JOURNAL
OF
THE PHYSICAL SOCIETY
OF JAPAN

Being a continuation of
"Proceedings of the Physico-Mathematical Society of Japan"

Volume 5
1950.

Office of the Society:
Faculty of Science, University of Tokyo.

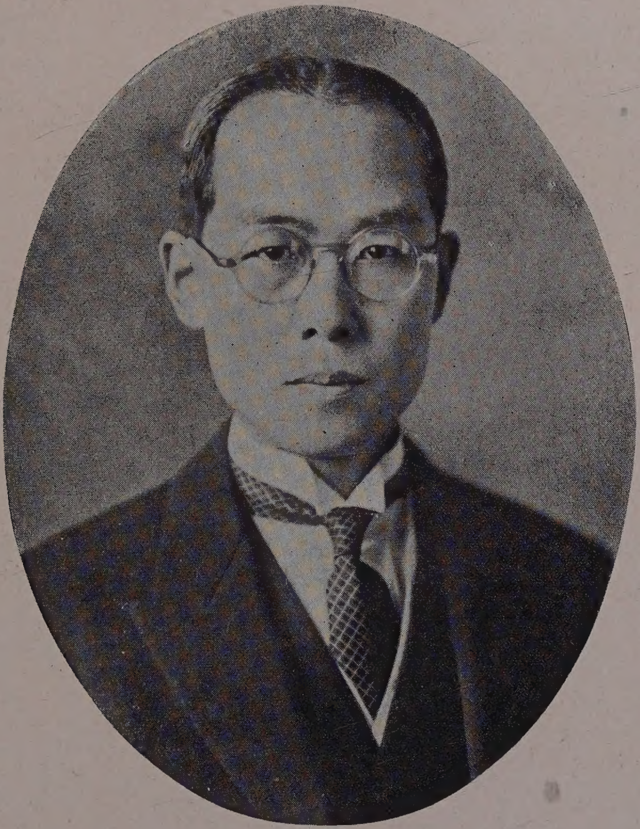

Professor HIDEKI YUKAWA
Nobel Laureate for Physics, 1949.

On the Mechanism of the Emission of the Auroral Green Light in the Night Sky.

By Michika MIYANISHI.

(Received May 4, 1949.)

It is well known that the auroral green line λ 5577 is emitted from the night sky. About the mechanism of its emission, however, reports are conflicting. In the present paper a new mechanism, which is to be considered rational, is proposed.

The photograph of the line have been taken by Wiechert(1), Slipher(2), Babcock(3), Rayleigh(4), Dufay(5), Sommer(6), Cabannes(7), Ramanathan and Karandikar(8), Gauzit(9) and others. The wave-length of the line was measured roughly by Sykora, Westman, Vegard and Slipher. Using a Fabry-Perot's interferometer Babcock(10) has measured it accurately and has obtained a value of λ 5577.350 ±0.005. About this line following natures are known.

(a) $OI(^1S_0-^1D_2)$: According to the result of the study of Zeeman effect on this line, which was made by McLennan(11) and others, the line is a forbidden one emitted by the transition from $^1S_0$ state to $^1D_2$ state in the singlet-triplet term schemes of atomic oxygen. By this term schemes the electron transitions of the red lines in the night sky light are also determined.

Green line λ 5577: $OI(^1S_0\rightarrow{}^1D_2)$

Red lines λ 6300: $OI(^1D_2\rightarrow{}^3P_2)$,

λ 6364: $OI(^1D_2\rightarrow{}^3P_1)$.

(b) The diurnal variation: Using photo-electric cells Rayleigh(12) measured the diurnal variation of the intensity of the line λ 5577, and it was found that the intensity reached a maximun at midnight. On the other hand McLennan(13) also measured it using an auroral filter, and a result similar to that of Rayleigh was obtained. Subsequent measurements were carried out by Dohrotin, Frank and Čerenkov(14), Chvostikov and Lebedev(15), Eropkin and Kozirev(16), Koiwai(17) and others, and it was noticed that the intensity maximum occured at midnight or an hour after it.

(c) The annual variation: According to the investigation of Rayleigh(18) the intensity maximum occurs in October in Northern hemisphere and in April in Southern hemisphere.

(d) The 11 year's periodic variation: In Addition to the annual variation, the result of Rayleigh's observationd in Englan during a long time has indicated a progressive increase in intensity. As this increase was parallel with that of sun spots, the former is thought by him to indicate a periodicity in the 11 year's period of the solar cycle.

About the mechanism of the emission of the auroral green line λ 5577, there are many investigations. Among them representative ones are shown in the following.

(1) Dissociation of ozone molecules by the light absorption: Mecke(19) showed the formation of excited oxygen atoms of $^1S_0$ state by the dissociation of ozone molecules as shown by the following relations (a) and (b).

(a) $O_3+h\nu(\lambda\ 2355)\rightarrow O_2(^3\Sigma)+O(^1S)$.

(b) $O_3+h\nu(\lambda\ 1800)\rightarrow O_2(^1\Sigma)+O(^1S)$.

(c) $O(^1S)\rightarrow O(^1D)+h\nu(\lambda\ 5577)$.

(2) Chapman's reaction: Chapman(20) expressed in his Bakerian lecture the view that "the energy of the green auroral line is previously energy of dissociation, which is transformed at the collisions of some particular type, one of the products being an excited neutral oxygen atom". Under this view he suggested the following reactions.

(a) $2O+O=O_2+5.06\ V+O=O_2+O(^1S)+$ [illegible] $0.89\ V$, in the atomic oxygen layer.

(b) $N_2^++O^-=N_2+O+9.4\ V,\ 2O+9.4\ V$ $=2O(S)+1.1\ V$, in the lower ionized layer.

(3) Kaplan's theory: The theory proposed by Kaplan is that the energy produced by the recombination of an ionized oxygen molecule and an electron is almost equal to the sum of the energy of dissocation (5.06 volts) of an oxygen molecule into two normal atoms and the energies of excitation (4.19×2 volts) of two normal atoms. This will be expressed by the following reactions.

$$O_2+13.50\rightarrow O_2^+,\quad O_2^+ + e + O_2 = 2O(^1S)+O_2 + 0.06\ \mathrm{V}.$$

(4) Kimura's theory: Kimura considered that the excited oxygen atom (^1S) is produced when an excited oxygen atom (^1D) collides with an excited nitrogen atom (^2D), and that the forbidden transition $^1S\rightarrow{}^1D$ occurs due to the molecular field of the nitrogen atom. The mechanism will be represented by the following reactions.

(a) $O_2+h\nu\rightarrow O(^3P)+O(^1D)$,

$N_2+h\nu\rightarrow N(^4S)+N(^2D)$.

(b) $O(^1D)+2.21\ \mathrm{V}\rightarrow O(^1S)$,

$N(^4S)+2.37\ \mathrm{V}\rightarrow N(^2D)$.

(c). $O(^1D)+N(^2D)\rightarrow O(^1S)+N(^4S)+0.16$. (Kinetic energy).

(5) Massey's theory: Massey(23) has proposed a mechanism of prodution of excited oxygen atoms (^1S), shown by the following reaction.

$$O^+ + O^- \rightarrow O(^1S)+O(^1S)+3\ \mathrm{V}\ (\text{Kinetic energy}).$$

It is known that the intensity of the night sky light increases with zenith distance. From this increase of the intensity Van Rhijn(24), Elvey, Roach and Gauzit(25), Uchiumi(26) and others have estimated the heights of the emission layers of the night sky light. A sudden fall of the intensity appears one hour before the astronomical twilight. This change in the intensity is thought by Furuhata(27) to be an effect of sun rise, and under the point of view he estimated the heights of the emission layers of the night sky light. The values of the heights, obtained by them are shown in Table I.

As shown in Table I. the height of the emission layer of λ 5577 is very different with the methods of estimation. The height, however, seems to be greater than 300 km and to be the same as that of F_2 layer or greater.

The compositions of high atmosphere, computed from the data at sea level, are given in the

Table I. Heights (km) of the emission layers of the night sky light.

	from zenith distance	from the effect of sun rise	Elvey, Roach and Gauzit	Uchiumi
5577	400	700, 650		340
5893 (*D*)	300	750, 650	130	
6300	120	750, 700, 700, 650		350
7000—7800	360	700, 580		
8500—11000	280	750, 650, 500, 390		
f_{F_2}		750, 650, 600, 260, 260, 200, 170		

f_{F_2} is the critical frequency of the F_2 layer.

Table II. Composition of high atmosphere.

height	100 v/V							Total pressure
	N	O	H_2O	A	CO	H	He	
140	0.01					99.15	0.84	0.0040
130	0.04					99.00	0.96	0.0046
120	0.19					98.74	1.07	0.0052
110	0.67	0.02	0.02	0.93	0.03	98.10	1.19	0.0059
100	2.95	0.11	0.05			98.58	1.31	0.0067
0	77.08	20.75	1.20			0.01		760.0000

v = volume of the gas contained in volume V of atmosphere, Unit of height = 1 km,
Unit of pressure = 1 mm Hg.

International Critical Table, Vol. I, p. 393. Some of them are shown in Table II.

There is a Laplace's equation to find a height of the atmosphere from its pressure.

$$h = 18400\ (\log B_0 - \log B)(1+\alpha t).$$

where h is the height (m), B_0 and B the atmospheric pressures of lower and higher points in the atmosphere, $\alpha = 0.00367$ the thermal expansion coefficient, t the mean temperature at the higher point. Using this equation the pressures at heights 100 km and 300 km were culculated by us, and the values of 0.00016 and 8.17×10^{-18} mm Hg respectively were obtained. In the calculation it is assumed that the temperature t is constant and that the value is -50°C. In such higher atmosphere the Laplace's equation will not be held satisfactorily, but the former is near that given in Table II and the latter will show that the pressure in the emission layer of λ 5577 is extremely small.

From the data given in Table II and the values obtained in the calculation it will be considered that the pressure in the emission layer of λ 5577 is extremely small and that the layer consisting of mainly hydrogen gas, oxygen, nitrogen and herium being the rare impurities in it. The mechanisms mentioned above are explained by the reactions between oxygen atoms or molecules or the reactions between an oxygen atom and a nitrogen atom. The densities of these gasses, however, will be too small to explain the mechanism by such mechanism. Now let us propose a new mechanism.

It is known that the center of the emission of fluorescence is the impurities of fluorescent substance and that the energy of the emission is taken from surrounding substance. A similar phenomenon in the emission of the auroral green line is considered in the present study. The mechanism thus obtained is shown in the following reactions.

$$\mathrm{H}+\mathrm{H}+\mathrm{O}(3P_{1,2}) \rightarrow \mathrm{H}_2+\mathrm{O}({}^1S_0), \qquad \text{(a)}$$

$$\mathrm{O}({}^1S_0) \rightarrow \mathrm{O}({}^1D_2)+h\nu(\lambda\ 5577), \qquad \text{(b)}$$

$$\mathrm{O}({}^1D_2) \rightarrow \mathrm{O}(3P_{1,2})+h\nu(\lambda\ 6364,\ \lambda\ 6300), \qquad \text{(c)}$$

$$\mathrm{H}+\mathrm{H}+\mathrm{O}(3P_{1,2}) \rightarrow \mathrm{H}_2+\mathrm{O}({}^1S_0). \qquad \text{(a)}$$

The heat of formation of hydrogen is 4.46 V and the energy of the transition of ${}^3P \rightarrow {}^1S$ is 4.1 V. Consequently there is a small excess energies in the reaction (a), but this will be transformed into kinetic energies. And neutral hydrogen atoms and oxygen atoms will be given by the dissociation of their molecules absorbing sun light or by neutralization of their ions, without forming molecules, since their densities are very rare. The number of hydrogen atoms may be extremely great as compared with that of oxygen atoms. Then the reactions (a), (b) and (c) will be repeated during a long time.

In this cyclic reactions, let n' be the number of oxygen atoms given due to the neutralization of their ions at a time t in the night, and it is assumed that $n' = a\sqrt{t}$, where a is a certain constant. Some oxygen atoms will be lost by the combination with hydrogen. Consequently initial total number n_0 of neutral oxygen atom will be decreased and this will be expressed by the equation $n'' = n_0 e^{-\mu t}$, where n'' is the number of oxygen atoms at the time t and μ a decay constant. In this equation $t = 0$ may be taken at the end of a astronomical twilight. Thus the total number of neutral oxygen atoms $n = n' + n''$ becomes

$$n = n' + n'' = a\sqrt{t} + n_0 e^{-\mu t},$$

$$\fallingdotseq n_0 + a t^{\frac{1}{2}} - n_0 \mu t. \qquad (1)$$

Consequently a maximum condition will be given by the following equations

$$\frac{dn}{dt} = \frac{a}{2} t^{-\frac{1}{2}} - n_0 \mu, \quad t = \frac{a^2}{4 n_0{}^2 \mu^2}.$$

Thus the existence of the intensity maximum of λ 5577 will be explained. The excited oxygen atom produced by the collision with two neutral hydrogen atoms has no valency. Consequently the atom will emits the green line λ 5577 adhering closely to the hydrogen molecule produced without combining. The forbidden transition ${}^1S_0 \rightarrow {}^1D_2$, therefore, may be given under the influence of the molecular field of the latter.

This study was helped by the research grant given from the Ministry of Education.

References.

(1) C. S. Wiechert: Phys. Zeits., 3 (1901), 365; (1902), 366.

(2) Ap. J. **49** (1919), 266; Astronom. S c. of the Pacific **41** (1929), 262.
(3) H. D. Babcock: Astrophys. J. **57** (1923), 209.
(4) Lord Rayleigh: Proc. Roy. Soc. **103** (1923), 45.
(5) J. Dufay: These de doctrat, Paris, (1928); Bull. Obs. Lyon (1928), 10; Comptes rendues, **198** (1934), 107, 2132; J. de phys. et rad., **5** (1934), 523, 603.
(6) L. A. Sommer: Zeits. f. Phys., **57** (1929), 582; Zeits. f. Phys., **77** (1932), 374.
(7) Cabannes: Comptes rendues **198** (1934), 2132; J. de phys. et rad., **5** (1934), 603.
(8) K. R. Ramanathan and J. V. Karaudikar: Nature, **129** (1932), 3251; **129** (1932), 3258; **132** (1933), 3341.
(9) Gauzit: Comptes redues, **199** (1934), 199; J. de phys. et rad. **5** (1934), 527.
(10) H. D. Babcock: ibid.
(11) J. C. McLennan and G. M. Shrum: Proc. Roy. Soc., A., **108** (1925), 501; J. C. McLennan and J. McLeod: Proc. Roy. Soc., A., **115** (1927), 515; J. C. McLennan, J. McLeod and W. C. McQuarrie: Proc. Roy. Soc., A., 114 (1927), 1; J. C. McLennan: Proc. Roy. Soc., A., **120** (1928), 327.
(12) Lord Rayleigh: Proc. Roy. Soc., A., **119** (1928), 19; **124** (1929), 395.
(13) J. C. McLennan: Proc. Roy. Soc., A., **120** (1928), 353.
(14) Dohrotin, Frank and Čerenkov: Comptes rendus, U. S. S. R., 1 (1935), 110.
(15) Chvostikov and Lebedev: Comptes rendus, U. S. S. R., **1** (1935), 119.
(16) Eropkin, Kozirev: Poulkov Obs. Circ., **13** (1935), 21.
(17) M. Koiwai: Kakioka Chijiki Kansokusho Yōhō, **1**, No. 1.
(18) Lord Rayleigh: Proc. Roy. Soc., A., **119** (1928), 11.
(19) R. Mecke: Zeits. f. Phys. Chem. B., Bodenstein-Fest Band, (1931), 395.
(20) S. Chapman: Proc. Roy. Soc., A **132** (1931), 353.
(21) J. Kaplan: Phys. Rev., **38** (1931), 1084.
(22) M. Kimura: Sc. Pap. I. P. C. R., **18** (1932), 116.
(23) H. S. W. Massey: Negative Ions, Cambridge, at the University Press, (1938).
(24) P. J. Van Rhijn: Pub. Astr. Lab. Groningen, No. **31** (1921).
(25) Gauzit: Astrophys. J., **85** (1937), 211.
(26) Uchiumi: Kakioka Chijiki Kansokusho Yōhō, **5**, No. 1 (1934).
(27) M. Furuhata: Collection of Papers of Denriso Kenkyu Tokubetsu Iinkai in Japan, No. 1.

Concentration Dependence of the Viscosity of High Polymer Solutions. I.

By Nobuhiko SAITÔ.

Kobayasi Institute of Physical Research, Kokubunzi, Tokyo.

(Read May 1; Received May 10, 1949)

§ 1. Introduction.

The intrinsic viscosity of high polymer solutions has been the center of the experimental and theoretical interest because it is related to the shapes and sizes of the molecules, or strictly speaking, to their molecular structures and molecular weights etc. Accordingly there are a great deal of experimental and theoretical researches concerning the intrinsic viscosity. Among them Kirkwood-Riseman's[1] and Debye-Bueche's[2] theories are prominent. Designating the intrinsic viscosity by a symbol $[\eta]$ we have

$$\eta_{sp} = [\eta]c \qquad (1)$$

for an infinitely dilute solution, where η_{sp} is the specific viscosity and c is the concentration in g/100 cc.

Experiments show, however, that the specific viscosity deviates from this linear relation with the concentration. Consequently experimental expressions have been proposed by several authors[3].

Recently some authors[4,5,6] have found experimentally a relation,

$$\eta_{sp} = [\eta]c + k[\eta]^2c^2 \qquad (2)$$

where k is a constant which does not depend on the molecular weight in a homologous series and is regarded to be invariable or slightly variable from solvent to solvent and by temperature. In this paper we intend to obtain a relation between the specific viscosity and the concentration and to derive theoretically the value of k.

§ 2. Method of Calculation.

It is assumed that the viscosimeter is the apparatus of Couette and the radii of its cylinders are considered infinite as compared with the distance between the two cylinders, which, on the other hand, can be regarded as two parallel planes situated at $y=h$, and $y=-h$. The fluid is flowing along the x-axis with the velocity gradient κ_0.

Burgers[7] treated elegantly the viscosities of the dilute colloidal solutions of rigid spheres, rods or ellipsoidal particles by Oseen's method. His method consists in calculating the perturbations in the velocity due to one suspended particle by replacing it with a set of forces which is determined by the boundary conditions. Kirkwood-Riseman[1] treated the intrinsic viscosity of solutions of linear polymers using this method. Following them, when a polymer molecule is introduced at a point (x, y, z) in the Couette apparatus described above, the perturbations in the velocity of the fluid at the origin of the coordinate system are given by

$$(u', v', w') = A\kappa_0\left(\frac{x^2y}{r^5}, \frac{xy^2}{r^5}, \frac{xyz}{r^5}\right) \tag{3}$$

where $r(r^2=x^2+y^2+z^2)$ is assumed to be large relative to the linear dimension of the molecule and A is a constant which can be determined by the molecular structure and some physical constants, but in our theory the details are not necessary. When the original velocity is represented by $(u=\kappa_0'y,\ v=\kappa_0''x,\ w=0)$, we have only to take $\kappa_0/2$ equal to the part of the dilatation of the flow, i.e., $(\kappa_0'+\kappa_0'')/2$. A high polymer molecule is composed of identical groups connected linearly or cross-linked by chemical bonds. In this theory it is assumed that such a group behaves as if it were a spherical particle when it moves in a fluid which is regarded as a viscous continuum, and the hydrodynamical resistance is expressed by Stokes' law. The resisting groups are therefore distributed within a molecule in a manner which is determined by the molecular structure and the statistical considerations. It is also assumed hat they are distributed in spherical symmetry and the molecule can be regarded roughly spherical. These assumptions are also adopted in the following.

The perturbation in the flow will decrease the velocities at the two parallel planes $y=h$, and $y=-h$, and will cause the decrease in the effective velocity gradient κ_{eff} which is to be observed in the experiment. On the other hand, since the shearing forces are proved to be invariant, the effective viscosity η_{eff} is found to increase by the relation

$$\kappa_{\mathrm{eff}}\,\eta_{\mathrm{eff}} = \kappa_0\eta_0 \tag{4}$$

where η_0 is the viscosity of the pure solvent. κ_{eff} is calculated by means of Eq. (3). (§ 4). Nevertheless the flow acting practically upon a molecule is influenced by the perturbations due to other molecules. In concentrated solutions κ_0 in Eq. (3) should be replaced by the one corrected for this effect. yz- and zx- components of the dilatation tensor of the flow acting upon a molecule will be zero, when averaged by integration over all the other molecules assuming that the distribution of the molecules is uniform outside a sphere of radius d and between the two planes. d is taken as a constant proportional to the root-mean-square distance of the groups from the center of mass of the polymer molecule and it is found to cancel out in the final result. Averaged xy-component $<\kappa>/2$ will be the same for all the molecules or precisely a function of y, i.e., a function of the distance from the parallel planes, considering the wall effect. But as is shown later, our method is valid for very small particles with strong Brownian motion, the wall effect can not be treated reasonably. It is sufficient to regard $<\kappa>$ to be constant. Our method is based on this averaging procedure, which makes the calculation much simpler and the limit of this approach will be discussed later in § 7.

§ 3. The Flow Acting Practically upon a Molecule.

The velocity gradient of the flow at the origin due to the perturbation by a molecule at (x, y, z)

is obtained by differentiating Eqs. (3),

$$\left.\begin{aligned}\kappa' &= -\frac{\partial u'}{\partial y} = -A\kappa_0\left(\frac{x^2}{r^5}-5\frac{x^2y^2}{r^7}\right)\\ \kappa'' &= -\frac{\partial v'}{\partial x} = -A\kappa_0\left(\frac{y^2}{r^5}-5\frac{x^2y^2}{r^7}\right)\end{aligned}\right\} \quad (5)$$

and the analogous equations when the original flow at (x, y, z) has yz- and zx-components of the dilatation. Therefore, they may vary from time to time according to the instantaneous configurations of the molecules arround the molecule under consideration. The rate of change in the configurations, however, is very rapid because of the strong-macro-Brownian motion of the molecules. Therefore, before a perturbation does reach to its steady state, the perturbations of the succeeding configurations which are regarded as perfectly disturbed ones from the preceding come to be added. In this way the tensor of the dilatation will not be so fluctuated as the case without Brownian motion,, and will have an averaged value independently of the instantaneous configuration. It is allowed to be replaced by $\langle\kappa\rangle$. From these considerations one obtains for the flow acting upon a molecule at the origin,

$$\langle\kappa\rangle = \kappa_0+\int n(\kappa'+\kappa'')dx\,dy\,dz \qquad (6)$$

where n is the number of the molecule per unit volume and the integration is carried out through the whole fluid except a sphere of radius d, substituting κ' and κ'' from Eqs. (5) with κ_0 replaced by $\langle\kappa\rangle$. First the integration is carried out in a plane $y=$ const., and is easily found to be zero when $|y|\geq d$.

Therefore we have

$$\begin{aligned}\langle\kappa\rangle &= \kappa_0-(A\pi n/d^5)\langle\kappa\rangle\int_{-d}^{+d}(d^2-y^2)(d^2-2y^2)dy\\ &= \kappa_0-(4/5)A\pi n\langle\kappa\rangle. \qquad (7)\end{aligned}$$

or

$$\langle\kappa\rangle = \kappa_0/[1+(4/5)A\pi n] \qquad (8)$$

In this connection attention must be paid to the order of integration of Eq. (6). The region of integration can be spread over the space except a sphere of radius d, if one neglects the wall effect. In fact, as is shown above, the integral vanishes over a plane $y=$ const. when $|y|\geq d$. If one integrate first over a surface of a sphere with the help of the polar coordinates and then integrate over radial direction, the integral vanishes. This integral is an example which can be evaluated to be any arbitrary value by different process of integration[8]. Physically ovr procedure is right, because there are two boundary planes which limits the region of integration, and makes the integrated value unique.

§4. Specific Viscosity.

The perturbation in the velocity at the plane $y=h$ is also calculated by Eq. (3), integrated over all the particles,

$$u' = -(2\pi/3)A\langle\kappa\rangle n\cdot 2h \qquad (9)$$

On the other hand at the plane $y=-h$, the perturbation is obviously $-u'$. Therefore, for the effective velocity gradient we obtain

$$\kappa_{\text{eff}} = \kappa_0+(2u'/2h) = \kappa_0-(4\pi/3)A\langle\kappa\rangle n \qquad (10)$$

Hence the specific viscosity is readily calculated by Eq. (4).

$$\eta_{\text{sp}} = \frac{\kappa_0-\kappa_{\text{eff}}}{\kappa_{\text{eff}}} = \frac{4\pi}{3}An\Big/\left(1-\frac{2}{5}\frac{4\pi}{3}An\right) \qquad (11)$$

or

$$\eta_{\text{sp}} = [\eta]c/(1-0.4[\eta]c), \qquad (12)$$

$$[\eta] = (4\pi/3)An/c. \qquad (13)$$

On expansion we have

$$\eta_{\text{sp}} = [\eta]c+0.4[\eta]^2c^2. \qquad (14)$$

§5. Suspensions of Spherical Particles.

An analogous treatment is also possible for suspensions of spherical rigid particles, provided that the particles are so small that the averaging procedure is allowable. The perturbation in the velocity at the origin by a particle at a point (x, y, z) in a laminar flow with the velocity gradient κ_0 is obtained by Burgers[7] with the result,

$$\left.\begin{aligned}u' &= A\kappa_0\frac{x^2y}{r^5}-B\kappa_0\left(\frac{3y}{r^5}-15\frac{x^2y}{r^7}\right)\\ v' &= A\kappa_0\frac{xy^2}{r^5}+B\kappa_0\left(\frac{3x}{r^5}-15\frac{xy^2}{r^7}\right)\\ w' &= A\kappa_0\frac{xyz}{r^5}+B\kappa_0\frac{15xyz}{r^7}\end{aligned}\right\} \quad (15)$$

where

$$A = (5/2)a^3, \qquad B = -(1/6)a^5$$

and a is the radius of suspended particles. The second terms containing B in the above equations being shown to contribute nothing as the result of averaging, the final result is the same as § 3, except that A is different from the above case. Thus we have

$$\eta_{sp} = (5/2)\phi/(1-\phi) \qquad (16)$$

$$= (5/2)\phi + (5/2)\phi^2 + \cdots \qquad (17)$$

where ϕ is the volume concentration $\phi = (4\pi/3)a^3n$.

§ 6. Comparison with the Experiments.

Eqs. (12) and (16) are nothing but the expression proposed experimentally by Fikentscher, Mark[9], and Sakurada[10].

$$\eta_{sp} = a\varphi c/(100-\varphi c) \qquad (18)$$

where a and φ are constants. This relation has been shown to be valid up to the concentration $\varphi c = 50$.

Table I.

Viscosity of polyvinyl acetate-acetone-water system in various ratio at 20°C (by Endô and Yosioka).

K means the coefficient of c^2 in Eq. (2), i.e. $k[\eta]^2$

Solvent water content in volume %	0	4.76	10	15.38	20	25
$[\eta]$	1.785	1.800	1.746	1.654	1.454	1.140
K	1.184	1.273	1.171	0.967	0.746	0.505
k	0.372	0.393	0.384	0.353	0.353	0.388

The experimental values of k are found to be 0.3−0.6, which are in fairly good agreement with our theoretical value 0.4. Recently Endô and Yosioka[11] have found that k is almost constant within 0.35−0.40 for polyvinyl acetate in the mixed solvents of acetone and water in various ratio, while the intrinsic viscosity varies anomalously with the increase in the water percentage (Table I). In general the value of k varies among the solvents. It decreases in one system[(2)] and increases in another[13], when the solvent becomes poorer. No definite conclusions can be derived as yet. In our calculation the molecule is assumed to be of spherical symmetry and the energetic interaction among the solvent and the polymer molecules is not taken account of, and hence k has constant value. If the solvent becomes better, the polymer molecules will be extended in some degree, and will not be regarded as spherical. The temperature and the solvent will change the statistical shape and the energetic interaction with the solvent and other polymer molecules. These effects will explain the change in k under different circumstances.

§ 7. Discussion.

The first term of Eq. (17) is the well-known factor of Einstein. Guth, Simha and Gold[14], having treated the interaction between the two particles, derived the second term,

$$\eta_{sp} = 2.5\,\phi + 14.1\,\phi^2 \qquad (19)$$

This is different from our result. Eq. (19) is valid for the particles without, or at most, with small Brownian motion. Guth and others first calculate the dissipation energy by the interaction of two particles in one configuration of the two and then take an average. This procedure is proper when there is no Brownian motion in the fluid with small velocity and consequently when a steady state is reached in each configuration of the particles. Eirich, Bunzl, and Margaretha[15] carried out some model experiments with glass particles etc., which are comparatively large, and obtained the coefficient of ϕ^2 to be 7−9.

Fikentscher and Mark derived Eq. (16) with certain hydrated polymer colloids, which may be regarded as spherical particles and yet have strong Brownian motion because they are extremely small. Our method is applied sucessfully in such a case.

In conclusion the author wishes to express his sincere thanks to Dr. S. Oka, Mr. A. Ookawa, and Mr. K. Yosioka for their valuable discussions given to this work.

References.

(1) J. G. Kirkwood, J. Riseman: J. Chem. Phys. **16** (1948), 565.

(2) P. Debye, A. M. Bueche: J. Chem. Phys. **16** (1948), 573.

(3) See for example, K. Meyer, H. Mark: *Hochpolymere Chemie* I (1940) p. 300.

(4) G. V. Schulz, F. Blaschke: J. prakt. Chem. **158** (1941), 130.

(5) D. J. Mead, R. M. Fuoss: J. Am. Chem. Soc. **64** (1942), 277.

(6) M. L. Huggins: J. Am. Chem. Soc. **64** (1942), 2716.

(7) J. M. Burgers: *Second report on viscosity and plasticity*, (1938), p. 113.

(8) E. Goursat: *Cours d'analyse mathématique.* I (1927), chap. 6. § 127.

(9) H. Fikentscher: H. Mark, Koll. Zeits. **49** (1929), 135.

(10) I. Sakurada: Koll. Zeits. **64** (1933), 195; **82** (1938), 345.

(11) K. Endô, K. Yosioka: Paper read at the 2nd annual meeting of the Chemical Society of Japan, April, 1949.

(12) A. Bartovics, H. Mark: J. Am. Chem. Soc. **65** (1943), 1901.

(13) T. Alfrey, J. D. Justice, S. J. Nelson: Trans. Faraday Soc. **42 B** (1946), 50.

(14) E. Guth, R. Simha, O. Gold: Koll. Zeits. **74** (1936), 266; *Ergebn. d. exak. Naturwiss.* **15** (1936), 1.

(15) F. Eirich, M. Bunzl, H. Margaretha: Koll. Zeits. **74** (1936), 276.

A Theory of Initial Permeability.

Syôhei MIYAHARA.

Physics Department, University of Nagoya.

(Received May 22, 1949).

Generally the initial permeability of ferromagnetics is determined by the energy variation ΔE^* with the magnetization, i. e.

$$\Delta E = \sum_i a_i \Delta I_i^2 - H \Delta I_i ,$$

$$\Delta I = \sum_i \Delta I_i ,$$

where ΔI_i is the variation of magnetization caused by the i-th mechanism. Then the ΔI_i is given by $\Delta E \doteq 0$. i. e.

$$\Delta I_i = H/2a_i ,$$

or

$$\kappa = \sum_i 1/2a_i . \tag{1}$$

The various mechanisms we know include (1): magnetization by continuous rotation, (2): magnetization by displacement of the boundaries of magnetic domains with microscopic crystal deformations and (3): boundary displacements without any crystal deformation.

On the other hand, the energy increase with magnetization is caused by the following origins; (α) anisotropy energy, (β) elastic energy and (γ) energy of boundary surface of domains, then

$$a_i = \sum a_i^\alpha ,$$

and consequently

$$\kappa = \sum_i (1/2 \sum_\alpha a_i^\alpha) \tag{2}$$

Thus the initial susceptibilities are completely determined by these nine quantities (some of which are evidently zero).

Now we shall consider the initial permeability due to a_3^γ only, which has not yet been considered previously.

First of all we must consider the reason for the existence of a 180°—boundary. Some authors hold the view that the domain boundary is formed at the place where the elastic energy is minimum. This conception can explain the existence of a 90°-boundary but it cannot explain the existence of a 180°-boundary, and those who take this standpoint, naturally doubt the existence of 180°-boundaries⁽¹⁾. But others believe that the domain boundaries are formed in order to minimize the sum of the magnetostatic and the boundary energies⁽²⁾. According to this, we cannot take into account, the elastic energy in the ordinary sense but we must pay attention to the fact that the displacement of the boundary is hindered by the existence of short range distortions of the crystal lattice such as the dislocations⁽³⁾, whose existence is doubtless nowadays in the theory of plasticity.

---

* Ordinarily the initial permeadility is measured adiabatically, so that we must take the energy instead of the free energy.

These kinds of distortions are severe even if the range is short, and must cause extremely high magnetic anisotropy in a few atom ranges around the dislocation centers. This consequently causes local and high boundary surface energy near the centers of dislocation.

Now we suppose that the boundary energy per unit area does not change, expect at the place of dislocation centers as the boundaries move, but the total energy changes owing to the increase in area of boundary surface by the linelike hinderances, and that the dislocation centers are distributed in the manner of a lattice specified by a single constant l of the dimension of length. Generally the volume of the magnetic domain is much greater than l^3, and the mean of the number of the unit lattices in a domain is much greater than one, so that the boundary surface of a domain is divided into two-dimensional lattices by the lines hindering the displacement of the boundary.

The total energy of boundaries of domains per unit volume is

$$E = \gamma S,$$

where S is the area of the boundary surface per unit volume and γ is the boundary energy per unit area. Small displacements of boundaries might not change the magnetostatic energy, and we can suppose that in our model, $E =$ min. i. e. $S =$ min. must be realized in $H = 0$.

If we take the length of a small displacement Δx of the midpoint of the unit surface lattice as a parameter determining the displacement of the boundary, then the increase in area is proportional to Δx^2, and the volume varies proportionally to Δx. Considering the dimensional relation, we have

$$\Delta A = c_1 \Delta x^2 \tag{3}$$

$$\Delta V = c_2 l^2 \Delta x, \tag{4}$$

where A and V are the area and the volume of a unit lattice determined by the distribution of dislocation centers, and c_1 and c_2 are dimensionless constants of the order of 1 (in a simple case $c_1 = \pi$, $c_2 = \pi/2$). When $\Delta x = 0$, the surface energy of a domain is $3n^{2/3}\gamma A$, and then the increase of total surface energy per unit volume is

$$\Delta E = 3n^{1/3} l^{-3} \gamma \Delta A, \tag{5}$$

From (3) and (4), the above expression (5) is written

$$\Delta E = 3cn^{-1/3} l^{-7} \gamma \Delta V^2, \tag{6}$$

where $c = c_1/c_2^2$. On the other hand, the change of the magnetization ΔI is

$$\Delta I = 6n^{-1/3} l^{-3} I_s \Delta V, \tag{7}$$

where I_s means the spontaneous magnetization. From the expression (6) and (7),

$$\Delta E = 1/12 \cdot c I_s^{-2} n^{1/3} l^{-1} \gamma \Delta I^2, \text{ where } n > 1, \tag{8}$$

or, if we use the total area S of the boundaries per unit volume instead of n,

$$\Delta E = 1/4 \cdot c I_s^{-2} l^{-2} S^{-1} \gamma \Delta I^2, \text{ where } S < 3/l \tag{9}$$

Then the initial susceptibility is given from (2) and (8) or (9),

$$\kappa = 6c^{-1} I_s^2 n^{-1/3} l \gamma^{-1} \tag{10}$$

or

$$\kappa = 2c^{-1} I_s^2 S l^2 \gamma^{-1}. \tag{11}$$

The initial permeabilities of iron have been discussed from the viewpoint of Becker-Kersten's theory, and $\frac{1}{\lambda\sigma}$ is considered as the important factor determining them. This consideration cannot be verified because we cannot evaluate the internal stresses independently, while the permeability determined by the displacement of 180°- or 90°-boundaries, that might not exist at the place expected from Becker-Kersten's, cannot be calculated from the above-mentioned theory.

In our theory, for iron,

$l = 10^{-4}$ cm (from the theory of plasticity)
$n = 1 \sim 10^6$
$I_s = 1.7 \cdot 10^3$

and

$\gamma = 4$ erg/cm^2 (from the Curie point)

then we have

$$4\pi\kappa = 10^2 \sim 10^4$$

The values agree satisfactorily with those obtained experimentally.

We can also understand the reason for the dependence of initial permeability on the manner of demagnetization, which is well known from experiments. In addition, we can derive the differences of the initial permeabilities of the single crystal rods with different directions. If we assume that the rods do not contain boundaries perpendicular to the axis of the rods, the total area of the 180°-boundaries in [100], [110], [111] rods is clearly in proportion of 1 : 1/2 : 1/3, and from (11).

$$\kappa_{[100]} : \kappa_{[110]} : \kappa_{[111]} = 6 : 3 : 2$$

This is the well known result obtained by Williams(4).

References.

(1) Becker & Döring: Ferromagnetismus, 148

(2) Landau & Lifschitz: Phys. Zeits. d. USSR, **8** (1935), 153.

(3) Talor: Proc. Roy. Soc., **145** (1934), 362; Seitz & Read: J. Appl. Phys., **12** (1941), 100, 170, 470, 538.

(4) Williams: Phys. Rev., **52** (1937), 747, 1004.

On the Interference Color of Thin Layers on Glass Surface.

By Hiroshi KUBOTA.

Second Faculty of Engineering, University of Tokyo.

(Received May, 27, 1949)

To effect the precise examination of the interference colors of the thin layer, the author calculated them in cases of the non-reflecting layer and the Newton's ring, by using the theory of color and plotted these values on the I. C. I. graph. Several results obtained from the graph were also examined.

§ 1. Introduction.

Along with the recent development of the study and industrialization of non-reflecting layers, the determination of the thickness of thin layers by observing their interference color has come to be employed frequently as the most simple but sufficiently accurate method. Newton studied the interference color of thin layer illuminated by white light in case of the Newton's ring(1) and there were some other records of experimental researches. Their descriptions, however, were very subjective, since the colors were specified by names, such as vivid yellow, pale pink, etc. Rayleigh calculated those colors, using Maxwell's result of measurements of colors(2).

The author has calculated the interference color, using the color table and the fundamental data concerning the color measurements given by I. C. I. and examined the results as described in the following.

§ 2. Calculation of Interference Color.

According to the theory of color, when a surface with the spectral reflectivity $R(\lambda)$ is illuminated by the light with the energy distribution $E(\lambda)$, the color of the reflected light is given by the following tristimulus values,

$$X = \int E\cdot\bar{x}\cdot R d\lambda, \quad Y = \int E\cdot\bar{y} R d\lambda,$$

$$Z = \int E\cdot\bar{z}\cdot R d\lambda \qquad (1)$$

In the above, the integration must cover the entire visible spectrum, and $\bar{x}$, $\bar{y}$, $\bar{z}$, are the three stimulus values of the spectrum. Normalizing them, we get the following trichromatic coordinates,

$$x = \frac{X}{S}, \quad y = \frac{Y}{S}, \quad z = \frac{Z}{S},$$

where $S = X + Y + Z$.

The color of the surface is shown by the point on the graph with those x and y as it's abscissa and ordinate, respectively. Therefore, to find the interference color of a thin layer, the spectral reflectivity of the layer $R(\lambda)$ must first be known.

When the glass with the refractive index n_g is coated by the thin layer of thickness d with the refractive index n, then $R(\lambda)$ of such a surface is given by,

$$R=\frac{B^2+C^2+2BC\cos\delta}{1+B^2+C^2+2BC\cos\delta}.$$

Where B and C are the reflectivity of the upper and lower boundaries of the layer, and in case of the perpendicular incidence,

$$B=\frac{1-n}{1+n},\quad C=\frac{n-n_g}{n+n_g},$$

and $\delta=\frac{4\pi}{\lambda}nd$ is the phase difference between these two light waves.

When the refractive index of the thin layer satisfies the amplitude condition of non-reflection, that is $n=\sqrt{n_g}$, then $B=C$.

If the squares of the above values are small compared with 1, formula (2) will become,

$$R\doteqdot 4B^2\cos^2\frac{\delta}{2}.$$

For the light source, we used the C light-source of I. C. I. We have integrated the equation (1) numerically, considering n and n_g as constant (that is, neglecting the dispersion). The results are correct for 3 figures, which are sufficiently exact for practical uses.

Fig. 1 shows these results plotted on the graph taking nd as a parameter.

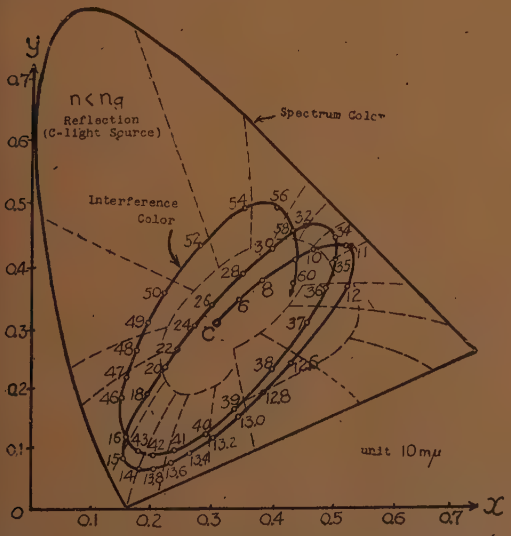

Fig. 1. Interference color in I. C. I. diagram.

§ 3. The Color of the Newton's Ring, etc.

In case of the so-called Newton's ring, there is a thin layer of air between the glass plates, so the reflectivity becomes somewhat different from those given above, and $B=-C$.

Therefore, $R=4B^2\sin^2\frac{\delta}{2}.$

So the interference color is the complementary color of that of non-reflecting layer. This will be easily obtained by using the above mentioned data. This is shown in Fig. 2.

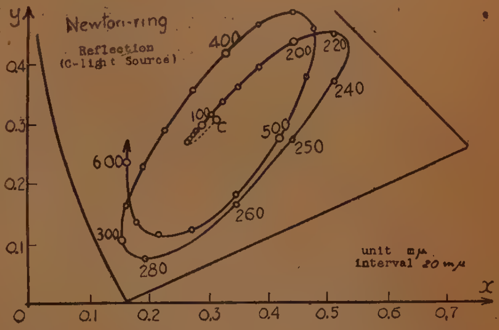

Fig. 2. Interference color of Newton's ring.

In case of the non-reflecting layer, for which $n\neq\sqrt{n_g}$, the formula (2) will become as below, assuming the denominator to be 1,

$$R=4BC\left(\varepsilon+\cos^2\frac{\delta}{2}\right) \tag{3}$$

where

$$\varepsilon=\frac{(B-C)^2}{4BC}=(n^2-n_g)^2/(n^2-1)(n_g^2-n^2)$$

Therefore, the tristimulus values (X', Y', Z') are

$$X'=\varepsilon\int E\cdot\bar{x}d\lambda+\int E\cdot\bar{x}\cos^2\frac{\delta}{2}d\lambda=a\varepsilon+X,$$

$$Y'=\varepsilon\int E\cdot\bar{y}d\lambda+\int E\cdot\bar{y}\cos^2\frac{\delta}{2}d\lambda=b\varepsilon+Y, \tag{4}$$

$$Z'=\varepsilon\int E\cdot\bar{z}d\lambda+\int E\cdot\bar{z}\cos^2\frac{\delta}{2}d\lambda=c\varepsilon+Z,$$

where a, b, c are the tristimulus values of the light source and X, Y, Z, are those of the reflected light when $n=\sqrt{n_g}$.

From these equations, we get the trichromatic coordinates (x', y', z') as follows;

$$x'=\frac{a\varepsilon+X}{k\varepsilon+S},\quad y'=\frac{b\varepsilon+Y}{k\varepsilon+S},\quad z'=\frac{c\varepsilon+z}{k\varepsilon+S},$$

where $k=a+b+c.$

As the above equations represent a straight line on the I. C. I. graph with parameter ε, the interference color for varying n will be given by the point on the straight line connecting the point showing the color of reflected light when $n=\sqrt{n_g}$ (given by formula (4) by making $\varepsilon=0$. Call this point P.) and the point showing the color of the light source (given by formula (4) by making $\varepsilon \doteq \infty$. Call this point Q.). Let the point given by (x', y') be R,

then $$PR/RQ = 1+\frac{k}{S}\varepsilon.$$

From formula (3), it is evident that, when $n<n_g$ then $\varepsilon>0$. Therefore, $\overline{PQ}$ is always larger than $\overline{RQ}$, which means that the point showing the interference color of the layer with $n=\sqrt{n_g}$ ($\varepsilon=0$) is farthest from Q. So the color is most clear having the largest degree of saturation. And the more it deviates from the condition $n=\sqrt{n_g}$, the nearer it approaches Q on the straight line PQ. This means gradual decrease in the degree of saturation without changing the dominant wave length, thus the color becoming more and more dull untill it finally becomes white at $n=n_g$ as shown in Fig. 3.

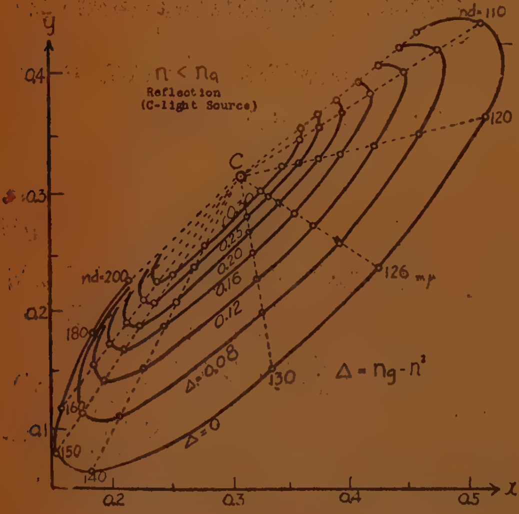

Fig. 3. Change in interference color with n. ($n<n_g$)

When n becomes larger than n_g, ε assumes a large negative value. Hence, $\overline{PQ}$ becomes negative, which means that the color is complementary with respect to the above case, having the greoter degree of saturation, receding from Q, as n becomes larger.

If we assume that formula (3) is available even when n is very large,(*) ε approaches to -1 as n increases. Therefore $R \sim \sin^2\frac{\delta}{2}$. So the interference colors become more and more similar to that of the reflected light of the Newton's ring.

The above procedure is shown in Fig. 4.

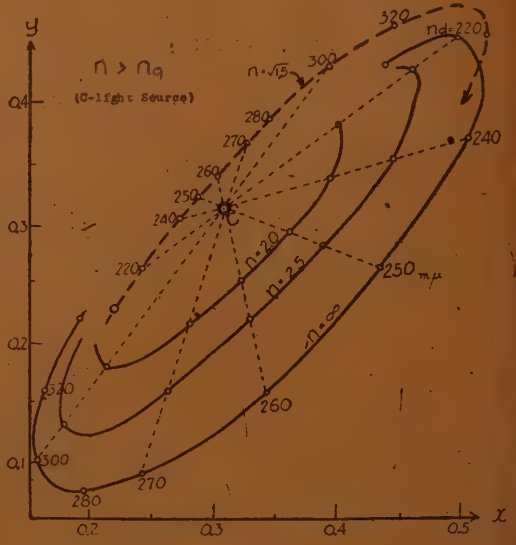

Fig. 4. Change in interference color with n. ($n>n_g$)

§ 4. On the Sensitive Color.

The intensity of light through a thin plate of uniaxial crystal placed between parallel nicol prisms is proportional to $\cos^2\delta$, where δ is the retardation between ordinary and extraordinary rays in the passage through crystal. So when white light is passed through such a system, its color is also shown by Fig. 1. In this case, it is a well known fact that, if the adequate retardation is given, there occurs the sensitive change in color with slight change in retardation. This is the phenomena called "sensitive color", and whose sensitivity can be given quantitatively by $\frac{\Delta S}{\Delta(nd)}$, where $\Delta(nd)$ is the change in retardation and ΔS is the corresponding change in color.

If we use the "uniform chromaticity scale" (U.C.S), ΔS of the two colors will be proportional to the distance between the two points on the graph, showing the two colors respectively.

(*) Practically, when n becomes very large, B, C, etc. are not negligible compared with 1. So, this assumption is not admissible.

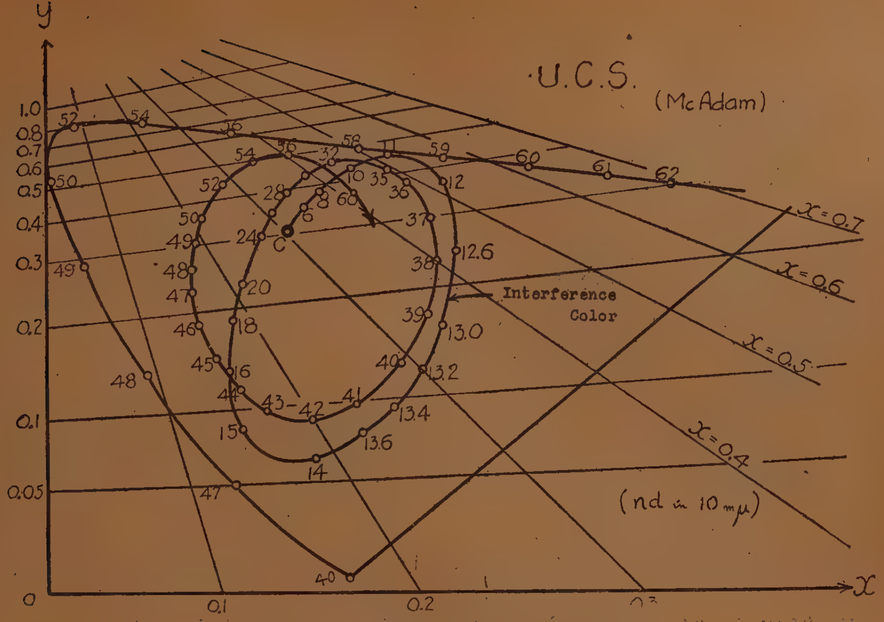

Fig. 5. Interference color in U.C.S.

Therefore, to study the sensitive color, we have to get the loci of the interference color on U.C.S. If we use MacAdam's U.C.S.(5), for example, we are able to get those loci by projecting Fig. 1 on this scale, as shown in Fig. 5.

From this graph, we can calculate $-\frac{\Delta S}{\Delta(nd)}$, as shown in Fig. 6.

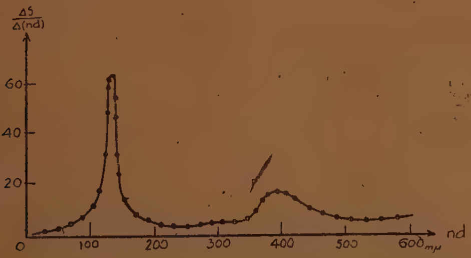

Fig. 6. Change in color sensitivity with thickness.

From the above, we learn that the neighborhood of purple in the 1st and 2nd order interference is the most sensitive part for the variation of thickness, which conforms with the phenomenon of "sensitive purple" in the case of double refraction by crystal.

In the case of the non-reflecting layer, this is also the thickness in which the brilliancy of the reflecting light (given by Y in formula (1)) is minimum and most effective thickness in reducing the reflection. But as shown above, at this thickness the color change is very sensitive and the irregularity of color is apt to appear, which often give rise to the troubles in the manufacturing process. We can avoid this unstable point of color by reducing or increasing the thickness of layer a little, but it will result in a negligible increase in reflectivity. Accordingly, the most practical color of the non-reflecting layer is not pure purple but it must be greenish purple or red pink.

5. The Use of Filter.

The interference color by using any light source other than C-light source may be found by the above method, if $E(\lambda)$ of the light source is known. Especially, the interference color of C-light source with filter thereon will be directly obtained by using the calculation hitherto mentioned, that is, by eliminating the absorbed part in numerical integration.

For example, in case of the yellow filter which absorbs below $\lambda = 550\ m\mu$, the stimulus value of z is zero, giving the tristimulus coordinates $(x, y, 0)$. So, all the colors lie on a straight line in I.C.I. diagram, as shown in Fig. 7.

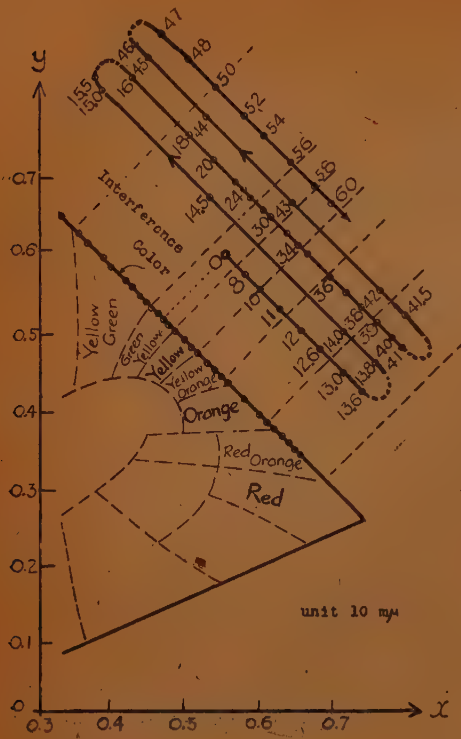

Fig. 7. Interference color with yellow light.

By Projecting Fig. 7. into U.C.S. and calculating $\frac{\Delta S}{\Delta(nd)}$ therefrom, we learn that the color also sensitively changes with thickness from orange to yellow at the neighborhood of $nd = 140\,\mathrm{m}\mu$. In this case, the sensitive color is not purple as before but yellow. From this, it is evident that the commonly known "sensitive purple" gets its purple color incidentally by a certain energy distribution of the light source and is not the inherent property of the purple color itself.

Aknowledgment.

The author wishes to acknowledge the valuable assistance, in performing the numerical integrations, of the members of my laboratory in the university, Miss. F. Saito, Messrs. T. Ara, T. Takemura, H. Nakamura and T. Ose.

References.

(1) Newton's Optics, (1939) London, 208.
(2) Rayleigh: Sci, Paper, II. (1886), 498.
(3) D. L. McAdam: J. O. S. A. **27** (1937), 294.

On the Theory of Recrystallization of Cold-Worked Metals.*

By Ryukiti HASIGUTI.

Faculty of Engineering, University of Tokyo.

(Received May 28, 1949).

§ 1. Introduction.

Cold-worked metals recrystallize, when they are heated suitably. Recrystallization takes place by means of nucleation and growth, i. e. new crystals grow at the expense of strained old matrix from nuclei formed in the matrix. The most remarkable characteristic of the rate of growth of new crystals is the fact that it is constant throughout a process from the beginning to the end, if the temperature is kept constant. This fact was widely proved experimentally, and especially by Mehl and others(1)(2) in the cases of silicon steel and aluminum in recent years, who have done very excellent and laborious works. The rate of growth G is known to have the following experimental relation to absolute temperature T; i. e.

$$G = A \exp(-E_e/RT), \qquad (1)$$

where A is a constant, E_e the experimental activation energy, and R the gas constant. The aim of this paper is to treat the rate of crystal growth theoretically.

§ 2. Theory.

Now let us consider the interface between a new crystal and the old matrix, where atoms in the old matrix move a little and rearrange themselves according to the crystal lattice of the newly formed crystal grain. This is the elementary process of the crystal growth. The reverse process will also take place, although its probability of occurrence may be very small. As it is not decided a priori how many atoms take part in an elementary process, we should, in general, consider a group of atoms as a unit of process, which is λ in length measured in parallel to the direction of growth. Let k_f be the number of times of occurrences of elementary processes of forward direction from the matrix to the new crystal in unit time, and k_b be those of backward direction from the new crystal to the matrix. As the net rate of growth mus be given by the difference between forward and backward processes, we get

---

* The preliminary account of this paper was published in the short note of this journal, Vol. 4, No. 4~6.

$$G = \lambda k_0\,, \qquad (2)$$

where $k_0 \equiv k_f - k_f$. As the strained matrix has higher internal energy compared with the newly formed crystal, the activation energy of forward movements is smaller than that of backward movements. We may assume that the difference of these activation energies is proportional to the energy E_i absorbed during the cold-working process. Hence we have

$$k_f = (1/\tau)\exp\{-(E-aE_i)/RT\}, \qquad (3)$$

$$k_b = (1/\tau)\exp(-E/RT), \qquad (4)$$

where τ is the time of relaxation for the movements of groups of atoms, a the constant of proportionality, and E the activation energy of backward movements, which may be approximately the same as the activation energy of the movements of groups of atoms from one unstrained crystal to another unstrained crystal. From equations (2), (3) and (4), we have

$$G = \lambda(k_f - k_b) = (\lambda/\tau)\exp(-E/RT)\{\exp(aE_i/RT) - 1\}. \qquad (5)$$

If the degrees of cold-working are small, we may assume that $aE_i \ll RT$. Then the equation (5) reduces to

$$G = (a\lambda E_i/\tau RT)\exp(-E/RT). \qquad (6)$$

From the experiments of thermal measurements of absorbed energies made by T. Suzuki(3), we can assume the following relation in the case of small degree of cold-working; i. e.

$$aE_i = bS^2, \qquad (7)$$

wherein b is a constant and S the strain produced during the cold-working. Hence we have

$$G = (b\lambda S^2/\tau RT)\exp(-E/RT). \qquad (8)$$

This last equation has the same form as that of expermentally obtained equation (1). But there is a problem to be considered. The experimental activation energies obtained from the experiments on aluminum made by Aderson and Mehl(2) are from 56,500 to 61,500 cal./mol. These values are larger than the sublimation heat of aluminum. This fact suggests that E_e must be a composite quantity. Moreover it is a remarkable fact that equation (8) yields a value of λ far greater than the atomic spacing.

Now it is probable that λ varies its value with temperature. If we assume, therefore, the following equation: i. e.

$$\lambda = \lambda_0 \exp(-E_1/RT), \qquad (9)$$

where λ_0 is a constant, we get

$$G = (b\lambda_0 S^2/\tau RT)\exp\{-(E+E_1)/RT\}. \qquad (10)$$

wherein $(E+E^1)$ corresponds to experimental activation energy E_e. This is the general equation for the rate of crystal growth in the case of recrystallization of cold-worked metals.

§ 3. Discussion.

Now let us compare this equation with experiments. When temperature is kept constant, the equation (10) reduces to the form

$$G = G_1 S^2, \qquad (11)$$

wherein G_1 is a constant, and its value is

$$G_1 = (b\lambda_0/\tau RT)\exp\{-(E+E_1)/RT\}. \qquad (12)$$

Plotting G against S^2 at constant temperatures using the experimental data obtained by Anderson and Mehl(2), we get straight lines as shown in Fig. 1 and 2, which justify the assumptions included in the equations (3) and (7). As we can get the values of G_1's for various temperatures from Fig. 1 and 2, we can make the $\log G_1$ versus reciprocals of absolute temperatures plotting like Fig. 3, which

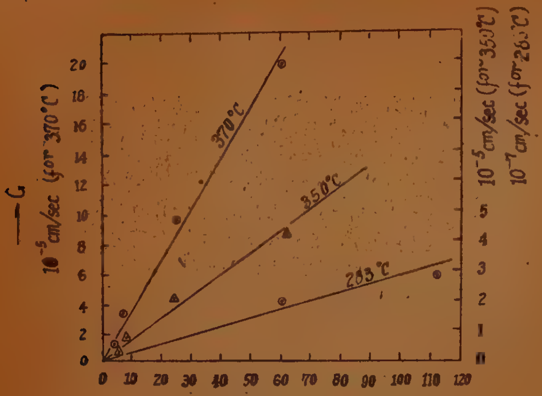

Fig. 1.

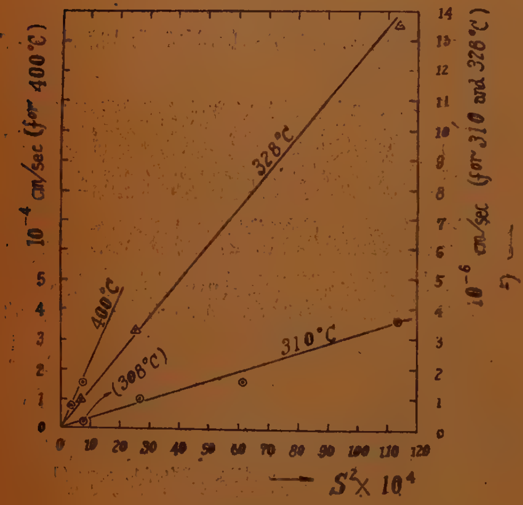

Fig. 2.

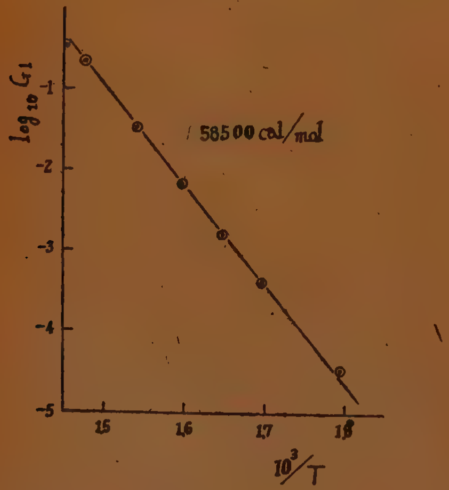

Fig. 3.

yields an activation energy of 58,500 cal./mol., which is the sum of E and E_1, as shown in equation (12).

The number of atoms in an unit of proces or in an atomic group which takes part in an elementary process seems to be considerably large. It may be improbable, therefore, that all the atoms in an unit move simultaneously get across a potential barrier in one jump. The atoms will jump across a barrier one by one, but successively one after another at very short intervals, like so to speak a chain reaction or an avalanche of reactions. A chain or an avalanche makes an elementary process. If this mechanism is true, the activation energy of an elementary process may be the same as that of the movement of a single atom.

The distance of movement of a single atom in a single jump in the case of crystal growth must be very much different from that of self-diffusion in metals. For on the one hand an atom moves at least one atomic distance in a single jump in the case of diffusion, and on the other hand an atom moves a very little distance only to rearrange itself in the case of crystal growth. The activation energy of crystal growth must, therefore, be smaller than that of self-difiusion. The latter is estimated to have the value 37,500 cal./mol. in the case of aluminum(4). We may, therefore, assume E to be about 30,000 cal./mol. Moreover we should rather put $E = E_1 = 29{,}250$ cal./mol. for simplicity.

Now from Fig. 3 and the values of S, which are less than ten per cent elongation, we can know the value of $b\lambda_0/\tau RT$ to be about 10^{18}. As bS^2 is far less than RT, and as τ is far larger than the time of relaxation of atomic vibration, λ_0 must be far larger than 10^3. Let us assume that λ_0 is equal to 10^4 cm., which will be perhaps the probable least value. Then from equation (9) and the value of $E_1 = 29{,}250$ cal./mol., we can obtain the length of an atomic group, which takes part in an elementary process. The numerical calculation shows that its value is 4 Å. at 283°K. and 320 Å. at 400°K. It is a very striking feature that the atomic group has considerable length, and therefore it contains a good many atoms.

§ 4. Conclusion.

The rates of crystal growth in the case of recrystallization of cold-worked metals were formulated. The unit of elementary process is not a single atom, but it is a group of atoms. The group contains considerable number of atoms.

References.

(1) J. K. Stanley, R. F. Mehl: Trans. Amer. Inst. Min. Met. Engr., **150** (1942), 260.

(2) W. A. Anderson, R. F. Mehl: Trans. Amer. Inst. Min. Met. Enger., **161** (1945), 140.

(3) T. Suzuki: Sci. Rep. Tohoku Univ., in press.

(4) T. S. Ke: Phys. Rev., **73** (1948), 267.

The New Dynamical Method for Measuring Young's Modulus and Internal Friction of Fibers and Films.

By Heiji KAWAI and Noboru TOKITA.

Kobayashi Institute of Physical Research, Kokubunji, Tokyo.

(Received May 28, 1949)

In spite of the numerous statical measurements of Young's moduli of some high-polymers, few dynamical measurements have been done. Recently the dynamical methods for measuring the vibrational properties were reported,(1) (2) (3) (4) but they are inconvenient for measuring the small samples.

The authors will report a new method by which the Young's moduli and damping coefficients of short fibers and films (about 1 cm in length) can be measured.

§ 1. Young's Modulus.

When an elastic fiber is tied at any point of a vibrating body, this natural frequency rises a little; on the other hand when a small mass is carried at same point, this frequency falls a little. If we decide the suitable mass which compensates the rise of frequency due to the fiber, we can calculate the elastic constant of the fiber.

As Fig. 1, we will now consider the lateral vibration of a metal bar *A*. *A* is clamped at one edge and carries a small load '*m*' at the point *P*, and at the same point *P* one end of a short and thin sample '*S*' is tied, which has a large load '*M*' at the other end of *S*.

Now we consider the vibration of coupled system. The mass of the sample, however, is assumed to be negligibly small.

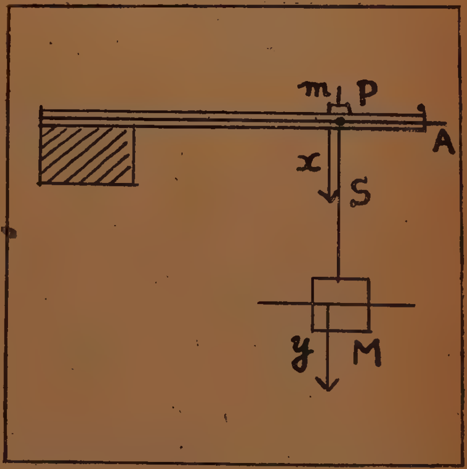

Fig. 1.

When the bar *A* vibrates laterally in *x*-direction and *M* in *y*-direction, the force *F* acted by the sample *S*, mass *m*, and *M* upon *P* is

$$F = -m\ddot{x} - E\sigma(x-y)/l_0 + (M+m)g, \qquad (1)$$

where x and y are respectively the displacements from the equilibrium positions of m and M, l_0 is the initial length of the sample, σ is the area of cross section of sample, and E is the Young's modulus of the sample S.

For the equation of motion of *M*, we have

$$M\ddot{y} - E\sigma(x-y)/l_0 = 0 \qquad (2)$$

If the natural frequenencies of metal bar *A* without *S*, *M*, and *m* are equal to them with *S*, *M*, and suitable mass *m*, which compensates the effect of sample,

$$F=(M+m)g. \qquad (3)$$

Accordingly,

$$m\ddot{x}+E\sigma(x-y)/l_0=0. \qquad (4)$$

Putting $x=x_0\exp(i\omega t)$, $y=y_0\exp(i\omega t)$, we have from the formula (2) and (4)

$$E=l_0\cdot\omega^2 m\cdot M/\sigma(m+M), \qquad (5)$$

where we assume that the natural frequency of the bar A is higher than that of the system coupled with S and M, namely

$$\omega^2>E\sigma/l_0M. \qquad (6)$$

§ 2. Internal Friction.

The phenomenon of internal friction may be treated phenomenologically in the theory of elasticity by regarding the elastic modulus as complex. The ratio of the real part of modulus to the imaginary part is denoted by Q.

If ΔE is the energy dissipated during one cycle, and E is the energy of vibration during the cycle, the ratio $\Delta E/E$ gives a measure of the internal friction.

Next, in the forced vibration, we can obtain another measure from a plot of the amplitude of vibration against the frequency of exciting force near a resonance frequency. Namely, this is the ratio of the half-width of the resonance curve Δf, to the resonance frequency f.

Provided the internal friction is so small, the relation between these various measures are as follows,

$$1/Q=\Delta E/2\pi E=\Delta f/\sqrt{3}f.$$

If Q_A, E_A, f_A, and Δf_A are respectively the notations for the metal bar A only; Q_S, E_S, and ΔE_S for the sample S only; and Q_{AS}, f_{AS}, and Δf_{AS} for the coupled system, we can obtain next relations,

$$1/Q_A=\Delta E_A/2\pi E_A=\Delta f_A/\sqrt{3}f_A \qquad (7)$$

$$1/Q_{AS}=(\Delta E_A+\Delta E_S)/2\pi(E_A+E_S)$$
$$=\Delta f_{AS}/\sqrt{3}f_{AS} \qquad (8)$$

where we postulate that the energy of coupled system is treated as the linear combination of each one at the first approximation.

When $E_A \gg E_S$ and $f_{AS}=f_A$, the equation (8) becomes

$$1/Q_{AS}=(\Delta E_A+\Delta E_S)/2\pi E_A=\Delta f_{AS}/\sqrt{3}\cdot f_A \qquad (9)$$

Accordingly,

$$1/Q_{AS}-1/Q_A\fallingdotseq\Delta E_S/2\pi E_A=(\Delta f_{AS}-\Delta f_A)/\sqrt{3}f_A \qquad (10)$$

Next, if δf is the difference between the resonance frequency of the bar A only, namely f_A, and the one of coupled system with S and M, *without* m, we can formulate as follows,

$$E_A=K\cdot f_A^2$$

and $$E_A+E_S=K\cdot(f_A+\delta f)^2,$$

where K is constant.

Accordingly,

$$(E_A+E_S)/E_A=(f_A+\delta f_A)^2/f_A^2=E_S/E_A+1.$$

$$\therefore\ E_S/E_A=(f_A+\delta f)^2/f_A^2-1\fallingdotseq 2\delta f/f_A. \qquad (11)$$

From the formula (10) and (11)

$$1/Q_S=\Delta E_S/2\pi E_S\fallingdotseq 1/2\sqrt{3}\cdot(\Delta f_{AS}-\Delta f_A)/\delta f. \qquad (12)$$

Then the measure of internal friction $1/Q_S$ is calculated by measuring δf, Δf_A and Δf_{AS}.

§ 3. Apparatus.

In Fig. 2, the outline of experimental apparatus is shown.

When the apparatus is constructed practically, the dimension of metal bar A must be decided by considering the character of the sample S and the range of measuring frequency.

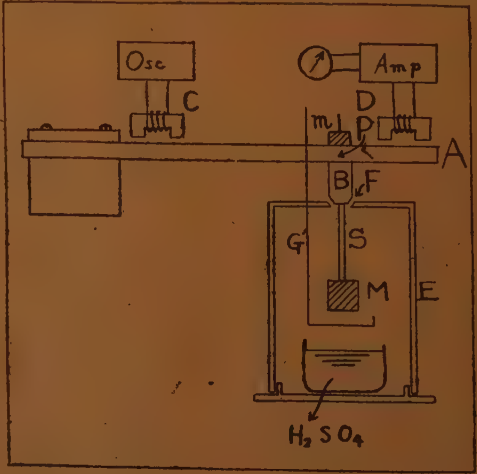

Fig. 2.

To eliminate the influence of the rotatory inertia of '*m*' the volume of '*m*' must be as small as possible, and '*m*' must be carried at the position near the loop of vibration.

The mass '*M*' must be as large as the formula (6) is satisfied.

In Fig. 2, *A* is an iron bar (maximum length 23.0 cm, width 1.5 cm, and thickness 0.3 cm) and its length can be varied by changing the clamped position. The metal chuck *B* which holds the sample is able to change its position along the long and narrow groove (length 11.0 cm, width 0.2 cm) in the center line of *A*.

The electro-magnetic driver '*C*' (constructed by winding insulated wire on an iron core and permanent magnet) excites the resonant vibration of *A* by an alternating current sent from the audio-frequency valve oscillator, and the similer electro-magnetic pick-up '*D*' detects the amplitude of the vibration.

'*m*' is a mass of lead, and sticked closely to *B* by a bit of oil clay.

'*E*' is the metal case which is kept at constant temperature and humidity, and the upper hole '*F*' of *E* is opened while the measurement so that *B* and *E* may not touch with each other when *A* vibrates.

§ 4. Measuring Method.

In the measurement, at first we support the mass '*M*' by holder *G*, and observe f_A and Δf_A. Next we remove *G* from *M*, and observe $f_A+\delta f$, and then $f_1, f_2, f_3 \ldots$ are observed when $m_1, m_2, m_3 \ldots$ are sticked on *P*.

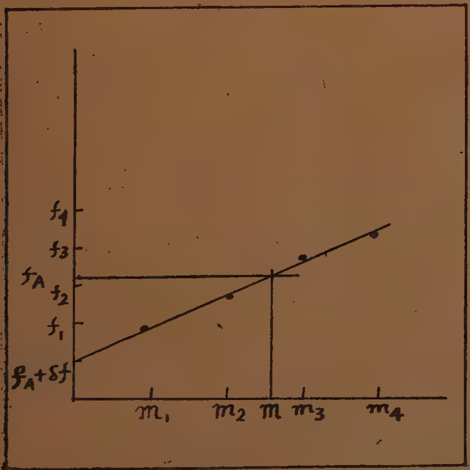

Fig. 3.

From these results the suitable value of '*m*' responding to f_A is found by graphical method as Fig. 3.

Then Δf_{AS} is observed when '*m*' is sticked on *P*. Using these values, E_S and $1/Q_S$ are calculated by the formulas (5) and (12), where for Δf_A, Δf_{AS} and δf the absolute values are not necessary.

The lateral vibration of the sample must be avoided in these measurements, for it gives a large error to the values of *E* and $1/Q$.

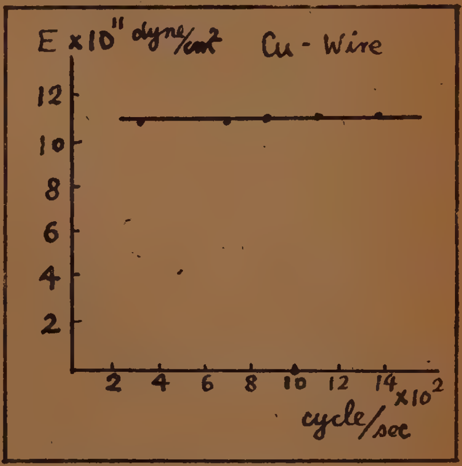

Fig. 4.

§ 5. Expetimental Results.

At first, in order to examine this method, we measured the Young's modulus of a fine 'Cu' wire (length 4.5 cm, diameter 7.2×10^{-3} cm).

Fig. 4 shows the results obtained by this method.

From this results, the Young's modulus of Cu-wire is constant from 200 cycle/sec to 1400 cycle/sec and its absolute value is $10.8\times10''$ dyne/cm².

We think that these values are very reasonable for Cu.

For example, Fig. 5 shows the relation obtained by this method between the frequencies and *E* of a raw silk fiber.

When the cross section of silk fiber is circle, the Young's modulus of it is 9.8×10^{10} dyne/cm².

Fig. 6 shows the relations between the freeness(5) *E* and $1/Q$ of paper (Sulphite pulp), these samples are about 10~20 mm in length, 3 mm in

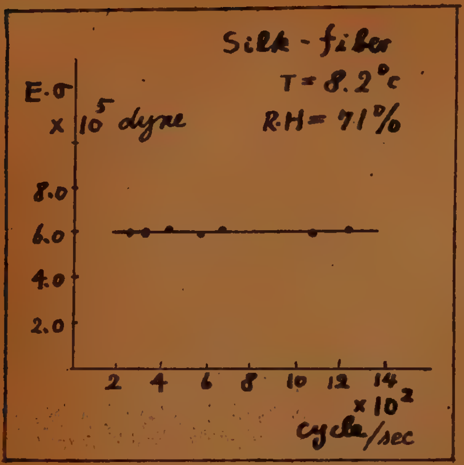

Fig. 5.

width, about 3×10^{-2} cm in thickness.

It was found that E and $1/Q$ of papers depend on the porosity, the amount of beating, sizing, and the kinds of fibers.

In Fig. 6, the abscissa refers to the freeness which is one of the measures of beating. It means that the smaller the value of freeness is, the more the quantity of beating.

As we are now measuring the vibrational properties of many high-polymers at various temperature and humidity, we will report these results in detail in the next paper.

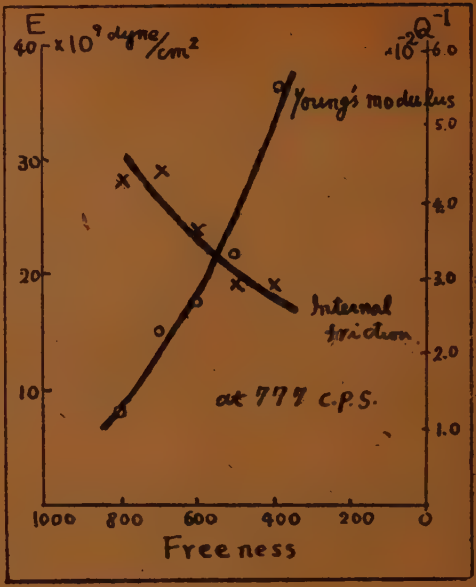

Fig. 6.

References.

(1) J. W. Ballou, & S. Silverman: J. Acous. Soc. Am. **16** (1944), 113.

(2) H. Wakeham, & E. Honold: J. App. Phys. **17** (1946), 698.

(3) H. S. Sack, J. Motz, H. L. Raub, & R. N. Work: J. App. Phys. **18** (1947), 450.

(4) W. J. Lyons, & I. B. Pretyman: J. App. Phys. **19** (1948), 473.

(5) W. Herzberg: Papierprüfung. p. 229.

Interaction of Beta Rays from RaE with Matter.

By Shoji KOJIMA and Shizuko HASHIMOTO.

Tokyo University of Literature and Science.

(Received June 13, 1949).

§ 1. Introduction and Method.

A fast electron passing through matter can create pairs, if its kinetic energy is larger than $2mc^2$. This process has been studied by many authors.(1) However, the experimental results with the methods of a cloud chamber or with a beta ray spectrometer are entirely inconsistent with the present theory. Feather and Dunworth(2) attacked this problem with a different method. The principle of the method is based on the coincidence counting of pair quanta which are emitted simultaneously in opposite directions when positrons annihilate. They studied on the beta rays from UX and obtained the results which accorded with other experiments. We have studied this problem on the beta rays from RaE. Our results are also close to those of other authors and contradict with the theory. This effect will be discussed on the standpoint of the double Bremsstrahlung.

§ 2. Absorption Measurements of Gamma Rays from RaE.

We have measured gamma rays from RaE by the aid of absorbers and a tube counter. A source of RaE was prepared as RaD which had been chemically separated from old radon tubes. Materials of the used absorbers are aluminum, copper, tin and lead. The tube counter was made of aluminum with wall thickness of 1 mm. The obtained absorption curves are reproduced in Fig. 1.

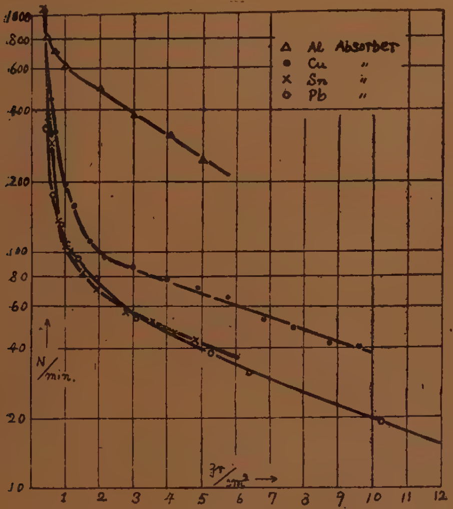

Fig. 1.

The soft part contains beta rays of RaE and gamma rays of RaD. The hard part yields following absorption coefficients: 0.88 cm^{-1} for copper and 1.57 cm^{-1} for lead which correspond to 0.37 MeV and 0.56 MeV respectively. The absorption curves are accordant with the Bremsstrahlung of RaE which was already studied by Droste(3) and confirmed to agree with the theory.

§ 3. Coincidence Measurements.

We have employed the Feather and Dunworth's method. The source was covered by metal sheets which have sufficient thickness to stop the beta rays such as 0.56 mm for copper, 0.65 mm for tin and 0.43 mm for lead. It was placed in the middle of the two coincidence counters.

Table I.

Absorber	Lead	Tin	Copper
Total time of observation (min).	700	1150	240
Total number of observed coincidences	272±16	230±15	203±14
Number of expected coincidences	230±14	191±12	198±12
Unexplained coincidences	42±22	39±19	5±18

The obtained results are given in Table I. In which the expected coincidences contain the chance coincidences and the natural coincidences. These are calculated from the effective resolving time of the coincidence apparatus. It was determined by observations with a gamma ray source of almost the same intensity as the coincidence experiment. From such observation over a total period of about 27 hours, the following result was obtained:

$$\tau = (5.12 \pm 0.31) \times 10^{-5} \text{ sec.}$$

The differences of the observed conincidences and the expected coincidences are unexplained coincidences. According to the interpretation by Feather and Dunworth, they are due to the pair creation of the kinetic energy of beta rays.

§ 4. The Cross Section of Pair Creation of the Kinetic Energy of Beta Rays.

To calculate the cross section it is necessary to know the number of the emitted beta rays and the efficiency of the counter. The intensity of the source was measured by an aluminium counter with wall thickness of 0.1 mm. The number of beta rays of the bare source was estimated by the extrapolation of absorption curves which had a linear character in semi-logarithmic plots. The number of beta rays was obtained as 9.6×10^7/min at the same position of the coincidence experiments.

The efficiency of a thick aluminium counter for gamma rays of 0.51 MeV had been obtained theoretically by Yukawa and Sakata(4) as 0.00272. we checked it experimentally by following two methods: (1) Gamma rays of the standard source which contains 2.9 mg Ra were measured by the counter. From the hard part of the absorption curve the energy of the hard gamma ray was estimated as 1.5 MeV on the average. Assuming that the number of emitted quanta was 2×10^5/min we obtained the efficiency for that energy as 0.006, which was reduced to 0.0018 for the 0.51 MeV gamma rays using a theoretical relation. (2) By the Droste's results it was known that the yield of the Bremsstrahlung having energy greater than 200 keV is 2.5×10^{-3} per disintegration after passing through 0.5 mm lead filter. Comparing the value with our experiments of gamma rays of RaE, the efficiency of the counter was obtained as 0,0021. From those we estimate the efficiency as 0.0022.

Using above results the cross sections of pair creation of kinetic energy of the beta rays which have the upper limit energy of 1.17 MeV are caculated as:

$$\sigma_{Pb}=(1.3\pm0.6)\times10^{-23}\,\text{cm}^2,$$
$$\sigma_{Sn}=(4.2\pm2.1)\times10^{-24}\,\text{cm}^2,$$
$$\sigma_{Cu}=(1.5\pm4.5)\times10^{-24}\,\text{cm}^2.$$

These cross sections are close to Feather and Dunworth's 1.4×10^{-23} cm² for the beta rays having upper limit of 2.3 MeV. On the contray the theoretcal value is less than 10^{-27} cm².

§ 5. Discussion.

The problem of the pair creation of kinetic energy of the beta ray is very conflicting between theory and experiments. By the experiments with the cloud chamber it is extremely difficult to distinguish a positron or an electron if i has not sufficient energy. The coincidence method has a definite advantage for this point. However, it remains a question whether the observed gamma rays are realy annihilation radiations having the energy of mc^2 or not. To interprete "unexplained coincidences" it may be possible to take the double Bremsstrahlung⁽⁵⁾. We shall estimate the ratio of the process to the single Bremsstrahlung by the assumption that all unexplained coincidences are due to the process. From the absorption curves the observed single Bremsstrahlungs passed through the absorber which just stops beta rays seem to have energies above 125 keV. The ratio of double Bremsstrahlung to those gamma rays are obtained as 1:50 provided that the average counter efficiency is 0.0023. Theoretically this ratio is of the order of 1:137 or smaller if the two quanta are not emitted in opposite directions. However, the interpretation of double Bremsstrahlung shows better agreement between the experiments and the theory than the pair creation.

References.

(1) Skobelizin and Stepanowa: J. de phys, **6** (1935), 1.
Da Silva: Comptes rendus, **202** (1936), 2070.
Champion and Barber: Nature, **140** (1937), 105.
Sizoo and Barendregt: Physica, **6** (1939), 1085.
(2) Feather and Dunworth, Proc. Camb. Phil. Soc., **43** (1938), 435.
(3) V. Droste: Zeits. f. Phys., **104** (1936), 335.
(4) Yukawa and Sakata: Sci. Papers I. P. C. R. (Tokyo), **686** (1937), 187.
(5) Heitler: "Quantum theory of radiation", Oxford.

On the Thermal Expansion of Cuprous Oxide.

By Ryosei UNO and Toshihiro OKADA.

Physical Institute, Faculty of Science, Kyushu University.

(Received June 18, 1949).

§ 1. Introduction.

There are a large number of researches on the electrical and optical properties of cuprous oxide and it is observed that the temperature dependence of the conductivity changes at the temperature of −70°C, 50°C, 150°C and 350°C(1). In order to explain these results, the simple theory of semi-conductor is perhaps not sufficient and the more detailed experimental researches, especially, about crystal structure may be necessary.

According to X-ray analysis cuprous oxide has a cubic lattice(2) and the change of the crystal structure was not observed from the room temperature to 350°C(1). On the thermal expansion, Auwers(3) reported that there might be a irregularity at 56°C and the influence of tempering was observed. When the sample was heatdd from the room temperature, its length was almost constant (the thermal expansion coefficient $\beta \lesssim 5\times 10^{-8}$) below 56°C and it began to decrease above 56°C. Then, when the temperature was lowered, the decreasing of the length was observed above 56°C, while its length was kept almost constant below 56°C. On the contrary, if the sample was heated and annealed in vacuum, its length decreased below 56°C ($\beta \sim 10^{-6}$) and was almost constant above 56°C. Another measurement about cuprite was cited by Mellor.(4) The results are shown in Table I.

Table I.

T°C	50	40	30	20	10	4.1	0
$\beta\times 10^{-8}$	+105.9	+82.3	+59.7	+36.7	+13.1	0	−0.95

The authors measured the thermal expansion from −150°C to 400°C.

§ 2. The Experimental Procedure.

The apparatus is shown in Fig. 1. The change in length of the sample relative to quartz is measured. If the sample becomes long, it lifts the quartz rod and the needle rotates, so the small mirror rotates. The apparatus has a metallic cover with a glass window to observe the angle of the rotation of the mirror by means of the telescope and scale, and the inside of the cover is pumped up to the vacuum of about 10^{-1} mm Hg.

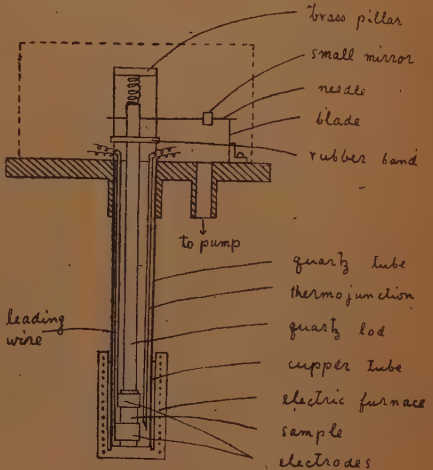

Fig. 1.

The temperature is measured by the cupper-constantan thermojunction. The sample has two electrodes (Au spattered) for measuring the electric conductivity.

In order to calibrate the scale, the thermal expansion of a cupper lod is measured. According to the data given in the Landolt-Börnstein table, 1 mm of the scale corresponds to 1.9×10^{-4} mm of the change in length of the sample.

The samples are prepared by heating the pure cupper strips in the electric furnace at about 900°C in air for about 50 hours. Its dimension is about $15\times 5\times 1.5$ mm³ and the distance between two electrodes is 4 mm.

It is observed that when the temperature is changed by some amount and thereafter kept constant, the length of the sample begins to vary and it takes several hours to saturate to the constant value. (We call this the "relaxation phenomenon".) So, the temperature is rendered to change after the length becomes constant for over 30 minutes.

§ 3. Results.

A. The curve of the saturated values.

The curve of the saturated values is shown in Fig. 2. The length of the sample is almost constant from —150°C to —50°C and then decreases at —50°C. From —50°C to 0°C it may be kept constant and above 0°C decreases gradually up to about 250°C. The expansion coefficient is about -1.8×10^{-6}. Above 300°C, its length increases having the expansion coefficient of about $+2.7\times10^{-6}$. According to the result, there may exist three irregular points at —50°C, 0°C and 300°C. The existence of the point reported by Auwers is not sure, while the irregular change is observed between 0°C and 100°C. But after one series of measurements the irregularity becomes smaller because of the sample being perhaps well annealed. The time written beside each point in Fig. 2 indicates the hours from the beginning of the measurement. Below the room temperature, it is difficult to keep the temperature constant for several hours. Therefore the results are rather unreliable.

B. The relaxation phenomena.

To describe the phenomena it is convenient to devide the range of the temperature into four parts.

i. From —150°C to 0°C.

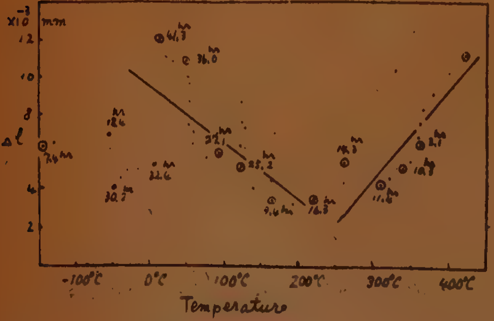

Fig. 2. ⊙···Saturated value. Two series of measurements, below 0°C and above 0°C are shown.

The relaxation phenomena are not surely observed; but contraction occurs gradually when the temperature is changed more rapidly.

ii. From 0°C to about 100°C.

The typical curve when heating is shown in Fig. 3. The length of the sample increases and decreases as the figure shows. There may be some complex phenomena in the sample. It is probable that the existence of cupric oxide as impurity and also vacancies of lattice sites may play a important rôle, because of this phenomena being influenced by the conditions of tempering and annealing. The curve when cooling is almost the same as when heating. If the sample is heated rapidly up to above 100°C, those phenomena are not observed.

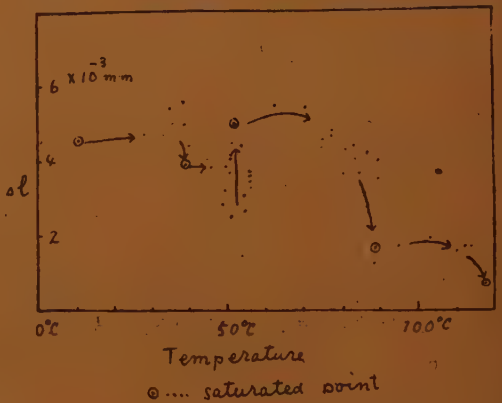

Fig. 3.

iii. From 100°C to about 250°C.

When heating, the sample expands by a small amount, and when the temperature is kept constant it contracts a little, while, when cooling, it contracts and when the temperature is kept constant it expands.

iv. Above 300°C.

The relaxation phenomena hardly exist and the reproducibility when heating and cooling is rather good.

C. The behavior when the temperature is changed rapidly.

The results are shown in Fig. 4. The relaxation times τ for the change in length are calculated about 1 hour as shown in Fig. 4. On the contrary, the conductivity follows the change in the temperature.

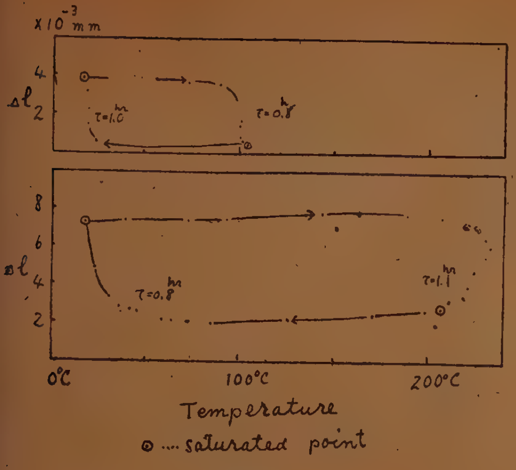

Fig. 4.

D. Relation between the conductivity and the thermal expansion.

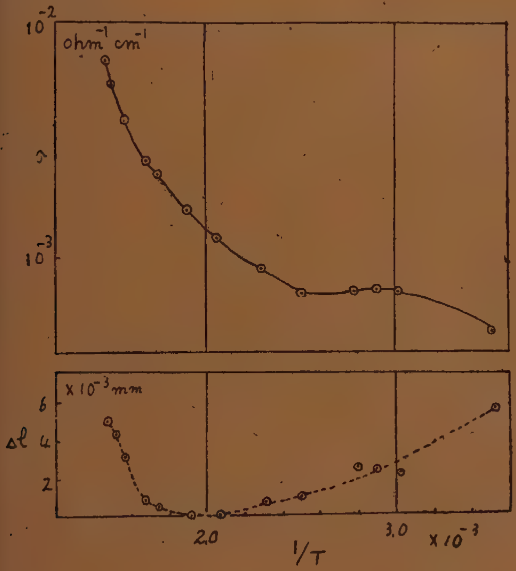

Fig. 5.

To investigate the relation between the conductivity and the thermal expansion, the both properties are observed at the same time. Fig. 5. shows the results. The singular points of both curves are observed at nearly the same temperature, but he correspondency is not sufficient.

§ 4. Conclusion.

Phenomenologically speaking, there may be five states, divided by the temperatures of −50°C, 0°C, 100°C and 250°C~300°C. We call these states α-, β-, γ-, δ- and ε-states from the higher temperature.

In the α-state, β is $+2.7\times10^{-6}$ and the relaxation phenomena are hardly observed. In the β- and γ-states, β is -1.8×10^{-6}. In the former the relaxation phenomena are observed and in the latter the length of the sample decreasing and increasing, the results are rather complex. In the γ- and ε-states, the sample keeps its length almost constant and when it transits from γ-state to ε-state, the expansion is observed.

The reason why the relaxation phenomena are observed and why the thermal expansion does not follow immediately the change of the temperature, is not clear.

Further research will be performed by means of the X-ray analysis about the single crystal to measure the thermal expansion of the lattice spacing. The relation between the conductivity and the thermal expansion will be discussed in the near future.

We are indebted to the Ministry of Education for the research grant.

References.

(1) T. Okada: The paper will be published in this journal.
(2) M. C. Neuberger: Zeits. Krist. **77** (1931) 169.
(3) O. von Auwers: Naturwiss. **19** (1931) 133.
(4) J. W. Mellor: *A comprehensive treatise on inorganic and theoretical chemistry*, Vol. III, P. 122.

On the Properties of Ferromagnetic Alloy of Manganese and Bismuth at Low Temperature, I. Magnetic, Dilatometric and Calorimetric Studies.

By Kenji KONDO.

Institute of Science and Technology, University of Tokyo.

(Received June 22, 1949).

§ 1. Introduction.

It is widely known, that manganese and chromium combine with various non-magnetic elements into ferromagnetic substances, e.g. Mn-N, Mn-P, Mn-Sb, Mn-Sn, Mn-As, Mn_2AlCu and so on. But the detailed mechanisms of their spontaneous magnetizations are scarcely known differing from that of iron, cobalt or nickel. Moreover, the experimental investigations show that some of the componds have abnormal properties, and their causes are not traced out.

The alloy of manganese and bismuth reported here, is one of the above-mentioned compounds and shows abnormal magnetic behaviour at low temperature(1). The part I of this paper involves the results of magnetic, dilatometric and calorimetric studies, and the part II the electric resistance, and the galvanomagnetic effects.

According to the state diagram determined by thermal analysis(2)(3), there are one or two intermetallic compounds, of which the one is ferromagnetic. The atomic constitutions of the ferromagnetic were supposed to be nearly 50 and 50 per cent. Thereafter, Fürst and Halla(4) concluded by X-ray analysis and measurement of specific gravity, that the intermetalic compounds were Mn_2Bi and $MnBi_2$, and the former was ferromagnetic. But Thielman(1) found the ferromagnetic MnBi-compound, using magnetic and chemical analysis simultaneously, pointed out that some new weak lines found in his photographic films of specimens of higher purity were not consistent with the results of Fürst and Halla's analysis, and supposed that the lattice structure of ferromagnetic MnBi is the nickel arsenide type.

§ 2. Production of Specimens.

The previous studies show that the system of manganese and bismuth is of two phases in fused state. They are not mixed up due to the great difference between their specific gravities and do not combine, even if heated beyond the melting point of manganese. And because manganese combines with gaseous hydrogen and nitrogen the former in the antiferromagnetic, the latter in the ferromagnetic, we must not use their atmospheres but that of inert gases, or employ the method in vacuo to avoid oxidation. Bismuth bites crucibles of quartz or of alumina at high temperature. On the other hand, the combining process is too inactive at the low temperature from 300° to 500°C to spare the time. Therefore, the author suspended the very fine powdered manganeses in fused bismuth held at the temperature of 700°C for some hours in a evacuated quartz tube. It is necessary to take a little more amount of manganese than stoichiometric quantity and to stir, because a small amount of it floats up to surface and does not react. A sample obtained in such a way includes the ferromagnetic part of 67 per cent and bismuth of 33 percent in volume. We may be able to get a more compound-rich sample by repeating this process more often.

The volume-fraction was determined as follows; To measure the length of each grain along straight lines across a microscopic photographic paper. The ratio of the sums of the length of each phase is necessarily the ratio of volumes, when grains distribute at random. The averaged percentages of volumes of ten photographs are the above-mentioned.

The density of the same sample was measured by the method of Archimedes and is found 8.82 grams per cubic centimetre. Considering the above-obtained volume fractions and the density of pure bismuth of 9.849 grams per cubic centimetre, we have that of the compound MnBi of 8.31 grams per cubic centimetre, while Thielmann's value by the X-ray analysis is 9.134 grams per cubic centimetre. The difference between them is not so small, but may be consistent, if we consider taht the density of bismuth-rich phase which includes very small quantity of mangese is more small than that of pure bismuth, and the sample may imply very small amount of manganese, air holes and intergranular regions (5).

The MnBi is very liable to be oxidized in atmospheric air. In microscopic view the Mn-Bi-phase is not found at first in a fresh well-polished surface, but gradually becomes gray after several minutes. Etched with dilute nitric acid, it becomes black at once. It is found spindle-shaped in the BiMn-poor sample but in the specimens, of which the author measured the various properties, they connect to each other like a net.

§ 3. Magnetic Properties.

1) Hysteresis loop at room temperature.

As the magnetization of this compound is hard to be saturated at room temperature, the electromagnet of Weiss-type was used, which can generate magnetizing field of 25000 Oersted. The measuring apparatus consists of a search coil, a ballistic galvanometer and a standard mutual inductance of 0.01 Henry. The object of this mutual inductance is to determine the constant of the galvanometer by noting the throw when a known current in the primary circuit is reversed. The specimen is a cylinder of 30 mm long and of 8.5 mm diameter. The search coil has 1000 windings and the mean sectional area of 1.674 cm^2. The pole pieces have the diameter of 20 mm, are bored of the diameter of 10 mm at their centres, and are seperated at intervals of 10 mm. When the specimen is introduced in the search coil between the pole pieces, two thirds of its length is placed within the holes of the pole pieces. As the magnetic field within a hole is weak and inhomogeneous, the demagnetizing field is unknown. The intensity of magnetization is calculated from the throw of the ballistic galvanometer when the specimen is removed along the holes rapidly and smoothly. But it is difficult to get the accurete value of magnetization from the measured magnetic flux, because the specimen is the mixture of ferromagnetic and non-ferromagnetic grains. Here we employ the approximate formula

$$\varphi = H + \frac{4\pi M f}{\sqrt{1+(R/L)^2}},$$

where φ is the density of magnetic flux within the search coil, H the true magnetic field, f the volume fraction of the non-ferromagnetic part, R and L are respectively a half of the diameter of the search coil and of the length of the specimen. The accuracy is good, when the diameter of the search coil is enough large than that of specimen and $R \ll L$. Although these conditions are not thoroughly satisfied in our case, it may be sufficient to measure the relative change in the magnetization,

We get the result represented in Fig. 1, where the intensity of magnetization is plotted against the true magnetizing field. The remanence of about 9 Gauss is very small compared to the saturated value, the hysteresis is observed in the magnetizing field beyond 10000 Oersteds, the hysteresis loop is very narrow and the magnetization increases gradually in the magnetizing field stronger than 20000 Oerstends. It cannot be decided now, whether these properties are intrinsic, or originated by the externally applied conditions, for instance the internal stress caused by the co-existence of two phases, in spite of careful annealing. In the stronger field than 11000 Oersteds, where the hysteresis disappears, the empirical relations between the magnetization and the magnetizing field is as follows:

$$J = 257\left(\frac{1-3.48.10^3}{H}\right).$$

Therefore, we obtain 257 Gauss as the saturated magnetization at room temperature (the dotted line in Fig. 1).

2) Influence of temperature on magnetization.

It is difficult to observe the behaviour of spontaneous magnetization while temperature arises

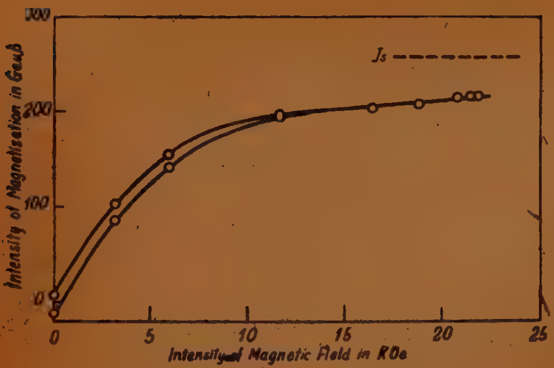

Fig. 1.

from liquid air temperature to room temperature, because of uneasy saturation. The measuring instrument is experesed in Fig. 2, Sc_1 and Sc_2 are two search coils, of which the winding directions are counterwise, and of which the winding numbers are the same 1000 turns. These coils are connected in series electrically, and arranged in parallel between the pole pieces in order to make the throw of ballistic galvanometer as small as possible, when the magnetizing current is reversed. The specimen S_p with the thermojunctions of copper and constantan is introduced into one search coil, and the search coils are enveloped with asbestos to make the rise of specimen's temperature moderately small. Then liquid air is poured into the Dewar's bottle. The throw of the ballistic galvanometer when we reverse the current is proportional to the magnetization. The calibration to absolute scale, i. e. the proportional factor, is determined by measurement of the known magnetization for which we fake the same specimen at room temperature. As soon as the liquid air evaporates out, the temperature rises rather rapidly at first and slowly at the end, with the speed of 2 degrees per minute on average. In Fig. 3 the magnetization is plotted against the temperature in the cases of the external magnetic field of 7500, 5800 and 4700 Oersteds. The magnetization decreases rapidly from −155° or −150°C and then gradually as the temperature rises, differently from the normal ferromagnetic substance or from the Weiss' theory. In these magnetic fields, the magnetization is not saturated yet, and this behaviour may be related to magnetic anisotropy constants. If we plot the magnetization aginst the field at every temperature, the fact is found, that the magnetization is near the saturation at the lowest temperature and at room temperature but remote at intermediate temperature. But if we assume the saturated value of 358 Gauss at −150°C, we obtain 304 Gauss at room temperature according to Weiss' theory. In Fig. 3 we plot this Weiss' curve. The difference between this calculated value and the observed 257 Gauss is too large to be neglected. Moreover, the saturated magnetization at −150°C is by far stronger than 358 Gauss and is considered to be about 500 Gauss at least from the behaviour of magnetization against magnetic field. Therefore, it is reasonable to consider that the spontaneous magnetization varies almost similarly as the curves in Fig. 3.

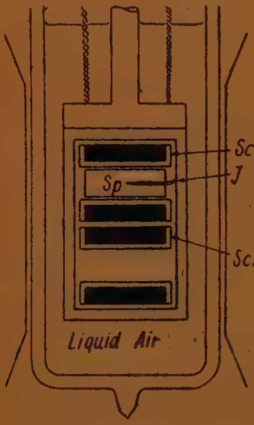

Fig. 2.

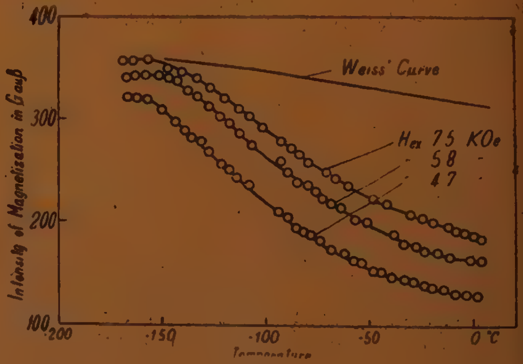

Fig. 3.

The observed region is too small to decide the behaviour at lower temperature than −150°C: whether it has a maximum at about −150°C or obeys the normal Weiss' theory, but the author thinks it to be the latter from many observations.

The magnetic moment of BiMn molecule can be calculated by the following formula in Bohr magneton ;

$$\mu = \frac{J_{Max} V}{\mu_B Z}$$

where J is the maximum magnetization, v the volume of an elementary cell, μ_B Bohr magneton, z is the number of molecules MnBi per an elementary cell. If we assume $J_{MAX} = 500$ Gauss, we get $\mu = 2.6$ Bohr magnetons or strictly $\mu > 2.6$ Bohr magnetons.

§ 4. Thermal Expansion.

The thermal expansion was measured by a usual differential dilatometer with optical lever. In order to increase the accuracy, an optical image was measured by a travelling microscope. The standard is a rod of pure copper. Since the thermal expansion coefficient of copper is unknown at low temperature, it is impossible to obtain the absolute value, but the relative measurement is sufficient for the detection of abnormal behaviour.

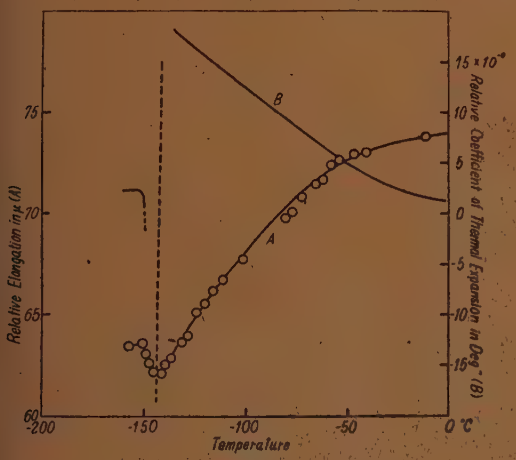

Fig. 4.

In Fig. 4, we plot the relative elongation (Curve A) and the relative value of expansion coefficient calculated from the curve A against the temperature. From −150°C to −142°C, MnBi contracts relatively. The relative coefficient changes from positive to negative and again to positive, and then diminishes gradually to a constant value.

§ 5. Specific Heat.

According to thermodynamics, the magnetic part of heat capacity is dependent upon the temperature-derivative of magnetization. There we may expect the abnormal specific heat. Moreover, the amount and the form of abnormal specific heat may give us some informations about the mechanisms.

1) Curie Temperature.

To determine the Curie point, we use the method of differential calorimetry, where the differential thermocouple consists of copper and constantan, and the standard is a rod of pure copper. To increase the included amount of MnBi in the specimen we broke the specimen into pieces and selected the ferromagnetic part by a magnet. The result is as follows : At 271°C, large latent heat of bismuth-rich part (Melting Point). At 350°C, a peak of specific heat of MnBi (Curie Temperature). At 293°C endothermic, and at 54°C exothermic reactions. To confirm this result, we measured the electric resistance. Knicks appeared manifestly at 54°C and faintly at 293°C and 350°C in curves of resistance against temperature. At 271°C, the resistance changes at 271°C irreversibly.

2) Specific Heat at low Temperature. The apparatus is shown in Fig. 5. In Fig. 5b, S is the sample, H_1 the heater of painted constantan wires, which supplies heat to sample, H_2 the nich rome wire wound around the case to diminish the radiactive and conductive loss from the sample, J_1 the differential thermometer indicating the temperature difference between the sample and the case, and J_2 the thermocouple, with which we measure the temperature of the sample. This ap-

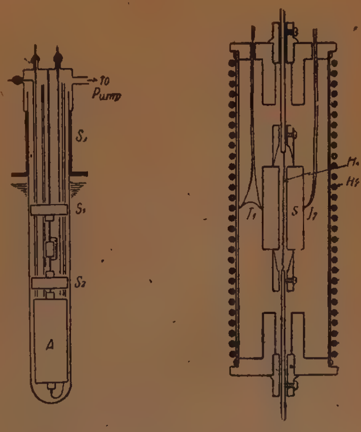

(a) (b)

Fig. 5.

paratus is placed at A in Fig. 5a. S_1, S_2 and S_3 are screens preventing the radioative and conductive inflow of heat. At first air is pumped out and then air is admitted through caustic soda, calcium chloride and a liquid air trap. The apparatus is dipped in liquid air. After the part A is cooled at constant temperature, air is pumped out. While we supply H_1 with constant power, 0.01 Watt, and adjust the power in H_2 so as to hold the temperature difference less than 0.05°C, we measure the temperature of the sample at equal intervals of time, 2 min. Time derivative of the temperature is proportional to the heat capacity. The obtained result is shown in fig. 6. The heat capacity increases abruptly at −155°C and then gradually approaches to Debye's curve. Unfortunately it is difficult to determine the deviation from Debye's theory, since there is scarecely normal region to calculate the Debye's characteristic temperature. But the above behaviour of heat capacity is considered in corformity with that of magnetization from the thermodynamical viewpoint.

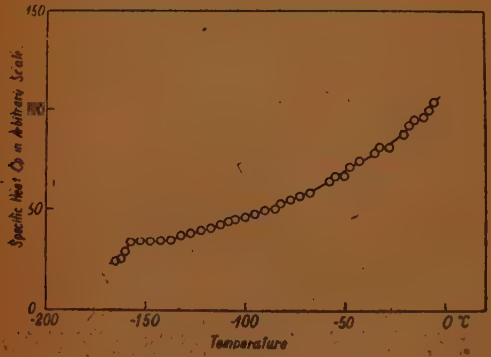

Fig. 6.

§ 6. Conclusion.

1) Ferromagnetic compound MnBi demands very high magnetic field to be saturated. This is reasonable, because the intensity of magnetizing field necessary for saturation increases in the order of the compound of manganese with nitrogen phosphor, arsenic and antimony. The increase in magnetization in high field beyond 20000 Oersteds may be due to a special mechanisms.

2) The magnetic moment per molecule is greater than 2.6 Bohr magentons. Therefore, the number of positive holes in d-band is large as compared with iron, cobalt and nickel.

3) The spontaneous magnetization decreases abnormally, at first rapidly and then gradually, while the temperature rises from −150°C to room temperature. The author considers it to be not attributed to the existence of two ferromagnetic substances with different Curie points.

4) Coefficient of thermal expansion shows small abnormal behaviour from −150°C to −148°C.

5) Curie temperature is about 350°C.

6) Anomalous specific heat arises suddenly at −150°C and diminishes gradually at higher tempearture, and its shape is qualitatively compatible with that of magnetization from the view-point of thermodynamics.

These anomalous phenomena may be accounted for not by transformation of lattice structure but by electronic transition.

In conclusion, the author wises to express his hearty thanks to Assistant Prof. Ren'ti Kimura, the instructor of Institute of Science and Technology, University of Tokyo for his excellent guidance and kind encouragement throughout this work, and to Prof. S. Kaya, University of Tokyo, for his kind support, offering the electromagnet and liquid air.

References and Note.

(1) K. Thielmann: Ann. d. Phys. **37** (1940) 41.

(2) E. Bekier: Zeits. f. Metallkunde **7** (1915) 83.

(3) P. Siebe; Zeits. f. anorg. u. allg. Chem. **108** (1919) 161.

(4) U. Fürst and F. Halla, Zeits. f. Phys. Chem. (B) **40** (1938) 283.

(5) Fürst and Halla measured the density using the pyknometer and got 8.95 grams per cubic centimeter. This value is not that of pure compound but of mixed samples. Comparing this with various possible structures, which X-ray analysis permitted, they adopted Mn_2Bi and the density of 9.24 grams per cubic centimeter.

Dissociation and Ionization of n-Propylalcohol by Electron Impact.

By Toyozo KAMBARA.

Hitachi Central Laboratory, Hitachi Ltd.

(Received June 28, 1949).

§ 1. Introduction.

From the experiments with the mass-spectrometer on the dissociation of organic molecules by electron impacts, it is possible to determine the nature of the ions produced from the parent molecules by the measurements of the M/e values, and also possible to give considerable information about the dissociation processes by the measurements of the appearance potentials of the formed ions. The appearance potential of the ion X is the sum of the following three quantities; namely (1) the dissociation energy $P(X)$ by which the neutral X is produced from the parent molecule, all product being in their lowes state, (2) the ionization potential of X, (3) the kinetic and excitational energy of the dissociation products. In general, the excitational and kinetic energy of the dissociation products can not be measured with the mass-spectrometer. Hence we can only obtain the upper limit of the ionization potential of X from difference between the appearance potential $A(X^+)$ and the dissociation energy $P(X)$. But the kinetic energy of the ions measured by Lozier and others is in the order of 1 eV or less in most cases.

Moreover the thermochemical and the spectroscopic data to be available for the analysis of the dissociation processes of the complex molecules is few. For these reasons the infarmations about the dissociation processes are uncertain to some extent. In the previous paper(1) we described the dissociation of the C_2H_5OH molecule by electron impact. In the water type molecule, like alcohol, the non-bonding electron of the oxygen atom is ionized at first by the Mulliken's theoretical prediction(2). This prediction seems to be sure in the C_2H_5OH molecule, for the CH_2OH^+ ion is the most abundant ion and its appearance potential is very low as the result of the trivalent property of O^+.

In this paper we describe the dissociation experiment of the n-C_3H_7OH by electron impact as a series of the previous works.

§ 2. Apparatus and Procedure.

The mass-spectrometer used in the present experiment is the same one as previously described.(3) The uniform magnetic field adopted for this apparatus is 60° type, and its radius is 22 cm. The cross-sectional view of the ion-source is shown in Fig. 1.

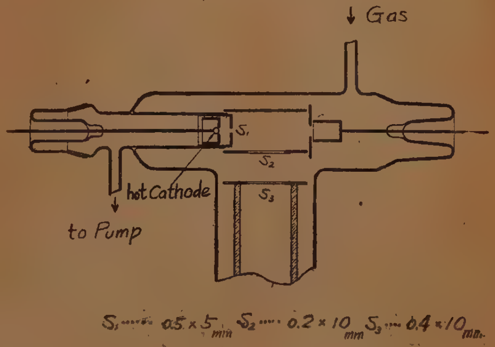
Gas
S_1
S_2
hot Cathode
S_3
to Pump
S_1 …… 0.5 × 5 mm S_2 …… 0.2 × 10 mm S_3 …… 0.4 × 10 mm.

Fig. 1. Ion Source.

The vapor of the purified sample is admitted into the ion-source through the glass gas leak such as to give a pressure of about 5×10^{-5} mm Hg. in the ion-source and less than 10^{-6} mm Hg. in the main point of the mass-spectrometer. The thermal decomposition of the vapor at the hot tungsten cathode is protected by the differential pumping method and also by lowering the filament temperature as much as possible.

The relative abundances of the formed ions by the electron impacts are measured from the peak heights of the photograph taken by the magnetic scanning method. The carbon isotope corrections are not carried out in this paper. The ion peaks which are supposed to be due to the impurities are always of low intensity and these ions are mainly produced from the diffusion pump oil. The important question in the investigation of this kind is whether the ions actually observed are the result of single electron impact. In this point we are convinced that the observations have been carried out under single electron impact. For the experiments show the results to be independent of pressure, electron current and filament temperature under the condition of operation.

The purification of the sample is as follows.

Merck's n-propyl alcohol is dried with the cupric sulphate and distilled. Its refractive index is $n_D^{20} = 1.3848$.

§ 3. Investigation on the n-Propylalcohol.

The n-C_3H_7OH molecule is a straight chain type one. The dissociation of this molecule by electron impact may perhaps be in the same manner as the C_2H_5OH molecule. The abundances of the ions produced from the n-C_3H_7OH molecule at the electron energy of 80 eV are summarized in Table I. The most abundant ion is the CH_2OH^+ ion.

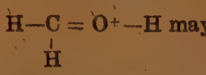

The structure of $\underset{\displaystyle H}{\overset{}{H-\underset{|}{C}}} = O^+-H$ may be stable on account of the trivalent property of O^+. The non-bonding electron of the oxygen atom in the n-C_3H_7OH molecule is first ionized and then the C—C bond next to the oxygen atom is broken since the strength of the C—C bond is weaker than the strength of the C—H bond. This causes to produce the CH_2OH^+ ion.

The abundance of the ion corresponding to $M/e = 28$ is also large. The photograph of the peaks of the ions produced from the n-C_3H_7OH molecule, taken by the magnetic scanning at the electron energy of 80 eV, is shown in Fig. 2.

The appearance potentials of the several ions are measured by the usual method and are corrected by the ionization potential of Ar. (15.7 eV). These values are shown in Table II.

Before one can make analysis of the processes by which the ions are formed, it is necessary to estimate the various values of the heat of dissociation involved. Now the heat of combustion of the n-C_3H_7OH is 482 Kcal/Mole by the measurement of Rossini(4). Its heat of vaporization is 9.8 Kcal/mole in the International Critical Tables. Hence the heat of formation of the n-C_3H_7OH is 65 Kcal/mole. The heat of sublimation of carbon which is involved in the thermochemical equation is still subject to some uncertainty, but in this work we have adopted the value $L(c) = 5.41$ eV as given by Herzberg.(5) Then the energy of dissociation of the n-C_3H_7OH to atoms in gaseous state is $D(nC_3H_7OH) = 39.5$ eV. The calculated energies $D(x)$ adopting $L(c) = 5.41$ eV used in the analysis of the data are as follows.

Table I. Nature and relative abundance of ions formed in n-propyl alcohol by electrons with 80 volts energy.

M/e	Ion	Abundance	
60	$C_3H_7OH^+$	1.00	2.03 %
59	$C_3H_6OH^+$	1.17	2.37
58	$C_3H_6O^+$	0.11	0.22
57	$C_3H_5O^+$	0.29	0.59
56	$C_3H_4O^+$	0.15	0.31
55	$C_3H_3O^+$	0.26	0.53
54	$C_3H_2O^+$	0.05	0.09
53	C_3HO^+	0.11	0.22
45	$C_2H_4OH^+$	0.59	1.20
44	$C_2H_4O^+$, $C_3H_8^+$	0.29	0.59
43	$C_2H_3O^+$, $C_3H_7^+$	1.15	2.34
42	$C_2H_2O^+$, $C_3H_6^+$	2.14	4.34
42	C_2HO^+, $C_3H_5^+$	2.41	4.89
40	C_2O^+, $C_3H_4^+$	0.52	1.06
39	$C_3H_2^+$	1.72	3.50
38	$C_2H_2^+$	0.49	1.00
37	C_3H^+	0.36	0.73
36	C_3^+	0.06	0.12
32	CH_3OH^+	0.35	0.72
31	CH_2OH^+	14.53	29.50
30	CH_2O^+, $C_2H_6^+$	0.49	1.00
29	CHO^+, $C_2H_5^+$	3.15	6.38
28	CO^+, $C_2H_4^+$	6.75	13.71
27	$C_2H_3^+$	4.30	8.73
26	$C_2H_2^+$	1.88	3.81
25	C_2H^+	0.31	0.62
24	C_2^+	0.06	0.12
19	H_3O^+	0.24	0.48
18	H_2O^+	0.42	0.84
17	HO^+	0.12	0.25
16	O^+, CH_4^+	0.48	0.97
15	CH_3^+	1.03	2.09
14	CH_2^+	0.45	0.91
13	CH^+	0.15	0.31
12	C^+	0.32	0.66
2	H_2^+	0.51	1.03
1	H^+	0.49	1.00

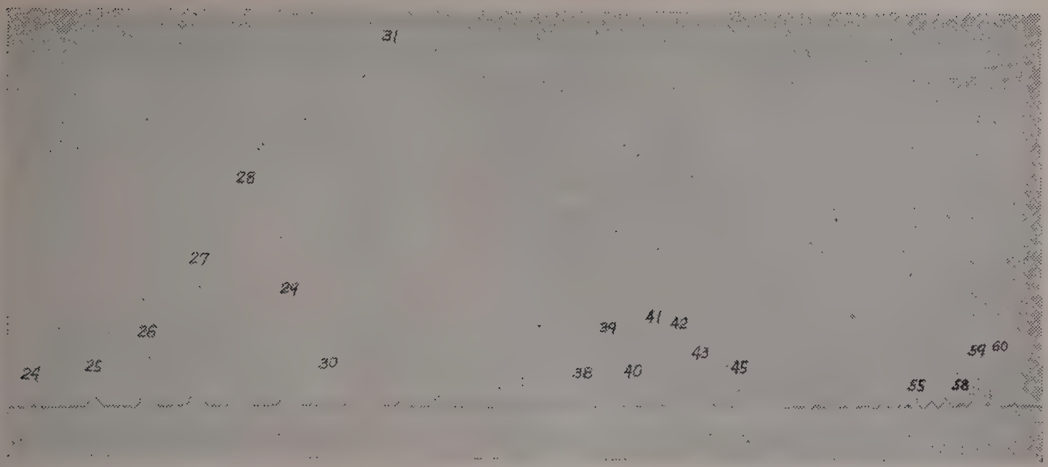

Fig. 2. Mass-spectrum obtained with n-C_3H_7 OH at the electron energy of 80 eV.

Table II. Appearance potentials of the ions produced from n-propylalcohol.

M/e	Ion	Appearance potential eV
60	$C_3H_7OH^+$	11.1 ± 0.2
59	$C_3H_6OH^+$	10.8 ± 0.2
42	$C_2H_2O^+$, $C_3H_6^+$	14.8 ± 0.2
41	C_2HO^+, $C_3H_5^+$	14.6 ± 0.1
39	$C_3H_3^+$	17.5 ± 0.1
31	CH_2OH^+	11.1 ± 0.2
29	$C_2H_5^+$, CHO^+	14.8 ± 0.1
28	$C_2H_4^+$, CO^+	12.6 ± 0.2
27	$C_2H_3^+$	14.8 ± 0.2

$D(H_2) = 4.5$ eV	$D(OH) = 4.3$ eV
$D(H_2O) = 9.5$ eV	$D(CH) = 3.5$ eV
$D(CH_2) = 7.1$ eV	$D(CH_3) = 10.7$ eV
$D(CH_4) = 15.2$ eV	$D(C_2H_2) = 13.0$ eV
$D(C_2H_3) = 16.2$ eV	$D(C_2H_4) = 19.3$ eV
$D(C_2H_5) = 22.2$ eV	$D(C_2H_6) = 25.2$ eV
$D(C_3H_3) = 19.6$ eV	$D(C_3H_5) = 26.5$ eV
$D(C_3H_6) = 29.6$ eV	$D(C_3H_7) = 32.5$ eV
$D(C_3H_8) = 35.4$ eV	$D(CH_3OH) = 19.0$ eV
$D(C_2H_5OH) = 29.3$ eV	

Table III lists the energies $P(x)$ of various combinations of three carbons, one oxygen and eight hydrogen atoms at the normal state with respect to the combination n-C_3H_7OH as zero.

Table III. Energies of dissociation of n-propylalcohol into its various constituents and interpretation of the appearance potentials.

No.	configuration	P(x)	A(x⁺)	I(x)
a	n-C_3H_7OH	0 eV	11.1 eV	I(n-C_3H_7OH) = 11.1 eV
b	$C_3H_6OH^+ + H$	11.1+2.9−3.6	10.8	
c	$C_3H_6 + H_2O$	0.4	14.8	$I(C_3H_6) = 10.0$
d	$C_3H_6 + O + H_2$	5.4		
e	$C_3H_6 + H + OH$	5.6		
f	$C_3H_5 + H_2 + OH$	4.2	14.6	$I(C_3H_5) \leq 10.4$
g	$C_3H_5 + H_2O + H$	3.5		
h	$C_3H_3 + 2H_2 + OH$	6.6	17.5	$I(C_3H_3) \leq 10.9$
i	$C_3H_3 + H_2O + H_2 + H$	5.9		
j	$CH_2OH^+ + C_2H_5$	10.1	11.1	
k	$C_2H_5 + CH + H_2O$	4.3	14.8	$I(C_2H_5) \leq 10.5$
l	$C_2H_5 + CH_2 + OH$	5.9		
m	$C_2H_4 + CH_3OH$	1.2	12.6	$I(C_2H_4) \leq 11.4$
n	$C_2H_4 + CH_2 + H_2O$	3.6		
o	$C_2H_3 + OH + CH_4$	3.8	14.8	$I(C_2H_3) \leq 11.0$
p	$C_2H_3 + H_2O + CH_2$	3.1		$I(C_2H_3) \leq 11.7$
q	3C+8H+O	39.5		

The difference between the observed value of the appearance potential $A(X^+)$ and the calculated value of the dissociation energy $P(X)$ gives the upper limit of the ionization potential. A summary of the results and their interpretation is also given in Table III. The discussion of some particular case will now be given.

1. $M/e = 60$

The appearance potential of the ion corresponding to this mass is $A(X^+) = 11.1 \pm 0.2$ eV. This could have been only the molecular ion.

$$I(\mathrm{nC_3H_7OH}) = A(\mathrm{nC_3H_7OH^+}) = 11.1\ \mathrm{eV}.$$

According to Mulliken's theoretical prediction non-bonding electrons of oxygen atom in the alcohol have the lowest ionization potentials of any of the electrons in the melecule by the charge transport effect. Let us assume that the ionization of the molecule represents the removal of one of these nonbonding electrons from the oxygen atom and the ionization potential remains constant as long as the molecular structure is not radically altered and that the value 11.1 eV is the ionization potential of the oxygen atom in the n-C_3H_7OH molecule. In the previous papers the similar assumption is justified by the experiment of the C_2H_5OH molecule.

As previously pointed out⁽³⁾, the ionization potential of the straight chain type hydrocarbon becomes smaller as the molecular weight increases. The ionization potential of the n-C_3H_7OH is 11.1 eV by the present work and the ionization potential of C_2H_5OH is 11.3 eV by Bleakney⁽⁶⁾, or 11.8 eV by the author. But the ionization potential of CH_3OH is the lower value as 10.8 eV given by Bleakney.

2. $M/e = 59$

The appearance potential of the ion corresponding to this mass is $A(X^+) = 10.8 \pm 0.2$ eV. This value is less than that of the parent molecular ion. If the C–H bond is broken when the oxygen atoms is ionized and becomes trivalent, this ion will appear.

For the energy to remove the hydrogen atom we shall use the value 2.9 eV assumed to be the strength of the first C–H bond in propane. For the difference between the C–O and C = O bond we shall use the value 3.6 eV the same as in the experiment of C_2H_5OH. For the ionization potential of the oxygen atom we shall use the value 11.1 eV found for the molecular ion. Then the appearance potential of $C_3H_6OH^+$ ion is $A(\mathrm{C_3H_6OH^+}) = 11.1 + 2.9 - 3.6 = 10.4$ eV. This is to be compared with the experimental value 10.8 eV. and can be considered to be in fairly good agreement.

If we assume that the O^+ is not trivalent, the upper process leads to the unreasonably low value $I(\mathrm{C_2H_5OH}) \leq 7.9$ eV.

3. $M/e = 42,\ 41$

The most parts of the ions corresponding to those masses may comprise no oxygen atom. If we assume that the $C_3H_6^+$ ion corresponds to $M/e = 24$, the process d is probable. If we assume that the $C_3H_5^+$ ion corresponds to $M/e = 41$, the process f is more probable than the process g. The former process leads to the value $I(\mathrm{C_3H_5}) \leq 10.4$ eV which is slightly higher compared with $I(\mathrm{C_3H_5}) \leq 9.7$ eV given by Delfosse and Bleakney.⁽⁷⁾

4. $M/e = 39$

The ion corresponding to this mass is the $C_3H_3^+$ ion. The value of $I(\mathrm{C_3H_3})$ given in either h or i process is about 2 eV higher than $I(\mathrm{C_3H_3}) < 9.0$ eV given by Bleakney.⁽⁷⁾

5. $M/e = 31$

The ion corresponding to this mass is the CH_2OH^+ ion. This ion is most abundant and its appearance potential is less than that of the parent ion. The only reasonable process is $\mathrm{nC_3H_7OH} \rightarrow \mathrm{CH_2OH^+} + \mathrm{C_2H_5}$. For the C–C bond energy in the n-C_3H_7OH molecule we shall use the value 2.5 eV assumed to be the C–C bond energy in propane. If we do not consider the trivalent property of O^+, the upper process leads to the unreasonably low value of $I(\mathrm{CH_2OH}) \leq 8.6$ eV. But considering the trivalent property of O^+ we can break the upper reaction down into the following chain only according to energy considerations.

a) $\mathrm{nC_3H_7OH} \rightarrow \mathrm{C_2H_4} + \mathrm{CH_3OH}$
b) $\mathrm{C_2H_4} + \mathrm{CH_3OH} \rightarrow \mathrm{CH_2OH^+} + \mathrm{C_2H_4} + \mathrm{H} + e$
c) $\mathrm{CH_2OH^+} + \mathrm{C_2H_4} + \mathrm{H} + e \rightarrow \mathrm{CH_2OH^+} + \mathrm{C_2H_5} + e$

The appearance potential will then be the algebraic sum of the energy involved in the three steps. The energy required for (a) is 1.2 eV. The energy required for (c) is -2.9 eV. According to Bleakney⁽⁶⁾ the energy required for (b) is 11.8 eV.

Then the calculated appearance potential is 10.1 eV and this is 1 eV lower than the experimental value. If this is true, the ion has the excess energy of 1 eV.

6. $M/e=29$.

The ion corresponding to this mass is chiefly considered to be the $C_2H_5^+$ ion. The process k leads to the reasonable value $I(C_2H_5)\leq 10.5$ eV. This value has the excess energy of 0.7 eV compared with $I(C_2H_5)\leq 9.8$ eV given by Bleakney.

7. $M/e=28$.

The appearance potential of this ion is 12.6 eV. The ion corresponding to this mass is the $C_2H_4^+$ ion, for the directly measured ionization potential of CO is 14.1 eV given by Tate.(8)

The energetically reasonable process is $nC_3H_7OH \rightarrow C_2H_4^+ + CH_3OH$ and this leads to the value $I(C_2H_4)\leq 11.4$ eV. The excess energy in this process 0.6 eV, for the ionization potential of the C_2H_4 molecule is 10.8 eV.

8. $M/e=27$.

The ion corresponding to this mass is the $C_2H_3^+$ ion. The processes O and p are both reasonable and the values $I(C_2H_3)$ in these processes are good agreement with the $I(C_2H_3)<11.2$ eV given by Bleakney.

§ 4. Conclusion.

The work reported here can be summarized briefly in the following way. The abundances and appearance potentials of the ions produced from the n-propyl alcohol by electron impact are measured. In the water type molecule like alcohol non-bonding electron of the oxygen atom is first locally ionized and then the C—C bond is easily broken satisfying the trivalent property of O^+. For this reason the CH_2OH^+ ion is most abundant in the n-C_3H_7OH like in the C_2H_5OH.

Moreover, the appearance potentials of the CH_2OH^+ and $C_3H_5OH^+$ ions are lower than the value of the parent molecular ion for the trivalent property of O^+. In fact, unless this concept is adopted, we are led to unreasonably low ionization potential and unsatisfactory interpretation of the result.

Our thanks are due to Dr. Y. Toriyama, Dr. S. Hamada and Dr. K. Yumoto for their kind guidances and encouragements.

We also wish to express our thanks to Mr. I. Kanomata, Mr. S. Kawamatsu and Mr. H. Tsuyama for their friendly cooperations.

References.

(1) T. Kambara and I. Kanomata: Nippon Butsuri Gakkaisi Vol. 4, No. 4 (1949).
(2) R. S. Mulliken: J. Chem. Phys. **3** (1935) 506.
(3) T. Kambara: J. Phys. Soc. Jap. **2** (1947) 25.
(4) F. D. Rossini: Nat. Bur. Stand. J. Research **13** (1934) 189.
(5) G. Herzberg: Molekülspectren u. Molekülstruktur. 1 (1939).
(6) C. S. Cummings II and W. Bleakney: Phys. Rev. **58** (1940) 787.
(7) J. Delfosse and W. Bleakney: Phys. Rev. **56** (1939) 256.
(8) Hagstrum and J. T. Tate: Phys. Rev. (1941) 354).

Dissociation and Ionization of iso-Propylalcohol by Electron Impact.

By Toyozo KAMBARA.

Hitachi Central Laboratory, Hitachi Ltd.

(Received June 28, 1949)

§ 1. Introduction.

In the previous papers(1) (2) we described the dissociation of ethyl and n-propylalcohol by electron impact. In the water-type molecule, like these alcohols, the non-bonding electrons of the oxygen atom have the lowest ionization potential by the charge transport effect.(3) When the oxygen atom in the molecule is ionized at first, the C—C bond next to the oxygen atom will be broken satisfying the trivalent property of O^+, for the C—C bond is weaker than that of the C—H bond.

Consequently the CH_2OH^+ ion is the most abundant one produced from the straight chain type alcohol as C_2H_5OH or n-C_3H_7OH. And the ion which is produced in the manner of knocking off the hydrogen atom from the parent molecule is also more abundant than the parent molecular ion.

Moreover the appearance potentials of these ions are lower than that of the parent molecular ion. These phenomena are considered to be due to the lowest ionization potential of the oxygen atom and the trivalent property of O^+.

In this paper we describe the dissociation of iso-propylalcohol by electron impact from the same viewpoint.

The apparatus and the experimental procedure are the same as previously described.(1)

The purification of the sample is as follows.

Takeda's iso-propylalcohol is dried with the cupric sulphate and twice distilled.

Its refractive index is $n_D^{25} = 1.3750$.

§ 2. Investigation on the Iso-propylalcohol.

The dissociation of the iso-C_3H_7OH molecule by electron impact may be different from the dissociation of the n-C_3H_7OH molecule, for the former has the CH_3 radical as the side chain.

The mass spectrum obtained with iso-C_3H_7OH is shown in Fig. 1. The abundances of the ions produced from the iso-C_3H_7OH are listed in the Table I.

It is reasonable for the structure of the iso-C_3H_7OH that the C_2H_4OH ion is most abundant, for the $C_2H_4OH^+$ ion should appear when the oxygen atom is first ionized and the C=C bond is broken.

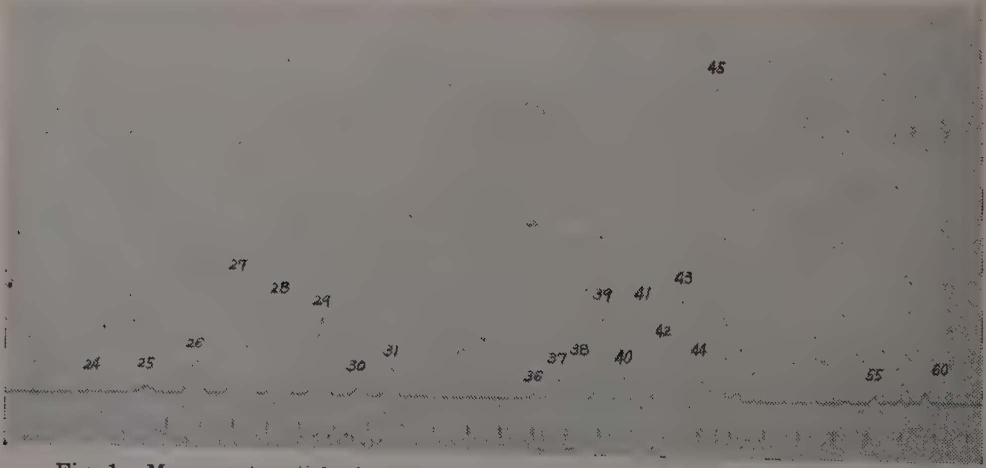

Fig. 1. Mass-spectrum obtained with iso-C_3H_7OH at the electron energy of 80 eV.

Moreover, in the iso-C_3H_7OH the ion corresponding to $M/e = 27$ is more abundant than the ion corresponding to $M/e = 28$.

The CH_3^+ ion from this molecule is also abundant than the same ion from the n-C_3H_7OH. But the abundanto of the ion corresponding to $M/e = 31$ in the iso-C_3H_7OH is less and its appearance potential is large compared with the same ion in the n-C_3H_7OH.

Table I. Nature and relative abundance of ions formed in iso-propylalcohol by electrons with 80 volts energy.

M/e	Ion	Abundance	
60	$C_3H_7OH^+$	1.00	0.17 %
59	$C_3H_6OH^+$	4.93	0.83
58	$C_3H_6O^+$	0.80	0.13
57	$C_3H_5O^+$	1.53	0.26
56	$C_3H_4O^+$	0.80	0.13
55	$C_3H_3O^+$	2.53	0.43
54	$C_3H_2O^+$	0.40	0.07
53	C_3HO^+	0.93	0.16
46	$C_2H_5OH^+$	3.60	0.61
45	$C_2H_4OH^+$	138.63	23.39
44	$C_2H_4O^+$, $C_3H_8^+$	9.00	1.52
43	$C_2H_3O^+$, $C_3H_7^+$	43.46	7.33
42	$C_2H_2O^+$, $C_3H_6^+$	23.46	3.96
41	C_2HO^+, $C_3H_5^+$	38.12	6.43
40	C_2O^+, $C_3H_4^+$	9.60	1.62
39	$C_3H_3^+$	35.86	6.05
38	$C_3H_2^+$	11.06	1.87
37	C_2H^+	8.00	1.35
36	C_2^+	1.27	0.21
32	CH_3OH^+	0.53	0.09
31	CH_2OH^+	11.46	1.93
30	CH_2O^+, $C_2H_6^+$	2.80	0.47
29	CHO^+, $C_2H_5^+$	32.93	5.56
28	CO^+, $C_2H_4^+$	43.32	7.31
27	$C_2H_3^+$	44.39	7.49
26	$C_2H_2^+$	13.46	2.27
25	C_2H^+	2.60	0.44
24	C_2^+	0.53	0.09
19	H_3O^+	15.46	2.61
18	H_2O^+	10.46	1.77
17	HO^+	3.20	0.54
16	O^+, CH_4^+	7.27	1.23
15	CH_3^+	31.59	5.33
14	CH_2^+	9.46	1.60
13	CH^+	2.60	0.44
12	C^+	6.33	1.07
2	H_2^+	9.73	1.64
1	H^+	9.46	1.60

Table II. Appearance potentials of the ions produced from iso-propylalcohol

M/e	Ion	Appearance potentials
60	iso-$C_3H_7OH^+$	— eV
45	$C_2H_4OH^+$	11.4±0.1
43	$C_2H_3O^+$, $C_3H_7^+$	14.4±0.1
42	$C_2H_2O^+$, $C_3H_6^+$	12.5±0.1
41	C_2HO^+, $C_3H_5^+$	15.0±0.2
39	$C_3H_3^+$	16.6±0.2
31	CH_2OH^+	17.0±0.2
29	$C_2H_5^+$, CHO^+	15.1±0.1
28	$C_2H_4^+$, CO^+	14.6±0.2
27	$C_2H_3^+$	16.1±0.1

The appearance potentials of the several abundant ions are measured. These are listed in Table II. But the appearance potential of the parent molecular ion could not be measured for its small abundance. The heat of combustion of the iso-C_3H_7OH is 479 Kcal/mole given by G. S. Parks & G. E. Moore.(4) The heat of vaporization is 9.6 Kcal/mole. Then the heat of formation is 68 Kcal/mole. The dissociation energy of the iso-C_3H_7OH to atoms in gaseous state is 39.64 eV by the same calculation as in the n-C_3H_7OH. Table III lists the energies $P(X)$ of various combinations of three carbons, one oxygen and eight hydrogen atoms at the normal state with respect to the combination iso-C_3H_7OH as zero. A summary of the results and their interpretation is also given in Table III.

The discussion of some particular cases will now be given.

1. *M/e* = 45.

The ion corresponding to this mass is the $C_2H_4OH^+$ ion. The only reasonable process to produce this ion is iso-$C_3H_7OH \rightarrow C_2H_4OH^+ + CH_3$. Now we can break this reaction down into the following chain according to energy considerations.

a) iso-$C_3H_7OH \rightarrow CH_2 + C_2H_5OH$
b) $CH_2 + C_2H_5OH \rightarrow CH^2 + H + C_2H_4OH^+ + e$
c) $CH_2 + H + C_2H_4OH^+ + e \rightarrow CH_3 + C_2H_4OH^+ + e$

The energy required for a) is 3.2 eV. According to the previous paper the energy required for b) is 11.8 eV.(2) The energy required for c) is −3.6 eV. Then the calculated appearance potential, the algebraic sum of the energy involved in the three steps, is 11.3 eV. This value is in very good agreement with the experimental value 11.4 eV.

Table III. Energies of dissociation of iso-propylalcohol into its constituents and interpretation of the appearance potentials.

No.	Configuration	P(x)	A(X+)	I(X)
a	iso C_3H_7OH	0 eV	— eV	—
b	$C_2H_4OH^+ + CH_3$	11.3	11.4	—
c	$C_3H_7 + OH$	2.8	14.4	$I(C_3H_7) \leq 11.6$
d	$C_3H_6 + H_2O$	0.5	12.5	$I(C_3H_6) \leq 12.0$
e	$C_3H_5 + H_2 + OH$	4.2	15.0	$I(C_3H_5) \leq 10.8$
f	$C_3H_5 + H + H_2O$	3.5		$I(C_3H_5) \leq 11.5$
g	$C_3H_3 + OH + 2H_2$	6.7	16.6	$I(C_3H_3) \leq 9.9$
h	$C_3H_3 + H_2O + H + H_2$	6.0		
i	$C_2H_5 + CH + H_2O$	4.4	15.1	$I(C_2H_5) \leq 10.7$
j	$C_2H_5 + CH_2 + OH$	6.0		
k	$C_2H_4 + CH_3OH$	1.3	14.6	
l	$C_2H_4 + CH_2 + H_2O$	3.7		$I(C_2H_4) \leq 10.9$
m	$CO + 2CH_4$	0.2		$I(CO) \leq 14.4$
n	$CO + C_2H_6 + H_2$	0.8		$I(CO) \leq 13.8$
o	$C_2H_3 + CH_3 + H_2O$	3.2	16.1	
p	$C_2H_3 + CH_4 + OH$	3.9		$I(C_2H_3) \leq 12.2$
q	$3C + 8H + O$	39.6		

2. *M/e* = 43.

The ion corresponding to this mass is more abundant than the same ion from the n-C_3H_7OH. From this fact both the $C_3H_7^+$ ion and the $C_2H_3O^+$ ion may be contained in this ion. If we assume that the appearance potential of this ion will be from the $C_3H_7^+$ ion, the only reasonable process *c* leads to the value $I(C_3H_7^+) \leq 11{,}6$ eV. But this value is 2 eV higher than $I(C_3H_7) \leq 9.0$ eV given by Bleakney.(5) If we assume that this appearance potential will be from the CH_3CO^+ ion, the following chain will be considered energetically.

a) iso $C_3H_7OH \rightarrow (CH_3)_2CO + H_2$

b) $(CH_3)_2CO + H_2 \rightarrow CH_3CO^+ + CH_3 + H_2 + e$

The energies required for a) and for b) are respectively 0.8 eV and 12.2 eV.(6) Then the appearance potential of the CH_3CO^+ is 13.0 eV. This value is about 1 eV lower than the experimental value.

3. *M/e* = 42, 41.

If we assume that the ion corresponding to *M/e* = 42 is the $C_3H_6^+$, we get the value $I(C_3H_6) \leq 12.0$ eV from the process *d*. This value is 2 eV higher than the directly measured ionization potential of the propylene $I(C_3H_6) = 10.0$ eV(5). If we assume that the ion corresponding to *M/e* = 41 is the $C_3H_5^+$, we get the value $I(C_3H_5) \leq 10.8$ eV from the process *e*. This value is 1.1 eV higher than the $I(C_3H_5) \leq 9.7$ eV given in propylene. In both cases we might consider about the ion $C_2H_2O^+$ and C_2HO^+.

4. *M/e* = 39.

The ion corresponding to this mass is the $C_3H_3^+$. The process *g* leads to the value $I(C_3H_3) \leq 9.9$ eV which is about 1 eV higher than the value $I(C_3H_3) \leq 9.0$ eV from the propane.

5. *M/e* = 29.

If we assume that the ion corresponding to this mass is the $C_2H_5^+$ ion, the process *i* may be most probable. The value $I(C_2H_5) \leq 10.7$ eV led from this process is about 1 eV higher than the value $I(C_2H_5) \leq 9.8$ eV from the propane.

6. *M/e* = 28.

The abundance of the ion corresponding to this mass is small in this molecule compared with the same ion in the n-C_3H_7OH. As above mentioned the appearance potential of this ion is that of the $C_2H_4^+$ ion in the n-C_3H_7OH. But in this molecule the appearance potential of the ion corresponding to this mass is 14.6 eV which is larger compared with the value $I(CO) = 14.1$ eV(7). If we assume that this ion is $C_2H_4^+$, the process *l* not *k* is the most probable process and this gives $I(C_2H_4) \leq 10.9$ in good agreement with the directly measured value $I(C_2H_4) = 10.8$ eV. If we assume that this ion is CO^+, the process *m* or *n* may be most probable and this gives $I(CO) \leq 14.4$ eV or 13.8 eV respectively.

7. *M/e* = 27.

The ion corresponding to this mass is the $C_2H_3^+$

ion. The process p in this molecule, the same as in the n-C_3H_7OH, is the most probable process and this gives the value $I(C_2H_3) \leq 12.2$ eV which is 1 eV higher than the value $I(C_2H_3) \leq 11.2$ eV given by Bleaknay.

§ 3. Conclusion.

The work reported here can be summarized briefly in the following way. The abundances and appearance potentials of the ions produced from the iso-propylalcohol by electron impact are measured. In the water type molecule like alcohol the non-bonding electron of the oxygen atom is first locally ionized and then the C−C bond is easily broken satisfying the taivalent property of O^+. For this reason the CH_2OH^+ ion is the most abundant one in the n-C_3H_7OH as previously described, but on the iso-C_3H_7OH the $C_2H_4OH^+$ ion is most abundant for the side-chain structure.

Moreover the appearance potentials of these ions are lower than the value of the parent molecular ions for the trivalent property of O^+. This concept seems to be sure not only in the normal alcohol, but also in the iso-type one. In fact, unless this concept is adopted, we are led to unreasonably low ionization potentials and unsatisfactory interpretation of the results.

Our thanks are due to Dr. Toriyama, Dr. S. Hamada and Dr. K. Yumoto for their kind guidance and encouragements.

We also wish to express our thanks to Mr. I. Kanomata, Mr. S. Kawamatsu and Mr. H. Tsuyama for their friendly cooperations.

Reference.

(1) T. Kambara: J. Phys. Soc. Jap. **5** (1950) 31.
(2) T. Kambara and I. Kanomata: Nippon Butsuri Gakkaisi. Vol. 4, No. 4 (1949).
(3) R. S. Mulliken; J. Chem. Phys. **3** (1935) 506.
(4) G. S. Parks and G. E. Moore: J. Chem. Phys. **7** (1939) 1066.
(5) J. Delfosse and W. Bleakney: Phys. Rev. **58** (1940) 787.
(6) T. Kambara: J. Phys. Soc. Jap. **5** (1950), No. 2. (in printing)
(7) Hagstrum and J. T. Tate: Phys. Rev. **59** (1941) 354.

The Time in which Equilibrium State of Auditions is Established. Part. I. The Damping Constant of the Inner Ear.*

By Yasuo MAKITA
The Research Institute of Acoustical Science, Osaka University.
and
Shin-ya MIYATANI.
The Research Institute of Science and Technology, Tokyo University.

(Received July 4, 1949)

Introduction

The time in which equilibrium state of audition is established, consists of two parts, one of which is due to the mechanical systems of the ear and the other is due to the nerve systems. In order to make clear the transient nature of auditory sensation, it is necessary to specify the time constants of these different systems.

Since Helmholtz made the experiments⑴ on the damping constant of the ear, a number of investigations⑵ have been conducted on this subject. It is, however, difficult to measure these values directly. It may, therefore, be valuable to make other contributions on this problem in order to increase reliablity of the results so far obtained.

---

* Presented at the meeting of the Acoustical Society of japan, November 15, 1947.

To find a damping constant of a vibrating system, there are two ways in general; measuring the resonance curve and the transient character. So far as the damping constant of the ear is concerned, the latter method has been often successfully used.

In the present paper, the results of calculation of the damping constant of the ear as a mechanical system are described, under the same assumption of the distribution of stimulus along the basilar membrane when a given pure tone is heard, as that was used in the previous paper(3) in which the relation between the differential pitch sensitivity and the differential intensity sensitivity was derived.

The numerical magnitude of the damping constant calculated, is consistent with the experimental results so far obtained and with our results by a new method which will be published in other paper.

Stimulus on the Basilar membrane Caused by a Pure Tone

In order to throw some light on the general nature of the masking effect of noise, the following empirical formula was found in our previous paper(4) to hold for the masking curve obtained by R. L. Wegel and C. E. Lane,(5) except for the frequency ranges near by that of the masking tone and its subjective harmonics,

$$M=\sum_i A(if_0,\alpha)\left(\frac{f_r}{if_0}\right)^{\mu}. \qquad (1)$$

Symbols in this formula have following meanings:

f_r: frequency per second of the masked tone

f_0: frequency per second of the masking tone,

M: threshold shift of the masked tone in decibels,

i: the ordinal number of subjective harmonics,

$A(if_0,\alpha)$ and μ; constants depending upon the sensation level of the masking tone and for the range $f_r < if_0$ or $f_r > if_0$, μ takes different values, n_{if_0} or $-{}_2n_{if_0}$ respectively. Table I shows the values of μ and $A(if_0, \alpha)$ obtained from Wegel-Lane's observations.

Table I.

$F_{req.}\ f_0$	d_s ^{db}	$A(f_0; \alpha)$	μ	
			$_1n_{f_0}$	$_2n_{f_0}$
200	60	53	2.0	—
200	80	70	1.6	—
400	40	30	3.9	1.8
400	60	49	3.2	—
400	80	63	2.3	—
800	40	38	4.6	3.5
800	60	50	4.6	—
800	80	77	4.6	—
1200	40	40	5.2	5.6
1200	60	55	5.2	—
1200	80	75	5.2	—
2400	40	30	4.6	6.3
2400	60	52	4.6	—
2400	80	80	4.7	—
3500	40	37	3.4	—
3500	60	58	2.8	—
3500	80	62	2.5	—

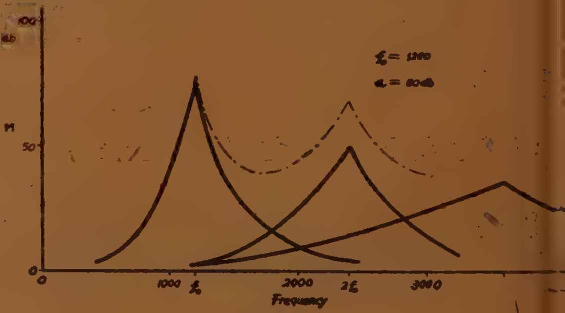

Fig. 1.

Fig. 1 shows an example of the curve calculated from the formula (1).

If it is assumed that M in the formula (1) represents the distribution of stimulus of a given tone of the frequency f_0 and the sensation level α at the position of f_r on the basilar membrane,(6) and that such a distribution of stimulus may be simply considered to take place by a great number of resonators changing their character continuously and being arranged in corresponding order along the basilar mambrane, we can easily calculate the damping constant of the inner ear.

Derivation of the Damping Constant of the Inner Ear

The mechanical parts of the inner ear including the fluid of the labyrinth, are generally considered to form a continuous and highly damped resonance system. But this continuous system is able to be replaceable by many discrete resonator distributed along the basilar membrane. Then, the damping constant of these assumed resonators can be deduced as follows.

In general, when a resonance curve of a simple resonance system was obtained, the damping constant or Q of the system can be calculated from the following well-known formula,

$$\frac{i_r^2-i_0^2}{i_0^2}=Q^2\left(\frac{f_r}{f_0}-\frac{f_0}{f_r}\right)^2, \tag{2}$$

where i_r is a quantity equivalent to the current at resonance for simple electrical resonance circuit, i_0 the current when the system is excited with an e.m.f. of frequency f_0 deviated from the resonance frequency f_r and Q is the quantity inversely proportional to the logarithmic decrement of the system.

Changing the form of the Eq. (2), we obtain

$$20\log\frac{i_0}{I}=10\log\left(\frac{i_r}{I}\right)^2\left\{Q\left(\frac{f_r}{f_0}-\frac{f_0}{f_r}\right)^2+1\right\}^{-1}, \tag{3}$$

where I is an arbitrary constant.

When the sensation level α of a pure tone is lower than 40 db and the frequency of it is higher than about 400, the subjective harmonics become negligibly small, so that the Eq. (1) can be written as follows.

$$M=A(f_0,\alpha)\left(\frac{f_r}{f_0}\right)^{\mu} \tag{4}$$

Thus, M in the formula (4) represents the magnitude of excitation expressed in decibels, given to the resonator at f_r by the pure tone of which frequency is f_0 and the sensation level α. $A(f_0,\alpha)$ is the value of M when f_0 is equal to f_r. Accordingly, we may express (4) by the following form,

$$20\log\frac{s_0}{S}=20\left(\frac{f_r}{f_0}\right)^{\mu}\log\frac{s_r}{S} \tag{5}$$

where s_0 and s_r are the velocity amplitude of the two resonators situated at the position designated by f_r and f_0 respectively under the exciting force of frequency f_0 and S is the velocity amplitude of each resonator corresponding to the threshold.

Comparing the Eq. (5) with the Eq. (3), we can take $20\log(i_0/I)$ as equivalent to M and $10\log(i_r/I)^2$ to $A(f_r,\alpha)$ (nearly equal to $A(f_0,\alpha)$ experimentally).

Since, however, any quantity of excitation of an assumed resonator in the ear smaller than that corresponding to the threshold will be observed as equal to the threshold value in the observation of masking effect, in other words, when the difference between f_r and f_0 becomes larger, the value of the Eq. (5) tends to null or s_0 tends to S, whereas i_0 tends to null.

It must be noted, therefore, that the substitution of M for $20\log(i_0/I)$ would be valid for the range in which the value of f_0/f_r or f_r/f_0 does not exceed about 4.

Putting M and A into (3), the following equation can be obtained.

$$M=A-10\log\left\{1+Q^2\left(\frac{f_r}{f_0}-\frac{f_0}{f_r}\right)\right\}. \tag{6}$$

From (4) and (6), we can express Q in terms of f_r, f_0, and A, namely

$$Q^2=\frac{10^{\frac{A}{10}(1-(f_r/f_0)^{\mu})}-1}{\left(\frac{f_r}{f_0}-\frac{f_0}{f_r}\right)^2}\doteqdot\frac{10^{\frac{A}{10}(1-(f_r/f_0)^{\mu})}}{\left(\frac{f_r}{f_0}-\frac{f_0}{f_r}\right)^2}. \tag{7}$$

When $\Delta f=|f_r-f_0|$ is small and $\Delta f/f_0<1$, we obtain the equation (8) neglecting the higher order of $\Delta f/f_0$,

$$Q^2=\frac{10^{\frac{\mu A\Delta f}{10f_0}}-1}{\left(2\frac{\Delta f}{f}\right)^2} \tag{8}$$

In order to simplify the result, we apply the following relation between the differential pitch sensitivity and the differential intensity sensitivity,(7)

$$A(f_0,\alpha)\ \mu\ (\Delta f/f_0)=10\log\left(1+\Delta J/J\right) \tag{9}$$

Putting (9) into (8), we obtain the simple relation between Q, $\Delta J/J$, and $\Delta f/f_0$, that is

$$Q=\frac{\sqrt{\Delta J/J}}{2\ \Delta f/f_0} \tag{10}$$

Numerical Calculation

We can calculate numerically the damping constant of the ear from the Eq. (7) and (8). Here it must be remembered that the mechanism of the inner ear is not so simple as we assumed, but it is composed of continuous systems. The mechanical resonance systems resposible for each tone in the audible frequency range are not discrete nor isolated, with the result that, the characteristic distribution of stimulus along the basilar membrane such as assumed may occur.

In the course of the numerical calculation, therefore, the damping constant of an assumed resonator at f_r should be given as an averaged value of what are obtained from (7) for different f_0, in other words, for different exciting frequencies.

Table II shows the value of Q and the logarithmic decrement δ, which are calculated from (7) using the values of A and μ in Table I.

Table III shows the Q and δ calculated from the Eq. (10) when f_r and f_0 are nearly equal, using the values of $\Delta J/J$ given by R. R. Riesz(8) and $\Delta f/f_0$ given by E. G. Shower and R. Biddulph.(9)

Table II.

f_r	f_0	$A(f_r, \alpha)$	μ	Q	mean	$\delta = \frac{\pi}{Q}$
400	800	30	4.6	19.6	19.4	0.16
400	1200	30	5.2	19.1		
800	1200	38	5.2	56.1	42.6	0.074
800	2400	38	4.6	29.0		
1200	400	40	−1.8	20.4	22.9	0.14
1200	800	40	−3.5	38.2		
1200	2400	40	4.6	10.0		
2400	800	30	−3.5	8.7	14.4	0.22
2400	1200	30	−5.6	20.0		
3500	1200	37	−5.6	27.0	43.0	0.073
3500	2400	34	−6.3	59.0		

Table III.

f_r	α	Q	δ
200	5	20	0.15
500	40	44	0.07
1000	5	54	0.06
1000	40	61	0.05
4000	5	73	0.04
4000	40	74	0.04

Conclusion

The empirical formula which holds for the masking curve of pure tones obtained by Wegel and Lane was assumed to represent the distribution of stimulus along the basilar membrane by the masking tone. Using this distribution function, the damping constant of the inner ear was calculated. The results obtained show rather good agreement with the experimental results so far obtained: the logarithmic decrement is about 0.1.

The relation between Q, $\Delta J/J$, and $\Delta f/f_0$ was also derived. The value of Q calculated from this relation into which the value of $\Delta J/J$ and $\Delta f/f$ were substituted, seems to be somewhat smaller. But as far as the order of magnitude is concerned, the assumed mechanism of hearing seems to offer the reasonable explanation for the sharp discrimination of frequency, in spite of the large damping constant.

In conclusion, the authors wish to express their hearty thanks to the late Prof. J. Obata for his kind suggestion throughout this work and they also have a pleasure to acknowledge the receipt of a grant in aid for the scientific research from Ministry of Education.

References.

(1) H. L. F. Helmholtz: Sensation of tone (trans. by A. J. Ellis) pp. 142–144, 4 ed. (1912).
(2) H. Barkhausen und G. Lewicki: Phys. Zeit., **25** (1924) 537.
G. V. Bekesy: Phys. Zeit., **22** (1928) 793.
30 (1929) 114.
Ann. d. Phys., **16** (1933) 845.
C. S. Hallpike, H. Hartridge, and A. F. Rawdon-Smith: Proc. Roy. Soc. London, B **122** (1937) 177.
S. Lifshitz: J. A. S. A., **7** (1936) 217.
5 (1933) 31.
W. Bürck, P. Kotowsky, and H. Lichite: E. N. T., **12** (1935) 278.
12 (1935) 355.
U. Steudel: Hochfrequenztechnik u. Elektroakust., **41** (1933) 116.
R. S. Hunt: J. A. S. A., **14** (1942) July.
W. A. Munson: J. A. S. A., **19** (1947) 584.
W. R. Garner: J. A. S. A. **19** (1947) 600.
R. H. Pumphrey: Nature, **160** (1947) 124.
(3) Y. Makita: Proc. Physich-Math. Soc. Japan, **24** (1942) 510.
(4) J. Obata, Y. Makita, and Y. Munetomo: Proc. Physico-Math. Soc. Japan, **25** (1943) 504, 511, 553.
(5) R. L. Wegel and C. E. Lane: Phys. Rev., **23** (1924) 266.
(6) H. Fletcher: Rev. Mod. Phys., **12** (1940) 47.
(7) Y. Makita: ibid.
(8) R. R. Riesz: Phys. Rev., **31** (1928) 861.
(9) E. G. Shower and R. Biddulph: J. A. S. A., **3** (1931) 275.

The Time in which Equilibrium State of Auditory Sensation is Established. Part II. The Time Constant of Building up or Decay of Auditory Sensation at the Threshold*.

By Yasuo MAKITA

The Research Institute of Acoustical Science, Osaka University.

and

Shin-ya MIYATANI.

The Research Institute of Science and Technology, Tokyo University.

(Received July 4, 1949).

Introduction.

In the previous paper(1), the authors reported the result of calculation of the damping constant of the inner ear, by assuming the distribution of stimulus on the basilar membrane when a pure tone was allowed to hear. It is then interesting to inquire into the time required in which equilibrium state of auditory sensation is established as a whole. This time is effected not only by the mechanical properties of the ear, but also would be effected by integral mechanism of nerve impulses in central nerve systems.

One of the authors experienced previously that the probability of perception of a tone of short duration, the intensity of which being in fluctuating region of the minimum audible threshold, was greater when the tone was allowed to hear with a short interval after another weak tone of short duration and the same frequency than otherwise(2). This phenomenon is reasonably understood by assuming the existence of the integral mechanism in the central nerve system.

In order to make clear the nature of the mechanism the investigation on the threshold of a tone of short duration and of interrupted tones was projected before the end of this war and completed in September, 1947. While the results in this paper are partly the same as those published recently by W. A. Munson(3), they may serve as the verification of the reproduciblity of the resluts.

I. The Threshold of a Tone of Short Duration.

It has been well known that the loudness of a tone decreases, in spite of its amplitude being kept constant, as the duration of the tone diminished. G. v. Békésy(4) has obtained the following relation between the loudness level α of tones and their duration t seconds,

$$\alpha = k \log t + c \qquad (1)$$

S. Lifshitz(5) has also found that the following relation holds between the apparent duration and the sensation level L,

$$Lt = k \qquad (2)$$

where k is constant.

These two relations may have close connection with the integral mechanism of auditory nerve system, but they do not show it explicitly. We measured, therefore, the amount of increase in intensity of a tone necessary to be just perceived when its duration diminished, for the purpose of obtaining the direct relation that would show the nature of building up or decay of the auditory sensation as a function of time. There were two reasons why we adopted the measurement of threshold instead of the loudness comparison; the first was that the probable error of the measurement of threshold was less than that of the loudness comparison,(6) the second was that the effect of adaptation hardly appears at threshold(7).

Experimental Procedure.

The experiments were carried out in a dead room (of about 6×5×3 cubic meters), a subject being situated in the sound field established at a distance of two meters in front of a dynamic loud speaker which was in a plane of one of the walls.

---

* Presented at the meeting of the Acoustical Society of Japan, November 15, 1947.

Shift of the threshold of the subject expressed in decibels, owing to shortening the duration of a tone, was measured by the following procedure. In the first place, a pure tone of 1000 cycles per second and of a given intensity sufficient to be perceptible was allowed the subject to listen with the duration of t seconds, by the key of the trigger circuit operated by the observer or the operator in the separated room while the intensity of the tone being reduced in one db steps by means of an attenuator. The observer worked at the key five times with irregular intervals of about two seconds at every attenuator setting.

The subject was provided with a push button which lighted a small electric lamp before the operator whenever and so long as the tone was perceived.

The observer was thus reducing the intensity of the tone and recorded the number of the tone exactly perceived in five interrupted tones at every attenuator setting, until the subject could no longer hear the tone. Then, the observer was increasing the intensity of the tone following the reverse procedure. Fig. (1) shows an example of the result obtained by these procedure. The numbers of exact responses are shown on the ordinate and the value of attenuation on the abscissa. The value of attenuation β correspondidg to the stage where the keying of 2.5 times in five were exactly perceived was taken as the value of threshold for the tone of duration t.(8).

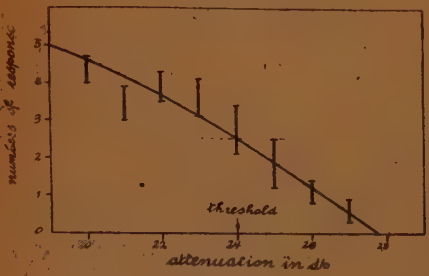

Fig. 1.

The values of β were measured for the different duration of the tone ranging from one second to 0.03 seconds on the three subjects. The amplitude of the tone at each attenuator setting was inspected to be unchanged irrespective of its duration by means of a moving coil microphon, an amplifier and a braun-tube oscillogragh.

Although the measurements were also performed using a telephone receiver instead of the dynamic speaker in order to inquire the effect of the reverberation of the dead room, even if it was very small, upon the experimental results, the difference of the results obtained by these two procedure was proved to be in the probable error of the experiment.

Results.

Let be denoted the reading of the attenuator setting at threshold as β_0 and β corresponding to tones of which durations are long enough and of t seconds respectively. Furthermore, let the intensity* of sound field established when the attenuator settings are β_0 and β be I_0 and I respectively.

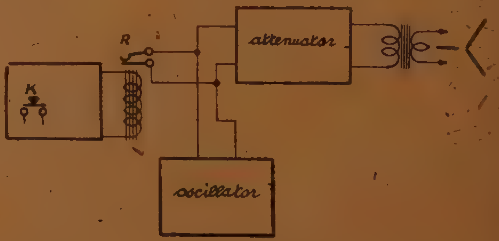

Fig. 2 (a).

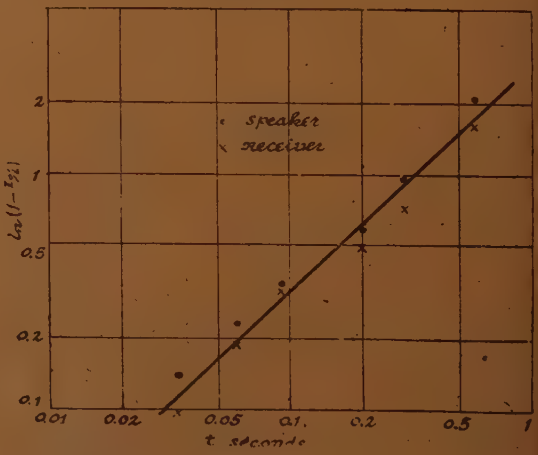

Fig. 2 (b).

---

* The term intensity used in this paper means that which is measured when the tone was kept on continuously.

Then, the following relation holds between them,

$$l_n\left(1-\frac{I_0}{I}\right) = \left(1-10^{\frac{\beta_0-\beta}{10}}\right). \tag{3}$$

The values of β_0 and β obtained for three subjects by the experimental procedure aforesaid were averaged and substituting them in the Eq. (3) the values of $ln\left(1-\frac{I_0}{I}\right)$ for corresponding duration of t seconds were calculated. Thus, Fig. 2 (b) shows that the following linear relation holds between $ln\left(1-\frac{I_0}{I}\right)$ and t,

$$ln\left(1-\frac{I_0}{I}\right) = -t/\tau$$

or

$$I\left(1-e^{-\frac{t}{\tau}}\right) = I_0 \tag{4}$$

where τ is a constant of value 0.2–0.4 sec. satisfying the experimental results.

Eq. (4) in other words means that the amount of sensation caused by a tone of duration t and of intensity I, is built up with the time contant τ after the starting of the tone and that the tone is not perceptible until the sensation builds up within the duration to the same value as is caused by the tone of intensity I_0, the intensity of threshold when the tone is kept on with long duration.

The time constant τ may, therefore, be taken as the time necessary in which auditory stimulation grows up to the value $1/e$ times the equilibrium state of stimulation owing to both the mechanical systems of the ear and the integrating character of the central nerve system. The time constant due to the mechanical systems of the ear, however, have generally been accepted as being a value smaller than about 0.06 seconds as described in the previous paper. Accordingly, the time constant τ obtained above may almost entirely ascribed to the central nerve systems.

Another statement is, therefore, capable concerning the integrating mechanism of nerve impulses, from which Eq. (4) can be reasonably deduced. If it is assumed that the number of nerve impulses sent to the cortex in unit time is proportional to the intensity of sound for the range above the thrshold of nerve impulses and that each impulse has the constant life time c in the cortex, then the rate of increase in the amount of nerve impulses integrated, comes to be equilibrated with the rate of decrease in the amount of nerve impulses by fading away. This statement can be mathematically expressed in the following.

Let the number of nerve impulses sent to the cortex in unit time due to the tone of intensity I be denoted by N, then the following relation holds between N and I;

$$N = kI.$$

where k is a positive constant for the range above the threshold of nerve impulses. Furthermore, the effective energy delivered by one nerve impulse is denoted by A and the time during which A decays to $1/e$ times of the first value, by τ. Thus we may write the amount of the integrated stimulation S at any instant t seconds after the presentation of the tone as follows,

$$S = \int_{t=0}^{t_0} ANe^{-\frac{t_0-t}{\tau}}$$

$$= AkI\int_{t=0}^{t_0} e^{-\frac{t_0-1}{\tau}}\,dt = AkI\tau\left(1-e^{-\frac{t_0}{\tau}}\right) \tag{5}$$

As already mentioned, the intensity of the tone just perceptible when it is sounded with infinitely long duration was denoted by I_0, Substituting I_0 in Eq. (5), we obtained S_0 corresponding to I_0, i. e.

$$S_0 = AkI_0\tau \tag{6}$$

We may, hence, deem that S_0 would represent the state of stimulation which is just perceptible, From Eq. (5) and Eq. (6) it is reasonably concluded that the intensity of a tone, duration of which is t seconds, must be increased as much as is given by the following relation in order that the tone may be perceptible,

$$AkI\tau\left(1-e^{-\frac{t}{\tau}}\right) \geqq AkI_0\tau$$

or

$$I\left(1-e^{-\frac{t}{\tau}}\right) \geqq I_0 \tag{7}$$

In the case of the threshold, we take

$$I\left(1-e^{-\frac{t}{\tau}}\right) = I_0 \tag{8}$$

Eq. (8) is identical with Eq. (4) obtained experimentally.

II. Threshold of Interrupted Tones.

In order to critisize the validity of Eq. (4) or Eq. (8) which are based on the assumption of the integral mechauism of nerve impulses sent to the central nerve system, we derived the expression for the intensity I of an interrupted tone just perceptible, in terms of the duration of the tone T_1 and that of silence T_2 from the Eq. (5) and compared it with the experimental results.

Let the instant an interrupted tone is allowed to hear, be the origin of time and consider the progress of the amount of stimulation in the central nerve system under the assumption of the integral mechanism of nerve impulses. Fig. (3) shows the assumed progress of the amount of stimulation with the elapse of time.

Let $S_1, S_2, \dots S_n, \dots S_\infty$, be the amount of stimulation at the time T_1, $2T_1+T_2, \dots +nT_1(n-1)T_2, \dots \infty$ respectively. Then, the mathematical expression of the progress shown in Fig. 3 can be easily derived from Eq. (5) as follows

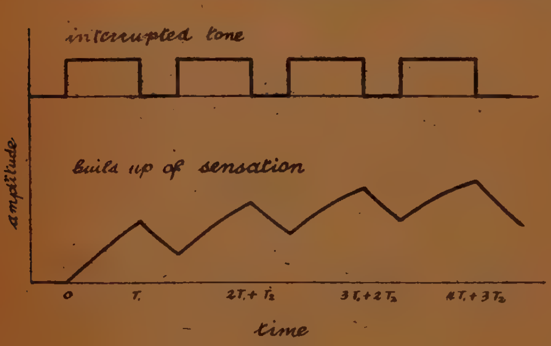

Fig. 3.

$$S_1 = AkI\tau(1-e^{-\frac{T_1}{\tau}})$$

$$S_2 = S_1(1+e^{-\frac{T_1+T_2}{\tau}})$$

$$\vdots$$

$$S_n = S_1(1+e^{-\frac{T_1+T_2}{\tau}}+e^{-\frac{2(T_1+T_2)}{\tau}}+\dots+e^{-\frac{(n-1)(T_1+T_2)}{\tau}})$$

$$S_\infty \doteqdot \frac{S_1}{1-e^{-\frac{T_1+T_2}{\tau}}} = \frac{AkI\tau(1-e^{-\frac{T_1}{\tau}})}{1-e^{-\frac{T_1+T_2}{\tau}}} \qquad (9)$$

Thereby, in order that the interrupted tone be perceived, the following condition must hold,

$$S_\infty \geqq AkI_0\tau\,, \qquad (10)$$

For the threshold of the interrupted tone, we take

$$S_\infty \doteqdot AkI_0\tau\;;$$

or

$$\frac{I(1-e^{-\frac{T_1}{\tau}})}{1-e^{-\frac{T_1+T_2}{\tau}}} = I_0\,. \qquad (11)$$

There are two special case which Eq. (11) should satisfy; one of them is the case when T_2 vanishes, the other is the case of the threshold of a tone of short duration, viz. the case when T_2 proceeds to infinity. It is really shown that in the former case, Eq. (11) is identical with $I = I_0$ consistent with our definition of I_0 and in the latter Eq. (11) is identical with Eq. (4) or Eq. (8).

Experimental Procedure.

In order to secure the validity of Eq. (11), we carried out the measurement of the threshold of a tone of 1000 c.p.s. interrupted after the manner of on-duration T_1 and off-duration T_2 being varied.

The procedure of the measurements was analogous to that mentioned in section I, except that the arrangements for generating a tone of short duration, i. e. the trigger circuit and the relay were replaced by a rotary electric motor. As is shown in Fig. (4), the switching device is composed of the same two metallic cylinders arranged adjacently on the motor shaft, and two brushes contacting with these cylinders respectively. The semi-circular surface of each cylider is inlayed with insulating material for instance bakelite and their position can be adjusted independently around the shaft of the driving motor.

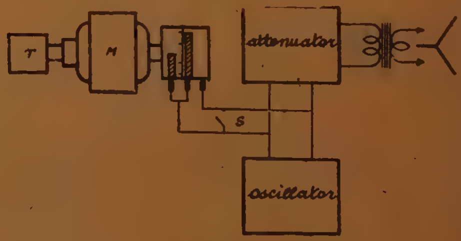

Fig. 4.

When either of the two brushes comes to contact with the insulating part of the corresponding cylinder, the output of the oscillator 0 being short circuited, the tone is stoped. On the other hand, the tone is kept on while both brushes are insulated at the same time. On-duration T_1 and off-duration T_2 could be, thus, adjusted by means of adjusting the number of revolution of cylinders and their relative position around the axis. Another switch S is inserted parallel with the rotating switches which is operated by the observer in order to measure the threshold by the same procedure described in section I.

The results, thus far obtained, being T_1 kept constant at the value of 0.057 seconds and $T_1/(T_1+T_2)$ varied from 0.01 to 1, are shown in Fig. (5). Here the abscissa shows the value of $T_1/(T_1+T_2)$ and the ordinate the value of $10 \log I/I_0$. Three curves in Fig. (5) are obtained by calculating from the following equation derived from Eq. (11) for three different values of τ: 0.57, 0.28 and 0.19.

$$10 \log (I/I_0) = 10 \log \left(\frac{1-e^{-\frac{T_1+T_2}{\tau}}}{1-e^{-\frac{T_1}{\tau}}} \right) \qquad (12)$$

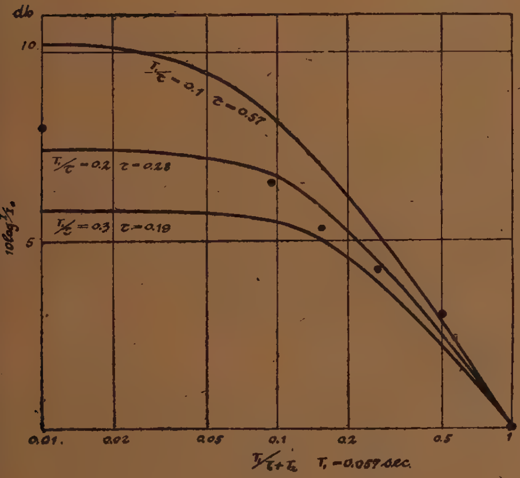

Fig. 5.

The dots represent the observed values averaged for three subjects being nearly on the curve 2 which is obtained by calculating in the case of $\tau = 0.28$. With the result we may be sure that Eq. (11) obtained by assuming the integral nature of nerve impulses in the central nerve system holds also in the case of interrupted tones as reasonably as a tone of short duration. Moreover the time constant τ obtained in section I and section II take almost equal value of 0.2–0.4 seconds.

Conclusion.

1) The intensity I of the tone of short duration t (0.03–1 sec.) just perceived was measured and was obtained Eq. (4), the relation between I and t which could be derived on the assumption of the integral nature of nerve impulses in the central nerve system.

2) It was shown that the value of the time constant of auditory sensation was 0.2–0.4 sec. which would be almost entirely ascribed to the integral mechanism of nerve impulses in the central nerve system and that τ meant the life time of one nerve impulse in the central system.

3) Results concerning the threshold of the tone of short duration was consistent with those of W. A. Munson except that the adaptation phenomenon did not appear in the present observation on account of the experiment being confined to the threshold measurement.

4) The result of G. v. Békésy, Eq. (1), can be derived by expanding Eq. (4) in power series of t and neglecting the terms of the higher order of t.

5) The just perceptible intensity I of interrupted tones of on-duration T_1 seconds and off-duration T_2 seconds was measured and it was shown that Eq. (11) held between I, T_1, and T_2. Eq. (11) was also derived on the same assumption of the integral nature of nerve impulses, the time constant obtained in this case being consistent with that obtained in connection with a tone of short duration. The parts of result of W. R. Garner⁽⁵⁾ may be summarized in Eq. (11).

6) Stimulation S may be transformed to sensation L by the operator T; for the range in which Fechner's law holds T is logarithm.

The authors wish to express their hearty thanks to the late Prof. J. Obata for his helpful suggestions and also have a pleaure to acknowledge the receipt of grants in aid for scientific research from Ministry of Education.

References.

(1) Y. Makita and S. Miyatani: J. Phys. Soc. Japan **5** (1950) 39.
(2) Y. Makita: unpublished.
(3) W. A. Munson: J.A.S.A., **19** (1947) 584.
(4) G. v. Békésy: Phys. Zeit., **30** (1927) 721.

(5) S. Lifshitz: J.A.S.A., **7** (1936) 213.
(6) J. C. Steinberg and W. A. Munson: J.A.S.A., **8** (1936) 71.
(7) G. v. Békésy: Phys. Zeit., **30** (1929) 115.
(8) S. Lifshitz: J.A.S.A., **11** (1939) 118.
(9) W. R. Garner: J.A.S.A., **19** (1947) 600.

On the Paramagnetic Susceptibilities of Some Polynuclear Complex Salts.

By Kenjiro KAMBE.

Faculty of Science, University of Tokyo

(Received Aug. 2, 1949)

§ 1. Introduction.

In the extensive experimental work on the magnetic susceptibilities of various salts, L. A. Welo[1] has measured the atomic paramagnetic susceptibilities χ_a of a number of polynuclear salts containing 3 atoms of iron or chromium. These measured χ_a obey the Curie-Weiss law in the temperature range used by his experiment; from the solid CO_2 temperature (about $-70°C$) up to the room temperature. The Curie-Weiss law is expressed by the formula

$$\chi_a = C/(T-\theta), \qquad (1)$$

where C and θ are constants for given salts, and T is the absolute temperature. As to the polynuclear salts in question, the values of C are the same as found with simple salts of iron or chromium, but the values of θ are large and negative. Among many results of Welo's measurements some typical examples are shown in the Table I. In this table reference numbers of salts are those used in the Welo's paper.

In the Welo's paper, large negative values of θ were explained by the electrostatic couplings between the iron and chromium ions, which were assumed to have permanent electric dipole moments, and the neighboring organic groups, which were also assumed to be permanent electric dipoles.

In this paper more reasonable explanations are suggested on the quantum-mechanical grounds. Ferromagnetic substances have paramagnetic susceptibilities obeying formula (1) above the curie-point, but in this case the values of θ are generally positive. In the theory of ferromagnetism θ are connected with the exchange integral which is positive for ferromagnetic substances. In analogy to this facts, we attempt to explain large negative values of θ by the exchange interaction between iron or chromium ions in a molecule, assuming the negative exchange integral.

§ 2. Assumptions.

To make the quantum mechanics applicable, we make the following assumptions concerning the structure of these salts.

(1) Metallic atoms in a molecule, Fe and Cr, are in the forms of ions, Fe^{3+} and Cr^{3+}. (2) All these ions are in S state. Fe^{3+} ions are in $S_{5/2}$ state. The ground state of Cr^{3+} ions in free state is ${}^4F_{3/2}$, but on account of the very strong electrostatic interactions between this and the neigh-

Table I. Atomic susceptibilities at 20°C, and constants C and θ.

No.	Salts	$\chi_a \times 10^6$ (20°C)	C	θ
1	$1/3[Fe_3(CH_3COO)_6(OH)_2]NO_3+6/3H_2O$	19.13	4.10	-577
4	$1/3[Fe_3(CH_2ClOO)_6(OH)_2]NO_3+5.5/3H_2O$	14.38	4.05	-593
11	$1/3[Cr_3(CH_3COO)_6(OH)_2]Cl+8/3H_2O$	22.35	1.92	-93
13	$1/3[Cr_3(CH_3COO)_6(OH_2)(NH_3)_3]I$	19.10	1.92	-116

boring ions only spin angular momentum is free, and orbital angular momentum is quenched(2), so Cr^{3+} ions are considered effectively in $S_{3/2}$ state, so far as the magnetism is concerned. (3) Metallic ions are the cause of the paramagnetism, other ions or organic groups in the salts will contribute only to the diamagnetism. Since the effect of the latter on the quenching of orbital moments of matallic ions has been considered in the assumption (2), we have to deal with only metallic ions in our calculation. (4) The interactions between molecules are neglected. Between metallic ions in a molecule only exchange interactions are considered. Dipole-dipole interactions are neglected, and this is reasonable except at very low temperatures. (5) The geometrical configuration of ions in a molecule is unknown. There are only three metallic ions, and we assume that they make a equiscecles triangle. In § 5, however, we see that this triangle must be nearly regular in order to obtain best agreements between our theory and the experiments.

§ 3. Energy Levels of a Molecule.

To deduce the susceptibility, we must know first the energy levels of a molecule. In the magnetic study, electronically excited states can be neglected. The ground state has fine structures because of the exchange interactions between metallic ions contained.

So in this section, the energy levels of system of three ions in S states are studied, when the exchange interactions are present. For this purpose the vector model is used.

For our purpose the essential part of the Hamiltonian of this system is

$$\mathrm{H} = -2[J_{12}(\boldsymbol{S}_1\boldsymbol{S}_2)+J_{23}(\boldsymbol{S}_2\boldsymbol{S}_3)+J_{31}(\boldsymbol{S}_3\boldsymbol{S}_1)],$$

where J_{ij} denotes the exchange integral between ith and jth ion, and $\boldsymbol{S}_i$ the spin vector of ith ion.

After the assumtion § 2. (5), we can put $J_{12} = J_{23} = J < 0$ and $J_{31} = \alpha J$. Then we have

$$\mathrm{H} = -2J[(\boldsymbol{S}_1\boldsymbol{S}_2)+(\boldsymbol{S}_2\boldsymbol{S}_3)+\alpha(\boldsymbol{S}_3\boldsymbol{S}_1)]. \tag{2}$$

Next we deduce the eigenvalues of (2), making use of the vector model. In this paper only the case, when the three ions composing the system are equal, will be treated, so the eigenvalues of $\boldsymbol{S}_i$ ($i = 1, 2, 3$) are equal, and we write it S. Then $(\boldsymbol{S}_i\boldsymbol{S}_i) = S(S+1)$.

We write $\boldsymbol{S}^* = \boldsymbol{S}_1+\boldsymbol{S}_3$, $\boldsymbol{S}' = \boldsymbol{S}_1+\boldsymbol{S}_2+\boldsymbol{S}_3$. Then we have

$$S^*(S^*+1) = 2S(S+1)+2(\boldsymbol{S}_1\boldsymbol{S}_3),$$

$$S'(S'+1) = 3S(S+1)+2(\boldsymbol{S}_1\boldsymbol{S}_2)+2(\boldsymbol{S}_2\boldsymbol{S}_3)+2(\boldsymbol{S}_3\boldsymbol{S}_1).$$

Hence

$$2(\boldsymbol{S}_1\boldsymbol{S}_3) = S^*(S^*+1)-2S(S+1),$$

$$2(\boldsymbol{S}_1\boldsymbol{S}_2)+2(\boldsymbol{S}_2\boldsymbol{S}_3) = S'(S'+1)-S^*(S^*+1)-S(S+1).$$

Putting these expressions into (2), we have

$$\mathrm{H} = -J[S'(S'+1)-(1-\alpha)S^*(S^*+1)-(1+2\alpha)S(S+1), \tag{3}$$

Here the allowed values of S^* are obtained by the addition rule of two spin vectors.

$$S^* = S_1+S_2,\ S_1+S_2-1,\ \ldots\ldots,\ |S_1-S_2|$$
$$= 2S,\ 2S-1,\ \ldots\ldots,\ 1,\ 0.$$

Also the allowed values of S' are determined by the same rule. For a given S^* values,

$$S' = S^*+S,\ S^*+S-1,\ \ldots\ldots,\ |S^*-S|.$$

For all the allowed values of S^*, we determine all the allowed values of S'. From this table we can conversely determine the allowed values of S^* corresponding to a given S'. Now we can calculate the eigenvalues of H easily, and the energy levels of the perturbed system can be given using the parameters, J and α. These energy values will be written as $W(S', S^*)$.

In coucluding this section we shall give the number of states having a given S' value. This is the number of the allowed S^* values for the given S' value. This number can be computed by a well-known formula(4);

$$\omega(S') = \Omega(S')-\Omega(S'+1), \tag{4}$$

where $\Omega(S')$ equals coefficient of $x^{S'}$ in the expansion of

$$(x^S+x^{S-1}+\ldots\ldots+x^{-S})^n,$$

and n is the number of atoms or ions composing the system. In our case $n = 3$.

§ 4. Derivation of the Paramagnetic Susceptibility.

When the system is placed under the influence of external homogenesus magnetic field (along the z-axis), the energy levels calculated in § 3 split further.

The first order Zeeman term $2M_{S'}\beta H$ must be added to the energy value $W(S', S^*)$, where β is the Bohr magneton. H is the field strength and $M_{S'}$ takes the valus S', $S'-1$, ..., $-S'+1$, $-S'$.

Now we can obtain the partition function Z for the system of molecules under the influence of homo geneous magnetic field;

$$Z = \sum_{S', S^*} \exp[-W(S', S^*)/kT] \cdot \sinh[(2S'+1)\beta H/kT]/\sinh[\beta H/kT]$$

Then the paramagnetic susceptibility per mole χ_m is

$$\chi_m = NkT \frac{1}{H} \frac{\partial}{\partial H} \log Z$$

$$= \frac{4N}{3kT} \frac{\sum S'(S'+1)(2S'+1)\exp[-W(S', S^*)/kT]}{\sum (2S'+1)\exp[-W(S', S^*)/kT}, \tag{5}$$

where N is the Avogadro's number.

The atomic susceptibility χ_a will be given by

$$\chi_a = \frac{1}{3}\chi_m. \tag{6}$$

For the comparison with the experiment, it is convenient to use the effective Bohr magneton instead of the susceptibility.

This is defined using the theoretical χ_a.

$$\mu_e = 3k\sqrt{\chi_a T/\beta^2 L}, \tag{7}$$

or directly from the experimental formula (1),

$$\mu_e' = 2.839\sqrt{\chi_a T}$$

$$= 2.839\sqrt{CT/(T-\theta)}. \tag{8}$$

§ 5. Polynuclear Salts of Iron Alone and Chromium Alone.

Let us apply the theory to the case of polynuclear salts containig Fe alone and Cr alone. Fe^{3+} ions are in $S_{5/2}$ state, so in this case $S = 5/2$. For Cr^{3+} ions, $S = 3/2$ (cf. § 2 (2)).

Performing the procedure explained in § 3, we obtain the energy values using the parameters J and α. And then by the formulas (5), (6), (7) we obtain the expression describing the temperature dependence of μ_e. The parameters J and α must be so adjusted that the theoretical μ_e (7) agree with the experimental μ_e'(8).

After brief preliminary calculations, we find that α must be approximately 1. So for simplicity, we assume $\alpha = 1$. This corresponds to assume three metallic ions in a molecule make a regular triangle. Then (5) becomes

$$\chi_m = \frac{4N}{3kT} \frac{\sum S'(S+1)(2S'+1)\omega(S')\exp[-W(S')/kT]}{\sum (2S'+1)\omega(S')\exp[-W(S')/kT]}, \tag{9}$$

where $W(S') = -J[S'(S'+1)-3S(S+1)]$.

From (4), (6), (7), (9) we have for $S = 5/2$;

$$\left.\begin{aligned} &\mu_e^2 = A/B \\ &A = 1+20\exp(-3x)+105\exp(-8x) \\ &\quad +210\exp(15x)+330\exp(-24x) \\ &\quad +429\exp(-35x)+455\exp(-48x) \\ &\quad +340\exp(-63x) \\ &B = 1+4\exp(-3x)+9\exp(-8x) \\ &\quad +10\exp(-15x)+10\exp(-24x) \\ &\quad +9\exp(-35x)+7\exp(-48x) \\ &\quad +4\exp(-63x). \end{aligned}\right\} \tag{10}$$

where $x = -J/kT$.

$$\text{For } S = 3/2: \quad \mu_e = P/Q$$

$$\left.\begin{aligned} &P = 2+40\exp(3x)+105\exp(-8x) \\ &\quad +168\exp(-15x)+165\exp(-24x), \\ &Q = 2+8\exp(3x)+9\exp(-8x)+8\exp(-15x) \\ &\quad +5\exp(-24x). \end{aligned}\right\} \tag{11}$$

Fig. 1 and Fig. 2 show the comparison of theoretical curves calculated from the above formulas with experimental curves computed from the formula (8). In calculating the theoretical curves, we took in the expression (10) $J = -38\,k$, $-40\,k$, $-42\,k$; in (11), $J = -14\,k$, $-16\,k$, $-18\,k$. These values are not unreasonable, and the agreement between theoretical curves and experimental curves are good, considering the rough approximations made in our calculations and the accuracy of experiments.

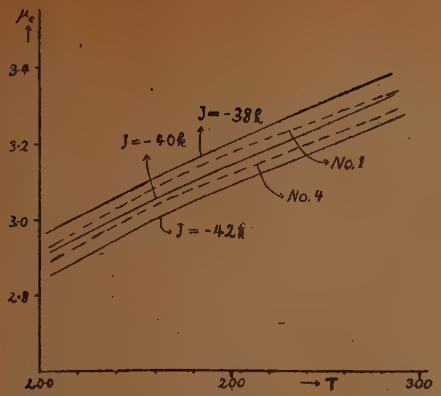

Fig. 1. Temperature variation of effective Bohr magnetons. For $S=5/2$.
——— theoretical curves calculated by the formula (10).
------ experimental curves calculated by (8), using the values of C and θ determined by Welo.

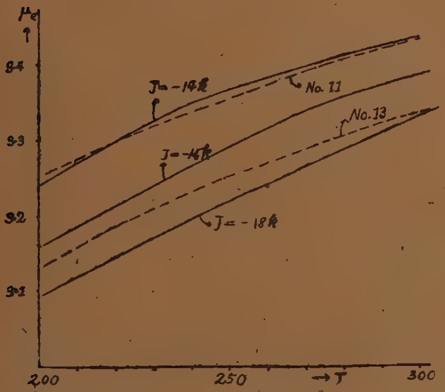

Fig. 2. For $S=3/2$.

§ 6. Mixed Polynuclear Salts.

Welo has measured three salts of this type; for example,

$$[Cr_2Fe(CH_3COO)_6(OH)_2]Cl+6H_2O,$$

$$\chi_m\times10^3(20°C)=16.80,\quad C=8.00,\quad \theta=-380,$$

where χ_m denotes the molecular susceptibility, C and θ are related to χ_m. Though the fundamental features of the susceptibilities of the salts of this type can be explained easily along the line of our theory, the quantitative comparison of the theory with the measurements will be premature before more measurements are made on salts of this type. So we will not give here the explicit formula of the susceptibility.

§ 8. Concluding Remarks.

To explain large negative values of θ, it seems possible to consider some other mechanism, e. g. to assume covalent bonds between metallic atoms and surrounding atoms, as in the case of Pauling's theory of magnetic susceptibilities of complex salts(5), but we could not succeed from this standpoint in obtaining a reasonable explanation of our problem.

In this paper we concluded from the analysis of the susceptibility data that the metallic ions form approximately regular triangles in a molecule. But to confirm this conclusion directly, the determination of the configuration of atoms in a molecule of our type by some other experimental method, e. g. X-ray diffraction method, is much desirable.

The measurement of the magnetic susceptibilities of polynuclear salts containing only two paramagnetic ions will be interesting.

In conclusion the author wishes to express his sincere thanks to Professor M. Kotani for his kind guidance.

References.

(1) L. A. Welo: Phil. Mag. 7th ser. **6**, (1928) 481.
(2) J. H. Van Vleck: "The theory of electric and magnetic susceptibilities" (1932), Chap. XI.
(3) ibid. Chap. XII.
(4) ibid. p. 324.
(5) L. Pauling: "The nature of chemical bond" (1940), Chap. III, § 16.

The Efficiency of the G-M Counter.

By Masateru SONODA.

Department of Physics, Faculty of Science, University of Kyoto.

(Read April 28, 1949; Received Feb. 15, 1949).

Abstract.

The efficiency, i. e. the counting probability per one quantum of the thick-walled γ-ray counter was computed theoretically, by making some simplifying assumptions for several energies between 10 mc^2 and 34 mc^2 (Li-p γ-ray) and for different wall thickness. The efficiency of the thin-walled counter was also discussed.

§ 1. Introduction.

In order to obtain the absolute intensity of the γ-ray from the measurements with a G-M counter, it is necessary to determine the efficiency of the counter. A few workers⁽¹⁾ have studied this problem only for the γ-ray of the comparatively low energies up to bout 5 mc^2, but there is no reliable knowledges for the high energy γ-rays such as those emitted by the (Li-p) or (F-p) reactions*. Since, however, in the experiments using these γ-rays, the knowledge of the efficiency of the counter for these energies is important, it is tried to obtain the efficiency for the energy range from 10 mc^2 to 35 mc^2, taking in mind the three processes; the pair creation, the Compton scattering and the photoelectric effect taking place in the wall of the counter. In determining the efficiency of the counter, it is necessary to know the range, the angular distribution, etc. of the secondary electrons produced by these processes. Since, however, these are scarcely known by experiments for such high energies, we are obliged to take the theoretically calculated values.

§ 2. Thick Walled Counter.

We have used the lead counter 6.5 mm thick in our experiments with 17 MV γ-ray of (Li-p) reaction⁽²⁾. The reason of selecting lead of 6.5 mm thickness is simply that the lead wall of this thickness can just prevent those electrons of 17 MV and less from entering into the counter which may be expelled from the surrounding materials by this γ-ray.

In calculating the efficiency of the lead counter, we used the theoretical values of the range of fast electrons calculated by W. Heitler⁽³⁾. The angular distribution of electrons was inferred immediately from Klein-Nishina's formula for the Compton recoil process, and from Hull's one for the photoelectric effect respectively, whose contributions were small in our energy ranges. It is, however, not known in detail for the pair creation process, which plays an important role in the lead wall for the range of such high energies. Moreover, the efficiency depends upon the shape and the thickness of the wall, and the energy of γ-ray quantum in a complicated manner, and further, the effect of multiple scattering of the secondary electrons makes the rigorous calculation more difficult.

Hence we must perform the merely approximate numerical calculations under the following simplifying assumptions. (1) Most of the pair components are emitted in the direction of the γ-ray quantum. This assumption is reasonable for the γ-rays of energies concerned and gives rise to little error⁽⁴⁾. (2) All the electrons are counted which are emitted from the layer x cm distant drom the inner surface of the counter and have the average range larger than x cm. (3) In the case of the pair creation, the two electrons (+ and −) are emitted at the same time. Therefore, both of these pair components can simultaneously penetrate into the effective space of the counter, when x is smaller than the critical value determined by the energy of the incident γ-ray. These two particles are assumed to cause only one discharge and counted as one*, because they may come into the effective space within the resolving time of the counter.

---

* A theoretical calculation was made by H. Yukawa and S. Sakata for the energies up to 10 MV⁽⁵⁾.

Further we replaced the cylindrical counter by a rectangular one with equal cross-section for simplification⁽⁵⁾. The direction of incidence of the γ-ray was assumed to be normal to a pair of planes with the same thickness as the cylindrical counter as shown in Fig. 1**. The necessary correction due to oblique incidence of the γ-ray would be considered later.

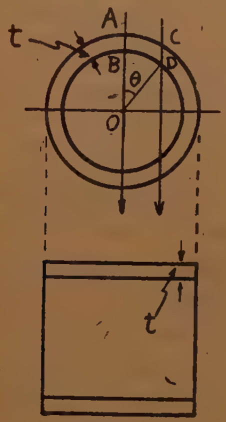

Fig. 1.

Now the efficiency η may be given by the sum of η_{ph}, η_c and η_{pa}, which denote the contributions due to the photoelectric effect, the Compton process and the pair creation process, respectively. Namely,

$$\eta_{\square} = \eta_{ph} + \eta_c + \eta_{pa}$$

and

$$\eta_{ph} = \int_0^{R(\epsilon_{ph})} \exp[-\tau(t-x)] \cdot N\phi_{ph}(x)dx$$

$$\eta_c = \int_0^{R(\epsilon_c)} \exp[-\tau(t-x)] \cdot NZ\phi_c(x)dx$$

$$\eta_{pa} = \int^{R(\epsilon_{pa})} \exp[-\tau(t-x)] \cdot N\phi_{pa}(x)dx$$

where $\phi(x)$ = the cross-section of each process in which the range of secondary electrons is greater than x cm.

ϵ = the maximum energy of electrons which can be emitted in each process.

τ = the total absorption coefficient in Pb.

t = the thickness of the wall

$R(\epsilon)$ = the range of electron whose energy is ϵmc^2.

N = the number of nuclei per unit volume.

and Z = the atomic number of the counter wall.

The results of numerical integration are given in Table I and II, which are graphically shown in Fig. 2 and 3. Table I and Fig. 2 give the efficiency of the lead counter of 6.5 mm thickness for various energies of the incident γ-rays, whereas Table II and Fig. 3 show the relation between the efficiency and the wall thickness for (Li-p) γ-ray (17 MV).

Further we have to consider the effect of the cylindrical shape of the counter instead of the rectangular one. If the γ-ray falls on the counter with the angle θ as indicated by the straight line CD in Fig. 1, the effective thickness t_e of the wall varies with θ. When the effective thickness t_e is smaller than the maximum range R_m of the secondary electrons, the contribution to the efficiency from the portion θ, $\theta+d\theta$ is given by

$$\eta_{te} \cos\theta d\theta, \qquad (t_e < R_m)$$

where η_{te} is the efficiency of the rectangular counter of thickness t_e which is shown in Fig. 3.

When $t_e > R_m$, the above quantity is given by

$$\eta_m \exp[-\tau(t_e - R_m)] \cdot \cos\theta d\theta$$

where η_m is the efficiency corresponding to the wall thickness R_m. The results of calculation are shown as $\eta_{\bigcirc}$ in the Table I, II and Figs. 2, 3*. It is seen from the figures that the efficiency increases at first approximately linearly with the thickness until the latter becomes roughly equal to the maximum range of the secondary electrons and then decreases owing to the futile absorption of the γ-ray. Moreover, the efficiency of the constant wall thickness is roughly proportional to the energy of the incident γ-ray quantum as shown in Fig. 2. These values may be diminished by a certain factor smaller than one owing to the effect of multiple scattering of the secondary electrons. This factor, however, will not differ appreciably from one for such high energies and may therefore be neglected without an appreciable error.

---

* All the workers so far considered that these particles were sometimes counted as two and the efficiency due to pair creation should be multiplied by a certain factor between 1 and 2, which could hardly be determined accurately.

** If we assume the forward emission of secondary electrons as described in the assumption (1) and neglect the effect of the bremsstrahlung, the lower part of the counter ($|\theta| > \pi/2$) shown in Fig. 1 may not be important.

* The results of Yukawa-Sakata are indicated for comparison in the figure by the dotted line, which was calculated for the lead counter of 3 mm thickness.

Table I. The Efficiency of the Lead Counter (Wall thickness 6.5 mm and inner diameter 2 cm)

$h\nu(mc^2)$	η_{pa}	η_c	η_{ph}	$\eta_\square(\%)$	$\eta_\bigcirc(\%)$
34	0.260	0.040	0.003	30.2	28.1
30	0.223	0.039	0.003	26.9	25.1
25	0.179	0.038	0.003	22.1	20.7
20	0.132	0.038	0.003	17.3	16.3
12	0.053	0.037	0.006	9.49	9.00

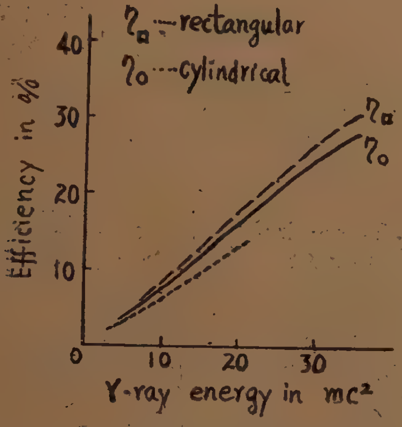

Fig. 2. The efficiency of the Pb counter of 6.5 mm thickness.

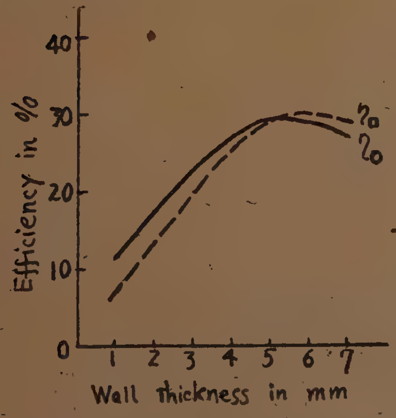

Fig. 3. The efficiency of the Pb counter for 34 mc^2 $h\nu$ (inner diameter 2 cm)

Table II. The Efficiency of the Lead Counter for 34 mc^2 $h\nu$ (Inner diameter 2 cm)

counter thickness (mm)	1	2	3	4	5	6	6.5
$\eta_\square$ (%)	7.1	13.6	20.0	25.7	29.5	30.3	30.2
$\eta_\bigcirc$ (%)	11.6	17.4	23.4	27.7	29.4	28.7	28.1

§ 3. Thin-Walled Counter

Next, we consider the counter of the wall thin compared with the range of the secondary electrons. In this case the efficiency of the counter is approximately given by

$$\eta = t(\tau_{pa}+\tau_c+\tau_{ph})$$

in which t is the wall thickness and τ is the absorption coefficient of each process.

By taking into account the effect of the oblique incidence, we get

$$\eta = \frac{\pi}{2}t(\tau_{pa}+\tau_c+\tau_{ph})$$

This value of η was calculated for the aluminium and lead counter of 1 mm thickness and shown in the Table III, IV and Fig. 4. The energy dependence is almost linear in both cases.

The ratio of these efficiencies η_{Pb}/η_{Al} is a function of the γ-ray energy alone, except an arbitrary constant factor, as is seen from Table V and Fig. 5. These values may be compared with the experimental results. The experiments, however, will be very difficult especially for the thin counter on account of the fact that the secondary electrons emitted from the surrounding substances are responsible for the discharge.

Table III. The Efficiency of the Lead Counter of 1 mm thickness

$h\nu$ (mc^2)	12	20	25	30	34
τ (cm^{-1})	0.509	0.622	0.652	0.698	0.735
η_{Pb} (%)	8.00	9.77	10.4	11.0	11.6

Table IV. The Efficiency of the *Al* Counter of 1 mm thickness

$h\nu$ (mc^2)	12	20	25	30	34
τ (cm^{-1})	0.0637	0.0514	0.0465	0.0439	0.0433
η_{Al} (%)	1.00	0.808	0.729	0.691	0.682

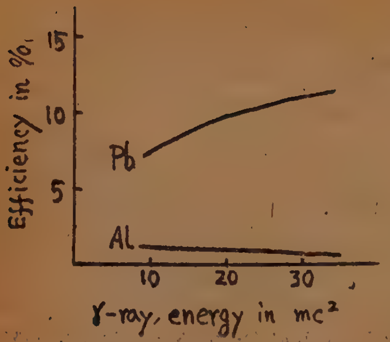

Fig. 4. The efficiency of the thin-walled counter

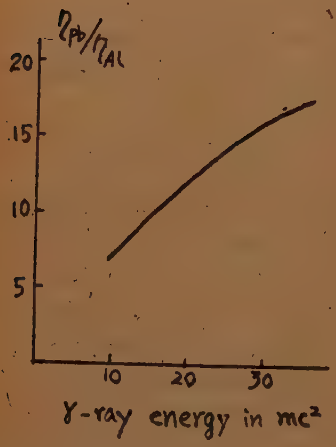

Fig. 5. The ratio of the efficiencies

Table V. The ratio of the efficiencies

$h\nu$ $(mc)^2$	12	20	25	30	34
η_{Pb}/η_{Al}	8.0	12.1	14.4	15.9	17.0

In conclusion the author wishes to express his cordial thanks to Prof. B. Arakatsu and the other members of the nuclear research laboratory of Kyoto University for helpful suggestions and valuable discussions.

References.

(1) H. J. v. Baeyer: Zeits. f. Phys., **95** (1935), 429.
G. F. v. Droste: Zeits. f. Phys., **100** (1936), 529.
G. J. Sizoo nnd H. Willemsen: Physica, **5** (1938), 105.
F. Norling: Phys. Rev., **58** (1940), 277.
J. v. Dunworth : Rev. Sci. Inst., **11** (1940), 107.
I. Nonaka: Proc. Phys-Math. Soc. Jap., **25** (1943), 227.
(2) B. Arakatsu and others: Proc. Phys-Math. Soc. Jap., **23** (1941), 440.
ibid, **23** (1941), 633.
ibid, **25** (1943), 173.
(3) See for instance W. Heitler: Quantum Theory of Radiation.
(4) H. Bethe and W. Heitler: Proc. Roy. Soc., **146** (1934), 83.
(5) H. Yukawa and S. Sakata: Sci. Pap. of Phys-Chem. Res., Inst. **31** (1937), 187.

On the Displacement Velocity of a Magnetic Domain Boundary by a Large Barkhausen Jump in a Ferromagnetic Substance.†

By Takasi HUZIMURA.

The Research Institute for Iron, Steel and other Metals, Tohoku University.

(Received Feb. 28. 1949)

It has often been assumed that the displacement velocity of a magnetic domain boundary in a ferromagnetic substance is governed by an inverse magnetic field due to an electric eddy current induced by the displacement of the boundary: On this basis a theoretical formula for the velocity has already been given by Sixtus and Tonks(1) Besides the aforesaid eddy current which determines the boundary displacement velocity, the probability of spin inversion as an elementary process of the displacement of the domain boundary is also to be taken into account. On this basis, Katayama(2) and Tsuya(3) elucidated another velocity formula for the displacement, so that it now becomes desirable to examine actual significance of both factors for the displacement velocity of the domain boundary in a ferromagnetic substance. Now, for example, if a ferromagnetic wire of permalloy is stretched by tension and magnetized to saturation, and if the magnetizing field is first diminished and subsequently increased again in an opposite direction, then a magnetic reversal through the whole wire takes place in a single Barkhausen jump when the strength of the magnetizing field reaches a certain value. If this reversal is caused by the displacement of a single domain boundary through the whole wire, one can measure directly its displacement velocity by observing the Barkhausen jump at the different points along the wire. In this way the writer measured the displacement velocity of the domain boundary in a perminvar wire under different tensions, at various temperatures ranging from –196°C to 200°C. From the data thus obtained the influence of the eddy current factor has been found to be of minor importance compared with that of the spin inversion factor even in a conducting ferromagnetic substance.

---

† Report of the Research Institute for Iron, Steel and other Metals. Tohoku University.

Specimen and Method of Velocity Measurement.

Specimens used are wires of Fe-Ni-Co (30 %, 45 % and 25 % respectively) alloy, the length and the diameter of which are 250 cm and 0.2 mm respectively. In order to eliminate mechanical strain, specimens are annealed at 800°C by flowing an alternating current in these specimens for 10 minutes. Since the magnetic anisotropy of the wire of the mentioned composition is small, its magnetostriction is isotropic and further its saturation value has a positive sign, its magnetization curve and hysteresis loop take a rectangular form under the action of a certain uniform tension along the wire: The axis of the wire becomes a unique preferential direction of the spontaneous magnetization and the reversal of magnetization occurs in a single Barkhausen jump. The field strength in which the Barkhausen jump occurs is denoted by H_s.

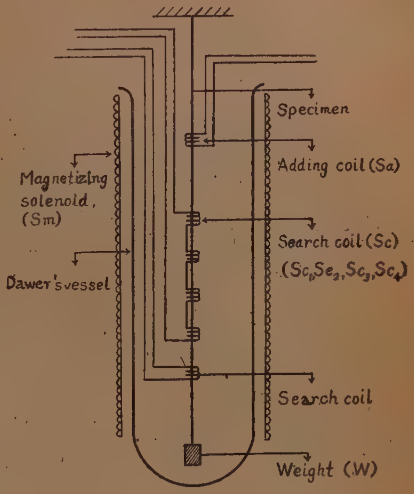

Fig. 1. Schematic diagram of apparatus for velocity measurement at –190°C.

An apparatus used for the velocity measurement at –190°C is schematically shown in Fig. 1. The specimen is stretched by a weight w, and four search coils, Sc_1, Sc_2, Sc_3, and Sc_4, are wound on the specimen at intervals of 30 cm. Those coils are jointed in series and connected to an electromagnetic oscillograph. Under the action of tension, the specimen is once magnetized to saturation in one direction; thereafter a smaller field H_m, the strength of which is smaller than H_s, is applied to the specimen in the opposite direction of magnetization by a solenoid S_m, (length 150 cm, turn number per cm 28). Next, a local field is applied by a short coil S_a (length 35 mm, total turn number 150) in the direction of the former field H_m. Owing to this local field a magnetic reversal occurs at first only in the region, covered by the coil S_a, of the mentioned wire and then the boundary between reversed and non-reversed regions displaces along the wire until the reversal of magnetization of the whole wire takes place. As the said search coils are connected in series, the peaks due to impulsive electromotive forces induced in each of the search coils by the passage of magnetic boundary are successively observed on the oscillogram. The distances between these peaks on the oscillogram, that is, the time intervals between these instants on which the boundary passes through the portions covered by each of the search coils, can be measured on the oscillogram. The displacement velocity of the boundary may be given by the ratio of the distance (30 cm each) between these search coils to the measured time intervals. In the case of measurement at high temperature, a Dewar's vessel in Fig. 1, is replaced by an electric furnace.

Results.

The displacement velocities of the magnetic boundary between reversed and non-reversed regions have been thus observed in the range from 2m/sec to 50 m/sec. To avoid the initial stage of the displacement, the velocity is calculated by the impulses induced in the search coils which are more than 100 cm apart from the adding coils S_a. The relation between the displacement velocity and the field strength is shown in Fig. 2 (at room temperature and at -190°C) and Fig. 3 (at room temperature and at 200°C), corresponding to different specimens respectively. For room temperature and 200°C the measurement of the velocity less than 10 m/sec is difficult, so that, in Fig. 4, the velocity-field relation is not given for this region.

Above the velocity range greater than 10 m/sec. the velocity varies almost linearly with the field strength for all temperatures. It is found that in this high velocity range the velocity-field relations are all parallel. However, it is also remarkable that the velocity-field curve is concave downwards at low temperature. The field strength

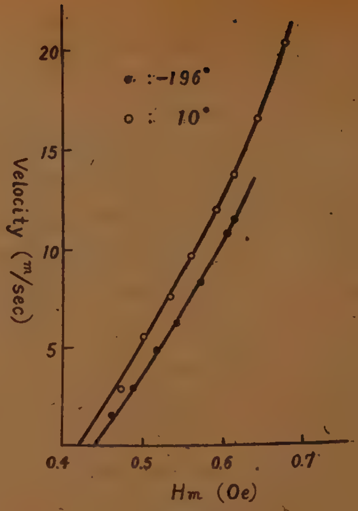

Fig. 2. Velocity-field curves for wire A.

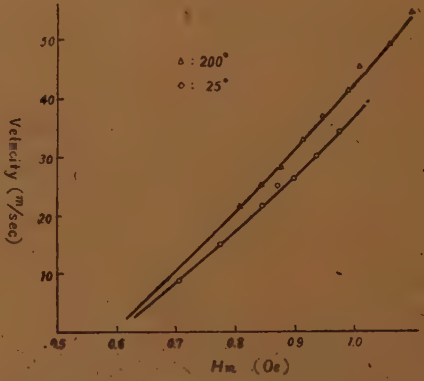

Fig. 3. Velocity-field curves for wire B.

Table I. (Measured at -190°C and 10°C with wire A).

Temperature	$H-H_0$	λ (cm)	Vcal (m/sec)	Vobs (m/sec)	$E_c\,(\times 10^2)$	$E_m\,(\times 10^2)$
−190°C	0.124	10.0	24.0	8.1	1.33	86
	0.095	9.4	16.6	6.2	1.17	66
	0.037	8.0	5.5	3.0	0.96	26
10°C	0.215	9.0	65.0	16.0	2.1	15
	0.157	7.0	37.0	9.6	1.6	11
	0.078	4.0	10.5	5.6	1.6	5

Table II. (Measured at 25°C and 200°C with wire B).

Temperature	$H-H_0$	λ (cm)	Vcal (m/sec)	Vobs (m/sec)	$E_c\,(\times 10^2)$	$E_m\,(\times 10^2)$
25°C	0.385	8.3	110	34	4.5	27
	0.317	7.7	84	26	3.7	22
	0.247	7.2	42	22	3.4	18
200°C	0.454	7.9	146	49	4.6	31
	0.353	6.5	94	37	4.1	24
	0.250	5.6	56	25	3.3	17

of the point at which V-H curve intersects with the axis of magnetic field is denoted by H_0. Now, if one denotes by δt the time interval between an instant in which the front of the boundary enters a search coil and that in which the end of the boundary leaves the same coil, then one can determine δt by measuring the duration time of an impulsive peak on the oscillogram. For the determination of δt the correction due to the natural period of the vibrators of the oscillograph is taken into account. Using the values of both the duration time of impulses and observed velocities we can estimate the length of the propagating boundary along the wire λ by $\lambda = V\delta t$. The values of λ determined by this equation are shown in column 3 in Tables I and II.

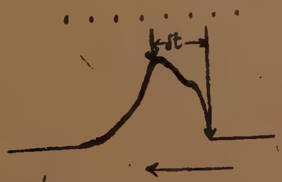

Fig. 4 Barkhausen Oscillogram. The duration time δt is determined by measuring the distance between two points on the impulsive peak, and the remaining part of the peak will be characteristic of the period of vibrator (75 cycles). This method of measurement of δt is certified by comparing another oscillogram, that is taken by using a vibrator period 3000 cycles.

The distance between upper spots indicates the time interval of 1/100 sec.

Discussion.

During the reversal of magnetization, the electromagnetic energy of the amount $H\cdot\Delta I$ should be transformed into heat energy. Here ΔI is the total change in magnetization during magnetic reversal (double the saturation of magnetization). Now the dissipation of the energy $H\cdot\Delta I$ occurs as (1) the Ohmic loss due to the eddy current by the boundary displacement in the ferromagnetic medium, and (2) that pointed out by Katayama: An interaction between the 3d electron and the crystal lattice arises due to the irregularity of the periodic field of crystal lattice potential by thermal vibration and by this interaction the inversion of electron spin, which composes the spontaneous magnetization of the wire, occurs at domain doundary. This inversion can be seen as an elementary process of the boundary displacement. It is shown by Katayama that energy of the spin magnetic moment against the external magnetic field is absorbed by the crystal lattice by the occurrence of the inversion. Now the displacement by the field strength H_0 takes place with exceedingly slow velocity, no eddy current loss will occur by this field. The dissipation of the energy $H\cdot\Delta I$ will occur by the direct energy exchange between the spin of electron and the crystal lattice*. If the field strength H is greater than H_0, the displacement takes place with non-vanishing velocity and in this case the displacement accompanies eddy current loss. If the velocity is essentially ruled by the accompanying eddy current, the excess energy $Em = (H-H_0)\Delta I$ will be wholly changed into the eddy current loss. A theoretical formula for eddy current loss E_e dissipated in the specimen by a magnetic domain boundary displacement with velocity V is given as follows:

$$E_e \doteq \frac{2\pi^3 a^4 (\Delta I)^4 V}{\rho\lambda}$$

In this formula a is the radius of the wire in cm, δ the specific resistance in ohm cm. The specific resistances ρ measured at various temperatures are shown in Table III. Now the values of the eddy current loss calculated using the observed velocity V_{obs} and λ are shown in column 5 and 3 in the Tables I and II. As they show, E_e is considerably small compared with the difference of

---

* Strictly speaking, the measured velocity is only an average over wide range along the wire: It is also possible to assume that at low average velocity the boundary makes an irregular motion due to the internal stresses distributed irregularly in the wire and the actual velocity varies from point to point along the wire. Basing upon this assumption microscopic eddy current will be supposed to be accompanied with boundary displacement even by vanishing average velocity. However, it will be concluded that even in this case the following conclusion in this section does not fall. A detailed discussion on this point will be given by Katayama in this journal.

Table III. Specific resistance.

Temperature	$\rho(\times 10^5)$ (ohm cm)
−190°C	1.49
10°C	2.62
20°C	2.72
200°C	4.17

energy $(H-H_0)\cdot\Delta I$, so that it is to be concluded that the loss of energy by exchange is also greatly influenced by the displacement velocity. Alternatively speaking if one assumes that the energy of the amount $(H-H_0)\cdot\Delta I$ be wholly consumed by eddy current loss, then the displacement velocity V_{cal} will be given by the Sixtus-Tonks formula(4)

$$V_{cal} = 0.25\cdot 10^8 \rho\lambda(H-H_0)/a^2\Delta I$$

The calculated values of this formula are shown in column 4 in Tables I and II. In these tables one can see that the calculated values are exceedingly larger than the observed values.

In conclusion, the loss of energy by the displacement of domain boundary is governed by accompanying eddy current as well as by the direct energy exchange between the spin of electron and the crystal lattice even in conductive ferromagnetic media. In the case of boundary displacement in a perminver wire, the latter proved to be the main factor for specifying the displacement velocity of the domain boundary.

The writer wishes to acknowledge his thanks to Dr. T. Hirone who supervised the present work. The present study was supported by the research grant of the Ministry of Education.

References.

(1) K. J. Sixtus and L. Tonks: Phys. Rev., **37** (1931) 931; **42** (1932) 419.

(2) T. Katayama: J. Phys. Soc. Jap., **4** (1948) 202.

(3) N. Tsuya: J. Phys. Soc. Jap., **3** (1948) 176.

(4) K. J. Sixtus and L. Tonks: Phys. Rev., **42** (1932) 419.

On the Discontinuous Elongation of Aluminium Crystal. I.

By Tomoyosi KAWADA.

The Mechanical Laboratory, Ministry of Commerce and Industry,
Suginami-ku, Tokyo.

(Read April 29, 1946; Received April 4, 1949).

§ 1. Introduction.

Joeffe and Ehrenfest(1) first observed in 1924 that plastic flow in rock-salt occurred discontinuously at temperature above 250°C. M. Clasen-Nekludowa(2) studied this phenomenon on rock-salt, α-brass and aluminium using a specially designed creep tester which magnified the elongation 10,000 times and observed that they elongated discontinuosly in a certain temperature range, the individual jump being of the order of micron. Later R. Becker and E. Orowan(3) studied the same phenomenon on single crystals of zinc; they photographed the stress-time curve magnifying the elongation 3,160 times and found that the average duration of jump was of the order of second at the room temperature and was of fraction of second at 70°C or 80°C. E. Schmid and N. A. Valouch(4) studied the tensile test of very pure zinc single crystals and found that the discontinuous jump occured when the slip plane was declined to the tensile direction more than 60° and the individual jump was from a few micron to a maximum tending to 80 micron. Later these phonomena were discussed by E. Orowan(5), F. Seitz and T. A. Read(6) and C. Zener(7) from the viewpoint of dislocation theory. The author studied this problem about aluminium crystals using a extensometer of electric capacity type.

§ 2. Experimental Procedure.

The tensile testing machine used for this experiment is shown in Fig. 1. The pulley R was driven by a d.c. motor and the specimen was elongated at constant speed. By changing the rotating speed of the motor the tensile speed could be controlled from 2.5 μ/sec to 10 μ/sec. To measure the load of the specimen, we used the bending of a flat spring S, which was supported by two knife edges set 10 cm apart and at the middle of this spring a loading rod connecting to the specimen at another end was hung by a knife edge. The bending of the spring was observed by a mirror M attached to the end of the spring, using a lamp and a scale.

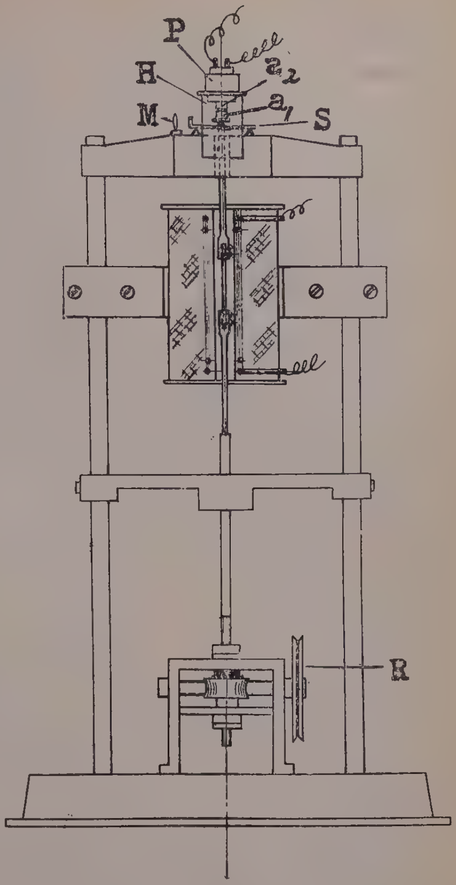

Fig. 1.

When the load increased or the discontinuous jump happened, the spring bent or relaxed. To record exactly this displacement of the middle point of the spring we used a extensometer of electric capacity type. Two brass cylinder a_1 and a_2 of diameter 10 mm and 8 mm facing each other at distance d were used as a air gap condenser, where a_1 was attached to the upper head of the loading rod and a_2 to the under part of the pick-up P. Thus the capacity varied as the spring bent or relaxed. The pick-up P could be moved by a micro-screw in the holder H to keep d in a definite range. The connecting diagram of the pick-up and the amplifier being shown in Fig. 2 where the output was connected to a electromagnetic oscillograph and recorded by a long recording camera. Whithin a certain range of d the output voltage was almost proportational to d and the ratio between the deflection of the oscillograph image and the change of d could be controlled from a few hundred to 20.000 continuously by regulating the variable condenser of the amplifier, but we used the magnification of 6,000 to 8,000 in this experiment. The

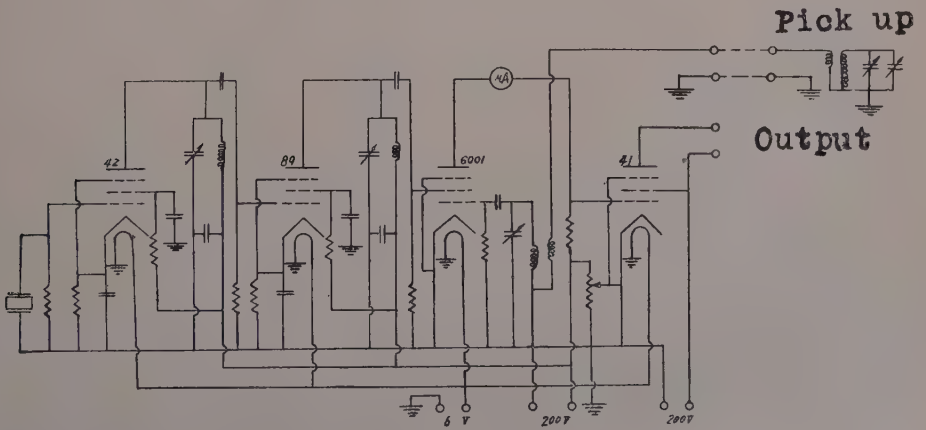

Fig. 2.

oscillogram thus obtained represents a stress-time curve and at the instance of discontinuous jump it represents the decrease of load and the elongation of the specimen if the duration of a jump is quick enough compared to the tensile speed.

We used four kinds of spring given in Table I, where *h* is the thickness and *b* the breadth of the spring, *a* is the amount of displacement at the middle of the spring when 1 g weight is loaded.

Table I.

No.	*h* mm	*b* mm	*a* μ
1	1.62	10.05	0.29
2	2.40	12.0	0.072
3	2.96	12.0	0.038
4	3.93	12.0	0.0165

The natural frequency of the oscillograph vibrator and the spring was above 1,000 cycles and the friction at the knife edges was thought to be so small that the accuracy of the time measurement was 1/1000 sec.

The size of specimen was 1 mm in thickness, 3 mm in breadth and 50 mm in gauge length.

The chemical compositions were as Table II.

Table II.

No.	Chemical Composition
1	99.99 % Al
2*	0.16 % Si, 0.16 % Fe, remainder Al
3	No. 2+5 % Zn
4	No. 2+10 % Zn
5	No.2+1 % Sn

* No. 2 was commerical aluminium.

By recrystalizing method we prepared the specimens of single crystal and coarse grain polycrystal and we determined the orientation of single crystal and bicrystal by X-ray Laue method.

§ 3. Result of Experiment.

We first studied the tensile test of commerical aluminium specimen under the condition of temperature 200°C, tensile speed 5 μ/sec and using spring No. 2. The stress-time curve in case of polycrystal was quite smooth as shown in Fig. 3. The stress time curve of single crystal is shown in Fig. 4. When the stress exceeded the critical shearing stress the curve fluctuated and the fluctuation continued till the elongation become 10 %.

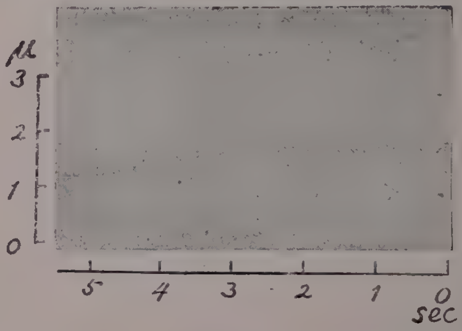

Fig. 3.

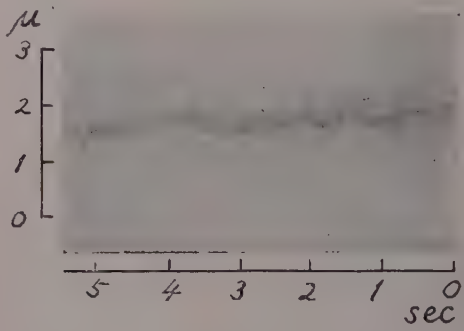

Fig. 4.

We tested the specimens of differently orientated single crystals, but the results were all similar. The amplitude of fluctuation was less than 0.5 μ and the drop of load was not so quick as to call it discontinuous jump, so we neglected this phenomemon in this experiment. In the case of coarse grain polycrystal the curves were quite different and one example of them is as follows. We photographed the stress-time curve of a specimen consisting of four crystals by a long recording camera from beginning till the elongation reached to 15 %. The curve was quite smooth when the stress was under critical shearing stress, but as soon as it exceeded critical shearing stress the discontinuous jump occurred as shown in Fig. 5 and repeating these jumps the load increased as a whole. When the total elongation exceeded about 10 % the discontinuous jump ceased to occur and the curve became smooth, only a few jumps occurred in groups several times till the elongation reached

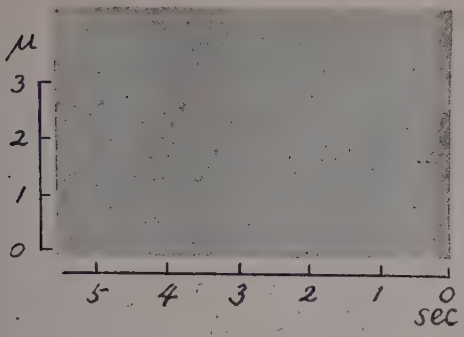

Fig. 5. A. Elongation 3%.

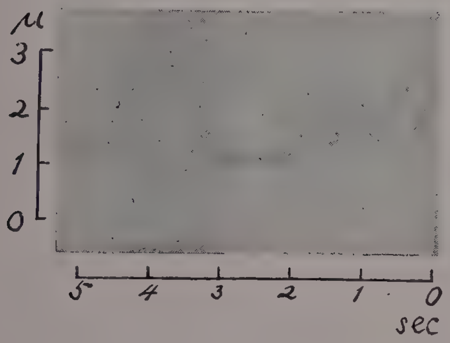

Fig. 5. B. Elongation 9%.

to 12%. We counted the number of jumps and measured the magnitude of each jump and expressed as follows. We classified the range of elongation of specimen into the interval of 0—2%, 2—3%, 3-4%.....and counted the number of jumps N and took the mean value of magnitude of jumps Δ in each interval and tabulated as Table III, where the interval 0—2%, 2—3%, 3—4%, ...were noted as <2%, 2%, 3%.....and Δ was measured in unit of μ.

Table III.

%	<2	2	3	4	5	6	7	8	9	>10
N	8	57	64	89	94	96	104	51	46	26
Δ	1.6	1.4	1.2	1.3	1.3	1.0	0.9	0.9	0.8	0.7

The fluctuation of the magnitude of the jump in each interval was as shown in Fig. 5. The total number of jumps N_t was 635 and the total elongation by the jumps was 680.6 μ and the mean magnitude of jump Δ_m was 1.07 μ. Similar results were obtained by other specimens differing to some extent from specimen to specimen and as extremum cases we got $N_t = 880$, $\Delta_m = 1.10\ \mu$ or $N_t = 470$, $\Delta_m = 1.22\ \mu$ but in those cases the distribution of number of jumps in each interval of elongation were similar. In the experiments of Part II we did not photographed the stress-time curve continuously from beginning to the elongation of 15% but photographed only about 30 sec at the beginning of each elongation stage of 2%, 3%, ... and took the number of jumps N in 10 sec and the mean of the magnitude of these jumps Δ. When the tensile speed was 5 μ/sec and the gauge length was 50 mm the elongation in 10 sec was 50 μ and this corresponded to the elogation of 0.1% so this N corresponded to 1/10 of that of Table III. We repeated the experiments a few times under the same condition using different specimen and picked up a typical one, so the data is thought to be fairly reliable.

References.

(1) A. Joffe: The Physics of Crystals, (1928), 50.

(2) M. Classen-Nekludowa: Zeits. Phys., **55** (1929), 555.

(3) R. Becker and E. Orowan: Zeits. Phys., **79** (1932), 566.

(4) E. Schmid and M. A. Valouch: Zeits. Phys., **75** (1932), 531.

(5) E. Orowan: Proc. Phys. Soc., **52** (1940), 8.

(6) F. Seitz and T. A. Read: J. App. Phys., **12** (1941), 470.

(7) C. Zener and J. H. Hollomon: J. App. Phys., **17** (1946), 69.

On the Discontinuous Elongation of Aluminium Crystal. II.

By Tomoyoshi KAWADA.

The Mechanical Labortory, Ministry of Commerce and Industry,
Suginami-ku, Tokyo.

(Read April 29, 1946; Received April 4, 1949).

§ 1. Introduction.

In the first report we described the experimental apparatus and an example of the experiment and confirmed that the discontinuous elongation of aluminium occurred when the specimen of coarse grain polycrystal was used. In this second report the results of detailed experiments of this phenomenon will be described.

§ 2. Effect of Spring.

It is well known that the results of tensile test are affected by testing conditions, so we first considered the effect of testing apparatus. As explained in the first report the testing apparatus was of the usual screw-and-spring type; one end of the specimen was pulled by screw, the other end being connected to the center of a flat spring. Bending of the spring produced the load while the displacement of the center of spring was the measured of load. When the specimen elongated, the spring contracted and the load could not be kept constant. So the effect of spring was first examined. We tested under the condition of tensile speed 5 μ/sec and temperature 200°C. The result is shown in Table I, where we have calculated the stress decrease at the jump by the Table I of the first report and represent it as Δ_s in unit g/mm^3. From this table we can see that N and Δ_s increases, Δ decreases with increasing strength of spring and $N \times \Delta$ is, roughly speaking, independent of strength of spring except the case of spring No. 4. In the following experiment we used the spring No. 2.

Table I.

Spring No. 1.

%	2	3	4	5	6	7	8	9
N	3	4	4	5	5	6	5	4
Δ	3.6	3.7	4.0	2.8	2.6	2.5	2.8	2.5
Δ_s	4.1	4.2	4.6	3.2	3.0	2.9	3.2	2.9

Spring No. 2.

%	2	3	4	5	6	7	8	9
N	5	6	9	9	10	10	5	5
Δ	1.4	1.1	1.3	1.3	1.0	0.9	0.9	0.7
Δ_s	6.5	5.1	6.0	6.0	4.6	4.2	4.2	3.2

Spring No. 3.

%	2	3	4	5	6	7	8	9
N	12	13	15	14	13	9	—	—
Δ	1.0	1.0	0.9	1.0	1.0	1.0	—	—
Δ_s	8.8	8.8	7.9	8.8	8.8	8.8	—	—

Spring No. 4.

%	2	3	4	5	6	7	8	9
N	9	6	4	2	—	—	—	—
Δ	0.6	0.6	0.6	0.4	—	—	—	—
Δ_s	12	12	12	0.4	—	—	—	—

§ 3. Effect of Tensile Temperature.

As described in the first report the discontinuous jump is closely related to temperature and especially M. Classen-Nekludowa found in her creep test of aluminium that the discontinuous jump occurred from 450°C to 550°C. In our experiment the discontinuous jump was observed above 100°C, and under 100°C the stress-time curve fluctuated but no jump was found and Above 350°C the jump did not occur and the stress-time curves were very smooth. The results are tabulated in Table II.

Table II.

100°C.

%	2	3	4	5	6	7	8	9
N	9	11	11	12	5	—	—	—
$\varDelta$	1.3	1.5	1.4	1.7	1.6	—	—	—

200°C.

%	2	3	4	5	6	7	8	9
N	5	6	9	9	10	10	5	5
$\varDelta$	1.4	1.1	1.3	1.3	1.0	0.9	0.9	0.7

300°C.

%	2	3	4	5	6	7	8	9
N	8	12	15	11	11	10	5	8
$\varDelta$	1.5	0.9	0.9	1.1	1.1	1.1	1.3	1.0

350°C

%	2	3	4	5	6	7	8	9
N	2	4	4	5	—	—	—	—
$\varDelta$	0.8	0.6	0.8	0.7	—	—	—	—

From this result we see that the magnitude of jump $\varDelta$ is the greatest at 100°C and become smaller as the temperature become higher while the number of jumps is almost equal between 100°C and 300°C. At 350°C it suddenly decreases.

§ 4. Effect of Tensile Speed.

The effect of tensile speed was tested by using the tensile speed of 2.5, 5 and 10 μ/sec under the tensile temperature 200°C and result is shown in Table III. As described in the first report we used N as the number of jumps during the elongation of 1/10 %, so the time interval necessary for this elongation was 20, 10 and 5 sec. corresponding to the tensile speed of 2.5, 5 and 10 μ/sec respectively.

In case of tensile speed of 10 μ/sec some fluctuations were seen in the stress-time curve and small jumps were some times indistinguishable from fluctuations so the result in this case was less reliable. We can see from the table that as the tensile speed becomes slower, jumps occur a little more frequently and the magnitude of jumps becomes greater.

Table III.

Tensile speed 2.5 μ/sec

%	2	3	4	5	6	7	8	9
N	10	10	8	8	10	14	12	10
$\varDelta$	1.5	2.4	2.4	2.4	2.3	1.7	1.6	1.6

Tensile speed 5 μ/sec

%	2	3	4	5	6	7	8	9
N	5	6	9	9	10	10	5	5
$\varDelta$	1.4	1.1	1.3	1.3	1.0	0.9	0.9	0.7

Tensile speed 10 μ/sec

%	2	3	4	5	6	7	8	9
N	4	4	5	7	5	5	6	4
$\varDelta$	0.9	1.2	0.8	0.7	0.9	0.8	0.8	0.7

§ 5. Effect of Difference of Orientation of Each Crystal in Bicrystal.

It is expected that the difference of orientation of neighbouring crystal will influence the discontinuous jump. For the relative orientation of neighbouring crystal affects the character of grain boundary(1) and the relative direction of the slip plane and the direction of slip of neignbouring crystal

Table IV.

1. $\chi_1 = 33°$, $\chi_2 = 32°$, $\alpha = 115°$, $\lambda_1 = 40°$, $\lambda_2 = 43°$, $\beta = 193°$

%	2	3	4	5	6	7	8	9
N	5	5	7	9	9	10	8	9
$\varDelta$	1.1	1.1	1.4	1.4	1.5	1.3	1.1	1.1

2. $\chi_1 = 41°$, $\chi_2 = 40°$, $\alpha = 2°$, $\lambda_1 = 47°$, $\lambda_2 = 46°$, $\beta = 2°$

%	2	3	4	5	6	7	8	9
N	4	4	5	5	2	1	—	—
$\varDelta$	1.5	1.4	1.1	0.9	0.9	1.2	—	—

3. $\chi_1 = 37°$, $\chi_2 = 35°$, $\alpha = 174°$, $\lambda_1 = 40°$, $\lambda_2 = 39°$, $\beta = 164°$

%	2	3	4	5	6	7	8	9
N	15	9	11	14	15	10	10	8
$\varDelta$	1.8	1.7	1.9	1.4	1.4	1.5	1.2	1.4

affect the deformation. Since in the preparatin of bicrystal we could not control the relative orientation of each crystal in a specimen, the orientation of each crystal was quite at random and moreover the grain boundary did not run straightly across the specimen but ran meanderigly.

Except a few specimen the neighbouring crystal has no special relative orientation and in Table IV, 1 we represent the result of one example of such a bicrystal under the condition of tensile speed 5 μ/sec and temperature 200°C.

where

χ = angle between the axis of the specimen and the direction of maximum slope of the slip plane,

λ = angle between the axis of the specimen and the direction of slip.

α = angle between two planes of the neighbouring crystal, each containing the axis of the specimen and the direction of maximum slope of the slip plane.

β = angle between two planes of the neighbouring crystal, each containing the axis of the specimen and the direction of slip.

The subscripts 1 or 2 refer to each of the neighbouring crystal.

In Table IV, 2 we represent the result for a bicrystal in which the neighbouring crystal has almost equal orientation, slip plane and direction of slip. IV, 3 is the result for a specimen in which relative direction of slip plane and direction of slip were almost 180°. IV, 2 and IV, 3 were the results for only one specimen, so they are less reliable. In VI, 1 the result is almost similar to Table III of the first report.

The fact that the result of bicrystal is almost similar to that of tricrystal or quadricrystal is worth noticing and we treated this problem in § 6. In IV, 2 when the relative orientation was quite similar the number of jumps was very few. In IV, 3 number of jumps and magnitude of jumps are greater than IV, 1.

§ 6. Effect of Crystal Size.

As no discontinuous jump occurred in polycrystal, we sought the minimum size of crystal grain in which jump occurred. Testing specimens of various grain size we found the minimum one was as follows; one crystal grain crossed the specimen and its length was about 3 mm or equal to the breadth of specimen and the existence of 2 or 3 of such crystal grains was necessary for the occurrance of the jump. The result of experiment of such specimen under the tensile speed of 5 μ/sec and temperature 200°C was shown in Table V, 1.

Table V.

1.

%	2	3	4	5	6	7	8	9	10	11
N	5	9	9	11	9	10	7	8	8	4
Δ	1.7	1.8	2.0	1.5	1.7	1.9	1.9	1.9	1.6	1.9

2.

%	2	3	4	5	6	7	8	9	10	11	12	13
N	4	7	8	11	11	12	14	12	10	8	9	7
Δ	2.6	1.8	2.6	3.4	3.4	2.6	2.1	1.7	1.8	1.1	1.4	1.1

In this case Δ was a little greater compared with the tricrystal or quadricrystal and jump occurred till the elongation reached to 12% or more, at one specimen jump occurred till it was cut at 15%.

Now when we pulled the coarse grain polycrystal the distortion near the grain boundary ceased to happen at the early stage of the elongation and after that time the distortion was mainly observed at the part far from the grain boundary and the discontinuous jump ceased to occur at about that time, while in the above cases the distortion of the specimen occurred severely in the larger crystal part and during pulling specimen the distored larger crystal was gradually elongated and distorted very near to the grain boundary nntil at last the specimen was cut at this part. Thus it seems that the distortion near the grain boundary is necessary for the occurrence of the discontinuous elongation.

As the special form of grain boundary we used a bicrystal in which grain boundary ran longitudinally about a quarter of specimen and there it went to one side. The result is shown in Table V, 2. In this case, too, Δ is grater than that in the usual case and the jump continued to occur till the elongation reached 13%. Inspecting the specimen we saw that the elongation of the specimen cccurred not only in the main 3/4 crystal part but also in 1/4 part where grain boundary ran.

Thus we see that the number of jumps increases not in proportion to the number of grain bonndaries, but increases only a little when the number of grain boundaries increases.

§ 7. Duration of Jump.

To test the duration of a jump more accurately we photographed by increasing the rotating speed of oscillograph camera and the example was shown in Fig. 1.

As described in § 2 of the first report the apparatus follows truly up to 1/1000 sec. The result was as follows. (1) The duration of a jump was quite at radom and the shortest was 25/1000 sec while the longest was 80/1000 sec. (2) The duration of a jump was quite independent of the magnitnde of the jump. For example, we observed as an extremum case a duration of 40/1000 sec for a jump of 2.4 μ while 55/1000 sec for a jump of 0.8 μ (3) It was also independent of the testing conditions such as spring, tensile speed and temperature.

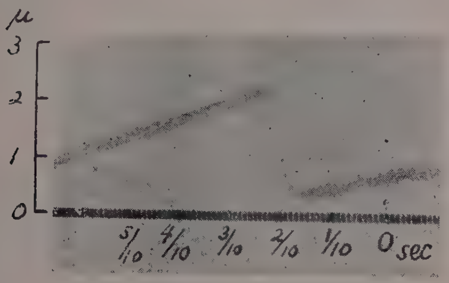

Fig. 1.

As seen from Fig. 1 a jump begins and ends rather suddenly and during a jump the load decreases almost linearly with time. This result seems to differ from that of R. Becker and E. Orowan where a jump began suddenly and ended very gradually and duration was very longer. Their experiment was the creep test while our experiment was the tensile test and the specimen was always pulling so the trailing of a jump should never be seen in our photograph. Thus it cannot be said that our result differs from the result of R. Becker and E. Orown.

§ 8. Effect of Purity and Alloying.

(1) 99.99 % Aluminium. Using specimen of 99.99 % aluminium, we found no discontinuous jump whatever tensile condition we tested when we used single crystal, polycrystal or coarse grain polycrystal specimen. From this result we know that the existence of some impurity is the necessary condition for the occurrance of discontinuous jump.

(2) Aluminium-zinc alloys. As the limit of solubility of zinc in aluminium is approximately 18.5 %, the alloys of aluminium containing 5 and 10 % of zinc are in the state of solid sloution and these alloys deform like aluminium(2). In these alloys the discontinuous jump occurred also in the coarse grain polycrystal only. The main difference between zinc alloy and commercial aluminium is that the temperature range for the occurrance of jump is narrower for zinc alloys, that is, in 5 % alloy it was between 100°C and 200°C while in 10 % alloy it was between 150°C and 200°C and the result is shown in Table VI where tensile speed was 5 μ/sec.

Table VI.

1. 5 % zinc alloy
   a. 100°C

%	2	3	4	5	6	7	8	9
N	3	4	5	3	3	—	—	—
Δ	1.1	1.0	1.0	1.4	1.3	—	—	—

b. 200°C

%	2	3	4	5	6	7	8	9
N	5	4	8	3	3	—	—	—
Δ	1.2	1.4	1.5	1.0	1.1	—	—	—

2. 10 % zinc alloy
   a. 150°C

%	2	3	4	5	6	7	8	9
N	3	4	5	5	3	—	—	—
Δ	1.7	1.4	1.7	1.4	1.2	—	—	—

b. 200°C

%	2	3	4	5	6	7	8	9
N	2	9	4	3	2	—	—	—
Δ	1.0	1.7	1.3	1.7	0.8	—	—	—

From this table we see that the jump ceases to occur at 7 % elongation and the number of jumps is less than commercial aluminium but the magnitude of jump is similar to that of commercial aluminium. In a word the occurrance of discontinuous jump became difficult when the percentage of zinc which is soluble in alminium increased.

(3) Alminium-tin alloy. Tin is almost insoluble in aluminium and alloy of aluminium containing 1% of tin becomes eutectics. In this alloy no discontinuous jump occurred except a few specimen in which jumps were found several times. Thus we know that a small amount of insoluble impurity which is contained in commercial aluminium is necessary for the occurance of jump but insoluble impurity of the order of 1 % hinders the occurance.

References.

(1) B. Chalmers: Proc. Roy. Soc. **A 162** (1937), 120.
(2) C. F. Elam: Proc. Roy. Soc. **A 109** (1925), 143; **115** (1927), 133.

On the Discontinuous Elongation of Aluminium Crystal III.

By Tomoyosi KAWADA.

The Mechanical Laboratory, Ministry of Commerce and Industry,
Suginami-ku, Tokyo.

(Read April 29, 1946, Received April 4, 1949)

In this third report we will discuss about the results of experiments.

E. Orowan, F. Seitz and T. A. Read and C. Zener discussed the cause of discontinuous elongation or the mechanism of occurrence of avalanche of dislocations in the case of single crystal. Discontinuous elongation occurring in our experiment differs in some respects from those found by M. Classen-Nekludowa, R. Becker and E. Orowan and E. Schmid and N. A. Valouch. They found the discontinuous jump in single crystal of pure metal while in our case the jump occurred not in single crystal but in coarse grain polycrystal specimen containing a little impurity, thus it may be natural to connect the grain boundary and impurity to the cause of discontinuous elongation.

The character and constitution of the grain boundary are discussed by many authors and according to B. Chalmers(1) the grain boundary consists of transitional lattice while the result of experiment of T'ing-Sui Kê(2) show that the grain boundaries in polycrystalline aluminium behave in a viscous manner, but at any rate the atomic arrangement at the grain boundary may be irregular. According to F. Seitz(3) when a dislocation moves to the grain boundary and hits on it, it would be difficult for the dislocation to move through it. And when a dislocation is stuck at grain boundary, the atomic arrangement there will be distorted and in the presence of an applied stress and at sufficient temperature the atomic arrangement at the grain boundary will change, for the atoms there are thought to be more mobile than in the crystal. As the result of this atomic rearrangement many nucleations of dislocation will be created on both sides of grain boundary for the width of the grain boundary is thought to be of the order of five interatomic distance. And in the presence of an applied stress they will start and grow to full line dislocations.

In this case it may be natural to suppose that the applied stress must be large enough to cause the atomic rearrangement and let the created nucleation start and grow. Moreover it is necessary that the started dislocations can move freely and do not hit on another grain boundary or the specimen must be a coarse grain polycrystal. When a jump occurs the stress decreases as we used the apparatus as described in the first report, and when the stress decrease to the magnitude that it cannot make the nucleation of dislocation start and move, jump will end. But we cannot say definitely that a jump ends after how many dislocations have moved or after how much the applied stress has decreased. For example at the elongation stage of about 10% the magnitude of a jump decreases and this may be explained considering that a dislocation become unmovable as the work hardening the specimen proceeds.

These assumptions may be adaptable only to the case of aluminium containing a little impurity and when the apparatus as described was used. In the following we will discuss the results of experiment with these assumptions.

In § 2 we find that $N\times\varDelta$ is independent of the strength of spring, *i. e.*, $\varDelta$ is proportional to $1/N$ or time interval between jumps. As shown in Fig. 5A of the first report the stress increases rapidly soon after a jump ends, and when it recovers large enough to cause the atomic rearrangement at grain boundary and let the created nucleation start and grow, the next jump occurs. The recovering speed of stress depends upon the testing condition such as temperature, tensile speed, etc., but may be independent of the strength of spring; so the time necessary to recover is roughly proportional to the magnitude of a jump or the magnitude of a jump is proportional to the time interval.

The character of grain boundary may be influenced by temperature. Above 350°C no jump was observed and this fact suggests that the character of grain boundary may change at about this temperature.

In §4 we find that the magnitude of jump becomes greater as the tensile speed becomes slower. As described in §7 the mean duration of a jump is about 5/100 sec so the elongation of specimen during a jump is about 0.125, 0.25 and 0.5μ corresponding to the tensile speed 2.5, 5 and 10μ/sec respectively, therefore we can expect that $\varDelta$ differs 0.12μ for the tensile speed 2.5 and 5μ/sec and 0.25μ for the tensile speed 5 and 10μ/sec as the effect of duration, but the above result shows the difference of about 5 and 10μ and thus this result cannot be explained by the effect of duration. As to the number of jumps we see in §4 that when the tensile speed becomes slower the magnitude of a jump becomes greater, so from the former discussion the number of jumps should be less for slower tensile speed, but the result of experiment shows that the number of jumps for the elongation of 1/10% of specimen becomes a little more great when the tensile speed becomes slower. This fact means that though the tensile speed becomes half, the speed of recovering of stress after a jump has ended do not become half but it is more than half. And the recovering of stress after a jump has ended is equal to the increasing of stress when we pull the specimen after it has been work hardened so in such case the speed of recovering of stress may not become half though the tensile speed becomes half.

We find in §5 that when the orientation of neighbouring crystal is nearly equal, the number of jumps is very few and the stress-time curve is just like Fig. 5B of the first report, *i. e.*, the jump does not occur successively. According to B. Chalmers⁽¹⁾ the atomic arrangement of grain boundary is rather regular in such a case, so it would be rather easy for the dislocations to pass through the grain boundary and only a few dislocations would be caught there, thus the number of jumps is very few.

The effect of grain size is such as discussed before and the effect of number of grain boundaries may be interpreted as follows. For the occurrance of a jump the stress must be large enough as described before and after a jump occurred the next jump occurs when the stress has recovered, and though a dislocation hits on the grain boundary during recovering, this does not develope to the avalanche of dislocation. Thus the number of jumps will not increase though there are many grain boundaries in a specimen and the number of the stuck dislocations becomes great.

The result on the duration of a jump shows that the rate of starting and moving of dislocations during a jump is quite independent of the tensile condition but it mainly depends upon the character of grain boundary and crystal where the jump is occurring.

In conclusion the author wishes to express his hearty thanks to Prof. S. Kaya to Tokyo University for his kind interest in this work.

References.

(1) B. Chalmers: Proc. Roy. Soc. A, **162** (1937), 120.
(2) T'ing-Sui Kê: Phys. Rev., **71** (1947), 533.
(3) F. Seitz: Physics of Metals, (1943), p. 108.

On the Oxidation of the Evaporated Barium Film

Tetsuya ARIZUMI and Seiichi KOTANI.

Kawanishi Machine Works Ltd., Kobe.*

(Received, July 20, 1949.)

§1. Introduction.

The getter acts as a kind of pump in manufacturing of vacuum tubes, making possible their mass production, while it acts as a keeper during their lives, absorbing gases released from various parts of a tube. In spite of such important characters, only a few studies⁽¹⁾ on the gettering process have been published, probably because of many technical difficulties and irreversibility. In this paper, the absorption of oxygen by the barium getter will be reported and the possible structure of the getter mirror will be discussed.

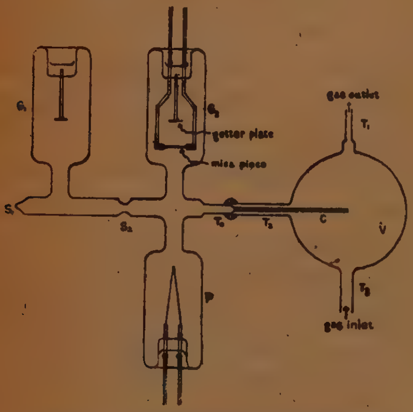

Fig. 1. Experimental apparatus

§2. Experimental Procedure.

The schematic diagram of the apparatus is shown in Fig. 1. It is divided into two parts, one of which is a main tube with two getter chambers G_1 and G_2, a Pirani gauge P and a fine and long glass capillary C. After the tube had been evacuated through S_1, the getter G_1 was flashed and the tube was sealed at S_1. After several hours the tube G_1 was tipped off at S_2 and then the second getter G_2 was flashed. During evacuation, all glass parts were baked for several hours and two getter plates were heated to dark-red by H. F. bombarder several times before the final flashing.

In the second getter chamber G_2, a small mica piece of $3 \times 1\,\mathrm{cm}^2$, is mounted 2 cm apart from getter plate. Some amount of evaporated barium is condensed onto the mica piece which is used to measure the resistance of the getter mirror. Both ends of the mica piece are silver plated and tightened through gold foils by thin nickel sheets to which the outer leads were welded.

The second tube V is a glass bulb of about 100 cc with three small glass tubes T_1, T_2, and T_3. The capillary of the first tube is inserted into V through the tube T_2. The tube T_3 was connected to an oxygen source through a purifier and a mercury manometer. Preceding to each experiment, oxygen was flowed into the bulb through T_3 and flowed out from T_1 and T_2 for several ten minutes to replace air in the bulb by oxygen, and it is flowed continuously during each experiment.

After air in V is replaced thoroughly by oxygen, the end of the capillary was pushed out slightly outside of T_4 and it was broken by hand. Then it was moved to the centre of the bulb. If necessary, T_0 and T_1 are jointed air-tightly by the small amount of vacuum clay. These processes were carried out as quickly as possible. When it is necessary to seal the capillary, the end is pushed out from T_4 and sealed by a weak burner.

The resistance of the getter mirror was measured by the deflection of a micro-ammeter in a bridge circuit, previously calibrated by standard resistances, since the rapidness is required in almost all cases. The measurement of pressure and the calibration of the capillary followed the methods described in the next paper.⁽²⁾

A batalum getter or an iron-clad barium getter was used for the experimental purpose. In the case of clad getter, the rapid sealing and evacuation is required to prevent the oxidation of the getter. The experiment was, in general, carried out at room temperature and after a series of experiments is finished, the total amount of the getter was dissolved in H_2SO_4 and weighted in the form of $BaSO_4$.

---

* New name, Kobe Kogyo Corp.

§ 3. Pressure Curve.

Even when oxygen begins to be introduced, the pressure is, in general, kept almost constant for a rather long time. Precisely speaking, however, it increases very slowly in many cases. It takes from several minutes to several hours to observe the rapid increase of the pressure. Such pressure change as shown in Fig. 2 is the most typical one, encountered in experiments most frequently, Even at the final stage of the rapid pressure increase, the getter has still an intense absorption ability; when the capillary is sealed, the pressure decreases rapidly to the original value.

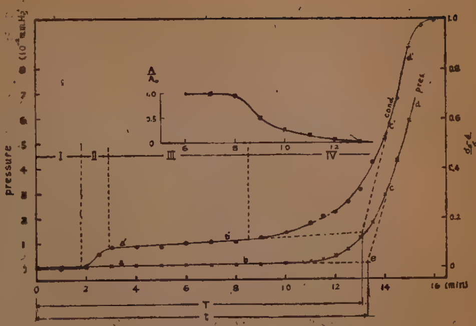

Fig. 2. Typical pressure and conductivity curves.

If the amount of gas introduced through the capillary, u, is smaller than v, that absorbed by the getter, the pressure is kept constant and if u is larger than v, it increases. Thus the cross point e of extrapolation of ab and cd, as shown in Fig. 2, may well be defined as a rough measure for the condition $u = v$. The length of oe, designated by T in the following, is supposed simply to depend upon the amount of barium, the size of the capillary and the structure of the getter mirror, but many

Table I.

tube No.	kind of gas	resistance initial (Ω)	amount of barium (g)	amount of gas flow (mol/min)	temperature (°C)	T (min)	t (min)	M (g)	Q (mol/g)	Remarks
1	O_2	1,750	—	7.4×10^{-8}	15	11	1	—	—	
2	air	4,624	—	—	—	1.5	0	—	—	
3	O_2	210	—	7.4×10^{-8}	18	124	3.1	—	—	
4	air	150	—	7.4×10^{-8}	—	27.3	—	—	—	
5	air	—	—	3.2×10^{-8}	—	10.6	—	—	—	
6	O_2	19	0.002	—	—	60	62	—	—	heat-treated
7	O_2	7.2	0.0014	5.0×10^{-8}	—	85.4	90	0.0026	2.9×10^{-3}	,,
8	O_2	75	0.0014	5.0×10^{-8}	—	52.5	0	0.0025	1.8×10^{-3}	batalum getter
9	O_2	1,500	0.0006	5.0×10^{-8}	—	3.6	1	0.0005	8×10^{-4}	
10	O_2	1.0	0.0094	2.9×10^{-7}	14	13.4	13.7	0.0127	3.7×10^{-4}	
11	O_2	0.88	0.0098	5.0×10^{-8}	14	220	220	0.0035	1.1×10^{-3}	broad maximum in pressure curve
12	O_2	1.6	0.0041	1.5×10^{-7}	14	24.1	25.6	0.0011	8.8×10^{-4}	
13	O_2	70.0	0.0032	2.7×10^{-7}	14	36.3	46.0	0.0030	3.1×10^{-3}	rapid increase of resistance in the initial stage
14	O_2	11.0	0.0038	2.7×10^{-7}	14	26.2	32.9	0.0025	2.2×10^{-3}	
15	O_2	9.0	0.0019	8.5×10^{-8}	14	14.6	13.9	0,00035	6.0×10^{-4}	
16	O_2	30.7	0.0041	8.5×10^{-8}	14	14.2	15.5	0.00039	3.0×10^{-4}	small maximum in pressure curve, rapid increase of resist. in the initial stage
17	O_2	4.2	0.0013	8.5×10^{-8}	14	7.3	0.6	0.00025	4.8×10^{-4}	
18	O_2	44.0	0.0025	1.0×10^{-7}	38	112	96.5	0.0058	8.5×10^{-3}	
19	O_2	0.7	0.0013	1.9×10^{-7}	50	35	0	0.0018	5.0×10^{-3}	
20	O_2	16.5	0.0038	1.9×10^{-7}	30	ca 77	—	—	3.9×10^{-3}	

results show that T is almost independent of the weight of barium and the amount of introduced oxygen, as summerized in Table I.

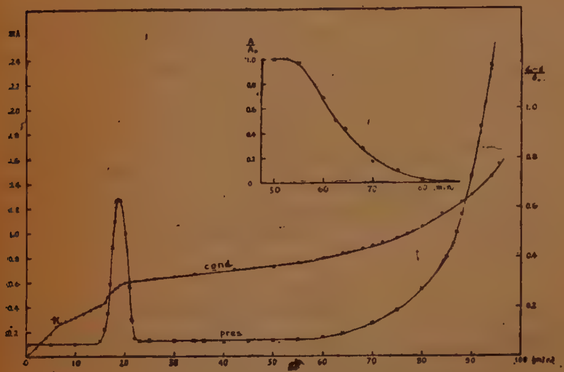

Fig. 3. Pressure and resistance curves of heat-treated getter.

Among many results, there are different types of pressure curves. The most remarkable anomaly was obtained in a heat-treated getter. Fig. 3 shows such an example, in which the getter chamber was baked at 350°C for 30 minutes. The pressure curve has a sharp maximum, but the pressure at both sides of the maximum is almost equal. The resistance of the getter mirror after the heat treatment differs slightly from the original one, suggesting the structure change of the mirror. Sometimes the pressure curves with a broad or a small maximum were obtained, which seems to show that the almost similar structure as the heat-treated one happens to be formed by the temperature rise of the glass wall being condensed by evaporated barium. It is found in Table I that T is much longer in abnormal pressure curves than in typical ones, giving the conclusion that the structure of the getter mirror has a remarkable effect upon T.

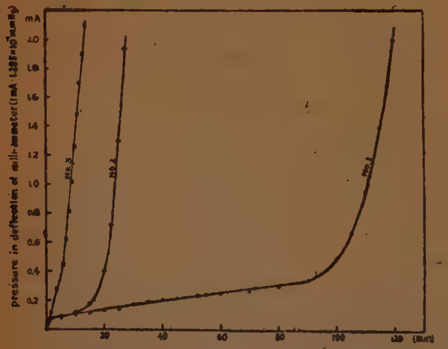

Fig. 4. Pressure curve of heat-treated getter (air)

Another example of the heat treated getter is reproduced in Fig. 4, in which dry air were introduced. The curve (1) is the pressure change of an untreated getter, while (2) and (3) are curves for the getters heated for 20 min. and for 30 min. at 350°C respectively. In spite of the same capillary being used, T differs largely. Although there is fluctuation caused by uncontrollable flashing conditions, such large difference in T is to be attributed to the structure change of the getter mirror. Differing from oxygen, however, the pressure begins to increase much sooner, without any bump, as the time of heat-treatment is longer. Such difference in the pressure curve in both kinds of gases will be discussed in the following.

Now the total amount of oxygen, absorbed by unit weight of barium in T min. is represented by

$$Q = \frac{sT}{W},$$

where W is the total weight of getter, and s the amount of oxygen through the capillary. Q is also given in Table I. With several exceptions it is found to be almost the same order at a constant temperature, independent of the amount of barium and of the introduced gas, supporting that the structure of the getter mirror is the most important factor. It also increases as the surrounding temperature becomes higher and thus another factor to determine Q is the temperature of the mirror.

§ 4. Conductivity.

The most typical change of the conductivity is shown in Fig. 2, in which $(\sigma_0-\sigma)/\sigma_0$ is plotted (σ is tne conductivity of the mirror and subscription 0 shows the initial value). Assuming that the thickness of the mirror is uniform everywhere, $(\sigma_0-\sigma)/\sigma_0$ represents the ratio of the thickness of oxide layer to that of initial layer.

At first the conductivity remains unchanged for a moment even after gas is flowed into, but this region is not always observed (region I). Then $(\sigma_0-\sigma)/\sigma_0$ begins to increase rather suddenly with a comparatively large velocity (II) and it is followed by a much slower increase (III). Finally

$(\sigma_0-\sigma)/\sigma_0$ again increase rapidly until the conductivity becomes to be almost zero (IV).

When the amount of the flashed getter is so small that the resistance may be larger than 1,000Ω, the constant part of resistance decrease remarkably and for the still smaller quantity they do not appear at all, showing that the structure of the mirror is not uniform but granular, because very thin film of barium connected between granules is oxidized to lose the conductivity.

In several cases the conductivity changes discontinuously. The most remarkable one of this kind is seen on the heat-treated getter. Besides the ordinary discontinuity marked by k in Fig. 3, a sudden decrease of the conductivity is observed just at the beginning of the hump in the pressure curve, suggesting that both phenomena are caused by the same effect. The sudden change of $(\sigma_0-\sigma)/\sigma_0$ means the discontinuous change in the oxidation velocity, which seems to be attributed to the dropping-off of the oxide layer or the development of cracks in it to expose fresh metallic barium to oxygen atmosphere. Similar phenomena have already been observed in the case of oxidation of copper at high temperature.(3)

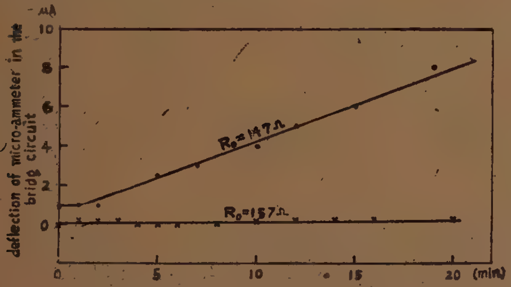

Fig. 5. Local difference of the getter mirror.

Sometimes such local non-uniformity of the structure as mentioned in the following is also observed. Two thin mica foils were mounted 1.5 cm and 2.5 cm respectively apart from the getter plate and on these foils the getter mirrors were formed. Introducting air through the capillary, both the pressure and resistance were measured, whose results are shown in Fig. 5. Although both initial resistances are almost equal, one remains almost unchanged during the introduction of air, while the other changes distinctly. Probably the former is of almost uniform structure and the latter of granular one. The structure of the getter mirror seems to be dependent largely upon the flashing conditions, as predicted from the electron diffraction studies on the getter mirror by Yamaguchi and Ichimiya.(4)

The total amount of barium consumed for the combination with introduced oxygen up to $\sigma/\sigma_0=10^{-1}$ is shown by M in Table I. If the mirror is of uniform thickness everywhere, M must be equal to the total amount of barium. In many experimental results, however, both quantities do not coincide with each other, disproving the uniform structure of the mirror.

§ 5. Correlation between Pressure and Resistance Curves.

The structure of the mirror can be inferred roughly from the correlation between both curves. To give a rough estimation for the length of the constant resistance part, e' is defined similarly to e in the pressure curve. These values designated by t are given in Table I; T must be longer than t in the granular structure because each isolated granules have still strong absorbing power even after the complete oxidation of thin film connected granules. In eight experimental tubes T is almost equal to t. In only two of these eight tubes, including heat-treated one, M is smaller than M' the total amount of barium, and in seven tubes t is much smaller than T, showing that in most cases the mirror is of granular structure. An example is presented in Fig. 6.

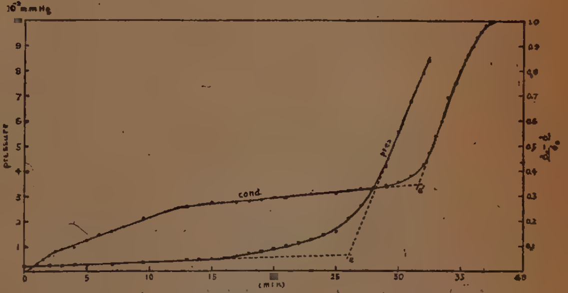

Fig. 6. Pressure and conductivity curves.

The heat treatment acts to diminish the porosity of the mirror and thus to decrease its true surface area. The appearance of the hump in the oxygen pressure curve of the heat-treated getter is due to the following mechanism: So long as the oxide layer covering the surface is still thin, the layer is perfectly compact and the oxidation velocity decreases gradually as the layer grows, resulting in the gradual increase in the pressure, followed by the rapid change, but as the thickness of the oxide layer goes over a definite value, many cracks are induced due to the volume contraction, exposing the fresh metallic surface. Thus the absorbing power recovers to decrease the pressure again and at the same time the oxidation velocity, that is, the type of the oxidation changes suddenly. Perhaps no cracks are induced in nitride layer and the reduction of the surface area by the heat treatment results immediately in the reduction of the absorbing ability and makes the pressure increase much earlier as shown in Fig. 4. The difference in the oxidation velocity between the region II and III in the typical curve will be attributed to the similar changes in the type of the oxidation. Several evidences for this conclusion were obtained: in several cases a small or a broad maximum appears on the pressure curve and in other cases dp/dt changes slightly, in the neighbourhood of the kink point from the region II to III. Perhaps the lack of uniformity and the local difference in the getter structure make it difficult to observe such a remarkable hump in the pressure curves as encountered in the heat treated getter. In the region III the oxidation becomes to proceed locally near crystal boundaries or at cracking points, as schematically shown in Fig. 7(a) resulting in the difference in the oxidation velocity. Perhaps the discontinuity corresponds to the change from the uniform oxidation to that along crystal boundaries.

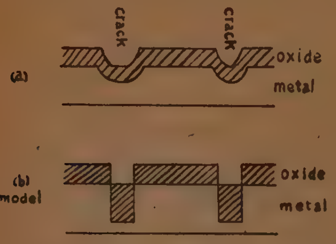

Fig. 7. Development of the oxide layer:

In the region I the resistance of the getter mirror does not change for a moment, while the pressure increases slightly, probably due to the mean free time of the gas and the surface adsorption.

As the amount of absorbed gas becomes so large that the thin layer connected between granules may be oxidized completely (refer to Fig. 8), the surface area decreases gradually, resulting in the simultaneous increases of the pressure and the resistance in the region IV, encountered in many cases. The surface area A can be calculated from the following formula:

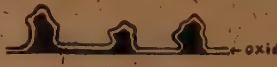

Fig. 8. Grannlar structnre.

$$st-\frac{v}{PL}p=\frac{Ax\rho}{M}=\frac{Ax_0\rho}{M}\frac{\sigma_0-\sigma}{\sigma_0}$$

where v represents the total volume of a experimental tube. x_0 and x thicknesses of the original barium layer and of the oxide layer respectively, ρ and N the density and the molecular weight of barium oxide, P standard pressure and L Loschmidt number. Differentiating and rearranging, we obtain

$$A=\frac{M\sigma_0}{\rho x_0}\left(s-\frac{V}{PL}\frac{dp}{dt}\right)\Big/\frac{d\sigma}{dt}$$

dp/dt and $d\sigma/dt$ are obtained from experimental curves. The calculated values of A/A_0 (A_0 is A value in $dp/dt=$ const. and $d\sigma/dt=$ const) shown in Figs. 2 and 3 begin to decrease just at the begining of the region IV, giving a support to the above assumption.

§ 6. Flashing Conditions.

Many studies on the evaporated film of metal have been carried out up to the present time. Picard and Duffenback⁽⁵⁾ concluded from their observation by the electron microscope that the evaporated film has the fine granular structure. The porosity of the film depends upon the pressure and the distance from the source⁽⁶⁾. This must hold for the flashing of the getter. In this case, however, a large amount of gases is released from the getter itself and the getter plate and thus the pressure reaches temporarily to from several mm. Hg. to several ten mm. Hg. One part of the released gases will be absorbed into the getter mirror and the other part will be exhausted by the pump to decrease the pressure rapidly. Thus the structure of the getter mirror formed at the initial stage of flashing is different from that formed at the final stage. When the getter is flashed at the pressure of several m.m. Hg. many isolated fine granules are observed visually to be formed on the glass wall at first and then they are covered by the uniform layer.

The structure depends largely upon the wall temperature onto which the mirror is formed. As the getter plate must be heated beyond 1,000°C at the flashing, the temperature of the glass wall is not constant in time and place, being another cause for the granular structure at the initial stage and moreover, for the local difference, together with unequality of the distance and the directivity of evaporation.

Thus, in general, the structure of the getter mirror near at the getter plate may well be considered as assumed in Fig. 8, while it is of thin and small granular structure apart from the getter plate, in agreement with Yamaguchi and Ichimiya's results. The intense absorption ability observed by Ehrke and Slack(5) on the getter flashed in argon atmosphere is attributed to the large surface area, characteristic of the remarkable granular structure.

§ 7. Conclusion.

In this paper the structure of the getter mirror and the mechanism of gas absorption were studied by the measurement of the pressure and resistance of the getter mirror and following results were obtained:

(1) The structure of the mirror is granular in most cases.

(2) The oxidation proceeds uniformly from the surface at first and then it proceeds along crystal boundaries.

(3) As the thickness of the oxide layer grows, many cracks are induced to recover the absorption ability.

In conclusion we acknowledge Mr. Imayeda and Mr. Shimizu for their sincere discussions.

References.

(1) O. Harashima: J. Elec. Comm. (in Japanese) **27** (6943) 548.
N. Kameyama: MUSEN SHIRYO (in Japanese) Dec. (1940).
L. Ehrke & M. C. Slack: J. App. Phys. **11** (1940) 129.
(2) T. Arisumi & K. Imayeda: J. Phy. Soc. Japan, **5** (1950) No. 3.
(3) J. S. Dunn, J. Inst. Metals, **46** (6931) 25.
(4) S. Yamaguchi & T. Ichimiya: Powder and Powder Metallurgy (in Japanese) **2** (1948) 11.
(5) R. G. Picard & O. S. Duffenback: J. App. Phys. **14** (1943) 291.
(6) K. Kobayashi, B. Shigihara & H. Kubota; OYOBUTSURI (in Japanese) **17** (1948) 225.

Statistics of the Three-Dimensional Ferromagnet (I)

By Takehiko OGUCHI.

Tokyo Institute of Technology, Oh-okayama, Tokyo.

(Received Aug. 11, 1949.)

§ 1. Outline of the Method.

Recently, the Ising model of ferromagnetism has been treated by the matrix method(1)(2). But so for it is mainly the one and two dimensional ferromagnets that have been discussed. If one wishes to treat the three-dimentional ferromagnet by this method, what should be thought of in the first place, is to regard one layer as a constituent element and to pile layers on one by one. Following this line of approach, however, one can hardly obtain any result owing to considerable mathematical difficulties, since the energy terms are so complicated and the matrix is filled solidly with elements.

Therefore, the author has given it up to regard each layer as a constituent element and, instead of it, extending the screw method, which was first given in the two-dimensional ferromagnet by Kramers and Wannier⁽¹⁾, to the three-dimensional one, adds a spin one by one.

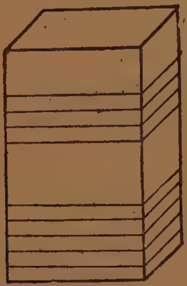

Fig. 1.

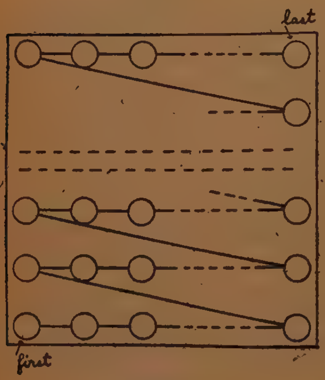

Fig. 2.

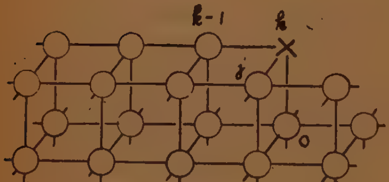

Fig. 3.

Let the ferromagnet of the simple cubic lattice be divided into many layers as shown in Fig. 1. In every layer, as shown in Fig. 2, the sequence of arrangement of spins is the following: —starting from the first position (for the sake of convenience, we shall take the first position at the corner of the layer, see Fig. 2), we add another spin beyond the one just placed previously, thus having arranged entirely one line. We then arrange the next line in the same sequence and so on, reaching to the last position. Then we move to the first position in the next layer and repeat the same operation. Now consider the case of arranging spins in the m-th layer. Let the spin which is to be added next be denoted by k (see Fig. 3). The number of spins in one layer is k. Since the interactions are restricted to only the immediate neighbors, the spins which interact with the k-th spin, are the $(k-1)$-th spin just placed previously and the j-th spin placed immediately beside it in a preceding line and the 0-th spin placed just under the k-th spin in the $(m-1)$-th layer. Let each of the spins be capable of two orientations which we characterize by $\mu_i=1$ and $\mu_i=-1$. We shall take interaction energies between parallel and antiparallel pairs to be $-\frac{1}{2}J$ and $+\frac{1}{2}J$ respectively, so that the three interaction energies which are just stated above, are the following:

$$-K\mu_k\mu_{k-1}\,,\quad -K\mu_k\mu_j\,,\quad -K\mu_k\mu_0\,,\tag{1.1}$$

where

$$K=J/2kT\,.\tag{1.2}$$

Let us call $A(\mu_{k-1},\cdots,\mu_{j-1}\cdots,\mu_0)$ the probability reffering to them alone, and $A(\mu_k,\cdots,\mu_j,\cdots,\mu_1)$ the one in which μ_1 occupies the place of μ_0, μ_2 of μ_1 and so forth. By rigorous Boltzmann statistics, these are related as follows:

$$\lambda A(\mu_k\cdots\mu_j\cdots\mu_1)=\sum_{\mu_0=\pm1}\exp\left[K\mu_k(\mu_{k-1}+\mu_j+\mu_0)\right]\,A(_{k-1}\cdots\mu_{j-1}\cdots\mu_0)\tag{1.3}$$

although the unknown factor λ enters because the Boltzmann exponentials are only proportional to probabilities, it becomes the eigenvalue ef Eq. (1.3).

The total energy E of our system at zero field takes the form:

$$E=-\frac{J}{2}\sum_{<i,k>}\mu_i\mu_k\tag{1.4}$$

where $\sum_{<i,k>}$ shall mean that the sum is carried out over all pairs (i, k) which are nearest neighbors. Thus the partition function f is

$$f=\sum_{\mu_1,\mu_2,\cdots\mu_N=\pm1}\exp\Big[K\sum_{i=k}^{(L+1)k-1}\mu_i\mu_{i+1}+K\sum_{i=1}^{Lk}\mu_{j+i}\mu_{k+i}+K\sum_{i=1}^{Lk}\mu_i\mu_{k+i}\Big]\tag{1.5}$$

where N denotes the total number of spins and L. denotes the total number of layers. The eigenvalue λ of Eq. (1.3) and the partition function f are related to each other as follows:—Since the matrix (1.3) is not symmetrical, we have to consider the left-handed eigenvectors which we call $B(\mu_k, \cdots, \mu_j, \cdots, \mu_1)$ and which satisfy the equations

$$\sum_{\mu_k} \exp[K\mu_k(\mu_{k-1}+\mu_j+\mu_0)]\, B(\mu_k, \cdots, \mu_j, \cdots, \mu_1) = \lambda B(\mu_{k-1}, \cdots, \mu_{j-1}, \cdots, \mu_0) \quad (1.6)$$

With proper normalization A_q and $\widetilde{B}_p$ can be made to satifsy orthogonality conditions:

$$\sum_{\mu_i} \widetilde{B}_p(\mu_k, \cdots; \mu_1)\, A_q(\mu_k, \cdots \mu_1) = \delta_{pq} \quad (1.7)$$

By repeating the matrix operation k times we obtain from Eqs. (1.3) and (1.6).

$$\sum_{\mu_1 \cdots \mu_k} \exp[K\sum_{i=k}^{2k-1} \mu_i\mu_{i+1} + K\sum_{i=1}^{k} \mu_{j+i}\mu_{k+i} + K\sum_{i=1}^{k} \mu_i\mu_{k+i}]\, A(\mu_k \cdots \mu_1) = \lambda^k A(\mu_{2k} \cdots \mu_{k+1}) \quad (1.8)$$

$$\sum_{\mu_{k+1} \cdots \mu_{2k}} \exp[K\sum_{i=k}^{2k-1} \mu_i\mu_{i+1} + K\sum_{i=1}^{k} \mu_{j+i}\mu_{k+i} + K\sum_{i=k}^{k} \mu_i\mu_{k+i}]\, B(\mu_{2k} \cdots \mu_{k+1}) = \lambda^k B(\mu_k \cdots \mu_1) \quad (1.9)$$

From Eqs. (1.7), (1.8) and (1.9),

$$\exp[K\sum_{i=k}^{2k-1} \mu_i\mu_{i+1} + K\sum_{i=1}^{k} \mu_{j+i}\mu_{k+i} + K\sum_{i=1}^{k} \mu_i\mu_{k+i}] = \sum_{p=1}^{2^k} \lambda_p^k A_p(\mu_{2k} \cdots \mu_{k+1})\, B_p(\mu_k \cdots \mu_1) \quad (1.10)$$

We can write down the same formula for the next layer:

$$\exp[K\sum_{i=2k}^{3k-1} \mu_i\mu_{i+1} + K\sum_{i=k+1}^{2k} \mu_{j+i}\mu_{k+i} + K\sum_{i=k+1}^{2k} \mu_i\mu_{k+i} = \sum_{p=1}^{2^k} \lambda_p^k A_p(\mu_{3k} \cdots \mu_{2k+1})\, B_p(\mu_{2k} \cdots \mu_{k+1}) \quad (1.11)$$

Now we multiply (1.10) and (1.11) and sum over the spins of the middle layer $\mu_{2k}, \cdots, \mu_{k+1}$. We get

$$\sum_{\mu_{k+1} \cdots \mu_{2k}} \exp[K\sum_{i=k}^{3k-1} \mu_j\mu_{i+1} + K\sum_{i=1}^{2k} \mu_{j+i}\mu_{k+i} + K\sum_{i=1}^{2k} \mu_i\mu_{k+i}] = \sum_{p=1}^{2^k} \lambda_p^{2k} A_p(\mu_{3k} \cdots \mu_{2k+1})\, B_p(\mu_k \cdots \mu_1) \quad (1.12)$$

We can continue the same process in each layer. To exclude the boundary effect, we shall put

$$\mu_{Lk+i} \equiv \mu_i \quad (1.13)$$

Using Eq. (1.15), we obtain,

$$f = \sum_{p=1}^{2k} \lambda_p^{Lk} = \sum_{p=1}^{2k} \lambda_p^N \simeq \lambda_{\max}^N \quad (1.14)$$

This shows that we can regard $\lambda_{\max}$ as the partition function per individual spin.

In the three-dimensional ferromagnet, the relation (1.13) and the interactions between the last spin in one layer and the first spin in the next layer are difficult to visualize in an actual model. But even if this treatment might cause some error from the boundary effect, we can make this error negligible by making N sufficiently large.

Thus if we solve the eigenvalue problem (1.3), we can obtain the partition function of the three-dimensional ferromagnet.

§ 2. The Properties for Low Temperatures.

Though the eigenvalue problem (1.3) has not yet been solved completely, the author has obtained the eigenvalue in the form of a power series valid at low temperatures by a perturbation treatment of the largest eigenvalues and eigenvectors. In the first place, let us use the dual number system to bring the matrix (1.3) into its customary square form. For the sake of convenience we shall use a system of order numbers each of which is greater than the corresponding dual number by an amount of unity. For example, let us write down several matrix elements:

configuration										ordinal number of row	ordinal number of column	element
k	$k-1$		⋯⋯	j	$j-1$		⋯⋯	1	0			
+	+	+	⋯⋯	+	+	+	⋯⋯	+	+	1	1	e^{3K}
+	+	+	⋯⋯	+	+	+	⋯⋯	+	−	1	2	e^{K}
+	+	+	⋯⋯	+	+	+	⋯⋯	−	+	2	3	e^{3K}
⋯⋯	⋯⋯	⋯⋯	⋯⋯	⋯⋯	⋯⋯	⋯⋯	⋯⋯	⋯⋯	⋯⋯	⋯⋯	⋯⋯	⋯⋯
+	+	+	⋯⋯	+	−	−	⋯⋯	−	−	2^{j-1}	2^j	e^{K}
+	+	+	⋯⋯	−	+	+	⋯⋯	+	+	$2^{j-1}+1$	2^j+1	e^{K}
+	+	+	⋯⋯	−	+	+	⋯⋯	+	−	$2^{j-1}+1$	2^j+2	e^{-K}
⋯⋯	⋯⋯	⋯⋯	⋯⋯	⋯⋯	⋯⋯	⋯⋯	⋯⋯	⋯⋯	⋯⋯	⋯⋯	⋯⋯	⋯⋯

It has already proved convenient to separate the configurations into two classes in accordance with the sign of $\mu_k^{(3)}$. The configurations of the class $\mu_k=+1$ consist of those with order number 1, 2, $\cdots$, 2^{k-1} and are arranged in that order. The remaining half of the configurations belong to the class $\mu_k=-1$ and are arranged in the order 2^k, 2^k-1, $\cdots$, $2^{k-1}+1$. Thus the complete matrix expression is the following:

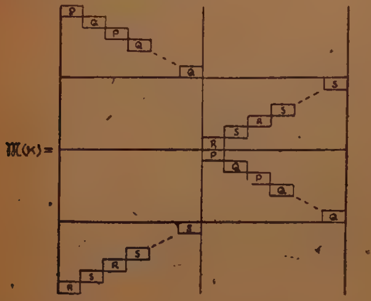

(2.1)

where

$$P=\begin{vmatrix} \xi^3\ \xi & & & \\ & \xi^3\ \xi & & \\ & & \ddots & \\ & & & \xi^3\ \xi \end{vmatrix},\qquad Q=\begin{vmatrix} \xi\ \eta & & & \\ & \xi\ \eta & & \\ & & \ddots & \\ & & & \xi\ \eta \end{vmatrix}$$

$$R=\begin{vmatrix} & & & \eta^3\ \eta \\ & & \iddots & \\ & \eta^3\ \eta & & \\ \eta^3\ \eta & & & \end{vmatrix},\qquad S=\begin{vmatrix} & & & \eta\ \xi \\ & & \iddots & \\ & \eta\ \xi & & \\ \eta\ \xi & & & \end{vmatrix} \tag{2.2}$$

$$\xi=e^K,\qquad \eta=e^{-K} \tag{2.3}$$

The order of the matrix $\mathfrak{M}(K)$ is 2^k. P, Q, R and S are subsidiary matrices and have 2^j columns and 2^{j-1} rows respectively. Though $\mathfrak{M}(K)$ is rather complicated compared with the one which was treated in the two-dimensional problem, $\mathfrak{M}(K)$ is easily seen to be reducible with an orthogonal transformation which is similar to that in the two-dimensional case. Thus two irreducible matrices V_+ and V_- are obtained of order 2^{k-1} and of the following form:

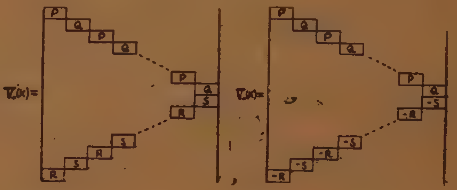

(2.4)

To obtain the eigenvalue valid at low temperatures, first let us transform $V_+(K)$ into $U_+(\eta^2)$,

$$V_+(K)=\frac{1}{\eta^3}U_+(\eta^2)=\frac{1}{\beta^{3/2}}U_+(\beta) \tag{2.5}$$

where $$\beta=\eta^2 \tag{2.6}$$

Second, let us expand $U_+(\beta)$ in the form,

$$U_+(\beta)=U_0+\beta U_1+\beta^2U_2+\beta^3U_3 \tag{2.7}$$

where

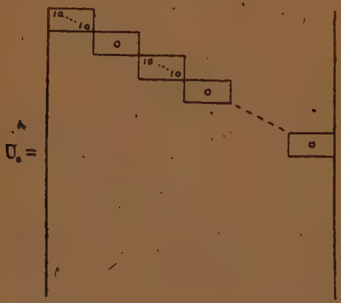

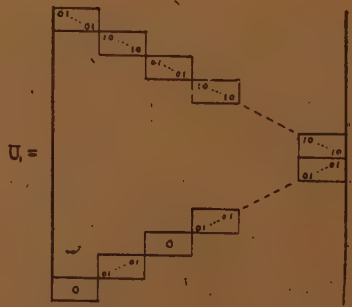

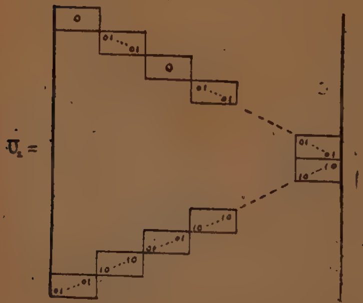

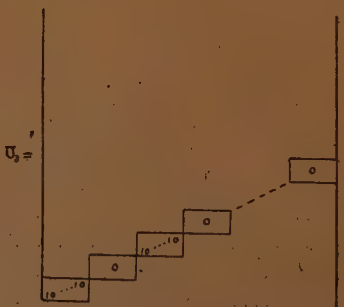

(2.8)

Table of components of the eigenvectors*

ψ_0	ψ_3	ψ_4	ψ_5	ψ_6	ψ_7
1 (1)	1 (2^{k-1})	$1\begin{cases}(2^a\cdot 2^j+1)\\ a=0\cdots k-2-j\end{cases}$	$1\begin{cases}(2^a+1)\\ a=0\cdots j-1\end{cases}$ 1 (2^{k-2})	$1\begin{cases}(3\cdot 2^a\cdot 2^j+1)\\ a=0\cdots k-3-j\end{cases}$ 1 $(2^{k-1}-2^{j-1})$	1 $(3\cdot 2^{j-1}+1)$ 1 (2^{k-3}) $1\begin{cases}2^a\cdot 2^j+2^{2j-k+a}+1)\\ a=0\cdots k-2-j\end{cases}$ $1\begin{cases}(2^{k-1}-2^a\cdot 2^j)\\ a=0\cdots k-3-j\end{cases}$ 1 (2^{k-1})

ϕ_0	ϕ_1	ϕ_2	ϕ^3
1 (1)	$1\begin{cases}(2^a+1)\\ a=0\cdots j-1\end{cases}$	$1\begin{cases}(2^b(2^a+1)+1)\\ a=1\cdots j-1\\ b=0\cdots j-1-a\end{cases}$ $1\begin{cases}(2^a\cdot 2^j+1\\ a=0\cdots k-2-j\end{cases}$	$1\begin{cases}(2^c\{2^b(2^a+1)+1\}+1)\\ a=1\cdots j-2\\ b=1\cdots j-1-a\\ c=0\cdots j-1-a-b\end{cases}$ $1\begin{cases}(2^b\cdot 2^j+2^a+1)\\ a=0\cdots j-1\\ b=0\cdots k-2-j\end{cases}$ 1 (2^{k-1})

* The number denotes the value of component, and the expression in parentheses denotes the order number of the component.

It is evident that U_0 has a single non-degenerate eigenvalue of unity and a $(2^{k-1}-1)$-fold degenerate value of zero. So we can expand $\mu_{\max}$ and $\phi_{\max}$ (maximum eigenvalue and eigenvector of U_+) in the form of power series in β,

$$\mu_{\max}=\mu_0+\beta\mu_1+\beta^2\mu_2+\cdots\cdots, \tag{2.9}$$

$$\phi_{\max}=\phi_0+\beta\phi_1+\beta^2\phi_2+\cdots\cdots \tag{2.10}$$

The eigenvalue equation at β^p is

$$U_0\phi_p+U_1\phi_{p-1}+U_2\phi_{p-2}+U_3\phi_{p-3}=\sum_{q=0}^{p}\mu_q\phi_{p-q}, \tag{2.11}$$

where ϕ_{-3}, ϕ_{-2} and ϕ_{-1} are zero.

As the method of perturbation has been given in detail by Ashkin and Lamb⁽³⁾, we shall not repeat its details except to emphasize the fact that both the left- and right-handed eigenvalues of V_+ and V_- tend to coincide for an infinite crystal.

The result is the following:

$$\lambda=\frac{1}{\beta^{3/2}}(1+\beta^6+3\beta^{10}-3\beta^{12}+15\beta^{14}-30\beta^{16}\cdots) \tag{2.12}$$

From the partition function we can evaluate the energy, specific heat, entropy, etc. by means of the thermodynamical treatment.

For instance the total energy is given by

$$\begin{aligned}E&=NJ\beta\frac{d\log\lambda}{d\beta}\\&=-\frac{3}{2}NJ+NJ(6\beta^6+30\beta^{10}-42\beta^{12}+210\beta^{14}-528\beta^{16}\cdots\end{aligned} \tag{2.13}$$

This completely agrees with the expression given by van der Waerden⁽⁴⁾ (the results given by him are quoted in reference (3), but at present his paper cannot be seen in Japan)*.

It is impossible to obtain the spontaneous magnetization from the partition function, because it does not contain the external field. But it is already known that the spontaneous magnetization is given by the formula,

$$\frac{I}{N\mu}=\frac{\tilde{\phi}_+\phi_-}{\tilde{\phi}_+\phi_+}, \tag{2.14}$$

where ϕ_+, ϕ_- are the right-handed largest eigenvectors of V_+ and V_- respectively and $\tilde{\phi}_+$ is the left-handed largest eigenvector of V_+. From the table of eigenvectors,

$$\begin{aligned}\tilde{\phi}_+\phi_-&=1+(k-2)\beta^6+(5k-j-11)\beta^{10}\\&\quad+\frac{1}{2}(k^2-15k+2j+26)\beta^{12}\cdots,\end{aligned} \tag{2.15}$$

---

* These series are preferably obtained by direct expansion, reference 1, page 264. The author thanks Prof. H. Takahashi and Prof. R. Kubo for this notice.

$$\tilde{\phi}_+\psi_+ = 1+k\beta^6+(5k-j+1)\beta^{10} + \frac{1}{2}(k^2-11k+2j-2)\beta^{12}\cdots\cdots \qquad (2.16)$$

Though both $\tilde{\phi}_+\psi_-$ and $\tilde{\phi}_+\psi_+$ contain k and j, their quotient, as may be expected, becomes independent of these parameters,

$$\frac{I}{N\mu} = 1-2\beta^6-12\beta^{10}+14\beta^{12}-90\beta^{14}+192\beta^{16}\cdots \qquad (2.17)$$

§ 3. Comparison with the results of Bethe-Takagi's Theory.

A straightforward treatment of ferromagnetism is the one developed by Bethe(5). Afterwards, Takagi(6) obtained the same results by a more elementary treatment of the combinatorial problem. In this method, it is customary to express the partition function using the parameters such as the long range order and the short range order. When the number of nearest neighbors is 2, 4, and 6, however, these parameters can easily be eliminated, and then the partition function and the spontaneous magnetization can he expressed in a form explicitly including only the temperature[*]. When the number of nearest neighbors is 6, these results are

$$\lambda = \frac{(1-\beta^2)^3(1+\sqrt{1+4\beta^2})^3}{4\beta^{3/2}\{1-6\beta^4+8\beta^6+(1+2\beta^2)\sqrt{1+4\beta^2}\}}, \qquad (3.1)$$

$$\frac{I}{N\mu} = \frac{\sqrt{2}\{1-6\beta^4+(1-2\beta^2)\sqrt{1+4\beta^2}\}^{\frac{1}{2}}}{1+(1-2\beta^2)\sqrt{1+4\beta^2}}, \qquad (3.2)$$

where β indicates the same temperature parameter as before. These may be expanded in power series of β as follows:

$$\lambda = \frac{1}{\beta^{3/2}}(1+\beta^6+3\beta^{10}-3\beta^{12}+15\beta^{14}-33\beta^{16}\cdots), \qquad (3.3)$$

$$\frac{I}{N\mu} = 1-2\beta^6-12\beta^{10}+14\beta^{12}-90\beta^{14}+216\beta^{16}\cdots \qquad (3.4)$$

Comparison between these results and (2.12) and (2.17) shows that Bethe-Takagi's approximation for the simple cubic ferromagnet at low temperatures is valid up to the terms of β^{14}.

The two-dimensional hexagonal lattice has the same number of nearest neighbors as that of the simple cubic lattice. As shown in Fig. 4 it can be treated by the screw method similar to that for the square net. One of the irreducible matrices is of the following form.

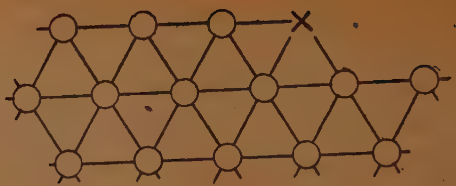

Fig. 4.

$$V_+(K) = \begin{vmatrix} \xi^3\xi & & & & \\ & \xi\eta & & & \\ & & \xi^3\xi & & \\ & & & \ddots & \\ & & & & \xi\eta \\ & & & & \eta\xi \\ & & & \iddots & \\ & & \eta^3\eta & & \\ & \eta\xi & & & \\ \eta^3\eta & & & & \end{vmatrix} \qquad (3.5)$$

The eigenvalue of this matrix for low temperatures can be obtained by the perturbation procedure with the results.

$$\lambda = \frac{1}{\beta^{3/2}}(1+\beta^6+3\beta^{10}-\beta^{12}\cdots), \qquad (3.6)$$

$$\frac{I}{N\mu} = 1-\beta^6-12\beta^{10}+2\beta^{12}\cdots \qquad (3.7)$$

These results show that λ and $I/N\mu$ agree with those of the simple cubic lattice up to the terms of the order β^{10}. These facts show that Bethe-Takagi's approximation, when the number of nearest neighbors is 6, is better for the simple cubic lattice than it is for the two-dimensional hexagonal lattice. This fact seems slightly surprising, because it is vaguely believed that the local field approximation would become successively poorer as the dimension is increased.

Let us denote by r and w the probability of the existence of parallel and antiparallel spin pairs. As total number of spin pairs is $3N$,

$$E = 3N\left(-\frac{1}{2}Jr+\frac{1}{2}Jw\right) = -\frac{3}{2}NJ(2r-1). \qquad (3.8)$$

Since the total energy has been given, we can obtain

$$r = 1-2\beta^6-10\beta^{10}+14\beta^{12}, \text{ for the simple cubic lattice;}$$

---

[*] These are obtained by a tedious calculation from the formulae (2-19), (2-20) in reference 6.

$r = 1-2\beta^{6}-10\beta^{10}+6\beta^{12}$, for the two dimensional hexagonal lattice.

This difference between two lattice types cannot be understood from the standpoint of the local field approximation.

The author desires to express his sincere thanks to Prof. Y. Takagi for his kind guidance and interest in the course of this work.

References.

(1) H. A. Kramers and G. H. Wannier: Phys. Rev., **60** (1941) 252, 263.

(2) E. W. Montroll: J. Chem. Phys. **10** (1942) 61.
R. Kubo: Busseiron Kenkyu, **1** (1943) 1, (in Japanese).
L. Onsagar: Phys. Rev., **65** (1944) 117.
G. H. Wannier: Rev. Mod. Phys. **17** (1945) 50.

(3) J. Ashkin and W. E. Lamb: Phys. Rev., **64** (1943) 159.

(4) v. d. Waerden: Zeits. f. Phys. **118** (1941) 473.

(5) H. A. Bethe: Proc. Roy. Soc., **150A** (1935) 552.

(6) Y. Takagi: Proc. Phys.-Math. Soc. Japan, **23** (1941) 44, 553.

A Note on the Structure of Amorphous Carbon.

By Mitsuo MIWA, Shôichi MAMIYA, Tatsuo IGARASHI and Yoshio ONAI.

Institute of Physics, Tokyo University of Literature and Science.

(Read May 22, 1948; Received August 13, 1949).

The structure of amorphous carbon has been studied by many workers by means of X-ray and electron diffraction and it was first believed that the amorphous carbon is not truely amorphous but merely fine powder of graphite. Arnfelt,(1) however, was aware of the absence of reflection by the net planes oblique to the principal axis such as *(101)*, *(112)*, etc. and suggested that *(001)* net planes of amorphous carbon are not so regularly arranged, though evenly spaced, as in graphite. Hofmann and Wilm(2) noticed that *(100)* and *(110)* lines of amorphous carbon broaden themselves outward only (i. e. on the side of large scattering angle) but not inward, when the size of crystallites becomes small. They also found a conspicuous change in the relative intensities of the two lines with the size of crystallites and concluded that amorphous carbon behaves itself like a two-dimensional lattice in the scatterig of X-rays. These characteristic features of the diffraction patterns of amorphous carbon were later confirmed by many investigators.(3)

One of the present writers(4) also studied various forms of carbon by means of electron diffraction and confirmed the results found by the former workers. He also measured their magnetic susceptibilities and found that the diamagnetic susceptibility of carbon decreases markedly and finally approaches to that of diamond as the size of crystallites diminishes. Summing up these facts, he thought that each *(001)* plane of amorphous carbon is probably splitted into two consecutive planes and that graphite may be indistiguishable from diamond in the ultimate limit of fine grain size as has only few atoms in every direction. According to Ott and others,(5) even the *(001)* plane of large graphite crystal is more or less splitted ("puckering" of *(001)* plane). In the later experiment of Hofmann and Wilm it was shown that *(004)* line fades more rapidly away than *(002)* line, as the grain size diminishes. This also seemed to be an evidence for a definite puckering of *(001)* plane of amorphous carbon. And yet no one seems to have hitherto discussed thereof. In the present experiment, following six forms of carbon have been examined by means of X-ray diffraction in order to investigate the said problem: (a) graphite, (b) carbon prepared by the reduction of CO gas with iron powder at 350~500°C, (c) retort carbon, (d) carbon prepared by the decomposition of C_2H_2 at 800°C, (e) cokes and (f) C_6H_6 soot.

The diffraction patterns were subjected to a microphotometer and the structure of diffraction lines and their relative integrated intensities (relative values of the area under the photometer curve) were determined. The results may be summarised as follows (see Table I and II): (1) as the grain size diminishes, the reflection by those planes oblique to the principal axis becomes weak and finally fades away entirely. (2) The structure of those lines corresponding to (*hk0*) planes become asymmetric. These lines broaden outward only. (3) Their relative intensities change greatly. In the coarse form (*100*) is much stronger than (*110*), while reverse is the case in the amorphous form. (4) The reflection of higher order by (*001*) plane fades rapidly away. (5) The spacing of (*001*) plane becomes larger. These characteristic features of diffraction pattern except (4) have been well known and their interpretation now seems to have been settled. In the following the item (4) will be discussed in detail.

Table I.

Observed relative intensities.

Sample \ (*hk1*)	(*002*)	(*100*)	(*101*)	(*004*)	(*110*)	(*112*)
Graphite	500	17	73	30	27	40
CO corbon (500°C)	500	36	50	15	20	9
CO carbon (350~400°C)	500	51	20	8	21	0
Retort carbon	500	59	—	10	29	—
Cokes	500	58	—	—	29	—
C_2H_2 carbon	500	55	—	—	26	—
C_6H_6 soot	500	60	—	—	27	—
Calculated	500	63	—	31	38	—

Table II.

sample	(*001*) spacing (Å)	grain size (Å)	
		⊥ (*001*)	// (*001*)
Graphite	6.69	—	—
CO carbon (500°C)	6.80	120	150(300)*
CO carbon (350~400°C)	6.80	60	60(120)
Retort carbon	6.90	40	50(100)
Cokes	6.83	45	60(120)
C_2H_2 carbon	6.85	50	60(120)
C_6H_6 soot	7.1~7.4	12	—

* Figures in the bracket correspond to the assumption of two-dimensional lattice (Warren).

The phenomena described in (1), (2) and (3) are closely related to each other and are interpreted as follows: The (*001*) planes of amorphous carbon are irregularly orientated, though evenly spaced, to each other, because of slipping along the plane in some case (Arnfelt) and rotation within the plane in other case (Warren). Reflections by adjacent (*001*) planes, therefore, are no more coherent to each other and the amorphous carbon behaves itself like a two-dimensional lattice in the scattering of X-rays.

Recently Warren[(6)] treated the scattering of X-rays by such a pseudo-plane lattice theoretically. According to him, the integrated intensity of a certain reflection by a plane lattice within the angular range $\theta_B \sim \theta$, where the scattering intensity is appreciable, is given by

$$P_{\parallel}(2\theta) = I_0 \frac{e^4}{m^2c^4} \frac{\lambda^2}{4\pi R} \frac{4a_3 M_0 j}{\sin\theta_B} \delta V < |F(\theta)|^2 > \\ < \frac{1+\cos^2 2\theta}{2} > \sin^{-1}[(1-\sin^2\theta_B/\sin^2\theta)^{1/2}/\cos\theta_B], * \tag{1}$$

where θ_B is the corresponding Bragg angle of three-dimensional lattice, R the distance between the sample and the point of observation, a_3 the thickness of the plane lattice or a half (*001*) spacing of three-dimensional lattice, M_0 the number of unit cells per unit volume in three-dimensional lattice, j the multiplicity of reflecting plane and δV the volume of a crystallite. The notation $< \; >$ denotes a mean value chosen appropriately.

The integrated intensity of reflection by randomly piled (*001*) planes, so far they are evenly spaced, is shown to be equal to that of the regularly piled ones. The latter is given by

$$P_{\perp}(2\theta) = I_0 \frac{e^4}{m^2c^4} \frac{\lambda^3}{16\pi R} \frac{1+\cos^2 2\theta_B}{\sin\theta_B \sin 2\theta_B} M^2 |F(\theta)|^2 \delta V \tag{2}$$

The relative integrated intensities of main lines of amorphous carbon calculated by the formulae (1) and (2) are given in the last row of Table I, in which the line breadth of reflection by two-dimensional lattice is assumed to be $1^1/_2°$ and the mean values $< \ >$ are replaced by the values corresponding to $\theta = \theta_B$. The calculated intensities except (*004*) will be found to agree with the experimental results fairly well.

---

* Here the factor N_1N_2M/A_a given in Warren's formula is replaced by $4a_3M_0\delta V$.

As for the rapid fading of higher order reflection by (*001*) plane, the following items were taken into consideration: (a) puckering of (*001*) plane, (b) fluctuation in the distance of (*001*) plane and (c) large error in the determination of intensity due to the large width of diffraction line. The third item, however, was found to be too small for the explanation of observed results. The second item or the fluctuation of (*001*) spacing, estimated from the broadening of diffraction line and the increase of spacing, also seemed to be too small. Thus we came to the conclusion that the splitting of (*001*) plane is the principal, though not the only, cause of rapid fall of (*004*) intensity. Splitting (u) in a large graphite crystal is said to be about 1/200 of d_{001} or more. The relative intensities of (*002*), (*100*) and (*004*) lines were calculated on the basis of the assumption of much large splitting. Some of them are given in Table III. If the splitting is assumed to be the only cause for the rapid fading of (*004*) line, it must amount to 1/20$\sim$1/15 in CO carbon.

Table III.

Variation of relative intensities with the degree of splitting of (*001*) plane.

u \ (*hkl*)	(*002*)	(*100*)	(*004*)	(*110*)
0	31.7	1.00	1.98	1.90
1/20	31.4	1.00	1.28	1.90
1/15	28.7	1.00	.88	1.90
1/13	25.8	1.00	.35	1.90
1/10	21.5	1.00	.03	1.90

It has been described above that the diamagnetic susceptibility of amorphous carbon is rather close to that of diamond. It will be questionable that this fact is really connected with the puckering of (*001*) plane. Large (*001*) spacing of amorphous carbon, however, seems to be favourable for our conclusion. Puckering also may have some connection with the fact that some form of amorphous carbon such as retort carbon is harder than graphite. Puckering will prevent the slipping along (*001*) plane.

References.

(1) H. Arnfelt: Ark. Mat. Ast. Fys., **23B** (1939), No. 2.
(2) U. Hofmann und D. Wilm: Zeits. Elektrochem. **42** (1936), 504.
(3) A. H. White and L. H. Germer: J. Chem. Phys. **9** (1941), 492; J. Bisoe and B.E. Warren: J. Appl. Phys. **13** (1942), 364.
(4) M. Miwa: Sci. Rep. Tôhoku Univ. **23** (1934), 242.
(5) H. Ott: Ann. Phys. **85** (1928), 81; A. W. Hull: Phys. Rev., **10** (1917), 661.
(6) B. E. Warren: Phys. Rev., **59** (1941), 693.

Dissociation and Ionization of Acetone and Acetic Acid Molecules by Electron Impacts.

By Toyozo KAMBARA.

Hitachi Central Laboratory, Hitachi Ltd.

(Received Aug. 19, 1949.)

§ 1. Introduction.

In the previous papers⑴ we described the dissociation of ethyl, *n*-propyl and isopropyl alcohols by the electron impacts.

In this paper we describe the dissociation of the acetone and acetic acid molecles which are more stable than the alcohol molecule for the resonance effect. The mass-spectrometer used in present experiment is the same one as previously described⑴.

The purified sample of acetone is prepared by Mr. Kawamatsu, the member of the chemical department in our laboratory.

Acetic acid is crystallized in several times and twice distilled avoiding the humidity. Its refractive index is $n_D^{20} = 1.3720$.

§ 2. Investigation on the Acetone.

The energy of C = O bond in the acetone molecule is 152 Kcal/mole given by Pauling. This value is 54 Kcal/mole higher than the arithmetical mean of C = C bond energy (100 Kcal/mole) and C = O bond energy (96 Kcal/mole). For this fact Pauling⑵ says that the acetone molecule is stabilized by the resonance effect between the two following structures, $(H_3C)_2C::\ddot{O}:$ and $(H_3C)_2\overset{+}{C}:\underset{\cdot\cdot}{\overset{\cdot\cdot}{O}}\overset{-}{:}$.

The abundance of the ion produced from the acetone molecule at the electron energy of 80 eV is listed in Table I.

The photograph of the peak of the ion produced from the acetone, taken by magnetic scanning method, is shown in Fig. 2.

The ion corresponding to the $M/e = 43$ is th most abundant one and its amount is about 40% of the total ion. When the oxygen atom is ionized and the C—C bond is broken satisfying the trivalent property of O^+, the ion CH_3CO^+ should appear.

Table I. Nature and relative abundance of ions produced from acetone by electron impact with 80 eV energy.

M/e	Ion	$(CH_3)_2CO^+ = 10$	%
58	$(CH_3)_2CO^+$	10	8.4_5
57	$C_3H_5O^+$	0.5_5	0.4_5
56	$C_3H_4O^+$	0.1_5	0.1
55	$C_3H_3O^+$	0.5_5	0.5
54	$C_3H_2O^+$	0.1	0.1
53	C_3HO^+	0.3	0.2_5
45	$C_2H_5O^+$	0.1_5	0.1_5
44	$C_2H_4O^+$	1.3	1.1
43	$C_2H_3O^+$	51.1_5	43.1
42	$C_2H_2O^+$, $C_3H_6^+$	4.5	3.8
41	C_2HO^+, $C_3H_5^+$	2.2	1.8_5
40	C_2O^+, $C_3H_4^+$	0.8_5	0.7
39	$C_3H_3^+$	3.2_5	2.7_5
38	$C_3H_2^+$	1.7	1.4_5
37	C_3H^+	1.5_5	1.3
36	C_3^+	0.4_5	0.3_5
31	CH_3O	0.2_5	0.2_5
30	CH_2O^+, $C_2H_6^+$	0.0_5	0.0_5
29	CHO^+, $C_2H_5^+$	2.9_5	2.5
28	CO^+, $C_2H_4^+$	2.0_5	1.7_5
27	$C_2H_3^+$	5.3_5	4.5_5
26	$C_2H_2^+$	3.8_5	3.2_5
25	C_2H^+	0.9_5	0.8
24	C_2^+	0.2_5	0.2
18	H_2O^+	0.5	0.4
17	HO^+	0.2_5	0.2
16	O^+, CH_4^+	0.6	0.5
15	CH_3^+	14.5_5	13.3
14	CH_2^+	3.5_5	3.0
13	CH^+	1.1_5	1.0
12	C^+	0.5_5	0.4_5
2	H_2^+	0.5_5	0.4_5
1	H^+	2.4_5	2.0_5

Moreover the undissociated molecular ion is considerably abundant is this case. The CH_3^+ ion is also abundant in the same manner as in the iso-C_3H_7OH.

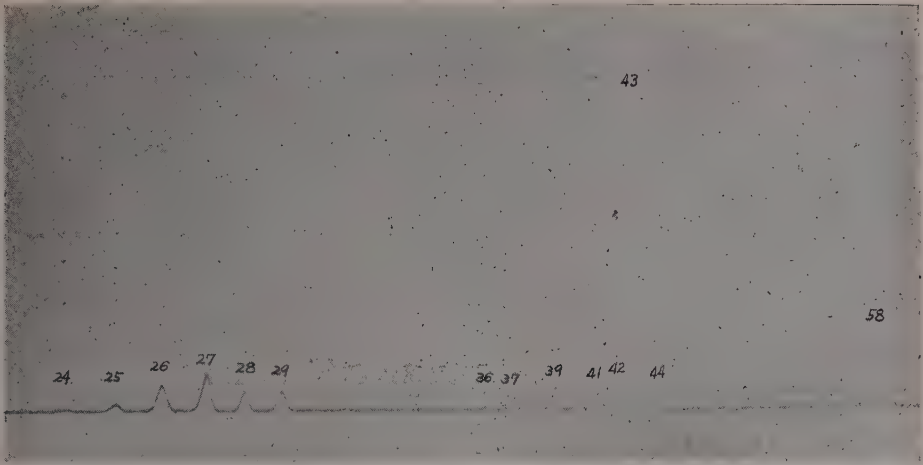

Fig. 1. Mass-spectrum obtained with $(CH_3)_2CO$ at the electron energy of 80 eV.

But it is strange that the amount of CO^+ ion is small. According to the experiment of the photodecomposition of the acetone molecule measured by Spence and Wild(4), the primary process of the decomposition in the ultraviolet region is $(CH_3)_2CH \rightarrow CH_3CO + CH_3$.

This process resembles to the dissociation of acetone by the electron impact. The appearance potentials of several ions are measured by the usual method and corrected by the ionization potential of Ar (15.7 eV). These value are shown in Table II.

Table II. Appearance potentials of ions produced from acetone.

M/e	Ion	$A(X^+)$
58	$(CH_3)_2CO^+$	10.4±0.1 eV
43	CH_3CO^+	12.2±0.1
42	CH_2CO^+, $C_3H_6^+$	15.5±0.2
41	$CHCO^+$, $C_3H_5^+$	16.1±0.1
39	$C_3H_3^+$	16.7±0.1
29	CHO^+, $C_2H_5^+$	17.1±0.1
28	CO^+, $C_2H_4^+$	16.5±0.1
27	$C_2H_3^+$	17.3±0.2
15	CH_3^+	16.0±0.1

Table III. Energies of dissociation of acetone into its various constituents and interpretation of the appearance potential.

No.	Configuration	$P(X)$	$A(X^+)$	$I(X)$
a	$(CH_3)_2CO$	0 eV	10.4 eV	$I((CH_3)_2CO) = 10.4$ eV
b	CH_3CO+CH_3	3.65	12.2	
c	C_3H_6+O	4.9	15.5	$I(C_3H_6) \leq 10.6$
d	C_3H_5+OH	3.7	16.1	
e	C_2H_5+C+H	8.0		
f	$C_3H_3+OH+H_2$	6.1	16.7	$I(C_3H_3) \leq 10.6$
g	$C_3H_3+H_2O+H$	5.4		$I(C_3H_3) \leq 11.3$
h	C_2H_5+CO+H	3.2	17.1	
i	C_2H_5+C+OH	8.0		
j	$HCO+CH_3+CH_2$	6.9	17.1	$I(HCO) \leq 10.2$
k	$CO+C_2H_4+H_2$	1.6	16.5	$I(CO) \leq 14.9$
l	$CO+CH_4+CH_2$	3.1		$I(CO) \leq 13.4$
m	$CO+2CH_3$	4.0		
n	$CO+C_2H_6$	0.2		
o	$C_2H_4+C+H_2O$	5.7		
p	$C_2H_3+CH_3+O$	7.6	17.3	
q	$C_2H_3+CO+H+H_2$	4.7		$I(C_2H_3) \leq 12.6$
r	$C_2H_3+H_2O+CH$	5.3		$I(C_2H_3) \leq 12.0$
s	$C_2H_3+OH+CH_2$	6.9		
t	CH_3+CH_3+CO	4.0	16.0	$I(CH_3) \leq 12.0$
u	$CH_3+C_2H_2+OH$	6.5		$I(CH_3) \leq 9.5$
v	$3C+6H+O$	34.5		

The heat of formation of the acetone vapor is 54 Kcal/mole. The heat of sublimation of carbon is still subject to some uncertainty, but we have adopted the Herzberg's value $L(c) = 5.41$ eV in this paper the same as in the previous paper. Then the dissociation energy of acetone to atoms in gaseous state is calculated to be 34.5 eV. Table III shows the energies $P(X)$ of various combinations of three carbons, one oxygen and six hydrogen atoms at the normal state with respect to the combination $(CH_3)_2CO$ as zero.

The difference between the observed value of the appearance potential $A(X^+)$ of the ion X and the above calculated energy $P(X)$ by which the neutral X is produced from the parent molecule gives the upper limit of the ionization potential of X. These values are also listed in Table III. The discussion of some particular cases will now be given.

1. $M/e = 58$

The ion corresponding to this mass should be the parent molecular ion.

$$A((CH_3)_2CO^+) = I((CH_3)_2CO) = 10.4 \text{ eV}.$$

Duncan(4) obtains the value 10.20 eV for the ionization potential of the acetone molecule from the experiment of the absorption spectrum. Noyes(6) gives 10.1 eV for this value measured with the two electrode tubes. From the precise measurements of the ionization potentials of the hydrocarbon molecules with the mass-spectrometer, Honig(7) concludes that the values of the ionization potentials measured by the electron impact method are 0.02 – 0.2 eV higher than the values obtained from the spectroscopic data. He gives the value 10.46 eV for the ionization potential of acetone. This is in good agreemeut with the value reported here. According to the Mulliken's theoretical prediction(3) $2p$ electrons of the oxygen atom in acetone have the lowest ionization potentials by the change transport effect. Now let us assume that the ionization of the molecule represents the removal of one of these non-bonding electrons from the non-mixing orbits of the oxygen atom and the ionization potential remains constant as ong as the molecular structure is not radically altered and that the value 10.4 eV is the ionization potential of the oxygen atom in the acetone molecule. The value of the ionization potential of acetone is considerably lower than that of alcohol. It seems to be reasonable that the oxygen atom in acetone is easily ionized for the resonance structure of $(H_3C)_2\overset{+}{C}:\underset{\cdot\cdot}{\overset{\cdot\cdot}{O}}\overset{-}{:}$.

2. $M/e = 43$

The ion corresponding to this mass is the most abundant one. The process by which this ion is produced is $(CH_2)_2CO \rightarrow CH_3C\overset{+}{O} + CH_3$.

Norrish, Crone and Saltmarsh(8) give the value of 96.5 Kcal/mole for the C–C bond energy of acetone from the experiment of the predissociation spectrum, but M. Burton(9) proposes 73.5 Kcal/mole for this value from the consideration of the reaction kinetics.

On the other hand Stevenson(10) obtains $B_{CC} = 82.6 \pm 9$ Kcal/mole for the C–C bond energy of ethane from the various data of the electron impact experiments. E. R. von Artsdalen and Valatin give nearly the same value of 85.6 ± 2.3 Kcal/mole and 82.78 Kcal/mole respectively for this energy. If we use the value 83 Kcal/mole for B_{CC} of ethane given by Stevenson and others and also use the value 84 Kcal/mole for B_{CC} of CH_3CHO and 84.5 Kcal/mole for B_{CC} of $(CH_3)_2CO$ as Burton presumes, the B_{CH} of CH_4 and HCHO are respectively calculated to be 100 Kcal/mole and 89.5 Kcal/mole. Now if we use 84.5 Kcal/mole for B_{CC} of acetone, the appearace potential $A(CH_3CO^+) = 12.2$ eV is led to the unreasonable value of $I(CH_3CO) \leq 8.5$ eV without the consideration of the trivalent property of O^+. In the alcohol molecule we use the value 3.6 eV for the difference between the $C = O$ and C C bond energy. In the acetone molecule let us define the value α for the difference between $C \equiv O$ and $C = O$ bond energy. If we use the value 10.4 eV for the ionization potential of the oxygen atom as previously assumed, the value α is approximately decided as follows; $10.4 + 3.7 - \alpha \leq 12.2$ eV, $\alpha \geq 1.9$ eV. Now if we compare the value α with the energy difference between $D(CO)$ and B_{CC} in acetone which is 2.5 eV, the approximately calculated value α is only 0.6 eV lower than the other. In considering the uncertainty of C–C bond energy the value α is in good agreement with the other.

3. $M/e=42$

The ion corresponding to this mass is either $C_3H_6^+$ or CH_2CO^+ ion. If we assume that the ion is $C_2H_6^+$, process C leads to the value $I(C_3H_6)\leq 10.6$ eV which is slightly highr than the $I(C_3H_6)=10.0\pm0.2$ eV given by Bleakney(13). If we assume that the ion is CH_2CO^+ and the energy to remove the hydrogen atom from CH_3CO is the same energy as to remove from CH_2, the calculated appearace potential of CH_2CO^+ is 15.9 eV. But the process *C* is more probable than this.

4. $M/e=41$.

If the ion corresponding to this mass is assumed to be $C_3H_5^+$, the process *d* or *e* leads the $I(C_3H_5)$ value considerably different from the $I(C_2H_5)\leq 9.7$ eV given by Bleakney. Perhaps we should consider $CHCO^+$ for this ion.

5. $M/e=39$.

This ion is the $C_3H_3^+$ ion. The process *f* led to $I(C_3H_3)\leq 10.6$ eV may be more probable than the process *g*, for the $I(C_3H_3)$ obtained from the isopropylalcohol is $I(C_3H_3)\leq 10.5$ eV.

6. $M/e=29$.

If the ion corresponding to this mass is assumed to be $C_2H_5^+$ ion, the value of $I(C_2H_5)$ led from the process *h* or *i* is considerably different from the value $I(C_2H_5)\leq 9.8$ eV obtained from propane. Assuming that the ion is HCO^+ ion, the process *j* leads to the value $I(HCO)\leq 10.2$ eV. The ionization potential of H_2CO is $11.3\pm0\ 5$ eV given by Jewitt(14). If the energy saving by the trivalent property of O^+ in formaldehyde is assumed to be the same value as in acetone, this process seems to be energetically probable.

7. $M/e=28$.

If the ion corresponding to this mass is assumed to be the CO^+ ion, the process *k* is the most probable one, for Vaughan gives the value 13.9 ± 0.2 eV and Tate(15) gives the value 14.1 ± 0.1 eV for the ionization potential of CO. In this paper we use the value $D(CO)=9.14$ eV given by Herzberg, but both Lozier(16) and Tate give the value $D(CO)=9.6$ eV to explain the experiment on the dissociation of CO by the electron impact. If we use the latter value, the process *l* is more probable. If the ion is assumed to be the $C_2H_4^+$ ion, the process O leads to the value $I(C_2H_4)\leq 10.8$ eV in good agreement with the directly measured value $I(C_2H_4)=10.8$ eV.

8. $M/e=27$.

The ion corresponding to this mass is the $C_2H_3^+$ ion. The most probable process is the process *r* which leads to the value $I(C_2H_3)\leq 12.0$ eV, for the $I(C_2H_3)$ obtained from propane and isopropylalcohol are respectively $I(C_2H_3)\leq 11.2$ eV and $I(C_2H_3)\leq 12.2$ eV.

9. $M/e=15$.

The ion corresponding to this mass is the CH_3^+ ion. The process *t* is the most probable process and leads to the value $I(CH_3)\leq 12.0$ eV.

The ion has the excess energy more than one electron volt comparing this value with the $I(CH_3^+)\leq 10.4$ eV given by Hipple, $I(CH_3)\leq 9.9$ eV given by Smith or $I(CH_3)=11.1\pm0.5$ eV given by Fraster and Jewitt.(17).

§ 3. Investigation on the Acetic Acid.

According to Pauling(2) the acetic acid molecule has the following resonance structures; namely

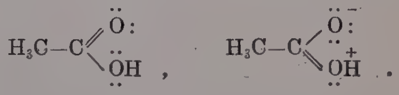

Table IV. Nature and relative abundance of ions produced from acetic acid by electron impact with 80 eV energy.

M/e	Ion	$CH_3COOH^+=10$	%
60	CH_3COOH^+	10.0	4.0
45	$COOH^+$	27.5	11.0
44	$C_2H_4O^+$, CO_2^+	3.9_5	1.5_5
43	CH_3CO^+	34.0	12.5
42	$C_2H_2O^+$	9.6	3.8
41	C_2HO^+	6.5	2.6
40	C_2O^+	1.1	0.4_5
31	CH_3O^+	2.9	1.1_5
30	CH_2O^+	0.4	0.1_5
29	CHO^+	11.2	4.4_5
28	CO^+, $C_2H_4^+$	44.2	17.9
27	$C_2H_3^+$	1.8	0.7_5
26	$C_2H_2^+$	1.6_5	0.6_5
25	C_2H^+	1.3	0.5
24	C_2^+	0.5_5	0.2
18	H_2O^+	7.0	2.8
17	HP^+	4.1	1.6
16	O^+, CH_4^+	10.8	4.3
15	CH_3^+	21.6	8.5_5
14	CH_2^+	14.7	5.8_5
13	CH^+	5.4	2.1_5
12	C^+	11.5	4.5_5
2	H_2^+	7.0	2.7_5
1	H^+	11.0	4.3_5

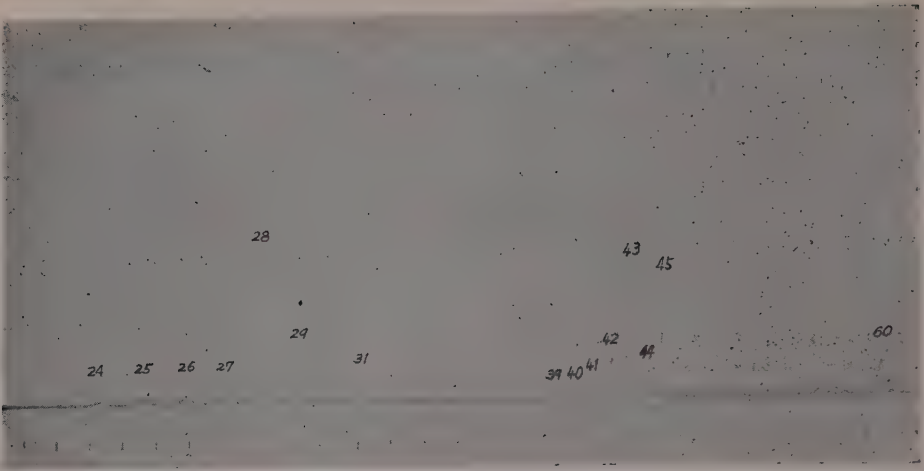

Fig. 2. Mass-spectrum obtained with CH_3COOH at the electron energy of 80 eV.

The resonance energy is 28 Kcal/mole. This molecule is more stable than acetone by this amount. In the acetic acid molecule as well as in the alcohol molecules, the oxygen atom is first ionized by Mulliken's theoretical prediction.

The abundances of the ions produced from the acetic acid at the electron energy of 80 eV are listed in Table IV.

The photograph of the ion peak at the electron energy of 80 eV taken by the magnetic scanning method is shown in Fig. 2.

In the Fig. 2 the ion peak corresponding to the $M/e = 39$ may perhaps be due to the impurity. Among the ions produced from the acetic acid the ions corresponding to the mass 45, 43 and 28 are abundant and moreover the ion corresponding to $M/e = 28$ is chiefly due to the CO^+ ion. The CH_3^+ ion is also abundant, but is not so much as in acetone. The ion C^+, H^+ and H_2^+ are more abundant in this molecule than in acetone. The primary process of the photodecomposition of acetic acid investigated by Burton(18) is $CH_3COOH \rightarrow CH_2COO + H$ or $CH_3COOH \rightarrow CH_4 + CO_2$. But the CO_2^+ ion almost disappears in the electron impact experiment. The appearance potentials of the abundant ion are listed in Table V.

Table V. Appearance potentials of ions produced from acetic acid.

M/e	Ion	$A(X)$
60	CH_3COOH^+	11.5±0.1 eV
45	$COOH^+$	14.3±0.1
43	CH_3CO^+	13.0±0.1
42	CH_2CO^+	12.0±0.2
28	CO^+, $C_2H_4^+$	14.6±0.1
15	CH_3^+	17.0±0.1

The heat of formation of acetic acid vapor is 111.7 Kcal/mole given by Rossini(19). Then the dissociation energy of acetic acid is calculated to be $D(CH_3COOH) = 29.6$ eV. The energies of $P(X)$ are shown in Table VI.

Some dissussions about the dissociation processes will now be given.

1. $M/e = 60$.

This ion should be the parent molecular ion.

Table VI. Energies of dissociation of acetic acid into its various constituents and interpretation of the appearance potential.

No.	Configuratian	$P(X)$	$A(X)$	$I(X)$
a	CH_3COOH	0 eV	11.5 eV	$I(CH_3COOH) = 11.5$ eV
b	$COOH+CH_3$	3.7	14.3	
c	CH_3CO+OH	5.1	13.0	
d	CH_2CO+H_2O		12.0	
e	$CO+CH_3OH$	1.5	14.6	$I(CO) \leq 13.1$
f	$C_2H_4+O^2$	6.2		
g	$CH_3+CO+OH$	5.5	17.0	$I(CH_3) \leq 11.5$
h	$2C+4H+2O$	29.6		

$A(CH_3COOH)=I(CH_3COOH)=11.5$ eV. Bleakney(20) investigates the dissociation of the formic acid by electron impact and gives the two ionization potentials, namely 11.0 eV for trans-type and 11.6 eV for cis-type formic acid. But we can only observe one ionization potential for the acetic acid. The ionization potential of acetic acid is the energy to remove the electron from the non-mixing orbit of oxygen atom and for the resonance structure the oxygen atom of $C=O$ bond seems to be more easily ionized than the oxygen atom of OH bond. But the ionization potential of acetic acid is about 1 eV higher than that of acetone and nearly equal to that of alcohol. For this reason it seems to be true that the hydrogen atom in OH bond may be labile and tends to jump from one oxygen atom to the other and raise the ionization potential of oxygen atom by diminishing the charge transport effect.

2, *M*/*e* = 45.

The ion corresponding to this mass is the $COOH^+$ ion. The process to produce this ion is $CH_3COOH \rightarrow CH_3+COOH^+ + e$.

If we assume that the B_{CC} of this molecule is the same value as the acetaldehyde and is 86 Kcal/mole (3.7 eV), the upper process will lead to the $I(COOH)\leq 10.6$ eV. Assuming that the ionization potential of the oxygen atom in 11.5 eV, the energy saving α for the trivalent property of O^+ is only ≥ 0.9 eV which is 1 eV lower than that of acetone.

But when we reduce the resonance energy 1.2 eV from the difference between $D(CO)$ and $B_{C=O}$, we get the value 1.3 eV. This value is nearly the same value as α. That is to say, the acid radical is more stable by the resonance energy. But in this point our result does not agree with the Bleakney's result obtained from the formic acid. For this reasons we consider that his B_{CH} value (4.48 eV) of HCOOH is considerably large compared with the B_{CH} value given by Burton or the author.

3. *M*/*e* = 43.

The ion corresponding to this mass is CH_3CO^+ ion.

The process C, namely $CH_3COOH \rightarrow CH_3CO^+ + OH + e$, is the most probable process, but without consideration of the trivalent property of O^+ this process leads to $I(CH_3CO)\leq 7.9$ eV which is much lower than the ionization potential of oxygen atom. But if we assume the ionization potential and energy saving in CH_3CO is the same value as in acetone, we can calculate the appearance potential of CH_3CO as $A(CH_3CO)\geq 10.4+5.1-1.9=13.6$ eV from the process C. This roughly estimated value of the appearance potential is 0.6 eV higher than the observed value. But if the value α is assumed to be 2.5 eV, the calculated appearance potential is in good agreement with the observed value.

4. *M*/*e* = 42.

The ion corresponding to this mass is CH_2CO^+. The appearance potential of this ion is very low. If we assume that the energy to remove the hydrogen atom from CH_3CO is the same value as from CH_3 and consider the energy difference between OH and OH_2 at the same time, the value of $A(CH_2CO^+)$ from the process *d* is roughly calculated to be 11.4 eV which is in fairly good agreement with the observed value.

5. *M*/*e* = 28.

The ion corresponding to this mass is the most abundant one in the acetic acid. If we assume that the ion is $C_2H_4^+$, the process *f* leads to the unreasonable value $I(C_2H_4)\leq 8.4$ eV compared with the directly measured value $I(C_2H_4) = 10.8$ eV. If we assume that the ion is CO^+, the process *e* in which the energy consumption is the lowest, leads to the lower value than the directly measured one, namely $I(CO)\leq 13.1$ eV. But if we use the value $D(CO) = 9.6$ eV as Lozier(16) and Tate(15), the the value $I(CO)$ from the process *e* is 13.6 eV. We consider that the value $D(CO)$ may be larger than the value $D(CO) = 9.14$ eV given by Herzberg, for the process is the only probable process.

6. *M*/*e* = 15.

The ion corresponding to this mass is the CH_3^+ ion. The process *g* is the most probable as in acetone and leads to the value $I(CH_3)\leq 11.5$ eV.

§ 4. Conclusion.

The works reported here can be summarized briefly in the following way. The most abundant ion produced from the acetone is the CH_3CO^+ ion. From the acetic acid CO^+ is the most abundant ion and the abundances of the $COOH^+$ and CH_3CO^+ ions are also large.

The appearance potential of the molecular ion of acetone is about 1 eV lower than that of alcohol, but the appearance potential of the molecular ion of acetic acid is nearly equal to the latter.

In these molecules the non-bonding electron of the oxygen atom is first ionized and O^+ has the trivalent property. The energy saving due to the trivalent property of O^+ is about ≥ 1.9 eV for acetone and ≥ 0.9 eV for acetic acid. The former value is nearly equal to the difference between D(CO) and $B_{C=O}$ in acetone, and the latter value is also nearly equal to the difference between the former value and the resonance energy of the acetic acid.

We wish to thank to Dr. Toriyama, Dr. Hamada and Dr. Yumoto for the their kindly guidance and encouragement. We also wish to thank to Mr. Kanomata Mr. Kawamatsu and Mr. Tsuyama for their friendly cooperation.

References.

(1) T. Kambara: J. Phys. Soc. Jap., **5** (1950) 31.
(2) L. Pauling: Nature of the chemical Bond.
(3) R. S. Mulliken: J. Chem. Phys., **3** (1935) 564.
(4) R. Spence and W. Wild: J. Chem., Soc. (1937) 352 Part. I.
(5) A. B. F. Duncan: J. Chem. Phys., **3** (1935) 131.
(6) W. A. Noyes: J. Chem. Phys., **3** (1935) 430.
(7) R. E. Honig: J. Chem. Phys., **16** (1948) 105.
(8) Norrish, Crone and Saltmarsh: J. Chem. Soc. (1934) 1456.
(9) M. Burton: J. Chem. Phys. **7** (1939) 1072.
(10) D. P. Stevenson: J. Chem. Phys., **10** (1942) 291.
(11) E. R. von Artsdalen: J. Chem. Phy.. **10** (1942) 653.
(12) Valatin J. G.: J. Chem. Phys., **16** (1948) 1018.
(13) J. Delfosse and W. Bleakney: Phys. Rev., **56** (1939) 256.
(14) Jewitt: Phys. Rev., **46** (1934) 616.
(15) J. T. Tate: Phys. Rev., **59** (1941) 354.
(16) W. W. Lozier: Phys. Rev., **46** (1934) 268.
(17) R. G. J. Fraster and T. N. Jewett: Phys. Rev., **50** (1936) 1091.
(18) M. Burton: J. Am. Chem. Soc., **58** (1936) 1645.
(19) F. R. Bichowsky and F. D. Rossini: Thermochemistry of Chemical Substance.
(20) T. Marier and W. Bleakney: Phys. Rev., **72** (1947) 792.

On the Resistance of Interface of Oxide-coated Cathode.

Hazimu KAWAMURA and Akira SHINOHARA.

Mazda Research Laboratory, Tokyo-Shibaura El. Co. Kawasaki, Kanagawa.

(Received Aug. 20, 1949).

It is said that the resistance of interface between core metal and oxide limits the pulsive emission of thermo-electron of few microseconds(1), and also that the "current spark" of oxide cathode under pulse operation is due to the breakdown of the interface.(2) (3) Fineman, Eisenstein(2) and Danforth, Goldwater(3) have found V-R characters similar to the rectifying layer by measuring the interface resistances under pulse operations. But conclusive results have not been obtained, because, in their experiments, the V-R characters were measured only in the direction such that electrons flow from metal to oxide. We have studied this behavior by measuring the resistance in both positive and negative directions.

Experimental Methode.

The tube used in our experiment were as shown in Fig. 1. The Ba-Sr carbonate sprayed on the sleeve of 45 mil dia. was stripped off leaving a rectangular part of 0.5 mm in width and 3 mm in length at the central portion. The two cathodes thus prepared were mounted such as the sprayed parts are in contact, and pressed by a tungsten spring as shown in Fig. 1. A nickel ribbon of 0.05 mm in thickness and 0.2 mm in width was inserted between the coating, which served as a probe. These parts were sealed in a glass bulb evacuated by a Hickman 3-stage oil diffusion pump for few hours under bulb baking of 200°C. The bulb was tipped off, after the carbonate was decomposed and the getter was flashed.

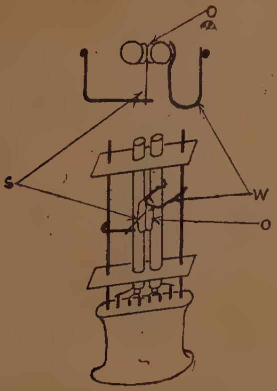

Fig. 1.

The V-R character were measured by oscilloscope through the circuit as shown in Fig. 2. The oscillation of saw teeth of about 1000 cycles was generated by a thyratron 66 G. This oscillating potential, after amplified by a beam power tube 807, is applied between the pair of cathodes of the measuring tube through resistance R_9 and R_{10} which are sufficiently greater than the risistance of oxide, so that the current through the circuit is strictly a saw teeth form irrespective of the V-R character of the sample. The potential drop generated between the probe and cathode of earth side, which is amplified by the triode part of DH-3, is applied to a deflecting plate of a oscilloscope. The potential drop amplified by DH-3 is differentiated by C_6 and R_{12}, and applied to the other plate of the oscilloscope after amplified by second DH-3. In order to obtain the scale of resistence, V-R character of a known ohmic resistance inserted between B and C, connecting A and B, is swept on the oscilloscope. The scale of voltage was obtained, by applying a known DC voltage to B and C. R_{10} was so adjusted according to the resistances of the samples as to generate about 1 volt between B and C.

Results and Discussions.

As it is said that the interface resistance is influenced by core metal,(1)(2)(3) we employed three sorts of core metals, as in Table I.

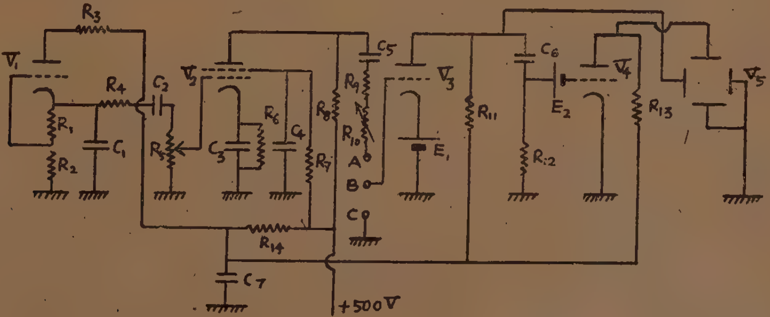

Fig. 2.

R_1	10 K	R_{11}	500 K	C_7	2.
R_2	500 K	R_{12}	100 K	E_1	1.5 V
R_3	100 K	R_{13}	500 K	E_2	1.5
R_4	500 K	R_{14}	20 K	V_1	66 G
R_5	200 K	C_1	0.03	V_2	807
R_6	200	C_2	0.2	V_3	DH 3
R_7	50 K	C_3	30	V_4	DH 3
R_8	2 K	C_4	2	V_5	osciloscope
R_9	2 K	C_5	8		
R_{10}	200 K	C_6	20 p		

Table I.

notion	main reducing impurities		
D	Mg~0.1%	Mn<0.2%	
R	Si~0.05%	Mn<0.2%	grad A nickel
E	no		electrolytic nickel

V-R character of "D" is shown in Fig. 3. The direction of easy flow is such that electrons flow from core to oxide. The form of the character, is almost independent of the temperature of the measurement. As the oxide is known to be a semiconductor of N-type, the direction of the rectification coincides with that of Wilson type(4). As the resistance r_e of the easy flow are thought to be the bulk resistance of the oxide, we can obtain the interface resistance by reducing r_e from the total resistance. Especially the interface resistance at $V=0$ is given by $\rho = r_0 - r_e$, where r_0 is the total resistance at $V \fallingdotseq 0$. r_e and ρ at 1000°K and the activation energy E_e and E_ρ of these values obtained by plotting logarithm vs. 1/T are tabulated in the 1st row of Table II. It is shown that both E_e and E_ρ are equal to 0.5 ~ 0.6 eV.

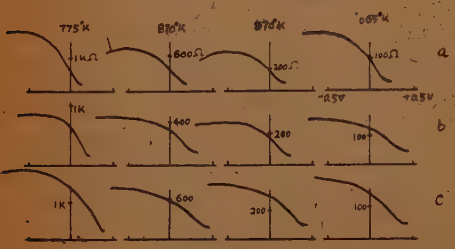

Fig. 3.

D-2 a) initial b) 1060°K, 250 min.
c) 1210°K, 50 min.

The direction of the rectification of electrolytic nickel "E" is coincide with that of Mott type(6), and the resistance itself is far greater than that of "D" as shown in Fig. 4 and Table II. E_ρ is greater than E_e by about 0.2 eV and the forms of the V-R characters are dependent on the measuring temperatures. When this sample was heat treated for 170 minutes at 1220°K, the resis-

Table II.

sample	treatment	type	r_e	E_e	ρ	E_ρ	r_0	E_0	ρ_-	E_-
D-2	initial	W	50	0.50	93	0.55				
	1060°K, 250 min	W	54	0.50	86	0.48				
	1210°K, 50 min	W	75	0.50	150	0.70				
D′-3	1110°K, 10 min	D					350	0.73	150	0.58
	1110°K, 230 min	W	90	0.63	81	0.62				
	1220°K, 90 min	W	60	0.57	105	0.57				
E-2	1100°K, 40 min	M					580	0.57		
	1100°K, 100 min	M	450	0.52	300	0.70	750	0.56		
	1220°K, 170 min	D					780	0.62	250	0.51
E-4	1110°K, 140 min	M	680	1.14	50					
	1220°K, 80 min	D					590	0.78	105	1.00
E′-3	1110°K, 10 min	D					750	0.60	46	0.85
	1110°K, 100 min	D					170	0.80	20	0.85
	1220°K, 90 min	D					250	0.77	51	0.92
E′-5	1110°K, 2 min	D					380	0.91	79	0.85
	1110°K, 140 min	D-M					350	0.94		
	1110°K, 260 min	M	550	0.77	100	1.20				
R-5	initial	D					520	0.85	80	0.66
	1090°K, 120 min	D					125	0.70	50	0.71
	1200°K, 50 min	D					67	0.57	12	0.73
R-6	initial	D					62	0.53	30	0.63
	1100°K, 370 min	D					340	1.02		
	1230°K, 400 min	D					106	0.61	37	0.73

(1) W, M, and D means the Wilson, Mott and double type.
(2) Sample D′ and E′ are heat treated at 1110°K for 60 minutes without getters were flashed, before the measurements are set about.

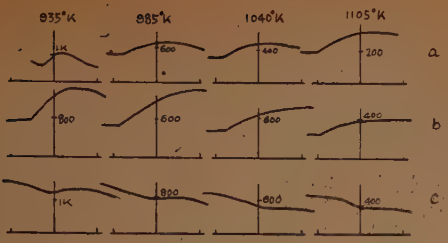

Fig. 4.
E-2 a) 1100°K, 40 min. b) 1100°K, 100 min.
c) 1220°K, 170 min.

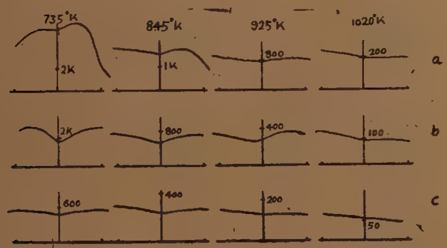

Fig. 5.
R-5 a) initial. b) 1090°K, 120 min.
c) 1200°K, 50 min.

tance of easy flow (negative direction) increased remarkably, and the V-R characters have a minimum point at about $V=0$ as shown in Fig. 4 c. In the case of "R", we can obtain this peculiar character having minimum at $V=0$, from the initial. We tabulated the total resistance r_0 at $V=0$ and the difference between r_0 and the resistance at $V=-0.5$ V (ρ_-) and these activation energy E_0, $E_{\rho-}$ in table II.

Now let us assume a thin layer of insulator at the interface and the potential gradient in the oxide due to the transfer of electrons from oxide to metal as shown in Fig. 6.(6). According to Davidov(5), if the thickness x_0 of the latter is smaller than the thickness d of the former, the electrons are carried by the tunnel effect and there appears the rectification of Wilson type(4). In this case, the contact resistance at $V=0$ is given by,

$$\rho = \frac{h^3}{4\pi me^2kTp}e^{E/2kT} \qquad (1)$$

where E is the energy difference between the impurity level and the conduction band, q is the transmission coefficient of electron through the potential barrier. The temperature dependence of ρ is the same as the bulk resistance of the oxide. Thus from the above results we can interpret the rectification of "D" as the Wilson type.

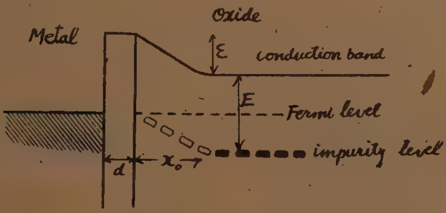

Fig. 6.

In the case of $x_0 > d$, thermo-electrons jump over the potential hill, and we can obtain the rectification of Mott type. The direction of the easy flow in this case is opposite to that in the case of Wilson type. The contact resistance at $V=0$ is given by

$$\rho = \frac{kT}{\varepsilon}\frac{x_0}{evn_0} \quad n_0 \doteqdot Ae^{-(E/2+\varepsilon)kT}, \qquad (2)$$

where n_0 is the electron density at the top of the potential hill, ε is the energy difference between potential hill and the conduction band far apart from the contact, v is the mobility of electron. Because in the case of the electrolytic nickel, the activity is far lower than in the case of "D", the impurity center must be ionized to the greater

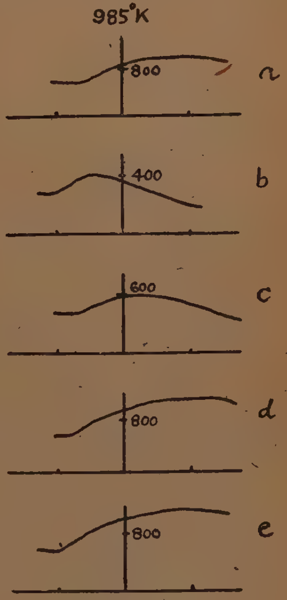

Fig. 7. E-2.
a) initial. b) 1100°K, metal—, oxide + 7 ma, 10 min.
c) 1100°K, 0 ma, 5 min.
d) 1100°K, 0 ma, 20 min.
e) 1100°K, metal + oxide— 5 ma, 5 min.

depth in order to get the equal surface charge. Therefore, the thickness x_0 of the potential gradient is far greater than in the case of "D", and accordingly it is likely to satisfy the condition $x_0 > d$. If this is the case in "E", we obtain the relation $E_e = E/2$ and $E_p = E/2+\varepsilon$. From the table II it can be seen that $E/2 = 0.5$ ev, $\varepsilon = 0.2$ ev. from eq. (2).

The V—R character of E—2 obtained after flowing the DC current of 7 mA from oxide to core at 1100°K for 10 minutes is shown in Fig. 7b. We can see that the direction of rectification is reversed accompanied by the reduction of the resistance, by this treatment. By flowing this DC current, the Ba ions are thought to be concentrated to the interface in the oxide, which increase the activity of this part and, therefore, reduce the thickness x_0. These concentrated active centers are diffused uniformly, by the heat treatment at 1100°K for 10 ~ 20 minutes without flowing current, and return to the initial state as shown in Fig. 7d. If we reverse the direction of DC current, the character does not change except the slight increase of the resistance as shown in Fig. 7e. These facts also show us that the rectification of "E" is the Mott type.

The peculiar character which appears in the case of "R" and E—2 after severe heat treatment seems to be due to the structure of interface composed of the rectifying layer of Mott type apeared in "E" and the rectifying layer of the reverse direction in series. We shall call this type of the character a "double" type, and shall discuss this behavior in the following. The V-R characters of samples "D" and "E", which were treated at 1100°K for 60 minutes without getter flashed, were measured treating at different conditions, after the batalum getters were flashed. In these cases the double type apears at first as shown in Fig. 8, 9, 10. For D′—3, but soon the Wilson type replaces the double type. But for electrolytic nickel, there appears the Mott type after long treatment at 1100°K as the case of E′—5, or the double type is conserved irrespective of the long treatment as in E′—3.

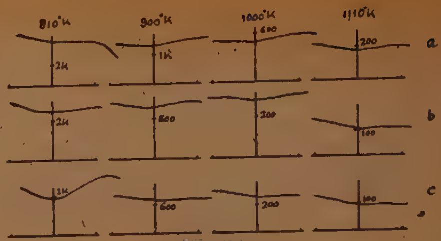

Fig. 8.

E′—3 a) 1110°K, 10 min. after getter flashing
b) 1110°K, 100 min. c) 1220°K, 90 min.

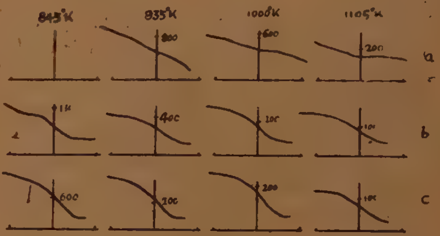

Fig. 9.

D′—3 a) 1110°K, 10 min. after getter flashing
b) 1110°K, 230 min. c) 1220°K, 90 min.

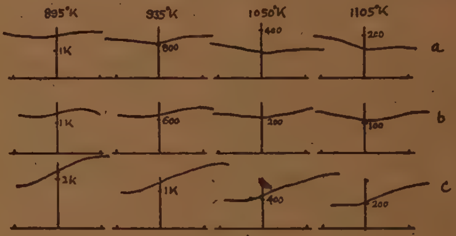

Fig. 10.

E′—5 a) 1110°K, 2 min. after getter flashing.
b) 1110°K, 140 min. c) 1110°K, 260 min.

It can be expected that Si contained in "R" sleeve should form a thick layer of Ba_2SiO_4 at the interface. If the contact between this layer and oxide has a rectifying property of Mott type as appeared in "E", and cotact between metal and this layer rectifies to the reverse direction, we may obtain the character of double type. Therefore, the appearance of the double type shows the existence of relatively thick interface layer. On the other hand, there seems to be but a very thin interface layer in "D" or "E", because Mg contained in "D" becomes MgO which is dissoloved in BaO and does not form a interstitial compound with BaO at the interface. But if the oxide is heat treated in bad vacuum, where getter is not flashed, there proceed the chemical reaction

$$Ni+O+BaO \rightarrow BaNiO_2$$

at the interface, and relatively thick interface layer is formed, and the character of double type is obtained. But Mg contained in "D" may reduce this interface compound, when the oxide is heated in good vacuum, and, therefore, Wilson type appears. The same variation occurs also in "E", if the vacuum is sufficiently high. But usually the reverse reaction, that is the oxidation, is apt to proceed, even if the getter is flashed as in the case of E−2.

The results of all samples are summarized in Table II, where the units of r_e etc. are ohms at 1000°K. From this table, we see that the activation energy of well activated oxide is about 0.55 eV, which is smaller than 0.7 ev(7) or 1.2 ev(8) so far reported. Hitherto, E_0 in our representation were measured as the activation energy, which is 0.6 ∼ 0.9 ev in the present report. But this is not rational, because of the complicated behavior of the resistance of interface. In accordance with the theory of Mott, we must assign the difference between the work functions of metal and oxide to ε. Therefore, ε must be equal to about 4 ev which is far geater than the value we obtained (0.2 ∼ 0.4 ev). But this theoretical value may become far smaller, if, for instance, a mono-atomic absorbed layer is assumed.

Conclusion.

We can summarize the above results as follows;

(1) If the impurity in core metal does not form a interstitial compound with the oxide at the interface, the contact resistance is Mott type or Wilson type, according to the activity is low or high.

(2) When the impurity forms a interstitial compound such as Ba_2SiO_4 at the interface, the V-R character shows the existence of double rectifying layer in series. (double type).

(3) Even in the case of (1), if heat treated in bad vacuum, the V-R character of double type appears

(4) The bulk resistance of the oxide is 0.55 ev which is smaller than the values so far reported.

As described above, it is necessary that the resistance of interface is small, for the pulse operation of oxide cathode. From above results we can say that the core metal containing the reducing impurities such as Mg, Ca, or Ba which do not form interface layer is desirable for this purpose.

In conclusion we wish to thank Dr. A. Kobayashi and Mr. M. Tomura, for their fruitful dicussion.

References.

(1) E. H. Coomes: J. App. Phys. **17** (1946), 647.
(2) A. Fineman and A. Eisenstein: J. App. Phys. **17** (1946), 663.
(3) W. E. Danforth and D. L. Goldwater: J. App. Phys. **20** (1949), 163.
(4) A. H. Wilson: Proc. Roy. Soc. (A) **136** (1932), 487.
(5) B. Davydov: J. Phys. U.S.S.R. **1** (1939), 166.
(6) N. F. Mott: Proc. Roy. Soc. (A) **171** (1939), 27.
(7) E. Nishibori and H. Kawamura: Proc. Phys-Math Soc. Jap. **22** (1940), 378.
(8) G. W. Mahlman: J. App. Phys. **20** (1949), 197.

Solar Limb Effect of the Spectral Lines in a Prominence Observed at the Total Eclipse in 1941.

By Tutomu TANAKA and Zyun KOANA.

Faculty of Science, Niigata University and Faculty of Science, Tokyo University.

(Read October 18, 1942; Received September 22, 1949.)

§ 1. Introduction.

The red shift of spectral lines at the limb of the sun has been investigated by several observers concerning the Fraunhofer lines as well as prominences(1)−(12). But most of the investigations have been made without regard to the eclipses. Evershed(8) mentions that it is desirable to obtain the limb spectra of the sun at some future eclipses, in order to get the values of the limb effect freer

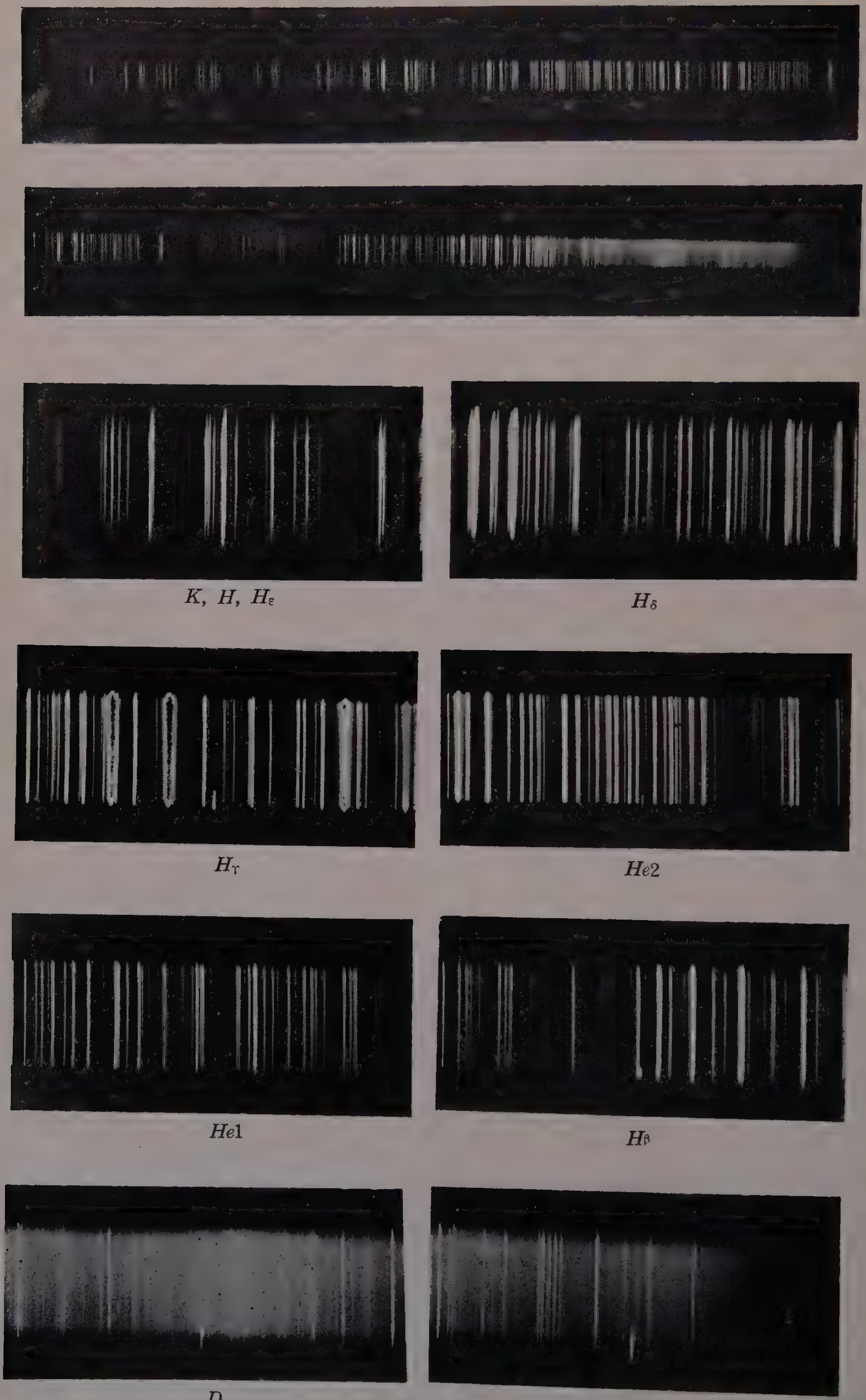

K, H, H_ε

H_δ

H_γ

$He2$

$He1$

H_β

D_3

H_α

Fig. 1.

from the effects of scattered light than under ordinary conditions. And he asserts that the values obtained without regard to the eclipses are probably under-estimated, owing to the influence of the scattered light. The present investigation is for the limb shift of the spectral lines of an eminent prominence which took its position just on the equator of the sun during the total eclipse in 1941.

The site of the observation selected was a table-land in a village near Hsienning (Kannei), Hupeh-sheng (Kohoku-syo), China. The weather was hazy. No coronal line was obtained by a very large three-prism spectrograph equipped with with a photographic lens of an effective aperture of about f/6.9. The time of exposure was about 150 seconds. Accidentally, the image of a large prominence came just on the east-corresponding side of the slit, which was put along the image of the equator of the sun. Fairly sharp images of ten or so prominence lines were seen, as shown in Fig. 1. The following is a report with respect to these spectral lines.

§ 2. Procedure of the Investigation.

The dispersion of the spectrum observed was from 4.59 to 15.6 Å./mm for the wave-length from 3933 to 4860 Å. This is shown in Fig. 2, while

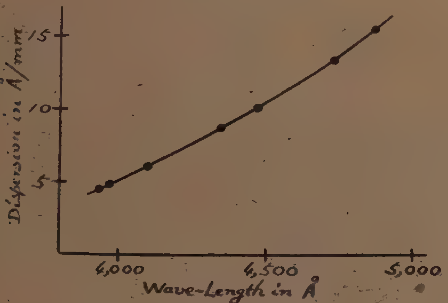

Fig. 2.

the resolving power of the apparatus was about 13.2×10^5 for H_γ. We might say that such a dispersion and resolving power are quite large, considering that it is for the spectrum taken in a solar total eclipse. But this might be insufficient to discuss the variation of wave-length of an order of 1/100 Å. or so with exactness. The images of the spectral lines were, however, quite sharp and the readings of the comparator used in their measurements were fairly consistent. Moreover, all the hydrogen lines in question are not mixed with other spectral lines, and the helium lines are distinguishable from the weaker components, though they are not resolved completely from the latter. This must make the result quite accurate. As in Fig. 3, let us draw an osculating curve through the points obtained by observation, to get rid of the effect of the error of each measurement. If in the discussion of this sort we are to use this osculating curve instead of the observed points themselves, it might be reasonable to take into consideration the quantity of an order of 1/100 Å, or so. But to discuss the result of this sort obtained from the part of dispersion less than 20 Å./mm, might be quite senseless. For this reason, we shall put off that part of the spectrum which contains H_α and D_3.

§ 3. The General View of the Result of the Measurements and Its Corrections.

The wave-lengths of the spectral lines have been determined in reference to iron-arc lines photographed in juxtaposition up to 0.001 I.A. Each point was measured repeating the comparator reading at least twenty times. At ten times the travelling microscope was moved in one direction, at the other ten times it was moved in the other direction, and the two sets of reading differences were verified to be nearly consistent. At five different points at least each spectral line was measured in the part where the prominence and comparison spectra are superposed. The wave-lengths thus obtained are to be added by the following corrections:

(1) Correction owing to the earth's revolution.
(2) Correction owing to the earth's rotation.
(3) Correction for the velocity in (4) owing to the inclination of the solar equator.
(4) Correction owing to the rotational velocity of the sun.

Our solar spectrum being at one-sided limb, the rotational velocity of the sun cannot be obtained from the plate, so far as the limb effect of spectral lines is not determined. Thus we adopted the value of the apparent rotation of 1.900 km/sec as an approximate value, considering the epoch of our observation fell in a decreasing sun-spot period. This might not be very exact. But the deviation might be small. This deviation will not alter essential points of the discussion in the subsequent sections.

§ 4. Determination of the Limb Effect.

The chief difficulty of the investigation of this kind is the lack of exact measurements of terrestrial wave-lengths for the lines in question as well as the iron-arc lines taken in reference. Most of them are not exactly determined up to 1/1,000 I.A. Even standard iron-arc lines, their wave-lengths are known to be agitated by the conditions of excitation. But the standard wave-lengths adopted by the International Astronomical Union in 1929 can be considered to be free from several errors and improper effects up to 1/1,000 I.A., if the conditions for the production of the arc are obeyed. By this reason, the wave-lengths of the iron-arc standard lines in Critical Tables in 1929 have been adopted, which practically coincide with the above ones.

Regarding the terrestrial wave-lengths for the lines in question, interferometer measures were mostly taken. More detailed description will be given in § 5.

The iron-arc lines in our spectrum show no clear evidence of being subjected to the pole-effect. All the lines, which belong to different groups with respect to the pole-effect, give the results practically equal to the wave-lengths which were measured by St. John and Babcock(1) using the spectra free from the pole-effect.

But to be sure to get rid of the pole-effect on the iron-arc lines(14), we used chiefly those of Group a or b, except in the case of H_β. Those of Group a and b are known to be practically free from the pole-effect. In the neighbourhood of H_β,

Table I.

Wave-length measured	Wave-lengths of Fe lines taken in reference	Correction	Wave-length corrected	Terrestrial wave-length	Residual
I.A.	I.A.	I.A.	I.A.	I.A.	I.A.
4861.298 (H_β)	4878.220 (c), 4872.145 (c), 4871.327 (c), 4859.747 (c), &c.	+0.038	4861.336	4861.327	+0.009
4713.119 (*H*e1)	4733.596 (a), 4710.287 (b), &c,	+0.037	4713.156	4713.145	+0.011
4471.451 (*H*e2)	4476.022 (b), 4466.556 (b), &c,	+0.035	4471.486	4471.476	+0.010
4340.442 (H_γ)	4337.050 (b), 4332.738 (b), &c.	+0.034	4340.476	4340.470	+0.006
4101.715 (H_δ)	4107.492 (b), 4098.183 (b), &c.	+0.032	4101.747	4101.738	+0.009
3970.053 (H_ε)	3971.324 (b), 3970.393 (b), 3969.260 (b), &c.	+0.031	3970.084	3970.074	+0.010
3968.457 (*H*)	3971.325 (b), 3970.393 (b), 3969.260 (b), &c.	+0.031	3968.488	3968.470	+0.018
3933.647 (*K*)	3935.816 (b), 3932.631 (b), &c.	+0.031	3933.678	3932.664	+0.014

there can be found no line belonging to these groups. For this, four lines belonging to Group c were used. The results, for which different reference lines were used, coincided with each other within the range of experimental errors. Moreover, for other lines, there can be found no evidence that shows the pole-effect of the lines of Group c on our plate. Therefore, our measurement for H_β was perhaps all right. The result is tabulated in Table I.

Table II(a).

	Residual	Relativity shift	Difference
	I.A.	I.A.	I.A.
H_β	+0.009	+0.0103	−0.001
*He*1	+0.011	+0.0099	+0.001
*He*2	+0.010	+0.0095	0.000
H_γ	+0.006	+0.0092	−0.003
H_δ	+0.009	+0.0087	0.000
H_ε	+0.010	+0.0084	+0.002
			Sum = −0.001

Table II(b).

	Residual	Relativity shift	Difference
	I.A.	I.A.	I.A.
H	+0.018	+0.0084	+0.010
K	+0.014	+0.0083	+0.006
			Sum = +0.016

For the first six lines the limb effect can hardly be seen. This is shown in Fig. 3. The effect, if any, must be so small that it cannot be found in a spectrum of such a dispersion as used by us. But for the last two lines something is left that suggests the limb effect.

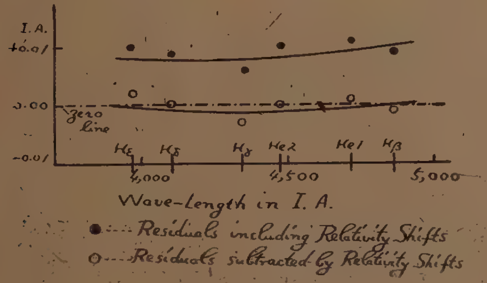

Fig. 3.

§ 5. Data for the Wave-Lengths of Different Lines.

(1) H_β.

Wave-length in I.A.	Observers
4861.327	Curtis(13)
4861.328	Gale, Monk and Lee(16)
4861.326	Evershed(3)
Mean 4861.327	

This mean value has been adopted as the terrestrial wave-length of H_β.

(2) Helium lines. The images of the two helium lines on our plate wer very sharp. The images of the weaker components of each triplet, one of which is not resolved completely from the principal one in question, could be easily distinguished.

Their terrestrial wave-lengths adopted are the mean value of the following two:

	Wave-length according to Fowler's Tables(13)	Wave-length according to Bacher and Goudsmit's Tables(14)	Mean
	I.A.	I.A.	I.A.
*He*1	4713.143*	4713.147	4713.145
*He*2	4471.477*	4471.474	4471.476

* These interferometer measures regard evidently the principal lines.

(3) H_γ.

Wave-length in I.A.	Observers
4340.470	Gale, Monk and Lee(16)
4340.469	Evershed, who recomputed from Curtis's formula(3)
Mean 4340.470	

(4) H_δ.

Wave-length in I.A.	Observers
4101.737	Gale, Monk and Lee(16)
4101.739	Evershed, who recomputed from Curtis's formula(3)
Mean 4101.738	

(5) H_ε.

Wave-length in I.A.	Observers
3970.075	Curtis[3]
3970.076	Evershed[3]
3970.070	Kent[17]
Mean 3970.074	

(6) *H* and *K*. Because they are known to undergo the pressure effect in a slight degree, their terrestrial wave-lengths were reduced to the case of the vacuum arc.

Wave-length in I.A.		Observers[5]
H 3968.474	*K* 3933.665	Adams
.473	.664	St. John
.469	.662	Burns and Meggers
.469	.669	Kiess
.467	.666	Warga
.468	.661	Evershed
.470	.663	”
.470	.664	Jackson
Mean 3968.470	3933.664	

For *H* and *K* in prominences, Evershed[1] found in 1927 that the mean of the residuals is 0.0109 I.A. Later, he found an unexpected increase of 0.003 I.A., so the residual amounts to 0.014 I.A. According to Jackson[5] it amounts to 0.015 I.A. Recently Evershed[12] remeasured it to be 0.015 I.A. According to our measurement, the same amounts to 0.016 I.A. (Table I), which is nearly equal to the above values. Thus, the limb effects for *H* and *K* in the prominence observed by us in the total eclipse of the sun, if any, are nearly equal to those observed hitherto in prominences without regard to an eclipse.

§ 6. Determination of the Linear Velocity of the Prominence due to the Sun's Rotation.

If we assume that the wave-lengths of H_β, H_γ, H_δ and two helium lines undergo no limb effect, we can determine the linear velocity of the prominence due to the sun's rotation. The result is tabulated in Table III.

Owing to (3), § 3, the result must be multiplied by 1.009 (=1/cos 7° 45′), so we obtain 1.93 km/sec.

To get the linear velocity due to the sun's sidereal rotation, the above velocity must be added by a velocity of 0.138 km/sec. Thus we have 2.07 km/sec as the linear velocity due to the sun's sidereal rotation. This agrees with that of the photosphere due to the sun's rotation, which is the origin-point of the prominence.

§ 7. Acknowledgements.

In conclusion, we wish to express our hearty thanks to the Hitati Factory and the Huzi Electric Factory for their supports.

§ 8. Summary.

(1) At the total eclipse of the sun in 1941, the limb shift of spectral lines has been investigated in a prominence situated on the east limb of the sun's equator. For H_γ the dispersion used by us was 8.7 Å./mm and the resolving power 1.32×10^5.

(2) The wave-lengths of four hydrogen, two ionized calcium and two helium lines were carefully measured.

(3) In a spectrum of such a dispersion as used by us for H_β, H_γ, H_δ, and the two helium lines no limb effect can be found. For H_ε the same can perhaps be said too.

Table III.

Wave-length measured	Correction except that due to the sun's rotation	Wave-length corrected	Terrestrial wave-length	Difference	Linear velocity due to rotation
I.A.	I.A.	I.A.	I.A.	I.A.	km/sec
4861.298	−0.0025	4861.295	4861.327	0.032	1.97
4713.119	25	4713.116	4713.145	0.029	1.85
4471.451	24	4471.449	4471.476	0.027	1.82
4340.442	23	4340.440	4340.470	0.030	2.07
4101.715	22	4101.713	4101.738	0.025	1.83
					Mean 1.91

(4) For H and K something exists that suggests the existence of the limb effect. Those amounts, if any, coincide with those found by Evershed without regard to the eclipses in the order of magnitude. Therefore, the values obtained without regard to the eclipses can hardly be considered as under-estimated, as they have ever been considered. But nothing definite can be said owing to the insufficient dispersion of the spectrum used.

(5) From the wave-lengths of H_β, H_γ, H_δ and the two helium lines the radial velocity of the prominence due to the sun's sidereal ratation is proved to be 2.07 km/sec.

References.

(1) Evershed: Roy. Astron. Soc., M.N. **88** (1927), 126.
(2) Evershed: Roy. Astron. Soc., M.N. **89** (1929), 250.
(3) Evershed: Roy. Astron. Soc., M.N. **90** (1930), 762.
(4) Evershed: Roy. Astron. Soc., M.N. **91** (1931), 260.
(5) Jackson: Roy. Astron. Soc., M.N. **93** (1932), 98.
(6) Hunter: Roy. Astron. Soc., M.N. **94** (1934), 594.
(7) McClea and Mitra: Observatory **57** (1934), 379.
(8) Evershed: Roy. Astron. Soc., M.N. **96** (1936), 152.
(9) Evershed: Observatory **60** (1937), 266.
(10) Thackeray: Roy. Astron. Soc., M. N. **97** (1937), 672.
(11) Roys: Roy. Astron. Soc., M.N. **97** (1937), 692.
(12) Evershed: Roy. Astron. Soc., M.N. **99** (1938), 120.
(13) Fowler: Report on Series in Line Spectra. 1922.
(14) Bacher and Goudsmit: Atomic Energy States. 1932.
(15) St. John and Babcock: Astrophys. J., **53** (1921), 260.
(16) Gale, Monk and Lee: Astrophys. J., **67** (1928), 89.
(17) Kent: Astrophys. J., **84** (1936), 585.

On the Solar Coronal Lines at the Total Eclipse in 1943.

By Tutomu TANAKA and Hirobumi OURA.

Faculty of Science, Niigata University and Research Institute for Low-Temperature Science, Hokkaido University.

(Read July 17, 1943; Received September 22, 1949).

§ 1. Introduction.

The total eclipse of February 5, 1943, gave a chance to observe a minimum type of the solar corona. The station adopted by our party was a a hill near Yubetu colliery, Hokkaido. The data concerning the eclipse and the eclipse station are shown in Table I.

Table I.

Location	Hill near Yubetu colliery
Longitude	144° 03.4′ E.
Latitude	43° 13.3′ N.
Elevation	500 metres
Altitude of the sun at 2nd contact	11° 4′
Altitude of the sun at 3rd contact	11° 21′
Time of totality	114 seconds
Apparent semidiameter at time of totality	
of the moon	16′ 37.0″
of the sun	16′ 13.3″
Computed time or 2nd contact	7^h 50^m 53^s Central Standard Time
Position angles of points of contact of the sun	
First contact	262° 5′
Second contact	81° 32′
Fourth contact	80° 4′
Position angle of the sun's axis of rotation	−13° 31′

These data we owe to Dr. Hukumi of the Tokyo Astronomical Observatory.

The altitude of the sun at the time of totality was very low, and this is a reason why the station was adopted on a hill of 500 metres above the sea-level.

The weather condition on the day in question cannot be said to have been perfect. Cloud, which might give some serious effect on the result, was not seen. But some trailings of haze, peculiar to early morning, might have existed, though the outline of the corona was clearly seen. At any rate, it is sure that the height of the observation station reduced to some extent the atmospheric obstruction, which might be produced by the atmospheric changes near the earth's surface in the early morning.

§ 2. Apparatus and Process of Photographing.

The spectrograph used was similar to that used in Syari(1). But the photographic lens was altered to a triplet made by Carl Zeiss, with a focal length of 70 cm. and an effective relative aperture of $f/6.9$, so that the dispersion of the spectrum was nearly doubled. Moreover, the surface of each prism and lens was covered with a thin film of CaF_2, to the effect that the transmission of the apparatus became about 1.5 times as much as before. A rotating prism was placed just before the slit, by which the image of the sun's equator was rotated to the orientation so that the image coincided exactly with the slit. During totality only one spectrogram was taken with an exposure time of 90 seconds, the exposure being commenced after 2 or 3 seconds from the beginning of totality. Immediately after that, four wedge-spectra of the standard lamp were photographed on the vacant part of the same plate with the same time of exposure. They were to serve as intensity scales for photometric purpose. A photographic plate named "KS-77" (backed) made by Huzi Photographic Film Co. was chosen. The size was 10 cm. ×25 cm. The process of developing was the same as before(1).

As it was known that the temperature in the open of that part of Hokkaido where the observation post was located averages −10° to −20°C. during the early part of February, it was feared that smooth operation of the diverse apparatus might suffer from low temperature. To obviate such difficulty, we used the aviation lublicant, which is said to have the capacity of withstanding the cold down to −30°C. It may have been due to this precaution that all the clockworks of the apparatus worked perfectly well. Moreover, nothing unfavourable happened concerning the groundwork of the observation post which was thoroughly protected against the effects of the frost.

§ 3. Intensity Distribution of Coronal Lines.

In the spectrograph used by us the slit was put along the sun's equator so that the radial distribution of the corona lines could directly be investigated, though our observation of course is to do with the proj ction on the plane perpendicular to the lines of collination. Among the coronal lines in our spectrogram, the lines of $\lambda\lambda$ 6374 Å. and 5303 Å. were fairly sharp, so their intensity distributions were measured by the method of photographic photometry. Regarding the line of λ 5303 Å., from the sun's east limb the eight heights were taken, which correspond to $0.08\,r$, $0.13\,r$, $0.18\,r$, $0.23\,r$, $0.28\,r$, $0.33\,r$, $0.38r$ and $0.43r$, where a height of $0.06\,r$ nearly equals to 1′, r being the sun's radius. And from the west limb, the eight heights corresponding to $0.09r$, $0.14r$, $0.19r$. $0.24r$, $0.29r$, $0.34r$, $0.39r$ and $0.44r$ were taken. Next, perpendicular to these vertical lines, the microphotometric curves were made (Fig. 1) and they were converted into intensity distribution curves by means of the intensity-scales by usual photographic-photometry method (Fig. 2). Since these curves represented peaks fairly sharp, the slitless correction for the microphotometer(2) were applied (Fig. 3). To say strictly, each curve obtained thus was never simply shaped. Neither its centre of gravity G nor the maximum point M was strictly on the middle vertical line PQ of this curve as shown in Fig. 4 for an example. This might

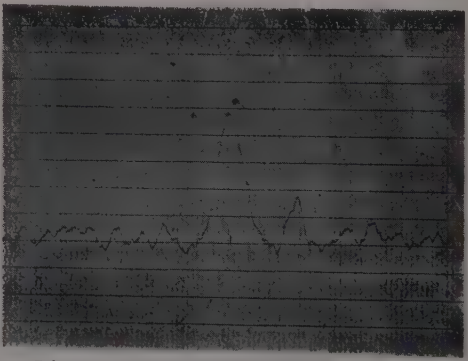

Fig. 1. Microphotometric Curve of λ 5303 Å

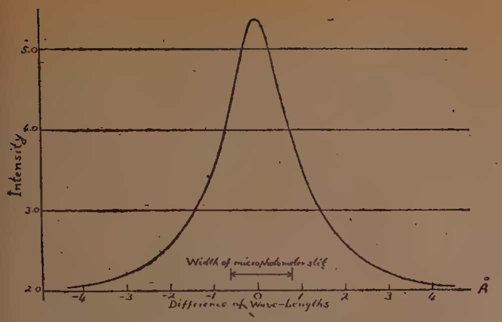

Fig. 2.

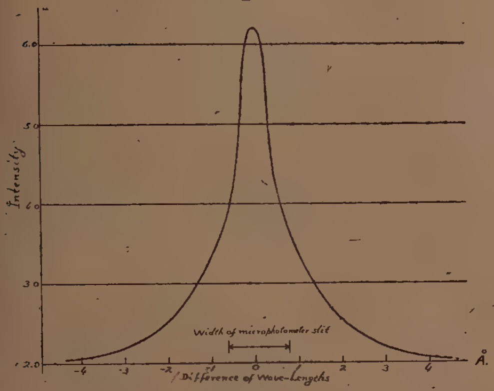

Fig. 3.

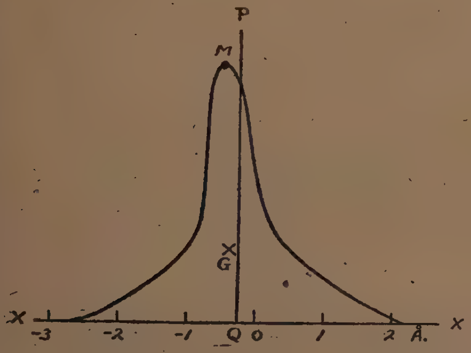

Fig. 4.

be due to turbulence occurring in various ways at different heights. To compare the intensities of different heights from the sun's limb in such a case, it might be the best to take each area of the part enclosed by the intensity-distribution curve and the ground line XX. The ground line was drawn at a height from which the parts due to the continuous spectrum of the corona, sky light and fogging were subtracted. Thus the integrated intensities of different heights were obtained. The processes with respect to different heights were quite independent. Nevertheless, when the values obtained thus are plotted against the distance from the sun's limb, a quite smooth curve can be obtained for each side of the sun's equator.

The value of the common logarithm of the brightness $B +$ constant is shown in Table II, where h represents the distance from the limb.

Table II.

East side		West side		Continuous spectrum*	
h	$\log_{10} B$ +const.	h	$\log_{10} B$ +const.		$\log_{10} B$ +const.
$0.08r$	0.822	$0.09r$	0.739	$0.2r$	0.700
$0.13r$	0.842	$0.14r$	0.722	$0.3r$	0.417
$0.18r$	0.766	$0.19r$	0.693	$0.4r$	0.074
$0.23r$	0.630	$0.24r$	0.581	$0.5r$	$\bar{1}.878$
$0.28r$	0.430	$0.29r$	0.477	$0.6r$	$\bar{1}.702$
$0.33r$	0.190	$0.34r$	0.372		
$0.38r$	0.099	$0.39r$	0.261		
$0.43r$	$\bar{1}.766$	$0.44r$	0.239		

* Regarding the data of this column, Part II of this paper is to be referred to.

The result is shown in Fig. 5(a).

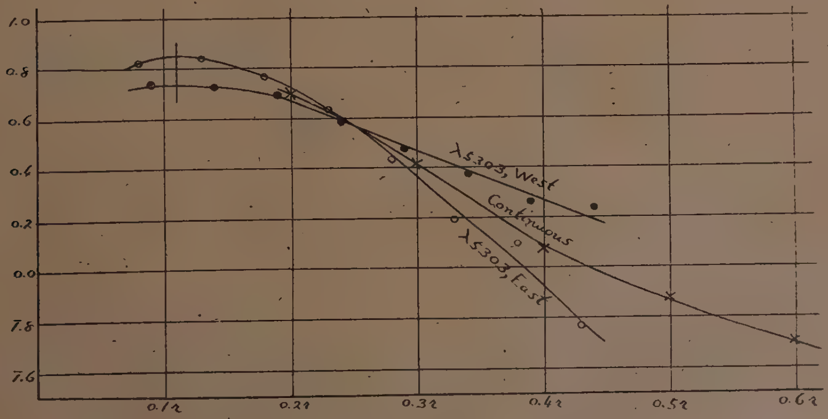

Fig. 5(a).

From the above data, it can be concluded:

(1) The parts of the corona of the opposite sides of the sun's equator show somewhat different intensity distributions, though those distributions do not much differ from that of the continuous spectrum of the corona.

(2) For the distance of 0.2r—0.5r from the sun's limb the slope of the curve for the continuous spectrum runs between those of the two curves for the east and west sides.

(3) The intensity is maximum at a distance near 0.11r or 1.8′ from the sun's limb, while the heights, at which the corona was partly concealed by the black moon during the time of exposure, and therefore the intensity distribution curve is not genuine, were less than 0.06r or 0.9′ from the sun's limb (notice Table I and the time of exposure),

Regarding tho line of λ 6374 Å., from the sun's west limb the five heights of 0.13r, 0.18r, 0.23r, 0.28r and 0.33r were taken. And the similar measurement was made. But, because of its faintness, the slitless correction was abandoned in this case. The curve obtained thus is shown in Fig. 5(b). while that for λ 5303 Å. without the slitless correction is shown in the same figure for comparison. The maximum height of the curve in this case occurs near 0.17 r or 2.7′ from the sun's limb. Comparing these curves, we can decidedly mention that the intensity distribution with respect to the distance from the sun's limb does not coincide for the two lines of λ 5303 Å. and λ 6374 Å.

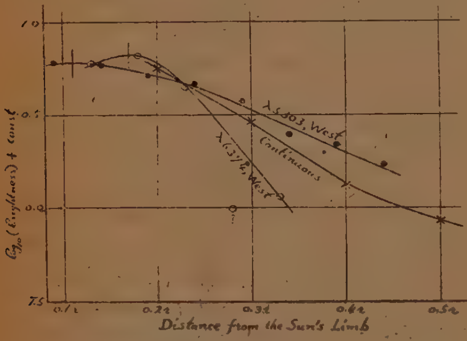

Fig. 5(b).

For 0.2r<h<0.3r, the distribution curve of the continuous spectrum observed in Syari coincides nearly with that observed in Yubetu, as it can be seen in Fig. 6. Therefore for h< 0.2r also, much difference might not occur. The same curve coincides also with that of the continuous spectrum observed by Grotrian⁽³⁾ well from h=0.2r to h=0.078r. But, according as h becomes less than 0.2r, our curves for the coronal lines become flat, and seem to deviate gradually from that of the continuous spectrum.

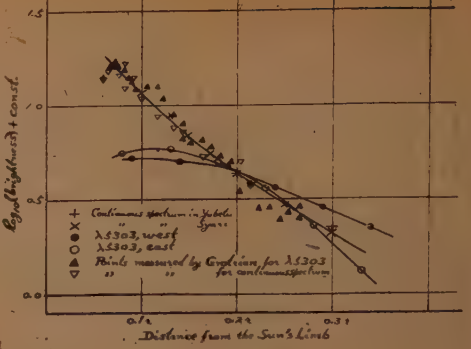

Fig. 6.

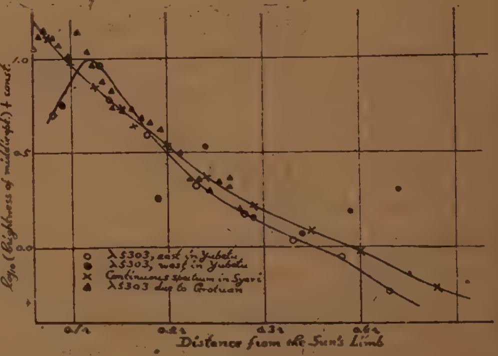

Fig. 7.

We used nearly the same apparatus and similar measuring methods in Syari and Yubetu, and for h<0.2r obtained quite different curves for the continuous and line spectra, the photographic densities used being medium in the both cases. Therefore this is to be considered to be genuine. The decay of intensity of the coronal lines being less for h < 0.2r, the coronal lines become more eminent at some distance from the sun's limb in comparison with the continuous spectrum, as can be seen directly.

Let us take the intensity of the middle point of the spectral line at each height as in Grotrian's curve, instead of the integrated intensity considered above. The result is shown in Fig. 7. As it can be seen, the curve of the east side is very near that obtained by Grotrian⁽³⁾ as well as that of the continuous spectrum. But the result for the west side diverges widely. Such a curve can hardly have important significance, as has been previously mentioned.

§ 3. Fluctuation of the Wave-lengths of Coronal Lines.

The wave-length of the centre of gravity of the line at each height seems to fluctuate by such an amount of wave-length as shown in Fig. 8 from each other. This figure can be obtained from the intensity distribution curves used in the preceding section. Such a fluctuation is perhaps due to a turbulence which might occur in the solar corona. The order of magnitude of such fluctuation coincides with the fluctuation of the value of the wave-length which was determined at different eclipses and the different observers. This is perhaps an important reason why the result of the measurement of the wave-length of each line is not consistent.

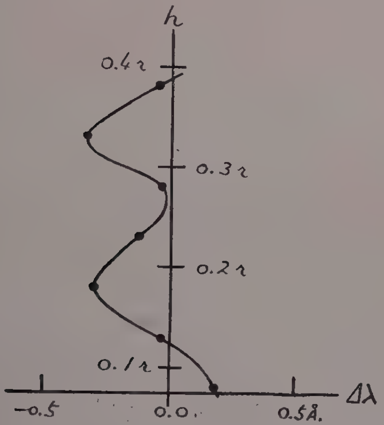

Fluctuation of C.G. from the middle point for the line λ5303 Å.

Fig. 8.

§ 5. Summary.

(1) For the middle solar corona the intensity distribution of the coronal lines of λλ 5303 Å. nnd 6374 Å. according to the distance from the sun's limb was investigated by photographic-photometry method.

(2) The intensity distribution for different lines as well as for different sides of the sun's limb is not common, though that does not make much difference from that of the continuous spectrum in the range of the distance from the sun's limb of $0.2r$—$0.4r$.

(3) For the distance from the sun's limb less than $0.2r$, the distribution curves of the coronal lines are flat, and deviate gradually from that of the continuous spectrum.

(4) The maximum of intensity exists at the distance of about $0.11r$ for λ 5303 Å. and of about $0.17r$ for λ 6374 Å. from the sun's limb.

Finally, we wish to express our hearty thanks to Dr. Koike, Director of Yubetu colliery, as well as several members of the same colliery, who kindly afforded us great facilities for the progress of the observation. We are also much indebted to Prof. Zyungo Yosida for his cooperation in the observation, and to the Hitati Factory, the Huzi Electric Co., and Dr. Keizo Tamura for their financial assistance.

References.

(1) Proc. Phys.-Math. Soc. of Japan 3, **19** (1937) 693.

(2) Zyun Koana: Proc. Phys.-Math. Soc. Japan 3, **25** (1943) 57.

(3) Zeits. f. Astrophys. **7** (1933) 26.

On the Continuous Spectrum of the Solar Corona at the Total Eclipse in 1943.

By Tutomu TANAKA, Hirobumi OURA, Tosio MURAKAMI and
Takio MITUNOBU.

Faculty of Science, Niigata University, Research Institute for Low Temperature Science, Hokkido University, and Huzi Electric Co.

(Read July 17, 1943; Received September 22, 1949).

§ 1. Polarization of the Continuous Spectrum of the Solar Corona.

The investigation of the polarization of the continuous spectrum of the solar corona affords a capital key to the nature of the corona. But the results published hitherto show remarkable inconsistence. Dufay and Grouiller(1) found that the polarization of the corona is independent of wave-length over the range 4,000 Å. – 5,000 Å., and concluded that the continuous spectrum of the corona is due to the scattering of sunlight by free electrons. Cohn(2), on the contrary, found that the amount of polarization for the light of different wave-lengths from 4,200 Å. to 6,680 Å. is different, and he concluded that the scattering is not due solely to free electrons. Thus the problem can never be said to have been solved. The present investigation is intended to throw a light on this. Unfortunately, the altitude of the sun during totality was very low (11° or so), the time was early morning at which the atmospheric conditions were changeable, and moreover the snow, not very heavy, covered the ground. So a great difficulty was met for accurate measurement, as it can be seen in the present report. But the weather was tolerably fair, and the observation was carried on as prearranged.

Regarding the data concerning the eclipse, Part I of this paper is to be referred to,

§ 2. Observational Procedure.

The apparatus used by us was a two-prism spectrograph, which consists of a collimator with a slit and converging lens of the focal length 40 cm. and of the aperture f/5, two heavy-flint glass (named F2) prisma, and a focusing lens manufactured by Nippon Kogaku Co. of the focal length 30 cm. and the aperture f/3.5. Next to the collimator lens, a Wollaston quartz biprism was put, by which two spectra were produced. The two spectra were sufficiently separated sidewards and corresponded to the vibrations of light parallel and perpendicular to the slit of the spectrograph. A diaphragm of the length 3.8 mm. was put in front of the slit of the collimator and in contact with it. And the image of the sun was put in an orientation, in which the image of the sun's equator coincided with the slit and the length of about 3.5 mm of the east side of the corona is uncovered by the diaphragm of the slit. So the spectrum

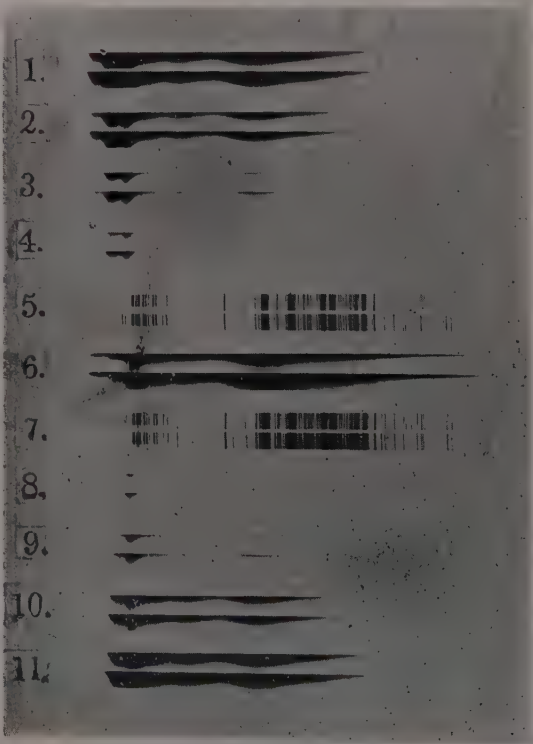

Fig. 1.

of the corona of the east side up to the height from the sun's limb nearly equal to the sun's diameter is produced. For the photographic plate, "KS-77" plate made by Huzi Photographic Co. was chosen.

Ninety second exposure was given, the slit being opened to 1 mm. This is shown in Fig. 1 (6). Figs. 1 (5) and (7) represent the wave-length scales of iron-arc lines. Just before and after totality, four sets of wedge-spectum with different intensities due to a standard tungsten lamp were made as intensity-scales by the same time of exposure. These are shown in (1)—(4) and (8)—(11) of Fig. 1. All the images are doubled, and the dependence of the transmission of the spectrograph on the direction of the light vibration does not influence the present result. The further treatment was similar to that in Part I of this paper.

§ 3. Polarizabilities for Different Wave-Lengths.

The polarizabilities for $\lambda\lambda$ 4200 Å., 4600 Å., 5000 Å., 5400 Å., 5800 Å., and 6200 Å. are tabulated in Table I, and shown in Fig. 2.

Table I.

h \ λ in Å.	4200	4600	5000	5400	5800	6200
	%	%	%	%	%	%
0.5r	34.3	—	37.9	37.3	30.5	—
0.6r	29.7	—	36.8	34.6	29.7	31.5
0.7r	29.7	18.6	30.7	29.9	26.3	32.8
0.8r	30.2	26.6	28.1	27.1	23.6	23.3
0.9r	29.8	27.0	26.2	23.0	21.6	17.7
1.0r	28.0	24.5	24.7	20.0	17.2	13.2
1.1r	26.5	22.7	22.3	17.4	16.0	9.7
1.2r	25.3	21.7	19.2	15.1	13.2	7.9
1.3r	24.1	20.7	15.2	13.7	10.6	5.8
1.4r	22.5	17.6	11.8	14.9	8.0	2.9

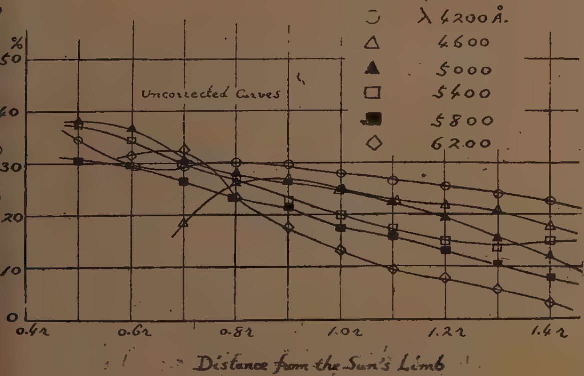

Fig. 2.

The sun itself was repeatedly photographed with the same polarigraph as we used in the eclipse, when the sun was near the position of totality. The spectra were always polarized in a slight degree. This cannot be considered to be due to some systematic error of the apparatus. If the polarization of the light emitted by the standard tungsten lamp which was used by us is investigated with the same apparatus, nothing similar can be found. The neutral glass used to reduce the sunlight has been proved at many occasions to produce no perceptible polarization to the light that transmits it normally. Thus it must be considered that this is due to the polarization of the natural light emitted from a light source outside the earth.

The optical phenomena of the sky near the horizon are quite complicated, especially when the sun's altitude is low. When a light source of low altitude outside the earth's atmosphere sends light through thick layers of atmospheric air, the light may undergo several modifications in complicated ways.

The polarization mentioned above can be a local phenomenon at our observation site, when the sun is at very low altitude. The condition of the sky in the same district at the same hour of each morning in the same season is very similar.

The polarization can be naturally assumed to be independent of the brightness of light source and can be applied to the case of the coronal light. Whatever reason of the polarization of this kind may be, the final result undergoes no serious modification. But, if this correction is added, the result is fairly simplified.

Let us denote the transmissions of the tangential and radial vibration with respect to the solar equator by κ_t and κ_r respectively. We observe the tangential and radial intensity of I_t' and I_r' instead of I_t and I_r, which are those without the influence of the earth's atmosphere. Thus we obtain

$$I_t' = \kappa_t I_t$$

and

$$I_r' = \kappa_r I_r .$$

Therefore

$$\frac{I_r'}{I_t'} = \frac{\kappa_r}{\kappa_t}\,\frac{I_r}{I_t} .$$

For the natural light $I_r = I_t$, $I_r'/I_t' = \kappa_r/\kappa_t = 1+\alpha$, where we are able to determine α by the sun's polarization.

Table II.

λ in Å.	4200	4600	5000	5400	5800	6200
α	0.167	0.135	0.127	0.135	0.138	0.208

But because

$$\frac{I_t}{I_r} = (1+\alpha)\frac{I_t'}{I_r'},$$

we have

$$\frac{I_t-I_r}{I_t+I_r} = \frac{(1+\alpha)I_t'-I_r'}{(1+\alpha)I_t'+I_r'}.$$

The polarizability of each wave-length genuine to the corona become a few per cent higher than the observed one. The corrected curves are shown in Table III and Fig. 3. In this figure, the end points of each curve are omitted on account of their ambiguity. At a glance, it can be seen that the arrangement of the curves has been much simplified.

Table III.

h \ λ in Å.	4200	4600	5000	5400	5800	6200
	%	%	%	%	%	%
0.5r	40.9	–	52.4	53.7	45.8	–
0.6r	36.5	–	40.9	40.0	35.4	39.7
0.7r	36.5	24.7	36.0	35.5	32.2	40.9
0.8r	37.0	32.4	33.5	32.8	29.6	32.0
0.9r	36.6	32.7	31.7	28.8	27.7	26.7
1.0r	34.9	30.2	30.2	26.0	25.3	22.4
1.1r	33.5	28.5	27.9	23.5	22.4	19.0
1.2r	32.4	27.7	24.9	21.3	19.5	17.2
1.3r	31.2	26.8	21.1	19.8	17.0	15.1
1.4r	29.7	23.7	17.6	21.0	14.3	12.2

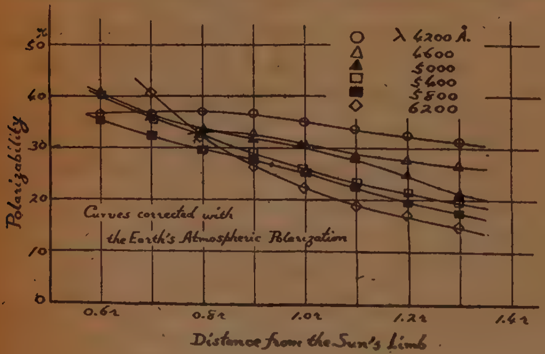

Fig. 3.

As it can be seen, the curves do not much deviate from each other. But the deviation of each curve from the mean curve is a little larger than the range of experimental errors. If the deviations are distributed irregularly according to the change of wave-length, they can be considered as the result of experimental errors. But these deviations are distributed quite regularly according to the change of wave-length, the polarizability being decreased when the wave-length is increased. Whether the variation of the polarizability of the corona due to the variation of wave-length is genuine to the corona or owes to some other resaon, it cannot be easily decided. Allen(3) found at the solar eclipse in 1940 a similar deviation. According to his result the polarizability in the middle corona for blue light was lager by about 5 % than that for red light, the sense of the deviation being the same as the present one, But he seems to have attributed this deviation to experimental errors. The following is another explanation for it, through it is of course not definite.

During totality there might have been a thin layer of cirrostratus (C_s) over the sky, as some observer asserts. If so, the cloud must be illuminated by the light from the ground, which was partially covered with snow and not covered by the moon. The light scattered by the cloud towards us might be polarized in some way. The details of this polarization cannot be known. But the following is an example of the polarizalbility of the light scattered by C_s in a similar case without eclipse and was measured by us :—

λ in Å	4200	4600	5000	5400	5800	6200
Polarizability in %	46	38	30	23	16	8

Here the incident beam was almost perpendicular to the visual line. To say strictly, the conditions in the two cases might be different. But let us provisionally assume that these polarizabilities hold good in the present case. Moreover, considering the circumstances, we may assume that in this polarization the tangential component with respect to the solar equator predominated. Next, let us consider that the cloud sent the light of which the mean brightness was equal to that of the corona at a distance of 1.5 r from the sun's limb. This intensity of the light from the cloud is chosen as large as its effect becomes negligible when the distance from the sun's limb h decreases to about 0.6 r, because for value of h less than about 0.6 r the deviations become smaller and are distributed in irregular order.

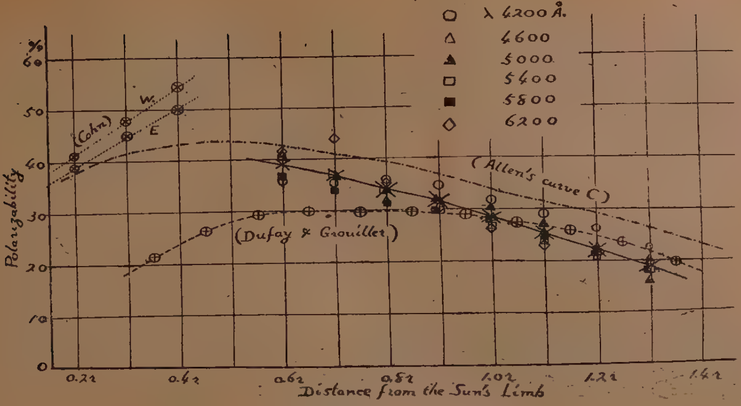

Fig. 4.

Under these assumptions, the intensity distribution genuine to the corona was calculated. The result is shown in Table IV and Fig. 4. The curves of different wave-lengths almost coincide with each other, at least for $0.6\,r < h < 1.3\,r$.

Table IV.

h \ λ in Å.	4200	4600	5000	5400	5800	6200	Mean
	%	%	%	%	%	%	%
$0.6r$	35.9	—	41.6	40.5	36.7	41.8	39.3
$0.7r$	35.4	—	36.6	36.7	33.9	44.3	37.4
$0.8r$	35.8	31.7	34.0	34.1	31.5	35.3	33.7
$0.9r$	34.9	31.6	32.0	29.9	30.0	30.3	31.6
$1.0r$	32.0	28.1	30.2	26.8	27.9	26.2	28.5
$1.1r$	29.1	25.2	27.1	23.7	24.6	22.9	25.4
$1.2r$	26.1	21.8	22.5	20.5	21.1	21.4	22.1
$1.3r$	22.2	20.0	15.7	17.8	17.7	19.4	18.8

The resultant curve is near that obtained by Dufay and Grouiller⁽¹⁾, of which the observation points are marked with (⊕) in Fig. 4. But, to say strictly, our curve is somewhat steeper. The ordinate-axis intercept of our curve at $h = 0.5\,r$ is almost at the mean height of those due to Dufay-Grouiller and Cohn.

Baumbach's coronal intensities are fitted to the formula

$$J_s(\rho) \fallingdotseq 0.0532\,\rho^{-2.5} + 1.425\,\rho^{-7} + 2.565\,\rho^{-17},$$

where ρ is the projected radial distance from the sun in terms of the sun's radius (i. e. $\rho = 1 + h/r$), the unit being 10^{-6} of the sun's central intensity. If it is considered that $\rho^{-2.5}$ term or the non-electron component is not polarized, while ρ^{-7} and ρ^{-17} terms or the electron components are partially polarized, Allen's curve C is obtained⁽⁴⁾. There is great variety among the polarization measurents but the tendency is to follow the curve C, as Allen asserts. As can be seen, the present curve shows a vivid resembrance to the curve C.

§ 4. Summary.

(1) For $0.6\,r < h < 1.3\,h$, the polarizability for each wave-length decreases gradually. Each polarizability curve does not much deviate from the straight line.

(2) The magnitude of the polarizability for each h decreases regularly as the wave-length increases. This deviation seems to be somewhat larger than the experimental error.

(3) But this variation might be due to the influence of intervening thin clouds. By reasonable assumptions, it can make the curves of different wave-lengths coincide with each other.

(4) The polarizability curve obtained thus is somewhat steeper than that due to Dufay and Grouiller, the value at $h = 1.02\,r$ being equal in the both cases.

(5) The same curve shows a vivid resemblance to Allen's curve C.

(6) At $h = 0.5\,r$, the present result (40 %) is nearly the mean of those by Cohn (54 %) and Dufay-Grouiller (29 %).

Finally, we wish to express our hearty thanks to Dr. Koike, Director of Yubetu colliery, as well as several members of the same colliery, who kindly afforded us great facilities for the progress of the observation. We are also much indebted to Prof. Zyngo Yosida for his cooperation in the observation, and to the Hitati Factory, the Huzi Electric Co., and Dr. Keizo Tamura for their financial assistance.

References.

(1) C. R., **203** (1936), 453.
(2) Astrophys. J., **87** (1938), 284.
(3) M. N., **101** (1941), 281.
(4) M. N., **107** (1947), 426.

Supplementary Report on the Continuous Spectrum of the Solar Corona.

By Tutomu TANAKA.

Faculty of Science, Niigata University.

(Read July 17, 1943; Received September 22, 1949).

§ 1. The Total Intensity Distribution according to the Distance of the Sun's Limb.

The question was attacked at the eclipse in 1936 by the author and Drs. Z. Koana and M. Kondo(1). The corona of that eclipse was of the maximum type, while that in 1943 was of the minimum. Thus to compare the results of the two cases affords special interest.

The method used in the present observation was similar to the former case. But, in this case, the total intensity B is given by the sum of the intensities of the components which were once resolved by a Wollaston prism for the purpose mentioned in the preceding paper.

In the region from λ 4200 Å. to λ 8600 Å., twelve wave-lengths were taken. For each wave-length the intensity distribution curve according to the distance from the sun's limb was obtained. The result is tabulated in Table I. The resulting curves, which are shown in Fig. 1, show small inconsistences. Meanwhile that of 6600 Å. is somewhat large. But the deviations show no regularity, and are almost within the range of experimental errors. Therefore it can be concluded that, the distribution curves of different wave-lengths can be said that they coincide with each other, as concluded in the report of 1938(1).

On the other hand, the decay curves are slightly steeper than those obtained in Syari for $h < 0.5\,r$ and somewhat flatter for $h > 0.6\,r$, as shown in Fig. 1. The difference might come from the difference of the type of the corona in the two cases. In the minimum type, the intensity decreases at first more rapidly in a slight degree and then more slowly in some degree, in comparison with that in the maximum type, though the deviation in the two cases is not large. If it is considered that we are regarding the sun's equator in both cases, such difference might be quite natural.

Next, let us consider the correction for the polarization due to the earth's atmosphere mentioned in the preceding paper. Adopting the previous notations, we have

$$\frac{I'_r}{I'_t} \doteq (1+\alpha)\frac{I_r}{I_t} = \frac{I_r}{I_t} + \alpha\frac{I_r}{I_t}.$$

Thus $$\frac{I'}{I_t'} = \frac{I}{I_t} + \alpha\frac{I_r}{I_t} = \frac{I}{I_t}\left(I + \alpha\frac{I_r}{I}\right).$$

Therefore $$I' = I\frac{I'_t}{I_t}\left(1+\alpha\frac{I_r}{I}\right) = I\left(1+\alpha\frac{I_r}{I}\right)\kappa_t,$$

or $$\log_{10}B' = \log_{10}B + \log_{10}\left(1+\alpha\frac{I_r}{I}\right) + \text{const.}$$

For the sake of the correction, $\log_{10}\left(I+\alpha\frac{I_r}{I}\right)$ must be subtracted from $\log_{10} B'$.

Put $k = \alpha\frac{I_r}{I}$, where $\frac{I_r}{I} \doteq \frac{1}{2}\left(1-\frac{I_t-I_r}{I_t+I_r}\right)$. This can be calculated from the mean value of α in Table II and the data in Table IV in the preceding paper.

Table I.

$\log_{10} B$ + const.

λ in Å. \ h	0.2 r	0.3 r	0.4 r	0.5 r	0.6 r	0.7 r	0.8 r	0.9 r	1.0 r	1.1 r	1.2 r	1.3 r	1.4 r
8600	—	3.081	2.654	2.370	—	—	—	—	—	—	—	—	—
8200	3.225	2.867	2.576	2.353	—	—	—	—	—	—	—	—	—
7800	3.290	2.973	2.664	2.420	2.232	—	—	—	—	—	—	—	—
7400	—	—	—	2.423	2.256	2.117	2.000	1.895	1.804	1.729	—	—	—
7000	—	—	—	—	2.224	2.117	2.000	1.884	1.780	1.695	—	—	—
6600	—	—	—	—	—	2.129	2.000	1.874	1.762	1.658	1.574	1.506	1.455
6200	—	—	—	—	2.272	2.142	2.000	1.896	1.802	1.722	1.655	1.602	1.569
5800	—	—	—	2.465	2.252	2.113	2.000	1.900	1.810	1.731	1.662	1.612	1.575
5400	—	—	—	2.497	2.287	2.131	2.000	1.897	1.809	1.732	1.666	1.616	1.562
5000	—	—	—	2.482	2.285	2.124	2.000	1.897	1.808	1.731	1.665	1.610	1.561
4600	—	—	—	—	—	2.143	2.000	1.903	1.827	1.761	1.705	1.661	1.618
4200	—	—	—	2.446	2.264	2.120	2.000	1.893	1.809	1.739	1.682	1.638	1.613
Mean	3.257	2.974	2.631	2.435	2.259	2.126	2.000	1.893	1.801	1.722	1.658	1.606	1.565

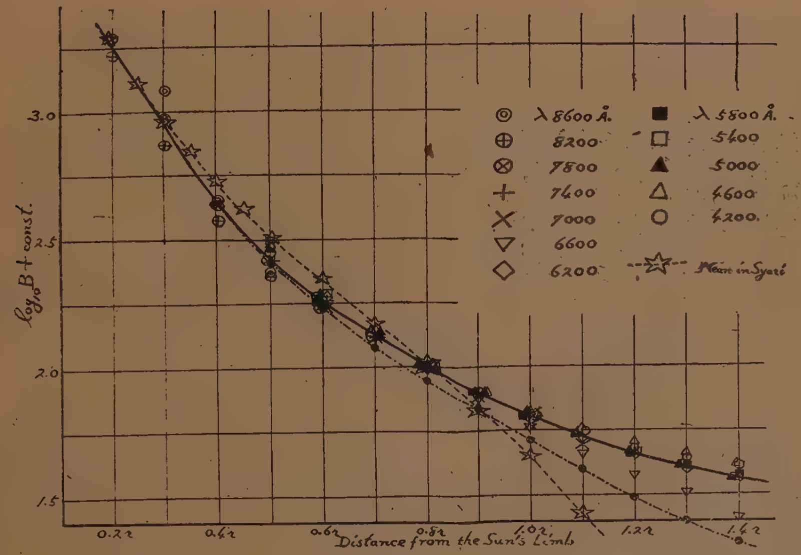

Fig. 1.

h	1.4r	1.3r	1.2r	1,2r	1.0r	0.9r	0.8r	0.7r	0.6r	0.5r	0.4r
k	$\frac{1}{1.28}$	$\frac{1}{1.65}$	$\frac{1}{2.14}$	$\frac{1}{2.85}$	$\frac{1}{3.81}$	$\frac{1}{5.19}$	$\frac{1}{7.18}$	$\frac{1}{10.1}$	$\frac{1}{14.5}$	$\frac{1}{21.2}$	$\frac{1}{32.4}$
$\log_{10}(1+k)$	0.251	0.206	0.166	0.131	0.101	0.077	0.057	0.041	0.029	0.020	0.013

The mean brightness curve corrected is shown in Fig. 1 by a chain line with marks (•).

For small values of h the curve of the relative brightness does not nearly alter. For larger values of h, the curve becomes steeper, but still flatter than that in Syari. The uncorrected curve seems too flat. Therefore, the above-mentioned conclusions hold good still.

§ 2. Results deduced from Cohn's Report.

Cohn(2) gave a voluminous report of 1932 and and 1934 eclipses regarding the polarization of the sun's corona. The detailed data given by him are indeed invaluable.

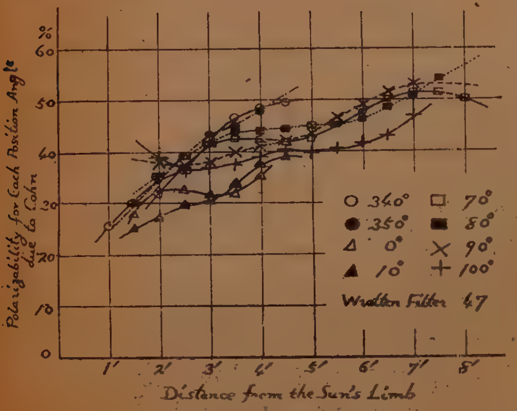

Fig. 2 (a).

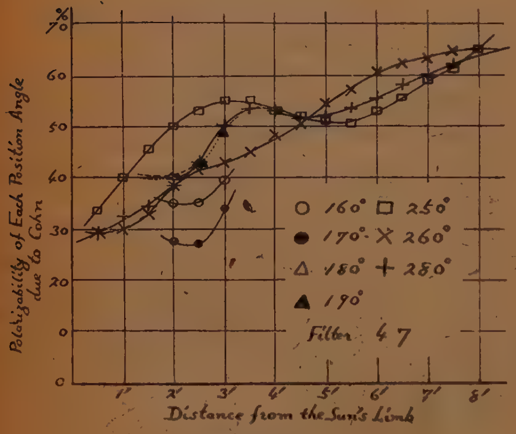

Fig. 2 (b).

The polarizability curves for different position-angles regarding each wave-length are very complicated [Figs. 2 (a) and 2 (b)]. But for each position angle, take the average of the polarizabilities for different colours. Put off the data in 1932 eclipse, because they are too meagre for this purpose. Moreover, if the deviations below 3.5% are admitted, a series of lines nearly straight can be drawn for each position angle [Figs. 3 (a) and 3 (b)]. This shows perhaps that the observational errors were cancelled to some extent by this process, and the complexity of the polarizability curves of different wave-lengths were chiefly due to the observational errors. From the figures, it can be known that the polarizabilities in oppsite sides of the sun's equator and of the sun's axis are approximately equal respectively. But according to the position-angle the polarizability varies to some extent, the polarizabilities near the equator being larger than those near the poles.

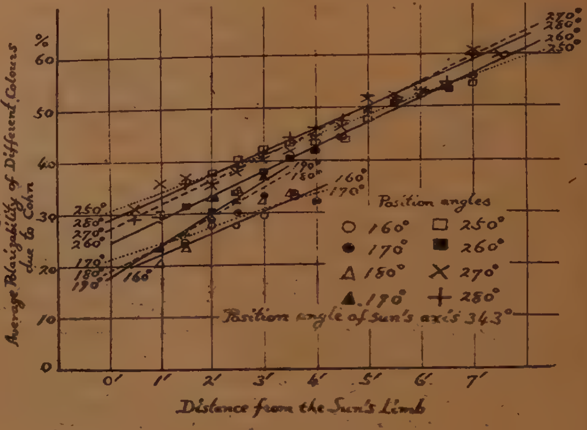

Fig. 3 (a).

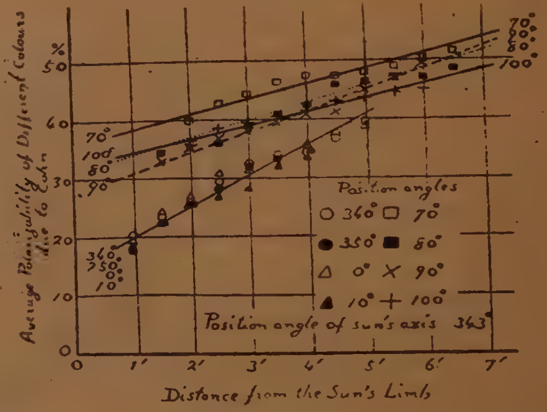

Fig. 3 (b).

From the data in 1932 eclipse, the similar conclusion can also be obtained in a rough degree, though the data are rather insufficient. For different eclipses, the polarizabilities coincide approximately with each other for each position-angle.

Thus the independency of the polarizability on the wave-length can perhaps be obtained from Cohn's data. Its dependency seems to be superficial.

§ 3. Effect of the Sky Light.

In our microphotometric curves the photographic density due to the sky light cannot be distinguished from that due to chemical fogging. It is so small that it can hardly be perceptible when resolved into the spectrum.

With respect to white light, the ratio of the brightness of square degree of the sky around the solar corona during totality against the brightness of the total solar corona has been reported by several observers.

Author	Altitude of the sun	Ratio of the brightness of square degree of the sky and that of the total corona
King(3)	18.3	0.0285
Kunz and Stabbins(4)	17.7	0.0336
,, (5)	36.5	0.0073
Parkhurst(5)	14.5	0.0073
La Baume Pluvinel and Barbier(6)	about 30	0.0156
		Mean 0.0184

The first three are regarding the same eclipse. Larger values of the first two observations are perhaps due to the deep snow which covered all the districts in the neighbourhood of the observation sites. Therefore these values might be too much. Though at our site the snow was not very deep, some parts of the ground in the neighbourhood were covered with snow. So these large values are not to be put off. The variation according to the sun's altitude is not evident. The brightness of the sky in our case was perhaps not so far from the above mean value.

If the above mean value is used, the intensity of the sky light is about $0.0184\times\pi\times\left(\frac{16}{60}\right)^2\times 2.95\times10^{-7}=12.2\times10^{-10}$ in terms of the sun's mean intensity. Here, in order to use the results by Schwarzschild(8) and Turner's law(9), we adopted $J_{\text{corona}}=2.95\times10^{-7}\,J_{\text{sun}}$, which is the integrated result of the intensity of each part of the corona expressed by the mean intensity of the sun by Schwarzschild.

Owing to Schwarzschild's results and Turner's law, the intensity of 12.2×10^{-10} is the intensity of the corona at 34.0′ or $2.1\,r$ from the sun's limb. At $h=0.6\,r$ and $h=1.3\,r$ from the sun's limb, which are the two limits of the range measured by us, the intensities of the coronal light are 645×10^{-10} and 73×10^{-10} respectively. The polarizability of the sky light might not be zero, but must be very small, because the light source and observer subtend an angle of nearly 180° at the scattering medium. Let us neglect it. In the corona the intensity distribution according to the distance from the sun's limb is common for different wave-length. So we can use a factor, which is independent of the distance, to get the intensity of each wave-length from that of white light. In the sky light the same can be mentioned. On the other hand, the colour of the sky light around the black moon during totality near the horizon cannot be known definitely, but can be mentioned to be quite white. Therefore we may assume for the present purpose the colours of the corona and the sky light of this case are similar. Thus we can use a common factor for the above-mentioned purpose regarding the corona and the sky light. This factor can be reduced in the following fractions. We shall omit it for simplicity. Represent the "mean" polarizability genuine to the corona of different wave-lengths by P; it can be obtained by

$$0.393=\frac{P_{0.6r}\times645}{645+12}\quad\text{and}\quad 0.188=\frac{P_{1.3r}\times73}{73+12},$$

or $P_{0.6r}=0.400$ and $P_{1.3r}=0.219$.

Thus the following table can be obtained:

h	$0.6r$	$0.7r$	$0.8r$	$0.9r$	$1.0r$	$1.1r$	$1.2r$	$1.3r$
P uncorrected in %	39.3	37.4	33.1	31.6	28.5	25.4	22.1	18.8
P corrected in %	40.0	38.3	34.9	33.1	30.5	27.8	24.9	21.9

In Fig. 4, the uncorrected points are marked with (×) and the corrected ones with (○).

According to the above result, the polarizability curve is not much altered by the effect of the sky light. The corrected curve in which the polarizability is expressed by percent is raised by about

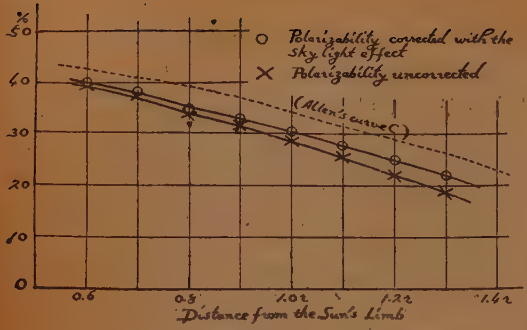

Fig. 4.

2% on the whole, the slope decreasing slightly.

§ 4. Summary.

(1) The total intensity distribution curves of different wave-lengths coincide with each other.

(2) The decay curves for the total intensity are somewhat steeper than those of the maximum type till the distance from the limb reaches some value and becomes flatter beyond this value.

(3) The independency of the polarizability on the wave-length can perhaps be obtained from Cohn's data.

(4) By adding the correction due to the effect of the sky light, the polarizability curve is raised by some few per cent, the slope of the curve decreasing slightly.

References.

(1) Phys. Math. Soc. Japan, Proc. **20** (1938), 52.
(2) Astrophys. J., **87** (1938), 284.
(3) H.C.O. Circular (1925), 286.
(4) Astrophys. J., **62** (1926), 114.
(5) Ditto.
(6) Astrophys. J., **64** (1926), 273.
(7) C. R., **196** (1933), 1345.
(8) Ast. Mitt. Göttingen, **13**.
(9) Proc. R. S., **66** (1900), 403.
(10) M.N., **107** (1947), 426.

On the Thickness of Plane Shock Waves in a Gas in Turbulent Motion.

By Akira SAKURAI.

Tokyo Electrical Engineering College

(Read October, 1948; Received Sept. 24, 1949).

§ 1. Introduction.

Theoretical discussions about shock waves⁽¹⁾ show that a plane discontinuity of velocity, pressure, density and temperature can exist in an ideal compressible fluid in which a relationship due to Rankine and Hugoniot is assumed. Also it is well known that dissipative forces such as viscosity, thermal conduction and radiation are capable of explaining the maintenance of a shock wave of permanent type which has a continuous layer of transition of finite thickness. But this theoretical thickness is too thin compared with the usual front thickness in an actual gas.

Now it should be noticed that in the theories mentioned above no account has been taken of apparent stresses due to turbulent motion which dissipates the energy more violently than the molecular motions do. Of course there can be flows which have very little or none of turbulence, and actually we have quite intense shock waves in such flows. But in most cases of actual flows, there must be considered to exist a remarkable amount of turbulence and perhaps the front will be broadened by this influence.

It is of much interest, therefore, to inquire whether a plane disturbance, which is of permanent type in the mean, can be propagated in a turbulent gas. In this paper this question will be discussed and answered in the affirmative.

§ 2. One-dimensional Steady Mean Flow.

The motion of an ideal compressible fluid can be determined by the Eulerian equations. Denoting the components of the velocity by u, v, w, the density of the fluid by ρ and the pressure by p, we have the equation of continuity:

$$\frac{\partial\rho}{\partial t}+\frac{\partial}{\partial x}(\rho u)+\frac{\partial}{\partial y}(\rho v)+\frac{\partial}{\partial z}(\rho w)=0, \tag{1}$$

and the equations for the dynamic equilibrium:

$$\frac{\partial}{\partial t}(\rho u)+\frac{\partial}{\partial x}(p+\rho u^2)+\frac{\partial}{\partial y}(\rho uv)+\frac{\partial}{\partial z}(\rho uw)=0, \tag{2}$$

and two similar equations.

It is assumed here that the mixture due to turbulence is so violent that the effect of viscosity, thermal conduction and radiation are negligible. In the absence of these quantities, we must take the relation between p and ρ of an ideal gas to be adiabatic, but, for simplicity, we assume that p and ρ are proportional to each other, so that

$$p=C_0^2\rho, \tag{3}$$

where C_0 is the velocity of sound.

If we take the mean values of these equations over a long period of time and assume that the mean flow is steady and its direction is parallel to the axis of x, then the average state of affairs may be supposed to be independent of t, y and z, so that, identically,

$$\frac{\partial\bar\rho}{\partial t},\ \frac{\partial\overline{\rho u}}{\partial t},\ \frac{\partial\overline{\rho uv}}{\partial y},\ \frac{\partial\overline{(p+\rho v^2)}}{\partial y},\ \frac{\partial\overline{\rho uw}}{\partial z},\cdots=0,$$

where the bar denotes the mean value.

Hence (1), (2) become

$$\frac{\partial\overline{\rho u}}{\partial t}=0,\ \frac{\partial\overline{(\rho+\rho u^2)}}{\partial x}=0,\ \frac{\partial\overline{\rho uv}}{\partial x}=0,\ \frac{\partial\overline{\rho uw}}{\partial x}=0.$$

Integrating these equations and substituting the relation (3), we have,

$$\overline{\rho u}=A,\ C_0^2\bar\rho+\overline{\rho u^2}=B,\ \overline{\rho uv}=C,\ \overline{\rho uw}=D, \tag{4}$$

where A, B, C, D are integration constants.

Now we separate the values u, v, w, ρ (of course, $\bar v$, $\overline{w}=0$) and superposed fluctuating values u', v', w', ρ' and we substitute $\bar u+u'$ for u, v' for v, w' for w and $\bar\rho+\rho'$ for ρ. Then (4) become respectively,

$$\bar\rho\,\bar u+\overline{\rho' u'}=A,$$

$$C_0\rho^2+\bar\rho\,\bar u^2+\bar\rho\,\overline{u'^2}+2\bar u\,\overline{\rho' u'}+\overline{\rho' u'^2}=B,$$

$$\bar\rho\,\overline{u'v'}+\bar u\,\overline{\rho' v'}+\overline{\rho' u'v'}=C,$$

$$\bar\rho\,\overline{u'w'}+\bar u\,\overline{\rho' w'}+\overline{\rho' u'w'}=D.$$

Because of the symmetrical property of the distributions of fluctuations u', v', w', ρ', the expressions $\overline{\rho' u'^2}$, $\overline{\rho' u'v'}$ and $\overline{\rho' u'w'}$ may be zero approximately. And thus the equations are transformed into

$$\bar\rho\,\bar u+\overline{\rho' u'}=A,$$

$$C_0^2\,\bar\rho-\bar\rho\,\bar u^2+2A\,\bar u+\bar\rho\,\overline{u'^2}=B, \tag{5}$$

$$\bar\rho\,\overline{u'v'}+\bar u\,\overline{\rho' v'}=C,$$

$$\bar\rho\,\overline{u'w'}+\bar u\,\overline{\rho' w'}=D.$$

§ 3. Relation between $\bar\rho$ and ρ' in Steady Flow.

We can find a relation between $\bar\rho$ and ρ' by a method similar to the "Generalized vorticity transfer theory" of G. I. Taylor⁽²⁾. The fluctuations at a definite point (x, y, z) are assumed to arise from the successive arrival of the elements of fluid which were initially at points (a, b, c) situated in the neighbourhood of the point (x, y, z). The change of density $\rho(x, y, z)$ from $\rho_0(a, b, c)$ due to the movement of an element of fluid from (a, b, c) to (x, y, z) may be given by the Lagrangian equation of continuity:

$$J\rho=\rho_0,\quad\text{where}\quad J=\frac{\partial(x,y,z)}{\partial(a,b,c)} \tag{6}$$

If we put, $x-a=l$, $y-b=m$, $z-c=n$, and neglect the second order terms in $\partial l/\partial a$, $\partial l/\partial b\cdots$, we have from (6),

$$J=1-\sum\frac{\partial l}{\partial a}$$

Moreover, as G. I. Taylor does, we assume that ρ_0 is also the mean density at (a, b, c); then if the mean motion is steady and only the first order terms in the Taylor series for $\bar\rho$ are retained,

$$\rho_0(a,b,c)=\bar\rho(x,y,z)-\sum(x-a)\frac{\partial\bar\rho(x,y,z)}{\partial x}$$
$$=\bar\rho-\sum l\frac{\partial\bar\rho}{\partial x}.$$

Substitution of this equation in (6) gives

$$\rho=\bar\rho+\rho'=\rho_0/J=\left(\bar\rho-\sum l\frac{\partial\bar\rho}{\partial x}\right)\Big/\left(1-\sum\frac{\partial l}{\partial a}\right)$$

$$=\bar\rho+\bar\rho\sum\frac{\partial l}{\partial a}-\sum l\frac{\partial\bar\rho}{\partial x},$$

whence $\rho'=\bar\rho\sum\frac{\partial l}{\partial x}-\sum l\frac{\partial\bar\rho}{\partial x}$

By the relation, $\partial l/\partial a=\partial l/\partial x$, ..., which are obtain d approximately with the assumption: l, m, $n\ll 1$, we have,

$$\rho'=\bar\rho\sum\frac{\partial l}{\partial x}-\sum l\frac{\partial\bar\rho}{\partial x}.$$

The second term on the right-hand side of this equation expresses the variation of density due to the initial distributions of density about that point, while the first term corresponds to the variation of density of a fluid element in its random motion. In the case of intense turbulent flow, the effect of the second part of ρ' is so large that the first term may be negligible, so that

$$\rho'=-\sum l\frac{\partial\bar\rho}{\partial x}. \tag{7}$$

The same result would be obtained directly, if we assume $\rho\fallingdotseq\rho_0$ instead of $J\rho=\rho_0$.

§ 4. Eddy Kinemaitc Viscosity.

In the mixture length theories it is usually assumed that the following relations hold between u', v', w' and $\bar u$, $\bar v$, $\bar w$,

$$u'=-\left(l\frac{\partial\bar u}{\partial x}+m\frac{\partial\bar u}{\partial y}+n\frac{\partial\bar u}{\partial z}\right),$$

and two similar equations for v' and w'.(3) Accordingly in our case, we may assume

$$u'=-l\frac{d\bar u}{dx}.$$

Hence we have,

$$\overline{u'^2}=-\overline{lu'}\frac{d\bar u}{dx}.$$

For simplicity, we adopt the relation (7)* for ρ', then,

$$\rho'u'=-lu'\frac{d\bar\rho}{dx}.$$

Let us substitute these expressions in the equations (5) and consider the eddy kinematic viscosity K** which is defined as:

$$K=\overline{lu'}=\overline{(x-a)u'}\ ^{***}$$

Then the equations (5) become

$$\bar\rho\bar u-K\frac{d\bar\rho}{dx}=A,$$

$$C_0^2\bar\rho-\bar\rho\bar u^2+2A\bar u-\bar\rho K\frac{d\bar u}{dx}=B:$$

Eliminating $\bar u$ from these equations, wn have an equation for $\bar\rho$:

$$C_0^2\bar\rho^2-B\bar\rho+A^2=-AK\frac{d\bar\rho}{dx}+K^2\bar\rho\frac{d^2\bar\rho}{dx^2}. \tag{8}$$

To determine the constants A, B, we consider the condition up-stream from the shock wave where the flow is uniform and

$$\bar\rho=\bar\rho_0,\quad \bar u=u_0,\quad \frac{d\bar u}{dx}=\frac{d\bar\rho}{dx}=0.$$

Using these equations, we can determine the values of A, B from the equation (8), as

$$A=\rho_0u_0,\quad B=\rho_0(C_0^2+u_0^2).$$

Then the equation (8) reduces to,

$$C_0^2\bar\rho^2-(C_0^2+u_0^2)\bar\rho+u_0^2\rho_0^2=-\rho_0u_0K\frac{d\bar\rho}{dx}+K^2\bar\rho\frac{d^2\bar\rho}{dx^2}.$$

If we introduce the quantities D, M defined as

$$\bar\rho/\rho_0=D,\quad u_0/C_0=M,$$

where M is nothing other than the Mach number of the on-coming flow, the equation becomes,

$$-M\frac{K}{C_0}\frac{dD}{dx}+\left(\frac{K}{C_0}\right)^2D\frac{d^2D}{dx^2}=D^2-(1+M^2)D+M^2$$
$$=(D-1)(D-M^2) \tag{9}$$

§ 5. Plane Shock Wave and its Front Thickness.

Though, $D=1$ and $D=M^2$ are both solutions of the equation (9), these present only a uniform flow, and therefore we must seek for other signi-

---

* It seems that no complication will result, if we adopt the full expression:

$$\rho'u'=\bar\rho\,u'\textstyle\sum\partial l/\partial a-lu'\,\partial\bar\rho/\partial x.$$

** In place of the eddy kinematic viscosity: lu', we can introduce other quantities such as the eddy viscosity: $\bar\rho\cdot lu$, and the mixture length: $(\bar{l^2})^{\frac{1}{2}}$, but in any case we may arrive at a similar result.

*** Strictly, we must introduce two different K corresponding to ρ' and u', respectively.

ficant solutions. It should be remarked that C_0 is, in general, much greater than K, which is reported to be of the order of 1 m/s in usual wind tunnels.(4) Then, if we neglect the term in $(K/C_0)^2$, the equation can be reduced to,

$$M\frac{K}{C_0}\frac{dD}{dx}=-(D-1)(D-M^2).$$

Integrating the above equation under the condition that the flow is super-sonic up-stream, we have

$$x=\frac{K}{C_0}\frac{M}{M^2-1}\log\frac{D-1}{M^2-D},$$

where the integration constant has been determined so that $D=(M^2+1)/2$ corresponds to $x=0$. The density distribution in the layer of transition represented by this equation is shown in the following figure.

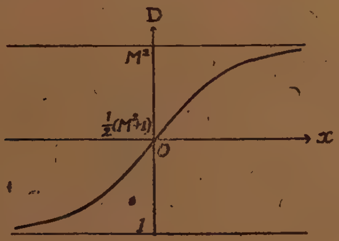

In the case in which the inclination of the above curve is great, we may consider this distribution of density as that in a shock wave. The thickness, T, of this layer of transition may be defined, as usual, by the distance between the two points where 8/10 of the change in D from M^2 to 1 occurs, thus

$$T=\frac{K}{C_0}\frac{M}{M^2-1}\log 9=2.2\frac{K}{C_0}\cdot\frac{M}{M^2-1}.$$

Or, if we denote $2.2K=L\cdot u^*$; $u^*/C_0=m$, above expression becomes,

$$T=L\cdot\frac{mM}{M^2-1},$$

where L represents the mixture length and m the Mach number of the velocity fluctuations approximately.

In conclusion the author wishes to express his gratitude to Prof. I. Imai for his guidance in this work.

References.

(1) See, for example, R. Becker: Zeits. f. Phys. 8 (1922) 32.
W. Durand: Aerodynamic Theory III. Div. H.
(2) G I. Taylor: Proc. Roy. Soc. A, **135** (1832) 697.
(3) For instance, H. Ertel: Sitz.-Ber. d. Pr. Akad. d. Wiss. Phys.-Math. Kl. **26** (1932).
(4) E. Inoue: J. Soc. Appl. Mech. Japan, **1** (1948) 15.

Polarization of Electrons*.

By Kenichi SHINOHARA and Norio RYU.

Department of Physics, Faculty of Science, Kyushu University.

(Read April 1949; Received Aug. 17, 1949).

Abstract.

An experiment was carried out to find out the palarization of electrons by double scattering. The scatterers used were gold foils of 5×10^{-5} mm thick and the energy of electrons ranged from 45 to 92 kev. The scattering angle at the first foil was taken as 90 degrees and that at the second foil 78 degrees. Polarization effect, as predicted by Mott, has been found, though its magnitude was somewhat smaller than that given by the theory. The values of 200 δ obtained was 3.6 ± 1.0, 4.0 ± 0.9, 6.8 ± 0.7, 9.0 ± 0.6, and 9.1 ± 1.0 for the electrons of energy 45, 60, 70, 90, and 92 kev, respectively.

§ 1. Introduction.

It was first shown theoretically by Mott⑴ that when high energy electrons are scattered twice at right angles by heavy atoms such as gold, a variation of the intensity at the second scattering with the azimuth is expected. The conditions to be fulfilled in order to realize the polarization are:

1) The velocity of electrons must be comparable with the velocity of light,

2) The atomic number of the scattering atoms must be large, so that $(Z/137)^2\sim1$,

3) Both angles of scattering must be large (i.e. comparable with 90°),

4) Both scattering must be single scatterings.

Dymond⑵, Thomson⑶ and Richer⑷ have each carried out experiments to verify the theory. But no polarization effect was found. Accordingly, several causes were examined, such as the effect of the crystal lattice, small angle multiple scatterings of electrons in the gold foils, but none was successful in explaining the discrepancy between the theory and the experiments.⑸⑹

In their experiments, the incident electron beam was scattered by a thin gold foil placed at an angle of 45° to the incident beam and the beam scattered back to the side of incidence was examined. We shall call this side, the reflection side, and the other, the transmission side. Now, Goertzel and Cox ⑺ have recently shown that on the reflection side a large number of electrons which had suffered two successive large angle scatterings in a single foil are mixed with those which had suffered a single 90° scattering, and pointed out that such electrons might have masked the polarization. Transmission side must be used to avoid this plural scattering. The calculation carried out by one of us also showed the existence of such doubly scattered electrons in large numbers. Shull, Chase, and Myers⑻ accordingly, using the beam scattered to the transmission side, obtained the polarization nearly coinciding with the theory, for the electrons of 400 kev energy.

The last of the four conditions mentioned, are most difficult to fulfill, especially when the observation is made on the reflection side. But the constancy of the energy of the electrons is also an important factor. Since the polarization effect to be expected is rather small and the number of electrons scattered twice by nucleus changes greatly with the energy, a large error might be introduced if there is a slight change of the accelerating voltage during the measurement. In this paper, an account will be given of the experiment which is carried out with the object of avoiding those errors.

---

* A preliminary report of this paper appeared in Phys. Rev., **75** (1949), 1762.

§ 2. Experimental Method and Procedure.

The electrons were emitted by a thoriated tungsten filament of 0.2 mm diameter in a Wehnelt cylinder and were accelerated by a voltage of 40—92 kv generated by a high tension equipment of the type of Cockcroft. The voltage was measured with a microammeter and a resistance of about 4000 MΩ. The resistance was made of 1 percent picric acid dissolved in a mixture of about 90 percent benzene and about 10 percent alcohol and contained in a glass tube.

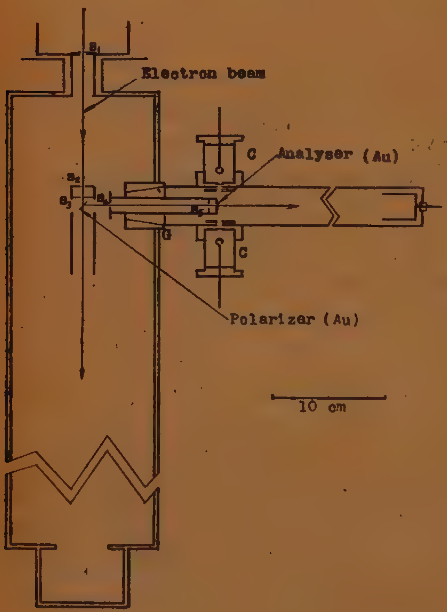

Fig. 1. Schematic diagram of the apparatus.

The scattering chamber is shown in Fig. 1. Three slits S_1 (diam. 1 mm), S_2 (diam. 1.5 mm) and S_3 (diam. 1.5 mm) defined the path of electrons which fell on the first gold foil (polarizer). This polarizer foil was supported by an aluminium plate, having approximately an elliptic hole whose longer and shorter axis are 6 and 4 mm, respectively. The foil was placed at the transmission position, as shown in Fig. 1, with its normal making an angle of 45° to the incident beam, and the longer axis of the hole being kept at 45° to the incident beam. Since the diameter of the slit S_3 was 1.5 mm, the beam falling on the foil did noth it the supporting aluminium plate. The electrons scattered at 90° by the polarizer, passed through two slits S_4 and S_5 and fell on the analyser foil placed perpendicular to the beam. The diameter of S_5 was 1.5 mm at an early stage of the experiment but was later changed to 0.75 mm for the reason stated below. Since the diameter of S_5 was either 1.5 mm or 0.75 mm and the analyser foil was supported by an aluminium plate having a hole of 2 mm diameter, the electrons did not hit the supporting aluminium plate. Two Geiger counters having thin mica windows of less than 1/100 mm thickness was placed at the positions shown in Fig. 1, to count electrons. The slits before the counter windows limited the path of the electrons so that only those scattered at an angle of 78° ± 4° entered the counters. Two scale-of-two counters were used and the counting rate was kept below 360/min. to avoid counting losses and also to avoid damaging the polarizer foil. The gold foils used as the polarizer and the analyser were both beaten gold foils of thick-ness about 5×10^{-5} mm.

The part of the scattering chamber housing the polarizer foil was made of 6″ brass tube and extended 45 cm from the foil in the direction of the incident beam and the part housing the analyser foil was made of $1\frac{1''}{4}$ brass tube and extended 30 cm from the analyser foil. The use of such large diameters and long extensions was done for the purpose of minimizing the disturbance due to stray electrons. Further precaution was taken by covering the inner surface of the chamber with thin aluminium plate, which at the same time reduced the emission of X-ray.

The part containing the analyser foil and two counters could be rotated as a whole by a ground joint G, and the positions of the counters could be interchanged and at the same time the analyser foil could be rotated in its plane, so that the difference of the counting efficiencies of the two counters and the possible slight difference of the geometry in this part of the apparatus could be eliminated.

If a/b is the ratio of the efficiencies of the two counters including its geometrical condition, the ratio x of the number of counts of the upper counter to that of the lower at one disponsition is

$$x = \frac{a}{b} \cdot \frac{1+\delta}{1-\delta} \qquad (1)$$

since the intensity of scattering should be proportional to $1+\delta$ and $1-\delta$, respectively, according to the theory of Mott. If, now, the analyser foil, together with the counters are rotated 180° by the ground joint, the ratio of the number of counts of the lower counter to the upper becomes

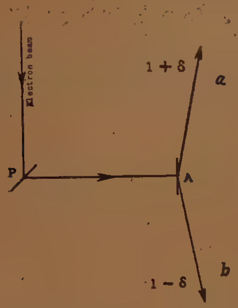

Fig. 2. Directions and intensities of the scattered electrons

$$y=\frac{a}{b}\cdot\frac{1-\delta}{1+\delta}, \qquad (2)$$

From the measurement of x and y, the magnitude of the polarization can be obtained as:

$$2\delta \doteqdot \frac{x-y}{x+y} \qquad (3)$$

since δ is a small quantity.

§ 3. Results.

Table I and Fig. 3 show the values of 200 δ for the electrons of energy 45—92 kev, obtained as described above. The experimental values are shown by $\underline{\overline{\odot}}$ in Fig. 3. The errors shown in Table I and also by vertical lines in Fig. 3 are the probable errors computed from the statistical fluctuations of the counting alone. The curves in Fig. 3 show the result of calculation by Mott,⑴ Massey and Mohr,⁽⁸⁾ and Bartlett and Watson,⁽¹⁰⁾ respectively. It is seen that the experimental result shows the existence of the polarization which is in the right direction, but its magnitude is smaller than that predicted by the theories. It is about half of that predicted by Massey and Mohr. The difference between the theoretical and the experimental values is more than the exprimental error.

Table I. Values of 200 δ.

Energy of electron (kev)	45	60	70	90	92
Experiment	3.6±1.0	4.0±0.9	6.8±0.7	9.0±0.6	9.1±1.0
Theory					
Mott⑴	3.0	6.4	9.0	13.4	13.6
Bartlett and Watson⁽²⁰⁾	8.3	10.1	11.2	12.4	12.5
Massey and Mohr	6.6	10.4	12.5	15.8	16.0

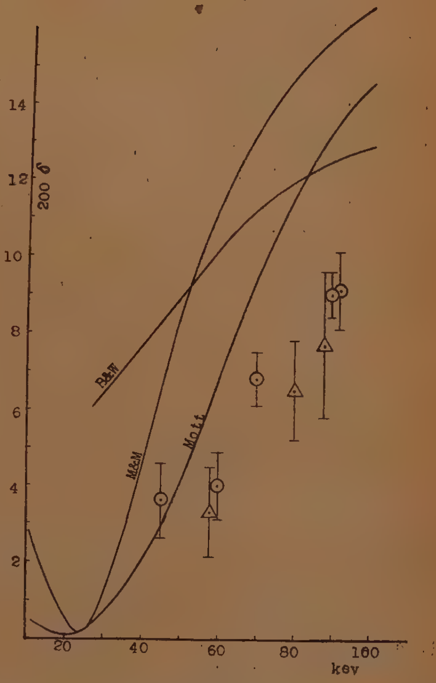

Fig. 3. Values of 200 δ as a function of the energy of electrons. Curves show the results of theoretical calculations.

§ 4. Possible Sources of Error.

Following causes can be considered as the possible sources of errors.

a. Effect of the unsteadiness of the accelerating voltage.

The cross section for the scattering of electrons by a nucleus changes proportinally to E^{-2}, where E is the energy of the electrons. Therefore, the intensity of the beam scattered twice is propotional to E^{-4}, and changes greatly with the accelerating voltage. In the experimental method such as used by Dymond and Thomson, a slight change of the accelerating voltage during a course of the experiment can give rise to a rather large error in the result. In our experiment, it was not possible to keep the accelerating voltage constant to within 1 percent of its value. However, since we used two counters placed at symetrical positions to the analyser foil and counted the scattered electrons simultaneously, no such error could be introduced. This arrangement, moreover, had the advantage of avoiding the ambiguity caused by the so-called reflection-transmission effect(7) of Goertzel and Cox.

b. Multiple Scattering.

The effect of multipe scattering resulting from small angle scatterings in the foil has been examined theoretically by Rose and Bethe.(6) It exerts no appreciable effect when the thickness of the foil is of the order of or less than 5×10^{-5} mm. But Goertzel and Cox(7) have pointed out that there is another kind of multiple scattering, or rather plural scattering, composed of two large angle scatterings which affect the result of polarization experiment in some cases. This kind of plural scatteaing is composed of one scattering of 45° or larger, when the incident beam falls on the foil at an angle of 45°, which brings the scattered electrons to proceed in the plane of the foil, succeeded by another scatteritg of 45° or larger, giving a total deflection of 90°. The electrons suffering such plural scatterings are mixed in large numbers when the foil is placed at a reflection position and were probably mainly responsible for masking the polarization in the experiment of Dymond, Thomson, and Richter. In the present experiment no such scattering occurs at the analyser foil. At the polarizer foil, its influence cannot be excluded but is very small. A rough calculation shows that, for 40 kev electron, 15 percent of the beam scattered at 90° to the transmission side had sufferred such plural scattering and 85 percent, single scattering. If the electrons originating from plural scattering are completely unpolarized, the measured final polarization effect would be reduced by 15 percent. For electrons of high energy, the effect of such plural scattering is smaller.

c. X-rays and Stray Electrons.

It was found that the materials in the neighborhood of S_1 and S_2 become strong sources of X-rays which reach the counters. To stop these X rays, more than 4 cm of lead was placed betwee S_1 and the counters and more than 2 cm of lea between S_2 and the counters. The counters wer further shielded from those X-rays by surroundin them with 4 mm of lead. X-rays originating i the neighbourhood of the analyser foil was prevent ed from entering the counters by placing in fron of each counter, two pieces of lead as shown l Fig. 4. The pieces of lead placed in the scatter ing chamber was always covered with thin alum nium plate to reduce stray electrons. These lea pieces are not shown in Fig. 1.

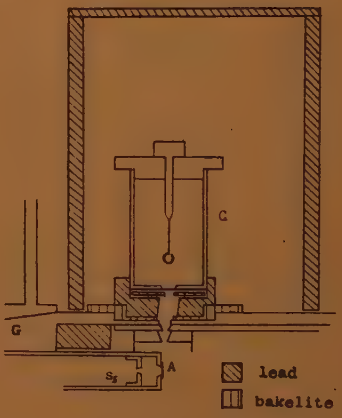

Fig. 4. Diagram of the counter and its lead shield.

In order to get the counts due to X-rays an stray electrons arising from chamber walls et counts were taken either with the polarizer fo or the analyser foil removed. Below 80 kev, th number of counts were is either case equal to th natural count of the counters, showing that n such radiations are entering the counters. Abo that voltage, slight effect of X-rays begun to ap pear, but its count was so few in number, at th energy as high as 92 kev, that no influence is ex pected on the value of the polarization obtaine It was also found that, by taking a count wit two foils in place and with the windows of th counters covered by thin aluminium plates, no ap preciable amounts of X-rays originats in the neigh bourhood of the analyser foil which enter th counters.

d. Faulty Geometry of the Apparatus.

Special care was taken in constructing the apparatus, so that the slits S_4, S_5, and the centre of the analyser foil all lie on the line of the rotation of the ground joint G (Fig. 1) and also that the two counters and slit system belonging to them lie at symmetrical positions of the axis. The height of the polarizer foil, which is the most probable source of error, as is already pointed out by Dymond, were made adjustable. Fig. 5 shows the result of the polarization measurement for 60 kev electrons at various height of the polarizer foil. If the foil is too high, the part of the beam coming from the foil is cut off by the upper edge of S_4 and the rest of it passing through S_4 and S_5 hits the analyser foil at some point lower than the centre. A smaller apparent polarization results. If the foil is too low, a larger polarization results. The number of counts naturally decreases greatly if the foil is too high or too low. The part giving a constant polarization shows the allowable range of the position of the foil. A smaller slit for S_5 gives a more flat curve than a larger one. Therefore the diameter of S_5, which was taken as 1.5 mm at the beginning, was later changed to 0.75 mm. Fig. 5 shows that the allowable range of the position of the foil is about 0.8 mm. This is what to be expected from the geometry of the apparatus when the diameter of S_5 is taken as 0.75 mm. The values of polarization marked with $\overline{\underline{\Delta}}$ in Fig. 3 are obtained when the foil is placed too high by about 0.5 mm corresponding to the position marked with $\overline{\underline{\Delta}}$ in Fig. 5. Slightly smaller polarization is obtained in this case.

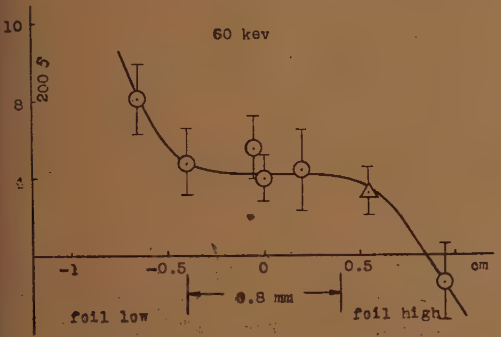

Fig. 5. Height of the polarizer and the value of the measured polarization.

§ 5. Discussion.

Our result shows the existence of the polarization contrary to those of Dymond, Thomson, and Richter. But our result does not contradict with theirs, since the plural scattering would probably have masked the effect, as is already stated above, in all of these experiments. The possible change of the accelerating voltage during the measurement also have probably influenced the experiments of Dymond and Thomson.

The experiment of Kikuchi(11), which claims to have obtained the polarization completely agreeing with the prediction of Mott,(1) uses a thick gold film of thickness 10^{-2} mm as the polarizer. As this films placed at the reflection position, plural scattering would have been even far more abundant, in this case, compared with the experiments of Dymond and others. In does not therefore at all conform to the condition (4) given above.

The experiment of Shull, Chase, and Myers(8) uses the transmission side and obtained, for the 400 kev electrons, a slightely larger polarization than is predicted by the theories. Their results are in accord with ours. But their method of reduction in getting the polarization from the measured quantities are rather complicated and does not seem to be free from introducing some error in their final result. Broer(12) has recently pointed out some inexactness in their results. Trounson and Simposon(13) has made some improvement in their apparatus and obtained 6.8 as the value of 200 δ at the same accelerating voltage, which is about 70 precent of the value given by the theories.

The value of the polarization we have obtained is about half of that predicted by the theory of Massey and Mohr. Part of such disagreement may be explained by the plural scattering at the polarizer foil and by the fact that the scattering angle at the analyser foil was 78° instead of 90°. The first cause, however, can decrease the effect to be measured as the polarization by about 15 percent at the utmost for the 40 kev electrons, and less than that at the higher energies. The effect of the smaller angle of scattering at the analyser is expected to reduce the difference between theories and the experiment but the theoretical prediction is still lacking on this point.

This work has been supported by the Scientific Research Expenditure of the Department of Education.

References.

(1) N. F. Mott: Proc. Roy. Soc., A **124** (1929), 425; A **135** (1932), 429.

(2) E. G. Dymond: Proc. Roy. Soc., A **136** (1932), 638; A **145** (1934), 657.

(3) G. P. Thomson: Phil. Mag., **7** (1934), 1058.

(4) H. Richter: Ann. d. Physik, **28** (1937), 533.

(5) R. A. Smith: Camb. Phil. Soc. Proc., **30** (1934), 520; M. F. Rose: Phys. Rev., **57** (1940), 280.

(6) M. F. Rose and H. A. Bethe: Phys. Rev., **55** (1939), 277.

(7) G. Goertzel and R. T. Cox: Phys. Rev., **63** (1943), 37.

(8) G. G. Shull. C. T. Chase, and F. E. Myers: Phys. Rev., **63** (1943), 29.

(9) H. S. W. Massey and C. B. O. Mohr: Proc. Roy. Soc., A **177** (1941), 341.

(10) J. H. Bartlett and R. E. Watson: Phys. Rev., **56** (1939), 612.

(11) K. Kikuchi: Proc. Phys-Math. Soc. Japan, **22** (1940), 805.

(12) L. J. Broer: Phys. Rev., **74** (1948), 1887

(13) E. Trounson and J. A. Simpson: Phys. Rev., **63** (1943), 55.

On the Energy Levels of the Configurations d^4p, d^5p and d^6p.*

By Takehiko ISHIDZU.

Department of Dynamics, 1st Faculty of Engineering, Tokyo University,

and

Shin-ya OBI,

Astronomy Department, Faculty of Science, Tokyo University.

(Read April 28, 1949; Received Sept. 5, 1949).

Abstract

The electrostatic energy matrices of the configurations d^4p, d^5p and d^6p were calculated by Racah's method of tensor operators. The results for the last configuration were compared with the observed values by J. C. Dobbie for Fe II, $3d^6 4p$.

§1. Calculation of the Matrix Elements.

The electrostatic energy matrices of d^np configuration can easily be calculated in SL scheme by the method of tensor operators which has been established by G. Racah(1). Referring to his original papers** for all notations and definitions, the energy of d^np is given by

$$W(d^np) = W(d^n)+W(d^n,\ p),$$

$$W(d^n,\ p) = nF_0(d,\ p)+f_2F_2(d,\ p)+g_1G_1(d,\ p)+g_3G_3(d,\ p),$$

where f_2, g_1 and g_3 are the matrix elements of the following scalar products of tensor operators

$$f_2 = 10\sqrt{21}\,(\boldsymbol{U}^{(2)}\cdot\boldsymbol{u}_p^{(2)}),$$

$$g_1 = -[n+(9\sqrt{5}/2)(\boldsymbol{U}^{(1)}\cdot\boldsymbol{u}_p^{(1)})+(5\sqrt{21}/2)(\boldsymbol{U}^{(2)}\cdot\boldsymbol{u}_p^{(2}$$
$$+4\,(\boldsymbol{S}\cdot\boldsymbol{s}_p)+18\sqrt{5}\,(\boldsymbol{V}^{(11)}\cdot\boldsymbol{v}_p^{(11)})$$
$$+10\sqrt{21}\,(\boldsymbol{V}^{(12)}\cdot\boldsymbol{v}_p^{(12)})],$$

---

[*] Although this paper is over the usual limitation of 6 pages it is published here, with the special approval of the Editorial Committee. (Editor)

[**] References 1 will be referred to in the following as RI, RII and RIII. Also see Reference 2.

$$\begin{aligned} g_3 = -[&(7n/2)-(21\sqrt{5}/2)(\boldsymbol{U}^{(1)}\cdot\boldsymbol{u}_p^{(1)}) \\ &+(5\sqrt{21}/2)(\boldsymbol{U}^{(2)}\cdot\boldsymbol{u}_p^{(2)})+14(\boldsymbol{S}\cdot\boldsymbol{s}_p) \\ &-42\sqrt{5}(\boldsymbol{V}^{(11)}\cdot\boldsymbol{v}_p^{(11)})+10\sqrt{21}(\boldsymbol{V}^{(12)}\cdot\boldsymbol{v}_p^{(12)})]. \end{aligned}$$

The operator $\boldsymbol{S}$ is the resultant spin vector of the core d^n and $\boldsymbol{s}_p$ the spin vector of the p electron. The other operators are

$$\boldsymbol{U}^{(k)} = \sum \boldsymbol{u}_i^{(k)}, \quad \boldsymbol{V}^{(1k)} = \sum \boldsymbol{s}_i\boldsymbol{u}_i^{(k)}, \quad \boldsymbol{v}_p^{(1k)} = \boldsymbol{s}_p\boldsymbol{u}_p^{(k)},$$

where the summation is extended over the n equivalent electrons and the suffix p refers to the p electron. The operator $\boldsymbol{u}^{(k)}$ is the "unit" tensor operator of the kth degree, defined by

$$(l\,||\,u^{(k)}\,||\,l') = \delta_{ll'}.$$

$\boldsymbol{u}^{(1)}$ is the constant multiple of the angular momentum vector $\boldsymbol{l}$; both are related together as

$$\boldsymbol{l} = \sqrt{l(l+1)(2l+1)}\,\boldsymbol{u}^{(1)}.$$

The matrix of $\boldsymbol{U}^{(1)}$ is therefore diagonal with respect to S, L and the seniority number††† v, and independent of S and v. The elements are given in general by⁽²⁾

$$(l^n vSL\,||\,U^{(1)}\,||\,l^n vSL) = \sqrt{\frac{L(L+1)(2L+1)}{l(l+1)(2l+1)}}.$$

The matrix of S is also diagonal with respect to v, S, L and depends on S, not on n. With the abbreviation:

$$(S\,||\,S\,||\,S) = (l^n vSL\,||\,S\,||\,l^n vSL)$$

one finds

$$\begin{aligned} &(0\,||\,S\,||\,0)=0, && (1/2\,||\,S\,||\,1/2)=\sqrt{6}/2, \\ &(1\,||\,S\,||\,1)=\sqrt{6}, && (3/2\,||\,S\,||\,3/2)=\sqrt{15}, \\ &(2\,||\,S\,||\,2)=\sqrt{30}, && (5/2\,||\,S\,||\,5/2)=\sqrt{210}/2, \end{aligned}$$

etc.

and for the scalar products

$$\begin{aligned} (l^n(v_1S_1L_1)l'SL\,|\,(\boldsymbol{S}\cdot\boldsymbol{s}')\,|\,l^n(v_1S_1L_1)l'SL) &= -(S_1+1)/2 \quad \text{for} \quad S=S_1-1/2, \\ &= S_1/2 \quad \text{for} \quad S=S_1+1/2. \end{aligned}$$

The matrix elements of $\boldsymbol{U}^{(2)}$, $\boldsymbol{V}^{(11)}$ and $\boldsymbol{V}^{(12)}$ were calculated by Racah for all configurations of p^n and d^n and listed in his paper (RII)*. From all these matrix elements the matrices of $W(d^n, p)$ for $n \leqq 2l+1=5$ are obtained straightforward, almost only by evaluation of the values of W-functions defined in RII**. For n values being more than five, i.e. for the so-called "almost closed shell" configurations, the matrix elements of $\boldsymbol{U}^{(k)}$ and $\boldsymbol{V}^{(1k)}$ are connected with those of their "conjugate" configurations by the formula (74) in RII***, which shows that we simply have to change the sign of all the tensor of even degree, i.e. of $\boldsymbol{U}^{(2)}$ and $\boldsymbol{V}^{(11)}$, in order to obtain the energy $W(d^n, p)$ from that of the conjugate configurations.

The internal energy $W(d^n)$ has been already calculated for all n values, but we need its matrix elements in vSL scheme. These elements are obtained with aid of the "coefficients of fractional parentage" $(l^n vSL\{|l^{n-1}(v_1S_1L_1)lSL)$**** successively by the formula

$$\begin{aligned} (l^n vSL\,|\,&W(d^n)\,|\,l^n v'SL) \\ &= (nC_2/{}_{n-1}C_2)\cdot(l^n vSL\,|\,W(d^{n-1})\,|\,l^n v'SL) \\ &= (nC_2/{}_{n-1}C_2)\sum_{v_1S_1L_1}\sum_{v_1'}(l^n vSL\{|l^{n-1}(v_1S_1L_1)lSL) \\ &\quad\times(l^{n-1}v_1S_1L_1\,|\,W(d^{n-1})\,|\,l^{n-1}v_1'S_1L_1) \\ &\quad\times(l^{n-1}(v_1'S_1L_1)lSL|\}l^n v'SL). \end{aligned}$$

The elements for d^4 (or d^6) and d^5 are listed in Table I and II in terms of the parameters:

$$\begin{aligned} &A = nC_2(F_0(d,d)-49F_4(d,d)), \\ &B = F_2(d,d)-5F_4(d,d) \text{ and } C = 35F_4(d,d). \end{aligned}$$

Adding the internal energy to $W(d^n, p)$ we find the total energy $W(d^n p)$.

Racah has calculated by his own method the energy of d^2p and d^8p, and compared the results with the observed values of Ti II and Ni II. Quite similar calculations were carried out by T. Yamanouchi⁽³⁾ with group-theoretical method and for d^3p and d^7p by A. Amemiya⁽⁴⁾ by the same method. Recently F. Rohrlich⁽²⁾ has calculated also for d^3p, d^7p and other configurations by means of Racah's method. In this paper we have calculated the energy matrices of the configurations d^4p, d^5p and and d^6p by Racah's method and compared the energy levels of d^6p with the observed values of J. C. Dobbie⁽⁵⁾ for Fe II, $3d^64p$ (in 1935).

---

††† See Reference 1, III, § 6.

* In his Table XIV (RIII, p. 375) the elements 3^2G-5^2F, and 3^4F-3^4G seem to be misprinted, while those 5^2F-3^2G and 3^4G-3^4F are correct.

** See Reference 1, II, § 3.

*** See Reference 1, II, § 6.

**** See Reference 1, III, § 3.

Table I. The Energy Matrices of d^4 or d^6 in vSL Scheme.

(The prefixes of the term symbol express the seniority number v.)

$$\begin{array}{c|cc} & 0^1S & 4^1S \\ \hline 0^1S & A+14(B+C) & 6\sqrt{21}B \\ 4^1S & & A+6(B+C) \end{array} \qquad \begin{array}{c|cc} & 2^3P & 4^3P \\ \hline 2^3P & A-7B+7C & 4\sqrt{14}B \\ 4^3P & & A-3B+4C \end{array} \qquad \begin{array}{c|cc} & 2^1D & 4^1D \\ \hline 2^1D & A+15B+9C & 12\sqrt{12}B \\ 4^1D & & A+3B+6C \end{array}$$

$$\begin{array}{c|cc} & 2^3F & 4^3F \\ \hline 2^3F & A-2B+7C & 12B \\ 4^3F & & A-8B+4C \end{array} \qquad \begin{array}{c|cc} & 2^1G & 4^1G \\ \hline 2^1G & A-6B+9C & 4\sqrt{11}B \\ 4^1G & & A-4B+6C \end{array}$$

Table II. The Energy Matrices of d^5 in vSL Scheme.

$$\begin{array}{c|cc} & 1^2D & 5^2D \\ \hline 1^2D & A+14C & -6\sqrt{14}B \\ 5^2D & & A-6B+8C \end{array} \qquad \begin{array}{c|c} & 3^2D \\ \hline 3^2D & A-4B+10C \end{array} \qquad \begin{array}{c|c} & 3^2F \\ \hline 3^2F & A-25B+10C \end{array} \qquad \begin{array}{c|c} & 5^2F \\ \hline 5^2F & A-9B+8C \end{array}$$

$$\begin{array}{c|c} & 3^2G \\ \hline 3^2G & A+3B+10C \end{array} \qquad \begin{array}{c|c} & 5^2G \\ \hline 5^2G & A-13B+8C \end{array}$$

Table III. The Matrices of $W(d^4, p)$.

Matrices of f_2 (coefficients of F_2)

$^{2,4}S$

$$\begin{array}{c|cc} & 2^3P & 4^3P \\ \hline 2^3P & -14/3 & 4\sqrt{14}/3 \\ 4^3P & & 38/3 \end{array}$$

$^{2,4}P$

$$\begin{array}{c|ccc} & 2^3P & 4^3P & 4^3D \\ \hline 2^3P & 7/3 & -2\sqrt{14}/3 & 4\sqrt{7} \\ 4^3P & — & 19/3 & 4\sqrt{2} \\ 4^3D & & & 1 \end{array}$$

^{2}P

$$\begin{array}{c|cccc} & 0^1S & 4^1S & 2^1D & 4^1D \\ \hline 0^1S & 0 & 0 & 2\sqrt{42} & 0 \\ 4^1S & & 0 & 6\sqrt{2} & 8 \\ 2^1D & & — & 1 & -6\sqrt{2} \\ 4^1D & & & — & 3 \end{array}$$

^{2}D

$$\begin{array}{c|ccc} & 2^1D & 4^1D & 4^1F \\ \hline 2^1D & 1 & 6\sqrt{2} & 0 \\ 4^1D & & 3 & -8 \\ 4^1F & & & 6 \end{array}$$

$^{4,6}P$

$$\begin{array}{c|c} & 4^5D \\ \hline 4^5D & -7 \end{array}$$

$^{4,6}D$

$$\begin{array}{c|c} & 4^5D \\ \hline 4^5D & 7 \end{array}$$

$^{2,4}D$

$$\begin{array}{c|ccccc} & 2^3P & 4^3P & 4^3D & 2^3F & 4^3F \\ \hline 2^3P & -7/15 & 2\sqrt{14}/15 & -4\sqrt{35}/5 & 4\sqrt{14}/5 & 8\sqrt{14}/5 \\ 4^3P & & 19/15 & -4\sqrt{10}/5 & 44/5 & 16/5 \\ 4^3D & & — & 1 & 8\sqrt{10}/5 & -8\sqrt{10}/5 \\ 2^3F & & & & 4/5 & 28/5 \\ 4^3F & & & & & 22/5 \end{array}$$

^{2}F

$$\begin{array}{c|ccccc} & 2^1D & 4^1D & 4^1F & 2^1G & 4^1G \\ \hline 2^1D & -2/7 & -12\sqrt{2}/7 & 0 & 8\sqrt{3}/7 & 16\sqrt{33}/7 \\ 4^1D & — & 6/7 & 4\sqrt{70}/7 & 20\sqrt{6}/7 & 4\sqrt{66}/7 \\ 4^1F & & — & 15/2 & \sqrt{105} & \sqrt{1155}/14 \\ 2^1G & & & & 55/21 & 5\sqrt{11}/21 \\ 4^1G & & & & — & 125/42 \end{array}$$

$^{2,4}F$

$$\begin{array}{c|cccc} & 4^3D & 2^3F & 4^3F & 4^3G \\ \hline 4^3D & 2/7 & -8\sqrt{7}/7 & 8\sqrt{7}/7 & 24\sqrt{5}/7 \\ 2^3F & — & 1 & -7 & 9\sqrt{35}/7 \\ 4^3F & & — & 11/2 & 3\sqrt{35}/14 \\ 4^3G & & & — & 11/14 \end{array}$$

$^{4,6}F$

$$\begin{array}{c|c} & 4^5D \\ \hline 4^5D & -2 \end{array}$$

^{2}I

$$\begin{array}{c|c} & 4^1I \\ \hline 4^1I & -5 \end{array}$$

$^{2,4}I$

$$\begin{array}{c|c} & 4^3H \\ \hline 4^3H & 1 \end{array}$$

^{2}K

$$\begin{array}{c|c} & 4^1I \\ \hline 4^1I & 2 \end{array}$$

^2G

$$\begin{array}{c|ccc} & 4^1F & 2^1G & 4^1G \\ \hline 4^1F & 5/2 & -7 & -\sqrt{11}/2 \\ 2^1G & & -11/3 & -\sqrt{11}/3 \\ 4^1G & & & 25/6 \end{array}$$

$^{2,4}G$

$$\begin{array}{c|cccc} & 2^3F & 4^3F & 4^3G & 4^3H \\ \hline 2^3F & 1/3 & 7/3 & -3\sqrt{3} & 4\sqrt{22}/3 \\ 4^3F & & 11/6 & -\sqrt{3}/2 & 4\sqrt{22}/3 \\ 4^3G & & & 11/10 & 4\sqrt{66}/5 \\ 4^3H & & & & 26/15 \end{array}$$

^2H

$$\begin{array}{c|ccc} & 2^1G & 4^1G & 4^1I \\ \hline 2^1G & 4/3 & 4\sqrt{11}/33 & -4\sqrt{429}/11 \\ 4^1G & & -50/33 & -16\sqrt{39}/11 \\ 4^1I & & & 35/11 \end{array}$$

$^{2,4}H$

$$\begin{array}{c|cc} & 4^3G & 4^3H \\ \hline 4^3G & -2/5 & -24/5 \\ 4^3H & & -13/5 \end{array}$$

Matrices of g_1 (coefficients of G_1)

^2S

$$\begin{array}{c|cc} & 2^3P & 4^3P \\ \hline 2^3P & -16/3 & 5\sqrt{14}/3 \\ 4^3P & & -5/3 \end{array}$$

^4S

$$\begin{array}{c|cc} & 2^3P & 4^3P \\ \hline 2^3P & 2/3 & -4\sqrt{14}/3 \\ 4^3P & & -23/3 \end{array}$$

^2P

$$\begin{array}{c|ccccccc} & 0^1S & 4^1S & 2^3P & 4^3P & 2^1D & 4^1D & 4^3D \\ \hline 0^1S & -4 & 0 & -9\sqrt{2}/2 & 0 & -\sqrt{42}/2 & 0 & 0 \\ 4^1S & & -4 & \sqrt{42}/2 & -2\sqrt{3} & -3\sqrt{2}/2 & -2 & -2\sqrt{6} \\ 2^3P & & & 19/6 & 7\sqrt{14}/6 & \sqrt{21}/2 & \sqrt{42}/2 & -\sqrt{7} \\ 4^3P & & & & 1/3 & \sqrt{6}/2 & 4\sqrt{3} & 2\sqrt{2} \\ 2^1D & & & & & -3/2 & 3\sqrt{2}/2 & 3\sqrt{3} \\ 4^1D & & & & & & -1 & -\sqrt{6} \\ 4^3D & & & & & & & 2 \end{array}$$

^4P

$$\begin{array}{c|cccc} & 2^3P & 4^3P & 4^3D & 4^5D \\ \hline 2^3P & -22/3 & -\sqrt{14}/3 & -\sqrt{7} & \sqrt{15} \\ 4^3P & & -8/3 & -5\sqrt{2}/2 & -\sqrt{210}/2 \\ 4^3D & & & -4 & 0 \\ 4^5D & & & & 0 \end{array}$$

^6P

$$\begin{array}{c|c} & 4^5D \\ \hline 4^5D & 0 \end{array}$$

^2D

$$\begin{array}{c|cccccccc} & 2^3P & 4^3P & 2^1D & 4^1D & 4^3D & 4^1F & 2^3F & 4^3F \\ \hline 2^3P & -5/6 & -31\sqrt{14}/30 & -3\sqrt{105}/10 & 3\sqrt{210}/10 & \sqrt{35}/5 & 0 & \sqrt{14} & -2\sqrt{14}/5 \\ 4^3P & & 2/15 & 3\sqrt{30}/10 & -3\sqrt{15}/5 & 7\sqrt{10}/5 & -6\sqrt{15}/5 & -11/5 & 8/5 \\ 2^1D & & & -7/2 & -3\sqrt{2}/2 & \sqrt{3} & 0 & 3\sqrt{30}/5 & -2\sqrt{30}/5 \\ 4^1D & & & & -4 & 0 & 2 & -\sqrt{15}/5 & 4\sqrt{15}/5 \\ 4^3D & & & & & 2 & 0 & 3\sqrt{10}/5 & -6\sqrt{10}/5 \\ 4^1F & & & & & & -5/2 & \sqrt{15} & 11\sqrt{15}/10 \\ 2^3F & & & & & & & 2 & 3/5 \\ 4^3F & & & & & & & & 17/10 \end{array}$$

^4D

$$\begin{array}{c|cccccc} & 2^3P & 4^3P & 4^3D & 4^5D & 2^3F & 4^3F \\ \hline 2^3P & -98/15 & 7\sqrt{14}/15 & \sqrt{35}/5 & 3\sqrt{3} & -4\sqrt{14}/5 & -2\sqrt{14}/5 \\ 4^3P & & -23/3 & -2\sqrt{10}/5 & 0 & -11/5 & -2 \\ 4^3D & & & -11/2 & \sqrt{105}/2 & -9\sqrt{10}/10 & 6\sqrt{10}/5 \\ 4^5D & & & & 5/2 & -\sqrt{42}/2 & 0 \\ 2^3F & & & & & -14/5 & -12/5 \\ 4^3F & & & & & & -4 \end{array}$$

^6D

$$\begin{array}{c|c} & 4^5D \\ \hline 4^5D & -10 \end{array}$$

^2F

	2^1D	4^1D	4^3D	4^1F	2^3F	4^3F	2^1G	4^1G	4^3G
2^1D	$-38/7$	$3\sqrt{2}/7$	$-2\sqrt{3}$	0	$-6\sqrt{21}/7$	$-4\sqrt{21}/7$	$-2\sqrt{3}/7$	$-4\sqrt{33}/7$	0
4^1D		$-37/7$	$3\sqrt{6}/7$	$-\sqrt{70}/7$	$-\sqrt{42}/7$	$4\sqrt{42}/7$	$-5\sqrt{6}/7$	$-\sqrt{66}/7$	$-6\sqrt{30}/7$
4^3D			$-16/7$	$-3\sqrt{105}/7$	$12\sqrt{7}/7$	$9\sqrt{7}/7$	0	$9\sqrt{11}/7$	$-3\sqrt{5}/7$
4^1F				$-11/8$	$\sqrt{15}/4$	$-5\sqrt{15}/8$	$-\sqrt{105}/4$	$-\sqrt{1155}/56$	$51\sqrt{21}/56$
2^3F					-1	$9/4$	$9\sqrt{7}/7$	$9\sqrt{77}/28$	$9\sqrt{35}/28$
4^3F						$31/8$	$45\sqrt{7}/28$	$-9\sqrt{77}/56$	$3\sqrt{35}/56$
2^1G							$-19/21$	$-5\sqrt{11}/84$	$3\sqrt{5}/4$
4^1G								$83/168$	$3\sqrt{55}/56$
4^3G									$51/56$

^4F

	4^3D	4^5D	2^3F	4^3F	4^3G
4^3D	$-101/14$	$-5\sqrt{105}/14$	$-3\sqrt{7}/7$	$-15\sqrt{7}/14$	$-15\sqrt{5}/14$
4^5D		$5/2$	$-\sqrt{15}$	$3\sqrt{15}/2$	$15\sqrt{21}/14$
2^3F			-4	$3/2$	$-9\sqrt{35}/14$
4^3F				$-19/4$	$-3\sqrt{35}/28$
4^3G					$-15/28$

^6F

	4^5D
4^5D	-10

^2G

	4^1F	2^3F	4^3F	2^1G	4^1G	4^3G	4^3H
4^1F	$-55/8$	$-3\sqrt{15}/4$	$-\sqrt{15}/8$	$7/4$	$\sqrt{11}/8$	$21\sqrt{5}/40$	$\sqrt{330}/5$
2^3F		$-1/3$	$-25/12$	$-\sqrt{15}$	$\sqrt{165}/4$	$13\sqrt{3}/4$	$-\sqrt{22}/3$
4^3F			$-95/24$	$5\sqrt{15}/4$	$-\sqrt{165}/8$	$-17\sqrt{3}/8$	$2\sqrt{22}/3$
2^1G				$-7/3$	$\sqrt{11}/12$	$3\sqrt{5}/20$	$\sqrt{330}/5$
4^1G					$-103/24$	$21\sqrt{55}/40$	$\sqrt{30}/5$
4^3G						$9/8$	0
4^3H							$-1/3$

^4G

	2^3F	4^3F	4^3G	4^3H
2^3F	$-28/3$	$1/6$	$-\sqrt{3}/2$	$-\sqrt{22}/3$
4^3F		$-97/12$	$5\sqrt{3}/4$	$-5\sqrt{22}/6$
4^3G			$-117/20$	$-3\sqrt{66}/10$
4^3H				$4/15$

^2H

	2^1G	4^1G	4^3G	4^3H	4^1I
2^1G	$-22/3$	$-\sqrt{11}/33$	$-3\sqrt{5}/5$	$9\sqrt{5}/5$	$\sqrt{429}/11$
4^1G		$-437/66$	$-51\sqrt{55}/110$	$-36\sqrt{55}/55$	$4\sqrt{39}/11$
4^3G			$-3/2$	6	$-6\sqrt{2145}/55$
4^3H				5	$-2\sqrt{2145}/55$
4^1I					$5/11$

^4H

	4^3G	4^3H
4^3G	$-48/5$	$-6/5$
4^3H		$-32/5$

^2I

	4^3H	4^1I
4^3H	-4	$-\sqrt{21}$
4^1I		-2

^4I

	4^3H
4^3H	-10

^2K

	4^1I
4^1I	-9

Matrices of g_3 (coefficients of G_3)

^2S

	2^3P	4^3P
2^3P	-7	$-5\sqrt{14}$
4^3P		0

^4S

	2^3P	4^3P
2^3P	-21	$2\sqrt{14}$
4^3P		-31

^2P

	0^1S	4^1S	2^3P	4^3P	2^1D	4^1D	4^3D
0^1S	-14	0	$21\sqrt{2}/2$	0	$-\sqrt{42}/2$	0	0
4^1S		-14	$-7\sqrt{42}/6$	$14\sqrt{3}/3$	$-3\sqrt{2}/2$	-2	$-2\sqrt{6}$
2^3P			$7/3$	$-13\sqrt{14}/6$	$4\sqrt{21}/3$	$-7\sqrt{42}/6$	$-\sqrt{7}$
4^3P				$7/6$	$-7\sqrt{6}/6$	$19\sqrt{3}/6$	$-11\sqrt{2}/2$
2^1D					-19	$3\sqrt{2}/2$	$-7\sqrt{3}$
4^1D						$-37/2$	$3\sqrt{6}/2$
4^3D							-8

^4P

	2^3P	4^3P	4^3D	4^5D
2^3P	$-77/3$	$4\sqrt{14}/3$	$-\sqrt{7}$	$-7\sqrt{15}/3$
4^3P		$-131/6$	$5\sqrt{2}/4$	$-\sqrt{210}/12$
4^3D			$-101/4$	$-5\sqrt{105}/4$
4^5D				$35/4$

^6P

	4^5D
4^5D	-35

^2D

	2^3P	4^3P	2^1D	4^1D	4^3D	4^1F	2^3F	4^3F
2^3P	0	$23\sqrt{14}/10$	$\sqrt{105}/5$	$-7\sqrt{210}/10$	$\sqrt{35}/5$	0	$\sqrt{14}$	$-2\sqrt{14}/5$
4^3P		$-7/10$	$-7\sqrt{30}/10$	$-11\sqrt{15}/10$	$-31\sqrt{10}/10$	$-6\sqrt{15}/5$	$-11/5$	$8/5$
2^1D			-16	$-3\sqrt{2}/2$	$-7\sqrt{3}/3$	0	$19\sqrt{30}/15$	$14\sqrt{30}/15$
4^1D				$-33/2$	$5\sqrt{6}/6$	2	$7\sqrt{15}/15$	$-28\sqrt{15}/15$
4^3D					$-4/3$	$10\sqrt{6}/3$	$-41\sqrt{10}/15$	$-28\sqrt{10}/15$
4^1F						$-45/2$	$-7\sqrt{15}/3$	$-17\sqrt{15}/30$
2^3F							$-4/3$	$-91/15$
4^3F								$-349/30$

^4D

	2^3P	4^3P	4^3D	4^5D	2^3F	4^3F
2^3P	$-91/5$	$-6\sqrt{14}/5$	$\sqrt{35}/5$	$-7\sqrt{3}$	$-4\sqrt{14}/5$	$-2\sqrt{14}/5$
4^3P		$-37/2$	$37\sqrt{10}/20$	$5\sqrt{42}/4$	$-11/5$	-2
4^3D			$-271/12$	$\sqrt{105}/12$	$23\sqrt{10}/30$	$23\sqrt{10}/15$
4^5D				$35/4$	$7\sqrt{42}/6$	$-5\sqrt{42}/3$
2^3F					$-467/15$	$14/15$
4^3F						$-82/3$

^6D

	4^5D
4^5D	-35

^2F

	2^1D	4^1D	4^3D	4^1F	2^3F	4^3F	2^1G	4^1G	4^3G
2^1D	$-73/7$	$3\sqrt{2}/7$	$14\sqrt{3}/3$	0	$2\sqrt{21}/21$	$4\sqrt{21}/3$	$-2\sqrt{3}/7$	$-4\sqrt{33}/7$	0
4^1D		$-72/7$	$-26\sqrt{6}/21$	$-\sqrt{70}/7$	$\sqrt{42}/3$	$-4\sqrt{42}/3$	$-5\sqrt{6}/7$	$-\sqrt{66}/7$	$-6\sqrt{30}/7$
4^3D			$92/21$	$11\sqrt{105}/21$	$-64\sqrt{7}/21$	$\sqrt{7}/3$	0	$9\sqrt{11}/7$	$-3\sqrt{5}/7$
4^1F				$-111/8$	$-7\sqrt{15}/12$	$-25\sqrt{15}/24$	$-\sqrt{105}/4$	$-\sqrt{1155}/56$	$-39\sqrt{21}/56$
2^3F					$-11/6$	$7/12$	$33\sqrt{7}/14$	$-3\sqrt{77}/4$	$-51\sqrt{35}/28$
4^3F						$13/24$	$-15\sqrt{7}/4$	$3\sqrt{77}/8$	$9\sqrt{35}/8$
2^1G							$-983/42$	$-5\sqrt{11}/84$	$-7\sqrt{5}/4$
4^1G								$-3697/168$	$-67\sqrt{55}/56$
4^3G									$-229/56$

^4F

$$\begin{array}{c|ccccc} & 4^3D & 4^5D & 2^3F & 4^3F & 4^3G \\ \hline 4^3D & -379/21 & 10\sqrt{105}/21 & 41\sqrt{7}/21 & -25\sqrt{7}/42 & -15\sqrt{5}/14 \\ 4^5D & & 5 & 7\sqrt{15}/3 & -11\sqrt{15}/6 & 15\sqrt{21}/14 \\ 2^3F & & & -67/3 & 7/3 & 3\sqrt{35}/7 \\ 4^3F & & & & -131/6 & -9\sqrt{35}/14 \\ 4^3G & & & & & -445/14 \end{array}$$

^6F

$$\begin{array}{c|c} & 4^5D \\ \hline 4^5D & -20 \end{array}$$

^2G

$$\begin{array}{c|ccccccc} & 4^1F & 2^3F & 4^3F & 2^1G & 4^1G & 4^3G & 4^3H \\ \hline 4^1F & -75/8 & 7\sqrt{15}/4 & 9\sqrt{15}/8 & 7/4 & \sqrt{11}/8 & -129\sqrt{5}/40 & \sqrt{330}/5 \\ 2^3F & & 13/6 & 35/12 & -\sqrt{15}/6 & -7\sqrt{165}/12 & -61\sqrt{3}/12 & -\sqrt{22}/3 \\ 4^3F & & & 145/24 & -35\sqrt{15}/12 & 7\sqrt{165}/24 & 49\sqrt{3}/24 & 2\sqrt{22}/3 \\ 2^1G & & & & -89/6 & \sqrt{11}/12 & -7\sqrt{5}/20 & -7\sqrt{330}/15 \\ 4^1G & & & & & -403/24 & 11\sqrt{55}/40 & 23\sqrt{30}/15 \\ 4^3G & & & & & & 1/8 & -4\sqrt{66}/3 \\ 4^3H & & & & & & & -28/3 \end{array}$$

^4G

$$\begin{array}{c|cccc} & 2^3F & 4^3F & 4^3G & 4^3H \\ \hline 2^3F & -43/3 & -7/3 & 11\sqrt{3}/3 & -\sqrt{22}/3 \\ 4^3F & & -101/6 & -5\sqrt{3}/6 & -5\sqrt{22}/6 \\ 4^3G & & & -241/10 & 11\sqrt{66}/30 \\ 4^3H & & & & -491/15 \end{array}$$

^4H

$$\begin{array}{c|cc} & 4^3G & 4^3H \\ \hline 4^3G & -58/5 & 24/5 \\ 4^3H & & -122/5 \end{array}$$

^2H

$$\begin{array}{c|ccccc} & 2^1G & 4^1G & 4^3G & 4^3H & 4^1I \\ \hline 2^1G & -22/3 & -\sqrt{11}/33 & 7\sqrt{5}/5 & -21\sqrt{5}/5 & \sqrt{429}/11 \\ 4^1G & & -437/66 & 59\sqrt{55}/110 & 24\sqrt{55}/55 & 4\sqrt{39}/11 \\ 4^3G & & & 5/2 & -6 & -6\sqrt{2145}/55 \\ 4^3H & & & & 7/2 & 21\sqrt{2145}/110 \\ 4^1I & & & & & -595/22 \end{array}$$

^2I

$$\begin{array}{c|cc} & 4^3H & 4^1I \\ \hline 4^3H & 7/2 & 3\sqrt{21}/2 \\ 4^1I & & -29/2 \end{array}$$

^4I

$$\begin{array}{c|c} & 4^3H \\ \hline 4^3H & -10 \end{array}$$

^2K

$$\begin{array}{c|c} & 4^1I \\ \hline 4^1I & -4 \end{array}$$

Table IV. The Matrices of $W(d^5, p)$.

Matrices of f_2 (coefficients of F_2)

$^{1,3}S$

$$\begin{array}{c|c} & 3^2P \\ \hline 3^2P & 0 \end{array}$$

$^{3,5}S$

$$\begin{array}{c|c} & 3^4P \\ \hline 3^4P & 0 \end{array}$$

$^{1,3}P$

$$\begin{array}{c|ccccc} & 5^2S & 3^2P & 1^2D & 3^2D & 5^2D \\ \hline 5^2S & 0 & 0 & 0 & 8\sqrt{2} & 0 \\ 3^2P & & 0 & 3\sqrt{14} & 0 & -15 \\ 1^2D & & & 0 & 3\sqrt{7} & 0 \\ 3^2D & & & & 0 & \sqrt{2} \\ 5^2D & & & & & 0 \end{array}$$

$^{3,5}P$

$$\begin{array}{c|cc} & 3^4P & 5^4D \\ \hline 3^4P & 0 & -3\sqrt{7} \\ 5^4D & & 0 \end{array}$$

$^{5,7}P$

$$\begin{array}{c|c} & 5^6S \\ \hline 5^6S & 0 \end{array}$$

$^{1,3}D$

$$\begin{array}{c|cccccc}
 & 3^2P & 1^2D & 3^2D & 5^2D & 3^2F & 5^2F \\
\hline
3^2P & 0 & -3\sqrt{70}/5 & 0 & 3\sqrt{5} & 0 & 24\sqrt{5}/5 \\
1^2D & & 0 & -3\sqrt{7} & 0 & 4\sqrt{70}/5 & 0 \\
3^2D & & & 0 & -\sqrt{2} & 0 & -4\sqrt{2} \\
5^2D & & & & 0 & 0 & 0 \\
3^2F & & & & & 0 & -12\sqrt{5}/5 \\
5^2F & & & & & & 0
\end{array}$$

$^{3,5}D$

$$\begin{array}{c|ccc}
 & 3^4P & 5^4D & 3^4F \\
\hline
3^4P & 0 & 3\sqrt{35}/5 & 0 \\
5^4D & & 0 & -16\sqrt{10}/5 \\
3^4F & & & 0
\end{array}$$

$^{1,3}F$

$$\begin{array}{c|ccccccc}
 & 1^2D & 3^2D & 5^2D & 3^2F & 5^2F & 3^2G & 5^2G \\
\hline
1^2D & 0 & 6\sqrt{7}/7 & 0 & -4 & 0 & -12\sqrt{35}/7 & 0 \\
3^2D & & 0 & 2\sqrt{2}/7 & 0 & 4\sqrt{35}/7 & 0 & -12\sqrt{33}/7 \\
5^2D & & & 0 & 0 & 0 & 24\sqrt{10}/7 & 0 \\
3^2F & & & & 0 & 3\sqrt{5} & 0 & 0 \\
5^2F & & & & & 0 & -12\sqrt{7}/7 & 0 \\
3^2G & & & & & & 0 & 3\sqrt{165}/7 \\
5^2G & & & & & & & 0
\end{array}$$

$^{3,5}F$

$$\begin{array}{c|ccc}
 & 5^4D & 3^4F & 5^4G \\
\hline
5^4D & 0 & 16\sqrt{7}/7 & 0 \\
3^4F & & 0 & -15\sqrt{21}/7 \\
5^4G & & & 0
\end{array}$$

$^{1,3}G$

$$\begin{array}{c|ccccc}
 & 3^2F & 5^2F & 3^2G & 5^2G & 3^2H \\
\hline
3^2F & 0 & -\sqrt{5} & 0 & 0 & 0 \\
5^2F & & 0 & 4\sqrt{15}/5 & 0 & -4\sqrt{110}/5 \\
3^2G & & & 0 & -3\sqrt{165}/5 & 0 \\
5^2G & & & & 0 & -12\sqrt{10}/5 \\
3^2H & & & & & 0
\end{array}$$

$^{3,5}G$

$$\begin{array}{c|cc}
 & 3^4F & 5^4G \\
\hline
3^4F & 0 & 3\sqrt{5} \\
5^4G & & 0
\end{array}$$

$^{3,5}H$

$$\begin{array}{c|c}
 & 5^4G \\
\hline
5^4G & 0
\end{array}$$

$^{1,3}H$

$$\begin{array}{c|cccc}
 & 3^2G & 5^2G & 3^2H & 5^2I \\
\hline
3^2G & 0 & 12\sqrt{165}/55 & 0 & 24\sqrt{715}/55 \\
5^2G & & 0 & 24\sqrt{165}/55 & 0 \\
3^2H & & & 0 & -7\sqrt{715}/55 \\
5^2I & & & & 0
\end{array}$$

$^{1,3}K$

$$\begin{array}{c|c}
 & 5^2I \\
\hline
5^2I & 0
\end{array}$$

$^{1,3}I$

$$\begin{array}{c|cc}
 & 3^2H & 5^2I \\
\hline
3^2H & 0 & \sqrt{7} \\
5^2I & & 0
\end{array}$$

Matrices of g_1 (coefficients of G_1)

^1S

$$\begin{array}{c|c}
 & 3^2P \\
\hline
3^2P & -10
\end{array}$$

^3S

$$\begin{array}{c|cc}
 & 3^2P & 3^4P \\
\hline
3^2P & -4/3 & 2\sqrt{14}/3 \\
3^4P & & 22/3
\end{array}$$

^5S

$$\begin{array}{c|c}
 & 3^4P \\
\hline
3^4P & -10
\end{array}$$

^1P

$$\begin{array}{c|ccccc}
 & 5^2S & 3^2P & 1^2D & 3^2D & 5^2D \\
\hline
5^2S & -2 & -6 & 0 & -2\sqrt{2} & -6 \\
3^2P & & 7/2 & -3\sqrt{14}/2 & -3\sqrt{2} & 9/2 \\
1^2D & & & 11/2 & 3\sqrt{7}/2 & 0 \\
3^2D & & & & -1/2 & -5\sqrt{2}/2 \\
5^2D & & & & & 5/2
\end{array}$$

^7P

$$\begin{array}{c|c}
 & 5^6S \\
\hline
5^6S & -10
\end{array}$$

^3P

	5^2S	3^2P	3^4P	1^2D	3^2D	5^2D	5^4D
5^2S	-6	2	$-\sqrt{14}$	0	$-2\sqrt{2}$	2	$3\sqrt{2}$
3^2P		$-41/6$	$-\sqrt{14}/3$	$-\sqrt{14}/2$	$\sqrt{2}$	$7/2$	$-\sqrt{2}$
3^4P			$-13/6$	-4	$2\sqrt{7}$	$-\sqrt{14}$	$-\sqrt{7}/2$
1^2D				$-11/2$	$-3\sqrt{7}/2$	0	0
3^2D					$-7/2$	$\sqrt{2}/2$	-6
5^2D						$-9/2$	$-3\sqrt{2}$
5^4D							$7/2$

^6P

	5^6S	3^4P	5^4D
5^6S	2	$3\sqrt{6}$	$\sqrt{42}$
3^4P		$-11/2$	$3\sqrt{7}/2$
5^4D			$-13/2$

^5D

	3^4P	5^4D	3^4F
3^4P	$-91/10$	$3\sqrt{35}/10$	$3\sqrt{14}/5$
5^4D		$-13/2$	$7\sqrt{10}/5$
3^4F			$-22/5$

^1D

	3^2P	1^2D	3^2D	5^2D	3^2F	5^2F
3^2P	$-37/10$	$-3\sqrt{70}/10$	$3\sqrt{10}/5$	$-3\sqrt{5}/10$	$-12/5$	$-6\sqrt{5}/5$
1^2D		$-13/2$	$3\sqrt{7}/2$	0	$2\sqrt{70}/5$	0
3^2D			$-1/2$	$-\sqrt{2}/2$	$6\sqrt{10}/5$	$-2\sqrt{2}$
5^2D				$-7/2$	$12\sqrt{5}/5$	6
3^2F					$-23/10$	$21\sqrt{5}/10$
5^2F						$-7/2$

^3D

	3^2P	3^4P	1^2D	3^2D	5^2D	5^4D	3^2F	5^2F	3^4F
3^2P	$-193/30$	$\sqrt{14}/15$	$3\sqrt{70}/10$	$-\sqrt{10}/5$	$-9\sqrt{5}/10$	$-3\sqrt{10}/5$	$4/5$	$-6\sqrt{5}/5$	$22/5$
3^4P		$-1/6$	$-12\sqrt{5}/5$	$-2\sqrt{35}/5$	$-3\sqrt{70}/5$	$-9\sqrt{35}/10$	$4\sqrt{14}/5$	0	$-\sqrt{14}$
1^2D			$-7/2$	$\sqrt{7}/2$	0	0	$-2\sqrt{70}/5$	0	$2\sqrt{70}/5$
3^2D				$-11/2$	$\sqrt{2}/2$	-2	$-2\sqrt{10}/5$	$2\sqrt{2}$	$4\sqrt{10}/5$
5^2D					$-9/2$	$3\sqrt{2}$	$-4\sqrt{5}/5$	-2	$2\sqrt{5}/5$
5^4D						$-1/2$	$4\sqrt{10}/5$	0	$-\sqrt{10}/5$
3^2F							$-19/10$	$\sqrt{5}/10$	$14/5$
5^2F								$-3/2$	$-2\sqrt{5}$
3^4F									2

^1F

	1^2D	3^2D	5^2D	3^2F	5^2F	3^2G	5^2G
1^2D	-2	$-12\sqrt{7}/7$	0	7	0	$3\sqrt{35}/7$	0
3^2D		$-26/7$	$10\sqrt{2}/7$	$-6\sqrt{7}/7$	$-\sqrt{35}$	$-18\sqrt{5}/7$	$3\sqrt{33}/7$
5^2D			$-20/7$	$12\sqrt{14}/7$	$-3\sqrt{70}/7$	$-6\sqrt{10}/7$	$-3\sqrt{66}/7$
3^2F				$23/8$	$-3\sqrt{5}/8$	$-9\sqrt{35}/56$	$-9\sqrt{231}/56$
5^2F					$35/8$	$15\sqrt{7}/8$	$-3\sqrt{1155}/56$
3^2G						$131/56$	$15\sqrt{165}/56$
5^2G							$223/56$

^6F

	5^4D	3^4F	5^4G
5^4D	$-68/7$	$2\sqrt{7}/7$	$6\sqrt{3}/7$
3^4F		-8	$6\sqrt{21}/7$
5^4G			$-16/7$

^3F

	1^2D	3^2D	5^2D	5^4D	3^2F	5^2F	3^4F	3^2G	5^2G	5^4G
1^2D	-8	$2\sqrt{7}/7$	0	0	-1	0	4	$3\sqrt{35}/7$	0	0
3^2D		$-52/7$	$-4\sqrt{2}/7$	4	$2\sqrt{7}/7$	$\sqrt{35}/7$	$-4\sqrt{7}/7$	$6\sqrt{5}/7$	$3\sqrt{33}/7$	0
5^2D			$-54/7$	$-6\sqrt{2}/7$	$-4\sqrt{14}/7$	$\sqrt{70}/7$	$2\sqrt{14}/7$	$-6\sqrt{10}/7$	$\sqrt{66}/7$	$10\sqrt{6}/7$
5^4D				$-8/7$	$8\sqrt{7}/7$	0	$-2\sqrt{7}$	0	$8\sqrt{33}/7$	$-10\sqrt{3}/7$
3^2F					$-53/8$	$-7\sqrt{5}/8$	$-7/2$	$3\sqrt{35}/56$	$3\sqrt{231}/56$	$-15\sqrt{21}/14$
5^2F						$-57/8$	$-\sqrt{5}/2$	$-3\sqrt{7}/56$	$\sqrt{1155}/56$	$\sqrt{105}/2$
3^4F							2	$9\sqrt{35}/14$	$-3\sqrt{231}/14$	0
3^2G								$-137/56$	$-13\sqrt{165}/56$	$-\sqrt{15}/2$
5^2G									$-503/168$	$5\sqrt{11}/42$
5^4G										$10/21$

^1G

	3^2F	5^2F	3^2G	5^2G	3^2H
3^2F	$-45/8$	$-7\sqrt{5}/8$	$3\sqrt{3}/8$	$-3\sqrt{55}/8$	$-\sqrt{22}$
5^2F		$-49/8$	$37\sqrt{15}/40$	$3\sqrt{11}/8$	$\sqrt{110}/5$
3^2G			$-83/40$	$9\sqrt{165}/40$	$-3\sqrt{66}/5$
5^2G				$-35/8$	$-3\sqrt{10}/5$
3^2H					$6/5$

^5G

	3^4F	5^4G
3^4F	-10	0
5^4G		-10

^3G

	3^2F	5^2F	3^4F	3^2G	5^2G	5^4G	3^2H
3^2F	$-187/24$	$5\sqrt{5}/8$	$7/6$	$-\sqrt{3}/8$	$\sqrt{55}/8$	$-5\sqrt{5}/2$	$\sqrt{22}/3$
5^2F		$-61/8$	$3\sqrt{5}/2$	$-23\sqrt{15}/40$	$-\sqrt{11}/8$	$-7/2$	$\sqrt{110}/5$
3^4F			$-8/3$	$-3\sqrt{3}/2$	$-\sqrt{55}/2$	$-2\sqrt{5}$	$2\sqrt{22}/3$
3^2G				$-199/40$	$\sqrt{165}/8$	$-\sqrt{15}/10$	$\sqrt{66}/5$
5^2G					$-101/24$	$-\sqrt{11}/6$	$\sqrt{10}$
5^4G						$16/3$	$-2\sqrt{110}/5$
3^2H							$-16/15$

^1H

	3^2G	5^2G	3^2H	5^2I
3^2G	$-47/10$	$-39\sqrt{165}/110$	$18/5$	$-6\sqrt{715}/55$
5^2G		$-85/22$	$-24\sqrt{165}/55$	$12\sqrt{39}/11$
3^2H			$7/10$	$-19\sqrt{715}/110$
5^2I				$19/22$

^5H

	5^4G
5^4G	-10

^3H

	3^2G	5^2G	5^4G	3^2H	5^2I
3^2G	$-91/10$	$\sqrt{165}/22$	$2\sqrt{15}/5$	$-6/5$	$-6\sqrt{715}/55$
5^2G		$-619/66$	$2\sqrt{11}/33$	0	$-4\sqrt{39}/11$
5^4G			$-14/3$	$-6\sqrt{15}/5$	$-2\sqrt{429}/11$
3^2H				$-59/10$	$\sqrt{715}/10$
5^2I					$1/22$

^1I

	3^2H	5^2I
3^2H	$-13/2$	$-5\sqrt{7}/2$
5^2I		$5/2$

^3I

	3^2H	5^2I
3^2H	$-19/2$	$\sqrt{7}/2$
5^2I		$-13/2$

^1K

	5^2I
5^2I	-8

^3K

	5^2I
5^2I	-10

Matrices of g_3 (coefficients of G_3)

^1S

$$\begin{array}{c|c|}
 & 3^2P \\
3^2P & -20
\end{array}$$

^3S

$$\begin{array}{c|cc|}
 & 3^2P & 3^4P \\
3^2P & -64/3 & 2\sqrt{14}/3 \\
3^4P & & 7/3
\end{array}$$

^5S

$$\begin{array}{c|c|}
 & 3^4P \\
3^4P & -35
\end{array}$$

^1P

$$\begin{array}{c|ccccc|}
 & 5^2S & 3^2P & 1^2D & 3^2D & 5^2D \\
5^2S & -7 & 14 & 0 & -2\sqrt{2} & -6 \\
3^2P & & -4 & \sqrt{14} & -3\sqrt{2} & 2 \\
1^2D & & & -7 & -6\sqrt{7} & 0 \\
3^2D & & & & -13 & 5\sqrt{2} \\
5^2D & & & & & -10
\end{array}$$

^7P

$$\begin{array}{c|c|}
 & 5^6S \\
5^6S & -35
\end{array}$$

^3P

$$\begin{array}{c|ccccccc|}
 & 5^2S & 3^2P & 3^4P & 1^2D & 3^2D & 5^2D & 5^4D \\
5^2S & -21 & -14/3 & 7\sqrt{14}/3 & 0 & -2\sqrt{2} & 2 & 3\sqrt{2} \\
3^2P & & -73/3 & -\sqrt{14}/3 & -4\sqrt{14}/3 & \sqrt{2} & 13/3 & 7\sqrt{2}/3 \\
3^4P & & & -14/3 & 28/3 & 2\sqrt{7} & 7\sqrt{14}/3 & 11\sqrt{7}/3 \\
1^2D & & & & -28 & \sqrt{7} & 0 & 0 \\
3^2D & & & & & -26 & -2\sqrt{2} & 14 \\
5^2D & & & & & & -27 & -3\sqrt{2} \\
5^4D & & & & & & & -4
\end{array}$$

^5P

$$\begin{array}{c|ccc|}
 & 5^6S & 3^4P & 5^4D \\
5^6S & 7 & -7\sqrt{6} & \sqrt{42} \\
3^4P & & -28 & -\sqrt{7} \\
5^4D & & & -34
\end{array}$$

^5D

$$\begin{array}{c|ccc|}
 & 3^4P & 5^4D & 3^4F \\
3^4P & -133/5 & -6\sqrt{35}/5 & 3\sqrt{14}/5 \\
5^4D & & -29 & -3\sqrt{10}/5 \\
3^4F & & & -172/5
\end{array}$$

^1D

$$\begin{array}{c|cccccc|}
 & 3^2P & 1^2D & 3^2D & 5^2D & 3^2F & 5^2F \\
3^2P & -31/5 & 6\sqrt{70}/5 & 3\sqrt{10}/5 & -9\sqrt{5}/5 & -12/5 & -6\sqrt{5}/5 \\
1^2D & & -14 & -\sqrt{7} & 0 & -8\sqrt{70}/5 & 0 \\
3^2D & & & -8 & 2\sqrt{2} & 6\sqrt{10}/5 & 8\sqrt{2} \\
5^2D & & & & -11 & -28\sqrt{5}/5 & 6 \\
3^2F & & & & & -173/10 & -29\sqrt{5}/10 \\
5^2F & & & & & & -37/2
\end{array}$$

^3D

$$\begin{array}{c|ccccccccc|}
 & 3^2P & 3^4P & 1^2D & 3^2D & 5^2D & 5^4D & 3^2F & 5^2F & 3^4F \\
3^2P & -284/15 & \sqrt{14}/15 & -\sqrt{70}/5 & -\sqrt{10}/5 & -2\sqrt{5}/5 & 7\sqrt{10}/5 & 4/5 & -6\sqrt{5}/5 & 22/5 \\
3^4P & & 7/3 & 28\sqrt{5}/5 & -2\sqrt{35}/5 & 7\sqrt{70}/5 & 8\sqrt{35}/5 & 4\sqrt{14}/5 & 0 & -\sqrt{14} \\
1^2D & & & -21 & 4\sqrt{7}/3 & 0 & 0 & 4\sqrt{70}/15 & 0 & -14\sqrt{70}/15 \\
3^2D & & & & -23 & -\sqrt{2}/3 & 14/3 & -2\sqrt{10}/5 & -4\sqrt{2}/3 & 4\sqrt{10}/5 \\
5^2D & & & & & -22 & 3\sqrt{2} & 28\sqrt{5}/15 & -2 & -14\sqrt{5}/15 \\
5^4D & & & & & & -3 & -28\sqrt{10}/15 & 0 & 47\sqrt{10}/15 \\
3^2F & & & & & & & -269/10 & 53\sqrt{5}/30 & 14/5 \\
5^2F & & & & & & & & -53/2 & 14\sqrt{5}/3 \\
3^4F & & & & & & & & & -8
\end{array}$$

^1F

	1^2D	3^2D	5^2D	3^2F	5^2F	3^2G	5^2G
1^2D	-2	$23\sqrt{7}/7$	0	-13	0	$3\sqrt{35}/7$	0
3^2D		$-26/7$	$-25\sqrt{2}/7$	$-6\sqrt{7}/7$	$13\sqrt{35}/7$	$-18\sqrt{5}/7$	$3\sqrt{33}/7$
5^2D			$-20/7$	$-4\sqrt{14}$	$-3\sqrt{70}/7$	$-6\sqrt{10}/7$	$-3\sqrt{66}/7$
3^2F				$-37/8$	$-13\sqrt{5}/8$	$-9\sqrt{35}/56$	$3\sqrt{231}/8$
5^2F					$-25/8$	$-165\sqrt{7}/56$	$-3\sqrt{1155}/56$
3^2G						$-849/56$	$-55\sqrt{165}/56$
5^2G							$-757/56$

^3F

	1^2D	3^2D	5^2D	5^4D	3^2F	5^2F	3^4F	3^2G	5^2G	5^4G
1^2D	-18	$-29\sqrt{7}/21$	0	0	$17/3$	0	$-28/3$	$3\sqrt{35}/7$	0	0
3^2D		$-122/7$	$23\sqrt{2}/21$	$-28/3$	$2\sqrt{7}/7$	$-17\sqrt{35}/21$	$-4\sqrt{7}/7$	$6\sqrt{5}/7$	$3\sqrt{33}/7$	0
5^2D			$-124/7$	$-6\sqrt{2}/7$	$4\sqrt{14}/3$	$\sqrt{70}/7$	$-2\sqrt{14}/3$	$-6\sqrt{10}/7$	$\sqrt{66}/7$	$10\sqrt{6}/7$
5^4D				$27/7$	$-8\sqrt{7}/3$	0	$58\sqrt{7}/21$	0	$8\sqrt{33}/7$	$-10\sqrt{3}/7$
3^2F					$-193/8$	$-11\sqrt{5}/24$	$-7/2$	$3\sqrt{35}/56$	$-\sqrt{231}/8$	$5\sqrt{21}/2$
5^2F						$-197/8$	$7\sqrt{5}/6$	$87\sqrt{7}/56$	$\sqrt{1155}/56$	$\sqrt{105}/2$
3^4F							$-1/2$	$9\sqrt{35}/14$	$\sqrt{231}/2$	$25\sqrt{21}/14$
3^2G								$-1677/56$	$31\sqrt{165}/168$	$7\sqrt{15}/6$
5^2G									$-5123/168$	$5\sqrt{11}/42$
5^4G										$-505/42$

^5F

	5^4D	3^4F	5^4G
5^4D	$-173/7$	$-18\sqrt{7}/7$	$6\sqrt{3}/7$
3^4F		$-61/2$	$-3\sqrt{21}/14$
5^4G			$-487/14$

^5G

	3^4F	5^4G
3^4F	$-45/2$	$-5\sqrt{5}/2$
5^4G		$-65/2$

^1G

	3^2F	5^2F	3^2G	5^2G	3^2H
3^2F	$-25/8$	$23\sqrt{5}/8$	$3\sqrt{3}/8$	$7\sqrt{55}/8$	$-\sqrt{22}$
5^2F		$-29/8$	$-113\sqrt{15}/40$	$3\sqrt{11}/8$	$\sqrt{110}/5$
3^2G			$-383/40$	$-\sqrt{165}/40$	$-3\sqrt{66}/5$
5^2G				$-95/8$	$17\sqrt{10}/5$
3^2H					$-94/5$

^3G

	3^2F	5^2F	3^4F	3^2G	5^2G	5^4G	3^2H
3^2F	$-367/24$	$-5\sqrt{5}/8$	$7/6$	$-\sqrt{3}/8$	$-7\sqrt{55}/24$	$35\sqrt{5}/6$	$\sqrt{22}/3$
5^2F		$-121/8$	$-7\sqrt{5}/2$	$27\sqrt{15}/40$	$-\sqrt{11}/8$	$-7/2$	$\sqrt{110}/5$
3^4F			$29/6$	$-3\sqrt{3}/2$	$7\sqrt{55}/6$	$13\sqrt{5}/6$	$2\sqrt{22}/3$
3^2G				$-899/40$	$5\sqrt{165}/24$	$7\sqrt{15}/30$	$\sqrt{66}/5$
5^2G					$-521/24$	$-\sqrt{11}/6$	$-\sqrt{10}/3$
5^4G						$17/6$	$14\sqrt{110}/15$
3^2H							$-466/15$

^1H

	3^2G	5^2G	3^2H	5^2I
3^2G	$3/10$	$71\sqrt{165}/110$	$18/5$	$-6\sqrt{715}/55$
5^2G		$25/22$	$36\sqrt{165}/55$	$12\sqrt{39}/11$
3^2H			$-34/5$	$28\sqrt{715}/55$
5^2I				$-238/11$

^5H

	5^4G
5^4G	-20

^3H

	3^2G	5^2G	5^4G	3^2H	5^2I
3^2G	$-141/10$	$-19\sqrt{165}/66$	$-14\sqrt{15}/15$	$-6/5$	$-6\sqrt{715}/55$
5^2G		$-949/66$	$2\sqrt{11}/33$	$-4\sqrt{165}/11$	$-4\sqrt{39}/11$
5^4G			$16/3$	$14\sqrt{15}/5$	$-2\sqrt{429}/11$
3^2H				$-117/5$	$-7\sqrt{715}/55$
5^2I					$-357/11$

^1I

	3^2H	5^2I
3^2H	1	$5\sqrt{7}$
5^2I		-5

^3I

	3^2H	5^2I
3^2H	-12	$-2\sqrt{7}$
5^2I		-24

^1K

	5^2I
5^2I	2

^3K

	5^2I
5^2I	-10

Table V. The Matrices of $W(d^6, p)$

Matrices of f_2 are obtained by changing the sign of those $W(d^4, p)$ in Table III.

Matrices of g_1 (coefficients of G_1)

^2S

	2^3P	4^3P
2^3P	$-23/3$	$-5\sqrt{14}/3$
4^3P		$20/3$

^4S

	2^3P	4^3P
2^3P	$-14/3$	$4\sqrt{14}/3$
4^3P		$-16/3$

^2P

	0^1S	4^1S	2^3P	4^3P	2^1D	4^1D	4^3D
0^1S	-6	0	$9\sqrt{2}/2$	0	$\sqrt{42}/2$	0	0
4^1S		-6	$-\sqrt{42}/2$	$2\sqrt{3}$	$3\sqrt{2}/2$	2	$-2\sqrt{6}$
2^3P			$10/3$	$-7\sqrt{14}/6$	$\sqrt{21}$	$-\sqrt{42}/2$	$\sqrt{7}$
4^3P				$-17/6$	$-\sqrt{6}/2$	$7\sqrt{3}/2$	$-\sqrt{2}/2$
2^1D					-4	$-3\sqrt{2}/2$	$-3\sqrt{3}$
4^1D						$-9/2$	$\sqrt{6}/2$
4^3D							-1

^4P

	2^3P	4^3P	4^3D	4^5D
2^3P	$-26/3$	$\sqrt{14}/3$	$\sqrt{7}$	$-\sqrt{15}$
4^3P		$-53/6$	$7\sqrt{2}/4$	$-\sqrt{210}/4$
4^3D			$-19/4$	$-3\sqrt{105}/4$
4^5D				$5/4$

^6P

	4^5D
4^5D	-10

^6D

	4^5D
4^5D	-10

^2D

	2^3P	4^3P	2^1D	4^1D	4^3D	4^1F	2^3F	4^3F
2^3P	$-61/15$	$31\sqrt{14}/30$	0	$-3\sqrt{210}/10$	$-\sqrt{35}/5$	0	$7\sqrt{14}/5$	$2\sqrt{14}/5$
4^3P		$-97/30$	$-3\sqrt{30}/10$	$-9\sqrt{15}/10$	$-17\sqrt{10}/10$	$-6\sqrt{15}/5$	$11/5$	$16/5$
2^1D			-5	$3\sqrt{2}/2$	$-\sqrt{3}$	0	$\sqrt{30}$	$2\sqrt{30}/5$
4^1D				$-9/2$	$\sqrt{6}/2$	-2	$\sqrt{15}/5$	$-4\sqrt{15}/5$
4^3D					-1	$2\sqrt{6}$	$-3\sqrt{10}/5$	$-12\sqrt{10}/5$
4^1F						$-3/2$	$-\sqrt{15}$	$\sqrt{15}/10$
2^3F							$22/5$	$-3/5$
4^3F								$-1/10$

D

	2^3P	4^3P	4^3D	4^5D	2^3F	4^3F
2^3P	$-124/15$	$-7\sqrt{14}/15$	$-\sqrt{35}/5$	$-3\sqrt{3}$	$-2\sqrt{14}/5$	$2\sqrt{14}/5$
4^3P		$-241/30$	$11\sqrt{10}/20$	$3\sqrt{42}/4$	$11/5$	$-2/5$
4^3D			$-31/4$	$\sqrt{105}/4$	$9\sqrt{10}/10$	$3\sqrt{10}/5$
4^5D				$25/4$	$\sqrt{42}/2$	$-\sqrt{42}$
2^3F					$-32/5$	$12/5$
4^3F						$-14/5$

F

	2^1D	4^1D	4^3D	4^1F	2^3F	4^3F	2^1G	4^1G	4^3G
2^1D	$-53/7$	$-3\sqrt{2}/7$	$2\sqrt{3}$	0	$-2\sqrt{21}/7$	$4\sqrt{21}/7$	$2\sqrt{3}/7$	$4\sqrt{33}/7$	0
4^1D		$-54/7$	$-4\sqrt{6}/7$	$\sqrt{70}/7$	$\sqrt{42}/7$	$-4\sqrt{42}/7$	$5\sqrt{6}/7$	$\sqrt{66}/7$	$-6\sqrt{30}/7$
4^3D			$-22/7$	$\sqrt{105}/7$	$-12\sqrt{7}/7$	$9\sqrt{7}/7$	0	$9\sqrt{11}/7$	$9\sqrt{5}/7$
4^1F				$-57/8$	$-\sqrt{15}/4$	$-7\sqrt{15}/8$	$\sqrt{105}/4$	$\sqrt{1155}/56$	$-3\sqrt{21}/56$
2^3F					$-5/2$	$-9/4$	$27\sqrt{7}/14$	$-9\sqrt{77}/28$	$-9\sqrt{35}/28$
4^3F						$-11/8$	$-45\sqrt{7}/28$	$9\sqrt{77}/56$	$45\sqrt{35}/56$
2^1G							$-67/42$	$5\sqrt{11}/84$	$-3\sqrt{5}/4$
4^1G								$-503/168$	$-39\sqrt{55}/56$
4^3G									$169/56$

F

	4^3D	4^5D	2^3F	4^3F	4^3G
4^3D	$-67/7$	$\sqrt{105}/7$	$3\sqrt{7}/7$	$-3\sqrt{7}/14$	$9\sqrt{5}/14$
4^5D		-5	$\sqrt{15}$	$-\sqrt{15}/2$	$15\sqrt{21}/14$
2^3F			-7	$-3/2$	$9\sqrt{35}/14$
4^3F				$-37/4$	$-9\sqrt{35}/28$
4^3G					$-145/28$

^6F

	4^5D
4^5D	-10

G

	4^1F	2^3F	4^3F	2^1G	4^1G	4^3G	4^3H
4^1F	$-61/8$	$3\sqrt{15}/4$	$5\sqrt{15}/8$	$-7/4$	$-\sqrt{11}/8$	$-69\sqrt{5}/40$	$\sqrt{330}/5$
2^3F		$-31/6$	$25/12$	$-\sqrt{15}/2$	$-\sqrt{165}/4$	$-13\sqrt{3}/4$	$\sqrt{22}/3$
4^3F			$-85/24$	$-5\sqrt{15}/4$	$\sqrt{165}/8$	$\sqrt{3}/8$	$4\sqrt{22}/3$
2^1G				$-37/6$	$-\sqrt{11}/12$	$-3\sqrt{5}/20$	$-\sqrt{330}/5$
4^1G					$-101/24$	$3\sqrt{55}/8$	$\sqrt{30}$
4^3G						$23/40$	$-2\sqrt{66}/5$
4^3H							$32/15$

G

	2^3F	4^3F	4^3G	4^3H
2^3F	$-29/3$	$-1/6$	$\sqrt{3}/2$	$\sqrt{22}/3$
4^3F		$-119/12$	$-\sqrt{3}/4$	$-\sqrt{22}/6$
4^3G			$-31/4$	$\sqrt{66}/2$
4^3H				$-8/3$

H

	2^1G	4^1G	4^3G	4^3H	4^1I
2^1G	$-26/3$	$\sqrt{11}/33$	$3\sqrt{5}/5$	$-9\sqrt{5}/5$	$-\sqrt{429}/11$
4^1G		$-619/66$	$3\sqrt{55}/22$	0	$-4\sqrt{39}/11$
4^3G			$-73/10$	$-18/5$	$-6\sqrt{2145}/55$
4^3H				$23/10$	$\sqrt{2145}/10$
4^1I					$1/22$

^4H

	4^3G	4^3H
4^3G	-10	$6/5$
4^3H		-10

^2I

$$\begin{array}{c|cc} & 4^3H & 4^1I \\ \hline 4^3H & -17/2 & \sqrt{21}/2 \\ 4^1I & & -13/2 \end{array}$$

^4I

$$\begin{array}{c|c} & 4^3H \\ \hline 4^3H & -10 \end{array}$$

^2K

$$\begin{array}{c|c} & 4^1I \\ \hline 4^1I & -10 \end{array}$$

Matrices of g_3 (coefficients of G_1)

^2S

$$\begin{array}{c|cc} & 2^3P & 4^3P \\ \hline 2^3P & -21 & 5\sqrt{14} \\ 4^3P & & -10 \end{array}$$

^4S

$$\begin{array}{c|cc} & 2^3P & 4^3P \\ \hline 2^3P & -28 & -2\sqrt{14} \\ 4^3P & & -27 \end{array}$$

^2P

$$\begin{array}{c|ccccccc} & 0^1S & 4^1S & 2^3P & 4^3P & 2^1D & 4^1D & 4^3D \\ \hline 0^1S & -21 & 0 & -21\sqrt{2}/2 & 0 & \sqrt{42}/2 & 0 & 0 \\ 4^1S & & -21 & 7\sqrt{42}/6 & -14\sqrt{3}/3 & 3\sqrt{2}/2 & 2 & -2\sqrt{6} \\ 2^3P & & & -35/6 & 13\sqrt{14}/6 & \sqrt{21}/6 & 7\sqrt{42}/6 & \sqrt{7} \\ 4^3P & & & & -41/3 & 7\sqrt{6}/6 & 13\sqrt{3}/3 & 7\sqrt{2} \\ 2^1D & & & & & -53/2 & -3\sqrt{2}/2 & 7\sqrt{3} \\ 4^1D & & & & & & -27 & -2\sqrt{6} \\ 4^3D & & & & & & & -11 \end{array}$$

^4P

$$\begin{array}{c|cccc} & 2^3P & 4^3P & 4^3D & 4^5D \\ \hline 2^3P & -91/3 & -4\sqrt{14}/3 & \sqrt{7} & 7\sqrt{15}/3 \\ 4^3P & & -89/3 & -2\sqrt{2} & -2\sqrt{210}/3 \\ 4^3D & & & -67/2 & \sqrt{105}/2 \\ 4^5D & & & & -35/2 \end{array}$$

^6P

$$\begin{array}{c|c} & 4^5D \\ \hline 4^5D & -35 \end{array}$$

^6D

$$\begin{array}{c|c} & 4^5D \\ \hline 4^5D & -35 \end{array}$$

^2D

$$\begin{array}{c|cccccccc} & 2^3P & 4^3P & 2^1D & 4^1D & 4^3D & 4^1F & 2^3F & 4^3F \\ \hline 2^3P & -49/10 & -23\sqrt{14}/10 & -\sqrt{105}/2 & 7\sqrt{210}/10 & -\sqrt{35}/5 & 0 & 7\sqrt{14}/5 & 2\sqrt{14}/5 \\ 4^3P & & -12/5 & 7\sqrt{30}/10 & -2\sqrt{15}/5 & 14\sqrt{10}/5 & -6\sqrt{15}/5 & 11/5 & 16/5 \\ 2^1D & & & -45/2 & 3\sqrt{2}/2 & 7\sqrt{3}/3 & 0 & \sqrt{30}/3 & -14\sqrt{30}/15 \\ 4^1D & & & & -22 & -\sqrt{6}/3 & -2 & -7\sqrt{15}/15 & 28\sqrt{15}/15 \\ 4^3D & & & & & -23/3 & -4\sqrt{6}/3 & 41\sqrt{10}/15 & -26\sqrt{10}/15 \\ 4^1F & & & & & & -53/2 & 7\sqrt{15}/3 & 58\sqrt{15}/30 \\ 2^3F & & & & & & & -259/15 & 91/15 \\ 4^3F & & & & & & & & -353/30 \end{array}$$

^4D

$$\begin{array}{c|cccccc} & 2^3P & 4^3P & 4^3D & 4^5D & 2^3F & 4^3F \\ \hline 2^3P & -133/5 & 6\sqrt{14}/5 & -\sqrt{35}/5 & 7\sqrt{3} & -2\sqrt{14}/5 & 2\sqrt{14}/5 \\ 4^3P & & -136/5 & -17\sqrt{10}/10 & -\sqrt{42}/2 & 11/5 & -2/5 \\ 4^3D & & & -92/3 & 2\sqrt{105}/3 & -23\sqrt{10}/30 & 4\sqrt{10}/15 \\ 4^5D & & & & 0 & -7\sqrt{42}/6 & 2\sqrt{42}/3 \\ 2^3F & & & & & -496/15 & -14/15 \\ 4^3F & & & & & & -517/15 \end{array}$$

^2F

	2^1D	4^1D	4^3D	4^1F	2^3F	4^3F	2^1G	4^1G	4^3G
2^1D	$-123/7$	$-3\sqrt{2}/7$	$-14\sqrt{3}/3$	0	$-26\sqrt{21}/21$	$-4\sqrt{21}/3$	$2\sqrt{3}/7$	$4\sqrt{33}/7$	0
4^1D		$-124/7$	$23\sqrt{6}/21$	$\sqrt{70}/7$	$-\sqrt{42}/3$	$4\sqrt{42}/3$	$5\sqrt{6}/7$	$\sqrt{66}/7$	$-6\sqrt{30}/7$
4^3D			$-101/21$	$-17\sqrt{105}/21$	$64\sqrt{7}/21$	$47\sqrt{7}/21$	0	$9\sqrt{11}/7$	$9\sqrt{5}/7$
4^1F				$-197/8$	$7\sqrt{15}/12$	$-11\sqrt{15}/24$	$\sqrt{105}/4$	$\sqrt{1155}/56$	$87\sqrt{21}/56$
2^3F					$-35/3$	$-7/12$	$6\sqrt{7}/7$	$3\sqrt{77}/4$	$51\sqrt{35}/28$
4^3F						$-193/24$	$15\sqrt{7}/4$	$-3\sqrt{77}/8$	$-15\sqrt{35}/56$
2^1G							$-611/21$	$5\sqrt{11}/84$	$7\sqrt{5}/4$
4^1G								$-5123/168$	$31\sqrt{55}/56$
4^3G									$-1231/56$

^4F

	4^3D	4^5D	2^3F	4^3F	4^3G
4^3D	$-997/42$	$-29\sqrt{105}/42$	$-41\sqrt{7}/21$	$-29\sqrt{7}/42$	$9\sqrt{5}/14$
4^5D		$15/2$	$-7\sqrt{15}/3$	$17\sqrt{15}/6$	$15\sqrt{21}/14$
2^3F			$-86/3$	$-7/3$	$-3\sqrt{35}/7$
4^3F				$-193/6$	$3\sqrt{35}/14$
4^3G					$-475/14$

^6F

	4^5D
4^5D	-35

^2G

	4^1F	2^3F	4^3F	2^1G	4^1G	4^3G	4^3H
4^1F	$-121/8$	$-7\sqrt{15}/4$	$-5\sqrt{15}/8$	$-7/4$	$-\sqrt{11}/8$	$81\sqrt{5}/40$	$\sqrt{330}/5$
2^3F		$7/3$	$-35/12$	$-4\sqrt{15}/3$	$7\sqrt{165}/12$	$61\sqrt{3}/12$	$\sqrt{22}/3$
4^3F			$-85/24$	$35\sqrt{15}/12$	$-7\sqrt{165}/24$	$-97\sqrt{3}/24$	$4\sqrt{22}/3$
2^1G				$-71/3$	$-\sqrt{11}/12$	$7\sqrt{5}/20$	$7\sqrt{330}/15$
4^1G					$-521/24$	$5\sqrt{55}/8$	$-\sqrt{30}/3$
4^2G						$-337/40$	$14\sqrt{66}/15$
4^3H							$-358/15$

^4G

	2^3F	4^3F	4^3G	4^3H
2^3F	$-74/3$	$7/3$	$-11\sqrt{3}/3$	$\sqrt{22}/3$
4^3F		$-127/6$	$11\sqrt{3}/6$	$-\sqrt{22}/6$
4^3G			$-59/2$	$-\sqrt{66}/6$
4^3H				$-104/3$

^2H

	2^1G	4^1G	4^3G	4^3H	4^1I
2^1G	$-41/3$	$\sqrt{11}/33$	$-7\sqrt{5}/5$	$21\sqrt{5}/5$	$-\sqrt{429}/11$
4^1G		$-949/66$	$-19\sqrt{55}/22$	$-12\sqrt{55}/11$	$-4\sqrt{39}/11$
4^3G			$37/10$	$42/5$	$-6\sqrt{2145}/55$
4^3H				$-31/5$	$-7\sqrt{2145}/55$
4^1I					$-357/11$

^4H

	4^3G	4^3H
4^3G	-23	-6
4^3H		-32

^2I

	4^3H	4^1I
4^3H	4	$-2\sqrt{21}$
4^1I		-24

^4I

	4^3H
4^3H	-20

^2K

	4^1I
4^1I	-10

§ 2. Comparison with the Terms of $3d^6 4p$ of Fe II.

Among the possible 68 terms of the configuration $3d^6 4p$ of Fe II, the 36 terms lying in the range from 38688 cm^{-1} to 74566 cm^{-1} were observed by J.C. Dobbie(5) in 1935. The parameters of the interaction $W(d, p)$: F_2, G_1 and G_3 are determined from the four terms ^6P, ^4P, ^4D and ^4F, all having the same parent term $3d^6 (4^5D)$. The results are

$$F_2(d, p) = 338\,\text{cm}^{-1},\quad G_1(d, p) = 301\,\text{cm}^{-1},$$
$$G_3(d, p) = 43\,\text{cm}^{-1}.$$

These values should be compared with other results obtained before for similar configurations what is done in Table VI.

Table VI. The Parameters F_2, G_1 and G_3 of $W(d, p)$ in $3d^n 4p$.

n	1	2		6		7	8		9
	Sc II	Ti II		Fe II		Co II	Ni II		Cu II
Ref.	(6)	(3)	(1)	(7)	ours	(8)	(3)	(1)	(8)
F_2 (cm^{-1})	242	301	290	320	338	357	361	364	351
G_1 („)		338	332		301		421	303	304
G_3 („)		23.4	18		43		32.7	54	36

Next using these values the parameters of the internal energy $W(d^6)$ were determined from the core energy of 4^5D, the energy of $d^6(4^3H)p\ ^4I$ and the sum of energies of the two ^4H terms. We find thus

$$A + 6F_0(d, p) = 59666\,\text{cm}^{-1},\quad B = 689\,\text{cm}^{-1},$$
$$C = 4434\,\text{cm}^{-1}.$$

Finally term energies have been calculated by use of these parameters by perturbation method and compared with observed values in Table VII and Figure 1. The agreement is not satisfactory for the terms derived from the parent terms 4^3P and 4^3F. These discrepancies have not yet been fully explained, but they are probably due partially to the configuration interaction with $3d^5 4s 4p$, partially to the wrong assignment of the experimental values.

Table VII. Comparison with $3d^6 4p$ of Fe II.

No.	Term	Obs. (cm^{-1})	Calc. (cm^{-1})	Dif.
1	$^6D(4^5D)$	38688	38316	− 372
2	$^6F(4^5D)$	42157	41358	− 799
3	$^6P(4^5D)$	43048	43048	0
4	$^4F(4^5D)$	44694	44546	− 148
5	$^4D(4^5D)$	44712	44401	− 311
6	$^4P(4^5D)$	47192	46865	− 327
7	$^4S(4^3P)$	59663	63734	4071
8	$^4P(4^3P)$	60751	65234	4483
9	$^4G(4^3H)$	60814	60510	− 304
10	$^4H(4^3H)$	60942	61180	238
11	$^2D(4^3P)$	61480	66548	5068
12	$^4I(4^3H)$	61482	61481	− 1
13	$^4F(4^3F)$	62141	63736	1595
14	$^2G(4^3H)$	62188	62315	127
15	$^4D(4^3P)$	62295	63977	1682
16	$^2I(4^3H)$	62462	62958	496
17	$^4D(4^3F)$	63183	65783	2600
18	$^4G(4^3F)$	63966	66105	2139
19	$^2F(4^3F)$	64344	67461	3117
20	$^2P(4^3P)$	64827	68232	3405
21	$^2G(4^3F)$	64941	66931	1990
22	$^2H(4^3H)$	65450	65169	− 281
23	$^4G(4^3G)$	65767	64584	−1183
24	$^2S(4^3P)$	66249	68914	2665
25	$^4F(4^3G)$	66300	66025	− 275
26	$^4H(4^3G)$	66512	65040	−1472
27	$^2D(4^3F)$	67103	67691	588
28	$^2H(4^3G)$	67734	67118	− 616
29	$^2F(4^3G)$	69625	68304	−1321
30	$^2G(4^3G)$	70406	69159	−1247
31	$^2H(4^1I)$	72203	72452	249
32	$^4F(4^3D)$	72418	71201	1217
33	$^4D(4^3D)$	72604	71891	− 713
34	$^2F(4^3D)$	73032	72993	− 39
35	$^2P(4^3D)$	73189	73048	− 141
36	$^2D(4^3D)$	74566	73304	−1262
37	$^4P(4^3D)$		70855	
38	$^2K(4^1I)$		71819	
39	$^2I(4^1I)$		74642	
40	$^2G(4^1G)$		75497	
41	$^2H(4^1G)$		77038	
42	$^2F(4^1G)$		77054	
43	$^2P(4^1D)$		78526	
44	$^2D(4^1D)$		80032	
45	$^2F(4^1D)$		80312	
46	$^2P(4^1S)$		82339	
47	$^2G(4^1F)$		82451	
48	$^2D(4^1F)$		84408	
49	$^2F(4^1F)$		85426	

No.	Term	Obs. (cm⁻¹)	Calc. (cm⁻¹)	Dif.
50	${}^4D(2^3P)$		86850	
51	${}^2S(2^3P)$		87964	
52	${}^4G(2^3F)$		88226	
53	${}^4S(2^3P)$		89403	
54	${}^4P(2^3P)$		89704	
55	${}^4D(2^3F)$		89952	
56	${}^2G(2^3F)$		90912	
57	${}^2D(2^3P)$		90954	
58	${}^4F(2^3F)$		91229	
59	${}^2P(2^3P)$		92561	
60	${}^2D(2^3F)$		92587	
61	${}^2F(2^3F)$		93006	
62	${}^2H(2^1G)$		96998	
63	${}^2G(2^1G)$		98883	
64	${}^2F(2^1G)$		99224	
65	${}^2D(2^2D)$		110824	
66	${}^2F(2^1D)$		112934	
67	${}^2P(2^1D)$		114496	
68	${}^2P(0^1S)$		136634	

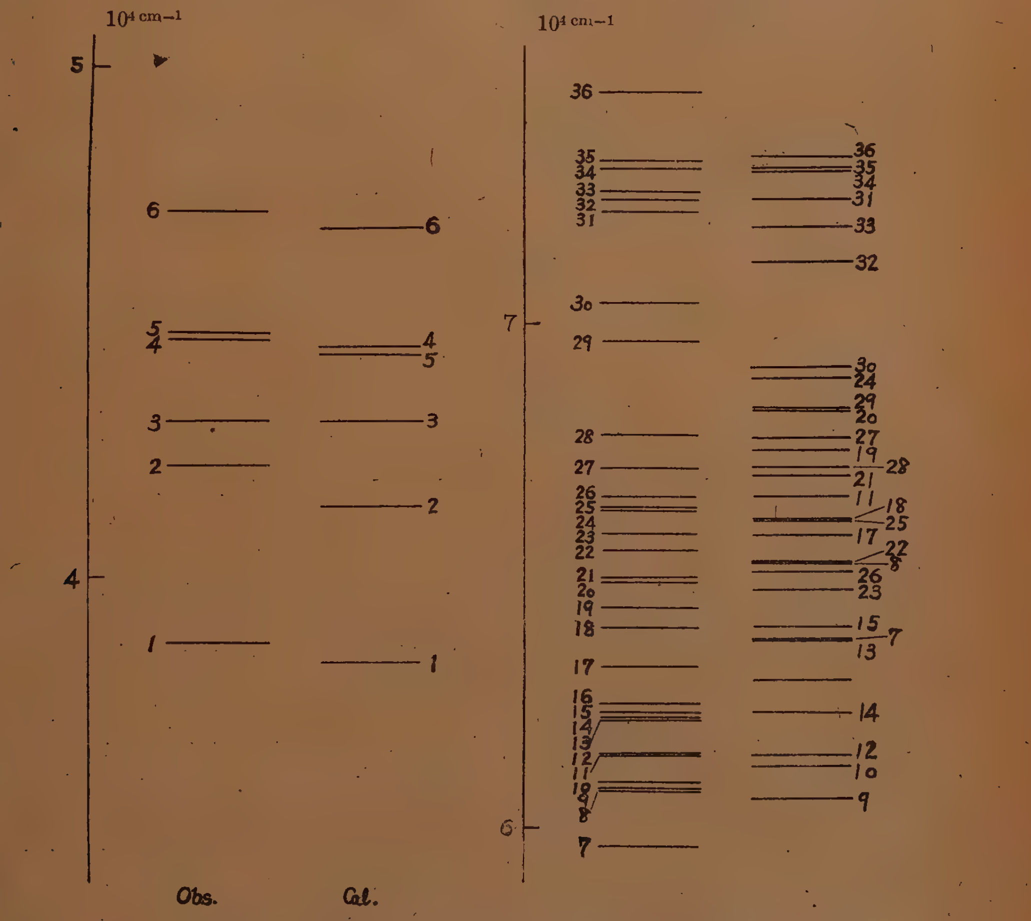

Fig. 1. Energy levels of $3d^64p$ of FeII (cf. Table VII).

In conclusion, we wish to thank Prof. T. Yamanouchi for his kind encouragement and Ass. Prof. A. Amemiya for many helpful advices, and also Miss Chizuko Mikoshiba for her help in numerical works.

References.

(1) G. Racah: Phys. Rev. **61**, 186 (1942); **62**, 438, (1942); **63**, 367 (1943). Especially cf. the second paper, Sec. 9.

(2) F. Rohrlich: Phys. Rev. **74**, 1372 (1948).

(3) T. Yamanouchi: Proc. Phys.-Math. Soc. Jap. **22**, 841 (1940).

(4) A. Amemiya: Nippon Sûgaku-Buturigakkai-si, **17**, 567 (1943) (Published by the Phys.-Math. Soc. Japan in Japanese).

(5) J. C. Dobbie: Proc. Roy. Soc. A **151**, 703 (1935).

(6) W. M. Cady: Phys. Rev. **43**, 322 (1933).

(7) T. Yamanouchi: Proc. Phys.-Math. Soc. Jap. **20**, 563 (1938).

(8) T. Yamanouchi: Proc. Phys.-Math. Soc. Jap. **19**, 166 (1937).

Note added in proof. Prof. G. Racah has written to us in reply to our sending of a copy of this manuscript and has pointed out, besides the errors remarked in footnote in p. 125, another mistake in Table XVIII of his third paper (RIII), where the elements 4^3G-4^3H and 4^3H-4^3G were given with the wrong sign. Owing to his remark our calculation have been corrected in this paper and the agreement with experiment has become somewhat better. We wish to express our gratitude to him for his kind remarks and also to Prof. F. Rohrlich for his valuable suggestions about our results, whom we have sent also a copy of this paper.

Structure of the f^n Electron Configurations. (I) Coefficients of Fractional Parentage of f^3.

By Takehiko ISHIDZU.

Department of Dynamics, First Faculty of Engineering, University of Tokyo,

and

Shin-ya OBI.

Astronomy Department, Faculty of Science, University of Tokyo.

(Read October 22, 1949; Received Nov. 21, 1949.)

Abstract

Racah's theory of the structure of the equivalent electron groups was applied to the f^n configurations. The coefficients of fractional parentage of f^3 terms were determined in this paper, and the electrostatic energies were re-calculated in $v\alpha SL$ scheme.

§1. Introduction and Summary.

G. Racah has established the theory of the structure of the equivalent electron groups in his third paper*⁽¹⁾ on the theory of complex spectra. With aid of the coefficients of fractional parentage and the seniority number v, he gave the matrix elements of the symmetric tensors $U^{(k)}$ and $V^{(1k)}$ for p^n and d^n configurations, which are available for the calculation of the electrostatic energies of the configurations such as p^nl or d^nl by his method of tensor operators. We have applied his theory to the configurations f^n and, as our first step, the coefficients of fractional parentage of f^3 terms are obtained in this article (I) and the matrices of the spin-orbit interaction for the same configuration are calculated in the next article (II). In f^3, as Racah has already pointed out, terms of the same kind can not be distinguished by seniority number alone and need another unspecified parameter α. From these results the electrostatic energies of f^3 were re-calculated in $v\alpha SL$ scheme.

§2. Coefficients of Fractional Parentage of f^3.

The coefficients of fractional parentage $(f^3\alpha SL\{|f^2(S'L')fSL)$ are defined as the coefficients of expansion of the eigenfunction corresponding to the term αSL of f^3 by those corresponding to the states in which the first two f electrons are at first coupled and construct a definite term $S'L'$

---

* References (1) and (2) shall be cited as RIII and RII in this and next papers.

of f^2, and then the third f electron is added to them, constructing the term SL of f^3 as a whole. These coefficients are so determined as, when the eigenfuction of $f^3(\alpha SL)$ are expanded by those corresponding to the states in which, by this time, the last two electrons construct at first a definite term $S''L''$ of ff and then the first electron is added to them, only allowed terms in f^2 may appear, that is, those for which $S''+L''=$ odd vanish. Thus the homogeneous simultaneous equations determining the parentages are written as follows:

$$\sum_{S'L'} (f^3\alpha SL\{\!\!|f^2(S'L')fSL)(f^2(S'L')fSL| f, ff(L''S''), SL)=0 \text{ for } S''+L''=\text{odd}. \quad (1)$$

Here $(f^2(S'L')fSL|f, ff(S''L''), SL)$ are the transformation coefficients between different coupling schemes of three angular momenta and are expressed in general by W-functions defined by the formula (36′) in Racah's second paper⁽²⁾ as follows:

$$(j_1j_2(J'), j_3J|j_1, j_2j_3(J''), J)=[(2J'+1)(2J''+1)]^{\frac{1}{2}} \times W(j_1j_2Jj_3;\, J'J''). \quad (2)$$

Hence

$$(f^2(S'L')fSL|f, ff(S''L''), SL) = [(2S'+1)(2S''+1)(2L'+1)(2L''+1)]^{\frac{1}{2}} \times W(\tfrac{1}{2}\tfrac{1}{2}S\tfrac{1}{2};\, S'S'')\times W(3\,3\,L\,3;\, L'L''). \quad (3)$$

With these values, the equations (1) for the C.F.P. (coefficients of fractional parentage) are solved; the number of independent non-vanishing solutions for a given SL depends upon the rank of the matrices of coefficients of the equations and equals the number of allowed terms of the same kind in f^3. Thus for each of ^2D, ^2F, ^2G and ^2H two solutions are found. For the case of ^2F it is possible to choose them that the C.F.P. from tbe state $f^2(^1S)$: $(f^3v\,^2F\{\!\!|f f^2(^1S)f\,^2F)$ is not zerof or the first solution, but zero for the second. Hence the C.F.P. $(f^3v\,^2F\{\!\!|f(^2F), f^2(^1S), {}^2F)$ is also not zero for the first, zero for the second; they have, therefore, the seniority number $v=1$ and 3 respectively ($1\,^2F$ and $3\,^2F$). For the cases of ^2D ^2G and ^2H, however, the C.F.P. from $f^2(^1S)$ are essentially zero, all these pairs of terms have the same seniority 3. It needs, therefore, another parameter besides v for distinguishing these terms of the same kind. In this paper each pair of terms is distinguished by the parameters α and β in such a way that for the states $3\alpha\,^2D$ and $3\alpha\,^2G$, the C.F.P. from the state $f^2(^3P)$: $(f^3 3\alpha\,^2D\{\!\!|f^2(^3P)f^2D)$ etc. are not zero, but for the states $3\beta\,^2D$ and $3\beta\,^2G$ they vanish, and for the state $3\alpha\,^2H$ the C.F.P. from the state $f^2(^1D)$ is not zero, but for $3\beta\,^2H$, it vanishes. Results thus obtained are given in Table I (N denotes the normalization factor).

Table I. The Coefficients of Fractional Parentage for f^3.
$(f^3v\alpha SL\{\!\!|f^2(v'S'L')fSL)$

		f^2						
f^3	N	$0\,^1S$	$2\,^3P$	$2\,^1D$	$2\,^3F$	$2\,^1G$	$2\,^1H$	$2\,^1I$
$3\,^4S$	1	0	0	0	1	0	0	0
$3\,^2P$	$42^{-\frac{1}{2}}$	0	0	$\sqrt{10}$	$-\sqrt{21}$	$-\sqrt{11}$	0	0
$3\alpha\,^2D$	$(4\cdot11\cdot21)^{-\frac{1}{2}}$	0	$2\sqrt{66}$	$3\sqrt{11}$	$-\sqrt{77}$	$11\sqrt{3}$	-11	0
$3\beta\,^2D$	42^{-1}	0	0	$3\sqrt{77}$	$7\sqrt{11}$	$-3\sqrt{21}$	$-7\sqrt{7}$	0
$3\,^4D$	$63^{-\frac{1}{2}}$	0	$3\sqrt{3}$	0	$\sqrt{14}$	0	$\sqrt{22}$	0
$1\,^2F$	$(9\cdot14)^{-\frac{1}{2}}$	6	-3	$-\sqrt{5}$	$-\sqrt{21}$	-3	$-\sqrt{33}$	$-\sqrt{13}$
$3\,^2F$	$(36\cdot77)^{-\frac{1}{2}}$	0	33	$-11\sqrt{5}$	0	-12	$-3\sqrt{33}$	$7\sqrt{13}$
$3\,^4F$	$42^{-\frac{1}{2}}$	0	$\sqrt{3}$	0	$-2\sqrt{7}$	0	$\sqrt{11}$	0
$3\alpha\,^2G$	$(36\cdot7\cdot31)^{-\frac{1}{2}}$	0	$31\sqrt{3}$	$-5\sqrt{15}$	$2\sqrt{77}$	$-18\sqrt{5}$	$\sqrt{13\cdot55}$	$-7\sqrt{39}$
$3\beta\,^2G$	$(9\cdot11\cdot14\cdot31)^{-\frac{1}{2}}$	0	0	$22\sqrt{13}$	$-\sqrt{13\cdot15\cdot77}$	$-17\sqrt{39}$	$14\sqrt{33}$	$28\sqrt{5}$
$3\,^4G$	$(9\cdot42)^{-\frac{1}{2}}$	0	$3\sqrt{11}$	0	$-2\sqrt{21}$	0	$-\sqrt{13\cdot15}$	0
$3\alpha\,^2H$	$(9\cdot11\cdot14\cdot37)^{-\frac{1}{2}}$	0	0	$37\sqrt{11}$	$-2\sqrt{15\cdot77}$	$-18\sqrt{13}$	$-7\sqrt{13\cdot33}$	$-7\sqrt{130}$
$3\beta\,^2H$	$(66\cdot37)^{-\frac{1}{2}}$	0	0	0	$\sqrt{7\cdot11\cdot13}$	$-7\sqrt{15}$	$-2\sqrt{55}$	$9\sqrt{6}$
$3\,^2I$	$(9\cdot22)^{-\frac{1}{2}}$	0	0	0	$\sqrt{77}$	$-3\sqrt{3}$	$\sqrt{22}$	$-6\sqrt{2}$
$3\,^4I$	3^{-1}	0	0	0	$\sqrt{2}$	0	$-\sqrt{7}$	0
$3\,^2K$	$66^{-\frac{1}{2}}$	0	0	0	0	4	$-\sqrt{33}$	$-\sqrt{17}$
$3\,^2L$	$2^{-\frac{1}{2}}$	0	0	0	0	0	1	-1

§ 3. Matrices of the Electrostatic Energies of f^3 in $v\alpha SL$ scheme.

The matrix elements of the electrostatic energies $W(f^3)$ in $v\alpha SL$ scheme are easily calculated by the formula*:

$$\begin{aligned}(f^3v\alpha SL\,|\,W(f^3)\,|\,f^3v'\alpha'SL) &= (f^3v\alpha SL\,|\sum_{i>j=1}^{3} e^2/r_{ij}\,|\,f^3v'\alpha'SL) \\ &= 3\,(f^3v\alpha SL\,|\,e^2/r_{12}\,|\,f^3v'\alpha'SL) \\ &= 3\sum_{v_1S_1L_1}(f^3v\alpha SL\{\!|f^2(v_1S_1L_1)fSL) \\ &\quad\times(f^2v_1S_1L_1\,|\,W(f^2)\,|\,f^2v_1S_1L_1) \\ &\quad\times(f^2(v_1S_1L_1)fSL|\!\}f^3v'\alpha'SL)\,. \qquad (4)\end{aligned}$$

Since the C.F.P. are given in Table I and the energies for f^2 are known, the calculations are straightforward. The results are shown in Table II, using the parameters:

$$A = F_0 - 21F_4 - 468F_6, \quad B = (5F_2+6F_4-91F_6)/5,$$
$$C = 7(F_4 - 6F_6)/5, \qquad D = 462F_6,$$

which give, of course, the same eigenvalues as Racah has given (RII, § 8)**. These matrices should be employed in calculating the electrostatic energies of f^n for $n>3$, or of the configurations such as f^nl in $v\alpha SL$ scheme.

Table II. The Electrostatic Energies of f^3 in $v\alpha SL$ scheme.

	$3\alpha\,{}^2D$	$3\beta\,{}^2D$
$3\alpha\,{}^2D$	$3A-3B+213C/2+3D$	$\sqrt{33}(4B-39C/2)$
$3\beta\,{}^2D$	$\sqrt{33}\,(4B-39C/2)$	$3A-11B-99C/2+3D$

	$1\,{}^2F$	$3\,{}^2F$
$1\,{}^2F$	$3A+40B+105C+9D$	$-10\sqrt{22}B$
$3\,{}^2F$	$-10\sqrt{22}B$	$3A+70B-30C+3D$

	$3\alpha\,{}^2G$	$3\beta\,{}^2G$
$3\alpha\,{}^2G$	$3A+\frac{1370}{31}B+\frac{1800}{31}C+3D$	$\frac{-5\sqrt{13\cdot15\cdot22}\,(4B-9C)}{31}$
$3\beta\,{}^2G$	$\frac{-5\sqrt{13\cdot15\cdot35}\,(4B-9C)}{31}$	$3A-\frac{936}{31}B+\frac{1703}{31}C+3D$

	$3\alpha\,{}^2H$	$3\beta\,{}^2H$
$3\alpha\,{}^2H$	$3A-\frac{547}{37}B-\frac{1344}{37}C+3D$	$\frac{-30\sqrt{13\cdot35}\,(2B-3C)}{37}$
$3\beta\,{}^2H$	$\frac{-30\sqrt{13\cdot35}\,(2B-3C)}{37}$	$3A-\frac{1155}{37}B+\frac{3675}{37}C+3D$

References.

(1) G. Racah: Phys. Rev. **63**, 367 (1943).
(2) G. Racah: Phys. Rev. **62**, 438 (1942).

---

* See also the authors' recent paper: "On the energy levels of the configurations d^4p, d^5p and d^6p", § 1, in this issue of this journal.

** A. Amemiya has also calculated the term energies of f^3 configulation by group-theoretical method. But a few errors are included in his results (Proc. Phys.-Math. Soc. Jap. **23**, 664, 1941): in his Table IIa, γ for ${}^4F$ is -858 instead of 868, for ${}^4D$ -1859 instead of -1850, and β for ${}^4S$ is -99 instead of -69, for ${}^2H$ -6 instead of 6; in Table IIb, e for ${}^2F$ is -451360 instead of -405600.

Structure of the f^n Electron Configurations. (II) Spin-orbit Interaction of the Configuration f^3.

By Takehiko ISHIDZU.

Department of Dynamics, First Faculty of Engineering, University of Tokyo.

and

Shin-ya OBI.

Astronomy Department, Faculty of Science, University of Tokyo.

(Read October 22, 1949; Received Nov. 21, 1949.)

Abstract

Utilizing the C.F.P. for f^3 terms obtained in the preceding article, the matrices of the spin-orbit interaction have been calculated in $v\alpha SL$ scheme. The results would be applicable to the spectra of Nd atoms.

The matrices of the angular part of the spin-orbit interaction $\sum_i (s_i l_i)$ are given in general by [RIII, (24), (25)]

$$(l^n\alpha SLJM \mid \sum_i (s_i l_i) \mid l^n\alpha' S'L'JM)$$
$$= (-1)^{S+L'-J}[l(l+1)(2l+1)]^{\frac{1}{2}}$$
$$\times (l^n\alpha SL \| V^{(11)} \| l^n\alpha' S'L') \times W(SLS'L';J1). \quad (1)$$

Since $\quad V^{(11)} = \sum_i s_i u_i$,

we obtain, by the relation (23) in RIII, for $l=3$,

$$(f^n\alpha SL \| V^{(11)} \| f^n\alpha' S'L')$$
$$= (-1)^{\frac{1}{2}-S'-L'}(n\sqrt{6}/2)[(2S+1)(2S'+1)(2L+1)$$
$$\times (2L'+1)]^{\frac{1}{2}} \sum_{\alpha_1 S_1 L_1} (-1)^{S_1+L_1} (f^n\alpha SL \{\!| f^{n-1}(\alpha_1 S_1 L_1) fSL)$$
$$\times (f^{n-1}(\alpha_1 S_1 L_1) fSL |\!\} f^n\alpha' S'L')$$
$$\times W(\tfrac{1}{2} S \tfrac{1}{2} S'; S_1 1)\, W(3L3L'; L_1 1), \quad (2)$$

where the W-functions are the same as occurred in (2) of the preceding article (I). Making use of the C.F.P. obtained in the article (I) the matrices of $V^{(11)}$ for f^3 terms were calculated; finally from (1) the whole matrix elements of the spin-orbit interaction were found. The results are shown in Table I and II.

In conclusion we wish to thank Prof. M. Kotani for his valuable advices* and Miss Chizuko Mikoshiba for her help in evaluation of W-functions.

---

* Prof. M. Kotani has also obtained already the matrices of the spin-orbit interaction for f^3 terms though in different scheme, except for $J=\frac{1}{2}$ and $\frac{3}{2}$.

Table 1. $(f^3 v\alpha SL \| V^{(11)} \| f^3 v'\alpha' S'L')$

	$3\,^4S$	$3\,^2P$	$3\alpha\,^2D$	$3\beta\,^2D$	$3\,^4D$	$1\,^2F$	$3\,^2F$	$3\,^4F$	$3\alpha\,^2G$	$3\beta\,^2G$	$3\,^4G$	$3\alpha\,^2H$	$3\beta^2\,H$	$3\,^2I$	$3\,^4I$	$3\,^2K$	$3\,^2L$
$3\,^4S$	0	$\frac{\sqrt{6}}{\sqrt{7}}$	0	0	0	0	0	0	0	0	0	0	0	0	0	0	0
$3\,^2P$	$\frac{\sqrt{6}}{\sqrt{7}}$	0	$-\frac{\sqrt{15}}{2\sqrt{14}}$	$\frac{\sqrt{55}}{2\sqrt{14}}$	$-\frac{\sqrt{5}}{\sqrt{14}}$	0	0	0	0	0	0	0	0	0	0	0	0
$3\alpha\,^2D$	0	$\frac{\sqrt{15}}{2\sqrt{14}}$	$-\frac{\sqrt{5}}{4\sqrt{21}}$	$\frac{\sqrt{55}}{4\sqrt{7}}$	$\frac{3\sqrt{5}}{2\sqrt{7}}$	$-\frac{\sqrt{10}}{\sqrt{21}}$	$-\frac{\sqrt{55}}{2\sqrt{21}}$	$\frac{\sqrt{5}}{2\sqrt{21}}$	0	0	0	0	0	0	0	0	0
$3\beta\,^2D$	0	$-\frac{\sqrt{55}}{2\sqrt{14}}$	$\frac{\sqrt{55}}{4\sqrt{7}}$	$\frac{\sqrt{35}}{4\sqrt{3}}$	$\frac{\sqrt{55}}{2\sqrt{21}}$	0	$-\frac{\sqrt{5}}{2\sqrt{7}}$	$-\frac{\sqrt{55}}{2\sqrt{7}}$	0	0	0	0	0	0	0	0	0
$3\,^4D$	0	$-\frac{\sqrt{5}}{\sqrt{14}}$	$-\frac{3\sqrt{5}}{2\sqrt{7}}$	$-\frac{\sqrt{55}}{2\sqrt{21}}$	$\frac{5}{\sqrt{42}}$	$\frac{\sqrt{10}}{\sqrt{7}}$	0	0	0	0	0	0	0	0	0	0	0
$1\,^2F$	0	0	$\frac{\sqrt{10}}{\sqrt{21}}$	0	$\frac{\sqrt{10}}{\sqrt{7}}$	$\frac{\sqrt{2}}{\sqrt{3}}$	$\frac{\sqrt{11}}{3\sqrt{3}}$	$\frac{1}{\sqrt{3}}$	$\frac{\sqrt{31}}{2\sqrt{7}}$	0	$\frac{\sqrt{11}}{\sqrt{7}}$	0	0	0	0	0	0
$3\,^2F$	0	0	$\frac{\sqrt{55}}{2\sqrt{21}}$	$\frac{\sqrt{5}}{2\sqrt{7}}$	0	$\frac{\sqrt{11}}{2\sqrt{3}}$	$-\frac{1}{\sqrt{6}}$	$\frac{\sqrt{11}}{2\sqrt{6}}$	$-\frac{\sqrt{11}}{\sqrt{14\cdot31}}$	$\frac{\sqrt{13\cdot15}}{2\sqrt{7\cdot31}}$	$\frac{\sqrt{7}}{2\sqrt{2}}$	0	0	0	0	0	0
$3\,^4F$	0	0	$\frac{\sqrt{5}}{2\sqrt{21}}$	$-\frac{\sqrt{55}}{2\sqrt{7}}$	0	$-\frac{1}{\sqrt{3}}$	$-\frac{\sqrt{11}}{2\sqrt{6}}$	$\frac{\sqrt{5}}{\sqrt{3}}$	$-\frac{9}{2\sqrt{14\cdot31}}$	$-\frac{\sqrt{33\cdot65}}{2\sqrt{7\cdot31}}$	0	0	0	0	0	0	0
$3\alpha\,^2G$	0	0	0	0	0	$-\frac{\sqrt{31}}{2\sqrt{7}}$	$\frac{\sqrt{11}}{\sqrt{14\cdot31}}$	$\frac{-9}{2\sqrt{14\cdot31}}$	$\frac{-19\sqrt{5}}{31\sqrt{14}}$	$\frac{3\sqrt{13\cdot33}}{62\sqrt{7}}$	$\frac{5\sqrt{55}}{2\sqrt{14\cdot31}}$	$\frac{\sqrt{11\cdot37}}{\sqrt{14\cdot31}}$	0	0	0	0	0
$3\beta\,^2G$	0	0	0	0	0	0	$-\frac{\sqrt{13\cdot15}}{2\sqrt{7\cdot31}}$	$-\frac{\sqrt{33\cdot65}}{2\sqrt{7\cdot31}}$	$\frac{3\sqrt{13\cdot33}}{62\sqrt{7}}$	$\frac{9\sqrt{14}}{31\sqrt{5}}$	$\frac{3\sqrt{39}}{2\sqrt{7\cdot31}}$	$\frac{16\sqrt{39}}{\sqrt{31\cdot35\cdot37}}$	$\frac{\sqrt{3\cdot31}}{\sqrt{37}}$	0	0	0	0
$3\,^4G$	0	0	0	0	0	$\frac{\sqrt{11}}{\sqrt{7}}$	$\frac{\sqrt{7}}{2\sqrt{2}}$	0	$\frac{-5\sqrt{55}}{2\sqrt{14\cdot31}}$	$\frac{-3\sqrt{39}}{2\sqrt{7\cdot31}}$	$\frac{5}{\sqrt{7}}$	$-\frac{\sqrt{37}}{\sqrt{14}}$	0	0	0	0	0
$3\alpha\,^2H$	0	0	0	0	0	0	0	0	$-\frac{\sqrt{11\cdot37}}{\sqrt{14\cdot31}}$	$\frac{-16\sqrt{39}}{\sqrt{31\cdot35\cdot37}}$	$-\frac{\sqrt{37}}{\sqrt{14}}$	$\frac{13\sqrt{11\cdot21}}{74\sqrt{5}}$	$\frac{\sqrt{13\cdot33}}{37}$	$\frac{\sqrt{65}}{\sqrt{37}}$	$\frac{2\sqrt{130}}{\sqrt{7\cdot37}}$	0	0
$3\beta\,^2H$	0	0	0	0	0	0	0	0	0	$-\frac{\sqrt{3\cdot31}}{\sqrt{37}}$	0	$\frac{\sqrt{13\cdot33}}{37}$	$\frac{2\sqrt{11\cdot15}}{37\sqrt{7}}$	$\frac{-17}{2\sqrt{7\cdot37}}$	$\frac{11}{\sqrt{2\cdot37}}$	0	0
$3\,^2I$	0	0	0	0	0	0	0	0	0	0	0	$-\frac{\sqrt{65}}{\sqrt{37}}$	$\frac{17}{2\sqrt{7\cdot37}}$	$\frac{\sqrt{13}}{7\sqrt{3}}$	$\frac{\sqrt{13}}{\sqrt{42}}$	$\frac{2\sqrt{10}}{7}$	0
$3\,^4I$	0	0	0	0	0	0	0	0	0	0	0	$\frac{2\sqrt{130}}{\sqrt{7\cdot37}}$	$\frac{11}{\sqrt{2\cdot37}}$	$-\frac{\sqrt{13}}{\sqrt{42}}$	$\frac{\sqrt{65}}{\sqrt{6}}$	$\frac{-2\sqrt{5}}{\sqrt{7}}$	0
$3\,^2K$	0	0	0	0	0	0	0	0	0	0	0	0	0	$\frac{-2\sqrt{10}}{7}$	$\frac{-2\sqrt{5}}{\sqrt{7}}$	$\frac{9\sqrt{15}}{28}$	$\frac{\sqrt{15\cdot17}}{4\sqrt{7}}$
$3\,^2L$	0	0	0	0	0	0	0	0	0	0	0	0	0	0	0	$-\frac{\sqrt{15\cdot17}}{4\sqrt{7}}$	$\frac{3\sqrt{17}}{4\sqrt{7}}$

Table II. Matrices of the Spin-orbit Interaction $\sum(s_i l_i)$ for f^3.

$J=\frac{1}{2}$

$$\begin{array}{c|cc}
 & 3\,{}^2P & 3\,{}^4D \\
\hline
3\,{}^2P & 0 & \frac{\sqrt{5}}{\sqrt{2}} \\
3\,{}^4D & & \frac{-3}{2}
\end{array}$$

$J=\frac{3}{2}$

$$\begin{array}{c|cccccc}
 & 3\,{}^4S & 3\,{}^2P & 3\alpha\,{}^2D & 3\beta\,{}^2D & 3\,{}^4D & 3\,{}^4F \\
\hline
3\,{}^4S & 0 & -\sqrt{6} & 0 & 0 & 0 & 0 \\
3\,{}^2P & & 0 & \frac{\sqrt{15}}{2\sqrt{2}} & -\frac{\sqrt{55}}{2\sqrt{2}} & \frac{\sqrt{5}}{2} & 0 \\
3\alpha\,{}^2D & & & \frac{1}{4} & -\frac{\sqrt{33}}{4} & \frac{3\sqrt{3}}{2\sqrt{2}} & \frac{-1}{2} \\
3\beta\,{}^2D & & & & \frac{-7}{4} & \frac{\sqrt{22}}{4} & \frac{\sqrt{33}}{2} \\
3\,{}^4D & & & & & -1 & 0 \\
3\,{}^4F & & & & & & -2
\end{array}$$

$J=\frac{5}{2}$

$$\begin{array}{c|ccccccc}
 & 3\alpha\,{}^2D & 3\beta^2\,D & 3\,{}^4D & 1\,{}^2F & 3\,{}^2F & 3\,{}^4F & 3\,{}^4G \\
\hline
3\alpha\,{}^2D & \frac{-1}{6} & \frac{\sqrt{11}}{2\sqrt{3}} & \frac{\sqrt{21}}{2} & \frac{2\sqrt{5}}{3} & \frac{\sqrt{55}}{3\sqrt{2}} & \frac{-1}{3} & 0 \\
3\beta\,{}^2D & & \frac{7}{6} & \frac{\sqrt{77}}{6} & 0 & \frac{\sqrt{5}}{\sqrt{6}} & \frac{\sqrt{11}}{\sqrt{3}} & 0 \\
3\,{}^4D & & & \frac{-1}{6} & \frac{-2\sqrt{5}}{\sqrt{21}} & 0 & 0 & 0 \\
1\,{}^2F & & & & \frac{-4}{3} & -\frac{\sqrt{22}}{3} & \frac{\sqrt{5}}{3} & -\frac{\sqrt{33}}{\sqrt{7}} \\
3\,{}^2F & & & & & \frac{2}{3} & \frac{\sqrt{55}}{6\sqrt{2}} & -\frac{\sqrt{21}}{2\sqrt{2}} \\
3\,{}^4F & & & & & & \frac{-7}{6} & 0 \\
3\,{}^4G & & & & & & & \frac{-5}{2}
\end{array}$$

$J=\frac{7}{2}$

$$\begin{array}{c|ccccccc}
 & 3\,{}^4D & 1\,{}^2F & 3\,{}^2F & 3\,{}^4F & 3\alpha\,{}^2G & 3\beta\,{}^2G & 3\,{}^4G \\
\hline
3\,{}^4D & 1 & -\frac{\sqrt{30}}{\sqrt{7}} & 0 & 0 & 0 & 0 & 0 \\
1\,{}^2F & & 1 & \frac{\sqrt{11}}{2\sqrt{2}} & \frac{\sqrt{3}}{2} & -\frac{\sqrt{31}}{2\sqrt{2}} & 0 & -\frac{\sqrt{55}}{2\sqrt{7}} \\
3\,{}^2F & & & \frac{-1}{2} & \frac{\sqrt{33}}{4\sqrt{2}} & \frac{\sqrt{11}}{2\sqrt{31}} & -\frac{\sqrt{13\cdot 15}}{2\sqrt{62}} & -\frac{\sqrt{35}}{4\sqrt{2}} \\
3\,{}^4F & & & & 0 & \frac{3\sqrt{3}}{4\sqrt{62}} & \frac{\sqrt{11\cdot 65}}{4\sqrt{31}} & 0 \\
3\alpha\,{}^2G & & & & & \frac{95}{6\cdot 31} & -\frac{\sqrt{33\cdot 65}}{62\sqrt{2}} & \frac{5\sqrt{11\cdot 35}}{12\sqrt{62}} \\
3\beta\,{}^2G & & & & & & \frac{-21}{31} & \frac{\sqrt{13\cdot 21}}{4\sqrt{31}} \\
3\,{}^4G & & & & & & & \frac{-4}{3}
\end{array}$$

$J=\frac{9}{2}$

	$3\,{}^4F$	$3\alpha\,{}^2G$	$3\beta\,{}^2G$	$3\,{}^4G$	$3\alpha\,{}^2H$	$3\beta\,{}^2H$	$3\,{}^4I$
$3\,{}^4F$	$\frac{3}{2}$	$\frac{3\sqrt{3}}{2\sqrt{62}}$	$\frac{\sqrt{11\cdot 65}}{2\sqrt{31}}$	0	0	0	0
$3\alpha\,{}^2G$		$\frac{-38}{3\cdot 31}$	$\frac{\sqrt{13\cdot 66}}{31\sqrt{5}}$	$\frac{55}{6\sqrt{62}}$	$-\frac{\sqrt{11\cdot 37}}{\sqrt{5\cdot 31}}$	0	0
$3\beta\,{}^2G$			$\frac{84}{5\cdot 31}$	$\frac{\sqrt{13\cdot 33}}{2\sqrt{5\cdot 31}}$	$\frac{-16\sqrt{6\cdot 13}}{5\sqrt{31\cdot 37}}$	$-\frac{\sqrt{31\cdot 42}}{\sqrt{5\cdot 37}}$	0
$3\,{}^4G$				$\frac{1}{6}$	$\frac{\sqrt{2\cdot 37}}{\sqrt{55}}$	0	0
$3\alpha\,{}^2H$					$\frac{-13\cdot 21}{5\cdot 37}$	$\frac{-6\sqrt{7\cdot 13}}{37\sqrt{5}}$	$\frac{-3\sqrt{390}}{\sqrt{11\cdot 37}}$
$3\beta\,{}^2H$						$\frac{-12}{37}$	$-\frac{\sqrt{11\cdot 21}}{\sqrt{2\cdot 37}}$
$3\,{}^4I$							$\frac{-7}{2}$

$J=\frac{11}{2}$

	$3\,{}^4G$	$3\alpha\,{}^2H$	$3\beta\,{}^2H$	$3\,{}^2I$	$3\,{}^4I$
$3\,{}^4G$	2	$\frac{\sqrt{3\cdot 37}}{\sqrt{22}}$	0	0	0
$3\alpha\,{}^2H$		$\frac{91}{74}$	$\frac{\sqrt{13\cdot 35}}{37}$	$-\frac{\sqrt{13\cdot 35}}{\sqrt{3\cdot 37}}$	$\frac{-2\sqrt{13\cdot 35}}{\sqrt{33\cdot 37}}$
$3\beta\,{}^2H$			$\frac{10}{37}$	$\frac{17}{2\sqrt{3\cdot 37}}$	$\frac{-7\sqrt{11}}{2\sqrt{3\cdot 37}}$
$3\,{}^2I$				$\frac{-1}{3}$	$\frac{\sqrt{11}}{6}$
$3\,{}^4I$					$\frac{-5}{3}$

$J=\frac{13}{2}$

	$3\,{}^2I$	$3\,{}^4I$	$3\,{}^2K$
$3\,{}^2I$	$\frac{2}{7}$	$\frac{\sqrt{5}}{\sqrt{14}}$	$\frac{-4\sqrt{5}}{7}$
$3\,{}^4I$		$\frac{1}{2}$	$\frac{2\sqrt{2}}{\sqrt{7}}$
$3\,{}^2K$			$\frac{-9}{7}$

$J=\frac{15}{2}$

	$3\,{}^4I$	$3\,{}^2K$	$3\,{}^2L$
$3\,{}^4I$	3	2	0
$3\,{}^2K$		$\frac{9}{8}$	$-\frac{\sqrt{15\cdot 17}}{8}$
$3\,{}^2L$			$\frac{-9}{8}$

$J=\frac{17}{2}$

	$3\,{}^2L$
$3\,{}^2L$	1

Ionization of the Negative Oxygen Ion by Electron Impact. III.

By Masaru WATANABE and Jun-ichi MIIDA.

Institute of Applied Mathematics, Second Faculty of Engineering, Tokyo University.

(Received Sept. 9, 1949).

§ 1. Introduction.

It has been ascertained both theoretically and experimentally that the negative oxygen ion should exist in the upper atmosphere. The negative ion is believed to be formed mainly by the electron attachment to the oxygen atom. The ion thus formed is stable at night, but is broken down and emit the electron by the solar radiation in the day-time.

To speak of the reflexion of the radio-wave by the ionosphere, the number of free electrons is the important factor, and the rôle of the negative ion should be related intimately to the variation of the number of free electrons. It is reported that the reflexion intensity of the radio wave increases, when meteors shoot into the ionosphere. It is probable that free electrons should be released from negative ions after the path of meteors.

There are two processes that the free electron detaches the negative ion, i. e. by the solar radiation and the collision of the other atom or molecule. The cross section of the former process amounts to the order of $10^{-17}\,\mathrm{cm}^2$ according to the calculation by Prof. Yamanouchi(1). Quantum mechanical calculation of detachment probability by collision is difficult and not carried out yet as far as the author knows. But the approximate calculation is possible on the collision between the electron and the negative ion.

The theoretical formula and the computation of the wave functions and their normalization have been published in the former paper(2). This report will give the final results, that is the calculation of the cross section for the electron detachment.

§ 2. Cross Section.

We consider the process

$$O^- + e \rightarrow O + e' + e'' \tag{1}$$

Using the perturbation method, the probability can be expressed as a sum of elementary processes(3):

$$W = \frac{16k'k''}{(2L+1)(2S+1)} \sum V_l^{l'l''}, \text{ (*)} \tag{2}$$

where k', k'' are the velocities of the scattered and ejected electron respectively, which satisfy the conservation law of energy which the incident electron's velocity k:

$$\frac{1}{2}k^2 = \frac{1}{2}k'^2 + \frac{1}{2}k''^2 + 0.1. \tag{3}$$

l, l' and l'' mean angular moment a of each electron, and the allowed combinations of l and (l', l'') are given by the selection rule. The first several examples are shown in Table I.

Table I.

l	l'	l''	κ
0	1	0	0
0	0	1	1
1	0	0	1
1	1	1	0,2

L and S are the orbital and spin angular momenta of the ion in the initial state. In our case $L=1$ and $S=\frac{1}{2}$. $V_l^{l'l''}$ means the partial cross section for the allowed transition and have been expressed as the square and procuct sum of double integrals, including the radial wave functions of free and atomic electrons:

$$R_\kappa(2p, k'l'; kl, k''l'') = \int_0^\infty \int \frac{r_<^\kappa}{r_>^{\kappa+1}} y_{2p}(r_1) y_{k'l'}(r_1) y_{kl}(r_2) y_{k''l''}(r_2) dr_1 dr_2 . \tag{4}$$

(*) All the physical quantities are measured in atomic units, uncless otherwise mentioned.

§ 3. Reduction of the Integral to the Differential Equation.

Hartree proposed the ingenious method of evaluating the double integral in his study on the calculation of the atomic energy level of the oxygen(4). He expressed the integral as follows:

$$R_\kappa = \int_0^\infty y_r y_\delta \left\{ \frac{1}{r_2^{\kappa+1}} \int_0^{r_2} r_1^\kappa y_\alpha y_\beta dr_1 \right.$$

$$\left. + r_2^\kappa \int_{r_2}^\infty \frac{1}{r_1^{\kappa+1}} y_\alpha y_\beta dr_1 \right\} dr_2 = \int_0^\infty y_\gamma y_\delta \left\{ I + J \right\} dr_2. \quad (5)$$

As the integrand changes so rapidy that it is inconvenient for direct integration, he differentiated the integrals I and J with respect to r and set up the differential equations (*),

$$\frac{dI}{dr} = -(\kappa+1)\frac{I}{r} + \frac{y_\alpha y_\beta}{r} \quad (6)$$

$$\frac{dJ}{dr} = \kappa \frac{J}{r} - \frac{y_\alpha y_\beta}{r}. \quad (7)$$

Then he solved these equations with appropriate conditions. But, with these devices, the labour for numerical integration is not saved in any way and so much time is required to get the desired results.

To economize labour and time, the calculating machine is the powerful tool and we have made use of the differential analyzer.

§ 4. Use of Differential Analyzer.

It is very convenient to introduce the logarithmic scale $\rho = \log r$, because not only the singularity at the origin is removed, but also the equation becomes to have constant co-efficient.

$$\frac{dI}{d\rho} = -(\kappa+1)I + y_\alpha y_\beta, \quad \frac{dJ}{d\rho} = \kappa J - y_\alpha y_\beta. \quad (8), \quad (9)$$

The schematie diagram for solving the I-equation (8) is shown in Fig. 1.

We have started at $r = 0.05$, where I has been obtained by direct integration of $y_\alpha y_\beta$ by Simpson's rule. The equation shows that I decrease as $\exp\{-(\kappa+1)\rho\} \doteqdot r^{-(\kappa+1)}$ for large ρ or r, so the solution tends to zero and the error diminishes, if exists.

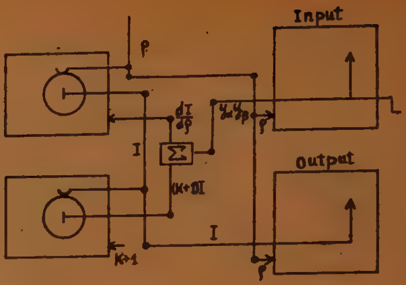

Fig. 1. $I = 1/r^{\kappa+1} \int_0^r r^k y_\alpha y_\beta dr$, $dI/d\rho = -(\kappa+1)I + y_\alpha y_\beta$
Schematic Diagram for solving the Equation: $dI/d\rho = -(\kappa+1)I + y_\alpha y_\beta$.

Next we attack J-equation (9). This can be treated as before, but we need not I and J separately, but $I+J$ as the final results, so it is a short-cut to solve the equation:

$$\frac{d(I+J)}{d\rho} = -(\kappa+1)I + \kappa J = \kappa(I+J) - (2\kappa+1)I \quad (10)$$

As this equation has the same form as (8), we can use the machine set-up with no change in the connection, inserting I as the input instead of $y_\alpha y_\beta$.

Near $r = 0$, $I \sim r^{l_\alpha + l_\beta + 1}$ and $J \sim r^\kappa \int_r^\infty \frac{1}{r^{\kappa+1}} y_\alpha y_\beta dr$ With the condition $|l_\alpha - l_\beta| \leqq \kappa \leqq l_\alpha + l_\beta$, $J \gg I$. Therefore we mustc alculate $\int_r^\infty \frac{1}{r^{\kappa+1}} y_\alpha y_\beta dr$ as the initial condition, but this is trobulesome to carry out. To avoid these difficulties, the equation has been solved backwards, starting at large $r (r = 8.0)$. $I(r = 8)$ has already been obtained in the former calculation. $J(r = 8)$ can be expressed asymptotically,

$$J = 8^\kappa \int_8^\infty \frac{0.983 \exp(-0.495r)}{r^{\kappa+1}} (c_1 F_l + c_2 G_l) d \quad (11)$$

where the expression in the bracket means the asymptotic form of the radial wave functions of the free electron. That of the atomic electron is expressed in the exponential form, which represents the Hartree's function in its significant figures.

Refer the appendix as to the estimation of this integral.

The second and more serious reason for backward integration is to prevent the accumulation of errors. The general form of the solution is $I+J = \exp(\kappa\rho)$+special solution of inhomogeneous

---

(*) These equations are slightly different from the original form of Hartree's.

equation and we seek for the solution which tends to zero at infinity. If we go forwards starting at $r=0$, small errors in the initial condition or arising in way of machine runnig, become large as $c\exp(\kappa\rho)$, which increases invincibly.

Backward integration reverse the situation. The errors tend to zero as the solution itself, and we get the results with high precision. On the machine, backward integration can be carried out simply by the inverse rotation of the axis of the independent variable. The results are shown in Fig. 2～9.

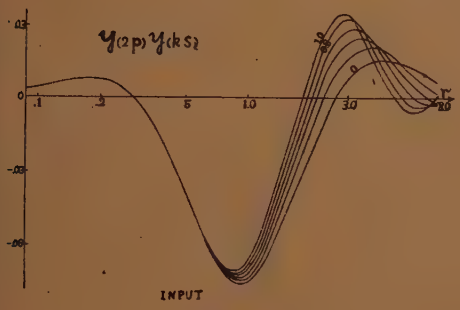

Fig. 2.

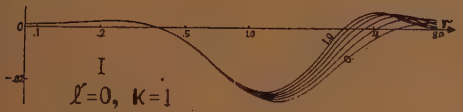

Fig. 3.

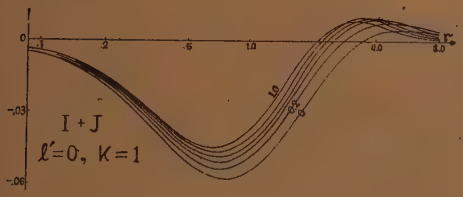

Fig. 4.

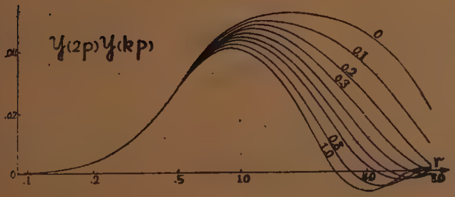

Fig. 5.

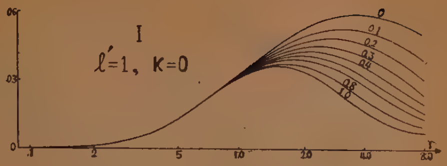

Fig. 6.

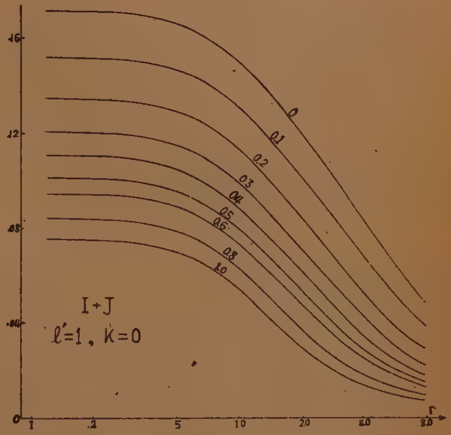

Fig. 7.

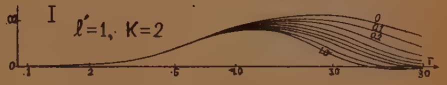

Fig. 8.

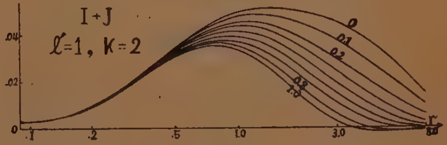

Fig. 9.

§ 5. Double Integral.

The schematic diagram for the second integration in the double integral

$$\int_0^\infty y_\gamma y_\delta\{I+J\}dr$$

are shown in Fig. 10.

Two input tables are required, one $I+J$ and the other $y_\gamma y_\delta$. The former is given in scale of ρ, and the latter in r. To save trouble to transform the scale severally, one integrator is available for generating $r=e^\rho$. The integrator on the right side end is to adjusted the scale factor of the exponetial function.

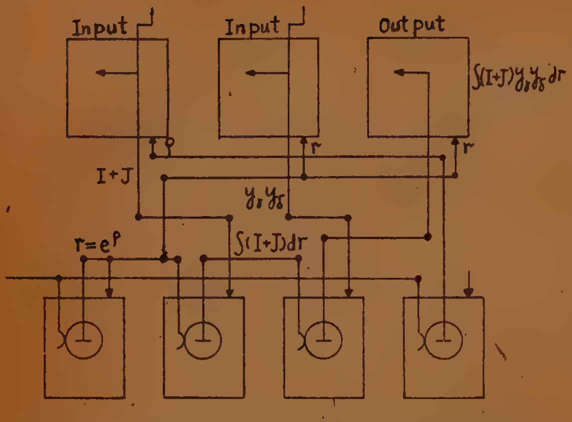

Fig. 10. Schematic Diagram for Integration: $\int y_T y_S \{I+J\} dr$.

The values of the double integrals thus obtained are shown in Fig. 11 ~ 15.

80 integrals have been computed in 4 days. The effective time might be reduced to half of this record, if we could save the time spent in repairing the broken belt of the amplifier, radiating the heat generating in the amplifier, or mis-setting in the initial condition.

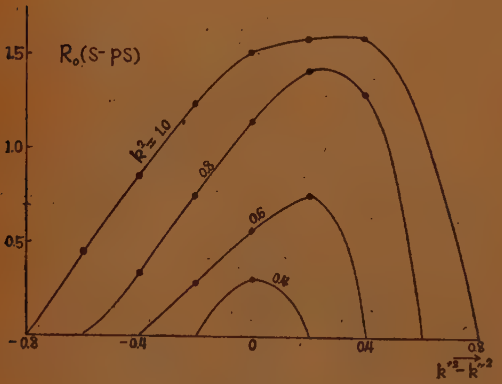

Fig. 11.

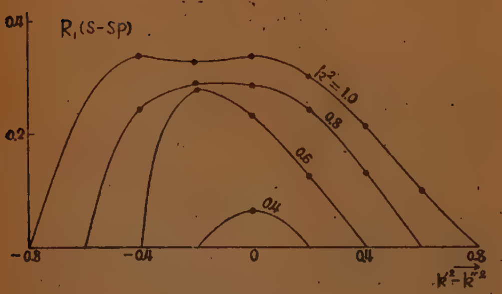

Fig. 12.

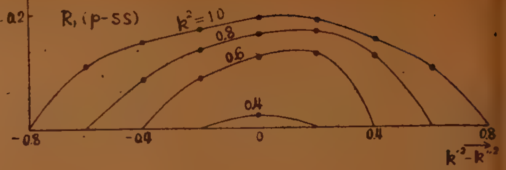

Fig. 13.

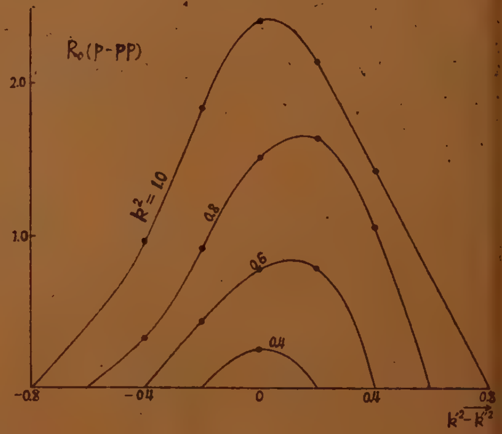

Fig. 14.

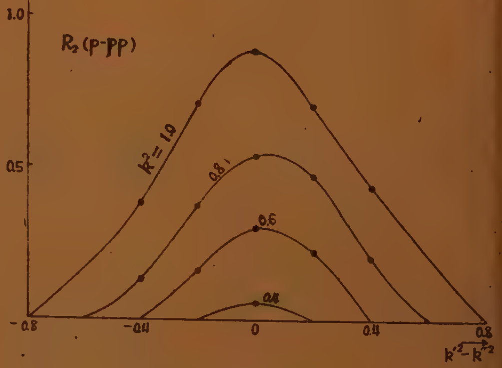

Fig. 15.

§ 6. Results.

The main features of the results are:

(1) *p-pp* cross sections are extraordinarily large.

(2) for small energy the probability that two electrons go out with same velocity is large.

Summing up the partial cross sections and multiplying the normalization constant and other numerical factor, we obtain the electron detachment probability against the energy of the incident electron. In Fig. 16 the abscissa and the ordinate are given in usual units.

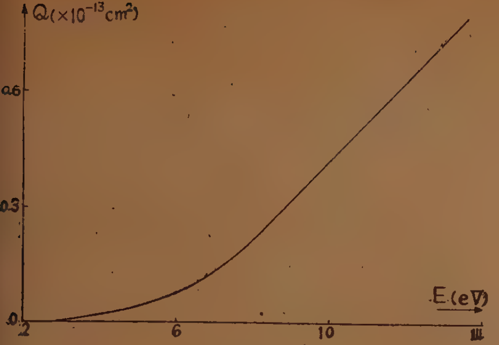

Fig. 16.

The large probability due to the anomalous property of p-electron⁽⁵⁾, suggests that the electron detachment easily occurs when the electron knocks on the negative ion with the energy larger than the electron affinity. Though the electron temperature of the ionosphere is too low to ionize the negative ion, it is probable that high speed electrons are sent from the sun or by some other origin as in the cosmic ray.

We wish to express our heartiest thanks to Prof. T. Yamanouchi for his continual encouragement throughout this work. We are indebted to Miss I. Ota for assisting the numerical computations and the mechanical operations.

Appendix.

The radial wave functions of free electron with energy $k^2/2$ and orbital angular moment l in the potential field $V(r)$ satisfy the equation

$$\frac{d^2y}{dr^2}+\left\{k^2-2V(r)-\frac{l(l+1)}{r^2}\right\}y=0.$$

If $V(r)$ vanishes faster than Coulombic potential $1/r$ for large r as in the atomic field ($r \geqq 8$ in our case), the equation reduces to

$$\frac{d^2y}{dr^2}+\left\{k^2-\frac{l(l+1)}{r^2}\right\}y=0,$$

whose solutions are the Bessel function of half-integer order, $F_l(kr)$ and $G_l(kr)$. Explict forms of them are

$$F_0=\sin kr,\quad F_1=(\sin kr)/kr-\cos kr,\ \ldots\ldots,$$

$$G_0=\cos kr,\quad G_1=-\sin kr-(\cos kr)/kr,\ \ldots.$$

The J-integrals at $r=8$,

$$J=8^\kappa\int_8^\infty\frac{0.934e^{-0.495r}}{r^{\kappa+1}}(c_1F_l+c_2G_l)dr,$$

can be expressed as linear combinations of

$$J_{ns}=\int_8^\infty\frac{1}{r^n}e^{ar}\sin krdr,$$

and $$J_{nc}=\int_8^\infty\frac{1}{r^n}e^{ar}\cos krdr.$$

Integrating by parts, we obtain the recurrence formula

$$J_{n,s}=\frac{1}{n-1}\left(\frac{e^{8\alpha}\sin 8k}{8^{n-1}}+kJ_{n-1,c}+\alpha J_{n-1,s}\right),$$

$$J_{n,c}=\frac{1}{n-1}\left(\frac{e^{8\alpha}\cos 8k}{8^{n-1}}-\alpha J_{n-1,c}-kJ_{n-1,s}\right),$$

The only integrals we must compute directly are

$$J_{1s}=\int_8^\infty\frac{e^{ar}}{r}\sin krdr,$$

$$J_{1c}=\int_8^\infty\frac{e^{ar}}{r}\cos krdr.$$

Differentiating J_{1s} with respect to the parameters k,

$$\frac{dJ_{1s}}{dk}=\int_8^\infty e^{ar}\cos krdr$$

which can be evaluated by elementary integration,

$$\frac{dJ_{1s}}{dk}=-\frac{e^{8\alpha}(\alpha\cos 8k+k\sin 8k)}{d^2+k^2}=f(k).$$

Similarly

$$\frac{dJ_{1s}}{dk}=-\frac{e^{8\alpha}(k\cos 8k-\alpha\sin 8k)}{\alpha^2+k^2}=g(k).$$

Again, integrating as to k,

$$J_{1s}(k)=\int_0^k f(k)dk,\ (J_{1s}=0\ \text{for}\ k=0)$$

$$J_{1c}(k)=\int_0^k g(k)dk+J_{1c}(k=0.)$$

$J_{1c}(k=0)=\int_8^\infty e^{ar}/rdr$ are tabulated as logarithmic exponental, e.g. in Jahnke-Emde's Table.

Though we can not dispense with numerical integration after all, our method here mentioned have several avdantages. At first, if we integrate J_{1s}, J_{1c} directly, the range extends to infinity and it is too lengthy and tedious to integrate until the integrands vanish practically. The transformed integrals are finite ones, and easily computed as with accuracy as desired. Secondly, if the integrals are wanted for various values of parameter k, our method is very convenient, because in the process of integration we can successively tabulate the values of the integrals with respect to k at once.

References.

(1) Yamanouchi, Proc. Phys.-Math. Soc. Japan, 22 (1940), 569.

(2) Watanabe, J. Phys. Soc. Japan, 4 (1949 203 and 208.

(3) Watanabe, ibid.

(4) Hartree and Black, Proc. Roy. Soc., A 13 (1933), 311.

(5) Yamanouchi, Inui and Amemiya, Proc. Phys Math. Soc. Sapan, 22 (1940), 847. Watanabe, ibid.

Probabilities of Excitation and De-excitation of Metastable States of Oxygen Atom by Collision of Slow Electron.

By Takahiko YAMANOUCHI.

Institute of Applied Mathematics, Second Faculty of Engineering, University of Tokyo.

(Received; Sept. 12, 1949).

§ 1. Introduction.

It is well known that the auraural line (5577) and the nebular line (6300) observed in the spectra of aurora, night-sky light and some of the planetary nebulae are due to the forbidden transitions between the metastable states ^1D and ^1S, and the ground state ^3P of the neutral oxygen atom, each arising from the normal configuration $1s^22s^22p^4$. These metastable states are mainly produced by the collision of free electrons in the ionosphere or the nebular atmosphere. We have already made a calculation(1) of the probability for the excitation from the ground state ^3P, but for the problems concerning the radiative equilibrium of these extremely rarefied gases, or the intesity ratio of the forbidden lines, it is necessary to find the probabilities of excitations and de-excitations for all possible transitions between these three states. In this paper, therefore, it is attempted to obtain the numerical values of all such probabilities. In the following, the three states ^3P, ^1D, and ^1S will be indicated by the suffixes 1, 2, and 3 respectively, and the probability of the transition of the ato from the state μ to the state ν will be denote by $W_{\mu\nu}$. Among them, $W_{ij}(i<j)$ is the probability of excitation, that is, the probability tha the electron gives energy to the atom, raising i to the higher energy state (collision of the firs kind), whereas W_{ji} is the probability of de-excitation, for which the atom loses energy by accelerating the electron (collision of the second kind) The general formulae for these probabilities bein already obtained(2), we have here performed necessary computations to find their numerical values Since most of the electrons contributing to thes processes have relatively small velocities, the calculations are carried out only for the energie just sufficient for causing transitions. Consequently, the variations of electron energies are take into account only in the distribution function an the normalizing factors of the wave functions Besides various approximations inevitable in th mathematical treatment of many-electron problems, many approximations and neglections ar also unavoidable in the numerical computation

so that the final results will give little more than the order of magnitude. Yet, I hope, it will serve as a data, hardly obtainable by experimental method, to investigate the physical conditions of upper atmosphere and the nebular interior.

§2. Probabilities of Excitation and De-excitation.

Let $w_{\mu\nu}(\varepsilon)$ be the probability for the excitation or de-excitation per unit time, of the atom from the state μ to ν, by the collision of electron with the energy ε. The density of the electron is taken to the unity. All the quantities are measured in atomic units, unless otherwise mentioned. The total probability due to the collision of electron having all the possible energies is then given by

$$W_{\mu\nu}=\int^{\infty}w_{\mu\nu}(\varepsilon)f(\varepsilon)d\varepsilon,$$

where $f(\varepsilon)$ is the energy-distribution function of the electron. The lower limit of the integral is the energy difference $\varepsilon_{ij}=\varepsilon_j-\varepsilon_i\ (j>i)$ for the excitation, and zero for the de-excitation. If we assume the Maxwellian distribution:

$$f(\varepsilon)=\frac{2\sqrt{\varepsilon}}{\sqrt{\pi}(\kappa T)^{3/2}}e^{-\varepsilon/\kappa T},$$

we have

$$\left.\begin{aligned}W_{ij}&=\frac{2}{\sqrt{\pi}(\kappa T)^{3/2}}\int_{\varepsilon_{ij}}^{\infty}w_{ij}(\varepsilon)\sqrt{\varepsilon}\,e^{-\varepsilon/\kappa T}d\varepsilon, \\ &\qquad\qquad\text{(excitation)} \\ W_{ji}&=\frac{2}{\sqrt{\pi}(\kappa T)^{3/2}}\int_{0}^{\infty}w_{ji}(\varepsilon)\sqrt{\varepsilon}\,e^{-\varepsilon/\kappa T}d\varepsilon. \\ &\qquad\qquad\text{(di-excitation)}\end{aligned}\right\}\quad(1)$$

n this integral, the Boltzmann's constant κ has the numerical value 3.17×10^{-6}, while the electron temperature T is at most of the order 10^4 degrees K, so that the integral is mainly determined by the values of integrand near the lower limit. We ave hence determined the value of $w_{\mu\nu}(\varepsilon)$ only or these "critical energies" $\varepsilon_{\mu\nu}$. Their numerical alues are $\varepsilon=0$, $\varepsilon_{12}=0.0720$, $\varepsilon_{13}=0.1535$, and $_{23}=0.0815$ respectively, for which the corresponding electron velocities are $k=0$, $k_{12}=0.379$, $k_{13}=$ .554, and $k_{23}=0.404$.

§3. Calculation of $w_{\mu\nu}$ (ε).

$w_{\mu\nu}(\varepsilon)$ is given by(2)

$$w_{\mu\nu}=\frac{16\pi k_{\nu}}{g_{\mu}}\sum V_{\mu\nu}(l,\ l'). \qquad (2)$$

g_μ is the weight $(2L_\mu+1)(2S_\mu+1)$(L and S are the quantum numbers for the orbital and spin angular momenta) and k_ν is the velocity of electron after the collision $k_\nu=\sqrt{k_\mu^2\mp2\varepsilon_{\mu\nu}}$ (the double sign corresponds to excitation and de-excitation). l is the order of spherical waves into which the incident wave function of the free electron are decomposed, and l is equal to l or $l\pm2$ for the transition (12), (23), and to l for the transition (13). The summation for l extends from 0 to infinity. $V_{\mu\nu}(l,l')$ is expressed as the quadratic form of

$$\left.\begin{aligned}Q_n&=\int_0^{\infty}\int\frac{r_<^{\,n}}{r_>^{\,n+1}} \\ &\qquad\times P_\mu(r_1)P_\nu(r_1)y(k_\mu l|r_2)y(k_\nu l'|r_2)dr_1dr_2 \\ \text{and}& \\ R_n&=\int_0^{\infty}\int\frac{r_<^{\,n}}{r_>^{\,n+1}} \\ &\qquad\times P_\nu(r_1)y(k_\mu l|r_1)P_\mu(r_2)y(k_\nu l'|r_2)dr_1dr_2\,,\end{aligned}\right\}\quad(3)$$

the explicit of forms of which will be given later. $f(kl|r)=y(kl|r)/r$ is the radial component of l-th spherical wave of free electron with the velocity k, and $f_\mu(r)=P_\mu(r)/r$ is the radial part of the orbital function of the $2p$ electron belonging to the oxygen atom in the state μ. $r_<$ and $r_>$ are the smaller and the larger of r_1 and r_2. As already mentioned, it is sufficient to find the numerical values of Q_n and R_n for the critical values of energy.

We shall omit here the detailed description of the method of determining the function $y(kl|r)$. In short, it is determined by the numerical integration of the Schrödinger equation of the electron moving in the average field of the oxygen atom, which is calculated for each state 1, 2, 3, using the Fock's function(4). The results show that the difference due to the small change of the energy of incident electron is negligible in the range of r, which makes the main contribution to the integral Q_n and R_n. Moreover, when the energy of the electron is small, we have to retain only few terms in the series (2). Therefore, we have taken the following nine functions for the subsequent calculations. (These are specified by s, p, d for $l=0$, 1, 2, according to the usual notations).

ϵ	^3P	^1D	^1S
0	—	s, p	s, p
ϵ_{12}	p, d	—	—
ϵ_{13}	p	—	—
ϵ_{23}	—	p, d	—

These numerically integrated wave functions are not however normalized, and will be distinguished by the accents: $y'(kl|r)$. $y(kl|r)$ in (2) is obtained by nomalizing them so as to take the asymptotic form: $\sin(kr-l\pi/2+\delta_l)/kr$ at the infinity. The normalizing factors β, defined by $y(kl|r)=\beta y'(kl|r)$, are as follows:

ϵ	ϵ_{12}		ϵ_{13}		ϵ_{23}	
μ	^3P		^3P		^1D	
	p	7.64	p	14.4	p	8.66
	d	0.0523			d	0.0597

For $k\to 0$, the normalizing factor γ_l is obtained from⁽⁵⁾

$$\gamma=1/\{1.3\ldots(2l+1)A\},$$

where A is determined by the equation:

$$y'(kl|r)=Ar^{l+1}+B/r^l,$$

for the value of r for which the field due to the atom vanishes practically. The numerical values of γ are a follows:

	s	p
^1D	14.0	16.0
^1S	13.6	17.0

Thus, if we retain only the powers of k arising in the normalizing factor for $k\to 0$ among the factors depending on ϵ in $V_{\mu\nu}(l, l')$, we have

$$V_{ij}(l, l')=k_j^{2l'}P_{ij}(l, l'),$$
$$V_{ji}(l, l')=k_j^{2l}P_{ij}(l, l'),$$

where

$$\left.\begin{aligned}P_{ij}(l, l')&=\alpha_{ij}(l, l')V_{ij}'(l, l')=P_{ij}(l', l),\\ \alpha_{ij}(l, l')&=\beta_l^2\gamma_{l'}^2=\alpha_{ji}(l', l),\end{aligned}\right\}\qquad(4)$$

and $V_{ij}'(l, l')$ means that Q_n and R_n are calculated by $y'(kl|r)$. The numerical values of $\alpha_{ij}(l, l')$ are given below:

i	j	l	l'	$\alpha_{ij}(l, l')$
^3P	^1D	p	p	14980
		d	s	0.533
^3P	^1D	p	p	60100
^1D	^1S	p	d	21800
		d	s	0.658

We obtain, by (2),

$$w_{ij}(\epsilon)=\frac{16\pi}{g_i}\sum P_{ij}(l, l')k_j^{2l'+1},$$
$$w_{ji}(\epsilon)=\frac{16\pi k_i}{g_j}\sum P_{ji}(l, l')k_j^{2l}.$$

§ 4. Expressions for Excitation and De excitation.

By performing the integrals (1) for

$$\epsilon=\epsilon_{ij}+k_j^2/2,\qquad\text{(excitation)}$$
$$k_j^2/2=\epsilon,\ k_i^2/2=\epsilon_{ij}\quad\text{(di-excitation)}$$

we find, from the formulae of Γ-function,

$$\left.\begin{aligned}W_{ij}&=\frac{16\pi}{g_i}k_{ij}\exp(-\epsilon_{ij}/\kappa T)\sum 1.3\ldots\\ &\qquad\times(2l+1)(\kappa T)^{l'}P_{ij}(l, l'),\\ W_{ji}&=\frac{1}{g_j}W_{ij}\exp(\epsilon_{ij}/\kappa T),\end{aligned}\right\}\qquad(5$$

which are expressed in the following forms

$$W_{ij}=U_{ij}\exp(-\epsilon_{ij}/\kappa T)/g_i,\quad W_{ji}=U_{ij}/g_j,\qquad(6$$

by putting

$$U_{ij}=16\pi k_{ij}\sum_{l,l'}1.3\ldots(2l'+1)(\kappa T)^{l'}P_{ij}(l, l').$$

Substituting the numerical values in these expres sion, we obtain

$$\begin{aligned}U_{12}&=10.15V_{12}'(ds)+2.71V_{12}'(pp)T,\\ U_{13}&=15.9V_{13}'(pp)T,\\ U_{23}&=18.4V_{23}'(ds)+4.20V_{23}'(pp)T.\end{aligned}\qquad(7$$

The expressions of $V_{ij}'(l, l')$ are as follows⁽²⁾

$$\left.\begin{aligned}V_{12}'(ps)&=3R_1'^2/2,\\ V_{12}'(pp)&=15(R_0'^2-R_0'R_2'/25+7R_2'^2/625),\\ V_{13}'(pp)&=3(R_0'-R_2'/5)^2,\\ V_{23}'(ds)&=2(2Q_2'/5-R_1'/3)^2,\\ V_{23}'(pp)&=24(2Q_2'/5-5R_0'/6-R_2'/30)^2/25\\ &\quad+(R_0'-R_2'/5)^2.\end{aligned}\right\}\qquad(8$$

The accents in Q_n and R_n mean that they ar calculated by $y'(kl|r)$. These integrals were eve luated numerically for small values of r, and ar alytically for large values of r. In the latter, we employed $P(r)=C_{\mu}\exp(-\alpha_{\mu}r)$ for the orbital functions, and the expressions of spherical waves of perfectly free electron for $y'(kl/r)$. The numerical values are:

$^3P\to{}^1D$ $R_1'(ds)=-0.0426$,
$R_0'(pp)=0.0177$, $R_2'(pp)=0.00694$;
$^3P\to{}^1S$ $R_0'(pp)=0.0147$, $R_2'(pp)=0.00578$;
$^1D\to{}^1S$ $Q_2'(ds)=0.414$, $R_1'(ds)=-0.0663$,
$Q_2'(pp)=0.0160$,
$R_0'(pp)=0.0174$, $R_2'(pp)=0.00680$.

Putting these values in (7) and (8), we obtain the following results:

$$\left.\begin{aligned}U_{12}&=0.0277+0.0156T,\\ U_{13}&=0.0088T,\\ U_{23}&=0.942\ +0.00137T,\end{aligned}\right\}\qquad(9)$$

which in ordinary cgs units are given by

$$\left.\begin{aligned}U_{12}&=\ 1.70+0.77\ T,\\ U_{13}&=\ 0.54T,\\ U_{23}&=57.7\ +0.084T,\end{aligned}\right\}\times10^{-10}\ (\mathrm{cm}^3\ \mathrm{sec}^{-1})\qquad(10)$$

The probabilities of excitation and de-excitation are then found by (6).

References.

(1) T. Yamanouchi, T. Inui and A. Amemiya, Proc. Phys.-Math. Soc. Japan, **22** (1940), 847.

(2) T. Yamanouchi and M. Kotani. Proc. Phys.-Math. Soc. Japan, **22** (1940), 14; T. Yamanouchi and M. Mashiko, Journ. Phys.-Math. Soc. Japan, **17** (1943), 581 (in Japanese).

(3) T. Yamanouchi and M. Kotani, Proc. Phys.-Math. Soc. Japan, **22** (1940), 60; T. Yamanouchi, ibid. **22** (1940), 569-

(4) D. R. Hartree, W. Hartree and B. Swirles, Phil. Trans. **238** (1939), 229.

(5) T. Yamanouchi, Journ. Phys.-Math. Soc. Japan, (1943), 5 (in Japanese).

On Experimental Methods of the Investigation of Turbulent Flow, I.

By Yutaka SHIGEMITSU.

Railway Technical Research Institute.

(Read July 23, 1949; Received Sept. 12, 1949).

Summary of Parts I–II.

This paper deals with experimental methods used for the study of turbulent flow in our laboratory. They are derived particularly for the investigation of non-isotropic turbulence in a wind tunnel experiment. We show methods of measuring u'-, v'-fluctuation, and $u'v'$-correlation coefficient, including the mean velocity of flow, by a hot-wire anemometer: which is particularly suitable for measuring in a small space of flow as the turbulent boundary layer. Concerning these methods, theoretical discussions and their experimental examinations are given, and as an example of the measurement, experimental results on turbulent boundary layer are shown.

§ 1. Introduction.

In the investigation of turbulent phenomena in fluid motion, the case of flow of so-called "isotropic turbulence" has been studied particularly in detail. Since G. I. Taylor had proposed his theory of isotropic turbulence, Th. von Kármán and many other investigators have developed theoretical aspects of this theory, and as experimental researches on it H. L. Dryden and others have made many contributions. He is the first who has found the method of compensation of the time lag of a hot-wire anemometer, and has developed the method of measuring the intensity of u'-

fluctuation, the scale of turbulence, and other important quantities concerning this theory.

On the other hand, in the case of "non-isotropic turbulence", we find many practically important problems to be solved in engineering, such as the turbulent boundary layer, the wake, and others. To study these problems and contribute to the theory of surface friction or heat tranfer in turbulent flow, it is fundamentally important to investigate, at first, the mechanism of non-isotropic turbulent flow. Since the transfer theory had been proposed, the momentum- or the vorticity-transfer theory has been developed, but concerning the mechanism of the turbulent flow of this type, we have few detailed knowledge in comparison with the case of "isotropic turbulence". It is because partly of the complicated charactor of this type of flow, and partly of the lack of an appropriate technique to measure the quantities which are necessary to construct the theory in this case.

When we take two dimensional flow of non-isotropic turbulence, at least the quantities of u', v', and $u'v'$ come to be necessary besides the mean velocity. The method of measuring u'-fluctuation by a hot-wire anemometer, has long been established and contributed greatly to the theory of "isotropic turbulence". As for the measurement of the intensity of v'-fluctuation, the method of heat diffusion has generally been used in isotropic turbulent flow. But in the case of non-isotropic turbulence, we know few methods of measurement. It is reported that H. Reichardt[1] measured with his "Dreidrahtsonde", v'-fluctuation and $u'v'$-correlation in turbulent channel flow. However, it seems that this method is not yet proper in the measurement in small space as in the turbulent boundary layer, and its theoretical discussions are inadequate.

As one of the methods of measurement of u'-fluctuation, there has been proposed the "constant resistance method". At first, the author gave more general theoretical ground on this method, and then taking it on foundation, has developed the measurement of v'-fluctuation or $u'v'$-correlation, which is preferable to be used in turbulent boundary layer. Thus, we will show these methods, including those of u'-fuctuation an mean velocity, and discuss from more genera theoretical point of view.

§ 2. Symbols.

The following symbols will be used in this paper:

x, y, z = three orthogonal coordinates, z-axis being taken parallel to the hot-wire

t = time.

V, θ, φ = three components of an instantaneous value of wind velocity in polar coordinates.

$\bar{V}$, V' = mean and fluctuational value of V.

$\bar{\theta}$, θ' = mean and fluctuational value of θ.

$\bar{\varphi}$, φ' = mean and fluctuational value of φ.

u, $\bar{u}$, u' = instantaneous, mean, and fluctuational value of the x-component of wind velocity.

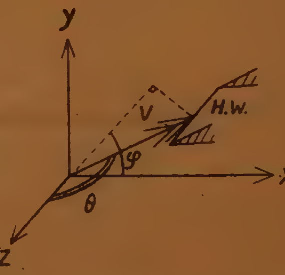

Fig. 1. Position of the hot-wire and wind direction.

v, $\bar{v}$, v' = instantaneous, mean, and fluctuational value of the y-component of wind velocity.

H = heat energy in the hot wire.

i_0 = electric current through the hot-wire to keep its mean resistance $\bar{R}$ equal to that of one arm of the Wheatstone's bridge in still air.

i = electric current through the hot-wire to keep its mean resistance $\bar{R}$ equal to that of one arm of the Wheatstone's bridge in a wind of velocity of (V, θ, φ).

I = electric current through the Wheatstone's bridge circuit ($I = 2i$).

T_0 = room temperature.

T = instantaneous temperature of the hot-wire when heated by the current i in a wind of velocity of (V, θ, φ).

R_0 = electric resistance of the hot-wire at temperature T_0.

R = instantaneous resistance of the hot-wire when heated by the current i in a wind of velocity of (V, θ, φ).

$\bar{R}$ = mean value of the above resistance R, and it is taken as constant, which is equal to that of one arm of the Wheatstone's bridge.

R' = fluctuational value of the above resistance R.

m = mass of the hot-wire.

s = specific heat of the hot-wire.

α = temperature coefficient of the resistance of the hot-wire.

M_0 = time constant of the hot-wire in still air.

M = time constant of the hot-wire in a wind of mean velocity $\bar{V}$.

§ 3. General Equation of Cooling of the Hot-Wire and the Measurement of Mean Velocity.

The general equation of cooling of the hot-wire in a three dimensional flow, is as follows;

$$\frac{dH}{dt} = i^2R - f(V, \theta, \varphi)(T - T_0), \qquad (3,1)$$

where in the right side, the first term is the Joule's heat in the hot-wire and the second is the heat loss from the wire to the flow. By the definitions,

$$H = 4{,}2msT,$$

and

$$T - T_0 = (R - R_0)/(R_0\alpha),$$

so, we can get the following equation

$$\frac{4{,}2ms}{R_0\alpha}\frac{dR}{dt} = i^2R - f(V, \theta, \varphi)\frac{R - R_0}{R_0\alpha}. \qquad (3,2)$$

This is the governing equation of the measurement of a hot-wire anemometer.

At first, we discuss the case in which all the fluctuational components of wind velocity are neglected, and an equilibrium of the heat exchange from the wire to the flow is kept. Then we obtain.

$$i^2\bar{R} = f(\bar{V}, \bar{\theta}, \bar{\varphi})(\bar{R} - R_0)/(R_0\alpha). \qquad (3,3)$$

when we make the wind direction parallel to the x-axis, (3,3) becomes.

$$i^2\bar{R} = f(\bar{V})(\bar{R} - R_0)/(R_0\alpha). \qquad (3,4)$$

In this case, $\bar{V}$ is generally expressed by a function of i and $\bar{R}$, but, for brevity, taking $\bar{R}$ constant, we can express $\bar{V}$ by a function of i only, thuse we take the "constant resistance method" in this paper. In (3, 4) King[2]) derived theoretically the form

$$f(\bar{V}) = K_1 + K_2\sqrt{\bar{V}} \qquad (3,5)$$

and the with (3, 4), we can get the following relation

$$I^2 = k_1 + k_2\sqrt{\bar{V}} \qquad (3,6)$$

where

$$k_1 = \frac{4(\bar{R} - R_0)}{\bar{R}R_0\alpha}K_1 \quad , k_2 = \frac{4(\bar{R} - R_0)}{\bar{R}R_0\alpha}K_2 .$$

When we connect the wire to an arm of a Wheatstone's bridge and keep its resistance $\bar{R}$ constaut as in Fig. 2, then by measuring the values of $\bar{V}$ and the total current I through the circuit $(I = 2i)$, we can derive these relation experimentally. Fig. 3 shows an example of this relation, and we recognize a good agreement of (3,6) with experimental data in the region of $\bar{V}$ above 5 m/s. With this calibration curve, we can measure unknown wind speed $\bar{V}$ by the value of I.

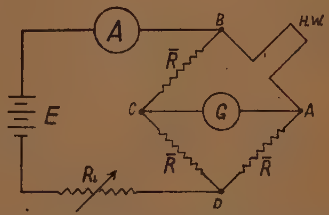

Fig. 2. The Wheatstone's bridge circuit in "constant resistance method."

In the isothermal flow of constant mean speed, if we change the relative direction of wind in the z, x-plane and keep an equlilibrium of its heat exchange, we get from (3,3).

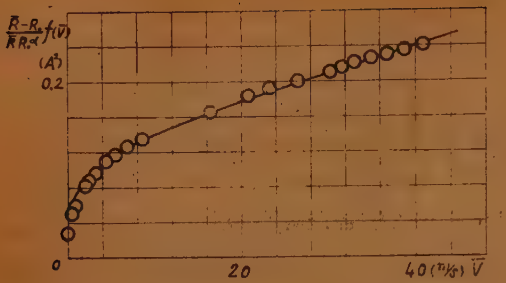

Fig. 3. A calibration curve of $f(\bar V)(\bar\theta =$ 90°, $\bar\varphi = 0°$) of a hot-wire. (It is a Nickel line of dia., 0,025 mm.) ○-points of measurement. Curve-theoretical form of (3,4).

$$i^2\bar R = f(\bar\theta)\bar R(\bar R - R_0)/(R_0\alpha), \qquad (3,7)$$

where all the fluctuations are neglected. So, by the "constant resistance method" as in Fig. 2, we can get a relation between $\bar\theta$ and I. Fig. 4 shows an experimental curve of this relation. Using this curve, we can easily measure the wind direction of $\bar\theta$.

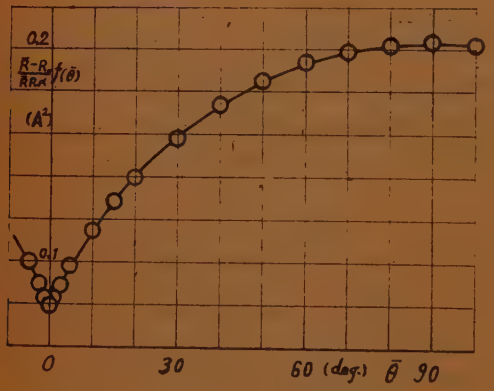

Fig. 4. A calculation curve of $f(\bar\theta)(\bar\varphi = 0$, $\bar V = 27$ m/s). (The wire is the same as that in Fig. 3).

As a direction-meter, there have been proposed many other methods: as an example, we take the following type of Thomas[3], and Baily[4]. It consists of two wires, each perpendicular to the x, y-plane. When we change the direction of wind in x, y-plane, the wire lying behind gets the effect of the heat wake of the front, and so the relation

$$i^2\bar R = f(\bar\varphi)(\bar R - R_0)/(R_0\alpha), \qquad (3,8)$$

holds for this wire in a flow of a constant mean speed. Thus in the "constant resistance method", we can get the relation between $\bar\varphi$ and I. Fig. 5 is an example of this experiment. This mthode is complicated as the direction-meter of the mean velocity, but as we describe later, it is useful when we measure v'-fluctuation of non-isotropic turbulent flow.

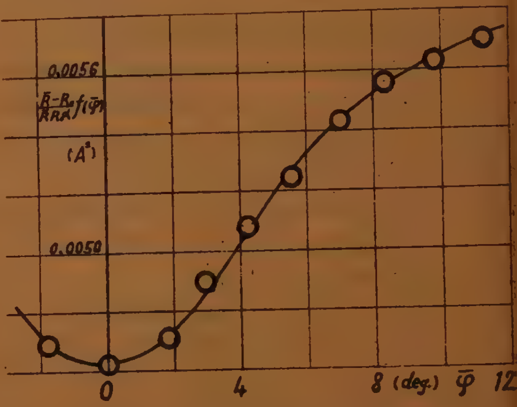

Fig. 5. A calibration curve of $f(\bar\varphi)(\bar\theta =$ 90°, $V = 14$m/s). (The wire is a Nickel line of dia., 0,007 mm.)

§ 4. Time Lag of the Hot-Wire.

As we proceed to measure fluctuations of the velocity of a fluid, the problem of the time lag of the wire occurs. It has previously been investigated by many writers in detail, and so in our method we show it briefly.

In the "constant resistance method" as shown in Fig. 2, when the flow constains fluctuations of the velocity, then the resistance R of the wire fluctuates correspondingly (then the current i through the wire comes to variate, but if we make $R_h \gg \bar R$, this variation can be neglected compared with that of the resistance R); when a velocity of turbulent flow is given by

$$V = \bar V + V', \ \theta = \bar\theta + \theta', \ \varphi = \bar\varphi + \varphi',$$

then the resistance is written correspondingly by

$$R = \bar R + R'.$$

When these are put in the fundamental equation (3,2), a condition of the equilibrium of the wire at the mean velocity is used, and the terms containing more than second order of fluctuations are neglected, then we get

$$M\frac{dR'}{dt} + R' = c_1 V' + c_2\theta' + c_3\varphi', \qquad (4,1)$$

where

$$M = \frac{A{,}2\, ms(\bar{R}-R_0)}{R_0{}^2 i^2 \alpha}, \tag{4,2}$$

$$c_1 = -\frac{(\bar{R}-R_0)^2}{R_0{}^2 i^2 \alpha}\left(\frac{\partial f}{\partial \bar{V}}\right)$$

$$c_2 = -\frac{(\bar{R}-R_0)^2}{R_0{}^2 i^2 \alpha}\left(\frac{\partial f}{\partial \bar{\theta}}\right) \tag{4,3}$$

$$c_3 = -\frac{(\bar{R}-R_0)^2}{R_0{}^2 i^2 \alpha}\left(\frac{\partial f}{\partial \bar{\varphi}}\right).$$

(4,1) is the fundamental equation of measuring velocity fluctuations by a hot-wire anemometer.

In three dimensional isothermal flow of turbulence, if the mean direction of wind is made parallel to the x-axis, the function $f(V,\ \theta,\ \varphi)$ is independent on φ, and by Fig. 4, $\left(\frac{\partial f}{\partial \theta}\right)_{90^\circ} = 0$, so c_2 and c_3 in (4,3) vanish and (4,1) becomes

$$M\frac{d\bar{R}}{dt} + R' = c_1 V'. \tag{4,4}$$

To formulate the relation between R' and V', we express V' and R' with a Fourier series of t respectively as

$$V' = \sum_n (a_n \cos \omega_n t + b_n \sin \omega_n t)$$

$$R' = \sum_n (c_n \cos \omega_n t + d_n \sin \omega_n t),$$

and put in (4,4), then we get the followings;

$$R' = \sum_n \frac{c_1}{\sqrt{(1+M^2\omega_n{}^2)}}\{a_n \cos(\omega_n t - \tau) + b_n \sin(\omega_n t - \tau)\}, \tag{4,5}$$

$$\tau = \tan^{-1}(M\omega_n).$$

Namely, in the above arrangement, when a turbulent fluctuation is given arbitrarily, the fluctuation of R' depends only on V'-component, and reduced in the ratio of

$$|c_1|/\sqrt{1+M^2\omega_n{}^2}$$

in amplitude, and retarded by the amount of

$$\tan^{-1}(M\omega_n)$$

in phase. Thus as for the intensity of these fluctuations, we get

$$\sqrt{\overline{R'^2}} = \frac{|c_1|}{\sqrt{(1+M^2\omega_n{}^2)}}\sqrt{\overline{V'^2}}. \tag{4,6}$$

It is generally called as the time lag of the wire, and M is called as the time constant of the wire. In the "constant resistance method", the value of M of a wire depends only on i, and by (4,2) we get the relation

$$M = M_0 \frac{I_0{}^2}{I^2}. \tag{4,7}$$

§ 5. Amplifier Used for Measuring Turbulent Fluctuations.

To measure turbulent fluctuation using a hot-wire, we need a valve amplifier, for the purpose of amplifying small voltage which is caused by this fluctuation, and compensating the time lag of the wire. Fig. 6 shows its diagram.

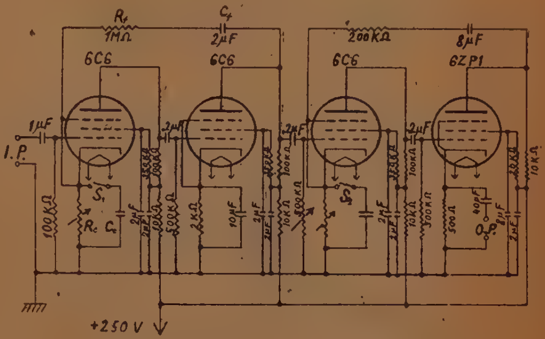

Fig. 6. Wiring diagram of the amplifier.

To compensate the time lag of the wire, we use the circuit of negative feed back. According to the theory of negative feed back, if A_f and β are taken as the amplitude and the ratio of the feed back,

$$A_f \doteqdot 1/\beta. \tag{5,1}$$

In the circuit of negative feed back of the first two stages in Fig. 6, when R_f, C_f, and Z_c are taken respectively as feed back resistance, its capacitance, and cathode impedance, we get

$$\beta = Z_c\Big/\left(R_f + \frac{1}{j\omega_n C_f} + Z_c\right).$$

However, in this circuit,

$$|R_f| \gg |1/(j\omega_n C_f)|,\ |Z_c|,$$

so we have

$$A_f \doteqdot R_f/Z_c.$$

Thus, when we shut the switch S_1 of the compensating circuit in the figure,

$$A_f \doteqdot \frac{R_f}{R_c}(1 + jR_c C_c \omega_n), \tag{5,2}$$

where R_c and C_c are cathode resistance and capacitance. So alternating voltage at the in-put is amplified in the ratio of

$$\sqrt{1+(R_cC_c)^2\omega_n^2}$$

in amplitude, and accelerated in the ratio of

$$\tan^{-1}(R_cC_c\omega_n)$$

in phase. Then if we choose R_cC_c, the constant of compensation, equal to the time constant M of the wire, the time lag can be compensated in amplitude and in phase. (When the above circuit gives inadequate compensation, we can also use the next feed back circuit.) Fig. 7 shows the frequency characteristics of the amplifier.

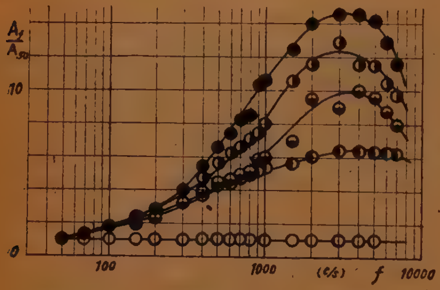

Fig. 7. Frequency characteristics of the amplifier. ●; $R_cC_c = 2{,}0\times10^{-3}$, ◑; $R_cC_c = 1{,}5\times10^{-3}$, ◒; $R_cC_c = 1{,}0\times10^{-3}$, ◐; $R_cC_c = 0{,}5\times10^{-3}$, ○; $R_cC_c = 0$.

§ 6. Compensation of Time Lag of the Wire.

When the fluctuations of a turbulent flow are measured, we must find the value of M of the wire and compensate it. At first, we show the relationship between R' and the fluctuating voltage e_G' between A and C in Fig. 2. Taking that the resistance of the wire changes in its value from $\bar{R}$ to $\bar{R}+R'$, the current i_G between AC (this resistance is shown by R_G) can be given by Kirchhoff's law;

$$i_G = \frac{\bar{R}^2-(\bar{R}+R')\bar{R}}{\varDelta}E, \tag{6,1}$$

where

$$\varDelta = \begin{vmatrix} 2\bar{R}+R'+R_G, & 2\bar{R}+R', & -\bar{R}, \\ 2\bar{R}+R', & 4\bar{R}+R', & -2\bar{R}, \\ -\bar{R}, & -2\bar{R}, & 2\bar{R}+R_b, \end{vmatrix}.$$

If the term containing R' are neglected in $\varDelta$, we get

$$i_G = -\frac{R'}{4(\bar{R}+R_G)(\bar{R}+R_b)}E.$$

But as $R_G \gg \bar{R}$, it becomes

$$i_G = \frac{I}{4}\frac{R'}{R_G}.$$

And so, when the resistance of the wire R variates in its value about the mean value $\bar{R}$, the intensity of the fluctuating voltage e_G' between AC, can be written as

$$\sqrt{\overline{e'_G{}^2}} = \frac{I}{4}\sqrt{\overline{R'^2}}. \tag{6,2}$$

To determine the value of M_0 of the wire, we first make the mean resistance equal to $\bar{R}$ of that of the bridge in still air (cf. Fig. 2), and add constant alternating current with a known frequency between BD, then the wire receives the same effect as it is cooled by the flow with a fluctuation of this frequency. So, if the fluctuating voltage e_G' of this case is amplified with an uncompensated amplifier, the out-put value I_0 must be shown as

$$I_0 \backsim 1/\sqrt{1+M_0^2\omega_n^2}.$$

With the above relation, we can determine the value of M_0. Fig. 8. shows examples of this relation. Then the value of M in a flow is given by (4,7). Thus we can determine the value of R_cC_c equal to this value and compensate the time

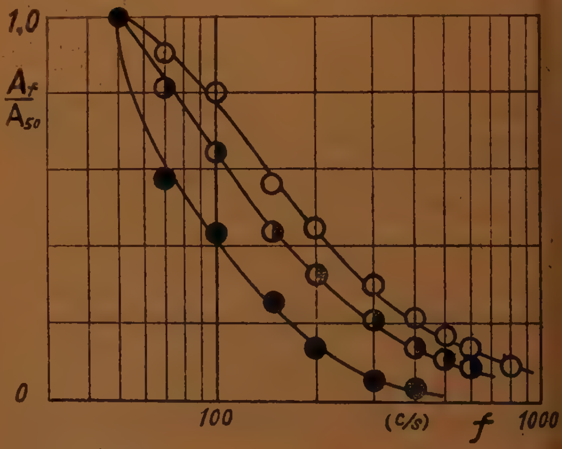

Fig. 8. Frequency characteristics of the uncompensated amplifier with hot-wires. ○; 0,010 mm Nickel, ◑; 0,015 mm Pt., ●; 0,030 mm Nickel.

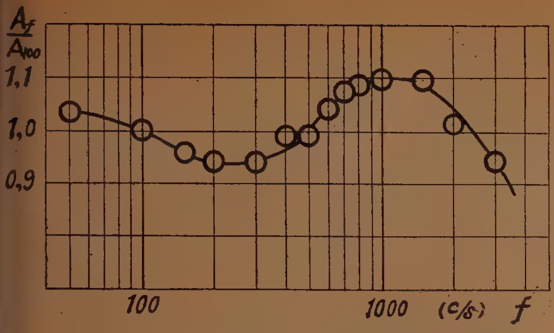

Fig. 9. Frequency characteristics of the compensated amplifier with a hot-wire (Nickel of dia., 0,010 mm).

lag of the wire in a turbulent flow, in its amplitude and phase. Fig. 9 shows an example of a frequency characteristics of the compensated amplifier with a hot-wire.

References.

(1) Reichardt, H.: Z. A. M. M. Bd. 18, 1938.
(2) King, L. V.: Phil. Trans. Roy. Soc., London A 214, 1914.
(3) Thomas, J. S. G.: Phil. Mag., 41. 1921.
(4) Baily, A.: A. R. C. Reports and Memoranda, No. 777, 1921.

On the Thoria Coated Cathode.

By Tetsuya ARIZUMI and Leona ESAKI.

Kobe Kogyo Corp.*

(Received, July 20, 1949).

§ 1. Introduction.

The stable cathode for large pulse current is indispensable in some kinds of transmitting tubes. The thoria coated cathode seems to be considerably promising for this purpose, but little has been known up to the present time. The authors have studied several thermionic properties of this cathode and found that the cathode becomes black and its emission increases very much, when it is activated at a high temperature or it is carburized. In this paper the activation of the cathode, its thermionic constants, effect of oxygen and the decay of emission shall be described together with their theories.

§ 2. Experimental Apparatus.

Several procedures are available for the preparation of the cathode without any difference in the thermionic properties, but the cataphoresis in lyophilic colloid is convenient for obtaining an uniform tight coating. Some amount of thoria powder, prepared by decomposing pure thorium nitrate in the hydrogen furnace at 800°C is suspended in the colloidal solution of nitrocellulose in buthyl acetate. The tungsten wire used as the cathode was coated in this lyophilic colloid in which thoria moves towards the positive electrode. The coating thickness of about 50 microns is most favourable.

The experimental tube is shown in Fig. 1 schematically. In the chamber (1) a batalum getter

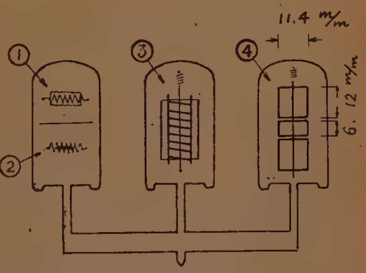

Fig. 1.
Schematic Diagram of Experimental Tube
(1) Batalum Getter
(2) Oxygen Source
(3) Ionization Gauge
(4) Diode for Studies

---

* Formerly, *Kawanishi Kikai Seisakusho, Ltd.*

is mounted and a small amount of cuprous oxide folded by tungsten coil in the chamber (2) is used as an oxygen source. The chamber (3) is a very sensitive and stable ionization gauge with a thoria coated cathode. The last one is a diode, conventional for thermionic studies, being composed of the thoria coated cathode of 0.129 mm tungsten wire, two auxiliary anodes and a central main anode.

Each tube was thoroughly evacuated on a three stage oil diffusion pump for several hours and then sealed off at a pressure of 10^{-6} mm Hg. During evacuation barium carbonate on batalum getter was decomposed into oxide, all metal parts were treated by H. F. bombarder, glass parts were baked above 300°C and the cathode was flashed at 2,500°K.

§ 3. Experimental Procedure.

The thermionic emission was measured by a galvanometer with the sensitivity of 10^{-7} ampere per one division and the period of 7.5 secs. Except the studies on effect of oxygen all experiments were carried out at the pressure below 10^{-7} mm Hg. For studying the effect of oxygen, it is required to control the oxygen pressure, which was made possible by the alternation of heating the folded cuprous oxide and flashing the batalum getter.

The temperature of the cathode was measured by a micro-optical pyrometer. For the normal white cathode Hanley's(2) empirical relation between true and brightness temperatures was available, but for carburized and gray cathodes, temperatures are not so rigorous, because the emissivility was assumed to be almost equal to that of carbon in the case of the carburized cathode and modified Hanley's relation is applied to the gray one.

For the carburization, the similar method as used for thoriated tungsten was followed; the cathode was heated in naphtalene vapour to give twenty percent increase of resistance at room temperature. The surface of the carburized cathode looks as the aggregation of charcoal particles.

§ 4. Experimental Results and Discussions.

(1) Activation

The activation of the cathode was carried out only by heating at some temperature between 2,000°K and 2,200°K, for about a quarter of an hour with the emission current being drawn. The colour of the activated cathode is white (the white cathode in the following). If the cathode is heated at a temperature beyond 2,500°K for several mins. or more, the colour becomes black, (the gray cathode). At a constant temperature it takes longer time to activate the cathode with thick coating than with thin coating, while the activation of the carburized cathode is much easier. These several results show that the activation is no more than the process of reducing some amount of thoria to metallic thorium by tungsten itself or carbon. When the gray cathode at lighting is exposed to the oxygen atomsphere, it turns out to white suggesting that the cathode differs from the mono-molecular layer one such as the thoriated tungsten. The emissions of the gray and carburized cathodes are much larger than that of the white cathode, perhaps because the emission depends upon the concentration of impurity thorium in thoria, similarly as in the case of alkaline earth oxide coated cathode. Differing from the latter, however, the thoria coated cathode is not poisoned substantially and is able to be activated completely, even if it is exposed to air on way of activation, perhaps because the reduced thorium is quite stable in the atmosphere. Thus no technical difficulties have been encountered in any experimental tube.

(2) Work function

For determining the thermionic emission at zero field, the variation of the emission current with applied potential are plotted in Fig. 2, in which full lines are those of the carburized cathode and dotted lines those of the gray cathode. In the carburized cathode the emission current increases very steeply with anode potential far different from theoretical Schottky lines, while in the white cathode the i-E relationship is almost similar as the fully activated thoriated tungsten. Such departure from the theoretical Schottky curve may well be understood by the patch effect, proposed by Becker(3).

Richardson lines plotted from emission currents at zero field are shown in Fig. 3 and obtained work

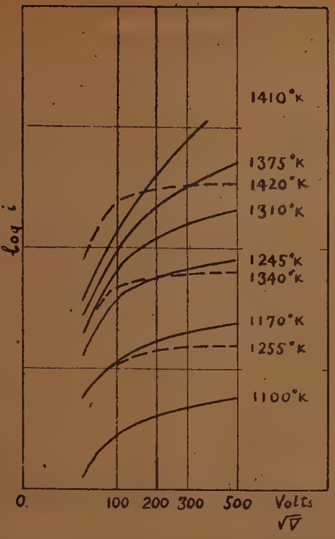

Fig. 2. log i versus $\sqrt{V}$
The full line corresponds to the carburized. The dotted line corresponds to the gray.

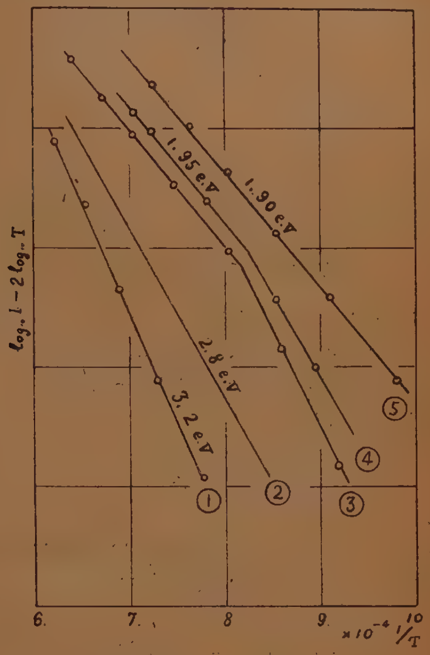

Fig. 3. Richardson Plots.
(1) The white
(2) Thoriated Tungsten
(3) (4) The gray
(5) The carburized

Table I. Thermionic constants of the thoria coated cathode.

Kind of Cathode	White cathode	Gray cathode		Carburized	Thoriated tungsten
Temperature range (°K)	1200–1600	less than 1,200	higher than 1,200	1,000–1,400	1,200–1,600
Work function (e. v.) Richardson constant (A/deg^2 cm^2)	3.2 5	3.2	1.95 1×10^{-2}	1.9 2×10^{-2}	2.8 5

function and Richardson constants are summerized in Table I, together with those of the fully activated thoriated tungsten. It is of great importance that the Richardson line for the gray cathode has a sharp discontinuity at about 1,200°K and above this temperature the work function is almost equal to that of the carburized one, while below this temperature it is almost equal to that of the white cathode. A similar discontinuity was observed in the case of the alkaline earth oxide coated cathode by one of the authors(4). Quite similarly as for this cathode, the emission current of the thoria coated one is probably represented by

$$i = An_0^{\frac{1}{2}}\mathrm{T}^{\frac{5}{4}} \exp\left\{-\frac{e}{kT}\left(\frac{E}{2}+V\right)\right\}^* \qquad (1)$$

in the higher temperature range, while in the lower temperature range it is given by

$$i = A'n_0T^2 \exp\left\{-\frac{e}{kT}(E+V)\right\} \qquad (2)$$

The abnormally small Richardson constants may well be understood in the similar way as for the alkaline earth oxide coated cathode.(4) (5)

(3) Effect of oxygen.

The emission of the gray cathode is very sensitive to the oxygen pressure. Even at the pressure of 10^{-7} mm Hg., the emission at a constant cathode temperature increases slightly for a while and then it begins to decrease as shown in Fig. 4. The inclination of $d(\log i)/dt$ becomes steeper as either the temperature or the pressure is higher. The time change of the emission at a constant pressure is shown in Fig. 4 as an example.

---

* Customary notations are used.

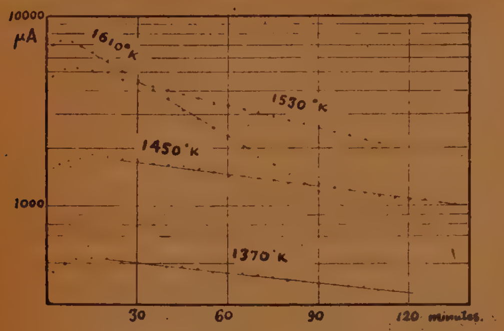

Fig. 4. log i versus time.

Probably the recombination of excess thorium and oxygen is responsible to this phenomena. If n_1 is the density of excess thorium atoms, the differential equation

$$-\frac{dn}{dt}=knp \qquad (3)$$

holds at a constant cathode temperature. The equation (3) is written in the form

$$-\frac{d}{dt}(\log i)=\frac{1}{2}kp \qquad (4)$$

making use of (1) in agreement with the experimental results shown in Fig. 5. In the equation (3), k is the constant of reaction, dependent upon the temperature T and it is represented by

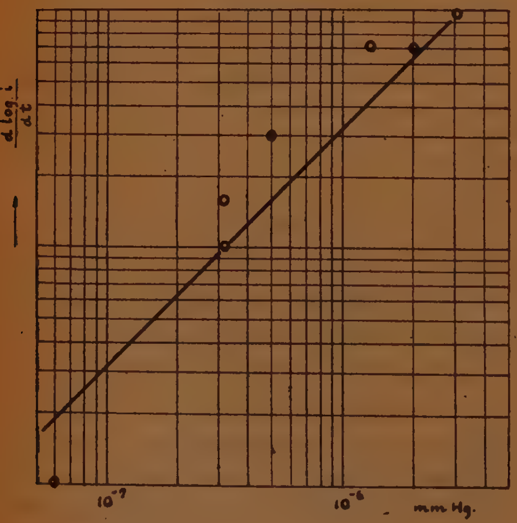

Fig. 5. $\frac{d}{dt}(\log i)$ versus pressure.

$$k=k_0\exp\left(-\frac{Q}{RT}\right) \qquad (5)$$

As seen in Fig. 6, log k is almost linear with $1/T$, giving the combination energy about 1.2 ev.

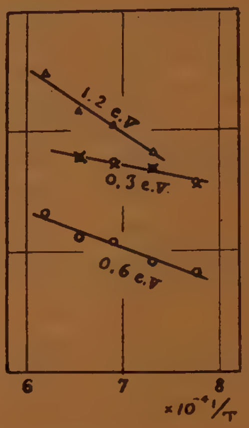

Fig. 6. log (various values) versus $1/T$
The upper triangle : Combination energy
The middle circle : Diffusion energy
from decay
Cross : from recovery
The lower circle : Depth of conduction band

The emissions of the white and carburized cathodes are almost independent of the oxygen pressure. In the white cathode, such time change of the emission as experienced in the gray one is not observed, as far as the emission current is continuously drawn and the cathode temperature is kept above 1,700°K. Fig. 7 gives an example. Even when the pressure is increased from 3×10^{-7} mm Hg to 3.5×10^{-5} mm Hg, step by step,

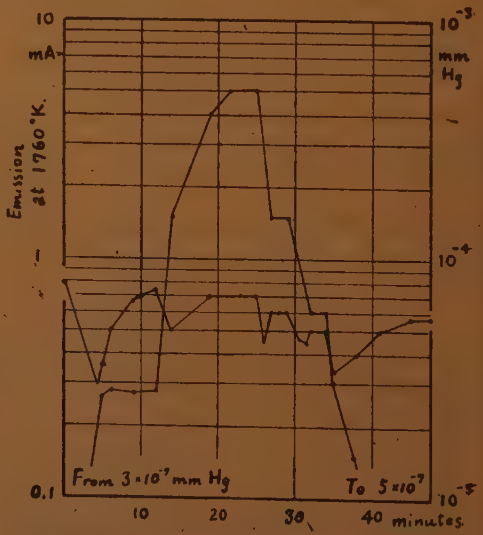

Fig. 7. The relation of oxygen pressure and emission.

the emission decreases just at the pressure change, but recovers gradually to the almost original value after a while. The similar changes of emission are observed when the oxygen is evacuated again. On the other hand the emission decreases monotonously when no potential is applied on the anodes. Both phenomena suggest that the electrolytic activation seems to be fairly effective above 1,700°K.

The emission of the carburized cathode falls down to one third or fourth at 1,400°K without the anode potential, when the pressure changes from 10^{-7} mm Hg to 10^{-4} mm Hg. The evacuation of oxygen recovers the emission if the cathode temperature is higher than 1,600°K. These results seem to show that the existence of carbon increases the reduction of thorium to prevent the remarkable effect of oxygen, playing the similar rolle as magnesium in the alkaline earth oxide coated cathode(6).

(4) Decay and recovery of emission.

When the emission current is drawn from the cathode, it decays rapidly at first and then approaches gradually to a final constant value. Then, if the applied potential is removed, the emission recovers to the initial value again, as illustrated in Fig. 8. Differing from the gas effect, the emission decays more remarkably in the better activated cathode. The short time emission change, however, was not observed in the present procedure.

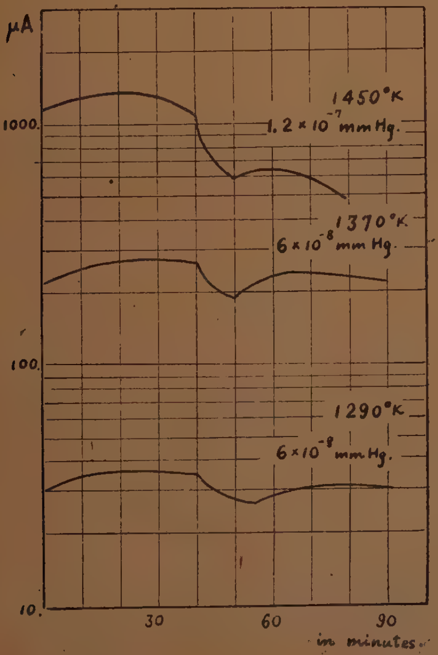

Fig. 8. Decay and recovery

Perhaps these phenomena are due to the transportation of thorium or oxygen atoms by electrolytic and concentration diffusion, just as barium atoms in the barium oxide coated cathode(7). In the following discussions, however, only the transportation of thorium atoms is taken into consideration. Of course the same discussion is applicable to the transportation of oxygen atoms. Assuming the uniformity of the electric field inside the layer, the equation,

$$F=-\frac{\partial\Psi}{\partial x} \quad \text{or} \quad \Psi=-xF \tag{6}$$

holds, where F is the field strength and Ψ the potential at the distance x from the surface. The field is represented by the electronic current i and the conductivity of the layer.

$$F=\frac{i}{\sigma}=\sqrt{\frac{kT}{2\pi m}}\exp\left(-\frac{e\phi}{kT}\right) \tag{7}$$

in which ϕ is the depth of conduction band, and k and m are the Boltzmann's constant and the effective mass of electron respectively. The number of thorium ion $n(x)$ at the equilibrium state is given by the Boltzmann's law,

$$n(x)=N\exp\left(-\frac{\Psi}{kT}\right)=N\exp\left(\frac{xF}{kT}\right) \tag{8}$$

If a is the thickness of the layer, $n(a/2)$ is equal to the number of thorium ions inside the layer at any time. Therefore

$$\log n\left(\frac{a}{2}\right)-\log n_\infty=\frac{a}{2}\frac{F}{kT} \tag{9}$$

is obtained. If i_0 and i_∞ are initial and final emissions respectively, (9) is represented in the form,

$$\log i_0-\log i_\infty=\frac{A}{\sqrt{T}}\exp\left(-\frac{e\phi}{kT}\right) \tag{10}$$

making use of (1), (7), and (8). Thus the depth of the conduction band, ϕ, can be estimated from the curve $\log(\log i_0/i_\infty)$ versus $1/T$. Experimental results are shown in Fig. 6 by circles, from which ϕ is determined to be about 0.6 e.v.

Next let us deal with the time change of the emission. The decreasing rate of thorium atoms is expressed by terms of the electrolytic conduction and thermal diffusion by Fick's law. Thus the following relation is obtained.

$$-nvF+D\frac{\partial n}{\partial x}=\Delta x\frac{\partial n}{\partial t} \tag{10}$$

v is the mobility of excess thorium ions and it is written as followed,

$$U=\frac{v_0}{kT}\exp\left(-\frac{U_0}{kT}\right) \tag{11}$$

The diffusion coefficient D is also given by

$$D=D_0\exp\left(-\frac{U_0}{kT}\right) \tag{12}$$

in which U_0 is the diffusion energy. X is of the order of electron mean free path inside the semiconductor. Substituting (11) and (12) into (10), and expressing by $\log n$ instead of n itself,

$$\left(-\frac{v_0}{kT}F+D\frac{\partial \log n}{\partial x}\right)\exp\left(-\frac{U_0}{kT}\right)=\Delta x\frac{\partial \log n}{\partial x} \tag{13}$$

At the equilibrium state, the relation

$$\frac{\partial \log n}{\partial x}=\frac{2}{a}\log\left(\frac{n}{n_\times}\right) \tag{14}$$

is obtained from the Boltzmann's law. Assuming that (14) holds at any time, the differential equation (13) can be solved with the solution

$$-Bt\exp\left(-\frac{U_0}{kT}\right)=\log\left(\frac{\log n-\log n_\infty}{\log n_0-\log n_\infty}\right) \tag{15}$$

Thus we obtain

$$-Bt\exp\left(-\frac{U_0}{kT}\right)=\log\left(\frac{\log i-\log i_\infty}{\log i_0-\log i_\infty}\right) \tag{16}$$

Experimental plotts of the right hand side in (16) are shown in Fig. 9 by circles. The relation

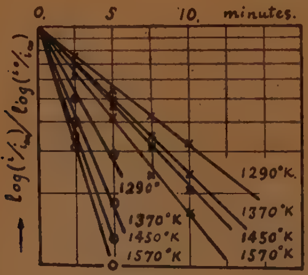

Fig. 9.
The circle : time versus $\log(i/i_\infty)/\log(i_0)$
The cross : time versus $\log(i/i_0)/\log(i_\infty)$

(16) holds at least for initial five minutes. Plotting these slopes at several temperatures, the middl curve in Fig. 6 was obtained and U_0 if found t be about 0.3 e.v.

Now we turn to the recovery of the emission The recovering curve has an almost inverted form of the decay curve. The almost similar procedure of analysis will be applicable for the decay, but in this case the atomic diffusion may well be assumed. The obtained result is

$$B't\exp\left(-\frac{U_0}{kT}\right)=\log\left(\frac{\log i-\log i_0}{\log i_\infty-\log i_0}\right) \tag{17}$$

Experimental plotts are shown by the cross in Fig. 9, in which, however, the time axis is about two times multiplied to that for B, as B is not always equal to B'. The theoretical expression (17) holds for almost all ranges of recovering. The diffusion energy calculated from these inclinations is 0.3 e.v. in agreement with the value obtaine from the decay curves.

§ 5. Conclusion.

The thoria coated cathode has many similar properties as the alkaline earth oxide coated cathode. Some amount of excess thorium atoms formed in the process of activation is the source of enhanced emission of this cathode and its emission is expressed in the similar form as that of the alkaline earth oxide coated cathode. The colour of this cathode varies from white to black and the work function becomes smaller as the activation progresses. The work function of the best activated one is 1.9 e.v., much smaller than that of the thoriated tungsten. The less activated white cathode is not sensitive to oxygen, but the gray cathode is very sensitive. Moreover, the similar time change of emission as experienced in the alkaline earth oxide coated cathode is observed and from these decay and recovery curves, the diffusion energy of thorium atoms was found to be about 0.3 e.v.

The energy state of this cathode will be discussed in a following paper together with results of conductity measurements. In conclution, we acknowledge all members in our laboratory for their valuable discussion.

References.

(1) T. Yabumoto, J Elec. Eng. Japan (in Japanese) **68** (1948) 319.

(2) T. E. Hanley, J. App. Phys. **19** (1948) 583.

(3) J. A. Becker, Rev. Mod. Phys. **7** (1935) 95.

(4) T. Arizumi & S. Narita, J. Phys. Soc. Japan **3** (1948) 356.

(5) T. Arizumi, J. Phys. Soc. Japan **3** (1948) 191.

(6) H. Kawamura, J. Phys. Math. Soc. Japan (in Japanese) **17** (1943) 159.

(7) J. P. Blewett, Phys. Rev. **55** (1939) 713.
H. Kawamura & N. Shinohara, Matsuda Kenkyu Jiho (in Japanese) **19** (1942) 453.

Absorption of Nitrogen by Evaporated Film of Barium.

By Tetsuya ARIZUMI and Kuninosuke IMAEDA.

Kobe Kogyo Corp.*

(Received Sept. 19, 1949).

§ 1. Procedure.

Following the preceding work, the absorption of nitrogen by the barium getter will be described in this paper. The precedure is almost similar, but a slight different method of analysis was applied. In other words, the temperature dependency of the absorption velocity was mainly studied. For this purpose the getter tube G_2 in Fig. 1 of the preceding paper was in most cases put in an oil bath or a small electric furnace.

The pressure was determined by the deflection of the balancing micro-ammeter of a bridge circuit with two Pirani gauges in its two arms, which are the gauge of the experimental tube and a standard one, evacuated to the lowest vacuum (about 10^{-7} m.m. Hg). The deflection of the ammeter was previously calibrated by a McLeod gauge for several kinds of gauges.

§ 2. Calibration of the Capillary.

The amount of gas introduced through the capillary was determined preceding to each experiment. It is given by

$$s = \frac{p_0 - p}{W} \tag{1}$$

where W is the resistance of the capillary and p_0 is the external gas pressure. If V be the total volume of the experimental tube, the pressure increase per unit time is

$$\frac{dp}{dt} = \frac{s}{V} = \frac{p_0 - p}{WV}$$

giving the solution

$$p = p_0\left\{1 - \exp\left(-\frac{t}{VW}\right)\right\} \tag{2}$$

because p is zero initially. So long as t is sufficiently small, the following relation holds.

$$\frac{1}{W} \doteqdot \frac{V}{t} \cdot \frac{p}{p_0} \tag{3}$$

Combination of (1) and (3) gives

$$s \doteqdot V\frac{p}{t} \tag{4}$$

Thus s can be calculated from time change of pressure and for many capillaries used in experiments it was of the order from 10^{-6} to 10^{-8} mol/min.

§ 3. Pressure Change at Room Temperature.

When the capillary is broken to introduce gas into the tube with a fresh getter mirror*, almost similar pressure curve as oxygen is always obtained. Slightly differing from oxygen, however, the pressure increases continuously without exception and all curves obtained by the same capillary can be represented by only one, by means of multiplying by some factor to the time axis as in Fig. 1. The result suggests that the process is almost similar in all cases.

---

* Formerly, *Kawanishi Kikai Seisakusho*, Ltd..

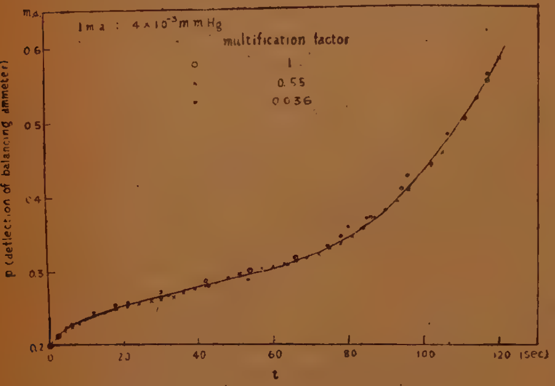

Fig. 1. Pressure curve.

Even after the pressure increases rapidly, the getter has still a strong absorbing ability. Sealing the capillary, the pressure begins to decrease immediately as shown by the curve II in Fig. 2. Introducing gas into the tube again, it increases much faster, while it decreases more slowly than the curve II if the capillary is sealed

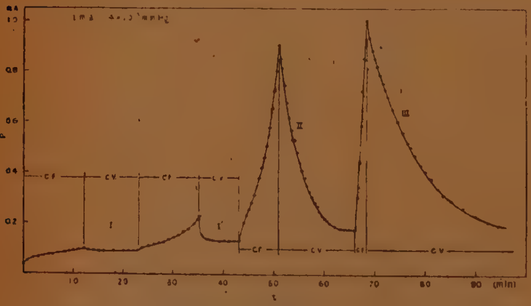

Fig. 2. Pressure change at aternations of c. f. and c. *v*. methods.

and at the same time the final value become slightly larger (curve III). Such behaviours becom remarkable as the time of repeating. The increase of the final pressure is experienced onl in the case of air because of the existence o rare gases.

Each curve in the c. v. method is represente by the relation,

$$p = p_0 \exp(-\alpha t) \quad (5)$$

as shown in Fig. 3, meaning that the time chang of pressure is given by the differential equation

$$\frac{\partial p}{\partial t} = -\alpha p \quad (6)$$

In the case of air p means, of course, the dif ference of a measured pressure and the residua one of rare gases. α is given by the inclination of each curve in Fig. 3 and it decreases almost linearly as the total amount of the introduce gas as in Fig. 4. However, α recovers slightly when the capillary remains sealed for a long time. For example No. 8 was obtained about two days after No. 7 and Nos 10 and 12 about one day after each preceding measurement. On the other hand No. 9 was measured soon after No. 8 an both α values apparently lie on a different line from the curve 1—7, suggesting the recovery of the absorption at No. 8.

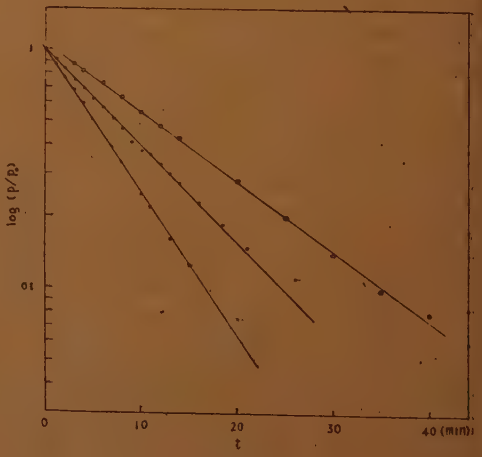

Fig. 3.

If the relation (6) always holds for the absorption, pressure change in the c. f. method will b represented by

---

* In the following the procedures to study the pressure change with gas being continuously flowed into and with the caplillary being sealed shall be called "constant flow" (c. f.) and "constant volume" (c. v.) methods respectively for briefness.

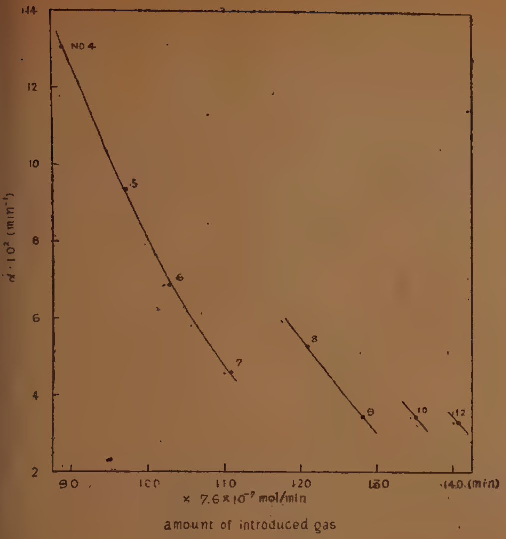

Fig. 4. Change of α.

$$\frac{dp}{dt}=\frac{s}{V}-\alpha p \qquad (7)$$

from which α is calculated. The result is also shown in Fig. 5 in which α is found to decrease rapidly to nearly zero.

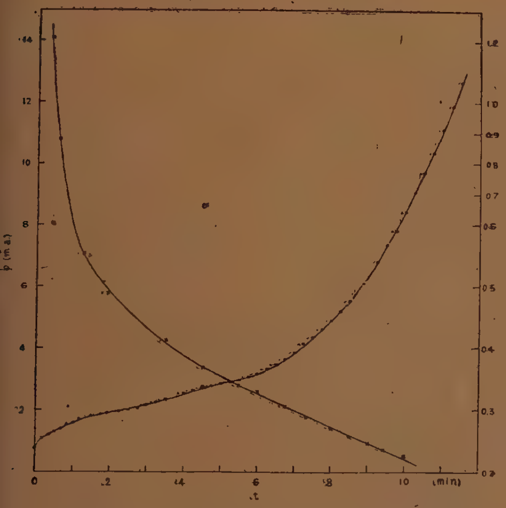

Fig. 5. Change of α in c. f. method.
●: pressure ×: α

§ 4. Effect of Temperature.

Curves I and II in Fig. 6 are similar changes of the pressure in the c. f. and c. v. methods at a constant temperature. Heating the getter chamber gradually, the pressure begins to decrease more rapidly at about 50°C and very rapidly beyond 65°C (curve III). Cooling to the room temperature the pressure does not increase. Repeating the similar procedure again, no remarkable pressure change is observed up to 90°C (IV), but beyond this temperature the pressure begins to decrease very rapidly. The pressure change in the c. f. method at about 320°C is much slower than the first time, in spite of having already absorbed a very large amount of gas (V, VIII). Moreover, the pressure begins to decrease immediately when the capillary is sealed at c and e. The pressure change in the c. v. method at these high temperature also satisfies the relation (5).

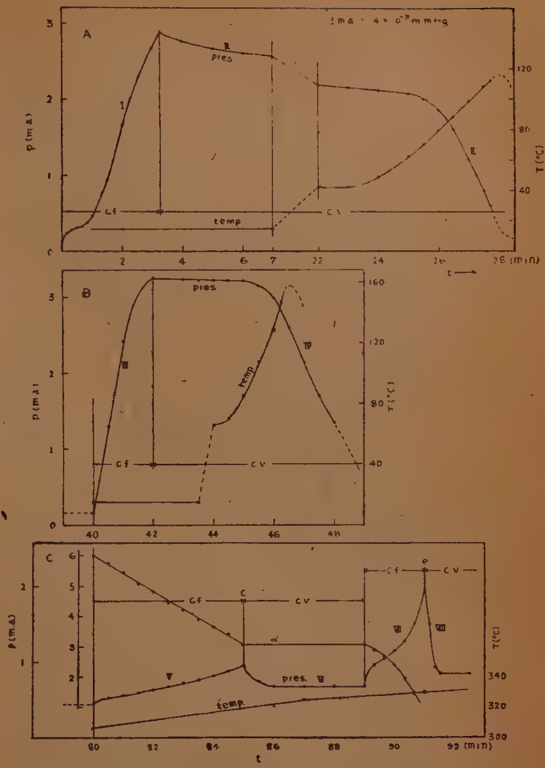

Fig. 6. Pressure change with varying temperature. B and C are continuations of A and B respectively.

As the temperature is changed continuously in the above experiment, the pressure change will be given by

$$\frac{dp}{dt}=\frac{\partial p}{\partial t}+\frac{dT}{dt}\frac{\partial p}{\partial T} \qquad (8)$$

Making use of the relation $pV=nRT$ and (6), we obtain

$$\alpha=-\frac{1}{p}\frac{dp}{dt}+\frac{1}{T}\frac{dT}{dt} \qquad (9)$$

In Fig. 7 a log α, calculated from the curve II in Fig. 6 are plotted agaist $1/T$ in which the curve is found to be almost linear and the inclination is estimated to be about 0.24 ev. Thus the following experimental formula will be obtained:

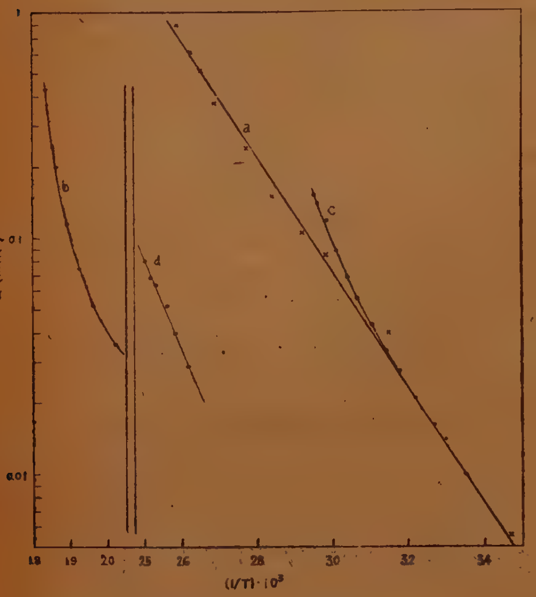

Fig. 7. α versus $1/T$ curves.

$$\alpha = \alpha_0 \exp\left(-\frac{Q}{kT}\right) \tag{10}$$

Fig. 8 is another example for the getter whose absorbing ability is already very weak at room temperature. Heating the getter chamber the pressure increase almost linearly at first and after passing through a broad maximum it begins to

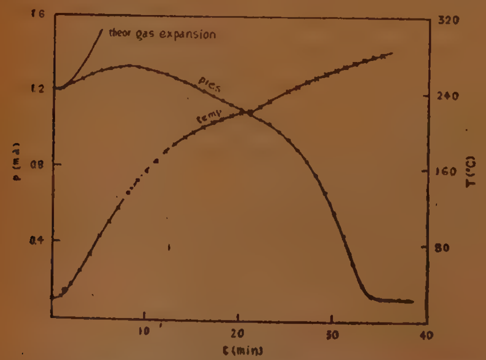

Fig. 8. Pressure change for the getter having absorbed a large amount of gas.

decrease. Above about 240°C its rate becomes much faster. Calculated values of α are shown in the Table I, in which α is found to be almos constant up to 218°C, but it begins to increas above this temperature. log α are also plotte in Fig. 5 (curve b) together with several example in which the inclinations are found to be differen each other. These results will be explained theo retically in the later section.

Table I.

t(min)	$(1/p)(dp/dt)$	$(1/T)(dT/dt)$	α
2	0.0187	0.056	0.037
3	0.0183	0.0533	0.035
4	0.0172	0.0506	0.033
5	0.0133	0.048	0.035
6	0.0084	0.0425	0.034
7	0	0.0346	0.035
10	−0.0078	0.0245	0.032
12	−0.0124	0.0205	0.033
14	−0.0170	0.0157	0.033
16	−0.0194	0.0109	0.030
18	−0.0202	0.0081	0.028
20	−0.0211	0.0063	0.027
22	−0.0238	0.0118	0.036
24	−0.041	0.0108	0.052
26	−0.066	0.0092	0.075
28	−0.106	0.0079	0.114
30	−0.194	0.0072	0.202
32	−0.425	0.0053	0.430

Many experimental results shows that the temperature above which α is represented by (10) becomes higher as the amount of absorbed gas.

Heating the getter having already a very large amount of gas, the first pressure increase is larger than the theoretical gas expansion, because of the desorption of gases. It is, however, doubtful whether these desorbed gases is originated from the getter or from other parts.

§ Discussion.

Nitrogen has been known to react with metalic barium to form barium nitride (Ba_3N_2) at high temperatures. Even at room temperature it is conclusive that the adsorption of nitrogen is not a simple absorption process, but that of forming barium nitride or its subnitrides. Thus the surface of the getter mirror is always covered by the complex layer unless it is still quite fresh. The first step of absorption will be begun by the adsorption on the complex layer, the velocity of which is given theoretically(2) by

$$v=\frac{p}{\sqrt{2\pi mkT}}\exp\left(-\frac{Q_a}{RT}\right) \qquad (11)$$

where Q_a is the activation energy for adsorption. The process of absorption, however, is not simple adsorption and therefore only nitrogen molecules striking on active centres may well be assumed to be captured. Thus the pressure change in the c. v. method is represented by the product of the density of active centres and the adsorption velocity, as followed,

$$-\frac{dp}{dt}=\lambda AN\frac{p}{\sqrt{2\pi mkT}}\exp\left(-\frac{Q_a}{RT}\right) \qquad (12)$$

where λ is constant, A the true surfacearea and N number of active centres per unit area. The experimental result that α is constant at low temperatures shows that the adsorption is predominant and moreover Q_a is nearly equal to zero. A and N in (12) decreases as the amount of absorbed gas, resulting in the gradual change of α in Figs. 4, 5 and 6. Its recoveries at Nos. 8, 10 and 12 in Fig. 4 are perhaps caused by the slight increase of N which is presumably determined by the diffusion of nitrogen from the surface to the interior or that of barium in inverse direction.

The active centre may well be considered to be the lattice sites which have not yet absorb a full amount of nitrogen, such as bare barium atoms or barium subnitride molecules. The diffusion of nitrogen atoms into the interior forms new active centres. Thus the concentration of nitrogen atoms on the surface should be formulated. If n be the number of nitrogen atoms at the surface it satisfies the Fick's diffusion equation, but the concentration gradiant may well be put n/x, because the layer is very thin. Thus we obtain

$$\frac{dn}{dt}=-D\frac{n}{x^2} \qquad (13)$$

Although the diffusion of nitrogen atoms results in the growth of the nitride layer, x may be assumed constant if the diffusion is sufficiently small. In this case the solution of (16) becomes to

$$n=n_0\exp\left(-D\frac{t}{x^2}\right) \qquad (14)$$

Substituting (17) in (13) together with the relation $N_t=N+n$, where N_t is the total number of possible sites for absorption,

$$-\frac{dp}{dt}=\lambda A\left\{N_t-(N_t-N_0)\exp\left(-D\frac{t}{x^2}\right)\right\}\cdot\frac{p}{\sqrt{2\pi mkT}}\exp\left(-\frac{Q_a}{RT}\right) \qquad (15)$$

The diffusion coefficient D is given by

$$D=D_0\exp\left(-\frac{Q_a}{RT}\right) \qquad (16)$$

as usual.

The formula (15) shows in good agreement with the experimental results that the absorption is predominant so long as D is very small or the nitride layer is sufficiently thick, while the diffusion becomes to determine the rate of pressure change when D is large, and even at high temperatures in which diffusion is the rate determining step, the relation (1) also holds. If proper conditions are satisfied, a crude approximation gives the result,

$$\frac{1}{p}\frac{dp}{dt}\fallingdotseq A'N_t\frac{t}{x^2}D \qquad (17)$$

as the adsorption term may well be assumed constant at high temperatures. Thus $Q=0.24$ e.v. obtained in Fig. 7 is probably an approximate value of diffusion energy.

At last it must be added that the rate determining process for the reaction of nitrogen with barium is always not adsorption, but diffusion, although the pressure change appears to present the counter-evidence, because even the surface reaction without diffusion makes the pressure change measurable in most cases.

References.

(1) T. Arizumi & S. Kotani, J. Phys. Soc. Japan 5 (1950) 70.
(2) S. Glasstane & others, the Theory of Rate Processes, (1941) McGraw-Hill.

Conductivity and Electronic Energy State of Thoria Coated Cathode.

By Tetsuya ARIZUMI and Leona ESAKI.

Kobe Kogyo Co., Kobe.

(Received October 13, 1949).

§ 1. Introduction.

The modern theory of semi-conductor predicts the intimate relation of its thermionic emission to conductivity. Numerous papers on the alkaline earth oxide coated cathode seem to support the theory. Following the previous paper(1) in which the thermionic properties of the thoria coated cathode has been reported, its conductivity and its possible electronic energy state will be described in this paper.

§ 2. Apparatus.

Because of the high operating temperature of the thoria coated cathode, it is, in general, directly heated, making the experimental techiques for the exact determination of the conductivity difficult. The main objection is the disturbance caused by the potential drop through the heater wire. To prevent this disturbance, the special construction, shown in Fig. 1, was adopted. Only the central part of a tungsten heater (diameter 0.129 m.m.) was coated cataphoretically with the thoria layer of about 50 microns thickness. The coating length was 5 m.m., to minimize the potential drop. Two fine tungsten wires (diameter, 0.015 m.m) S_1 and S_2 were welded just at the ends of the coating and both probes were connected together to a lead R. Anothor tungsten wire S_3 of the same size was tightly wound around the middle of the coating only by one turn, on which the thin layer of thoria was sprayed.

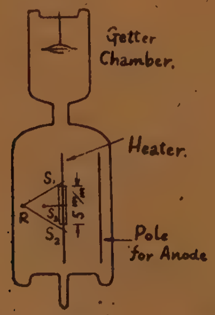

Fig. 1. The construction of the experimental tube.

A straight nickel wire P was served as an anode. The assembled tube was evacuated carefully: the glass baking, the cathode flashing and the degassing of all metal parts were carred out sufficiently and then the tube was sealed off immediately after flashing a barium getter.

§ 3. Procedure and results.

Initially the cathode was activated and aged until the emission reached to the steady state. The measurement of conductivity was carried out in the following way by a circuit in Fig. 2. Even when no external voltage was applied between S_3 and R, a small amount of current was always observed. Thus, preceding to each measurement, the applied voltage was so adjusted that no current might be flowed through the galvanometer G. This applied voltage is somehow dependent on the cathode temperature and seems to be caused by the electromotive force between the base metal and the surface of thoria at slightly lower tem-

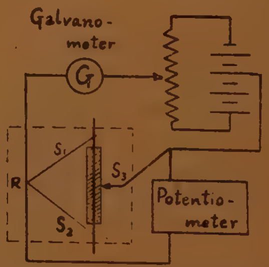

Fig. 2. Schematic diagram of measuring circuit.

perature and the spurious effect of the heating current. Fig. 3 shows the effective potential difference between S_3 and R versus the current, in which the plus sign means R is positive.

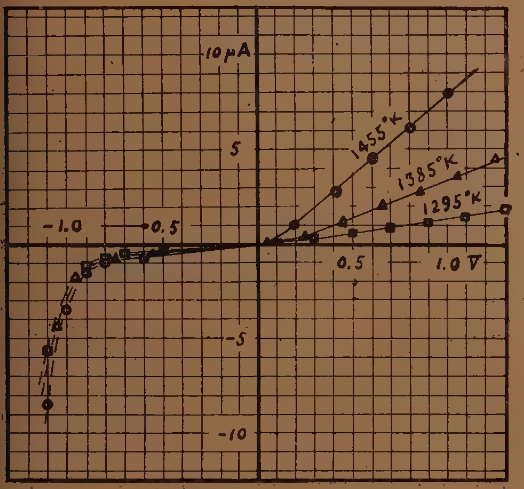

Fig. 3. The diffration potential difference versus current.

The current in the minus side is much smaller than the plus side so long as the potential difference is smaller than one volt, but it tends to increase gradually with time when the potential difference exceeds this limit. In the plus side, however, the voltage-current relation is almost ohmic except the neighbourhood of zero point and no time change is observed below 1,500°K. The conductivity may well be represented by the ohmic range in the plus side as discussed later. In Fig. 4 conductivities are plotted against $1/T$, together with thermionic emissions, in which the parallel relations between both quantities are found to hold in any case. Both work functions and activation energies for the conductivity are summerized in Table 1.

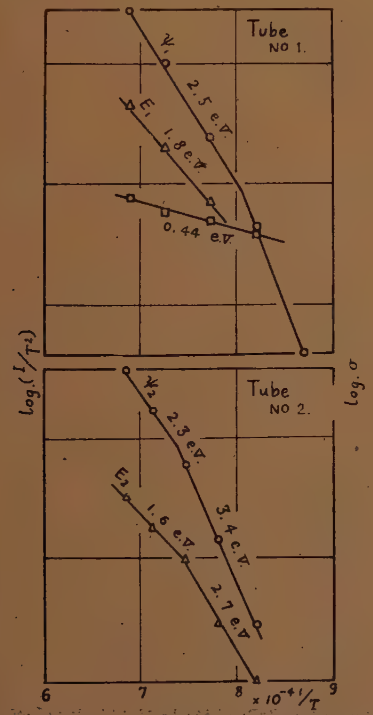

Fig. 4. The electronic conductivity and thermionic emission versus $1/T$. The rectangular mark is the plot of $(\partial i/\partial V)_{V=0}$ against $1/T$.

Table I.

Tube No.	Temp. (°k)	Work function (e.v.)	Activation energy for conductivity (e.v.)	Difference (e.v.)
1	1200	2.5	1.8	0.7
2	1300	2.3	1.6	0.7
	1300	3.4	2.7	0.7

§ 4. Discussion.

The contact area of the probe S_3 and thoria is about 0.034 mm², while that of the heater and thoria is larger than 2 mm². As the ratio of both contact areas exceeds the rectification ratio, the current-voltage characteristics in Fig. 3 may well be considered to be caused by a point contact of thoria and tungsten and the fact that the direction from tungsten to thoria is easy flow suggests that thoria is a N-type semi-conductor.

Thus in the hard flow direction, the applied potential is almost dropped at the point contact, while in the easy flow direction it is almost uniform through the thoria layer, showing that the ohmic law must hold only for the easy flow direction. This is the theoretical reason that the conductivity was evaluated in the easy flow region.

The thermionic current i and the conductivity σ are given by

$$i = ne\rho D\left(\frac{kT}{2\pi m}\right)^{\frac{1}{2}} \exp\left(-\frac{e\phi}{kT}\right) \tag{1}$$

and

$$\sigma = nev \tag{2}$$

respectively, where

n : number of condution electrons
v : mobility of conduction electron
ρ : roughness factor of the cathode surface
D : transmission coefficient
ϕ : depth of condction band

and other notations are those customarily used. According to Nijboer's theory⁽²⁾ on semi-conductor, the number of conduction electrons n is expressed by

$$\frac{n(n+N)}{n_0-n}=\left(\frac{2\pi mkT}{h^2}\right)^{\frac{3}{2}}\exp\left\{-\frac{e}{kT}(\varepsilon-\zeta)\right\} \tag{3}$$

in which n_0 is the number of impurity levels and N that of "frozen-in" holes. ζ is the potential at impurity levels and ε that at the bottom of conduction band.

In general, the apparent work function and the activation energy of the conductivity are given by

$$\Psi=-\frac{k}{e}\frac{\partial\left(\log\frac{i}{T^2}\right)}{\partial\left(\frac{1}{T}\right)} \tag{4}$$

and

$$E=-\frac{k}{e}\frac{\partial(\log\sigma)}{\partial\left(\frac{1}{T}\right)} \tag{5}$$

respectively. Differentiating (1), (2) and (3) and rearranging, Ψ and E are written as follows:

$$\Psi=\frac{3}{2}\frac{kT}{e}+\phi+\frac{\frac{3}{2}\frac{kT}{e}+(\varepsilon-\zeta)}{1+\frac{n}{N+n}+\frac{n}{n_0-n}} \tag{6}$$

$$E=\frac{\frac{3}{2}\frac{kT}{e}+(\varepsilon-\zeta)}{1+\frac{n}{N+n}+\frac{n}{n_0-n}} \tag{7}$$

giving the simple relation

$$\Psi-E=-\frac{3}{2}\frac{kT}{e}+\phi \tag{8}$$

The relation (8) shows that in any case the difference of the work function and the activation energy of the conductivity is equal to ϕ, so long as kT/e is neglisibly small. In good agreement with the theory, the experimental results, summerized in table 1, shows that $\phi=\Psi-E$ is always constant, 0.7 e.v.

The formulae (6) and (7) suggest that both the work function and the activation energy of the conductivity vary gradually as the progress of activation. Several results,⁽³⁾~⁽⁶⁾ hitherto obtained, are summerized in table 2, in which the work functions are found to distribute in a rather wide range, as expected from the theory. The large change of the Richardson constant having been described in the previous paper⁽¹⁾ will be explained qualitively in the similar manner as the barium oxide coated cathode⁽⁷⁾.

In the extreme case, $n > N$, (6) becomes

$$\Psi=\phi+\frac{\varepsilon-\zeta}{2} \tag{9}$$

while in case, $n > N$, it becomes

$$\Psi=\phi+(\varepsilon-\zeta) \tag{10}$$

In the previous paper⁽¹⁾ it has been revealed that the work function of the fully activated cathode was 1.95 e.v. Therefore we may well put

Table II.

Author	Richardson const. (A/deg², cm²)	Work function (e. v.)	remarks
D. A. Wright⁽³⁾ (1947)	7.5	2.6 (2)	Pulsed emission
	2.5	2.5 (4)	D. C. emission
T. Yabumoto⁽⁴⁾ (1948)	—	3.0	D. C.
T. E. Hanley⁽⁵⁾ (1948)	5.62	2.55	Pulsed
	2.63	2.67	D. C.
H. Y. Fan⁽⁶⁾ (1949)	37.8	3.14	Sintered cathode
T. Arizumi and L. Esaki⁽¹⁾ (1949)	5.0—1×10⁻²	3.2—1.95	D. C.

$$\phi+\frac{\varepsilon-\zeta}{2}=1.95(\text{e.v.})$$

ϕ being 0.7 e.v., gives $\varepsilon-\zeta=2{,}5$ e.v. and this results in

$$\phi+(\varepsilon-\zeta)=3.2(\text{e.v.})$$

in satisfactory agreement with the work function of the deactivated cathode. Therefore the energy diagram of thoria will be represented as schematically shown in Fig. 5.

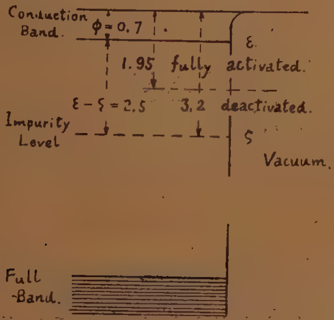

Fig. 5. The schematic diagram of the electronic energy state for thoria.

According to the diode theory⁽⁸⁾ on the point contact, the current through the contact is expressed by

$$i=A\exp\left(-\frac{e|\varphi|}{kT}\right)\left\{\exp\left(\frac{eV}{kT}\right)-1\right\} \tag{11}$$

in which V is the potential drop at the contact and φ is the difference of the contact potential. Differentiating (11) by V, we obtain

$$\left(\frac{\partial i}{\partial V}\right)_{V=0}=A\frac{e}{kT}\exp\left(-\frac{e|\varphi|}{kT}\right) \tag{12}$$

Thus, φ can be estimated from the inclination through the origin in the voltage-current characteristics in Fig. 3. The rectangular mark in Fig. 4 is the semi-logarismic plot of $(\partial i/\partial V)_{V=0}$ versus $1/T$. The curve is almost straight and gives $\varphi=0.44$ e.v. In general both the image force and the tunnel effect tend to lower the height of the potential barrier. Even applying the Courant's⁽⁹⁾ correction on these effects, φ becomes 0.62 e.v. This is far smaller than the value expected from the difference of work functions, probably because of the imperfect point contact and several other effects.

§ 5. Conclusion.

The results are summerized as follows:

(1) The conductivity was measured by inbedded probe method. The parallel relation between the thermionic emission and the conductivity was found to hold as in the case of barium oxide cathode, and the depth of the conduction band was estimated 0.7 e.v. The energy difference between the impurity level and the bottom of the conduction band was also evaluated to be 2.5 e.v.

(2) The rectifying property at the contact of thoria and tungsten has shown that thoria was N-type semi-conductor, but the difference of contact potentials, experimentally obtained from the rectification phenomema was much smaller than the difference of work functions.

References.

(1) T. Arizumi and L. Esaki, J. Phys. Soc. Japan (now in press).
(2) B. R. A. Nijboer, Proc. Phys. Soc. (A) **51** (1939) 575.
(3) D. A. Wright, Nature **160** (1947) 129.
(4) T. Yabumoto, J. Eect. Japan, **68** (1948) 319.
(5) T. E. Hanley, J. App. Phys. **19** (1948) 583.
(6) H. Y. Fan, J. App. phys. **20** (1949) 682.
(7) T. Arizumi and S. Narita, J. Phys. Soc. Japan **3** (1948) 356.
(8) H. C. Torrey and C. A. Whitmer, Crystal Rectifiers (McGraw-Hill Book Company 1949), P 81.
(9) E. Courant, Phys. Rev. **69** (1946) 684.

Researches and Developments on the Spiral Orbit Spectrometer (I).

By Mitsuo SAKAI.

Department of Physics, University of Tokyo.

(Received September 21, 1949).

Introduction.

In 1943 Dr. G. Miyamoto(1)* performed several experiments on his ingenious, new type of β ray spectrometer. It's principle was based on the consideration that when a charged particle starts radially from a central axis of a heterogeneous magnetic field of axial symmetry with outerward gradual decrease, it will discribe a spiral orbit. In case a certain relation between the field strength and the momentum of the emitted particle is fulfilled, its orbit will converge to a difinite circle. According to the trajectory of the emitted particles, this type of spectrometer has been named the Spiral Orbit Spectrometer" by its founder. Its theory was developed by G. Iwata, G. Miyamoto and M. Kotani(2)**, but experimentally only one attempt(3) was made on further study of properties of this apparatus due to the interference of the War.

Recently the present author carried out some investigations on the properties of the spectrometer and made several developments of it. In the course of these experiments and calculations, it soon became evident that this type of spectrometer has many good features. The following description gives the several theoretical and experimental results mainly related to the case of accelerated thermoelectrons.

§ 1. Description of Apparatus.

The apparatus used for this experiment is the one used formerly for γ ray experiments by R. Sagane *et al* and has a pair of pole pieces, 70 mm in diameter with their gap distance of 40 mm. It is shown diagrammatically in Fig. 1. The intensity distribution of the magnetic field and the radius

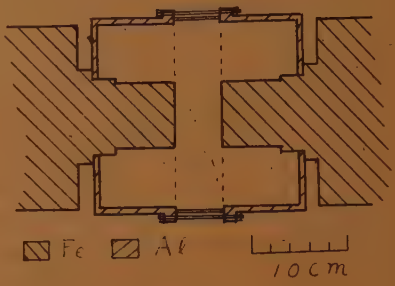

Fig. 1.

of converging circle is also shown in Fig. 2. The source of electrons is made of a tungsten wire stretched by a holder which may be adjusted so that the filament will be coaxial to the magnetic field. This wire has a diameter of 0.1 mm and

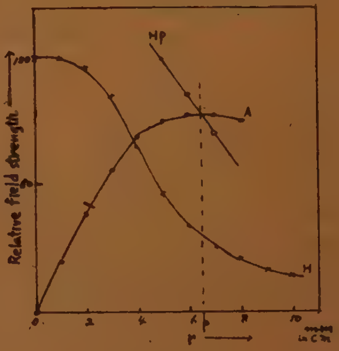

Fig. 2.

is heated by a D.C. current from a storage battery. In order to adjust the position of the wire easily and accurately, its image was projected by means of a lens system with a magnification of several times upon a screen outside of the apparatus. In this way it was possible to adjust it within the accuracy of 0.05 mm. The thermoelectron emitted from the source wire was accelerated radially by a cylindrical grid situated concentric to it. It was deflected by magnetic field and received by a Faraday cage placed on the converging circle. Keeping constant the accelerating voltage, the current to the Faraday cage was measured with the variation of the exciting current of the magntic field. A peak was found in the former current when the convering condition was fulfilled. The electric circuits are described schematically in Fig. 3. The heating system of the filament was insulated from the earth perfectly by the use of a certain technique*. The accelerating voltage was supplied by usual high tension stabilizing circuit used formerly for counter experiments, which has the range from 400 Volts to 1200 Volts.

---

* This report will be referred to as (I).
** This report will be referred to as (II).

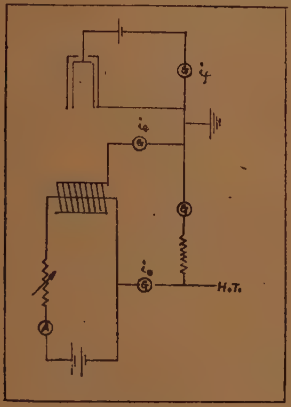

Fig. 3.

§ 2. General Theoretical Discussions.

Now discussions are given on several problems in the case of accelerated thermoelectron according to the theory given by (II).

(1). General conclusions of the theory.

The authers of (II) showed that, if v be the velocity of an electron which starts from the source, with an angle α to its radius, B be the vector potential on the converging circle, fulfilling the condition of covergence and ΔB be its variation corresponding to that of the magnetic field, then the probability I that the electron will be captured by the detector, (having width 2 d and being adjusted on the radius of converging circle ρ, c. f. Fig 4), is given by the following equations corrosponding to Eq. (23) of (II):

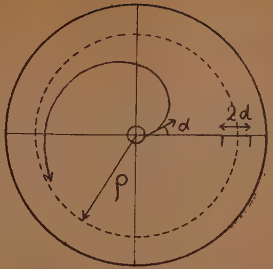

Fig. 4.

$$I=\frac{\kappa\sqrt{2}}{2\pi}\cosh^{-1}\frac{\delta}{\kappa}\left(\frac{\Delta B}{B}+C_0\right)^{-\frac{1}{2}}+O(\delta);\ \frac{\Delta B}{B}+C_0>0, \quad (1)$$

$$I=\frac{\kappa\sqrt{2}}{2\pi}\sinh^{-1}\frac{\delta}{\kappa}\left|\frac{\Delta B}{B}+C_0\right|^{-\frac{1}{2}}+O(\delta);\ \frac{\Delta B}{B}+C_0<0. \quad (2)$$

κ, C_0 and δ are defined respectively by the following equations:

$$A(r)/A(\rho)=1-(1-x)^2/\kappa^2;\ x=v/\rho, \qquad (3)$$

$$C_0=r_0/\rho\sin x-r_0A_0/\rho B, \qquad (4)$$

$$\delta=d/\rho \qquad (5)$$

where r_0 is the radius of the source and A_0 the vector potential at the surface of it. And $O(\delta)$ is the small correction term of order δ compared with the first term†. In our case, particles start normal to the surface and therefore α is zero and C_0 becomes $-r_0A_0/\rho B$ which is usually very small in quantity and is deemed to be negligible.

If we set C_0 equal to zero in Eq. (1) and (2), we get

$$I=\frac{\kappa\sqrt{2}}{2\pi}\cosh^{-1}\frac{\delta}{\kappa}\left(\frac{\Delta B}{B}\right)^{-\frac{1}{2}};\ \Delta B>0, \qquad (1')$$

$$I=\frac{\kappa\sqrt{2}}{2\pi}\sinh^{-1}\frac{\delta}{\kappa}\left|\frac{\Delta B}{B}\right|^{-\frac{1}{2}};\ \Delta B<0. \qquad (2')$$

These equations may be called as the fundamental probability equation and the curve which is obtained by the variation of ΔB may be called as the fundamental probability curve. Then this curve plays a very important role in the construction of apparatus, the determination of constants of the measuring system in any experiment and also to derive theoretical estimation for the shape of the expected lines.

---

* One can easily overcome the imperfect insulation due to wet surface of the insulator by winding several turns of a heated wire around the bushings of the insulating supporter.

† For usual experimental conditions this term will be only several percents.

(2) Position of the source

Dr. Miyamoto has already pointed out that the adjustment of the source to the axis of magnetic field was essential for this type of spectrometer. The theoretical meaning of this fact is as follows:

Let the centre of the sourse S be apart from the centre C of the magnetic field by R as shown in Fig. 5. The electron starting from a point A on the surface of the source has a certain capture probability which is given by Eq. (1) and (2) and from these equations we can expect that this probability depends only on $\overline{AC}\sin\alpha$. By applying since formula to the triangle $\varDelta ACS$, we can obtain:

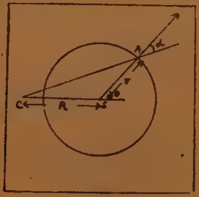

Fig. 5.

$$\overline{AC}\sin\alpha = R\sin\theta \tag{6}$$

Therefore, the condition of our case may be reduced to that of a infinitely thin line source S located at R apart from the centre. Suppose a virtual tube of radius R placed coaxial to the magnetic field, then the emission of the particles from S corresponds to the emission of particles outerward from this virtual tube surface. This type of a source was already treated as a β ray source in (II). Accordingly the effect of the excentricity of this type of a source is easily calculated from the formula (II)*.

One remark is to be added here that in the case of accelerated thermoelectrons the thickness of a source has no influence on the shape of the peak except the shift of the position of its maximum point by $r_0A_0/\rho B$ as one may expect clearly from Eq. (1) and (2).

(3) Grid.

Suppose the central axis of the grid to be eccentric by a from that of the filament, which is adjusted coaxial to the magnetic field as shown in Fig. 6, and let r_0 and R be the radius of filament and grid respectively. Here, let the grid be considered as a source which emits particles from its surface with a certain angle α to its normal, and apply the above theory on this virtual source. Since in this case the distance between the emitting point and the central axis is large, it is necessary to consider the effect of the correction term. Nevertheless it may be sufficient to examine the quantity C_0, because in Eq. (1) and (2) this distance is only envolved in this term. In this point of view, r_0 in Eq. (4) is to be replaced by r. Then,

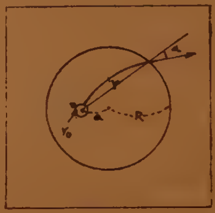

Fig. 6.

$$C_0 = r/\rho\sin\alpha - rA_0/\rho B \tag{4'}$$

If we integrate the θ component of the equation of motion in the vicinity of the central axis, we obtain:

$$r\dot{\vartheta} = \frac{eH_0}{2rm}(r^2 - r_0^2) \tag{7}$$

In the derivation of this formula we make use of the fact that the magnetic field near the centre is uniform. Using the equation of the condition of convergence, we get:

$$\sin\alpha = \frac{r\dot{\vartheta}}{v} = \frac{1}{2}\frac{r^2 - r_0^2}{r\rho}\frac{H_0}{H(\rho)}; \tag{8}$$

$$\begin{aligned} C_0 &= \frac{1}{2}\frac{r^2 - r_0^2}{\rho^2}\frac{H_0}{H(\rho)} - \frac{1}{2}\frac{r^2}{\rho^2}\frac{H_0}{H(\rho)} \\ &= -\frac{1}{2}\frac{r_0^2}{\rho^2}\frac{H_0}{H(\rho)} = -\frac{r_0}{\rho}\frac{A_0'}{B}, \end{aligned} \tag{9}$$

where A_0' is the vector potential on r_0. Considering Eq. (1), (2), (4) and (9), we can conclude that lectrons accelerated by the grid are equivalent o electrons which start normal to the surface f the source on the central axis, although the rid may be situated eccentrically.

---

* This consideration is approximate one because the effect of the relative position between source and detector is not accounted for but this effect is small as we see in § 4, (2) of (I). In the case of a β ray source this effect can also be treated theoretically by some interesting considerations but the results can not be given here because of the limited space.

4) Position of the detector.

From the theory of (II) we easily obtain the quation of probability as the following equations hich correspond to each of the cases that the uterside, middle or innerside of the Faraday cage s adjusted to the converging circle respectively :

1 st. Case
Outerside coincides)

$$I = \frac{\kappa\sqrt{2}}{2\pi}\cosh^{-1}\frac{2\delta}{\kappa}\left(\frac{\Delta B}{B}+\frac{r_0}{\rho}\sin\alpha\right)^{-\frac{1}{2}}; \qquad \frac{\Delta B}{B}+\frac{r_0}{\rho}\sin\alpha > 0,$$

$$I = \frac{\kappa\sqrt{4}}{4\pi}\sinh^{-1}\frac{2\delta}{\kappa}\left|\frac{\Delta B}{B}+\frac{r_0}{\rho}\sin\alpha\right|^{-\frac{1}{2}}; \qquad \frac{\Delta B}{B}+\frac{r_0}{\rho}\sin\alpha < 0. \tag{10}$$

nd. Case
(Middle coincides.)

$$I = \frac{\kappa\sqrt{2}}{2\pi}\cosh^{-1}\frac{\delta}{\tau}\left(\frac{\Delta B}{B}+\frac{r_0}{\rho}\sin\alpha\right)^{-\frac{1}{2}}; \qquad \frac{\Delta B}{B}+\frac{r_0}{\rho}\sin\alpha > 0,$$

$$I = \frac{\kappa\sqrt{2}}{2\pi}\sinh^{-1}\frac{\delta}{\kappa}\left|\frac{\Delta B}{B}+\frac{r_0}{\rho}\sin\alpha\right|^{-\frac{1}{2}}; \qquad \frac{\Delta B}{B}+\frac{r_0}{\rho}\sin\alpha < 0. \tag{11}$$

3 rd. Case
Innerside coincides)

$$I = 0;\ \frac{\Delta B}{B}+\frac{r_0}{\rho}\sin\alpha > 0,$$

$$I = \frac{\kappa\sqrt{2}}{4\pi}\sinh^{-1}\frac{2\delta}{\kappa}\left|\frac{\Delta B}{B}+\frac{r_0}{\rho}\sin\alpha\right|^{-\frac{1}{2}}; \qquad \frac{\Delta B}{B}+\frac{r_0}{\rho}\sin\alpha < 0. \tag{12}$$

f course in our case of the acceleration of thermo-lectrons we must take α equal to zero in these quations. Using these equations, Fig. 7 is drawn s the fundamental probability curves in the above hree cases, assuming $\kappa = 1.6$, $2d = 5.6$ mm and $= 65.5$ mm as the constants of the apparatus nd 0.2% as the spread of initial velocity distri-ution of the emitted particles. In this procedure ome precaution must be taken as pointed out in § 3 of the following paper. The adopted constants are the same as those of our apparatus. The curves A, B and C correspond to Eq. (12), (11) and (10) and we have 0.40%, 0.30% and 0.35% as the resolving power, $\Delta B/B$ for the full width at half maximum and 0.28, 0.39 and 0.53 as the maximum probability for each case. Therefore it is clear that to adjust the outerside of the detector to the converging circle is most preferable, if we have little regard to the resolving power and the deviation of the maximum position.

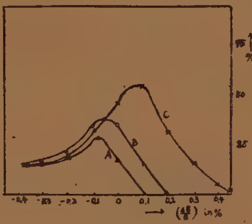

Fig. 7.

(5) Magnetic focusing action of the axial direction*.

It is a very interesting problem to consider the effect of the magnetic focussing action on the behaviour of the particle which does not start from the median plane. But this problem can be solved only by numerical integration. Therefore we must be satisfied by the following estimation.

According to eq. (34) of (II), we put the vector potential as,

$$A(r, z) = A_0(r) + z^2 A_1(r). \tag{13}$$

Then the equations of motion and the first integrals can be written in the form :

$$\frac{d^2r}{dt^2} = -\frac{e^2}{m^2}\left\{\frac{1}{2}\frac{dA_0^2(r)}{dr} + z^2\frac{dA_0(r)A_1(r)}{dr} + \frac{z^4}{2}\frac{dA_1^2(r)}{dr}\right\} \tag{14}$$

$$\frac{d^2z}{dt^2} = -\frac{e^2}{m^2}\{2zA_0(r)A_1(r) + 2z^3A_1^2(r)\} \tag{15}$$

$$\left(\frac{dr}{dt}\right)^2 = v^2 - \frac{e^2}{m^2}A_0^2(r) - 2\frac{e^2}{m^2}\int_0^r z^2\frac{d(A_0(r)A_1(r))}{dr}dr - \frac{e^2}{m^2}\int_0^r z^4\frac{dA_1^2(r)}{dr}dr \tag{16}$$

---

* The author thanks Mr. C. Ookawa for his valuable discussions.

$$\left(\frac{dz}{dt}\right)^3=-4\frac{e^2}{m^2}\int_{z_0}^{z}\times A_0(r)A_1(r)z\,dz-4\frac{e^2}{m^2}\int_{z_0}^{z}A_1^2(r)z^2dz \quad (17)$$

where the particle is assumed, as shown in Fig. 8, to start from the center of the magnetic field with only the normal velocity component v. Therefore the returning point r_0 is determined by putting the right hand side of eq. (16) equal to zero:

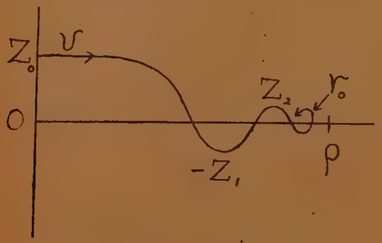

Fig. 8.

$$v^2=\frac{e^2}{m^2}A_0^2(r_0)+2\frac{e^2}{m^2}\int_0^{r_0}z^2\frac{d(A_0(r)A_1(r))}{dr}dr+\frac{e^2}{m^2}\int_0^{r_0}z^4\frac{dA_1^2(r)}{dr}dr \quad (18)$$

As the second and the third terms of the right hand side of this equation are positive, we may conclude that r_0 is smaller than the radius of converging circle ρ. But this difference may be considered to be small because of the smallness of these termes.

Let the points which satisfy the equation $\frac{dz}{dt}=0$, be $z_0, -z_1, z_2, \ldots$ Neglecting the second small term of the right hand side of eq. (17), we have,

$$\int_0^{z_0}A_0(r)A_1(r)z\,dz-\int_0^{z_1}A_0(r)A_1(r)z\,dz=0. \quad (19)$$

Since the integrand of the second term is greater than that of the first term, we obtain,

$$z_0>z_1.$$

By the similar discussion we have,

$$z_0>z_1>z_2>\ldots \quad (20)$$

Thus we may say that the particle approaches to the median plane making a damped oscillation and turns back near the converging circle.

§ 3. Experimental Results and Comparison with the Theretical Conclusions.

The available solid angle is idealy defined in the present case as the tratio i_f/i_a, where i_f is th current to the Faraday cage at the peak poin and i_a is that which is not captured by the gri and flows in the median plane. In order to determine not only i_a experimentally, but also to chec the effect of the magnetic focusing action in th axial direction as discussed in (5), (§2), the curren distribution in this direction was first measure by means of a small Faraday cage placed on th radius ρ which can be translated smoothly from outside by the use of the Wilson seal. The result are shown in Fig. 9. In this figure A and are the cases where the filament has the effective length with regard to emission, of abou 4 mm and 8 mm respectively. The Faraday cag

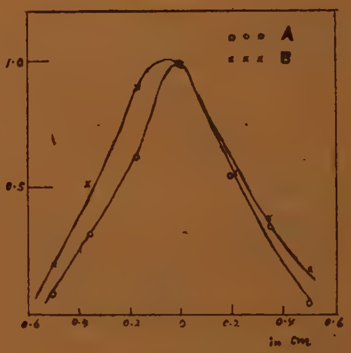

Fig. 9.

used has the dimensions of 3 mm in width, 5.6 m height and 10 mm long. The fact that A and has almost the same type of shape is a clear evidence of the magnetic focusing action which ha been expected by the above theoretical discussion From this measurement, furthermore, we can conclude that almost all particles flowing near th median plane are captured, if we use a Farada cage with its width of 10 mm. In this respect, the demensions of the Faraday cage wa chosen as 10 mm in width, 5,6 mm in height an 10 mm long, although the latter two quantitie may be selected somewhat arbitrarily. Fo the reason stated in (4), (§2), the outersid of the Faraday cage was adjusted to the radiu of the converging circle. Then the peak form was taken by the procedure described in §1 and als the grid current i_g was measured. In Fig. 10 dat are given in the case of the acceleration voltage

1200 volts. The sharp increment of i_g at the peak point means the fact that the particles which pass through the grid turn back by the magnetic field and are captured by the grid and if the particles flow in the median plane, i_g must be equal to the emission current i_0 at any part over the peak. But this is not the case as shown in experimental curve and this means that the fraction of the particles which pass through the grid do not follow their orbit near the median plane. Therefore in deriving the solid angle as defined above we must take into account of this fact. To do this, we estimate somewhat arbitrary i_a as defined above as $i_{g_A}-i_{g_0}$ in Fig. 10, where i_{g_A} is represented as i_g at the "cut off" point of i_f curve. Then one has 35.0 % as the available solid angle and 0.51 % as the resolving power as defined in (4) (§ 2).

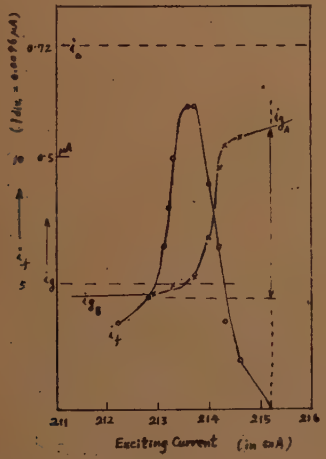

Fig. 10.

The thoretical curves and experimental curve are given in Fig. 11. In drawing those curves we use the fundametal probability curve with the above constants and assume the apparent initial velocity distribution of the particles and also make an assumption that the source is adjusted precisely to the centre, because we can adjust it by the lens system. As one may find from Fig. 11, the 0.4 % distribution curve is consistent with the experimental curve. The voltage drop along the filament is about 0.1 % in the case of accelerating voltage of 1200 volts. The reason, why the velocity distribution spreads more than three times as expected from the above voltage drop, may be mainly the scattering of the particles with the residual gas molecules in the vacuum vessel and also the small eccentricity of the source. To test the former point, the variation of peak value was measured by changing the pressure of residual gas. Fig. 12 shows this effect. From this curve we can estimate this effect and obtain 39 % as corrected solid angle*.

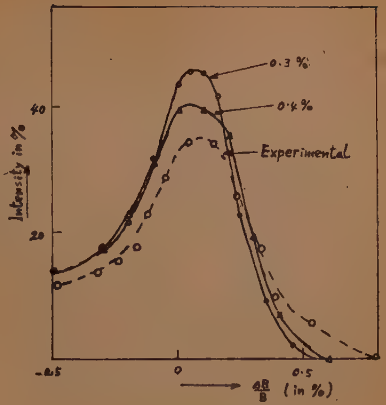

Fig. 11.

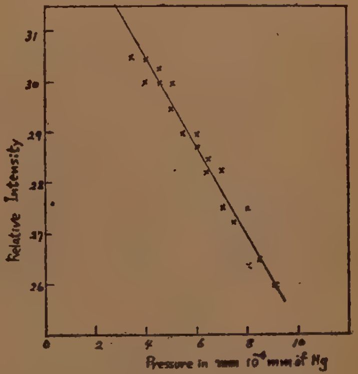

Fig. 12.

Finally we add some experimental results on the effect of the eccentricity of the position of the source as considered in (2), (§ 2). In this experiment we used a tungsten wire of a diameter 0.12 mm and moved it up and down from the position of centre and the quantity of the displacement is measured by that of its image outside the apparatus. Thus we got the peak form and the resolving power *vs.* displacement as Fig. 13. The curve derived from the theory assuming 0.4 %

---

* The comparison between this type of spsctrometer and the semicircular magnetic focusing spectrometer will soon appear in this Journal.

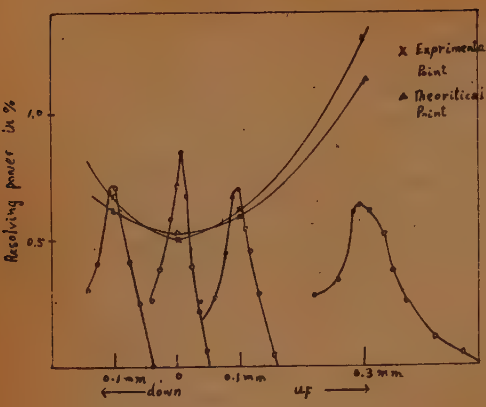

Fig. 13.

initial velocity spread agrees well with the experimental curve. This fact is the evidence that the conclusion in (2), (§ 2) is right.

Reference.

(1) G. Miyamoto: Proc. Phys.-Math. Soc. Japan (in Japanese) **17** (1943) 587.

(2) G. Iwata, G. Miyamoto and M. Kotani: Journal. Phys. Soc. Japan (in Japanese) **2** (1947) 1.

(3) R. Sagane, G. Miyamoto, K. Nakamura and Takechi: Proc. Phys.-Math. Soc. Japan. **25**(1943) 274.

Researches and Developments on the Spiral Orbit Spectrometer (II.)

By Mitsuo SAKAI.

Department of Physics, University of Tokyo.

(Received Sept. 21, 1949.)

Abstract.

In the present paper the effect of intensity distribution of the magnetic field upon resolving power and solid angle is discussed. Analogous to the shimming of a cyclotron, an additional pole piece will increase the intensity without any degeneration of resolving power. Some experimental results on this subject is given here.*

§ 1. Theoretical Consideration.

The leading principle is the idea that if we could increase κ by any means and also increase δ in order to keep δ/κ constant, we may have κ times as large a probability without any sacrifice of the resolving power, because the argument in hyperbolic function in Eqs. (1) and (2) of (III) remains constant. Furthermore, if we consider the fact that to increase κ only is equivalent to make d small and κ is directly effective to increase the probability, we can expect to have a good resolving power with little sacrifice of intensity. For the illustration, the theoretical curve obtained in a case of a β ray source is shown in Fig. 1 with different values of κ.

Expanding the vector potential in the vicinity of ρ, we find:

$$A(r) = A(\rho)-(\rho-r)\left(\frac{\partial A}{\partial r}\right)_{\rho}+\frac{(\rho-r)^2}{2}\left(\frac{\partial^2 A}{\partial r^2}\right)_{\rho} \qquad (1)$$

and comparing Eq. (I) with Eq. (3) of (III) and with the relation $(\partial A/\partial r)_{\rho}=0$, we get:

$$-A(\rho)/\rho^2\kappa^2=\frac{1}{2}\left(\frac{\partial^2 A}{\partial r^2}\right)_{\rho}. \qquad (2)$$

and

$$\kappa^2=2RH(\rho)/\rho, \qquad (3)$$

---

* The notations appearing in the following description are the same as the preceding paper. We refer this paper as (III). The notations of the reference (I) and (II) are also the same as in (III).

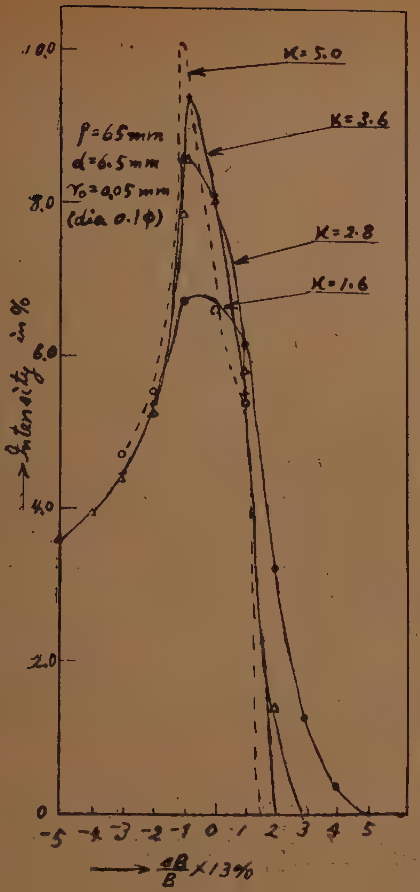

Fig. 1.

where R is the radius of curvature of $A(r)$ at the point of ρ. Next we take 1 st. and 2 nd. derivative of A as follows:

$$\frac{\partial A}{\partial r}=\frac{\partial}{\partial r}\frac{1}{r}\int_0^r Hrdr=-\frac{1}{r^2}\int_0^r Hrdr+H, \tag{4}$$

$$\frac{\partial^2 A}{\partial r^2}=\frac{2}{r^3}\int_0^r Hrdr-\frac{H}{r}+\frac{\partial H}{\partial r} \tag{5}$$

and asuming H as $H=H(\rho)\left(\frac{\rho}{r}\right)^n$ near the converging circle, we easily find:

$$\left(\frac{\partial^2 A}{\partial r^2}\right)_\rho=(1-n)\frac{A(\rho)}{\rho} \tag{6}$$

and from Eq. (2) we have another representation of κ;

$$k^2=\frac{2}{n-1} \tag{7}$$

Of course this formula is connected implicitly with Eq. (3) and one may use this equation in the derivation of κ. From Eq. (3) and (7) it is concluded that in order to increase κ we should make the maximum of curve $A(r)$ as flat as possible and the power factor n of the magnetic distribution r^{-n} near ρ must have the value as equal to unity as possible*. Furthermore to find the physical meaning of κ in respect of the kinematics of particles, we interoduce a variable x as defined $r=\rho+x$ into r component of the equation of motion near the converging circle and take the term of order x^3. Then we get:

$$\dot{x}=\left(\frac{eB}{m\rho}\right)^2\frac{2}{k^2}x+O(x^3), \tag{8}$$

$$=\frac{2\omega_r{}^2}{\kappa^2}x+O(x^3) \tag{8'}$$

$$\fallingdotseq\omega_r{}^2(n-1)x+O(x^3), \tag{8''}$$

where ω_r is the frequency of revolution of particles on the converging circle. Therefore we may understand clearly the meaning of κ if we notice that the stability of motion of particles on the converging circle depends on the square of κ and the more we can increase κ, the larger will be the probability of capture. But in general this consideration is true only in approximation since to derive the average probability with α, we must average with I instead of with θ as done by the authors of (II).

It may be correct to write:

$$I_{\text{av}}\fallingdotseq\frac{1}{\pi}\int_{-\frac{\pi}{2}}^{\frac{\pi}{2}}\text{Min}\left[\frac{\kappa\sqrt{2}}{2\pi}f(\alpha)\,;\,I\right]d\alpha, \tag{9}$$

where Min[ ] means to take the smaller one of the two values in the bracket. But this effect is small usually as shown later in Fig. 5 and 6.

§ 2. Improvement of the Magnetic field.

In order to obtain the magnetic field of larger κ, we first made a preliminary test, using a small model and varying the field by the various additional pole pieces. Then we measured the field distribution for the present apparatus just as used in (1II) with enlarged additional pole pieces. The configuration B in fig. 2 is the one adopted finally.

---

* Notice in our case $n>1$ but $n<1$ in betatron.

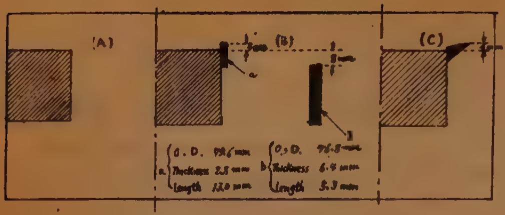

Fig. 2.

For the sake of comparison, A, the normal configuration, and C which gives smaller κ are also given. Distribution of the strength of the magnetic field and the curves of $A(r)$ in each case in $A(r)/A(\rho)$ *vs.* x are represented in Fig. 3 and Fig. 4 respectively. From these figures we find A, B and C have respectively $\rho=6.5$ cm, 8.2 cm and 6.4 cm and $\kappa=1.6$, 3.8 and 0.85, where the values of κ are taken on the innerside of maximum point of A (r), because the detector is placed on this region as discussed in (4), § 2 of (III).

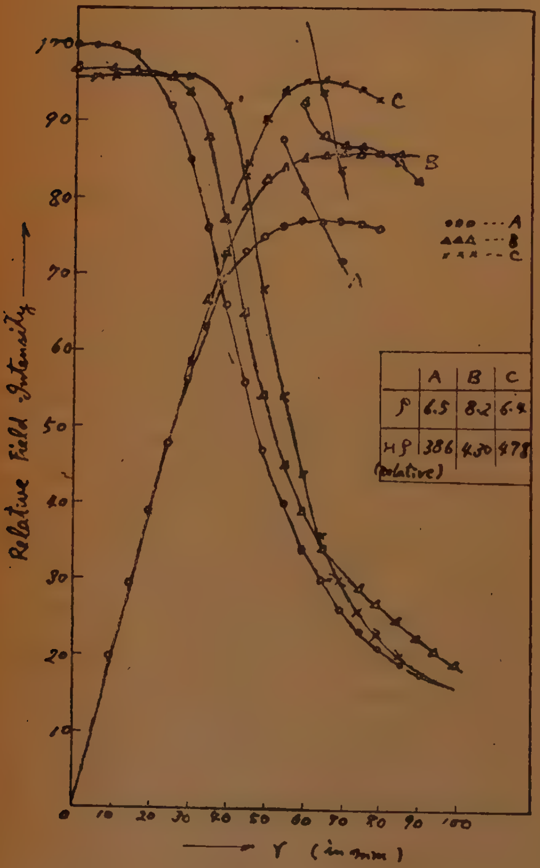

Fig. 3.

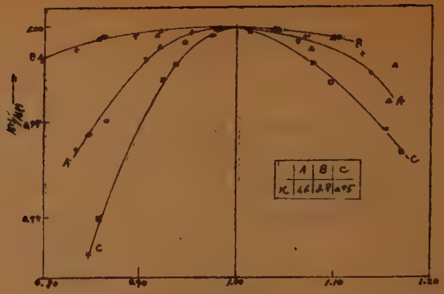

Fig. 4.

§ 3. Examination of the Fundamental Probability Curve.

To keep κ/δ constant in the case of A and B we choose 5.6 mm and 16.7 mm for the value of $2d$. Taking into account of the conclusion in (4), § 2, of (III) the outerside of the Faraday cage is adjusted on ρ, and from Eq. (10) of (III) we may get the fundamental probability curve as in Fig. 5. Using this curve we can easily obtain the curve for the intensity distribution with any kind of an assumption for the initial velocity distribution. For instance, Fig. 6 is represented with the case of 0.4% velocity spread with uniform intensity. As alluded in the preceeding section the maximum intensity in B is two times as large as in A, although κ is 2.4 times in the former case. And also one may notice a slight degeneration of the resolving power.

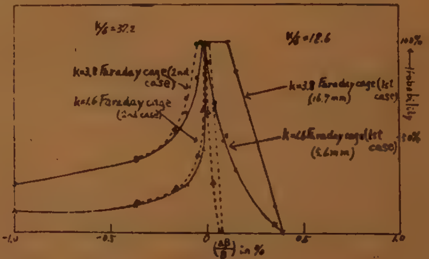

Fig. 5.

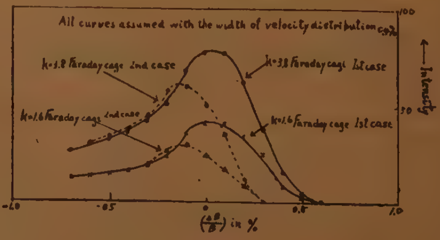

Fig. 6.

§ 4. Experimental Results and Acknowledgement.

For the confirmation of the above theoretical consideration some experiments were done with the same apparatus as used in (III). In this experiment, a Faraday cage with $2d = 16.7$ mm, outerside of which was adjusted to the converging circle, was adopted owing to the consideration of the preceeding section. The peak obtained and that with the same δ/κ in (III) are compared in Fig. 7. The intensity and the resolving power are 78 % and 1.25 % respectively and are in rather good agreement with the value 79 % and 0.5 % as expected in Fig. 6. The degeneration of the resolving power may be mainly due to the particles scattered by the obstacles such as lenses and lamps placed close to the converging circle, since in this case we must use the enlarged radius of converging circle. To verify this point it may be sufficient to notice the fact that the measured peak has more particles in low energy side as compared in A, whereas it has the same sharpness of "cut off" in high energy side.

In this way we may conclude that to make κ large is very efficient in all respect in the spiral orbit spectrometer.

The present author wishes to express his sincere thanks to Prof. R. Sagane for his kind constant guidance, without which these researchs would have been impossible. His hearty thanks are also due to Prof. M. Kotani and Mr. G. Iwata for their valuable theoretical discussions and to Mr. Y. Kamezawa for his sincere experimental cooperation.

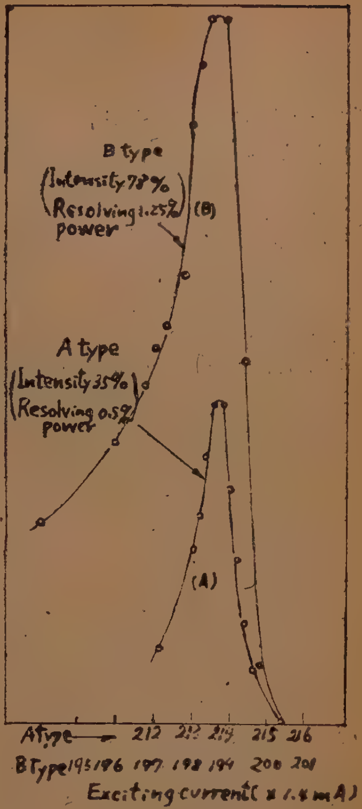

Fig. 7.

Application of the Double Slit Interferometer to the Measurement of Phase Shift of Light Transmitted through Thin Films.

By Kōzō Isiguro.

Department of Physics, University of Tokyo.

(Received September 29, 1949).

§ 1. Introduction.

As regards the phase shift undergone by the light transmitted through thin films, there has been no direct measurements performed, since Quincke(2) and Hurion originated such measurements about 3/4 centuries ago, though for the reflected light some works are known(1). The present writer, experimenting with a simple double slit interferometer(7) (Rayleigh's refractometer modified a little), found that it serves to sufficiently accurate determination of the phase changes. In the following it is intended to give some results of his observations concerning the phase shift of the light during transmission through thin films metallic and non-metallic by means of this instrument.

§ 2. Apparatus.

As shown in Fig. 1, the light taken from a monochromater *A* is made parallel by a collimator *B*, is transmitted through the specimen plate *D*, and illuminates double slit *E*. It is there diffracted, and after passing through a compensator *F* and a double image prism *G*, enters into an ordinary telescope *H* of somewhat large magnification. The eye-piece of cylindrical lense as used in the Rayleigh's refractometer was not employed. To the upper half of *E* a very weak prism, which has been selected among "plane" eye-glasses, is attached in order to deviate the light through the upper half from that through the lower half. The specimen plate *D* is a plane-parallel glass plate (B K 7) 10 mm thick, on which in the central portion two fine parallel streaks 10 mm apart are drawn with carborundum point.

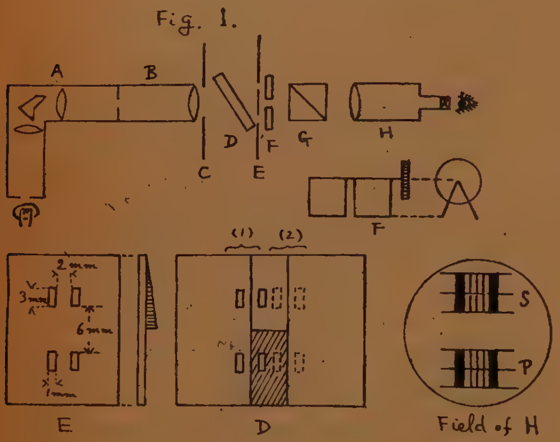

Fig. 1.

The film to be examined is deposited on the lower half of the space between the two streaks. The light transmitted through the film goes to the lower half of only one of the slits of *E* and is brought to interference with the light passing through the lower half of the other slit. The light passing through the upper halves of the both slits produces interference fringes separated from those obtained by the lower halves and serves to comparison (reference fringes). The compensater is to shift sideways the reference fringes alone. It consists of two thin glass plates attached laterally to a common horizontal axis by their edges side by side and making an angle about 15 degrees with each other. They are situated each just behind the upper half of one of the slits, and can be tilted as a whole, the angle of tilt being accurately measurable. The angle of tilt α_0 to bring out the shift of one interference fringe is about 160 minutes. Actually the two compensator plates are obtained by cutting a cover-glass for microscope into two, and the axis to which they are attached is at one end fixed to the centre of the prism-table of a spectrometer in tumbled position.

The double-image prism *G* serves to separate the light of perpendicular and parallel polarization in the field of telescope *H*, so that observation for both polarization can be made at the same time. *C* is a rectangular aperture of 5 mm width and can be moved sideways. If we choose the thickness of the glass plate *D* for 10 mm, the unnecessary reflected light in the glass plate for the large incident angle of 70 degrees will not enter the double slit. *D* can rotate around the axis perpendicular to the paper to change the incident angle and also can move sideways.

At first *D* is placed in the position (1) relative to the double slit *E* (Fig. 1), and F is adjusted to make the reference fringes just coincide to the fringes to be tested. Then *D* is translated to the position (2) and *F* readjusted to the displaced test fringes, the angle of rotation α of the compensator plates being read. Then the phase-shift is determined by the equation

$$\Delta = \frac{1}{2}\frac{\alpha}{\alpha_0} \qquad (1)$$

To get sufficient accuracy, it was necessary to take about 10 readings for each positions to take mean value.

In this paper, when the advance of phase occurs by the film, it is said that Δ is positive and vice versa. For example, the retardations of $\lambda/4$ and λ, correspond to $\Delta = -0.25$ and -1.00 respectively.

The observations can be done for the wave length regeon of 5000 ∼ 7000 Å (with some effort 4800 ∼ 7200 Å).

According to Tolansky(3), the present apparatus is of the two beam interference type and the interference fringes are not so sharp as the multi-beam type. But, in practise, perhaps owing to the logarithmic response of the eyes, the dark frings are fairly sharp and pretty acurrate measurements are possible. The simplicity of the present method may be rather advantageous comparing with the other methods.

§ 3. Observations.

(1) Silver films

Silver was prepared by burning silver nitrate, and it was evaporated from heated tungsten coil in vacuum of the order of 10^{-4} mm Hg. The glass plate to be silvered was placed 10 cm upward the tungsten coil. The observations were done alone for $\lambda = 5890$ Å (with about 50 Å width of wave length) and mainly for the incident angle $\varphi = 0°$ and 70°. The angle 70° was the maximum value by which the measurements can be made without much difficulties with our instrument.

In Fig. 2, 3, 4, (A), the phase shifts of silver films are plotted against theco sine of the incident angle. The thickness of films are respectively about 250, 170, and 300 Å. They were determined from the evaporated quantities of silver by the formula

$$l = M/(4\pi\rho r^2) \quad\dots\dots\dots\dots\dots \quad (2)$$

where M = the evaporated quantities of silver
r = the distance between the coil and glass plate
ρ = the density of silver.

Δ_p means the phase shift of the perpendicularly polarized light (namely, with the magnetic vector parallel to the incident plane) and Δ_s that of the parallel polarized light.

For smaller angles than 70°, Δ_p, Δ_s are not exactly on the straight lines connecting the values for $\varphi = 0°$ and 70°, ($\cos 70° = 0.342$) although they form fairly smooth curves. The broken straight lines merely connect the calculated values for $\varphi = 0°$ and 70°, the calculation being made by the assumption of $n = 0.18$, $k = 3.64$ for silver films and of adequate thicknesses for each films (≃ 210, 180, 300 Å), that is, thicknesses so chosen that the calculated and the measured phase shift for normal incidence coincide.

With the increasing incident angles, the visibility of the fringe of the Δ_p component became gradually worse, while Δ_s component gradually better.

The values of Δ_p do not change remarkably from the value for $\varphi = 0$ and have the positive sign, that is, the phase advances in the silver film rather than in the air of equall thickness. On the contray the values of Δ_s decrease almost straightly and some times change its sign for large angles.

The advancing of phase for $\varphi = 0$ in silver film has been already recognized by Quinke(2) and the differences between Δ_p and Δ_s are known indirectly by polarimetric experiments(4) and directly by Blau(5) and Tolansky(3). But the author is not aware of reports which treated the problem in the most direct way as in the present paper.

Behaviours of the phase shift mentioned above may be presumed from the electromagnetic theory by the assumption that the film consists of uniform material bounded by two geometrical planes(6). But such discussions together with more accurate measurements concerning with silver will be given in a near future.

Fig 2 shows also the change (B) undergone when the opened bottle of HCl was approached for several minutes to the specimen after the measurement (A), and represents an example how the silver film is sensitive to contaminations.

Fig. 3, 4 concern the specimen which were after the measurement (A) changed to AgBr, having been placed in the vessel filled with Br_2 vapour about 1 hour or more, and measured after the evacuation of several minutes (B). These AgBr films have native phase shifts and pre s ent large irregularity.

The field of telescope bacame in this case somewhat blurred perhaps due to scattering.

In Fig. 3, the AgBr film had been illuminated for several minutes by the quartz mercury lamp

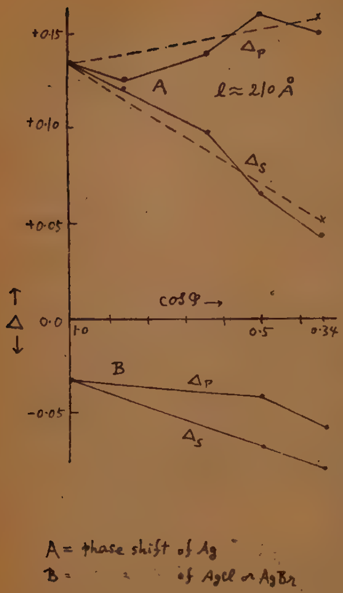

Fig. 2.

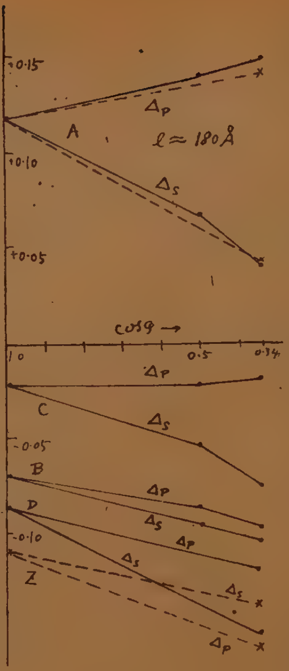

Fig. 3.

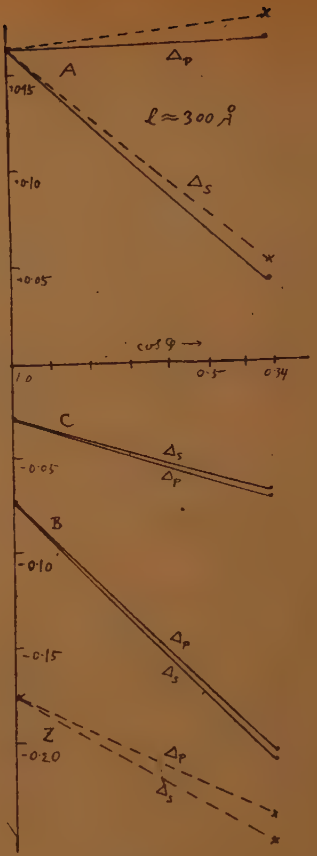

Fig 4.

(in that stage distinct change was not observed) and then blackend by M. Q. developer (C), then again exposed to the Br_2 vapour (D). In Fig. 4 the AgBr film had been exposed to the sun beam about 5 hours (C). After the exposure, the film became very transparent and the scattering decreased. The phase shifts had the very small negative values. Any deposition of metalic silver was not observed, and the blackening, or noticeable phase changes did not occured by developement. Any how, the observed phase shifts (B) are always fairly small compared with the calculations (Z), which were done under the assumption that Ag film turned completely to AgBr ($n = 2.253$).

(2) Pb films

The measurements of phase shift were done only for the normal incidence, while intensity measurements of the transmitted light were added, all for $\lambda = 5890$ Å. In Fig. 5 transmission T_0', by which the ratio of the transmitted intensities

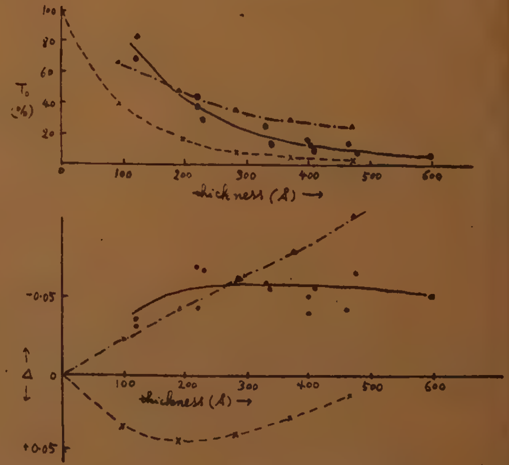

Fig. 5. Phase shift $\varDelta$

● Full lines = observations

× —·— — — = calculations for $n = 2.01$, $k = 3.48$

△ —·—·— = calculations for $n = 2.6$, $k = 1.2$

through the film and the bare glass plate is meant, is given for various thicknesses. The broken line represents the the theoretical values calculated by the use of the Drude's optical constants for lead $n = 2.01$ and $k = 3.48$. The full smoothed experimental curve does not coincide with it, so that apparaently our determination of the film thicknesses is not correct. The disagreement with theory is, however, more remarkable for phase shifts, as phase retardations of about $-0.05(\lambda/20)$ were ovserved for all the thicknesses, while theoretically there ought to be advancing of phase. If we take the optical constants as $n = 2.0 \sim 2.5$ and $k = 1.0 \sim 2.0$, the measured values may be somewhat accordant (the lines —·—·—·— in the graps correspond to $n = 2.6$, $k = 1.2$). But the origin of the inconsistency is not yet clear. If there occurred some oxidation of Pd film during the process of evaporation, such behaviors might be explainable. (The purity of the used lead was of the order of chemically pure.)

(3) ZnS films

Several specimens of different thickness were made by evaporation. By the intensity measurement, the wave lengths of maximum and minimum transmission of the films were determined. (The intensity measurement was made fairly accurately with photo-cells and UX-54 tube. The details of the measuring apparatus and the observed curves of the transmitted and reflected intensities will be given later in another place.)

With these wave lengths, λ_m, the relation

$$nl = m\lambda_m/4 \qquad m = 1, 2, 3, \ldots\ldots\ldots \quad (3)$$

must hold, where

$n =$ the refractive index of ZnS film and

$l =$ the thickness of film,

while the phase shifts are represented by

$$\Delta_m = (l - nl)/\lambda_m \ldots\ldots\ldots\ldots\ldots \quad (4)$$

From (3), (4), eliminating l,

$$n = 1/(1 + 4\Delta_m/m)$$

In this equation, m is easily determined by inspection of the intensity curves, and as Δ_m are measurable, it is possible to determine the refractive index of ZnS film.

The results of such determination are represented in Tab. I, and Fig. 6.

Tab. I.

Specimen	No. 1		No. 2		No. 3		No. 4	No. 5
$\lambda_m(\mu)$	0.512	0.590	0.550	0.680	0.535	0.685	0.660	0.610
Δ_m	−0.885	−0.741	−0.700	−0.549	−0.579	−0.431	−0.275	−0.142
m	6	5	5	4	4	3	2	1
Δ_m/m	−0.148	−0.148	−0.140	−0.137	−0.145	−0.144	−0.138	−0.142
n	2.43	2.47	2.28	2.22	2.38	2.35	2.22	2.31

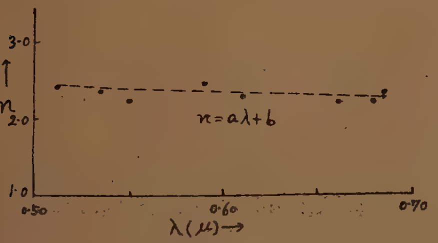

Fig. 6. Refractive index of ZnS.

Assuming a linear relation $n \doteqdot a\lambda + b$ simply, the constant a and b were calculated by the method of least squares with the values in Tab. I. The values $a = -0.927\ (\mu)^{-1}$ $b = 2.89$ were thus obtained, and from these constants, the refractive index for $\lambda = 0.589\ \mu$ was determined as

$$n = 2.34 \pm 0.06$$

which shows fairly good agreement with the refractive index given for spharelite

$$n = 2.37$$

§ 4. Conclusion.

From the several examples given above, it can be said that the simple double slit interferometer serves to measurements of phase shifts and is fairly useful for the investigation of thin films, especially when it is combined with the intensity measurement.

The author wishes to express his thanks to Prof. M. Kiuchi for the kind guidance and also to Mr. G. Kuwahara of our institute, who made the intensity measurements for him and to Mr. M. Inoue of the Hitachi Kameari Works, by whom the pure silver was presented to him.

References.

(1) Winkelmann's Hand. d. Phys. VI (1906) 1311.
(2) G. H. Quinke: Pogg. Ann. **142** (1871) 177.
(3) S. Tolansky: Multi-Beam Interferometry of Surfeces and Films (1947).
(4) B. Pogany: Ann. d. Phys. **49** (1916) 531. G. Essers-Rheindorf: Ann. d. Phys. **28** (1937) 297.
(5) L. W. Clau, R. R. Thompson: Zeits. f. Inst. Kund. **49** (1929) 57.
(6) For example, the fundamental equations of H. Wolter: Z. P. **105** (1937) 269.
(7) K. Ishiguro: Ōyō Butsuri **15** (1946) 11 (in Japanese).

On the Vapour Flow in the Diffusion Pump.*

By Seiichi ŌYAMA.

Institute of Science and Technology, University of Tokyo.

(Received November 17, 1949).

§ 1 Introduction.

The back flow of vapour towards the vacuum vessel is an important factor affecting the pumping speed of a diffusion pump, but the theoretical treatment has not yet been presented except one by Molthan(1), which is too simple to be applied for practical purposes. In fact he assumed that when the vapour is effusing through a small hole into a vacuum the vapour molecules obey the Maxwell law of velocity distribution but the angular distribution of the molecules with a definite speed v has a spherical symmetry. If the vapour is flowing as a whole along the wall at a constant speed V, the above-mentioned spherical distribution is displaced uniformly towards the flow direction by an amount V and thus all the molecules with speed v smaller than V are to be carried away completely to the right hand side of y-axis (cf. Fig. 1). Some of the molecules having speed v larger than V, however, are able to effuse into the left hand side of y-axis; and Molthan assumed that these molecules might be considered to produce the back flow. He calculated the amount of the back flow by integration over the possible values of v ranging from V to infinity in accordance with the velocity distribution of Maxwell. The assumption of spherical symmetry, however, is not justified to be valid from the viewpoints of either hydrodynamics or kinetic theory of gases. When a gas is allowed to discharge into vacuum, its compressibility should of course be taken into account in the hydrodynamical treatment, which leads to the invalidity of the above assumption, and further, it is well known according to gas-kinetic theory of effusive flow through a small hole, that the angular distribution obeys the cosine law(2). Besides, his defini-

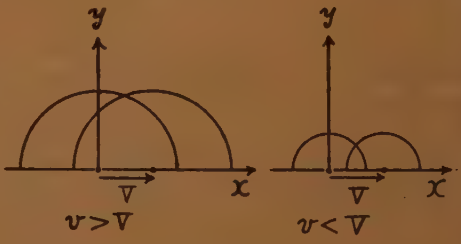

Fig. 1.

---

* The content of the paper was read already in the annual meeting of the Physical Society of Japan held in May, 1948.

ion of the back flow is too simple to take acount of the effect of the geometrical structure f the pump. Finally, it may be pointed out that e did not pay any attention to the fact that the apour shows the tendency of forming small liquid rops during its expansion; indeed the correct reationship between pressure and density is unnown. In view of the mentioned situation his reatment may be considered to be only a first trial f attack of the phenomena in question, so it will e worth while to propose here the author's method.

The pressure of the working vapour of a difusion pump is usually about 1 mm Hg in a nozzle nd therefore its mean free path is much smaller han the scale of the nozzle so that hydrodynamial treatment may still be permissible. Morever, we can expect the appearance of a superonic flow under a suitable design of the nozzle and the fore-vacuum. Therefore, we first apply the Prandtl-Meyer theory of supersonic gas flow around a corner(3) to the vapour flow in the nozzle, and then, to discuss the region of highly rarefied vapour, we make use of the kinetic theory of gases. Thus we find the manner in which the intensity of the back flow is affected by the presure of a working vapour, by its Mach number, and by the width of the clearance connecting the working section of the pump with a vessel to be evacuated. As a results, it is found that the supersonic velocity of vapor flow is much profitable for increasing the pumping speed.

§ 2. Vapour Flow from a Nozzle.

For simplicity we confine the problem to two limensions and then assume one of the walls of nozzle to be removed infinitely distant in order o avoid the interference of two expansion waves ent out from both edges of the nozzle. Thus we re able to apply the Prandtl-Meyer theory of he supersonic flow around a corner to the vapour low under consideration, but after enough exansion for its mean free path to be 1 mm (cf. ig. 2 Line ON) we cease application of the theory nd consider the stream to be flowing away arallel to OB with the velocity V correspondng to the state on the line ON. Then we make se of the kinetic theory to estimate the number of melecules evaporating from the surface OB. To start such a calculation we mnst be given such quantities as the speed V and the position of line OB etc., which can be determined as functions of the state before expansion (corresponding to the region AOM). For convenience' sake it is arbitrally decided that the both treatments, hydrodynamical and gas-kinetical, should be connected at the line ON where the mean free path attains 1 mm.

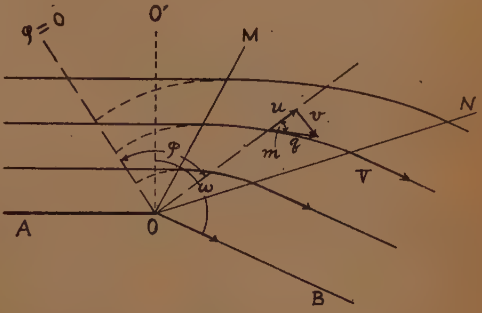

Fig. 2.

Taking into consideration the fact that the vapour pressures, p, of mercury is nearly proportional to T^{20} (T being absolute temperature) near $p=1$ mm Hg, $T=399°$, we shall consider the vapour flow as an adiabatic process of an imaginary gas whose γ, the ratio of the two specific heats, takes 20/19 passing through the state $p=1$ mm Hg and $T=399°$. Further, we shall also make brief calculation with the value 5/3 for γ in view of the fact that the formation of small liquid drops has not yet been experimentally confirmed in such a low pressure, and so it might be conceivable that the vapour would be also to remain in a supersaturated state. The correct treatment of the vapour flow accompanied with the formation of fog is very difficult, and detailed investigation in future will be necessary.

Let us introduce polar coordinates r, φ, taking the origin at the edge of a nozzle. When the constant of integration is made to vanish by measuring φ from the radius at which $u=0$, the results of the Prandtl-Meyer theory are

$$q^2=\frac{2\gamma p_0}{(\gamma-1)\rho_0}\left\{1-\frac{1-\lambda^2}{2}(1+\cos 2\lambda\varphi)\right\}, \tag{2.1}$$

$$\frac{p}{p_0}=\left(\frac{\rho}{\rho_0}\right)^{\gamma}=\left(\frac{T}{T_0}\right)^{\gamma/\gamma-1}=\left\{\frac{1}{\gamma+1}(1+\cos 2\lambda\varphi)\right\}^{\gamma/\gamma-1} \tag{2.2}$$

$$\tan m \equiv v/u = \lambda \cot \lambda\varphi, \qquad (2.3)$$

where (u, v), q, ρ, m are respectively the velocity, its magnitude, the density of vapour, local Mach angle and $\lambda^2 = (\gamma-1)/(\gamma+1)$.

Henceforth let us discriminate the various states by suffixes, thus giving suffix $_0$ for the stagnation point, $*$ for the state where the velocity q attains the local sound velocity, $_1$ just before expansion and $_2$ for the state in the region NOB where the mean free path equals 1 mm.

If we consider a molecule to be a rigid sphere, then the mean free path l can be related to n, the number of molecules per unit volume, and its diameter σ as follows[(4)]:

$$l = (\sqrt{2}\pi n\sigma^2)^{-1}. \qquad (24)$$

Neglecting small variation in σ with T, we can take

$$\sigma = 4.26\times10^{-8}\,\mathrm{cm}$$

from the experimental data of viscosity. Then l is given by

$$l = 0.01712(T/p)$$

which serves to determine the line ON or the direction OB. Thus we can get the desired quantities φ_2, $q_2 \equiv V$ and T_2 as functions of p_1 and Mach number M_1, which is the ratio of q_1 and the sound velocity at the point.

§ 3. Effusive Molecular Flow.

It is well known that the two-dimensional angular distribution of molecules effusing from a slit with the speed v is given by

$$f(v, \theta) = (n\beta^2 v^2/\pi) \sin \theta e^{-\beta^2 v^2} \qquad (3.1)$$

where θ is measured from the x-axis' and

$$\beta = (m/2kT)^{1/2} = 2/(\sqrt{\pi}\,\bar{v})$$

(cf. Fig. 3).

But when a gas is flowing away with the speed V parallel to the plane $x'x$, the mentioned distribution is displaced towards the flow direction so that the forward part becomes predominant. Now we shall estimate the angular distribution in this case. Those molecules which, in a coordinate system moving with the flow (C-system have a speed v in the direction making an ang α with the x-axis will have a velocity (v', θ) i a system at rest (R-system) such that (cf. Fig.

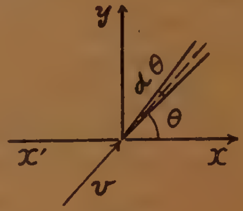

Fig. 3

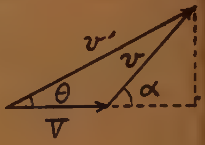

Fig. 4.

$$\left.\begin{aligned} v' \cos \theta &= V + v \cos \alpha, \\ v' \sin \theta &= v \sin \alpha. \end{aligned}\right\} \qquad (3.2$$

Hence

$$v/V = (\cot \theta \cdot \sin \alpha - \cos \alpha)^{-1} \qquad (3.3$$

$$\frac{d\theta}{d\alpha} \; \frac{v(V \cos \alpha + v)}{V^2 + 2Vv \cos \alpha + v^2} \qquad (3.4)$$

So the distribution function $g(v, \theta)$ in the R-system where v represents the speed due to the heat mo tion, can be related to $f(v, \alpha)$ in the C-system a follows:

$$\begin{aligned} g(v, \theta) &= f(v, \alpha) d\alpha/d\theta \\ &= \frac{n\beta^2 v}{\pi} \sin \alpha \cdot e^{-\beta^2 v^2} \frac{V^2 + 2Vv \cos \alpha + v^2}{V \cos \alpha + v} \end{aligned} \qquad (3.5)$$

We can get the anglar distribution $I(\theta)$ in th R-system by integrating (3.5) over all the possibl values of v. Thus

$$I(\theta) = \frac{n\beta^2 V^3}{\pi} \int_\theta^\pi \frac{\sin^2 \alpha}{\sin^2 \theta} \left(\frac{v}{V}\right)^4 e^{-\beta^2 V^2 (v/V)^2} d\alpha, \qquad (3.6$$

where v/V is a function of α with a paramete θ and its behabiour is shown in Fig. 5. Fo numerical calculation it is convenient to tabulat (v/V^2) and $(\sin^2 \alpha/\sin^2 \theta)(v/V)^4$.

§ 4. Numerical Results.

Let us denote the minimum section of a nozz by S_*. When the fore-vacuum is good, the ve locity of the flow attains here the sound velocity If the area of the aperture S_1 is equal to S_*, th flow will effuse with the sound velocity (i.e. M_1 = 1). In order to get the supersonic flow ($M_1 >$ we must design the nozzle like a Laval nozzle, a the necessary relation can be obtained from th continuity equation $S_1\rho_1 q_1 = S_*\rho_* q_*$. Next, the structure of the clearance connecting with the vacuum vessel will be assumed to be such as shown in Fig. 6, and the width d may be varied by a diaphragm. Thus we define the intensity of the back flow H by the number of molecules aiming at the clearance d. The position of line OB is determined by $\omega \equiv \angle O'OB$ which is obtained from the relation

$$\omega = (\varphi_2+m_2)-(\varphi_1+m_1)+90°$$

(cf, Fig. 2 and Fig. 6).

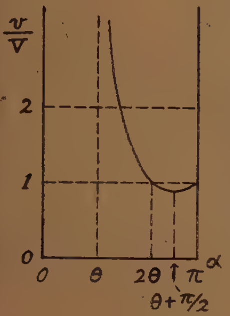

Fig. 5

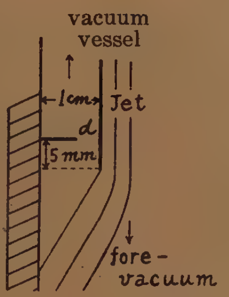

6.

We shall investigate the effects of the pressure p_*, the Mach number M_1 and the width d of the clearance upon the back flow H. It must be pointed out that p_* is a certain measure of the heating current of the pump and M_1 is related to the cross section S of a nozzle. We have calculated for the cases when p_* is 5, 1, 0.1 mm Hg and M_1 is 1, 1.406, 2.262 respectively for the flow of imaginary gas with $\gamma = 20/19$. In Table I various quantities necessary for the calculation are given, where c denotes $[2\gamma/(\gamma-1)\cdot p_0/\rho_0]^{1/2}$ Also the results for $\gamma = 5/3$ are given. Fig. 7 shows $I(\theta)$ for these cases. Although the value ω is affected by Mach number M_1, $I(\theta)$ itself does not depend on M_1 and can be determined only by p_*. When p_* is high, the value V becomes so large that the distribution of the forward part tends to be more predominant. As regards the case $\gamma = 5/3$, temperature drop during the expansion is so rapid and consequently the heat motion becomes so weak that the backward distribution is practically zero (cf. Fig. 7, dotted line). Of course this is desirable, but it is hardly conceivable that the formation of fog does not occur during such rapid cooling. Therefore we did not attempt further study in this case.

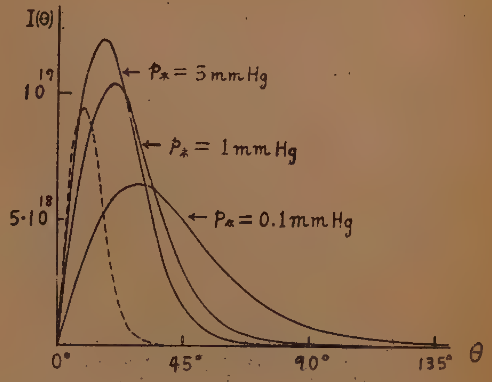

Fig. 7. dotted line is for $\gamma = 5/3$, $p_* = 1$mm Hg.

Having obtained the situation of line OB and the angular distribtion $I(\theta)$ or $Z(\theta) \equiv \int_\theta^\pi I(\alpha)d\alpha$, we can estimate the back flow H for the given structure of the pump. As shown in the definition of the back flow, we assumed the condensation at the wall to be complete. In Fig. 8 H is plotted against clearance d. We can see that highly supersonic flow is effective for reducing the back flow, particulaly when p_* is high. In Fig. 9 curves of H versus p_* are shown with d as a parameter. It will be seen that the pressure minimizing H tends to decrease with increasing d. Now, it is obvious that with larger V and smaller ω back flow will be less. But with increasing p_* both V and ω increase, and thus H is determined by the balance of these two effects.

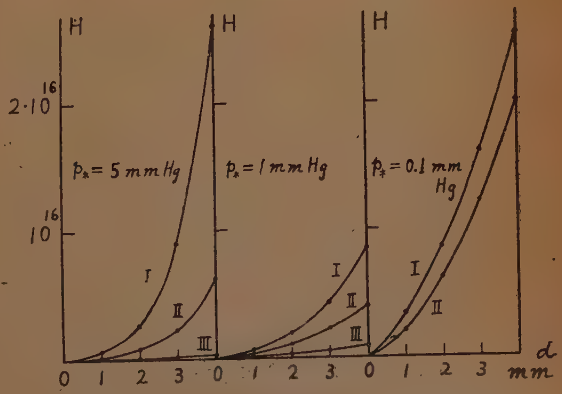

Fig. 8. The Intensity of the Back Flow versusthe Clearance.
I: $M_1 = 1$, II: $M_1 = 1.406$, III: $M_1 = 2.262$

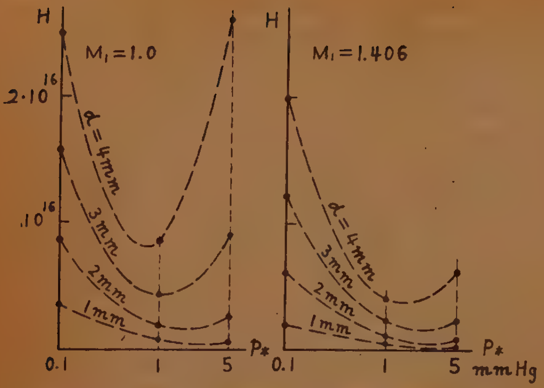

Fig. 9. The Intensity of the Back Flow versus the Vapour Pressure.

In view of these general tendencies obtained above, it may be recommended to use a vapour of pressure of several mm Hg and make a fairly wide clearance, and to design a nozzle in the form of a Laval nozzle so as to produce a highly supersonic flow. These are also profitable to give air molecules a sufficiently large momentum towards fore-vacuum. It seems to the author that when a pump is well designed, the effect of incomple condensation at the wall surface becomes remar able compaired with the above-mentioned dire back flow.

§ 5. Summary.

Investigating the vapour flow in a diffusio pump by a method proposed here by the preser author, the general tendencies of the effects the working vapour pressure, its Mach numbe and the clearance connecting with a vacuu vessel upon the back flow of the vapour can seen and the advantage of a supersonic flow emphasized. As the working pressure of th vapour is at most several mm Hg, and consequen ly the Reynolds number of the flow is very smal the sepration of the flow or the formation of shock wave may probably be much delayed s that we can expect the presence of the super sonic flow without great difficulty. But on th other hand we are using a vapour and not a

Table I. (denotes that the value in the left neighbouring column should be taken.)

	$\gamma=\frac{20}{19}$								$\gamma=\frac{5}{3}$
	$p_*=5$ mm Hg $=6666.1$ C.G.S.			$p_*=1$ mm Hg $=1333.2$ CGS			$p_*=0.1$ mm Hg $=133.32$ C.G.S		$p_*=1$ mm Hg
$2\varphi_1/\sqrt{39}$	0°	18°	36°	0°	18°	36°	0°	18°	
p_1(C.G.S.)	6666.1	4061.5	895.65	1333.2	812.30	179.13	133.32	81.23	1333.2
M_1	1	1.406	2.262	1	1.406	2.262	1	1.406	1
S_1/S_*	1	1.153	3.128	1	1.153	3.128	1	1.153	1
φ_1	0	56°13′	112°25′	0	56°13′	112°25′	0	56°13′	0
m_1	90°	45°19′	26°14′	90°	45°19′	26°14′	90°	45°19′	90°
φ_2	170°41′	,,	,,	139°47′	,,	,,	72°19′	,,	136°27′
m_2	17°12′	,,	,,	21°15′	,,	,,	37°39′	,,	11°18′
ω	187°53′	176°22′	139°15′	161° 2′	149°31′	112°24′	109°58′	98°27′	147°45′
T_0	443.82°	,,	,,	409.50°	,,	,,	364.97°	,,	532.00°
c(cm/sec)	85780	,,	,,	82390	,,	,,	77790	,,	33200
V(cm/sec)	41230	,,	,,	33660	,,	,,	19820	,,	31440
T_2	341.2°	,,	,,	,,	,,	,,	,,	,,	54.98°
β^2	35.35×10^{-10}	,,	,,	,,	,,	,,	,,	,,	2.194×10^{-8}
n_2	1.241×10^{15}	,,	,,	,,	,,	,,	,,	,,	,,

eternal gas, so that much consideration should always be given to the formation of fog during the expansion, although its influence has not yet been investigated. The author desires first of all that experiments will be made in order to confirm if or not the vapour flow in the diffusion pump is really supersonic, and secondly, if the flow proves not to be supersonic, that the supersonic flow will be acieved by improvement of the design of fore-vacuum or a nozzle and by trial such as superheating of the vapour before expansion.

In the present paper some simplifications are made, which, the author believes, do not change much the above-mentioned general tendencies. Finally, it was not attempted to study the case of subsonic vapour flow, because according to hydrodynamics the intensity H of the back flow in this case seems to be considerably greater. Also, even if a supersonic region appears near the throat of the nozzle, it may happen that the region is very small and immediately followed by a shock wave, thus the flow becoming subsonic downstream. In such a case, H will again be large. It seems to the author that these case may correspond to the state such that the diffusion pump does not work efficiently due to bad fore-vacuum condition.

In conclusion the author wishes to express his cordial thanks to Dr. I. Imai for his kind interest and encouragement.

References.

(1) W. Molthan: Zeits. f. techn. Phys. **8** (1926) 377.
(2) E. H. Kennard: Kinetic Theory of Gases, (1938) 62.
(3) W. F. Durand: Aerodyamic Theory, **3** (1934) 243.
(4) E. H. Kennard: loc. cit. 113.

Short Notes

On the Magnetostriction Vibrator as a Source of Suppersonics.

By Yoshihito Takesada.

Institute of Geophysics, Kyoto University.

(Recived Oct. 25, 1948).

Introduction.

The vibrator of magnetostriction is employed for the radiation and reception of supersonic (about to 60 Kc). In the case of the exciting current applied to the vibrator, the vibrator of Al about 13 % Fe-alloy (Alfer) has the same order efficiency as that of the vibrator of Ni. When the high power sound waves are radiated, the air bubbles are generated in the neighbourhood of the vibrator and a large abnormal absorption will occur by the air bubbles. Accordingly, the transmitting power of the sound will be much decreased in the neighbourhood of the vibrator. The absorption coefficient of the weak sound waves may be taken from Stokes formula for practical purposes. But there still remains the necessity of computation of the absorption coefficient of the high power sound waves in the neighbourhood of the vibrator.

§ 1. Alfer Vibrator and its Wave Transmission.

The magnetic property of the Fe-Al system alloy was studied by A. Schulze*. He obtained the value of 33.8×10^{-6} for $\delta l/l$ (l means length) in the external magnetic field of 350 *Oe* for 10.52 % Al-Fe alloy. Dr. H. Masumoto determined experimentally the relation between magnetostriction and intensity of magnetization for Fe-Al alloy of 16.56 % Al in the mgnetic field of 0 to 1200 Oe. The metal of Al 12.68 % Fe-alloy is named by Dr. H. Masumoto as Alfer. The $\delta l/l$-H curve for Alfer obtained by him is shown in figure

(1). By the exprimental method illustrated in figure (2), we have obtained the result which is given in figure (3). The dependence of the efficiency upon its position is shown in figure (4) with respect to the Alfer vibrator. When we put the vibrator in the depth of 3-M in the sea with disturbing surface and measured sound intensity, we get the lowest curve in figure (4). It shows that the disturbance of medium is a large factor for the attenuation of sound. In this measurement, the radiating surface of vibrator is 18.8 cm×10 cm, the thickness of which being 0.5 mm, the resonance frequency, 23.6 Kc and temperature of the water, 27°C.

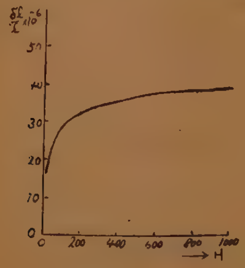

Fig. 1.

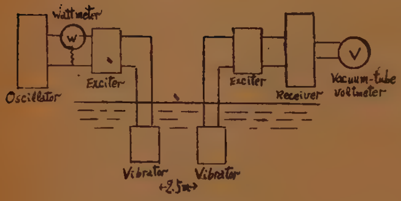

Fig. 2.

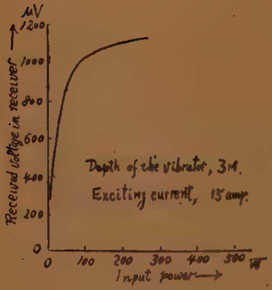

Fig. 3.

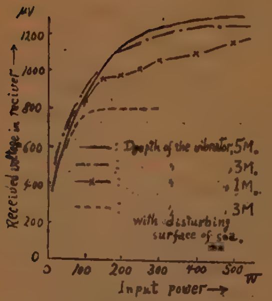

Fig. 4.

§ 2. The sound waves near the vibrator.

When the intense waves are radiated to the medium, the air bubbles which are generated by the sound waves will raise the damping of sound intensity. In the case of the magnetostriction vibrator (radiating surface is 18.8 cm × 10 cm) driven by the power of about 0.7 watt/cm^2, practically the cavitation phenomena appear in the vicinity of the vibrator due to the large intensity of sound wave. When the vibrator is placed in the sea near the bottom, we shall have a long distance of sound propagtaion in comparison with the vibrator which is placed in the sea near the surface. The intensity of the sound transmitted from the the vibrator to the surrounding medium, has various balues based on acoustic resistance ρc for the medium.

Put the wave equation as, $\partial^2\Delta\rho/\partial t^2 = \partial^2\Delta p/\partial x^2$. The phase difference between $\Delta\rho$ and Δp is denoted by φ, and the variation quantity of density and pressure is given by $\Delta\rho = \Delta\rho_0 \exp[i\{\omega(t-x/c)\}-\alpha x]$ and $\Delta p = \Delta p_0 \exp[i\{\omega(t-x/c)+\varphi\}-\alpha x]$ respectively. From this we find $(1-ic/\omega\cdot\alpha)\exp(i\varphi/2) = 1$ where $C^2 \equiv (\Delta p/\Delta\rho)_0$ for the practical velocity of sound in fluid mixtures. If the medium is adiabaticaly changed by the sound waves we have the relation $\Delta p/p_0 = \gamma\Delta\rho/\rho_0$. And then $\exp(i\varphi/2) = V/C$ where $V \equiv \sqrt{\gamma p_0/\rho_0}$ for the velocity constant of sound in water. Therefore absorption coefficient will become $\alpha = |\omega/V(V/C-1)|$. The absorption coefficient for the sound waves of large intensity is derived from $|V-C|$. The absorption coefficient for various $|V/C-1|$ is shown in figure (5).

Conclusion.

The vibrator of Alfer is employed by supplying the proper exciting current.

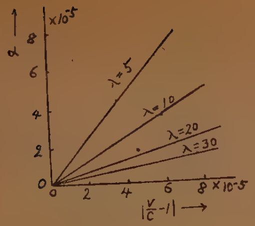

Fig. 5.

The absorption coefficient of the sound intensity near vibrator is indicated by $\alpha = |\omega/V(V/C-1)|$. In order to obtain an effective sound radiation, we must give the high static pressure to the medium around the vibrator.

Reference.

* A. Schulze. Z. Phy. **50** (1928) 495.

On the Structure of Adsorbed Organic Long-Chain Molecules on the Clevage Surface of Molybdenite.

Yoshiro Kainuma and Ryozi Uyeda.

Physical Institute, Faculty of Science, Nagoya University.

(Received September 18, 1949.)

Several years ago, one of us(1) observed unidentified patterns as illustrated schematically in Fig. 1 in the electron diffraction photographs of the cleavage surface of molydenite. Recently the other of us explained the patterns by assuming the adsorption of long-chain hydrocarbon molecules on the cleavage surface of molybdenite. They are oriented on the surface of molybdenite as shown in Fig. 2. The plane of the zigzag chain of the molecule is parallel to the surface and the chain is parallel to the side of the hexagon of the base crystal. The number of chains oriented parallel to each other is at least 40 or 50, because the pattern of the a-azimuth is very sharp (Fig. 1a). From the distance r in Fig. 1a the distance between the chains is calculated to be 4.63A. (Fig. 2). If the C-C distance and the bond angle(2) are assumed as given in Fig. 2, the van der Waals radius of methylene radical turns out to be 1.99A, in good accordance with the available data.(3) From the sharpness of the pattern in the b-azimuth, which is rather diffuse, the number of carbon atoms in the molecule is estimated to be about 30.

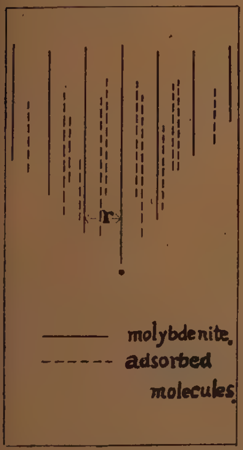

Fig 1a. Diffraction pattern of the a-azimuth.

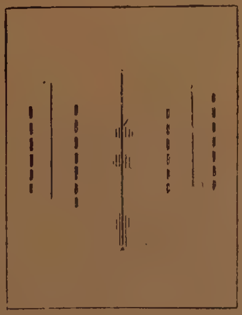

Fig. 1b. Diffraction pattern of the b-azimuth.

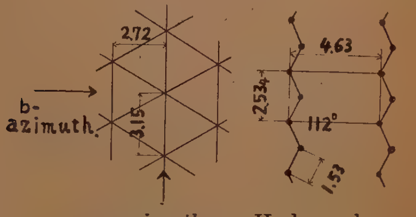

a-azimuth Hydrocarbons.
Molybdenite

Fig. 2. Orientation of hydrocarbons on the cleavage surface of molybdenite.

It is also worth being mentioned that we observed satellites on both sides of the principal reflection spectrum, as shown in Fig. 1b. They appear only in the b-azimuth (with one exception) when intensity of the pattern described above becomes strong. They may be due to the long spacing of the adsorbed layer, although their sharpness is difficult to be explained. If this is the case, the long spacing is calculated to be about 38A in good accordance with that calculated from the breadth of the layer line.

The origin of the adsorbed molecules is not yet clear, but it may be the vapour of oil or grease in the vacuum apparatus.

We observed that these patterns disappear at high temperatures(4). It is rather remarkable that the organic molecules lie flat on the base surface in contrast to the most of the reported cases(5) in which they stand vertically on it. It is also interesting to study the mechanism how the above orientation is produced, but we postpone the discussions until more data are available.

References.

(1) R. Uyeda: Proc. Phys.-Math. Soc. Jap. **18** (1936), 563, **20** (1936) 556.
(2) C. W. Bunn: Trans. Faraday Soc. **35** (1939) 482.
(3) L. Pauling: The Nature of the Chemical Bond. p. 190.
(4) R. Uyeda: Proc. Phys.-Math. Soc. Jap. **24** (1942) 812.
(5) G. P. Thomson and W. Cochrane: Theory and Practice of Electron Diffraction. p. 197.

Absorption Spectra of Colored Potassium Chloride Containing Several Kinds of Impurities.

By Sei-ichi KONDO, and Tokuo SUITA.

Faculty of Engineering, Osaka University.

(Received Nov. 15, 1949.)

The absorption spectrum of additively colored potassium chlorides containing a small quantity of thallium chloride was observed by O. Stasiw,(1) and an absorption band at about 4000 Å named K was found. On the origin of it's absorption center, however, nothing has been known.

We have carried out some experiments, and tried a qualitative interpretation of this phenomenon.

We made single crystals from melted potassium chlorides mixed with several mol per cent of NaCl, AgCl, TlCl, $PbCl_2$, $BaCl_2$, etc. by Kyropoulos' method(2). The crystals thus grown have, in general, about 0.1 mol per cent impurities. These crystals can not be colored uniformly by the additive coloration, and become opaque with colloidal appearance. But those irradiated with X-rays show the characteristic colors to their impurities. For example, the crystals containing AgCl color in red brown, NaCl weak yellow blue, TlCl red-purple, and $BaCl_2$ weak yellow. These colors fade out easily by the white light like the ordinary F-band of pure crystals. We have taken the absorption curves at the visible region of these colored crystals by the aide of a simple optical instrument. Since the color produced with X-rays disappears by white light owing to the neutralisation process of electrons with positive holes, the colored specimen was set behind a narrow and long slit, and transmitted with very weak light dispersed by a glass prism. The transmitted light falls upon a rubidium photo-electric tube, and the photo-current thus produced was measured by a duBridge-Brown circuit using a UX-54 tube and a galvanometer of sensibility 10^{-8} amp/mm.

The results are shown in Fig. 1. The ordinate represents the value $x = \kappa l$, which is defined by

$$I = I_0 e^{-\kappa l}$$

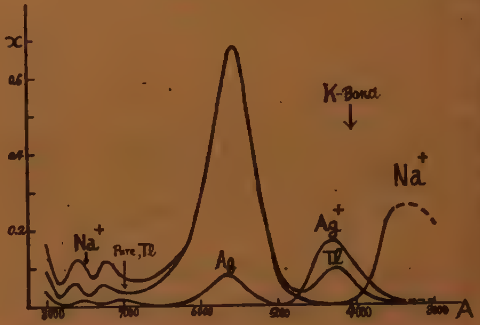

Fig. 1. Absorption Curves of KCl Krystals containing NaCl, AgCl and TlCl.

where I_0 is the intensity of the light transmitting the non-colored crystal and I is that of colored crystals. If the thickness l of the colored region were 0.05 mm as in the case of I. Estermann(4), the absorption coefficient κ of F-band may be 10 ∼ 20 which is reasonable. In our instrument the red-side of the spectra is worse in accuracy, but comparatively good in violet side. The 5790. Å and 5769.6 Å lines of the Hg atomic spectra used as standard were easily separated.

In addition, we have measured the dielectric properties of the crystals used above and also some mixed crystals of Na-KCl system at the constant frequency 2.6 M.C., and found anomalou dielectric dispersion of the Breckenridge's type(5) characteristic to its impurites. The anomalous behavior of pure alkali halides found by Breckenridge is supposed to be due to the dipolar rotation of pairs of vacancies in an electric field. Thus the rotational motion is composed of the displacement of an anion attached to the vacancies, and its activation energy determines the dispersion temperature. The anomalous behaviors of these crystals correspond to the previous optical experiment as results.

From these results we imagine a mechanism of the impurity absorption as follows. The negative ion vacancies may prefer to come to the neighboring site of the impurity anion from the nature of bonding energy. If the electron were trapped in such a vacancy, an electronic state characteristic to its impurity may be formed, and this state is different from that of F-centers. From a simple consideration of the potential box influenced by the impurity ion, the system consisting of electron and vacancy may be more stable. Thus the observed wave lengths of maximum absorption may be shorter than the F-band. The activation energy of impurity ions required to cross the potential barrier may differ from that of the native ion. Their colors produced with X-rays seem to be almost unchanged by their impurity concentration. As for example, in K-NaCl system, the color changes abruptly at Na:K=6:4, and at each region of impurity concentration the color remains nearly constant. These results appear to contradict with the Ivey's suggestion(6).

References.

(1) O. Stasiw: Gött. Nachr. **1** (1936).
(2) S. Kyropoulos: Zeits. f. anorg. allgem. chem., **154**, 308 (1926).
(3) L. A. Dubridge, and H. Brown: Rev. Sci. Instrument (1933).
(4) I. Estermann, W. J. Leivo, and O. Stern: Phys. Rev. **75**, 621 (1949).
(5) R. G. Breckenridge: J. Chem. Phys., **16**, 959 (1949).
(6) H. F. Ivey: Phys. Rev. **72**, 341 (1947).

Probable Distribution of Segments of a Polymer Around the Center of Gravity.

By Akira ISIHARA.
Faculty of Science, University of Tokyo.

(Received November 14, 1949).

Most of the calculations concerning the shape of a high polymer molecules are confined to the case where one end of the polymer is fixed. We can calculate also the probable distribution of its segments around the center of gravity. If their number is N and the length of a chain is l, the coordinate of i-th segment is given by

$$r_i = \frac{l}{N}\{\alpha_1+2\alpha_2+\cdots+(i-1)\alpha_{i-1}$$
$$-(N-i)\alpha_i-(N-i-1)\alpha_{i+1}-\cdots-\alpha_{N-1}\},$$

where α_i is the unit vector in the direction of the i-th bond. By ordinary Markoff's method, we can at once obtain the distribution function $(W)R$:

$$W(R)=\Sigma\left(\frac{C_i^2}{\pi}\right)^{3/2}\exp(-C_i^2R^2),$$

$$C_i^{-2}=\frac{1}{9}\left(\frac{l}{N}\right)^2$$
$$\cdot\{N(N+1)(2N+1)-6iN(N+1)+6i^2N\},$$

from which we can calculate $<R^2>_{av}=Nl^2/6$ and other averages. These quantities are more important than the corresponding averages of the distance between both ends of a polymer, especially to discuss the shape of a polymer in the solutions.

On the Solution of Differential Equations of the Two-Dimensional Steady Flow of Compressible Fluid.

By Osamu SAITO and Ayao AMEMIYA.
Department of Dynamics, First Faculty of Engineering, University of Tokyo.

(Received April 12, 1950).

Several methods have been developed to study the two-dimensional steady flow of compressible fluid. Although hodograph method gives us a rigorous solution of this problem, the determination of arbitrary functions involved in this expression by the boundary condition is much troublesome, so we will treat it by another method. Using new independent variable such as $w=w(q)$ and Ψ, our equations will be given as follows:

$$\frac{\partial_2 F}{\partial w^2}\frac{\partial^2 F}{\partial \Psi^2}-\left(\frac{\partial^2 F}{\partial w\,\partial \Psi}\right)^2=f(w), \qquad (1)$$

$$f(w)=\frac{1}{\rho^2}-\frac{d}{dw}\left(\frac{1}{\rho}\right),$$

$$w=\int\frac{\rho}{q}dq,$$

and ρ is density.

The velocity potential ϕ and stream angle θ, then, will be obtained from the following relations:

$$\phi = \frac{\partial F}{\partial w}, \quad \theta = -\frac{\partial F}{\partial \Psi}.$$

The coordinates x and y are also given by

$$dx = \frac{\cos\theta}{v} d\phi - \frac{\sin\theta}{\rho q} d\Psi$$

$$dy = \frac{\sin\theta}{q} d\phi + \frac{\cos\theta}{\rho q} d\Psi.$$

Assuming that the equation (1) has an intermediate integral, the solution of (1) will get the following form:

$$F = \pm \Psi \int \sqrt{-f(w)}\, dw + \alpha \Psi + G(w). \tag{2}$$

where α is an arbitray constant and G is an arbitray function of w. This represents supersonic flow. From (2) we will get x and y as follows:

$$x = h(q^2) \mp \frac{1}{q}\left(\sqrt{-f} \cos \mp \frac{1}{\rho} \sin\theta\right)\Psi,$$

$$y = \Gamma\{h(q^2)\} \mp \frac{1}{q}\left(\sqrt{-f} \sin\theta \mp \frac{1}{\rho} \cos\theta\right)\Psi,$$

where $y_0 = \Gamma(x_0)$ means the boundary and from $\Gamma'(x_0) = \tan\theta$ we get $x_0 = h(q^2)$.

Furthermore there will be found another solution of the following type:

$$F = \frac{(\Psi + C)^2}{Aw + B}$$

$$+ \frac{1}{2} \int dw \int (Aw + B) f(w)\, dw + E\Psi + Fw + H,$$

where A, B, C, E, F and H are arbitrary constants.

Phycical discussions and detailed investigations will be given later.

Electromagnetic Phenomena on Ribbon Elements Grating.

By Tokio SAKURAI.

Electrical Communication Laboratory, Ministry of Telecommunications.

(Received April 21, 1949)

Electromagnetic phenomena on ribbon elements grating are investigated to serve for investigation of electromagnetic devices, particularly for non-reflective metal lens antenna.

§ 1. Electromagnetic Oscillation Modes near the Ribbon Elements Grating.

A grating plane constructed by equal and equidistant metallic ribbon elements is placed on yz-plane of rectangular x. y, z-coordinates. Each ribbon element is directed parallel to z-axis. The breadth and interval of ribbon elements are both considered to be very small compared with the wave length to electromagnetic wave. The orthogonal section of the grating by xy-plane is shown in Fig. 1. Let us take orthogonal curvilinear doordinates u_1, u_2 on xy-plane combined by

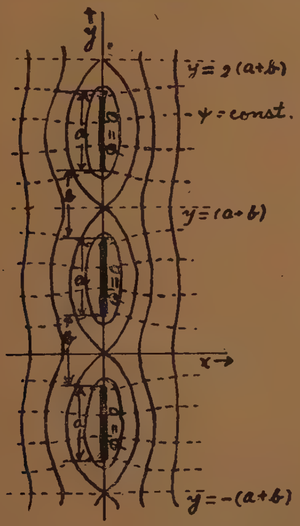

Fig. 1. Orthogonal Section of Ribbon Elements Grating.

$$(dx)^2+(dy)^2 = h_1^2\,(du_1)^2+h_2^2\,(du_2)^2\,. \qquad (1)$$

Since the space near the grating is of cylindrical form, the field near the grating is the fields derived from electric Hertz vector component Π_z and magnetic Hertz vector component $\Pi_z{}^*$ of the forms

$$\Pi_z = C\phi\,(u_1\,,\ u_2)\,e^{j\omega t\pm jhz} \qquad (2)$$

$$\Pi_z{}^* = C^*\phi^*\,(u_1\,,\ u_2)\,e^{j\omega t\pm jhz} \qquad (3)$$

by following formulas

$$\left.\begin{aligned} &E_1=\frac{1}{h_1}\frac{\partial^2\Pi_z}{\partial z\partial u_1}, \quad E_2=\frac{1}{h_2}\frac{\partial^2\Pi_z}{\partial z\partial u_2}, \quad E_z=(k^2-k^2)\Pi_z\,, \\ &H_1=\frac{j\omega\varepsilon}{h_2}\frac{\partial\Pi_z}{\partial u_2}, \quad H_2=-\frac{j\omega\varepsilon}{h_1}\frac{\partial\Pi_z}{\partial u_1}, \quad H_z=0\,. \end{aligned}\right\}(4)$$

$$\left.\begin{aligned} &E_1=-\frac{j\omega\mu}{h_2}\frac{\partial\Pi_z{}^*}{\partial u_2}, \quad E_2=\frac{j\omega\mu}{h_1}\frac{\partial\Pi_z{}^*}{\partial u_1}, \quad E_z=0\,, \\ &H_1=\frac{1}{h_1}\frac{\partial^2\Pi_z{}^*}{\partial z\partial u_1}, \quad H_2=\frac{1}{h_2}\frac{\partial^2\Pi_z{}^*}{\partial z\partial u_2}, \quad H_z=(k^2-h^2)\Pi_z{}^*. \end{aligned}\right\}(5)$$

ϕ, ϕ^* in (2), (3) satisfy

$$\varDelta\phi+(k^2-h^2)\phi = 0\,, \qquad \varDelta\phi^*+(k^2-h^2)\phi^* = 0\,. \qquad (6)$$

where $\varDelta$ express two-dimensional Laplacian on xy-plane. But since the varation of the field on xy-plane is large, the terms with the coefficient (k^2-h^2) is negligible with respect to the terms with $\varDelta$. Hence (6) becomes approximately

$$\varDelta\phi = 0\,, \qquad \varDelta\phi^* = 0\,. \qquad (7)$$

Since the tangential electric and normal magnetic components of the field vanish on conductor surface, the boundary conditions of ϕ, ϕ^* are

$$\phi = 0\,; \qquad \partial\phi^*/\partial\nu = 0 \qquad (8)$$

(on ribbon elements of the grating)

where ν is the normal of the ribbon elements surfaces.

(7) and (8) are most conveniently solved by applying the comformal representation. Let w and z be complex variables defined by

$$w = \phi+j\psi\,, \qquad z = x+jy \qquad (9)$$

combined by the relation

$$\cosh w = m\cosh\{\pi z/(a+b)\}\,, \qquad (10)$$

where

$$m = \sec\{\pi b/2(a+b)\} = \operatorname{cosec}\{\pi a/2(a+b)\}. \quad (11)$$

The formula (10) gives

$$\left.\begin{aligned} \cosh\phi\cos\psi &= m\cosh\{\pi x/(a+b)\}\cos\{\pi y/(a+b)\}, \\ \sinh\phi\sin\psi &= m\sinh\{\pi x/(a+b)\}\sin\{\pi y/(a+b)\}. \end{aligned}\right\} \quad (12)$$

The curves $\phi =$ const. are traced in full lines, while the curves $\psi =$ const. are traced in dotted lines in Fig. 1. The lines $\psi = 0$, $\psi = \pm\pi$, $\psi = \pm 2\pi$, ...coincide with the lines $y = 0$, $y = \pm(a+b)$, $y = \pm(a+b)$, ...respectively. The locus $\phi = 0$ consists the line segments of the length a placed with equal intervening distance b along y-axis.

There are two groups of ϕ and ψ satisfying (12). For the first time we consider the case where at points symetrically situated on opposite side of y-axis the values of ϕ are identical, while those of ψ are equal in magnitude but of opposite signs. If we regard the line segments of length a on y-axis expressed by $\phi = 0$ as the sections of ribbon elements, then the first relations in (7) and (8) are automatically satisfied. Hence the field evaluated by (2) and (4) using this ϕ is the field of electric type.

Now we consider the remaining case that at points symmetrically situated on opposite sides of y-axis the values of ϕ are equal in magnitude but of opposite signs, while those of ψ are identical. Hence of we consider the portions of length a expressed by $\phi = 0$ as the intervening interval of ribbon elements, the second equations in (7) and (8) are automatically satisfied. Hence if we denote this ϕ by ϕ^* and substitute in (3) and (5), we get the field of magnetic type.

§ 2. Macroscopic Boundary Value Problems.

From (10) for large values of $|x|$

$$\left.\begin{aligned} &\phi \simeq \log m + \pi|x|/(a+b), \quad (x \gtrless 0) \\ &\qquad \text{(for electric type field)} \end{aligned}\right\} \quad (13)$$

$$\left.\begin{aligned} \phi^* &\simeq \log m + \pi|x|/(a+b), && (x > 0) \\ &\simeq -\log m - \pi|x|/(a+b), && (x < 0) \\ &\qquad \text{(both for magnetic type field)} \end{aligned}\right\} \quad (14)$$

For small values of $|x|$, as it is clear from Fig. 1., the functional form of ϕ is complicated. But to solve macroscopic problems it is convenient to consider that (13) and (14) still hold for small value of $|x|$. For the field obtained by solving the boundary value problem founded on the fact that (13) and (14) hold for small values of $|x|$ satisfies that founded on (13) and (14) and consequently coincides with the field bounded by ribbon elements grating except the microscopic differences in the neighbourhood of the grating. Hence substituting (13) in (2) and (4) we have

$$\left.\begin{aligned} E_z &= (k^2-h^2)\,C\log m, && (\text{for } x = \pm 0) \\ H_y{}^{(1)} &= -j\omega\varepsilon C\frac{\pi}{a+b}, && (\text{for } x = +0) \\ H_y{}^{(2)} &= j\omega\varepsilon C\frac{\pi}{a+b}, && (\text{for } x = -0) \\ E_x{}^{(1)} &= \pm jhC\frac{\pi}{a+b}, && (\text{for } x = +0) \\ E_x{}^{(2)} &= \mp jhC\frac{\pi}{a+b}, && (\text{for } x = -0) \end{aligned}\right\} \quad (15)$$

The common factor $e^{j\omega t \pm jhz}$ is omitted for simplicity in above expression. But in reality this factor must be multiplied in above expressions. The field components not w;itten in (15) are zero. If we substitute (14) in (3) and (5), we have

$$\left.\begin{aligned} H_z{}^{(1)} &= (k^2-h^2)\,C^*\log m, && (\text{for } x = +0) \\ H_z{}^{(2)} &= -(k^2-h^2)\,C^*\log m, && (\text{for } x = -0) \\ E_y &= j\omega\mu C^*\frac{\pi}{a+b}, && (\text{for } x = \pm 0) \\ H_x &= \pm jhC^*\frac{\pi}{a+b}, && (\text{for } x = \pm 0) \end{aligned}\right\} \quad (16)$$

Since it is arbitrary to add uniform magnetic field $H^{(0)}$ parallel to grating plane and uniform electric field $E^{(0)}$ perpendicular to grating plane on both sides of the grating, the fields on both sides of grating plane for both electric and magnetic type are as follows by (15) and (16) :

$$\left.\begin{aligned} E_z{}^{(1)} &= E_z{}^{(2)} = (k^2-h^2)\,C\log m\, e^{j\omega t \pm jhz} \\ H_y{}^{(1)} &= \left\{H_y{}^{(0)} - j\omega\varepsilon C\frac{\pi}{a+b}\right\} e^{j\omega t \pm jhz} \\ H_y{}^{(2)} &= \left\{H_y{}^{(0)} + j\omega\varepsilon C\frac{\pi}{a+b}\right\} e^{j\omega t \pm jhz} \\ E_x{}^{(1)} &= \left\{E_x{}^{(0)} \pm jhC\frac{\pi}{a+b}\right\} e^{j\omega t \pm jhz} \\ E_x{}^{(2} &= \left\{E_x{}^{(0)} \mp jhC\frac{\pi}{a+b}\right\} e^{j\omega t \pm jhz} \\ &\qquad \text{(for electric type case)} \end{aligned}\right\} \quad (17)$$

---

(1) Cf. Lamb, Hydrodynamic, p. 534, Sixth Ed.

$$\left.\begin{aligned}
&H_z^{(1)}=\left\{H_z^{(0)}+(k^2-h^2)\,C^*\log m\right\}e^{j\omega t\pm jhz}\\
&H_z^{(2)}=\left\{H_z^{(0)}-(k^2-h^2)\,C^*\log m\right\}e^{j\omega t\pm jhz}\\
&E_y^{(1)}=E_y^{(2)}=j\omega\mu C^*\frac{\pi}{a+b}e^{j\omega t\pm jhz}\\
&H_x^{(1)}=H_x^{(2)}=\pm jhC^*\frac{\pi}{a+b}e^{j\omega t\pm jhz}\\
&\qquad\text{(for magnetic type case)}
\end{aligned}\right\}\quad(18)$$

where suffix (1) and (2) express the quantities on positive x-side and negative x-side of the grating respectively. Eliminating C and C^* between equations of (17) and (18), we have

$$\left.\begin{aligned}
&E_z=\frac{p}{k}\left\{j\omega\mu(H_y^{(1)}-H_y^{(2)})+\frac{\partial}{\partial z}(E_x^{(1)}-E_x^{(2)})\right\},\\
&H_z^{(1)}-H_z^{(2)}=\frac{4p^*}{k}\left\{-j\omega\varepsilon E_y+\frac{\partial H_x}{\partial z}\right\},\\
&E_z^{(1)}=E_z^{(2)}\,,\quad E_y^{(1)}=E_y^{(2)}\,,\quad H_x^{(1)}=H_x^{(2)}\,.
\end{aligned}\right\}(19)$$

If we denote by $\boldsymbol{k}$ the unit vector directed along the ribbon elements of the grating (*i. e.* z-direction in Fig. 1.) and by $\boldsymbol{n}$ the unit normal of the grating from (2) side to (1) side (*i. e.* x-direction in Fig. 1.) and rewrite the results of (19) in vector forms, we have

$$\left.\begin{aligned}
&\boldsymbol{k}\cdot=\boldsymbol{E}\frac{p}{k}\boldsymbol{k}\cdot\{j\omega\mu\,\boldsymbol{n}\times(\boldsymbol{H}^{(1)}-\boldsymbol{H}^{(2)})\\
&\qquad\qquad+\nabla[\boldsymbol{n}\cdot(\boldsymbol{E}^{(1)}-\boldsymbol{E}^{(2)})]\},\\
&\boldsymbol{k}\cdot(\boldsymbol{H}^{(1)}-\boldsymbol{H}^{(2)})=\frac{4p^*}{k}\boldsymbol{k}\cdot\{-j\omega\varepsilon\,\boldsymbol{n}\times\boldsymbol{E}\\
&\qquad\qquad+\nabla(\boldsymbol{n}\cdot\boldsymbol{H})\},\\
&\boldsymbol{n}\times\boldsymbol{E}^{(1)}=\boldsymbol{n}\times\boldsymbol{E}^{(2)},\qquad \boldsymbol{n}\cdot\boldsymbol{H}^{(1)}=\boldsymbol{n}\cdot\boldsymbol{H}^{(2)},
\end{aligned}\right\}(20)^\dagger$$

where p and p^* in above formulas expressed by the same formula as follows:

$$p,\ p^*\doteq\{a+b\}/\lambda\}\log m\,. \qquad (21)$$

If we denote by η the breadth of ribbon elements of the grating and express the relations between p, p^* and η in graphs, we get Fig. 2. As it is clear from (21), the expressions of p and p^* are of the same formula. But since $\eta=a$ for p and $\eta=b$ for p^*, the graphs of p and p^* are different as shown in Fig. 2. The length $a+b$ expresses the distance between the similar positions on neighbouring two elements, and in consequence $\eta=a+b$ in Fig. 2, expresses the case when the breadth of ribbon elements become maximum and intervening space the elements vanish. $p=\infty$ when $\eta=0$, p decreases as η increases, and finally $p=0$ when $\eta=a+b$. On the other hand $p^*=0$ when $\eta=0$, p^* increases with η, and finally $p^*=\infty$ when $\eta=a+b$.

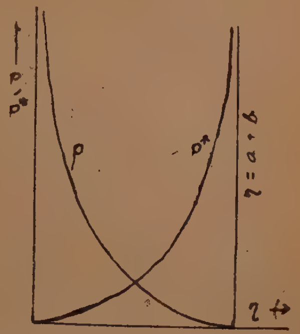

Fig. 2. The Graphs of p and p^*.

Let us now investigate transmitting and reflecting phenomena of plane electromagnetic wave propagating along x-axis on ribbon elements grating. If we denote by $\boldsymbol{E}^{(2+)}$, $\boldsymbol{H}^{(2+)}$ the field of incident wave and by $\boldsymbol{E}^{(2-)}$, $\boldsymbol{H}^{(2-)}$ the field of reflecting wave on negative x-side of the grating and by $\boldsymbol{E}^{(1+)}$, $\boldsymbol{H}^{(1+)}$ the field of transmitting wave, there are two kinds of polarizing waves of following expressions:

$$\left.\begin{aligned}
&H_z^{(2+)}=B^{(+)}e^{-jkx}, && E_y^{(2+)}=\sqrt{\mu/\varepsilon}\,B^{(+)}\,e^{-jkx}\\
&H_z^{(2-)}=B^{(-)}e^{jkx}, && E_y^{(2-)}=-\sqrt{\mu/\varepsilon}\,B^{(-)}\,e^{jkx}\\
&H_z^{(1+)}=A^{(+)}e^{-jkx}, && E_y^{(1+)}=\sqrt{\mu/\varepsilon}\,A^{(+)}\,e^{-jkx}
\end{aligned}\right\}(22)$$

$$\left.\begin{aligned}
&H_y^{(2+)}=B^{(+)}e^{-jkx}, && E_z^{(2+)}=-\sqrt{\mu/\varepsilon}\,B^{(+)}e^{-jkx}\\
&H_y^{(2-)}=B^{(-)}e^{jkx}, && E_z^{(2-)}=\sqrt{\mu/\varepsilon}\,B^{(-)}\,e^{jkx}\\
&H_y^{(1+)}=A^{(+)}e^{-jkx}, && E_z^{(1+)}=-\sqrt{\mu/\varepsilon}\,A^{(+)}e^{-jkx}
\end{aligned}\right\}(23)$$

where time factors are omitted. The field $\boldsymbol{E}^{(2)}$, $\boldsymbol{H}^{(2)}$ on the negative x-side of the grating is the superposition of incident and reflecting field, while the field $\boldsymbol{E}^{(1)}$, $\boldsymbol{H}^{(1)}$ on the positive x-side of the grating is only transmitting field. Hence

$$\left.\begin{aligned}
&\boldsymbol{E}^{(2)}=\boldsymbol{E}^{(2+)}+\boldsymbol{E}^{(2-)}, && \boldsymbol{H}^{(2)}=\boldsymbol{H}^{(2+)}+\boldsymbol{H}^{(2-)},\\
&\boldsymbol{E}^{(1)}=\boldsymbol{E}^{(1+)}, && \boldsymbol{H}^{(1)}=\boldsymbol{H}^{(1+)}.
\end{aligned}\right\}\quad(24)$$

If we substitute (23), (24) in (19), we get

$$\left.\begin{aligned}
&A^{(+)}=\frac{2jpB^{(+)}}{1+2jp},\qquad B^{(1)}=\frac{B^{(+)}}{1+2jp},\\
&\text{(for the plane wave whose electric}\\
&\text{field is parallel to the elements of}\\
&\text{grating.)}
\end{aligned}\right\}\quad(25)$$

---

† $\boldsymbol{n}\cdot\boldsymbol{H}^{(1)}=\boldsymbol{n}\cdot\boldsymbol{H}^{(2)}$ is not independent condition, for this is deducible from $\boldsymbol{n}\times\boldsymbol{E}^{(1)}=\boldsymbol{n}\times\boldsymbol{E}^{(2)}$ and Maxwell's equations.

$$\left.\begin{aligned} &A^{(+)} = \frac{B^{(+)}}{1+2jp^*}, \quad B^{(-)} = \frac{2jp^*B^{(+)}}{1+2jp^*}, \\ &\text{(for the plane wave whose electric} \\ &\text{field is perpendicular to the ele-} \\ &\text{ments of grating.)} \end{aligned}\right\} \quad (26)$$

(25) and (26) express the relations of the amplitudes of transmitting and reflecting waves with respect to the amplitude of incident wave.

§ 3. Non-reflective Metal Lens Antenna.

As the preparation of the investigation of non-reflective metal lens antenna the device of the following construction is to be first considered. Ribbon elements gratings are placed on parallel equidistant grating planes with the coordinates $x=0$, $x=\pm c$, $x=\pm 2c, \ldots\ldots$, and the construction of each ribbon elements grating is the same as shown in Fig. 1. The electromagnetic waves of H_{10} type are propagating in each space between two neighbouring grating planes along y-axis and the propagation mode in each space is expressed by the formula.

$$H_y^* = \Gamma e^{-jhy} e^{j\omega t} \sin \gamma x_n, \quad (27)$$

where
$$\gamma^2 = k^2 - h^2. \quad (28)$$

x_n is the coordinates taken along x-axis with the origin at the center of n-th space. Consequently x_n is related with x by

$$x_n = x-(2n-1)c/2. \quad (29)$$

The coordinate of grating planes bounding the n-th space are by (29)

$$x_n = \pm c/2. \quad (30)$$

Owing to the periodicity of the field, the field in the positive x-side of the grating plane $x_n=c/2$ is equal to the field in the positive x-side of the grating plane $x_n=-c/2$. If we substitute (27) in (5) and make use of the fact just related, we can evaluate the fields on both sides of grating plane at $x_n=c/2$. If we notice that y in (27) corresponds to z in (5), z in (27) corresponds to $-u_2$ in (5), and x in (27) corresponds to u_1 in (5), we get the results as follows:

$$\left.\begin{aligned} &E_z^{(1)} = E_z^{(2)} = -j\omega\mu\gamma\Gamma e^{-jhy} e^{j\omega t} \cos \gamma c/2, \\ &-H_y^{(1)} = H_y^{(2)} = \gamma^2 \Gamma e^{-jhy} e^{j\omega t} \sin \gamma c/2, \\ &H_x^{(1)} = H_x^{(2)} = -jh\gamma\Gamma e^{-jhy} e^{j\omega t} \cos \gamma c/2, \\ &E_y^{(1)} = E_y^{(2)} = 0, \quad E_x^{(1)} = E_x^{(2)} = 0, \\ &H_z^{(1)} = H_z^{(2)} = 0. \end{aligned}\right\} \quad (31)$$

All conditions of (19) except the first are automatically satisfied by (31). If we substitute (31) in the first condition of (19) and make use of the fact $k=2\pi/\lambda$, we get

$$\frac{\pi c}{2p\lambda} = \frac{\gamma c}{2} \tan \frac{\gamma c}{2}. \quad (32)$$

It is clear Fig. 2. that $1/p$ increases from zero to infinity as the breadth of ribbon elements grows from zero to full breadth.†† If we combine this fact with (32), we can easily see that increases from zero to π/c as the breadth of ribbon elements grows from zero to full breadth. Hence by (28) the propagating constant h of the electromagnetic wave along the space between grating planes is equal to the propagation constant k in the free space when the breadth of ribbon element is zero, but h becomes smaller and smaller as the breadth of ribbon element grows large. Finally h reaches the propagation constant of H_{10} wave in wave guide of breadth c as the breadth of ribbon element becomes full breadth. This principle explains the action of non-reflective metal lens,

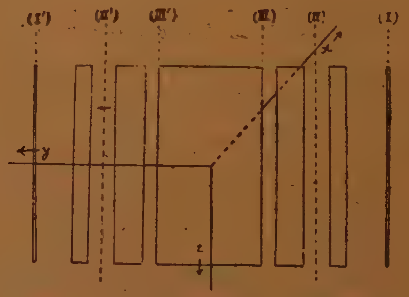

Fig. 3. The Gratings of slowly varying breadth.

which is constructed by parallel equidistant grating planes as shown in Fig. 3, placed at $x=0$, $x=\pm c$, $x=\pm 2c, \ldots.$ parallel to yz-plane. The grating plane shown in Fig. 3, is constructed by placing ribbon elements on both sides of plate conductor between (III) and (III'). The breadth of these ribbon elements grows smaller and smaller and vanishes at (I) and (I'). Now suppose that plane electromagnetic wave whose electric field is directed in z-direction and whose magnetic field is directed in x-direction is travelling in y-direction until the moment when the wave front reaches the dotted line (I) in Fig. 3., the wave travels in free space with the propagation constant k. But after the wave has passed the line (I), the wave enters into the space bounded by the ribbon elements. Now we shall denote by the dotted line (II) in Fig. 3. the wave front in the moment when the wave front is in the halfway passing the space bounded by ribbon elements. The behavior of the electromagnetic wave in this moment is approximately equal to that of the wave passing through the space bounded by two parallel ribbon elements gratings shown in Fig. 1. Hence the propagation constant h in this moment is equal to h evaluated by (28) and (32). Therefore as wave front (II) moves from the position shown by the dotted line (I) to the position shown by the dotted line (III) in Fig. 3., the propagation constant h decreases continuously from the starting value k. Finally when the wave front (II) coincides the line (III), the propagation constant h reaches the progagation constant of H_{10} wave in the wave guide of breadth c. The wave propagates further with this propagation constant of H_{10} wave until wave front comes on the dotted line (III′). Thenceforth the propagation constant increases continuously and reaches the value k, when the wave front comes on the dotted line (I′). Afterwards the wave propagates with the propagation constant k in the free space. Thus there is no sudden change in propagation constant in passing through the space between parallel gratings shown in Fig. 3. Hence if we construct metal lens with these gratings, there will be no reflection of electromagnetic wave in passing through the lens.

---

†† Full breadth means the breadth of the ribbon element when the intervening space vanishes, i.e., $\eta=a+b$.

On Experimental Methods of the Investigation of Turbulent Flow, II.

By Yutaka SHIGEMITSU.

Railway Technical Research Institute.

(Read July 23, 1949; Received Sept. 19, 1949)

Abstract.

In the previous part of the paper⁽¹⁾ we discussed the fundamentals of cooling of a hot-wire and proposed a methed to compensate its thermal lag. Then in this paper, taking foundation on these theoretical results, we will show several methods to measure turbulent velocity fluctuations. We use the same symbols as in the previous paper⁽¹⁾.

§1. Measurement of u'-Fluctuation.

In a turbulent flow, the deviation of the direction of wind from its mean value is ordinarily so small, that when the mean direction is made parallel to the x-axis, u'-fluctuation may be written as

$$u' = (\bar{V}+V')\cos\theta'\cos\varphi' - \bar{V}\cos\theta'\cos\varphi' \fallingdotseq V'$$

If a hot-wire is put in a turbulent flow perpendicular to the x, y-plane making its mean direction parallel to the x-axis, and its mean resistance is made equal to $\bar{R}$, then we get easily

$$\sqrt{\bar{e}_G'^2} \fallingdotseq \bar{c}_1 \frac{1}{\sqrt{(1+M^2\omega^2{}_n)}}\sqrt{\bar{u}'^2}, \qquad (1,1)$$

where

$$\bar{c}_1 = \frac{(\bar{R}-R_0)^2}{2R_0{}^2 i\alpha}\frac{\partial f}{\partial \bar{V}}. \qquad (1,2)$$

In the above expressions, $\sqrt{\overline{e_G'^2}}$ can be measured with a compensated amplifier and $\bar{c}_1$ can be got by the calibration curve of $\frac{\bar{R}-R_0}{\bar{R}R_0\alpha}f(\bar{V})$, so, we can calculate the value of $\sqrt{\overline{u'^2}}$ by (1,1).

In a flow of non-isotropic turbulence, the mean velocity also changes ordinarily in its value from place to place. We will show the procedure of the experiment to measure u'-fluctuation:

(i) By a measurement of mean speed, make a calibration curve of $\bar{V}$ and I (or $\sqrt{\bar{V}}$ and I^2), and get the relation between $\bar{c}_1$ and I.

(ii) Determine the value of M_0.

(iii) Read the value of I, by which the mean resistance is made equal to $\bar{R}$ in a flow, and know the values of $\bar{V}$, $\bar{c}_1$, and M.

(iv) Adjust the constant of the compensation circuit equal to M.

(v) With this compensated amplifier, measure the intensity of the in-put voltage e_G', by the method of substitution with an alternating current of a known frequency (we use that of 50 cycle/sec.).

(vi) Then we can calculate the value of $\sqrt{\overline{u'^2}}$ as follows;

$$\sqrt{\overline{u'^2}} = \sqrt{\overline{e_G'^2}}\frac{\sqrt{1+M^2(2\pi\times 50)^2}}{\bar{c}_1}. \tag{1,3}$$

§ 2. Measurement of v'-Fuctuation.

In a three dimensional flow in which the mean direction is made parallel to the x-axis, v'-fluctuation is defined as

$$v' = (\bar{V}+V')\cos\theta'\sin\varphi' \doteqdot \bar{V}\varphi'.$$

In the fundamental equation

$$M\frac{dR'}{dt}+R' = c_1V'+c_2\theta'+c_3\varphi', \tag{2,1}$$

where

$$M = \frac{4{,}2\,ms(\bar{R}-R_0)}{R_0^2i^2\alpha},$$

$$c_1 = -\frac{(\bar{R}-R^0)^2}{R_0^2i^2\alpha}\frac{\partial f}{\partial\bar{V}}$$

$$c_2 = -\frac{(\bar{R}-R_0)^2}{R_0^2i^2\alpha}\frac{\partial f}{\partial\bar{\theta}}$$

$$c_3 \doteqdot -\frac{(\bar{R}-R_0)^2}{R_0^2i^2\alpha}\frac{\partial f}{\partial\bar{\varphi}},$$

as far as the wire is put perpendicular to the x, y-plane, c_2 vanishes, and if the effect of the first term in the right side is vanished and that of the third is made to appear itself, we get a possibility that φ'-fluctuation can be measured in the same way as u'-fluctuation. To cancel the effect of the first term, we need at least two wires which have the same value of c_1, and to get the effect of the third, need a direction-meter as described previously. From this point of view, we will shows several methods to measure v'-fluctuation.

It is known that H. Reichardt measured v'-fluctuation with his "Dreidrahtsonde". At first, we discuss this method from our theoretical point of view. "Dreidrahtsonde" consists of three equal wires; two of them are in the heat wake of the other, on both sides of its center as shown in Fig. 1. When these are put in a flow of mean velocity of $\bar{V}$ perpendicular to the x, y-plane, and connecting the wires (2) and (3) to the two arms of a Wheatstone's bridge, we make these resistance equal to $\bar{R}$ (cf. Fig. 2), then by (2,1), we have

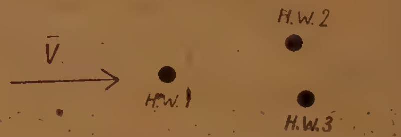

Fig. 1. Arrangement of "Dreidrahtsonde".

$$M_2\frac{dR_2'}{dt}+R_2'$$
$$=\left\{-\frac{(\bar{R}-R_0)^2}{R_0^2i^2\alpha}\right\}\left(\frac{\partial f_2}{\partial\bar{V}_2}\right)V_2'+\left\{-\frac{(\bar{R}-R_0)^2}{R_0^2i^2\alpha}\right\}\left(\frac{\partial f_2}{\partial\bar{\varphi}_2}\right)\varphi_2' \tag{2,2}$$

$$M_3\frac{dR_3'}{dt}+R_3'$$
$$=\left\{-\frac{(\bar{R}-R_0)^2}{R_0^2i^2\alpha}\right\}\left(\frac{\partial f_3}{\partial\bar{V}_3}\right)V_3'+\left\{-\frac{(\bar{R}-R_0)^2}{R_0^2i^2\alpha}\right\}\left(\frac{\partial f_3}{\partial\bar{\varphi}_3}\right)\varphi_3',$$

(in (2,1) $\frac{\partial f_2}{\partial\bar{\theta}_2}$ and $\frac{\partial f_3}{\partial\bar{\theta}_3}$ vanish in this arragement) where the suffix 2 and 3 show the wires (2) and (3). As we choose these two wires equal,

$$M_2 = M_3 \doteqdot M,$$

moreover we can expect that

$$\frac{\partial f_2}{\partial\bar{V}_2} = \frac{\partial f_3}{\partial\bar{V}_3} \tag{2,3}$$

The wires are so small, that the wire (1) does not participate in causing new turbulence behind it (in our measurement, the Reynolds number of the flow around the wire (1) is ordinarily less than 10), and their distances are so small as compared with the scale of turbulence in the flow (the distance between the wires (1) and (2) is usually about 0,3 mm), so that

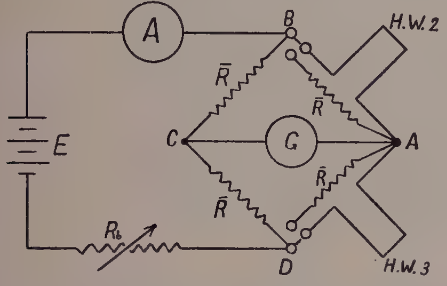

Fig. 2. The Wheatstone's bridge circuit in measureing v'-fluction.

$$V_2' = V_3' = V' \qquad (2,4)$$
$$\varphi_2' = \varphi_3' = \varphi',$$

where V' and φ' are designated as the two components of turbulent fluctuations at a point. Thus by (2,2), (2,3), and (2,4), we have

$$M\frac{dR'}{dt}+R' = c_2\varphi', \qquad (2,5)$$

where in this case,

$$R' = R_2'-R_3',$$
$$M = \frac{4{,}2\, ms(\bar R-R_0)}{R_0{}^2 i^2\alpha}, \qquad (2,6)$$
$$c_2 = \left\{-\frac{(\bar R-R_0)^2}{R_0{}^2 i^2\alpha}\right\}\left\{\left(\frac{\partial f_2}{\partial\bar\varphi_2}\right)-\left(\frac{\partial f_3}{\partial\bar\varphi^3}\right)\right\}.$$

(2,5) gives a theoretical ground to measure φ'-fluctuation, and it is the same form as the fundamental equation to measure u'-fluctuation. Thus the previously described theoretical discussions can be similarly adapted in the case of φ'-fluctuation. We first get the value of M_0 of the wire (2) (or (3)) in still air, and next read the value of the current I to keep the mean resistance of the wires (2) and (3) equal to $\bar R$ in Fig. 2, then by the relation of $MI^2 = M_0 I_0{}^2$, we can easily determine the value of M in this case. So, in the "constant resistance method" as shown in Fig. 2, we can calculate the intensity of φ', in the same way as u'-fluctuation. The above discussions can be adapted in the case of not necessarily symmetrical arrangement of the three wires as proposed by H. Reichardt.

To avoid technical difficulty to arrange three wires very closely, we have the following method. We put three wires as in Fig. 2, but in this case, only the wire (3) is put in the heat wake of (1), and (2) is apart from it. Then in the "constant resistance method", we have

$$M_2\frac{dR_2'}{dt}+R_2' = \left\{-\frac{(\bar R-R_0)^2}{R_0{}^2 i^2\alpha}\right\}\left(\frac{\partial f_2}{\partial\bar V_2}\right) V_2'$$
$$M_3\frac{dR_3'}{dt}+R_3' \qquad (2,2')$$
$$= \left\{-\frac{(\bar R-R_0)_3}{R_0{}^2 i^2\alpha}\right\}\left(\frac{\partial f_3}{\partial\bar V_8}\right)V_3'+\left\{-\frac{(\bar R-R_0)^2}{R_0{}^2 i^2\alpha}\right\}\left(\frac{\partial f_3}{\partial\bar\varphi_3}\right)\varphi_3'.$$

When the distance between (2) and (3) is not so large compared with the scale of turbulence, V_2' can be taken equal to V_3' and $\frac{\partial f_2}{\partial\bar V_2}$ to $\frac{\partial f_3}{\partial\bar V_3}$, and then we get, in the same way, the following formula

$$M\frac{dR'}{dt}+R' = c_2\varphi', \qquad (2,5')$$

where

$$R' = R_2'-R_3',$$
$$M = \frac{4{,}2ms\,(\bar R-R_0)}{R_0{}^2 i^2\alpha} \qquad (2,6')$$
$$c_2 = \frac{(\bar R-R_0)^2}{R_0{}^2 i^2\alpha}\left(\frac{\partial f_3}{\partial\bar\varphi_3}\right).$$

So, φ'-fluctuation can also be measured by this method. It seems to be useful especially when the scale of turbulence is not so small.

In turbulent boundary layer, the scale of turbulence seems to be very small, and it is preferable to put each wire as closely as possible. From this point of view, the author developed a direction-meter of Thomas and Baily's type, to be useful in measuring v'-fluctuation in this case. When one wire is put in the heat wake of the other, as shown in Fig. 3, then as for the wires

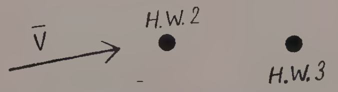

Fig. 3. Arrangement of Thomas and Baily's type.

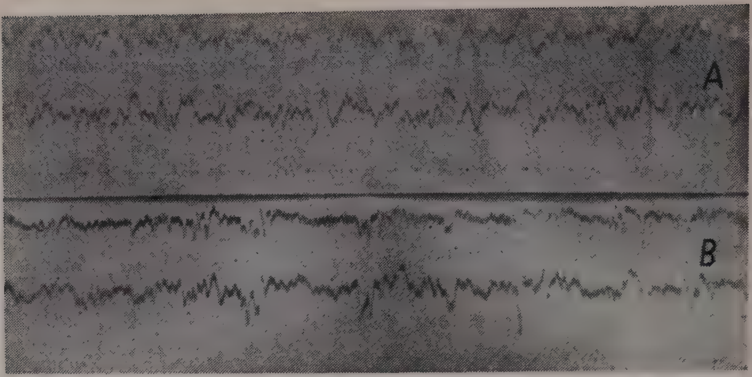

Fig. 4. Simultaneous oscillograph records of u'-fluctuations at two points. A is potential flow (the distance is 0,6 mm). B is turbulent boundary layer flow (the distance is 0,9 mm). For the convenience of comparison, two uncompensated aplifiers are used. Each timing mark is 1/100 sec.

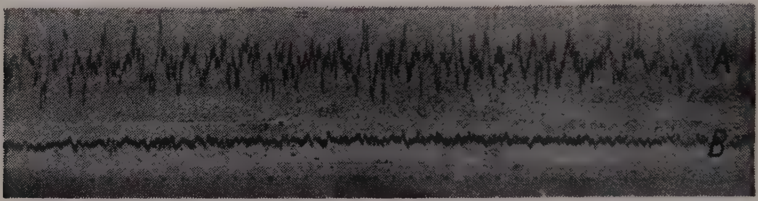

Fig. 5. Comparison of fluctuating voltages between AC in the Wheatstone's bridge circuit (cf. Fig. 2). A is the case when the wire (1) is put in the front. B is the case when (1) is taken off. In both cases, one compensated amplifier under the same state is used.

(2) and (3), the formulas (2,2′), (2,5′), and (2,6′) also hold in the "constant resistance method" of this system, and similarly we can measure the intensity of φ'’fluctuation.

Then, we will give several experimental checks on the assumptions of theoretical grounds of the above methods. Fig. 4 shows the simultaneous oscillograph records of u'-fluctuations at two points perpendicular to the mean direction of the velocity, in two cases of flow. By these figures, we can estimate the range of distance of the two wires, in which the correlation coefficient of u' at these points is almost equal to the unity. Then it is assumed that when the wire (1) is taken off in Fig. 1, the resistance fluctuations of the wires (2) and (3) are cancelled and we can scarcely find fluctuating voltage between A and C in Fig. 2, compared with the case, in which the wire (1) is put in front of them and the heat wake is turned on. Fig. 5 shows an experimental result of this comparison, in a potential flow. Fig. 6 shows an experimental curves of $\frac{\overline{R}-R_0}{R_0\overline{R}\alpha}f(\overline{V})$ (where $\overline{\varphi}$ is taken constant) and $\frac{\overline{R}-R_0}{R_0\overline{R}\alpha}f(\overline{\varphi})$ ($\overline{V}$ is constant) of the wires (2) and (3) in Fig. 1. By these figures, the voltage fluctuation of e_G' between A and C in the "constant resistance method" in Fig. 2, is assumed to depend largely on φ'-fluctuation and scarcely on u'-fluctuation of the flow.

In non-isotropic turbulent flow, it is supposed that not only the value of mean velocity, but also the form of heat wake of the wire changes from

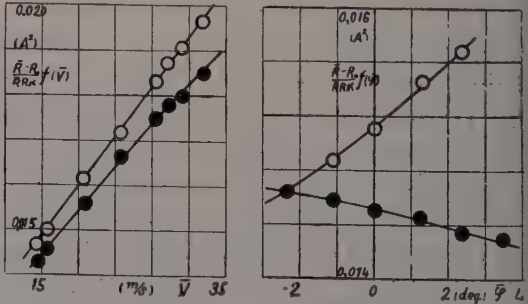

Fig. 6. Experimental curves of $\frac{\overline{R}-R_0}{R_0\overline{R}\alpha}f(\overline{V})$ and $\frac{\overline{R}-R_0}{R_0\overline{R}\alpha}f(\overline{\varphi})$ of the wires (2) (○) and (3) (●) in Fig. 1.

place to place, and the calibraton in the procedure of measuring v'-fluctuation is complicated. We show it as follows;

(i) With a direction-meter mentioned above, make a calibration curves of $\bar{\varphi}$ and I as shown in Fig. 6 and get the relation between $\bar{c}_2$ and I. ($\bar{c}_2 = \frac{I}{4}|C_2|$, where c_2 is expressed by (2,6) or (2,6′) in each case.)

(ii) Determine the value of M_0 of one wire, in the same manner as the case of u'-fluctuation.

(iii) Put the direction-meter at an angle to the mean direction of the flow, so that the difference of the values of tangents of the above calibration curves may be large.

(iv) Read the value of I, by which the mean resistances of the wires are equal to $\bar{R}$, and know the values of $\bar{c}_2$ and M.

(v) Adjust the value of the constant of the compensation circuit equal to M.

(vi) With this compensated amplifier, measure the intentity of e_G' by the method of substitution with an alternating current of a known frequency (for instance of 50 cycle/sec.).

(vii) With the wire which lies ahead in the direction-meter, measure the value of $\bar{V}$.

(viii) Then we can calculate the value of $\sqrt{\overline{V'^2}}$ as follows;

$$\sqrt{\overline{V'^2}} = \bar{V}\sqrt{\overline{e_G'^2}}\,\frac{\sqrt{1+M^2(2\pi\times 50)^2}}{\bar{c}_2}. \qquad (2,7)$$

§ 3. Measurement of u′v′-Correlation.

In the investigation of non-isotropic turbulent flow, it is important to measure the intensity of Reynolds' shearing stress, $-\rho\overline{u'v'}$, but as for an experimental techique, it is easy to measure a correlation coefficient of u' and v';

$$(\overline{u'v'})/(\sqrt{\overline{u'^2}}\sqrt{\overline{v'^2}}). \qquad (3,1)$$

In the previously described direction-meter, we can measure u'-fluctuation by the wire lying ahead. Thus, fluctuating voltages which correspond to u'- and v'-fluctuations, can be taken simultaneously. And so, there opens a way to measure these correlation coefficient, as those of u'-correlation at two points, which have been proposed by many writers. In a direction-meter shown in Fig. 1, all the wires are connected as shown in Fig. 7, and the constants of the compensation circuits of the amplifiers A_1 and A_2 are made respectively equal to the time constants of the wires (1) and (2), then we can measure u'- and v'-fluctuation simultaneously with the two amplifiers. when $\bar{I}_1$ and $\bar{I}_2$ are taken respectively as the out-put values of the amplifies A_1 and A_2, and I_0 as the value of the difference of those of A_1 and A_2, measured with thermal-type milliammeters, then we can take as

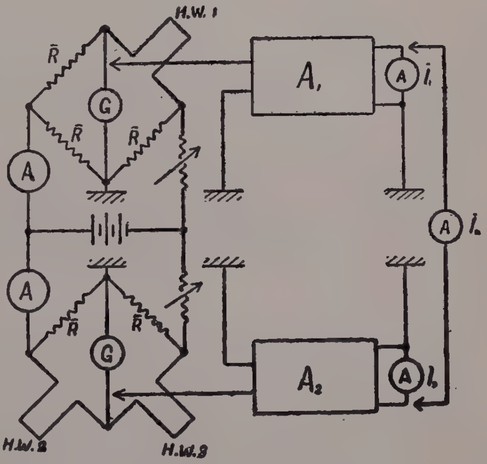

Fig. 7. The Wheatstone's bridge circuit in measuring $u'v'$-correlation.

$$\bar{I}_1 = \alpha\sqrt{\overline{u'^2}},\quad \bar{I}_2 = \beta\sqrt{\overline{v'^2}},\quad \bar{I}_0 = \sqrt{\overline{(\alpha u'-\beta v')^2}}, \qquad (3,2)$$

where α and β are constants of ratio. By a simple calculation, (3,2) leads to the following relation

$$\frac{\overline{u'v'}}{\sqrt{\overline{u'^2}}\sqrt{\overline{v'^2}}} = \frac{\bar{I}_1+\bar{I}_2-\bar{I}_0}{2\bar{I}_1\bar{I}_2}. \qquad (3,3)$$

Thus we can calculate the correlation coefficient of u' and v' by this relation, and further get the value of shearing stress, $-\rho\overline{u'v'}$, by measuring $\sqrt{\overline{u'^2}}$ and $\sqrt{\overline{v'^2}}$. In the case of the direction-meter shown in Fig. 3, the fluctuating voltage which dicates u', is taken from the side AB in Fig. 2, and $u'v'$-correlation coefficient can also be measured.

When we measure u'- and v'-fluctuations simultaneously by the "constant resistance method", as we choose the values of $\bar{R}$ of the two bridges equal (cf. Fig. 7), the difference of the time constants depends only on that of the heating current, and its difference is usually so small that it is not so erroneous to take these constants equal. Then it is possible to measure the above correlation coefficient with one amplifier, as in the measurement of u'-correlation at two points. Taking the value of $R_c C_c$ of the compensated amplifier equal to these mean value, the methods of measuring u'-correlation coefficient proposed by G. I. Taylor(2) or H. L. Dryden(3), can be applied to that of u' and v' at one point.

For the purpose of investigating the aspect of $u'v'$-correlation qualitatively, it is convenient to use the method of a braun-tube oscillograph; when the two out-put voltages in Fig. 7, are in the two orthogonal axis of a braun-tube oscillograph, we can evaluate at least the order of the value of the correlation coefficient, by the figure upon the tube which shows itself a frequency distributing function of u and v about the mean velocity.

§ 4. An Example of the Measurement.

As an example of measurements, we show an experimental result on the flow in turbulent boundary layer, which is along a flat plate with a slightly positive pressure gradient. Fig. 8 shows the distributions of $\overline{V}$, $\sqrt{\overline{u'^2}}$, $\sqrt{\overline{v'^2}}$, and $\overline{(u'v')}/(\sqrt{\overline{u'^2}}\sqrt{\overline{v'^2}})$. Fig. 9 shows simultaneous oscilograph records of u'- and v'-fluctuation in it, and Fig. 10 shows a figure which shows frequency distributing function, the photograph being taken by the expossure of about 20 seconds upon the surface of a braun-tube oscillograph.

In conclusion, it is a pleassure to record here a debt of gratitude to Mr. M. Siotani, for his kind guidance particularly in the early period of this investigation, and also the author desires to acknowledge the laborious assistances by Mr. N. Matsumoto and Mr. T. Uchida in our laboratory.

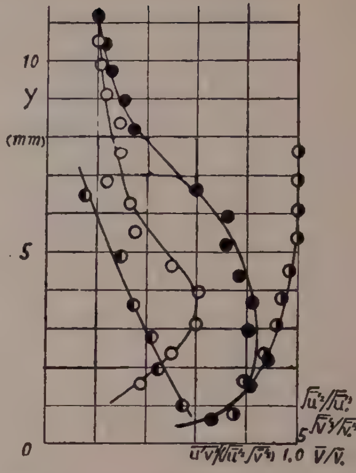

Fig. 8. Distributions of $\overline{V}/\overline{V}_0$(◑), $\sqrt{\overline{u'^2}}/\sqrt{\overline{u_0'^2}}$(●), $\sqrt{\overline{v'^2}}/\sqrt{\overline{v_0'^2}}$(○), and $\overline{(u'v')}/(\sqrt{\overline{u'^2}}\sqrt{\overline{v'^2}})$(◐) in turbulent boundary layer. The suffix 0 shows the potential flow outside the layer. $\overline{V}_0 = 14{,}3$ m/s, $\sqrt{\overline{u_0'^2}}/\overline{V}_0 = 0{,}006$, $\sqrt{\overline{v_0'^2}}/\overline{V} = 0.006$.

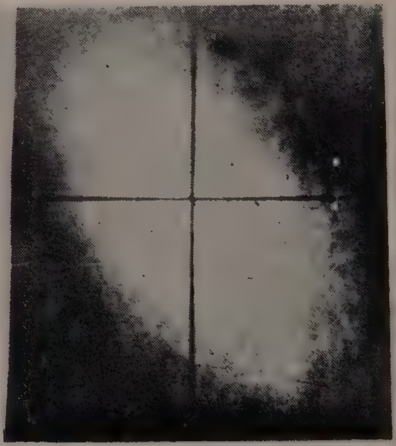

Fig. 10. A photograph which shows the frequency distributing function of u (abscissa) and v (ordinate) about their mean value at a point in turbulent boundary layer.

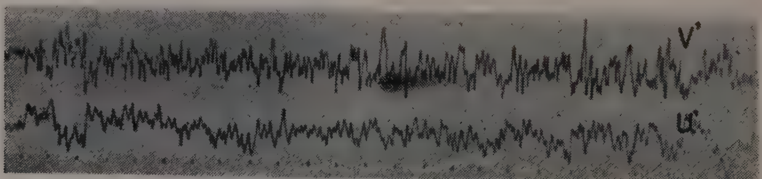

Fig. 9. Simultaneous oscillograph records of u'- and v'-fluctuation in turbulent boundary layer.

References.

(1) Shigemitsu, Y.: J. Phys. Soc. Japan, Vol. 5, No. 3, 1950.
(2) Taylor, G. I.: Proc. Roy. Soc. London, A 157, 1936.
(3) Dryden, H. L., Schubauer, G. B., Mock, W. C., and Skramstadt, H. K.: N. A. C. A., Tech. Rep. No. 581, 1937.

Transport Phenomena in Degenerate Systems.
I. General Theory in a Mixed System.

By Akira Isihara.

Faculty of Science, University of Tokyo.

(Received November 14, 1949)

§ 1. Introduction.

The methods of treating the transport phenomena of gases which have been developed mainly by Enskog, Chapman and others(1), must be somewhat altered if we wish to treat the phenomena in quantummechanically degenerate gases at very low temperatures. Actually, when the mean de Broglie wave length $h/2\pi mkT$ corresponding to the mean temperature motion becomes comparable to or larger than the diameter r_0 of the colliding molecules, the product of the mean free path l and the desity ρ becomes to depend upon the density and the temperature. Thus, Uehling and Uhlenbeck(2) found in a quantummechanical generalization of the method of Enskog and others that it comes from the alteration of the "Stosszählen Ansatz" and the deviation of the quantummechanical cross section from the classical one, and also confirmed the ingenious estimation of Enskog(3) and the procedure given by Massey and Mohr(4) who took into account the quantummechanical corrections by introducing the quantummechanical cross section into the classical expressions of Chapman for the gas coefficients.

On the other hand, for the degenerate gases at very temperatures it is no more satisfactory to do with the small quantummechanical corrections to the classical formulas for gas coefficients, so that the further extension of the theory is required. Moreover, recent progresses on the experiments with the isotopes He_3 and He_4 promote us to extend the theory furthermore to include mixed systems also. In the present article, therefore, we want to treat the mixed gases obeying different statistics in general. Applications to the degenerate Bose-Einstein gases and to the other special cases will be discussed in the following papers. Since the general procedures of solution of the fundamental equations are the same as those of Chapman and Uehling(2), we want to describe our theory briefly omitting the explanations of obvious notations such as time t, Boltzmann's constant k.

§ 2. Fundamental Equations.

The fundamental equations of our theory are the Boltzmann's equations which are expressed by,

$$\left.\begin{aligned} D_1 f_1 &= \frac{\partial f_1}{\partial t} + \boldsymbol{r}\cdot\frac{\partial f_1}{\partial \boldsymbol{X}} + \boldsymbol{X}\cdot\frac{\partial f_1}{\partial \boldsymbol{r}} = -J_{11}(f_1) - J_{12}(f_1), \\ D_2 f_2 &= \frac{\partial f_2}{\partial t} + \boldsymbol{s}\cdot\frac{\partial f_2}{\partial \boldsymbol{X}} + \boldsymbol{Y}\cdot\frac{\partial f_2}{\partial \boldsymbol{s}} = -J_{21}(f_2) - J_{22}(f_2), \end{aligned}\right\} \tag{1}$$

where

$$\begin{aligned} J_{ij}(f_i) = \int \{ & f_i f_j (1+\theta_i f_i')(1+\theta_j f_j') \\ & - f_i' f_j' (1+\theta_i f_i)(1+\theta_j f_j)\} gw(\vartheta, g)\, d\Omega\, d\phi_j . \end{aligned} \tag{2}$$

The suffices ij represent the colliding two molecules, and the suffices 1 and 2 represent the two species of molecules obeying the statistics represented by the parameter θ; $\theta = 1$, 0 and -1

correspond to the case of Bose-Einstein, Boltzmann and Fermi-Dirac statistics respectively. $\boldsymbol{r}$ and $\boldsymbol{X}$ represent the velocity and the acceleration of the molecule 1 respectively, $\boldsymbol{s}$ and $\boldsymbol{Y}$ are those of the molecule 2. $gw(\vartheta, g)$ is the effective cross section that the relative velocity, the magnitude of which is g, is deflected after collision by ϑ, $d\Omega$ is the surface element of the direction, $d\phi$ is the volume element in velocity space and these are expressed as:

$$\left.\begin{aligned} d\Omega &= \sin\vartheta\, d\vartheta\, d\varphi\,, \\ d\phi_1 &= G_1 (m_1/h)^3\, d\boldsymbol{r}\,. \end{aligned}\right\} \tag{3}$$

where G is the weight factor, m the mass and h is the Plank's constant. The integrations over the velocities of the integral of $J_{ij}(f_i)$ are performed over the arguments correspond to the latter suffix j. In the Eq. (2) we do not give the expressions of $d\phi_2$, because it has the same form as $d\phi_1$. When it answers the purpose, we wish to put up with such one representative equation hereafter.

To solve the above equations we consider the deviation from the thermal equilibrium to be very small and put:

$$\begin{aligned} &f = f^{(0)}(1+\phi)\,; \quad \chi = \phi/(1+\theta f^{(0)})\,, \\ &f^{(0)} = 1\Big/\left(\frac{1}{A}\exp\frac{m}{2kT}U^2-\theta\right). \end{aligned} \tag{4}$$

Introducing these equations into Eq. (1) and if we confine ourselves to take the zeroth approximation in the left hand members, we obtain:

$$\left.\begin{aligned} D_1 f_1^{(0)} &= -J_{11}(\chi_1)-J_{12}(\chi_1)\,, \\ D_2 f_2^{(0)} &= -J_{21}(\chi_2)-J_{22}(\chi_2)\,, \end{aligned}\right\} \tag{5}$$

$$\begin{aligned} J_{11}(\chi_1) = \int & f_1^{(0)} f^{(0)} (1+\theta_1 f_1^{(0)\prime})(1+\theta_1 f^{(0)\prime}) \\ & \times(\chi_1+\chi-\chi_1'-\chi')\, gw(\vartheta, g)\, d\Omega\, d\phi\,. \end{aligned} \tag{6}$$

Therefore, it is the fundamental problem to solve these equations satisfying the following mass, momentum and energy conservation laws:

$$\left.\begin{aligned} &\int f_1\, d\phi_1 = \int f_1^{(0)} d\phi_1 = n_1\,, \\ &\int f_1 m_1 \boldsymbol{U}_1 d\phi_1 + \int f_2 m_2 \boldsymbol{U}_2 d\phi_2 \\ &\qquad = \int f_1^{(0)} m_1 \boldsymbol{U}_1 d\phi_1 + \int f_2^{(0)} m_2 \boldsymbol{U}_2 d\phi_2\,, \\ &\int f_1 \frac{m_1}{2} U_1^2 d\phi_1 + \int f_2 \frac{m_2}{2} U_2^2 d\phi_2 \\ &\qquad = \int f_1^{(0)} \frac{m_1}{2} U_1^2 d\phi_1 + \int f_2^{(0)} \frac{m_2}{2} U_2^2 d\phi_2\,. \end{aligned}\right\} \tag{7}$$

For this purpose, we use the thermodynamical and hydrodynamical equations:

$$\left.\begin{aligned} &\rho_1 = m_1 \int f_1^{(0)} d\phi_1\,; \quad \boldsymbol{u}_1 = \frac{1}{\rho_1}\int f_1^{(0)} m_1 \boldsymbol{r}\, d\phi_1\,, \\ &\qquad n_1 \boldsymbol{u}_1 + n_2 \boldsymbol{u}_2 = n\boldsymbol{u}\,, \end{aligned}\right\} \tag{8}$$

$$\left.\begin{aligned} n_1 &= G_1 (2\pi mkT/h^2)^{3/2} F^{(1)}_{1/2}\,, \\ p_1 &= \frac{2}{3}\varepsilon_1\rho_1 = G_1 kT (2\pi m_1 kT/h^2)^{3/2} F^{(1)}_{3/2}\,, \end{aligned}\right\} \tag{9}$$

$$F_s^{(1)} = F_s(A_1) = \frac{1}{\Gamma(s+1)}\int \frac{Z^s dz}{\exp Z/A_1 - 1}\,, \tag{10}$$

$$\left.\begin{aligned} &\frac{d\rho_1}{dt} + \rho_1 \frac{\partial}{\partial \boldsymbol{x}}\cdot\boldsymbol{u} = 0\,, \\ &\rho\frac{d\boldsymbol{u}}{dt} = \rho_1 \boldsymbol{X} + \rho_2 \boldsymbol{Y} - \frac{\partial p}{\partial \boldsymbol{x}}\,, \\ &\frac{d}{dt}\left(\frac{p}{\rho}\right) = -\frac{2}{3}\frac{p}{\rho}\frac{\partial}{\partial \boldsymbol{x}}\cdot\boldsymbol{u}\,. \end{aligned}\right\} \tag{11}$$

If we use the following abbreviations:

$$\left.\begin{aligned} \boldsymbol{\xi}_1 &= \boldsymbol{U}_1 c_1^{1/2} = (\boldsymbol{r}-\boldsymbol{u})\, c_1^{1/2}\,, \\ \tau_1^2 &= \xi_1^2 + \eta_1^2 + \zeta_1^2\,, \\ c_1 &= m_1/2kT\,, \end{aligned}\right\} \tag{12}$$

then the Eq. (5) becomes:

$$\begin{aligned} \frac{f_1^{(0)2}}{A_1\exp(-\tau_1^2)} \Bigg[& \frac{\boldsymbol{\xi}_1}{c_1^{1/2} T}\cdot\frac{\partial T}{\partial \boldsymbol{x}}\left(\tau_1^2 - \frac{5}{2}\frac{p_1}{n_1 kT}\right) \\ & + 2\cdot\left(\boldsymbol{\xi}_1\boldsymbol{\xi}_1 - \frac{\tau^2}{3}\boldsymbol{1}\right) : \frac{\partial}{\partial \boldsymbol{x}}\boldsymbol{u} \\ & + \frac{2\boldsymbol{\xi}_1 c_1^{1/3}}{\rho_1 \rho}\cdot\left\{\rho_2 \frac{\partial p_1}{\partial \boldsymbol{x}} - \rho_1 \frac{\partial p_2}{\partial \boldsymbol{x}} - \rho_1\rho_2(\boldsymbol{X}-\boldsymbol{Y})\right\}\Bigg] \\ = & -J_{11}(\chi_1) - J_{12}(\chi_1)\,. \end{aligned} \tag{13}$$

Therefore, the solutions of the equations of these types have the form:

$$\chi_1 = -\boldsymbol{A}_1\cdot\frac{\partial \log T}{\partial \boldsymbol{x}} - \boldsymbol{\mathit{II}}_1 : \frac{\partial}{\partial \boldsymbol{x}}\boldsymbol{u} - n\boldsymbol{D}\cdot\boldsymbol{F}_{12}\,, \tag{14}$$

$$\boldsymbol{F}_{12} = \frac{1}{nkT\rho}\left\{\rho_2 \frac{\partial p_1}{\partial \boldsymbol{x}} - \rho_1 \frac{\partial p_2}{\partial \boldsymbol{x}} - \rho_1\rho_2(\boldsymbol{X}-\boldsymbol{Y})\right\}\,, \tag{15}$$

where $\boldsymbol{A}_1$, $\boldsymbol{\mathit{II}}_1$ and $\boldsymbol{D}$ are the functions satisfying the following integral equations:

$$\left.\begin{aligned} &\boldsymbol{\xi}_1 f_1^{(0)2}\left(\tau_1^2 - \frac{5}{2}\frac{p_1}{n_1 kT}\right)\Big/ A_1 \exp(-\tau_1^2)\, c_1^{1/2} \\ &\qquad\qquad = J_{11}(\boldsymbol{A}_1) + J_{12}(\boldsymbol{A}_1)\,, \\ &\qquad\qquad \cdots\cdots\cdots\cdots\cdots\cdots \end{aligned}\right\} \tag{16}$$

$$\left.\begin{aligned} &2\left(\boldsymbol{\xi}_1\boldsymbol{\xi}_1 - \frac{\tau_1^2}{3}\boldsymbol{1}\right) f_1^{(0)2}/A_1\exp(-\tau_1^2) \\ &\qquad\qquad = J_{11}(\boldsymbol{\mathit{II}}_1) + J_{12}(\boldsymbol{\mathit{II}}_1)\,, \\ &\qquad\qquad \cdots\cdots\cdots\cdots\cdots\cdots \end{aligned}\right\} \tag{17}$$

$$\left.\begin{aligned}\boldsymbol{\xi}_1 f_1^{(0)2}/A_1 \exp(-\tau_1^2)\, c_1^{1/2} n_1 &\\ &= J_{11}(\boldsymbol{D}_1)+J_{12}(\boldsymbol{D}_1)\,,\\ -\boldsymbol{\xi}_2 f_2^{(0)2}/A_2 \exp(-\tau_2^2)\, c_2^{1/2} n_2 &\\ &= J_{21}(\boldsymbol{D}_2)+J_{22}(\boldsymbol{D}_2)\,.\end{aligned}\right\} \quad (18)$$

Aa a matter of course, the left hand members of these equations approach their classical forms as the temperature increases. And similarly(1):

$$\boldsymbol{\xi}_1\cdot\boldsymbol{F}_{12}/c_1^{1/2}$$
$$\rightarrow \boldsymbol{U}_1\cdot\left\{\frac{\partial n_1/n}{\partial x}+\frac{n_1 n_2}{n\rho}(m_2-m_1)\frac{\partial \log p}{\partial x}\right\}. \quad (19)$$

To obtain the definite solutions of these integral equations, we impose on χ the five conditions given by Eq. (7). As the functions $\boldsymbol{\Lambda}$, $\boldsymbol{\Pi}$ and $\boldsymbol{D}$ should have the forms

$$\left.\begin{aligned}\boldsymbol{\Lambda} &= \boldsymbol{\xi}\,\chi_a(\tau^2)\,,\\ \boldsymbol{\Pi} &= \left(\boldsymbol{\xi}\boldsymbol{\xi}-\frac{\tau^2}{3}\mathbf{1}\right)\chi_b(\tau^2)\,,\\ \boldsymbol{D} &= \boldsymbol{\xi}\,\chi_d(\tau^2)\,,\end{aligned}\right\} \quad (20)$$

the conditions (7) reduce to:

$$\sum mc^{-1/2}\int f^{(0)}(1+\theta f^{(0)})\,\boldsymbol{\xi}\cdot\boldsymbol{\Lambda}\, d\phi = 0\,,$$
$$\sum mc^{-1/2}\int f^{(0)}(1+\theta f^{(0)})\,\boldsymbol{\xi}\cdot\boldsymbol{D}\, d\phi = 0\,.$$

Using Eq. (20), these are transformed into

$$\left.\begin{aligned}\sum mc^{-1/2}\int \tau^4 f^{(0)}(1+\theta f^{(0)})\,\chi_a(\tau^2)\,d\tau &= 0\,,\\ \sum mc^{-1/2}\int \tau^4 f^{(0)}(1+\theta f^{(0)})\,\chi_d(\tau^2)\,d\tau &= 0\,.\end{aligned}\right\} \quad (21)$$

Though we must add the solutions of the homogenous integral equations to the particular solutions of Eqs. (16) ~ (18) to obtain the general solutions, the results thus obtained do not alter the forms of the equations such as Eq. (14). Therefore, we may regard the Eq. (14) as the general solution of the original equations. Thus in the first approximation the solutions are given by as follows:

$$\left.\begin{aligned}f_1 = f_1^{(0)}\Big[1&-\frac{f_1^{(0)}\exp(\tau_1^2)}{A_1 T}\boldsymbol{\Lambda}_1\cdot\frac{\partial T}{\partial x}\\ &-\frac{f_1^{(0)2}\exp(\tau_1^2)}{A_1}\boldsymbol{\Pi}:\frac{\partial}{\partial x}\boldsymbol{u}\\ &-\frac{f_1^{(0)}\exp(\tau_1^2)}{A_1}n\boldsymbol{D}\cdot\boldsymbol{F}_{12}\Big]\,,\\ &\cdots\cdots\cdots\cdots\cdots\cdots\end{aligned}\right\} \quad (22)$$

From Eq. (22) we can calculate the viscosity and other gas coefficients. For this purpose, we define the following notations.

$$\left.\begin{aligned}\{\boldsymbol{\Lambda},\boldsymbol{a}\} &= \sum\int\frac{f_1^{(0)2}\,\boldsymbol{\xi}_1\cdot\boldsymbol{a}_1}{A_1 c_1^{1/2}\exp(-\tau_1^2)}\\ &\qquad\times\left(\tau_1^2-\frac{5}{2}\frac{p_1}{n_1 kT}\right)d\phi_1\,,\\ \{\boldsymbol{\Pi},\boldsymbol{b}\} &= \sum\int\frac{f_1^{(0)2}\,\boldsymbol{b}}{A_1\exp(-\tau_1^2)}:\\ &\qquad\left(\boldsymbol{\xi}_1\boldsymbol{\xi}_1-\frac{\tau_1^2}{3}\mathbf{1}\right)d\phi_1\,,\\ \{\boldsymbol{D},\boldsymbol{a}\} &= \int\frac{f_1^{(0)2}\,\boldsymbol{\xi}_1\cdot\boldsymbol{a}_1}{A_1 n_1 c_1^{1/2}\exp(-\tau_1^2)}\,d\phi_1\\ &\qquad-\int\frac{f_2^{(0)2}\,\boldsymbol{\xi}_2\cdot\boldsymbol{a}_2}{A_2 n_2 c_2^{1/2}\exp(-\tau_2^2)}\,d\phi_2\,.\end{aligned}\right\} \quad (23)$$

§ 3. The Gas Coefficients.

From Eq. (22), noting the first and the third terms of the equation do not contribute the mean velocity, we can calculate the diffusion velocity of tho two species of molecules relative to one another as follows:

$$\bar{\boldsymbol{U}}_1-\bar{\boldsymbol{U}}_2 = -\frac{1}{3}\left[\{\boldsymbol{D},\boldsymbol{D}\}n\boldsymbol{F}_{12}+\{\boldsymbol{D},\boldsymbol{\Lambda}\}\frac{\partial \log T}{\partial x}\right]. \quad (24)$$

When no force acts on the molecules, and the pressure and temperature of the gas are uniform $\boldsymbol{F}_{12}$ reduces to:

$$\boldsymbol{F}_{12} = \frac{n_1}{n}\frac{d\log A_1}{dn_1}\frac{\partial n_1}{\partial x}. \quad (25)$$

Therefore, the diffusion coefficient D_{12} defined by

$$\bar{\boldsymbol{u}}_1-\bar{\boldsymbol{u}}_2 = -D_{12}\left(\frac{1}{n_1}\frac{\partial n_1}{\partial x}-\frac{1}{n_2}\frac{\partial n_2}{\partial x}\right), \quad (26)$$

becomes

$$D_{12} = \frac{n_1 n_2}{3n}\{\boldsymbol{D},\boldsymbol{D}\}\frac{d\log A_1}{d\log n_1}. \quad (27)$$

For the thermal diffusion coefficient D_T and the relative diffusion velocity we obtain the expressions:

$$D_T = \frac{n_1 n_2}{3n^2}\{\boldsymbol{D},\boldsymbol{\Lambda}\}\frac{d\log A_1}{d\log n_1}, \quad (28)$$

$$\bar{\boldsymbol{U}}_1-\bar{\boldsymbol{U}}_2 = -\frac{n^2}{n_1 n_2}\frac{d\log n_1}{d\log A_1}D_{12}\left\{\boldsymbol{F}_{12}+k_T\frac{\partial\log T}{\partial x}\right\}, \quad (29)$$

where $k_T = D_T/D_{12}$ is the thermal diffusion ratio. On the other hand, the thermal flux $\boldsymbol{q}$ given by

$$\boldsymbol{q} = \sum\int f\frac{m}{2}U^2\boldsymbol{U}\,d\phi\,, \quad (30)$$

can be transformed into the following form by using Eq. (23):

$$\frac{\boldsymbol{q}}{kT}-\frac{5}{2}\left(\frac{p_1\bar{\boldsymbol{U}}_1}{kT}+\frac{p_2\bar{\boldsymbol{U}}_2}{kT}\right)$$
$$=-\frac{1}{3}\left[\{\boldsymbol{\Lambda},\boldsymbol{D}\}\,n\boldsymbol{F}_{12}+\{\boldsymbol{\Lambda},\boldsymbol{\Lambda}\}\frac{\partial\log T}{\partial x}\right].$$

Eliminating $\boldsymbol{F}_{12}$ with use of Eq. (24), and considering the symmetrical relation $\{\boldsymbol{\Lambda},\boldsymbol{D}\}=\{\boldsymbol{D},\boldsymbol{\Lambda}\}$, we obtain:

$$\boldsymbol{q}=\frac{5}{2}(p_1\bar{\boldsymbol{U}}_1+p_2\bar{\boldsymbol{U}}_2)+kT(\bar{\boldsymbol{U}}_1-\bar{\boldsymbol{U}}_2)\frac{\{\boldsymbol{\Lambda},\boldsymbol{D}\}}{\{\boldsymbol{D},\boldsymbol{D}\}}-\lambda\frac{\partial T}{\partial x},\tag{31}$$

$$\lambda=\frac{k}{3}\left[\{\boldsymbol{\Lambda},\boldsymbol{\Lambda}\}-\frac{\{\boldsymbol{\Lambda},\boldsymbol{D}\}^2}{\{\boldsymbol{D},\boldsymbol{D}\}}\right],\tag{32}$$

where λ is the coefficient of thermal conduction.

In the same way, the coefficient of viscosity μ is given by,

$$p_{xx}-p=-\frac{2\mu}{3}\left(2\frac{\partial u}{\partial x}-\frac{\partial v}{\partial y}-\frac{\partial w}{\partial z}\right),$$
$$\mu=\frac{1}{10}kT\{\boldsymbol{\Pi},\boldsymbol{\Pi}\}.\tag{33}$$

To calculate these expressions, we assume $\boldsymbol{\Lambda}$, $\boldsymbol{\Pi}$ and $\boldsymbol{D}$ are constructed as a liner combinations of functions $\boldsymbol{h}^{(r)}$, $\boldsymbol{k}^{(r)}$ and $\boldsymbol{h}^{(r)}$ respectively, where r assumes the values extending from $-\infty$ to ∞. The typical form of the expansion is given by

$$\boldsymbol{\Pi}=\sum_{-\infty}^{\infty}c_r\boldsymbol{k}^{(r)}.\tag{34}$$

If we assume further that the functions $\chi_a(\tau^2)$, $\chi_b(\tau^2)$ and $\chi_c(\tau^2)$ are analytic functions of the argument τ^2, and if we think of the condition (20) and (21), $\boldsymbol{h}^{(r)}$ and $\boldsymbol{k}^{(r)}$ can be fixed as follows:

$$\begin{array}{lll} & r\geq 1 & r\leq 1 \\ \boldsymbol{h}_1^{(r)}= & \boldsymbol{\xi}_1\left[\tau_1^{2r}-\frac{\Gamma(r+5/2)}{\Gamma(5/2)}\frac{F^{(1)}_{r+1/2}}{F^{(1)}_{1/2}}\right]; & =0, \\ \boldsymbol{h}_2^{(r)}=0; & & =\boldsymbol{\xi}_2\left[\tau_2^{2r}-\frac{\Gamma(r+5/2)}{\Gamma(5/2)}\frac{F^{(2)}_{r+1/2}}{F^{(2)}_{1/2}}\right] \\ \boldsymbol{k}_1^{(r)}= & \left(\boldsymbol{\xi}_1\boldsymbol{\xi}_1-\frac{\tau_1^2}{3}\mathbf{1}\right)\tau_1^{2r-2}; & =0, \\ \boldsymbol{k}_2^{(r)}=0; & & =\left(\boldsymbol{\xi}_2\boldsymbol{\xi}_2-\frac{\tau_2^2}{3}\mathbf{1}\right)\tau_2^{2r-2}. \end{array}\tag{55}$$

To determine the coefficients of expansions of Eq. (34) we require, for example, that the expression

$$H^{(n)}=\{\boldsymbol{\Pi}-\boldsymbol{\Pi}^{(n)},\ \boldsymbol{\Pi}-\boldsymbol{\Pi}^{(n)}\},\tag{36}$$

which is always positive, assumes the minimum value for a given n. Here $\boldsymbol{\Pi}^{(n)}$ is the nth approximation for $\boldsymbol{\Pi}$. Therefore, if we define b_{rs} and β_r by

$$b_{rs}=\{\boldsymbol{k}^{(r)},\boldsymbol{k}^{(s)}\},\tag{37}$$

$$\beta_r=\{\boldsymbol{\Pi},\boldsymbol{k}^{(r)}\},\tag{38}$$

and by B the determinant $|b_{rs}|$ and $B_{\beta r}$ the one obtained by replacing rth column of B by β_r, then c_r is determined as follows:

$$c_r=B_{\beta r}/B.\tag{39}$$

Thus, the coefficient of viscosity μ is found to be (the degree of approximation is determined by the degree of the determinant):

$$\mu=-\frac{kT}{10}B_{\beta\beta}/B,\tag{40}$$

where $B_{\beta\beta}$ is the determinant obtained from B by bordering the final row and column with β_r, the common element of which being zero.

In the same way. the coefficient of thermal conduction becomes

$$\lambda=-\frac{k}{3}\frac{A_{\alpha\alpha\gamma\gamma}}{A_{\gamma\gamma}},\tag{41}$$

$$D_{12}=-\frac{n_1n_2}{3n}\frac{d\log A_1}{d\log n_1}\frac{A_{\gamma\gamma}}{A},$$

$$D_T=-\frac{n_1n_2}{3n}\frac{d\log A_1}{d\log n_1}\frac{A_{\alpha\gamma}}{A}.\tag{42}$$

where $A_{\alpha\gamma}$ (or $A_{\alpha\alpha\gamma\gamma}$) is the determinant obtained from the determinant $A=|a_{rs}|$ by bordering it by final rows and columns (or by two final rows and columns), the common element (or elements) being zero, the other elements being α_r and γ_s (or α_r, γ_r and α_s, γ_s). $A_{\gamma\gamma}$ is similar to $B_{\gamma\gamma}$ or $B_{\beta\beta}$. a_{rs}, α_r and γ_r are the following integrals

$$a_{rs}=\{\boldsymbol{h}^{(r)},\boldsymbol{h}^{(s)}\},\tag{43}$$

$$\alpha_r=\{\boldsymbol{\Lambda},\boldsymbol{h}^{(r)}\};\quad\gamma_r=\{\boldsymbol{D},\boldsymbol{h}^{(r)}\}.\tag{44}$$

Thus, we have arrived at the final formulas for the gas coefficients. These formulas have the same symbolycal expressions as the classical formulas of Chapman and others, but the explicit formulas are different from them. We wish to consider the situation in the following articles.

References.

(1) Chapman and Cowling: Mathematical Theory of Non Uniform Gases. Cambridge 1939.

(2) Uehling and Uhlenbeck: Phys. Rev. **43** (1933), 552. Uehling: Phys. Rev. **46** (1934), 917.

(3) Enskog: Svenska Vetenskapsakademien Hadlungar **63** (1921), 5.

(4) Massey and Mohr: Proc. Roy. Soc. **141**, (1933), 434; **144** (1934), 188.

Transport Phenomena in Degenerate Systems.
II. Degenerate Bose-Einstein Gas.

By Akira ISIHARA.

Faculty of Science, University of Tokyo.

(Received November 14, 1949)

(Read October 23, 1949)

§ 1. Introduction.

Many papers have been published concerning the condensation of Bose-Einstein gas. Most of them, however, treat only the equilibrium properties. Recently Band⁽¹⁾ has proposed a theory concerning the transport phenomena in Bose-Einstein gas, and examined the effect of condensation on them. Obeying the current conceptions, he considered the normal and super molecules. Their velocity distribution functions and their manners of deviation from the equilibrium distributions are different from each other. He, thus calculated the coefficient of thermal conductivity which represents the experimental one qualitatively. His fundamental equations, however, include such phenomenological parameters as relaxation times, which are determined by the condition that the net flow of particles is zero, and which cannot be satisfied at temperatures below the λ-point T_0. He adopted the fundamental equations hoping to connect the results with "liquid" helium, but we think it is also necessary to examine the effect of condensation on the coefficients in the case of ideal Bose-Einstein "gas". When the temperature is high enough, the gas coefficients do not depend on the density, but when it becomes very low this is not the case owing to the quantum effect. Therefore, it is expected that some changes in the coefficients will appear at the condensation. In the next section we want to calculate these, following the theory of Uhlenbeck and Uehling with respect to the transport phenomena in gases⁽²⁾,

§ 2. The Gas Coefficients.

At first we want to calculate the coefficient of thermal conductivity κ of degenerate helium gas. In the similar way as explained in § 3 of the first paper of this series it is calculated as follows:

$$\kappa = \frac{k}{3}\int \Phi(\tau) \boldsymbol{A} \cdot \boldsymbol{\xi}\, d\sigma , \tag{1}$$

$$\Phi(\tau) = f^{(0)2}/\exp(-\tau^2)\, c^{1/2} \cdot \left(\tau^2 - \frac{5}{2}\,\frac{p}{n_1 kT}\right) , \tag{2}$$

where,

$$\tau^2 = \frac{m}{2kT} U^2 = \xi^2 + \eta^2 + \zeta^2 , \tag{3}$$

$$c = m/2kT , \tag{4}$$

$$\boldsymbol{\xi} = (\xi, \eta, \zeta) = c^{1/2} \boldsymbol{U} ; \quad |\boldsymbol{U}| = U , \tag{5}$$

$$d\sigma = VG(m/h)^3\, d\xi\, d\eta\, d\zeta , \tag{6}$$

and in the region of He II the equilibrium distribution function $f^{(0)}$ is given by

$$f^{(0)} = 1/\exp(\tau^2) - 1 . \tag{7}$$

n_1 is the number density of the normal component of helium. The reason of its appearance in Eq. (2) is that the other component- the "super," the number density of which is denoted by n_2-does not contribute the pressure. Λ is a function satisfying the following integral equation, which comes from the linearized Boltzmann's equation,

$$\xi \Phi(\tau) = J(\Lambda)\,, \tag{8}$$

$$J(\Lambda) = \int f_1^{(0)} f^{(0)} (1+f_1^{(0)\prime})(1+f^{(0)\prime})(\Lambda_1+\Lambda-\Lambda_1'-\Lambda') \times gw(\vartheta,\, g)\, d\sigma_1\, d\Omega\,, \tag{9}$$

where $gw(\vartheta, g)$ is the effective cross section that the relative velocity g is deflected by ϑ after collision, and

$$d\Omega = \sin\vartheta\, d\vartheta\, d\varphi\,. \tag{10}$$

The other notations are as usual, and we may omit the explanations. The function Λ satisfying Eq. (8) can be expanded in power series of τ which is expressed in x-direction as follows:

$$\Lambda = \Sigma\, c_r h_r\,,$$
$$c_r = A_{\alpha r}/A\,, \tag{11}$$

where $A = |a_{rs}|$, and $A_{\alpha r}$ is the determinent obtained from A by replacing its r-th column by α_r. α_r and a_{rs} are the following integrals:

$$\alpha_r = \int \xi\, \Phi(\tau)\, h_r\, d\sigma\,, \tag{12}$$

$$a_{rs} = \int J(h_r)\, h_s\, d\sigma\,. \tag{13}$$

Introducing Eq. (11) into Eq. (1), κ is determined as follows:

$$\kappa = -k\,\frac{A_{\alpha\alpha}}{A}\,, \tag{14}$$

where $A_{\alpha\alpha}$ is the determinant obtained from A by bordering its final row and column with α_r, the common element of which being zero.

While the integration of Eq. (12) can be easily performed, the integration of Eq. (13) must be somewhat carefully done. As in the case of London's theory on the Bose-Einstein condensation, we must pay an attention to the fact that because of the form of Eq. (6) the zero-state will have weight zero if we calculate the integral as it is though the contribution from the "super" to the integral is not zero. This situation does not occur in the integration of Eq. (12) where the term corresponding to the zero state vanishes. On the other hand, in Eq. (13), though the velocities of the thermal motions of the super molecules are zero, their non-vanishing relative velocities to the normal particles make us to consider the contribution to the integral from the collisions between the super and the normal and that of the inverse collisions. We want to denote these contributions to a_{rs} by $[h_r h_s]_{01}$, whereas those come from the remaining collisions by $[h_r h_s]_{11}$, and to call the former collisions as s-collisions whereas the latter as n-collisions. Then Eq. (13) becomes:

$$a_{rs} = [h_r h_s]_{01} + [h_r h_s]_{11}\,. \tag{15}$$

To calculate these terms we separate the integrals with respect to the velocity l of the center of gravity from the one with respect to the relative velocity g of colliding molecules. The transformation in the case of n-collisions is given by the equations:

$$\lambda = l(m/kT)^{1/2}\,;\ \gamma = g(m/4kT)^{1/2}\,, \tag{16}$$

$$\xi = \left\{ \frac{\lambda}{\sqrt{2}}\mathbf{1} + \frac{\gamma}{\sqrt{2}} \begin{pmatrix} \cos\alpha\cos\theta\,, & -\sin\alpha\sin\theta\cos\varepsilon\,, & 0 \\ \cos\alpha\sin\theta\cos\delta\,, & \sin\alpha\cos\theta\cos\varepsilon\cos\delta\,, & -\sin\alpha\sin\varepsilon\sin\delta \\ \cos\alpha\sin\theta\sin\delta\,, & \sin\alpha\cos\theta\cos\varepsilon\sin\delta\,, & \sin\alpha\sin\varepsilon\cos\delta \end{pmatrix} \begin{pmatrix} \cos\theta \\ \sin\theta \\ \sin\theta\cos\delta \end{pmatrix} \right\}, \tag{17}$$

where λ, θ, α, and γ, δ, ε are the polar coordinates corresponding to the velocity of the center of gravity and that of the relative velocity respectively. From Eq. (8) and the conditions of mass, momentum and energy conservation the form of h_r is determined as follows

$$h^r = \xi\left(\tau^{2r} - \frac{\Gamma(r+5/2)}{\Gamma(5/2)}\,\frac{F^{r+1/2}}{F_{1/2}}\right), \tag{18}$$

so that the main parts of its component which actually give non-vanishing contribution to $[h_r h_s]_{11}$ are given by

$$\left.\begin{aligned} h_r &= 2^{-r-1/2}[\lambda\cos\theta+\gamma(\cos\alpha\cos\theta \\ &\qquad -\sin\alpha\sin\theta\cos\varepsilon)](\lambda^2+\gamma^2+2\gamma\lambda\cos\alpha)^r, \\ h_{r1} &= 2^{-r-1/2}[\lambda\cos\theta-\gamma(\cos\alpha\cos\theta \\ &\qquad -\sin\alpha\sin\theta\cos\varepsilon)](\lambda^2+\gamma^2-2\gamma\lambda\cos\alpha)^r. \end{aligned}\right\} \tag{19}$$

If we take such approximations to the calculations of α_r or a_{rs} as used in the theory of London-condensation and if we think of its condition:

$$n_1 = N(T/T_0)^{3/2}; \quad T_0 = \left(\frac{N}{VF_{1/2}}\right)^{2/3} \frac{h^2}{2\pi mk}, \tag{20}$$

we obtain for α_r given by Eq. (12):

$$\alpha_r = c^{-1/2} n_1 \frac{2\pi^{-1/2}}{3} \frac{\Gamma\left(\frac{2r+7}{2}\right)}{F_{1/2}} \times\left[F_{r+1/2} - \frac{5}{2r+5} \frac{F_{r+1/2} F_{3/2}}{F_{1/2}}\right], \tag{21}$$

$$F_s = \frac{1}{\Gamma(s+1)} \int z^s dz/(\exp z - 1),$$

and for $[h_r h_s]_{11}$

$$[h_r h_s]_{11} = \frac{n_1^2}{2}\left(\frac{2}{c}\right)^{1/2} \frac{1}{F_{1/2}^2} \int d\omega\, \alpha\omega_1\, \gamma I(\vartheta, \gamma)\, d\Omega \times f^{(0)} f_1^{(0)} (1+f^{(0)\prime})(1+f_1^{(0)\prime}) \times (h_r + h_{r1} - h_r' - h_{r1}')(h_s + h_{s1}), \tag{22}$$

where $\gamma I(\vartheta, \gamma)$ is the differential cross section with respect to the center of gravity and $d\omega$ is

$$d\omega = d\xi\, d\eta\, d\zeta. \tag{23}$$

Taking the first approximation to the evaluation of Eq. (22) we obtain for $[h_1 h_1]_{11}$, which is necessary to calculate κ in the first approximation,

$$[h_1 h_1]_{11} = n_1^2 \left(\frac{2}{c}\right)^{1/2} \frac{8\sqrt{\pi}}{9} \frac{P_1}{F_{1/2}^2}, \tag{24}$$

$$P_1 = \int \exp(-\gamma^2)\cdot \gamma^7 \theta(\gamma)\, d\gamma, \tag{25}$$

$$\theta(\gamma) = \int [1 - P_2(\cos\vartheta)]\, I(\vartheta\gamma) \sin\vartheta\, d\vartheta\cdot \tag{26}$$

In the case of s-collisions corresponding to the first term of Eq. (15), regarding the members with suffix 1 to correspond to the super, we obtain:

$$\boldsymbol{\xi} = \sqrt{2}\,\boldsymbol{\gamma}; \; \boldsymbol{g} = \boldsymbol{\gamma}(2/c)^{1/2}; \; d\Gamma = \gamma^2 \sin\theta\, d\gamma\, d\theta\, d\delta; \tag{27}$$

$$\tau^2 = 2\gamma^2; \; \tau'^2 = \gamma^2(1+\cos\vartheta), \; \tau_1'^2 = \gamma^2(1-\cos\vartheta),$$

$$\boldsymbol{\xi} = \frac{\gamma}{\sqrt{2}} \begin{pmatrix} 1+\cos\theta, & -\sin\theta, & 0 \\ \sin\theta\cos\delta, & 1+\cos\theta\cos\delta, & -\sin\delta \\ \sin\theta\sin\delta, & \cos\theta\sin\delta, & 1+\cos\delta \end{pmatrix} \times \begin{pmatrix} \cos\vartheta \\ \sin\vartheta\cos\varphi \\ \sin\vartheta\sin\varphi \end{pmatrix}, \tag{28}$$

and for the main parts of h_1 etc.:

$$\left.\begin{aligned} h_1 &= 2\sqrt{2}\gamma^3\cos\theta, \\ h_1' &= \frac{\gamma^3}{\sqrt{2}}\{\cos\theta(1+\cos\vartheta) \\ &\qquad -\sin\theta\sin\vartheta\cos\varphi\}(1+\cos\vartheta), \\ h_{11}' &= \frac{\gamma^3}{\sqrt{2}}\{\cos\theta(1-\cos\vartheta) \\ &\qquad +\sin\theta\sin\vartheta\cos\varphi\}(1-\cos\vartheta). \end{aligned}\right\} \tag{29}$$

Therefore, we arrive at:

$$[h_1 h_1]_{01} = n_1 n_2 (2\pi)^{-3/2} c^{-1/2}/F_{1/2} \times \int \gamma I(\vartheta, \gamma)\, d\Omega\, f^{(0)} (1+f^{(0)\prime})(1+f_1^{(0)\prime}) \times (h_1 - h_1' - h_{11}')^2\, d\Gamma, \tag{30}$$

$$= n_1 n_2 \left(\frac{2}{c}\right)^{1/2} \frac{8\sqrt{\pi}}{9} \frac{P_2}{F_{1/2}^2}, \tag{31}$$

$$P_2 = F_{1/2} \int \exp(-2\gamma^2)\cdot\gamma^9 \theta(\gamma)\, d\gamma. \tag{32}$$

Thus, from Eqs. (14), (15), (21), (24) and (31) κ is given by in the first approximation as follows:

$$\kappa \simeq \frac{25}{32\pi^{1/2}} \frac{3k}{2m} (mkT)^{1/2} \frac{3n_1}{2(n_1 P_1 + n_2 P_2)}. \tag{33}$$

In the same way the coefficient of viscosity η can be shown to be

$$\eta = -3kT \frac{B_{\beta\beta}}{B}, \tag{34}$$

$$\beta_r = \int \frac{f^{(0)2}}{\exp(-\tau^2)} k_r \left(\xi^2 - \frac{\tau^2}{3}\right) d\sigma, \tag{35}$$

$$b_{rs} = \int J(k_r)\, k_s\, d\sigma = [k_r k_s]_{01} + [k_r k_s]_{11}, \tag{36}$$

$$k_r = \left(\boldsymbol{\xi}\boldsymbol{\xi} - \frac{\tau^2}{3}\mathbf{1}\right)\tau^{2r-2}. \tag{37}$$

Here $B = |b_{rs}|$, and $B_{\beta\beta}$ is the determinant similar to $A_{\alpha\alpha}$, and β_r is calculated as follows:

$$\beta_r = \frac{8\pi^{-1/2}}{45} \Gamma\left(\frac{2r+5}{2}\right) \frac{F_{r+1/2}}{F_{1/2}} n_1. \tag{38}$$

With respect to n-collisions, the main parts of the x-component of k_r are given by:

$$\begin{aligned} k_{11} = 2^{-1}\Big[&\left(\cos^2\theta - \frac{1}{3}\right)(\lambda^2 + \gamma^2 + 2\gamma\lambda\cos\alpha) \\ &+\gamma^2\sin^2\theta\sin^2\alpha\cos^2\varepsilon - \gamma^2\cos^2\theta\sin^2\alpha \\ &-2\gamma\lambda\sin\theta\cos\theta\sin\alpha\cos\varepsilon \\ &-\gamma^2\sin\theta\cos\theta\sin 2\alpha\cos\varepsilon\Big], \end{aligned} \tag{39}$$

$$\begin{aligned} k_1 = 2^{-1}\Big[&\left(\cos^2\theta - \frac{1}{3}\right)(\lambda^2 + \gamma^2 - 2\gamma\lambda\cos\alpha) \\ &\gamma^2\sin\theta\sin^2\alpha\cos^2\varepsilon - \gamma^2\cos^2\theta\sin^2\alpha \\ &+2\gamma\lambda\sin\theta\cos\theta\sin\alpha\cos\varepsilon \\ &-\gamma^2\sin\theta\cos\theta\sin 2\alpha\cos\varepsilon\Big], \end{aligned}$$

and therefore

$$[k_1 k_1]_{11} \doteqdot n_1^2 \left(\frac{2}{c}\right)^{1/2} \frac{16\sqrt{\pi}}{45} \frac{Q_1}{F_{1/2}^2}, \tag{40}$$

$$Q_1 \doteqdot P_1. \tag{41}$$

With respect to s-collisions:

$$\left.\begin{aligned} k_1 &= 2r^2 \cos^2 \theta, \\ k_1' &= \frac{r^2}{2}\{\cos\theta^2 (1+\cos\vartheta)^2 + \sin^2\theta \sin^2\vartheta \cos^2\varphi \\ &\quad -2\sin\theta\cos\theta\sin\vartheta(1+\cos\vartheta)\cos\varphi\}, \\ k_{11}' &= \frac{r^2}{2}\{\cos^2\theta(1-\cos\vartheta)^2 + \sin^2\theta\sin^2\vartheta\cos^2\varphi \\ &\quad +2\sin\theta\cos\theta\sin\vartheta(1-\cos\vartheta)\cos\varphi\}, \end{aligned}\right\} \tag{42}$$

$$[k_1 k_1]_{01} = n_1 n_2 \left(\frac{2}{c}\right)^{1/2} \frac{16\sqrt{\pi}}{45} \frac{Q_2}{F_{1/2}^2}, \tag{43}$$

$$Q_2 = F_{1/2} \int \exp(-2r^2)\, r^7\, \theta(r)\, dr. \tag{44}$$

Introducing these into Eq. (34), we can obtain the following expression for the viscosity:

$$\eta = \frac{15}{32} \frac{(mkT)^{1/2} (F_{3/2})^2 n_1}{\sqrt{\pi}(n_1 Q_1 + n_2 Q_2)}. \tag{45}$$

To calculate the effective cross sections P or Q, we adopt the rigid elastic model. In this case $I(\vartheta, r)$ is given by

$$\begin{aligned} I(\vartheta, r) &= r_0^2 \frac{2}{y^2} \Sigma (4n+1)(4m+1) P_{2n}(\cos\vartheta) \\ &\quad \times P_{2m}(\cos\vartheta) \cos(\delta_{2n} - \delta_{2m}) \sin\delta_{2n} \sin\delta_{2m}, \end{aligned} \tag{46}$$

$$\delta_l = \arctan (-1)^l \frac{J_{l+1/2}(y)}{J_{-l-1/2}(y)},$$

$$r = \frac{y}{r_0} \lambda_0 = \frac{yh}{r_0 2\pi (mkT)^{1/2}}. \tag{47}$$

where r_0 is the diameter of the molecule and λ_0 is the de Broglie wave length corresponding to the mean temperature motion. Introducing this into Eq. (26), and evaluting the integration by the method of steepest descent which is accurate for very low temperature, we obtain for $\theta(r)$ the following expression:

$$\theta(r) = 4r_0^2 \left(1 - \frac{r^2}{3}\left(\frac{\lambda_0}{r_0}\right)^{-2} - \frac{61 r^4}{15\cdot 12}\left(\frac{\lambda_0}{r_0}\right)^{-4} + \cdots\right). \tag{48}$$

Inserting this into Eqs. (25), (32) and (44), we obtain:

$$\begin{aligned} P_1 &= 12 r_0^2 \left\{1 - \frac{4}{3}\left(\frac{\lambda_0}{r_0}\right)^{-2} - \frac{61}{9}\left(\frac{\lambda_0}{r_0}\right)^{-4}\right\}, \\ P_2 &= \frac{3}{2} r_0^2 \left\{1 - \frac{5}{6}\left(\frac{\lambda_0}{r_0}\right)^{-2} - \frac{61}{24}\left(\frac{\lambda_0}{r_0}\right)^{-4}\right\} F_{1/2}, \\ Q_1 &= \frac{3}{4} r_0^2 \left\{1 - \frac{2}{3}\left(\frac{\lambda}{r_0}\right)^{-2} - \frac{61}{36}\left(\frac{\lambda}{r_0}\right)^{-4}\right\} F_{1/2}, \end{aligned} \tag{49}$$

Therefore, the gas coefficients become:

$$\kappa = \left(\frac{kT}{\pi m}\right)^{1/2} \frac{125k}{64 r_0^2} \frac{n_1}{(8n_1 + F_{1/2} n_2)}, \tag{50}$$

$$\eta = \left(\frac{mkT}{\pi}\right)^{1/2} \frac{5F_{3/2}^2}{8r_0^2} \frac{n_1}{(16n_1 + F_{1/2} n_2)}. \tag{51}$$

§ 3. Discussions.

The results thus obtained are illustrated in Fig. 1 and 2.

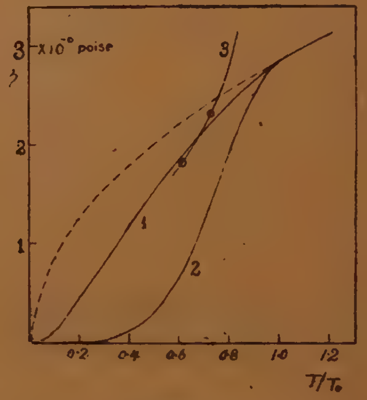

Fig. 1.
Viscosity—temperature curves.

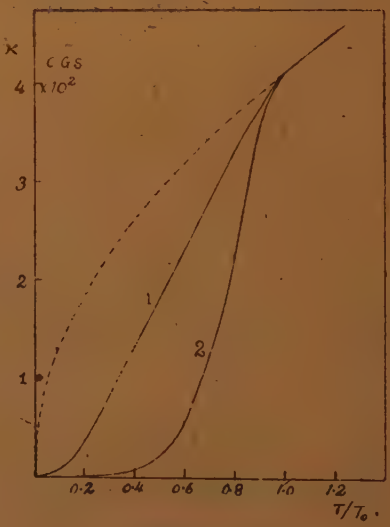

Fig. 2.
Thermal conductivity—temperature curues.

The curves with figure 1 correspond to purely theoretical calculation. In this case n_1 was determined from Eq. (20). Since this London's result does not fit the experiment, we illustrate in curves 2, though it has no theoretical grounds.

the case where n_1 and n_2 vary with the empirical formulas:

$$n_1 = N(T/T_0)^{5.5},$$
$$n_2 = N(1-(T/T_0)^{5.5}), \qquad (52)$$

in Eq. (50) or (51), allowing the other terms remain as they are. The curve 3 in Fig. 1 corresponds to the experiment of Keesom-MacWood(3). As we can see from the figure, the thermal conductivity thus calculated does not resemble the experimental curves so well. The fundamental process of heat transfer in liquid helium may differ from the process of momentum transfer. On the other hand, though the experimental results on the viscosity of liquid helium differ considerably from each other, their general features resemble the theoretical curves in Fig. 1.

At any rate, the physical meaning of the theoretical equations (33) and (46) is obvious. In the classical theory, the gas coefficients are given by

$$\kappa \sim \eta \approx \rho \bar{v} l \qquad (53)$$

where ρ is the density of the gas, l the mean free path. Therefore, the theoretical equations mean that only the normal component transfer the momentum, whereas the mean free path depends on the density of the other component also; l is expressed in a mixed system as follows:

$$l = 1/\pi\sqrt{2}(n_1P_1+n_2P_2), \qquad (54)$$

In liquid He I, the viscosity is almost gas-like and is expressed by the following empirical formula obtained from the experiment of Keesom-MacWood:

$$\eta_1 = 1.46\times10^{-5}\sqrt{T} \text{ C.G.S.} \qquad (55)$$

At the λ-point it shows a knick or dicontinuity and decreases very rapidly as the temperature decreases. With respect to the experiment, Tisza(4) pointed out that Keesom and MacWood measured $\eta\rho_n$ whereas they thought that they had measured $\eta\rho$. The curve of η thus corrected reveals a minimum in the neighborhood of 1.64°K, as is illustrated by curve 2 in Fig. 3. We can see from the slope of the curve 1 in the figure that the correction to the Keesom-MacWood's results is still too small to smooth out the curve from the region of He I to that of He II in the neighborhood of T_0 while it becomes larger in the lower temperature region. This result is somewhat curious and demands some explanation of us. If we leave the correction out of consideration, the theoretical expression for the viscosity such as given by Eq. (51) is appropriate rather in the lower part of temperatures. This comes partly from the fact that we have evaluated the integrals for P and Q by the method of steepest descent, which is accurate near the absolute zero, and that the gas coefficients are sensitive to them. The discrepancy of the experiment and the present theory is reasonable if we remember that the theory of ideal Bose-Einstein condensation can only explain the general features of the λ-transition, and also that we have adopted the rigid sphere model for the calculation of the cross sections P and Q. In the calculation, we have taken

$$m = 3.2998\times10^{-24} \text{ gr.}; \quad r_0 = 2.10\times10^{-8} \text{ cm},$$

which are reasonable values to explain the viscosity of gas at higher temperatures. We may however be able, to explain the corrected curve 2 in Fig. 3 qualitatively based on the model somewhat analogous to that of Landau(5), but such a discussion is beyond the scope of this paper.

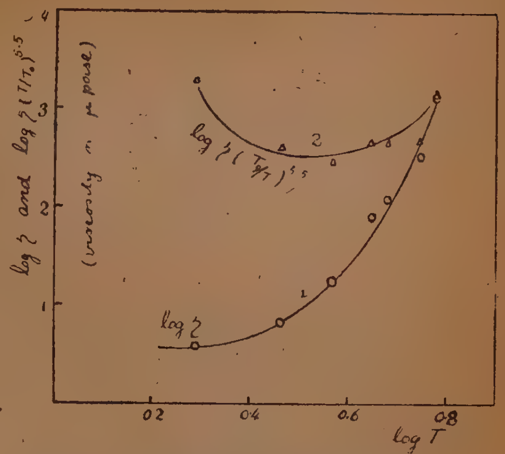

Fig. 3. Keesom—Macwood's experiment for viscosity of liquid He.

In conclusion, the author wishes to make an acknowledgement to Professors T. Sakai and M. Kotani for their valuable suggestions.

References.

(1) W. Band: Phys. Rev. 75 (1949), 339.
(2) E. A. Uehling and G. E. Uhlenbeck: Phys. Rev. 43 (1933), 552; E. A. Uehling: Phys. Rev. 46 (1934), 917; A. Isihara: J. Phys. Soc Jap. 5 (1950), 213.
(3) W. H. Keesom and G. E. MacWood: Physica 5 (1938), 737.
(4) L. Tisza: Phys. Rev. 72 (1947), 838.
(5) L. Landau: F. Phys. U,S.S.R. 5 (1941), 71.

On the Electric Formation of the Selenium Rectifier.

By Masao TOMURA.

Matsuda Research Laboratory of Tokyo Shibaura Electric Co., Ltd., Kawasaki.

(Read, April 29, 1949; Received, Oct. 24, 1949)

§ 1. Introduction.

In the preceding report⁽¹⁾, by researching a process of heat formation in manufacturing the selenium rectifier, the present author has made clear a phenomenon of selenide formation in the barrier layer and in this paper he will pursue a mechanism of process of electric formation which follows the heat formation.

The selenium rectifier which has suffered only the heat formation shows no sufficient ratio of rectification and has so large current in the blocking direction that we cannot use it for normal purpose, owing to its shortening and melting of the front electrode for application of high voltages. When we apply a high D. C. voltage for a while in the blocking direction, so called the electric formation takes place and the hard flow becomes very small, while the easy flow decreases little. Thus the ratio of rectification becomes very large and the rectifier gains desirable natures for normal uses.

Up to this time, no researches have been carried on the electric formation and by a mere empirical fact that makes the characteristics better this process of formation has been carried on. It is the purpose of the present survery to improve the characteristics of the selenium rectifier by studying on the mechanism of the process of electric formation.

§ 2. The Preparation of the Sample and the Method of the Electric Formation.

The selenium material which is used in this experiment comes from the Nikko. Co., Ltd. and suffered distillations in air twice and in vacuum once, after which 0.2 wt. % of sulphur and 0.02 % of iodine are added to it. The front electrode alloy is composed of 50 % of Bi, 20 % of Cd, 30 % of Sn and 0.5 % of Tl. And processes of manufacture are follows. After coating of melted selenium on a metal base electrode, the element suffers the first heat treatment of 2 hours at 130°C under high pressure and next by the second heat treatment of 4 hours at 215°C the selenium is converted to a semiconductor which has good conductivity. Thus the surface of the selenium semiconductor is covered with the front electrode alloy by the spraying method. After that the third heat treatment of 6 hours at 90°C is added to the element. This last process is called as the heat formation. The effective area of the element is 10 cm^2.

As a method of the electric formation which is carried on after the above heat formation, a D. C. voltage is applied in the blocking direction till the formation shows no progression, by elevating the voltage from 20 V to 40 V, taking care of avoiding to make the front electrode melt. In the present study it is not examined in detail how is the electric formation carried on, because the purpose of this survery is in observing the difference between rectification characteristics before and after the formation.

The static characteristics of rectification of the sample are shown in Fig. 1. The figure shows reduction of currents in the forward and blocking directions, but little in the former and large in the later. The ratios of the currents before and after the formation at various voltages are shown in Fig. 2. From these facts it is known that the electric formation is a very useful method in manufacturing the selenium rectifier. Then investigations of the mechanism of the formation will make the natures of that rectifier clear and give a key of improving its characteristics.

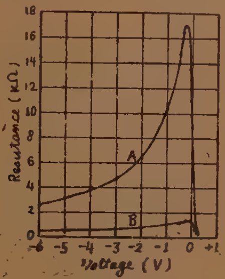

Fig. 1. The rectification characteristics of the selenium rectifier.
A: after the electric formation
B: before the electric formation

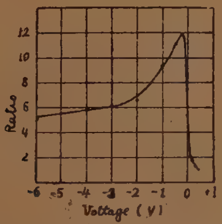

Fig. 2. Ratio of the rectification resistances before and after the electric formation.

§ 3. The Temperature Variation of the Rectification before the Electric Formation.

Next, D. C. characteristics of the easy and hard flows over the temperature range from 10°C to 90°C are measured in a thermostat which is filled with turbine oil. Measurements are carried on as follows: the easy and hard flows for various voltages at each temperature are measured and the duration of applying voltage is maintained so short as several seconds that the progress of the formation cannot take place by the D. C. voltages in the blocking direction. The results are shown in Fig. 3.

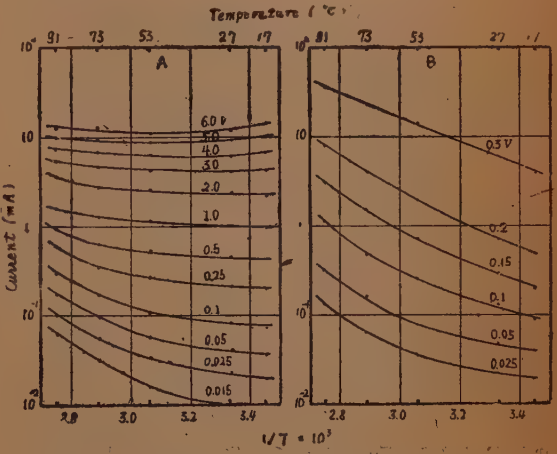

Fig. 3. The current *vs.* 1/T curves before the electric formation.
A: for hard flow
B: for easy flow

The author has reported(2), that the charateristics of the selenium rectifier were explained by the Mott's theory approximately at higher temperatures than the room temperature and then the current density i is shown by the next equation(3).

$$\left.\begin{aligned} i &= \frac{V_0-V-E_0/e}{\rho_\infty} \\ &\quad\times\exp\left[e^{3/2}\frac{\sqrt{V_0-V}-\sqrt{V_0}}{\sqrt{\kappa d}\,kT}\right]\left(e^{\frac{eV}{kT}}-1\right) \\ \rho_\infty &= \frac{d}{evn_0} \\ n_0 &= 2\left(\frac{2\pi mkT}{h^2}\right)^{\frac{3}{2}}e^{-\frac{eV_0}{kT}} \end{aligned}\right\}\cdots (1)$$

Here e is the electronic charge, m the electronic mass, k Boltzmann's constant. h Planck's constant, T the absolute temperature, d the thickness of the barrier layer, κ the dielectric constant of the barrier layer, v the mobility of the current carrier, V_0 the contact potential, E_0 the activation energy of the conductivity of selenium semiconductor and V the applied voltage through the barrier layer. Both i and V have plus signs in the forward direction and minus in the opposite direction. Eq. (1) means that the relation between log i and $1/T$ is shown as a straight line which changes its slope easier with V, by the term $\exp(eV/kT)$ in the forward direction and by the image force effect term $\exp[e^{3/2}(\sqrt{V_0-V}-\sqrt{V_0})/(\sqrt{\kappa d}\,kT)$ in the blocking direction.

Fig. 3 shows that the experimental results are satisfied with Eq. (1) in the temperature range over 80°C, but deviations from Eq. (1) are large at lower temperatures.

The same results have been observed with the silicon crystal detector and the deviations have been attributed to the tunnel effect of current carriers(4). As the figures show, the smaller the applied voltage in the forward direction and the larger the applied voltage in the blocking direction, the larger are the deviations from straight lines. That is to say, the larger the internal field in the barrier layer, the larger are the deviations, because they are due to the tunnel effect which becomes remarkable with the intensity of the internal field owing to the increase of the transmission by that effect. Thus the current by the tunnel effect in the blocking direction is larger than the one in the reverse direction and they superpose the currents attributed to the thermoionic effect shown by Eq. (1), making the ratio of rectification worse. Considering that the rectification by the tunnel effect shows the opposite direction to the one by the thermoionic effect, we can easily understand the above facts.

The rectification current by the tunnel effect is shown as(5)

$$i=\frac{4\pi mk^2T^2}{h^3}pe^{-\frac{E_0}{kT}}\left(e^{\frac{eV}{kT}}-1\right) \qquad \text{(2)}$$

Here p is the transmission coefficient through the barrier layer. As the direction of the tunnel effect rectification is reverse to the one of the rectification shown by Eq. (1), we must notice that i in Eq. (2) takes a plus sign for a minus sign of V. At $V=0$, i in Eq. (1) and Eq. (2) vary with $\exp(-V_0/kT)$ and $\exp(-E_0/kT)$ respectively. V_0 is obtained as 0.65 V from the slope of the curve extraporated to $V=0$ at high temperatures in Fig. 3 and E_0 as 0.072 eV from the relation between the spreading resistance R_s and $1/T$ shown in Fig. 4. R_s can be obtained from the constant part of the differential resistance in the forward direction. Thus the current by the tunnel effect will overcome the current by the thermoionic effect at lower temperatures and *vice versa* at higher temperatures.

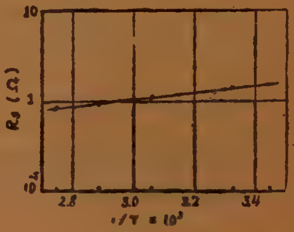

Fig. 4. The sapreading resistance *vs.* 1/T curve.

§ 4. The Temperature Variation of the Rectification after the Formation.

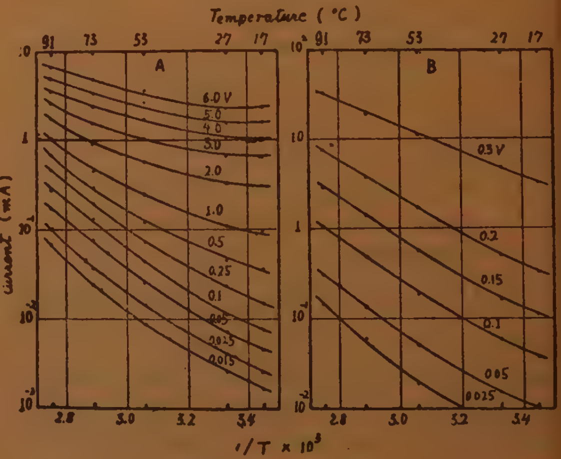

Fig. 5. The current *vs.* 1/T curves after the electric formation.
A: for hard flow.
B: for easy flow.

Fig. 5 shows the D. C. characteristics of the sample which have suffered the electric formation. It is the same sample as the one of which the characteristics before the formation are shown in Fig. 3. Conspicuous points which these figures show are that the deviations of curves log i *vs.* $1/T$ from straight lines are very small even at low temperatures, and the difference between the currents before and after the formation is large at high voltages in the blocking direction even though at high temperatures. We can conclude from these points that the formation diminishes the current by the tunnel effect by some way. The curves at small voltage after the formation approach to the one shown by Eq. (1) in the temperature range down to 40°C. We must notice the tunnel effect occuring at high voltages in the blocking direction even at 90°C.

The method of the electric formation mentioned in § 2. is not sufficient to make the tunnel effect disappear completely, because the curve log *i vs.* 1/T does not shift to a perfect straight line. So then it is important to study on the electric formation in detail in order to avoid the existence of the current by the tunnel effect which makes the characteristics of the rectifier bad.

§ 5. The Non-Uniform Structure of the Barrier Layer.

As the above mentioned, the current by the tunnel effect is important in discussing the selenium rectifier and then we must decide whether it flows through the whole area of the barrier layer, that is to say, through the upper thin part of the whole potential barrier; or it flows through only the local spots where the barrier layer is thin.

To study on this problem, the author makes a sample which has a thin cadmium front electrode by vacuum evaportation on the surface of selenium semiconductor and adds it a electric formation. The cadmium films is so thin that any changes at the contact between the cadmium electrode and selenium semiconductor are able to be observed through the electrode from the outside. The results are as follows. There appear many colored spots on the surface of the sample as Fig. 6 shows, at which spots heavy currents flow by high inverse voltages, making some chemical reactions occur. Thus the author would point out that there were many local spots of small area through which the currents flowed for the most part by the tunnel effect owing to their thin barrier layers.

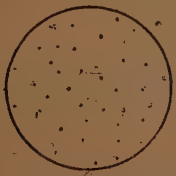

Fig. 6. Appearance of the local spots on the Cd-Se contact by the electric formation.

That the contact potential V_0 before and after the formation are just equal as known from Fig. 3 and Fig. 5 is consistent with the above suggestion. If the tunnel effect occurs at the whole area of the barrier layer, the decrease of the current by the formation must be due to growth of the upper part of the potential barrier any way which makes the contact potential higher. So it can be concluded that the tunnel effect occurs only at the local spots and perhaps the decrease of the current will be due to diminution of the area of the local spots by the formation. This diminution cannot influence the contact potential and the thickness of the barrier layer on the whole, resulting in no alteration of the flows at high temperatures excepting the region of high inverse voltages. From the fact that the easy flow at high voltage and high temperature changes only a little by the formation, it is supposed that the effective total area of the spots is much smaller than the whole area of the barrier layer (compare Fig. 3 and Fig. 5). Because the easy flow acts on the pure thermoionic effect at high voltage and high temperature, and the currents flow through the whole area of the barrier layer, while they flow through only the local spots in the fairly main part at very low temperatures. The author will report on this problem in the next report. So it can be concluded clearly that the diminution of the total area of the local spots is so small that we can observe no alteration of the easy flow at the above conditions. Then considering that the diminished part of the area of the spots can be estimated in the order of fraction to the total area of the spots before the formation from the amount of derease of the curcent, the total area of the spots itself is much smaller than the whole area of the barrier layer.

Concering with these problems the author presents a suggestion that the Joule's heat produced by heavy currents through the local spots by the formation may melt the selenium semiconductor there, changing it to another modification which is an insulator and diminishing the effective area of the spots through which currents can flow.

Above discusssion points out the non-uniform nature of the barrier layer concerning with the local spots where the barrier layer is thin. Jearian(6) has suggested another non-uniform nature of the barrier layer on the silicon and germanium detector; that is, on account of the distribution of the contact potential, the experimental value of e/kT obtained by an analysis of the curve according to Eq. (1) is found smaller than the theoretical one.

We can show the forward characteristic as the next form.

$$i = A(e^{\frac{e}{kT}(V_a - iR_s)} - 1) \quad \ldots\ldots\ldots\ldots (3)$$

Here V_a is the applied voltage through the total rectifier, R_s the spreading resistane and A a constant. By plotting $\log(i+A)$ *versus* $V_a - iR_s$, and determing A and R_s by trial to produce a straight line of intercept A, we can analize the data and obtain the slope e/kT of the line.

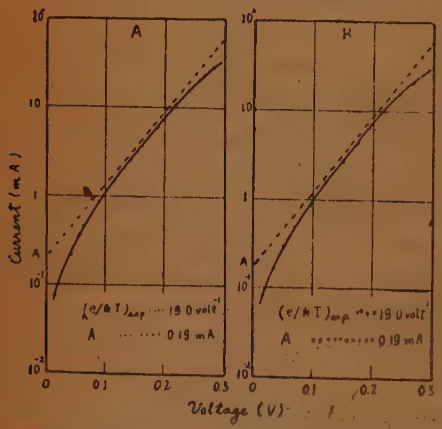

Fig. 7. The current *vs.* voltage curves.
A : before the electric formation
B : after the electric formation

(See Fig. 7.) The curves at low temperatures are not sufficient for analysis on account of the existence of the tunnel effect, so the author will take up only the data at 90°C. The slopes of the curves before and after the formation are closely equal and both values are 19.0 volt^{-1} against the theoretical value 31.8 volt^{-1}. Thus we can find the non-uniformity of the contact potential with the selenium rectifier also. Then heavy currents will flow through points of low contact potential by the formation, occurring some reaction and diminishing the effective area at these points. Diminishing of the area of the points of low contact potential will make the slope of the straight line steeper. But the experiment shows a contray result on account of which we may conclude that the formation does not take place at the points of low contact potential, but only the points with thin barrier layer. At the same time, A is also kept constant in spite of the formation, so the thickness and effective area of the barrier layer does not change in the least. From this it is known that the barrier layer on the whole suffers no reactions by the formation.

§ 6. Conclusion.

The author finds the current by the tunnel effect superposed on the current of the Mott's type by measuring the dependence of the rectification charactersistics of the selenium rectifier on the temperature. And the former current flows through only local spots at which the barrier layer is thin.

Next the electric formation is decided as process of diminishing the effective area of the spots, making the current by the tunnel effect smaller and the characteristics of the rectification better.

And two types of the non-uniform nature of the rectifier are pointed out: the existence of local spots where the barrier layer is thin and the distribution of the contact potential. The one which is improved by the electric formation is the former type.

The author thanks Dr. A. Kobayashi for his kind encouragement in the course of this research.

References.

(1) M. Tomura: Bull. Chem. Soc. Jap., **22** (1949), 82.
(2) M. Tomura: Tsushin Kogyo (in Japanese), **2** (1946), 20.
(3) N. F. Mott: Proc. Roy. Soc. A, **171** (1939), 27.

(4) A. Kobayashi: J. Phys. Soc. Jap., **3** (1949), 41.
(5) e. g. R. H. Fowler: "Statistical Mechanics" 2nd Ed., 432, Cambridge Univ. Press, (1936).
(6) e. g. H. C. Torrey and C. A. Whitmer: "Crystal Rectifier", 83 McGraw-Hill Press, (1948).

D. C. Resistance of Barium Titanate and Its Solid Solutions Ceramics.

By Shoichiro NOMURA and Shozo SAWADA.

Institute of Science and Technology, University of Tokyo.

(Received Nov. 22, 1949)

§ 1. Introduction.

Although the physical and chemical properties of barium titanate have been observed experimentally by many investigators, any detailed measurement of D.C. resistance has not been attempted.

D. C. Swanson⁽¹⁾ reported that the D.C. specific resistance of barium titanate was varied widely from 10^6 to 10^{15} ohm·cm. Further, T. Ogawa⁽²⁾ measured the temperature-dependnecy of D.C. resistance in air and observed an anomaly at the Curie point. We have measured the voltage-and temperature-dependencies of the D. C. resistance of barium titanate, barium·strontium titanate and barium·lead titanates ceramics from room temperature to about 150° C. in vacuum in order to avoid moisture. For the temperature dependency of resistance of barium titanate ceramics, we have already reported briefly⁽³⁾. It is very difficult to measure the true D. C. resistance without influence of absorption current, because its magnitude and relaxation time are very large in comparison with those of non-ferroelectric substances which have no domain structure.

The temperature dependency of D. C. resistance resembles to that of semi-conductors, and we can easily find the activation energy above and below the Curie temperatue. On the standpoint of investigating the essential properties of barium titanate, however, the measurements of resistance are not so powerfull, but for solid solutions, namely, barium strontium-and barium lead-titanates, it is quite interesting, for elucidating the atomic structure and, further, for various applications, to observe the variation with temperature and composition of specific resestance and activation energy.

§ 2. Preparation of Samples and Experimental Method.

After preparing barium-, strontinm-and lead-titanates ceramics separately by the usual method, we smashed them into powders, whose sizes were smaller than 150 meshes. Then they were mixed together with distilled water at the required molar ratio, and when nearly dry up, they were pressed into small disks, which were fired, in a gas furnace, at temperatures of 1300°C. to 1450°C. for 3 to 4 hours. After firing, a disk was remaked into a sheet, which was about 1 mm. to 0.5 mm. thickness and 1 cm², area. Electrodes of fired on silver paste were applied. Fig. 1 shows the apparatus of

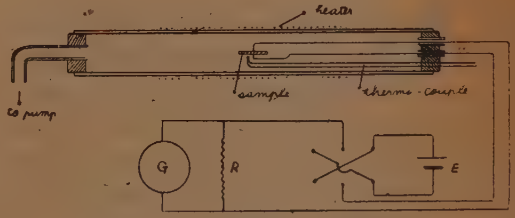

Fig. 1.

measurement of D. C. resistance, where *G* is a galvanometer, *R* a shunt resistance, and *S* a sample placed in a vacuum electric furnace ($10^{-1}\sim 10^{-2}$ mm. Hg). Fused quartz was used at contact points between lead-wires and other parts to remove electric leakage, since its influence is very large in this case, and there was no discernible deflection at 1 m. scale distance when the circuit was opened near the sample.

Strictly speaking, D. C. resistance must be measured in the state in which the so-called absorption current is excluded. As a matter of fact, however, it is nearly impossible to do so for this substance. We shall perhaps be able to get better result, in principle, if a measurement is performed at a very later time after switching in. It, however, increases external disturbances in the measuring apparatus; zero-point fluctuation of galvanometer and unnecessary changes in quality of the samples.

Furthermore, when temperature rises beyond room temperature, needless currents flow the circuit, owing to a thermo-electromotive force.

In order to remove the influence of the undesirable currents stated above and zero-point deflection, our observations were made alternatively for opposite directions of the impressed e. m. f., always at about ten minutes later after switching in and these two groups of observed values were graphically averaged.

§ 3. Absorption Current and Ohmic Law.

Fig. 2 (a) and (b) show the behaviour of D. C. current after switching in. The ordinate in logarithmic scale represents the ratio of transient current to ten minutes later current which is nearly stationary. We can separate this into two parts before and after one minute. The former depends sensiblly upon the circuit constants of galvanometer, while the latter does not. It is the reason why (a) and (b) are different, these being measured with different galvanometere. The latter is likely to follow the well-known law of At^{-n}, where *A* and *n* are constants. Therefore, we can write as

$$i(t) = i_{stationary} + Bt^{-n}, \tag{1}$$

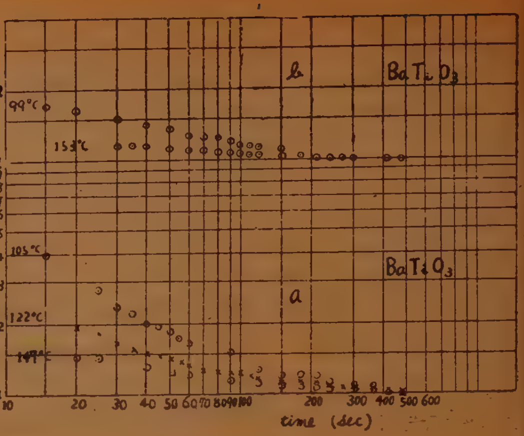

Fig. 2.

where we may suppose that *B* and *n* are the constants dependent upon temperature. As seen from Fig. 2, *B* seems to vary slightly with temperature.

The voltage-dependency of conductance is given in Fig. 3*, which shows the ohmic law except for the cases (*c*) and (*d*), in which the deviation may perhaps be caused by appreciable temperature rise by conduction current, while the other reasons, for instance, the translation of twin boundaries, might be considered. It, however, is not important for our purpose because ceramics are perhaps composed of a great number of very small domains.

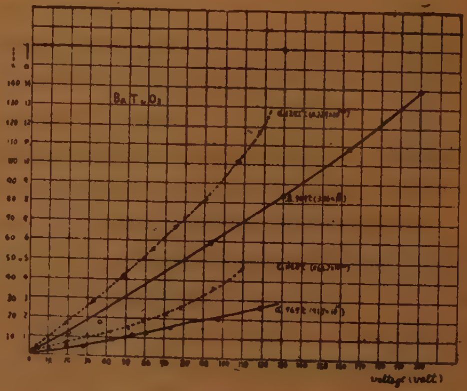

F;g. 3.

From the above state of affairs we can hardly assert that our measurements are free from absorption phonemena since most absorption currents are apt to be proportional to applied voltage.

---

* The ordinate shows $i_{stationary}$ in an arbitrary scale and the values in parentheses the specific resistance in ohm·cm. at each temperature respectively.

§ 4. Temperature Dependencies.

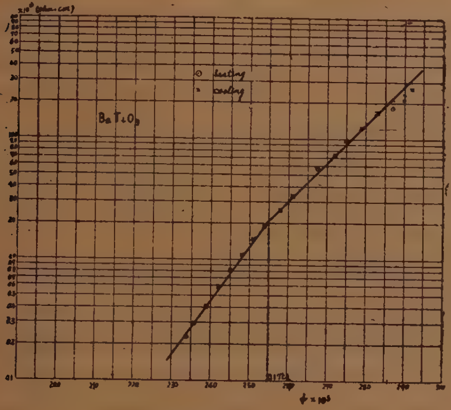

Fig. 4 (a).

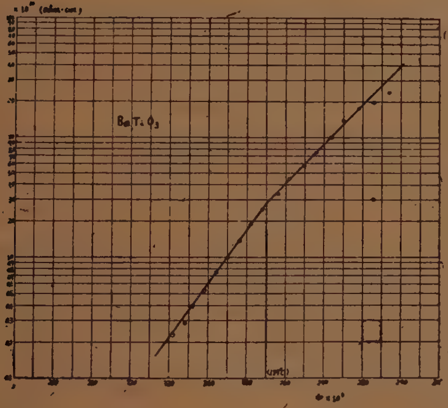

Fig. 4 (b).

Fig. 4 (a) and (b) show the temperature dependencies of the resistivity of pure barium titanate ceramics (Curie-point 117°C.) from room temperature to 150°C., in which increasing and decreasing time rates of temperature are 0.7°C./sec. and 0.3°C./sec. respectively. The obseved behaviours of $\rho(T)$ in Fig. 4 may be represented by the following empirical formula,

$$\rho = Ke^{\frac{\phi}{KT}}, \quad \begin{cases} \phi = \phi_e & T < Tc \\ \phi = \phi_h & T > Tc, \end{cases} \qquad (2)$$

where K is a constant and ϕ_h, ϕ_e are the activation energies above and below the Curie temperature respectively. The values of the two cases of increasing and decreasing temperature are consistent with each other within experimental error. The activation energies estimated from the observed data in Fig. 4 are

$$\begin{array}{lll} & \text{(a)} & \text{(b)} \\ \phi_h & 0.89\ \text{e. v.} & 0.89\ \text{e. v.} \\ \phi_e & 0.62\ \text{e. v.} & 0.65\ \text{e. v.} \end{array} \qquad (3)$$

The activation energy of (a) is seen a little smaller than that of (b). This is because the time rate of increase in temperature is different in both cases and the time interval from switching in to observation is smaller for (a) than for (b). But the difference of activation energy is far small than that of both time rates, which fact seems to show that the value of ϕ obtained above is not meaningless.

Figs. 5 and 6 are the observed data of barium-strontium (90–10)-and barium-lead (90–10)-titanates. In these cases also the sormula (2) is satisfied, Curie point being lower for the former and higher for the latter than that of pure barium titanate.

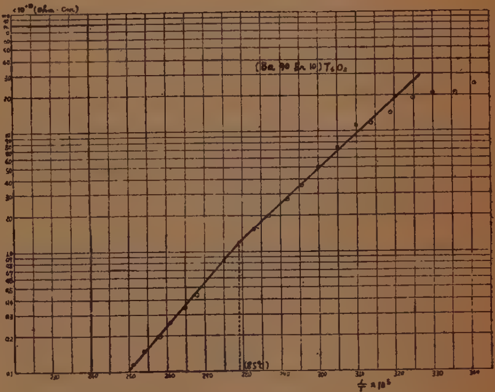

Fig. 5.

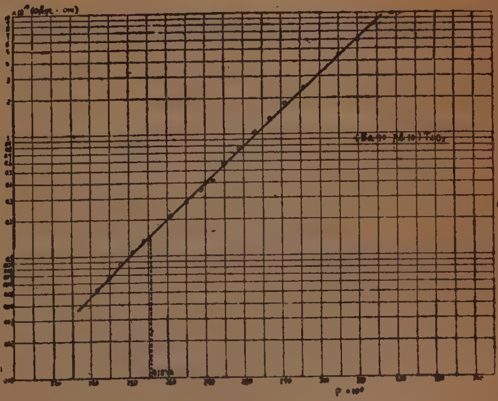

Fig. 6.

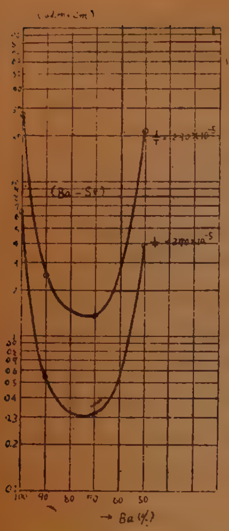

Fig. 7.

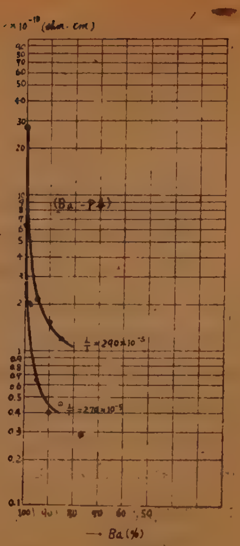

Fig. 8.

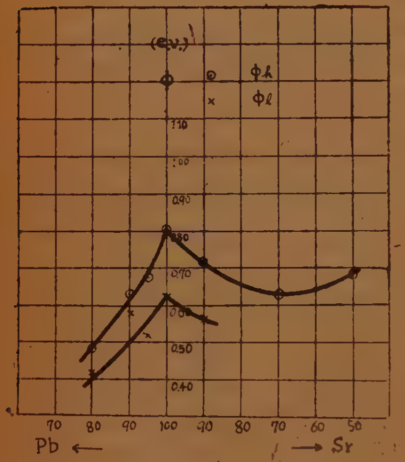

Fig. 9.

Figs. 7 and 8 show the variation with molar ratio of mixture of the resistance for barium-strontium-and barium-lead-titanate respectively at two temperatures*. How the activation energy varies with molar is shown in Fig. 9. ϕ_e of barium-strontium titanaie cannot be measured because of the descent of Curie point below the room temperature**.

§ 5. Discussion.

As we noticed repeatedly, it seems to be very complicated to measure the D.C. resistance of barium titanate groups, especially in ceramic state, because of their ferroelectric characters. On neglecting ferroelectric phenomena such as immigration of domain boundaries by the field, we are forced to take into account very large absorption current, since the dielectric constant of a-axis is larger than that of c-axis. We, however, may suppose that the obtained results are reliable values of D. C. resistance, especially regarding activation energy.

It is reasonable that the activation energy is of the order of 0.6 e. v., being intermediate between those of electronic and ionic conductions, which fact may be supposed to be useful data for our understanding of the electronic structure of the mentioned substance. We are not allowed to discuss in detail the variations with molar ratio of activation energies and resistivity, without considering that optimum sintering temperature of ceramics varies with composition, but in our experimental condition lattice deformation or irregularity may be possible reasons for such variation. The reappearance of increase of the resistivity of barium strontium (50—50) titanate may be said to correspond to a sort of lattice-ordering, if we suppose for the current to be mainly of ionic type.

The authors wish to express their hearty thank to Prof T. Muto for his kind criticism and advice.

References

(1) D. C. Swanson: Phys. Rev., **69** (1946), 546.
(2) T. Ogawa: Busseiron Kenkyu, No. 6 (1947), 1.
(3) S. Sawada, G. Shirane and S. Nomura: Oyobutsuri, **18** (1949), 85.

---

* The pure barium titanate of these samples is not the same as that in Figs. 2 and 4, but is the same one in Fig. 5.

** The Curie points of lead series are a little low perhaps because of impurities.

Specific Heat and Thermal Expansion of Barium-Strontium Titanate Ceramics.

By Shozo SAWADA and Shoichiro NOMURA.

Instiute of Science and Technology, University of Tokyo.

(Received Nov. 22, 1949)

§ 1. Introduction.

Barium-and strontium-titanates ceramics have been reported to form solid solutions for the whole range of concentration of component molecules and, for the molecular concentrations of $10 \sim 20\%$ strontium titanate, their permittivity has been observed to become 10^4 or more(1),(2),(3). The mentioned results seem to be quite reasonable in view of the fact the ionic radius of strontium is only a little smaller than that of barium, although the detailed properties of such ceramics are not to be discussed without consideration of the sintering con ditions i. e., firing temperature or firing time. Owing to the lack of detailed knowledge about the physical properties of the interesting solid solutions mentioned above, we have been working experimentally the investigations of the variation with molecular concentration of the permittivity, the specific heat and the thermal expansion of such materials.

Now, since a maximum of the permittivity seems to appear in the neighbourhood of 85% barium titanate, we have observed experimentally the specific heat and the thermal expansion of the sample containing 90% barium titanate with the expectation that some exaggerated anamalies might be observed if the ferro-electricity is exalted for this solid solution than for pure barium titanate.

§ 2. Preparation of Sample.

Barium-and strotium-titanates ceramics were prepared separately by the usual method, firing temperature being about 1250°C. These ceramics were pulverized and next were mixed in the concentration of 90% $BaTiO_3$ and 10% $SrTiO_3$, which mixture was re-fired at about 1400°C. Chemical analysis has not yet been performed. So the true composition of the sample may be different from the above value.

The experimental methods and apparatus for measuring the specific heat and themal expansion were described in detail in our papers regarding pure barium titanate(4). In addition, we measured the permittivity and loss factor by the usual resonance method.

§ 3. Results of Observations.

Fig. 1 shows the temperature variations of ε', ε'' and loss factor tan δ, where ε', and ε'' are the real and imaginary parts of permittivity. Figs.

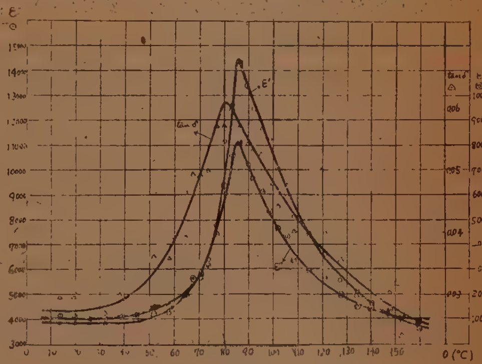

Fig. 1.

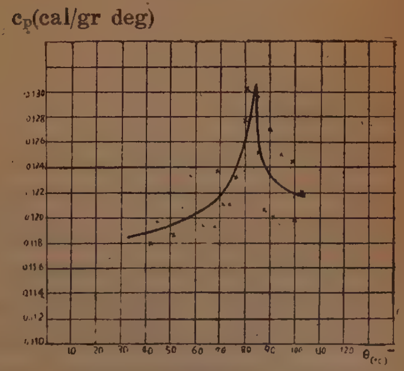

Fig. 2.

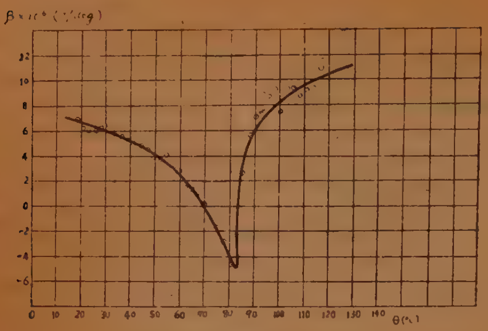

Fig. 3.

2 and 3 show the specific heat C_p and thermal expansion β respectively. As seen in Figures, the Curie temperatures of ε', ε'' tan δ, C_p and β are found to lie at 85.5°C, 86°C, 81°C, and 84°C. respectively, where that of β is defined as a temperature of maximum contraction.

The value of normal specific heat and the amount of anomaly at the Curie temperature are nearly equal to those of pure barium tetanate. The value of normal thermal expansion is a little larger than that of pure barium titanate and the amount of anomaly at the Curie temperature is about three times larger.

§4. Discussion.

The amount of anomaly of thermal expansion at the Curie temperature is large as expected, but that of specific heat is not. It might be said that the exaltation of ferro-electricity in this solid solution, which itself is not undoubtful, increases the anomaly of thermal expansion but not that of specific heat. But we can not derive any conclusion without more thorough investigations, as the observation of specific heat of svch insulating substances is especially difficult.

The study of variation of specific heat and thermal expansion with respect to the whole range of molecular concentration is very desirable, though it would be considerablly laborious.

The authors wish to express their sincere thank to Prof. T. Muto for his kind criticism and advice.

Reserences.

(1) S. Roberts: Phys. Rev., **71** (1947), 890.
(2) B. Matthias and A. von Hippel: Phys. Rev., **73** (1948), 1261.
(3) J. G. Powless, Nature, **161** (1948), 655.
(4) S. Sawada and G. Shirane and H. Sugawara: Phys. Soc. Jap., **2** (1947), 90.
S. Sawada and G. Shirane: Phys. Soc. Jap., **4** (1949), 52.

Statistical Thermodyamics of Multimolecular Adsorption. I.

By Syû Ono.

Institute of Applied Science, Faculty of Engineering, Kyushu University.

(Received Nov. 28, 1949).

§1. Introduction.

Recently the author(1) has deduced the difference equation which determines the change in the structure and composition at the surface layer between the liquid and vapor phase, and has shown that the surface is a layer of several molecules thick, by making use of the hole theory of liquid(1)(2). And he applied this theory to the adsorption at the interface between two regular solutions(3) and also to the adsorption on a solid wall in contact with a regular solution(4). In the present paper we shall apply this statistical method to the adsorption on a solid wall from gases. And the hole theory of liquid proposed in the previous paper(1)(3) in which the change of the free volume of the molecule with relative concentration of molecules and holes is approximately taken into account, is applied, too.

§ 2. Bragg-Williams Approximation to the Hole Theory.

Let us divide a whole space inside the container into L cells having the equal volume and the same shape, L being larger than the number of molecules N. And we assume that the centers of these cells constitute the lattice points in a face-centered cubic array. Suppose the cell occupied by the ith molecule is surrounded by $w_i Z$ vacant cells and $(1-w_i)Z$ occupied ones, Z beging the number of the nearest neighbors; $Z=12$ for the face-centered cubic lattice. If these molecules are situated at the centers of their own cells, the potential energy of the ith molecule is expressed by $(1-w_i)Z\varepsilon$, where ε denotes the potential energy of a pair molecules at the centers of two nearest neighbor-cells. The interactions between the molecules which are not in the adjacent cells are neglected; this is valid when the force between molecules decreases as rapidly as the van der Waals attraction.

Let us denote by u_i the potential energy of the ith molecule. Here we shall use the value of the potential energy of the molecules surrounded by the neighboring molecules at the centers of their own cells as the approximated value of u_i so that we may assume that this potential energy depends only on the positional coordinates of ith molecule and w_i; that is $u_i = u(x_i, y_i, z_i; w_i)$. Then the partition function for the ith molecule is

$$q(w_i) = \int_\tau \exp\left[-\frac{u(x_i, y_i, z_i; w_i)-(1-w_i)Z\varepsilon}{kT}\right] dv_i, \tag{1}$$

where dv_i is the volume element of the ith molecule and the integration extends over the cell. And the partition function $Q(\mathbf{s})$ appropriate to the given configuration $\mathbf{s}$ can be written in the from

$$Q(\mathbf{s}) = \phi^N \prod_{i=1}^{N} q(w_i), \tag{2}$$

where ϕ is $(2\pi mkT)^{3/2} j(T)/h^3$, $j(T)$ being the partition function for the internal degrees of freedom of a molecule. When each molecule rests at the center of its cell, the potential energy of the system is

$$E(\mathbf{s}) = \frac{(N-X)Z\varepsilon}{2}, \tag{3}$$

where X is defined by

$$X = \sum_{i=1}^{N} w_i. \tag{4}$$

Neglecting the configuration in which two or more molecules occupy a single cell, we may express the partition function of the syetem in the from

$$f(T) = \sum_{\mathbf{s}} \exp\left(-\frac{E(\mathbf{s})}{kT}\right) Q(\mathbf{s}), \tag{5}$$

where the sum extends over all configurations, $\mathbf{s}$, of the system, the word "configuration" being employed in a special sense here to desigate a specific distribution of the N molecules among L cells.

In order to make further progress it is necessary to know $q(w)$ as a function of w. It is obvious that $q(1) = \tau$, being the volume of a cell, because the integrand in (1) is unity if $w=1$. And we denote $q(0)=\omega$. ω can be calculated from the interatomic potential function, by making use of the cage model of liquid⁽²⁾. Generally, ω may be a function of T. For an intermediate value of w, $q(w)$ is approximately interpolated in the way adopted in the previous papers⁽¹⁾⁽²⁾:

$$q(w) = \omega^{1-w}\tau^{w}. \tag{6}$$

If we substitute (2) and (3) into (5) we have according to (4) and (6)

$$f(T) = \left\{\exp\left(-\frac{Z\varepsilon}{kT}\right)\phi\omega\right\}^N \sum_X g(N, X)\eta^X, \tag{7}$$

where

$$\eta = \exp\left(-\frac{\zeta}{kT}\right), \tag{8}$$

and

$$2\zeta = -\varepsilon - 2kT \ln\frac{\tau}{\omega}, \tag{9}$$

$g(N, X)$ being the number of the distinguishable arrangement of N molecules in L cells with the specified value of X. And here we have the relation

$$\sum g(N, X) = \frac{N!(L-N)!}{L!}. \tag{10}$$

Denoting the average value of X in the canonical ensemble by $\bar{X}$, it is expressed in the form

$$X=\eta\frac{\partial\ln f(T)}{\partial\eta}. \tag{11}$$

And from this and the relation between the partition function and the Helmholtz free energy F, we obtain

$$F=-kT\ln f(T)=-kT\int^{\eta}X\frac{d\eta}{\eta}. \tag{12}$$

Here we assume that the mixing of molecules and holes is completely random. Then out of Z neighbors of any cell, on the average Zx will be occupied, $Z(1-x)$ unoccupied, x being the relative concentration of melecules, N/L. Since ZX is the total number of pairs of cells, of which the one is occupied and the other is unoccupied, we have

$$X=Lx(1-x) \tag{13}$$

which is independent of η. (13) is characteristic for the Bragg-Williams approximation. Substituting (13) into (12) we obtain

$$F=L\zeta x(1-x)+\frac{NZ\varepsilon}{2}+NkT\ln\phi\omega$$

$$+LkT\{x\ln x+(1-x)\ln(1-x)\}, \tag{14}$$

where the constant of integration is determined by (7) and (10), Stirling's formula being used. Then the equation of states is given by

$$p=-\frac{NkT}{Vx}\Big(\ln(1-z)+\frac{x^2\varsigma}{kT}\Big\}, \tag{15}$$

where the relation between the concentration x and the volume V is expressed by $Vx=N\tau$. The equations which determine x_G and x_L, the values of x in the vapor and liquid phases respectively, become

$$\frac{\varsigma}{kT}(2x_G-1)=\ln\frac{x_G}{1-x_G} \tag{16}$$

$$x_G+x_L=1. \tag{17}$$

It will be seen from the above derivation that this hole model is applicable to the vapor phase. And we can prove that the free energy (14) becomes identical with that of the perfact gas in the limit of increasing volume.

§ 3. Statistical Mechanics of the System Contacting with an Adsorbing Wall

We shall extend the treatment shown in the preceding section to the case of the inhomogeneous system. In reality, the concentration near the wall may vary with the distance from the wall. The theory for the inhomogeneous regular solution has been shown in the peceding papers⁽³⁾⁽⁴⁾.

Let us consider the system surrounded by two horizontal plane walls mutually parallel and by a vertical cylindrical wall. And we shall investigate the change in the concentration near one of the plane walls. We shall assume that [100] planes of the face-centered cubic lattice are placed parallel to the plane walls for the sake of convenience. And we refer to these parallel planes as equipotential layers or briefly layers; then we number them from 1 to m. In the present case, each layer has equal number of cells in it. We denote by n_r the number of moleculecules in the rth layer; they satisfy the following relation:

$$\sum_{r=1}^{m}n_r=N, \tag{18}$$

N being the total number of molecules.

The number of neighboring cells of molecules is ZN in all, out of which ZX neighbors are vacant and $n_1Z/3$ are the wall molecules, if we neglect the effect of the other walls than the one contacts with the first layer. In this point, the author takes a different aspect from that of Guggenheim⁽⁵⁾. Then the number of pairs both occupied is $(N-X-n_1/3)Z/2$. Hence the static energy of the system in a given configuration s is expressed by

$$E_s(s)=\frac{(3N-3X-n_1)Z\varepsilon}{6}+\frac{Zu_1}{3}\varphi. \tag{19}$$

as with (4), where φ stands for the interaction between a gas molecule and a wall molecule, the interaction between the wall and a molecule in higher layer being neglected. This neglection will be valid if the intermolcular potential between a gas molecule and a wall molecule decreases as rapidly as one between the gas molecules.

Then the partition function for the molecule in the first layer if surround by wZ vacant cells will be approximately exprssed by

$$q(w) = \omega^{\frac{2}{3}-w}\tau^{w}\beta^{\frac{1}{3}}, \tag{20}$$

β being the factor due to the effect of the wall. For the molecules in higher layers, we adopt (7) as before. (2) is applicable also to the inhomogeneous systems, and substitution of (2) and (7) into (3) leads to

$$Q(s) = (\phi\omega)^{N}\left(\frac{\tau}{\omega}\right)^{X}\left(\frac{\beta}{\omega}\right)^{\frac{Zn_1}{3}}. \tag{21}$$

According to (19) and (21) the partition function for the system, which is expressed by (6), can be written in the form

$$f_i(T) = \left\{\phi\omega \exp\left(-\frac{Z\varepsilon}{2kT}\right)\right\}^{N} \sum_{n_1 n_2 \cdots n_m} J(n_1, u_2, \ldots, u_m), \tag{22}$$

with

$$\lambda = \frac{1}{3}Z\left(\varphi - \frac{\varepsilon}{2} + kT\ln\frac{\omega}{\beta}\right), \tag{23}$$

$$J(n_1, n_2, \ldots, n_m) = \exp\left(\frac{n_1\lambda}{kT}\right)\sum_{X} g(n_1, n_2, \ldots, n_m, X)\exp\left(-\frac{X\varsigma}{kT}\right), \tag{24}$$

where $g(n_1, n_2, \ldots, n_m, X)$ is the number of configurations with specified values of X, and n_1, $n_2, \ldots, n_m$. Here we have

$$\sum_{X} g(n_1, n_2, \ldots, n_m, X) = \prod_{r=1}^{m} \frac{n_r!(n-n_r)!}{n!}, \tag{25}$$

n being the number of the cells in each layer. As usual, it would be sufficiently accurate to replace the series (22) by its maximum term(6), and it follows that

$$f_i(T) = \left\{\phi\omega \exp\left(-\frac{Z\varepsilon}{ekT}\right)\right\}^{N} J(n_1^*, n_2^*, \ldots, n_m^*), \tag{26}$$

where $n_1^*, n_2^*, \ldots, n_m^*$ are the value of $n_1, n_2, \ldots, n_m$ which maximize $J(n_1, n_2, \ldots, n_m)$ consistent with the condition (18). We can determine these values by

$$\frac{\partial \ln J(n_1^*, n_2^*, \ldots n_m^*)}{\partial n_r^*} = -\frac{\mu^*}{kT} \tag{27}$$

and (18), μ^* being undetermined multiplier. As with (11) the mean value of X in canonical ensemble is given by

$$X = \eta\frac{\partial \ln f(T)}{\partial\eta} \tag{28}$$

η being defined by (8). From (26) and (28), we have

$$\ln J(n_1^*, n_2^*, \ldots, n_m^*) = \int^{\eta} X\frac{d\eta}{\eta}. \tag{29}$$

Since n_r^* is nearly equal to the mean value of n_r, the mean value of the number of the pairs of cells, of which the one is occupied in the $r+1$th layer and the other is unoccupied in the rth layer, will be $Z(1-n_r^*)n^*_{r+1}/3n$, if the mixing in each layer is completely random as in the Bragg-Williams approximation; and since ZX is the sum of these numbers, we obtain, taking into account the effect of the wall,

$$\begin{aligned} X = \frac{n}{6}[\{&2x_1(1-x_1)+x_2(1-x_1) \\ &+x_1(1-x_2)\}+\textstyle\sum 2x_r(1-x_r)+x_r(1-x_{r-1}) \\ &+x_{r-1}(1-x_r)+x_r(1-x_{r+1})+x_{r+1}(1-x_r)\}], \end{aligned} \tag{30}$$

where x_r is the average concentration of molecules in the rth layer defined by $x_r = n_r^*/n$, the effect of the other walls being neglected for the sake of simplicity. Substituting (30) into (29), we obtain, as with (14),

$$\begin{aligned} \ln J(x_1, x_2, \ldots, x_m) = -n\Big[&\frac{\varsigma}{kT}\{2x_1(1-x_1)+x_2(1-x_1) \\ &+x_2(1-x_1)\}+x_1\ln x_1+(1-x_1)\ln(1-x_1)\Big] \\ -n\sum_{r=2}^{m}\Big[&\frac{\varsigma}{6kT}\{2x_r(1-x_r)+x_r(1-x_{r-1})+x_{r-1}(1-x_r) \\ &+x_r(1-x_{r+1}) \\ &+x_{r+1}(1-x_r)+x_r\ln x_r+(1-x_r)\ln(1-x_r)\}\Big], \end{aligned} \tag{31}$$

the constant of integration being determined from (24) and (25). Substituting (31) into (27), we have

$$\frac{2\zeta}{3}(1-x_1-x_2)-\lambda+kT\ln\frac{1-x_1}{x_1} = \mu^*, \tag{32a}$$

and

$$\frac{\zeta}{3}(3-2x_{r-1}-2x_r-2x_{r+1})+kT\ln\frac{x_r}{1-x_r} = \mu^*. \tag{32b}$$

x_r's approach x_G, the concentration in the gaseous phase, at great distance from the wall, so they satisfy the following relation,

$$\lim_{r\to\infty} x_r = x_G. \tag{33}$$

Then substituting (33) into (32b) we can determine the constant μ^* by

$$\mu^* = \zeta(1-2x_G)+kT\ln\frac{x_G}{1-x_q}. \tag{34}$$

Using the differences

$$\begin{aligned} \Delta x_r &= x_{r+1}-x_r \\ \Delta^2 x_r &= \Delta x_{r+1}-\Delta x_r \end{aligned} \tag{35}$$

and substituting (34) into (32a) and (32b), we obtain

$$\Delta x_1 = \left(3x_G-2x_1-\frac{1}{2}\right) + \frac{3kT}{2\zeta}\left\{\ln\frac{x_1}{1-x_1}-\ln\frac{x_G}{1-x_G}\right\}-\frac{3\zeta}{2\lambda}, \tag{36a}$$

$$\Delta^2 x_{r-1} = 3(x_G-x_r)+\frac{3kT}{2\zeta}\left\{\ln\frac{x_r}{1-x_r}-\ln\frac{x_G}{1-x_G}\right\}. \tag{36b}$$

(36b) is a difference equation.

§ 4. Comparison with Experiment.

The method used in solving the difference equations appeared in the previous papers⑴⑷ is applicable to solve (36b). In the present case Δx_1 and, accordingly x_2 is calculable from x_1 by making use of (36a), if T, ζ and λ are given. And from (36b) we obtain $\Delta^2 x_1$ and Δx_2 and x_3. Repeating these processes we can determine all x_r's. Thus there exists a solution for each value of x_1. We try to calculate the appropriate solutions which obey (33). For the values of x_1 larger than a critical value x_1^* the oscillatory types of solutions are obtained, and for the values smaller than x_1^* the ones decreasing without limit are obtained. Then we see that the solution for this critical value, x_1^*, behaves properly at great distance from the wall as required from (33). Thus we can obtain the solution of (36b) with condition (33) and (36a) by very careful selection of x_1. For some values of x_G, we have three critical values, x_1^*, x_1^{**}, and $x_1^{***}(x_1^* < x_1^{**} < x_1^{***})$. x_1^* and x_1^{***} have the above-mentioned property. On the other hand, the solutions for the values larger than x_1^{**} decrease without limit and the ones for the values smaller than x_1^{**} oscillate.

Let us take $\zeta = 3.210\times10^{-13}$ ergs $\lambda = 3.586\times10^{-13}$ ergs and $T = 284.1$(11°C). These values are estimated from the vapor pressure of carbon tetracholoride at 11°C, and the surface tensions of carbon tetrachloride and mercury, and the interface tension between benzene and mercuy. The interface tension between mercury and benzene which has almost equal values of critical and surface constants is used, because there are no avaliable data for the one between carbon tetrachloride and mercury. Calculated appropriate solutions for $x_1 = 0.00001$; and $x_1 = 0.0003$ are shown in Table I. And we see that the defference of the surface from the bulk is confined to almost unimolecular layer.

Let us consider as the amouut of adsorbed molecules the surface excess amount defined by

$$\Delta n = n\sum_{r=1}^{m}(x_r-x_G). \tag{37}$$

Here we use the quantity x defined by

$$x = \frac{\Delta n}{n} = \sum_{r=1}^{m}(x_r-x_G), \tag{38}$$

Table I.

x_G	x_1	x_2	x_3	x_4
0.00001	0.996	0.002	0.00001	0.00001
0.0003	1.000	0.096	0.0003	0.0003

which becomes unity when only the first layer is completely covered. x_r's can be calculated by means of (36a) and (36b) for the different values of x_G, and p being given by (15) as a function of x_G. Thus we obtain a plot of x against $\log p$ as shown in Fig. 1. This is an adsorption isotherm. Some portions of this isothem intersect a vertical line at three points. But real substance cannot have three values of x. And thermodynamics tells us that the one with the lowest Gibbs free energy will be the stable state. The Helmholtz free energy or the approximated Gibbs free energy can be computed from x_r by means of (26) and (31). In the case where the adsorption occurs, we must take the numbers of the molecules supplied from reservoir into consideration, which is equal to nx. Then the Gibbs free energy of the reservoir decreases $nx\mu$, where μ is the chemical potential. Hence the stable state must have the smallest value of $F-nx\mu$. From (14), (26) and (31) we obtain

$$\begin{aligned} F-nx\mu = &+n\Big[\frac{\zeta}{6kT}\{2x_1(1-x_1)+x_2(1-x_1)+x_1(1-x_2)\} \\ &+x_1\ln x_1+(1-x_1)\ln(1-x_2)-\frac{x_1\lambda}{kT}\Big] \\ &+\frac{n\zeta}{6kT}\sum_{r=1}^{m}\Big[\{2x_r(1-x_r)+x_r(1+x_{r-1})+x_{r-1}(1-x_r) \\ &+x_r(1-x_{r+1})+x_{r+1}(1-x_r)+x_r\ln x_r \\ &+(1-x_r)\ln(x-x_r)\}\Big]+\frac{nx}{kT}\Big\{\varsigma(2x_G-1)-kT\ln\frac{x_G}{1-x_G}\Big\}. \end{aligned} \tag{39}$$

Thus we obtain the corrected curve shown in Fig. 1, in which dotted portions represent unstable phases. The pressure correspoding to the point C is equal to the vapor pressure, and stable gaseous phase cannot exist beyond this point.

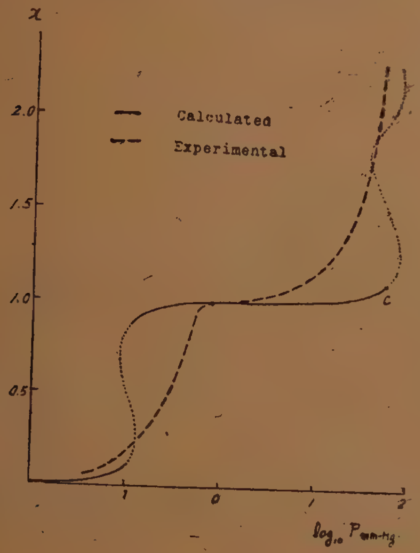

Fig. 1.

From the above calculation and the results obtained in the preceding paper⁽⁴⁾, we can conclude that the adsorption is effectively monomolecular except immediate neighborhood of the condensing point as far as the interactions between the molecules in the second or more distant layer and wall are neglected. The broken curve shown in Fig. 1 is the experimental isotherm of the adsorption from gaseous carbon tetrachloride on mercury surface, in which multimolecular adsorption seems to be fairly effective. This experimental curve has been calculated from Cassel's experiment⁽⁷⁾. We find considerable discrepancy between theory and experiment, especially in high pressure region. This discrepancy may be due to the neglection of the interactions between wall and farther molecules. The theory of multimolecular adsoption taking into account such interaction will appear in near future.

The author wishes to express his thanks to Ass. Prof. Tomoyasu Tanaka of the Faculty of Science of this university for his aid. And he is indebted to Special Research-Committee of Theoretical Physics, National Research Council of Ministry of Education for financial aid.

References.

(1) S. Ono: Mem. Faculty of Engineering, Kyushu Univ. **10** (1947), 195.
(2) T. Sato and S. Ono: J. Phys. Soc. Japan **4** (1949), 103.
(3) S. Ono and M. Kunimune: Busseiron Kenkyu **15** (1949), 15.
(4) S. Ono: Mem. Faculty of Engineering, Kyushu Univ. **12** (1950), 1.
(5) E. A. Guggeheim: Trans. Faraday Sac. **41** (1945), 150.
(6) R. H. Fowler and E. A. Guggenheim: Statistical Thermodynamics, Cambridge, 1939.
(7) H. Cassel: Trans, Faraday Soc. **28** (1932), 177.

Measurement of Thermal Diffusion Ratio by "Bending Balance"

By Kazuhisa MATSUDA and Naoki ONO.

Physics Department, Tokyo Institute of Technology.

(Received Nov. 30, 1949)

§1. Introduction.

The main part of this thermal diffusion apparatus is made of two glass bulbs which are connected with a short glass tube. After introducing the binary mixture of gases into these bulbs, we heat one of the bulbs and cool the other, resulting in the change in the concentrations of the mixture in the two bulbs. This change in concentrations of one component depends on the nature of both components, their mixing ratio and the temperature of the both bulbs. The relation is expressed theoretically by the following formula,⁽¹⁾

$$\Delta C = -k_T \log T_h/T_c$$

where ΔC is the difference of concentrations of one component in the two bulbs, k_T a constant which depends on the nature of the gases and their mixing ratio, the so-called thermal diffusion ratio, and T_h and T_c the absolute temperatures of hot and cold chambers, respectively. Therefore, the measurement of thermal diffusion ratio is reduced to the measurements of three quantities, i.e. ΔC, T_h and T_c. Since ΔC is in general a small quantity, we must use an accurate method for the measurement of ΔC. For this purpose, various methods have been adopted, such as (a) chemical gas analysis, (b) katharometer method⁽²⁾ (measurement of thermal conductivity), (c) stream method (measurement of viscosity), (d) the method using interferometer,⁽³⁾ etc.

In our experiment, we used "bending balance"⁽⁴⁾. As this instrument gives us very accurate data on the specific gravity of gases, we can expect the more direct knowledge concerning the change in concentration than the other methods.

§2. Experimental Method.

The outline of the apparatus is shown in Fig. 1. The gas to be measured is introduced into the glass chamber A and B. A is inserted in a cylindrical electric furnance and used as a hot chamber. B is kept at room temperature or in an ice vessel and used as a cold chamber. After closing the cocks C_1 and C_2, opening the cock C_3, we heat the hot chamber up to the appropriate temperature. These temperatures were measured by using a chromel-alumel thermocouple.

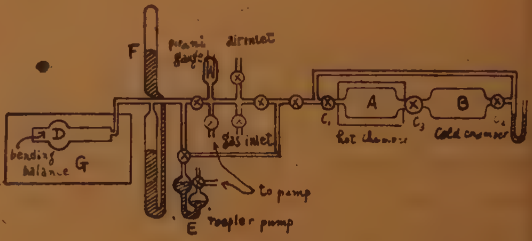

Fig. 1.

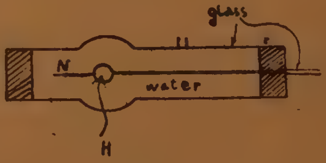

Fig. 2.

We found by several experiments that, in our apparatus the steady states could be reached in five hours or so.

Then, we closed the cock C_3 and opened C_1, and transferred the gas contained in A to the bending balance D by a Töpler pump E. The pressure of the gas in the balance was measured by a manometer F, whose diameter is 30 mm, and a cathetometer which can be read with the accuracy of 1/500 mm. This pressure of the gas was kept at about 30 cm Hg. The balance was kept at constant temperature in the thermostat G.

A measure of the weight of the gas was given by the displacement of the pointing needle of the bending balance (N in Fig. 2), when H, once evacuated, was filled with gas to an appropriate pressure. Similar measurement was performed on the gas contained in B. ΔC was determined from the difference of the specific gravities of the gases in A and B.

§ 3. Results I: Thermal Diffusion Ratio at Various Mixing Ratios.

We performed experiments on the mixtures of hydrogen and nitrogen, and measured the separation caused by thermal diffusion at several mixing ratios from 6.4 percent to 85.0 percent nitrogen. Hydrogen was prepared by the electrolysis of KOH 20 percent aqueous solution. The oxygen, conceivable as the impurity, was combined to water by passing the gas over a red heated platinum wire and then removed by phosphorous pentoxide. Nitrogen used was obtained from a bomb of nitrogen. Impurity oxygen was removed by passing it through a quartz tube containing red heated copper net. By measuring the specific gravities of the prepared gases by the bending balance, we found that the impurities are less than 1 percent in the hydrogen and 0.5 percent in the nitrogen, provided that the impurity was oxygen alone.

Table I.

% of N_2	T_h°C	T_c°C	ΔC %	k_T (obs)	k_T (elastic)	R_T
6.4	200	27	0.94	0.0207	0.0593	0.349
12.3	200	27	2.15	0.0472	0.0970	0.487
15.3	200	28	2.50	0.0556	0.1112	0.500
20.3	200	30	2.91	0.0654	0.129	0.506
25.3	200	30	3.60	0.0809	0.142	0.572
28.7	200	27	3.90	0.0857	0.146	0.585
33.3	200	30	3.75	0.0842	0.151	0.559
34.7	200	29	3.97	0.0884	0.151	0.584
41.6	200	27	4.91	0.0881	0.150	0.586
50.4	200	27	3.49	0.0767	0.141	0.543
68.8	200	27	2.11	0.0464	0.103	0.449
85.0	100	0	0.69	0.0220	0.0551	0.399

The experimental data of ΔC and k_T are shown in Table 1. Fig. 3 shows the result of our experiment with those of Ibbs-Underwood and O. Blüh-G. Blüh, for comparison. The curve 1 in Fig. 3 is the theoretical curve, which was obtained from the Chapman-Enskog's theory of transport phenomena of gases for the molecular model of rigid elastic sphere.

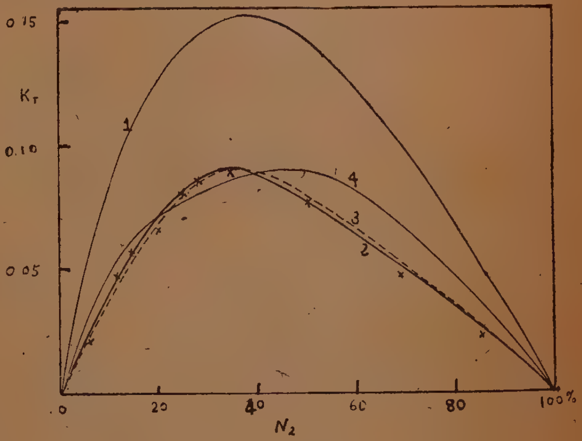

Fig. 3.

curve 1; k_T elastic sphere model
2: k_T our experiment
3: k_T Ibbs and Underwood
4: k_T O. Blüh and G. Blüh

Fig. 4 shows the thermal separation ratio R_T of these experiments and theoretical R_T. R_T is defined by the following formula.

$$R_T = k_T / k_T \text{ (elastic sphere)}$$

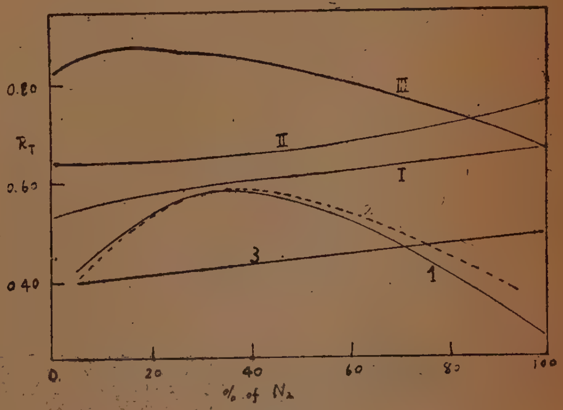

Fig. 4.

curve 1: R_T of ours
2: R_T of Ibbs-Underwood
3: R_T of O. Blüh-G. Blüh
curve I: R_T for $n = 8.2$
II: R_T for $n = 10$
III: R_T for Lennard-Jones Model

§ 4. Results II: Change in Thermal Diffusion Ratio with Temperature.

Next, we measured k_T at four different temperatures and the results are shown in Table II. The difference in k_T were very small and our accuracy was insufficient to deduce any decisive conclusion, but we may say that k_T is constant within the accuracy of our experiment.

Table II

T_c	T_h	% of N_2	ΔC %	k_T
24	100	48.8	1.84	0.0826
24	200	47.0	3.70	0.0820
24	300	48.1	5.65	0.0864
24	400	47.3	6.77	0.0837

§ 5. Theoretical Curves.

In order to know to what extent theory of Chapman-Enskog can explain our results using the accepted values of molecular constants, we calculated the following three curves. If we assume a model that the mutual repulsive force between hydrogen and nitrogen is proportional to the inverse n-th power of their distance, and if we take the index n to be 8.2 and 10, we shall obtain the curve I and II of Fig. 4, respectively, by following the Chapman's method(5) faithfully. Next, if we assume a Lennard-Jones model $-\mu/r^6 + \nu/r^{12}$ and follow the calcuration of Kihara and Kotani,(6) we shall obtain the cure III. As to the constant μ and ν of mutual force between hydrogen and nitrogen, we calculated by Lennard-Jones and Cook's method(7) from the Vershoyle's data of virtial coefficients of this binary mixture, and obtained $\mu = 0.34 \times 10^6$ erg Å and $\mu = 570 \times 10^{12}$ erg Å. In this calculation we assumed that the temperature is 373°K since k_T varies little in our temperature rang.

§ 6. Discussion and Conclusion.

The experimental errors of our experiment are less than 5 percent which are mainly due to the insufficient constancy of the thermostat temperature (±3/1000°C), the effects caused by the fluctuation of the room temperature and the variation of T_h and T_c.

Thus we obtained the following conclusions.

(1) Our results agree with those of Ibbs-Underwood, but not with those of O. Blüh-G. Blüh. So that many experiments with the katharometer by Ibbs and his collaborator may be correct.

(2) The method of bending balance is effective for the analysis of the binary gas mixtures. In order to make more exact experiment, however we must improve the apparatus and reduce the above mentioned errors.

(3) Theoretical calculation does not agree with the experimental curve (Fig. 4). The shape of the curve of R_T based on the Lennard-Jones model is similar to the experimental one, but its absolute value differs considerably. The height of the curves depends largely on the power index of the inverse repulsive force. We can see this by the comparison of the curve I and II in Fig. 4.

The authors are grateful to Dr. Yeiichi Takeda under whose direction this work was carried out, and to Prof. J. Oishi and the members of our department who lent us various equipments and gave us many kind suggestions.

References.

(1) Chapman and Cowling: The mathematical theory of non-uniform gases (1940) p. 252-255.

(2) G.T.L. Ibbs and L. Underwood: Proc. Phys. Soc. **39** (1927) 227 and other Ibbs's reports.

(3) O. Blüh and G. Blüh: Zeits. f. Physik. **90** (1934) 12.
H. G. Dreckman. S. L. Downey and N. C. Pierce: J. Chem. Phys. **17** (1949) 408, etc.

(4) Y. Takeda: Pro. Phys. Math. Soc. Japan **23** (1941) 1920.
Bulletin of Tokio Institute of Technology **13** (1948) 58.

(5) S. Chapman: Proc. Roy. Soc. **A 177** (1940) 38.

(6) T. Kihara and M. Kotani: Proc. Phys. Math. Soc. Japan **25** (1943) 602. The similar method particulary on binary mixtures, has been developed recently. See J.O. Hirschfelder, R. B. Birdand, E. L. Spetz: J. Chem. Phys. **44** (1948) 968 Chem. Rev. **44** (1949) 205.

(7) Lennard-Jones and Cook: Proc. Roy. Soc. **A 115** (1929) 4.

(8) Vershoyle: Proc. Roy. Soc. **A 111** (1926) 552.

The Time in which Equilibrium State of Audition is Established.
Part 3. A New Method of Measuring the Damping Constant of the Mechanical Systems of the Ear.

By Yasuo MAKITA* and Shin-ya MIYATANI†.

* *The Research Institute of Acoustical Science, University of Osaka.*
† *The Research Institute of Science and Technology, University of Tokyo.*

(Received Dec. 10, 1949)

§ 1. Introduction.

In the previous papers(1)·(2), the damping constant of the mechanical systems of the inner ear was calculated by assuming the distribution pattern of stimulus along the basilar membrane and the time constant of auditory stimulation was inquired. The time constant of auditory stimulation which was obtained by measuring the time in which the equilibrium state of audition was established, was effected by both the mechanical character of the ear and the integration mechanism in the nervous system.

In the present paper, a new measuring method capable of differentiation of the time constant of the mechanical system of the ear from that of the nervous system was described.

When an external force whose frequency is increasing or decreasing as a function of time, is applied to a mechanical vibrating system, the amplitude of the vibration of the system at resonance becomes smaller and smaller as the changing velocity of the frequency of the applied force becomes larger. This amplitude of the system at resonance depends upon the magnitude of the applied force, the damping coefficient of the system, and the changing velocity of the frequency.

If we know the relation between the changes of the amplitude at resonance and the changing velocity of the frequency of the external force at different values of the damping constant as a parameter, we can inversely estimate the damping constant of other vibrating systems by measuring the changes of amplitute at resonance when the external force of vibration whose frequency varies at various velocity.

Applying this relation thus obtained to the ear, we are able to estimate the damping constant of the mechanical systems of the ear.

§ 2. An Experiment on the Electrical Circuit of One Degree of Freedom.

In order to make clear the relation between the damping constant of the system and changing velocity of the frequency of an applied force, the following experiment was carried out.

For simplicity, an electromotive force whose frequency varies with a constant rate, was applied to a simple series resonance electric circuit composed of L, C, and R, and the relation between the peak value of an induced e.m.f. in the inductance L when the frequency of the applied e.m.f. is coincident with the resonance frequency of the system N, was measured varying N and Q of the circuit.

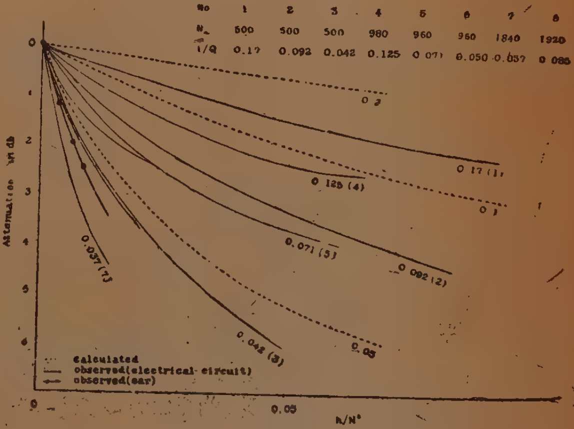

Fig. 1.

Fig. 1 shows the results of this experiment, but these of calculation(3) are, so tedious that only three dotted curves are shown in the same figure, in which N is the resonance frequencies, Q is $\omega L/R$; the sharpness of the resonance. The abscissa represents h/N^2, where h is the changing rate of the frequency, viz df/dt, and the ordinate gives the value α which represents the ratio of the induced electric potential in the inductance L expressed in decibels when the frequency of the applied electromotive force is coincident with the resonance frequency of the circuit N, to that when the frequency of applied e.m.f. was kept constant at N. When Q is kept constant, the relation between h/N^2 and α is given by one curve.

§ 3. The Measurement of the Damping Constant of the Mechanical System of the Ear by the Tone of the Frequency Varying with Uniform Rates.

If it is allowed to assume that the inner ear is equivalent to a system composed of many resonators and that each of them would act as an resonance system of one degree of freedom, as is above described. Q of the mechanical systems of the ear may be obtained from fig. 1 by measuring the sensitivity of the ear for the tone of the frequency varying with uniform rates. That is to say, when the subject is allowed to hear the tone of varying frequency, the amplitude of vibration of basilar membrane decreases according to the rate of frequency change being increased, with the result that the threshold for this tone will be raised.

It should be, however, noticed that the ear is not composed of a single resonator but of continuous resonating system or many resonators and that its frequency character is not uniform. Therefore it is necessary to measure the threshold shift dividing the audible frequency range into small freqnency regions in which the ear has almost uniform sensitivity.

The procedure of the experiment is analogous to that described in the previous paper⁽²⁾. Fig. 2 shows the Schematic connection of the experimental apparatus.

In order to generate a tone of the frequency varying with an uniform rate, the loudspeaker is sounded by such a current that is given by a bea oscillator through an power amplifier. The frequency of the electromotive force generated by the beat oscillator, is varied by means of a capacity in the oscillatory circuit being varied.

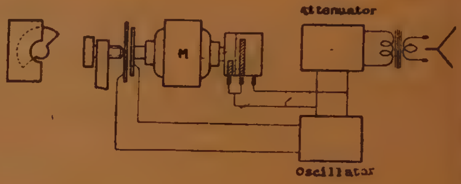

Fig. 1.

This capacity is composed of one fixed metal plate and a half circular metal plate which is rotated by an electric motor. By changing the number of revolution and distance of the two plates, it is capable of adjusting the rate of frequency change and the extent.

By this arrangement the electro-motive force whose frequency is being changed as a manner of triangle-waves is generated. To dividing the audible frequency range into small frequency regions, using the rotary switch driven by the same electric motor (as was used to produce the tone of short duration in Part 2)⁽²⁾, the tone whose frequency is increasing or decreasing uniformly from f_1 c.p.s. to f_2 c.p.s., was produced once every revolution. The sound thus produced, has a short duration T_1 and the frequency varying from f_1 c.p.s. to f_2 c.p.s. in that duration as is shown in fig. 3.

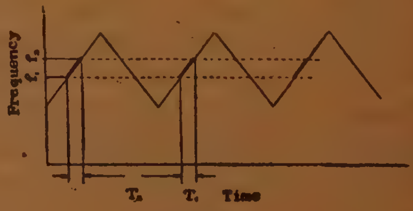

Fig. 3.

When we measured the threshold shift for the sound, two effects may be superposed, one of which is csused by the duration of the tone the other, by the change of frequency. The character of the former is seemed to be almost central nervous as described in Part 2⁽²⁾, and the latter may be peripheral.

Therefore, the difference between S_a and S_b, the threshold shift of the pure tone of frequency $\frac{f_1+f_2}{2}$ c.p.s. and of the duration T_1 seconds, and that of the tone of the frequency varying from f_1 c.p.s. to f_2 c.p.s. and the duration T_1 seconds, may be considered to represent the effect of the pure mechanical part of the ear.

The measuring procedure of the threshold and the subjects were same as described in the previous paper$^{(2)}$.

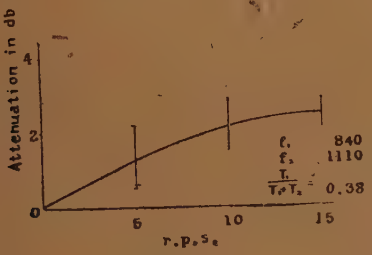

Fig. 4.

Fig. 4 shows the results of the experiments, the abscissa represents the number of revolutions per second of the rotary condenser plate, and the ordinate, the difference between S_a and S_b.

The velocity of the variation of the frequency h is increased proportional to the number of revolutions n with the following relation,

$$h=\frac{(f_2-f_1)\times 2\pi n}{\theta}=\frac{n(f_2-f_1)}{\dfrac{T_1}{T_1+T_2}}$$

where θ is a constant depending upon f_2 and f_1; T_1 and T_2 are onduration and off-duration of the tone respectively. In Fig. 4 it is shown that the difference becomes larger as h increases. Then the damping constant or Q of the mechanical systems of the ear for a given frequency can be obtained by putting the experimental results thus obtained into Fig. 1.

The observed values are on the solid curve between the curves (3) and (7) in Fig. 1, with the result that the value of Q of the mechanical systems of the ear for 1000 c.p.s. may be estimated as between about 24 and 27 corresponding to the logarithmic decrements of 0.13 and 0.12 respectively.

The logarithmic decrement of the mechanical system of the ear obtained by the new experimental method made sure of that so far presumed by many investigators and also was consistent with our previous calculation.

§ 4. Conclusion.

1. The new method of investigation of the damping constant of the mechanical parts of the ear is devised.
2. The logarithmic decrement of the mechanical system of the ear obtained by this method is about 0.13 which is consistent with the value so far obtained and the results of our calculacion.
3. It is shown that the time in which equilibrium state of Audition is established in nervous system is longer than the time constant of the mechanical part of the ear, the former is 0.2–0.4 seconds except adaptation phenomena, but the latter is 0.006 – 0.009 seconds.

The authors express their hearty thanks to the late Prof. Obata for his helpful suggestions and also have a pleasure to acknowledge the receipt of grants in aid for Scientific research from Ministry of Education.

Referenccs.

(1) Y. Makita and S. Miyatani: J. Phys. Soc. Jap. **5**, (1950) 39.
(2) Y. Makita and S. Miyatani: ibid.
(3) F.M. Lewis: A.S.M.E. APM-54-24 (1932).

On The Stark Effect of Helium in Strong Electric Field (I).

By Seiichi SUEOKA.

Institute of Applied Mathematics, Second Faculty of Engineering, University of Tokyo.

(Read April 28, 1949, Received December 26, 1949)

§1. Introduction.

The Stark effect of helium atom has been discussed by many authors from different viewpoints. When the strength of electric field is considerably weak, the quadratic effect is observed and the calculations based on the Schrödinger's perturbation method have proved to be in good agreement with the experimental results(1). In the case for which the strength of field ranges from the intermediate to the strong, Foster(2) has obtained the results from his experiment, which indicate the predominant linear effect, and he has explained his data from the theoretical side.

In the very strong electric field, on the other hand; Y. Ishida(3) and H. Kubota(4) have observed a peculiar phenomenon which is called the resonance. The resonance effect consists of two aspects. The first is the repulsion of two lines such as $6^1P \rightarrow 2^1P$ and $7^1D \rightarrow 2^1P$. This would be interpreted qualitatively by the J. von Neumann and E. Wigner's general consideration,(5) taking into account of the matrix elements between the states differing in principal quantum numbers. The second is the abnormality of the intensities of Stark lines which appears as an extraordinary amount of radiation at the vertex of one line of resonance hyperbola,(3) for example, $6^1P \rightarrow 2^1P$ line, and which often shows the vanishing intensity after encounter.

We intend to explain these resonance effects more quantitatively. In order to perform the calculations taking into account of the matrix elements between the states of different principal quantum numbers, we come upon a trouble of solving the secular equation of very large dimensions. To avoid this trouble formally, we have adopted the method of hypermatrix,(6) making use of the symmetry of the Hamiltonian matrix, and have obtained the simplification of the secular equation.

§2. Hypermatrix of Hamiltonian.

The Hamiltonian of helium atom in the electric field is given as a sum of H_0, the unperturbed part, and H' the perturbing energy due to the presence of the electric field. The explicit expressions of H_0 and H' in atmic units are as follows:

$$H_0 = -\frac{1}{2}\Delta_1 - \frac{1}{2}\Delta_2 - \frac{Z}{r_1} - \frac{Z}{r_2} + \frac{1}{r_{12}},$$
$$H' = F(z_1+z_2),$$

where F denotes the field strength and the other notations have the usual meanings.(7) For very strong field, we may neglect the mutual interaction of electrons as compared to H'. Then the zero-th order wave function of helium in symmetrized form may be written as,

$$U_{n,l,m} = \frac{1}{\sqrt{2}}\{u_1(1)\,u_{n,l,m}(2) \pm u_1(2)\,u_{n,l,m}(1)\}$$

in n, l, m state, where u_1 and $u_{n,l,m}$ represent the normalized wave functions of hydrogen in the ground and $n, l,$ state respectively. $u_{n,l,m}$ is expressed as the product of radial function $R_{n,l}(r)$ and spherical harmonics $Y_{l,m}(\theta,\varphi)$. The matrix element of H' between the n, l, m state and n', l', m' state is given

$$(n, l, m\,|\,H'\,|\,n', l'\, m')$$
$$= \iint U^*_{n,l,m} \cdot F(z_1+z_2) \cdot U_{n',l',m'}\, d\tau_1 d\tau_2$$
$$= F\cdot\delta_{m,m'} \cdot \int R_{n,l}(r)\, R_{n',l'}(r)\, r^3 dr$$
$$\times \iint Y^*_{l,m}(\theta,\varphi)\, Y_{l',m'}(\theta,\varphi) \cos\theta \sin\theta\, d\theta\, d\varphi.$$

Owing to the selection rule of the angular part, the non-vanishing elements are only two followings,

$$(n, l, m|H'|n', l+1, m)$$

$$=F\cdot\sqrt{\frac{(l+1)^2-m^2}{4(l+1)^2-1}}\cdot\int_0^\infty R_{n,l}(r)\,R_{n',l+1}(r)\,r^3dr,$$

$$(n, l, m|H'|n', l-1, m)$$

$$=F\cdot\sqrt{\frac{l^2-m^2}{4l^2-1}}\cdot\int_0^\infty R_{n,l}(r)\,R_{n',l-1}(r)\,r^3dr. \quad (1)$$

The radial integral is the same as that appearing in the theory of transition probability of hydrogen atom, of which the general expression was given by Gordon.[(8)]

On account of the diagonality of the matrix of H' in m, we may instead of full matrix of H_0+H' consider the part for $m=\text{const.}$ So it suffices to take $U_{n,l,m}\,(m\leqq l\leqq n-1)$, $U_{n',l',m'}$ $(m\leqq l'\leqq n'-1)$ as bases. The dimension of the matrix is then $n+n'-2m$. In the matrix of H_0+H', H_0 has of course only the diagonal elements, while H' gives non-vanishing elements on both sides of the principal diagonal at the nearest seats, and also at the corresponding part in the interaction part of n and n'. This appearance of elements suggests a suitable choice of arranging the bases in the order of $U_{n,m,m}$, $U_{n'm,m}$, $U_{n,m+1,m}$, $U_{n',m+1,m}$, $\cdots$, $U_{n,n-1,m}$, $U_{n',n-1,m}$ and $U_{n',n,m}$. (Here we assume $n'>n$). As there is no matrix element between $U_{n',l,m}\,(l>n)$ and $U_{n,l,m}\,(m\leqq l\leqq n-1)$, we may omit the former out of our consideration. Then the shematic form of matrix, extracting the part near $l=l$, is as follows:

$(n,l-1\|H_0\|n,l-1)$, $\quad 0$ $0 \quad ,(n',l-1\|H_0\|n',l-1)$	$(n,l-1\|H'\|n,l)$, $(n,l-1\|H'\|n',l)$ $(n',l-1\|H'\|n',l)$,$(n',l-1\|H'\|n',l)$	$0 \quad , \quad 0$ $0 \quad , \quad 0$
$(n,l\|H'\|n,l-1)$, $(n,l\|H'\|n',l-1)$ $(n',l\|H'\|n,l-1)$, $(n',l\|H'\|n',l-1)$	$(n,l\|H_0\|n,l) \quad , \quad 0$ $0 \quad , (n',l\|H_0\|n',l)$	$(n,l\|H'\|n,l+1)$, $(n,l\|H'\|n',l+1)$ $(n',l\|H_0\|n,l+1)$, $(n',l\|H'\|n',l+1)$
$0 \quad , \quad 0$ $0 \quad , \quad 0$	$(n,l+1\|H'\|n,l)$, $(n,l+1\|H'\|n',l)$ $(n',l+1\|H'\|n,l)$, $(n',l+1\|H'\|n',l)$	$(n,l+1\|H_0\|n,l+1)$, $\quad 0$ $0 \quad (n',l+1\|H_0\|n',l+1)$

At a glance on this form, we find at once that the non-vanishing part appears in a form of sub-matrix of two rows and columns. Therefore, it is convenient for us to consider the H_0+H' matrix as a hypermatrix, of which elements are two dimensional matrices. If we denotes these elements by

$$E_l=\begin{pmatrix}(n,l|H_0|n,l), & 0\\ 0, & (n',l|H_0|n',l)\end{pmatrix},$$

$$A_l=\begin{pmatrix}(n,l|H'|n,l+1), & (n,l|H'|n',l+1)\\ (n',l|H'|n,l+1), & (n',l|H'|n',l+1)\end{pmatrix}, \quad (2)$$

then the hypermatrix of H_0+H' has the following form.

$$\begin{pmatrix}E_m, & A_m, & 0, & 0, & & & \\ \tilde{A}_m, & E_{m+1}, & A_{m+1}, & 0, & & & \\ 0, & \tilde{A}_{m+1}, & E_{m+2}, & A_{m+2}, & & & \\ & & \cdot & \cdot & \cdot & & \\ & & & \cdot & \cdot & \cdot & \\ & & & & \cdot & \cdot & \cdot \\ & & & & E_{n-2}, & A_{n-2}, & 0\\ & & & & \tilde{A}_{n-2}, & E_{n-1}, & A'_{n-1}\\ & & & & 0, & \tilde{A}'_{n-1}, & E'_n\end{pmatrix} \quad (3)$$

where $\tilde{A}_l$ represents the transposed (conjugate) matrix of A_l, with the exception that A'_{n-1} or $\tilde{A}'_{n-1}$ are the matrix of one row, two columns or two rows, one column and $E_n'=(n',n,m|H_0|n',n,m)$.

§ 3. Simplification of Secular Equation.

Next, we shall give the method of obtaining the eigenvalues of hypermatrix (3), making correspondence with the means which we make use for usual matrix. Regarding $2(n-m)+1$ dimensional X vector as a hypervector and assuming that X consists of $n-m+1$ vectors, X_1, X_2, $\cdots$, X_{n-m+1}, these are the two-dimensional vectors except the last one which is one-dimensional. We may then consider the hypervector X as a operand of hypermatrix and obtain the following associated matrix equations, corresponding usual algebraic associated equations.

$$\begin{aligned}&E_mX_1+A_mX_2=\lambda EX_1,\\ &\tilde{A}_mX_1+E_{m+1}X_2+A_{m+1}X_3=\lambda EX_2,\\ &\tilde{A}_{m+1}X_2+E_{m+2}X_3+A_{m+2}X_4=\lambda EX_3,\\ &\cdots\cdots\cdots\cdots\cdots\cdots\cdots\cdots,\\ &\cdots\cdots\cdots\cdots\cdots\cdots\cdots\cdots,\\ &\tilde{A}_{n-2}X_{n-m-1}+E_{n-1}X_{n-m}+A'_{n-1}X_{n-m+1}=\lambda EX_{n-m},\\ &\tilde{A}'_{n-1}X_{n-m}+E'_nX_{n-m+1}=\lambda EX_{n-m+1},\end{aligned} \quad (4)$$

where λ is a eigenvalue and E is a unit matrix of two rows and columns. From these equations, we may eliminate the X_i one after another, namely,

$$\begin{aligned} X_2 &= A_m^{-1}\Lambda_m X_1\,, \\ X_3 &= A_{m+1}^{-1}(\Lambda_{m+1}A_m^{-1}\Lambda_m-\tilde{A}_m)\,X_1\,, \\ X_i &= A_{m+i-2}^{-1}(\Lambda_{m+i-2}X_{i-1}-\tilde{A}_{m+i-3}X_{i-2}) \qquad (5) \\ & \qquad\qquad (i=3,\ 4,\ \cdots\cdots,\ n-m), \end{aligned}$$

where Λ_n denotes $\lambda E-E_n$. We notice that there exists the inverse matrix A_i^{-1}, because of the non-singularity of A_i. By continuing the above procedure of elimination, we obtain

$$X_{n-m-1} = BX_1\,;\quad X_{n-m} = CX_1\,, \qquad (6)$$

where B and C are the matrices of two rows and columns. These are the functions of $A_i(\tilde{A}_i)$, $E_i\,(m \leqq i \leqq n-2)$ and λ. Substituting (6) into the last two equations of (4), following matrix equations are obtained:

$$\begin{aligned} \{\Lambda_{n-1}C-\tilde{A}_{n-2}B\}X_1-A'_{n-1}X_{n-m+1} &= 0\,, \\ \tilde{A}'_{n-1}C\,X_1-(\lambda-E'_n)\,X_{n-m+1} &= 0\,. \qquad (7) \end{aligned}$$

As a necessary condition for the existence of non-vanishing X_1 and X_{n-m+1}, we obtain the following determinantal equation of three dimensions which corresponds to the secular equation of usual matrix.

$$\left\| \begin{matrix} \Lambda_{n-1}C-A_{n-2}B\,, & A'_{n-1} \\ \tilde{A}'_{n-1}C\,, & \lambda-E_n' \end{matrix} \right\| = 0\,, \qquad (8)$$

where $A'_{n-1}C$ and A'_{n-1} are matrices of one row, two columns and two rows, one column respectively, and the notation $\|\ \|$ is used in the following sense:

$$\left\| \begin{matrix} A, & B \\ C, & D \end{matrix} \right\| = \left| \begin{matrix} A_{11}\,, & A_{12}\,, & B_{11}\,, & B_{12} \\ A_{21}\,, & A_{22}\,, & B_{21}\,, & B_{22} \\ C_{11}\,, & C_{12}\,, & D_{11}\,, & D_{12} \\ C_{21}\,, & C_{22}\,, & D_{21}\,, & D_{22} \end{matrix} \right| .$$

The dimension of (8) being $2(n-m)+1$ for the given value of m, all the roots of secular equation of original matrix, the dimensions of which are $2(n-m)+1$, will be contained in (8).

§ 4. Calculations in the case of $n=4$, $n'=5$.

We shall calculate the energy of the states of $n=4$ and $n'=5$, as a simple example of application of the preceding method. It may be able to extract the part of given value of m, for which the azimuthal quantum number ranges from $l=m$ to $l=3$ and $l=4$ in the case of $n=4$ and $n'=5$ respectively. For example, we shall take the case $m=0$, for which the dimension of the energy matrix is largest. In this case, the hypermatrix (3) may be written as follows:

$$\begin{pmatrix} E_0\,, & A_0F, & 0, & 0, & 0 \\ \tilde{A}_0F, & E_1\,, & A_1F, & 0, & 0 \\ 0, & \tilde{A}_1F, & E_2\,, & A_2F, & 0 \\ 0, & 0, & \tilde{A}_2F, & E_3\,, & A'_3F \\ 0, & 0, & 0, & \tilde{A}_3'F, & E_4' \end{pmatrix} \qquad (9)$$

Making use of the procedure mentioned in the previous section, we obtain the following secular equation.

$$\left\| \begin{matrix} \Lambda_3A_2^{-4}\Lambda_2A_1^{-1}\Lambda_1A_0^{-1}\Lambda_0-F^2 & A_3' \\ \quad\times(\Lambda_3A_2^{-1}\Lambda_2A_1^{-1}\tilde{A}_0+\Lambda_3A_2^{-1}\tilde{A}_1A_0^{-1}\Lambda_0 & \\ \quad+\tilde{A}_2A_1^{-1}\Lambda_1A_0^{-1}\Lambda_0)+F^4\cdot\tilde{A}_2A_1^{-1}\tilde{A}_0\,, & \\ \tilde{A}_3'\{A_2^{-1}\Lambda_2A_1^{-\prime}\Lambda_1A_0^{-1}\Lambda_0 & \lambda-E'_4 \\ \qquad-F^2(A_1^{-1}\Lambda_2A_1^{-1}\tilde{A}_0 & \\ \quad+A_1^{2-}\tilde{A}_1A_0^{-1}\Lambda_0)\}, & \end{matrix} \right\| = 0. \qquad (10)$$

For simplicity, we assume the interaction between $l=3$ and $l=4$ is negligible. This approximation, corresponding to the fact that A_3' is considered to be zero, may be permissible, so far as the energy levels with $l=0,\ 1,\ 2$ are concerned at least. Then the equation (10) may be reduced to the following determinantal equation of two dimensions.

$$\begin{aligned} \| \Lambda_3A_2^{-1}\Lambda_2A_1^{-1}\Lambda_1A_0^{-1}\Lambda_0-F^2\,(\Lambda_3A_1^{-1}\Lambda_2A_1^{-1}\tilde{A}_0 & \\ +\Lambda_3A_2^{-1}\tilde{A}_1A_0^{-1}\Lambda_0+\tilde{A}_2A_1^{-1}\Lambda_1A_0^{-1}\Lambda_0) & \qquad (11) \\ +F^4\cdot\tilde{A}_2A_1^{-1}\tilde{A}_0\,\| &= 0. \end{aligned}$$

The non-diagonal elements of (9), $A_l\,(l=0,1,2,3)$, are given by (2) and the numerical values of which can be obtained from the results calculated by Bethe(9).

$$A_0 = \frac{1}{\sqrt{3}}\begin{pmatrix} -23.24, & 3.521 \\ 4.604, & -33.54 \end{pmatrix},$$

$$A_1 = \frac{2}{\sqrt{15}}\begin{pmatrix} -20.78, & 11.04 \\ 3.017, & -34.37 \end{pmatrix},$$

$$A_2 = \frac{3}{\sqrt{35}}\begin{pmatrix} -15.89, & 14.00 \\ 1.158, & -30.00 \end{pmatrix}.$$

On the other hand, the diagonal element E_l has the following form

$$E_l = \begin{pmatrix} \varepsilon_{4l}, & 0 \\ 0, & \varepsilon_{5l} \end{pmatrix},$$

where ε_{nl} denotes the energy of the stationary state of helium atom in the absence of electric field and is measured from ε_{42} (4*D* level).

In the case of par-helium, for example, the values in atomic units are

$$\begin{aligned} &\varepsilon_{40} = -0.002279, \quad \varepsilon_{41} = 0.000203, \quad \varepsilon_{42} = 0, \\ &\varepsilon_{43} = 0.000029, \quad \varepsilon_{50} = 0.010110, \quad \varepsilon_{51} = 0.011368, \\ &\varepsilon_{52} = 0.011262, \quad \varepsilon_{53} = 0.011279. \end{aligned}$$

Using these numerical values, we may obtain the following algebraic equation for F^2, after expanding the determinant (11).

$$y^4 + a(\lambda)y^3 + b(\lambda)y^2 + c(\lambda)y + d(\lambda) = 0 \tag{12}$$

where $y = 10^6 F^2$. The coefficients are the functions of λ:

$$\begin{aligned} a(\lambda) &= -522.5\,\lambda^2 + 3.140\,\lambda - 0.01348, \\ b(\lambda) &= 54380\,\lambda^4 - 885.7\,\lambda^3 + 4.944\,\lambda^2 - 0.0^2 4765\,\lambda \\ &\quad + 0.0^4 1957, \\ c(\lambda) &= -1695 \times 10^3\,\lambda^6 + 453 \times 10^2\,\lambda^5 - 421.9\,\lambda^4 \\ &\quad + 1.789\,\lambda^3 - 0.0^2 3439\,\lambda^2 - 0.0^5 7172\,\lambda + 0.0^9 6660, \\ d(\lambda) &= 0.1211\,\lambda\,(\lambda + 0.002279)(\lambda - 0.000203) \\ &\quad \times (\lambda - 0.000029)(\lambda - 0.010110)(\lambda - 0.011368) \\ &\quad \times (\lambda - 0.011262)(\lambda - 0.011279). \end{aligned}$$

The equation (12) is fourth degree in F^2, while eighth degree in λ. It is convenient, therefore, to solve (12) for F^2 or y, regarding λ as a parameter. For given values of λ that are changed from −0.006 to 0.018 with the interval of 0.001 or 0.0005, the quartic equations for y are solved. That roots in the first approximation are obtained by the Differential Analyser set at The Institute of Science and Technology, University of Tokyo.

The accuracy of the values are raised by Horner's method. The results are given in Table I. The manner of changes of the energy values with the strength of the field are shown in Fig. 1, where the dotted lines, representing the diagram in the case in which the interactions between the states with $n = 4$ and $n' = 5$ are neglected, are added for the sake of comparison. It may be seen at once from Fig. 1 that there exist four points in the neighbourhood of the strength of the field being $F \sim 0.00025$, $F \sim 0.00035$, $F \sim 0.00045$ and $F \sim 0.0007$ respectively, where the two levels do not cross but repel each other. It may be interpreted that the two levels cause the so-called resonance effect, on account of the partly mixing states such as 4, l and 5, $l-1$.

Table I.

λ	$F \times 10^3$			
−0.008	2.331	1.005	0.07865	0.3635
−0.006	1.994	0.7729	0.6807	0.2769
−0.005	1.832	0.6531	0.6241	0.2249
−0.004	1.675	0.5899	0.5067	0.1687
−0.002	1.375	0.4953	0.2293	—
−0.001	1.230	0.4547	0.9272	—
0	1.087	0.4116	0	—
0.0005	1.015	0.3905	0.02884	0.1481
0.001	0.9394	0.3647	0.06261	0.2579
0.0015	0.8582	—	0.09484	—
0.002	0.7560	0.3417	0.1264	0.4740
0.0025	—	0.3173	0.1577	—
0.003	—	0.2968	0.18888	—
0.004	—	—	—	—
0.005	—	0.2185	0.3151	—
0.0055	—	0.1995	0.3475	—
0.006	0.5620	0.1811	0.3810	0.9225
0.0065	—	0.1605	—	1.044
0.007	—	0.1423	—	1.151
0.0075	0.3612	0.1251	0.4658	1.252
0.008	0.3003	0.1066	0.5013	1.352
0.009	0.1936	0.06745	0.5667	1.545
0.010	0.08683	0.01961	0.6345	1.738
0.012	0.09489	0.02786	0.7692	2.125
0.014	0.2827	0.09911	0.9071	2.506
0.016	0.4585	0.1680	1.048	2.892
0.018	0.6274	0.2359	1.193	3.279

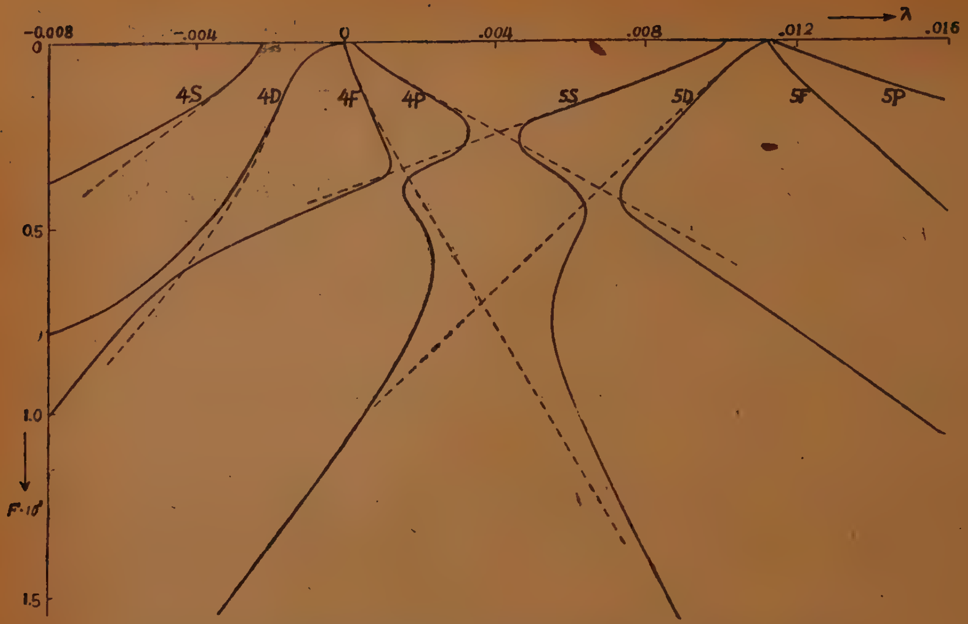

Fig. 1. The energy and field strength diagram in atomic units.
The case of $n = 4$, $n' = 5$ and $m = 0$.

§ 5. Conclusion.

In this work, the numerical computations are performed only in a simple case to explain the essential features of the resonance phenomena of Stark effect. Such strong fields as produce the resonance in the case of $n = 4$ and $n = 5$, has not been realized in the experiment, therefore we are not able to compare the result directly with the experimental data. The comparison with experimental results in the case of $n = 6$ and $n = 7$, and also the calculation of the line strength will be given in a future issue of this Journal.

The author wishes to express his hearty thanks to Prof. T. Yamanouchi for his kind encouragement and valuable advides, and Prof. H. Kubota for his suggestion of this problem and kindness of lending me unpublished photographs, and to Prof. T. Inui and Ass. Prof. A. Amemiya for their valuable discussions, and to Mr. J. Miida for his giving benefit on using the Differential Analyser and to Miss. I. Ōta for her assistance in numerical computations. The author is also indebted to The Educational Ministry for the financial aid.

References.

(1) H.A. Bethe: Handbuch der Physik, 24/I (1933), p. 419.
(2) J.S. Foster: Proc. Roy. Soc. London, **117** (1928) 137.
(3) Y. Ishida: Sc. Pap. I.P.C.R., **14** (1930) 49.
(4) H. Kubota: Private Communication.
(5) J. von Neumann and E. Wigner: Phys. Zeits., **30** (1930) 467.
(6) M. Born and P. Jordan: Elementare Quantenmechanik (1930), p. 28, and S. Sueoka: J. Phys. Soc. Jap., **4** (1949), 361.
(7) H.A. Bethe: Hand. d. Phys., p. 324 & 419.
(8) W. Gordon: Ann. d. Phys., **2** (1929) 1031.
(9) H. A. Bethe: Hand. d. Phys., p. 442, or E. U. Condon and G.H. Shortley: The Theory of Atomic Spectra (1935), p. 133.

The Determination of Sound Absorption Coefficient.

By Juichi IGARASHI.

Kobayashi Institute of Physical Research Tokyo.

(Read May 1 1949 Received Jan. 6, 1950)

§ 1. Introduction.

In recent years a very useful theory on room acoustics has been developed by P.M.Morse(1), R. H. Bolt and others. But it is not yet easy to apply to the architectural engineering. The absorption coefficient which has been used for the detemination of the reverberation time is a very convenient conceptionfor the acoustical design of the room. The coefficients of various wall materials were measured at many laboratories, the results of the same material obtained at different places, however, have shown some different values(2).

This disagreement may be attributed to the contradiction between the non-uniform field in the reverberation chamber and the assumption of the uniform field in the reverberation formula. The non-uniform field is caused partly by the effects of the normal vibrations of the room and many workers endeavoured to make the sound field uniform.

But as the reverberation method involves nonuniform distribution of wall materials, the uniform field can not be expetced usually. Accordingly when we determine the absorption coefficient from the reverberation time, we must introduce a suitable formula which represents the non-uniform sound field caused by the distribution of different materials.

On the other hand, the normal coefficient which was determined by the stationary wave method or others, has not been applied to the engineering purpose, for the reason that the normal coefficient is limited for the normally incident sound only. If we can determine the absorption coefficient, however, as the function of incident angles, the normal coefficient will be more useful for the acoustical design.

In this paper the author will report on the results of the measurements about the reverberation method and a new method which determines the normal coefficients.

1. The reverberation time was measured in a small rectangular box. To eliminate the effects of normal vibrations of the room the thyratron noise was used as a sound source and the experiments were performed for various frequency ranges.

2. The author introduced the modified approximate formula for the reverberation of sound, when the materials of different coefficients were distributed in the room. Thus from the experimental results above mentioned the absorption coefficients were determined.

3. Normal coefficients can be determined easily from the decay time of normal vibrations of the tube.

4. According to the relation between absorption coefficients and incident angles of sound we can determine average coefficients from the values of normal coefficients. They were compared with the values measured by the reverberation method.

§ 2. Measurements by the Reverberation Method.

For a reverberation chamber a rectangular box was used (Fig. 1).

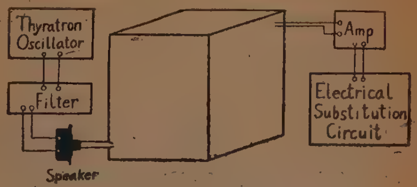

Fig. 1. Mode of Reverberation chamber.

It is made of concrete and dimentions of which are $50\times46\times42$ cm^3. The wall is 5 cm. thick. At a corner of the side walla small pipe connecting to a loudspraker, is inserted as a high impedance source of sound(3). The thyratron noise is amplified and supplied to the speaker. The frequency band is determined arbitrary by the band pass filter in the electric circuit. A small crystal microphone which is set at an another corner of the box picks up the sound pressure. The decay time is measured by the method of the electrical substiution which will be mentioned later.

At first, absorption coefficients of the concrete wall must be determined at various frequency bands. The decay time τ (the reverberation time $T = 6.9\,\tau$) and calculated coefficients are shown in Table I.

The sample to be measured is set on a floor of the box as it covers the whole plane. Then the box is closed and by the same method the decay time is measured. The results for the felt 1 cm. thick are also shown in the same table.

Table I.

	Concrete wall		Felt 1 cm.
Freq.Band	[τ]	[α]	[τ]
	sec.		sec.
500 5000	0.072	0.025	0.02
—3500	75	24	
—2500	77	23	0.025
—1800	77	23	
—1200	78	23	0.028
—800	83	22	
1000—5000	68	27	
2000—5000	63	29	
3500—5000	.55	32	
1000—2000	.70	26	
1000—1800			0.022
1000—2500			0.020

§ 3. The Modified Reverberation Formula for the Non-uniform Field.

In the measurement above mentioned the author intended to eliminate the effects of the normal vibrations by using the thyratron noise. Even in such a small box we can expect fairly uniform distribution of sound except low frequencies. The values of the coefficients at various frequencies are averaged. Besides the normal modes, however the cause of a non-uniform field is the distribution of materials. According to the statistical method the following consideration is possible.

If we choose P, as the power out put of the speaker and p, as the mean free path of the room, then the energy density at p/c sec, after the power supply to the speaker was stopped, is

$$E_0 = P_0\, p/cV$$

c: sound velocity
V: volume of the room

After the first reflection,

$$E_1 = E_0 \sum R_i S_i / S$$

S: total surface area of the room.

At the second reflection we can assume that the sound reflected previously from one surface does not incident upon the same surface butdiffuses to another surfaces proportional to their area.

Therefore the sound density after the second reflection is

$$E_2 = E_0 \Sigma' \Sigma' S_i S_j R_i R_j / S(S - S_i)$$

dash means excluding i = j.

Similarly after the third reflection we get

$$E_3 = \Sigma' \Sigma' E_1 S_i S_j R_i R_j / S(S - S_i)$$
$$= E_0 \Sigma' \Sigma' (S_i R_i / S)^2 S_j R_j / (S - S_i)$$

After the fourth reflection

$$E_4 \doteq E_0 \{\Sigma' \Sigma' S_i S_j R_i R_j / S(S - S_i)\}^2$$

Thus the sonnd density after the 2n-th reflection

$$E_{2n} = E_0 \{\Sigma' \Sigma' S_i S_j R_i R_j / S(S - S_i)\}^n$$
$$= E_0 \exp[n \ln\{\Sigma' \Sigma' S_i S_j R_i R_j / S(S - S_i)\}]$$

The time elapced until this moment is

$$t = 2np/c$$

As the mean free path p is statisticaly $4V/S$,

$$n = Sct/8V$$

$$E = E_0 \exp[(Sct/8V) \times \ln\{\Sigma' \Sigma' S_i S_j R_i R_j / S(S - S_i)\}] \dots\dots\dots\dots (1)$$

Therefore we can introduce the reverbration formula

$$T = 2KV/[S \ln\{\Sigma' \Sigma' S_i S_j R_i R_j / S(S - S_i)\}] \dots (2)$$

T: reverberation time
K: −0.162 (meterunit)

The formula (2) can be made simplify, if the area of each surface and the absorption coefficient of the bare room are known.

In the present experiment

$$\ln(0.36\,RR_0+0.64\,R_0^2)=-0.025/T\ldots\ldots\ldots \quad (3)$$

$R_0=1-\alpha_0$: reflecting power of the concrete wall

The relation between α and T calculated by (3) is shown in Fig. 2 (dotted line), full line by Sabine's formula.

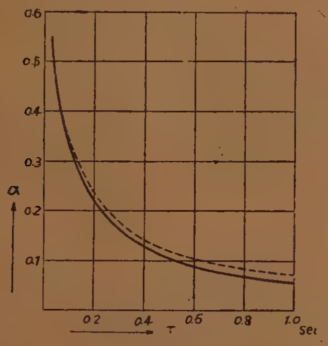

Fig. 2.

The relation between α and T.

From the results obtained in the preceding section, absorption coefficients of the material at various frequency bands are determined. The values for the felt 1 cm. thick are illustrated in Fig. 6.

§ 4. A New Method for the Measurement of Normal Coefficient.

The normal coefficient of sound has been measured by various methods. Results obtained coincide well with each other. The author tried also a new method for determining it.

The sample is set at the one end of a cylindrical brass tube (length 100 cm.; diameter 10 cm.) while at the another end, there is a small hole to which a high impedance source is inserted. The frequency is adjusted at one of the normal frequencies of the tube and the sound pressure is measured by the crystal microphone, which is situated at a source side of the tube. The electrical circuit of this method is shown in Fig. 3.

Voltage induced in the microphone is amplified and rectified. Condencer C_2 is charged at the same potential as that induced between A and E. Then the power supply to the speaker and the charging current to C_2 is cut off simultaniously. If the decay time of the sound in the tube and that of R_2 C_2 circuit coinside each other, an out put meter does not deflect. So the decay time is determined in terms of R_2 and C_2. From the decay time we can calulate the absorption coefficients of materials as follows.

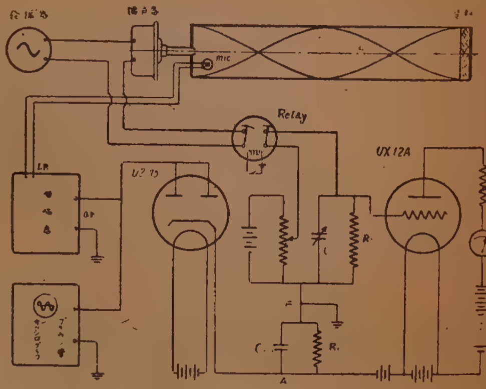

Fig. 3.

The electrical substitution circuit.

If the sound is absorbed only at one end which has absorbing material, at the stationaly state the sound density is

$$E_s=E_0(1+R+R^2+R^3+R^4+-)=E_0/(1-R)\ldots \quad (4)$$

$E_0=P_0p/cV$ as preceding section.

Therefore the Sound density at t sec. later after n reflections from the time at which the power supply was stopped, is

$$E_n=E_0 \times(R^n+R^{n+1}+R^{n+2}+R^{n+3}+---)=E_0R^n/(1-R)$$

$$E_n/E_s=\exp\{(ct/2l)\ln R\}$$

where $n\doteq ct/2l$ l: length of a tube,

If we choose τ as the time in which the sound pressure becomes $1/e$,

$$E_n/E_s=\exp\{(c\tau/2l)\ln R\}=1/e^2$$

$$\tau=-4l/(c\ln R)$$

In this case we assumed that the sound energy is not lost except at the material, but we must consider the absorption at the other parts of the tube. If we measure the decay time without the material the absorption rate of the tube itself is known. Then the formula (4) becomes

$$E_s = E_0\{1+RR'+(RR')^2+(RR')^3+---\}$$
$$E_n/E_s = 1/e^2 \doteqdot \exp\{(c\tau'\ln RR')/2l\}$$

dash means values with material.

$$\ln R' = \ln(1-\alpha') \doteqdot (4l/c)(1/\tau-1/\tau') \dots\dots\dots \quad (5)$$

From values τ, τ', l, c the absorption coefficient α is determined.

In Fig. 4 the values obtained for the felt 1 cm. 2 cm. 3 cm. and the tex 1 cm. thick, are illustrated.

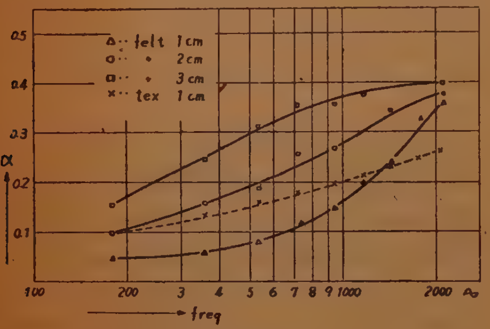

Fig. 4.

The absorption coefficient. (Normal coef).

The results obtaioned by this method coincide well with the coefficients by the stationary wave method.

§ 5. Comparison of the Absorption Coefficients.

When we compare the absorption coefficient by the reverberation method with the normal coefficient, the latter is smaller than the former. This is because that the absorption coefficient is a function of incident angles.

Paris(4) reported the relation between the absorption coefficient at arbitraly angle and the normal impedance Z_n, that is

$$\alpha_\theta = 1-|(Z_n\cos\theta-\rho c)/(Z_n\cos\theta+\rho c)|$$

ρ: density of the air

θ: incident adgle of the sound upon the material.

Willig(5) and Hunt(6) measured α_θ by different methods and confirmed the Paris's relation.

Willig proposed also the conception of the average coefficient $\bar{\alpha}$. He calculated the relation between $\bar{\alpha}$ and α_n; this is shown in Fig. 5.

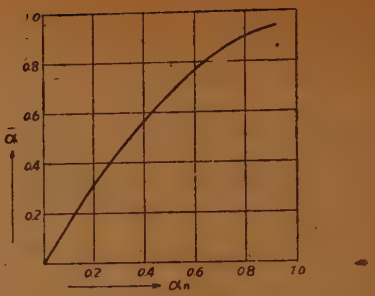

Fig. 5.

The relation between the average coefficient and the normal coefficient (after Willig).

The results obtained in the present experiment by the reverberation method are illustrated in Fig. 6, the abssisa being the frequency and the ordinate, α.

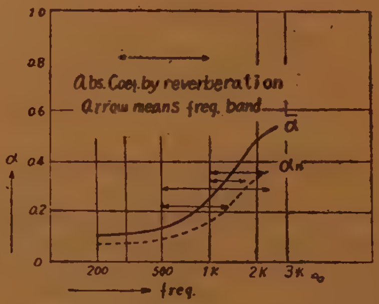

Fig. 6.

Comparison of the coefficients.

The straight lines are the observed values for the felt 1 cm. thick and the arrows mean the frequency ranges. The full line curve is the average coefficients determined from the normal coefficients which were already shown in Fig. 4, (dotted curve).

§ 6. Conclusion.

When we adopt the reverberation method as described in this paper we must use the larger box as a reverberation chamber for the reason that the numbers of normal vibrations can not be excited in a small box, especially at low frequencies.

The various methods for determining absorption coefficients were discussed but the tube method is a very convenient one because the frequency charactor of coefficients are determined accurately and easily. The normal coefficients will be more useful for the acoustical design of the room, by transforming them to the average coefficients.

In conclusion the author wishes to express his hearty thanks to Professor K. Sato for his kind guidance.

References.

(1) P.M.Morse and R.H.Bolt. Rev. Mod. Phys. **16** (1944) 69.
(2) Simposium on Absorption Coefficients. J.A.S.A. **11** (1939) 61.
(3) F.V.Hunt J.A.S.A. **10** (1939) 216.
(4) Paris. Nature **9** (1930) 126.
(5) F.J.Willig J.A.S.A. **10** (1939) 293.
(6) F.V.Hunt Loc.cit.

On the Mathematical Analysis of the Problem of the Conduction of Heat when Emissivity is Variable.

By Tunezo SATOH.

(Received January 10, 1950).

The mathematical statement for the problem of the conduction of heat with the heat transfer phenomena in a semi-infinite body, initially at constant temperature is as follows:

Obtain the solution $v(x, t)$ of

$$\frac{\partial v}{\partial t} = \frac{\partial^2 v}{\partial x^2} \quad (x > 0,\ t > 0) \tag{1}$$

such that

$$v(x, +0) = v_0 \quad (x > 0) \tag{2}$$

$$-\frac{\partial v}{\partial x} + hv = 0 \quad (\text{at } x = +0). \tag{3}$$

In the usual treatment such as above stated, h in (3) has been treated to be constant, but for the present paper we will cosider it to be variable.

Suppose that $v(x, t) = 0 (x < 0)$ and

$$v(x, t) = O(e^{cx}) \tag{4}$$

for some $c > 0$ and all values of t, with similar conditions on any of partial derives which occur⁽¹⁾

Let

$$V(\zeta, t) = \frac{1}{\sqrt{2\pi}} \int_9^\infty v(x, t) e^{i\zeta x} dx, \tag{5}$$

where $\zeta = \xi + i\eta \quad \eta > c$.

Thus we get

$$\frac{\partial V}{\partial t} + \zeta^2 V = \frac{1}{\sqrt{2\pi}} (i\zeta - h(t)) v(+0,\ t).$$

If we solve this,

$$V(\zeta, t) = \frac{1}{\sqrt{2\pi}} \Big[A(\zeta) e^{-t\zeta^2}$$
$$+ e^{-t\zeta^2} \int_0^t \{i\zeta - h(u)\} v(+0,\ u) e^{u\zeta^2} du \Big], \tag{6}$$

where $A(\zeta)$ may be determined by

$$A(\zeta) = \sqrt{2\pi}\ V(\zeta, +0) = \int_0^\infty v(x, +0) e^{i\zeta x} dx = -\frac{v_0}{i\zeta}. \tag{7}$$

Now since it is known⁽²⁾ that for every point x, for which $f(x+0)$ and $f(x-0)$ exist,

$$f(x+0) \int_0^\infty K(u) du$$
$$+ f(x-0) \int_{-\infty}^0 K(u) du = \lim_{\lambda \to \infty} \lambda \int_{-\infty}^\infty f(u) K(\lambda(u - x)) du,$$

when the following statement is ture: $f(u) \in L_1(-\infty, \infty)$, $K(u) \in L_1$ and bounded, and $K(u) = O(|u|^{-1})$, if we put

$$f(u) = 0, \quad \text{for } u < 0,$$

$$K(u) = e^u, \ \text{for } u \leq 0\,; \quad = 0, \ \text{for } u > 0,$$

then the above equation will take the following form:

$$\lim_{\lambda \to \infty} \lambda \int_0^x f(u) e^{-\lambda(x-u)} du = f(x-0).$$

Hence if we suppose the functions $v(+0, t)$,

$h(t)v(+0, t)$ to satisfy the same conditions as those on $f(t)$,

$$\lim_{|\xi|\to\infty} \xi^2 e^{-t\xi^2}\int_0^t v(+0, u)e^{u\xi^2}du = v(+0, t-0),$$

$$\lim_{|\xi|\to\infty} \xi^2 e^{-t\xi^2}\int_0^t h(u)v(+0, u)e^{u\xi^2}du = h(t-0)v(+0, t-0), \qquad t>0.$$

Thus we can conclude that, for any finite $\eta > c$,

$$V(\zeta,\ t) = O(|\xi|^{-1}).$$

Now using L_2-theory and the residue theorem, we obtain

$$v(x,\ t) = \frac{2v_0}{\sqrt{\pi}}\int_0^{x/2\sqrt{t}} e^{-u^2}du$$

$$+\frac{x}{2\sqrt{\pi}}\int_0^t \frac{v(+0,u)}{(t-u)^{3/2}}e^{-x^2/4(t-u)}du, \qquad (8)$$

$$v(x,\ t) = v_0-\frac{1}{\sqrt{\pi}}\int_0^t \frac{h(u)v(+0,u)}{\sqrt{t-u}}e^{-x^2/4(t-u)}du. \qquad (9)$$

The last result (9) tends to

$$\varphi(t) = 1-\frac{1}{\sqrt{\pi}}\int_0^t \frac{h(u)\varphi(u)}{\sqrt{t-u}}du \qquad (10)$$

with $x \to +0$, where $v(+0, t) = v_0\varphi(t)$.

Especically, let h be constant. Then the equation (10) will be

$$\varphi(t) = 1-\frac{h}{\sqrt{\pi}}\int_0^t \frac{\varphi(u)}{\sqrt{t-u}}du,$$

from which

$$\int_0^t \frac{\varphi(u)du}{\sqrt{t-u}} = 2\sqrt{t}-h\sqrt{\pi}\int_0^t \varphi(u)du.$$

follows. By combining both equations

$$\varphi(t)-h^2\int_0^t \varphi(u)du = 1-\frac{2h}{\sqrt{\pi}}\sqrt{t}.$$

Thus we have

$$\varphi(t) = \frac{2}{\sqrt{\pi}}e^{h^2t}\int_{h\sqrt{t}}^\infty e^{-u^2}du \qquad (11)$$

which is none but the usual result as well known.

Consequently in general, as in above particular case, when either of emissivity $h(t)$ or temperature at surface $v(+0, t)$ i. e. $\varphi(t)$ is known, another is determined by the equation (10).

Finally, we would like to show the asymptotic properties of $h(t)$, $\varphi(t)$ as $t \to \infty$ and $t \to +0$. For a particular case when h is constant, it is

$$\sqrt{t}\,h\varphi(t) \to 1/\sqrt{\pi},\ \text{as}\ t\to\infty,$$

and

$$\varphi(t) \to 1,\ \text{as}\ t \to 0.$$

Now in general, by the physical meaning we may assume

$$\varphi(t) \to 0,\ \text{as}\ t \to \infty.$$

Therefore from (10)

$$\lim_{t\to\infty}\int_0^t \frac{h(u)\varphi(u)}{\sqrt{t-u}}du = \sqrt{\pi}$$

from which we deduce

$$\lim_{t\to\infty}\frac{1}{\sqrt{t}}\int_0^t h(u)\varphi(u)du = 2/\sqrt{\pi}. \qquad (12)$$

Since the continuity of $h(t)\varphi(t)$ for $t > 0$ should be secured in practical problems, from (12) we obtain

$$\sqrt{t}\,h(t)\varphi(t) \to 1/\sqrt{\pi},\ \text{as}\ t \to \infty. \qquad (13)$$

In the sequal, let $t \to +0$ be in (10). For the present case we may assume that

$$\varphi(t) \to 1,\ \text{as}\ t \to +0.$$

Hence from (10)

$$\lim_{t\to+0}\int_0^t \frac{h(u)\varphi(u)}{\sqrt{t-u}}du = 0.$$

Now if we put

$$\int_0^t \frac{h(u)\varphi(u)}{\sqrt{t-u}}du = g(t),$$

where $g(t) \to 0$ as $t \to 0$, then

$$\pi\int_0^t h(u)\varphi(u)du = \int_0^t \frac{g(u)}{\sqrt{t-u}}du = \sqrt{t}\int_0^1 \frac{g(t\theta)d\theta}{\sqrt{1-\theta}}.$$

Hence we deduce from this result that

$$\frac{1}{\sqrt{t}}\int_0^t h(u)\varphi(u)du \to 0\ \text{as}\ t \to 0.$$

If we assume the continuity or $h(t)\varphi(t)$, we have

$$\sqrt{t}\,h(t) \to 0\ \text{as}\ t \to +0.$$

These results explain the experimental results done by Prof. N. Nishiwaki, Engineering Depart., Tokio University (being pressed shortly) very well.

References.

(1) E. C. Titchmarsh: Theory of Fourier Integrals (Oxford), pp. 284–6, 1937.

(2) S. Bochner: Vorlesungen uber Fouriersche Integrale, pp. 19–21 (1932).

A Symmetrical Six-arms Waveguide Circuit for Microwave Bridge.

By Koichi SHIMODA.

Department of Physics, Faculty of Science, University of Tokyo.

(Read Oct. 22, 1949; Received Jan. 27, 1950)

§ 1. Introduction.

A symmetrical six-arms waveguide circuit [illegible] described which may be used as a microwave bridge for measuring reflection coefficients or impedances of microwave systems. The six-arms waveguide circuit was devised in 1948 by the aid fo S. Tomonaga's general theory of microwave circuits(1). This circuit shows tetrahedral symmmetry, having six waveguide openings.

A theoretical analysis has been developed for a perfect symmetrical six-arms waveguide circuit. The devised circuit has been built and tested. And it is shown that it can be used favorably for microwave bridge as predicted.

A so-called magic-tee(2) is generally used as a balanced circuit, which is often called a bridge circuit. But it is only a sort of compensated circuits, which requires calibrated attenuators for measuring reflection coefficients. Moreover, a simple E-H tee is not a magic-tee which requires matching rods or irises in the structure. Since the matching in the magic-tee arms is realised only for one certain frequency, the magic-tee may be used only within a limited frequency band of a few percent width.

On the other hand, because the six arms circuit does not require any matchiug component and its charcteristic is determined mainly by its geometrical symmetry, it may be used at any frequencies, provided the waveguide allows to transmit only one mode of waves through it. It is shown by theoretical treatment that the elements of the "characteristic matrix" of the six-arms circuit are determined entirely by measuring any one of the matrix elements.

§ 2. Characteristic Matrix of the Circuit.

The six-arms circuit was devised in 1948 in consideration of the "characterisic matrix" introduced by S. Tomonaga(1). And this is also one of the good examples of his theory. Though his theory treats general circuits of waveguides which may transmit many modes of waves, but practical waveguides are usually designed to transmit only one mode of waves. Therefore, we shall assume hereafter that the higher modes are cut off and the fundamental mode alone is to be considered. A theory of microwave circuits whose waveguides are restricted to one mode is described.

A waveguide circuit having some waveguide openings as terminals is considered. Some of the the waveguides may be concentric cables or Lecher wires, provided the radiation losses and coupling losses may be neglected. When the complex amplitude of waves in the waveguide is defined taking the time facter, exp $(j\omega t)$, so that the square of the magnitude of the amplitude represents total energy-flow in the waveguide, we may write

$$S_k = p_k^2 - q_i^2, \tag{1}$$

where S_k is the total energy-flow outward in the k-th waveguide; p_k and q_k represents the amplitude of the outgoing and incoming waves respectively.

Then the amplitude of an outgoing wave can be expressed by a linear combination of the amplitudes of incoming waves in the circuit.

$$p_i = \sum_i a_{ik} q_k \tag{2}$$

Here, $A = (a_{ik})$ is called the characteristic matrix of the waveguide circuit. By the reciprocity relation the characteristic matrix is symmetrical. That is,

$$a_{ik} = a_{ki}. \tag{3}$$

If the circuit losses can be neglected, the chracteristic matrix is unitary, and the next equation holds.

$$\sum_k \overset{*}{a}_{ik} a_{kh} = \delta_{ih} \qquad (4)$$

Where $\overset{*}{a}_{ik}$ denotes the complex conjugate of a_{ik}; $\delta_{ih}=0$ when $i \neq h$, and $\delta_{ii}=1$. Although the characterisic matrix of a waveguide circuit having n openings has n^2 elements, but the number of independent elements are less than n^2, since there exist above relations.

A magic-tee or a hybrid ring which has four openings is an excellent construction and widely used in microwave measurements. In practice, however, it has a defect of being frequency sensitive. Some trials to make it frequency insensitive proved to be failure, and it was found that if we use a six-arms circuit, it is possible to realise a better microwave bridge. The six-arms circuit is described in the following.

The regular polyhedron having minimun number of edges is a regular tetrahedron which has six edges. The antipodal pair of edges of the tetrahedron are orthogonal to each other, and the whole system is symmetrical for the three axses. Therefore, if we build a microwave circuit in the form of regular tetrahedron whose edges are opened and connected to rectangular waveguides as shown in Fig. 1, then the characteristic of this circuit will show good symmetry. That is to say, the characteristic matrix of this circuit will be simple.

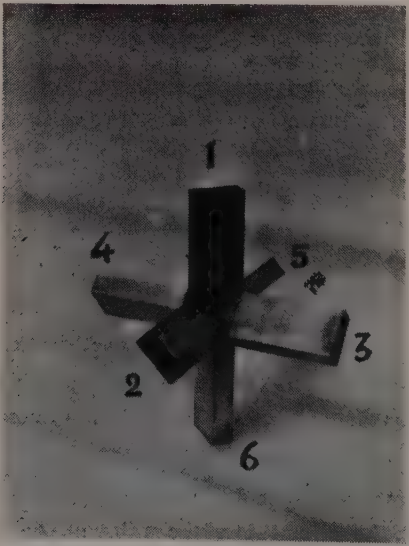

Fig. 1.
A symmetrical six-arms waveguide circuit.

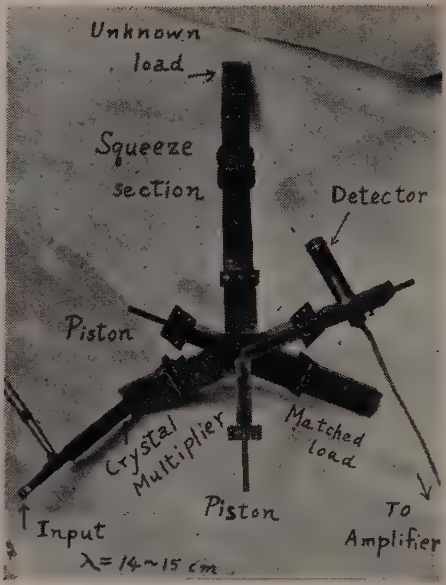

Fig. 2.
An arrangement of the waveguide bridge for 6200 Mc/sec.

It is seen from its geometrical symmetry that the three elements of the characteristic matrix of the circuit are zeros.

$$a_{16} = a_{25} = a_{34} = 0$$

Here, the waveguides are denoted as shown in Fig. 1. Also

$$a_{11} = a_{22} = a_{33} = a_{44} = a_{55} = a_{66},$$

and other elements are all equall in their absolute values.

As the phase of the waves in the waveguide is arbitrarily determined, the phase-reference-plane in the waveguide may be chosen so as to make the non-diagonal matrix elements, $a_{ik} (i \neq k$ and $i+k \neq 7)$, real. Then, from equations (3) and (4), it is shown that the elements, a_{ii}, are pure imaginary numbers.

In this way, the characteristic matrix of the symmetrcal six-arms waveguide circuit is represented as

$$A = \begin{Bmatrix} jr & a & a & a & a & 0 \\ a & jr & -a & a & 0 & -a \\ a & -a & jr & 0 & a & a \\ a & a & 0 & jr & -a & a \\ a & 0 & a & -a & jr & -a \\ 0 & -a & a & a & -a & jr \end{Bmatrix} \qquad (5)$$

and

$$r^2 + 4a^2 = 1. \qquad (6)$$

This ciruit is quite analogous to the Wheatstone bridge, and may be used as a microwave bridge for measuring reflection coefficients and for other applications. For example, it may be used as follows: the arm-1 is connected to a generator; the arm-6 is to a detector; the arm-2 and arm-3 are equally loaded; the arm-4 is loaded by a calibrated adjustable load; and arm-5 is loaded by an unknown impedance. Then the bridge is balanced when the unknown impedance and the adjustable load becomes equall for the operating frequency.

In the case when the diagonal element, $a_{ii}=jr$, equalls zero, this circuit plays a role of a perfect microwave Wheatstone bridge. But if not, it may be used as a microwave bridge as will be described.

§ 3. Analysis as a Microwave Bridge.

In microwave circuit, it is easy to use a nearly perfect reflection of variable phase, which is realised by moving a metallic piston in the waveguide. To avoid contact losses, a piston with quarter-wavelength choke is gederally used.

In order to vary the magnitude of the reflection coefficient, it is necessary to use a variable attenuator or a transformer, which is unavoidably accompanied by some phase shift. Besides, the calibration of an attenuator or a transformer is generall frequency dependent, and it is laborious to accomplish it precisely. And so, if possible, it is better not to use an attenuator or a transformer.

When the two arms of the six-arms circuit are loaded by lossless pistons, and one of the other arm is terminated by a matched load, it is possible to balance the circuit by adjusting pistons.

Let r_n be the reflection coefficient of the load in the n-th waveguide seen from the reference plane of the arm. Then the detector output becomes zero, when the following balancing condition is satisfied.

$$(r_2-r_3)[r_4r_5-1+jr(r_4-r_5)] = (r_4-r_5)[r_2r_3-1+jr(r_2+r_3)]. \tag{7}$$

If the arm-4 is terminated by a matched load, $r_4=0$; and if r_5 is unknown, equation (7) may be written as follows.

$$jr-\frac{1}{r_5}=\frac{r_2r_3-1+jr(r_2+r_3)}{r_2-r_3}. \tag{8}$$

When arm-2 and arm-3 are loaded by lossless pistons,

$$r_2=-\exp(-2j\theta_2), \text{ and } r_3=-\exp(-2j\theta_3),$$

where θ expresses the electrical length measured from the reference plane to the face of the piston in the waveguide. Using θ_2 and θ_3, the balancing condition is given by

$$jr-\frac{1}{r_5}=\frac{\sin(\theta_3+\theta_2)+r\cos(\theta_3-\theta_2)}{\sin(\theta_3-\theta_2)}. \tag{9}$$

In order to establish the bridge-balance for a certain load, it is not necessary to adjust both, r_2 and r_3. Therefore, we may set $\theta_2=\pi/4$ for example. Then,

$$jr-\frac{1}{r_5}=-(1+r)\tan(\theta_3+\frac{\pi}{4}). \tag{10}$$

Though the magnitude of the right-hand side of the above equation can be varied from $-\infty$ to ∞, it remains real. Therefore, it is required to adjust the phase of the unknown reflection coefficient using a phase shifter or other devices, so as to make the left-hand side of the equatihn (10) real. This is always possible, since $|r|$ is smaller than 1 and $|1/r_5|$ is greater than 1.

If the load to be measured is located at a distance $\lambda_g.\theta/2\pi$ from the phase reference plane in the arm-5,

$$r_5=r_L.\exp(-2j\theta_5),$$

where r_L is the reflection coefficient of the load at the point, ane r_5 is that of at the reference plane. When the bridge is balanced by adjusting θ_3 and θ_5, r_L is represented by

$$r_L=\frac{\exp(2j\theta_5)}{jr+(1+r)\tan(\theta_3+\frac{\pi}{4})}. \tag{11}$$

For practical measurement, experimental determinations of the matrix element, r, and the phase reference planes are required. Although there are several methods for the purpose, but the following method would be the simplest.

It is shown from the equation (7) that the bridge output becomes zero for any value of r_4 and r_5, if r_2 and r_3 obey the next equation.

$$\begin{aligned} &r_2 - r_3 = 0, \\ &r_2 r_3 - 1 + jr(r_2 \pm r_3) = 0. \end{aligned} \tag{12}$$

The bridge balance of this type can be obtained by using lossless pistions in arm-2 and arm-3. But it is now necssary to adjust the position of the both pistons. Putting

$$r_2 = -\exp(-2j\theta_2),\ r_3 = -\exp(-2j\theta_3),$$

equation (12) may be written as

$$\begin{aligned} &\theta_2 = \theta_3 + n\pi, \\ &\exp(-2j\theta_2) = jr \pm (1-r^2)^{\frac{1}{2}} = jr \pm 2a. \end{aligned} \tag{13}$$

In is shown by this result that the bridge-balance which is independent of r_4 and r_5 is found at four different pairs of positions of the pistons in the arm-2 and arm-3 within the interval of a guide wavelength long.

These bridge-balance can be experimentally determined, and the four positions of the piston can be scaled from an arbitrary point, which are denoted l', l'', l''', and l''''. Here

$$l''' = l' + \frac{1}{2}\lambda_g, \text{ and } l'''' = l'' + \frac{1}{2}\lambda_g.$$

And also it is shown from equation (13) that the position of the phase reference plane (where $\theta = 0$) is given by

$$l_0 = \frac{1}{2}(l' + l'') - \frac{1}{8}\lambda_g. \tag{14}$$

In this way, the phase reference plane for the two arms can be determined experimentally. If necessary, the reference plane for other arms may be determined by interchanging the roles of the arms.

The matrix element, r and a, may also be given by l' and l''.

$$\begin{aligned} r &= -\sin 2\theta' = -\sin 2\theta'', \\ \text{and} \quad a &= \pm\frac{1}{2}\cos 2\theta' = \mp\frac{1}{2}\cos 2\theta'', \end{aligned} \tag{15}$$

where $\theta' = 2\pi(l' - l_0)/\lambda_g$, and $\theta'' = 2\pi(l'' - l_0)/\lambda_g$.

§ 4. Experimental Results.

A symmetrical six-arms waveguide circuit was designed and tested at the wavelength near 4.8 centimeters, since it was easier to construct and test at about this wavelength.

The construction is of a form shown in Fig. 1 (without waveguide flange), which has been made of phosphor-bronze plates. In order to minimize circuit losses, it would be better to silver the waveguide. The cross-section of the waveguide is rectangular, and the inner dimension is 15×35 millimeters. The six arms are connected each other by four large and four small regular triangles. The inner dimension of the side of large and small triangles is 35 and 15 millimeters respectively. In the arms, there are no irises or other matching elements.

As already mentioned, this circuit is used as a microwave bridge, the arrangement of which is shown by a photograph in Fig. 2. The generator used is a crystal multiplier which generates third harmonics from 14 to 15 centimeter waves. The fundamental wave is generated by a mag-

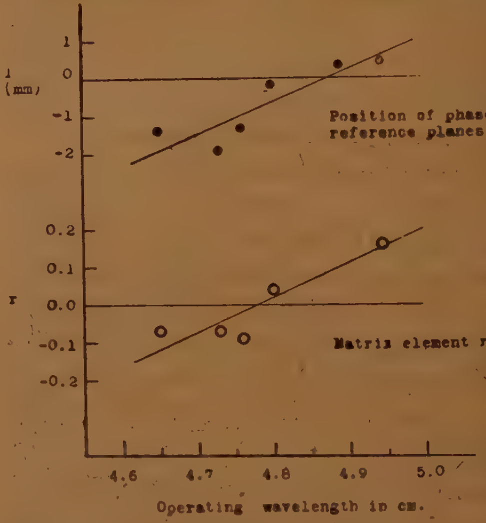

Fig. 3.
Observed characteristics of the wrveguide bridge.

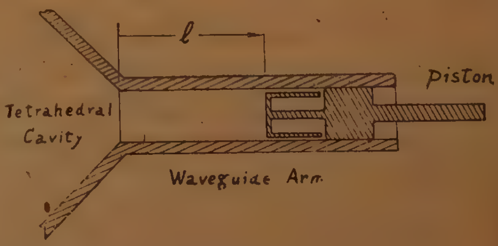

Fig. 4.
One arm of the six-arms circuit and a piston.

netron, ML-15 (produced by Japan Radio Company). The detector attatched to the opposite arm consists of a silicon-tungsten rectifier.

Two arms of the remaining four arms are loaded by shorting pistons (quarter wavelength choke section type), and the third is terminated by a wide band matched load, and the fourth is connected to a load to be measured through a squeeze section. The matched load is made of magnetite sand, filled tapered in the waveguide. The squeeze section is not a good phase shifter for measurement use. But it is simpler and appropriate for the preliminary test.

In order to determine the phase reference planes and the matrix elements. the waveguide of the arm-5 is opened and a small electric fan with many wings is rotated near the waveguide opening so as to vary the reflection coefficient of the arm-5. And by adjusting the two pistons, the bridge can be balanced for the time-varying load.

From the positions of the pistons when the bridge is balanced, the positions of the phase reference planes are determined by equation (14). The result of this model is shown in Fig. 3, as a function of operating wavelength. The positions are scaled from the openings of the polyhedral cavity, which is not resonating, as shown in Fig. 4.

The observed matrix element, r, is also shown in Fig. 3, as a function of wavelength. Since the positions of the pistons were measured by a calliper, and since the pistons were neither screwnor rack-and-pinion drived, there may be errors of about 0.2 millimeters. This causes the error of about 0.04 in the value of matrix element, r, which explains the fluctuation of the above result.

If the circuit is not perfectly symmetrical, the characteristic of the circuit will be seen different from different arms. In practice however, because of the above mentioned position errors, the asymmetry of the characteristic was not found in the measurement of this model.

The more accurate and precise construction with fine drive-mechanisms of pistons will enable to measure microwave impedances with sufficient accuracy. This microwave impedance meter seems to be a proper microwave measuring instrument.

References.

(1) S. Tomonaga: J. Phys. Soc. Japan, **2** (1947) 158; **3** (1948) 93.

(2) W. A. Tyrrell: Proc. I. R. E., **35** (1947) 1294.

On the Steady Surface Ripples of a Cylindrical Flow.

Yoshimasa WADA.

Yamanashi University.

(Read Nov. 8, 1949; Received Jan. 28, 1950)

When an obstacle is held stationary in moving fluid, or, on the contrary, a solid is moved forward with a definite velocity through still water, we see there a beautiful pattern of ripples and waves. These phenomena were investigated by many authors especially for the case of plane surface. Among them Lord Kelvin⁽¹⁾ gave a formula of the relation between the velocity of the obstacle v and k ($=2\pi/\lambda$), where λ is ripple-or wave-length, thus

$$v^2=\frac{Tk}{\rho}+\frac{g}{k}, \tag{1}$$

where T represents the surface tension and ρ the density of fluid and g is the gravitational acceleration. Thereafter Lord Rayleigh⁽²⁾ investigated mathematically the form of waves which occurs when the disturbances are given with pressure striking the surface along a straight line or at a point. Since the right-hand-side of (1) is a formula representing the velocity of surface ripples and waves, which gave him the foundation of his method of measuring the surface tension with ripples, the equation (1) means that we can observe only the ripples of wave-length corresponding to the velocity which is equal to that of the solid.

In the sase of cylindrical flow, similar phenomena are observed, and K. Prosad and B. N. Chosh⁽³⁾ utilizing these phenomena obtained the value 71.6 c.g.s. for the surface tension of water at 20°C by measuring the ripple length and velocity of flow and using Lord Kelvin's equation (1); of course, for their calculation, neglecting the term involving gravity, they used

$$W^2 = \frac{Tk}{\rho} = \frac{2\pi T}{\rho\lambda}. \qquad (2)$$

Neverthless, as these expressions are essentially to be applied to the flow, such that the surface of it is an infinitely wide plane, for the cylindrical flow they have to be used under some limitations. So that the author found a more general expression corresponding to (2), investigated the differenece between them, and compared them with the experimental results.

Using cylindrical coordinates with positive z-axis downwards, when the fluid has a common velocity W in that direction, the velocity potential is

$$\phi = AJ_0(ikr)\,e^{i(kz+nt)} - Wz. \qquad (3)$$

If we take a to be the mean radius of the cylinder, the form of surface is given by

$$r = a+\zeta = a+\alpha e^{i(kz+nt)}. \qquad (4)$$

For $r = a$,

$$-\left(\frac{\partial\phi}{\partial r}\right)_{r=a} = \frac{\partial\zeta}{\partial t} + W\frac{\partial\zeta}{\partial z}, \qquad (5)$$

so that $\phi = -\dfrac{(n+kW)\alpha}{kJ_0'(ika)}J_0(ikr)e^{i(kz+nt)} - Wz.$ (6)

Using (6) and the equation of pressure:

$$\frac{p}{\rho} = \frac{\partial\phi}{\partial t} - \frac{1}{2}q^2, \qquad (7)$$

we find, neglecting α^2,

$$\frac{T}{\rho}\left(k^2-\frac{1}{a^2}\right) = -\frac{i(n+kW)^2}{k}\,\frac{J_0(ika)}{J_0'(ika)}, \qquad (8)$$

or

$$(n+kW)^2 = \frac{T(k^2a^2-1)}{\rho a^2}\cdot\frac{ikJ_0'(ika)}{J_0(ika} \qquad (9)$$

If $W = O$, (9) becomes Lord Rayleigh's⁽⁴⁾ equation for the surface ripples of the cylindrical column of still fluid. On the contrary, if we take n to be zero, it represents a steady state, namely,

$$k^2W^2 = \frac{T(k^2a^2-1)}{\rho a^2}\,\frac{ikJ_0'(ika)}{J_0(ika)} \qquad (10)$$

In order to make this correspond to (2), dividing the both sides by k^2, we find

$$W^2 = \frac{Tk}{\rho}\left(1-\frac{1}{k^2a^2}\right)\frac{I_1(ka)}{I_0(ka)}. \qquad (11)$$

When k is finite and a increases to infinity, (11) takes the same form as (2); this is consistent physically with the fact that the cylindrical flow is reduced to a plane flow when its radius increases indefinitely. Thus we must use (2) in the case of very large value of ka, and when a is finite, we ought to take into account the correction facter for cylindrical case, a function of ka only,

$$f(ka) = \left(1-\frac{1}{k^2a^2}\right)\frac{I_1(ka)}{I_0(ka)}, \qquad (12)$$

First, we consider the variation of $f(ka)$ with the values of ka, and then we require the solution of (11), which is written as

$$W^2 = \frac{Tk}{\rho}f(ka) \qquad (13)$$

in simplified expression.

By mathematical tables for small values of ka and by asymptotic expansions for large values, (12) can be evaluated. The curve in Fig. 1 represents it, where, if $ka = 1$, $f(ka) = 0$, and with increasing ka, $f(ka)$ approrches to unity asymptotically, and $f(ka)$ differs from unity by about 6% for $ka = 10$ and about 1% ever for $ka = 50$.

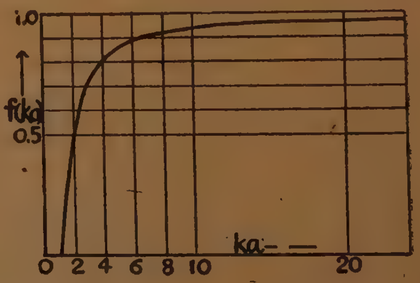

Fig. 1.
Curve of $f(ka)$.

In the second place, in order to get the solution of (13), we transform it as follows.

$$k = \frac{\rho W^2}{T f(ka)}. \qquad (14)$$

Since it involves a factor $f(ka)$ in the denominator it is not easy to solve, but as we have already obtained the values of $f(ka)$ for any value of ka, we can have graphically the desired relationship of ka and W as a family of curves having a as parameters. Fig. 2 represents such examples, where $T = 73$ and $\rho = 1$ in c. g. s. units. These curves are like parabolas, allhaving their vertexes on the k-axis, i. e. at $W = 0$, and the only one which represents (2), having infinitely large a, is strictly a parabola. It is in the lowermost. For finite a with decreasing W, k does not become zero but approaches to the finite value $1/a$, and, as the real jet in which the velocity of flow increases and the radius decreases downwards, in the upper portion as well as in the lower portion the differences from the case of plane flow cannot be so small that (2) may be applicable. In addition, since the velocity in (1) has a minimum value, when the velocity of flow is less than this limitation we can see any steady ripples and waves neither in front nor in rear of an obstacle. For cylindrical flow, on the contrary, as (15) holds there instead of (1), we can see steady ripples as long as W becomes zero, and at last the ripple length is given by the formula $k = 1/a$, i. e. $\lambda = 2\pi a$. It is very interesting that this ripple length was introduced by Lord Rayleigh as it gave the border-land between stable and unstable conditions for disintegration of jet.

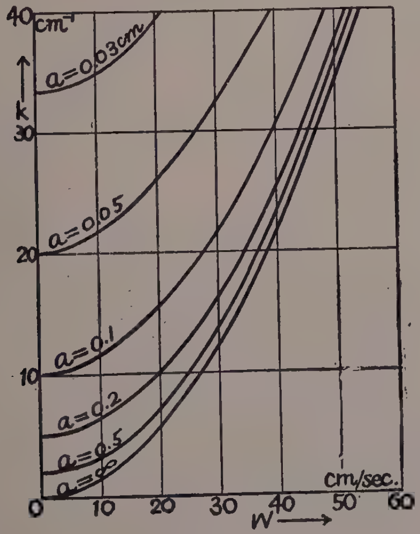

Fig. 2.
k versus velocity W, for various jet radius a.

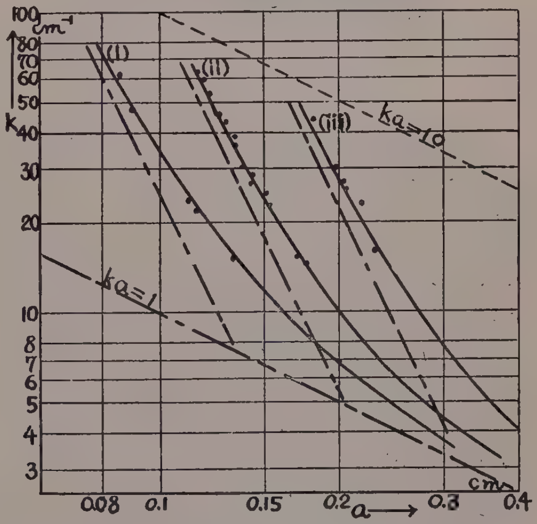

Fig. 3. k versus jet radius a, for various quantity of flow Q.
(i) $Q = 1.37$ cc/sec
(ii) $Q = 2.48$,,
(iii) $Q = 5.14$,,

Although Fig. 3 is convenient to consider theoretically the character of (14), it is difficult to compare with experimental results, as W and a do vary with the height in a same jet. So that we transform it again as to represent the relationship of a and k with parameter Q, the quantity of flow. This is Fig. 3, where the logarithmic scale is used. With increasing Q the curves shift right-and-downwards sustaining a similar form, and they have two asymptotes on the sides of larger and smaller values of ka; the former represents the equation (2) of Prosad and Ghosh for the same value of Q, and the latter $ka = 1$, and this is a common asymptote to all a—k curves. These sides correspond to the uppermost and lowermost portion of a jet. But, in real case, fluid is flowing down from an orifice of a finite cross section with finite velocity, and disintegration of fluid column occurs where the velocity increases over a certain value. So that what we can observe easily is the phenomena in the central portion where the curve of Fig. 3 deviates utmost from the two asymptotes.

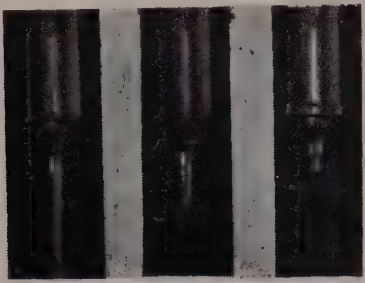
(i) (ii) (iii)

Fig. 4. (a) Q = 2.48 cc/sec.

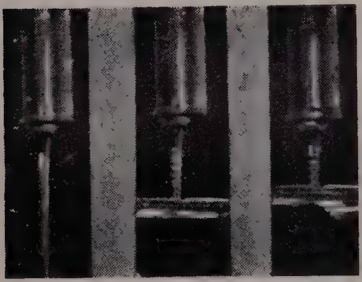
(i) (ii) (iii)

Fig. 4. (b) Q = 5.14 cc/sec.

In the case of real perpendicular jet, where a varies continuously, k also varies continuously. Such an aspect is illustrated in Fig. 4, where (i) is of an undisturbed jet in every case. By the influence of viscosity the ripple pattern cannot be observed on the whole surface of a jet at once, the height of the obstacle was varied a few times, thus the experimental values were obtained for the range as wide as possible. To get a and k from these photographs the following method was used. For example, the distances of the two succeding ridges of ripples, z_1 and z_2, were measured from the orifice. The mean position z of z_1 and z_2 was taken as the position of the ripple. And then in the undisturbed jet the radius a_0 at the distance z from the orifice was determined. Subtracting z_1 from z_2, ripple length λ was obtained, and k was taken as $2\pi/\lambda$. Since, for cylindrical flow of equation (4), the relationship of a and the radius of undisturbed flow a_0 is given by

$$a = a_0\left(1-\frac{1}{4}\frac{\alpha^2}{a_0^2}\right),$$

this equation was applied to get a from a_0. α was measured from the photograph for the same ripple. Thus a number of pairs of a and k for various portion on a jet were obtained. These values were plotted in Fig. 3 for comparison with the calculation. There are given three experimental examples, curves (ii) and (iii) corresponding respectively to photographs (a) and (b).

According to the above investigation, in order to utilize the equation of plane surface, we must pursue the measurement in the portion as low as possible, though it is very troublesome. In Fig. 3 the inclination of the variation of experimental values seems a little steeper than the calculated curve. Although this discordance is qualitatively explained by the effect of insertion of obstacle, for further arguments viscosity which is neglected in the calculation has to be taken into account and the precision of the experiments is to be increased.

I express my gratitude to Professors K. Honda and I. Imai in Tokyo University and Professor T. Yasaki in Yamanashi University for their kind instruction.

References.

(1) Lord Kelvin: Phil. Mag. **42**, (1871) 370.
(2) Loyd Rayleigh: Proc. London Math. Soc. **15**, (1883) 69.
(3) K. Prosad and B. N. Ghosh, Ind. Journ. Phys. **10**, (1937) 31.
(4) Lord Rayleigh: Proc. Roy. Soc. **29**, (1879) 71.

On the Phenomena of Burning of Insulators Caused by Gliding Spark Discharges.

By Seikichi SAITO.

Hitachi Central Laboratory.

(Received, July 22, 1949)

§ 1. Introduction.

The phenomenon that the surface of insulator becomes worse and is spoiled by the surface discharge is a dangerous matter in an practical case. Owing to the complexity of the phenomenon, however, its research is far from being completed(1).

Hitherto the many works about this problem seem to be chiefly concerned with the material of the insulator. However, in this paper, we try to examine analytically the burning phenomenon in connection with the forms of the spark discharge.

§ 2. The Forms of the Spark Discharge.

The surface burning of the insulator expands gradually by the repeated discharge, so that the phenomenon of the burning has been observed by repeating the spark discharge on the surface of insulating materials.

The spark discharge circuit (as shown in Fig. 1) consists of a repeating impulse voltage generator (a high tension magneto-generator is used in this experiment), variable resistance R, variable capacity C, and a gliding spark gap g (needle to needle). The forms of the surface discharge can be changed from one to the other, by controlling these variable elements. On the other hand, the spark is studied by taking the photograph of spectrum.

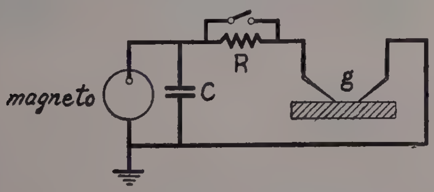

Fig. 1. Spark discharge circuit.

As is well-known the forms of the spark discharge can be classified into the following two forms.

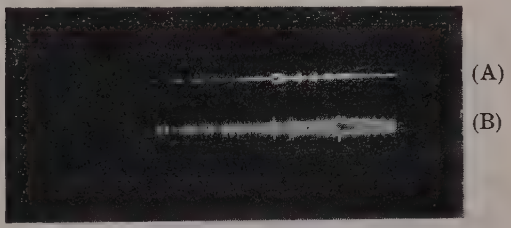

Fig. 2. Spectra of flame and flash discharge.
(A) g = 10 mm C = 360 $\mu\mu$F R = 10 kΩ
(B) g = 10 mm C = 360 $\mu\mu$F R = 0
Numbers of the repeated spark discharges are 96/sec in both cases.

(A) The flame discharge having the violet coloured and weak brightness all over the gap.

This form is appeared when R is large, and gives a band spectrum of the air (mainly N_2 and

Table I. The Insulator which are examined in our experiments.

Condensed Polymers	Phenol resin Xyrenol resin Anilin resin Phenol-furfurorol resin
Polymerized Polymers	Polystyrene Polyvinyl chloride Polymethacryl methyl ester Polyvinyl acetate Polyvinyl alcohol Polyethlene Paraffin wax
Gum	Ebonite Vulcanized gum vulcanize < 8 % 14 % 26 %
Cellulose and its derivatives	Fibre Acetyl cellulose Nitrocellose Benzil cellulose Ethyl cellulose Celluloide

N_2^+ band). This form corresponds to so-called "glow discharge".

(B) The flash discharge having the white coloured and very strong brightness all over the gap. This form appeares when R is small, and gives the line spectrum of the electrode metal (mainly spark line or arc-line). This corresponds to so-called "spark discharge"

Now, the experiments have been carried out how the surface burning depends on these discharge forms. The insulators, which are examined in our experiments, are listed in Table I.

§ 3. The Forms of the Surface Burning

(A) Flame Discharge.

When the material of the insulator is bakelite, the surface burning is classified into two forms. One of them occurs when the both electrodes are approached towards the surface (as shown in Fig. 3 (A), without contacting it. In this case, the flame appears all over the surface between electrodes, and the insulator burns being accompanied with a violent evaporation. At first, a dark brown groove begins to appear, and it becomes deeper and deeper. A remarkable feature of this burning is that the spark can be always observed on the surface, and yet the spark voltage is maintained at the constant value. The reason is considered to be the fact that, owing to its high temperature, the evaporation becomes active and the flaming up is followed in its scattering process, therefore no carbide remains there. This form of the burning is named "evaporation burning".

The other burning occurs when the both electrodes are brought into direct contact with the bakelite surface, as shown in Fig. 3 (B). In this case, at first, a yellow coloured fire spot with very strong brightness appears at the top of negative electrode, and then the spot moves gradually towards the positive electrode at the speed of about 2.5 mm/sec. The trace of the spot is carbonized and formed a shallow ditch. In this case the spark voltage falls down gradually, as if the negative electrode moves towards the positive one.

When the spot reaches the positive electrode, the spark voltage decreases suddenly, and the discharge current flows through the conductive carbonized ditch, so that the visible spark is no more observed. There exists a hyperbolic relation between the time for the disappearance of spark and the numbers of repeated sparks per second, as shown in Fig. 4.

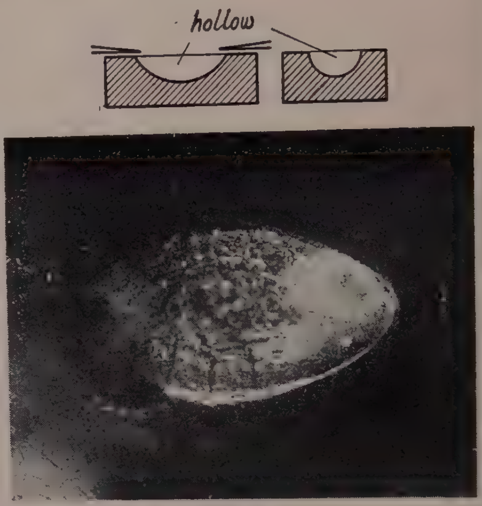

Fig. 3 (A).
Evaporation burning.

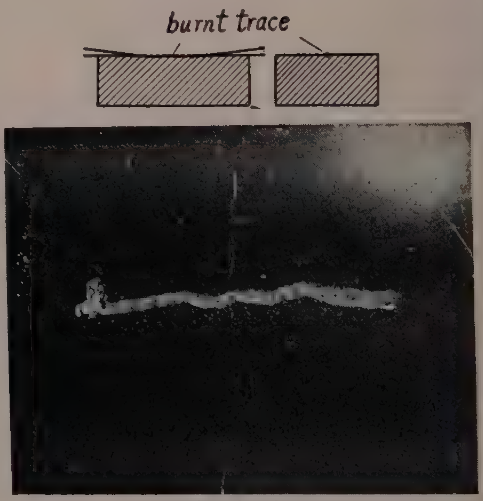

Fig. 3 (B).
Carbonization burning.

Considering from the fact that the spark voltage diminishes as mentioned above, the form of this burning is fatal for the purpose of insulation. This form of burning is named "carbonization burning".

The evaporation burning digs the insulator in the vertical direction, but the carbonization

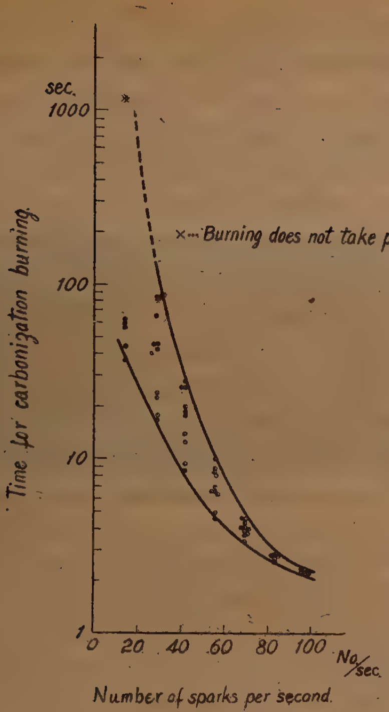

Fig. 4 Relation between the time for carbonization burning and the numbers of sparks per second.

burning expands along the surface of the insulator.

In the case of carbonization burning, the burning begins from the negative side. But, if the top of the negative electrode is separated only about 0,25 mm from the surface of bakelite, the "carbonization burning" can be prevented. On the contrary, even if the top of the positive electrode is separated from the surface, the carbonization burning occurs, unless the negative one is separated. In other words, the occurrance of this burning depends upon whether the cathode is in contact with the surface or not, and does not depend on the anode condition. These results are shown in Fig. 5.

In the case of other insulators, except gum in Table I, the burning takes place in the similar processes to those of bakelite. The difference among the burnings of the various materials may depend only on the speed of these burning process.

In the case of ebonite, however, the phenomenon of burning is somewhat different from that of bakelite. In the case of baklite, the evaporation burning is accompanied with the evaporation and the flame, but in the case of ebonite, the flame is more active, and is accompanied with the smoking. Moreover, the surface of ebonite between electrodes is used to fall in melting state. A carbonized substance that looks like soot, floats over that melted parts and is heaped up gradually, at last the spark current comes to flow through the floating carbonized substance and the spark voltage becomes extremely low. On the other hand, the carbonization burning in ebonite are as follows. At first, a bright spot appears on the negative side, and then the ebonite under the spot begins to melt

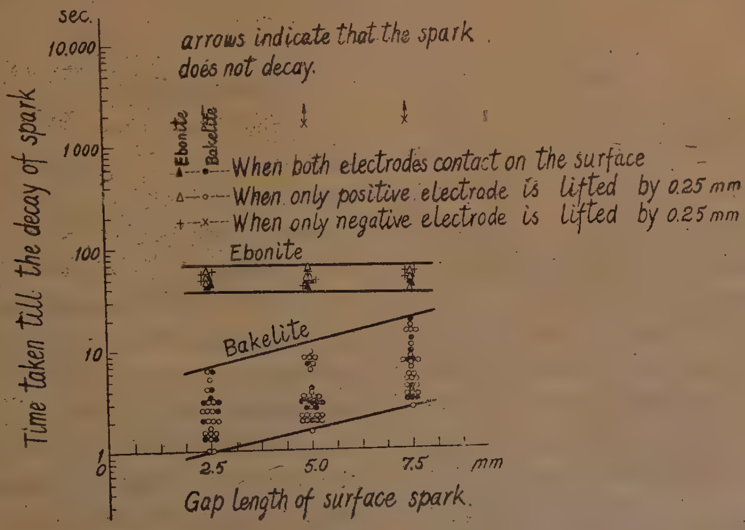

Fig. 5. Relation between the time for the decay of spark and the gap length.

and the melting part gradually extends towards positive side. However, the spot remains at the top of negative electrode without moving. And then a carbonized substance, which is floating on a melted part, is heaped up and comes to bridge over the gap between electrodes. Therefore the electric current flows across this bridge, and the gap becomes conductive.

As mentioned, in the above, the phenomenon of burning of bakelite is somewhat different from that of ebonite, and for this reason it is considered that the former soon carbonizes by the flame discharge, but the latter melts. Which type of the burning takes place depends only on the property of the material for the evaporation and the melting.

As above described, the fatal burning of the insulator by the surface spark discharge is caused by the bright spot which appears at the negative electrode. Therefore it is necessary to examine the conditions of the top of negative electrode in detail. Concerning these matters the following facts are found.

By connecting a thermo-junction (copper-constantan) to the electrode (as shown in Fig. 6,) the induced electro-motive-force can be measured, and its results are shown in Fig. 7. When the junction is connected to the negative electrode, a remarkable deflection is observed as shown in curve (I_-), but, on the contrary, when it is connected to the positive electrode, the deflection is very small as shown in curve (I_+). From these resluts, it is recognized that the top of negative electrode becomes very hot, and owing to its high temperature, the insulator which is just in contact with the negative electrode begins to burn from this point.

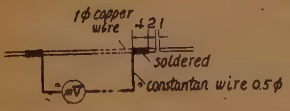

Fig. 6. Measuring circuit.

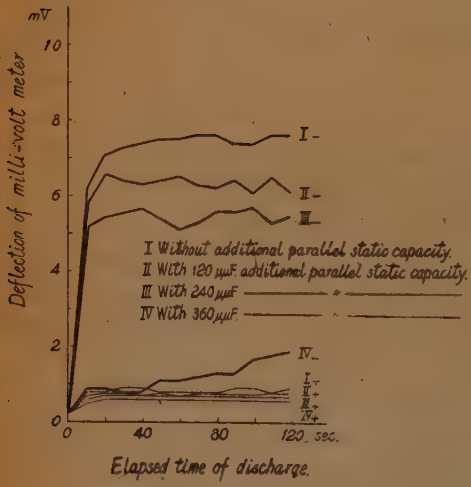

Fig. 7. Temperature rises of negative and positive electrodes.

In the case that the gap length is longer than 15 mm, a small bright spot often appears from the positive electrode too, and it moves fast towards the cathode, and collides with the other spot from the negative electrode. This positive spot appeares frequently when the carbonized particles or moisture adheres to the surface of the electrode or the insulator.

The appearance of the positive spot is not so stable as that of the negative one. Because, it seems that the appearance of the positive spot does not depend on the materials of the insulator, but only on the physical and chemical conditions of the surfaces of anode and insulator. For example, when we paint a comparatively heat proof paint on the surface, the bright spot from the positive electrode hardly appears, but the bright spot from the negative electrode burns the paint in the neibourhood and the carbonization ditch developes.

(B) Flash Discharge.

In the circuit shown in Fig. 1, if the resistance R, which is in series with the surface spark gap g, is zero and C is increased gradually, the flame discharge becomes to change into the flash discharge. In this case, the temperature of the cathode also becomes lower as shown in Fig. 6 II III and IV, and the burning phenomena of insulator, not only evaporation burning but also carbonization burning, do not occur whatever the material may be, (as shown in Fig. 8). However, the surface of insulator is engraved along the path of the spark as if the spark falls into the insulator. And the colour of the insulator in the ditch does not change. So that the formation of the carbonized ditch, and the sudden decrease of spark voltage cannot be observed. Therefore, the realization of "the harmless discharge" can be expected, by connecting the suitable capacity in parallel with the spark gap, or by widening the gap and raising the spark voltage.

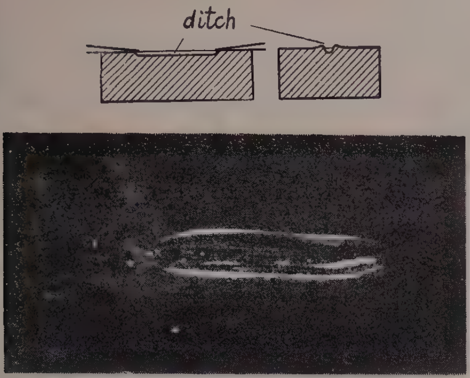

Fig. 8. Harmless deformation.

Furthermore, as well-known, the duration of the flash discharge is very short, but the flame discharge continues for several milli-seconds. Therefore, if the induction period—which exists in the case of ignition phenomenon—exists in the case of burning (that is, evaporation or carbonization), it is reasonable that the bruning does not occur in the flash discharge. On the other hand, the repeated discharge of the above two types are examined with the electrodes enclosed in a glass tube (as shown in Fig. 9). The temperature rise of gas in each case is obtained as shown in Fig. 10. From these results, it is understood that, in the case of the flash discharge, the temperature rise is remarkably smaller than that of the flame discharge.

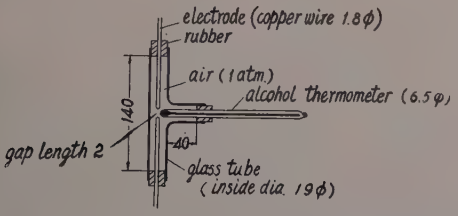

Fig. 9. Measurement of temperature rise.

To examine the temperature difference between the flash and the flame discharges in the same spark energy, C is maintained at a constant value. In the case of the flash discharge, as above description, the temperature rises of the electrode itself and of atmospheric gas are both small. So that, in the case of flash discharge, in spite of the fact that there is no loss of thermal energy in series-resistance R, the generation of thermal energy is smaller than that of the flame discharge On the other hand, it is evident from the result obtained in the spectrum analysis that the electrode is remarkably consumed by the flash discharge. Accordingly, in the case of flash discharge, the most part of the discharge energy seems to be consumed to evaporate the electrode metal. As is described above, in the case of flash discharge, not only the duration of discharge is short, but also thermal energy itself is small. These facts are one of reasons why the ability of burning is small.

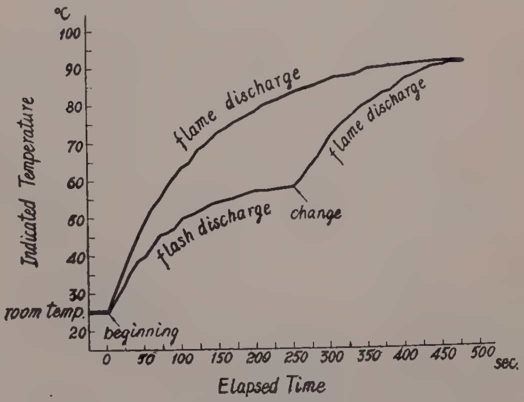

Fig. 10. Temperature rise of flame and flash discharges.

§ 4. Conclusion.

As the results of qualitative experiments on the burning of insulator by the gliding spark, it becomes to be clear that the states of burning are much dependent on the type of spark discharge.

In the case of the flame discharge, there are two kinds of burnings, the evaporation burning and the carbonization burning, and the degree of the damage caused by these burnings depends on the material of the insulator.

The former consumes the insulator, by the evaporation and the flame burning, but the spark voltage does not fall down. In the latter case, the carbonization begins from the negative side, and extends gradually, and at last the gap between the electrodes is bridged over by a carbonized material and becomes conductive. The carbonization burning begins to occur from the heated point on the negative electrode. And so, a great attention must be paid to this point.

In the case of the flash discharge, whatever the material may be, the burning phenomena are not observed, and the spark voltage is maintained at constant. For this reason we should consider not only the existence of the induction period for burning, but also the smallness of the thermal energy of the flash discharge. We should also remember that this fact suggests a possibility of some method to prevent the surface burning of insulators.

In conclusion, the author wishes to express his sincere thanks to Dr. Toriyama, director of our laboratory, for his advices.

Reference.

(1) H. H. Race and F. W. Warner; G. E. Rev., **38** (1935) 97.

Effects of the Transformation Process on the Thermoelectric Power of the Superlattice Alloy Cu_3Au.

By Takao SATO.

Faculty of Engineering, University of Kyushu.

(Received Dec. 12, 1949)

§ 1. Introduction.

The thermoelectric properties of the Cu_3Au superlattice alloy was first treated by Takagi and the writer.(1) There, we used the quenched specimen coupled with pure nickel wire and measured the thermo-electromotive force between 0°C and 100°C. And we found the relation between the electrical resistance and the thermo-electromotive force. It is easily seen that this method is not suitable for studying the behavior in the neighborhood of the transformation point. Now the writer has measured the temperature dependency of the thermoelectric power of the Cu_3Au superlattice by the same method as used by the writer(2) in the Ni_3Mn superlattice alloy.

The present investigation may be intersting from the point of view that the transformation mechanism of the Cu_3Au superlattice alloy has been more clearly understood, particularly, from the researches of Sykes and his collaborators(3) than other superlattice alloys.

§ 2. Experimental Details and Results.

The materials used were pure gold and electrolytic copper. They were melted together in Tammann tube of graphite and casted to a wire of about 1 mm in diameter and about 50 mm in length. The specimen was annealed at about 800°C for 2 hrs. and slowly cooled about 15 hrs.

Firstly, the electrical resistance was measured by the usual current-potential method, in order to examine the ordered state of the specimen. The results are shown in Fig. 1, where the ordinate represents the potential drop in mV. The curve I shows the variation of the resistance on cooling from 500°C to 330°C at the rate of about 1°C/min. and the curve II shows the result obtained in the process of heating from 330°C to 500°C at the same rate. From these curves it is seen that the transformation points are 375°C on cooling and 392°C on heating, respectively. The curve III shows the result obtained on cooling from 500°C to 250°C at the another rate of 10°C/hr. In this case, the transformation point is 381°C. It is interesting that a small flat part appears in the temperature region 10–15°C just above the critical point in these curves.

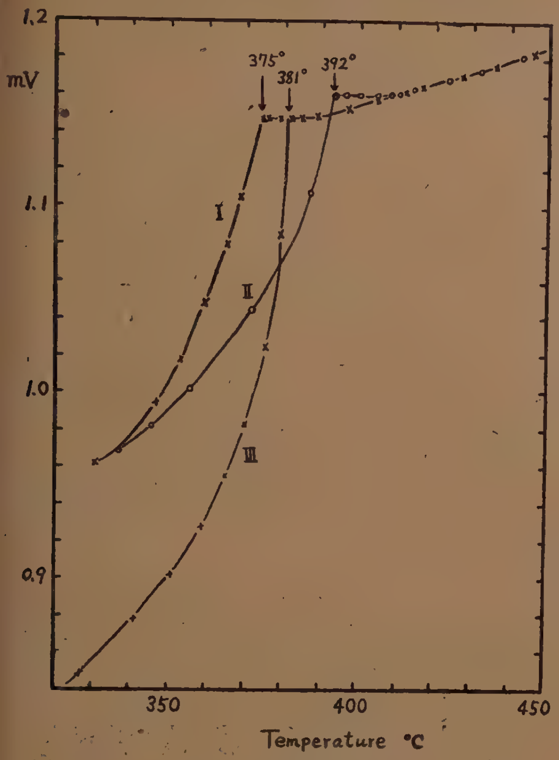

Fig. 1. The electrical resistance *versus* temperature curves.
Curve I : cooling at 1°C/min.
Curve II : heating at 1°C/min.
Curve III : cooling at 10°C/hr.

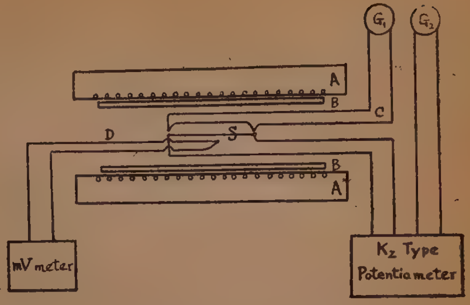

Fig. 2. Apparatus for the thermoelectric power measurement.
A : Nichrome wire winding furnace.
B : Copper pipe.
C : Pt-PtRh differential thermocouple.
D : Pt-PtRh thermocouple.
G_1 : Galvanometer for the temperature difference.
G_2 : Galvanometer for the thermoelectromotive force.
S : Specimen.

For the measurement of the thermoelectric power, the writer has adopted the method similar to that used for the measurement of anomalous behaviors of the thermoelectric power of the Ni_3Mn superlattice alloy(3). The essential features of the apparatus are shown in Fig. 2. The thermoelectric power was obtained by measuring directly the thermoelectromotive froce of the sample coupled with a platinum wire, a small temperature difference between two ends of the sample being kept. This temperature difference was about 1–3°C which occured in the furnace. We used a Pt-PtRh differential couple for the measurement of these temperature differences. The thermoelectromotive force and the temprature difference were measured, respectively, by two galvanometers (G_1 and G_2) which have a short period (5 sec) and a high voltage sensitivity ($1,8\times10^{-7}$V). The thermoelectric power was obtained from the thermoelectromotive force and the temperature difference at each temperature assuming the linearity relation. The results are shown in Figs. 3 and 4. Fig. 3 is the case of heating, in which the curves I and II are the results for the rates of 1°C/min. and 20°C/hr., respectively. Fig. 4 is the case of cool-

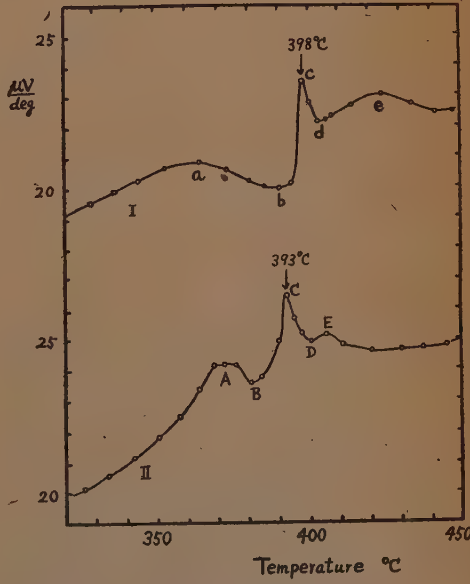

Fig. 3. The thermoelectric power *vs.* temperature curves on heating. Curve I : rate 1°C/min. Curve II : rate 20°/hr.

ing in which the curve I and II are the results for the rates of 1°C/min. and 20°C/hr., respectively. The sign of the thermoelectric power coupled with a platinum wire is positive.

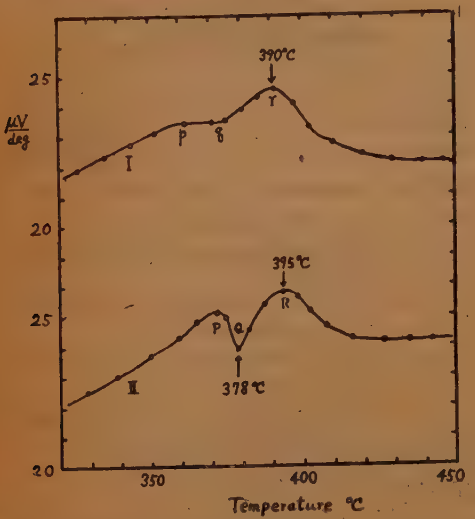

Fig. 4. The thermoelectric power *vs.* temperature curves on cooling. Curve I: rate 1°C/min. Curve II: rate 20°/hr.

There is a remarkable difference between Fig. 3 and Fig. 4. In Fig. 3, there are sharp maxima at 398°C in the curve I and at 393°C in the curve II. On the other hand, in the curve I of Fig. 4, there is a broad hill whose maximum point is about 390°C, but in the curve II there are a broad hill whose maximum point is about 393°C and a valley at about 378C°.

§ 3. Discussion of the Results.

As mentioned above, there are sharp peaks at 398°C and 393°C in the curves I and II of Fig. 3, respectively. Such temperatures are not the transformation points and it will be seen from the resistance *versus* temperature curve of Fig. 1 that the real transformation point exists just below these peaks. It is noteworthy that there is the chief change of the thermoelectric power near these peaks which correspond to the anomalous resistance regions just above the critical points as seen in Fig. 1. The behaviors of the heating curves in Fig. 3 depend on the heating rates used and it may be considered that *a*, *b*, *c*, *d*, and *e* of the curve I correspond to *A*, *B*, *C*, *D*, and *E* of the curve II, respectively.

In regard to the part of *a*, the variation is more broad in the case of 1°C/min. then in the case of 20°C/hr. But, on the contrary, the change from *b* to *c* is more steep in the case of 1°C/min. than in the case of 20°C/hr. and the change of *e* → *E* is similar to that of *a* → *A*.

In the case of Fig. 4, there is no sharp change as in Fig. 3. Though there is no such a distinct valley in the curve I as in the curve II, *p*, *q*, and *r* in the curve I seem to correspond to *P*, *Q*, and *R* in the curve II, respectively.

It may be considered that *A*, *B*, and *C* of the curve II in Fig. 3 correspond to *P*, *Q*, and *R* of the curve II in Fig. 4, respectively but in Fig. 4 there are no points corresponding to *D* and *E* in Fig. 3. The features of the part of *A* similar to those of *P*, but the features in the neighborhood of *C* are very different from those in *R*.

We may assume that the appearance of the parts *A* and *C* should be due to something in the growing processes of the long range order and the short range order, respectively. There are considerable differences between heating and cooling at the rate of 1°C/min. but the corresponding parts B and *Q* occur in the case of the rate of 20°C/hr. From this point of view, we may expect that the difference between heating and cooling decreases with the decreasing rate.

In the resistance-temperature curve the transformation points on heating and on cooling are slightly different, and there is no difference in other features. Whilst, it is while to notice that, as mentioned above, there is the essential difference between heating and cooling in the thermoelectric power *versus* temperature curve at the rates of 1°C/min and 20°/hr. From this fact it may be considered that the internal behaviors of the order → disorder process and the disorder → order process may have different effects on the physical quantity of the second order such as the thermoelectric power.

In the case of the Cu_3Au superlattice the thermoelectric power may be not appreciably influenced by the growing process of the local order. Consequently, on cooling we can not observe a fluctuating change of the thermoelectric power just above the critical temperature. Such a so-called pre-transformation phenomena can not be observed in the case of β-brass(4) also, weile this phenomena is clearly observed in the case of the superlattice alloys Mg_3Cd, MgCd, and $MgCd_3$ in magnesium-cadmium system(5). Therefore, no further detail discussions can be made on the fact that the pre-transformation phenomena in the case of the Cu_3Au superlattice is not observed.

Komar and Sidorow(6) found that the Hall coefficient changes its sign from minus to plus in the transformation of the Cu_3Au superlattice from the disordered state to the ordered one. As the themoelectric power is proportional to the electronic change e as the Hall coefficient, we will examine the sign of the thermoelectric power before and after the transformation.

Generally, an order of magnitude of the absolute thermoelectric power (A.T.E.P.) of ordinary metals and alloys is 1–10μV/deg. and a sign of the relative thermoelectric power (R.T.E.P.) depends on the kind of a coupled metal. The sign of the R.T.E.P. of the Cu_3Au superlattice coupled with a platinum wire is positive, as shown in Fig. 3 and 4. The A.T.E.P. of platinum is $-11.3\ \mu V$/deg. at 350°C and $-13.1\ \mu V$/deg. at 450°C. Since the A.T.E.P. of the Cu_3Au superlattice alloy is given by $S-|S_{Pt}|$ where S is the R.T.E.P. of the alloy measured and $|S_{Pt}|$ is the absolute magnitude of the A.T.E.P. of platinum, the sign of the A.T.E.P. of the Cu_3Au superlattice must be positive for both the ordered and the disordered states. Thus, this result is not consistent with the sign of the Hall coefficient.

According to Muto's(7) theoretical consideration on the electronic structure of the Cu_3Au superlattice, in the ordered state the Fermi surface cuts across some of the boundary planes of the Brillouin zone, since the first Brillouin zone of the disordered state is divided into zones of smaller volume in the ordered state. Owing to this change of the electronic structure in the transformation, it will be understood that the Hall constant changes its sign from minus to plus during the ordering process. Though the signs of the Hall constant and the thermoelectric power are both proportional to the electronic charge e, other factors which determine their signs are by no means identical. To calculate the thermoelectric power it is required to have the more accurate knowledge of the energy levels and the assumption that the electrons are free is not such a appropriate one in this case as in the Hall effect. For these reasons it may be considerered that the inconsistency in the signs of the Hall effect and the thermoelectric power is not essential and depends upon some special features of the electronic structure of the Cu_3Au superlattice.

Now, it is remarked that the temperature dependency of the A.T.E.P. of the superlattice alloy Cu_3Au decreases with rising temperature in the region of the disorderd state, as the A.T.E.P. of platium decreases with rising temperature. Therefore, in the present no further detailed discussions can be made on the problem whether the disordered state has the larger thermoelectric power than the ordered state or not, and on the dependency of the thermoelecric power of a superlattice alloy upon its degree of order as Wilson(8) has been pointed out.

Sykes and Jones(3) noticed that since a considerable amount of atomic rearrangement can take place before either the lattice structure or electrical resistance is affected, the detailed consideration of the transformatoin process is not appropriate without the measurement of other physical quantities, for example, specific heat. The present results of the thermoelectric power seem to show more obviously the complex behavior of the order-disorder transformation than the results of the speciffc heat. Since the specific heat has a simple meaning and is intuitive, quantitative discussions of the results of the specific heat can be made. On the contray, as the thermoelectric power depends, directly or indirectly, on the delicate states of the electronic structure of solids its maning is not so simple as that of the specific heat. The thermoelectric power should be affected by the delicate internal state of a specimen which can not be found by the measurement of the specific heat. However, the present knowledge of the thermoelectric power lacks in ability of examing the question that what sorts of internal changes in solids have any influences on the thermoelectric power.

The writer is indebted to Prof. A. Okazaki for his valuable discussions and to Prof. K. Omori for his kind encouragement and continued interest. The expense of this research has been defrayed from the Scientiffc Research Expenditure of the Educational Ministry.

References.

(1) Y. Takagi-T. Sato: Proc. Phys. Math. Soc. Jap. **21** (1939) 251.

(2) T. Sato: J. Phys. Soc. Jap. **3** (1948) 251.

(3) C. Sykes-H. Evans: J. Inst. Metals **58** (1936) 255.
C. Sykes-F. W. Jones: Proc. Roy. Soc. **157** (1936) 213.
C. Sykes-F. W. Jones: Proc. Roy. Soc. **166** (1938) 376.

(4), (5) Unpublished

(6) A. Komar-S. Sidorov: J. Phys. USSR **4** (1941) 552.

(7) T. Muto: Sc. Pap. I.P.C.R. **34** (1938) 377.

(8) A. H. Wilson: Proc. Roy. Soc. **167** (1938) 580.

On the Anomalies of the Small Angle Reflection of Cathode Rays from the Surface of a Single Crystal.

Part 3. The Effect of Absorption.

By Kazutake KOHRA.

Institute of Applied Science, Faculty of Eng'neering, Kyushu University.

(Received May 28, 1949)

Abstract.

The effect of absorption on the electron eiffraction is studied by introducing the imaginary potential into the Schrödinger equation. The interpretation of anomalies in the lower order reflections carried out in Part 2, is made more complete by considering the absorption. Finally, the several problems as to the lower order reflections are discussed.

§ 1. Introduction.

Electrons suffer inelastic scattering besides elastic scattering in a crystal and the effect of the former on the diffraction phenomenon is not negligible. However, it is so difficult to treat exactly the diffraction taking into accout both scatterings that the effect of inelastic scattering has been usually considerd by replacing it with absorption. There has been two principal methods of considering absorption in the dynamical theory, correspoding to the two types of the treatments described in Part 1(1). The one, adopted by Slater(2) and K. Moliére(3), introduces the imaginary potential into the Schödinger equation* and the other, adopted by Harding(6) correponds to those of Darwin(7) and Prins(8) in X-ray diffraction.

There are some inconsistencies and ambiguities among the results obtained by different authors. While the result of Slater(9) indicated that the position of the reflection is not shifted by the effect of absorption, that of K. Moliére(10), on the contray, indicates that it is shifted. In this paper we will carry out the calculation as exactly as possible by introducing the imaginary potential of variour types and examine the effect of absorption in details, and moreover, make the consideration of the small angle reflection, which has been done in Part 2, more complete.

---

* It corresponds to the one used by Kohler(4) and G. Moliere(5).

§ 2. Introduction of Absorption by the Aid of the Imaginary Potential.

The state of the electron in a crystal is given by the following equation.

$$\Delta\psi+\frac{8\pi^2me}{h^2}(E+V)\Psi=0. \tag{1}$$

As shown in Part 1, V presents the periodic field of the crystal and has usually the real value. If we add the imaginary constant term iv_0' to the real potential, we get the damped wave as follows: Suppose that only incident wave is strong in the crystal, its wave vector is given by

$$k_0=\pm\sqrt{K^2+v_0+iv_0'}, \tag{2}$$

in place of $\pm\sqrt{k^2+v_0}$, and we have the wave functions;

$$\phi_0 e^{i\vec{k}_0\vec{r}}=\phi_0 e^{i\sqrt{K_0^2+v_0}(\vec{s}_0\vec{r})}e^{-\frac{1}{2}\frac{v_0'}{\sqrt{K^2+v_0}}(\vec{s}_0\vec{r})} \tag{3}$$

where s_0 means the unit vector in the incident direction and the other symbols have the same meanigs as in Part 1. When v_0' is positive, we have the damped wave by adopting the (−) sign.

We introduce further the following periodic imaginary potential with a crude analogy;

$$\frac{8\pi^2me}{h^2}V=\sum(v_g+iv_g')e^{2\Pi i\vec{g}\vec{r}} \tag{4}$$

The procedure of the calculation is essentially the same as the one in Part 1. In the present case, however, the resonnance error δ is always complex and there is no strict selective reflection. When the thickness of the crystal L is sufficiently large, the reflction coefficient is always given by

$$\left|\frac{\phi_h}{\phi_0}\right|^2=|V_{12}(N-D-\delta)+(v_0+iv_0'-V_{11}+N^2-(D-\delta)^2)(N+D-\delta)|^2\div|V_{12}(N+D-\delta)+(v_0+iv_0'-V_{11}+N^2-(D-\delta)^2)(N+D-\delta)|^2 \tag{5}$$

and is independent of L*.

§ 3. The Value of the Potential.

Before we carry out the numerical calculation of the reflection coefficient by (5), each term of the various types of potentials involved in (5) is determined in the following way.

(A) The real potential.

The periodic terms of real potential v_g is given, as well known, in terms of the structure factor according to eq. (26) in Part 2,

$$v_g=\frac{8\pi^2me}{h^2g^2a^3}\sum_i e^{2\Pi i\vec{g}\vec{R}_i}(Z_g^i-f_g^I).$$

It is to be noted that the phase factors of some v_g are varied by the position of the surface. Now we consider two typical cases (Fig. 1.) In one case, the surface is assumed to coincide with the atomic plase (xy-Plane), in another case, we put it at the middle of two atomic planes ($x'y'$-plane).

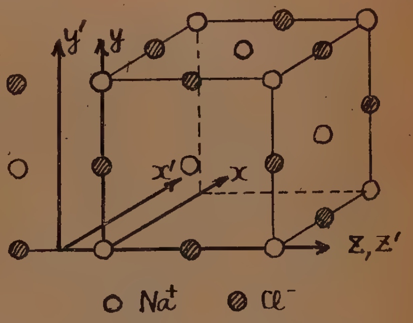

Fig. 1. The position of the surface.

For instance, there is no difference in the value of for g = (004n) between two cases;

$$v_g=\frac{8\pi^2me}{h^2g^2a^3}\times4\{(Z_g^{Na}-f_g^{Na})+(Z_g^{cl}-f_g^{cl})\}, \tag{7}$$

while, for g = (004n+2), there is a difference in the sign

$$v_g=\left\{\pm\right\}\frac{8\pi^2me}{h^2g^2a^3}\times4\{(Z_g^{Na}-f^{Na})+(Z_g^{cl}-f^{cl})\}. \tag{7'}$$

This fact has the influence on the tail part of the (00 4n+2) reflection, but not of the (004n) reflcection as shown in Fig. 2.

---

* When there is no absorption, this expression holds only whithin the range of selective reflection.

(B) The imaginary potential.

(a) The constant potential.

Suppose that the amplitude of the incident wave decreases to $1/e$ in traveling a distance l by absoption, and we obtain the following relation from eq. (3);

$$v_0' = \frac{2\sqrt{K^2+v_0}}{l}, \qquad (8)$$

for the accelerating voltage of about of 40 kv, we get

$$v_0' \doteqdot \frac{400}{l}. \quad (l \text{ in } A) \qquad (8)$$

The value of v_0 can be determined half-experimentally from eq. (9).

(b) The periodic term v_g'.

The procedure of determining the values q_G' which is theoretically acceptable, is not yet known to us. We assume now the following two methods of determining its value.

(i) First, we consider the value of v_g' as proportional to the corresponding term of the real potential as adopted by K. Molière, that is,

$$v_g' = v_g \times \frac{v_0'}{v_0} \qquad (9)$$

(ii) In the other method, we represent v_g' in terms of the generalized structure factor by the crude analogy with the representation of v_g in terms of the structure factor as follows;

$$v_g' = \frac{8\pi me^2}{h^2 g^2 a^3}\sqrt{\sum_i \sum_m \sum_n |f_g^{mn}|^2}, \qquad (10)$$

where $\sum_i$ means the summation over the all atoms in the unit cell and $\sqrt{\sum_m \sum_n |f_g^{mn}|^2}$ is the so-called generalized structure factor, the table of which is given by Heisenberg and Bewilogua⁽¹²⁾*.

§ 4. Numerical calculation of the reflection coefficient.

The reflection coefficient and resonnance error δ for the (002) and (004) reflections have been calculated as a function of N for the several cases in which the various types of the imaginary potential are introduced besides the usual real one. Fig. 2 shows the numerical results on the (002) reflection for various values of the

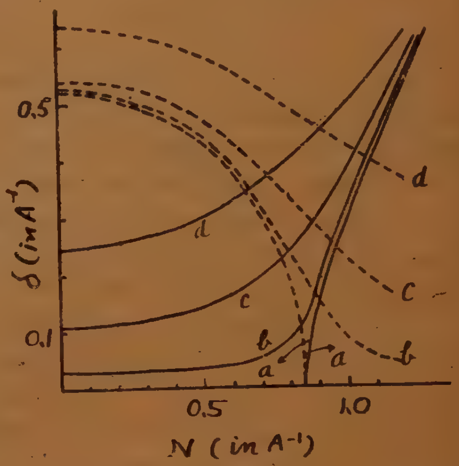

Fig. 2. (a).
— : The real part of, - - - - - : The imaginary part of δ.

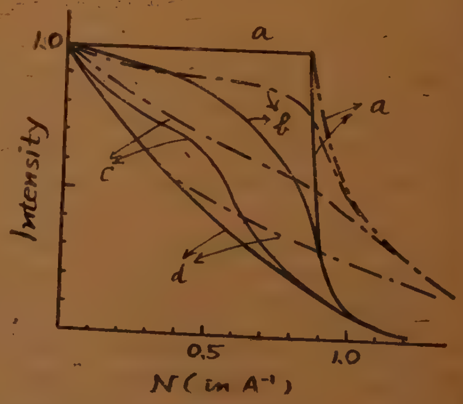

Fig. 2. (b).
δ and reflection coefficient as a function of N for different values of v_0'.
— : Surface at ($x'y'$-plane), — - — - — : at (xy-plane). $V_{11} = -0.261$, $V_{12} = \pm 1.645$, $v_0 = 1.87$.* (a) $v_0' = 0$, (b) $v_0' \doteqdot 0.1$, (c) $v_0' = 0.4$, (d) $v_0' = 1.0$.

---

* In the present case, $\sum_i$ is used instead of $\sum_i \exp(-2\pi i \vec{g}\vec{R}_i)$, as it is assumed that there is no phase relation among the inelastically scattered waves. The generalized structure factor is the one for the isolated atom, although it seems to be more suitable to use the one for the crystal. According to Pisardnko⁽¹³⁾ who calculated the corresponding quantity to ours using Frenkel's excitation function, v_g' terns out to be negligibly small. This fact seems to suggest that the assumptions of this type of the imaginary potential is meaningless. But, as our intention is to study if the essential feature of the intensity curve is affected by various types of the imaginary potential, the values determined in the above way will be of some use.

* $v_0 = 1.87$ corresponds to $E_0 = 7.2$ volts. The values of v_0' in (b) (c) and (d) corresponds respectively to $l = 2{,}000{,}500$ and 200 A.

constant imaginary potential v_0'. In Fig. 3 and 4, the periodic terms of imaginary potential v_g' are taken into account besides the constant term v_0'. Fig. 5 shows the result on the (004) reflection for various types of imaginary potential.

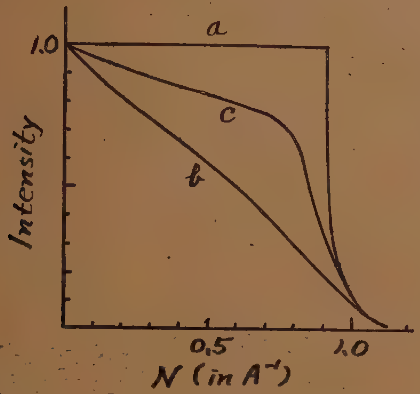

Fig. 3.
$V_{11}=0, V_{12}=-(v_{002}+iv'_{002})=-(-1.485+iv'_{002})$, $v_0=1.87$**. (a) no absorption, (b) uniform absorption $v_0'=0.4$, (c) periodic absorption, $v_0'=0.4$, $v'_{002}=v_{002}\,v_0'/v_0=\pm 0.312$.

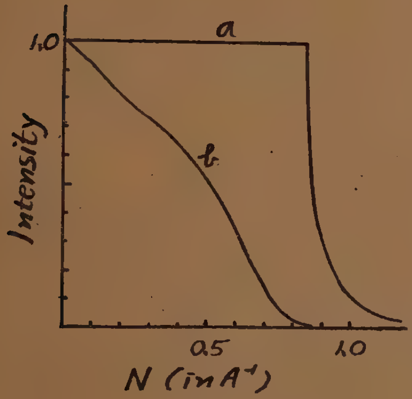

Fig. 4.
v_g' are determined in terms of the genelalized structure fector. (a) no absorption, the same one as (a) in Fig. 2, (b) $V_{11}=-0.75+0.16i$, $V_{12}=-1.79-0.32i$, $v_0'=0.4$.

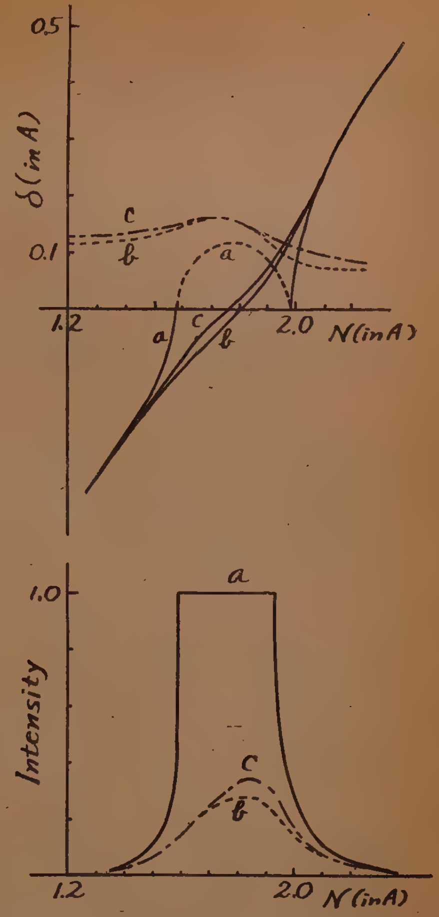

Fig. 5. δ and reflection coefficient. $V_{11}=0, V_{12}=-(v_{004}+iv'_{004})=-(0.612+iv_{004})$ $v_0=1.87$*; (a) no absorption, (b) uniform absorption, $v_0'=0.4$, (c) periodic absorption, $v_0'=0.4$. $v'_{004}=v_{004}\cdot v_0'/v_0\doteq 0.131$.

§ 5. The correction for the apparent mean inner potential.

The actual intensity curve can be obtained by considering both effects of absorption and the effectiveness of the incident beam striking the surface. The latter effect has already considered in Part 2. It may be concluded that generally the peak of reflection shifts from the center of selective reflection, except the lowest order reflection. By the use of eqs. (19) (20) and (22) in Part 1, we obtain the new correction for the apparent mean inner potential;

$$\Delta E=\frac{8\pi^2 me}{h^2}(V_{11}+0.8|V_{12}|), \qquad (11)$$

** All v_g and v_g' except $g=(000)$ and (002) are taken to be zero for the sake of simplicity.

In Fig. 3 and 4, the surface is put on $x'y'$-plane.

* $v_g=v_g'=0$ ($g\neq(000), (004)$).

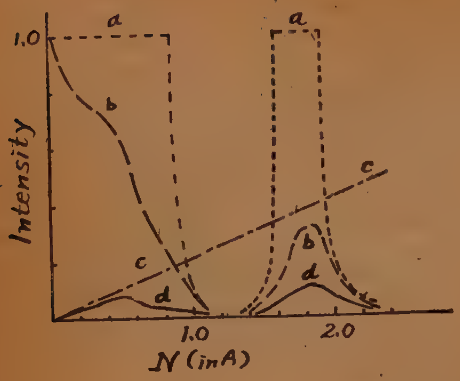

Fig. 6. The intensity curve with the consideration of the effectiveness of the incident beam. (a) no absorption, (b) $v_0' = 0.4$, (c) effective beam, (b) the curve to be expected from (b) and (c).

only the first term of which was considered in Part 1. The correction for the lowest order reflection must be oftained immediately from the curve in Fig. 6. The new correction values for the apparent mean inner potential are compared with the previous and the experimental data of Yamaguti(14) in table I and Fig. 7. It is seen that the anomalies at the lower order reflections are qualitatively explained*.

Table I. The correction value. (in volts).

order of reflection	Yamaguti's result	Old correction	New correction
002	6.95	(−1.00)	3.6
004	1.64	0.93	1.77
006	0.48	0.50	0.83
008	0.11	0.28	0.49
0010	0.31	0.17	0.29
0012	0.12	0.12	0.18

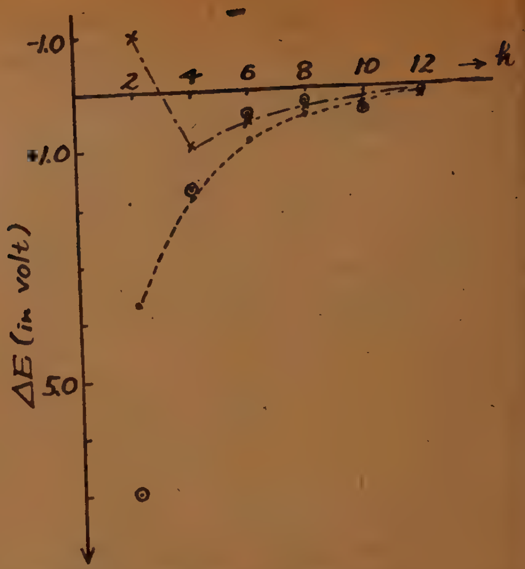

Fig. 7. The correction for the apparent mean inner potential for each order reflection.
⊙ : Observed value, × : Old corrected value,
● : Our new corrected value.

§ 6. Discussions.

(a) It is concluded from the above figures that the increasing value of absorption generally decreases the reflection. Furthermore, there seems not to be essential difference in the results among various assumptions made on the imaginary potential, although a problem what kind of imaginary potential is theoretically most acceptable, remains unsolved.

(b) In the (002) reflection, the peak which is actually observed in the experiment cannot be expected from the theory in any type of imaginary potential, but by taking into account the effectivenses of the incident beam.

(c) According to our result for (004) reflection, the peak of the intensity curve shift towards the upper limit of the range of selective reflection for the uniform absorption as well as for the periodic one. This result agrees with that of K. Molière, and not with that of Slater. The disagreement with that of Slater may be considered to arise from the poorness of his approximation.

(d) The width of reflection is decreased by a small value of absorption as most authors mentioned, while, it becomes broad surely for a large value of absorption as Slater pointed out. Furthermore, it is broadened by taking account of the effectiveness of the incident beam as seen in Fig. 6. As for the experimental results, Kikuchi(11) and Beeching(17) observed the width 10–20 times that to be expected from the simple dynamical theory, on the other hand, Miyake's result(18) agrees approximately with the prediction of the theory. In fact, other causes than absorption such as the adsorbed layer and the irregularities of the spacings near the surface will have their influences upon the width of reflection. In the present stage, it seems not to be possible to enter quantative discussions on this problem.

---

* In our calculation of the intensity curve, the value of the mean inner potential 7.28 volt is used as the most probable, juding from the results obtained by various methods(15). This value is considerably different from 8.48 volts by the Yamaguti's experiment, the data in which is compared with ours. However, these values have not so much influence with the correction value itself.

(e) As seen in Fig. 2, the tail part of the intensity curve is influenced by the position of the surface. The potential near the surface, in fact, would be more complicated and have its influence upon the tail part.

(f) The correction value for the lowest order reflection is still smaller than the one expected from the experiment. The discrepancy may be caused by the following conditions; As there are many small step-like projections on the surface, the part of transmission increases and the effect of refraction will be reduced.

In conclusion the author should like to express his sincere thanks to Prof. Shinohara for his guidance and Prof. Muto and Prof. Nogami for their kind advices and encouragements during the course of this work.

References.

(1) K. Kohra and K. Shinohara: Jour. Phys. Soc. Jap. **4** (1949) 155.
(2) J. C. Slater: Phys. Rev. **51** (1937) 840.
(3) K. Molière: Ann. d. Phys. **34** (1939) 461.
(4) M. Kohler: Berliner Ber. Phys.-Math. **Kl, XIX** (1935) 1.
(5) G. Molière: Ann. d. Phys. **35** (1939) 272 and 297.
(6) J. W. Harding: Phil. Mag. **23** (1937) 271.
(7) C. G. Drawin: Phil. Mag. **27** (1914) 675.
(8) J. A. Prins: Zeits. f. Phys. **63** (1930) 477.
(9) J. C. Slater: cf. (2).
(10) K. Molière: cf. (3).
(11) K. Kohra and K. Shinohara: cf. (1).
(12) W. Heisenbering; Phys. Zeits. **32** (1931) 737.
L. Bewilogua: Phys. Zeits. **32** (1931) 740.
(13) N. Pisarenko: Phys. Zeits. d. Sowj. **7** (1935) 26.
(14) T. Yamaguti: Proc. Phys.-Math. Soc. Jap. **23** (1941) 433.
(15) S. Miyake: Proc-Phys.-Math. Soc.-Jap. **22** (1940) 666.
(16) S. Kikuchi: Sci. Pap. I. P. C. R. **24** (1935) 225.
(17) R. Beeching: Phil. Mag. **20** (1925) 841.
(18) S. Miyake: Sci. Pap. I. P. C. R. **26** (1935) 261.

Short Notes

On the Rate of Nucleation of Ice.

By Hirobumi OURA.

Institute of Low Temperature Science, Hokkaido University.

(Received Jan, 6, 1950)

The supercooling of water is a common phenomenon which we meet frequently. It has been believed that the freezing of supercooled water starts from points called nuclei and the freezing does not occur in pure water which contains no nuclei. In like manner, production of ice crystal by sublimation in air has been believed to need sublimation nuclei. But the experiment by R. S. Johannsen(1) about freezing of supercooled water and the experiment by V. J. Schaefer(2) about production of snow in supercooled fog showed that nuclei appeared spontaneously in supercooled water or in supersaturated water vapour even if there were no nuclei. These spontaneous nuclei must be very small particles of ice and the probability of production of such small particles by statistical thermal fractuation may be fairly large. The author calculated the rate of nucleation using the equation derived by O. Turnbull and J. C. Fisher(5), and explained quantitatively the results of experiments of Johannsen and Schaefer. The interfacial free energy between ice and water and that between air and ice were also calculated.

According to Johannsen's experiment, pure water can be supercooled by −20°±1°C, and it begins to freeze only when it has been cooled below this critical temperatur. It is noted that the width of this critical temperatur is very narrow.

Schaefer moved about a copper rod cooled to various temperatures below 0°C in artificially produced water fog of temperature about -15°C. He found that small crystals of snow appeared in the fog when the temperature of the copper rod was below −39°C. He concluded that the sublimation nuclei of ice were produced spontaneously of air supersaturated with water vapoure were decreased to −39°C or more.

According to Turnbull and Fisher, the number of nucleation per second r^* in a system of N molecules is

$$r^* \sim NkT/h.\exp[-(\Delta F^*+\Delta f^*)/kT],$$

where ΔF^* is a maximum value of $\Delta F=(Ai^{\frac{2}{3}}+Bi)$ kT. ΔF is the difference between the free energy of a ice particle composed of i molecules before freezing. $Ai^{\frac{2}{3}}kT$ is the interfacial free energy and $BikT$ is the bulk free energy difference in absence of free surface. Δf^* is the free energy of activation when a nucleus of i molecules and a molecule of water or water vapour combines to a nucleus of $i+1$ molecules. Δf^* is neglected in the following calculation.

In case of nucleation in supercooled water BkT is the difference between free energy of water and that of ice and is deduced from the vapour pressures of ice and water. A is assumed to be 3.6 at −20°C in order to be consistent with the experimental results. This is the same thing as to put the value of interfacial free energy between ice and water to 18.5 erg/cm². Johannsen cooled the water in a vessel at its bottom and let the water freez. The author considered it suitable to take N as number of water molecules in 20 molecular layers attached to the bottom of the vessel and r^* calculated is shown in Table I.

Table I.

t°C	r^*/scc
−19	4×10^{-3}
−20	3
−21	8×2^2

At −19°C it takes about 5 minutes for one nucleus to be made, but at −20°C about 3 nucleus is made per second and at −21°C about 800 nucleus per second. From this result we can understand the fact the spontaneous nucleation can or cannot occur practically with such a slight difference of temperature as one degree in the neighbourhood of −20°C.

To explain the results of Schaefer's experiment, the calculation is performed similarly. The values of BkT at various temperatures are calculated, assuming the vapour to be cooled suddenly with its pressure in equilibrium with that of the supercooled water at −15°C. The interfacial free energy between ice and air is taken as 98.5 erg/cm² and the value of A is determined. 98.5 erg/cm² is the sum of the free energy of the surface between air and water and that of the interface between water and ice which the author assumed above as 18.5 erg/cm². As N, the number of watervapour molecules in 1000 cubic centimeter is considered, r^* thus calculated is shown in Table II. From this we can explain the critical temperature −39°C.

Table II.

t°C	r^*/sec
−38	4×10^{-3}
−39	1
−40	2×10^2

The phenomena that sufficiently supercooled water and water vapour can make themselves the nucleus of ice crystal and that these phenomena occur or not with a slight difference of temperature, can be explained quantitatively. The interfacial free energy between air and ice

98.5 erg/cm² and that between ice and water 18.5 erg/cm² may not be far from the truth.

References.

(1) R.S.Johannsen; Science **108** (1948) 652.
(2) V.J.Schaefer: Chem. Rev. **44** (1949) 291.
(3) O.Turnbull and J.C.Fisher: J.Chem. Phys. **17** (1949) 71.

On the Anomalous Dielectric Properties of Mixtures of Lead Titanate and Strontium Titanate.

By Shoichiro NOMURA and Shozo SAWADA.

Institute of Science and Technology, University of Tokyo.

(Received March 1, 1950)

Recently, it has been discovered experimentally that many of the perovskite-type crystals, namely, $NaCbO_3$, $KCbO_3$, $NaTaO_3$, etc⁽¹⁾. and tungsten oxide WO_3⁽²⁾ are ferroelectric substances, as in the case of barium titanate which is well-known to have spontaneous polarization in certain regions of temperatures. In this connection it should be noted that Matthias pointed out the experimental conditions for a crystal to be ferroelectric and emphasized that barium titanate is not so particular kind of ferroelectric substance⁽¹⁾.

On the similar viewpoint to Matthias, we have been studying the dielectric properties of solid solutions of $BaTiO_3$ & $SrTiO_3$ and $BaTiO_3$ & $PbTiO_3$ and the Curie points of these mixtures have been found to become lower for the former and higher for the latter in comparision with that of pure $BaTiO_3$.

Now it is quite interesiting to work out the behaviours of solid solution of $PbTiO_3$ & $SrTiO_3$, since we may expect for it to have rather different anomalous properties from those of the already known substances described above, because of the strong coupling between Pb^{++} and Sr^{++} and of their interactions with Ti^{++++} and O^{--} involved in the mentioned crystals.

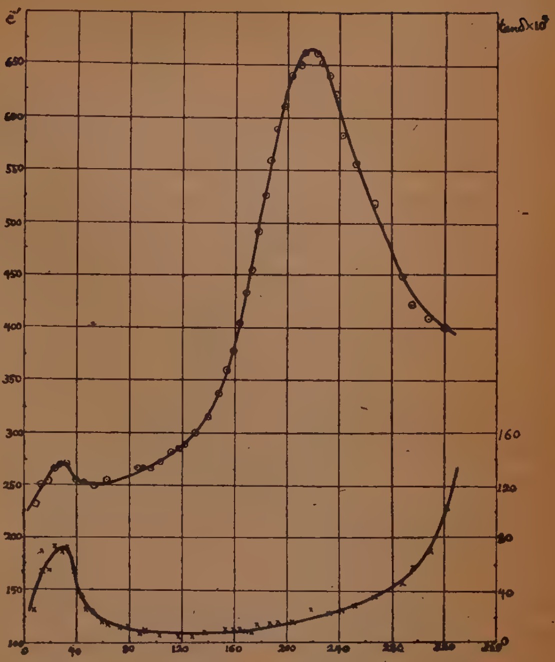

Fig. 1. ⊙..... ε' temperature ×..... tan δ

Samples are made from $PbTiO_3$ and $SrTiO_3$ powders. These are mixed, pressed into disk, and then fired at about 1200°C by electric furnace. Fig. 1 shows the temperature dependencies of both permittivity and loss factor of the sample (50% $PbTiO_3$+50% $SrTiO_3$) from room temperature to 300°C, being measured at 940 KC. As seen in Fig. 1 there are two anomalous point, in this region, similar to those of $BaTiO_3$. Although the permittivity is about 250 at room temperature, it becomes 2.6 times of the room temperature value at the upper Curie point of about 218°C. At the lower point of about 35°C, a discontinous change of permittivity occours, and, further, above the upper Cnrie point, Curie-Weiss law of permittivity is substantiated experimentally for its mentioned substance, namely,

$$\varepsilon' = \frac{C}{T-T_c},$$

where C is a constant, being equal to 0.94×10^5 deg. in our case⁽³⁾.

Fig. 2 shows the relation between Curie temperature and mixing weight-percentage. With decreasing weight-percentage of $PbTiO_3$, the upper Curie point is observed to displace rather linearly to the lower temperature side, while,

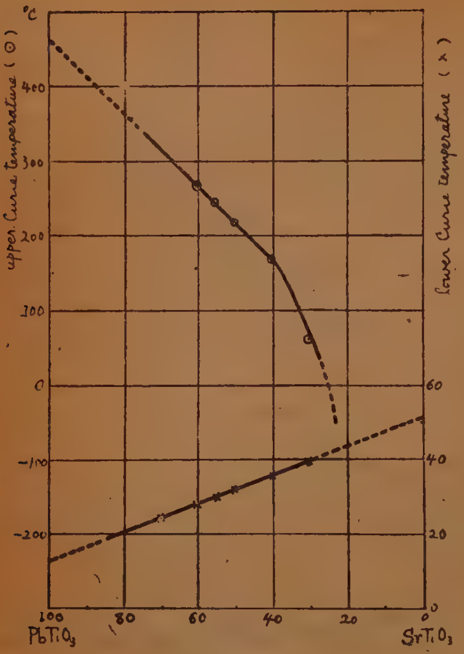

Fig. 2.

lower one to the higher temperature side, together with the predominance in the peak value of permittivity at the lower Curie point. For the sample of (30% $PbTiO_3$+70% $SrTiO_3$), the two Curie points tend to nearly coincide at about 50°C.

Unfortunately, we cannot make sure the existance of Curie point for pure $PbTiO_3$ by our present method of measurement because of its large loss factor prevailing at higher temperatures.

Hysteresis phenomena of polalization with respect to the applied field appear below the upper Curie temperature, which phenomena are able to be clearly observed by the use of cathode ray oscillograph.

Thermal properties of the mentioned substance, i. e. their specific heats and thermal expansions were also measured, showing anomalies at two Curie points in a similar way to the case of electrical properties.

These experimental results seem to show that $(Pb\text{-}Sr)TiO_3$ is ferroelectric substance as in the case of barium titanate. Details of our results will be reported shortly in this Journal.

References.

(1) B.T.Matthias, Phys. Rev., **75** (1949). 1771.
(2) B.T.Matthias, Phys. Rev., **76** (1949). 430.
(3) T.H.Van Santen and G.H.Jonker, Nature, **159** (1947), 333.

On Fast Neutron in Cosmic Rays.

By Giichi Yoshii.

Central Meteorological Observatory.

(Received May 23, 1950)

To measure the number of fast neutrons in cosmic rays, an arrangement as Figure 1. was designed, consisting of G.M. counter trays (upper row), a proportional counter (middle) and a G.M. counter (lower). The fast neutrons, which do not cause discharge in the upper counters, will knock out protons in the thin paraffin layer (1 cm thick) between the upper and the middle, and by counting these protons with the proportional counter, we are able to measure the number of fast neutrons indirectly. Accordingly electric circuits are made of the coincidence between the middle and the lower in order to restrict the direction of these protons in the vertical, and the anticoincidence between the upper and the above coincidence.

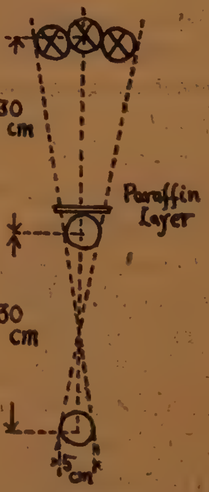

Fig. 1.

A description is given of the details of the instrument. The proportional counter which contains 25 mm Hg Argon and 75 mm Hg Ether was found very satisfactory, i. e. the variation of ionmultiplication was about twice, when the counter voltage was raised by 100 volts in usual range (700 to 1300 volts)(1). This is connected directly to the linear amplifier, which is a three stage one using pliotron (FP 54) as first tube to ensure high grid resistance and small capacity, and has the amplification factor 2.10^3. The pulses of about 5.10^{-4} to 10^{-1} volts can be measured by this amplifier without distortion. The coincidence circuit is a usual one with two one-shot multivibrater, and has the resolving time of the order 10^{-5} sec. The efficiency of the anticoincidence with neon tubes in place of Rossi tubes is nearly 100% and in the condition of our experiment its blocking effect was not more than 0.5%.

Now, the fast neutrons will be regarded almost equal to the knocked out protons, for they are ejected only in the vertical on account of the coincidence method. Then the upper limit of the fast neuton energy is settled by discriminating the pulses amplified, and is about 100 MeV. The lower limit depends on the proton energy, penetrating the walls of both coincidence counters and is no less than 15 MeV. Considering the ionisation losses of the protons in the paraffin layer, the energy range of the fast neutron will have to be 20 MeV to 200 MeV in place of the above range. The experimental results are as follows:

$$N_1=2.1\pm0.04 \text{ counts/hr} \quad N_2=2.5\pm0.4 \text{ counts/hr}$$
$$N_3=10.0\pm0.3 \text{ counts/hr}$$

Here N_1 is the counting without paraffin, and shows the background counting; N_2 is the counting with paraffin, and shows the sum of the background and the fast neutrons; N_3 is the counting of only the coincidence counter, and shows the sum of the background and the protons in cosmic rays. Accordingly $N_2-N_1=0.4\pm0.4$ counts/hr shows the counting of the fast neutrous, and $N_3-N_1=7.9\pm0.3$ counts/hr $=1.4\times10^{-4}$ counts/sec cm^2 steradian, shows the counting of the protons(2)(3). But as, in the former, the efficiency has to be taken account of, which is the product of the cross section between proton and neutron, and the number of the protons in the paraffin layer, so it is estimated as 20 ± 20 counts/hr.

In conclusion, the number of the fast neutrons in these energy ranges will be not more than several times that of the fast protons. However, owing to the great number of the countings of background, we cannot deduce correctly the absolute value of fast neutrons and the relation between the protons and the neutrons.

The experiment was made at the Meteorological Research Institute.

Refereuces.

(1) M.E. Rose and S.A. Korff: Phys. Rev. **59** (1941), 850.
(2) C.D. Anderson: Rev. Mod. Phys, **20** (1948) 334.
(3) D.H. Perkins: Proc, Roy. Soc. **191** (1949) 325.

On the Electrical Conductivity of Magnetite.

By
Hiroshi WATANABE and Noboru TSUYA.

Research Institute for Iron, Steel and Other Metals.
Tohoku University, Sendai.

(Received May 25, 1950)

It has been known that magnetite undergoes transformation at −160° c.c.a., at which it shows a markable change in magnetization, 2 sharp maximum of specific heat and also some anomalies in other physical properties.(1) Several attempts have been made by a number of Japanese theoretists(2) to account for this transformation, but there remain some points to be criticized, either in interpretation of the experimental data on the one hand, or in the interpretation of the data themselves on the other. For instance, we may notice the following points: (1) Since this transformation spreads over a certain range of temperature, it must be expected that the same behavior will be found in that of conductivity. But it is difficult to find such breadth of transformation from the data on the electrical conductivity. Further, if the transformation is of the first kind, obscured by the inhomogeniety of substance or by some other reasons, some type of jump in the value of electrical conductivity at the transformation may be expected. Such jump has been found only in one of Verwey's(3) data and not in others. (2) Previous theories, whether they are based on the localized electron model or the itinerant electron picture, have interpreted the change of magnetization at the transformation temperature to be that of the spontaneous magnetization. But since this change vanishes in high magnetic fields, it must be an inevitable conclusion from this standpoint that the transformation itself vanishes with such field. If it were true, the conductivity curve in high fields would be a straight line having no anomalies on it. In other words, a very wide variation of conductivity with the applied magnetic field—amounting to several thousands percent—would be expected.

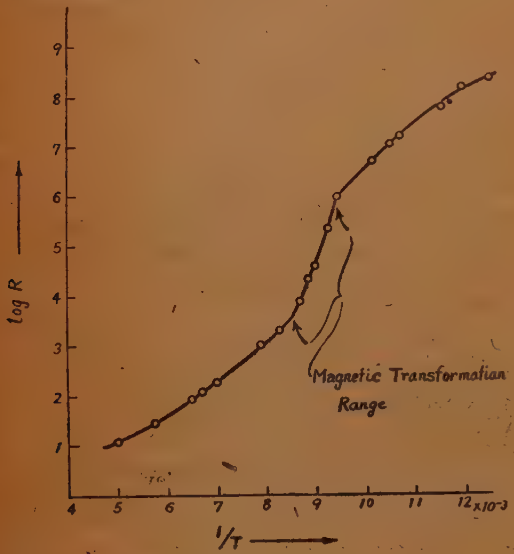

Fig. 1. Single Crystal of Magnetite from Kamaishi, Iwate Prefecture.

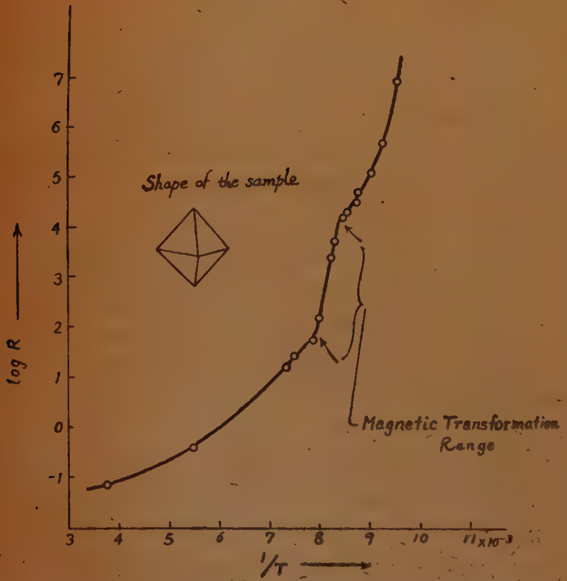

Fig. 2. Single Crystal of Magnetite from Nagasaki Prefecture.

The purpose of our experiment is to make clear these mentioned points. So we measured first the temperature dependence of the electrical conductivity of natural magnetite with special precautions near the transformation temperature. The results obtained are given in Figs. 1 and 2. Fig. 1 refers to a single crystal of magnetite from Kamaishi, Iwate Prefecture, while Fig. 2 to a specimen from Nagasaki Prefecture, whose shape is also shown in the figure. We have found it difficult to obtain correct data of conductivity for poly-crystals, because of the grain boundaries which may act as series resistances in the measurement. In this respect we believe that the sample in Fig. 2 contains no such cracks.

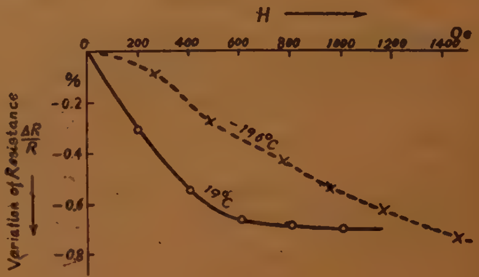

Fig. 3.

As can be seen from the figure, the transformation begins at −154° c and is completed at −146° c and the activation energy of conductivity of the lower temperature side is 0.16 ev. while that of the higher temperature side is 0.069 ev. A jump of about 10 times in the value of conductivity is also found in the figure.

Secondly we have measured the variation of conductivity with the applied magnetic field. This is shown in Fig. 3. The magnetic field has little influence on conductivity both below and above transformation temperature.(4) We interpret this fact as indicating that the transformation cannot be wiped out by the applied magnetic field. This may be corroborated by the measurements on thermoelectromotive force, magnetostriction and specific heat in high fields which data will be reported in the future.

We are indebted to the Ministry of Education for the research grant and to Drs. K. Honda and T. Hirone for their supervision.

References.

(1) P. Weiss and R. Forrer: Ann. d. Phys. **12** (1929) 276.
T. Okamura: Sci. Rep. Toh. Univ. **21** (1932) 231.
(2) T. Hirone and N. Tsuya; Riken-iho **23** No. 7 (1944) 177 (in Japanese).
T. Nagamiya: Kagaku **14** (1944) 87 (in Japanese).
K. Yoshida: Bussei-Ron Keokyu **12** (1948) 14 (in Japanese).
M. Shimizu: Read on April, 11, 1948 at the Meeting of the Phys. Soc. Jap.
H. Shimazu and K. Yoshida: Nippon Butsuri-Gakkaishi: **4** (1949) 74 (in Japanese).
(3) E.J.W. Verwey: Nature **144** (1939), 327.
(4) Similar results have already been obtained by Y. Shirakawa: Phys. Rev. **60** (1941) 835.

Long Beaded Counters for X-Ray Measurements.

By Itaru NONAKA and Zitsuo SHIMAZU.

Matsuda Research Laboratory, Tokyo Shibaura Electric Co.

(Received May 27, 1950).

Recently Geiger-Müller counters are frequently used in X-ray studies of crystal structures. The most efficient method is to use a long counter letting the X-rays to pass through in the axial direction. For example, a counter which is 20 cm in length and contains 150 mm Hg of argon and 15 mm Hg of C_2H_5OH vapour has a quantum efficiency of 56 per cent for CuKα line (1.54Å). In such a counter, however, the counting losses due to the dead time (of the order of 10^{-4} sec.) of the counter become considerable when slightly intense X-rays are measured.

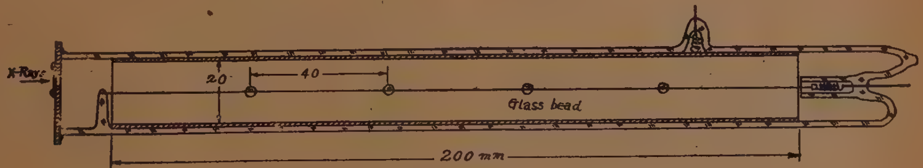

Fig. 1.

To reduce the above counting losses to a considerable extent we tried to use a long counter having several glass beads on its central wire. In such a beaded counter the discharge along the central wire can not spread beyond the beads(1) and is constricted within the section between two adjacent beads. Therefore, a secondary electron created even within τ seconds (dead time) after the preceding one has produced a discharge can be counted so long as it is created in any section other than that of the preceeding electron. A rough consideration indicates that the counting losses of a beaded counter of n sections are $1/n$ of those of a non-beaded one.

The counter constructed by us is shown in Fig. 1. The length of the cathode is 20 cm and the number of sections is five. The filling gas is a mixture of argon at 152 mm Hg and C_2H_5OH vapour at 15 mm Hg. We also contructed a couuter of the same dimensions as above but has no glass beads, and compared the counting losses of these two counters. The method of the measurements is as follows; the absorption by thin mica sheets of a CuKα_1 X-ray beam monochromatised by a calcite crystal is measured by the above two counters respectively.

The results of the measurements are shown in Fig. 2. In the case of the non-beaded counter, at counting rates higher than about 30000/min. counting losses appear as deviations from the straight line and at 60000/min. the losses amount to as much as 14 per cent. From these values of counting losses we obtained the dead time of the counter to be 1.2×10^{-4} sec. On the other hand, in the case of the beaded counter the point of 60000/min. lies strictly on the straight line indicating no obvious counting losses are present. We used a scale of 64 circuit for recording the counter pulses and it saturated at a counting rate of about 75000/min., so we could not measure at higher counting rates than about 60000/min..

In addition, the absorption coefficient of mica

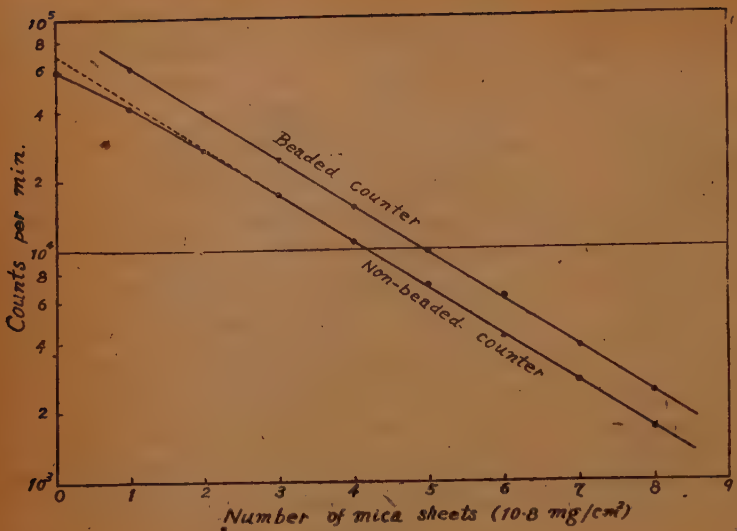

Fig. 2.

for CuKα_1(1.537Å) was obtained to be $\mu = 44.2$ cm²/g or 124 cm^{-1}($\rho = 2.8$ g/cm³). This agrees with the value of Williams(2) $\mu = 120$ cm^{-1} in the limits of our accuracy of measurements.

Theoretical considerations on the counting losses of beaded counters will be reported in future.

This mork is indebted to the Ministry of Education for the research grant.

References.

(1) H. G. Stever: Phys. Rev. **59** (1941), 765.
(2) J. H. Williams: Phys. Rev. **44** (1933), 146.

On Sneddon and Fulton's Solution for the Irrotational Flow of a Perfect Fluid Past Two Spheres.

By Isao Imai.

Department of Physics, Faculty of Science, University of Tokyo.

(Received June 9, 1950)

Recently Sneddon and Fulton [3] have dealt with the irrotational flow of a perfect incompressible fluid past two spheres by the use of Weiss' formula [4]. They have obtained a closed expression, in terms of elementary functions, for the velocity potential in the general case of arbitrary relative position and magnitude of the two spheres. Further they have considered in some detail the special case in which the uniform flow takes place in the direction parallel to the line joining the centres of the two spheres. Thus they have obtained the expressions for the pressure distributions on the spheres as well as for the resultant forces acting on them.

In view of the fact that the results of previous investigators, e.g. Endô [1] and Mitra [2], on the same subject were all given in the form of infinite series (involving Legendre's functions), Sneddon and Fulton's result would seem very remarkable. However, it seems to the present writer that there are unfortunately some misunderstandings in their application of the Weiss formula.

The Weiss formula reads as follows. If the irrotational flow of an incompressible, inviscid fluid, characterized by a velocity potential $\phi_0(x, y, z)$, is disturbed by the introduction of the sphere with equation

$$x^2+y^2+z^2 = a^2,$$

then the velocity potential of the disturbed flow is given by the expression

$$\phi(x, y, z) = \phi_0(x, y, z)+\phi_1(x, y, z), \qquad (1)$$

where the perturbation term ϕ_1 is defined in terms of the original potential function $\phi_0(x, y, z)$ by the equation

$$\phi_1(x, y, z) = \frac{a}{r}\phi_0\left(\frac{a^2x}{r^2}, \frac{a^2y}{r^2}, \frac{a^2z}{r^2}\right) - \frac{2}{ar}\int_0^a \lambda\phi_0\left(\frac{\lambda^2x}{r^2}, \frac{\lambda^2y}{r^2}, \frac{\lambda^2z}{r^2}\right)d\lambda \qquad (2)$$

and $r^2 = x^2+y^2+z^2$.

Sneddon and Fulton consider the case in which two spheres, one (A) of radius a with its centre at the origin, and the other (B) of radius b with its centre at (α, β, γ), are streamed past by a uniform flow of velocity U in the direction of the x-axis. For this purpose they take

$$\phi_0 = -Ux - \frac{1}{2}Ub^3(x-\alpha)\{(x-\alpha)^2+(y-\beta)^2+(z-\gamma)^2\}^{-3/2} \tag{3}$$

as the unperturbed potential and calculate the perturbation potential ϕ_1 by means of (2). Since ϕ_0, as given by (3), is nothing other than the velocity potential for a uniform flow past a single sphere (B) of radius b with centre at (α, β, γ), it might at first sight appear that their analysis would lead to a correct result. But really, the Weiss formula is only applicable to an infinite flow region which is to be disturbed only by the introduction of the sphere $r=a$. Thus the sphere B should not be regarded as the boundary of the flow field. In fact, (3) is the velocity potential for the uniform flow in the presence of a doublet at (α, β, γ), and so the result of application of the Weiss formula gives only the flow past a sphere $r=a$ in the presence of a doublet at (α, β, γ). Hence, the sphere B will no longer be along stream lines.

The above-mentioned situation may most clearly be seen in the figures in Sneddon and Fulton's paper, showing pressure distributions on the sphere A, for the special case in which the line of centres of the two spheres is parallel to the undisturbed flow. Thus a strange fact is observed that when the two spheres are situated very near to each other stagnation and then reversal of flow direction take place on the surface of the sphere. Such a flow pattern, which would be quite inconceivable for flow past two spheres, can be readily understood for flow past a sphere in the presence of a doublet at a small distance behind it.

Thus, Sneddon and Fulton's result does not present a correct answer to the problem of two spheres. However, it may be expected to give some useful informations on the interaction of a sphere and a nearly spherical body placed in a uniform flow. In particular, if the two bodies are not too close to each other, their solution may be regarded as a good approximation to the flow past two spheres. Indeed, the shape of the second body is expected to become increasingly nearer to a true sphere, as the distance of the doublet from the sphere becomes larger.

References.

(1) Endô, D.: Proc. Phys.-Math. Soc. Japan **20** (1938), 667.

(2) Mitra, S. K.: Bull. Calcutta Math. Soc. **36** (1944), 31.

(3) Sneddon, I. N. and Fulton. J.: Proc. Camb. Phil. Soc. **45** (1949), 81.

(4) Weiss, P.: Proc. Camb. Phil. Soc. **40** (1944), 259.

On the Perfect Velocity Focusing Mass Spectrogtaph.

By Mitsuo Sakai.

Department of Physics, Tokyo University.

(Received June 16, 1950).

Recently the present author performed several preliminary experiments on a new type of mass spectrograph. Fig. 1 shows a schematic longitudinal section of this apparatus. The ions are produced at one end of the axis of the cylindrical chamber and first accelerated radially by the grid. Then they are deflected by the second electric field which is applied normal to the first direction. Thereafter they fly the equipotential space and at last reach the receiver. In the space of the separation, there is uniform magnetic field which is excited by magnet coils and the direction of this field is parallel to the second electric field, that is, to the axial direction.

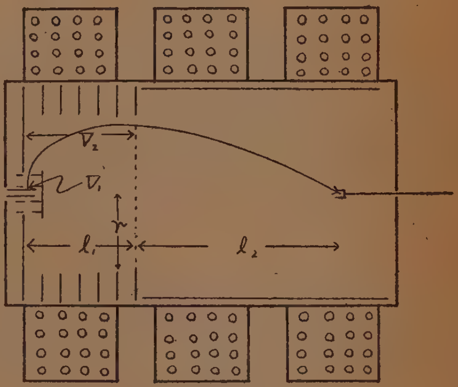

Fig. 1.

By the simple consideration for the trajectory, we obtain the following equations as the converging condition and the dispersion formula.

$$\frac{(2l_1+l_2)}{2\pi}H=\sqrt{\frac{2mV_2}{e}}\quad\cdots\cdots\text{(1)}$$

$$\frac{dl_2}{dm}=\frac{2\pi}{H}\sqrt{\frac{V_2}{2me}}\quad\cdots\cdots\text{(2)}$$

From the above equations and the configuration of this apparatus we conclude the following point as merits of this spectrograph.

(1) The converging condition does not contain V_1. Therefore the initial velocity of ions has no effect on the resolving power, so that we may say that this spectrograph has the property of the perfect velocity focusing. This is a very profitable characteristic and we can reduce considerably the accelerating voltage.

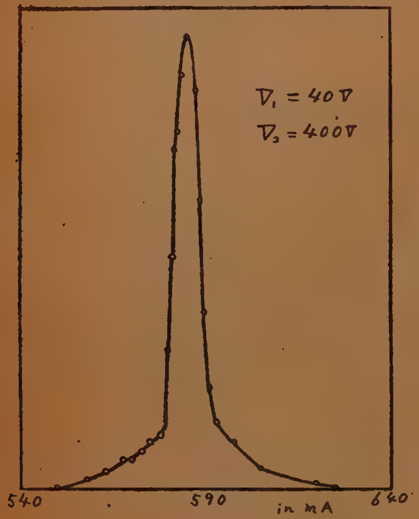

Fig. 2.

(2) The dispersion is π times as large as the ordinary semicircular spectrograph.

(3) As the source has an axial symmetry, the apparatus has a very high luminosity.

In the apparatus used for the preliminary test, radius was 5 cm, l_1, 6.8cm, l_2, 17cm. The electron mass spectrum by thermoelectrons is shown in Fig. 2 and the deviation of the position at the peak point by accelerating voltage, V_1, is plotted in Fig. 3. The small deviation in Fig. 3 is probably accounted for the non-uniformity of the magnetic field. The spectrum has 1.3% as the resolving power at half maximum. If we use an apparatus more accurately constructed, this resolving power might be increased considerably.

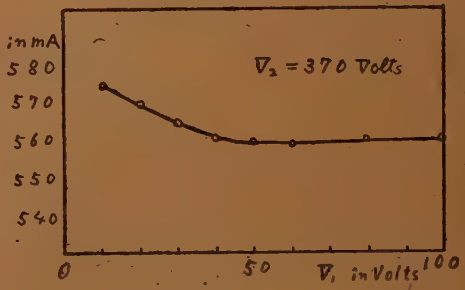

Fig. 3.

On Some Properties of the Cu-Mn Alloy System.

By Takao SATO.

Faculty of Engineering, University of Kyushu.

(Received Dec. 13, 1949)

§ 1. Introduction.

Feussner-Lindeck⁽¹⁾ found that the temperature coefficient of the electrical resistance of the Cu-Mn alloy system becomes negative when the content of manganese is more than about 10 atomic percent. Generally speaking, it is the common sense that the electrical resistance of metals and alloys increases with rising temperature and it is not understood easily that the electrical resistance decreases with rising temperature.

Many researches⁽²⁾ on the temperature variation of the electrical resistance of the Cu-Mn system were done with the practical interest, but apart from the practical points the electrical properties for all concentrations of the Cu-Mn system were investigated by Grube, Oestreichen and Winkler.⁽³⁾ They intended to have the diagram, but did not discuss why the temperature coefficient of the resistance in the Cu-Mn alloy becomes negative.

Further, there is a problem whether a superlattice is present or not. Valentiner-Becker⁽⁴⁾ studied the relation between the magnetic susceptibility and the manganese concentration of the Cu-Mn alloy, and found that the magnetic susceptibility becomes very large in the neighborhood of the 25 atomic percent magnanese at low temperatures and considered that this anomalous phenomena are due to the superlattice of the composition Cu_3Mn. Recently, Ellsworth-Blake⁽⁵⁾ reported that their results of x-ray analysis were not consistent with the equilibrium diagram and the superlattice might be present in Cu-Mn alloys though they did not succeed to photograph the superlattice lines.

The writer has studied mainly the temperature dependency of the electrical resistance for Cu-Mn alloys, in which the content of manganese extends from 10 to 70 atomic percent, in order to study why the temperature coefficient of the resistance becomes negative and whether the superlattice is present or not in Cu-Mn alloys. Above all, the writer studied in details for the 25 atomic percent manganese alloy which corresponds to the composition Cu_3Mn, if a superlattice is present.

§ 2. The Measurement of the Resistance and its Results.

We made alloys of manganese content from 10 to 70 atomic percent in a cylindrical form of, 5 mm in diameter, about 100 mm in length and annealed about 5 hrs. at 800°C.

The electrical resistance R was measured by the usual current-potential method at the rate of about 2–3°C/min. on heating and cooling. The resistance *vs.* temperature curves for each atomic percent of manganese are shown in Figs. 1–1, 1–2, and 1–3. In these figures the ordinates represent the ratio R/R_0 where R_0 is the resistance at room temperature.

By comparing the present results with those of Grube, Oestreichen and Winkler, it will be seen that the behaviors at the high temperature region are widely different. Namely, in their results, for example, the resultance has nearly constant up to the high temperature of 800°C in the case of 10 % Mn and the temperature coefficient of the resistance is negative up to 800°C in the case of 20 % Mn. In the present results, however, the temperature coefficient of the resistance changes from negative to positive at about 500–600°C. Furthermore, the writer found the unexpectedly large change of the resistance at about 850°C while they made the measurements till 800°C for the concentration up

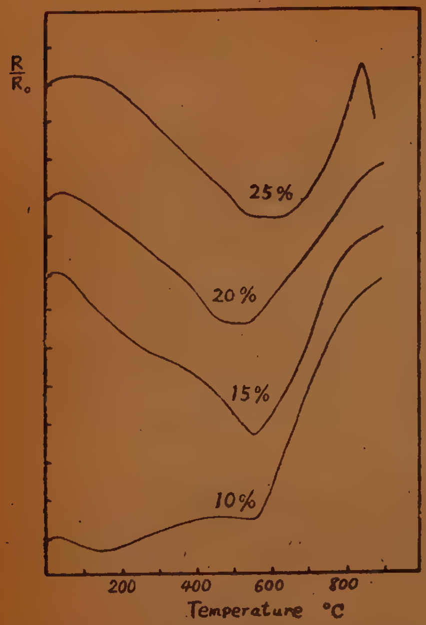

Fig. 1-1. The resistance *vs.* temperature curves for 10, 15, 20, and 25 atomic percent manganese. One graduation of the ordinate is 0.01.

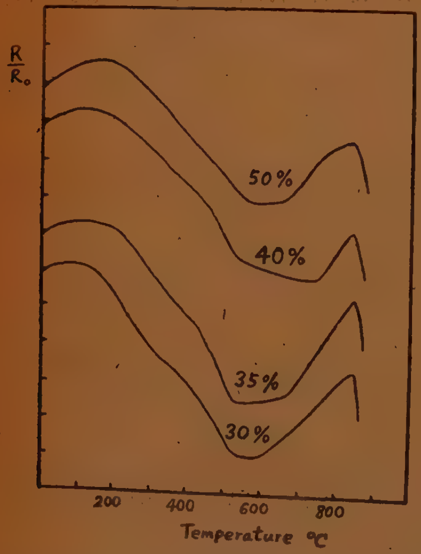

Fig. 1-2. The resistance *vs.* temperature curues for 30, 35, 40, and 50 atomic percent manganese. One graduation of the ordinate is 0.01.

to the 70 % Mn. Especially, we found the drastic change of the resistance, which seems to correspond to the first order phase change for 25-60 % Mn. Stillmore, the temperature variation of the resistance in the region of about 500-600°C is interesting and the temperature coefficients of this region have the small negative or positive value.

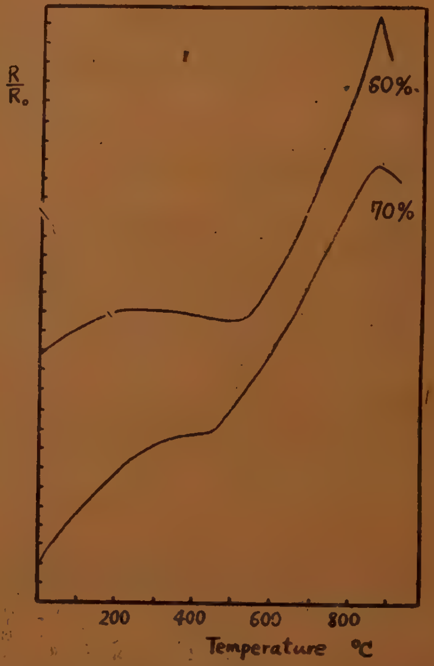

Fig. 1-3. The resistance *vs.* temperature curves for 60 and 70 atomic percent manganese. One graduation of the ordinate is 0.01 for 60 % Mn while that is 0.02 for 70 % Mn.

The values of the resistance increase with manganese content and the maximum point of

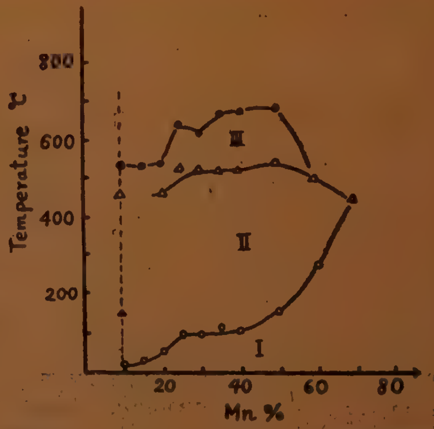

Fig. 2. Change of the temperature coefficient of the resistance with manganese concentration. Region I: the positive temperature coefficient, region II: the negative temperature coefficient, region III: the positive or negative temperature coefficient.

R/R_0, where the temperature coefficient of the resistance changes from positive to negative, displaces to the higher temperature side with the increasing content of manganese. Fig. 2 shows how the temperature coefficient of the resistance changes with manganese content.

There is no the first order phase change at about 850°C in the diagrams of Persson(6) and Grube-Oestreichen-Winkler(4) which were based on the x-ray analysis, but this temperature corresponds to the change $\alpha+\alpha$ Mn $=\alpha+\gamma$ Mn in the diagram of Ishihara(7) which was determined by the microscopic study and the thermal analysis. But the circumstance seems not so simple that we have some conclusions for the diagram only from the above mentioned results.

§ 3. The Behavior of the Resistance of the Cu Alloy of 25 Atomic Pecent Manganese.

Since Valentiner-Becker suggested that there exists the superlattice alloy Cu_3Mn, the writer measured the electrical resistance for the specimen of 25% Mn in several external conditions. The results obtained for this alloy seems to not lose general characteristics of Cu-Mn alloys.

The remarkable fact for this alloy is that the value of the resistance, its temperature coefficient and the maximum point of R/R_0 curve were largely affected by a small oxidization.

As manganese has a large affinity with oxygen, the black oxide of manganese grows on the surface of the alloy by remarkable selective oxidization, and the layer of clean copper remains between the oxide layer and the ground alloy. It is considered that this layer of copper affects the resistance of the alloy considerably. When the alloy is oxdized, the specified temperature, where the temperature coefficient of the resistance changes from positive to negative, decreases. And, owing to further oxidization the region of the negative temperature coefficient of the resistance disappear as shown in the curve *c* of Fig. 3.

In this way, the electrical properties of the alloy is affected by the positive temperature coefficient of the resistance of copper layer on the surface. If we strip off the oxidization film and layer of copper from the specimen, whose temperature coefficient becomes positive the considerable oxidization, we obtain the normal resistance temperature curve. This phenomena can proved simply by plating the un-oxidized specimen with copper. In Fig. 3, the curve *a* is the normal resistance temperature curve and the curve *c* shows that the region of the negative temperature coefficient of the curve *a* disappears by oxidization.

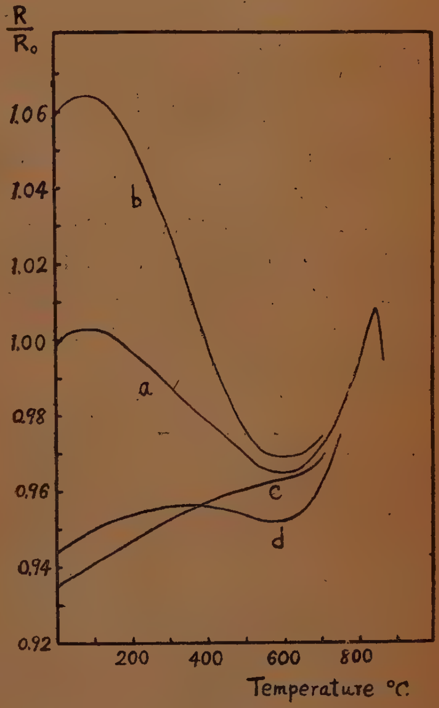

Fig. 3. The resistance *vs.* temperature curve on heating for the alloy of 25 atomic percent manganese. Curve *a*: normal heating curve. Curve *b*: the specimen quenched into water from 700°C. Curve *c*: the specimen oxidized considerably. Curve *d*: the specimen used for the curve *c* and quenched from the high temperature 700°C.

In Fig. 3, the heating curve of the un-oxidized specimen which was quenched into water from 700°C is the curve *b* where the larger negative temperature coefficient appears. Hence, when the specimen, whose negative temperature coefficient disapeared by oxidization, was quenched, the negative temperature coefficient has come to appear i. e. when the specimen used for the curve *c* was quenched from the high temperature of 700°C we obtained the curve *d*.

§ 4. The Thermal Analysis and the Measurement of the Thermoelectric Power.

From the temperature dependency of the resistance for alloys of several contents of manganese obtained here, it seems difficult to expect the presence of the superlattice, but further the differential thermal analysis and the measurement of the thermoelectric power for the alloy 25 % Mn were made.

The specimen for the thermal analysis is 10 mm in diameter and 25 mm in length and copper is used as the neutral substance. The differential thermocouple used is a Pt-PtRh thermocouple. The result is shown in Fig. 4 (a). The latent heat corresponding to the first order phase change clearly appear at about 850°C as expected from the temperature dependency of the resistance in Fig. 1-1.

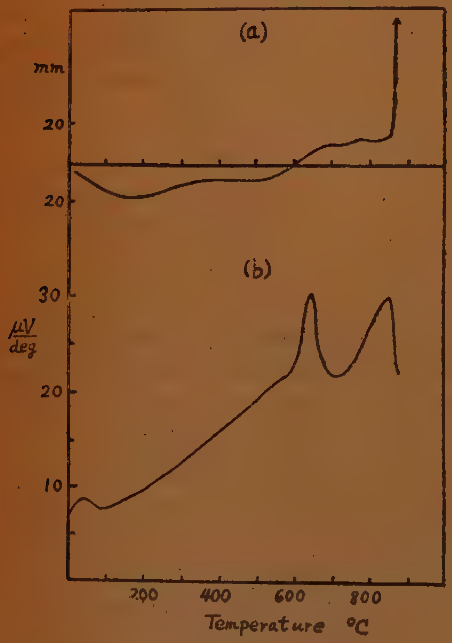

Fig. 4. (*a*) Result of the differemental thermal analysis for the 25 % Mn alloy. The ordinate is the deflection of galvanometer. (*b*) Temperature variation of the thermoelectric power of the 35 % Mn alloy coupled with platinum.

The method of the measurement of the thermoelectric power in the same as used in the previous investigation of order-disorder transformation(8). The result obtained here is shown in Fig. 4 (*b*). The sign of the thermoelectric power coupled with platinum is positive. There are peaks at about 40°, 650°, and 850°C.

The peak at about 40°C corresponds to the temperature in which the temperature coefficient of the resistance changes from positive to negative and the peak at about 650°C to the temperature coefficient of the resistance changes from negative to positive. Furthermore, the remarkable decrease at about 850°C is due to the first order phase change which is clearly found in the measurements of the resistance and the thermal analysis, as mentioned above.

§ 5. Consideration for the Problem Whether the Superlattice is Present or Not.

Valentiner-Becker and Ellsworth-Blake suggest that there is the superlattice alloy in the Cu-Mn system. However, from their experimental results, we may not agree with the conclusion that the superlattice alloy exists. Namely, a superlattice line in the x-ray analysis, which is the direct confirmation of a superlattice, has not been found and any characterstic variations for a superlattice have not been found by powerful indirect method, electrical and thermal, also.

Though there is no direct confirmation by x-ray, according to an indirect method such as thermal, and magnetic, the Ni_3Mn alloy(9) has been considered as a superlattice alloy. Furthermore, for the research of the superlattice, there are some cases that a direct confirmation by x-ray appeared latter than an indirect method in our past experience. Consequently, it will be overhasty that we conclude, that there is no superlattice, only by the fact that the superlattice line is not found. However, the writer considers that it will be powerful that any characteristic features of order-disorder transformation are not found in an indirect method such as electric and thermal.

According to Valentiner-Becker the magnetic susceptibility of the Cu alloy of about 25% Mn content becomes large at the low temperature. If we consider that manganese have a characteristic electronic structure, this fact will be understood. As the magnetic properties have the intimate connection with the electronic structure of the alloy, it seems unnecessary to consider that the above anomaly of the magnetic susceptibility is due to the creation of the superlattice.

It is the remarkable property that several manganese alloys become ferromagnetic. It is sure that the atom primarily responsible for this magnetism, for example, of the Heusler alloy, which has the composition such as Cu_2MnAl, is manganese.

The state density at the Fermi surface of the 3d shell and the magnitude of the exchange energy between the electrons belonging to 3*d* shell influence the condition of ferromagnetism. This exchange energy is considerably sensitive to the interatomic distance. The writer conceives that in the Cu_3Mn alloy, the exchange energy does not satisfy the condition of ferromagnetism, though the state density of 3*d* band satisfies it. However, the Heusler alloy Cu_2MnAl, which is produced by replacing one Cu atom by Al atom in the Cu_3Mn alloy, becomes frromagnetic statisfing the condition of the exchange energy also. So far the Cu_2Al alloy have been considered as the mother alloy of the Heusler alloy, but it seems rather natural that the Cu_3Mn alloy might be considered as the mother alloy from its magnetic property.

§ 6. Consideration of the Negative Temperature Coefficient of the Resistance.

There are alloys which have the negative temperature coefficient of the resistance, but it should be noted that these alloy have one or two transition metals as their constituents. It is well known that the transition metals have the incomplete *d*-shell and their physical properties are more complex than other metals.

The temperature variation of the resistance of the Cu-Mn alloy sensitively depends on the effect of the third element, the oxidization of the surface and the working-up of the specimen. These facts shows that the electrical properties of this alloy depend on the delicate electronic structure of this alloy. As the value of its thermoelectric power is the same order as transition metals, the negative temperature coefficient of the Cu–Mn alloy may be not understood from the idea that the small number of electrons as in semiconductors change with temperature. Consequently, the negative temperature coefficient of the Cu-Mn alloy seems to depend on the characteristic affairs of the Fermi surface of the 3*d* energy band of the alloy.

Generally, the electrical properties of the transition metals is determined mainly by the behaviors of the *s* electrons, but there is an empty part of *d*-band, which has considerably larger state density than *s*-band. The electrical resistance of the transition metals is more affected by the $s \to d$ transition of the conduction electrons than the $s \to s$ transition. Hence, if the state density of the Fermi surface of the *d*-band remarkably decreases with rising temperature in suitable combination of copper and manganese, the negative temperature coefficient will be possible.

This idea has been applied by Mott(10) for Pd, Pt, and Ta, of which the resistance temperature ratio R/T decreases with increasing temperature and for the copper-nickel alloy (Constantan) whose temperature coefficient of the resistance is negative. It is considered that the above mentioned effect is predominate in Cu–Mn alloys. The resistance of an alloy is made up of two part, i. e. $R = R_0 + R_T$ where the resistance R_0 is due to the disorder and the electronic structure and R_T is due to the thermal vibration of atoms. Considering the part of R_0 which is due to s—d transition, the resistance at the temperature T given by

$$\text{const.}\, T\left[1-\frac{\pi^2}{6}\left(\frac{T}{T_0}\right)^2\right] \qquad (1)$$

where T_0 is the degeneray temperature for the *d*-band. This formula gives a good approximation if T is small compared with T_0.

In the alloy of 25% Mn, for example, if we assume roughly that the temperature dependency will be given by formula (1), we obtain about $T_0 \sim 1000°K$ from the maximum point in the curve *a* in Fig. 3. Namely, the state density of the Fermi surface decrease very fast with increasing energy in the range of $kT = 0.1 \sim 0.05$ eV (k = Boltzmann's const,).

As shown in the curve *b* of Fig. 3, the resistance and the negative temperature coefficient are larger than the normal specimen (curve *a*). This fact is explained as follows: the breath of 3*d* band of quenched state will be narrower than an unquenched state, and hence the state density of the quenched state i. e. its resistance will become large. Furthermore, the state density near the Fermi surface in the quenched state decrease faster than the unquenched state with increasing temperature. Hence, the negative temperature coefficient of the quenched specimen becomes larger than the unquenched specimen. Though Cu alloys containing about $10 \sim 60\%$ Mn have the negative coefficient, as shown in Fig. 2, the maximum point at the low temperature is displaced toward higher temperature side with increasing concentration of manganese. This fact means that the empty space of the 3*d*-band, where the state density near the Fermi surface is nearly constant, increases with manganese content. In the alloy of 70% Mn, it will be considered that the negative temperature coefficient of the resistance does not appear at the temperature, where the state density near the Fermi surface decrease with increasing energy, owing to some thermal effects.

There are several alloys having the negative temperature coefficient of the resistance without including transition metals. These alloys almost have not metallic characteristic such as the plastic properties or the good conductor of electricity. For example, there are some alloys of bismuth$^{(11)}$ and the intermetallic compounds. These are the intermediate materials between metals and semi-conductors.

The writer is indebted to Prof. A. Okazaki for his valuable discussions and to Prof. K. Omori for his kind encouragement and continued interest. The expense of this research has been defrayed from the Scientific Research Expenditure of the Educational Ministry.

References.

(1) K. F. Feussner-St. Lindeck: Wiss. Abh. d. phys. Techn. Reichsanstalt **2** (1895) 501.
(2) K. F. Feussner-St. Lindeck: Wiss. Abh. d. phys. Techn. Reichsanstalt **2** (1895) 601.
E. F. Bash: Trans. Amer. Inst. Min. Met. Eng. **11** (1921) 261.
M. A. Hunter-J. W. Bacon: Trans. Amer. Electrochemical Soc. **36** (1919) 323.
S. Kimura-Z. Isawa: Researches Electrotech. Lab. **103** (1921).
S. Kimura-Z. Isawa: Researches Electrotech. Lab. **103** (1922).
(3) G. Grube-E. Oestreichen-O. Winkler: Z. f. Elektrochemie **45** (1939) 776.
(4) S. Valentiner-G. Becker: Z. f. Phys. **80** (1933) 735.
(5) L. D. Ellsworth-F. C. Blake: J. Appl. Phys. **15** (1944) 507.
(6) E. Persson: Z. Phys. Chem. (B) **9** (1930) 25.
(7) T. Ishihara: Tohoku Imp. Univ. Sci. Rept. **19** (1930) 499.
(8) T. Sato: J. Phys. Soc. Japan. **3** (1948) 198.
(9) S. Kaya-A. Kussmann: Z. f. Phys. **72** (1931) 292.
S. Kaya-M. Nakayama: Proc. Phys.-Math. Soc. Japan **22** (1940) 126.
M. Thompson: Proc. Phys. Soc. **52** (1940) 217.
(10) N. F. Mott: Proc. Roy. Soc. **153** (1936) 699.
(11) N. T. Thompson: Proc. Roy. Soc. **155** (1936) 111.

On the Barkhausen Jumps in the Course of Magnetic After-Effect*

By Takasi HUZIMURA.

The Research Institute for Iron, Steel and Other Metals, Tohoku University

(Read April, 1949; Received Dec. 13, 1949)

Summary.

When a magnetic field applied to a ferromagnetic substance suddenly changes, its magnetization instantly approaches a final equilibrium value. However, small changes of magnetization follow even after the change of magnetic field is quite completed. This phenomenon is known as magnetic after-effect. Based upon recent theories on the mechanism of magnetization, retardation of the displacement of magnetic domain boundaries has been taken into account in a discussion of this phenomenon.(1) In explaining magnetic after-effect, only gradual changes of magnetization are discussed, but, it is not yet clear whether this change is really continuous or not. The present writer has detected discontinuous changes of magnetization (Barkhausen jump) in the course of magnetic after-effect under various conditions; in this paper a method and results of measurement of the discontinuous change of magnetization in the course of magnetic after-effect are described, and a discussion on the mechanism of magnetic after-effect is given based upon the results obtained.

§ 1. Specimen and the Methods of Observation.

Specimens used were rods of cold-drawn Cr-permalloy (Fe-10%, Ni-86%, Cr-4%), and a single crystal of Magnetite (semi-conductor). The dimensions of these specimens are given in the following table.

Specimen	Length (mm)	Section (mm)
Cr-permalloy	23	2 (diameter)
Magnetite	15	2×2

The specimen was inserted inside a search coil of 10000 turns, the length of which is 25 mm. Electromotive force induced in the search coil by the change of magnetization of the specimen was magnified by an amplifier of the resistance coupling type and recorded on moving photographic films of an electromagnetic oscillograph connected to the amplifier (natural frequency of the vibrater used is about 6,000 cycles). Now, the specimen was first magnetized to saturation and then by suddenly changing the applied magnetic field, the magnetization of the specimen was brought to the desired point on the descending branch of the hysteresis curve. Most part of the corresponding change of magnetization then occurred instantaneously, but at the same time, numerous Barkhausen jumps were recorded periodically in succession on the oscillogram, which continued for more than 20 seconds after the change of external magnetic field was quite completed.** Consideration must here be given to the decaying period of the electric current passing through the magnetizing solenoid after the circuit is opened. However, if we denote by L and R the inductance and the resistance respectively of the magnetizing circuit, the decaying period is given by $2L/R$, which for the present case of $L=0.1$ henry, $R=8\Omega$ is 0.025 sec., and its effect is thus out of the question with the present arrangement. These Barkhausen jumps recorded on the oscillograms are counted for their number of occurrence after 0.2 sec. from the instant at which the intensity of magnetic field was changed.

§ 2. Experimental Results.

A rod of cold-drawn Cr-permalloy was first magnetized to saturation and subsequently, by sudden decreasing of the applied magnetic field its magnetization was brought to a point I_f on the descending branch of the hysteresis curve. This caused many Barkhausen jumps to be observed intermittently on the oscillogram after the change of magnetic field had been quite completed.*) The number of Barkhausen jumps that occurred during each time interval of 0.1 sec. after 0.2 sec. from the instant at which the magnetic field changed, was counted on the oscillograms and plotted against the lapse of time. The result is given in curve a in Fig. 1 for $I_f=-110$ gauss. As is shown, the number of Barkhausen jumps occurring each time interval (0.1 sec.) decreased continuously with the lapse of time and after 0.6 sec. the number reached half the initial value. The Barkhausen jumps, however, can be observed intermittently even beyond the lapse of 20 sec. from the change of the external magnetic field.

---

*) The report from the Research Institute for Iron, Steel and Other Metals, Tohoku University. A part of the fund for this investigation is due to the Grants-in-Aid of Fundamental Scientific Researches of the Ministry of Education for 1949. (Item # D, 387; "The experiment on the displacement of domain boundaries in a ferromagnetic substance".)

**) If a Braun-tube oscillograph is used in place of an electromagnetic one, Barkhausen jumps are observed intermittently during 20 seconds.

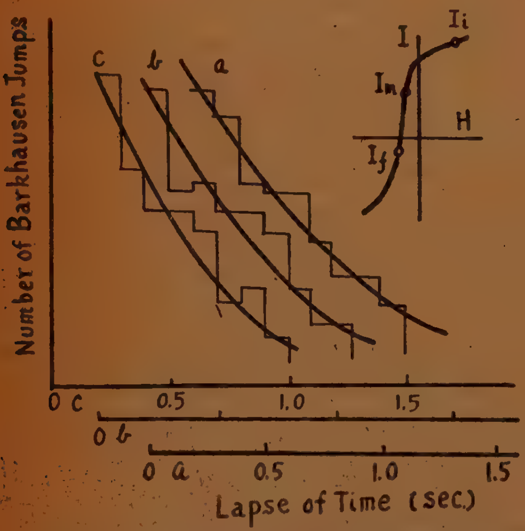

Fig. 1. Distribution curves of Barkhausen jumps in the course of magnetic after-effect for a Cr-permalloy.

		I_i	I_m	I_f
(a)	I;	500		−110
(b)	I;	500	10	−110
(c)	I;	500	−70	−110

Next, the magnetization of this specimen was first brought to an intermediate stage of magnetization I_m by changing the magnetic field, and after one or two seconds brought to a final stage of magnetization I_f, whereafter the occurrence of Barkhausen impulses in the course of after-effect was observed. The results are given in curves b and c in Fig. 1, wherein $I_m=10$ g., $I_f=-110$ g. for b, and $I_m=-70$ g., $I_f=-110$ g. for c. As can be seen from the figure, the three distribution curves a, b and c do not differ in form from each other, from which it will be concluded that if the initial and final stages of magnetization, I_i and I_f, are not altered, condition of magnetization in the intermediate stages I_m do not have any influence on the distribution of the occurrence of Barkhausen jumps in the course of after-effect.

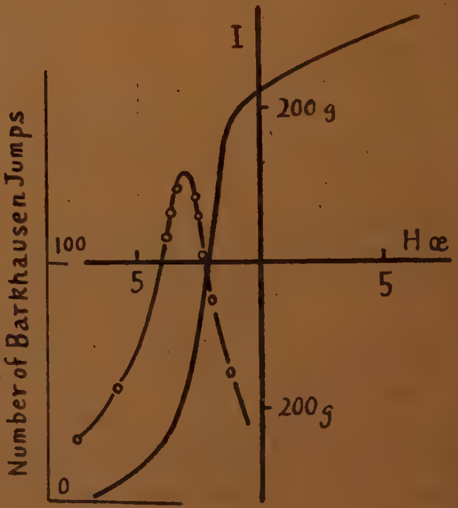

Fig. 2. Number of Barkhausen jumps that occurred in the course of magnetic after-effect and the hysteresis curve measured at 15° C.

In the next experiment, the occurrence of Barkhausen jumps after the sudden change of the magnetizing field was observed at different stages of magnetization on the descending branch of hysteresis curve: The specimen (Cr-permalloy) was first magnetized to saturation, then immediately brought to the various points on the descending branch of hysteresis curve. In Fig. 2, the total number of Barkhausen jumps that occurred in a interval ranging from 0.3 sec. to 1.3 sec. after the change of external field are plotted against various final stages of magnetization. If the difference between the initial and final magnetic field is small, the numbers of Barkhausen jumps are also exceedingly small, but the numbers increase with the decrease of the final field, reaching a maximum and then decreasing again. This maximum point of the occurrence curve of Barkhausen jumps is found near the steepest part of the descending branch of the hysteresis curve. However, the exact form of this hysteresis curve can not be determined, since the demagnetizing factor N of the specimen is very large ($N=0.14$), and the form of the specimen is a little different from the true ellipsoid of rotation. Consequently, the precise coincidence of the maximum point with the point of the steepest inclination of the hysteresis curve could not be conclusively decided by the present experiment.

---

*) Barkhausen jumps in the course of after-effect may also be observed when both specimen and the search coil are pulled out of the solenoid, in which a stationary electric current is passing.

Similar observations were carried out at various temperatures ranging from −190° C to 100° C, and the results are shown in Fig. 3 (100° C and 15° C) and 4 (15° C and −190° C). As is shown, there is no appreciable dependence on the temperature of the total number of the occurrence of Barkhausen jumps between 0.3 sec. and 1.3 sec. in the course of magnetic after-effect with the final field H_f; a sharp maximum is found near the steepest part of the descending branch of hysteresis curve at each temperature.

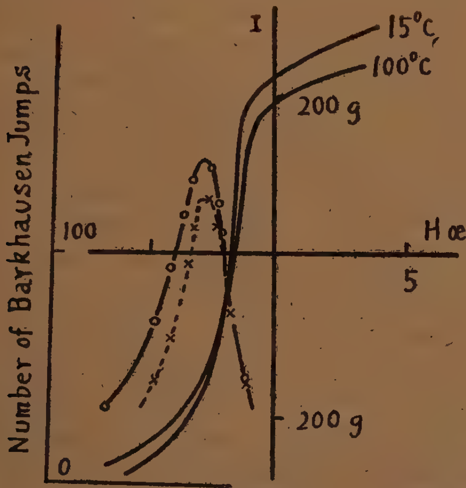

Fig. 3. Number of Barkhausen jumps and the hysteresis curves measured at 15° C and 100° C.
0 : 15° C.   × : 100° C

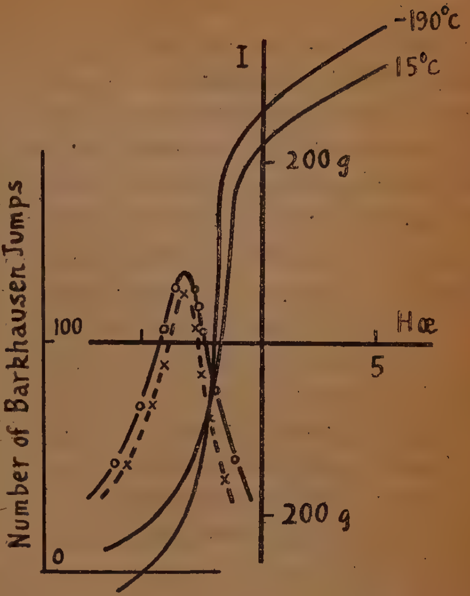

Fig. 4. Number of Barkhausen jumps and the hysteresis curves measured at 15° C and −190° C.
0 : 15° C.   × : −190° C.

An observation of Barkhausen jumps in the course of after-effect for a ferromagnetic semiconductor was also carried out. For this experiment a needle of single crystal of natural Magnetite was chosen; the number of Barkhausen jumps at various time interval after the change of magnetic field are plotted in Fig. 5. As seen

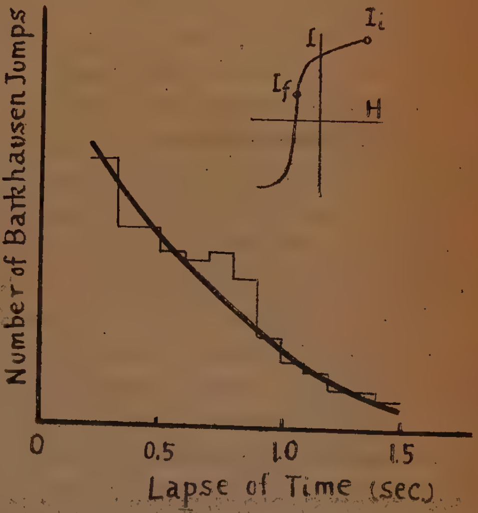

Fig. 5. Distribution curve of Barkhausen jumps in the course of magnetic after-effect for a Magnetite.

from the figure the results are similar to that of Cr-permalloy. In this case, however, there exist no local magnetic fields due to induced microscopic eddy current which would have occurred during the displacement of magnetic domain boundaries in a ferromagnetic metal. Consequently, it might be concluded that the influence of the said local magnetic field is not an essential factor in the retardation of the discontinuous process of magnetization.

§ 3. Discussion.

It is usually assumed that the elementary processes of magnetization are the reversible and irreversible displacements of domain boundaries and the continuous rotation of spontaneous magnetization, the irreversible being the origin of the Barkhausen jumps. With regard to the velocity V of the irreversible boundary displacement, Sixtus and Tonks[2)] found the following equation

$$V = a(H - H_0) \dots\dots\dots\dots\dots (A)$$

where a is a constant, H_0 the strength of the so-called critical field. This expression is based on the assumption that the boundary displaces without changing its form. The quantity H_0 depends on the amount and distribution of internal stress and changes from point to point in the ferromagnetic substance. Now, in the actual process of magnetization, however, this assumption will not hold. Due to the change in the boundary forms, variations occur in the surface energy of the magnetic domain boundaries and in local magnetic fields due to free magnetism on the boundaries and hence some corrections should be added to the velocity formula of boundary displacement; but even in this case, the formula (A) will hold if the definition of H_0 is amended and those factors above mentioned are included to the quantity H_0. Now, if the magnetizing field is suddenly changed, most part of the unstable boundaries of magnetic domain displace instantaneously to the new equilibrium positions. However, if in some regions of the ferromagnetic substance the critical field H_0 assumes a very close value to the external field H, and if the domain boundaries happen to lie in those regions, they should then displace with very small velocity. Consequently, it would take a certain time interval for the boundary to pass through that region. If the value of H_0 for the boundary diminishes after passing the said region, the boundary would displace suddenly after passing the same region, and on the occasion, Barkhausen jumps may occur as will be seen in Fig. 6. Accordingly, these retarded Barkhausen jumps would be observed even after the change of magnetization has been completed. Such Barkhausen jumps can be seen in the recorded discontinuous changes of magnetization in the course of magnetic after-effect. According to this consideration on the mechanism of the occurrence of Barkhausen jumps during after-effect, the number of discontinuous changes of magnetization is determined by the number of domain boundaries of the form shown by Fig. 6, depending only on the initial stage and the final field of the process. Consequently, it is reasonable to conclude that the occurrence of Barkhausen jumps during after-effect is not affected by bringing its magnetization to the intermediate stage as described in the early page of this report and is only dependent on the final stage of magnetization.

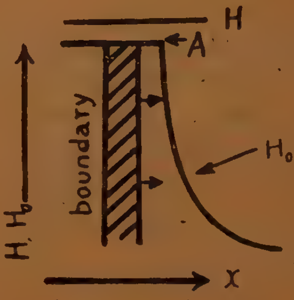

Fig. 6. Owing to the small value $H-H_0$ a magnetic domain boundary moves slowly till A and then displaces suddenly.

These considerations were based on the discontinuous displacements of the 180°-boundary and hence the said Barkhausen jumps would be found abundantly in the steep part of the hysteresis curve, where displacements of 180°-boundary predominate. These theoretical results are supported by the facts already described (in Fig. 2, 3, 4) that the maximum point of the after-effect falls on the steepest part of the descending branch of hysteresis curve. The form of the hysteresis curve does not change appreciably with variations in temperature and consequently no serious error would be introduced, if we assume that only slight changes occur in the distribution of the critical field strength H_0 throughout the specimen with the rise or fall of temperature. Therefore, it may be expected that the number of Barkhausen jumps in the course of after-effect has little dependence on temperature.

Lastly, on the basis of the present results some remark may be made regarding Preisach's discussion[3] of the magnetic after-effect. He observed the magnetic after-effect on a Fe-Ni alloy and concluded from his results that the displacement of magnetic domain boundary receives two types of retardation; (1), the retardation due to inverse local magnetic field, caused by microscopic eddy currents induced in the specimen while a magnetic domain boundary is displacing; (2), the change in H_0 due to changes in distribution and intensity of internal stress accompanying thermal fluctuation. A magnetic domain boundary which ceases its displacement at a point at which H_0 is slightly larger than H will displaces again when H_0 becomes smaller than H due to a thermal fluctuation of internal stress. Under these influences a number of magnetic domain boundaries have its displacement retarded in the course of magnetic after-effect. According to the considerations developed by Preisach, it is to be concluded that Barkhausen effect is directly related with magnetic after-effect and that maximum value of magnetic after-effect will be observed mainly in the range of discontinuous magnetization (steep part of hysteresis curve), which agree with the results of the present experiments. However, as the Barkhausen jumps in the course of after-effect are observed also in a semi-conductor (Magnetite) with characteristics more or less similar to those of the ferromagnetic metals, it will be evident that the influence of microscopic eddy currents mentioned is not an essential factor in magnetic after-effect. Furthermore, according to Preisach's opinion, the distribution of H_0 changes with thermal fluctuation, and accordingly it is to be expected that the magnetic after-effect may greatly depend on temperature. However, according to the results of the present experiment, the occurrence of Barkhausen jumps in the course of magnetic after-effect seems almost independent of temperature. Consequently, it would not be unreasonable to conclude that there is no intimate relation between the thermal fluctuation of internal stress and the magnetic after-effect, though Barkhausen jumps certainly are observed in the course of magnetic after-effect.

The writer wishes to acknowledge his thanks to Prof. T. Hirone who supervised the present work and also to Dr. T. Katayama for his helpful suggestions.

References.

(1) J. L. Snoek: Physica, Haag., **8** (1938), 663.
F. Preisach: Zeits. Phys., **94** (1935), 277.
(2) K. J. Sixtus and L. Tonks: Phys. Rev., **42** (1932), 419.
(3) F. Preisach: Zeits. Phys., **94** (1935), 277.

On Velocity Fluctuations in the Laminar Boundary Layer, I.

By Yutaka SHIGEMITSU.

Railway Technical Research Institute.

(Read Oct. 15, 1948; Received Dec. 24, 1949)

Summary of Parts I—II.

This paper deals with experimental studies of the velocity fluctuations in the laminar boundary layer near a plate in a wind tunnel flow. In Part I, the general aspects of the relation between the velocity fluctuations and the state of the free stream outside the layer are shown, and some discussions are given for the problem of transition. In Part II, the existence of a finite value of $u'v'$-correlation in the laminar boundary layer is proved by experimental results, and its effect on the mean velocity distribution is discussed.

Parts I. Relationship between Laminar Boundary Layer Oscillations and Transition.

§ 1. Introduction.

The conception of the laminar boundary layer was first introduced by L. Prandtl, and since he derived its equations of motion, many investigations have been carried out on these solutions. However, there exists, more or less, turbulent velocity fluctuations in the real state of flow. They affect on the boundary layer flow and bring forth many phenomena in it which cannot be explained by these equations. In other words, in practical cases of the boundary layer flow, we have few examples in which the above conception can completely be adapted in its whole region. Then, from the practical point of view, it becomes necessary to investigate the real state of flow in the laminar boundary layer, apart from the studies on the above equations of motion.

One of the significant phenomena which cannot be clarified by the equations of motion is that of transition from laminar to turbulent flow. Since the Reynolds' experiment on transition in a tube flow, there have been presented many detailed investigations on it,—for example, the theory of local separation or the theory of stability. But it is doubtful whether the problem of transition which is found in many cases of real flow, may be explained completely by these theories. As the effects of the turbulence in the main flow upon the laminar boundary layer, H. L. Dryden(1) had previously pointed out the characteristic "laminar boundary layer oscillations" near a plate in a wind tunnel flow. Then he and his colleagues(2) proceeded the measurements on the Tollmien-Schichting waves in the boundary layer by the method of "forced" oscillation using a wind tunnel with very low turbulence and got many fruitful experimental results on the theory of stability proposed by W. Heisenberg and others. On the other hand, concerning the above "free" oscillations found in the flow with a moderate degree of turbulence, we have heard few more detailed investigations.

Thus for the purpose of surveying general aspecs of the real state of the laminar boundary layer, we made further experiments on it with our recent equipments for measuring velocity fluctuations and will propose several experimental results and these discussions.

§ 2. Experimental Equipments and Preliminary Measurements.

In this experiment, we used the 1,5 m × 1,0 m elliptic wind tunnel of Göttingen type in our laboratory. The plate used in the measurements was 0,024 m thick, 0,4 m wide, and 2,0 m long, made of polished mahogany, and the shape of the leading edge is a semi-ellipse, whose major axis is 3,0 cm and minor is 1,2 cm. If needed, we changed the pressure gradient with two end plates or an interference plate, as shown in Fig. 1. All the measurements were made with a hot-wire anemometer whose wire was made of nickel of 0,010 mm in diameter and 3 mm long. As the investigation of velocity fluctuation in this part of the paper, we measured u'-fluctuation by the "constant resistance method".(3)

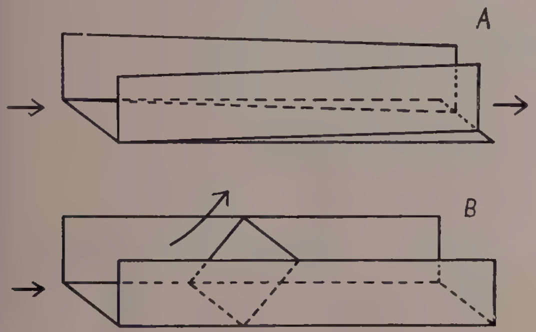

Fig. 1. Schematic diagram of the equipments of adjusting the pressure gradient. A: $dp/dx < 0$. B. $dp/dx > 0$.

The measurements were made in three states of flow of the pressure distribution along the plate. They are shown in Fig. 2, by the curves of the velocity distribution of the main flow along the plate. The turbulence in the flow is supposed to be caused mainly by the rectifying screen lying 2,0 m ahead of the plate and its percentage is about 0,45 at a mean speed of 14,3 m/s along the plate. In the above three states of flow, any conspicuous difference could not be found in the distribution of the intensity of turbulence in the main flow.

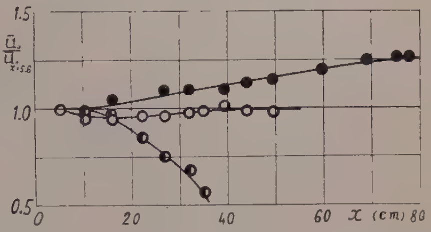

Fig. 2. Distributions of the mean speed along the plate. The suffix O designates the main flow outside the layer.

§ 3. General Aspects of the Laminar Boundary Layer Oscillations.

It has previously been pointed out, that when the turbulence in the main flow is not so small, there exist large velocity fluctuations of very low frequency in the laminar boundary layer. In our measurements, we could also find these "boundary layer oscillations". As an example, we show in Fig. 3, the distribution of its intensity

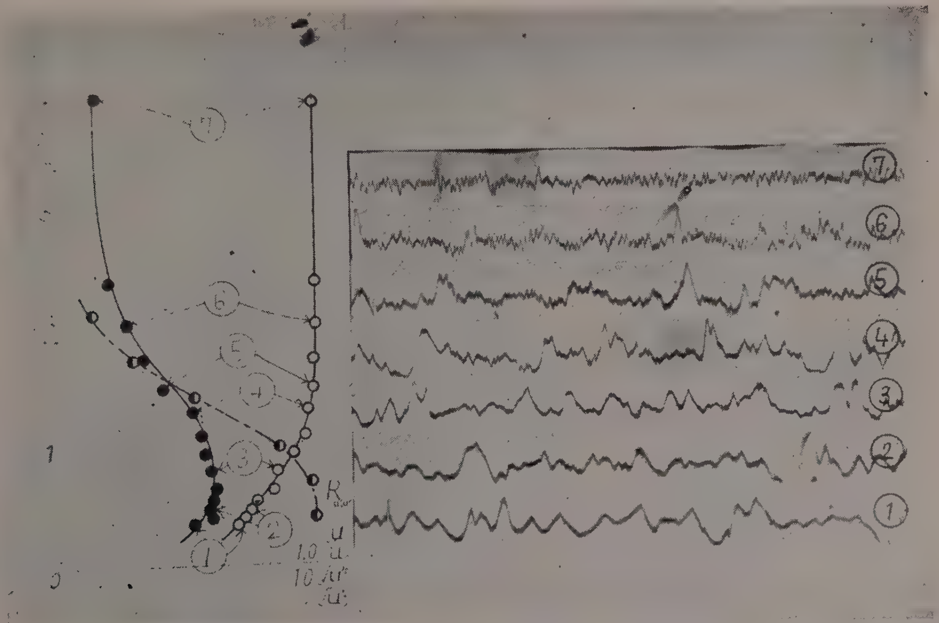

Fig. 3. State of the "laminar boundary layer oscillations" along the plate ($dp/dx = 0$) at the position of $x = 35$ cm. $\bar{u}_0$ and u_0' are the mean and fluctuational velocity outside the layer. Numbers on the figure are the corresponding points of measurement. ○—mean velocity. ●—fluctuational velocity. Each timing mark is 1/100 sec. Chain line is the distribution of u'-correlation coefficient ($R_{u'u'}$).

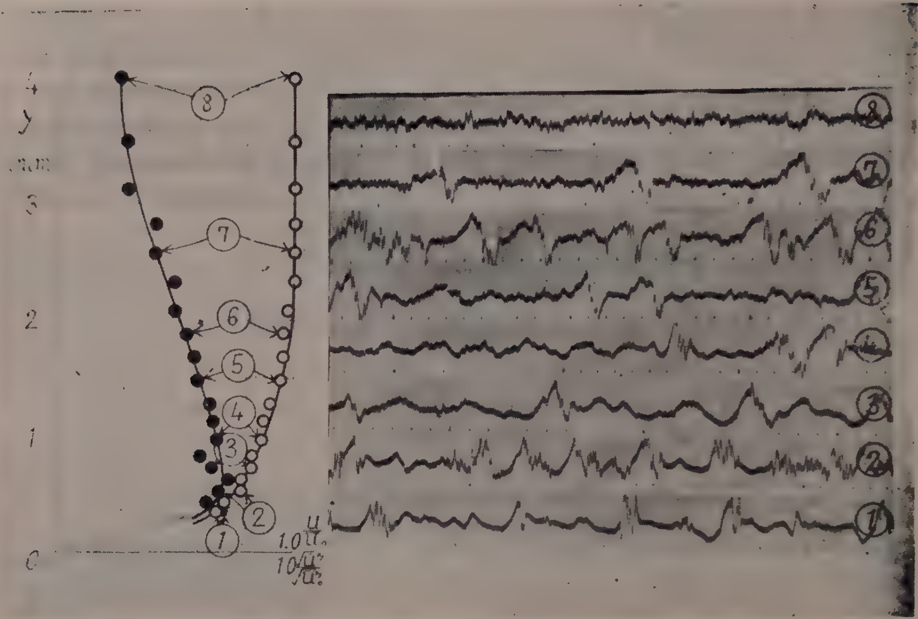

Fig. 6. General view of the velocity fluctuations in the transition region along the plate ($dp/dx = 0$) at a point of $x = 49$ cm. Symbols and numbers in the figure have the same meaning as in Fig. 5.

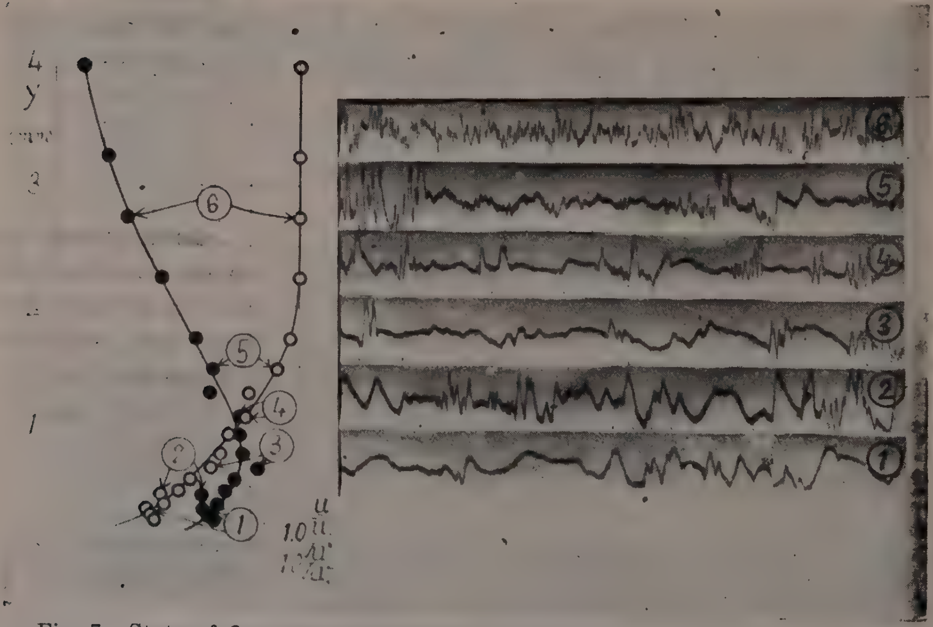

Fig. 7. State of flow near the separation point in the case of $dp/dx>0$. Symbols and numbers in the figure have the same meaning as in Fig. 5.

and the oscillograph records of its fluctuations at the point of $x=35$ cm. (x is a distance from the leading edge.) These measurements were made in the main flow of constant speed of 14,3 m/s, in which case the laminar boundary layer began to break down at about $x=42$ cm. By these figures, we can recognize that the flow in the boundary layer has a completely different character in its velocity fluctuation from that in the main flow outside of it.

To investigate further detailed characteristics of these oscillations, we have made some experiments on it. In Fig. 3, it is supposed that the "oscillations" do not depend directly on the turbulence of the main flow outside the layer at this point. To ascertain it, we investigated the distribution of u'-correlation coefficient in the layer with two hot-wires, one of them being fixed at a point of $y=0,4$ mm. This result is also shown in Fig. 3, and by this curve, we can recognize that the oscillation occurs almost uniformly in the layer and moreover they are independent upon the state of turbulence outside the layer. To investigate the aspect of the development of the oscillations along the plate, we plotted the relation between the maximum value of its intensity in the layer at a point and its distance from the leading edge. Fig. 4 shows these experimental results in the three states of flow. Then we can find that the intensity of the "boundary layer oscillations" at a point is increasing as it goes far from the stagnation point, while the state of turbulence outside the layer cannot be recognized to change. Moreover, the rates of the increase of its intensity along the surface, are different by the pressure distribution along the plate.

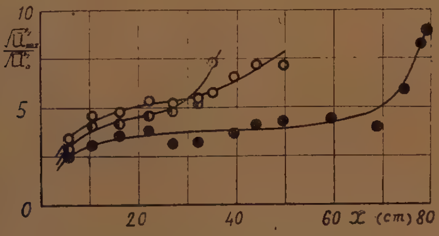

Fig. 4. Distributions of the maximum intensity of the "oscillations" in the boundary layer. ○ $dp/dx=0$. ● $dp/dx<0$. ◐ $dp/dx>0$.

In the laminar boundary layer, the state of flow near the forward stagnation point is necessary to be studied as the beginning of the layer. Fig. 5 shows the distributions of the mean and fluctuational velocity, and in this figure we find that the fluctuation of velocity do not vanish so rapidly as the mean velocity toward the stagnation point. So, we can suppose that at the stagnation point, the flow comes to stop but the velocity fluctuation gives large effects upon the laminar boundary layer.

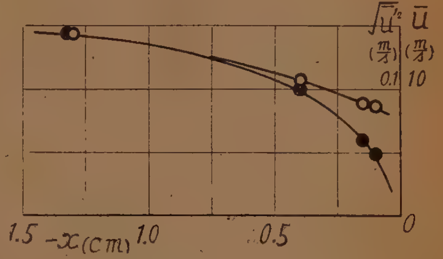

Fig. 5. Distributions of the intensity of mean and fluctuational velocity near the stagnation point. ● mean velocity. ○ fluctuational velocity.

By the above measurements, we can get the following results. The velocity fluctuations usually found in the laminar boundary layer, have a characteristic to develop along the surface of a body under a constant state of turbulence in the main flow, which is different depending on the pressure gradient along the surface, and there is no direct relation between the above "oscillations" and the turbulence outside the layer at this point. As for the cause of the origin of "boundary layer oscillations", we cannot get a definite conclusion from the above measurements, but it is likely that the state of these oscillations depend largely upon that of the turbulence in the main flow near the forward stagnation point.

§ 4. State of Flow in the Transition Region.

One of the important feature derived by the equations of motion of laminar boundary layer, is a phenomenon of laminar separation. In th real state of flow, however, we can hardly find the steady separation as derived by the theory, but the phenomenon of so-called "transition" usually occurs. As for the problem of transition, there have been done many systematic investigations, but in this section, for the purpose of displaying real state of transition which is usually found in many cases of flow containing moderate degree of turbulence, we will give some experimental results on it.

It is generally known that, there is a large part of region along the surface of a body between the positions where the laminar boundary layer begins to break down and where it changes into fully developed turbulent boundary layer. This is called as the transition region. In our measurement in the case of $dp/dx = 0$, the transition region was found to be about from $x = 42$ cm to 60 cm. Fig. 6 shows a general view of the velocity fluctuations in this region ($x = 49$ cm). The most characteristic feature in this figure is the intermittent outbreak of high frequency fluctuations. This character was found in all the previously published experimental investigations on transition. In the case of the accelerated flow, we could also find transition. It began at about $x = 77$ cm. In this case, we could also find the discontinuity of the frequency of velocity fluctuations.

In the previously mentioned state of flow of $dp/dx > 0$, the flow separated from the plate keeping its state of laminar flow (cf. Fig. 1). By the methd of kerosene-and-lampblack, we determined the laminar separation point ($x = 34$ cm) and then we investigated the state of velocity fluctuation near this point by a hot-wire anemometer. Fig. 7 shows the state of flow at $x = 35$ cm. In this figure, we find also the discontinuous change in the frequency of velocity fluctuations. By moving a hot-wire along the surface near the separation point, we noticed that there was some region of distance between the points where the discontinuity of the velocity fluctuation began to appear and where the low frequency of laminar boundary layer flow completely disappeared. It was found to be about from $x = 32$ cm to 37 cm in this case. Namely, it was recognized that in the real state of flow, laminar boundary layer did not separate at one point as designated by a theoretical solution, but the separation point fluctuated in its position. It may be proper to call it generally as a "laminar separation region".

§ 5. Discussions.

In the above measurements, the conditions of the turbulence in the main flow is complicated, and it is difficult to draw any quantitatively definite conclusions on the velocity fluctuations in the boundary layer. So, taking foundation on the previously mentioned experimental results, we will give some qualitative discussions on the real state of flow in the laminar boundary layer.

As for the state of flow in the separation region (cf. Fig. 7), we can easily explain it as follows. In general, when the steady laminar boundary layer separates from the surface of a body, an unstable vortex is usually formed by the retarded flow, but in the real state of laminar boundary layer, the location of this separation point fluctuates owing to the pressure fluctuation in the layer. Namely, when λ is taken as the parameter of the state of laminar boundary layer flow ($\lambda = -(dp/dx)(\delta^2/\mu U)$ where δ is the thickness of the layer and U, the speed of the flow outside of it), its value fluctuates about it mean value:

$$\lambda = \bar{\lambda} + \lambda' , \qquad (5,1)$$

where

$$\bar{\lambda} = -\frac{d\bar{p}}{dx}\frac{\bar{\delta}^2}{\mu \bar{U}} , \qquad \lambda' = -\frac{dp'}{dx}\frac{\bar{\delta}^2}{\mu \bar{U}} , \qquad (5,2)$$

where p and p' are respectively mean and fluctuational value of the pressure. When the above fluctuating value reaches its constant critical value of separation, λ_s (in Kármán-Pohlhausen's theory, it is taken as -12), a momentary separation occurs, and the range of the distance along the plate in which this separation occurs, can be taken as a "separation region". As to the discontinuity of the frequency of oscillograph records in Fig. 7, it can be interpreted that the parts of the low frequency indicate the laminar boundary layer and the parts of high frequency, the flow in the unstable vortex caused by a momentary laminar separation.

The characteristic feature of the flow in the transition region is also the intermittent discontinuity of the velocity fluctuation as shown in Fig. 6. Such a discontinuity of the velocity fluctuation was first found in Reynolds' experiment on the flow in a tube. In the recent experiments on the Tollmien-Schlichting waves made by H. L. Dryden and others(2), it was also reported, that in transition region, these regular waves exhibited intermittent burst of high frequency fluctuations, and he supposed that they were intermittent laminar separation. When these characteristics in transition flow are compared with the state of flow in separation region shown in Fig. 7, it is naturally concluded, although it cannot be proved at present, that all the phenomena of transition are an unsteady laminar separation.

As for the velocity fluctuation in the laminar boundary layer, there has been proposed an interpretation that it is the fluctuation of the thickness of the boundary layer, and in our measurements in this part of the paper, we cannot get any more definite results on its mechanism than that is described qualitatively in § 3. However, it is the fact that under the main flow with a moderate degree of turbulence, there exists larger velocity fluctuation in the boundary layer than in the main flow. On such a state of flow, we will investigate the effects of the velocity fluctuations in the laminar boundary layer. We express the velocity components by these mean and fluctuational values;

$$u = \bar{u} + u'$$
$$v = \bar{v} + v',$$

and when these are put in the Navier-Stokes' equations of motion and the mean values are taken, they reduce to

$$\bar{u}\frac{\partial \bar{u}}{\partial x} + \bar{v}\frac{\partial \bar{u}}{\partial y} = -\frac{1}{\rho}\frac{d}{dx}(P_l + \rho\overline{u'^2}) + \nu\left(\frac{\partial^2 \bar{u}}{\partial x^2} + \frac{\partial^2 \bar{u}}{\partial y^2}\right) - \frac{\partial \overline{u'v'}}{\partial y} \qquad (5,3)$$

$$\bar{u}\frac{\partial \bar{v}}{\partial x} + \bar{v}\frac{\partial \bar{v}}{\partial y} = -\frac{1}{\rho}\frac{d}{dy}(P_l + \rho\overline{v'^2}) + \nu\left(\frac{\partial^2 \bar{v}}{\partial x^2} + \frac{\partial^2 \bar{v}}{\partial y^2}\right) - \frac{\partial \overline{u'v'}}{\partial x},$$

where P_l is the pressure when the effects of velocity fluctuations are neglected. If we neglect all the fluctuating values, (5,3) can be simplified to Prandtl's equations of motion of laminar boundary layer supposing

$$\delta/L \ll 1, \qquad (5,4)$$

where L is a standard length along the x-axis. Then the pressure in the layer is easily proved to be equal to that in the main flow outside the layer. When we consider the velocity fluctuations, however, (5,3) and (5,4) do not participate in determining the distribution of the intensity of pressure fluctuation in the layer, but it is decided entirely depending on the velocity fluctuation at this point. (The mean values of the intensity of pressure caused by u'- and v'-fluctuation are expressed respectively of $\rho\overline{u'^2}$ and $\rho\overline{v'^2}$, and so the total pressure is increased in its mean value by the velocity fluctuations.) Thus, in the laminar boundary layer, there exists large pressure fluctuation caused by the "boundary layer oscillations", which are different from that in the main flow outside the layer. The above discussions can be adapted in the case of boundary layer flow in which velocity fluctuations are caused by "forced" oscillation.

The theory of local separation derived by G. I. Taylor(4), depends on the assumption that the value of p' in (5,2) is equal to the pressure fluctuation in the main flow, and a functional relation between the critical Reynolds number and Taylor number is derived. It has been ascertained by experimental results on sphere or elliptic cylinders, but in the case of flow along a flat plate, we have not a complete agreement with experimental results as the above cases. It is assumed that in the case of flow around a sphere or an elliptic cylinder, the range of the laminar boundary layer along the main flow is narrow and the difference between the boundary layer oscillation and the turbulence outside the layer is not large at transition point, while for the flow along a flat plate, its range is large and the above difference becomes conspicuous. This is believed to cause the discrepancy between the theoretical and experimental results in the case of flow along a flat plate. Further, by this theory we cannot explain the phenomena of transition caused by "forced" oscillation in a flow with very low turbulence.

From the above point of view, the author will propose the following interpretation on the phenomenon of transition. The phenomenon of transition is an unsteady laminar separation, and in the case of laminar boundary layer it occurs in such a condition that

$$-\frac{\bar{\delta}^2}{\mu\bar{U}}\frac{d}{dx}(p+p')=\lambda_s \qquad (5,5)$$

is fulfilled. In this formula, δ, $\bar{U}$, p, and p' are respectively mean thickness of the layer, mean velocity outside the layer, mean pressure which is almost equal to that outside the layer, and pressure fluctuation which is entirely caused by the velocity fluctuations of the "boundary layer oscillations" which are caused by the free turbulence in the main flow or caused by the forced oscillation in the boundary layer. Namely the most important effects of the "oscillations" upon the transition are their intensity and frequency. To prove this interpretation, however, we need more detailed experimental investigations.

On Velocity Fluctuations in the Laminar Boundary Layer, II.

By Yutaka SHIGEMITSU.

Railway Technical Research Institute.

(Read July 23, 1949 Received Dec. 24, 1949)

Part II. Existence of $u'v'$-Correlation in the Laminar Boundary Layer.

§ 1. Distribution of $u'v'$-Correlation Coefficient.

Since H. L. Dryden(1) found large velocity fluctuations in the laminar boundary layer, the distinction between turbulent and laminar boundary layer flow could not be considered to depend upon the existence of the velocity fluctuation in the flow, but it was supposed to exist in these frequncy or in the shearing stress produced by their velocity fluctuations. Namely, it has been believed that in the turbulent boundary layer, the Reynolds shearing stress, $-\rho\overline{u'v'}$, ought to exist, while in the laminar boundary layer, this value vanishes. In the definition of laminar boundary layer derived by L. Prandtl, the existence of the Reynolds shearing stress cannot be considered. As for the mechanism of the laminar boundary layer oscillations, we have no definite knowledge, but when we colcrlated experimentally its frequency distribution function of u'-fluctuation, we got such a curve as shown in Fig. 1. By this

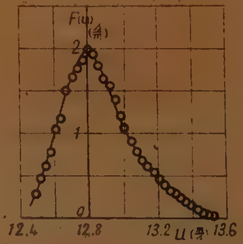

Fig. 1. Frequency distribution curve of u about its mean value of the "laminar boundary layer oscillation".

curve, we can recognize that the oscillation is not merely a periodic motion as Kármán vortex, but it shows rather an aspect of "turbulence". Thus, in the real state of boundary layer flow, we have still a question whether these oscillations may have a contribution to the Reynolds shearing stress.

Recently, for the purpose of investigating non-isotropic turbulent flow, we have devised a simple method of measuring $u'v'$-correlation coefficient by a hot-wire anemometer. It is codsisted of two or three hot-wires, one of them lying ahead and the others in its heat wake. We can measure u'- and v'-flucutations simultaneously by the wires lying ahead and in its heat wake respectively, and we can easily evaluate the value

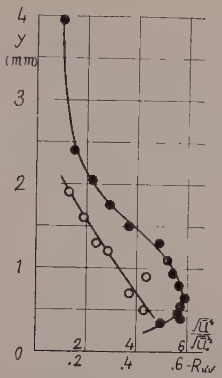

Fig. 2. Distribution of the intensity of u'-fluctuation (●) and $u'v'$-correlation coefficient (○) in the laminar boundary layer along the plate ($dp/dx = 0$) at the point of $x = 35$ cm.

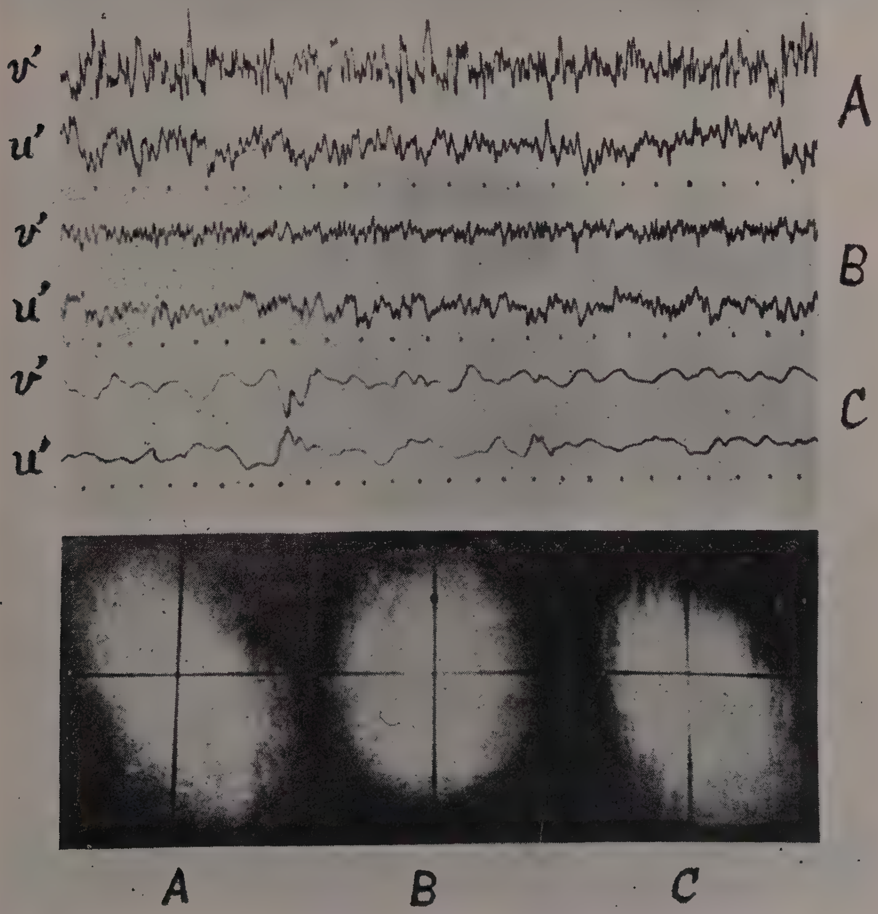

Fig. 3. States of the velocity fluctuations in three cases of flow. A-turbulent boundary layer. B-main flow of the wind tunnel. C-laminar boundary layer. In the above figures, the each timing mark is 1/100 sec. In the below figures, the origin of coordidates is the position of the mean value of u and v, the abscissa being u'-fluctuation and the ordinate, v'-fluctuation.

of $u'v'$-correlation coefficient. When u'- and v'-fluctuating voltages are simultaneously put equally in the two orthogonal axes of a braun-tube oscillograph, we can get a figure which indicates the frequency distribution function of u and v about their mean values. The detailed discussions on these methods are described in reference 3.

By this method, we investigated the existence of shearing stress produced by the laminar boundary layer oscillations. The measurements were made in the same state of the main flow of the constant speed along the plate as described in Part I. We repeated the measurements at the point of $x = 35$ cm, by the method of the two or three wires, and at this point, we found obviously the existence of a negative value of the correlation coefficient of u' and v'. Fig. 2 shows the distributions of its value and the intensity of u'-fluctuation. For comparison, we also made measurements in the turbulent boundary layer and in the main flow. In Fig. 3, the above figures show the simultaneous oscillograph records of u'- and v'-fluctuations in the three states of flow, and the below, the corresponding frequency distribution functions of u and v, taken by photographing with exposures of about 20 seconds upon the surface of a braun-tube. By these results, we can recognize the existence of a negative value of $u'v'$-correlation in the laminar boundary layer as in the turbulent boundary layer.

§ 2. Effects of $u'v'$-Correlation on the Mean Velocity Distribution.

The above measurements are concerned with the $u'v'$-correlation coefficient, and not with the value of $-\rho\overline{u'v'}$. To evaluate the Reynolds shearing stress, we need moreover a measurement of the intensity of v'-fluctuation. In general, in the laminar boundary layer, such a measurement is very difficult, owing to its small thickness, and so at present, we cannot evaluate the effect of Reynolds shearing stress on the mean velocity distribution. But it is the fact that at this point there exists a finite value of Reynolds shearing stress, and its effect on the distribution of the mean velocity ought to appear itself. Fig. 4 shows comparisons with the theoretical curve.

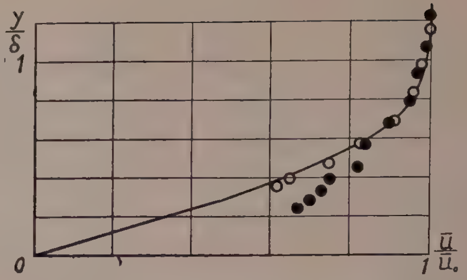

Fig. 4. Comparison of the mean velocity distributions which are derived theoretically and experimentally. Full line-theoretical. ○— measured points at $x = 10$ cm. ●—$x = 35$ cm.

Concerning the discrepancy between them shown in this figure, we can take such an interpretation that as the boundary layer develops along the plate, the effect of the shearing stress by the oscillations comes to be conspicuous. In general, by many experiments on the mean velocity distribution in the laminar boundary layer along a flat plate, we recognize that it becomes gradually to differ from the theoretical result derived by Blasius, when the measuring point upon the plate is put so far from the leading edge, and as it goes still farther, the velocity distribution changes into the 1/7-power law of the fully developed turbulent boundary layer. But when we investigate the state of the velocity fluctuation in the layer by a hot-wire anemometer, we often meet the cases in which the mean velocity distribution differs from the theoretical result before an intermittent discontinuity of the frequency is found. This fact is supposed to be due to the Reynolds shearing stress in the laminar bonndary layer.

In conclusion, the author desires to record here a debt of gratitude to Dr. T. Maekawa for his valuable advice during the work and to express his thanking Mr. N. Matsumoto and Mr. T. Uchida for their assistances in the measurements.

References of Parts I–II.

(1) Dryden, H. L.: N. A. C. A. Tech. Rep. No. 562, 1936.
(2) Dryden, H. L.: Advances in Applied Mechanics. 1, 1948.
(3) Shigemitsu, Y.: Journal of the Physical Society of Japan Vol. 5 1950.
(4) Taylor, G. I.: Proc. Roy. Soc. A 156, 1936.

On the Properties of Ferromagnetic Alloy of Manganese and Bismuth at Low Temperature.

II. Electric Conduction and Galvanomagnetic Effects.

By Kenzi KONDO.

Institute of Science and Technology, Uuiversity of Tokyo.

(Received Jan. 7, 1949)

Summary.

In Part I,(1) the results of magnetic, dilatometric and calorimetric studies of the ferromagnetic MnBi was reported. This compound was found to show abnormal behaviour in the above properties at low temperature. This paper includes the electric and galvanomagnetic studies, where the specimen is the same as in part I.

§ 1. Apparatus.

The shape of specimen is a circular cylinder or a rectangular parallelopiped. In Fig. 1a, C's are the current terminals, and R's are the potential terminals used in measurements of electric resistance and of its change in magnetic field. They are of copper wire soldered with Wood's metal. A current of 1 A and of 0.5A are passed through C respectively in measuring Hall E.M.F. and electric resistance or its change in magnetic field, which are supplied from a battery of large power. The potential terminals R's are at a distance of 13.15 mm along a axis in the middle of the side plane. The wedge-shaped H's of the same alloy as the specimen are Hall potential terminals, which soldered with Wood's metal along a plane perpendicular to the axis on upper and lower sides. J is a thermocouple of copper and constatan and is attached to the specimen with shelac. The specimen and its attachments are varnished to avoid the influence of moisture, and are covered by a case of copper (C in Fig. 1b). A generator of magnetic field for galvanomagnetic effects is a electromagnet of Weiss type, of which the pole pieces are of the diameter of 50 mm and apart at the intervals of 60 mm. To measure the potential difference we use a galvanometer of voltage sensitivity 1 μV/mm.

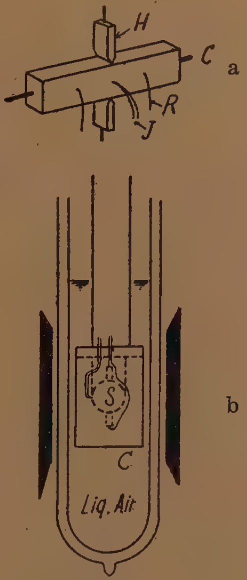

Fig. 1.

§ 2. Electric Resistance.

The specimen is a circular cylinder of diameter 8.87 mm and of length 30 mm, and involves the compound MnBi of 67 percents.

1) Specific resistivity at room temperature.

The specific resistance of the specimen is 230 $\mu\Omega$ cm at room temperature and is greater than that of bismuth and manganese, i.e., 119 and 5.0 $\mu\Omega$ cm. Since the specific resistance of mixture is remarkably influenced by lower resistance, we may expect very high specific resistivity of MnBi. In such a case, it is difficult to know the exact resistivity of higher resistance, because the specific conductivity varies markedly from place to place and the microscopic equipotential surface deviates from the macroscopic. Moreover, the specific resistivity of the bismuth-rich component may be lower than that of pure bismuth. To get the approximate value, we neglect such facts and employ the following formula:

$$\frac{1}{\rho_{\mathrm{obs}}} = \frac{f_{\mathrm{B}}}{\rho_{\mathrm{Bi}}} + \frac{f_{\mathrm{MB}}}{\rho_{\mathrm{MB}}}$$

where ρ_{obs}, ρ_{Bi} and ρ_{MB} are respectively the specific resistance of the specimen, bismuth and MnBi, and f_{Bi} and f_{MB} are the volume fractions of bismuth and of MnBi. If we adopt the following values:

$$\rho_{obs}=230\,,\quad \rho_{Bi}=119\,,\quad f_{MB}=0.67 \text{ and } f_{Bi}=0.33\,,$$

we get $\rho_{MB}=424\,\mu\Omega$ cm. This is very large compared with that of usually alloy, and may be ascribed to poor electrons in a conduction band.

2) Temperature coefficient.

The specific resistance of the specimen if plotted against temperature from −174°C to −15°C in Fig. 2. It shows a monotonous increase and not any anomalous behaviour except at −154°C. Under the same assumption as in previous paragraph,

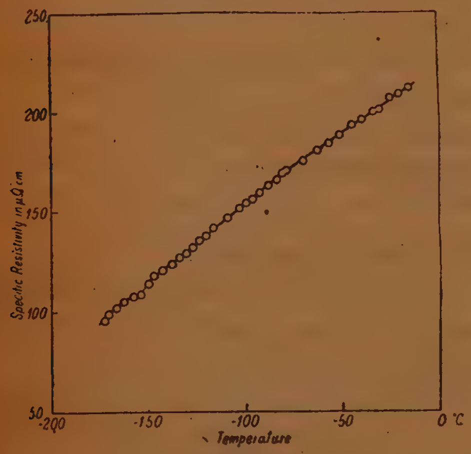

Fig 2.

$$\frac{\alpha_{obs}}{\rho_{obs}}=\frac{\alpha_{Bi}f_{Bi}}{\rho_{Bi}}+\frac{\alpha_{MB}f_{MB}}{\rho_{MB}}\,.$$

where $\alpha=\dfrac{1}{\rho}\dfrac{d\rho}{dt}$, the temperature coefficient of resistance. Assuming that $\alpha_{obs}=0.003$ and $\alpha_{Bi}=0.004$ at room temperature, we get $\alpha_{MB}=0.001$. Although this is rather small among metalls, MnBi is not a semi-conductor.

In Fig. 2 the decrease of resistance happens at −154°C, but this is not sure, because this behaviour is not reproducible and the measured values fluctuate. Contrary to magnetization, thermal expansion and specific heat, specific resistivity does not exhibit any abnormal changes. This may be ascribed to the slight influence on electrons in conduction band and to the poor accuracy of measurement for measurable change of resistivity and its temperature coefficient must be greater than respectively 10% and 30%. In spite of these rather severe restrictions, we may conclude that an anomalous behaviour of resistance is very small as compared with that of spontaneous magnetization.

§ 3. Hall Effect.

1) Hall effect is one of the effects which expose us the circumstance of d-band, on which the unusual appearance of magnetization is dependent. From its sign we shall be able to know the relative effective numbers of conduction electrons and of positive holes. But we do not derive reliable results in consequence of the following reasons: (1) Bi, which the specimen involves, shows conspicously large Hall E.M.F., as widely known. If Hall E.M.F. of MnBi is small compared with that of Bi, we are not able to separate clearly two electromotive forces, and that of MnBi may be within the error of measurement. (2) Beside Hall E.M.F., the thermo-electromotive force appears necessarily owing to the temperature difference of Ettinghausen effect at the grain boundaries between Bi and MnBi. But we can remove this secondary effect to some extent, if we measure electromotive force instantaneously as quick as we apply magnetic field, because Ettinhausen effect has a large time lag as compared with that of Hall effect.

2) Hall electromotive force at room temperature.

The specimen is a rectangular parallelepiped of section 6.40×7.20 and of length 30.75 in mms. (Fig. 1a) The observed sign is negative, and its magnetic field dependency is similar to magnetization curve. For bismuth and ferromagnetic substances, the usual formula as Hall E.M.F. = $RHiL$ is not suitable where R is a Hall constant, H magnetic field, i current density, and L the distance between two potential terminals, for in weak magnetic field R is not constant but very much dependent on magnetic field. Therefore we employ the quantity $\eta=R\cdot H$ in the place of usual R. If we assume Hall E.M.F. additive, for mixture, we get total Hall F.M.F. $=\int_0^L \eta i\,dx$

in the place of $R \cdot H \cdot \imath \cdot L$, where dx is the linear element along L. Under the same assumption as in resistance, that the component of electric field along the axis of the specimen is almost constant in the perpendicular surface to the axis, we get

$$\text{total Hall E.M.F.} = E \int_0^L \frac{\eta}{\rho} dx$$

where E is the electric field along the axis and ρ is the specific resistance dependent upon magnetic field. If we set total length of MnBi and of Bi along L respectively l_{MB} and l_{Bi}, we obtain

Total Hall E.M.F.

$$= E \frac{\eta_{\text{obs}} L}{\rho_{\text{obs}}} = E \left(\frac{\eta_{\text{MB}} l_{\text{MB}}}{\rho_{\text{MB}}} + \frac{\eta_{\text{Bi}} l_{\text{Bi}}}{\rho_{\text{Bi}}} \right).$$

Since l_{MB}/L and l_{Bi}/L are equal to the volume fractions of MnBi and of Bi phase,

$$\frac{\eta_{\text{obs}}}{\rho_{\text{obs}}} = \frac{\eta_{\text{MB}} f_{\text{MB}}}{\rho_{\text{MB}}} + \frac{\eta_{\text{Bi}} f_{\text{Bi}}}{\rho_{\text{Bi}}}.$$

Introducing the observed values of η_{obs}, η_{Bi}, ρ_{obs}, ρ_{Bi}, f_{MB}, f_{Bi} and the calculated values of ρ_{MB} in the above equation, we get η_{MB} as plotted against the magnetization in Fig. 3 (⊙), and at the same time we plot the behaviour of the usual quantity (○), η_{MB}/H against magnetic field.

The sign of η_{MB} is positive, that is, the number of positive hole is grater than that of conduction electron. This result consists with the large magnetic moment per moleculs and the small conductivity. In a ferromagnetic substance Hall E.M.F. is a function of magnetization M as well as of magnetic field H. Assuming a linear function of M and H, we get a empirical formula as follows:

$$\eta_{\text{MB}} = 6.5\,H + 289\,M \text{ in E.M.U.},$$

which is plotted against the magnetization in Fig. 3 (curve).

The coincidence of the calculated value with the measured is fairly good. The two coefficients are same, however strong the intensity of the magnetic field or the magnetization is, we may conclude that Hall electromotive force is a linear function of three components of magnetization and of magnetic fields, and we can know the Hall electromotive force in strong field from that in weak field. Since the coefficients of the magnetization is very large compared with that of magnetic field, Hall electromotive force is not dependent upon magnetic induction, and does not originate only in local magnetic field, for instance, $289/6.05 = 47.8$ is very greater than Lorentz's local field $4\pi/3 = 4.19$.

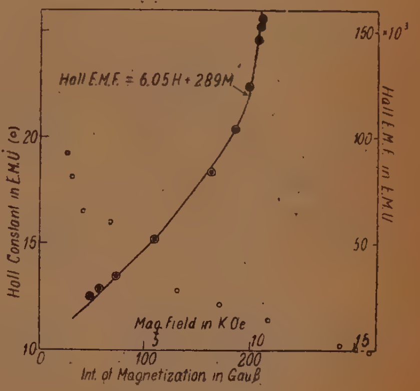

Fig. 3.

3) The influence of temperature on Hall electromotive force.

The observed Hall electromotive force of the specimen is shown in Fig. 4 from −175°C to −10°C. We did not calculate the Hall electromotive force or the coefficient of MnBi as it is difficult to obtain them with sufficient accuracy according to the abnormal Hall effect of bismuth at low temperature, but we can guess qualita-

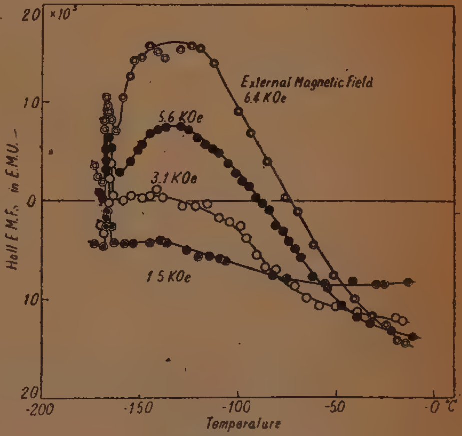

Fig. 4.

tively the behaviour of MnBi. The sharp minimum appeared from —160°C to —165°C is not proper to MnBi but due to biemuth. Accordingly the Hall electromotive force of MnBi increases rapidly at about —170°C and then gradually decreases through a very broad maximum till room temperature. Its sign may be positive at every temperature. Although the applied magnetic field is too weak to saturate the magnetization, we shall be admitted to conclude that we obtain the essentialy similar results even in the saturated magnetization as we saw in the previous section. On one hand, this anomalous Hall electromotive force is ascribed to the anomalous magnetization, and on the other hand to the two Hall coefficients themselves. The cause of the latter may be the abnormal change of effective number of electrons.

§ 4. Change of Resistance in Magnetic Field.

It is widely known that the change of resistance of ferromagnetic substance in magnetic field is dependent upon magnetic field, spontaneous magnetization and its compoment along the impressed current. And it is impossible to infer the resistance of the saturated state from that in weak field as in Hall effect. Moreover, the change of resistance is small in cantrast to that of bismuth, and we could not gain the sure and reproducible value for Mn. In Fig. 5 we show the change of resistance of the specimen (not of MnBi) at low temperature. The large values is chiefly due to bismuth, and those of MnBi are nearly the same in longitudinal and transverse effects. From -172°C to -10°C, there is not found any abnormality. This is probably due to insufficient accuracy, and at -150°C in 6400 Oersteds, the abnomal change of $\Delta\rho/\rho$ and its temperature coefficient of MnBi are less than 15 percents and 40 percents.

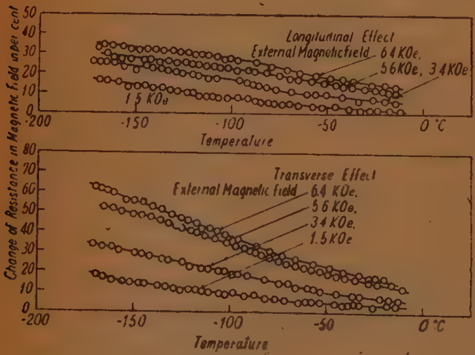

Fig. 5.

§ 4. Conclusion.

1) The specific resistivity of MnBi is rather great among alloys. Then number of electrons in a conduction band is small.

The temperature coefficient of resistivity of MnBi is small, but positive, that is, MnBi is not semi-conductor.

At -150°C MnBi does not show remarkable anomalous behaviour in resistivity, that is, the influcence upon conduction electron is slight.

2) In every magnetic field Hall electromotive force of MnBi is represented by common linear function of magnetic field and of magdeization, and its sign is positive. Therefore, the number of positive holes in *d*-band is markedly more than that of electron in a conduction band.

The Hall constants of MnBi is very much greater than that of other ferromagnetic substances.

At low temperature the Hall electromotive force show a large and broad maximum, of which the shape is asymmetric.

3) The change of resistance of MnBi in magnetic field is large compared with other metals except bismuth. But it does not show any remarkable abnormality.

In conclusion, the authors wishes to express his hearty thanks to Assis. Prof. Ren'ti Kimura. Institute of Science and Technology, University of Tokyo for his excellent guidance and kind encouragement throught this work, and to Prof. S. Kaya, University of Tokyo for his kind support, offering the electromagnet and liquid air.

References.

(1) K. Kondo, J. Phys. Soc. Japan 4 (1950).

The Change in Thermal E. M. F. Produced by a Magnetization of a Single Crystal of Iron.

By Zenya FUNATOGAWA.

Yokohama National University.

(Received January 25, 1950)

§ 1. Introduction.

It was first observed by Sir Wm. Thomson in 1856 that a thermocouple may be constructed entirely of iron or nickel provided the two parts are in different states of magnetization. Numerous investigations(1) have since been made of the effect with conflicting results.

In a longitudinal magnetic field, some authors(1) (2) found the e.m.f. of opposite sign for iron and nickel, but others (1) (3) (4) have found the e.m.f. positive, i.e., from magnetized to non-magnetized metal at a cold junction, in both cases. The e.m.f. of iron was sometimes observed to increase rapidly with magnetization to a maximum and then decrease to a constant value in a strong field, but some obtained a reversal of sign in a strohg field. This decrease or reversal in a strong field suggested to some authors a connection with the similar change in length on magnetization.

In many previous works the effect has been studied with a wide temperature difference, i.e. 100° or more because the e.m.f. of this thermocouple is very small. It is inadequate to discuss the results from theoretical viewpoints, because the magnetization and also ordinary thermoelectric powers may not change with temperature in a linear relation, so we must define and measure this e.m.f. as a mean value between $t°$ and $t°+dt°$ as in the case of an ordinary thermocouple. For simplicity the defined e.m.f. is called the "magneto-thermal e.m.f. per degree" or the "magneto-thermoelectric power" at a given temperature $t°$.

The phenomena have been measured hitherto only in an ordinary soft iron consisting of an indeterminate mass of small crystals, so that there has been no information as to the subject of Thomson thermomagnetic effect. It is, therefore, desirable to measure the effect on single crystals. The formula of the magneto-thermoelectric power of a single crystal or a single magnetic domain that is magnetized to saturation was given by N. Akulov(5) as follows:

$$(E_m)_{\alpha\beta\gamma}=a_0+a_1\sum\alpha_i^2\beta_i\gamma_i+a_2\sum_{i\neq j}\alpha_i\beta_i\alpha_j\gamma_j\ldots\ldots(1)$$

$$a_0=-\frac{a_1}{3}\quad\ldots\ldots\ldots\ldots\ldots\ldots\ldots\ldots\ldots\ldots\ldots(2)$$

where $(E_m)_{\alpha\beta\gamma}$ is the induced magneto-thermoelectric power measured along a direction with direction cosines β_1, β_2, β_3 with respect to the principal axes of a cubic crystal, when the crystal is magnetized in a direction α_1, α_2, α_3, and with a temperature gradient along a direction γ_1, γ_2, γ_3. a_1 and a_2 are so-called anisotropy constants of cubic crystals. In our case $\beta_i=\gamma_i$, so we get

$$(E_m)_{\alpha\beta}=a_0+a_1\sum\alpha_i^2\beta_i^2+a_2\sum_{i\neq j}\alpha_i\alpha_j\beta_i\beta_j\ldots(3)$$

If (E_m) in Eq. (3) is subsituated by $\left(\frac{\delta l}{l}\right)$ we get the well known magnetostrictive formula.

In order to make the measurement of the anisotropy constants in Eq. (3) by using a real crystal, it is necessary to specify a standard state. As pointed out by S. Kaya and H. Takaki(6) on distributions of magnetic domains in a single crystal of iron rod, the domains were not distributed equally in the six directions of the easiest magnetization even when the crystal-rod as a whole was in a state of demagnetization. They adopted, therefore, as a standard state the breaking point (remanence) of a descending hysteresis curve and determined the magnetostrictive constants of iron. From these considerations, the magnitudes of magneto-thermoelectric powers between the saturation and the remanence of a crystal rod are given as follows:

$$(E_m)_{\text{sat.}-\text{rem.}} = a_1\left[1 - \frac{\beta_1{}^3+\beta_2{}^3+\beta_3{}^3}{\beta_1+\beta_2+\beta_3}\right] +2(a_2-a_1)(\beta_1{}^2\beta_2{}^2+\beta_2{}^2\beta_3{}^2+\beta_3{}^2\beta_1{}^2)\ldots\ldots(4)$$

It is the purpose of this experiment to know the dependency of magneto-thermoelectric powers on the directions in a crystal of iron at an ordinary temperature (25° C) and also to give a fundamental clue to consideration of the mutual interaction between 3d- and 4s-electrons.

§ 2. Experimental Methods and Samples.

The magneto-thermal e.m.f. is a difference of the thermal e.m.f. between a demagnetized specimen and the magnetized one, each of which is measured against copper, first for the demagnetized state and then when subjected to uniform longitudinal magnetic fields under the same temperature differenec. It is necessary, as described above, that the temperature difference should be as small as possible in measurement. In our case the hot junction is 5° C~20° C higher than the cold junction which is kept at room temperature (25° C). Experimental arrangements are shown in Fig. 1. Each end of a specimen was fastened, respectively, to copper leads and copper-constantan thermocouple. The specimen was then placed in a quartz tube carrying two independent non-inductive windings, I and II, of nichrome wire, the former being used for heat treatment and the latter for controlling the temperature difference of each end of the specimen. The tube was placed inside a water jacket, through which the water kept constant in temperature was driven. The ordinary thermal e.m.f. arising from the couple was nearly balanced by connecting the couple leads as usual to a potentiometer. The magneto-thermal e.m.f. set up by a magnetic field was determined by noting the deflection of a sensitive galvanometer.

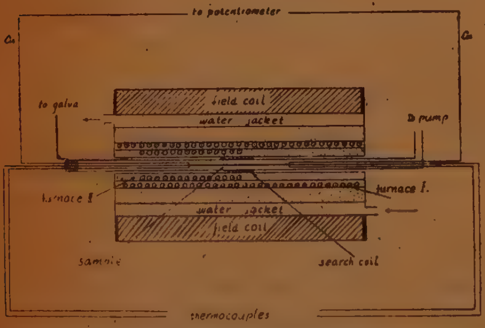

Fig. 1. Schematic representation of apparatus.

Magnetostrictions were measured by the similar methods used by S. Kaya and H. Takaki (loc. cit.).

Specimens used for this experiment were cylindrical rods made by Edward's recrystalization method from electrolytic Swedish iron. The diameter, length, direction cosines of rod-axis with respect to the principal axes and the observed and calculated values of remanence given by

$$J_{r.\ \text{calc.}} = \frac{J_\infty}{\beta_1+\beta_2+\beta_3}\ \ldots\ldots\ldots\ldots\ldots\ldots(5)$$

are shown in Table I.

The specimens are divided into three classes; viz., No. 10 is a tetragonal-, No. 20 a diagonal-, and No. 105 a trigonal-crystal respectively.

§ 3. Experimental Results.

The magneto-thermoelectric powers and magnetostrictions at every point on the progressive magnetization and on descending hysteresis curves, after thoroughly demagnetized by A. C., are shown in Figs. 2, 4, 5, and 6. Remembering that the normal e.m.f. against copper is positive for iron below about 275° C, we find that the positive magneto-thermoelectric power represents an actual increase of the

Table I.

Sample number	Diam. (mm.)	Length (mm.)	Direction cosines			$J_{r.\ \text{calc.}}$	$J_{r.\ \text{obs.}}$
			β_1	β_2	β_3		
10	2.842	189.6	0.996	0.065	0.054	1533	1535
20	1.960	172.5	0.732	0.676	0.083	1147	1121
105	1.955	230.4	0.659	0.542	0.522	992	995

magnitude of the total thermal e.m.f. as the result of magnetization.

Fig. 2 is the results of the tetragonal crystal No. 10. We know that both the curves of the magneto-thermoelectric power and of the magnetostriction change their styles in the same manner. External appearances of the magnetostriction curves differ from the well known ordinary styles of tetragonal crystals, but the difference is due to the initial distributions of magnetic domains affected by an small external condition or heat treatment etc., nevertheless, the magnitude between the saturation and the remanence has not been effected by them and almost remains constant. Fig. 3 shows this fact in the case of the magneto-thermoelectric power. In the figure the "absolute curves" are the results of No. 10 which is thermally demagnetized at 820° C and the "A.C. demagnetized curves I" are the results of the same sample which was demagnetized several times by A.C. after thermally demagnetized at the same temperature. The "A.C. demagnetized curves II" which are same ones in Fig. 1. We know that the apparent saturation values diminish gradually by A.C. demagnetization.

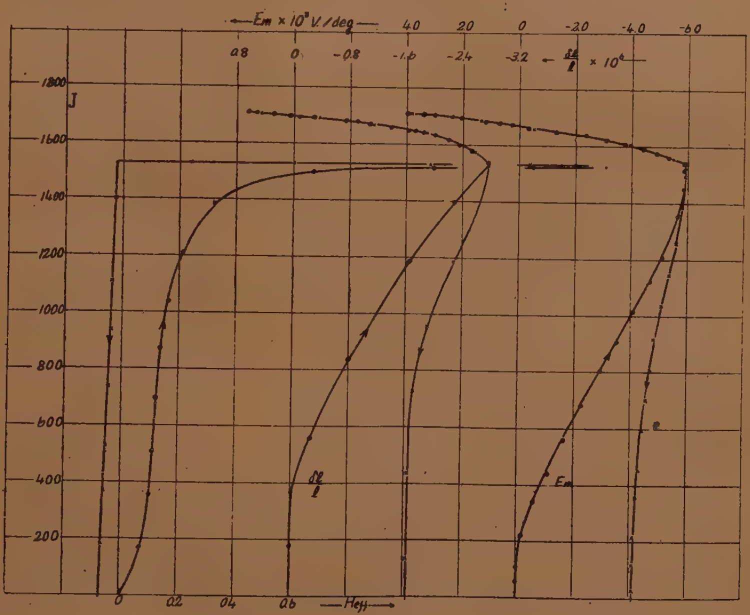

Fig. 2. Tetragonal crystal No. 10.

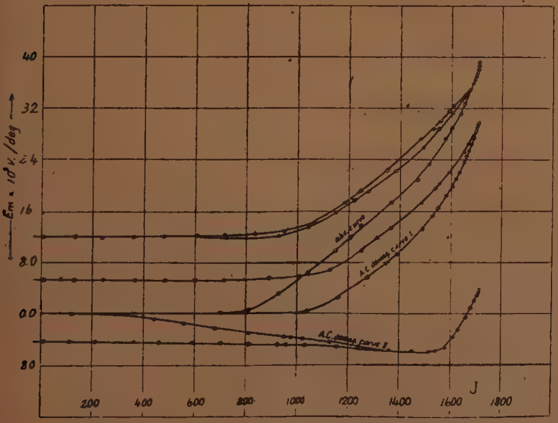

Fig. 3. Effect of demagnetization.

Fig. 4 is the results of the diagonal-crystal No. 20. Provided that this sample is a perfect diagonal crystal, we may except that the magnetostriction or magneto-thermoelectric power increases monotonously with magnetization up to the remanence and then decreases up to the saturation, but the results of this sample continue their increasing tolerably above the remanence in both cases, especially prominent for the magneto-thermoelectric power, until $J = 1200 \sim 1250$. This fact is caused by 90°-reversals of magnetic domains which have been residued at the remanence from one of principal axes perpendicular to the bar axis to another principal axes inclined 45° to the bar axis and also we can see this reversals experimentally as sharp Barkhausen jumps. The "absolute curves" in Fig. 4 are the results of the same sample demagnetized thermally at 820° C. The magneto-thermoelectric power of this sample does not change its sign even when it is saturated, but the point of inflection where the increasing turns to the decreasing occurs at the same value as in the case of the magnetostriction.

Fig. 5 is the results of the trigonal crystal No. 105. The styles of the curves of magnetostrictions or of magneto-thermoelectric powers are very simple, namely most parts of changes concentrate in the regions of rotational magnetization between the remanence and the saturation, and also represent only very small hysteresis.

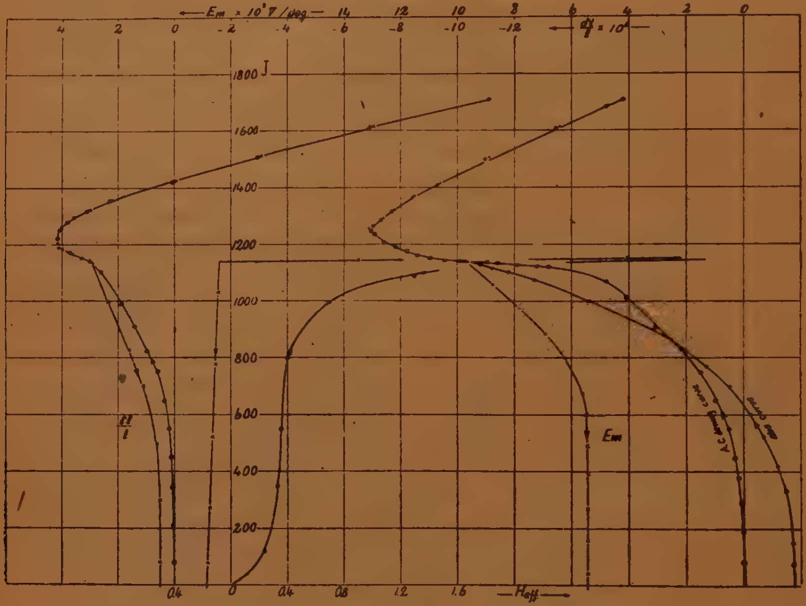

Fig. 4. Diagonal crystal No. 20.

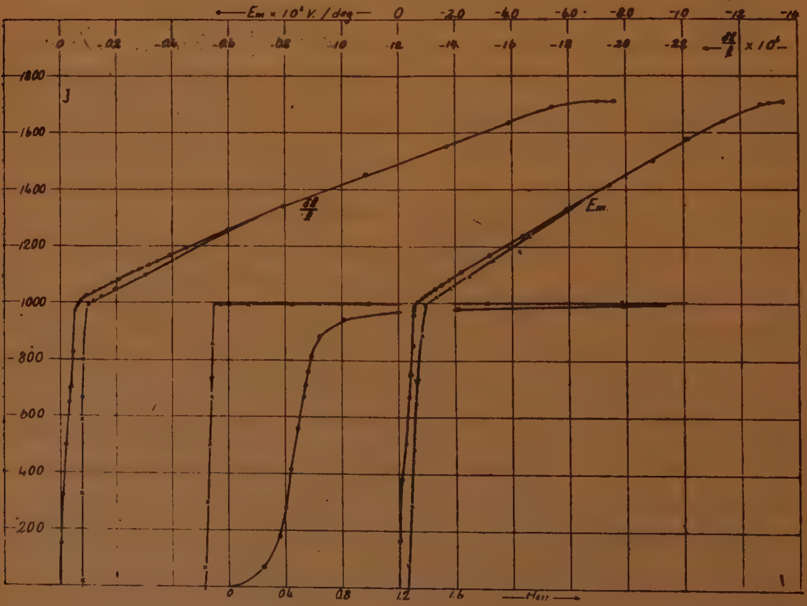

Fig. 5. Trigonal crystal No. 105.

We could not detect any effect of processes of demagnetization. We may expect these results from the symmetry properties of trigonal crystals.

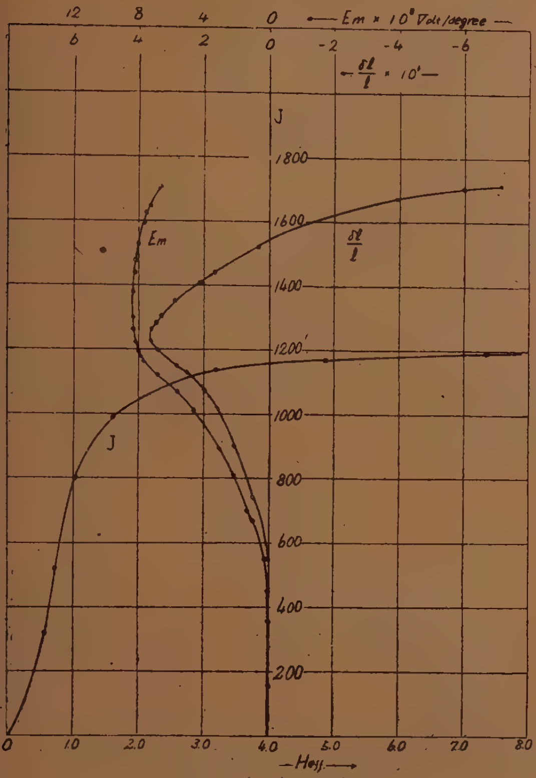

Fig. 6. Polycrystal.

Fig. 6 is the results of a polycrystal. The magnetostriction reverses its sign in a strong field, but the magneto-thermoelectric power, as most results of previous works, does not reverse its sign in any field.

§ 4. Discussion.

By measurement of the difference of magneto-thermoelectric powers between the remanence and the saturation we can calculate the anisotropy constants a_1 and a_2, and get next equations for our samples as follows:

No. 105 $0.0072a_1 + 0.6518a_2 = -12.3 \times 10^{-8}$
No. 20 $0.0298a_1 + 0.4996a_2 = -5.4 \times 10^{-8}$
No. 10 $0.0993a_1 + 0.0142a_2 = 9.8 \times 10^{-8}$

Solving the normal equations of these we get

$a_1 = 104 \times 10^{-8}$ Volt/deg.
$a_2 = -18.9 \times 10^{-8}$ Volt/deg.

In a similar way we get next equations to calculate the anisotropy constants of magnetostrictions as follows:

No. 105 $0.0072a_1' + 0.6518a_2' = -18.6 \times 10^{-6}$
No. 20 $0.0298a_1' + 0.4996a_2' = -13.0 \times 10^{-6}$
No. 10 $0.0993a_1' + 0.0142a_2' = 3.4 \times 10^{-6}$

From these equations we get

$a_1' = 38.9 \times 10^{-6}$
$a_2' = -28.7 \times 10^{-6}$

The values obtained by S. Kaya and H. Takaki (loc. cit.) who used many crystal-rods including our samples are $a_1' = 38.4 \times 10^{-6}$ and $a_2' = -28.3 \times 10^{-6}$. It is difficult to determine the constants a_1 or a_1' from our samples, because any of the bar axis coincides nearly with the symmetry axis of the crystals and so that the coefficients of a_1 or a_1' in the above equations are very small. Assuming that half of all domains in No. 10 in a thoroughly demagnetized final state by A. C. distributes respectively in the direction of [100] or [1̄00] that is nearest to the bar axis, the magnitude of the magneto-thermoelectric power between the demagnetized state and the remanence is given as follows:

$$(E_m)_{0-\text{rem.}} = a_1\left[\beta_1^2 - \frac{\beta_1^3+\beta_2^3+\beta_3^3}{\beta_1+\beta_2+\beta_3}\right] \cdots\cdots (6)$$

From the observed value $(E_m)_{0-\text{rem.}} = 4.8 \times 10^{-8}$ we get $a_1 = 54 \times 10^{-8}$ Volt/deg. In the same way we get also $a_1' = 26.0 \times 10^{-6}$. Both the values are smaller than that already obtained. Contrary to our expectation we may conclude that the initial demagnetized state has already had the domains perpendicular to the bar axis. It is difficult to determine a_1 or a_1' from the measurement on tetragonal crystals while a_2 or a_2' is accurately determined from the measurement on diagonal- or trigonal-crystals. On account of the value of a_1 or a_1' being probably a little too large to explain numerically the results of the polycrystal we are trying to repeat more measurements on other polycrystals.

An ordinary absolute thermoelectric power of iron which shows abrupt change below the Curie-point by appearances of a spontaneous magnetization is independent of the direction of the magnetization of domains. A qualitative explanation was given by N. F. Mott(7) from the standpoint of the modern theory of metal. The magneto-thermoelectric power depends upon the directions of the magnetization of domains. It is not at present certain whether these properties are directly related to ferromagnetism or only indirectly related — through the magnetostrictive lattice distortion, for instance, as was first pointed out by Ewing. According to our measurements on the series of Fe-Ni alloys we can conclude that the magneto-thermoelectric force is not directly related to the magnetostrictive lattice distortion because the magneto-thermoelectric power of a 18.5% Fe-Ni alloy which is almost free from change in length on magnetization is several times greater than that of pure iron.

§ 5. Conclusion.

We measured the change in thermo-electric power of iron crystals against copper produced by a magnetization at room temperature. As the results we found that the changes were very similar to the change in length on magnetization. Corresponding to the magnetostrictive constants

$$\lambda_{100} = \frac{2}{3}a_1' = 25.9 \times 10^{-6}$$

$$\lambda_{111} = \frac{2}{3}a_2' \doteq -19.1 \times 10^{-6}$$

we get the constants as follows:

$$(E_m)_{100} = \frac{2}{3}a_1 = 7.0 \times 10^{-8} \text{ Volt/deg.}$$

$$(E_m)_{111} = \frac{2}{3}a_2 \doteq -1.3 \times 10^{-8} \text{ Volt/deg.}$$

The magneto-thermoelectric power; viz., $(E_m)_{100}$ and $(E_m)_{111}$ may generally depend on temperature. We are now measuring this temperature dependency, results of which will give some fundamental clues to the solution of the mechanisms of the magneto-thermoelectric forces. We will undertake, in future, to investigate from the modern theory of solid the mechanisms of magnetization by using our results which may depend upon the mutual interaction between 3d- and 4s-electrons as in the case of the change of electrical resistance on magnetization.

The crystals used in this investigation were supplied by Professor Dr. S. Kaya to whom the author is indebted for much valuable discussion and suggestion. It is also a pleasure to thank Professor Dr. T. Muto for generous advice.

References.

(1) A survey of early literature is given by L. L. Campbell in "Galvanomagnetic and Thermomagnetic Effect", and by G. Masing in "Handbuch der Metallphysik, Bd. I, I Teil, 1935".

(2) H. Broili: Ann. d. Physik, **14** (1932), 259.

(3) W. H. Ross: Phys. Rev., **38** (1931), 179.

(4) F. E. Lowance and F. W. Constant: Phys. Rev., **48** (1935), 257.

(5) N. Akulov: Zeits. f. Phys., **87** (1934), 768.

(6) S. Kaya and H. Takaki: Sci. Rep. Tohoku. Anni. vol. dedicated to Prof. Honda, (1936), 314.

(7) N. F. Mott: Proc. Roy. Soc., **156** (1936), 368.

On the Negative Energy Photon Hypothesis*.

By Tamotsu AWANO.

(Received Jan. 25., 1950)

§ 1. Introduction.

In 1942 Dirac⁽¹⁾ proposed a method of field quantization which uses an indefinite metric in the Hilbert space of quantum states and introduces negative energy photons. This method was able to overcome well-known convergence difficulties of the field theories, if it is coupled with the λ-limiting process⁽²⁾. However, it failed in the theory of generation and annihilation of pairs of positive and negative electrons.

Tomonaga⁽³⁾ and Schwinger⁽⁴⁾ have developed, independently, a covariant formulation and introduced a mixed Heisenberg-Shroedinger representation, the interaction representation. In this theory the divergence arising from the vacuum polarization phenomenon occurs in a factor that alters the strength of all charges, an disavoided by a formal renormalization of the charge. Also, diverging electromagnetic proper mass makes it necessary to renormalize the electron mass.

---

* In this paper, the same notation as in the Schwinger's paper is used.

In the present paper, the theory of negative energy photon is considered in the Schwinger's covariant formalism. The electromagnetic proper mass of the electron is calculated according to Schwinger's method, and it is found that it diverges. Finally, a note on the λ-limiting process is added.

§ 2. Negative Energy Photon.

The usual method of decomposing the electromagnetic potential into Fourier components is done according to

$$A_\mu(x) = V^{-\frac{1}{2}} \sum_k \left(\frac{\hbar c}{2k_0}\right)^{\frac{1}{2}} \times [A_\mu(k) \exp(ik_\nu x_\nu) + A_\mu{}^*(k) \exp(-ik_\nu x_\nu)], \quad (2.1)$$

where $k_\mu{}^2 = 0$ and we define k_0 as positive. After Dirac we decompose $A_\mu(x)$ into two complex fields $U_\mu(x)$, $U_\mu{}^*(x)$:

$$A_\mu(x) = \frac{1}{\sqrt{2}}[U_\mu(x) + U_\mu{}^*(x)], \quad (2.2)$$

and quantize the oscillators of $U_\mu(x)$ with $k_4 x_4$ in the phase factor in the usual way, while the other part of the oscillators of $U_\mu(x)$ with $-k_4 x_4$ in the phase factor is quantized with the method of negative energy oscillator, where * indicates the adjoint operator. This means that we must put

$$\left.\begin{aligned} U_\mu(x) &= V^{-\frac{1}{2}} \sum_k \left(\frac{\hbar c}{2k_0}\right)^{\frac{1}{2}} [U_{\mu+}(k) \\ &\quad \times \exp(ik_\lambda x_\lambda) + U_{\mu-}(k) \exp(-ik_\lambda x_\lambda), \\ U_\mu{}^*(x) &= V^{-\frac{1}{2}} \sum_k \left(\frac{\hbar c}{2k_0}\right)^{\frac{1}{2}} [U_{\mu+}{}^*(k) \\ &\quad \times \exp(-ik_\lambda x_\lambda) + U_{\mu-}{}^*(k) \exp(ik_\lambda x_\lambda), \end{aligned}\right\} \quad (2.3)$$

$U_{\mu+}(k)$ and $U_{\mu-}(k)$ correspond to the positive and negative energy photons, respectively. If η_+ and η_- denote the metric of the Hilbert space corresponding to the positive and negative energy oscillators, respectively, then

$$U_{\mu+}{}^*(k) = \eta_+{}^{-1} U_{\mu+}{}^\dagger(k) \eta_+(k),$$
$$U_{\mu-}{}^*(k) = \eta_-{}^{1-}(k) U_{\mu-}{}^\dagger(k) \eta_-(k),$$

† denoting the Hermitian conjugate operator. The energy and momentum are assumed as

$$\left.\begin{aligned} E &= \frac{1}{2}\int\left\{\frac{\partial U_\lambda{}^*}{\partial x_i}\frac{\partial U_\lambda}{\partial x_i}\right. \\ &\quad \left. + \frac{\partial U_\lambda{}^*}{\partial x_0}\frac{\partial U_\lambda}{\partial x_0} + \frac{\partial U_\lambda}{\partial x_i}\frac{\partial U_\lambda{}^*}{\partial x_i} + \frac{\partial U_\lambda}{\partial x_0}\frac{\partial U_\lambda{}^*}{\partial x_0}\right\} dv, \\ G_i &= -\frac{1}{2c}\int\left\{\frac{\partial U_\lambda{}^*}{\partial x_0}\frac{\partial U_\lambda}{\partial x_i}\right. \\ &\quad \left. + \frac{\partial U_\lambda}{\partial x_0}\frac{\partial U_\lambda{}^*}{\partial x_i} + \frac{\partial U_\lambda}{\partial x_i}\frac{\partial U_\lambda{}^*}{\partial x_0} + \frac{\partial U_\lambda{}^*}{\partial x_i}\frac{\partial U_\lambda}{\partial x_0}\right\} dv, \end{aligned}\right\} \quad (2.4)$$

and the commutation relations are given by

$$\left.\begin{aligned} [U_{\mu+}(k), U_{\nu+}{}^*(k')] &= \delta_{\mu\nu}\delta_{k_1 k_1'}\delta_{k_2 k_2'}\delta_{k_3 k_3'}, \\ [U_{\mu-}(k), U_{\nu-}{}^*(k')] &= -\delta_{\mu\nu}\delta_{k_1 k_1'}\zeta_{k_2 k_2'}\delta_{k_3 k_3'} \end{aligned}\right\} \quad (2.5)$$

The quantities $N_{\mu+}(k)$, $N_{\mu-}(k)$ defined by

$$N_{\mu+}(k) = U_{\mu+}{}^*(k) U_{\mu+}(k), \quad N_{\mu-}(k) = -U_{\mu-}{}^*(k) U_{\mu-}(k) \quad (2.6)$$

have the eigenvalues 0, 1, 2,.....which represent the numbers of the positive and negative energy photons, respectively. The commutative law for $U_\mu(x)$, $U_\mu{}^*(x)$ is derived from (2.5)

$$\left.\begin{aligned} [U_\mu(x), U_\nu{}^*(x')] &= i\hbar c\delta_{\mu\nu} D(x-x'), \\ [U_\mu(x), U_\nu(x') &= [U_\mu{}^*(x), U_\nu{}^*(x')] = 0. \end{aligned}\right\} \quad (2.7)$$

In view of the property $D(-x) = -D(x)$ the commutative law for $A_\mu(x)$ is

$$[A_\mu(x), A_\nu(x')] = i\hbar c\delta_{\mu\nu} D(x-x'), \quad (2.8)$$

The above procedure is equivalent to introducing besides the usual potential field $A_\mu(x)$, the adjoint of which is $A_\mu{}^*(x) = A_\mu(x)$ satisfying the commutative law (2.8), another field $B_\mu(x)$, the adjoint of which is $B_\mu{}^*(x) = -B_\mu(x)$, satisfying the commutative law

$$[B_\mu(x), B_\nu(x')] = -i\hbar c\delta_{\mu\nu} D(x-x'), \quad (2.9)$$

and putting

$$\left.\begin{aligned} U_\mu(x) &= \frac{1}{\sqrt{2}}[A_\mu(x) + B_\mu(x)], \\ U_\mu{}^*(x) &= \frac{1}{\sqrt{2}}[A_\mu(x) - B_\mu(x)]; \end{aligned}\right\} \quad (2.10)$$

assuming the energy and momentum expressions

$$\left.\begin{aligned} E&=\frac{1}{2}\int\Big[\frac{\partial A_\mu}{\partial x_i}\frac{\partial A_\mu}{\partial x_i}\\ &\quad+\frac{\partial A_\mu}{\partial x_0}\frac{\partial A_\mu}{\partial x_0}-\frac{\partial B_\mu}{\partial x_i}\frac{\partial B_\mu}{\partial x_i}-\frac{\partial B_\mu}{\partial x_0}\frac{\partial B_\mu}{\partial x_0}\Big]dv,\\ G_i&=-\frac{1}{2c}\int\Big[\frac{\partial A_\mu}{\partial x_0}\frac{\partial A_\mu}{\partial x_i}\\ &\quad+\frac{\partial A_\mu}{\partial x_i}\frac{\partial A_\mu}{\partial x_0}-\frac{\partial B_\mu}{\partial x_0}\frac{\partial B_\mu}{\partial x_i}-\frac{\partial B_\mu}{\partial x_i}\frac{\partial B_\mu}{\partial x_0}\Big]dv. \end{aligned}\right\} \quad (2.11)$$

Assuming that the field $A_\mu(x)$ only interacts with the material field, the Lagrangian function is assumed as follows:

$$\begin{aligned} L&=-\frac{1}{2}\frac{\partial A_\mu(x)}{\partial x_\nu}\frac{\partial A_\mu(x)}{\partial x_\nu}+\frac{1}{2}\frac{\partial B_\mu(x)}{\partial x_\nu}\frac{\partial B_\mu(x)}{\partial x_\nu}\\ &\quad-\frac{\hbar c}{2}\bar{\psi}(x)\Big[\gamma_\mu\Big(\frac{\partial}{\partial x_\mu}-\frac{ie}{\hbar c}A_\mu(x)\Big)+\kappa_0\Big]\psi(x)\\ &\quad-\frac{\hbar c}{2}\bar{\psi}'(x)\Big[\gamma_\mu\Big(\frac{\partial}{\partial x_\mu}+\frac{ie}{\hbar c}A_\mu(x)\Big)+\kappa_0\Big]\psi'(x). \end{aligned} \quad (2.12)$$

The equation of motion for $U_\mu(x)$, $U_\mu^*(x)$ are derived as

$$\left.\begin{aligned} \Box U_\mu(x)&=-\frac{1}{\sqrt{2}}\frac{1}{c}j_\mu(x),\\ \Box U_\mu^*(x)&=-\frac{1}{\sqrt{2}}\frac{1}{c}j_\mu(x). \end{aligned}\right\} \quad (2.13)$$

The Fermi condition is given in terms of $U_\mu(x)$, $U_\mu^*(x)$ as follows:

$$\frac{\partial U_\mu(x)}{\partial x_\mu}\Phi=0,\quad \frac{\partial U_\mu^*(x)}{\partial x_\mu}\Phi=0. \quad (2.14)$$

§ 3. Interaction Representation.

In Tomonaga-Schwinger's theory, the equation of motion for state vector is given by

$$i\hbar c\frac{\delta\Psi[\sigma]}{\delta\sigma(x)}=H(x)\Psi[\sigma]. \quad (3.1)$$

Now the theory developed in the preceding section is expressed in the interaction representation chosing $H(x)$ as

$$H(x)=\frac{-1}{\sqrt{2}}\frac{1}{c}j_\mu(x)[U_\mu(x)+U_\mu^*(x)]. \quad (3.2)$$

The Fermi condition is expressed. in this representation, as

$$\left.\begin{aligned} &\Big[\frac{\partial U_\mu(x)}{\partial x_\mu}-\frac{1}{\sqrt{2}}\frac{1}{c}\int_\sigma D(x-x')j_\mu(x)d\sigma_\mu'\Big]\Psi[\sigma]=0,\\ &\Big[\frac{\partial U_\mu^*(x)}{\partial x_\mu}-\frac{1}{\sqrt{2}}\frac{1}{c}\int_\sigma D(x-x')j_\mu(x)d\sigma_\mu'\Big]\Psi[\sigma]=0, \end{aligned}\right\} (3.3)$$

x being an arbitrary point not necessarily lie on σ.

Owing to the divergence-less character expressed by the supplementary condition (2.14), it is possible to eliminate the longitudinal parts of the $U_\mu(x)$, $U_\mu^*(x)$ fields. Introducing an arbitrary time-like unit vector n_μ, $n_\mu^2=-1$, we decompose $U_\mu(x)$ into the gradient in the time-like direction specified by n_μ of a scalar field $\Lambda(x)$, the gradient in the space-like direction orthogonal to n_μ of a scalar field $\Lambda'(x)$ and the vector field $u_\mu(x)$ which has no component in the direction n_μ, and is didergence-less:

$$\begin{aligned} U_\mu(x)&=n_\mu n_\nu\frac{\partial}{\partial x_\nu}\Lambda(x)\\ &\quad-\Big(\frac{\partial}{\partial x_\mu}+n_\mu n_\nu\frac{\partial}{\partial x_\nu}\Big)\Lambda'(x)+u_\mu(x), \end{aligned} \quad (3.4)$$

where

$$n_\mu u_\mu(x)=0,\quad \frac{\partial}{\partial x_\mu}u_\mu(x)=0.$$

It is assumed that $\Lambda(x)$, $\Lambda'(x)$ and $u_\mu(x)$ satisfy the field equation:

$$\Box\Lambda(x)=\Box\Lambda'(u)=\Box u_\mu(x)=0.$$

Commutative law

$$\left.\begin{aligned} [\Lambda(x),\Lambda^*(x')]&=i\hbar c\mathfrak{D}(x-x'),\\ [\Lambda'(x),\Lambda^*(x')]&=i\hbar c\mathfrak{D}(x-x'),\\ [u_\mu(x),u_\nu^*(x')]&=i\hbar c\delta_{\mu\nu}D(x-x')-i\hbar c\Big\{\frac{\partial}{\partial x_\mu}\\ &\quad\times\frac{\partial}{\partial x_\nu}+\Big(n_\mu\frac{\partial}{\partial x_\nu}+n_\nu\frac{\partial}{\partial x_\mu}\Big)n_\lambda\frac{\partial}{\partial x_\lambda}\Big\}\mathfrak{D}(x-x') \end{aligned}\right\} (3.5)$$

are derived from (3.4), (2.7). In terms of these quantities, the equation of motion for $\Psi[\sigma]$, and supplementary conditions are expressed as follows:

$$\begin{aligned} i\hbar c\frac{\delta\Psi[\sigma]}{\delta\sigma(x)}&=\Big[-\frac{1}{\sqrt{2}}\frac{1}{c}j_\mu(x)\\ &\quad\times\{u_\mu(x)+u_\mu^*(x)\}-\frac{1}{c^2}\int_\sigma\Big(\frac{1}{2}\frac{\partial\mathfrak{D}(x-x')}{\partial x_\mu}\\ &\quad+n_\mu n_\nu\frac{\partial\mathfrak{D}(x-x')}{\partial x_\nu}\Big)j_\mu(x)j_\lambda(x')d\sigma_\lambda'\Big]\Psi[\sigma], \end{aligned} \quad (3.6)$$

$$\left.\begin{aligned} \{\Lambda(x)-\Lambda'(x)\}\Psi[\sigma]&=0,\\ \{\Lambda^*(x)-\Lambda'^*(x)\}\Psi[\sigma]&=0. \end{aligned}\right\}$$

§ 4. Coupling between the Fields.

According to the preceding considerations the coupling between the electromagnetic and electron fields can be described in two equivalent ways: either employing the complete electromagnetic field, together with suplementary conditions, or using the transverse vector field, which requires no explicit use of the supplementary condition. The first-order coupling between the fields corresponds to the emission or absorption of a light quantum by a free electron, and such processes are all virtual. Hence it is convenient to have an equation of motion for $\Psi[\sigma]$ from which the first-order interaction term has been eliminated. In order to carry out this program, we introduce into (3.6) the gauge transformation

$$\Psi[\sigma] \rightarrow e^{-iS[\sigma]}\Psi[\sigma],$$

where

$$\left.\begin{aligned} S[\sigma] &= -\frac{1}{2\sqrt{2}}\frac{1}{\hbar c^2} \\ &\times \int_{-\infty}^{\infty} j_\mu(x')\{u_\mu(x)+u_\mu^*(x)\}\epsilon[\sigma,\sigma']d\omega'. \end{aligned}\right\} \tag{4.1}$$

The volume integral is extended over whole space-time. If we consider only the terms up to the second-order with respect to the interaction, we obtain the equation of motion

$$\begin{aligned} i\hbar c\frac{\delta\Psi[\sigma]}{\delta\sigma(x)} &= \Big[-\frac{i}{8\hbar c^3}\int_{-\infty}^{\infty} \\ &[j_\mu(x)\{u_\mu(x)+u_\mu^*(x)\}, j_\nu(x')\{u_\nu(x') \\ &+u_\nu^*(x')\}]\epsilon[\sigma,\sigma']d\omega' - \frac{1}{c^2}\int_\sigma \Big(\frac{1}{2}\frac{\partial\mathfrak{D}(x-x')}{\partial x_\mu} \\ &+n_\mu n_\nu\frac{\partial\mathfrak{D}(x-x')}{\partial x_\nu}\Big)j_\mu(x)j_\lambda(x)d\sigma_\lambda'\Big]\Psi[\sigma]. \end{aligned} \tag{4.2}$$

Similarly we introduce for (3.2), (3.3) the gauge transformation

$$\Psi[\sigma] \rightarrow e^{-iR[\sigma]}\Psi[\sigma],$$

where

$$\left.\begin{aligned} R[\sigma] &= -\frac{1}{2\sqrt{2}\hbar c^2} \\ &\times \int_{-\infty}^{\infty} j_\mu(x')\{U_\mu(x')+U_\mu^*(x')\}\epsilon[\sigma,\sigma']d\omega'. \end{aligned}\right\} \tag{4.3}$$

The new equation of motion is

$$\begin{aligned} i\hbar c\frac{\delta\Psi[\sigma]}{\delta\sigma(x)} &= \frac{1}{8c^2}\int_{-\infty}^{\infty} \\ &\times\{j_\mu(x), j_\nu(x')\}D(x-x')\epsilon[\sigma,\sigma']d\omega'\Psi[\sigma] \\ &-\frac{i}{16\hbar c^3}\int_{-\infty}^{\infty}[j_\mu(x), j_\nu(x')]\{(U_\mu(x)+U_\mu^*(x)), \\ &(U_\nu(x')+U_\nu^*(x'))\}\epsilon[\sigma,\sigma']d\omega'\Psi[\sigma] \end{aligned} \tag{4.4}$$

and the new supplementary conditions are

$$\begin{aligned} \Big[\frac{\partial U_\mu(x)}{\partial x_\mu} &+ \frac{1}{\sqrt{2}c}\int_\sigma D(x-x')j_\mu(x')d\sigma_\mu' \\ &-\frac{1}{\sqrt{2}c}\int_\sigma D(x-x')j_\mu(x')d\sigma_\mu' \\ &+\frac{i}{4\hbar c^3}\int_\sigma d\sigma_\mu' D(x-x')\int_{-\infty}^{\infty}d\omega''[j_\nu(x''), j_\mu(x)] \\ &\times\{U_\nu(x'')+U_\nu^*(x'')\}\epsilon[\sigma,\sigma'']\Big]\Psi[\sigma]=0 \end{aligned}$$

and the adjoint equation. In consequence of the gauge transformation (4.3), the new potential and current are given by

$$e^{iR[\sigma]}U_\mu(x)e^{-iR[\sigma]} = U_\mu(x)+\delta U_\mu(x),$$

$$e^{iR[\sigma]}j_\mu(x)e^{-iR[\sigma]} = j_\mu(x)+\delta j_\mu(x),$$

where

$$\delta U_\mu(x) = -\frac{1}{2\sqrt{2}c}\int_{-\infty}^{\infty} j_\mu(x')D(x-x')\epsilon[\sigma,\sigma']d\omega', \tag{4.5}$$

$$\begin{aligned} \delta j_\mu(x) &= \frac{i}{2\sqrt{2}\hbar c^2}\int_{-\infty}^{\infty}[j_\mu(x), j_\nu(x')] \\ &\times\{U_\nu(x')+U_\nu^*(x')\}\epsilon[\sigma,\sigma']d\omega'. \end{aligned} \tag{4.6}$$

Thus, the equation of motion (4.4) can be written as

$$\begin{aligned} i\hbar c\frac{\delta\Psi[\sigma]}{\delta\sigma(x)} &= \Big[-\frac{1}{4\sqrt{2}c}\{j_\mu(x), (\delta U_\mu(x)+\delta U_\mu^*(x))\} \\ &-\frac{1}{4\sqrt{2}c}\{(U_\mu(x)+U_\mu^*(x)), \delta j_\mu(x)\}\Big]]\Psi[\sigma]. \end{aligned} \tag{4.7}$$

Next, we transform (4.2) in the form which gives its obvious physical meaning. The additional term produced by the gauge transformation (4.1) is

$$\begin{aligned} \delta u_\mu(x) &= -\frac{1}{2\sqrt{2}c}\int_{-\infty}^{\infty} j_\mu(x')D(x-x')\epsilon[\sigma,\sigma']d\omega' \\ &-\frac{1}{\sqrt{2}c}\int_\sigma\Big(\frac{\partial}{\partial x_\mu}+2n_\mu n_\nu\frac{\partial}{\partial x_\mu}\Big) \\ &\times\mathfrak{D}(x-x')j_\lambda'(x')d\sigma_\lambda' + \frac{1}{2\sqrt{2}c}\frac{\partial}{\partial x_\mu} \\ &\times\Big\{\int_{-\infty}^{\infty} n_\lambda\frac{\partial}{\partial x_\lambda}\mathfrak{D}(x-x')n_\nu j_\nu(x')\epsilon[\sigma,\sigma]d\omega'\Big\}. \end{aligned}$$

The gradient term on the right hand side can be completely eliminated, in the approximation of retaining only second-order quantities, by a suitable gauge transformation, and we have

$$\begin{aligned} \delta u_\mu(x) &= \delta U_\mu(x) - \frac{1}{\sqrt{2}c} \\ &\times\int_\sigma\Big(\frac{\partial}{\partial x_\mu}+2n_\mu n_\nu\frac{\partial}{\partial x_\nu}\Big)\mathfrak{D}(x-x)j_\lambda(x')d\sigma_\lambda'. \end{aligned} \tag{4.8}$$

The additional term for $j_\mu(x)$ is, in this case,

$$\delta j_\mu(x) = \frac{i}{2\sqrt{2}\,\hbar c_2}\int_{-\infty}^{\infty}[j_\mu(x), j_\nu(x')] \times \{u_\nu(x')+u_\nu{}^*(x')\}\,\epsilon[\sigma, \sigma']d\omega'. \tag{4.9}$$

Thus, we have the equation of motion

$$i\hbar c\frac{\delta\Psi[\sigma]}{\delta\sigma(x)} = \Big[-\frac{1}{4\sqrt{2}\,c}\{j_\mu(x), (\delta U_\mu(x)+\delta U_\mu{}^*(x))\} -\frac{1}{4\sqrt{2}\,c}\{(u_\mu(x)+u_\mu{}^*(x)), \delta j_\mu(x)\}\Big]\Psi[\sigma]. \tag{4.10}$$

Finally, the current introduced by the electromagnetic field is divided into two parts, that existing in the absence of the electron field, and that associated with the presence of charged particles

$$\delta j_\mu(x) = (\delta j_\mu(x))_0 + (\delta j_\mu(x))_1,$$

where

$$(\delta j_\mu(x))_0 = \frac{i}{2\sqrt{2}\,\hbar c^2}\int_{-\infty}^{\infty} <[j_\mu(x), j_\nu(x')]>_0 \times \{u_\nu(x')+u_\nu{}^*(x')\,\epsilon[\sigma, \sigma']d\omega, \tag{4.11}$$

$$(\delta j_\mu(x))_1 = \frac{i}{2\sqrt{2}\,\hbar c^2}\int_{-\infty}^{\infty}[j_\mu(x), j_\nu(x')]_1 \times \{u_\nu(x')+u_\nu{}^*(x')\}\,\epsilon[\sigma, \sigma']d\omega', \tag{4.12}$$

the subscript 1 indicates the difference between the quantity and its vacuum expectation value. Decomposing the matter interaction term into one-particle and two-particle terms:

$$\{j_\mu(x), j_\mu(x')\} = \{j_\mu(x), j_\mu(x')\}_0 + \{j_\mu(x), j_\mu(x')\}_1 + \{j_\mu(x), j_\mu(x')\}_2,$$

the equation of motion for $\Psi[\sigma]$ is written as

$$i\hbar c\frac{\delta\Psi[\sigma]}{\delta\sigma(x)} = \{H_{0,0}+H_{1,0}+H_{2,0}+{}_{1,1}\}\Psi[\sigma] \tag{4.13}$$

where

$$H_{0,0} = \frac{1}{8c^2}\int_{-\infty}^{\infty}\{j_\mu(x), j_\mu(x')\}_0 D(x-x')\,\epsilon[\sigma, \sigma']d\omega', \tag{4.14}$$

$$H_{1,0} = -\frac{i}{16\hbar c^3}\int_{-\infty}^{\infty}[j_\mu(x), j_\nu(x')]_1 <\{(u_\mu(x)+u_\mu{}^*(x)), (u_\nu(x')+u_\nu{}^*(x'))\}>_0\,\epsilon[\sigma, \sigma']d\omega' + \frac{1}{8c^2}\int_{-\infty}^{\infty}\{i_\mu(x), j_\mu(x')\}_1 D(x-x')\,\epsilon[\sigma, \sigma]d\omega', \tag{4.15}$$

$$H_{2,0} = \frac{1}{8c^2}\int_{-\infty}^{\infty}\{j_\mu(x), j_\mu(x')\}_2 D(x-x')\,\epsilon[\sigma, \sigma']d\omega'.$$

$$H_{1,1} = -\frac{i}{16\hbar c^3}\int_{-\infty}^{\infty}[j_\mu(x), j_\nu(x')]_1 \times \{(u_\mu(x)+u_\mu{}^*(x)),(u_\nu(x')+u_\nu{}^*(x'))\}_1\epsilon[\sigma, \sigma']d\omega'.$$

The subscripts of these quantities refer to the number of electrons and light quanta whose transitions are described by the term in question. The explicit forms of $\{j_\mu(x), j_\mu(x')\}_0$ and $\{j_\mu(x), j_\mu(x')\}_1$ were given by Schwinger.

§ 5. Vacuum Condition, Electromagnetic Self-Energy.

The vacuum of the isolated electromagnetic field may be that state where exist no light quanta. This condition is expressed by

$$u_\mu(x)\Psi_0 = 0, \tag{5.0}$$

where Ψ_0 represents the vacuum of the electromagnetic field. Now, the vacuum expectation value in (4.15) can be calculated

$$H_{1,0} = \frac{1}{8c^2}\int_{-\infty}^{\infty}\{j_\mu(x), j_\mu(x')\}_1 D(x-x')\,\epsilon[\sigma, \sigma']d\omega$$
$$= \frac{e^2}{16}\int_{-\infty}^{\infty}\Big\{[\bar{\psi}(x), \gamma_\mu\Big(\gamma_\lambda\frac{\partial}{\partial x_\lambda}-\kappa_0\Big) \times \Delta^{(1)}(x-x')\gamma_\mu\bar{\psi}(x')]_1 + [\bar{\psi}(x')\gamma_\mu\Big(\gamma_\lambda\frac{\partial}{\partial x_\lambda'}-\kappa_0\Big) \times \Delta^{(1)}(x'-x)\gamma_{\mu 1}\bar{\psi}(x)]_1\Big\}D(x-x')\,\epsilon[\sigma, \sigma']d\omega'.$$

Introducing a function $F(\lambda)$ defined by

$$\frac{dF(\lambda)}{d\lambda} = D(x-x')\frac{d\Delta^{(1)}(x-x')}{d\lambda}$$

where $\lambda = -(x_\mu - x_\mu')^2$, we have

$$H_{1,0} = \frac{e^2}{8}k_0\Big\{\Big[\bar{\psi}(x), \int_{-\infty}^{\infty}\{F(\lambda)-2D(x-x')\Delta^{(1)}(x-x')\} \times \psi(x')d\omega'\Big]_1 + \Big[\int_{-\infty}^{\infty}\bar{\psi}(x')\{F(\lambda)-2D(x-x') \times \Delta^{(1)}(x-x')\}d\omega', \psi(x)\Big]_1\Big\}.$$

Using the integral representation of $D(x)$, $\Delta^{(1)}(x)$ and $\exp(iA\lambda)$, we have

$$H_{1,0} = K\cdot\frac{1}{2}[\bar{\psi}(x), \psi(x)]_1$$

where

$$K = \frac{e^2\kappa_0}{2(4\pi)^2}\int_{-\infty}^{\infty}d\xi\int_{-\infty}^{\infty}d\eta\frac{1}{(\xi+\eta)|\xi+\eta|} \times e^{-i\frac{\kappa_0{}^2}{4(\xi+\eta)}+i\frac{\kappa_0{}^2}{4\xi}}\Big(2-\frac{\xi}{\xi+\eta}\Big)\frac{\xi}{|\xi|}$$
$$= -\frac{\alpha}{16\pi}m_0c^2\int_0^{\infty}\chi d\chi\cdot\lim_{\omega_0\to 0}\log\frac{1}{\gamma\omega_0}$$

where α is the fine structure constant, and $\log\gamma$ is Euler's constant. Showing that it is possible to remove the term $H_{1,0}(x)$ from (4.13) and thereby alter the equation of motion for the electron field into that of a particle of mass $m=m_0+\frac{K}{c^2}$, it is justified that $\frac{K^2}{c^2}$ represents the electromagnetic mass of electron.

§ 6. Concluding Remark.

It was shown by Dirac, that a translation of the λ-limiting method into quantum theory can easily be described by a change of the commutation relation between the potentials according to

$$[A_\mu(x),A_\nu(x')]=\frac{i\hbar c}{2}\delta_{\mu\nu}[D(x-x'+\lambda)+D(x-x'-\lambda)],$$

where the four-vector λ_ν has to be time-like, $\lambda_0^2>\lambda_i^2$.

We may consider the λ-limiting process in the Tomonaga-Schwinger's formalism. Taking $H(x)$ in (3.1) as $-\frac{1}{c}j_\mu(x)A_\mu(x)$, we pass on a Heisenberg-Schroedinger mixed representation, in which the equation of motion for the electromagnetic field is

$$\Box A_\mu(x)=\frac{i}{2\hbar c^2}\frac{\partial}{\partial x_\nu}\int_\sigma j_\mu(x)$$
$$\times\{D(x-x'+\lambda)+D(x-x'-\lambda)\}d\sigma_\nu',$$

which differs from that of the field in vacuum. Therefore, we cannot arive at the interaction representation in this manner and cannot simply combine the negative energy photon hypothesis with the λ-limiting process in the interaction represention.

References

(1) P. A. M. Dirac, Proc. Roy. Soc. **A 180,** (1942) 1; cf. also W. Pauli, Rev. Mod. Phys. **15,** (1943) 175.

(2) G. Wentzel, Zeits. f. Phys. **86,** (1933) 479 and 635; **87,** (1934) 726.
P. A. M. Dirac, Ann. de l'Inst. Poincare **9,** (1939) 13.

(3) S. Tomonaga, Prog. Theor. Phys. **1,** (1946) 27.

(4) J. Schwinger, Phys. Rev. **74,** (1948) 1439; **75,** (1949) 651.

The Vibrational Properties of Wood I.

By Eiichi FUKADA.

Kobayashi Institute of Physical Research, Kokubunji, Tokyo.

(Read May 1, 1949; Received January 26, 1950)

§ 1. Introduction.

The vibrational properties of wood are very interesting as it is used popularly in many musical instruments. They are very different according to its original location in the tree, the direction of fibers, the moisture content, the temperature, and the previous treatment. Therefore it is desirable to repeat the measurement so many times that the reliable results could be obtained. We have measured the logarithmic decrement and the Young's modulus of wood by means of a new method which seems to be comparatively simpler than the previously reported ones(1)(2)(3). In the present paper we will report the data on the various woods under the condition of air-dried state.

§ 2. Measuring Method.

Fig. 1. gives the schematic diagram of measuring apparatus. The dimensions of test piece M are about 30 cm long, 2 cm wide, and 0.5 cm thick. We suspend it with two fine threads F at the nodal lines corresponding to each mode of lateral vibration. The thin iron piece P is attached on both ends of specimen and a pole of the electromagnetic coil L_1, L_2, is respectively set with a small air gap toward it. When the alternating current of the valve oscillator is sent through coil L_1, the specimen begins the lateral forced vibration and the induced electromotive force arises in coil L_2. When the frequency of alternating current in exciting coil L_1 is adjusted to coincide with the natural frequency of wood specimen, the induced electromotive force in receiving coil L_2 has a maximum value. This maximum is determined by the microammeter A. The Young's modulus of wood is calculated from this frequency f according to the following formula;

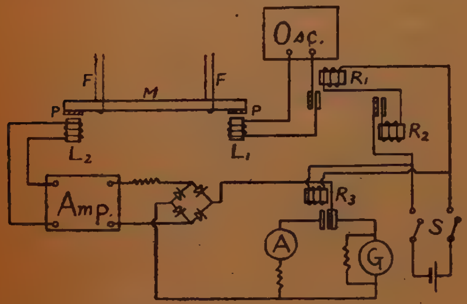

Fig. 1. The schematic diagram of measuring apparatus.

$$E = \frac{48\pi^2}{m^4} \cdot \frac{l^2}{a^4} \cdot \rho \cdot f^2, \tag{1}$$

where l is the length, a the thickness, ρ the density of specimen, and m the numerical constant determined by the mode of vibration.

The method of measuring the logarithmic decrement is as follows; on the condition of resonance we switch off the exciting current and rectify the damping current in receiving coil L_2 caused by the damping vibration of specimen and measure its total charge by a ballistic galvanometer G. When a switch S is closed and the contact of relay R_2 is touched with hand, then relay R_1 operates and the alternating current flows through the exciting coil L_1, which makes the specimen vibrate. The alternating current induced in the receiving coil L_2 is amplified and full-wave rectified. When the switch S is open, the contact of relay R_1 separates, and the exciting current disappears, and the specimen ceases to vibrate. If the switch S is closed again, as the contact of relay R_2 separates, the exciting current does not flow and the specimen does not vibrate. When the switch S is opened, the contact of relay R_3 touches on the side of ballistic galvanometer G, by which the total charge of rectified damping current caused by the damping oscillation of specimen is measured. Owing to the relay R_2 we can also measure the charge in the arbitrary time interval while the switch S is open, and reduce the error due to the hum of amplifier by opening the switch S only for the necessary small interval. It is already known that the damping of vibration of wood is just exponential at small amplitude(3). Therefore the amplitude of alternating current induced in the receiving coil L_2 decreases as $\exp(-\alpha t)$ with the time t, where α is the damping constant. Denoting the initial amplitude of current I_0 and its angular frequency ω, the total charge obtained is

$$Q = \int_0^\infty I_0 \exp(-\alpha t) |\cos \omega t| dt$$

$$= I_0 \left(\frac{\alpha}{\alpha^2 + \omega^2} + \frac{\omega}{\alpha^2 + \omega^2} \operatorname{cosech} \frac{\pi \alpha}{2\omega} \right) \tag{2}$$

As $\omega^2 \gg \alpha^2$,

$$Q = I_0 \cdot \frac{2}{\pi \alpha}. \tag{3}$$

When the specimen is vibrating steadily, the current I in the microammeter is

$$I = \frac{\omega}{2\pi} \int_0^{\frac{2\pi}{\omega}} I_0 |\cos \omega t| dt = I_0 \frac{2}{\pi}. \tag{4}$$

From (3) and (4), we have

$$Q = I/\alpha. \tag{5}$$

This is the same as the representation of the total charge of the direct current the amplitude of which is initialy I and attenuates as $\exp(-\alpha t)$. The logarithmic decrement λ is defined as

$$\lambda = \log e^{\alpha T} = \alpha T = \alpha / f. \tag{6}$$

where T is the period of vibration. From (5)

$$\lambda = I / f Q. \tag{7}$$

Using this relation the logarithmic decrement λ can be calculated.

But here is an indispensable correction. For after opening the switch S and separating the contact of relay R_1, a finite time interval Δt

elapses before the contact of relay R_3 touches on the side of ballistic galvanometer. Accordingly the electric charge do not flow in this interval through the galvanometer and it causes the systematic error. Now if the direct current I decreases as exp $(-\alpha t)$, its total charge Q is

$$Q=\int_0^{\Delta t} Ie^{-\alpha t}dt+\int_{\Delta t}^{\infty} Ie^{-\alpha t}dt$$
$$=\Delta Q+Q_m, \qquad (8)$$

where Q_m is the measured charge and ΔQ the unmeasured charge. We indicate by λ_m the logarithmic decrement calculated from Q_m using the relation (7) and by λ the true logarithmic decrement, then

$$\frac{\lambda}{\lambda_m}=\frac{Q_m}{Q}=\frac{Q-\Delta Q}{Q}=1-(1-e^{-\alpha\Delta t})$$
$$=e^{-\alpha\Delta t}=1-\alpha\Delta t+\frac{\alpha^2\Delta t^2}{2}. \qquad (9)$$

Therefore we must add the correction term $\Delta\lambda$ to the measured value λ_m, that is,

$$\lambda=\lambda_m-\Delta\lambda, \qquad (10)$$

where

$$\Delta\lambda=\lambda_m^2\cdot f\cdot\Delta t\,(1-\lambda_m\cdot f\cdot\Delta t/2). \qquad (11)$$

To determine this time interval Δt we charged a condenser C to which a resistance R was connected in parallel and discharged the charge on this condenser through the relays used in the apparatus and measured the difference between the discharged charge when the parallel resistance is connected and that when not connected. From this amount and the value of R and C, Δt was obtained after a simple calculation. In our apparatus Δt was about 2×10^{-3} seconds. Further by appling the voltage of exciting coil L_1 and that of ballistic galvanometer G simultaneously to the oscillograph, we photographed the change of the exciting and damping current. This photograph showed that Δt was of the above-mentioned order of magnitude. The correction containing Δt is considerably large when the frequency of vibration or the logarithmic decrement is large, so that this correction must not be neglected.

In the range of about 100—5000 cycles per second we used the resonance at each mode of vibration and the highest mode of vibration used was about sixth overtone. According to each mode of vibration each nodal line was suspended by thread. Though the suspending position deviated a few millimeters from the true nodal line its effect was negligibly small⁽³⁾. The amplitude of vibration was less than the order of one tenth millimeters and the logarithmic decrement was indifferent to the amplitude.

§ 3. Experimental Results.

Fig. 2 and 3 give respectively the experimen-

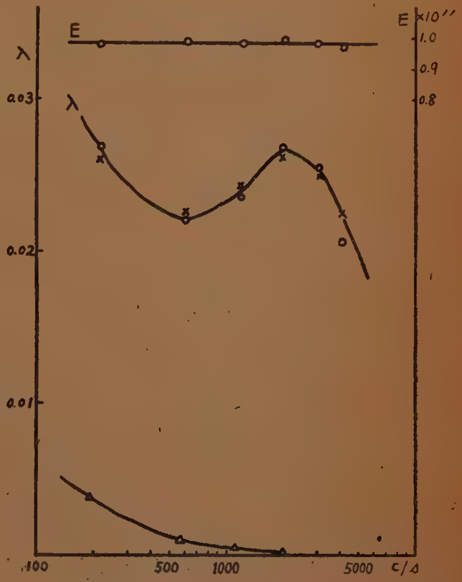

Fig. 2. The Young's modulus and the logarithmic decrement of air-dried Tabu.

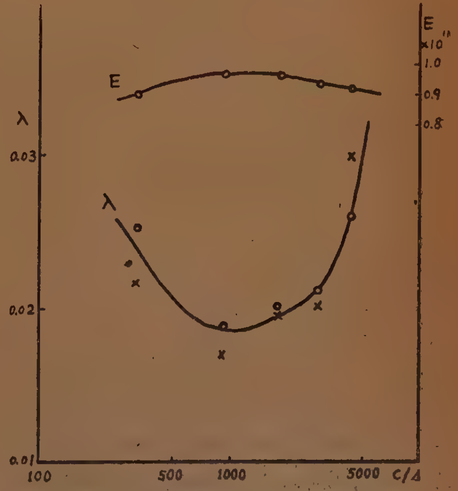

Fig. 3. The Young's modulus and the logarithmic decrement of air-dried Momi.

tal results (the mark ○) for Tabu (a broad-leaved tree) and Momi (a needle-leaf tree). To confirm the precision of the new method the values measured by the resonance method are shown with the mark ×. When we denote by Δt the frequency interval at which the amplitude of receiving current takes the half value of the maximum at resonance and f_r the resonant frequency, the logarithmic decrement λ is given as follows;

$$\lambda \doteqdot \frac{\pi}{\sqrt{3}} \frac{\Delta f}{f_r} \qquad (12)$$

It is seen that the two methods give the same results. The value obtained from the photograph of damping current taken by the oscillograph also nearly coincided with the above results. The measured values for the same specimen, the length of which was cut half or one third of original one, could be also plotted on the same curve within the limit of error. Therefore the variation of λ due to frequency is not originated from the mode of vibration but from the frequency itself.

The lower curve in Fig. 2. shows the attenuation due to air, that is, the difference of the logarithmic decrement measured in the atmospheric pressure from that measured in about 10 mm Hg vaccum. The logarithmic decrement of wood itself is, therefore, the measured decrement minus this decrement due to air.

In the measurable frequency range (about 100—5000 c.p.s.) the Young's modulus shows hardly any variation but the decrement varies remarkably with frequency and its behavior differs according to the kind of wood. After investigation of about 30 kinds of wood, we have found that the frequency characters of the logarithmic decrement could be divided into two main types. One is such that the decrement increases gradually with the frequency (A), to which the needle-leaf trees belong. The other is such that the decrement decreases with a maximum value on the way (B), in some cases this maximum disappears (B'). The broad- leaved trees belong to this type. Fig. 4 gives the measured results for Sugi. Hinoki, and Ezomatsu as the examples of the first type, these are all the needle-leaf trees. Fig. 5 gives the data for Kaede, Harunire, and Karamatsu as the examples of the second type, where the former two are the broad-leaved trees but the last is the needle-leaf tree. The eighteen kinds of needle-leaf tree used in the experiment showed the first type (A) with only one exception of Karamatsu and the ten kinds of broad-leaved tree all showed the second type (B) or (B'). The distinction between B and B' is almost meaningless, for both change to

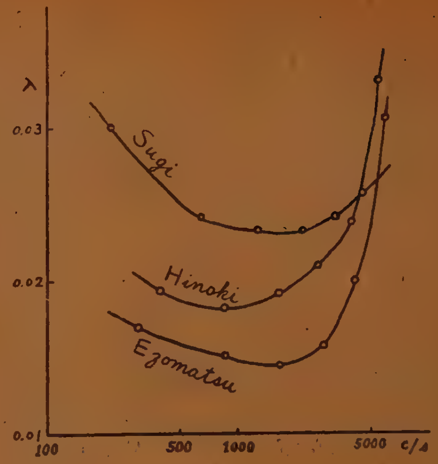

Fig. 4. The logarithmic decrement *vs.* frequency; A type.

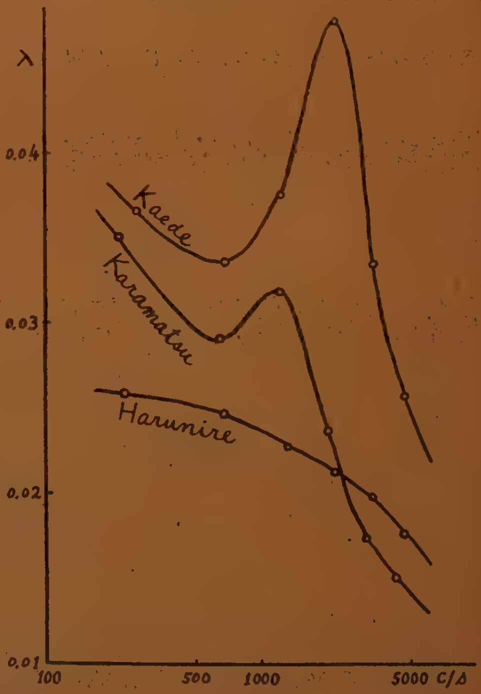

Fig. 5. The logarithmic decrement *vs.* frequency; Band B' type.

each other and the height of maximum in the B state also varies according to the moisture content. These precise relations are still unknown.

Table 1 shows the kind of wood, density, Young's modulus, and the logarithmic decrement at the frequency of fundamental mode (in the neighbourhood of 100—200 c.p.s.), and the frequency character of the logarithmic decrement. The meaning of the notation A, B, B' was above described. The woods denoted by No. 1 to No. 18 are the needle-leaf trees and those from No. 19 to No. 20 are the broad-leaved trees. It is seen that the frequency character of the logarithmic decrement is distinctly discriminated according to the kind of tree. These specimens were all in the state of so-called air-dried, namely, dried by being left in the atmosphere for a long time and their moisture content would be about 15 percents by weight. The temerature of measurement was the room temperature in winter namely about 10°C. It must be noticed that the different results would be obtained under the different conditions of moisture content or temperature.

All the specimens in the above table are such that their fibers are orientated in the direction of the length of specimens. The different results might be expected when the fibers are orientated perpendicular to the direction of the length of specimen. Fig. 6 and Fig. 7 show the comparison of two cases for Bishūhinoki. It is seen that the Young's modulus is about one tenth

Table I.

The Experimental Results of the Various Woods.

No.	Local Name.	Botanical Name.	Density	Young's modulus	Logarithmic decrement	Type
1	Sawara	Chamaecyparis pisifera Endl.	0.278	0.58×10^{11}	2.45×10^{-2}	A
2	Sugi (Japan cedar)	Cryptomeria japonica D. Don.	0.358	0.52	3.10	A
3	Sirabe	Abies Veitchii Lindl.	0.390	0.90	1.74	A
4	Hinoki (Japan cypress)	Chamaecyparis obtusa Endl.	0.397	0.95	1.95	A
5	Bishūhinoki	ditto (produced at Bishū).	0.356	0.84	2.31	A
6	Ōtakihinoki	ditto (produced at Ōtaki).	0.377	0.80	1.80	A
7	Taiwanhinoki	ditto (produced at Taiwan).	0.424	1.00	1.73	A
8	Miurehinoki	ditto (produced at Miure).	0.453	1.12	2.00	A
9	Kisohinoki	ditto (produced at Kiso).	0.472	0.98	2.45	A
10	Kōchihinoki	ditto (produced at Kōchi).	0.487	0.66	2.18	A
11	Ezomatsu (Spruce)	Picea jezoensis Carr.	0.399	1.11	1.70	A
12	Todomatsu	Abies sachalinensis.	0.407	0.91	1.85	A
13	Momi (Fir)	Abies firma Sieb. et Zucc.	0.413	0.90	2.38	A
14	Tōhi	Picea hondoensis Mayr. Monog.	0.420	1.15	1.90	A
15	Asunaro	Thujoposis dolabrata Sieb. et Zucc.	0.487	0.90	1.85	A
16	Akamatsu (Red pine)	Pinus densiflora Sieb. et Zucc.	0.516	0.89	2.43	A
17	Tsuga	Tsuga Sieboldii Carr.	0.550	1.28	1.91	A
18	Karamatsu (Larch)	Larix leptolepis Murray.	0.590	0.87	3.50	B
19	Shina (Bass wood)	Tilia japonica Simk.	0.389	0.58	3.10	B′
20	Tochi (Horse-chestnut)	Aesculus turbinata Bl.	0.493	0.79	2.91	B′
21	Harunire	Ulmus davidiana Planch.	0.526	0.94	2.58	B′
22	Nire (Elm)	Ulmus parvifolia Jacq.	0.546	1.14	2.77	B′
23	Kaede (Maple)	Acer palmatum Thunb.	0.635	1.15	3.65	B
24	Buna (Beech)	Fagus crenata Bl.	0.649	1.15	3.90	B
25	Keyaki	Zelkova serrata Makino.	0.669	0.85	2.01	B′
26	Tabu	Machilus Thunbergii Sieb. et Zucc.	0.682	0.98	2.65	B
27	Nara	Quercus serrata Thunb.	0.708	1.24	3.03	B′
28	Kaba (Birch)	Betula Tauschii Koidz.	0.793	1.72	2.46	B

and the logarithmic decrement is about thrice in the case that the direction of fibers are perpendicular to that of the length as compared with the case of parallel. The Young's modulus decreases at the high frequency in the specimen which the fibers are orientated perpendicular to the length. In order to examine whether this is due to the effect of the iron pieces, we attached further a thin iron piece on the previously attached one (about 0.1 grams) in both ends, but the measured results was the same. Therefore it seems that the decrease of Young's modulus at higher frequency is not the effect by the iron pieces.

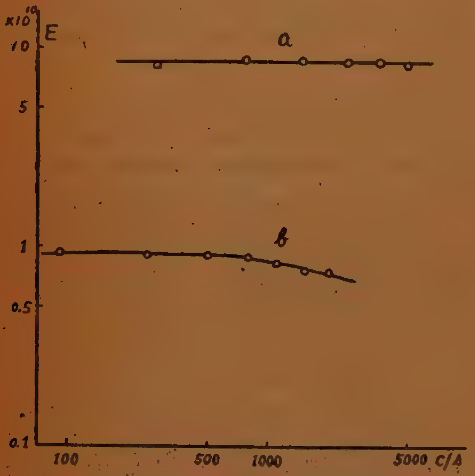

Fig. 6. The Young's modulus of Bishūhinoki.
a: The direction of fibers is parallel to the length of specimen.
b: The direction of fibers is perpendicular to the length of specimen.

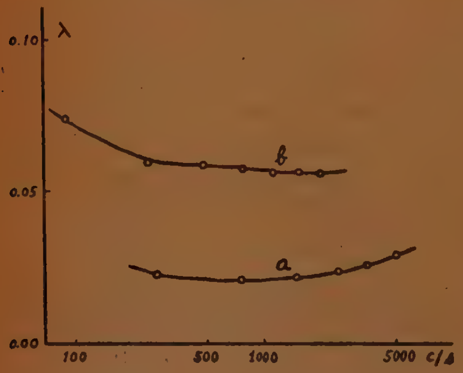

Fig. 7. The logarithmic decrement of Bishūhinoki.
a: The direction of fibers is parallel to the length of specimen.
b: The direction of fibers is perpendicular to the length of specimen.

§ 4. Remarks.

We have measured the Young's modulus of various wood from the resonant frequency of lateral vibration and the logarithmic decrement from the electric charge which summed up the rectified damping current after stopping the excitation. In the main audiofrequency range the Young's modulus does not change while the logarithmic decrement shows an interesting variation and its behaviour is characteristic for the needle-leaf trees and the broad-leaved trees respectively. These two kinds of wood are plainly distinguished with only one exception. But these results were obtained under the condition of the air-dried state and in room temperature of winter. It is to be noticed that this character changes rather sensitively with the moisture content and temperature. It was surposed that even in the needle-leaf trees the logarithmic decrement would decrease through a maximum value at the higher frequency. And it was actualy confirmed. The measurement by the resonance method in the longitudinal vibration of the specimen of the needle-leaf tree showed that the logarithmic decrement had a maximum value between 5000 c.p.s. and 10000 c.p.s. The difference of the above described two types A and B is, therefore, only due to the difference of the relaxation time which causes the maximum in the decrement vs. frequency curve. This relaxation time is considered to be given as the reciprocal of the frequency at maximum and may be related to some internal structure of the wood. The further investigation for these behaviours, especially the relations with the moisture content and the temperature are very interesting and their results will be reported in the next paper.

In conclusion the author wishes to express his sincerest gratitude to Dr. Heiji Kawai. Without his original idea and his kindest guidance this work would not have been performed. The author also wishes to thank Mr. Akira Akiyama who has kindly transfered his precious specimens. This study was helped by the research grant from the Ministry of Education.

References.

(1) F. Krüger and E. Rohloff: Zeits. f. Physik. **110**, (1938), 58.

(2) R. B. Abbott and G. H. Purcell: J. Acous. Soc. Am. **13**, (1941), 54.

(3) A. Akiyama: Rep. Inst. Sci. Techn. Univ. Tokyo. **1**, (1947), 38. (in Japanese.)

Ferromagnetic Properties and Superlattice Formation of Iron Nickel Alloys (I)*.

By Sōshin Chikazumi

Department of Physics, University of Tokyo.

(Received January 31, 1950)

§ 1. Introduction.

Iron-nickel alloys of the composition near Ni_3Fe have unusual magnetic properties sensitive to heat treatment. They develop extremely high permeabilities when cooled rapidly from 600°C. Annealing below this temperature or cooling slowly, they lose this property of practical importance. Furthermore, when cooled from 600°C in a magnetic field, they exhibit high maximum permeabilities only in the direction parallel to the field applied during heat treatment. J.F. Dillinger and R.M. Bozorth[1)] investigated this effect in detail, especially as to the temperature range responsible for this effect. They explained this effect in terms of plastic release of internal stress produced by magnetostriction. On the other hand, attempts to explain these characteristics, which are called the permalloy problem, have lead to the discovery of the superlattice Ni_3Fe.[2)] S. Kaya[3)] investigated the formation of this superlattice by measuring specific resistance and specific heat. He found that the superlattice is formed very gradually during annealing at its critical ordering temperature (490°C), and that the state of perfect order is reached after about 160 hours. Since that time, its formation has been supposed to be a dominant factor for the anomalous magnetic magnetic behavior of these alloys. The true origin, however, has not been established.

In this connection the writer performed an experiment as described below for the purpose of explaining these anomalous magnetic properties.

§ 2. Change in Magnetic Properties by Superlattice Formation under Various Field Conditions.

The specimen alloys are prepared by melting electrolytic iron and nickel, with 0.5% manganese added, in a high frequency vacuum induction furnace. The samples used are rods of 21.5% Fe-Ni, 1.3 mm in diameter, 30 cm in length. Their ends are made into nearly ellipsoidal shape to eliminate severe inhomogeneity of demagnetizing fields. They are first annealed at 1000°C for one hour, cooled slowly to 600°C and then quenched on a copper plate. Formation of superlattice is effectuated by inserting the specimen into the furnace kept at 490°C. It is annealed at this temperature for a desired time and then quenched to measure its magnetic property. Superlattice grows additively through the repetition of this process. This procedure has been carried out under the following three conditions:

---

* The experiments in this paper was made from 1946 to 1948.

(1) without field, (2) with longitudinal (20 Oe), and (3) with circular magnetic field (10 Oe on the surface). In case (3) circular field is produced by D.C. current (3 amps.) flowing through the specimen rod itself. This field may be enough to turn the intrinsic magnetization towards circular direction throughout the specimen except for a small part near the axis.

The process of superlattice formation appears through the change of electric resistance as shown in Fig. 1. Anomalously slow rate of formation which sets in after several hours of annealing can be seen regardless of annealing condition. The magnetization curves for case (1), (2) and (3) are shown in Figs. 2, 3 and 4 respectively. In the case (1) or (3), the high maximum permeability obtained by quenching from 600°C rapidly breaks down by the superlattice formation. On the contrary, it increases appreciably by the treatment of the case (2). This anomalous behavior can be explained by assuming that the intrinsic magnetization in each domain becomes stable in the same direction as it has been during heat treatment. (We shall call this effect "domain fixing" for convenience, sake). When this stable direction is not parallel to the axis, as is the case for (1) or (3), rotation of the intrinsic magnetization from this direction requires some external work. This is the reason why magnetization curve lies down. When this direction is parallel to the axis, as in the case (2), magnetizing process takes place through the displacement of 180° walls and does not require so much work.

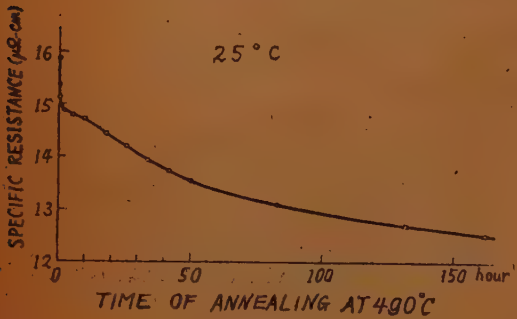

Fig. 1. Change in specific resistance due to superlattice formation.

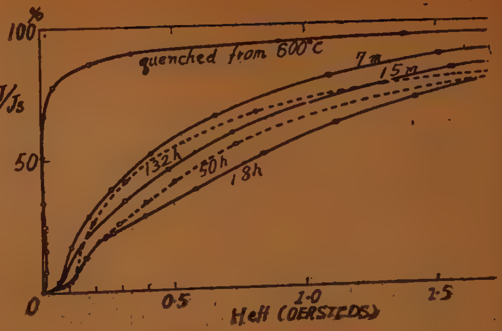

Fig. 2. Variation of magnetization curve by annealing at 490°C without magnetic field.

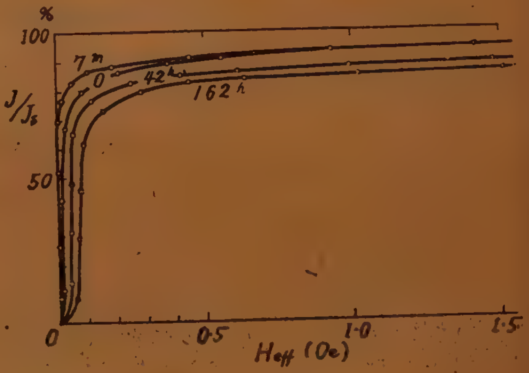

Fig. 3. Variation of magnetization curve by annealing at 490°C in a longitudinal magnetic field.

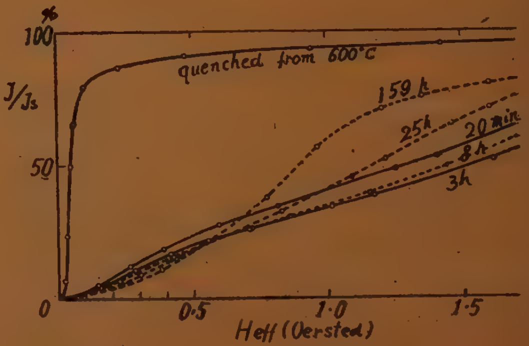

Fig. 4. Variation of magnetization curve by annealing at 490°C in a circular magnetic field.

Evidence for this description can be seen in the behavior of magneto-resistance effect as shown in Fig. 5. It is the change of direction of the intrinsic magnetization and not of its sense which gives rise to resistace change. Curve *b* in the figure, therefore, shows that the rotation does not take place in the case (2) for the most part of magnetizing process.

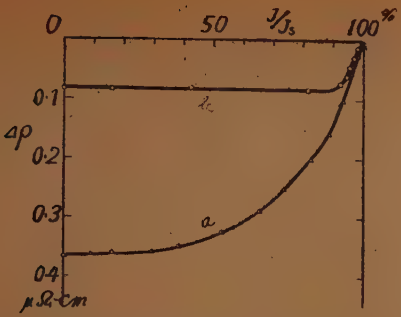

Fig. 5. Magneto-resistance effect. Annealed for 15 minutes at 490°C, a: without, b: with longitudinal magnetic field.

Thus a total change of specific resistance from demagnetized to saturated state gives useful information as to the domain distribution. This quantity, denoted by $\Delta\rho$ hereafter, is proportional to $\cos^2 \vartheta$, where ϑ is an angle between the stable direction of intrinsic magnetization and the electric current. For the case of random distribution, therefore, this quantity should be 2/3 ($=\overline{\cos^2 \vartheta}$) of the one for the case in which the direction of fixing is perpendicular to the axis. And it should be zero for the case of fixing in longitudinal direction. Variation of $\Delta\rho$ with superlattice formation are shown in Fig. 6 for the three conditions of annealing. Here one can see the theoretical ratio 3:2:0 approximately realized at the first stage of annealing. These characteristic domain distributions, however, break down with the approach to perfect order.

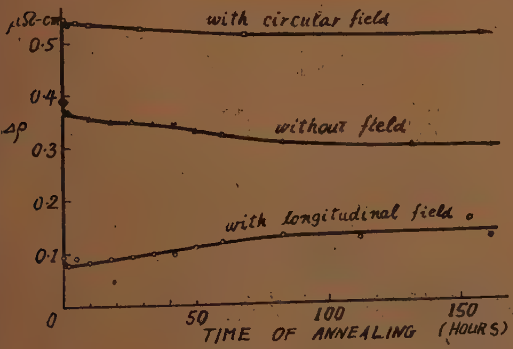

Fig. 6. Variation of $\Delta\rho$ with time of annealing for various field conditions.

Another evidence for domain fixing can also be seen in the variation of residual magnetization. (Fig. 7). Its ratio to the saturation magnetization, J_R/Js, can be calculated for some simple cases. When the crystal anisotropy is superior, domains may orient in the specific [100] direction which forms the least angle with the direction of the previous field. In this case the value should be 83.1%[4] for polycrystal which consists of randomly oriented crystallites. When the internal stress favors one of the three easy directions, this value decreases to one-third of the above value, i.e. to 27.7%.[5] For, if the favored direction is not the one which forms the least angle, the intrinsic magnetization rotates at first towards the latter direction as the field decreases and then changes over to the favored direction. This final orientation, however, can take with equal probability either one sense or the opposite; so it can not contribute statistically to the residual magnetization. Only the case in which it does contribute is when the easy direction which forms the least angle is favored by internal stress. As this happens with the probability 1/3, the value J_R/Js reduces to the one mentioned above.

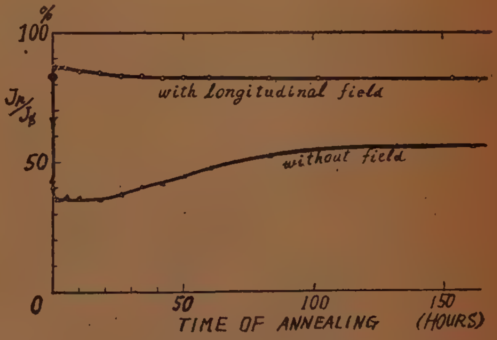

Fig. 7. Variation of residual magnetization with time of annealing.

We may see the value corresponding to these extreme cases in Fig. 7. The starting value 83% and the minimum value 35% are in fair agreement with the theoretical ones. This shows that when annealed without field the intrinsic magnetization is fixed in the easy direction in which it has accidentally been lying during the heat treatment. Gradual recovery of J_R/Js after long annealing may be caused by the break-down of domain-fixing effect. When annealed in a longitudinal field, the value increases to 87% as a result of one-directional fixing of domains.

The most striking evidence of domain fixing is a linear form of the magnetization curve obtained after annealing in a circular magnetic field (Fig. 4). This shape is theoretically expected as will be explained in § 3. Since the susceptibility of this linear part is inversely proportional to the magnitude of internal stress, we are able to know the variation of internal stress (or strength of domain fixing) directly through the behavior of curves in Fig. 4. This knowledge is a good assurance for the above-mentioned characteristic behavior of the domain fixing.

It should be added that the initial permeability decreases rapidly even by annealing in longitudinal field, and that it does not recover by further treatment (Fig. 8). This is probably due to breakdown of some special magnetic structure which is responsible for the unusual high initial permeability of this alloy. Slight existence of superlattice may be a prerequisite for this structure.

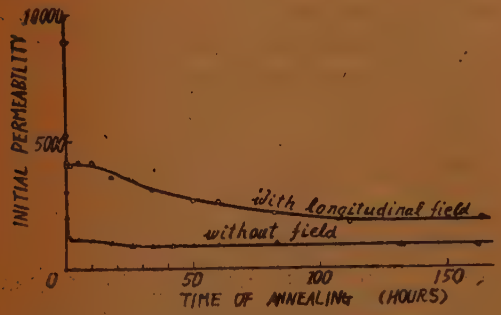

Fig. 8. Variation of initial permeability with time of annealing.

Further, the high induction part of the magnetization curve steps down gradually with the progress of order regardless of the field condition of annealing. This is probably caused by an increase of crystal anisotropy energy, as proved by E.M. Grabbe.[7] These two ranges, initial and final, therefore, are out of present consideration as far as the domain-fixing effect is concerned.

§ 3. Estimation of a Magnitude of Internal Stress Responsible for Domain Fixing.

In order to estimate the magnitude of internal stress, effect of the external tension on the susceptibility of the linear magnetization curve (as shown in Fig. 4) were measured. When the intrinsic magnetization is forced to turn on one hand by internal stress σ_i, and on the other hand by external stress σ and field H in the direction perpendicular to σ_i, an energy per unit volume is expressed by[5]

$$E=-(3/2)\lambda\sigma_i \sin^2\vartheta-(3/2)\lambda\sigma\cos^2\vartheta-J_sH\cos\vartheta \quad (1)$$

where λ is a saturation value of magnetostriction, assumed to be isotropic and positive, J_s is saturation magnetization, and ϑ is an angle between J_s and H. Then the equilibrium direction of J_s is given by minimizing the energy,

$$dE/d\theta=-3\lambda(\sigma_i-\sigma)\sin\theta\cos\theta+J_sH\sin\theta=0 \quad (2)$$

So we have

$$J=J_s\cos\theta=(J_s^2/3\lambda(\sigma_i-\sigma))H \quad (3)$$

which gives a linear magnetization curve. An extrapolation of this linear part intersects with $J=J_s$ line at a point with abscissa

$$H_\sigma=3\lambda(\sigma_i-\sigma)/J_s. \quad (4)$$

The linearity of the observed curves as shown in Fig. 9 agrees with the theory but for the fact that they do not pass the origin. If, however, the first rise in the magnetization curve is due to a magnetization of the region which has not been affected by the fixing effect and is consequently easier to magnetize, the value H_σ should give the theoretical one regardless of the presence of such initial rise. Values of H_σ obtained from Fig. 9 are plotted in Fig. 10 as a

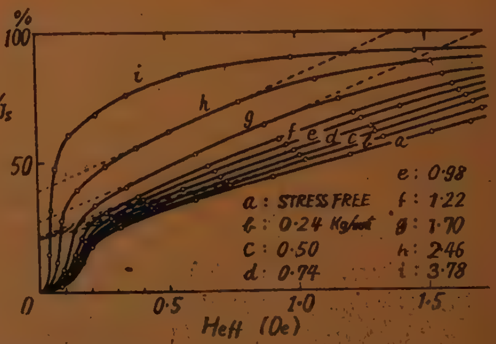

Fig. 9. Effect of tension on the magnetization curve for 21.5% Fe-Ni alloy annealed for one hour at 490°C in a circular magnetic field.

function of σ. Δρ curve in the same figure means a variation of domain distribution in the demagnetizing state. The linearity of $H_\sigma-\sigma$ relation is good so long as the domain distritution is not affected by external tension. The slope of this line and its intersection point with abscissa give the value of λ and σ_i respectively:

$$\lambda=2.7\times10^{-6},\quad \sigma_i=3.4\ \text{kg/mm}^2.$$

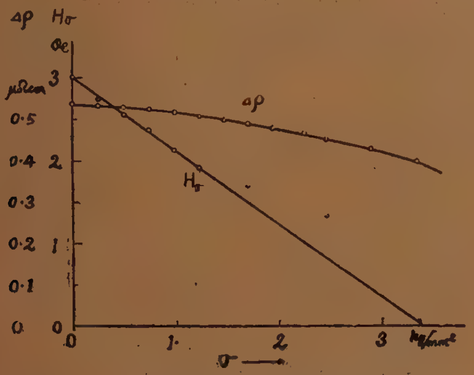

Fig. 10. Variation of H_σ and Δρ with tension. Cf. Fig. 9.

This value of λ comes to fair agreement with the directly observed one3), and so is a justification to this procedure. The value of σ_i may also be right, since the magnetization curve rises by external tension of the same order. This, however, is unexpectedly large as compaired with the estimation proposed by Bozorth and Dillinger. Their explanation is as follows: The internal stress produced by the magnetostrictive strain of each domain would be released by the plastic flow during annealing. So, the rotation of intrinsic magnetization forced by the applied field should produce a new elastic energy by the amount (9/4) λ^2 E at most, where E is a Young's modulus. For this reason the original direction must be stable. Comparing this elastic energy with the one used in Eq. (1), it follows $\sigma_i=(3/2)\lambda E$. Using $E=2\times10^{12}$ dyne/cm² and $\lambda=2.7\times10^{-6}$ for this alloy, this is found to be 0.08 kg/mm². The observed value is about forty times larger than this estimation.

Similar experiment was carried out for 15% Fe-Ni, in which the formation of superlattice is comparatively weak. Since this alloy has a negative magnetostriction, magnetization curve flattens down by external tension as shown in Fig. 11. When this is annealed in a longitudinal field the curves become steeper as shown by the dotted line. From the $H_\sigma-\sigma$ curve shown in Fig. 12 the value of σ_i is found to be 0.22~0.38 kg/mm² for annealings at various temperatures. On the other hand, using $\lambda=-8.3\times10^{-6}$ and $E=2\times10^{12}$ dyne/cm², (3/2) λE is found to be 0.25 kg/mm² which is in good agreement with the observed value. Thus the λ—E estimation seems to give fairly reasonable value for ordinary substance. The large descrepancy may be the characteristics of the superlattice alloy.

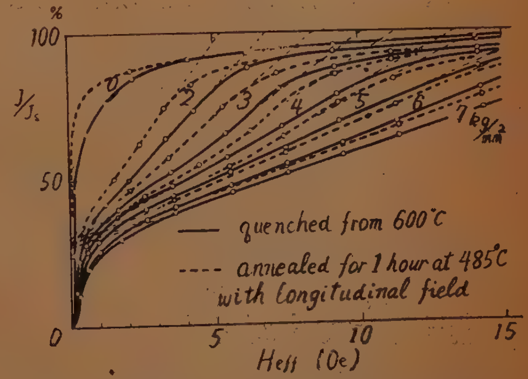

Fig. 11. Effect of tension on the magnetization curve for 15% Fe-Ni alloy for two sorts of annealing.

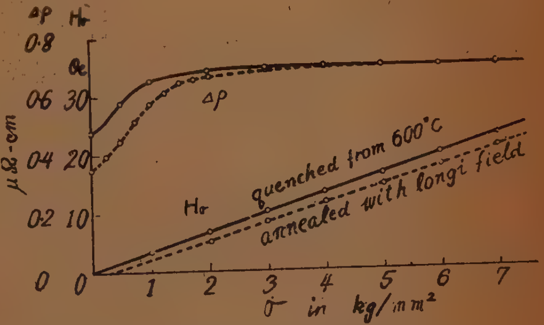

Fig. 12. Variation of H_σ and Δρ with tension. Cf, Fig. 11.

We have so far been using the term internal "stress" for convenience' sake, but the origin which affects a direction of intrinsic magnetization should be a deformation in lattice, whether it is caused by the stress or by other factors. The stress of 3.4 kg/mm² is equivalent to a strain of $\sigma_i/E=1.7\times10^{-4}$. This is found to be the same order as the fractional contraction of length observed during superlattice formation. Fig. 13 shows a change of length in 24.1% Fe-Ni alloy measured by dilatometer while maintaining the constant temperature of 490°C. The total contraction of length is 4.4×10^{-4}. It may be concluded, therefore, that a mechanism of domain fixing is closely related to a volume change which takes place during superlattice formation.

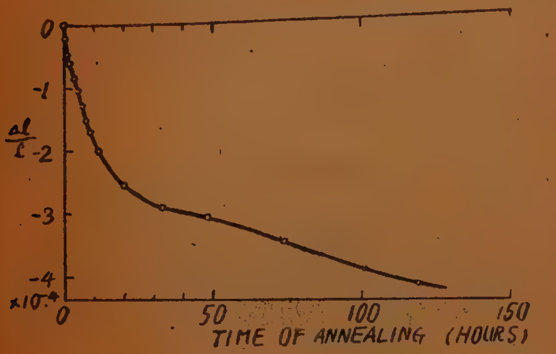

Fig. 13. Contraction of length during superlattice formation observed at 490° C for 24.1% Fe-Ni alloy.

§ 4. Rotation of Fixing Direction and Relaxation Time.

Investigation was made upon the changes of magnetization curve when the sample which had previously undergone the domain fixing in one direction was annealed with the field of other direction. The mathod is as follows: The specimen (21.5% Fe-Ni) previously annealed in a circular field for desired time is inserted into the 490°C furnace with a longitudinal field of 20 Oe, annealed for 5 minutes and then quenched on a copper plate. This five minutes' annealing is repeated until the magnetization curve ceased to rise any further. The curve measured after each annealing is shown in Fig. 14 for several stages of superlattice formation. Rotation of fixing direction occurs very quickly at the early stage of ordering, but it reqires several times of annealing at later stages. The course of change of H_σ and $\Delta\rho$ for all stages are summarised in Fig. 15. The value $\Delta\rho$ does not change at first, although H_σ decreases rapidly. This means that the fixing strength alone at first decreases while maintaining its original direction, then its direction rotates towards the axis.

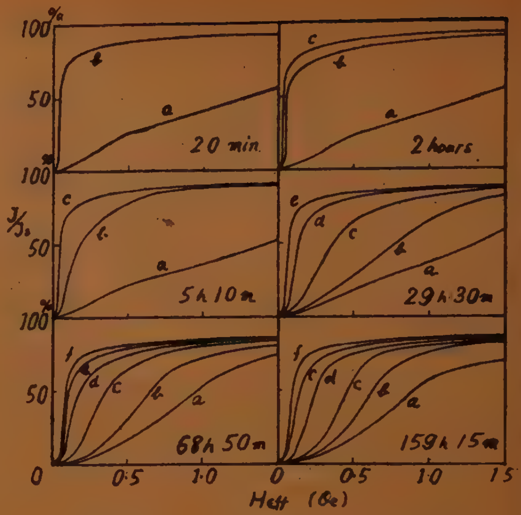

Fig. 14. Variation of magnetization curve due to rotation of fixing direction. Curve *a*: annealed in circular field, *b*: then annealed for five minutes in longitudinal field, and so on. Number in the figure means total time of annealing at 490°C.

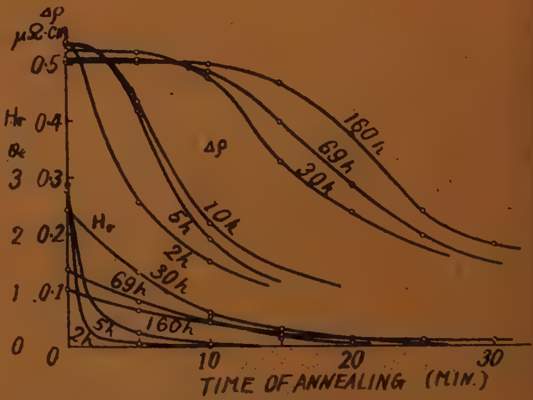

Fig. 15. Variation of H_σ and $\Delta\rho$ with time of annealing. Cf. Fig. 14.

Eq. (4), where $\sigma=0$ for the present case, therefor, is valid at the first stage where $\Delta\rho$ remains unchanged. So, the relaxation time is determined from the initial decrease of H_σ curve. This is ploted in Fig. 16. It increases along with the progress of superlattice formation, but seems to saturate as it approaches perfect order. If the domain fixing were to be caused by the internal stress produced by local growth of ordered phase, the relaxation time would increase more rapidly at the later stage of annealing. We had better consider the relaxation time as dependent upon the frequency of atomic re-arrangement which may be larger at non-equilibrium disordered state and may decrease to a constant value with approach to thermal equilibrium ordered state. This suggest that the domain fixing may have its origin in a characteristic arrangement of two sorts of atoms in the lattice.

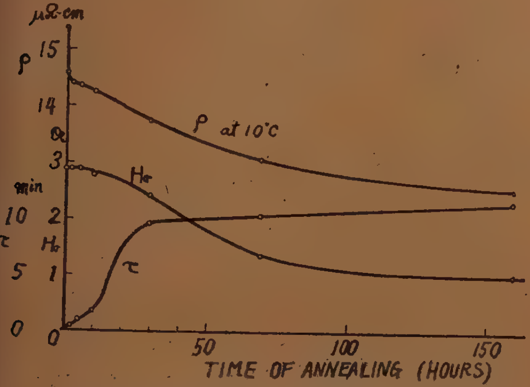

Fig. 16. Changes in relaxation time τ, H_σ and ρ with the progress of superlattice formation.

§ 5. Conclusion.

By the heat treatment at the critical ordering temperature the intrinsic magnetization is fixed in the same direction as has been orinted during the treatment. A strength of fixing increases at first with the progress of order but finally decreases and loses its characteristic distribution as it approaches perfect order. A magnitude of internal strain responsible for domain fixing is the same order as the length-contraction observed during superlattice formation. The measurement of relaxation time suggests that the origin consists in a characteristic arrangement of atoms in the lattice.

Reserences.

(1) J.F. Dillinger and R.M. Bozorth: Physics **6**, (1935) 279, 285.
(2) O. Dahl: Zeits. f. Metallkunde, **28** (1936) 133.
(3) S. Kaya: J. Fac. Sci., Hokkaido Imp. Univ. **2** (1938) 29.
(4) R. Becker u. W. Döring: Ferromagnetismus, S. 288.
(5) R. Becker u. W. Döring: Ferromagnetismus, S. 131.
(6) R.M. Bozorth: Zeits. f. Phys. **124** (1948) 519.
(7) E.M. Grabbe: Phys. Rev. **57** (1940) 728.

Ferromagnetic Properties and Superlattice Formation of Iron-Nickel Alloys (II)*.

By Sōshin Chikazumi.

Department of Physics, University of Tokyo.

(Received January 31, 1950).

§ 1. Introduction.

In the preceding paper(1) the writer reported investigations on the domain fixing phenomena and its relation to the superlattice formation. The magnetic measurements there were made at room temperature after annealing at 490°C. In this paper measurements at high temperature are made to see how the magnetic properties vary during cooling. The mechanism of domain fixing is also discussed on the basis of the obtained results. It is seen that a possible explanation of these phenomena can be made by assuming an existence of "directional order". A trial to prove its existence has been made.

§ 2. Magnetic Properties at Elevated Temperature.

The specimen used is a rod of 21.5% Fe-Ni

---

[*] The experiments here were made from 1948 to 1949.

alloy, same as described in the preceding paper. The method of magnetic measurement is the usual commutation method. The secondary coil consists of 707 turns of copper wire insulated by alumina and mica. Fluctuations in the read of the galvanometer were completely avoided by inserting an earthed copper plate between the furnace and field solenoid. All measurements of magnetization curve were made at constant temperature.

The sample is firstly annealed at 1000°C' and then quenched from 600°C. When this is heated in a longitudinal field of 10 Oe, the magnetization curve does not lose its high maximum permeability even when heated at the ordering temperature (Fig. 1). This is doubtlessly caused by domain fixing in the longitudinal direction. To detect the occurrence of domain fixing more clearly, a similar experiment was made by heating it in a circular magnetic field** (Fig. 2). The fixing of domains cannot be observed below approximately 400°C. Thereupon the curve suddenly reveals a linear form which is characteristic for the domain fixing in circular direction. When cooled from 600°C in a circular field, it gradually reveals a linear form, as shown in Fig. 3. The curve varies almost reversibly when reheated.

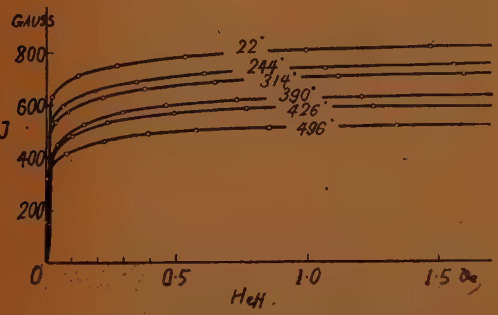

Fig. 1. Variation of magnetization curve by heating in a longitudinal field. Preliminarily quenched from 600°C.

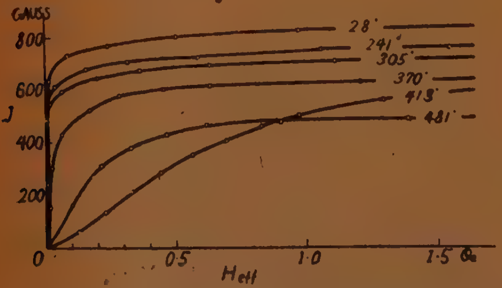

Fig. 2. Variation of magnetization curve by heating in a circular magnetic field. Preliminarily quenched from 600°C.

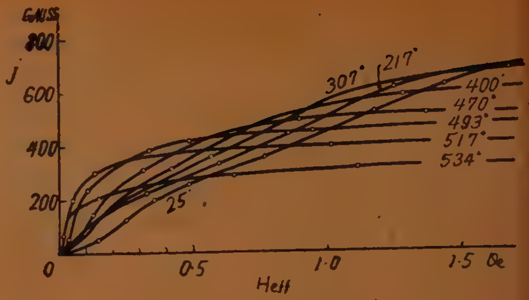

Fig. 3. Variation of magnetization curve by cooling in a circular magnetic field from above 600°C.

To summarized these results, the energy W required in magnetizing to saturation are plotted as a function of temperature in Fig. 4. This energy is obtained from the area surrounded by the magnetization curve, ordinate and $J=J_s$ line. It is interesting to note that the curves *b* and *c* fairly correspond to the initial permeability *versus* temperature curve obtained by G. W. Elmen(2) and by S. Kaya(3).

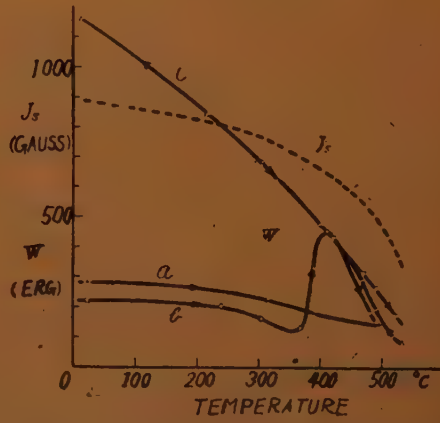

Fig. 4. Variation of W and J_s with temperature. a: heated in a longitudinal field, b: heated in a circular field, c: coold and heated in a circular field. Cf. Figs. 1, 2, and 3.

It must be noticed that the magnetization curve measured above 350°C depends upon the time required for measurement. For instance

---

** This field is produced by a D.C. current flowiug through the specimen rod itself, as described in the preceding paper.

the intensity of magnetization varies with time at 490°C as shown in Fig. 5 (a). This corresponds to the variation of the magnetization curve from A to B in Fig. 5 (b). This obviously is due to the rotation of fixing direction from perpendicular to parallel to the axis, as explained in § 4. in the preceding paper. The relaxation time obtained from Fig. (a) is a few minutes. This is the same order as obtained in the preceding paper.

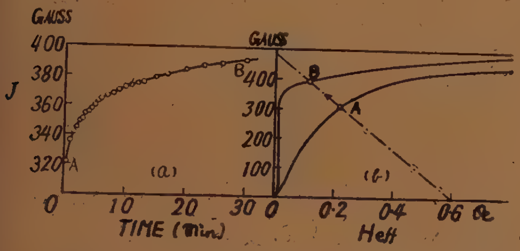

Fig. 5 (a) Time dependency of the intensity of magnetization at 0.6 Oe of external field, observed at 490°C, (b) The corresponding variation of magnetization curve.

Therefore, the circular field was cut off only when the measurement of each point on the magnetization curve was made. The relaxation time, however, seems to increase rapidly with the decrease of temperature. In fact the domain fixing does not take place below 350°C during the time interval required for measurement, as can be seen from curve *b* of Fig. 4. Nevertheless, the magnetization curve in Fig. 3 continues to vary below this temperature and gradually approaches the ideal linear form. This can be explained for some extent by referring to the change of magnetostriction which increases with the decrease of temperature. However, while the energy W, which should be expressed by $(3/2)\ \lambda\sigma_i$*** here, varies more rapidly than the magnetostriction (curve *c* in Fig. 4), it seems to be inadequate to account for the behavior by considering the change of magnetostriction as a principal factor.

In order to see how the internal stress σ_i itself varies with temperature, the effect of external tension on the magnetization curve was measured at several temperature. The specimen was previously annealed for one hour at 490°C in a circular field. The results are shown in Fig. 6. The curves without tension were exactly reproduced after the maximum tension was removed. The values H_σ were obtained from the intersection points of the $J = Js$ line and the linear parts. These are plotted in Fig. 7 as a function of external tension σ. Each statisfies the expected linear relation. The derived values of λ and σ_i are tabulated in Tab. I.

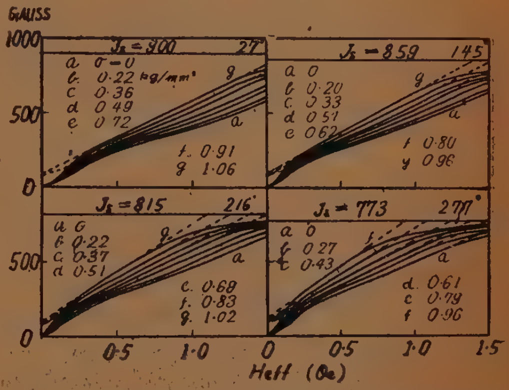

Fig. 6. Effect of tension on the magnetization curves at various temperature. Specimen was previously annealed for one hour at 490°C in a circular magnetic field.

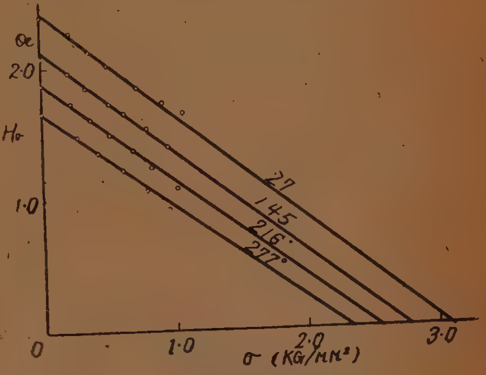

Fig. 7. H_σ versus σ curves for various temperature. cf. Fig. 6.

Table I. Variation of various quantities with temperature.

Temp.	Js	σ_i	λ	σ_i/λ	λ / J_s^2
°C	Gauss	kg/mm²	$\times 10^{-6}$		
27	900	3.10	2.39	1.29_5	2.95
145	859	2.79	2.22	1.25_7	3.01
216	815	2.57	2.02	1.27_1	3.04
277	773	2.34	1.86	1.25_7	3.11

*** In this expression λ is a saturation value of the magnetostriction and σ_i is the internal stress responsible for domain fixing. Cf. Eq. (1) in the preceding paper.

The results show that the internal stress σ_i decreases with the increase of temperature, the rate of its variation proportional to λ. This fact, except for quantitative discrepancies, seems to support the $\lambda-E$ estimation, which follows the relation $\sigma_i=(3/2)\lambda E$, where E the Young's modulus is nearly independent of temperature. This means that as the temperature decreases, the domains stabilize their direction by the successive release of the internal stress produced by the gradual increase of magnetostriction. If, therefore, the direction of the applied field is changed on the way of cooling, subsequent plastic flows will not strengthen but rather weaken the stability of domains in the original direction. To prove the matter the experiment below was made.

The specimen is cooled from 600°C, with a circular field continuously applied, annealed for one hour at 490°C and cooled to 352°C. The field is then switched to the longitudinal direction and cooled further to 282°C. The magnetization curves measured at each temperature are shown in Fig. 8. Contrariwise to the presumption the curve at 282°C is flatter than that of 352°C, proving further increase of fixing strength in the circular direction*. Further cooling to 218°C and 152°C in a longitudinal field reveals the same tendency. Moreover, the magnetization curve were not affected by the prolonged annealing (21 hours) at 250°C in a longitudinal field.

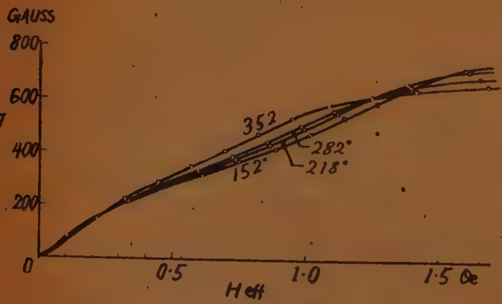

Fig. 8. Variation of magnetization curve by cooling in a circular field above 352°C and in a longitudinal field below 352°C.

As seen from the above experiments, the direction of domain fixing cannot be altered by any treatment below 350°C. The cooling effect is only to intensify the characteristic of domain fixing in the original direction. We may, therefore, regard the behaviour of the magnetization curves at room temperature mentioned in the preceding paper as to correspond to that of 490°C. The magnitude of internal stress at 490°C can be obtained by extrapolating the values of σ_i in Tab. I. The obtained value lies in the range between 1.7 kg/mm² obtained by linear extrapolation and 1.1 kg/mm² obtained by assuming the proportionality to λ or Js^2. This value also gives rise to a strain of the same order as the fractional contraction of length observed during superlattice formation as mentioned in the preceding paper.

§ 3. Possible Mechanism of Domain Fixing.

The basic character of domain fixing is that the domain distribution during annealing become stable at room temperature. The $\lambda-E$ estimation gives a qualitative explanation of this basic character and seems to be valid for ordinary substances but fails to yield results in accord with experimental facts for the superlatticed alloy. Since the fixing direction is determined during annealing above 400°C, i. e. where the ordering of atoms can occur, there is no doubt that domain fixing has its origin in the superlattice formation. Moreover, it seems to be in close connection with the volume contraction accompanying the ordering process. If the superlattice were to develop by the local growth of ordered phases, fairly strong internal stress of about 30 kg/mm² should be produced about such regions. As such regions develop, the whole body will contract thus releasing the internal stress. This corresponds to the observed behavior of internal stress. However, this explanation has a fatal defect in explaining the one-directional fixing, for the one-directional stress which would contribute to such fixing cannot exist without external tension. Furthermore, the fact that the volume contraction occurs from the initial stage

---

* Since the observed λ is proportional to Js^2 as seen in Tab. I, which has also been confirmed by W. Doering(4) for Ni, it follows from Eq. (3) of the preceding paper

$$\chi=J/H=Js^2/3\lambda\sigma_i\propto 1/\sigma_i.$$

The relative variation of σ_i, therefore, can be derived by comparing the inclination of the magnetization curves.

of superlattice formation (Fig. 13 in the preceding paper), and that the relaxation time does not correspond to the natural growth of superlattice do not favor this explanation. A similar explanation has frequently been used to explain the decrease of permeability by mere cooling or annealing. This also incorrect, because this effect is one of the special cases of domain fixing as shown in the preceding paper.

Now, in order to describe the one-directional fixing, we must conclude that there should be a deformation in the lattice without any stress, in the same manner as the spontaneous magnetostriction but about 40 time larger in magnitude R. Becker and W. Döring⁽⁵⁾ attributed this deformation to the tetragonality of the lattice. Now the origin of this tetragonality can be described on the basis of the experimental facts as follows. Since the progress of order means an increase of the concentration of unlike-atom pairs, we can ascribe the contraction of volume to a slight difference of the pair length, shorter for unlike-atom pairs than like-atom pairs. If, therefore, the atoms arrange so that the concentration of like-atom pairs in one direction is larger than the other, the lattice will be deformed spontaneously. We shall call such an arrangement "directional order". Since the fractional difference of the pair length should be the same as the total fractional contraction of length accompanying the ordering process, i.e. 4.4×10^{-4}, the spontaneous deformation caused by directional order will also be the same order. This agrees with the experimental fact.

In a ferromagnetic crystal the lattice is always forced to strain in the direction of intrinsic magnetization, and usually gives rise to a finite strain called "magnetostriction" counter-balanced by elastic force. When the alloy is annealed at the temperature where the ordering of atom takes place, the magnetostrictive force should favor the directional ordering of atoms which has a strain in the same direction and of the same sign but of larger magnitude as the usual magnetostriction. After the specimen is cooled to a temperature where the re-arrangement of atoms cannot take place, the directional order will, in a manner, "freeze". A considerable amount of work by the external field will then be necessary to rotate the intrinsic magnetization out of its freezed direction. When the alloy is sufficiently annealed and approaches perfect order, the number of like-atom pairs will become scarce. The lack of such pairs will cause a break-down in the directional order and, consequently, in domain fixing.

Moreover, if the thermal expansion coefficient differs slightly between the two sorts of atom pair, larger for unlike-atom pairs than like-atom pairs, the cooling process will result in an increase of the strain of directional order. The fractional difference of thermal expansion coefficient between two sorts of pairs should be 1 % in order to explain the experimental fact quantitatively. A fractional difference of 1 % is not altogether unnatural.

Thus the description based on the assumption of directional order gives a thorough explanation of all experimental facts. It is, therefore, desirable to prove its existence directly by experiment.

§ 4. Experimental Proof of the Existence of Directional Order.

The specimen used is a cross-formed thin plate of 24.1 % Fe—Ni alloy as shown in Fig. 9. This is preliminarily annealed for 2 hours at 1200°C in hydrogen atmosphere. This is then put into a frame made of the same material for

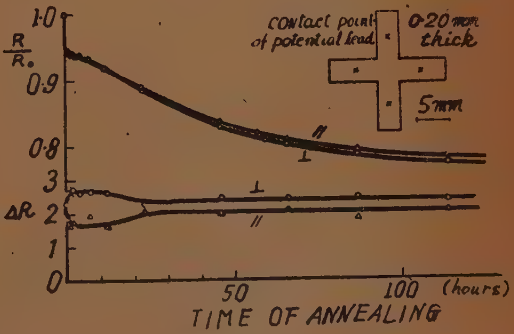

Fig. 9. · Variation of electric resistance and the magneto-resistance effect with superlattice formation. Each curve corresponds to the measurement along the each arm, parallel or perpendicular to the field direction applied during annealing.

the purpose of reducing the demagnetizing field and annealed at 490°C with a magnetic field of 300 Oe, applied parallel to one of the arms. The field was continuously applied during the quanching process. The electric resistance for each arm was carefully measured by observing the potential drop between two fine dots as shown in the figure, employing a current of 445 mA. The measurements were carried out for demagnetized and saturated (parallel to the current) states. The temperature was kept constant (20.4° ~ 20.6°C) during the whole measurement.

The fractional change of the resistance is shown in Fig. 9 as a function of the time of annealing. Value ΔR in the same figure signifies a change of resistance from demagnetized to saturated state. When the domain fixing takes place, the ΔR value measured along the fixing direction should decrease and the one measured perpendicular to it should increase. The observed curves show this tendency. If domain fixing is due to the appearance of directional order, which has more unlike-atom pairs in the perpendicular than in the parallel direction, the resistance should be smaller for the former than the latter direction. The result shows the expected difference in the latter stage of andealing, but no difference can be seen in the early stage where the domain fixing appears markedly as seen from ΔR curves. As the directional order is characterized by the concentration of unlike-atom pairs, which is classified as "short range order", this result is reasonable, for such "short range order" has no considerable effect on resistance. As ordering proceeds and the periodicity of atomic arrangement becomes nearly perfect, the small number of residual like-atom pairs may affect the periodicity in a way as to give rise to the small difference of resistance.

If the origin is thus related to the short range order, domain fixing should also occur when annealed above the critical ordering temperature. Experimentally this has already been recongnized by J. F. Dillinger and R. M. Bozorth⁽⁶⁾ and by Y. Tomono⁽⁷⁾, although no interpretation from the point of view of superlattice formation has ever succeeded for it.

§ 5. Conclusion.

The domain fixing takes place above 350°C and its fixing direction cannot be altered by any treatment below this temperature. The fixing strength, however, increase gradually in the original direction as the temperature decreases. The description in terms of "directional order" gives a thorough explanation of all experimental facts. A trial to prove its existence directly by measuring the resistance change yields a self-consistent result but failed in giving a conclusive proof. In order to obtain a more distinct proof and to examine its character, investigation must be made on a quantity more sensitive to the short range order and possessing directional character. Unfortunately the writer has not yet been informed of such a quantity.

The writer wishes to express his sincere thanks to Professor S. Kaya for his ready advice and for stimulating discussions throughout the course of this work.

References.

(1) S. Chikazumi: J. Phys. Soc. Japan. **5** (1950).

(2) G. W. Elmen: J. Frankline Inst., **207** (1929), 583.

(3) S. Kaya: J. Fac. Sci., Hokkaido Imp. Univ. **2** (1938), 29.

(4) W. Döring: Z. Phys. **103** (1936), 560. R. Becker und W. Döring: Ferromagnetismus S. 132.

(5) R. Becker und W. Döring: Ferromagnetismus S. 421.

(6) J. F. Dillinger and R. M. Bozorth: Physics, **6** (1935) 279, 285.

(7) Y. Tomono: J. Phys. Soc. Japan, **4** (1949) 298.

On the Motion of Electrons in a B—K Tube*.

By Masaki HIRASHIMA.

Mazda Research Laboratory, Tokyo-Shibaura Electric Co. Ltd.,
Kawasaki City.

(Received February 2, 1950)

§ 1. Introduction.

It seems to be very important to know about motions of electrons in B—K tubes when the mechanism of rectification and oscillation is to be considered more or less quantitatively. In 1938 Gundlach and Kleinsteuber in Germany published a paper⑴, in which they described calculations based on the assumption that electrons could enter the retarding field (grid-plate space) only a single time, almost all of these electrons being captured by the grid wires when they were leaving this space. They claimed fairly good agreement between the theory and experiment. Their assumption was based upon graphical calculations regarding the electron paths drawn on the equipotential maps which were obtained by means of an electrolytic tank with an enlarged model of their B—K tube. As is to be expected at once, the space charges in the interelectrode spaces do not manifest their effect at all in this case and there is likely left some room for doubt in this connection. Apparently, no previous investigators except those quoted above have studied the problem in very great detail. The present writer undertook the study of this problem during the last war, following the method employed by E. G. Linder for the case of magnetons⑵. Somewhat interesting results were obtained.

The present paper concerns a B—K tube to which only electrosatic fields are applied, and the case of superimposed high-frequency fields will be discussed in a forthcoming paper. The discussion will be directly applicable to such tubes as ionization gauge and reflex klystron.

§ 2. Construction of and Potential Distribution in the B—K Tube.

The B—K tube used in the present experiments was constructed as shown in Fig. 1, in which K is a filamentary cathode of tungsten 0.05 mm thick; G is a grid made of molybdenum spiral of mean diameter 3.25 mm, pitch 1.5 mm, wire thickness 0.25 mm; P is a mesh plate (about 2500 meshes/sq.cm) of diameter 7.5 mm, made of very thin nickel wires (0.05 mm thick) spaced 0.2 mm apart; and C is a collecting electrode of inner diameter 12 mm, made of nickel plate, the latter being used for measuring energy distribution of electrons under receiving conditions. The length of the electrodes is about 15 mm. On each side of these electrodes are placed the end plates EP, which are kept at a negative potential with respect to the cathode and serve to prevent stray electrons from disturbing the operation of the tube. Great care was paid to mount these electrodes as perfectly concentrically as practicably possible.

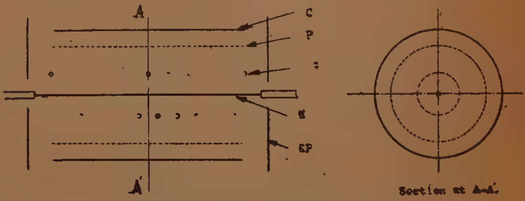

Fig. 1. Construction of the B—K tube actually used.

As is to be explained elsewhere, when the tube was used for reception of a very weak incoming wave of wavelength 58 cm, the voltages of the electrodes at the optimum receiving condition were, for example, $V_g = 134$ volts, $V_p \approx 0$ volt and $V_{ep} = -150$ volts. As the grid saturation voltage is of the order of $60 \sim 80$ volts (see, for example, Fig. 7), we can safely neglect the effect of space charge in the K–G space at the optimum condition. Therefore, the potential distribution in this space is given by

---

* A part of the oral publication made at the Fall Meeting of I.E.E. of Japan held in Tokyo on November 2, 1948.

$$V = V_g \frac{\ln (r/r_k)}{\ln (r_g/r_k)} \qquad (1)$$

where r is the distance from the axis of the cathode of any point whose potential is V, and r_k and r_g are the radii of the cathode and grid respectively. ln denotes the natural logarithm.

In the grid-plate space there is formed very close to the plate a virtual cathode where the electrons having penetrated through the grid openings into this space turn back toward the grid. For the sake of simplicity, assume the virtual cathode to coincide with the surface of the plate as a first approximation; then the potential distribution in this space becomes nearly equal to that in a cylindrical diode, in which a space charge-limited electron current* flows from the outside cathode considered located at the surface of the plate to the inner anode placed at the position of the grid, and is nearly given by

$$V = V_g \left\{ \frac{r(-\beta)^2}{r_g(-\beta_g)^2} \right\}^{2/3} \qquad (2)$$

where r has the same meaning as in Eq. (1), $(-\beta)$ is Langmuir's coefficient for the cylindrical diode with an outside cathode and an inner anode⁽³⁾, and $(-\beta_g)$ is the value of $(-\beta)$ for $r = r_g$.

Fig. 2 shows the potential distribution curves thus obtained from (1) and (2). The broken lines show the same for a plane electrode system.

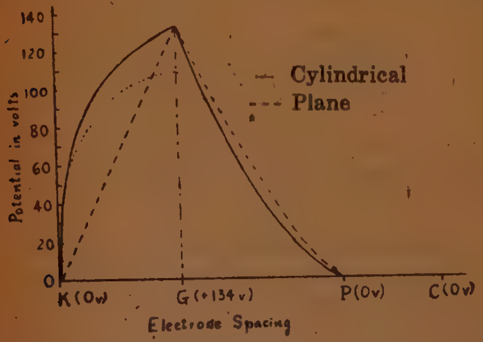

Fig. 2. Potential distribution in the B–K tube.

The difference in the form of this potential distribution curve for the cylindrical case from that for plane one is no doubt responsible for the longer transit time of electrons in this space with the former arrangement.

§3. Pendulum Motion of Electrons and Space Charge in the B–K Tube.

3. 1. Calculation of the Mean Number of Electron Oscillations.

We shall first consider how many times electrons execute pendulum motion on the average through the grid openings in the B–K tube. Assume that a fraction α of dN electrons, emitted from the cathode K, Fig. 3, in an interval of time dt and accelerated by the grid maintained at a high positive potential, V_g, is captured by the grid wire, and the remainder then penetrates into the grid-plate space. After approaching the plate closely, a fraction $(1-\sigma)$ is forced to turn back by the plate kept at zero or somewhat negative potential with respect to the cathode. On the return transit from the plate to the cathode, a fraction δ of the electrons is captured again by the grid wire and finally, a fraction $(1-\delta)$ which has had a chance to escape capture by the grid wire can reach the vicinity of the cathode. The returning electrons then start from the cathode region upon a second revolution without being captured by the cathode to any appreciable extent (A very small fraction γ is assumed to be captured). The time required for their passage past the cathode will be dt. During that time interval, another group of dN electrons will be emitted. Hence the total number starting on the second cycle will be

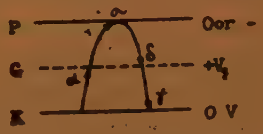

Fig. 3. Absorption of electrons by the electrodes.

$$dN\{1 + (1-\alpha)(1-\sigma)(1-\delta)(1-\gamma)\}.$$

If the radial oscillations are repeated indefinitely, the total number of electrons leaving the cathode in an interval of time dt will be

---

* As will be seen later, this is given by $2I_k(1-\alpha)/(1-\eta)$.

$$n=\frac{dN}{1-(1-\alpha)(1-\sigma)(1-\delta)(1-\gamma)}=\frac{dN}{1-\eta}. \qquad (3)$$

where η stands for $(1-\alpha)(1-\sigma)(1-\delta)(1-\gamma)$ for the sake of brevity. It is assumed here that the fraction lost on successive revolutions are constant. This is probably not strictly true, so that α, σ, δ and γ should be regarded as mean values. It is of some interest to consider some particular cases at this place. (1) If $\alpha=\sigma=\delta=\gamma=0$, then $n=\infty$. This would be the case if no electrons were collected by the electrodes, and nearly corresponds to the case of a magnetron without any grid inside the tube. This means that a very small filament emission may cause a large space charge by virtue of the electrons making many oscillations before being captured. (2) If $\alpha\doteq\sigma\doteq 1$, then $n=dN$. This would be the case if all the electrons were captured by the grid or plate, and nearly corresponds to the case of a B−K tube with a grid of very thick wire and very small pitch. As will be shown later, it is safely assumed that $\sigma\approx 0$ and $\gamma\approx 0$ as compared with unity, so that in practical cases η is put approximately as follows:

$$\eta\approx(1-\alpha)(1-\delta) \qquad (4)$$

Now, of these $dN/(1-\eta)$ electrons leaving the cathode region in an interval of time dt, $dN\cdot\alpha/(1-\eta)$ are captured by the grid directly and the remaining electrons, $dN(1-\alpha)/(1-\eta)$, penetrate througth the grid openings into the G−P space. After approaching the plate very closely, a fraction $(1-\sigma)$ of these electrons is pushed back toward the grid, by which a fraction δ is captured. The remainder, $(1-\delta)$, passes through the grid openings toward the cathode again. Let us denote the transit times of electrons from K to G, from G to P and from K to K via G and P by τ_1, τ_2 and $\tau=2(\tau_1+\tau_2)$, respectively. Then, $dN\alpha\tau_1/(1-\eta)\,\tau$ is the mean number of electrons making one entire trip, taken account of the electrons landing on the grid on the way from K to P. Since $\sigma\approx 0$ (see below), the mean number of the electrons captured by the grid on the return transit from P to K, averaged over one entire path, is given by $dN(1-\alpha)(\tau_1+2\tau_2)\cdot\delta/(1-\eta)\,\tau$. In a similar way $dN(1-\alpha)(1-\delta)\cdot 2(\tau_1+\tau_2)/(1-\eta)\tau$ is the mean number of the electrons which have fortunately escaped capture by the grid wire twice and execute one entire radial oscillation.

Thus, the total average number of electrons making one complete radial oscillation is given by the sum of these as follows:

$$\frac{dN}{1-\eta}\cdot\frac{1}{\tau}\{\alpha\tau_1+(1-\alpha)(\tau_1+2\tau_2)\delta+\tau(1-\alpha)(1-\delta)\}.$$

Since the time taken by electrons to complete one radial oscillation is τ, the total number N of electrons existing in the interelectrode space at any instant is τ/dt times the value given above, i. e.,

$$N\doteq\{\alpha\tau_1+(1-\alpha)(\tau_1+2\tau_2)\delta+(1-\alpha)(1-\delta)\tau\}\frac{1}{1-\eta}\cdot\frac{dN}{dt}.$$

On the other hand, denoting the mean number of radial oscillations of the electrons by R, N may be given by $N=R\tau\cdot dN/dt$. Hence

$$R=\frac{1}{1-\eta}\left\{\frac{x}{\tau}\tau_1+(1-\alpha)\cdot\delta\cdot\frac{\tau_1+2\tau_2}{\tau}+(1-\alpha)(1-\delta)\right\}. \qquad (5)$$

By knowing the values of α, δ, η, τ_1, t_2 and τ for the dimensions and the voltages of the electrodes given, we can deduce from Eq. (5) how many times the electrons make radial oscillations on the average within the tube.

Our considerations hereafter are confined only to the voltage condition: $V_g=134$ volts, $V_p\approx 0$ volt and $V_{ep}=-150$ volts.

3. 2. Determination of η.

We shall first take up the determination of α. The procedure of measurement is as follows: The grid G, plate P and collector C respectively are connected together by ammeters, and a d-c voltage V_g is impressed between these electrodes and the cathode K. The currents flowing through these ammeters, I_g (grid current), I_p (plate current) and I_c (collector current), are measured as functions of the grid voltage V_g, and $\alpha'=I_g/(I_g+I_p+I_c)$ is calculated. This is shown in Fig. 4 by a full line. While the measurements were conducted with $I_f=0.66$, 0.68, 0.70 amp. respectively, a fairly good agreement among these three curves was observed. The end-plate voltage V_{ep} was kept constant throughout the experiments at -150 volts with respect to the cathode. This gave the highest sensitivity under receiving condition. This α' must, however, not be used in place of α, for the former was obtained with $V_g = V_p = V_c$, while the plate voltage V_p was kept at nearly zero voltage in the actual receiving condition. When $V_p = 0$, the effective potential on the grid plane is somewhat lowered, and the grid voltage must be raised by the amount V_g/μ in order to attain the same effective potential on the grid plane as before, μ, the amplification factor of the grid with respect to the plate, being nearly equal to 6 in the present case. The α-curve in Fig. 4 is thus obtained, and is considered to represent approximately the absorption coefficient of the grid for electrons moving in the direction K → P. But in reality, the irregularities in the field distribution in the vicinity of the grid wire are likely to act in fovor of a larger value of α than that obtained above.

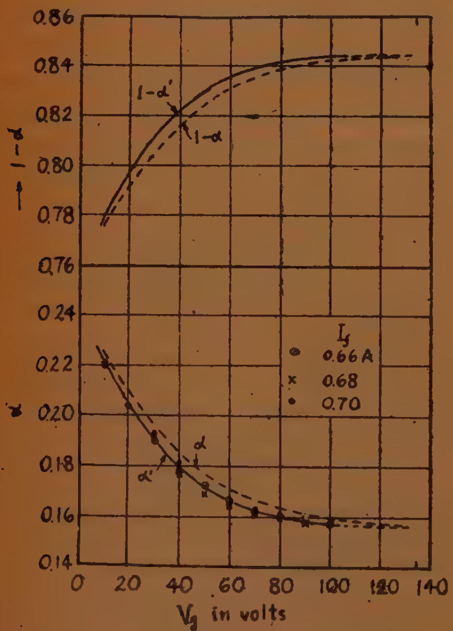

Fig. 4. Determination of α.

The α-curve in Fig 4 shows that the value of α decreases gradually on increasing V_g, giving $\alpha \approx 0.156$ at $V_g = 134$ volts. While this value of α is somewhat smaller than the screening factor of the grid ($0.25/1.5 = 0.17$), the discrepancy between these two values is perhaps attributable to deformations of the electrode structures and also to secondary electrons emitted by the grid. The fact that the value of α becomes larger for the smaller values of V_g might be due to (1) a potential minimum formed close to the grid by space charge in the grid-plate space, by which a part of the electrons having had chances to escape capture by the grid wire is forced to turn back toward the grid again; (2) the increase of the effective diameter of the filamentary cathode due to space charge: all the space charge-limited cylindrical diodes with $r_g/r_k > 10$ have the same capacity as a space charge-free one with $r_g/r_k = 4.5$(4); and (3) shift of the virtual cathode initially located very near around the filament toward the grid surface on decreasing V_g. On increasing V_g, the value of α is likely to tend to a definite value. This is what it ought to be in the temperature-limited region (current division between the electrodes)(5). It is at least not unreasonable that there is little discrepancy between the curves α and α', if we take into consideration the facts that the B—K tube under consideration has a concentric structure with very thin cathode, and the field intensity near the cathode is so strong that paths of electrons emitted from the cathode are determined mainly by the field distribution right around the cathode without being influenced appreciably by the field irregularities around the grid wire. In Fig. 5 are shown the field distributions in a B—K tube, measured in an electrolytic tank with a model about twenty times larger than the real one in question. These serve as an illustration of the relations above mentioned. In this figure four patterns are shown which correspond to $V_g = 20$, 60, 100 and 140 volts respectively, and in each case with $V_p = 0$ and with space charge neglected.

In Fig. 4 is shown also the curve $(1-\alpha)$, the transmission coefficient of the grid for electrons moving in the direction K → P, which gives the value 0.844 at $V_g = 134$ volts.

We shall next consider the determination of σ. By connecting the plate P and collector C, respectively, by ammeters to earth potential and giving the grid $+V_g$ volts the ratio $\sigma' = (I_p + I_c)/I_k(1-\alpha)$ is calculated, where $I_k = I_g + I_p + I_c$. Strictly speaking, the true value of σ is smaller

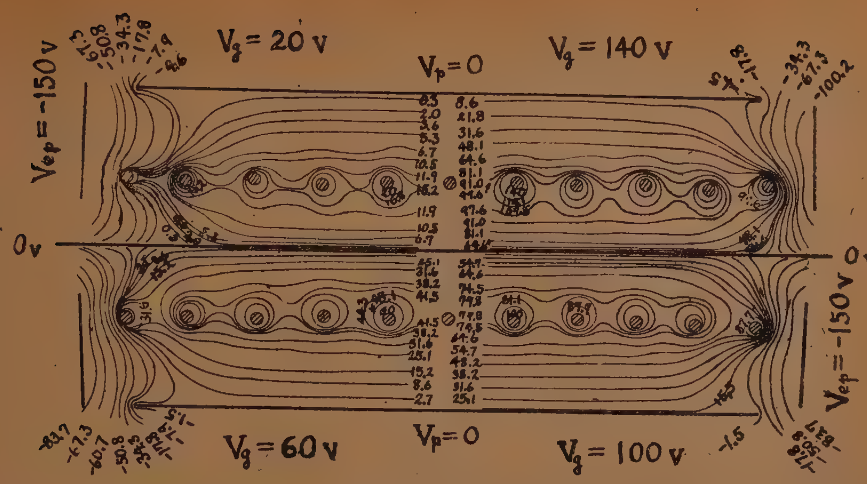

Fig. 5. Field distributions in the B—K tube. Measured in an electrolytic tank.

than σ', because the electron stream penetrating into the grid-plate space is not $I_k(1-\alpha)$ but $I_k(1-\alpha)/(1-\gamma)$ and so it is quite safe to take up σ' in place of σ in order to see if σ would be of such an order of magnitude as to be negligible. The results of experiments are shown in Fig. 6. The reason the value of σ' for $I_f = 0.70$ amp. is larger than that for $I_f = 0.66$ amp. may well be explainable by the higher initial velocities of electrons emitted by the cathode for the former than for the latter. The irregularities in the potential distribution in the grid plane are relatively larger for higher V_g than for lower one, which in turn exercise larger effects upon the deflection of electron paths in the grid-plate space, the radial component of electron velocity thus being relatively more strongly affected for the case of higher V_g than that for lower one. Besides, the lower V_g becomes, the nearer the virtual cathode around the filament approaches the grid surface as mentioned above so that electrons having higher initial velocities increase in relative number in the grid-plate space, electrons having lower initial velocities being captured by the grid directly. The result is that σ increases on decreasing V_g, although the absolute value of the electron current entering the grid-plate space is smaller. These curves show clearly that σ is of an order of magnitude which is negligibly small as compared with α.

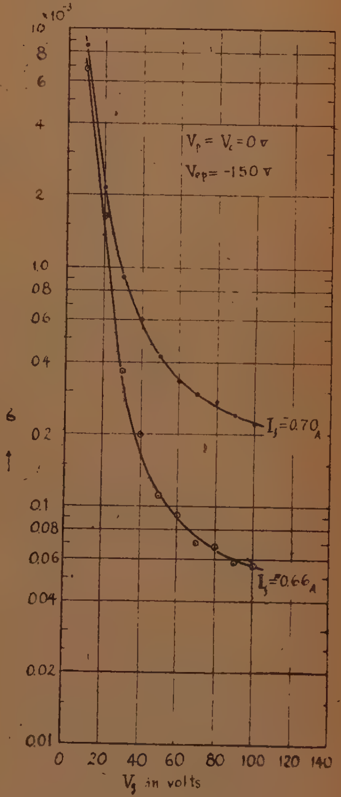

Fig. 6. Determination of σ.

As to the absorption coefficient of the cathode, γ, it will not be unreasonable to suppose that γ is nearly of the same order as or somewhat smaller than σ, taking into consideration the facts that the cathode is a very thin filament, and that no virtual cathode is formed around this filament under the voltage conditions under consideration. This point was also confirmed experimentally by probe method.

Finally, we are in a position to consider the determination of δ, the absorption coefficient of the grid for the electrons moving in the reverse direction from P to K. In the space charge-limited region the space potential near the cathode is lowered very much by the space charge due to the returning electrons. This in turn reduces the electron current density emitted from the cathode surface, the maximum current density being attained at zero potential gradient on that surface if the initial velocities of the thermal electrons be assumed zero. Analysis shows that the following equation is obtained by assuming an equivalent cylindrical diode, whose anode and cathode respectively coincide with the grid and cathode of the B—K tube in question:

$$I_g = (1-\eta)\times 14.68\times 10^{-6}\frac{V_g^{3/2}}{r_g\beta^2}\ \text{A/cm.} \qquad (6)$$

where β is the well-known Langmuir's coefficient and is nearly equal to 1 in the present case, since $r_g/r_k = 0.325/0.005 = 65$. Eq. (6) indicates that the existence of the oscillating electrons gives rise to the space charge effect producing a reduction of the currrent obtained.

In Fig. 7 are shown some experimental data obtained with our B—K tube. In this figure the curve I shows the current I_k as a function of V_g, obtained with the grid, plate and collector connected together and $+V_g$ volts applied with respect to the cathode, while the curve II shows the current I_g as a function of V_g, obtained with the plate and collector connected together to the cathode (zero potential). It is to be noted here that the curves I and II must not be compared directly, for the effective potential on the grid plane differs somewhat for these two cases, the effective potential for the case of the curve II being below that for the case of the curve I. In order to keep the effective potentials on the grid plane equal for the both cases the abscissae for the curve II must be shifted to left by the amount $V_g/(\mu+1) \approx V_g/7$, the curve III being thus obtained.

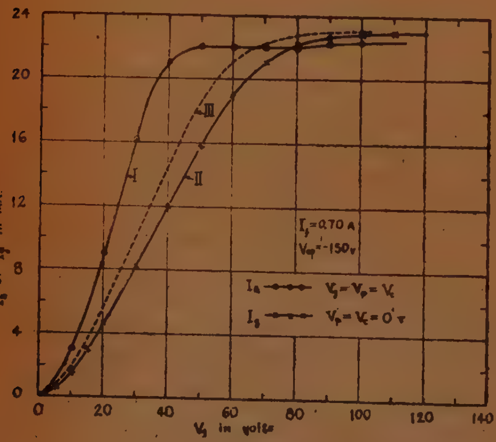

Fig. 7. Increase of space charge by virtue of oscillating electrons.

In the space charge-limited region the following equations hold good, by referring to Eq. (6):

$$\text{for Curve I, } I_k = GV_g^{3/2} \qquad (7)$$

$$\text{for Curve III, } I_g = G(1-\eta)V_{g0}^{3/2} \qquad (8)$$

where G is the perviance and V_{g0} denotes V_g for the curve III. From Eqs. (7) and (8) we get, by putting $I_k = I_g$:

$$\delta \approx \frac{(V_g/V_{g0})^{3/2}-\alpha}{1-\alpha} \qquad (9)$$

Referring to the curves I and III in Fig. 7 and the curves α and $(1-\alpha)$ in Fig. 4, we are able to calculate δ, which is plotted in Fig. 8 as a function of the grid voltage V_g. It is seen in Fig. 8 that we can estimate, as a rough approximation, $\delta \doteqdot 0.4$ and $1-\delta \approx 0.6$ at $V_g = 134$ volts and $V_p \doteqdot 0$ volt.

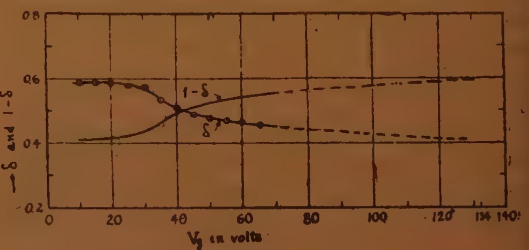

Fig. 8. Determination of δ.

It is of some interest that the value of δ thus obtained is somewhat larger than α determined above. This is attributable, in the writer's opinion, to the facts that the grid-plate space approaches a plane electrode system more closely than the grid-cathode space, and hence the field intensity near the virtual cathode formed very close to the plate is not as strong as in the grid-cathode space (see Fig. 2), and furthermore, deflections of electron paths due to the irregularities of potential distribution near the grid wire act in favor of increase of δ rather than α.

Thus, the values of η and $1-\eta$ at $V_g = 134$ volts and $V_p = 0$ volt are given by

$$\left.\begin{aligned} \eta &\approx (1-\alpha)(1-\delta) = 0.51 \\ 1-\eta &\approx 0.49 \end{aligned}\right\} \qquad (10)$$

3. 3. Calculation of the Transit Times.

In calculating the transit times of electrons between the electrodes the grid voltage V_g itself may not be used but the mean grid voltage $V_{g\mathrm{mean}}$ as shown by the dotted line in Fig. 2 must be adopted. By reference to Fig. 5 it is deduced that $V_{g\mathrm{mean}}$ is about 110 volts for $V_g = 134$ volts. Transit time τ_1 of electrons from K to G is calculated by the formula derived by Scheibe(6) and is equal in the present case to $\tau_1 = 3.03 \times 10^{-10}$sec., while the transit time τ_2 from G to P is calculated by the use of the formula derived by Fortescue(7), which runs in our case as follows: $\tau_2 = 12.35 \times 10^{-10}$sec. The transit time τ taken by electrons to make an entire trip is, then, given by $\tau = 2(\tau_1 + \tau_2) = 30.76 \times 10^{-10}$sec.

3. 4. Results.

Using the data obtained above and Eq. (5), we get $R = 1.7$ as the mean number of electron oscillations. This value of R for the B—K tube is far smaller than that obtained previously by Linder(2) for a magnetron, and the existence of the grid in the former case is responsible for this result.

We shall consider the motion of electrons in the B—K tube in somewhat more detail. Assume that 100 electrons are emitted by the cathode at any instant; then it is deduced that about 50 per cent of them can execute a single revolution, about 26 per cent two revolutions, about 13 per cent three revolutions, about 7 per cent four revolutions and only 3 per cent can approach the cathode after executing cyclic motions five times.

In conclusion, the writer wishes to express his sincere thanks to Dr. T. Okabe for his cordial guidance and to Mr. M. Yamamoto for his assistance in making the sample tube. His best thanks are also due to Dr. M. A. Pomerantz of Bartol Research Foundation of the Franklin Institute, U.S.A., but for whose kind corrections for many grammatical mistakes the paper would not have taken its present form.

References.

(1) F. W. Gundlach and W. Kleinsteuber: Zeits. f. techn. Phys. **22** (1941), 57.

(2) E. G. Linder: Phys. Rev. **26** (1938), 346.

(3) I. Langmuir: Phys. Rev. **22** (1923), 347.

(4) W. G. Dow: Fundamentals of Engineering Electronics (John Wiley & Sons, New York, 1937), p. 117

(5) B. van der Pol: Zeits. f. Hochfreq. **25** (1925), 121.

(6) A. Scheibe: Ann. d. Phys. **73** (1924), 54.

(7) C. L. Fortescue: Wireless Eng. **12** (1935), 310.

Dispersion of Ultrasonic Velocity in the Liquid Fatty Acids.

By Yasaka WADA, Sotoshi SHIMBO and Minoru ODA.

First Faculty of Engineering, University of Tokyo.

(Received February 15, 1950).

§ 1. Introduction.

Very little is known about the dispersion of of ultrasonic velocity in liquid fatty acids. The only information was given by B. G. Spakovskij(1 in the case of acetic acid. According to his results, a difference of 0.9 percent was detected between sound velocities in the two frequency ranges, 0.24–0.27 M.C. and 2.4–3.4 M.C., and the dispersion was ascribed to relaxation of the dissociation of a dimer to monomers with a relaxation time of 10^{-7}sec.. But the sample was for industrial use, containing water, and was yellowish.

The authors wanted to detect the dispersion also in the case of higher fatty acids, expecting a longer relaxation time than that of acetic acid. The experiment was carried out for stearic, palmitic and lauric acid in a frequency range of 0.61–6.28 M.C., at temperatures from 95°C to solidifying points.

Against our expectation, however, no dispersion was observed in higher temperature range. But near the solidifying point the sound velocity became maximum at a certain frequency, which was the lower, the higher the acid was. This phenomenon may be called "Resonant dispersion".

§ 2. Experimental.

For the measurement of ultrasonic velocity is used the ultrasonic interferometer, which was reported in our previous paper(2) The vessel, containing 20 c.c. liquid to be studied, is immersed in an oil bath. As the temperature difference between the liquid and the bath is not negligible, particularly in high temperatures, the temperature in the vessel is directly observed by means of a thermocouple. The measurement is carried out always from the high temperature to the solidifying point at each frequency.

To prevent the sample from local warming by ultrasonics, sound of small intensity (less than 0.2 W/cm^2) is always used, and the sound wave, produced by a piezoquartz plate which is placed outside the vessel, is transmitted into the vessel through a thin mica foil. The intensity of sound is estimated by a torsion vane. Special cautions are paid to the parallelism between the quartz plate and the reflector.

The error of measurements of the wave length is within a few per mille and somewhat larger at elevated temperatures because of fluctuations of the temperature during the measurement. The reflections of sound by the walls of the vessel is checked to have no effect on the precision. The frequency is calibrated from the wave length in the water.

Fig. 1 shows a schematic diagram of the apparatus. The frequencies of the main oscillator and the signal generator are adjusted to be slightly different from each other and the beat between them is amplified and transmitted from a loud-speaker. When the reflector is moved by a micrometer screw towards the quartz, the frequency of the main oscillator and accordingly the pitch of the beat vary periodically. The wave length of sound can be determined from intervals of positions of the reflector giving the maximum pitch of the beat. The intensity of sound is adjusted by varying the plate voltage of the main oscilator.

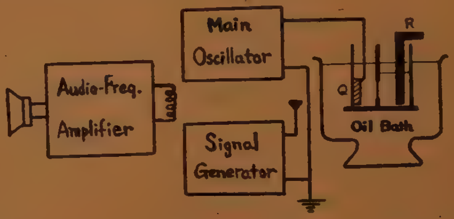

Fig. 1. Schematic diagram of the apparatus.
R: Reflector. Q: Quartz plate.

Four different thicknesses of X-cut quartz plate are used, 5, 3, 2, 1.3 mm, supplying the frequencies 0.61, 1.00, 1.45, 2.12 M.C. as the fundamental vibrations and 1.63, 2.87, 4.28, 6.28 M.C. as the first over-vibrations. To test the reliability of the apparatus, some preliminary experiments are performed for paraffin (M.P. ca. 50°C) and cetyl alcohol (M.P. 50°C). The results show no dispersion and the sound velocity decreases linearly with temperature.

The adopted samples of higher fatty acids are steartic acid (M.P. 6.45–66°C), palmitic acip (M.P. 65 57°C) and lauric acid (M.P. 43.5°C), among which the lauric acid is the purest and the palmitic acid contains some water and has yellowish appearance.

§ 3. Results.

In table I are listed the data of the sound velocity in the fatty acids. Fig. 2 shows the relations between the sound velocity and the frequency at the temperature near the solidifying point.

As alread mentioned in the introduction of this paper, the observed sound velocity of the higher fatty acids near the solidifying point has maximum at a certain frequency, which is the lower, the higher the acid is: 1.0, 1.8, and 2.6 M.C. for strearic, palmitc and lauric acid respectively. The abnormally remarkable dispersion of the palmitic acid seems to be ascribed to impurities.

Table I. Sound velocity in fatty acids.

(A) Stearic acid

Temp.(°C) / Freq. (M.C.)	65	70	80	90
0.61	1264	1257	1225	1191
1.00	1277	1264	1225	1191
1.45	1268	1258	1227	1192
2.12	1260	1255	1228	1189

(B) Palmitic acid

Temp. / Freq.	65	70	80	90
0.61	1265	1258	1232	1200
1.00	1278	1267	1230	1198
1.45	1302	1279	1232	1198
2.12	1313	1290	1237	1202
2.87	1291	1277	1240	1200
4.28	1279	1265	1232	1200
6.28	1263	1257	1233	1204

(C) Laurid acid.

Temp. / Freq.	40	45	55	65
0.61	1297	1289	1248	1219
1.00	1307	1290	1255	1221
2.12	1313	1291	1256	1221
2.87	1314	1294	1256	1220
2.28	1304	1292	1255	1218

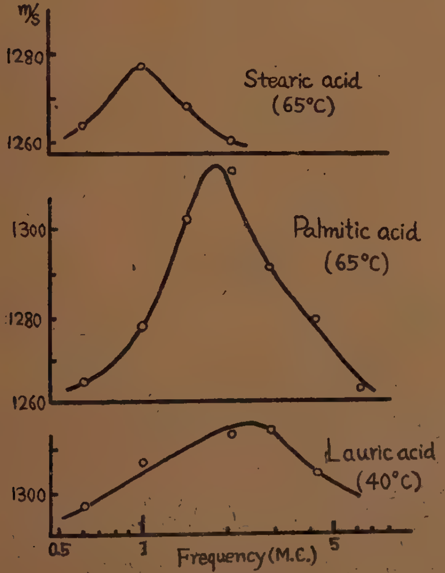

Fig. 2. Dispersion of sound velocity in fatty acids.

§ 4. Discussion.

The observed dispersion in the fatty acids may be explained as superposition of two relaxational phenomena, one giving a positive dispersion (sound velocity increasing with frequency) and the other giving a negative one (sound velocity decreasing with frequency). From another point of view, however, it may be ascribed to a sort of resonant phenomena.

It has been shown by one of the authors⁽³⁾ that moelecules of higher fatty acids, as well as lower ones, form dimers up to the temperature far above the melting point. Therefore, the dispersion, observed only near the solidifying point, can not be reasonably attributed to the dimer-monomer dissociation. From the reasons above, the dispersion seems to be explained rather as a resonant phenomenon than a relaxational one.

It may be plausible to assume that there exist many cybotactic (solid-like) groups in the higher fatty acid near the solidifying point. A further assumption is made that these groups have nearly the same proper angular frequencies with the average value ω_0. When the sound with the angular frequency ω passes through the medium, the cybotactic groups are set into forced vibrations with the amplitude D, which is given as

$$D^2 = \frac{I}{m^2(\omega_0^2-\omega^2)^2+\mu^2\omega^2}, \tag{1}$$

where m is the mass of the group, μ the coefficient of resistance and I a constant propertional to the sound intensity.

The vibrations of the groups cause themselves to dissociate into more disordered (liquid-like) state and consequently increase the specific volume v (or the pressure p, if the volume is kept constant) and the internal energy u by the amount proportional to the intensity of the bibrations. Denoting the pressure and the internal energy as p_0 and u_0 respectively when there exists no sound, and p and u when the sound passes, it follows

$$p = p_0(v, T)(1+kD^2) \tag{2}$$

and

$$u = u_0(v, T)(1+kD^2), \tag{3}$$

where k is a constant. The relations among the infinitesimal change of pressure, volume and temperature can be written as

$$\Delta p=\left(\frac{\partial p_0}{\partial v}\Delta v+\frac{\partial p_0}{\partial T}\Delta T\right)(1+kD^2) \tag{4}$$

and

$$\Delta u=\left(\frac{\partial u_0}{\partial v}\Delta v+\frac{\partial u_0}{\Delta T}\Delta T\right)(1+kD^2). \tag{5}$$

Furthermore for an adiabatic process

$$\Delta u=-p\Delta v. \tag{6}$$

From (4), (5) and (6), the sound velocity V, given by

$$V^2=-\frac{v}{\rho}\frac{\Delta p}{\Delta v}, \tag{7}$$

becomes

$$V^2=V_0^2(1+kD^2), \tag{8}$$

where V_0 is the sound velocity of zero intensity and can be represented as

$$V_0^2=\frac{v}{\rho}\left[\left(p_0+\frac{\partial u_0}{\partial v}\right)\frac{\dfrac{\partial p_0}{\partial T}}{\dfrac{\partial u_0}{\partial T}}-\frac{\partial p_0}{\partial v}\right]. \tag{9}$$

On substituting (1) to (8), it follows the following formula expressing the resonant dispersion,

$$V^2=V_0^2\left(1+\frac{kI}{m^2(\omega_0^2-\omega^2)^2+\mu^2\omega^2}\right). \tag{10}$$

According to the last expression, the amount of the dispersion is proportional to the intensity of sound. Fig. 3 shows the dependence of sound velocity of the palmitic acid on sound intensity. In the higher temperature range the sound velocity does not vary with the intensity, but near the solidifying point, where the dispersion occurs, the velocity increases with the intensity, in accordance with our expection.

It seems very unnatural, however, to assume, that the cybotactic groups have their proper frequency so low as a few mega cycle and the authors should be much obliged if the readers take the trouble to comment upon it. Anyhow the dispersion of this type, which shows a charcteristic "resonant frequency" in each fatty acid, may offer the possibility of the qualitative analysis of fatty acids.

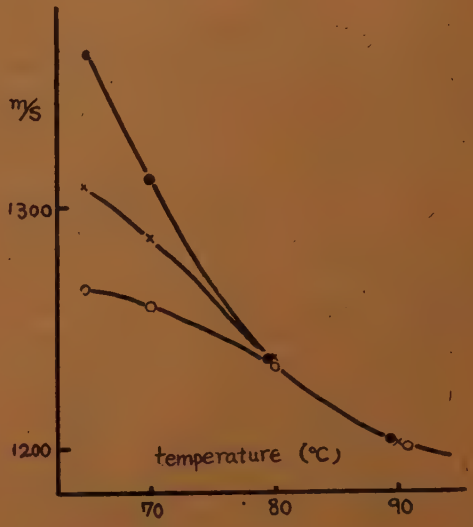

Eig. 3. Dependence of sound velocity in palmitic acid on sound intensity.
● : 2.12 M.C. 1.8 W/cm²
× : 2.12 M.C. 0.5 W/cm²
○ : 0.61 M.C. where the dispersion disappears.

In conclusion the authors wish to express their great appreciations to Professor Yoshio Suge and others in their department, who gave the continued encouragement and the valuable discussion. The authors are also indepted to Dr. T. Tsuchiya and Mr. H. Fukuba who offered the samples and to Mr. S. Ishii who took the trouble to determine the melting points of the samples.

References.

(1) B. G. Spakovskij: C. R. USSR., **18** (1938) 169, 173.
(2) Y. Wada S. Shimbo & M. Oda: Oyobutsuri (J. Appl. Phys. Japan), **18** (1949) 351
(3) Y. Wada: ibid., **18** (1949) 156.

On the Characteristics of the Selenium Rectifier at Low Temperatures and the Electric Formation.

By Masao Tomura.

Matsude Research Laboratory of the Tokyo Shibaura Electric Co., Ltd., Kawasaki.

(Read, April 29 and Nov. 8, 1949; Received, March 4, 1950)

§ 1. Introduction.

The author has reported on the temperature variations of the rectification of the selenium rectifier in the temperature region higher than the room temperature and how influenced the electric formation on the characteristics of rectification(1). According to him the current by tunnel effect superposed on the one of thermoionic type(2) plays an important rôle in a case of the selenium rectifier and it makes natures of the rectifier worse. As the latter current decreases exponentially with decrease of temperature, inspite of constancy of the former, measurements at low temperatures will make the tunnel effect conspicuous about which we hope to know in detail.

On the ather hand, the manufacturing process of electric formation is a very useful method to improve the characters of the rectifier and it has been concluded(1) that the process diminished the tunnel effect which took place through local spots where the berrier layers were thin.

In order to study on the electric formation precisely, it is desirable to measure the characteristics of the rectifier at low temperatures.

§ 2. Description of Experiments.

The selenium rectifier which is used for measurements is manufactured just in the same way as the one reported in the preceeding survey(1). Its area is 2.0 cm^2. Measurements are carried on as follows: the easy and hard flows for various d.c. voltages at each temperature are measured and the duration of applying voltage is maintained so short as a few seconds that progress of the electric formation cannot take place by high d.c. voltages in the blocking direction especially before the formation and the Joule's heat produced in the barrier layer cannot disturb results so much especially for the high inverse voltage. The reproducibility is not very good, but no obstacles appear for the following discussions.

The thermostat which contains the sample is a normal type of liquid air thermostat which is controled by a inside heater separated by vacuum from the outside liquid air. The temperature of the sample is measured by a copper-constantan thermocouple and the atmosphere of the vessel is substituted by dried air.

The resistance of selenium semi-conductor is measured for a rod sample of 0.8 cm in length and 0.2 cm in diameter which is made from the same material as the one used for the rectifier, and has graphite electrodes. And small interface resistances at each electode are eliminated from voltage versus current curves.

§ 3. Temperature Variation of the Hard Flow.

The results of the measurements of the easy and hard flows before and after the formation are shown in Fig. 1 and Fig. 2. The characteristics of the rectifier in the temperature range higher than about −30°C are same as the ones reported before. Namely there appear currents by tunnel effect superposed on currents of the Mott's type. While in the temperature region lower than −30°C, only the former type of current is observed owing to disappearance of the latter as expected.

Next an interesting result is found which shows a reverse temperature coefficient at high voltages to the one at higher temperature. The reason of this effect is not yet understood. The author tried to calculate theoretically by assuming that the electron distribution in the barrier

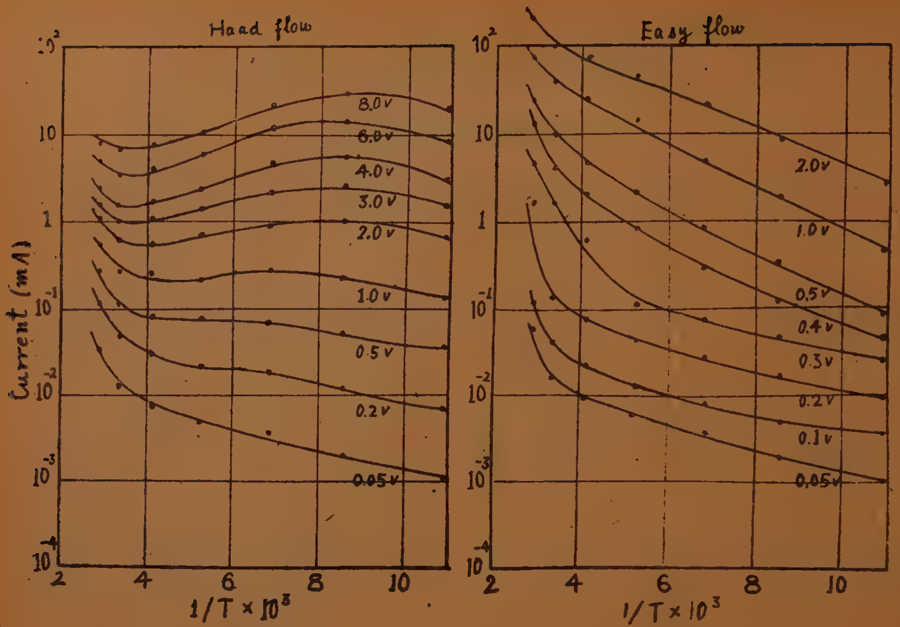

Fig. 1. Characteristics of the hard and easy flows before the electric formation.

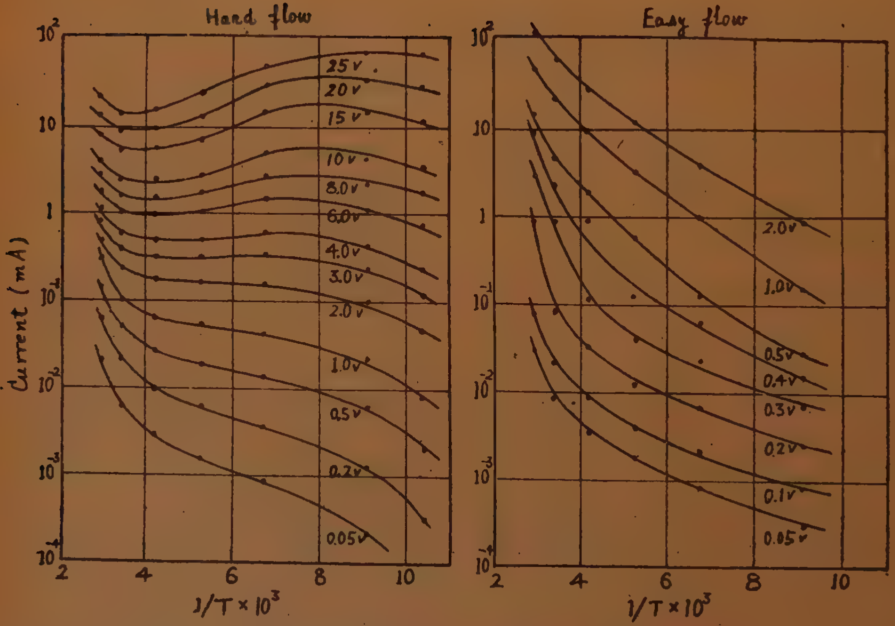

Fig. 2. Characteristics of the hard and easy flows after the electric formation.

layer become diffused by elevating temperature, making the effective thickness of the barrier layer larger, but failed to explain so large temperature dependence of the effect⁽³⁾. Perhaps positive holes accerlated by a very high field will make this problem clear.

§ 4. Characteristice at Highe Reverse Voltages.

At high reverse voltages the tunnel effect converts into the field emission, for the internal field in the barrier layer becomes so large such as $10^6 \sim 10^7$ volt/cm. Thus we can use the next equation for the hard flow at high voltages⁽⁴⁾.

$$i = AF^2 \exp\{-\alpha(eV_0)^{3/2}\} \quad \cdots\cdots\cdots\cdots \quad (1)$$

$$\alpha = \frac{8\pi}{3}\frac{\sqrt{2m}}{ehF}.$$

Here i is the current by field emission, F the internal field in the barrier layer, V_0 the contact potential, m the electron mass, h Planck's constant, e the electronic charge and A a constant. From Eq. (1)

$$\log\{i/(V_0+V)^2\} \simeq \text{const.} - \frac{8\pi}{3}\frac{\sqrt{2m}}{eh}(eV_0)^{3/2}\frac{d}{(V_0+V)} \quad \cdots\cdots\cdots \quad (2)$$

is obtained and the thickness of the barrier layer d can be evaluated from the slope of the curve $\log\{i/(V_0+V)^2\}$ *versus* $1/(V_0+V)$ at high voltage in the blocking direction. The curves are shown in Fig. 3.

At low temperatures the spreading resistance becomes so large that an applied voltage is not a real voltage impressed through the barrier layer, and corrections must be taken. d obtained from Fig. 3. is shown in Table I.

As these values of d are obtained by assuming the internal field constant in the barrier layer and a relation $d=(V_0+V)/F$ to hold, the upper part of the barrier is so thiner than 50Å～100Å that the tunnel effect will occur easily. At the same time this effect will convert into field emission for voltages higher than several volts, for the internal field exceeds 10^6v/cm. These order of thickness of the barier layer is less by one than that which is obtained as $10^{-5} \sim 10^{-6}$ cm above the room temperature⁽⁵⁾. This fact supports the mechanism which is reported previously⁽¹⁾; rectification acts on the Mott's type at higher temperatures and on the type of tunnel effect at lower temperatures.

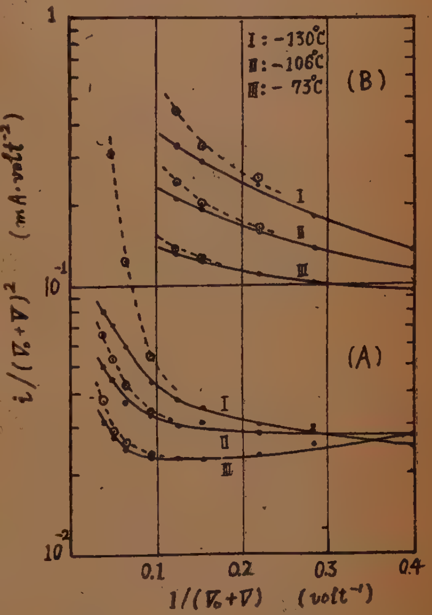

Fig. 3. The field emission curves before (B) and after (A) the electric formation. Real lines are observed curves and dotted lines calibrated curves.

Table I. The calculated values of d from Eq. (2) before and after the electric formation. V_0 is taken as 0.4 volt*.

Temperature	Before the formation	After the formation
−130°C	ca. 60 Å	ca. 250 Å
−106°C	ca. 30 Å	ca. 90 Å
− 73°C	ca. 20 Å	ca. 110 Å

Increase of d from ca.50 Å to 100Å by the formation means growth of the thickness of the barrier layer, resulting decrease of transmission of charge carrier through the barrier and diminishing the current by the tunnel effect.

§ 5. Temperature Variation of Spreading Resistance and Resistance of Selenium Semiconductor.

The spreading resistance R_s of the rectifier can be obtained graphically from a current versus voltage curve in the forward direction in high voltage region where the differential resistance has a constant value. (See Fig. 4). As the spreading resistance comes from the bulk semiconductor, that is, selenium semiconductor, its temperature dependency must be same as one of resistance of selenium semiconductor itself.

---

* Here V_0 is meant as a real contact potential, so then the value at high temperature must be taken.

The results of observation are shown in Fig. 5 and Fig. 6. The resistance of the semiconductor shows two kinds of activation enegy which may perhaps be attributed to two species of impurity: the one is iodine which is mixed artificially, the other unknown impurity which have remained inspite of purification(6).

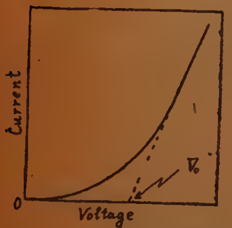

Fig. 4. A current *versus* voltage curve in the forward direction. V_0 is the contact potential.

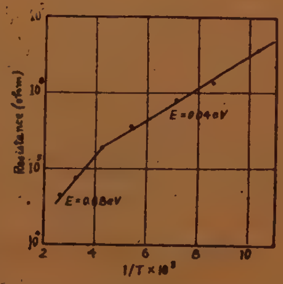

Fig. 5. The resistance *versus* 1/T curve of the selenium semiconductor.

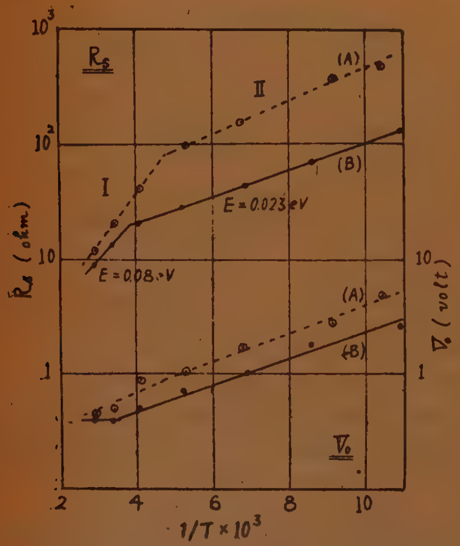

Fig. 6. R_s and V_0 versus 1/T curves before (B) and after (A) the electric formation.

The curve of R_s versus 1/T also consists of two parts I and II. Discrepancy between activation energies of R_s and the body resistance may be owing to difference of materials used.

We must notice that R_s in the II part increase several times by the electric formation, while it is almost constant in the I part. Thus R_s in the II part is not considered as a spreading resistance in the normal meaning, but will be the *local spreading resistance*(9) which exists at local small patches. When the current flows through only these small local spots, it is limited not by the spreading resistance on the whole, but by local spreading resistances for the most part. Thus assuming that the effective area of local spots is diminished by the formation, resulting increase of the effective value of the local spreading resistance, large increase of R_s by the formation can be explained. These discussions are consistent completely with the stand point of the previous work(1) that tunnel effect occure only at local spots where the barrier layers are thin. (See Fig. 7.)

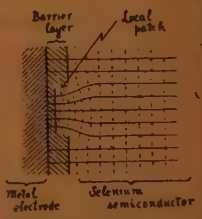

Fig. 7. A local patchin the barrier layer: Real lines are flows of current and dotted lines equipotential surfaces.

As the local spreading resistance is schown in a form of $\alpha\exp(E/kT)$, α_a/α_b gives the ratio of the effective areas before and after the formation, and is nearly 4 for our sample. Here and α_a are α_b before and after the formation. But this ratio in the I part is nearly one, meaning that R_s in this part is the normal spreading resistance which cannot be changed by the formation.

Next, an interesting consideration must be added. The fact that a large change of R_s occurs only in the II part where the activation energy due to one kind of impurities is observed shows localization of the local spreading resistance only in the neighbourhood of that impurity centre or perhaps its aggregation.

§ 6. Contact Potential.

Usually, a straight part appears in a current *versus* voltage curve at high voltages in the forward direction. This fact means that the internal field in the barrier layer flattens owing to a forward applied voltage and then a linear relation between current and voltage shows an ohmic spreading resistance. So the intercept of the straight line and the voltage axis shows the voltage V_0 which is necessary to flatten the internal field. As the activation energy of selenium semiconductor is small, V_0 is approximately equal to the contact potential at the interface. (See Fig. 4)

The temperature variation of contact potential is shown in Fig. 6. It is recognized that V_0 tends to have a constant value at high temperatures before and after the formation and its temperature dependency at low temperatures is exponential. In the I part the rectification acts on the Mott's type, so the contact potential must have a definite value. But in the II part the nature of rectification comes from the tunnel effect at the local spots and the contact potential obtained by the above method has another meaning from that in the I part. In this case V_0 means a voltage at which transmission coefficient of the tunnel effect becomes one, resulting no hinderance to the current through the barrier and making appearance of the current *versus* voltage curve of the ohmic local spreading resistance.

No studies have been carried on concerning with the temperature variation of transmission by tunnel effect at high voltage in rectification.

V_0 increases 1.6 times by the formation in the II part as the figure shows. As increase of V_0 by the formation means growth of the barrier layer at local spots and V_0 means a voltage necessary for a perfect transmission, we may conclude that the thickness of the barrier layer increases 1.6 times approximately by the formation. This increase of thickness in just consistent in order with the one mentioned in § 4.

§ 7. Conclusion.

Temperature variations of several characteristics of the selenium rectifier before and after the formation are measured between +70°C∼−180°C. Main results obtained are as follows.

(1) Currents at high reverse voltages show abnormal characters at two temperatures.

(2) Currents in the low temperature region are ones of tunnel effect type in either directions.

(3) Hard flows at high reverse voltages convert rather into field emission.

(4) Two kinds of impurity centres are observed in our selenium Semiconductor material and only the one is related to the non-uniform nature(1) of the rectifier, that is to say, to local spots where the barrier layer is thin and through which tunnel effect currents flows. And then these spots suffer from the electrical formation.

(5) Local spreading resistance which has been offered only in concept is really observed.

(6) The electrical formation brings about growth of the barrier layer and diminishing of effective area of local spots, which are observed by changes of R_s and V_0 by the formation respectively.

(7) Contact potential obtained by a usual method has a essentially different meaning at low temperatures and means rather a transmission coefficient.

The author thanks Dr. A. Kobayashi for his kind encouragement in the course of this work.

References.

(1) M. Tomura: J. Phys. Soc. Japan. **5** (1950) 5. Read at the annual meeting of the Phy. Soc. Jap. April 29, 1949 (Tokyo).
(2) N. F. Mott: Proc. Roy. Soc., **A. 171** (1939) 27.
(3) M. Tomura: Read at the annual meeting of the Phy. Soc. Jap. April 29, 1949 (Tokyo).
(4) e. g. A. Kobayashi: J. Phys. Soc. Japan, **3** (1948) 41.
(5) M. Tomura: Tsushin Kogyo (in Japanese), **2** (1946) 20.
(6) M. Tomura: Kagaku Butsuri (in Japanese), **2** (1950) 28.
(7) e. g. H. C. Torrey and C. A. Whitmer: "Crystal Rectifier", 88 Mc Graw-Hill Press, (1948).

On the Structure of Na_2O-SiO_2 Glasses.

By Ryosuke YOKOTA.

Matsuda Research Laboratory, Tokyo Shibaura Electric Co. Ltd. Kawasaki, Kanagawa.ken.

(Read Oct. 23, 1949; Received March 8, 1950)

§ 1. Introduction.

On the structure of Na_2O-SiO_2 glasses, the random network theory of B. E. Warren and his co-workers(1) is generally admitted. B. E. Warren and J. Biscoe(1) obtained a X-ray diffraction pattern of Na_2O-SiO_2 glasses and came to the conclusion as follows. The silicons and oxygens form a three dimensional random network in which each silicon is surrounded by 4 oxygens each at the corners of a tetrahedron. Some of the oxygens are bonded to 2 silicons and some to 1 silicon. There are holes in this random network in which the sodium atoms lie surrounded by about 6 oxygens, and with increasing Na_2O-SiO_2 content, the single bonded oxygens and holes increase continuously and uniformly.

But the curves of the physical properties, for example, density and refractive index (n_D) and the composition are always represented by some straight lines having breaks at definite compositions.

Therefore, it is clear that there is necessity of refinement of random uetwork theory of B. E. Warren. On the other hand, according to W. L. Bragg[2], silicate part of the structure in silicate crystals is a three dimensional network SiO_2; a sheet as in the mica group $(Si_2O_5)^{2-}$; a chain as in the amphiboles $(Si_4O_{11})^{2-}$ or in the pyroxenes $(SiO_3)^{2-}$ or a ring as in the beninoite $(Si_3O_9)^{2-}$. In 1940, M. L. Huggins(3) published a remarkable opinion that silicate glasses may have the similar arrangement of SiO_4 tetrahedra as the silicate crystals do.

§ 2. Analysis of X-Ray Diffraction Pattern of Na_2O-SiO_2 Glasses.

The author analysed the X-ray diffraction pattern obtained by B. E. Warren and J. Biscoe as follows; The compositions of the samples are represented by $(Na_2O)_x\ (SiO_2)_{1-x}$ and silicon-oxygen ratio (N_{Si}) is determined from

$$N_{Si} = (1-x)/(2-x)$$

and the curve of intensity of diffraction and N_{Si} is obtained by taking $\sin\theta/\lambda$ as a parameter. This is shown in Fig. 1.

In Fig. 1, the curves of $\sin\theta/\lambda = 0.1$, 0.2, 0.3, and 0.4 are seen to change discontinuously at the neighorhood of $N_{Si} = 0.435$ and 0.40.

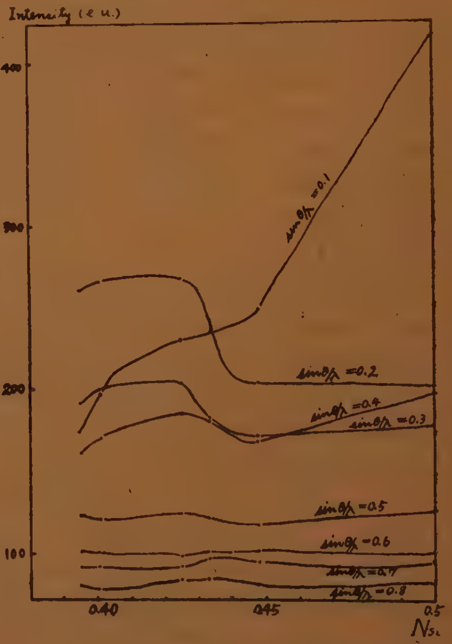

Fig. 1. Relation between X-ray diffraction intensity and N_{Si}, taking $\sin\theta/\lambda$ as a parameter.

At the intensity of diffraction at large diffracted angles has the tendency to approch the constant value independent of the compositions, the differences by composition for $\sin\theta/\lambda \geqq 0.5$ are negligibly small.

Next let us consider tne first peak of X-ray diffraction pattern. The position of the first peak of X-ray diffraction pattern of liquids is very distinguished and can be measured more accurately than the intensity of diffraction. Let us assume the X-ray diffraction patertns of liquid A 100% and liquid B 100% to be represented in Fig. 2 in the neighborhood of the first peaks.

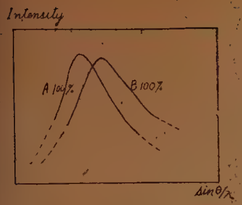

Fig. 2. X-ray intensity of diffraction of liquid A 100% and B 100%.

If liquid A and B do not associate each other and if the interaction of molecules of liquid A and B are considerably weak, an approximate additivity holds for the X-ray intensity of diffraction when liquid A ahd B are mixed in different proportions. In this case, if the mean half-width of the two peaks is w, and separation of the two maxima is s, the compounded curve of the two peaks has not two maxima but a single maximum when $s/w < 0.9$. Denote the values of $1/2 \sin\theta/\lambda$, corresponding to this single new maximum as [d], and plot [d] with x, and so we find the relation of [d] and x is linear. But when the mixed liquids associate, the relation of [d] and x is not linear. As the glass is considered a super-cooled liquid and X-ray diffraction pattern of glass resembles that of liquid, we can apply the above reasoning to the case of Na_2O-SiO_2 glasses.

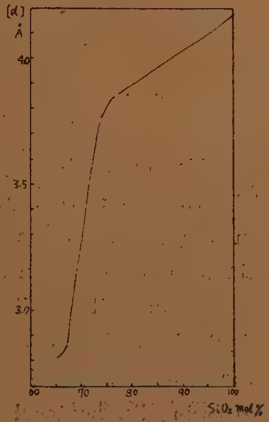

Fig. 3. Relation between [d] and SiO_2 mole %.

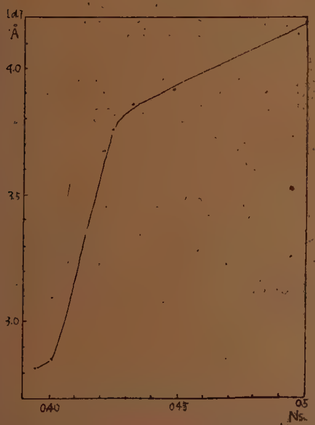

Fig. 4. Relation between [d] and N_{Si}.

Thus, Fig. 3 and 4 are obtained in order to represent the relations of [d] with SiO_2 mole percent and N_{Si} respectively.

From these figures, we can see that [d] deviates strongly from a straight line and the deviation is approximately represented by straight lines with the breaks in the neighborhood of $N_{Si} = 0.435$ and 0.40.

§ 3. Considerations from Viscosity.

H. R. Lillie[4] has measured the viscosity of Na_2O-SiO_2 glasses from 800°C and 1400°C with the concentric cylinder method. His results can be represented by the relation $\eta = C\exp(Q/RT)$ in which η is viscosity, C and Q are constants, and R is the gas constant. In the range from 1200°C and 1400°C ($\eta \approx 10^1 \sim 10^3$ poises) each curve of $\log\eta$ versus $1/T$ can be represented as a straight line completely. The relation of the activation energy and the composition (N_{Si}) is shown in Fig. 5.

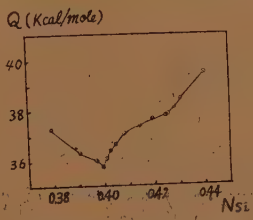

Fig. 5. Relation between activation energy and N_{Si} at high temperature.

In Fig. 5 there is a inflection point at the neighbourhood of $N_{Si} = 0.435$ and a sharp minimum at $N_{Si} = 0.40$. At high temperatures such as 1200°C~1400°C, Na-O bonds have already broken which bind the sheets of SiO_4 tetrahedra at $N_{Si} = 0.40$. This is the reason why there is a sharp minimum in activation energy at $N_{Si} \doteq 0.40$.

Next let us consider the viscosity of Na_2O-SiO_2 glasses at the annealing temperature measured by J. P. Poole.(5) The curve of the activation energy and the composition is shown in Fig. 6.

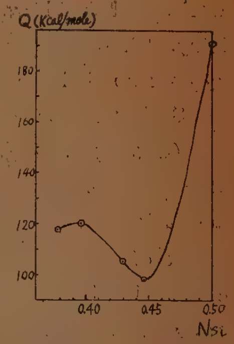

Fig. 6. Relation between activation energyand N_{Si} at the annealing temperature.

At the annealing temperture ($\eta \approx 10^{10} \sim 10^{14}$ poises) no Na-O bonds are broken and the large part of the activation energy is that of hole formation. Therefore the activation energy is related chiefly to the Si-O bond strength which changes with the configurations of SiO_4 tetrahedra. In Fig. 6 SiO_2 ($N_{Si} = 0.50$) has the extremely large activation energy owing to the there-dimensional network structure having the most stable and tight Si-O bond.

With the introduction of Na_2O the cristobalite-like structure of SiO_2 changes to the more compact structure having weaker Si-O bond. But at the neighbourhood of $N_{Si} = 0.40$ the configuration of SiO_4 tetrahedra becomes the sheets as in mica and Si-O bond strength is restored. This is the reason why there is a maximum in activation energy at $N_{Si} = 0.40$.

§ 4. Discussions and Conclusions.

As the X-ray diffraction pattern corresponds directly to the structure, the change of the X-ray diffraction pattern in Na_2O-SiO_2 glasses must be related to the structure change with the composition in these glasses. The breaks of $N_{Si} = 0.435$ and 0.40 which I found in X-ray diffraction pattern correspond to the compositions of $3Na_2O{\cdot}10SiO_2$ and $Na_2O{\cdot}2SiO_2$ respectively. From this fact, it may be interpretable that $3Na_2O{\cdot}10SiO_2$ $Na_2O{\cdot}2SiO_2$ and $Na_2O{\cdot}SiO_2$ are "compounds" and Na_2O-SiO_2 glasses are composed of mixtures of SiO_2 and $3Na_2O{\cdot}10SiO_2$ between $N_{Si} = 0.5$ and 0.435, and mixtures of $3Na_2O{\cdot}10SiO_2$ and $Na_2O{\cdot}2SiO_2$ between 0.435 and 0.40 and so on. But the concept of "compound"—discrete molecule of $Na_2O{\cdot}SiO_2$, $Na_2O{\cdot}2SiO_2$ and $3Na_2O{\cdot}10SiO_2$ — is ruled out because these are inconsistent with the well established laws of structural silicate chemistry. Therefore generally the "compound" theory does not hold the whole silicate glasses.

Seeing the curve of the specific volume and N_{Si} (Fig. 7.) of Na_2O-SiO_2 glasses from the data of Morey and Merwin(6) and the curves of the activation energy and N_{Si} (Fig. 5 and 6), the break of $N_{Si} = 0.435$ can be regarded that the cristobalite-like structure of SiO_2 having many holes and therefore high specific volume, changes partially to the more compact structure by the introduction of Na_2O and this change saturates at $N_{Si} = 0.435$ and that the SiO_4 tetrahedra are approximately in a cloce-packed arrangement below $N_{Si} = 0.435$ and some of them are more loosely packed above $N_{Si} = 0.435$.

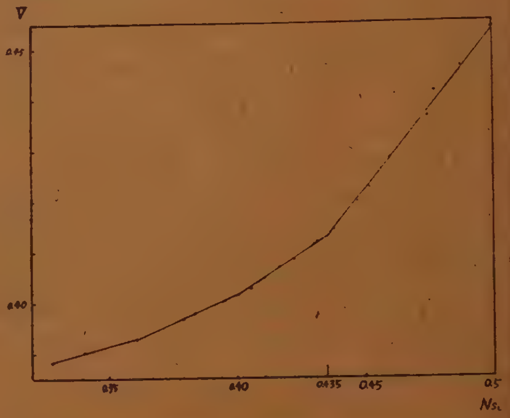

Fig. 7. Relation between the specific volume and N_{Si}.

Also in K_2O-SiO_2 glasses and Na_2O-CaO-SiO_2 glasses the curves of the density and refractive index (n_D) with the composition have breaks at the same composition as in Na_2O-SiO_2 glasses.

Because all the silicate crystals have the configurations of SiO_4 tetrahedra above mentioned, the same configurations of SiO_4 tetrahedra must exist in all silicate glasses.

References.

(1) B. E. Warren and H. Krutter: J. Amer. Ceram. Soc. **19**. (1936) 202; J. Biscoe and B. E. Warren ibid. **21**. (1938) 259.
(2) W. L. Bragg, Atomic Structure of Minerals, Ithaca, New York, Cornell University press 1937.
(3) M. L. Huggins: J. Amer Ceram. Soc. **26**, (1942) 4; J. Opt. Soc. Amer. **30**, (1940) 420.
(4) H. R. Lillie: J. Amer. Ceram. Soc. **23**, (1939) 367.
(5) J. P. Poole: J. Amer. Ceram. Soc. **32**, (1949) 215.
(6) G. W. Morey and H. E. Merwin: J. Opt. Soc. Amer. **22**, (1932) 632.

Probe Measurements for High Frequency Discharge II.

By Shoji Kojima and Kazuo Takayama.

Tokyo University of Literature and Science.

(Received March 20, 1950)

We have been studying electron temperatures of high frequency discharges by means of a double-probe method.(1) Recently Johnson and Malter reported a new method.(2) Though the two methods use same characters of a double-probe the deductions of electron temperature are based on different idea. Then we have tried to compared them.

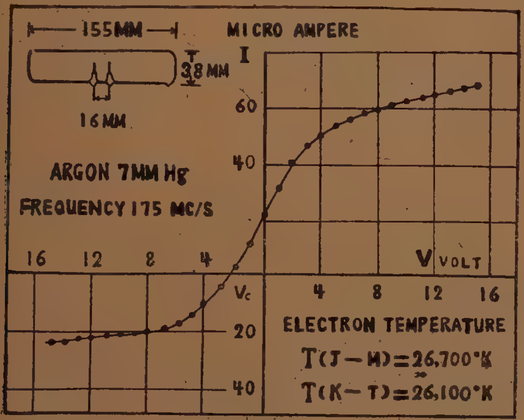

Fig. 1.

A typical characteristic curve of double-probe current I *vs,* its voltage V is shown in Fig. 1. In high frequency discharges the curves have same type when the probes are set in neutral position of the field as mentioned in the previous paper. This fact enables to use probe methods in high frequency plasma as direct current.

Johnson and Malter obtained the following formula for a same area double-probe in direct current plasma:

$$\frac{I_1-I}{I_2-I}=\frac{I_2}{I_2}\exp\left[\frac{e(V_c-V)}{kT}\right] \qquad (1)$$

where T is electron temperature, e electronic charge, k Boltzmann's constant, I_1 and I_2 are saturation current of probe 1 and 2. V_c is the voltage when double-probe current I vanishes. From semi-logarithmic plots of (1), electron temperatures are determined. In our method the voltage V_c is used. Considering origin of this voltage it is concluded that this rises from the difference of the electron density at the pair of probes. From the fact that this voltage is the potential difference needed to prevent the diffusion of electrons following formula is deduced:

$$V_c=-\frac{kT}{e}\ln\frac{I_2}{I_1} \qquad (2)$$

provided that electron densities are proportional to saturation currents and that mobilities of ions are much smaller than electrons. We can determine electron temperature by the measurements of I_1, I_2 and V_c with the aid of formula (2).

First we have derived the electron temperature from the curve shown in Fig. 1 by these two methods. The result by Johnson-Malter's method gives 26,700°K and by our method it is obtained 26,100°K. The agreement is excellent. Some other results are shown in Table I. In these cases one plasma is measured at three different probe positions i.e. at the middle of plasma, near its periphery and at a intermiate position. The table contains saturation currents which may be used as the indication of the field strength. The value obtained by our method agree with Johnson and Malter's one except high intensity discharges where V_c comes not only from diffusion of electrons but also from some other sources.(1)

Above results also indicate for the nature of high frequency discharges that the electron temperature at any point in a plasma is same and that the electron temperature rise is rather small compared with the increase of the density of plasma.

Table I.

Probe position		Weak discharge	Medium discharge	Strong discharge
Middle	I_1	22 μA	34 μA	54 μA
	I_2	4.5 μA	30.5 μA	53 μA
	V_c	31.5 V	0.25 V	0.07 V
	T(J-M)	23,200 °K	25,200 °K	26,700 °K
	T(K-T)	22,800 °K	25,500 °K	45,000 °K
Intermediate	I_1	18 μA	34 μA	54 μA
	I_2	3.5 μA	21.5 μA	52 μA
	V_c	3.35 V	1.0 V	0.15 V
	T(J-M)	23,700 °K	26,200 °K	28,200 °K
	T(K-T)	23,600 °K	25,000 °K	45,700 °K
Periphery	I_1	17 μA	32 μA	56 μA
	I_2	1.8 μA	12.5 μA	46.5 μA
	V_c	4.0 V	2.2 V	0.8 V
	T(J-M)	23,200 °K	27,200 °K	26,700 °K
	T(K-T)	20,400 °K	27,000 °K	49,400 °K

References.

(1) S. Kojima and K. Takayama, Jour. Phys. Soc. Japan **4** (1949) 349.
(2) K. O. Johnson and L. Malter, Phys. Rev. **76** (1949) 14 1.

On the Magnetic After Effect due to the Irreversible Displacement of Domain Boundary (I).*

By Seijiro MAEDA.

Physics Department, Faculty of Science. Tohoku University.

(Read Apr. 1949; Received April 10, 1950)

§ 1. Introduction.

Various types of magnetic after effect have been reported(1) since Ewing(2) first pointed out that sudden changes of magnetization in ferromagnetic substances accompanies a strong magnetic after effect. However, no comprehensive discussions have been published concerning the manifold behaviors of this phenomenon. The author has studied(3) this effect in a wide range of magnetic fields with special reference to the irreversible boundary displacement of the ferromagnetic substance, and has been able to ascertain several points regarding the significance of the irreversible process over the magnetic after effect. The results obtained diverge widely from the investigations of Richter.(4) In the following pages are described the methods and results of measurement on the transient behavior of the said after effect of a Cr-permalloy, and a discussion on the mechanism of magnetic after effect is then given, based upon the results obtained.

---

* This investigation was financed in part by the Grant-in-Aid of Fundamental Scientific Researches of the Ministry of Education for 1949. Item #D392, "On the Magnetic After Effect of the Iron Alloys".

§ 2. Experimental Arrangements and Specimen.

If the magnetic field H_i under which the specimen is magnetized to induction B_i changes suddenly to the field H_f, then the magnetization is instantly brought to the value B_f' and thereafter changes slowly till it reaches the final state B_f. This slow change of magnetization is called a magnetic after effect. For the purpose of measuring the slow change of magnetization, a search coil was wound on the specimen and connected to a ballistic galvanometer (period; 22 seconds). If the galvanometer circuit is closed at time t, shortly after the change of the magnetizing field, and should deflectons of the galvanometer be recorded for various values of t, these deflections would correspond to the total change of magnetic induction B during the lapse of time from t to ∞, practically so long as the decaying period of the after effect is shorter than the quarter period of the ballistic galvanometer. The magnetizing coil used is 120 *cm* long and 15 *cm* in diameter, and has a coil constant of 15 *Oe/Amp*, the search coil is 3 *cm* long and 1.5 *mm* in diameter, with a total of 5000 turns, the circuit of the ballistic galvanometer has a magnetic sensibility 0.010 *gauss* per deflection of 1 *mm*. A special mechanical time switch was devised in order to close the circuit after the lapse of time t from the moment of field change.

Special considerations should be given to two point with regard to the apparent magnetic retardations accompanying a change of the magnetic field. One is the retardation due to inductance L and resistance R in the circuit of the magnetizing coil and the other is the retardation due to the eddy current in the specimen caused by a sudden change of the magnetization. However, as $R = 100\,\Omega$ and $L = 2\,mH$ in our case, the relaxation constant $2L/R$ of the former is of the order of 10^{-5} seconds, which has no effect on our measurements. The relaxation time in the latter case is given by the Rayleigh's formula $\tau = 4\pi r \rho \mu / 5.78$ on the assumption that permeability is approximately independent of the magnetic field in the region in consideration; here ρ is the specific electrical resistance and r is the radius of the cylindrical specimen; therefore for $r = 0.06\,cm$, and for the specimen described in the next paragraph, (at room temperature $\rho = 7.6 \times 10^{-5}\,\Omega\,cm$ and maximum permeability $\mu = 15{,}700$) the value of calculated τ is of the order of 10^{-4} seconds which is negligible in our measurement. It is also observed that, the characteristic properties of the after effect are not affected by the change of measuring conditions due to the change of the resistance in the circuit of the magnetizing coil and cross sectional area of the specimen used.

The specimen in question is a wire of Cr-permalloy (Ni 85%; Cr 4.1% Ti 0.6%; balance Fe), the length and diameter of which are 60 *cm* and 1.2 *mm.* respectively. After being annealed at 950°*C* for 5 hrs in a dry hydrogen atmosphere and coolled in the furnace, its magnetic hysteresis curve at 25°*C* is as shown in Fig. 2.

§ 3. The Dependency of the Magnetic after Effect on the Magnetizing Field.

The total amount of the slow change of magnetization $B_n(t)$ following the elapse of t seconds after the decrease of magnetic field $H_i \rightarrow H_f$ is measured for each value of t by means of the measuring process mentioned above. Several results of such measurement are given in Fig. 1. In which the relations between $B_n(t)$ and t for various values of H_f are given. As it shows, the relation between $\log B_n(t)$ and $\log t$ is expressed by a linear equation

$$\log B_n(t) = C - \log t \tag{1}$$

for various values of H_f. It is worth noticing that all the curves have a common inclination which value is minus unity; alternatively speaking $B_n(t)$ is inversely proportional to t, namely

$$B_n(t) = B_{n0}\, t_0 / t \tag{2}$$

where B_{n0} is the amount of the total change of magnetization during the period from $t_0 = 1/100$ seconds after the instant of the breaking of the

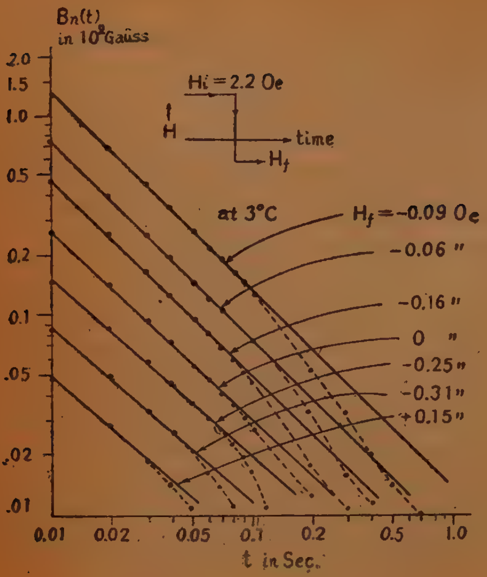

Fig. 1. Decaying characters of after effect. Mode of field change is shown in upper.

magnetizing circuit to the time at which the change of magnetization practically finishes. Hereafter B_{no} is chosen as a parameter representing the amount of magnetic after effect. This relation diverges widely from Richter's⁽⁴⁾ results, which were obtained from static measurements on the magnetic after effect of carbonyl-iron, and which propounded that the decaying character could be described by the relationship, $B_n(t) \propto \log t$, for a wide range of t. Further, Richter thought that the after effect strongly depended on the duration time ϑ of the initially applied magnetizing field, but in our measurements the dependency on ϑ is not observed so long as ϑ is longer than 1/100 second. Consequently, in our measurement ϑ is choosen as 10 seconds.**

Next, let us describe the relation between the after effect B_{no} and the parameter H_f. In Fig. 2 the value of B_{no} is shown as a function of H_f. As can be seen from it, the after effect is not observed in the range of H_f which lies between the saturation field H_s and 0.35 Oe. As the hysteresis curve of our specimen shows, the change of magnetization in this region is mainly

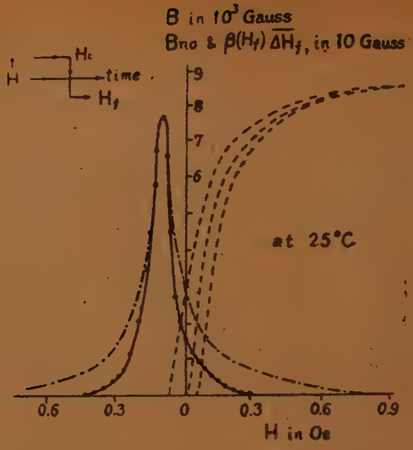

Fig. 2. ———————— B_{no} vs H_f curve.
– – – – – – – – B—H curve.
·—·—·—·— $\beta(H_f)\overline{\Delta H_f}$ vs H_f curve.

due to the rotation of spontaneous magnetization and irreversible displacement scarcely contributes to it. The change of magnetization in this region should be so rapidly performed, as to assume that after effect will obviously not occur therein. By further decreasing H_f beyond this region, the after effect first appears and B_{no} shows a maximum when H_f reaches the value −0.09 Oe at 25°C; this value of H_f coincides exactly with the position of the maximum value of $|dB/dH|$ in the descending branch of the hysteresis loop. With continued decrease of the final magnetic field H_f, the after effect again decreases, and in the region of magnetic field of less than say 0.43 Oe., the after effect finally disappears. Now it is to be noted that the after effect does not depend on the method of changing the field, and is dependent only on the values of initial and final fields. Provided that the field is not changed instantaneously to the final field H_f but is made to rest for a certain time interval at an intermediate field H_m and is then suddenly changed to the field H_f, no change on the mode of after effect is observed. Fig. 3 shows the after effect in such a case. In the figure, $B_n(t)$ vs t curves are given for various values of the intermediate field H_m. As can be seen from the figure the curves obtained for various H_m are all identical.

Next, measurements analogous to above are carried out for various initial field H_i,

---

** It is to be noticed that if ϑ is less than 10^{-3} seconds, the effect of the former field can be observed, a detailed description will be published later.

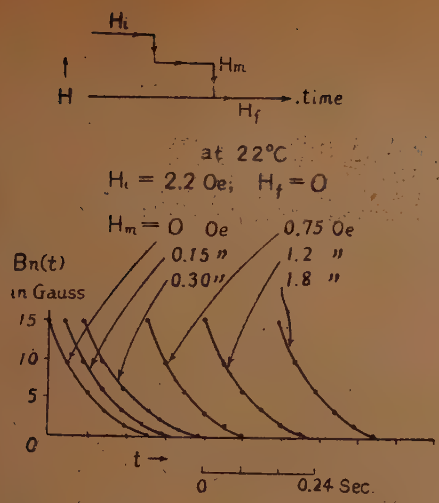

Fig. 3. Effect of intermediate field H_m; Decaying characters for various H_m are shown respectively.

the results being shown in Fig. 4. The upper curves in Fig. 4, show the hysteresis-loops for various maximum fields H_i, the lower curves in the same figure showing the relation between B_{no} and H_f in the after effect, referred to the various hysteresis loops shown in the upper curves. As can be seen from the lower curves in Fig. 4, the relation between B_{no} and H_f is similar, on the whole, to the case in which H_i corresponds to the saturation field, as was shown in Fig. 2, yet the position of the maximum value of B_{no} displaces in the direction of smaller H_f when H_i is decreasing. In the case where H_i, is smaller than 0.18 *Oe*, a maximum value of B_{no} does not appear and B_{no} attains the largest value when the magnetic field H_i changes to $H_f = -|H_i|$, this character corresponds to that of $|dB/dH|$ calculated from the measured hysteresis loop. With further decrease of H_i, the amount of after effect gradually diminishes and finally disappears. The area of the hysteresis loop also gradually diminishes and finally approaches zero. It is to be noted that the region in hysteresis loop and the range in which the after effect disappears coincide perfectly with each other. Fig. 5 shows the $B_{no}-H_f$ curves of after effect which accompany field changes $H_i \to -|H_i|$ (curve II) and $H_i \to 0$ (curve I) in a transitional region from the reversible to the irreversible magnetization, that is, Rayleigh's region; for the sake of reference the $B-H$ and B_r-H curves also shown in the same figure. As can be seen from the figure, the residual magnetization and after effect are first observed as soon as H_i exceeds this reversible region of magnetization, that is, when the irreversible process begins to occur, and in such a region B_{no} increases almost proportionaly to B_r. The curve I in Fig. 6 shows B_{no} in relation to the change of magnetization from the demagnetized state to any point

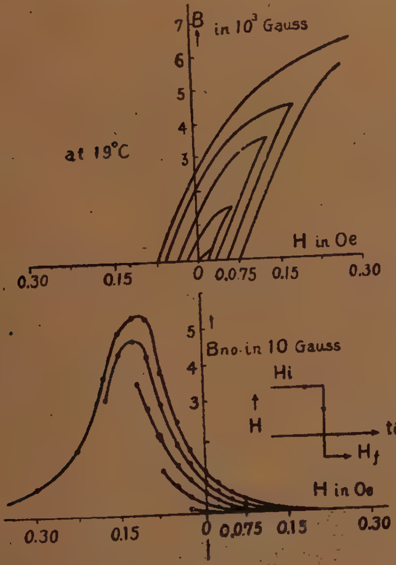

Fig. 4. upper. $B-H$ curve
lower; B_{no} *vs* H_f curves for various initial fields H_i.

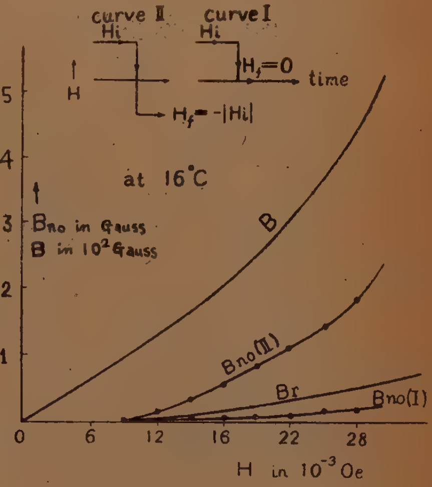

Fig. 5. $B-H$ Curve, B_r-H Curve and after effect in Rayleigh's region.

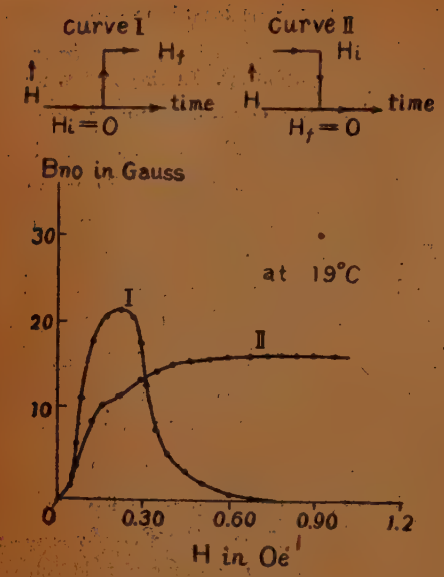

Fig. 6. B_{no} curves for various H_i or H_f.

on the virgin curve of magnetization. In this case also maximum after effect appears at a point in which the irreversible displacement of the domain boundary occurs most frequently, and in the upper region of the magnetization curve the after effect decreases again and finally vanishes when H_f is brought to the rotational region. Curve II in Fig. 6, shows B_{no} in the case of $H_f = 0$, for various values of H_i ranging from zero to saturation field, in this case B_{no} increases at first rapidly with H_i and finally reaches a nearly constant value for H_i in the region of continuous rotation. These facts also suggest that the observed after effect is mainly caused by the irreversible displacement of the domain boundary and that the rotational process of spontaneous magnetization does not contribute to it.

§ 4. Discussion on the Experimental Results.

It has been confirmed from experimental results of large Barkhausen effects that when the external field becomes larger than a certain critical field H_0, a 180° domain boundary commences to displace; that if the boundary displaces without changing its form, displacement velocity v is expressed(5) by

$$V = a(H_f - H_0). \tag{3}$$

where a is a constant. In general cases, however, the form of the boundary changes with displacement of the boundary itself, and consequently the displacement of the boundary in the actual magnetization process is not so simple as mentioned above. However, in this case, the relation between displacement velocity and the magnetic field will be expressed in form by a type of equation similer to the above, if we assume that these factors are absorbed in H_0, and we take $H_0(r)$ as a function of the location r of the domain boundary. Moreover, in the ferromagnetic substance, the local magnetic field $H_i(r)$ due to the free magnetism of other domain boundaries do exist, and this field must be added to the external magnetizing field H_f in the velocity formula, thus,

$$V = a[H_f + H_i(r) - H_0(r)] \tag{4}$$

No serious error will be introduced if one assumes that an analogous formula also hold for the case of the 90° domain boundary. Now, the critical field strength changes from point to point in the medium, and the values of H_0 take its maximum values at various point in the same medium. If the difference $H_f + H_i$ over the peak values of $H_0(r)$ is very small at certain special regions of the ferromagnetic material the displacement velocity of the boundary will assume a very small value when the boundary is passing over this region. The said distribution of $H_0(r)$ at such a region is schematically expressed in Fig. 7 though the actual distribution of $H_0(r)$ might be expressed by something like the dotted curve. But for the sake of brevity it is supposed that the distribution is expressed by the full curve. The critical field H_0 takes its highest value H_{om} in the region AB and it is supposed that $H_f + H_i - H_{om}$ assumes a very small value. If after passing AB the boundary reaches a region CD of a smaller H_0 value, the boundary commences a rapid displacement from the first. Consequently, in such a case, if the magnetic field changes suddenly from H_i to H_f, a comparatively long time is required for the change of magnetization, due to the slow displacement in

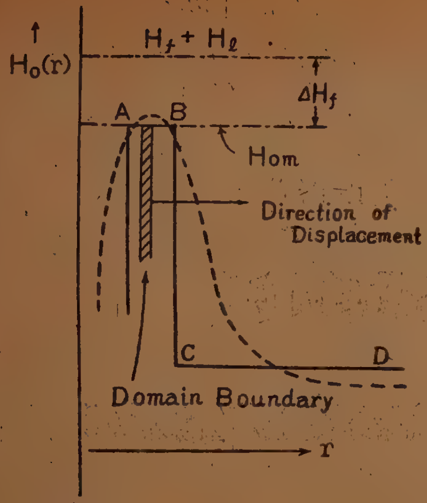

Fig. 7. Schematic $H_0(r)$ curve.

this region *AB*.*** Further, we suppose that such regions are found everywhere in the substance, and the superposition of these retardations of magnetization are observed as an after effect in the present measurement. Viewed from this standpoint, the time required for the processes depends both on the values of $H_f+H_l-H_{om}$ and the size of the range in which $H_f+H_l-H_{om}$ assumes a very small value. But in the following discussion, for the sake of brevity, the ranges are assumed to be of the same value as *D*, and that boundary always starts from the end of the region *AB*. The main change of magnetization also is assumed to occure from the discontinuous parts *CD*, and the small effect of the continuous change due to the parts *AB* is neglected.

We must now consider the decaying form of the after effect. For the domain boundary at which slow displacement is completed and where rapid displacement commences at time *t*, under the action of final field H_f+H_l, the value of H_{om} must be given by the relation (4), namely

$$D/v = D/[a(H_f+H_l-H_{om})] = t \qquad (5)$$

consequently, for the domain boundaries which complete its slow displacement between *t* and $t+dt$, the value of H_{om} lies between

$$H_{om} \text{ and } H_{om}+(dH_{om}/dt)dt$$
$$= H_{om}+[a(H_f+H_l-H_{om})^2/D]\,dt$$

The number of such domain boundaries ndt which complete their displacement during this small time interval is proportional to $(dH_{om}/dt)dt$, hence

$$ndt = k(H_{om}/dt)\,dt$$
$$= k[a(H_f+H_l-H_{om})^2/D]\,dt = kD/(at^2)dt^{****} \qquad (6)$$

Here *k* is a constant. If all the domain boundaries give the same amount of induction change b_n due to the rapid displacement, $B_n(t)$ can be expressed by the equation.

$$B_n(t) = k\,b_n\,D/a\int_t^\infty t^{-2}dt \text{ or } B_n(t) = K/t \qquad (7)$$

Here *K* is a constant, and from experimental results (eq. (2)) it should be identified as $B_{no}t_o$. Hence we obtain finally

$$\log B_n(t) = \text{const}-\log t \qquad (8)$$

According to this consideration, $B_n(t)$ takes a similar decaying form for different values of both H_i and H_f: a linear relation with a common inclination minus unity holds between $\log B_n(t)$ and $\log t$. These results coincide well with the experimental results shown in Fig. 2. However, in the region of relatively larger values of *t*, the coincidence is not so good; for the measured curve, $\log B_n(t)$ *vs* $\log t$, shows a larger inclination than the expected value minus unity.

Next, we should consider the dependency of the amount of after effect on the final field H_f from the viewpoint mentioned above. The parameter B_{no} represents the change of induction during the period from 1/100 seconds after the change of field to the time at which the after effect practically finishes. Hence, if we denote the small difference $H_f+H_l-H_{om}$ by ΔH_f, then after 1/100 seconds from the instant of change of the field, the domain boundary, for which the difference $\overline{\Delta H_f}$ takes a definite value, expressed by

---

*** T. Fujimura's[7] recent studies "on the Barkhausen jumps in the course of magnetic after effect" with specimens of Cr-permally and magnetite support our view that such a slow displacement of domain boundary does definitely occur in a ferromagnetic substance.

**** The equation (6) does not hold when *t* approaches zero because at $t=0$ dH_{om}/dt assumes the value infinity, and at this singular point the width $(dH_{om}/dt)dt$ does not represent the actual breadth.

$$1/100 = D/(a\overline{\Delta H}_f) \quad \text{or} \quad \overline{\Delta H}_f = 100D/a \qquad (9)$$

makes a sudden displacement. Then, subsequent displacements of the domain boundary, for which the values of ΔH_f are less than $\overline{\Delta H}_f$, occur in succession finally ending at the boundary for which H_{om} coincides with $H_f + H_i$. Consequently B_{no} be equal to the change of magnetic induction due to the whole of the sudden displacement of the domain boundaries for which H_{om} takes a value between $H_f + H_i$ and $H_f + H_i + \overline{\Delta H}_f$. In other words if we denote by $\beta(H_f)\overline{\Delta H}_f$ the total change of induction B by sudden displacements of the domain boundaries during the change of the magnetizing field $H_f \rightarrow H_f + \Delta H_f$, then B_{no} is determined by the total change of magnetization due to the subsequent Barkhausen jumps which follow the slow displacement of the total domain boundaries mentioned above, for which the highest value H_{om} of the critidal field H_o lies in the range from $H_f + H_i$ to $H_f + H_i + \overline{\Delta H}_f$ for the definite value of $\overline{\Delta H}_f$ which is determined by the relation*****

$$t_o = D/(a\overline{\Delta H}_f) \quad \text{or} \quad \overline{\Delta H}_f = D/(at_o) \qquad (10)$$

Now from the above considerations B_{no} should be equal to $\beta(H_f) \times \overline{\Delta H}_f$, that is

$$B_{no} = \beta(H_f) \times \overline{\Delta H}_f \quad \text{or} \quad B_{no} = \beta(H_f)D/(at_o) \qquad (11)$$

as $\overline{\Delta H}_f$ is independent of H_f; B_{no} is proportional to $\beta(H_f)$, which depends only on the final field H_f. Consequently, it would now be required to find the form of $\beta(H_f)$. During the course of the actual magnetization process, its change is caused by the reversible and irreversible displacements of the domain boundary, as well as by the continuous rotation of Spontaneous magnetization. But in the present case, we are considering the region of magnetization curve in which the irreversible displacement of the domain boundary plays a leading part in the change of magnetization, hence it would be possible to assume that the change of induction ΔB due to the change of the magnetizing field ΔH_f along the descending branch of the hysteresis curve is expressed by $\beta(H_f) \times \Delta H_f$, that is,

$$\beta(H_f) = |\Delta B/\Delta H| \qquad (12)$$

The value of $\overline{\Delta H}_f$ in eq. (10) can be determined, based on the value of $\beta(H_f)$ thus obtained. As seen from Fig. 2 the value of $\beta(H_f)$ at the steepest point of the descending branch of the hysteresis loop is 6.3×10^4 *gauss/Oe*, while the value of B_{no} for the corresponding value of H_f is 78 *gauss* at 25°*C*. The value of $\overline{\Delta H}_f$ is once for all determined by

$$\Delta H_f = (78/6.3) \times 10^{-4} = 1.2 \times 10^{-3}\ Oe$$

Hence, from $\beta(H_f)$ B_{no} can be calculated by being multiplyied by $\overline{\Delta H}_f = 1.2 \times 10^{-3}\ Oe$. Calculated values of B_{no} as a function of the final field H_f have of course the same form as $\beta(H_f)$. Comparison with experimental results are shown in Fig. 2, where the position of the maximum values and the orders of magnitude of $\beta(H_f)\overline{\Delta H}_f$ coincide well with that of the measured after effect. Therefore, we finally obtain an expression for the after effect due to the irreversible displacement of the domain boundary, is, then,

$$B_n(t) = \beta(H_f)\overline{\Delta H}_f t_o/t \quad \text{or} \quad B_n(t) = |\Delta B/\Delta H|\,\overline{\Delta H}_f t_o/t \qquad (13)$$

The experimental results in Fig. 3 were to be expected from the above consideration; as $\beta(H_f)$ only depend on H_f, the after effect depends only on the final field H_f, and the effect of stopping its magnetization at an intermediate field H_m is not observed when the initial state maintains constancy and provided that the difference $H_f - H_m$ greater than $\overline{\Delta H}_f$.

The author wishes to acknowledge his thanks to Prof. T. Hirone who supervised the present work.

References.

(1) See, for example; R. Becker & W. Döring: Ferromagnetismus, Berlin, (1939) p. 242.

(2) J.A. Ewing: Phil. Trans. Roy. Soc., Lond. Vol. **176** (1885).

(3) S. Maeda: Nippon Butsurigakkaishi Vol **4**, No. **1** (1949) p. 5 (Published by the Phys. Soc. Japan, in Japanese.

(4) G. Richter: Ann. Phys., Lpz. Bd. Vol. **29** (1937), p. 605.

(5) J.G. Snoek: Physica. Haag, Vol. **8** (1939), p. 663.

(6) K.J. Sixtus & L. Tonks: Phys. Rev., Vol. **42** (1932), p. 419.

(7) To be published shortly in J. Phys. Soc., Japan.

***** According to the equation (10) $\overline{\Delta H}_f$ assumes a very large value for exceedingly small value of t_o and for such a case, the following consideration does not hold true.

On the Young's Moduli and the Internal Friction of Papers.

By Heiji KAWAI and Noboru TOKITA.

Kobayashi Institute of Physical Research, Kokubunji, Tokyo.

(Received April 18, 1950)

§ 1. Introduction.

The vibrational properties of papers have serious effects upon the characters of loud speakers and acoustical instruments which have the paper diaphragms. Therefore the measurements of the Young's moduli and the internal friction of papers are important in practical use.

Using the new dynamical method which was reported in the previous paper(1) by the authors, the Young's moduli and the internal friction of papers have been studied at the various conditions.

They are affected by the various conditions, for example, the freeness, the frequency of vibration, the humidity and the amplitude of vibration. In this paper we will report the experimental results and the models of internal friction.

§ 2. Measuring Method.

In the region 200—2000 *c.p.s*, the method reported in the previous paper(1) has been used. In the region 30 *kc*—200 *kc*, the method was adopted by which Nolle, Ballou, Witte and co-workers has measured the vibrational properties of rubber and some high-polymers.(2)(3)(4)(5)

The dimensions of samples in the region 200—2000 *c.p.s.* and in the region 30—200 *kc* are the small rectangular ribbons (about 4 *mm* width, 25 *mm* length) and the long one (about 3 *mm* width and 1000 *mm* length) respectively.

The samples are composed of the various kinds of fibers, for example, sulphite-pulp (*S.P.*), cotton, bamboo, wool and a papermulberry (Japanese name, *Kôzo*).

Table I.

Experimental resutls of various papers at 780 *c.p.s.*

Sample	$E\times10^9$ dyne/cm^2	$\dfrac{\Delta W}{2\pi W}\times10^{-2}$	$d\times10^{-2}$cm	ρ
S.P. (Pressed) fr, 400	47.5	2.9	2.4	0.43
,, fr, 500	23.0	2.9	3.2	0.35
,, fr, 600	18.0	3.6	2.5	0.46
,, fr, 800	8.5	4.3	4.0	0.46
S.P. (//-Roll)	43.0	3.7	0.65	0.77
S.P. (⊥ Roll)	22.0	4.5	0.65	0.77
S.P. (not Pressed)	10.0	3.8	0.70	
Bamboo (,,)	6.3	3.2	3.5	0.28
Craft (,,)	11.5	5.0	3.0	0.40
Cotton (,,)	8.7	7.0	3.9	0.48
Wool 50% S.P. 50%	0.7	5.7	3.1	0.38
Wool-fiber	65.5		diameter 0.38	
Kôzo 100%	4.0	5.4	4.3	

§ 3. Experimental Results.

A part of the experimental results is shown in Table (I), where ΔW, W are the energy dissipated during one cycle and the vibrational energy, respectively and the relationship between Q^{-1} and $\frac{\Delta W}{2\pi W}$ is

$$Q^{-1} = \frac{1}{2\pi}\log\left(1-\frac{\Delta W}{W}\right),$$

and $\frac{\Delta W}{W}$ being smaller than 1

$$Q^{-1} \fallingdotseq \frac{1}{2\pi}\frac{\Delta W}{W}.$$

(1) The effect of freeness.

The Young's moduli and the internal friction of papers which are composed of the same kind of fiber are affected by the freeness (proporting to the reciprocal of beating degree)⁽⁶⁾. Fig. 1 shows the results of freeness dependence of *S.P.* papers. In general, as the freeness increases, the Young's modulus decrease and the internal friction increases.

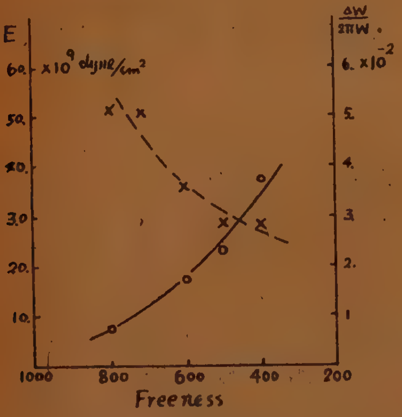

Fig. 1. Freeness dependence for *S. P.* papers.

(2) The effect of frequency.

Fig. 2 shows the result of frequency dependence of the Young's modulus and the internal friction for the *S.P* 100% paper. The fibers of this paper are short (below 0.1 mm) and combined tightly with each other. Fig. 3 shows the result of the paper composed of wool 50% and *S. P.* 50%, whose fibers are long (about 10 *mm*) and combined loosely with each other.

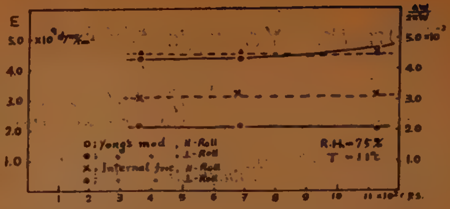

Fig. 2. Frequency dependence for *S. P.* 100% paper.

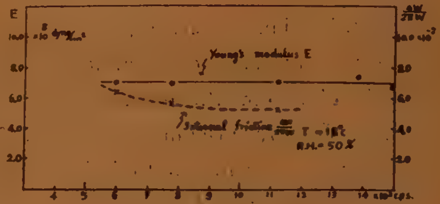

Fig. 3. Frequency dependence for wool 50%, *S. P.* 50% paper.

In general, in the region 200—2000 *c.p.s.* the Young moduli and the internal friction are constant at each temperature and humidity. Fig. 4 shows internal friction for two different *S. P.* papers in the region 30—200 *kc.*

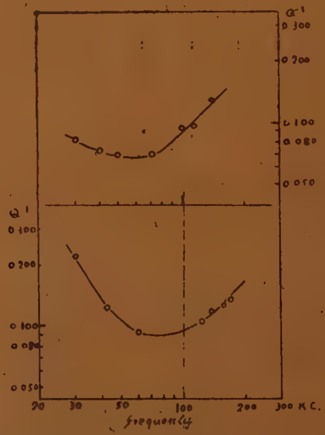

Fig. 4. Internal friction Q^{-1} *vs.* frequency for *S. P.* paper in the region 30—200 *kc.*

Above 100 *kc*, Q^{-1} increases lineally as the frequencies. Below 100 *kc*, however, it is found that Q^{-1} shifts from this straight line.

Though we think that there may be a dispersion in the vicinity of 10 *kc*, the measurement of this region has not been yet carried out on account of the difficulty of measuring.

We infer that the behaviour above 100 *kc* depends upon the property of cellulose fiber itself.

(3) The effect of humidity.

The mechanical properties of papers are sensitive to the humidity. The relative humidity (hereafter written *R. H.* in short) was varied at will by alterning the concentration of H_2SO_4 in the case.

First the measurement was done from *R. H.* 0% to *R. H.* 100%, next inversely it was done from *R. H.* 100% to *R. H.* 0%. They were repeated twice or three times at each sample and these results were reproducible. Fig. 5 is the result for the *S. P.* 100% paper.

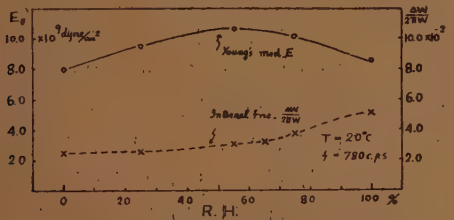

Fig. 5. Humidity dependence for *S. P.* 100% paper at 780 *c.p.s.*

It is interesting that the Young's modulus of this paper has the maximum value in the vicinity of *R. H.* 55%. We think that it may be due to to the cellulose property of *S. P*, as Wakenam and co-workers reported that the Young's modulus of cellulose fiber has the greatest value in the vicinity of 4—5% moisture contents⑺. In Fig. 6, the result for paper composed of wool 50% and *S. P.* 50% is shown. The Young's modulus increases with *R. H.* and has not a maximum value. It may be thought that the maximum value of *S. P.* paper disappear on account of the large effect for humidty of wool fiber.

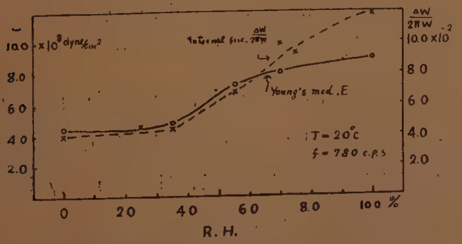

Fig. 6. Humidity depence for wool 50% paper at 780 *c.p.s.*

(4) The effect of amplitude of vibration.

We measured the effects of amplitude for two typical samples which was reported in the previous section §3 (2), namely one is the *S. P.* 100% paper and the other is the wool 50% paper.

Fig. 7 shows the plots of internal friction *versus* amplitude of vibration. They have been measured by the aid of a microscope. As the results of measurements, we obtained two typical curves. One is the curve for the wool 50% paper, that the internal friction increases rapidly with the amplitude in first and has the maximum value at some amplitude and then decreases gradually. The other is the curve for the *S. P.* 100% paper, that the internal friction is independent upon the amplitude. The Young's moduli, however, are independent upon the amplitude for both cases.

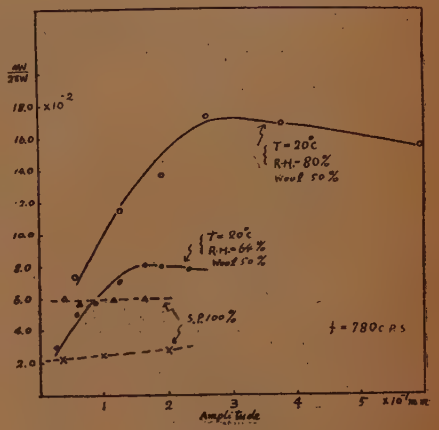

Fig. 7. Internal friction $\varDelta W/2\pi W$ *vs.* amplitude of vibration for *S. P.* 100% and wool 50% papers at 780 *c.p.s.*

§4. On the Mechanism of Internal Friction.

(1) The case in whicn it depends on the amplitude.

As an explanation of visco-elastic behaviour, the Voigt model has been adopted that in the simplest case consists of a purely elastic element or spring and a purely viscous one or dash-pot whose viscosity causes the internal friction.

In the paper whose fibers are combined loosely with each other, for example, as the wool 50% paper, it may be considered that the kinetic friction of the binding portions causes the internal friction. As the paper is a kind of visco-elastic material, we devised a kind of Voigt model as shown in Fig. 8 where instead of a dash-pot, the mechanism of kinetic friction was considered. In Fig. 8, K_1, K_2 are the elastic constants of springs, F is the kinetic frictional force that is constant in slipping, l is the slipping distance of the end of spring (2) against this kinetic frictional force at any elongation x. When this model is elongated by x, the potential energy stored in springs (1) and (2) are

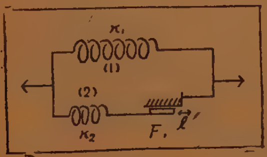

Fig. 8. A visco-elastic model for papers.

$$W_1 = 1/2.\kappa_1 . x^2, \tag{1}$$

$$W_2 = 1/2.\kappa_2 \cdot (x-l)^2, \tag{2}$$

respectively, and the energy dissipated during this motion is

$$\varDelta W = F \cdot l. \tag{3}$$

As the frictional force F is dynamically balanced to the elastic force of spring (2), the following relation is obtained

$$F = \kappa_2 \cdot (x-l). \tag{4}$$

If $\frac{2\pi W}{\varDelta W}$ is used as a measure of the internal friction, from eq. (1) (2) (3) and (4)

$$2\pi \frac{W_1 + W_2}{\varDelta W} = \pi \left(\frac{\kappa_1 \cdot x^2}{F \cdot \left(x - \frac{F}{\kappa_2}\right)} + \frac{F}{\kappa_2 \cdot \left(x - \frac{F}{\kappa_2}\right)} \right). \tag{5}$$

In eq. (5) the first term increases as x lineally, and the second term decreases as x reciprocally. Thus $\frac{2\pi W}{\varDelta W}$ has a minimum at some elongation x_0. The values of x_0 and $\left(\frac{2\pi W}{\varDelta W}\right)_{\min}$ are

$$x_0 = \frac{2F}{\kappa_2}, \quad \left(\frac{2\pi W}{\varDelta W}\right)_{\min} = \frac{1}{2} \frac{4\kappa_1 + \kappa_2}{\kappa_2}.$$

Accordingly it is able to explain the experimental results qualitatively by this model. Namely $\frac{\varDelta W}{2\pi W}$ increases so far as the amplitude of vibration x_0 in first, and beyond this point it decreases.

The physical meaning of this behaviour is as follows. When the amplitude of vibration is small, namely small strain, the fibers do not slip with each other due to the frictional force, thus the vibrational energy is not dissipated at the binding portions at all. When the strain of paper becomes large and the fibers begin to slip with each other, $\frac{\varDelta W}{2\pi W}$ increases in first and soon decreases, for $\varDelta W$ increases as x and W increases as x^2.

(2) The case in which it does not depend on the amplitude.

In the paper whose fibers are combined tightly with each other, the different mechanism from the previous one has to be devised, because the binding portions do not slip as easily as the previous case. Thus we considered the mechanism as shown in Fig. 9, where the both ends of a fiber are tightly clamped and the intermediate part of a fiber is able to transfer from one equilibrium position A to the other one B by the stress across a barrier of an activiation energy. Hereafter we call such a protion "*defect*" in short. In Fig. 9, U is the activiation energy which a movable fiber in this *defect* requires to transfer from A to B, and $2a$ is the average distance between two equilibrium positions.

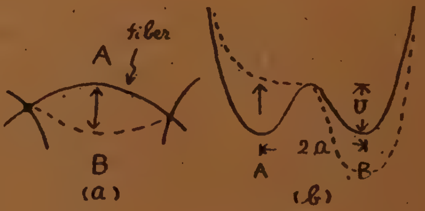

Fig. 9. The model of *defect*.
(a). configuration of fibers.
(b). potential diagram.

If assuming that the numbers of these *defects* are under the Boltzmann distribution, the numbers of *defects* having the activation energy between U and $U+dU$ are

$$dN = N_0 \exp\left(-\frac{U}{U_0}\right) \frac{dU}{U_0}, \tag{6}$$

where N_0 and U_0 are the total numbers of *defects* and the average activiation energy of these *defects* respectively. When the fiber is subjected to the stress and then one bottom of the potential curve, for example A, is raised to U, the fiber is able to transfer from A to B across the barrier. Now assuming that the work $F\cdot a$ is done upon these *defects* in this case, the numbers of *defects* which transfer across these barriers are as follows,

$$\begin{aligned} N &= \int_0^{F\cdot a} N_0 \exp\left(-\frac{U}{U_0}\right)\frac{dU}{U_0} \\ &= N_0\left(1-\exp\left(-\frac{F\cdot a}{U_0}\right)\right)\sim\frac{N_0}{U_0}\cdot F\cdot a, \text{ for } F\cdot a \ll U_0. \end{aligned} \tag{7}$$

Whenever a *defect* transfer between two equilibrium positions, the energy $F\cdot a$ is dissipated as a heat energy. Thus if the *defects* are subjected to the oscillating stress, the dissipated energy per one cycle, $\varDelta W$, is expressed as follows,

$$\varDelta W = 2F\cdot a \times N = 2\frac{N_0}{U_0}(F\cdot a)^2. \tag{8}$$

Then

$$\frac{1}{2\pi}\frac{\varDelta W}{W} = \frac{1}{2\pi}\frac{2\dfrac{N_0}{U_0}(F\cdot a)^2}{\dfrac{F^2}{2\kappa}} = \frac{2\kappa}{\pi}\cdot\frac{N_0}{U_0}\cdot a^2, \tag{9}$$

where W is the vibrational energy of this sample and κ is the elastic modulus. As shown in eq. (9), the internal friction of this model is independent upon the stress F, namely the amplitude of vibration.

§ 5. Conclusions.

In the region of the audiofrequencies, the Young's moduli and the internal friction of various papers are almost independent on the frequencies, but they are very sensitive to the humidity. The effect of humidity depends upon the property of fiber itself composing the paper. In the region above 100 *kc* the internal friction Q^{-1} increases lineally as frequency, but below 100 *kc* Q^{-1} shifts from this straight line. We think that the behaviour above 100 *kc* depends upon the property of fiber itself. In general the internal friction of papers is the sum of three different parts of internal friction, namely the first is the internal friction due to the fibers themselves composing the papers, the second is due to the effect of kinetic friction for binding portions of fibers and depends upon the amplitude of vibration, and the last is contributed by the *defects* of papers and independent upon the amplitude of vibration.

Reference.

(1) H. Kawai and N. Tokita; J. Phys. Soc. Jap. **5** (1950) 17.
(2) J. Ballou and S. Silverman; J. A. S. A **16** (1944) 113.
(3) A. Nolle; J. A. S. A. **19** (1949) 194.
(4) J. Ballou and J. Smith; J. App. Phys. **20** (1949) 493.
(5) R. Witte, B. Mrowca and E. Guth; J. App. Phys. **20** (1949) 481.
(6) W. Herzberg; Papierprüfung, s. 227.
(7) H. Wakeham and E. Honold; J. App. Phys. **17** (1946) 698.

Anomalous Specific Heat and Molecular Rotation in Normal Solid Alcohols.

By Yoshinobu KAKIUCHI, Tosio SAKURAI and Tadasu SUZUKI.

Institute of Science and Technology, University of Tokyo.

(Received April 20, 1950)

§ 1. Introduction.

Certain normal higher alcohols are known for their anomalous dielectric properties, and they are often attributed to molecular rotation.(1)(2)(3) Baker and Smyth(2) suggested the rotation of molecules around their long axis.

A. Müller(4) has concluded from his X-ray measurements, molecules of normal paraffines whose carbon numbers ranging from 21 to 27 rotate around their long axis above certain critical temperatures which are several degrees below their melting points.

Malkin(5) has observed exactly the similar phenomena in some normal alcohols of odd carbon number, and one of the authors(6) in hexadecyl alcohol, and confirmed the existence of molecular rotation.* It is highly desirable, however, to study the behavior of their specific heat near the transformation point, in order to elucidate the nature of the problem.

The present authors(7) have observed the specific heat of tetradecyl and hexadecyl alcohol and found the anomaly as described in the following.

§ 2. Preparations of the samples.

For a preliminary study, commercial crude cetyl alcohol made by Takeda Chemical Company, which is the same one in former X-ray studies was also used. As the transformation point is affected greatly by the purity of the sample, it was distilled at a reduced pressure, and the effect of distillation was closely observed. As the experiment preceeded, authors have realized that the influence of impurities were so great that they resolved to complete further purification.

Crude cetyl alcohol was once fractionated at a reduced pressure (3∼5 mmHg) using Claisen's flask, the side tube of which was packed with small fragments of glass rods in order to make the path of the vapor as long as possible. Each fraction, which corresponds to the temperature range of roughly ten degrees centigrade near the melting point of the pure substance, was then turned into acetate, acetic acid anhydride being used as acetylating agent. Acetates were carefully seperated by repeated fractional distillation and then saponified. And the product was once distilled again.

Hexadecyl alcohol thus obtained was recrystallized from methanol solution four times, and beautiful white crystallites were obtained. As for tetradecyl alcohol, the amount contained in mother material was very small, the quantity of the final product was not sufficient to repeat recrystalization, and therefore it was served directly to measurement. The melting and solidification points of hexadecyl alcohol were 49.1°C and 48.2°C, and that of tetradecyl alcohol were 32.4°C and 31.5°C respectively.

§ 3 Methods and apparatus for measurements.

The calorimeter was made of copper, containing equally spaced copper disks which facilitates the heat conduction. A heating coil of a manganin wire, whose diameter is 0.1 mm and its total resistance was 90∼100 ohms, was fitted in the calorimeter. The total weight of the calorimeter was about 54 grams and the entire surfaces were nickel plated in order to prevent the chemical reaction between the sample and copper, and also to minimize the radiation loss. The molten sample was poured into the calorimeter and then solidified.

When the glass calorimeter, as described by Nagasaki and Takagi(8) was used, there may exist some nonuniform temperature distribution throughout the sample, owing to the poor conductivity of the substance, but the results of the measurements were not essentially different from that of the case where the matallic one was used. Therefore, the glass calorimeter was used in most measurement, because of its simplicity in its treatment and the lack of fear for the chemical reaction with the sample.

The calorimeter was hung in a cylindrical vacuum tight brass vessel the inner surface of which was nickel plated. A copper-constantan thermojunction was inserted in the calorimeter and another differential thermojunction, which also consists of copper and constantan wires, was attached between the surface of the calorimeter and the outer vessel. The pressure in the vessel was reduced to 5×10^{-2} mm Hg in order to eliminate the effect of water vapor, but the heat transfer through the air was not be successfully eliminated. Further reduction of the pressure would be necessary for that pourpose. The process of evacuation may safely be om sample was sealed in the calorimeter under reduced pressure.

---

* According to Hoffman and Smyth(3), Otto recognized rotation in hexadecyl alcohol, but not in dodecyl. Authors have no opportunity of seeing original paper.

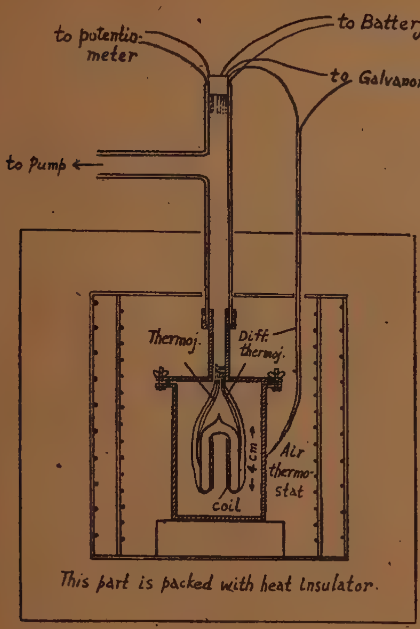

Fig. 1.

The heat capacity was measured by a method described by Nagasaki and Takagi(8), which is an improvement of Sykes(9), and a constant current was made to flow through the heating coil. Then the time required to raise the temperature of the calorimeter by 0.3°C was recorded by a stop watch. The electromotive force of thermojunctions were detected by sensitive galvanometers, and as for the one reading the temperature of the calorimeter, a potentiometer was used in combination.

The temperature of the vessel was always kept constant evual to that of the calorimeter by adjusting the current flowing through the coil of a thermostat in which the vessel was arranged in order to prevent the radiation loss.

The maximum value of the time rate of the temperature rise was about 0.5°C per minute, but much smaller at near the transition and melting points.

The heat capacity of the calorimeter containing the sample was determined from the current flowed, and the resistance of the heating coil and the time rate of the temperature rise. The capacity of the calorimeter when empty, determined in a similar manner was subtracted from the above result, and the net heat capacity of the sample was thus obtained.

In the measurement of specific heat by lowering the temperature, the temperature difference between the calorimeter and the surrounding vessel was kept constant, and the time rate of the lowering of the temperature of the calorimter was recorded, thus being able to estimate the specific heat.

The loss of heat energy due to radiation and conduction during the measurement was estimated to be small. For instance, in the measurement by lowering the temperature, the temperature difference was kept to the value corresponding to 175 mm scale of the galvanometer deflection and the time nescessary for the calorimeter to cool from the melting point to the temperature lower than the transition point was less than three hours. In usual measurements, in which the temperature was raised through the corresponding range in less than two hours, the temperature difference was adjusted less than 3 mm scale of the galvanometer deflection. Therefore, the error in the total value of heat of fusion and of rotational transformation is less than 2 percents.

§ 4. Results of the experiments.

One of the results of the experiments with crude cetyl alcohol, which is the same sample used in former X-ray studies, is shown in Fig. 2, curve A. The anomaly exists at exactly the same temperature (20°C) where the lattice transformation corresponding to rotational transition sets in. The sample obtained by distilling once the crude alcohol at a reduced pressure, gives the result as shown in curve B. The results show that the transformation point shifts to the higher temperature side by purification.

The heat of transformation sometimes reaches to nearly half the value of the heat of fusion. The results are, however, greatly affected by the thermal history, and it is nescessary to cool the sample well below the transformation temperature, otherwise the specific heat anomaly almost disappears. In Fig. 3, curve A correspond

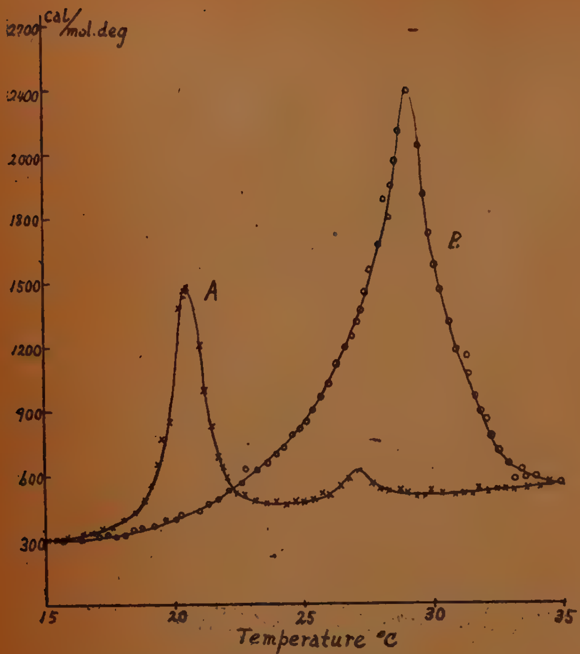

Fig. 2. Specific Heat of crude hexadecyl alcohol.

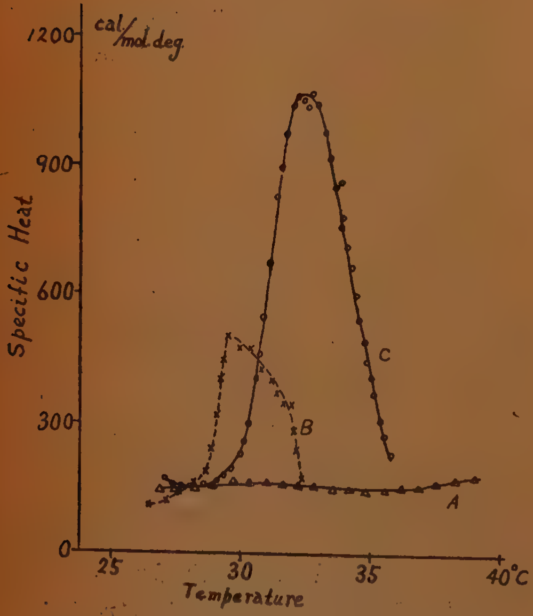

Fig. 3. The effect of thermal treatment.

to the case where the measurement was done right after solidification of the sample and shows no anomaly. The curve B is the one measured after being left overnight at the room temperature, and the curve C corresponds to the case where the sample was slowly cooled to the temperature of melting ice.

Fig. 4 is the specific heat curve for pure hexadecyl alcohol, which shows a sharper anomaly than in the case of the crude one. In this case the curve is far more reproducible, and the effect of thermal treatment seems to be negligible.

The heat of transformation and the heat of fusion are estimated from the heat energy supplied, and their figures are 5.92 and 7.37 kcal/mol respectively. It may be of some value to mention that the heat of transition is roughly the same amount with that of fusion in this case. As seen in the figure, there is a little hump at the tail of the anomalus specific heat curve for melting, and the corresponding heat quantity is about 0.36 kcal/mol (c.f. Table I).

The result for tetradecyl alcohol is shown in Fig. 5. The curve A corresponds to the case where the temperature is lowered and B, C and D for the case where the temperature is raised during the measurement. Because the sample is not pure enough a rather large hysteresis is observed. The curve B which is for the measurement right after solidification from its melts, shows a comparatively little anomaly, which indicates that the crystal does not yet reach its equilibrium state. If the sample is left overnight

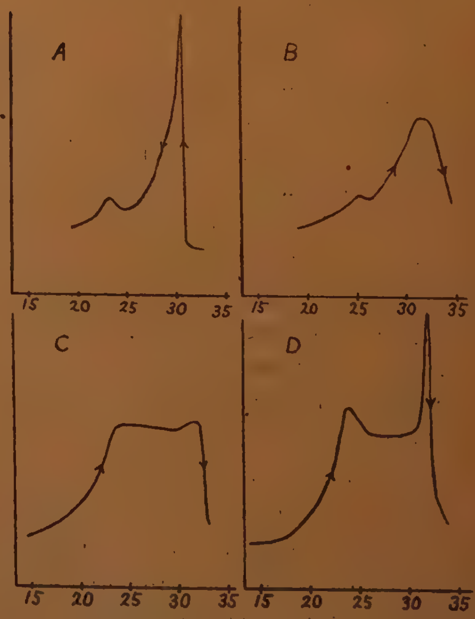

Fig. 5. Specific Heat of tetradecyl alcohol.

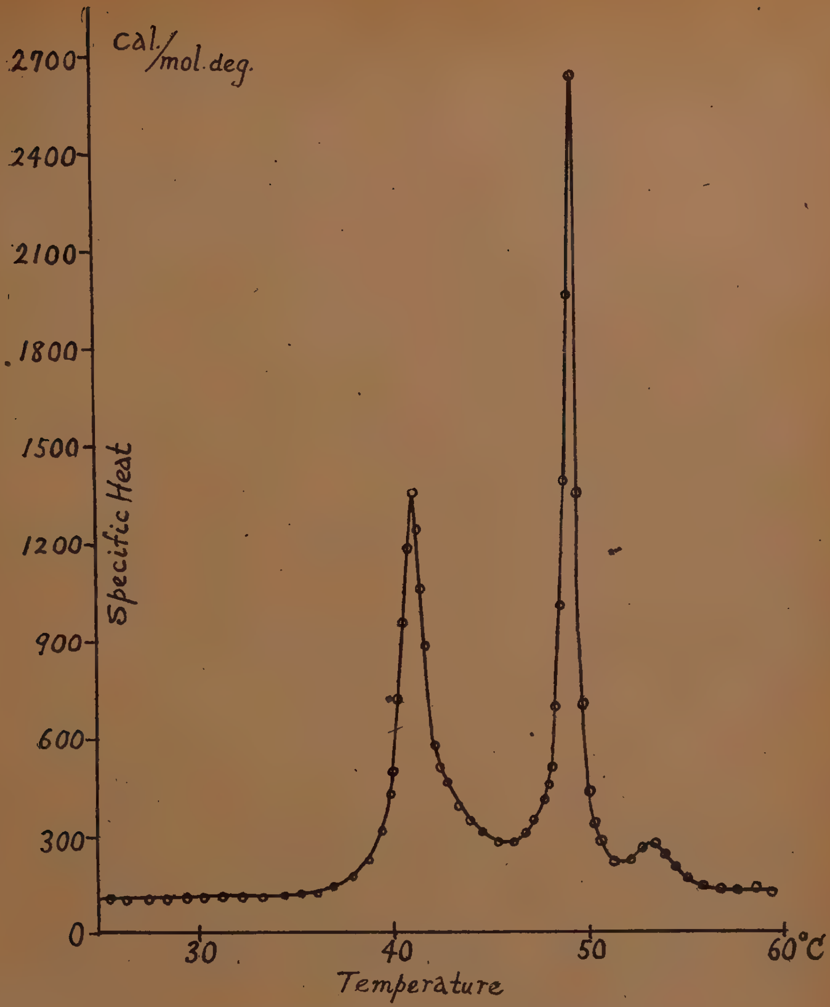

Fig. 4. Specific heat curve for pure hexadecyl alcohol.

Table I.

		Heat of transition (Kcal/mol)	Heat of fusion (Kcal/mol)		Total (Kcal/mol)
Tamman[10]		—	8.18		—
Parks[11]		3.97	8.45		12.4
Present measurements	Takeda (crude)	1.6	3.1		4.1
	Takeda (distilled)	3.7	6.5	(hump)	10.2
	Pure hexadecyl alcohol	5.87 5.97 mean 5.92	7.52 7.22 mean 7.37	0.31 0.41 mean 0.36	13.70 13.60 mean 13.65

and then measured, it recovers the specific heat anomaly to some extent, but heat of fusion is not so conspicuous (curve C). When the sample is cooled to the temperature of melting ice, the sharp peak reappears at the melting point (curve D).

§ 5. Discussions.

For the crude hexadecyl alcohol, the specific heat anomaly exisists at the temperature where the lattice symmetry changes from orthorhombic to hexagonal,(6) and this temperature also coincides with that at which the dielectric constant* begin to increase. Although X-ray studies for purified sample are now in progress, no definite information is available yet. The rise of the dielectric constant* is seen, however, exactly at the temperature corresponding to the specific heat anomaly in case of pure samples too.

From the knowledge about van der Waals radius of atoms and internuclear distances in the molecule, it seems hardly possible for the perfect free rotation to occur even above the transition point, and only the cog-wheel like rotation is supposed to be possible. Hence the problem may well be interpreted as the order-disorder transition, where the ordered state corresponds to the molecular arrangement stable at lower temperatures, disordered state corresponding to the case where the molecules have equal probability of finding themselves in several possible positions. The rotational state hitherto mentioned may thus be interpreted as the disordered state, and perhaps the molecules would really rotate when they change the position from one of the possible orientation to the other, and spend some of their times in librating around one position.

The shape of the specific heat curve is not of λ-type and rather of symmetrical one, which shows that the considerable amount of ordering still persists above the transition point. Anyhow, the cog-wheel like retation of the molecules is believed to be highly plausible.

The effect of long chain impurities upon hysteresis may also be interpreted from these points of view. Namely, if the alcohols of different carbon number are contained in the crystal, the lattice may be somewhat distorted and molecules having random orientation return to their original position with some difficulties even at low temperatures, and this may in turn prevent the lattice distortion to be removed easily. The fact that the hysteresis hardly exists in the sample of high purity is also clearly seen in dielectric measurements. That is, the difference between dielectric constants measured by raising and lowering the temperature is very large for the sample of low purity, which almost disappears by careful purification.

The heat of transition and of fusion is tabulated in Table I together with the data from former investigations.

Parks⁽¹¹⁾ has obtained the sum total of the heat of transition and of fusion by the extrapolation from the heat of solution in alcohols of lower carbon number, and estimated the ratio between them from heating curve. His value is a little too low which may be the effect of some impurities, and the percentage of the heat of fusion seems to be too large owing to somewhat uncertain method of estimation.

The experimental data on the transformation of alcolols are tabulated in the following (Table

Table II.

	author \ carbon number	12	13	14	15	16	17	18	19	20	21	22
Thermal analysis	Phillips-Mumford⁽¹⁾	±	+	+		+	+	+	+			
	Higasi-Kubo⁽²⁾					+		+				
Specific Heat	Kakiuchi-Sakurai –Suzuki			+		+						
Dielectric constant	Baker-Smyth⁽¹⁾					+						
	Hoffman-Smyth⁽³⁾	—		+		+		+				+
	Higasi-Kubo⁽²⁾					+		+				
	Kakiuchi-Komatsu*			+		+		+				
X-ray	Bernal⁽¹²⁾	+										
	Malkin⁽⁵⁾		+		+		+					
	Sano-Kakiuchi⁽⁶⁾					+						
	Ott	—				+						

* to be published soon.

---

* The data on dielectrictric measurements are to be published soon.

II). In the table, + sign means that the result is affirmative for a transition, and — means negative results. Bernal(12) has reported the rotational transition in ease of dodecylalchol, but Hoffman and Smyth(3) has not fouhd any dielectric anomaly. According to Philips and Mumford(13), the knick appears only id the cooling curve, and no transition ean be detected by thermal analysis in case of heating. Therefore the rotational state can exist only as a supercooled state in dodecyl alcohol. Anyhow, it may safely be concluded from the results listed in Tabel II, that alcohols with carbon number from 13 to 22 have high temperature modification with rotating molecules.

§ 6. Acknowledgements.

The authors express their hearty thanks to Prof. S. Wakayama and Prof. C. Hata for their giving them sampls and many valuable directions for the purification. They are also indebted to the Ministry of Education for financial aids.

References.

(1) O. Baker and C. P. Smyth: J. Amer. Soc. **60** (1938) 1229.
(2) K. Higasi and M. Kubo: Sci. Pap. I. P. C. R. **36** (1939) 286.
(3) J. D. Hoffman and C. P. Smyth: J. Amer. Chem. Soc. **71** (1949) 431.
(4) A. Müller: Proc. Roy. Soc. **A138** (1932) 514.
(5) T. Malkin: J. Chem. Soc. (1935) 720.
(6) K. Sano and Y. Kakiuchi: J. Phys. Soc. Jap. **4** (1949) 365.
(7) Y. Kakiuchi and T. Sakurai: J. Phys. Soc. Jap. **4** (1949) 365.
(8) S. Nagasaki and Y. Takagi: Oyobuturi: **17** (1948) 104.
(9) Sykes and Jones: J. Inst. Metal **12** (1936) 257.
(10) Tamman: Z. F. Phys. Chem. **85** (1913) 273.
(11) Parks: J. Chem. Phys. **14** (1946) 507.
(12) J. D. Bernal: Nature 123 (1932) 870.
(13) Phillips and Mumford: J. Chem. Soc. (1934) 663.

Dielectric Dispersions of Alkali Halide Crystals.

By Seiichi Kondo and Tokuo Suita.

Faculty of Engineering, Osaka University.

(Received April 28, 1950)

§ 1. Introduction.

The crystals of Alkali halides except the cesium compounds have the face-centered cubic symmetry, and positive and negative ions are alternately located regularly in ideal crystals. The real states, however, are considered to differ slightly from the ideal arrangement of atoms. Namely there are lattice defects of the so called "Schottky" or "Frenkel" types(1) in a crystal in thermal eqilibrium, and by these irregularities the mechanisms of such phenomena as ionic conductivity, thermal diffusion, color-center, plastic properties and etc. can be explained. In the caystals of alkali halides there are plenty of Schottky type defects composed of the same number of positive and negative ion vacancies. The isolated ionic vacancies which have apparent electric charges, will tend to form neutral pairs or more stable groups of vacancies(2). At ordinary temperatures, therefore, there must be many types of vacancies in the crystals, and some of these may have apparent electric dipole moment having different activation energies of orientation in an alternating electric field.

Breckenridge(3) has found anomalies of dielectric properties in many alkali halides typical for the anomalous dispersions of polar compounds, and explained them in terms of dipole of the negative and positive pair of vacancies, and calculated the activation energy with a simple theory, for example, 0.78 e.v. in potassium chlorides. But these values appeared to be too great for the neutral pairs, as pointed out by Grimley⁽⁴⁾, and calculated by Dienes⁽⁵⁾.

We have measured the dielectric properties of sodium and potassium chlorides at several frequencies near 3 M.C., and found the anomalous behavior of loss angles and dielectric constants.

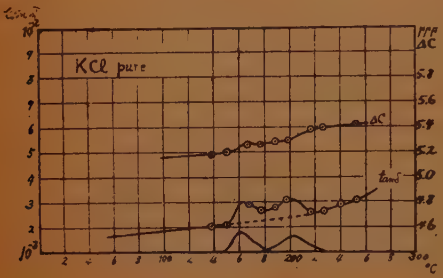

Fig. 1. Dielectric properties of KCl crystals at 2.6 M.C.

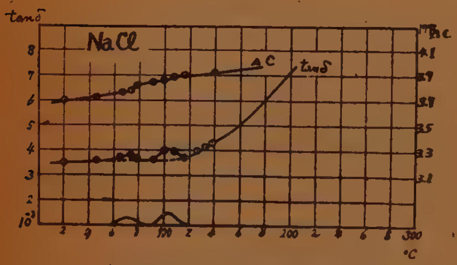

Fig. 2. Dielectric properties of NaCl crystals. at 2.6 M.C.

§ 2. Experimental Procedure.

The samples used for the measurement were prepared by the Kyropoulos' method, from the melted pure or impure salt. The single crystals were cut parallel to the plane (100), made to plates 1 mm thick and 1.5 cm square, and circles of diameter 1.0 cm were painted with Acquadag on each surface. The nickel or silver plates, a little smaller than the circles, were put on them and then dried carefully. All the samples for observation were quenched from 600°C to room temperature in about 10 minute.

The loss angle tan δ and the capacities were measured by means of the substitution method. The experimental error of the capacity was about ±0.003 P.F., and that of tan δ was about $\pm 1 \times 10^{-4}$. The error of measuring temperature was ±1°C.

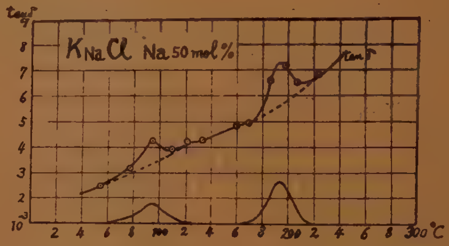

Fig. 3. Capacity and tan δ of Na—KCl having great peak. at 2.6 M.C.

§ 3. Results and Discussions.

(a) The dielectric properties of the crystals in Fig. 1 and 2 were observed with crystals treated as previously illustrated. The survey of these curves shows us two or three peaks of tan δ and a slight increases of capacity at each peak. The height of these peaks seems to depend upon the thermal treatment, and X-ray irradiation. For example, the peak of Fig. 3 is three times larger than the ordinary value of the peaks tan $\delta = 0.5 \times 10^{-3}$. The sample used in the measurement of Fig. 3 was made from the melted salt poured out to the graphite vessel and quenched very rapidly to room temperature, but the samples of other cases were quenched from about 600°C to room temperature comparatively slowly. Another example is Fig. 4. The

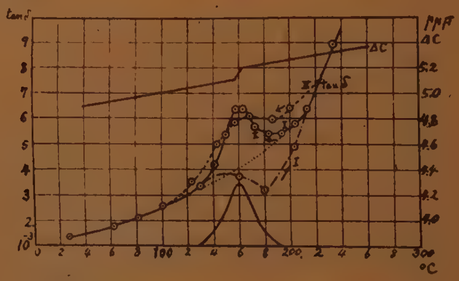

Fig. 4. tan δ of KCl. at 2.6 M.C.

peak at 160°C becomes lower by the successive observations slowly ascending and descending the temperature; curve I represents the results of the first proccess and II that of the second. This will mean the annealing effect of the crystals, which shows that the anomalies relate directly to the lattice vacancies mentioned in section I.

Breckenridge has calculated the activation energy of the analogous dielectric anomalies at lower frequencies by the equation,

$$\tau = \tau_0 \, e^{U/kT} \qquad (1)$$

where U is the activation energy, τ is the time of relaxation $1/2\pi f$—f is the measuring frequency —, and τ_0 which is the reciprocal of the maximum frequency of the lattice vibration of the crystal is a constant independent of the temperature. But the more reasonable value of U is to be obtained from the $\log f$—$1/T$ diagram as usual.

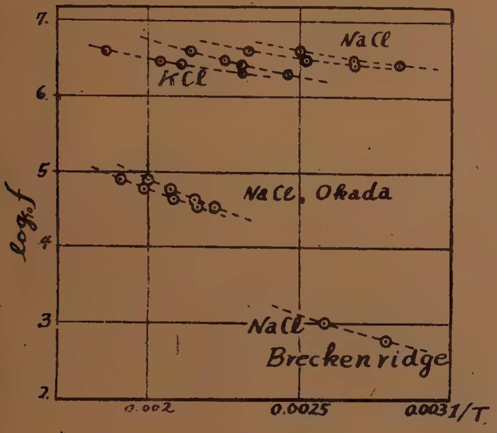

Fig. 5. Frequency—temperature relation of the anomalous Dispersions.

We have therefore observed the frequency effect of the dispersions in Fig. 5. The curves of the figure show a slight curvature alike those obtained by Okada(6). The most simple experimental formula for these curves is not the equation (1) in which U is dependent upon temperature, but the following equation

$$\tau = A/T \, e^{U'/kT} \qquad (2)$$

where A is a aconstant, and T is the absolute temperature of the dispersion. Following the theory of chemical rate process(7), the theoretical equation of such relaxation phenomena is

$$1/T_{\nu} = \frac{kT}{h} e^{-\Delta F/kT} = \frac{kT}{h} e^{\Delta S/k} \, e^{-\Delta U/kT} \qquad (3)$$

there h is Plank's constant, ΔF, ΔS and ΔU are the free energy, entropy and heat of activation respectively. The usual activation energy is ΔU in this equation. Although this theory may cause some question in view of the kinetic theory, by the equation (3) we calculated the value ΔS, ΔU and ΔF of the dispersion of us, Okada, and Breckenridge in which the two values of sodium chlorides seemed to be the frequency effect of the same origin. In Table I the energy of activation is comparatively small in each case, and the entropy has almost the same value having the negative sign. The same values of entropy may show the analogous mechanism of the relaxation phenomena, but the negative sign cannot be interpreted sufficiently at the present stage. The different values of activation energo ΔU are also unable to be explained. One of the reasons for these may lie in the fact that there exist many types of vacancies in the crystal and the activation energies must be different for different types of assembly. For example, the triplet may orient itself more easily to the electric field by the motion of the cation surrounded by the two anion vacancies of the neighboring positive vacancies than in the case of doublet vacancies. Many kinds of the electronic optical absorption centers called F, M, R_1, R_2(2), K(8), (9) and N(10) may seem to be a proof of the presence of many types of vacancies.

Table I.

	Kondo	Okada	Brecken-ridge
ΔF	0.42 *e.v*	0.70 *e.v*	0.66 *e.v*
ΔU	0.08	0.24	0.18 *e.v*
ΔS	$-0.93 \times 10^{-3} \frac{e.v.}{°C}$	$-0.99 \times 10^{-3} \frac{e.v.}{°C}$	$-1.3 \times 10^{-3} \frac{e.v.}{°C}$

(b) If there were impurity cation near the vacant site, the activation energy of the impurity cation near the vacant site—the activation energy of the impurity cation crossing the potential barrier would differ from that of native ion. In the Table II there are some peaks at 70°C—200°C. The peak at 200°C exists in every case of potassium chlorides. When the molal ratio of potassium chlorides to sodium chlorides are varied, the change of the dispersion

Table II.

	Temperature of Dispersion °C	Δ tan δ
Pure	200	3×10^{-4}
Containing Na	160	5×10^{-4}
Containing Tl	195	4×10^{-4}
	155	4×19^{-4}
	120	6×10^{-4}
Containing Pb	200	2×10^{-4}
	150	4×10^{-4}
	95	6×10^{-4}
Containing Ag	190	7×10^{-4}
	75	7×10^{-4}

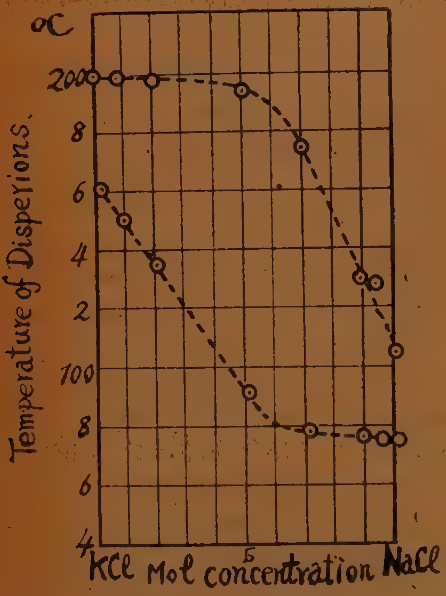

Fig. 6. Dispersion temperature and molal ratio of NACl and KCl mixed crystals.

temperatures in Fig. 6 show some interesting phenomena. The curves are separated into two parts of different quality. The effect of X-ray irradiation upon the color of the crystals is as follows; from 0 to 60 mol per cent of sodium the color is violet, at 60 mol per cent dark, and 60 to 100 mol per cent sodium the color orange. If there were comparatively large micro crystals of potassium and sodium chlorides in the solid solution, the color might be dark corresponding to the quantity of either salt, or in mixed crystals the color must change gradually⁽¹¹⁾. The above experimental facts deny this consideration and a more different mechanism may play the role. for example, two pure and impure phases mixing like the water-oil emulsion. With such a model, the horizontal part of the curves may originate in the pure phases; that is to say, in potassium chlorides 200°C and in sodium chlorides 80°C. The dispersions in another temperature have greater peaks than that mentioned above, which shows the stronger mechanical stress, or greater numbers of vacancies than in the pure phase. But this is an imagination and a more precise examination is necessary. Moreover, the potassium-sodium chloride solid solution is not a good example of stable mixed crystals.

§ 4. summary.

We have found the dielectric anomalous dispersions different from those of Breckenridge and Okada. The difference of these three anomalies may originate in different types of assemblies of vacancies. The activation energies of Breckenridge are not correct as pointed out by Grimley. Further investigations are necessary about the strictly pure salt, and another mixed crystals. We are gratefull for many sugestions of Prof. T. Nagamiya.

References.

(1) N. F. Mott and R. W. Gurney: Electronic processes in Ionic crystals. Cambridge (1941).

(2) F. Seitz: Rev. Mod. Phys., **16** (1946) 384.

(3) R. G. Breckenridge: J. Chem. Phys. **16** (1949) 959.

(4) T. B. Grimley: J. Chem. Phys. **17** (1949) 496.

(5) G.J. Dienes; ibid. **16** (1948) 620.

(6) T. Okada: Busseiron Kenkyu, **20** (1949) 171; Nov..

(7) H. Eyring: The theory of Rate process, (1941).
W. Kaumann: Rev. Med. Phys. **14** (1949) 12.

(8) O. Stasiw: Gött. Nachr. **1** (1936) 1.
T. Suita & S. Kondo: J. Phys. Soc. Japan, **5** (1950) 200.

(9) Y. Uchida: ibid., **4** (1949) 57.

(10) H. Burstein and J. J. Oberly: Phys. Rev. **76** (1949) 1254.

(11) H.F. Ivey: Phys. Rev., **72** (1947) 341.

Short Notes

On the Noise of Rochelle Salt, II. Barkhausen Effect.

By Shoji Kojima and Kiyoe Kato.

(Received June 24, 1950)

In the previous paper⁽¹⁾ we reported that in Rochelle salt the ferro-electric Barkhausen noise can be observed separating from Schönfeld's surface noise. This note describes some results for the Barkhausen noise.

The pulse of the noise obtained by reversing the field from —300 to +300 volts have been studied using the apparatus described in the previous paper. And a thyratron counting device is applied to count the number of pulses and to determine the pulse size distribution.

(1) *Size distribution.* The full curves in Fig. 1 give the total number of pulses at 8°C and 20°C as the function of the thyratron bias voltage. Differentiating the curve of 8°C we obtain the size-distribution as shown by the dotted curve in Fig. 1.

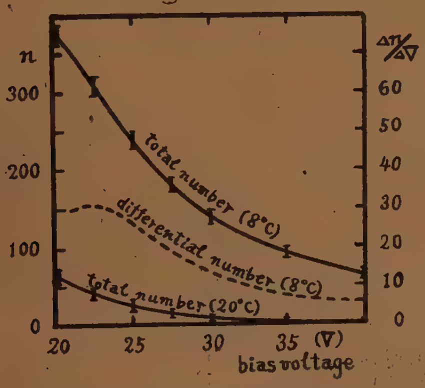

Fig. 1. Sile distribution.

(2) *The volume of Barkhausen region.* The height of the largest pulses observed in the oscilloscope is about 1.68 cm at 8°C. Since the time constant of the circuit of Rochelle salt is larger than the time of polarization, the height of pulses corresponds to the total charge transfered during orientation of a Barkhausen region. The known sensitivity of the apparatus gives that 1 cm height corresponds to 3.5×10^{-14} coulombs. The observed charge Q relates to the equivalent volume of Barkhausen region v by the following formula⁽²⁾:

$$Q = 2pv/L$$

where p is the polarization and L the distance between electrodes. Putting $Q = 7.22 \times 10^{-14}$ coul., $p = 2.45 \times 10^{-7}$ coul/cm³, and $L = 0.5$ cm, we have $v = 7.35 \times 10^{-8}$ cm³. This is the largest equivalent volume at 8°C.

(3) *The propagation velocity of polarization.* Since the rise time of pulses is caused by the time of polarization, the propagation velocity of polarization can be calculated using the above obtained volume of Barkhausen region. The observed rise time of 2×10^{-4} sec. gives the velocity as 20 cm/sec provided that the length of the region is 4×10^{-3} cm.

(4) *Temperature dependence.* The pulse size and the number of pulses have been measured as the function of temperature lowering very slowly from 30°C to the room temperature of 6°C. In this measurement the humidity was fixed about 60%. The results are shown by the curves h nnd n in Fig. 2. The curve v shows the volumes of Barkhausen region which are computed from the curve h using the known values of polariza-

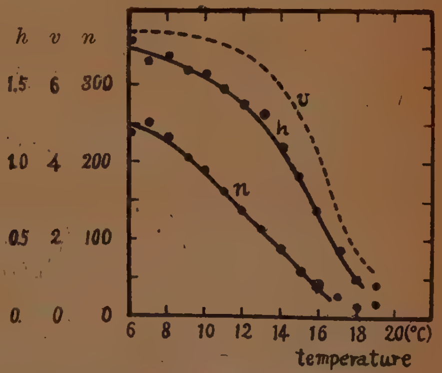

Fig. 2. h: maximum height of pulse (cm), n: numberof pules, v: volume of Barkhausen region ($\times 10^{-8}$ cm³).

tion(3)(4). These curves indicate that the Barkhausen effect increases with decreasing temperature.

We are indepted to the Ministry of Education for the research grant.

References

(1) Kojima and Kato, J. Phys. Soc. Japan **4** (1949) 362.
(2) Newton, Ahearn and McKay, Phys. Rev. **75** (1949) 103.
(3) Schwartz, E. N. T. **9** (1932) 481.
(4) Hablützel, Helv. Phys. Acta. **8** (1935) 498.

An Experiment on 16 Times Amplification of the Phase-Shift of Thin Films.

By Kōzō Ishiguro.

Physics Department, Faculty of Science, University of Tokyo.

(Received July 3. 1950)

In a previous paper(1), the author reported on the application of the double slit interferometer to the phase shift measurements. In the course of experiments, it was noticed that the phase-shift sensitivity could be increased by the choice of the adequate type of the deposition of films. In Fig. 1, the shadowed parts are the places where the film is deposited. As in the previous paper, the phase of light transmitted through the film relative to the light through the bare basic glass is denoted by $2\pi\Delta$. At first, the specimen is placed in position A relative to the double slit and the interference fringe of the parts [I] and [II] is adjusted to make the straight lines by the rotation of the compensator, then the specimen is translated to the position B and the caused shift of fringe between the parts [I] and [II] is re-adjusted. The rotation of the compensator gives the quantity which corresponds to the phase-shift Δ. With the specimen deposited as (a) of Fig. 1, the value observed by the above procedure gives only Δ, but by the specimen of the type (b), it gives 2Δ and by (c) 4Δ. Therefore the type (c) is most effective. When the two samples of type (c) are superposed, the sensitivity of the instrument is increased to 8Δ. Moreover, when it is possible to lay the same films also on the back surfaces and only the observation for the normal incidence is required, the sensitivity can be increased to 16Δ.

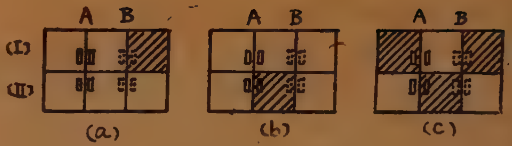

Fig. 1.

Actually the author tried such measurements. On the shadowed parts of type (c) of the cleanly washed glasses (BK7), whose dimension is 3×2 cm and 3 mm in thickness, the commercial anti-fogging lens cleaner made of good soap was painted and then wiped cleanly by the absorbent gauze. With such specimens, the observed phase-shift was $\Delta = \frac{-0.133-\varepsilon}{16} = -0.008_8$ for $\lambda = 0.59\mu$ (where $\varepsilon = 0.014$ is the basic glass correction). When the refractive index of the films is assumed to be $n = 1.5$ or 1.4, the film thickness calculated from the above observation is 110 Å and 140 Å respectively. The formula for the calculation is given by $\Delta = \frac{l}{\lambda}\frac{1-n^2}{1+n_0}$ (where $n_0 \approx 1.52$ is the refractive index of the basic glass).

For the surfaces wiped by the silicon oil paper lens cleaner, Δ was -0.005_0 which corresponded to the film thckness of 60 Å ($n = 1.5$) or 80 Å ($n = 1.4$).

The author believes that by piling up much more glass plates of good optical uniformity, further amplification is not impossible.

Reference.

(1) K. Ishiguro: J. Phys. Soc. Jap. **5** (1950) 187.

Absorption Spectrum of Cuprous Oxide.

By Masakazu Hayashi.

Faculty of Science, Hokkaido Uuiversity.

and

Kiichiro Katsuki.

Muroran College of Technology.

(Received July 12, 1950)

Schoenwald(1) studied the inner photo-electric effect of cuprous oxide and found the absorption edges at 0.63μ (2.0 ev), 0.8μ (1.5 ev) and 2.0μ (0.6 ev). According to Mott and Gurney's interpretation(2), 2.0 ev corresponds to the energy difference between the full band and the empty band, and 0.6 ev to that between the full band and an impurity level, the difference between this level and the empty band being 1.5 ev.

Now we have succeeded in obtaining the absorption spectrum of cuprous oxide in the visible region. The spectrograph used was of Hilger E_1 type whose dispersion in the region in question was 40 Å/mm. Light source was an incandescent lamp (400 W).

Fig. 1 is the reproduction of the absorption spectrograms of cuprous oxide taken at room temperature. As will be seen from Fig. 1 (a) there appear two sharp absorption edges at 0.628$_2\mu$ (1.973 ev) and 0.637$_3\mu$ (1.947 ev). The spectrogram (Fig. 1 (b)) which was taken with longer exposure, shows anotherabsorption edge at 0.605$_7\mu$ (2.047 ev). Thus the absorption edge 0.63μ discovered by Schoenwald proves to be not a single absorption edge, but consist of three absorption edges. The electronic transition corresponding to these three edges are shown in Fig. 2.

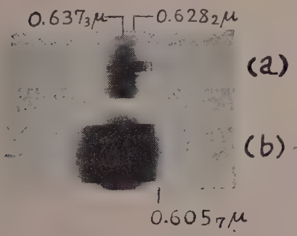

Fig. 1.

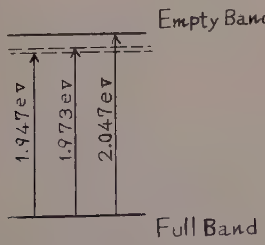

Fig. 2.

Next, we studied the temperature dependency of the absorption (from −135°C to +150°C). The results are given in Fig. 3, of which the curves indicated by (b) show the behavior as functions of temperature of the two absorption edges appearing at 0.628μ and 0.637μ at room temperature, and that indicated by (a) shows the similar behavior of the edge that appears at 0.605μ at room temperature. From these curves we can see the facts: 1) the vertical distance (the energy difference) between the two curves (b) is nearly constant; 2) at higher temperatures above 0°C the energy changes linearly with temperature; 3) at lower temperatures below 0°C the dependency is not so simple.

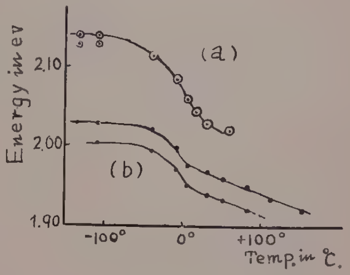

Fig. 3.

At very low temperatures (<−100°C) three new absorption edges manifest themselves at 0.580$_5\mu$ (2.136 ev), 0.577$_0\mu$ (2.149 ev) and 0.575$_9\mu$ (2.154 ev) These do not seem to be shifted with change of temperature.

The investigation is still in progress. The details of experimental procedure and the results obtained as well as their theoretical interpretation will be reported in a separate paper.

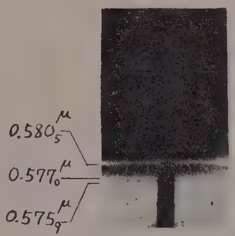

Fig. 4.

In conclusion, the authors wish to express their thanks to Prof. T. Hori for his continued interest in the work and the many valuable suggestions he made during the investigation.

References.

(1) B. Schoenwald, Ann. der Physik, (5) **15,** 395 (1932).
(2) N. F. Mott and R. W. Gurney, *Electronic Processes in Ionic Crystals,* Oxford, (1940).

On Some Regularities in the Isotope Effect in the Spectrum of Lead.

By Kiyoshi Murakawa and Shigeki Suwa.

Institute of Science and Technology,
Komaba-machi, Meguro-ku, Tokyo.

(Received Aug. 3, 1950)

§ 1. Introduction and Experimental Arrangement.

In two papers[1)2)] the authors described the regularities existing in the isotope effect in the spectra of heavy elements. In this paper experimental basis coming from the lead spectrum will be presented.

In order to obtain a bright spectrum of lead, a hollow cathode discharge tube of the type described previously[3)] was used, and the tube was filled with neon or helium. The fine structure was examined with a Febry-Pérot etalon and a glass and a quartz Lummer plate. As an example of the interference pattern taken by us, the photograph of λ5609 and λ5545 (Pb II) is reproduced in Fig. 1.

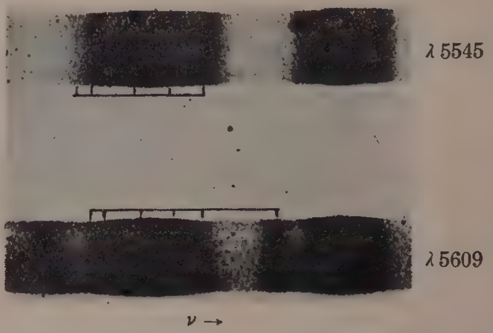

Fig. 1. Interference pattern of Pb II λλ5609 and 5545 taken with a 11 mm etalon

§ 2. Results.

The fine structure of the lead spectrum has

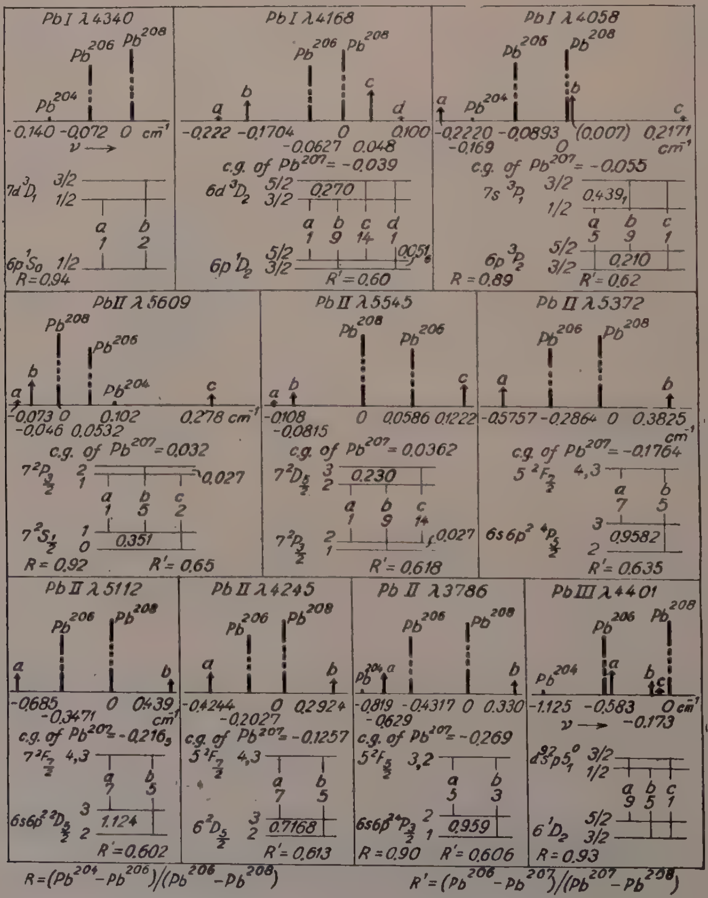
Pb I λ 4340
Pb^{206} Pb^{208} Pb^{204}
-0.140 -0.072 0 cm^{-1}
ν ⟶
7d $^3D_1$ 3/2 1/2
a b 1 2
6p $^1S_0$ 1/2
R=0.94
Pb I λ 4168
Pb^{206} Pb^{208} a b c d
-0.222 -0.1704 0 0.100 -0.0627 0.048
c.g. of Pb^{207} = -0.039
6d $^3D_2$ 5/2 3/2 0.270
a b c d 1 9 14 1
6p $^1D_2$ 5/2 3/2 0.051$_6$
R'=0.60
Pb I λ 4058
Pb^{206} Pb^{208} a Pb^{204} b c
-0.2220 -0.0893 (0.007) 0.2171 -0.169 0 cm^{-1}
c.g. of Pb^{207} = -0.055
7s $^3P_1$ 3/2 1/2 0.439$_1$
a b c 5 9 1
6p $^3P_2$ 5/2 3/2 0.210
R = 0.89 R' = 0.62
PbII λ 5609
Pb^{208} Pb^{206} Pb^{204} a b c
-0.073 0 0.102 0.278 cm^{-1} -0.046 0.0532
c.g. of Pb^{207} = 0.032
7 $^2P_{3/2}$ 2 1 0.027
a b c 1 5 2
7 $^2S_{1/2}$ 1 0 0.351
R= 0.92 R'= 0.65
Pb II λ 5545
Pb^{208} Pb^{206} a b c
-0.108 0 0.0586 0.1222 -0.0815
c.g. of Pb^{207} = 0.0362
7 $^2D_{5/2}$ 3 2 0.230
a b c 1 9 14
7 $^2P_{3/2}$ 2 1 0.027
R'= 0.618
Pb II λ 5372
Pb^{206} Pb^{208} a b
-0.5757 -0.2864 0 0.3825 cm^{-1}
c.g. of Pb^{207} = -0.1764
5 $^2F_{7/2}$ 4,3
a b 7 5
6s6p^2 $^4P_{5/2}$ 3 2 0.9582
R'= 0.635
Pb II λ 5112
Pb^{206} Pb^{208} a b
-0.685 0 0.439 -0.3471 cm^{-1}
c.g. of Pb^{207} = -0.216$_5$
7 $^2F_{7/2}$ 4,3
a b 7 5
6s6p^2 $^2D_{5/2}$ 3 2 1.124
R'=0.602
Pb II λ 4245
Pb^{206} Pb^{208} a b
-0.4244 0 0.2924 -0.2027
c.g. of Pb^{207} = -0.1257
5 $^2F_{7/2}$ 4,3
a b 7 5
6 $^2D_{5/2}$ 3 2 0.7168
R'= 0.613
Pb II λ 3786
Pb^{206} Pb^{208} Pb^{204} a b
-0.819 -0.4317 0 0.330 -0.629
c.g. of Pb^{207} = -0.269
5 $^2F_{5/2}$ 3,2
a b 5 3
6s6p^2 $^4P_{3/2}$ 2 1 0.959
R=0.90 R'= 0.606
Pb III λ 4401
Pb^{206} Pb^{208} Pb^{204} a b c
-1.125 -0.583 0 cm^{-1} -0.173
ν ⟶
d^{9}p5$_1^0$ 3/2 1/2
a b c 9 5 1
6 $^1D_2$ 5/2 3/2
R = 0.93
R=(Pb^{204}–Pb^{206})/(Pb^{206}–Pb^{208})
R'=(Pb^{206}–Pb^{207})/(Pb^{207}–Pb^{208})

Fig. 2. Hyperfine structure of lead lines.

been measured by numerous spectroscopists, but there has been no paper that has been concerned with the regularities to be described below. Only the recent work of Manning, Anderson and Watson[4] may be mentioned.

The structure of the lines that we measured as carefully as possible is given in Fig. 2, the same type of expression as in the case of reference 2 being used.[5] Under each structure diagram, the transition scheme for Pb^{207} $(I=1/2)$ is given. The splitting of the term $6p^3P_2$ of Pb^{207} was determined from the structure of $\lambda 2873$* $(6p^3\,P_2-6d^3\,D_2)$, and was used to interpret the structure of $\lambda 4058$ (Pb I).

We are interested in the ratio of the distances of the neighbouring even isotope components, namely (Pb^{204}—Pb^{206})/(Pb^{206}—Pb^{208}), which will be denoted as R for the sake of brevity. The value of R is given for each line (where possible) in Fig. 2. The abundance of Pb^{204} being very small, the measurement of R is not so accurate, but it may be assumed from Fig. 2 that R is constant for every line within experimental error, and the mean value of R is about 0.93. The component due to Pb^{204} being weak, the interference pattern seems as if it is attracted to a neighbouring strong component, so that a correction was carried out photometrically for every distance Pb^{204}—Pb^{206}. The amount of correction that was given actually seems to have been a little larger than just necessary, so that the value 0.93 can be regarded as an upper limit of R. In any case it has been confirmed that R is less than 1.

Manning et al.,[4] using a sample enriched in the isotope Pb^{204}, measured the isotope effect in the Pb I lines $\lambda 4058-2802$, and obtained the value of R ranging from 0.85 to 0.94, the mean value being about 0.87. This is in good agreement with our value, when the above mentioned remark is taken into account.

As to the value of the ratio (Pb^{206}—Pb^{207})/(Pb^{207}—Pb^{208}) which will be denoted as R', it may be seen from Fig. 2 that R' is also constant for all lines at least in the first approximation, and the mean value of R' is about 0.615.

The theory about the value of R' proposed recently by Breit[6] is based on the Schmidt model[7] of the atomic nuclei, and according to this theory, the value of R' seems to depend on the structure of the lead nuclei only, so that the constancy of R' is in harmony with the theory.

---

* The accuracy of this determination is not so good, being of the order of ±0.005 cm^{-1}.

References.

(1) K. Murakawa: Phys. Rev. **78** (1950), 480.

(2) K. Marakawa and S. Suwa: Jour. Phys. Soc. Japan **5** (1950) in press.

(3) K. Murakawa: Sci. Pap. Inst. Phys. Chem. Res. Tokyo **18** (1932), 191.

(4) T. E. Manning, C. E. Anderson and W. W. Watson: Phys. Rev. **73** (1950), 417.

(5) The classification of Pb I, Pb II and Pb III was given by H. Gieseler and W. Grotrian (Zeits. f. Phys. **39** (1926), 377), L.T. Earls and R.A. Sawyer (Phys. Rev. **47** (1935), 115) and A.M. Crooker (Canad. Jour. Res. **14** (1936), 115) respectively.

(6) G. Breit: Phys. Rev. **78** (1950), 470.

(7) T. Schmidt: Zeits. f. Phys. **106** (1937), 358.

Photo-elastic Method for Determination of Stress in Powdered Mass.

By Takao WAKABAYASHI.

The Tokyo Technical College of Chiba University, Matsudo, Chiba.

(Received July 21, 1950)

It is difficult to determine experimentally the stress distribution in powdered mass without any serious disturbances, Even a slight displacement of the measuring device(1) affects it considerably. Here, it is attempted to adopt a photo-elastic method for eliminating such defect.

When the sand of transparent material such as glass is immersed in the liquid medium whose refractive index is identical to the sand, it becomes transparent for the light within a certain range of wave-length. This principle has already been applied successfully to the Christiansen filter(2). In a vessel provided with two windows of thick glass plates on both sides, the sand of glass and the solution of carbon-disulphide and benzene are filled. The quantity of liquid is chosen sufficiently large to submerge the surface of sand mass, and bubbles are expelled completely from the interior in order to eliminate the influence of the surface tension to the stress distribution. A small ring-shaped piece of phenolite is placed in the sand where the stress is to be determined, and load is applied to the surface of the sand. The inner hole of this phenolite ring is stuffed with cotton-wool, so that the sand does not enter into the hole, and the force acting upon this test-piece is determined by the ordinary method of photoelasticity. When such test-piece is too tender to deform appreciably, the surrounding sand particles lead to some state of equilibrium by the arch effect, and the stress estimated by the photo-elastic figure of the test-piece should not be accepted as true one. It is supposed, however, from a rough estimation that the influence of such effect is of no significance, so far as

$$\frac{r-r_0}{r} > \frac{E_0}{10\,E},$$

where E, E_0, being the Young's modulus of the test-piece and that of the sand respectively; r, r_0, the outer and inner radius of the test-piece. Even if E/E_0 is about 1/20, necessary condition is $(r-r_0)/r>1/200$. In the present experiment, $E_0=5\times10^4\text{kg/cm}^2$, $E=2\times10^3\text{kg/cm}^2$, and $r=3.5$ mm, $r_0=1.5$mm, the necessary condition described above is fulfilled. From the isochromatic and isoclinic lines thus observed in the test-piece, the stress around the outer contour of it or the ellipse of stress in the sand can be obtained. This means the simultaneous measurement of direction and magnitude of stress, corresponding to the little hole method(3) in the case of thin elastic plate. Thus, when the stress distribution in the sand mass is required, a number of test-pieces are arranged in some adequate positions. When the applied load is gradually changed, the corresponding variation of stress in sand shows considerable hysteresis as shown in Fig. 1.

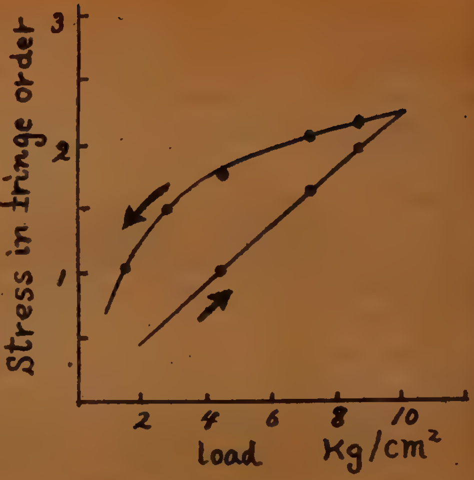

Fig. 1.

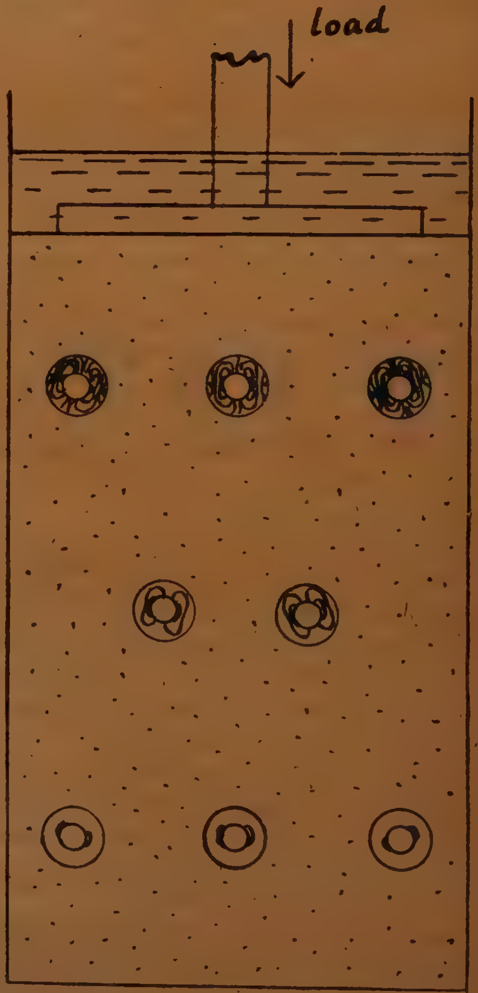

Fig. 2.

When the load is applied suddenly to the surface of sand, it is interesting to observe that the stress is propagated gradually to the bottom. This velocity is so slow that it is easy to follow with naked eyes. An example is shown in in Fig. 2 which is a sketch of the photogram taken when the applied load is 150 kg and the vessel is a pillar of rectangular cross section, 5×5 cm². As is clearly shown by the isochromatic lines of these pieces, the direction of the principal stress is not vertical, but is inclined towards the wall, indicating the fact that an appreciable part of load is supported by the wall. When the sand is filled in the vessel step bo step with sufficiently large compression, it is observed that the propagation velocity of stress within sand due to the applied load is large, and comparatively large amount of stress is exerted to the bottom.

Further experiment is now going on with some other kinds of transparent powder and with more sensitive test-pieces.

The author wishes to express his sincere thanks to Prof. M. Hirata, Prof. K. Yuasa and Mr. Mori for their kind suggestions and encouragements.

Reference.

(1) Kögler u. Scheidig: Bautechnik (1927) Heft 29 u. 31.
(2) John Strong: Procedure in experimental physics. p. 372.
(3) P. Laurent and A. Popoff: La Photoélasticité. Rev. Metal. 35 (1938) p. 363, 407, 448.

X Ray Analysis on Selenium Layers of Selenium Rectifiers.

By J. YAMAGUCHI, and S. KATAYAMA.
Faculty of Engineering, Osaka University.

(Received August 10, 1950)

Zhdanov reported that the layer of selenium rectifiers, which were annealed at 210°C. after having been treated under a pressure of 7 tons/sq. cm. at 135°C., show a fibre diagram with $[11\bar{2}0]$ as the fibre axis which is oriented normal to the layer plane.

In this paper the orientation of selenium crystallites in selenium rectifiers, which are treated at various conditions, is studied by the X-ray method. The method of determination of fibre axis and its porallel degree is described below. When an X-ray beam falls on a fibrous specimen with a inclination of β from its axis, positions of interference spots on cylindrical photographic films are shown by the relation,

$$\cot\delta' = \frac{\sqrt{1+\sec^2 2\theta\cot^2\delta}}{\tan 2\theta}\times\tan^{-1}(\cos\delta\ \tan 2\theta),$$

where

$$\cos\delta \doteqdot \frac{\cos\rho-\cos\beta\sin\theta}{\sin\beta\cos\theta},$$

δ: inclination between two planes; one involves incident and diffracted beams, the other incident beam and the fibre axis.

θ: Bragg's glancing angle.

ρ: angle between normal to the net plane of crystal and the fibre axis.

δ': inclination of the line passing the interference spot and the center from the horizontal line on the unfolded photographic film.

The selenium layer of ractifier is set with the inclination of 5°～45° (the interval being 5°) from the direction of incident beam and diffracted beams are recorded on cylindrical photographic films. We have observed that the intensities of diffraction rings of $(11\bar{2}0)$ and $(12\bar{3}0)$ are maximum appearing at the region near the horizontal line when the inclination is 20°. This fact seems to show that if the fibre axis is oriented normal to the base plate, $[11\bar{2}0]$ is the fibre axis. This assumption is justified, from the calculation of δ's about every crystal planes with various inclinations comparing with the observed values. This result agrees with Zhdanev's⁽¹⁾.

We have determined the parallel degree (P) expressed by the equation,

$$P = \frac{(90^\circ-H^\circ)}{90^\circ}\times 100,$$

where $2H^\circ$ is half value breath, from the intensity distribution measured along $(11\bar{2}0)$ ring recorded on a cylindrical film, whose axis coincides with

Table I. Parallel Degree of Selenium Crystallites.

Pressure at 1st* heat treatment (kg./sq.cm.)	Without 2nd* heat treatment	Temperature at 2nd heat treatment. °C.*		
		170	190	210
5	0	0	0	0
30	79 ± 7	0	0	0
50	78 ± 8	76 ± 4	76 ± 4	72 ± 3
100	79 ± 6	71 ± 3	71 ± 2	70 ± 4

*Specimens are obtained as follows; steel plated by nickel, is coated with selenium, subjected to pressures 5, 30, 50 and 100 kg./sq.cm. at about 130°C. for an hour and annealed for four hours at 170, 190 and 210°C.

the incident beam, inclination of the layer being 20°.

Rectifying characteristics and specific resistance of specimens are measured. They do not seem to depend on the orientation of selenium crystallites.

Conclusions.

1) When selenium crystallites in selenium rectifier show preferred orientation, the fibre axis is [11$\bar{2}$0] and is perpendicular to the base plate.

2) The selenium crystallites show random orientation when the specimens pressed at a pressure lower than 30 kg./sq.cm., and become to have preferred orientation when pressed above 30 kg./sq.cm. Its parallel degree decreases with increasing temperature at the second heat treatment.

References.

(1) G.S. Zhdanov and V. Sharvin, J. Phys. Chem. (U.S.S.R.) **19** (1945) 160.

On Cadmium Selenide of Selenium Rectifiers.

By J. YAMAGUCHI, and S. KATAYAMA.

Faculty of Engineering, Osaka University.

(Received August 10, 1950)

Whether cadmium set on the surface of selenium rectifier forms selenide and whether it, if formed, has a role in the rectifying action is not as yet clear. We shall show the results of X-ray studies on this subject.

We have examined a specimen made in the following manner: steel plate, plated by nickel, is coated with molten selenium, pressed at a pressure of 30 kg./sq.cm. at 130°C. for six hours and annealed at 210°C. for four hours. On this selenium film cadmium is deposited by cathode sputtering (Specimen No. 1). A voltage of 6 volts is applied to the rectifier plate of specimen No. 1 in the hard flow direction for three hours (Specimen No. 2). The plate of specimen No. 1 is heated at 80°C. for five hours (Specimen No. 3 or 4).

By the reflection method using Cr-Kα, diffraction patterns of these specimens are recorded on cylindrical photographic films. These patterns show three kinds of diffraction rings due to selenium, cadmium selenide and cadmium. Cadmium selenide is known to have two modifications, which are isomorphous with zinc blende (cubic) and wurtzite (hexagonal). Nearly all the lines due to the two modifications are superposed, and we made use of (0002) and (10$\bar{1}$1) for the identification of the hexagonal form. Further, the lines (10$\bar{1}$2) and (10$\bar{1}$3) are superposed with (10$\bar{1}$0) of cadmium and (11$\bar{2}$1) of selenium, which are however distinguishable from the latters by the photometer curves. Using these as the criterion, we have confirmed that Nos. 1, 2 and 3 contain cadmium seledide in the hexagonal form while No. 4 is of the cubic modification.

Next the thickness of cadmium selenide layer is measured by Shimazu's method. We have modified it as a form to be applicable to more general cases. Its principle is as follows: on a powder photograph taken with a substance consisting two layers, upper and lower, there appear two kinds of diffractions due to each layer, and the intensities of the diffracted beams due to the lower layer are cut down by the absorption of the uppear layer. Therefore, by measuring the intensity ratios of the diffracted beams due to both layers, the thickness of the upper layer can be calculated. This relation is given by

$$\frac{I_1}{I_2}=\frac{N_1^2p_1F_1^2\mu_2y_2L(\theta_1)}{N_2^2p_2F_2^2\mu_1y_1L(\theta_2)}\;\frac{1-\exp(-\mu_1y_1l)}{\exp(-\mu_1y_2l)},$$

where I is intensity of diffracted beam, l is the thickness of the upper layer, N, p, F, μ, θ, $L(\theta)$ are respectively number of unit cells per unit volume, multiplicity of the lattice plane, structure factor, linear absorption coefficient, Bragg's glancing angle and Lorentz factor,

$$y=\{1/\sin(2\theta-\alpha)\},$$

α: inclination, and suffix 1, 2 shows the quantity of the upper or lower layer.

Comparing the intensities of diffractions (10$\bar{1}$0) of CdSe to (10$\bar{1}$1) of Se, and (11$\bar{2}$0) or (220) of CdSe to (11$\bar{2}$0) of Se, the thickness of CdSe were calculated. Results obtained are shown in Table I.

Table I.

Specimen	Thickness of CdSe layer.
No. 1	$(1.0\sim1.2)\times10^{-4}$ cm.
2	$(1.0\sim1.4)\times10^{-4}$ cm.
3	$(0.7\sim0.9)\times10^{-4}$ cm.
4	$(1.2\sim1.4)\times10^{-4}$ cm.

In order to see under what conditions either of the two modifications of cadmium selenide were formed, and in order to measure the conductivity, we have prepared it using both the dry and the wet methods. Cadmium powder is mixed with $10\sim15\%$ excess selenium powder. The mixture is heated to above 360°C. till reaction begins. The product is powdered and heated at about 1,350°C. for a few minuits. By X-ray analysis it was confirmed that cadmium selenide prepared by this method is of the hexagonal modification. The powder photograph of cadmium selenide prepared by the wet method shows, however, no diffraction ring. The specimen pressed and heated at 200°C. becomes to give a powder photograph which has three diffuse diffraction rings, due to both the hexagonal and the cubic modifications. (Table IIa).

Table II. Powder Photographs of CdSe Prepared By The Wet Method and Pressed.

a) Observed Values

Lattice Spacing (A)	Intensity
2.14	s.
1.96	v.w.
1.83	s.

b) Calculated Values

Hexagonal System			Cubic System		
Spacing (A)	Index	Intensity	Spacing (A)	Index	Intensity
2.15	(11$\bar{2}$0)	10	2.15	(220)	20
1.980	(10$\bar{1}$3)	10	—	—	—
1.832	(11$\bar{2}$2)	7	1.833	(311)	6

Conclusion.

1) It was found cadmium selenide of the hexagonal modification is formed on the surface of selenium rectifiers by sputtering with cadmium. This form of cadmium selenide does not change by the treatment of current in the direction of hard flow, while after the third heat treatment it transforms to the cubic form in some instance.

2) The thickness of the cadmium selenide layers is estimated to be about 10^{-4} cm.

3) Cadmium selenide prepared by the wet method is amorphous and becomes to be a mixture of both the cubic and the hexagonal modifications by heating at 200°C.

The Theory of "Metal Plates Dielectric"†

By Tokio SAKURAI.

Electrical Communication Laboratory, Ministry of Telecommunications.

(Received June 23, 1948)

Since the device made by group of parallel metal plates whose distances between neighbouring plates are very small compared with half wave length displays similar properties for electromagnetic wave as polarizing material for visible light, I call this device *metal plates dielectric* and investigate its fundamental properties.

§ 1. Boundary Conditions.

The Fig. 1. shows the orthogonal cross section of the metal plates dielectric perpendicular to the plates group. *Plate line* in the figure denotes the cross section of the metal plate and *boundary line* shows the cross section of the boundary plane of the metal plates dielectric passing through the edges of the metal plates. Rectangular x, y, z coordinates are so chosen that zx-plane is parallel to each plate and x-axis coincides one of the plates lines in Fig. 1. Plate lines are all parallel to x-axis and lies at $y=0$, $\pm b$, $\pm 2b, \dots$, and the boundary line cuts x-axis at $x=a$ and inclined with y-axis at an angle δ.

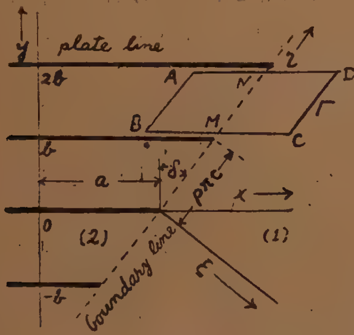

Fig. 1. Orthogonal Section of Metal Plates Dielectric,

Since the variations of field intensity in xy-plane are large compared with those with respect to time and z-direction, we can neglect the derivatives with respect to x and y. Therefore we get from Maxwell's four field equations

$$\left.\begin{aligned} \partial E_z/\partial u_1 = \partial E_z/\partial u_2 = 0\,, \\ \partial H_z/\partial u_1 = \partial H_z/\partial u_2 = 0\,, \end{aligned}\right\} \tag{1.1}$$

$$\left.\begin{aligned} \frac{\partial}{\partial u_1}(h_2E_1)+\frac{\partial}{\partial u_2}(h_1E_2)=0\,, \\ \frac{\partial}{\partial u_1}(h_2E_2)-\frac{\partial}{\partial u_2}(h_1E_1)=0\,, \end{aligned}\right\} \tag{1.2}$$

$$\left.\begin{aligned} \frac{\partial}{\partial u_1}(h_2H_1)+\frac{\partial}{\partial u_2}(h_1H_2)=0\,, \\ \frac{\partial}{\partial u_1}(h_2H_2)-\frac{\partial}{\partial u_2}(h_1H_1)=0\,, \end{aligned}\right\} \tag{1.3}$$

where u_1, u_2 are rectangular curvilinear coordinates in xy-plane and

$$(dx)^2+(dy)^2=h_1^2(du_1)^2+h_2^2(du_2)^2\,. \tag{1.4}$$

(1,1) shows that E_z and H_z are constant throughout xy-plane. Hence remembering that the tangential electric components vanish on metal plate surfaces

$$E_z=0\,,\quad H_z=\text{const.},\quad \text{(throughout } xy\text{-plane.)} \tag{1.5}$$

(1.2) and (1.3) show that both electric and magnetic fields are derivable from generating functions ϕ and ϕ^* as follows:

$$E_1=\frac{1}{h_1}\frac{\partial\phi}{\partial u_1}\,,\qquad E_2=\frac{1}{h_2}\frac{\partial\phi}{\partial u_2}\,, \tag{1.6}$$

$$H_1=-\frac{1}{h_2}\frac{\partial\phi^*}{\partial u_2}\,,\qquad H_2=\frac{1}{h_1}\frac{\partial\phi^*}{\partial u_1} \tag{1.7}$$

where

$$\Delta\phi=\Delta\phi^*=0\,,\quad \text{(throughout } xy\text{-plane)} \tag{1.8}$$

where Δ represents Laplacian in xy-plane. If we remember that tangential electric and normal magnetic components vanish on metal plate surface, we easily find the boundary conditions of ψ and ψ^* on plate lines are

---

† This paper was originally prepared as the following two papers by the same author: *Fundamental Theory of Metal Plates Dielectric*, (received on 23 June 1948). *Electromagnetic Phenomena on Metal Plates Dielectric of Sheet Structure*, (received on 17 August 1948).

$$\psi = C, \quad \psi^* = C^* \quad \text{(on plate lines)} \tag{1.8}$$

where C, C^* are some constants.

ψ satisfying (1.8) and (1.6) can be written in the form

$$\psi = Ay + \psi^i. \tag{1.10}$$

Ay expresses the part of ψ due to external field, ψ^i expresses the part due to the change on metal plates induced by the external field and is most conveniently obtained by comformal representation in the following manner.

Suppose that two complex variables

$$z = x + jy, \quad w = u + jv \tag{1.11}$$

are combined by the relation

$$\exp\{[z/(c\cos\delta)] - w\tan\delta\} = \sin(w/p), \tag{1.12}$$

where

$$\left.\begin{aligned} a &= pc\,(\pi/2+\delta)\sin\delta + c\cos\delta\log(\cos\delta), \\ b &= \pi pc\cos\delta. \end{aligned}\right\} \tag{1.13}$$

$v=0$ expresses plates lines in Fig. 1. in the complex z-plane. Since v satisfies relations:

$$\begin{aligned} \varDelta v &= 0, \quad \text{(throughout } xy\text{-plane)}, \\ v &= 0, \quad \text{(on plate line.)} \end{aligned} \tag{1.14}$$

If we put

$$\psi^i = Bv, \quad (B \text{ being constant}) \tag{1.15}$$

ψ given by (1.10) satisfies (1.8) and (1.9). Thus the form of ψ is determined with the aid of comformal representation. Similarly we can determine ψ^* and get

$$\psi^* = A^*y + \psi^{i*}, \tag{1.16}$$

where A^*y expresses the part of ψ^* due to external field and ψ^{i*} expresses the part due to current on metal plates induced by external field and is of the form

$$\psi^{i*} = B^*v. \tag{1.17}$$

Now we shall consider the macroscopic boundary conditions at the boundary of the metal plates dielectric. Let us now take rectangular coordinates ξ, η, ζ so that its origin is on the end of the plate line on which x-axis is chosen, ξ, η-plane coincides with xy-plane, and in consequence ζ-axis is parallel to z-axis and lies along a metal plate edge and η-axis is along the boundary line. Hence if we denote by upper suffix (1) the field outside and by (2) the field inside the boundary plane of the metal plates electric, we have by (1.5)

$$E_\zeta^{(2)} = E_\zeta^{(1)} = 0, \quad H_\zeta^{(2)} = H_\zeta^{(1)}. \tag{1.18}$$

By (1.12) we get

$$\frac{dw}{dz} = \frac{(1/c)\sin(w/p)}{\cos(w/p-\delta)}, \tag{1.19}$$

from which we have

$$\left.\begin{aligned} &\lim_{x\to-\infty}\left|\frac{dw}{dz}\right| \to \text{exponentially to zero}, \\ &\lim_{v\to+\infty}\left(\frac{dw}{dz}\right) = \frac{1}{c}e^{j\left(\frac{\pi}{2}-\delta\right)} \end{aligned}\right\} \tag{1.20}$$

where $v = +\infty$ expresses by (1.12) the place outside the metal plates dielectric apart from the boundary line at a distance far greater than that between plates lines. Since the distance between plate line is very small in macroscopic consideration we can regard approximately that the field properties at $x=-\infty$ at those near the boundary line inside and the field properties at $v=+\infty$ as those near the boundary outside the metal plates dielectric. Hence by (1.6), (1.10), (1.15) and (1.20) we get

$$E_\eta^{(2)} = E_\eta^{(1)} \,(= A\cos\delta). \tag{1.21}$$

Similarly by (1.7), (1.16), (1.17) and (1.20)

$$H_\xi^{(2)} = H_\xi^{(1)} \,(= -A^*\cos\delta). \tag{1.22}$$

By Maxwell's field equation

$$j\omega\mu H_\xi + \left(\frac{\partial E_\zeta}{\partial\eta} - \frac{\partial E_\eta}{\partial\zeta}\right) = 0. \tag{1.23}$$

If we combine (1.23) with the first equation of (1.18), we recognize that (1.21) and (1.22) are same equations. Therefore the independent boundary conditions on the boundary plane of the metal plates dielectric are only (1.18) and (1.21).

These boundary conditions can be extended even in the case where the dielectric constant ε and permuability μ vary near the boundary plane of metal plates dielectric. Even when ε and μ

vary continuously or jumpwisely, (1.1) holds unchanged. Hence (1.5) deduced from (1.1) still holds. Consequently (1.18) deduced from (1.5) also holds. In order to prove that (1.21) holds even when ε and μ are variable we introduce two dimensional vectors on xy-plane defined by following equations:

$$\boldsymbol{E} = E_1\boldsymbol{i}_1 + E_2\boldsymbol{i}_2, \quad d\boldsymbol{s} = h_1\boldsymbol{i}_1 du_1 + h_2\boldsymbol{i}_2 du_2, \tag{1.24}$$

where $\boldsymbol{i}_1$ and $\boldsymbol{i}_2$ are unit vectors along u_1 and u_2 lines. Even ε and μ are variables, the second equation of (1.2) still holds. Hence

$$\int_\Gamma \boldsymbol{E}\cdot d\boldsymbol{s} = 0, \tag{1.25}$$

where the integrating path Γ is taken around a parallelogram $ABCD$ counter clockwisely, in Fig. 1. If we assume that ε and μ vary similarly in each space between metal plates, electric fields on BC and AD sides are equal to each other and (1.25) is simplified into

$$\int_{BA} \boldsymbol{E}\cdot d\boldsymbol{s} = \int_{CD} \boldsymbol{E}\cdot d\boldsymbol{s}. \tag{1.26}$$

If AB and CD sides are taken sufficiently apart from the boundary line, the effect of metal plates edges becomes small and the fields can be regarded as uniform. Hence

$$\boldsymbol{E} = \text{const.}, \quad (\text{on } AB \text{ or } CD \text{ side.}) \tag{1.27}$$

Substituting (1.27) in (1.25) we find that (1.21) holds even when ε and μ are variable near the bonndary plane of plates dielectric.

§ 2. Analysis of Plane Electromagnetic Wave on Metal Plates Dielectric.

Let us now suppose that the boundary plane of the metal plates dielectric discussed in foregoing section is of infinite breadth and plane electromagnetic wave is incident on the boundary plane. Let us denote by $\boldsymbol{i}$, $\boldsymbol{j}$, $\boldsymbol{k}$ the unit vectors directed along ξ, η, ζ-axis, by $\boldsymbol{n}^{(+)}$ the unit vector expressing the propagation direction of a plane wave, and by γ_1/k_1, p/k_1, q/k_1 its direction cosines. Then there exist

$$k_1^2 = \gamma_1^2 + p^2 + q^2, \quad k_1^2 = \omega^2\varepsilon_1\mu_1, \tag{2.1}$$

$$k\boldsymbol{n}^{(+)} = \gamma_1\boldsymbol{i} + p\boldsymbol{j} + q\boldsymbol{k}, \tag{2.2}$$

where ε_1, μ_1 are the electromagnetic constants of the space outside the metal plates dielectric. Let us introduce wave function $\phi^{(+)}$ and vectors $\boldsymbol{M}^{(+)}$, $\boldsymbol{N}^{(+)}$ defined by

$$\phi^{(+)} = \exp\{j\omega t - j(\gamma_1\xi + p\eta + q\zeta)\} \tag{2.3}$$

$$\left.\begin{aligned} \boldsymbol{M}^{(+)} &= j\phi^{(+)}\boldsymbol{i}\times k_1\boldsymbol{n}^{(+)} = j\phi^{(+)}(-q\boldsymbol{j} + p\boldsymbol{k}), \\ \boldsymbol{N}^{(+)} &= -\phi^{(+)}(\boldsymbol{i}\times k_1\boldsymbol{n}^{(+)})\times\boldsymbol{n}^{(+)} \\ &= -(\phi^{(+)}/k_1)\{(\gamma_1^2 - k_1^2)\boldsymbol{i} - \gamma_1(p\boldsymbol{j} + q\boldsymbol{k})\}. \end{aligned}\right\} \tag{2.4}$$

Electromagnetic field $\boldsymbol{E}^{(+)}$, $\boldsymbol{H}^{(+)}$ of the plane wave propagating in the direction $\boldsymbol{n}^{(+)}$ is expressed with the aid of $\boldsymbol{M}^{(+)}$, $\boldsymbol{N}^{(+)}$ as follows:

$$\left.\begin{aligned} \boldsymbol{E}^{(+)} &= \frac{1}{k_1^2 - \gamma_1^2}\left\{C^{(+)}\left(\frac{\gamma_1 q}{k_1}\boldsymbol{M}^{(+)} + jp\boldsymbol{N}^{(+)}\right)\right. \\ &\qquad \left. + D^{(+)}\left(\frac{\gamma_1 p}{k_1}\boldsymbol{M}^{(+)} - jq\boldsymbol{N}^{(+)}\right)\right\}, \\ \boldsymbol{H}^{(+)} &= -\sqrt{\frac{\varepsilon_1}{\mu_1}}\frac{1}{k_1^2 - \gamma_1^2}\left\{C^{(+)}\left(p\boldsymbol{M}^{(+)} - j\frac{\gamma_1 q}{k_1}\boldsymbol{N}^{(+)}\right)\right. \\ &\qquad \left. - D^{(+)}\left(q\boldsymbol{M}^{(+)} + j\frac{\gamma_1 p}{k_1}\boldsymbol{N}^{(+)}\right)\right\}. \end{aligned}\right\} \tag{2,5}$$

Let us consider the unit vector $\boldsymbol{n}^{(-)}$ and $\phi^{(-)}$, $\boldsymbol{M}^{(-)}$, $\boldsymbol{N}^{(-)}$ defined by

$$\boldsymbol{n}^{(-)} = -\gamma_1\boldsymbol{i} + p\boldsymbol{j} + q\boldsymbol{k}, \tag{2.6}$$

$$\phi^{(-)} = \exp\{j\omega t - j(-\gamma_1\xi + p\eta + q\zeta)\}, \tag{2.7}$$

$$\left.\begin{aligned} \boldsymbol{M}^{(-)} &= j\phi^{(-)}\boldsymbol{i}\times k_1\boldsymbol{n}^{(-)} = j\phi^{(-)}(-q\boldsymbol{j} + p\boldsymbol{k}), \\ \boldsymbol{N}^{(-)} &= -\phi^{(-)}(\boldsymbol{i}\times k_1\boldsymbol{n}^{(-)})\times\boldsymbol{n}^{(-)} \\ &= -(\phi^{(-)}/k_1)\{(\gamma_1^2 - k_1^2)\boldsymbol{i} - \gamma_1(p\boldsymbol{j} + q\boldsymbol{k})\}. \end{aligned}\right\} \tag{2.8}$$

Electromagnetic field $\boldsymbol{E}^{(-)}$, $\boldsymbol{H}^{(-)}$ of plane wave propagating in the direction $\boldsymbol{n}^{(-)}$ is

$$\left.\begin{aligned} \boldsymbol{E}^{(-)} &= -\frac{1}{k_1^2 - \gamma_1^2}\left\{C^{(-)}\left(\frac{\gamma_1 q}{k_1}\boldsymbol{M}^{(-)} - jp\boldsymbol{N}^{(-)}\right)\right. \\ &\qquad \left. + D^{(-)}\left(\frac{\gamma_1 p}{k_1}\boldsymbol{M}^{(-)} + jq\boldsymbol{N}^{(-)}\right)\right\}, \\ \boldsymbol{H}^{(-)} &= -\sqrt{\frac{\varepsilon_1}{\mu_1}}\frac{1}{k_1^2 - \gamma_1^2}\left\{C^{(-)}\left(p\boldsymbol{M}^{(-)} + j\frac{\gamma_1 q}{k_1}\boldsymbol{N}^{(-)}\right)\right. \\ &\qquad \left. - D^{(-)}\left(q\boldsymbol{M}^{(-)} - j\frac{\gamma_1 p}{k_1}\boldsymbol{N}^{(-)}\right)\right\}. \end{aligned}\right\} \tag{2.9}$$

If we consider that the electromagnetic field outside the metal plates dielectric is the superposition of both fields given by (2.5) and (2.9), field must satisfy the first condition in (1.18). Hence there must exist the relation

$$D^{(+)} = D^{(-)} \tag{2.10}$$

between the coefficients of (2.5) and (2.9). But $C^{(+)}$ and $C^{(-)}$ do not subject any restriction. (2.10) shows that the part of the wave field expressed by the term with $D^{(-)}$ in (2.9) is all reflected back by the boundary plane and becomes the part of the wave (2.5) expressed by the term with $D^{(+)}$. Therefore the terms with $D^{(+)}$ and $D^{(-)}$ in (2.5) and (2.9) have no relation with the field inside the metal plates dielectric. Therefore if we consider only the terms with $C^{(+)}$ and $C^{(-)}$, (2.5) and (2.9) becomes

$$\left.\begin{aligned} \boldsymbol{E}^{(1+)} &= \frac{C^{(+)}}{k_1^2-\gamma_1^2}\left(\frac{\gamma_1 q}{k_1}\boldsymbol{M}^{(+)}+jp\boldsymbol{N}^{(+)}\right), \\ \boldsymbol{H}^{(1+)} &= -\sqrt{\frac{\varepsilon_1}{\mu_1}}\frac{C^{(+)}}{k_1^2-\gamma_1^2}\left(p\boldsymbol{M}^{(+)}-j\frac{\gamma_1 q}{k_1}\boldsymbol{N}^{(+)}\right). \end{aligned}\right\} \quad (2.11)$$

$$\left.\begin{aligned} \boldsymbol{E}^{(1-)} &= -\frac{C^{(-)}}{k_1^2-\gamma_1^2}\left(\frac{\gamma_1 q}{k_1}\boldsymbol{M}^{(-)}-jp\boldsymbol{N}^{(-)}\right), \\ \boldsymbol{H}^{(1-)} &= -\sqrt{\frac{\varepsilon_1}{\mu_1}}\frac{C^{(-)}}{k_1^2-\gamma_1^2}\left(p\boldsymbol{M}^{(-)}+j\frac{\gamma_1 q}{k_1}\boldsymbol{N}^{(-)}\right). \end{aligned}\right\} \quad (2.12)$$

Hence η and ζ components of the resultant field

$$\boldsymbol{E}^{(1)}=\boldsymbol{E}^{(1+)}+\boldsymbol{E}^{(1-)}, \quad \boldsymbol{H}^{(1)}=\boldsymbol{H}^{(1+)}+\boldsymbol{H}^{(1-)} \quad (2.13)$$

become by (2.4) and (2.8)

$$\left.\begin{aligned} E_\eta^{(1)} &= -\frac{j\gamma_1}{k_1}\{C^{(+)}\psi^{(+)}-C^{(-)}\psi^{(-)}\}, \quad E_\zeta^{(1)}=0, \\ H_\eta^{(1)} &= j\sqrt{\frac{\varepsilon_1}{\mu_1}}\frac{pq}{k_1^2}\{C^{(+)}\psi^{(+)}+C^{(-)}\psi^{(-)}\}, \\ H_\zeta^{(1)} &= -j\sqrt{\frac{\varepsilon_1}{\mu_1}}\frac{\gamma_1^2 q^2+p^2 k_1^2}{k_1^2(p^2+q^2)} \\ &\qquad \times\{C^{(+)}\psi^{(+)}+C^{(-)}\psi^{(-)}\}. \end{aligned}\right\} \quad (2.14)$$

If we remember that electromagnetic waves in each space between metal plates are evaluated by the same method as that of evaluating H_{10} in rectangular wave guide and these electromagnetic waves propagate with constant phase differences with each other, we find that the electromagnetic waves in the spaces between metal plates constructing metal plates dielectric are deduced from x-compoment of following Hertz vector of magnetic type

$$\Pi_x^* = \frac{1}{j\omega q}\left(\Gamma^{(-)}e^{j\gamma_2^* x}+\Gamma^{(+)}e^{-j\gamma_2^* x}\right) \times e^{-jpy/\cos\delta}e^{-jqz}e^{j\omega t}, \quad (2.15)$$

where

$$\gamma_2^* = k_2^2-q^2, \quad k_2^2 = \omega^2\varepsilon_2\mu_2. \quad (2.16)$$

ε_2, μ_2 are the electromagnetic constants of the spaces inside the metal plates dielectric. The η and ζ components of the field are evaluated by substituting (2.15) in following eqations:

$$\left.\begin{aligned} E_\eta^{(2)} &= -j\omega\mu_2\cos\delta\,\partial\Pi_x^*/\partial z, \\ E_\zeta^{(2)} &= 0, \quad H_\zeta^{(2)} = \partial^2\Pi_x^*/\partial x\,\partial z. \end{aligned}\right. \quad (2.17)$$

If we substitute (2.15) in (2.17) and substitute (2.3), (2.7) in (2.14), and if we again substitute these results in the second condition of (1.18) and (1.21), we get

$$\left.\begin{aligned} \mu_2 k_1\cos\delta\,(\Gamma^{(-)}+\Gamma^{(+)}) &= \gamma_1(C^{(-)}-C^{(+)}), \\ \mu_1 k_1\gamma_2^*\,(\Gamma^{(-)}-\Gamma^{(+)}) & \\ &= \frac{\gamma_1^2 q^2+k_1^2 p^2}{p^2+q^2}(C^{(-)}+C^{(+)}). \end{aligned}\right\} \quad (2.18)$$

§ 3. Plane Electromagnetic Wave Phenomena on Metal Plates Dielectric.

Let us first consider the case when the plane electromagnetic wave is incident on the infinite boundary plane coinciding with η, ζ-plane from positive ξ side and the negative ξ side of η, ζ-plane is wholly occupied by metal plates dielectric of infinite breadth. If we denote by θ the incident angle and by φ the angle of the inclination of the orthogonal projection of propagating direction on η, ζ-plane with η-axis, we have by (2.2)

$$\gamma_1=k_1\cos\theta, \quad p=k_1\sin\theta\cos\varphi, \quad q=k_1\sin\theta\sin\varphi. \quad (3.1)$$

Since there is no returning wave in metal plates dielectric, we have by (2.15) $\Gamma^{(+)}=0$. If we substitute this in (2.18) and solve two equations of (2.18) simaltaneously,

$$\left.\begin{aligned} C^{(+)} &= \frac{\gamma_2^*\sqrt{\mu_1/\varepsilon_1}\cos\theta-\omega\mu_2\cos\delta\sin^2\psi_1}{\gamma_2^*\sqrt{\mu_1/\varepsilon_1}\cos\theta+\omega\mu_2\cos\delta\sin^2\psi_1}C^{(-)}, \\ \Gamma^{(-)} &= \frac{2\omega\cos\theta\sin^2\psi}{\gamma_2^*\sqrt{\mu_1/\varepsilon_1}\cos\theta+\omega\mu_2\cos\delta\sin^2\psi_1}C^{(-)}, \end{aligned}\right\} \quad (3.2)$$

where ψ_1 is the *complementary incident angle* in free space and is defined by the angle of inclination of propagating direction in free space with ζ-axis along the metal plate edge, and consequently

$$\cos\psi_1 = \sin\theta\sin\varphi. \quad (3.3)$$

The propagation constant γ_2^* in metal plates dielectric is imaginary when $\varepsilon_2\mu_2<\varepsilon_1\mu_1\cos\psi_1$ by (2.16), (3.1) and (3.3) and consequently by the first relation of (3.2)

$$|C^{(+)}| = |C^{(-)}|, \quad (\text{when } \varepsilon_2\mu_2<\varepsilon_1\mu_1\cos\psi_1) \quad (3.4)$$

This means that if $\varepsilon_2\mu_2 < \varepsilon_1\mu_1 \cos\phi_1$ the incident wave is totally reflected by the boundary plane and the space inside the metal plates dielectric displays attenuating property and consequently no transmitting wave can propagates inside the metal plates dielectric. γ_2^* becomes real, when $\varepsilon_2\mu_2 > \varepsilon_1\mu_1 \cos\phi_1$ by (2.16), (3.1) and (3.3), and by the second relation of (3.2)

$$|C^{(+)}| < |C^{(-)}|, \quad (\text{when } \varepsilon_2\mu_2 > \varepsilon_1\mu_1 \cos\phi_1) \qquad (3.5)$$

This means that if $\varepsilon_2\mu_2 > \varepsilon_1\mu_1 \cos\phi_1$ the reflected wave is weaker than incident wave and the transmitted wave travels without attenuation inside the metal plates dielectric.

If we combine (3.1) with (2.2), (2.6), we find that the law of reflection of electromagnetic wave on the plane of metal plates electric is the same as that of light reflection *i. e.*, the direction of incident and reflected wave are both on incident plane perpendicular to the boundary plane and the incident and reflection angle equal in absolute value but opposite in sign with each other.

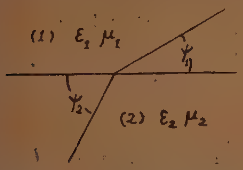

Fig. 2. Complementary transmission angles.

If we denote now by ϕ_2 the *complementary transmission angle* defined by the angle of the inclination of propagation direction of transmitted wave in the space inside the metal plates dielectric with negative direction of ζ-axis along the metal plate edge, we have by (2.16)

$$q = k_2 \cos\phi_2, \quad \gamma_2^* = k_2 \sin\phi_2 . \qquad (3.6)$$

Hence by (3.1), (3.3) and (3.6)

$$k_1 \cos\phi_1 = k_2 \cos\phi_2 . \qquad (3.7)$$

Let v_1 and v_2 be denoted the phase velocities of electromagnetic waves in free space and the space inside the metal plates dielectric respectively, then $k_1 = 1/v_1$, $k_2 = 1/v_2$. Therefore (3.7) becomes

$$v_1/v_2 = \cos\phi_1/\cos\phi_2, \qquad (3.8)$$

which is *the transmission law corresponding to Snell's law.*

Now we consider the case when the plane electromagnetic wave propagating in the space inside the metal plates dielectric is incident on the boundary plane. Since there is no returning wave in free space in this case, we have by (2.14) $C^{(-)} = 0$. If we substitute this and (2.1), (3.6) in (2.18), and solve (2.18) simaltaneously, we have

$$\left.\begin{aligned} \Gamma^{(+)} &= \frac{\mu_1\gamma_1 k_1 k_2 \sin\phi_2 - \mu_2 k_1 \cos\delta\,(k_1^2 - k_2^2\cos^2\phi_2)}{\mu_1\gamma_1 k_1 k_2 \sin\phi_2 + \mu_2 k_1 \cos\delta\,(k_1^2 - k_2^2\cos^2\phi_2)}\,\Gamma^{(-)}, \\ C^{(+)} &= -\frac{2\mu_1\mu_2 k_1^2 k_2 \cos\delta \sin\phi_2}{\mu_1\gamma_1 k_1 k_2 \sin\phi_2 + \mu_2 k_1 \cos\delta\,(k_1^2 - k_2^2\cos^2\phi_2)}\,\Gamma^{(-)} \end{aligned}\right\} \qquad (3.9)$$

By (2.1), (3.6) and (3.9) we get

$$\left.\begin{array}{l} |\Gamma^{(+)}| = |\Gamma^{(-)}| \quad \text{and } \gamma_1 \text{ is imaginary,} \\ \qquad (\text{when } k_1^2 - k_2^2\cos^2\phi_2 < p^2) \end{array}\right\} \qquad (3.10)$$

$$\left.\begin{array}{l} |\Gamma^{(+)}| < |\Gamma^{(-)}| \quad \text{and } \gamma_1 \text{ is real,} \\ \qquad (\text{when } k_1^2 - k_2^2\cos^2\phi_2 > p^2) \end{array}\right\} \qquad (3.11)$$

(3.10) shows that the incident wave is totally reflected by the boundary plane and the transmitting wave out of the boundary attenuates away in free space. (3.11) shows that the incident wave is partly reflected by the boundary and the transmitted wave travels without attenuation in free space. It is notable that the plane of incidence is not perpendicular to the boundary plane as in the case of reflection of wave incident in free space. The plane of incidence is parallel to metal plates constructing the metal plates dielectric, and incident and reflected waves are both on this plane. The angles of inclinations of incident and reflected waves to the normal lying on the plane of incidence and perpendicular to metal plate edge are called the angles of incidence and reflection respectively in the case of wave propagating inside the metal plates dielectric, and these angles are equal in magnitude but opposite in sign by (2.15). The relation between the propagating direction of incident and transmitted waves is the same as shown in Fig. 2., provided that the direction of propagation in opposite in sign. Therefore ϕ_1 becomes the complementary incident angle and ϕ_1 becomes the complementary transmission angle, and the relation (3.7) and (3.8) hold as before.

"Artificial Matter" for Electromagnetic Wave.

By Tokio SAKURAI.

Electrical Communication Laboratory, Ministry of Telecommunications.

(Read April 29, 1949; Received May 27, 1949)

If the body is constructed by blocks of materials, and if the breadth of these blocks is very small compared with the wave length of electromagnetic wave, the behavior of the body is not blockish for the electromagnetic wave. The body behaves as if it was constructed by uniform material. Therefore by using the various kinds of blocks we can get bodies exhibiting various uniform electromagnetic properties. Hence the author calls the body thus constructed *artificial matter*, and the general theoretical treatments of which shall be discussed in this paper.

§ 1. General Theoretical Treatments.

If the body is of periodic structure in three dimension, there exist in necessity three directions, in which the structure of the body is repeated periodically. Let oblique coordinates x, y, z be chosen so that x, y and z axes are parallel to these three directions, and let a, b and c be the lengths of fundamental periods in these directions respectively, then the function f expressing the structure has following property

$$f(x, y, z) = f(x+n_1 a,\ y+n_2 b,\ z+n_3 c)\,, \qquad (1)$$

where n_1, n_2, n_3 are any integers positive or negative.

Since the parallelepiped whose edges are of lengths a, b and c and are parallel to x, y and z axes respectively is the unit of periodicity, it shall be called *unit periodic parallelepiped*. Since the structure of the body is blockish, the electromagnetic field distribution is too complicated to suffer analytical treatment. It is convenient to introduce the idea of macroscopic field expressing average field in the certain neighbourhood of the observing point, which fits analytical treatment owing to its slowly varying functional properties in space.

Let us define the macroscopic quantity at any observing point P as the mean value of the quantity over the whole volume of the unit periodic parallelepiped whose center is at the point P. This is interpreted analytically as follows. Let the coordinates of the point P be (x, y, z) in oblique x, y, z-coordinates, then the macroscopic quantity $\bar{g}$ of the quantity g is expressed by the following integral

$$\bar{g} = \frac{1}{a\,b\,c}\int_{x-a/2}^{x+a/2}\int_{y-b/2}^{y+b/2}\int_{z-c/2}^{z+c/2} g\,dx\,dy\,dz\,. \qquad (2)$$

The electromagnetic field distribution in the artificial matter always accompanies the rapid variation varying with the periodic structure of the body. Hence if g represents the field component, it must be of the form

$$g = wf\,, \qquad (3)$$

where f is the function having the property (1), and w is the function of position varying slowly compared with the periodic variation of the structure of the body. If we substitute (3) in the integral (2) and make use of the fact that w can be regarded as a constant over the range of the integral, we have

$$\bar{g} = \frac{w}{a\,b\,c}\int_{x-a/2}^{x+a/2}\int_{y-b/2}^{y+b/2}\int_{z-c/2}^{z+c/2} f\,dx\,dy\,dz\,. \qquad (4)$$

Owing to the property (1) the integral on the right-hand side of (4) is a constant quantity (say Γ) independent of x, y, z. Hence (4) becomes

$$\bar{g} = w\Gamma\,/\,a\,b\,c\,, \qquad (5)$$

which shows that macroscopic field component $\bar{g}$ varies slowly compared with the periodic variation of the structure of the artificial matter.

Consequently it is appropriate to define the macroscopic quantity by (2).

Let us now try to get the macroscopic field equations. Let us write down Maxwell's equations

$$\nabla \times \boldsymbol{E} + j\omega \boldsymbol{B} = 0\,, \quad \nabla \times \boldsymbol{H} - j\omega \boldsymbol{D} = \boldsymbol{J}\,. \qquad (6)$$

If we operate both sides of the equations (6) by the operator

$$\frac{1}{abc}\int_{x-a/2}^{x+a/2}\int_{y-b/2}^{y+b/2}\int_{z-c/2}^{z+c/2} dx\,dg\,dz\,, \qquad (7)$$

and make use of the fact that the operator ∇ and the operator (7) are commutative with each other, we obtain

$$\nabla \times \bar{\boldsymbol{E}} + j\omega \bar{\boldsymbol{B}} = 0\,, \quad \nabla \times \bar{\boldsymbol{H}} - j\omega \bar{\boldsymbol{D}} = \bar{\boldsymbol{J}}, \qquad (8)$$

where bar represents the macroscopic corresponding quantities.

If we define mascroscopic dielectric constant $\bar{\varepsilon}$, macroscopic permuability $\bar{\mu}$, and macroscopic conductivity $\bar{\sigma}$ by the relations

$$\bar{\boldsymbol{D}} = \bar{\varepsilon}\bar{\boldsymbol{E}}, \quad \bar{\boldsymbol{B}} = \bar{\mu}\bar{\boldsymbol{H}}, \quad \bar{\boldsymbol{J}} = \bar{\sigma}\bar{\boldsymbol{E}}. \qquad (9)$$

(8) and (9) make same field equations as common electromagnetic field equations, Hence macroscopic field vectors satisfies common electromagnetic field equations.

The above results for the body of periodic structure are also applicable for the body of statistically uniform structure. In this case lengths of the edges of unit periodic parallelepiped are chosen such a manner that the shapes and numbers of blocks included in the parallelepiped are statistically invariant wherever it may be removed in the body.

§ 2. Spherical Particles in Uniform Solvent.

Spherical particles of equal magnitude are distributed in uniform solvent so that their centers are at $(n_1 a, n_2 b, n_3 c)$ in x, y, z-coordinates, which are assumed orthogonal in this section to avoid the unnecessary complexity, and where n_1, n_2, n_3 are zero and all integers positive and negative. In this case unit periodic parallelepiped becomes rectangular which shall be called *unit rectangular parallelepiped* hereafter.

Now we shall consider electric field distribution in the neighbourhood of a spherical particle. Since the radius r_1 of the spherical particle is very small compared with wave length, electric field can be treated statically and put

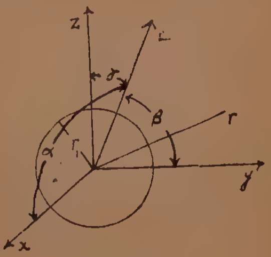

Fig. 1.

$$\boldsymbol{E} = -\nabla\phi\,. \qquad (10)$$

The boundary conditions of ϕ at the surface of spherical particle are

$$\phi_0 = \phi_1\,,\ \varepsilon_0\frac{\partial\phi_0}{\partial r} = \varepsilon_1\frac{\partial\phi_1}{\partial r}, \quad (\text{at } r = r_1) \qquad (11)$$

where r is the radius vector with the origin at the center of the spherical particle, whose coordinates are (0, 0, 0) in x, y, z-coordinates. The suffix 1 expresses the quantities of the spherical particle, while the suffix 0 expresses the quantities of the solvent. ϕ_0 and ϕ_1 both satisfy three dimentional Laplace's equation. If we solve this equation so as to satisfy (11), we get ϕ_0 and ϕ_1 as follows:

$$\left.\begin{aligned} \phi_0 &= -E_0\,(x\cos\alpha + y\cos\beta + z\cos\gamma) \\ &\qquad \times\left(1 - \frac{\varepsilon_1 - \varepsilon_0}{\varepsilon_1 + 2\varepsilon_0}\,\frac{r_1^3}{r^3}\right), \\ \phi_1 &= -\frac{3\,\varepsilon_0}{\varepsilon_1 + 2\varepsilon_0}\,E_0\,(x\cos\alpha + y\cos\beta \\ &\qquad + z\cos\gamma), \end{aligned}\right\} \qquad (12)$$

where E_0 and α, β, γ have following meanings. In the space apart from spherical particle the disturbance of the field by the particle becomes weak, and the electric field may nearly be regarded uniform, this field is denoted by $\boldsymbol{E}_0$ and its intensity by E_0, the angles of inclinations of $\boldsymbol{E}_0$ with x, y, z-axes are denoted by α, β, γ respectively.

Now we shall evaluated macroscopic electric field $\bar{\boldsymbol{E}}$ using the formula (2). As already explained in obtaining (5) from (4), the value of macroscopic quantity is independent of the position of unit rectangular parallelepiped, therefore we may chose the center of the unit rectangular parallelepiped on the center of the spherical particle and substitute (10) in (2). Thence we get

$$\bar{\boldsymbol{E}} = -\frac{\boldsymbol{i}}{abc}\int_{-b/2}^{b/2}\int_{-c/2}^{c/2}\left\{[\phi_0]_{x=a/2}-[\phi_0]_{x=-a/2}\right\}dy\,dz$$
$$-\frac{\boldsymbol{j}}{abc}\int_{-a/2}^{a/2}\int_{-c/2}^{c/2}\left\{[\phi_0]_{y=b/2}-[\phi_0]_{y=-b/2}\right\}dx\,dz$$
$$-\frac{\boldsymbol{k}}{abc}\int_{-a/2}^{a/2}\int_{-b/2}^{b/2}\left\{[\phi_0]_{z=c/2}-[\phi_0]_{z=-c/2}\right\}dx\,dy. \qquad (13)$$

If we substitute (12) in (13) and neglect the value of r_1^3/r^3 on the surface of the unit rectangular parallelepiped compared with unity, (13) becomes

$$\bar{\boldsymbol{E}} = \boldsymbol{i}E_0\cos\alpha+\boldsymbol{j}\,E_0\cos\beta+\boldsymbol{k}\,E_0\cos\gamma = \boldsymbol{E}_0\,, \qquad (14)$$

where $\boldsymbol{i}$, $\boldsymbol{j}$, $\boldsymbol{k}$ are unit vectors directed in x, y, z-axes.

If the dielectric constant in the unit rectangular parallelepiped were ε_0 in everywhere, the macroscopic electric induction $\bar{\boldsymbol{D}}$ would be $\varepsilon_0\boldsymbol{E}_0$ by (14). But in fact the dielectric constant of the spherical particle is ε_1 instead of ε_0, this difference must be adjusted. Therefore

$$\bar{\boldsymbol{D}} = \varepsilon_0\boldsymbol{E}_0+\{(\varepsilon_1-\varepsilon_0)\,/\,V\}\textstyle\int_{V_1}\boldsymbol{E}_1 dv\,, \qquad (15)$$

where V_1 and V are volumes of the spherical particle and the unit rectangular parallelepiped respectively. If we evaluate $\boldsymbol{E}_1$ by substituting ϕ_1 of (12) in (10), and if we substitute the value $\boldsymbol{E}_1$ thus obtained in (15), we get

$$\bar{\boldsymbol{D}} = \varepsilon_0\boldsymbol{E}_0\left\{1+\frac{4\pi r_1^3}{V}\,\frac{\varepsilon_1-\varepsilon_0}{\varepsilon_1+2\varepsilon_0}\right\}. \qquad (16)$$

Hence by combining (14) and (16) with the first relation of (9) we have

$$\bar{\varepsilon} = \varepsilon_0\left\{1+\frac{4\pi r_1^3}{V}\,\frac{\varepsilon_1-\varepsilon_0}{\varepsilon_1+2\varepsilon_0}\right\}. \qquad (17)$$

If the spherical particle is conductive and its conductivity is expressed by σ_1, the boundary condition of the surface of the particle becomes

$$\phi_0 = \phi_1\,,\ \varepsilon_0\frac{\partial\phi_0}{\partial r} = (\varepsilon_1-j\sigma_1\,/\,\omega)\frac{\partial\phi_1}{\partial r}\,,\ (\text{at } r=r_1) \qquad (18)$$

in stead of (11). Hence

$$\varepsilon_1' = \varepsilon_1-j\sigma_1\,/\,\omega \qquad (19)$$

plays the part of ε in non-conductive case. Therefore if ε_1' is replaced in place of ε_1 in the result of non-conductive case, the corresponding result of conductive case is obtained. Thus the expession obtained by replacing ε_1 in the right-hand side of (16) by ε_1' must express the macroscopic quantity defined by replacing ε_1 in the right-hand side of (15) by ε_1'. Since this macroscopic quantity is the mean value of the vector expressing $\varepsilon_0\boldsymbol{E}=\boldsymbol{D}$ in the solvent and $\varepsilon_1'\boldsymbol{E}=(\varepsilon_1-j\sigma_1/\omega)\boldsymbol{E}=\boldsymbol{D}_1-j\boldsymbol{J}_1/\omega$ in the spherical particle, *i.e.*, the mean value of $\boldsymbol{D}-j\boldsymbol{J}/\omega$ over the unit rectangular parallelepiped, this macroscopic quantity must be $\bar{\boldsymbol{D}}-j\bar{\boldsymbol{J}}/\omega$. Hence

$$\bar{\boldsymbol{D}}-j\bar{\boldsymbol{J}}\,/\,\omega=\varepsilon_0\boldsymbol{E}_0\left\{1+\frac{4\pi r_1^3}{V}\,\frac{\varepsilon_1'-\varepsilon_0}{\varepsilon_1'+2\varepsilon_0}\right\}. \qquad (20)$$

Therefore by the first and third relations of (9)

$$(\bar{\varepsilon}-j\bar{\sigma}/\omega)\,\bar{\boldsymbol{E}}=\varepsilon_0\boldsymbol{E}_0\left\{1+\frac{4\pi r_1^3}{V}\,\frac{\varepsilon_1'-\varepsilon_0}{\varepsilon_1'+2\varepsilon_0}\right\}. \qquad (21)$$

Comparing (21) with (14), we get

$$\bar{\varepsilon}-\frac{j\bar{\sigma}}{\omega}=\varepsilon_0\left\{1+\frac{4\pi r_1^3}{V}\,\frac{\varepsilon_1'-\varepsilon_0}{\varepsilon_1'+2\varepsilon_0}\right\}. \qquad (22)$$

Specially $\sigma_1\to\infty$, (22) becomes

$$\bar{\varepsilon} = \varepsilon_0\left(1+\frac{4\pi r_1^3}{V}\right). \qquad (23)$$

When the spherical partical is made of metal, σ_1 may be regarded infinity. The result (23) tells us that if the small metallic spheres are arranged in space, the space behaves as dielectric matter whose macroscopic dielectric constant is given by (23). This artificial dielectric made out of metallic spheres only is called by the author "*metal balls dielectric*".

With regard to macroscopic permuability $\bar{\mu}$ the same arguments used for macroscopic dielectric constant are applied, and the result

$$\bar{\mu} = \mu_0\left\{1+\frac{4\pi r_1^3}{V}\,\frac{\mu_1-\mu_0}{\mu_1+2\mu_0}\right\} \qquad (24)$$

is obtained. Specially $\mu_1\to\infty$, (24) becomes

$$\bar{\mu} = \mu_0\left(1+\frac{4\pi r_1^3}{V}\right). \qquad (25)$$

The result (25) tell us that the material of high permuability can not be obtained by mixing particles of high permuability with the solvent of low permuability.

The above results for the artificial matter of periodic structure are easily extended to those of the matter of statistically uniform structure. In this case the volume of unit rectangular parallelepiped is that of the smallest rectangular parallelepiped which always contain particles statistically equal in shape and number wherever it may remove in the solvent. The results corresponding to (17), (22) and (24) become

$$\bar{\varepsilon} = \varepsilon_0\left\{1+\sum_{i=1}^{n}\frac{4\pi r_i^3}{V}\,\frac{\varepsilon_i-\varepsilon_0}{\varepsilon_i+2\varepsilon_0}\right\}, \tag{26}$$

$$\bar{\varepsilon}-\frac{j\bar{\sigma}}{\omega} = \varepsilon_0\left\{1+\sum_{i=1}^{n}\frac{4\pi r_i^3}{V}\,\frac{\varepsilon_i'-\varepsilon_0}{\varepsilon_i'+2\varepsilon_0}\right\}, \tag{27}$$

$$\bar{\mu} = \mu_0\left\{1+\sum_{i=1}^{n}\frac{4\pi r_i^3}{V}\,\frac{\mu_i-\mu_0}{\mu_i+2\mu_0}\right\}, \tag{28}$$

where the suffix i means the quantity of the ith spherical particle and n is the total number of the particles contained in the unit rectangular parallelepiped.

§ 3. Artificial Matter of Sandwich Type.

The body made by piling up several kinds of plates alternately is called "*artificial matter of sandwitch type*". The artificial matter made by

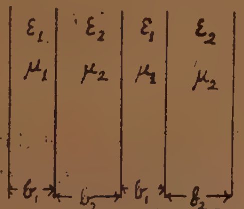

Fig. 2. Orthogonal Section of Artificial Matter of Sandwich Type.

piling up two kinds of plates with electromagnetic constants ε_1, μ_1 and ε_2, μ_2 shall be discussed in this section. The thicknesses b_1 and b_2 of two kinds of plates are assumed very small compared with the wave length of electromagnetic wave. In this case the edge-lengths of unit rectangular parallelepiped are $b = b_1+b_2$ in direction perpendicular and are arbitrary in directions parallel to elementary plates.

We first consider the case that the electric field vector $\boldsymbol{E}$ is same in values in neighbouring two elementary plates, consequently $\boldsymbol{D}_1 = \varepsilon_1 \boldsymbol{E}$ and $\boldsymbol{D}_2 = \varepsilon_2 \boldsymbol{E}$ in two plates respectively. Therefore their macroscopic values $\bar{\boldsymbol{E}}$ and $\bar{\boldsymbol{D}}$ are

$$\bar{\boldsymbol{E}} = \boldsymbol{E}, \quad \bar{\boldsymbol{D}} = (\varepsilon_1 b_1+\varepsilon_2 b_2)\boldsymbol{E}/(b_1+b_2). \tag{29}$$

Hence macroscopic dielectric constant $\bar{\varepsilon}$ becomes

$$\bar{\varepsilon} = (\varepsilon_1 b_1+\varepsilon_2 b_2)/(b_1+b_2), \quad (\boldsymbol{E}/\!/\text{ plates.}) \tag{30}$$

When the electric field is perpendicular to elementary plates, the induction vector $\boldsymbol{D}$ is same in values in neighbouring elementary plates. Consequently $\boldsymbol{E}_1 = \boldsymbol{D}/\varepsilon_1$ and $\boldsymbol{E}_2 = \boldsymbol{D}/\varepsilon_2$ in two neighbouring plates respectively. Therefore their macroscopic values $\bar{\boldsymbol{D}}$ and $\bar{\boldsymbol{E}}$ are

$$\bar{\boldsymbol{D}} = \boldsymbol{D}, \quad \bar{\boldsymbol{E}} = (b_1/\varepsilon_1+b_2/\varepsilon_2)\boldsymbol{D}/(b_1+b_2). \tag{31}$$

Hence macroscopic dielectric constant $\bar{\varepsilon}$ becomes

$$\bar{\varepsilon} = (b_1+b_2)/(b_1/\varepsilon_1+b_2/\varepsilon_2); \quad (\boldsymbol{E}\perp\text{ plates.}) \tag{32}$$

Specially in the case $\varepsilon_1 \ll \varepsilon_2$, (30) and (32) becomes

$$\bar{\varepsilon} = \varepsilon_2 b_2/(b_1+b_2), \quad (\boldsymbol{E}/\!/\text{ plates.}) \tag{33}$$

$$\bar{\varepsilon} = \varepsilon_1 (b_1+b_2)/b_1, \quad (\boldsymbol{E}\perp\text{ plates.}) \tag{34}$$

Hence for the artificial matter composed with two kinds of elementary platetes of very different dielectric constants the macroscopic dielectric constant is of same order with the larger dielectric constant when the electric field is parallel to the plates, while it is of same order with the smaller dielectric constant when the electric is parpendicular to the plates.

When two elementary plates are conductive, ε_1' and ε_2' defined by

$$\varepsilon_1' = \varepsilon_1 - j\sigma_1/\omega, \quad \varepsilon_2' = \varepsilon_2 - j\sigma_2/\omega \tag{35}$$

play the parts of ε_1 and ε_2 in non-conductive case. By using the same argument as used to get (21) from (19), we have

$$\bar{\varepsilon}-j\bar{\sigma}/\omega = (\varepsilon_1' b_1+\varepsilon_2' b_2)/(b_1+b_2), \quad (\boldsymbol{E}/\!/\text{ plates.}) \tag{36}$$

$$\bar{\varepsilon}-j\bar{\sigma}/\omega = (b_1+b_2)/(b_1/\varepsilon_1'+b_2/\varepsilon_2'); \quad (\boldsymbol{E}\perp\text{ plates.}) \tag{37}$$

If σ_1 vanishes for all direction of $\boldsymbol{E}$, and if

$$\sigma_2 = 0, \ (\boldsymbol{E}/\!/\text{ plates.}) \quad \sigma_2 = \infty, \ (\boldsymbol{E}\perp\text{ plates.}) \tag{38}$$

(36) and (37) become

$$\bar{\varepsilon} = \varepsilon_1, \quad (\boldsymbol{E}/\!/\text{ plates.})$$

$$\bar{\varepsilon} = (b_1+b_2)\,\varepsilon_1/b_1, \quad (\boldsymbol{E}\perp\text{ plates.}) \tag{39}$$

(38) takes place when many metal needles are arranged parpendicularly to elementary plates over the whole spaces in the plates with dielectric constant ε_2. Such an artificial matter shall be called *metal needles dielectric.*

Proceeding in the same manner as we have obtained (30) and (32), we can evaluate the values of macroscopic permuability $\bar{\mu}$ in two cases when the magnetic field ***H*** is parallel and perpendicular to elementary plates as follows:

$$\bar{\mu} = (\mu_1 b_1 + \mu_2 b_2) / (b_1 + b_2), \quad (\boldsymbol{H} \,//\, \text{plates.}) \qquad (40)$$

$$\bar{\mu} = (b_1 + b_2) / (b_1 / \mu_1 + b_2 / \mu_2), \quad (\boldsymbol{H} \perp \text{plates.}) \qquad (41)$$

If we combine these results with (30) and (32), we can get the macroscopic propagation constant $\bar{\kappa}$ of plane wave given by the formula

$$\bar{\kappa}^2 = \bar{\varepsilon}\, \bar{\mu}\, \omega^2. \qquad (42)$$

When the plane wave propagates perpendicularly to elementary plates, ***E*** and ***H*** are both parallel to the plates. Hence by substituting (30) and (40) in (42) we get

$$\bar{\kappa}^2 = \omega^2 (\varepsilon_1 b_1 + \varepsilon_2 b_2)(\mu_1 b_1 + \mu_2 b_2) / (b_1 + b_2)^2. \qquad (43)$$

When the plane wave propagates along elementary plates, there are two cases when ***E*** is parallel and ***H*** is perpendicular to the plates and when ***E*** is perpendicular and ***H*** is parallel to the plates. In the first case by (30), (41) and (42)

$$\bar{\kappa}^2 = \omega^2 (\varepsilon_1 b_1 + \varepsilon_2 b_2) / (b_1 / \mu_1 + b_2 / \mu_2). \qquad (44)$$

In the second case by (32), (40) and (42)

$$\bar{\kappa}^2 = \omega^2 (\mu_1 b_1 + \mu_2 b_2) / (b_1 / \varepsilon_1 + b_2 / \varepsilon_2). \qquad (45)$$

Radioactivity of Thoriated Tungsten Wire.

By Itaru NONAKA and Shoji TANABE.

Matsuda Research Laboratory, Tokyo Shibaura Electric Co. Ltd.

(Read April 28, 1949, Received April 5, 1950)

§ 1. Introduction.

We have introduced a method of determing simply and quickly the thorium content of thoriated tungsten wire by measuring the β-ray activity by thin walled Geiger-Müller counters(1). In this method, however, only the relative content can be determined because of the complication of absorption of β-rays in the wire itself, and the absolute value must be determined by ordinary chemical analyses.

To determine the absolute value of content by the radioactivity method, it seems that the γ-rays should be measured. But, in effect, the results of the γ-ray method do not coincide with those of the chemical method. For example, when the chemical method gives a value of 2.0 per cent of ThO_2, the γ-ray method gives a value of only 1.3 per cent. As for the origin of this discrepancy, it seems to be that some parts of the radiocative elements of thorium series had evaporated away in the course of high temperature treatment (ca. 3000°C) of the thoriated tungsten ingot.

The β-rays and the γ-rays, which are measured in our method with G-M counters of thin aluminium wall (0.2 mm) and thick brass wall (2 mm) respectively, are those emitted by $MsTh_2$ and $Th(C+C'+C'')$. If some of the atoms of the above elements or their parents $MsTh_1$ or RdTh evaporate away, some changes of the activity will occur after the heat treatment. Th itself is in a state of oxide and is considered to be difficult to evaporate, or even if it evaporates to some extent the reduction of the content will also appear in the result of chemical analysis.

In a sample of thoria which has passed more than five years after its refinement from ore, the greater parts of RdTh* and all of the other radioactive elements are in the state of element, so their facilities for evaporation can be estimated from their melting points in metalic state. ThB, ThC and ThC″, being istopes of Pb, Bi and Tl respectively, have their melting points near 300°C and are considered to be very easy to exaporate. ThX and MsTh$_1$, being isotopes of Ra, have melting point of 960°C and are considered to have medium hardness for evaporation. RdTh in metalic state has melting point of as high as 1845°C, so it is very hard to evaporate.

From a practical point of view, it is important to make clear the variation of radioactivity of thoriated tungsten with time. For long period variation extending for several years, direct measurements are uneasy to be applied. For such purposes, therefore, it seems to be suitable to know the degrees of evaporation of the radioactive elements during the heat treatment and to calculate the time variation of radioactivity from these evaporation data.

As the first step of such problems, we treated pure ThO$_2$ specimens at several temperrtures between 1500°C and 2300°C and tried to know the degrees of evaporation from the time variation of the radioactivity.

In the second step we applied the same method to ingots of thoriated tungsten and estimated the long period variation of radioactivity of thoriated tungsten wire.

§ 2. Theoretical Considerations.

At any time not less than one hour after the heat treatment the intensity of γ-rays or β-rays is determined altogether by the number of atoms of MsTh$_2$ and ThC disintegrating per unit time. Accordingly, the intensity of γ-rays I_γ and of β-rays I_β are expressed as follows,

$$\left.\begin{aligned} I_\gamma &= 0.67\lambda_2 N_2 + \lambda_c N_c \\ I_\beta &= \lambda_2 N_2 + \lambda_c N_c \end{aligned}\right\} \qquad (1)$$

where N_2 and N_c are the number of atoms of MsTh$_2$ and ThC respectively, λ_2 and λ_c are their disintegration constants, and the numerical coefficient 0.67 is a factor(2) indicating the difference of sensitivities to be detected of the γ-rays form MsTh$_2$ and Th(C+C′+C″).

Now, we denote by k, k', k'', and k''' the proportions of the atoms of RdTh, MsTh$_1$, MsTh$_2$, and ThB (or ThC)* respectively which did not evaporated by the heat treatment, and by N_1, N_2, N_R, N_X, N_B, N_c, and λ_1, λ_2, λ_R, λ_X, λ_B, λ_c the numbers of atoms and disintegration constants of MsTh$_1$, MsTh$_2$, RdTh, ThX, ThB, and ThC respectively. Before the heat treatment, there exist transient equilibriums between MsTh$_1$ and MsTh$_2$, and between RdTh and the succeeding elements. Accordingly, if we denote the quantities before the heat treatment by $^{(0)}$ marks on their shoulders, there exist next relations,

$$\left.\begin{aligned} &(\lambda_1 N_1)^{(0)} = (\lambda_2 N_2)^{(0)} = A \\ &(\lambda_R N_R)^{(0)} = (\lambda_X N_X)^{(0)} = (\lambda_B N_B)^{(0)} = (\lambda_c N_c)^{(0)} = B \end{aligned}\right\} \qquad (2)$$

where A and B are considered to be constants during a period of the order of months.

The values of N_2 after the heat treatment is obtained by the following differential equation,

$$\left.\begin{aligned} &\frac{dN_2}{dt} = \lambda_1 N_1 - \lambda_2 N_2 \\ &\lambda_1 N_1 = k'(\lambda_1 N_1)^{(0)} = k'A \text{ (const.)} \\ \text{at } t=0;\ &\lambda_2 N_2 = k''(\lambda_2 N_2)^{(0)} = k''A \text{ (const.)} \end{aligned}\right\} \qquad (3)$$

and we obtain the following solution,

$$\lambda_2 N_2 = k'A + (k'' - k')Ae^{-\lambda_2 t} \qquad (4)$$

Secondly, the values of N_c can be obtained by the following simultaneous differential equations,

$$\left.\begin{aligned} &\frac{dN_c}{dt} = \lambda_B N_B - \lambda_c N_c \\ &\frac{dN_B}{dt} = \lambda_X N_X - \lambda_B N_B \\ &\frac{dN_X}{dt} = \lambda_R N_R - \lambda_X N_X \\ &\lambda_R N_R = k(\lambda_R N_R)^{(0)} = kB \text{ (const.)} \\ \text{at } t=0;\ &\lambda_c N_c = k'''B \text{ (const.)} \\ &\lambda_B N_B = k'''B \text{ (,,)} \\ &\lambda_X N_X = k'B \text{ (,,)} \end{aligned}\right\} \qquad (5)$$

---

* As RdTh is an isotope of Th, some RdTh atoms are those which had accompanied Th in the process of refinement from ore.

We assumed for simplicity the proportions of ThB and ThC are equal.

We can solve these equations successively and obtain the following solution for N_c,

$$\lambda_c N_c = B\Big[k - \frac{\lambda_B}{\lambda_B-\lambda_X}\cdot\frac{\lambda_c}{\lambda_c-\lambda_X}(k-k')\,e^{-\lambda_X t}$$
$$-\frac{\lambda_c}{\lambda_c-\lambda_B}\Big\{(k-k''')-\frac{\lambda_B}{\lambda_B-\lambda_X}(k-k')\Big]e^{-\lambda_B t}$$
$$+\frac{\lambda_B}{\lambda_c-\lambda_B}\Big\{(k-k''')-\frac{\lambda_c}{\lambda_c-\lambda_X}(k-k')\Big\}e^{-\lambda_c t}\Big] \tag{6}$$

Putting (4) and (6) into (1) we finally obtain the following expressions for I_β and I_γ,

$$I_\gamma(t) = I_\gamma(\infty)+0.67A\,(k''-k')\,e^{-\lambda_2 t}$$
$$-1.15B\,(k-k')\,e^{-\lambda_X t}$$
$$-B\,\{1.10\,(k-k''')-1.25\,(k-k')\}\,e^{-\lambda_B t}$$
$$-B\{(0.10\,(k-k''')-0.10\,(k-k')\}\,e^{-\lambda_c t}.$$
$$I_\beta(t) = I_\beta(\infty)+A\,(k''-k')\,e^{-\lambda_2 t}$$
$$-1.15B\,(k-k')\,e^{-\lambda_X t}$$
$$-B\,\{1.10\,(k-k''')-1.25\,(k-k')\}\,e^{-\lambda_B t}$$
$$-B\,\{0.10\,(k-k''')-0.10\,(k-k')\}\,e^{-\lambda_c t}. \tag{8}$$

They contain two parameters A and B, but when the age of the original ThO_2 is greater than five years the ratio of them is considered to be constant with fairly goon approximation, or

$$\frac{A}{B} = \frac{(\lambda_1 N_1)^{(0)}}{(\lambda_R N_R)^{(0)}} = 1.10 \tag{9}$$

Still more, we can obtain following relations between $I_\gamma(0)$, $I_\gamma(\infty)$ and $I_\gamma{}^{(0)}$,

$$\left.\begin{aligned}\frac{I_\gamma(0)}{I_\gamma{}^{(0)}} &= \frac{0.738\,k''-k'''}{1.738}\\ \frac{I_\gamma(\infty)}{I_\gamma{}^{(0)}} &= \frac{0.738\,k'-k}{1.738}\end{aligned}\right\} \tag{10}$$

And the similar relations for I_β 's

$$\left.\begin{aligned}\frac{I_\beta(0)}{I_\beta{}^{(0)}} &= \frac{1.10\,k''-k'''}{2.10}\\ \frac{I_\beta(\infty)}{I_\beta{}^{(0)}} &= \frac{1.10\,k'-k}{2.10}\end{aligned}\right\} \tag{11}$$

The left hand sides of (10) and (11) are measurable quantities, so the values of $I_\gamma(t)$ or $I_\beta(t)$ at more two points can determine the values of k, k', k'', and k'''.

§ 3. Experiments on Pure ThO₂ Specimens.

In the first step we performed an experiment on pure thoria. The specimens of pure thoria are in forms of rods, 3 mm in diameter and about 2 cm in length. They were heated in a tungsten coil at 1500°C, 2000°C and 2300°C respectively for ten minuits in a stream of argon gas. Then the specimens were wrapped in thin aluminium foils of 0.1 mm thick and their activities were measured by Geiger-Müller counters for four months long. The γ-rays were measured by a brass counter of 15 mm in inner diameter, 5 cm in length and 2 mm in wall thickness, and the β-rays by an aluminium counter of the same dimmension as above except the wall thickness of 0.2 mm. As the aluminium counter is also sensible to γ-rays, the β-ray intensities were obtained after correcting the percentage of γ-ray countings.

The results of the measurements are shown in Fig. 1, 2, and 3. At 1500°C the depression of activity is slight and recovers about two days

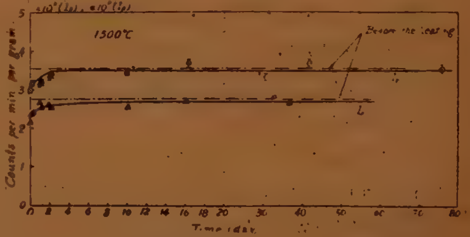

Fig. 1. Radioactivity of ThO_2 heated at 1500°C for 10 min.

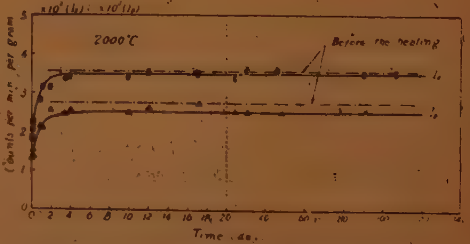

Fig. 2. Radioactivity of ThO_2 heated at 2000°C for 10 min.

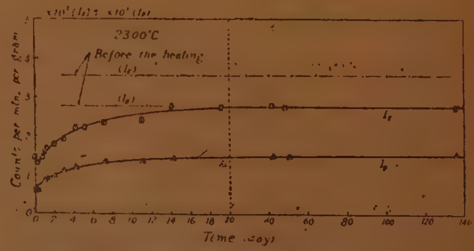

Fig. 3. Radioactivity of ThO_2 heated at 2300°C for 10 min.

after, but as the temperature becomes higher the depression becomes greater and its recovering is slower. These facts indicate that at lower temperature only ThB and ThC evaporate, but at higher temperature ThX begins to evaporate.

From the formulas (7), (8), (9), (10) and (11) we can evaluate the four qurntities k, k', k'', and k''' which express the proportions of the elements not evaporated in the heat treatment. The results of these evaluation are shown in Table I. The The solid curves in Fig. 1, 2, and 3 are those calculated by the formulas (7) and (8) with the above values of k's.

In the case of β-rays we are observing the phenomena effectively in a layer about 0.1 mm deep from the outer surface of the speciemen, and in the case of γ-rays the average throughout the speciemen.

§ 4. Experiments on Thoriated Tungsten Ingots.

In the second step we performed an experiment on thoriated tungsten ingots. Ingots are heated as high as 3000°C in the course of their production. The ingots used in this experiment was 6 mm square in section and about 30 cm in length. The temperature of heating is not perfectly uniform throughout the total length, so we prepared two speciemens of about 2 cm in length, one from the portion of the highest temperature and the other from the portion of the lowest temperature. And in the former speciemen one of the side faces was scraped off about 0.5 mm in thickness. Then we measured on three cases "high temp. (outer)", "high temp. (inner)", and "low temp. (outer)". The results are shown in Fig. 4.

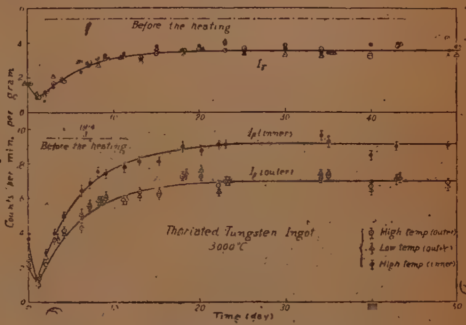

Fig. 4. Radioactivity of ingot after heat treatment.

In the case of γ-rays there was no difference between above three cases, so the analysis was performed on the average of them. In the case of β-rays there were marked differences between "high temp. (outer)" and "high temp. (inner)", but no difference between "high temp. (outer)" and "low temp. (outer)". The depresfion of activity is very striking compared with that of the pure ThO_2 specimens.

The values of k's obtained are shown in Table I. Even in the average throughout the

Table I. Proportions of radioactive elements not evaporated in the heat treatment.

	γ-Rays				β-Rays			
	RdTh k	MsTh₁ ThX k'	MsTh₂ k''	ThB ThC k'''	RdTh k	MsTh₁ ThX k'	MsTh₂ k''	ThB ThC k'''
Pure ThO_2 1500°C	(1.00)	0.97 ±0.06	(1.00)	0.71 ±0.05	(1.00)	0.96 ±0.05	(1.00)	0.58 ±0.08
2000°C	(1.00)	0.97 ±0.02	(1.00)	0.16 ±0.03	(1.00)	0.87 ±0.02	0.86 ±0.03	(0.0)
2300°C	1.01 ±0.03	0.45 ±0.03	0.95 ±0.03	(0.0)	0.78 ±0.03	0.33 ±0.02	0.50 ±0.02	(0.0)
Ingot 3000°C	1.10 ±0.13	0.08 ±0.07	0.73 ±0.05	(0.0)	(1) 0.71 ±0.05	0.05 ±0.02	0.23 ±0.02	(0.0)
					(2) 0.93 ±0.06	0.06 ±0.03	0.37 ±0.02	(0.0)

(1) Outer surface. (2) Inner layer 0.5 mm deep.

specimen (γ-ray case) MsTh$_1$ and ThX evaporate almost entirely, and in the surface (β-ray case), MsTh$_2$ also evaporate almost entirely.

From those results on Table I, it is known that MsTh$_2$ is harder to evaporate than MsTh$_1$ or ThX, and perhaps have higher melting point than that of MsTh$_1$ (960°C). The solid curves in Fig. 4 are those calculated by the formulas (7) and (8).

§ 5. Long Period Variation of Activity.

From the results of the preceding section we can calculate the long period variation of the activity of thoriated tungsten measured by years.

At any time more than one month after the manufacturing of the ingot there exist transient radioactive equilibriums between MsTh$_1$ and MsMn$_3$ and between RdTh and its daughter elements. At this stage the β-ray activity is determined by the amonnts of MsTh$_1$ and RdTh, or

$$I_\beta(t) = \lambda_1 N_1 + \lambda_R N_R \tag{12}$$

If we take the time of high temperature treatment as the origin of time, then at $t=0$ (in a sense measured by years) we can put as follows,

$$\left.\begin{aligned}(\lambda_1 N_1)_{t=0} &= k'A \cong 0\\ (\lambda_R N_R)_{t=0} &= kB \cong B\end{aligned}\right\} \tag{13}$$

With this initial condition we obtain for $(\lambda_1 N_1)$ and $(\lambda_R N_R)$ as follows,

$$\left.\begin{aligned}\lambda_1 N_1 &= (\lambda N)_{Th}(1-e^{-\lambda_1 t})\\ \lambda_R N_R &= (\lambda N)_{Th}\Big\{1-\frac{\lambda_R}{\lambda_R-\lambda_1}e^{-\lambda_1 t}\\ &\qquad +\Big(\frac{B}{(\lambda N)_{Th}}+\frac{\lambda_1}{\lambda_R-\lambda_1}\Big)e^{-\lambda_R t}\Big\}\end{aligned}\right\} \tag{14}$$

On the other hand, the quantity of RdTh in the original ThO$_2$ sample varies as a function of time T since it had been refined from ore. After a simple calculation we obtain for $(\lambda_R N_R)^{(0)}$ as follows,

$$(\lambda_R N_R)^{(0)} = B = (\lambda N)_{Th}\Big\{1-\frac{\lambda_R}{\lambda_R-\lambda_1}(e^{-\lambda_1 T}-e^{-\lambda_R T})\Big\} \tag{15}$$

From (12), (14) and (15) we can calculate $I_\beta(t)$, where T is considered as a parameter. The results of these calculations are shown in Fig. 5, where an example of observed values is also shown.

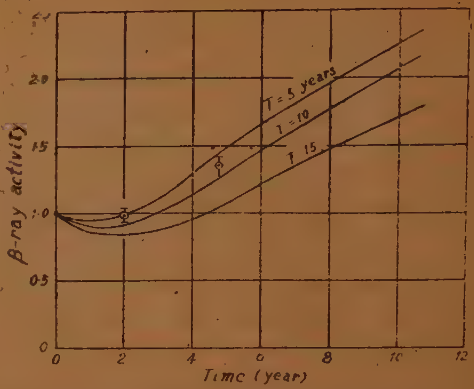

Fig. 5. Long period variation of the β-ray activity of thoriated tungsten wire.

Unfortunately, however, the age T of the original ThO$_2$ is not known and it is certain only that the age is not younger than five years.

It seems very natural that the observed points lie between the calculated curves of $T=5$ and 10 years respectively.

§ 6. Conclusions.

From these facts described above we must attend to the following points when we are going to determine the Th content of thoriated tungsten wire by activity measurement;

(i) Measurement activity of new wire must be performed at least two weeks after its manufacturing.

(ii) Determination of the absolute value of content must be performed by comparing with a chemically analysed standard wire.

(iii) During a period counted by years the activity varies cocsiderably.

In conclusion the authors express their cordial thanks to Mr. R. Akiyama of our research laboratory for his kind preparations of thoriated tungsten ingots, and also to the Ministry of Education for financial aids.

References.

(1) I. Nonaka and M. Yokota: Toshiba Review, 2 (1947), 41. (in Japanese).
(2) Madame Pierre Curie: "Radioactivité" p. 463. (1935).

The Efficiency of the Geiger-Müller Counter for the High Energy γ-Rays II.

By Masateru SONODA.

Department of Physics, Faculty of Science, University of Kyoto.

(Received April 13, 1950)

§ 1. Introduction.

In order to obtain the absolute number of the incident β particles or γ-quanta from the measurements with counter, it is always necessary to determine the efficiency of the counter, i. e. the counting property per one particle or quantum.

For β counter, the window foil is generally thin as compared to the range of the β particle and the absorption of β particles in the foil itself can be neglected. According to Danforth and Ramsey(1), the β particle coming into the effective domain of the counter can be counted at the rate of nearly 100% when the gas pressure in the counter is more than about 8 cmHg. Since an ordinary counter is used at the pressure greater than this value, the efficiency for β particle can be practically considered to be 100% when the absorption in the window foil can be neglected. When this condition is not valid, the penetration probability of the β particle discussed later must be considered.

For the γ-rays, the problem is more complicated. A few workers2)-8)23) studied this problem for the γ-rays of comparatively low energies up to about 5 mc^2, and some rasults were obtained for the brass or aluminium counter. There is, however, no reliable knowledge for the high energy γ-rays such as emitted by the (Li-p) or (F-p) reactions*. The author tried in the preceding paper** to calculate theoretically the efficiency of the thick walled lead counter for the high energy γ-rays which is generally used in our laboratory, since the experimental determination belongs to a very difficult thing in the present state of matter. In that paper, the effects of multiple scattering and radiation loss of the secondary electrons were neglected in the consideration for the sake of simplicity. This assumption is, however, not rigorously true, since actually the secondary electrons suffer the multiple scattering and the radiation loss. Furthermore, these effects are more important for the wall substance of the larger atomic number such as lead and therefore the numerical values calculated in the preceding paper give only the upper limit of the efficiency. A new calculation has been made in this paper by taking these effects into account.

§ 2. General Method.

In order to simplify the calculation, we presumably replace at first the cylindrical counter by a rectangular one with equal cross section. The direction of the incident γ-ray was assumed to be normal to a pair of plates of the same thickness as the cylindrical counter as shown in Fig 1. The necessary correction due to the oblique incidence of the γ-ray would be considered later.

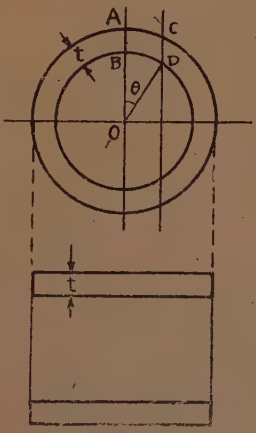

Fig. 1.

Now at first we must consider the angular distribution of the secondary electrons. It can be infered immediately from Klein-Nishina's formula(11) for the Compton recoil process which shows that most of secondary electrons are emitted in the forward direction. The photoelectric effect is extremely small in our energy range(10) and therefore can be neglected without serious error.

---

* A preliminary report of this paper was given at the meeting of the Institute for Chemical Research, Kyoto University. November, 1949. Rep. of Inst. Chem Res. Kyoto Univ. 20 in print.

* A theoretical calculation was made by H. Yukawa and S. Sakata for the energies up to 10 Mev9).

** Reference (10): hereafter cited as I.

On the contrary, the pair creation process contributes consriderably to the efficiency in such high energy region. H. Bethe(11) has calculated theoretically the angular distribution of the pair components and shown that the solid angle θ in which the electrons are emitted is of the order of $\theta \sim mc^2/h\nu$ and that the great majority of electrons are emitted in the direction of the incident γ-ray*.

Accordingly we can reasonably assume in the following calculation that all the electrons produced are emitted in the forward direction.

The the efficiency $\eta_{\square}(h\nu,t)$ of the rectangular counter of the thickness t for the γ-quantum of enecrgy $h\nu$ may be given by the following expession

$$\eta_{\square}(h\nu,t) = \int \exp[-\tau(t-x)]dx \int [\sigma_c(h\nu,E)p(E,x) + \{2\sigma_p(h\nu,E)p(E,x) - \sigma_p(h\nu,E)p(E,x) \times p(h\nu-E,x)\}]dE \quad \text{........ (1)}$$

where τ	is the absorption coefficient of the γ-quantum considered, from the inner surface of wall where the secondary electron is produced, and
$\sigma_c(h\nu,E)$	are the probability for the production of secondary electron of energy E by the incident γ-quantum of energy $h\nu$ by the Compton effect and the pair creation process respectively, and
$p(E,x)$	is the probability with which the electron of energy E can penetrate through the thickness x of the wall.

In the case of the pair creation, the two electrons (positive and negative) are emitted at the same time. Therefore both of these components can simultaneously penetrate into the effective space of the counter when x is smaller than a certain critical value determined by the energy of the incident γ-ray. These two particles are assumed to cause only one discharge and counted as one because they may come into the effective space within the resolving time of the counter. This fact is expressed in Eq (1) by the expression

$$2\sigma_p(h\nu,E)p(E,x) - \sigma_p(h\nu,E)p(E,x)p(h\nu-E,x)$$

which means the total probability that either positive or negative component or both of them simultaneously come into the counting space. The probability for the production of the secondary electron σ_c and σ_p can be calculated by the ordinary theory of quantum mechanics(11).

§ 3. Probability of Penetration.

In order to calculate the probability of the penetration of the secondary electrons, the losses by the scattering and the radiation must be taken into account. We consider at first the effect of the multiple scattering by the method of Fowler and others(13)*.

(I) *Multiple Scattering*

The electron beam of homogeneous energy which is initially parallel is diverged by multiple scattering and the number of electrons moving in the initial direction decreases gradually with the distance. Finally the divergence of the beam becomes so large that the complete diffusion of electrons occurs and an "apparent absorption coefficient" may be used in the calculation.

In the region of the multiple scattering, the probability $p_c(E,x)$ of an electron of energy E remaining within a cone of angle ϕ after travelling a distance x is given, according to W. Bothe(14) by the expression

$$p_c(E,x) = 1 - \int_{\phi}^{\infty} \frac{\theta}{\lambda_2} e^{-\theta^2/2\lambda^2} d\theta = 1 - \exp[-\phi^2/2\lambda^2] \quad ..(2)$$

λ is the most probable scattering angle and is given by

$$\lambda^2(E,x) = 4\pi r_0^2 NZ\left(\frac{E}{E^2-1}\right)^2\left(\log\frac{R}{p_1} - \frac{11}{12}\right)x \quad ...(3)$$

where N and Z are the number of atoms per cc and the atomic number of the wall substance respectively, $r_0 = e^2/mc^2$ is the classical electron radius, R is the atomic radius ($\approx 1.5 \times 10^{-8}$), and p_1 is the lower limit of impact parameter ($\approx 10^{-10}$). E is measured in mc^2 unit.

---

* Recently a series of observations with Wilson chamber has been made for 17 Mevγ -ray in our laboratory(19). The results are taken to agree well with the theoretical expectation though these are not decidedly conclusive because the number of the observed tracks is not sufficiently large.

* The calculated the efficiency of the aluminium counter, when the wallthick ness is great compared to the range of secondary electron. Their wall thickness must, therefore, be greater than 2·5 cm for the (Li-p) γ-ray. This is not practical.

Substituting the approximate values of R and p_1, we obtain

$$\lambda^2(E,x) = c^2x/E^2 \qquad (3')$$

$$\text{where } c^2 = 16\pi r_0^2 NZ \qquad (4)$$

In the case of the lead wall

$$c^2 = 8.87 \times 10^2 \qquad (4')$$

We must determine λ^2 when an electron of initial energy E_0 traverses the thickness x. λ^2 is proportional to the mean square scattering. The mean square scattering in x is equal to the sum of the values in each elementary thickness dx and so we have

$$\lambda^2(E_0,x) = \int_0^x c^2/E^2\, dx \qquad (5)$$

where

$$E = E_0 - \int_0^x -(dE/dx)_{coll}\, dx \qquad (6)$$

The integrand $-(dE/dx)_{coll}$ means the energy loss by the collision only. It was calculated by several workers(11). According to them, it is nearly constant in the region of high energy considered and is approximately equal to 21.3 mc²/cm for Pb and namely

$$-(dE/dx)_{coll} \doteq k = 21.3 \qquad (7)$$

Then Eq (6) and (5) become

$$E = E_0 - kx$$

$$\lambda^2 = \frac{c^2x}{E_0(E_0-kx)} \qquad (5')$$

Substituting these values into Eq (2), we obtain for Pb

$$p_c(E_0,x) = 1-\exp\left[-E_0(E_0-kx)\phi^2/2c^2x\right] \qquad (8)$$

$$= 1-\exp\left[-E_0(E_0-21.3x)\phi^2/1.77\times 10^3\right] \qquad (8')$$

In our case ϕ is given by

$$\phi = \arccos\, x/R_0(E_0)$$

where $R_0(E_0)$ is the average range of electron of energy E_0, when only the collision process is considered (excluding the radiation loss). It can be written as

$$R_0(E_0) = \int_0^{E_0} \frac{dE}{-(dE/dx)_{coll}} \qquad (10)$$

With Eqq (9), (10) and (8), $p_c(E_0,x)$ can be calculated for the region of multiple scattering.

The beam of electrons is diverged more and more for the larger x and the complete diffusion begins in the long run at a certain value of x. The above formula becomes invalid beyond this critical value.

W. Bothe(14) has theoretically found that the critical value of the most probable scattering angle is 33° = 0.576 radian*

The formula (8) for the multiple scattering will hold until λ becomes equal to 0.576. So that the thickness of penetration d, above which the diffusion appears, is given from Eq (5′) as

$$d = \lambda_d E_0^2/(c^2+\lambda_d^2 E_0 k) \qquad (11)$$

where $\lambda_d = 0.576$. Numerical values of d for several initial energies E_0, are shown in Fig 2 in the case of Pb.

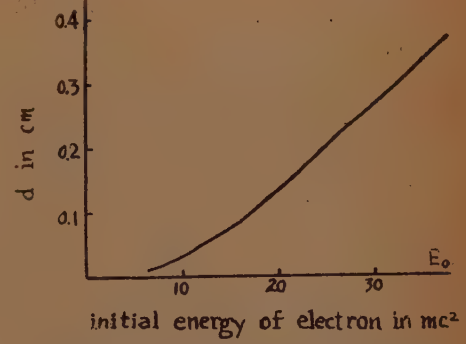

Fig. 2. Relation between d and E_0

In the diffusion region (i. e. $x > d$), the probability of penetration is given by the following formula in which $1.3\lambda^2/x$ is the so-called "apparent absorption coefficient"(14).

$$-(1/p)(dp/dx) = 1.3\lambda^2/x = 1.3c^2/E^2 \qquad (12)$$

Then

$$p_c(E_0,x) = p_d \exp\left[-1.3c^2\int_d^x \frac{dx}{E^2}\right] \qquad (13)^{**}$$

---

* The experimental value is between 30° and 34°.

** Fowler and others assumed that $-(dE/dx)$ is also constant in this case. This assumption is, however, not rigorously true, since the electrons are near the end of their range in the case of complete diffusion and their energy may be considerably smaller than in the multiple scattering.

in which E is given by Eq (6). $p_c(E_0,x)$ can be calculated numerically from the above equation. The constant of integration p_d must be chosen so that Eq (13) may be fitted smoothly to Eq (8) at the point $x=d$, where the diffusion beginns. Namely

$$p_d = p(E_0,d)$$

(*II*) *Radiation Effect.*

Throughout the range, the effect of radiation loss must be supperposed. W. A. Fowler(15) considered that the radiation usually results in large energy loss by a relatively few particles and therefore the contribution due to the radiation loss would be given by the following equation.

$$(1/p_r)(dp_r/dx) = -N\phi_{rad} \qquad (14)$$

where $N\phi_{rad}$ is the radiation probability in the wall substance and is considered to be nearly constant in the energy range under consideration. In a rough approximation, therefore, we have

$$N\phi_{rad} = 1.1\mathrm{cm}^{-1} \quad \text{for Pb} \qquad (15)$$

On integration of Eq (14), the effect of radiation can be expressed by

$$p_r = \exp(-N\phi_{rad}x) \qquad (16)$$

The total probability of penetration may therefore be given as the product of $p_o(E_0,x)$ and $p_r(E_0,x)$, and written as follows

$$p(E_0,x) = \exp(-1.1\,x)$$
$$\times[1-\exp\{-E_0(E_0-21.3x)\phi^2/1.77\times10^8\}] \qquad (17)$$

in the multiple scattering region and

$$p(E_0,x) = \exp(-1.1x)p_d\exp\left[-1.3c^2\int_d^x\frac{dx}{E^2}\right]. \qquad (17')$$

in the diffusion region.

§ 4. Effect of Secondary Radiation.

The secondary electrons emitted by an incident γ-quantum falling on the counter can radiate $h\nu'$ by the brehmstrahlung effect. This brehmstrahlung can emit another electron and may be counted by the counter. The effect of this additive counts must be considered.

The number of secondary electrons of energy E_0 emitted at a point x distant from the inner surface of the counter is given by

$$n(E_0,x)dx = \exp[-\tau(t-x)]\sigma(h\nu,E_0)\,dx \qquad (18)$$

where $\sigma(h\nu,E_0)$ is the probability for the production of the electron of energy E_0 by the γ-quantum $h\nu$.

These electrons will decrease in number by scattering and radiation during the penetration of distance y. This decrease was discussed in the preceding section and is given as follows

$$n(E_0,x)\,dx\,p(E_0,y) \qquad (19)$$

The number of the quanta of the secondary radiation emittad at the point y is therefore

$$n(E_0,x)\,dx\,p(E_0,y)\,N\phi_{rad}dy \qquad (20)$$

If the average energy of secondary radiation emitted by the electron of energy E_0 is denoted by $\overline{h\nu}(E_0)$, the counting probability for the above mentioned secondary radiation is given by

$$n(E_0,x)\,dx\,p(E_0,y)N\phi_{rad}dy\eta(\overline{h\nu},x-y) \qquad (21)$$

The total effect of the secondary radiation is, therefore, given by the integration of Eq. (21), and namely

$$\iiint n(E_0,x)p(E_0,y)N\phi_{rad}\eta(\overline{h\nu},x\text{-}y)\,dx\,dy\,dE_0$$
$$=\iiint\exp[-\tau(t-x)]\sigma(h\nu,E_0)p(E_0,y)$$
$$\times N\phi_{rad}\eta(\overline{h\nu},x-y)dx.dy\,dE_0 \qquad (22)$$

In calculating the above integral, we must determine the average γ-ray energy $\overline{h\nu}(E_0)$. This quantity is given by

$$\overline{h\nu}(E_0) = \int h\nu'\varphi(E_0,h\nu')d(h\nu')\Big/\int\varphi(E_0,h\nu')d(h\nu') \qquad (23)$$

where $\varphi(E_0,h\nu')$ is the differential probability of emitting the secondary radiation of energy $h\nu'$ by an electron of energy E_0. φ can be given by the results of the quantum mechanical calculation(11). Unfortunately, however, this quantity diverges for the small value of $h\nu'$. (infrared catastrophe). We must therefore perform the process of cutting off at a certain small value of $h\nu'$. By actual trials, the energy value of the out-off point turns out not to affect the final results seriously. We therefore select the cut-off value of $h\nu'$ as $h\nu' = 1\ \mathrm{mc}^2$.

This means the assumption that the γ-quanta of energy below 1 mc^2 do not contribute seriously to the result and is consistent with the neglection of the annihilation γ-quanta of positron emitted by the pair creation.

Then Eq. (23) can be calculated and is found to be less than 10 mc^2 for the electron enrgy below 35 mc^2.

Since the value of $\eta(\overline{h\nu},x-y)$ is only 3% at most in such a low energy region, we can take in a rough approximation as follows,

$$\eta(\overline{h\nu},x-y) = \text{const} = 1.5\%$$

Then Eq (22) becomes

$$1.65\int_0^t \exp[-\tau(t-x)]dx\int_0^x dy\int_0^{h\nu}\sigma(h\nu,E_0)p(E_0,y)dE_0 \tag{24}$$

The integration is performed by the graphical method and is found to be only 0.5% for $h\nu = 34$ mc^2 and $t = 0.65$ cm.

§ 5. Results.

Substituting Eqq. (17) and (17′) into Eq. (1), we can calculate the efficiency $\eta_\square(h\nu,t)$ of the rectangular counter. The results are shown in Table I and Figg. 3, 4.

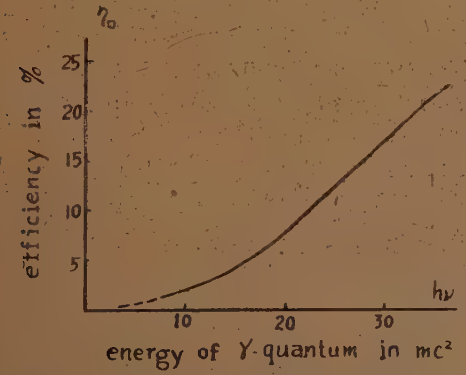

Fig. 3. Efficiency of Rectangular Lead Counter of Wall Thickness 6.5 mm.

In the actual cases, however, the cylindrical counters are commonly used and so the correction due to the cylindrical shape must be considered.

If the γ-ray falls on the cylindrical counter with the angle θ as indicated by the straight line CD in Fig 1, the effective thickness of the wall varies with the angle θ, and so the efficiency also

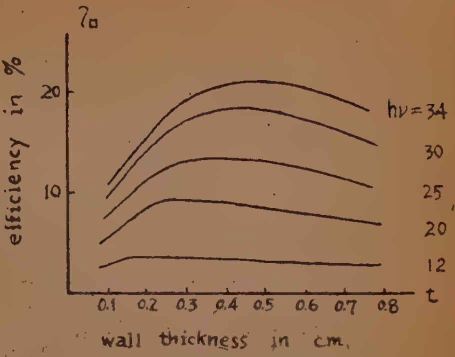

Fig. 4. Efficiency of Rectangular Lead Counter of Different Wall Thickness for Various γ-Ray Energies.

Tabie I. The Efficiency of the Rectangular Counter

wall thickness in cm	energy of γ-ray quantum in mc^2 12	20	25	30	34
0.65	3.0%	7.8%	12.4%	17.0%	20.2%
0.60	3.1	8.1	12.8	17.5	20.7
0.50	3.3	8.7	13.3	18.2	21.4
0.40	3.4	9.2	13.6	18.4	21.0
0.30	3.6	9.4	13.4	17.6	19.6
0.20	3.7	8.9	11.9	14.7	16.0
0.10	3.3	6.4	8.3	10.1	11.2

varies with θ. The efficiency η_0 for the cylindrical counter is given by

$$\eta_0 = \int\eta(\theta)\cos\theta\, d\theta \tag{25}$$

in which $\eta(\theta)$ can be obtained from the results for the rectangular counter. The numerical values obtained for the counter of inner diameter 2 cm are shown in Table II and Figg. 5 and 6.

Table II. The Efficiency of the Cylindrical Counter (inner diameter 2 cm)

wall thickness in cm	energy of γ-ray quantum in cm^2 12	20	25	35	34
0.65	2.9%	7.6%	12.0%	16.4%	19.3%
0.60	3.0	7.8	12.3	17.0	20.1
0.50	3.3	8.4	13.0	18.1	21.4
0.40	3.5	9.0	13.6	18.7	21.7
0.30	3.7	9.5	13.6	18.5	21.0
0.20	3.7	9.3	13.3	16.3	18.1

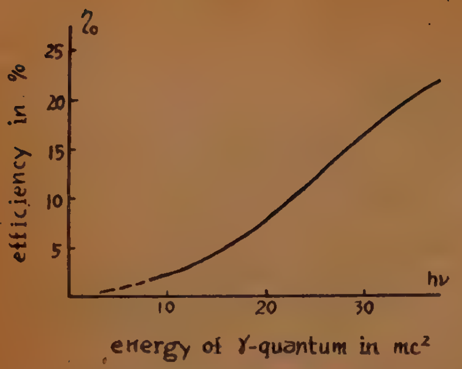

Fig. 5. Efficiency of Cylindrical Lead Counter of Wall Thickness of 6.5 mm and Inner Diameter 2 cm.

Fig. 5 shows the relation between the efficiency and the energy of the incident γ-ray for the lead counter of the wall thickness 6.5 mm and the inner diameter 2 cm, which we are daily using in the experiments determining the absolute values of the cross section of various photonuclear effects. Fig. 6 is the efficiencies for various thicknesses of the lead counter of the inner diameter 2 cm.

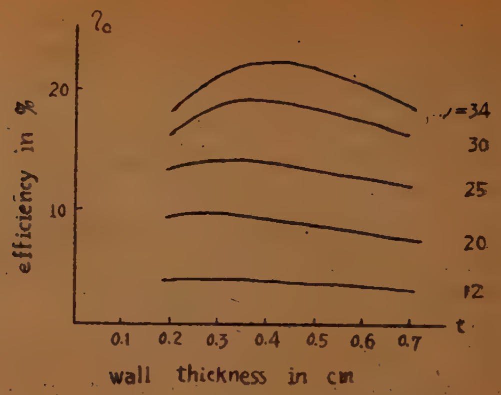

Fig. 6. Relation between Efficiency and Wall Thickness of Cylindrical Lead Counter of Inner Diameter 2 cm for Various γ-Ray Energies.

The Efficiency of the Geiger-Müller Counter for the High Energy γ-Rays III.

By Masateru SONODA.

Department of Physics, Faculty of Science, University of Kyoto.

(Received April 13, 1950.)

In the calculation described in the paper II, the effect of radiation was assumed to be expressed by the equation (16). In the brehmstrahlung effect, however, the quantum of smaller energy is radiated with greater probability and most of electrons still possess the considerable energies after the emission of brehmstrahlung. These electrons can therefore penetrate into the effective space of the counter. They were assumed not to be counted in that paper. The value of $p_r(E_0, x)$ calculated there might be somewhat underestimated.

Generally speaking, there may occur the multiplication process like the cosmic ray shower, when an electron or a γ-quantum of high energy enters into a substance. The theory of the comic ray shower[15] has been developed by many authors since the original papers of Bhabha-Heitler[16] and Oppenheimer-Carlson[17] were published.

We try in this paper to investigate the penetration probability in a method similar to the shower theory.

§ 6. Consideration by Shower Theory.

Now if $n_e(E, x)$ is the number of the electrons of energy E produced by the multiplication process at the depth of x distant from the point where the initial electron of energy E_0 is produced. (See Fig. 7).

The total probability of penetration with which the electron of energy E_0 can travel through the distance x will be given by

$$p_r(E_0, x) = \int_1^{E_0} n_e(E, x)\, dE \tag{26}$$

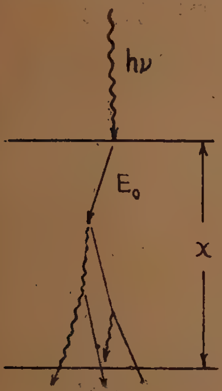

Fig. 7.

As in the shower theory, the equation satisfied by $n_e(E, x)$ can be obtained as follows. In the given thickness dx, the number of electrons with energy between E and $E+dE$ undergoes the change because of the following effects.

(a) Photons with energy $h\nu$ larger than E produce a certain number of electrons in the energy range $(E, E+dE)$. This number is

$$dE\, dx \int_{h\nu>E} n_\nu(h\nu, x)\,[\sigma_c(h\nu, E)+2\sigma_p(h\nu, E)]\, d(h\nu) \tag{27}$$

where $n_\nu(h\nu, x)$ is the number of photons of energy $h\nu$, produced by an electron of initial energy E_0.

(b) Some electrons with energy E' larger than E enter into the interval $(E, E+dE)$ by radiating part of their energy $E'-E$. Their number is

$$dE\, dx \int_E^{E_0} n_e(E', x)\,\varphi(E', E'-E)\, dE' \tag{28}$$

where $\varphi(E', h\nu)$ is the probability with which an electron of energy E' radiates a quantum of energy $h\nu$.

(c) Some electrons initially in the interval $(E, E+dE)$ leave this interval by the radiation loss. Their number is

$$n_e(E, x)\int_0^{E-1} \varphi(E, h\nu)\, d(h\nu) \tag{29}$$

The number of photons $n_\nu(h\nu, x)$ undergoes a similar change.

(d) Electrons with energy E' larger than $h\nu$ radiate a certain number of photons in the energy interval $(h\nu, h\nu+d(h\nu))$. This number is

$$d(h\nu)\, dx \int_{h\nu}^{E_0} n_e(E', x)\,\varphi(E', h\nu)\, dE' \tag{30}$$

(e) Some photons initially in the interval $(h\nu, h\nu+d(h\nu))$ are absorbed by the pair creation and the Compton effect. Their number is

$$d(h\nu)\, dx\, n_\nu(h\nu, x)\,\tau(h\nu) \tag{31}$$

where $\tau(h\nu)$ is the absorption coefficient of the γ-quantum of energy $h\nu$.

Therefore

$$\frac{\partial n_e(E, x)}{\partial x} = \int_{h\nu>E} n_\nu(h\nu, x)[\sigma_c(h\nu, E)+2\sigma_p(h\nu, E)]\, d(h\nu) + \int_E^{E_0} n_e(E', x)\,\varphi(E', E'-E)\, dE' - n_e(E, x) \times \int_0^{E-1} \varphi(E, h\nu)\, d(h\nu) \tag{32}$$

$$\frac{\partial n_\nu(h\nu, x)}{\partial x} = \int_{h\nu}^{E_0} n_e(E', x)\,\varphi(E', h\nu)\, dE' - n_\nu(h\nu, x)\,\tau(h\nu) \tag{33}$$

In the shower theory, we can make use of the assumption that E_0 is infinitely large and therefore Eqq. (32) and (33) can be solved. This assumption is, however, not valid is our case and the problem becomes very difficult. Accordingly the following simplified method was adopted.

An electron of energy E can radiate a photon of energy between 0 and E with a certain probability. However, we consider for simplicity that the electron emits a photon of the mean energy $\overline{h\nu}(E)$ with the total radiation probability. $\overline{h\nu}$ is given by Eq. (23) in the paper II. Namely

$$\overline{h\nu}(E) = \int_0^{E-1} h\nu\,\varphi(E, h\nu)\, d(h\nu) \quad \int_0^{E-1} \varphi(E, h\nu)\, d(h\nu) \tag{23}$$

Then Eqq. (32) and (33) are simplified as follows.

$$\frac{\partial n_e(E, x)}{\partial x} = \int_{h\nu>E} n_\nu(h\nu, x)[\sigma_c(h\nu, E)+2\sigma_p(h\nu, E)]\, d(h\nu) + n_e(\bar{E}', x)\,\phi(\bar{E}') - n_e(E, x)\,\phi(E) \tag{32'}$$

$$\frac{\partial n_\nu(h\nu, x)}{\partial x} = n_e(\bar{E}'', x)\,\phi(\bar{E}'') - n_\nu(h\nu, x)\,\tau(h\nu) \tag{33'}$$

where $\phi(E)$ is the radiation probability of the electron of energy E.

Namely

$$\phi(E)=\int\varphi(E,h\nu)\,d(h\nu) \qquad (34)$$

$\bar{E}'$ is the energy such that an electron of energy $\bar{E}'$ radiates a photon of a certain mean energy $\bar{h\nu}'$ and falls to the state of the energy E. (i.e. $\bar{E}'=E+\bar{h\nu}'$). And $\bar{E}''$ is the energy such that an electron of energy $\bar{E}''$ radiates a photon of the mean energy $h\nu$.

If the energy E_0 of the initial electron is given, Eqq. (32′) and (33′) can be successively solved for each value of E.

Then we can calculate $p_r(E_0, x)$ by Eq. (26). The results obtained are shown in Table 3 and Fig. 8. In Fig. 8, the values by Fowler method are also shown for comparison.

Table 3. Probability $p_r(E_0, x)$

E_0 in mc²	Thickness t In cm.									
	0.1	0.2	0.3	0.4	0.5	0.6	0.7	0.8	0.9	1.0
34	0.99	0.96	0.93	0.89	0.84	0.78	0.71	0.66	0.60	0.55
30	0.99	0.96	0.93	0.88	0.82	0.75	0.70	0.65	0.60	0.55
26	0.99	0.96	0.93	0.88	0.83	0.77	0.71	0.66	0.61	
22	0.99	0.96	0.98	0.88	0.84	0.78	0.74			
18	0.99	0.96	0.93	0.89	0.85	0.80				
14	0.99	0.97	0.94	0.90						
10	0.99	0.98	0.95	0.92						

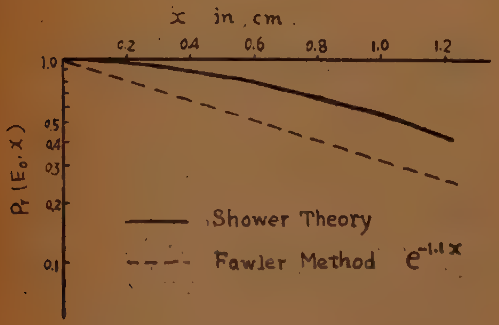

Fig. 8. Probability $p_r(E_0, x)$ for $E_0=34\,mc^2$

The total probability of penetration $p(E_0, x)$ is given similarly to Eqq. (17) and (17′) in the paper II. Namely

$$p(E_0, x)=p_r(E_0, x)\times[1-\exp\{-E_0(E_0-21.3x)\phi^2/1.77\times10^3\}] \qquad (35)$$

in the multiple scattering region and

$$p(E_0, x)=p_r(E_0, x)\,p_d\exp\left[-1.3\,c^2\int_0^x\frac{dx}{E^2}\right] \qquad (35')$$

in the region of the complete diffusion.

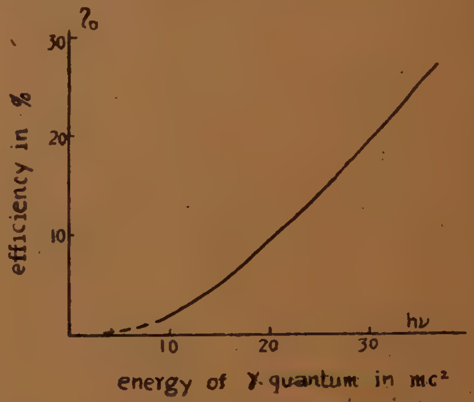

Fig. 9. Efficiency of Rectangular Lead Counter of Wall Thickness 6.5 mm.

Using Eqq. (35) and (35′) the counting efficiency for the rectangular counter can be calculated by Eq. (1) and is shown in Table 4 and Fig. 9, 10.

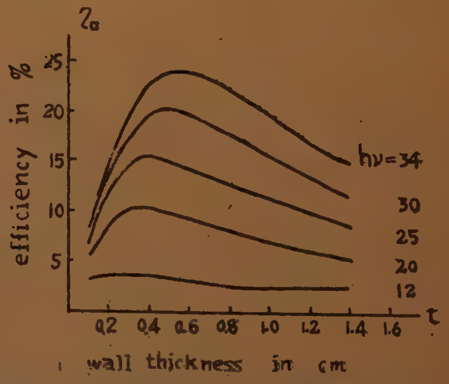

Fig. 10. Relation between Efficiency and Wall Thickness of Rectangular Lead Counter for Various γ-Ray Energies.

Table 4. The Efficiency of the Rectangular Counter.

Wall thickness in cm.	Energy of γ-ray quantum in mc²				
	12	20	25	30	34
0.10	3.1%	5.7%	6.9%	7.5%	7.6%
0.20	3.6	9.0	12.4	14.0	14.7
0.30	3.5	10.4	15.0	18.1	20.0
0.40	3.4	10.3	15.3	19.6	22.8
0.50	3.3	10.0	15.0	20.0	23.7
0.60	3.2	9.4	14.5	19.6	23.8
0.65	3.1	9.2	14.1	19.1	23.6
0.70	3.1	8.9	13.7	18.7	23.2

Table 5. The Efficiency of the Cylindrical Counter (inner diameter 2 cm.).

Wall thickness in cm.	Energy of γ-ray quantum in mc²				
	12	20	25	30	34
0.20	3.7%	9.7%	13.6%	16.0%	17.4%
0.30	3.6	10.4	15.2	19.1	21.8
0.40	3.4	10.2	15.0	19.8	23.5
0.50	3.2	9.7	14.4	19.6	23.7
0.60	3.1	9.0	13.8	18.8	23.2
0.65	3.0	8.7	13.5	18.3	22.8

The correction for the cylindrical shape was made by Eq. (25) as in the Fowler method. The results for the cylindrical lead counter described in the preceding paper, are listed in Table 5 and shown in Fig. 11 and 12.

It is seen from the figures that the efficiency increases at first with the thickness and then it decreases owing to the futile absorption of the γ-ray. Moreover, the efficiency of the constant wall thickness is roughly proportional to the energy of the incident γ-quantum except for the case of the very thin wall thickness.

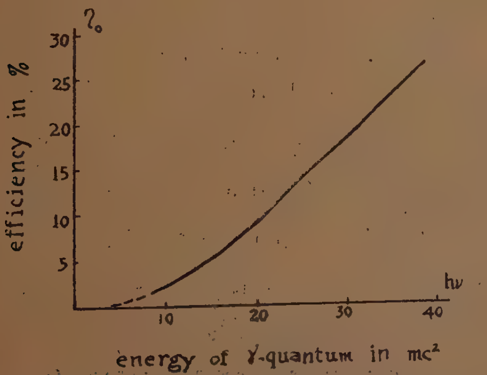

Fig. 11. Efficiency of Cylindrical Lead Counter of Wall Thickness 6.5 mm. and Inner Diameter 2 cm.

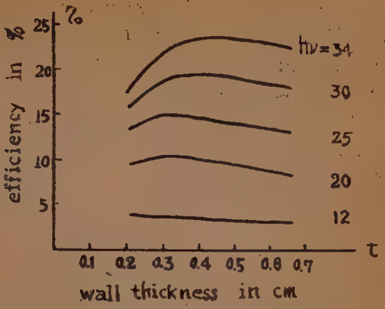

Fig. 12. Relation between Efficiency and Wall Thickness of Cylindrical Lead Counter of Inner Diameter 2 cm. for Various γ-ray Energies.

These values have been used in our laboratory for obtaining the cross sections of various photonuclear effects produced by the (Li-p) and (F-p) γ-rays and have been proved to be satisfactorily useful.

In conclusion the author wishes to express his cordial gratitude to Prof. B. Arakatsu, Prof. M. Kobayashi and Prof. K. Kimura for helpful suggestions and valuable discussions.

References.

(1) W. E. Danfoth and W. E. Ramsey: Phys. Rev. **49**, 854 (1936).
(2) H. J. v. Baeyer: ZS. f. Phys. **95**, 429 (1935).
(3) G. F. v. Droste: ZS. f. Phys. **100**, 529 (1936).
(4) G. J. Sizoo and H. Willemsen: Physica **5**, 105 (1936).
(5) F. Norling: Phys. Rev. **58**, 277 (1940).
(6) J. v. Dunworth: Rev. Sci. Inst. **11**, 107 (1940).
(7) I. Nonaka; Proc. Phys-Math. Soc. Jap. **25**, 227 (1943).
(8) K. Buchmann: Phys. Zeits. **38**, 817 (1937).
(9) H. Yukawa and S. Sakata: Sci. Pap. Phys-Chem. Res. **31**, 187 (1937).
(10) M. Sonoda: Journ. Phys. Soc. Jap. **5**, 53 (1950).
(11) See for example W. Heitler: Quantum Theory of Radiation 1936 Oxford Press.
(12) H. Bethe: Proc. Cambr. Phil. Soc. **30**, 524 (1934).
(13) W. A. Fowler, C. C. Lauritsen and T. Lauritsen: Rev. Mod. Phys. **20**, 258 (1948).
(14) W. Bothe: Handbuch der Physik, XX, II/2 (1933).

(15) See for example B. Rossi and K. Greisen: Rev. Mod. Phys. **13**, 240 (1941).
(16) H. J. Bhabha and W. Heitler: Proc. Roy. Soc. **159**, 432 (1937).
(17) J. F. Carlson and J. R. Oppenheimer: Phys. Rev. **51**, 220 (1937).
(18) B. Arakatsu and others: Proc. Phys-Math. Soc. Jap. **23**, 440, 633 (1941); ibid. **25**, 173 (1943); Journ. Phys. Soc. Jap. **1**, 24 (1946).
(19) S. Shimizu and J. Muto: Memo. Coll. Sci. Kyoto Univ. A **25**, No. 2, Art. 11 (1949).
(20) A. Roberts, J. R. Downing and M. Deutsch: Phys. Rev. **60**, 544 (1941).

On the Spectrum of Turbulence.

By Ken-ichi KUZUKAWA.

Physical Institute, Faculty of Science, Tôkyô Metropolitan University.

(Received April 27, 1950)

§ 1. Introduction.

About the spectrum of turbulence, many authors have already discussed in these days. Thus Taylor, Kármán and Howarth etc. have discussed the functional relation between the spectrum function and the correlation function, but their theories are semi-empirical. Recently, C. F. von Weizsäcker and W. Heisenberg have deduced that the spectrum of the energy in one dimension is proportional to $-5/3$ power of the wave number, from the fundamental assumption of "mechanical similarity".

This theory, however, is correct only in the case that the considered vortex is sufficiently larger than the smallest vortex, and sufficiently smaller than the largest vortex. And the experiment shows that this condition is not satisfied in the usual wind tunnel. Now, present writer will show the quantum-theoretical method by which the spectrum of the turbulence can be deduced. This spectrum will be compared to the measurement of Taylor in the last paragraph.

§ 2. Fundamental Equation.

The fundamental equation of the viscous fluid is

$$\rho\partial V/\partial t+\rho(V,\ \mathrm{grad}\ V)=-\mathrm{grad}\,p+\rho\nu\Delta V \qquad (2,1)$$

Then we can introduce scalar and vector potentials by the following definition.

$$V=\mathrm{grad}\,\Phi+\mathrm{rot}\,\Psi. \qquad (2,2)$$

Now we shall take the cartesian coordinates which are fixed with respect to the general flow. Considering the case where Reynolds number is very small, or

$$R_L=|V|L/\nu\ll 1 \qquad (2,3)$$

We can neglect the inertia term of the equation (2,1).

"L" in the condition (2, 3), is the characteristic length, which is represented by the radius of the vortex. Therefore we may consider the condition (2.3) is correct at the final period in the wind tunnel.

From the equations (2,1), (2,2), and (2,3), we can obtain the following equation

$$\rho\partial/\partial t\,\mathrm{rot}\,\Psi=-\mathrm{grad}\,p+\rho\nu\Delta\,\mathrm{rot}\,\Psi. \qquad (2,4)$$

Introducing tne function S by the formula

$$p/\rho=\partial S/\partial t \qquad (2,5)$$

the equation (2,4) can be written in the following form

$$\rho\partial/\partial t\,(\mathrm{rot}\,\Psi+\mathrm{grad}\,S)=\rho\nu\Delta\,\mathrm{rot}\,\Psi. \qquad (2,6)$$

Introducing also the function ω by the following expression

$$\mathrm{rot}\,\boldsymbol{\Psi}+\mathrm{grad}\,S=\partial\boldsymbol{\omega}/\partial t \tag{2,7}$$

where

$$\boldsymbol{\omega}=(\xi,\ \eta,\ \zeta), \tag{2,8}$$

the fundamental equation takes the following form

$$\rho\partial^2\boldsymbol{\omega}/\partial t^2=\rho\nu\Delta\,\mathrm{rot}\,\boldsymbol{\Psi}. \tag{2,9}$$

Calculating the rotation of the equation (2,7)

$$-\Delta\boldsymbol{\Psi}=\partial/\partial t\,\mathrm{rot}\,\boldsymbol{\omega}. \tag{2,10}$$

From (2,9) and (2,10), we obtain

$$\rho\partial^2\boldsymbol{\omega}/\partial t^2=\rho\nu\partial\Delta\boldsymbol{\omega}/\partial t. \tag{2,11}$$

Integrating this we have

$$\partial\boldsymbol{\omega}/\partial t=\nu\Delta\boldsymbol{\omega}+\boldsymbol{U}(x,\ y,\ z), \tag{2,12}$$

where we consider ρ and ν are constants, and $\boldsymbol{U}(x, y, z)$ is an arbitrary function.
Substituting (2,12) in (2,11), we get the following form as the fundamental equation.

$$\rho\,\partial^2\boldsymbol{\omega}/\partial t^2=\rho\nu^2\Delta\Delta\boldsymbol{\omega}+\rho\nu\Delta\boldsymbol{U}(x,\ y,\ z). \tag{2,13}$$

§ 3. Lagrangian.

The "Lagrangian" or the function, from which the fundamental equation (2,13) can be derived by the variation method, can be given in the form:

$$L=\rho/2\,(\dot{\boldsymbol{\omega}},\dot{\boldsymbol{\omega}})+\rho\nu^2/2\,(\Delta\boldsymbol{\omega},\ \Delta\boldsymbol{\omega})+\rho\nu\,(\boldsymbol{\omega},\ \boldsymbol{U})$$
$$-(\alpha,\beta,\gamma)\begin{pmatrix}\xi_x, & \eta_x, & \zeta_x\\ \xi_y, & \eta_y, & \zeta_y\\ \xi_z, & \eta_z, & \zeta_z\end{pmatrix}\begin{pmatrix}\xi\\ \eta\\ \zeta\end{pmatrix}+C, \tag{3,1}$$

where the vector $\boldsymbol{A}=(\alpha, \beta, \gamma)$ is a vector function of time only, and C is a scalar constant.

§ 4. Canonical Variables, Hamiltonian, and Canonical Equations.

First we shall introduce the canonical variables in the following way.

$$(\xi,\ \eta,\ \zeta)=(Q_1\ Q_2\ Q_3), \tag{4,1}$$

$$\left.\begin{aligned}P_1&=\partial L/\partial\dot{Q}_1=\rho\dot{\xi},\\ P_2&=\partial L/\partial\dot{Q}_2=\rho\dot{\eta},\\ P_3&=\partial L/\partial\dot{Q}_3=\rho\dot{\zeta}.\end{aligned}\right\} \tag{4,2}$$

Then Hamiltonian may have the following form

$$H=\sum P\dot{Q}-L=1/2\rho\,(\boldsymbol{P},\ \boldsymbol{P})-\rho\nu^2/2\,(\Delta\boldsymbol{Q},\ \Delta\boldsymbol{Q})$$
$$-\rho\nu\,(\boldsymbol{Q},\ \boldsymbol{U})+(\alpha\,\beta\,\gamma)\begin{pmatrix}\xi_x, & \eta_x, & \zeta_x\\ \xi_y, & \eta_y, & \zeta_y\\ \xi_z, & \eta_z, & \zeta_z\end{pmatrix}\begin{pmatrix}\xi\\ \eta\\ \zeta\end{pmatrix}-C \tag{4,3}$$

The canonical variables are connected by the following relations, which are called Hamilton's canonical equations.

$$\bar{H}=\iiint H\,dx\,dy\,dz,$$
$$\begin{aligned}\dot{Q}_1&=\delta\bar{H}/\delta P_1, & \dot{P}_1&=-\delta\bar{H}/\delta Q_1,\\ \dot{Q}_2&=\delta\bar{H}/\delta P_2, & \dot{P}_2&=-\delta\bar{H}/\delta Q_2,\\ \dot{Q}_3&=\delta\bar{H}/\delta P_3, & \dot{P}_3&=-\delta\bar{H}/\delta Q_3.\end{aligned} \tag{4,4}$$

§ 5. Quantisation and Wave Epuation.

We shall quantise the equation (4,4) by the following relations.

$$\left.\begin{aligned}&[P_i(\boldsymbol{r}),\ Q_j(\boldsymbol{r}')]=-ik\,\delta_{ij}\,\delta(\boldsymbol{r},\ \boldsymbol{r}'),\\ &[P_i(\boldsymbol{r}),\ P_j(\boldsymbol{r}')]=0,\\ &[Q_i(\boldsymbol{r}),\ Q_j(\boldsymbol{r}')]=0,\end{aligned}\right\} \tag{5,1}$$

where, $\delta(\boldsymbol{r}, \boldsymbol{r}')$ is defined by the equation

$$\int F(\boldsymbol{r})\,\delta(\boldsymbol{r},\ \boldsymbol{r}')\,d\tau=F(\boldsymbol{r}').$$

Here, the universal constant "k" which is corresponding to Planck's constant "$\hbar$" in the quantum theory, should be determined by the character of the molecular motion of the considered fluid. We shall discuss the detail about this important constant in a later paragraph.

Now the wave equation becomes

$$\bar{H}\Psi=E\Psi. \tag{5.2}$$

§ 6. Development of the Variables in Fourier Series.

We shall develop the canonical variables $\boldsymbol{Q}(Q_1, Q_2, Q_3)$ and $\boldsymbol{P}(P_1, P_2, P_3)$ in Fourier series

$$P_j=\sum_{N=-\infty}^{\infty}p_{j,N}(t)\,l^{-3/2}\exp\{2\pi i(\boldsymbol{N}.\ \boldsymbol{r})/l\}$$
$$Q_j=\sum_{N=-\infty}^{\infty}q_{j,N}(t)\,l^{-3/2}\exp\{-2\pi i(\boldsymbol{N},\ \boldsymbol{r})/l\}. \tag{6,1}$$

where

$$p_{j,N}=\int_0^l\!\!\int_0^l\!\!\int_0^l P_j\,l^{-3/2}\exp\{-2\pi i(\boldsymbol{N},\ \boldsymbol{r})/l\}\,dx\,dy\,dz,$$
$$q_{j,N}=\int_0^l\!\!\int_0^l\!\!\int_0^l Q_j\,l^{-3/2}\exp\{2\pi i(\boldsymbol{N},\ \boldsymbol{r})/l\}\,dx\,dy\,dz. \tag{6,2}$$

Here "l" is a characteristic length which represents the largest special period of Q_j and P_j, and may be determined by some typical length of the wind tunnel or the mesh.

Considering the relations (5,1), we can derive the following relations between coefficients of the development.

$$\left.\begin{aligned} &[p_i\boldsymbol{N}_k,\ q_j\boldsymbol{N}_l] = -ik\delta_{ij}\delta_{\boldsymbol{N}_k\boldsymbol{N}_l} \\ \text{and of course } &[q_j\boldsymbol{N}_k,\ q_j\boldsymbol{N}_l] = 0,\ [p_j\boldsymbol{N}_k,\ p_j\boldsymbol{N}_l] = 0. \end{aligned}\right\} \tag{6,3}$$

Setting

$$\left.\begin{aligned} &\boldsymbol{A} = i\boldsymbol{A}^* = i(\alpha^*,\ \beta^*,\ \gamma^*) \\ &|\boldsymbol{A}^*|\cos(\boldsymbol{A}^*, \boldsymbol{N}) = \sigma.\quad |\boldsymbol{N}| = N, \end{aligned}\right\} \tag{6,4}$$

and the additional constant being

$$-3k(2\rho)^{-1/2}\sum(2\pi\sigma)^{1/2}l^{-1}N^{1/2} \tag{6,5}$$

the function $\bar{H}$ can be developed in the following form

$$\begin{aligned} \bar{H} = &(1/2\rho)\sum_{\boldsymbol{N}}(p_1{}^2\boldsymbol{N} + p_2{}^2\boldsymbol{N} + p_3{}^2\boldsymbol{N}) \\ &+ (2\pi/l)\sum\sigma N(q_1{}^2\boldsymbol{N} + q_2{}^2\boldsymbol{N} + q_3{}^2\boldsymbol{N}) \\ &- (\rho\nu^2/2)(16\pi^4/l^4)\sum N^4(q_1{}^2\boldsymbol{N} + q_2{}^2\boldsymbol{N} + q_3{}^2\boldsymbol{N}) \\ &- 3k(2\rho)^{-1/2}\sum(2\pi\sigma)^{-1/2}l^{-1/2}N^{1/2} \end{aligned} \tag{6,6}$$

Substituting $(k/i)\partial/\partial q_{j\boldsymbol{N}}$ for $p_{j\boldsymbol{N}}$, we obtain the wave equation

$$\bar{H}(q_{j\boldsymbol{N}},\ (k/i)\partial/\partial q_{j\boldsymbol{N}})\Psi = E\Psi, \tag{6,7}$$

where α^*, β^* and γ^* are real functions of time.

§ 7. Stationary State and Perturbation Theory.

We shall presume the term of the viscosity to be that of perturbation, or,

$$\bar{H} = \bar{H}_0 + \bar{H}',$$

where

$$\begin{aligned} \bar{H}_0 = &-\frac{k^2}{2\rho}\sum\left(\frac{\partial^2}{\partial q_1{}^2\boldsymbol{N}} + \frac{\partial^2}{\partial q_2{}^2\boldsymbol{N}} + \frac{\partial^2}{\partial q_3{}^2\boldsymbol{N}}\right) \\ &+ \sum\frac{2\pi\sigma}{l}N(q_1{}^2\boldsymbol{N} + q_2{}^2\boldsymbol{N} + q_3{}^2\boldsymbol{N}) \\ &- 3k(2\rho)^{-1/2}\sum(2\pi\sigma)^{1/2}l^{-1}N^{1/2} \\ \bar{H}' = &-(\rho\nu^2/2)(16\pi^4/l^4)\sum N^4(q_1{}^2\boldsymbol{N} + q_2{}^2\boldsymbol{N} + q_3{}^2\boldsymbol{N}), \end{aligned} \tag{7,1}$$

Now we shall search for the non-perturbed wave function.

Or we shall consider the following differential equation.

$$\bar{H}_0\varphi = E_0\varphi. \tag{7,2}$$

When σ is positive, this problem is same as the calculation of the characteristic functions for the simple harmonic oscillators. Then, the energy of the characteristic states is

$$\varepsilon_{j\boldsymbol{N}} = (m-1)h^*\sqrt{N},\quad m = 1, 2, \ldots\ldots \tag{7,3}$$

where $h^* = 2k\sqrt{\pi\sigma}/\sqrt{\rho l}$.

When σ is negative, the equation (7,2) has no characteristic function.

Now, we calculate the transition probability by means of the perturbation theory.

The probability by which the physical system removes from "m"-state to "$m-2$"-state on account of the absorption of two vortex-quanta by the thermal motion should be represented by the following expression.

$$P_{\mathrm{trans}} = (\sqrt{m(m-1)}/2\alpha)^2 = m(m-1)/4\alpha^2 \tag{7,4}$$

And then, the probability by which the physical system removes from "m"-state to "$m+2$"-state on account of the emission of two vortex-quanta by the thermal motion, should be represented by the following expression.

$$P_{\mathrm{trans}} = (\sqrt{(m+1)(m+2)}/2\alpha)^2 = (m+1)(m+2)/4\alpha^2 \tag{7,5}$$

We shall consider two states of thermal motion, "a" and "b", which are in equilibrium with the "m".state of the vortex-quantum.

E_a and E_b denoting the thermal energies of "a"-state and "b"-state of the thermal motion respectively, the probability of existence in those states may be proportional to $\exp\{-E_a/\kappa T\}$ and $\exp\{-E_b/\kappa T\}$ respectively (where κ denotes Boltzmann constant, and T is the absolute temperature), if we assume the canonical ensemble about the thermal motion. Remembering the transition probability (7,4) and (7,5), the condition of the thermal equilibrium may be expressed by the following formula.

$$\begin{aligned} &\exp\{-E_b/\kappa T)m_N(m_N-1) \\ &\qquad = \exp\{-E_a/\kappa T\}(m_N+1)(m_N+2), \end{aligned}$$

where $E_a - E_b$ must be

$$2h^*\sqrt{N},\quad h^* = 2k\sqrt{\pi\sigma}/\sqrt{\rho l} \tag{7,6}$$

From the above formula, the quantum number corresponeing to the wave number N/l can be obtained in the following form

$$m_N = 2^{-1}[\exp(\theta)-1]^{-1}[\{\exp(\sqrt{N}\theta)-3\} \div\{\exp(2\sqrt{N}\theta)+14\exp(\sqrt{N}\theta)+1\}^{1/2}] \quad (7,7)$$

with $\theta = 2h^*/\kappa T$.

The physical meaning of "$m_N dN$" is the probability of the existence of the vortex-quanta with the wave numbers which are between

$$N/l \text{ and } (N+dN)/l.$$

§ 8. The Spectrum of the Turbulence.

h^* is generally a function of time. But, if the turbulence is completely polarized, or A is a constant independent of time, h^* is simply a universal constant. Therefore the distribution function of the energy in one-degree of freedom, can be calculated from (7,3)

$$f_E(N) = \varepsilon_{jN} = (m_N-1)h^*\sqrt{N}. \quad (8,1)$$

Approximately (8,1) is represented by the following form after normalization.

$$f_E(N) = \frac{4h^{*3}\sqrt{N}}{\zeta(3,1)\cdot\Gamma(3)\cdot\kappa^3T^3[\exp\{(2h^*/\kappa T)\sqrt{N}\}-1]}$$

$$= \frac{h^{*3}}{0.601\kappa^3T^3}\,\frac{\sqrt{N}}{[\exp\{(2h^*/\kappa T)\sqrt{N}\}-1]} \quad (8,2)$$

§ 9. The Phyiscal Meaning of Hamiltonian.

In Hamiltonian (4,3), if we neglect the term of viscosity in the equation of motion, the term $(1/2\rho)(\boldsymbol{P},\boldsymbol{P})$ is equal to

$$(\rho/2)(\boldsymbol{V},\boldsymbol{V})+p$$

or the energy in the usual meaning. Therefore the first term of Hamiltonian (6,6) is the energy in the usual meaning, and the second term represents the irregular motion which has not stream lines, and whose energy is not involved in the first term.

The third term represents the correlation effect between the mechanical motion and the viscosity, Finally, the additional constant

$$3k(2\rho)^{-1/2}\sum(2\pi\sigma/l)^{1/2}N^{1/2}$$

may be considered as some energy which is initially excited and cannot be observed by the usual hydrodynamical treatment, so that this energy must be subtracted if the theory shall be compared with the usual hydrodynamical experiment: This energy may be the spinning energy of the smallest drop of fluild.

§ 10. The Physical Meaning of the Constant "k".

The constant "k" in the commutation relation (6,1) is corresponding to Planck's constant "$\hbar$" in the quantum theory.

We shall write the following expression analogously to the uncertain principle by Heisenberg.

$$\Delta Q_1 \Delta P_1 \geq k. \quad (10,1)$$

From (10,1), we have

$$\rho\Delta u\Delta x \geq k/4 \quad (10,2)$$

where u is the x-component of the velocity.

If we consider the velocity of flow microscopically we must average the velocity of the molecules in a certain volume,

Then the fluctuation of the mean value Δu will be inversely proportional to the number of the molecules in the considered volume, and proportional to the average value of the molecular motion.

If we permit the error of the x-coordinate Δx about the position where we endeavour to survey the velocity of the flow, we can average the velocity of the molecules, which are on the line-element Δx at a certain moment.

Then the number of the molecules whose average velocity determines the velocity of the flow is $\pi D^2 n\Delta x$, where D is the diameter of the molecule and n is the number of the molecules in unit volume.

Then we have

$$\Delta u \geq cv'/(\pi D^2 n\Delta x) \quad (10,3)$$

where c is a universal constant and v' is the average value of the molecular motion. From the kinetic theory of gas, the viscosity being proportional to $\rho v'/(\pi D^2 n)$, (10,3) reduces to $k=\gamma\eta$ where γ is a universal constant, and η is the coefficient of the viscosity.

Thus "k" is proportional to the viscosity.

§ 11. The Comparison with the Experiment.

We shall compare the theoretical expression (8,2) with Taylor's experiment.

We can set $N/l = \mu/\bar{U}$ or $N = (\mu/\bar{U})l$ (11,1)

where N/l is the wave number, μ is the frequency and $\bar{U}$ is the velocity of the general flow.

Using the frequency μ instead of N, from the expression (8,2) we have

$$U f_E(\mu) \doteqdot \frac{\delta^3\sqrt{\mu/\bar{U}}}{4.808\,[\exp(\delta\sqrt{\mu/\bar{U}})-1]} \qquad (11,2)$$

where $\delta = 2h^*\sqrt{l}/\kappa T$

Then, assuming the energy of flow is determined almost only by the velocity, the present theory can be compared Taylor's experiment.

The following figure shows the Taylor's experiment, in comparison with the theoretical formula (11,2), whose constant γ is assumed as "1.3". It will be seen that the theory is very satisfactory.

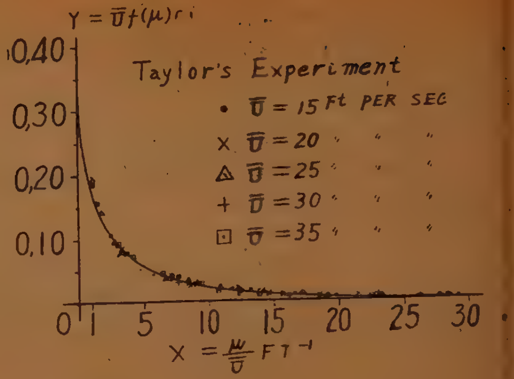

Fig. 1.

References.

(1) G.I. Taylor: Proc. Roy. Soc. A, **164** (1938), 476.

(2) Th. von Kármán and L. Howarth: Proc. Roy. Soc. A, **164** (1938), 192.

(3) G. K. Batchelor: Quart. Appl. Math. **6** (1948), 97.

(4) C.F. von Welzsäcker: Z. Phys. **124** (1948), 416.

(5) W. Heisenberg: Z. Phys. **124** (1948), 628.

(6) W. Heisenberg: Proc. Roy. Soc. A, **195** (1948), 402.

Natural β-Ray Spectrum of RaC.

By Mitsuo MIWA.

Physical Institute, Tokyo University of Literature and Science,

and Seizaburo KAGEYAMA.

Radiological Department, Japanese Foundation for Cancer Research.

(Received May 9, 1950).

§ 1. Introduction.

The probability of the internal conversion of γ-ray depends both on the energy and the character of the ray and so gives an important information on the spin of the nuclear energy states concerned. The conversion coefficient may be studied either by comparing the intensities of γ-line estimated by the observation of conversion electron with the corresponding intensities determined by the observation of recoil electron or photoelectron or, in the case of α-active body by comparing the former intensities with the spectral intensities of α-rays. It has hitherto been studied by many investigators on natural radioactive substances. Their results however are not still in accord with each other in some respects.

Ellis and Aston⁽¹⁾ performed years ago a detailed investigation of natural β-ray spectrum of RaC, using a magnetic spectrograph of semi-circular focusing type, and determined the intensities of conversion lines from the blackening of photographic plate. Later Constantinov and Latyshev⑵ also studied the same spectrum. They however employed two G–M counters working in coincidence for the detection of electron. Their results differ from those of English authors in following points:

(1) According to Constantinov and Latyshev, the intensity of conversion line *K*1379 KeV (where *K* denotes the electron shell of atom where conversion of the γ-ray takes place and 1379 KeV the energy of the γ-ray) is 3.5×10^{-4} per disintegration, while it is only 0.9×10^{-4} in Ellis and Aston's report. Constantinov and Latyshev concluded from their findings that this γ-ray would be of quadrupole character.

(2) The conversion lines *L*1414 and *M*1414 are not resolved in the spctrum of Ukrainian authors. They futher supposed the superposition of a weak conversion peak emitted by the γ-ray 1520 KeV on the two.

(3) The intensity of *K*1414 line reported by Ukrainian authors is about 40 percent larger than that found by English authors.

We have re-examined the β-ray spectrum of RaC and studied these points in question carefully. The experimental method adopted was nearly the same as Ukrainian writers', but the resolving power of our spectrometer was much better than theirs.

§ 2. Experimental Arrangement and Procedure.

The β-ray spectrometer used was of usual semicircular focusing tyye, with an electromagnet made of silicon steel sheets. The depth of vacuum chamber was 3 cm and the distance between the β-ray source and the slit of the first counter 20 cm. After Neary⑶, baffles made of aluminium sheet of 3 cm in thickness were so arranged as to subtend minimum solid angle at the source. The width of slit in the first baffle plate was so chosen that the divergence of the electron beam available was two degrees at the source.

The variation of the susceptibility of iron core with temperature is a trouble in a magnetic spectrometer of high resolving power. The strength of magnetic field changes gradually with rise of core temperature caused by heat evolution in the coil, even if the exciting current is kept strictly constant. The temperature of the core therefore was kept practically constant by inserting water-cooled jackets between the core and the exciting coils.

The strength of magnetic field was determined only relatively through exciting current, the *Hρ*-values of main peaks of natural β-ray spectrum of RaC given by Ellis and Aston being taken as reference. Owing to the high resolving power of our spectrometer, however, an ordinary precision ammeter was found insufficient for a fine control of magnetic field. So a galvanometer coil carrying constant current was suspended between the pole pieces of the magnet and its deflection was observed by lamp and scale. The sensitivity of this arrangement was 6–8 gauss. cm per scale division. Observation records were usually taken at an interval of 2-4 scale divisions in the continuous region of the spectrum and 1–1/2 scale division around the conversion peak.

The electron was detected by two G—M counters working in coincidence. The slit of the first counter was 0.4×10 mm^2 and a mica foil of about 0.85 mg/cm^2 served as the separator of counter and vacuum chamber in the main experiment. A foil of 0.5 mg/cm^2 was also used for checking the absorption effect of the foil in lower energy region.

The coincidence circuit employed was of Rossi type, the resolving time of which being about 6.10^{-6} sec. A 32-scaling circuit of vacuum triodes UY56 served as the recorder.

Radon up to 150 mc sealed in a small glass ampule was used as the source of β-rays, the thickness of ampule beging about 2.8 mg/cm^2.

§ 3. Experimental Results.

The experimental results are shown in Figs. 1-6 and also taaulated in the Tables I and II. Fig. 1 represents the exprimental results on natural β-rays of RaC in *Hρ*-scale without recalculation. The numbers near the conversion peaks denote the energies of the corresponding

γ-lines in KeV. The energy spectrum was recalculated for equal energy interval and is given in Fig. 2. Figs. 3–6 depict separate parts of the spectrum, where the conversion peaks from individual γ-line are most clearly seen. The area

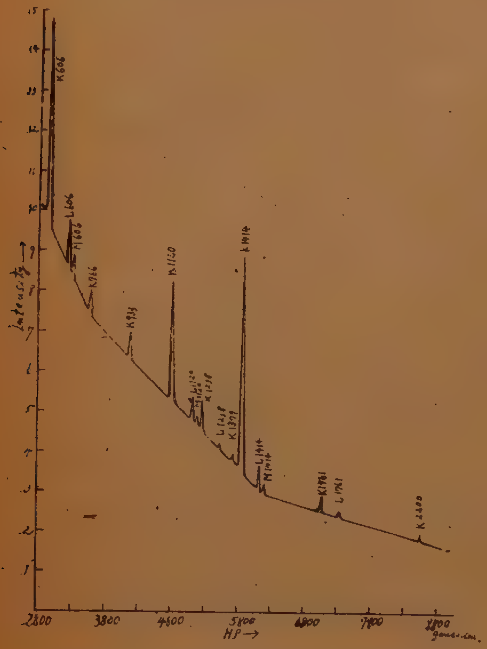

Fig. 1. Natural β-spectrum of RaC.

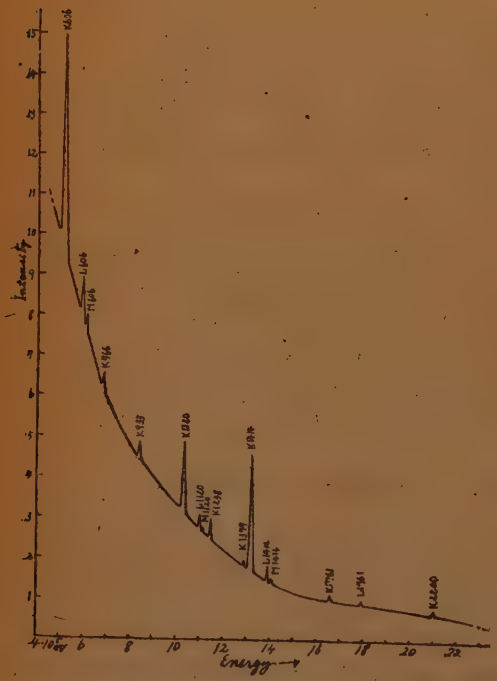

Fig. 2. Natural β-spectrum of RaC.

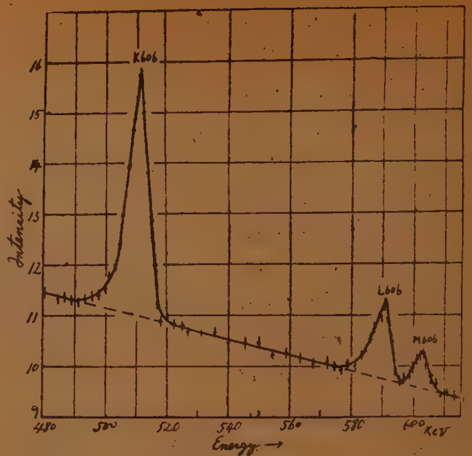

Fig. 3. Conversion peaks K606, L606 and M606 KeV.

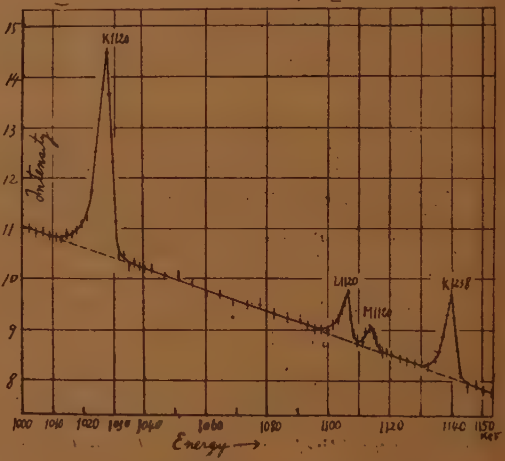

Fig. 4. Conversion peaks K1120, L1120, M1120 and K1238 KeV.

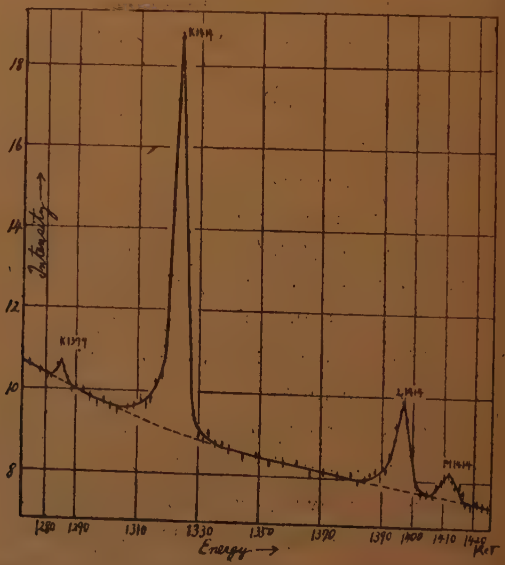

Fig. 5. Conversion peaks K1379, K1414, L1414 and M1414 KeV.

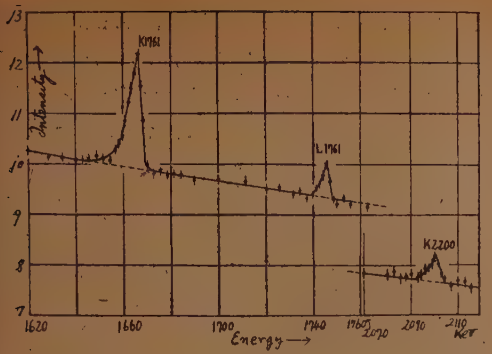

Fig. 6. Conversion peaks K1761, L1761 and K2200 KeV.

of individual conversion peak is evidently proportional to the number of conversion electrons of the given γ-line, i. e., to the intensity of the γ-line (p) multiplied by its conversion coefficient (α). The relative intensities of the internal conversion electrons of RaC estimated from the energy spectrum given above are shown in Table I, together with those obtained by Ellis-Aston and Constantinov-Latyshev. The ratios of the internal conversion coefficients of different energy levels for main γ-lines are also given in Table II.

Table I. Relative spectral intensities of conversion electrons of RaC.

Energy of γ-ray in KeV	Conversion level	Relative Intensities		
		Ellis and Aston	Latyshev and Constantinov	Present Writers
606	K	49	40	40
	L	9	—	7.4 ±0.5
	M	1.6	—	2.8 ±0.3
766	K	3.2	—	3.0 ±0.5
933	K	4.1	—	4.0 ±0.5
1120	K	18.0	12.4	12.4 ±0.7
	L	2.1	1.9	1.8 ±0.2
	M	1.0	—	0.87±0.2
1238	K	3.6	2.5	2.9 ±0.4
	L	0.85	—	0.5 ±0.2
1379	K	0.9	3.5	0.98±0.15
1414	K	25.0	34.5	24.4 ±1.5
	L	3.7	(8.5)	3.6 ±0.3
	M	1.4	—	1.3 ±0.2
1761	K	4.2	4.8	4.1 ±0.5
	L	0.95	1.1	0.62±0.2
2200	K	0.95	1.5	0.85±0.3
	L	0.2	—	—

Table II. Ratios of the internal conversion coefficients of the main γ-lines of RaC for different energy levels.

γ-ray (KeV)	α_L/α_K			α_M/α_K	
	Ellis and Aston	Latyshev and Constantinov	Present writers	Ellis and Aston	Present writers
606	0.22	—	0.18	0.04	0.07
1120	0.16	0.19	0.15	0.08	0.07
1414	0.14	(0.245)	0.15	0.056	0.05
1761	0.22	0.23	0.15		
Theoretical value			0.15		—

§ 4. Discussions.

(I) As is mentioned in the introduction, there is a great divergence between the intensity of conversion line K 1379 observed by Ellis and Aston and that found by Constantinov and Latyshev. In consequence of this divergence, the conversion coefficient given by English writers implies dipole nature of the said γ-ray, while the results of Ukrainian writers is favourable for a quadrupole transition. Our result is in complete agreement with Ellis and Aston, as shown in Table I.

According to Constantinov and Latyshev, the intensity of conversion peak K1379 is about one-tenth of K1414. If so, when the conversion peaks L1414 and M1414 are completely resolved, the peak K1379 will be slightly weaker then L1414. Or it will be about twice as intense as M1414. We studied this point carefully with radon tubes of varying thickness. The peak K1379, however, was always found to be weaker than M1414. We believe that the accuray of our measurement was surely better than Ukrainian writers', because the peak K1379 was superposed by the tail of the intense peak K1414 in their report. The two peaks were completely resolved from each other in our spectrum. The error in the estimation of general background also will probably be larger than ours. The reason is that the experimental points given by them, between the peak K1414 and L1414 for example, seems too few to draw a reliable background line.

Our findings in this connection were in accord with English writers' as described above. But there are some questions whether the said γ-line is really of dipole nature or not. The intensities of the γ-line found by different authors do not agree with each other. The discussion on this point therefore will be postponed until our experiment on RaC γ-ray now undertaken will be completed.

(2) According to Constantinov and Latyshev, there exists 1520 KeV γ-line of quadrupale nature in the γ-ray spectrum of RaC and its intensity is about 0.7, the intensity of 2200 KeV γ-line being taken as unity. As to the intensity of the line Itoh and Watase(4) also came to the same conclusion. Constantinov and Latyshev concluded the quadrupole character of the γ-ray from their findings on the internal conversion positron. Owing to the poor resolution of their spectrometer, however, the K conversion peak corresponding to the γ-line is not found in their β-ray spectrum. They must have supposed that it is not resolved from the conversion lines L1414 and M1414, the three lines amalgamating into a single peak.

The conversion lines L1414 and M1414 are completely resolved in our spectrum, as is shown in Fig. 5. Therefore, if the γ-line be really of quadrupole nature and have the said intensity, the K conversion peak should be found on the right hand of the peak M1414 in our spectrum. The distance between the expected peak and the peak M1414 will be comparable with that between L1414 and M1414. And its intensity is expected to be about one half of M1414 line or nearly equal to K2200 line. But no trace of such a conversion peak was detected in our experiment, even though the region in question was surveyed carefully.

Thus it is highly probable that 1520 KeV γ-line is a dipole radiation instead of a quadrupole radiation. The probability of internal conversion for a dipole radiation is expected to be about three times weaker than that for a quadrupole radiation of the same quantum energy(5). It may also be suggested that the energy of the γ-line is a little lower than 1520 KeV (for example 1500 KeV or so) and its K conversion line become superposed on M1414 line. In that case, however, the intensity of the conversion peak M1414 should be far stronger than given above. Thus the quadrupole character of the γ-line in question is again very improbable.

(3) The intensity of the conversion line K1414 found by us was again in good agreement with the result of English authors, but not with that of Ukrainian authors'. The measurement of its relative intensity to the conversion line K606 was repeated several times, because this line was taken as sub-standard in the higher energy region in our experiment. So we believe the value given above to be the most exact.

(4) The ratio of the internal conversion

coefficients a_L/a_K of the γ-line 606 KeV is a little larger that those of the other main lines, although the difference is not so large as in the results of Ellis and Aston. According to Fisk⁽⁶⁾, the theoretical value of the ratio is 0.15, irrespective of the nature of radiation, in the energy region in quesion. The difference between the observed value of 606 Kev line and the theoretical value seems to exceed the statistical error.

As for the origin of this discrepancy, the following items may be taken into consideration: (1) the scattering by the mica window of the counter and (2) the superposition of conversion electrons generated by an unknown weak γ-line. To investigate the effect of scattering, we repeated the measurement with counters having mica window 0.5 mg/cm^2 in thickness, whose absorption effect of electrons may be entirely neglected in the energy range studied. But the ratio a_L/a_K was unchanged within the statistical error. If it were the superposition of a weak γ-line, it could not be decided by our experiment.

In conclusion, the present authors express their thanks to the aid given by the Scientific Research Expenditure of the Department of Education.

Reference.

(1) C. D. Ellis and G. H. Aston, Proc. Roy. Soc. **A 129** (1930) 180.
(2) A. A. Constantinov and G. D. Latyshev, J. Phys. U.S.S.R. **5** (1941) 249.
G. D. Latyshev, Rev. Mod. Phys. **19** (1947) 132.
(3) G. J. Neary, Proc. Roy. Soc. **A 175** (1940) 71.
(4) J. Itoh and Y. Watase, Proc. Phys. Math. Soc. Jap. **23** (1941) 142.
(5) H. R. Hulm, N. F. Mott, F. Oppenheimer, and H. M. Taylor, Proc. Roy. Soc. **A 155** (1936) 315.
(6) J. B. Fisk, Proc. Roy. Soc. **A 143** (1934) 674.

Further Remarks on Araki's Theory of Inverted Alkali Doublets.

TA-YOU-WU.

National Research Council Ottawa, Canada.

(Received May 10, 1950).

Abstracts.

In a reply to the writer's criticism on his theory of the inverted doublets in certain alkali spectra, Araki takes exception to the first of the criticisms that the effective charge for the f electron wave functions in Cu should be unity instead of 7.6. The present note presents arguments for this criticism and shows that the contention of Araki is untenable.

In a note⁽¹⁾ the writer points out that the idea of Araki that the inversion of the doublet $4f^2F$ in Cu is due to the spin-orbit interaction between the valence and the core electrons is untenable for two reasons, namely, the assumption of the high value 7.6 for the effective charge for the f electron by Araki has been mainly responsible for the agreement claimed, and the "over-screening" found by Araki really is due to some numerical errors in his calculation.

In a reply⁽²⁾, Araki defends the assumption of the high value 7.6 for the effective charge of the f electrons. In the following note, we shall show why the effective charge should be very close to unity.

Consider the one-electron problem of an f electron in the field of the nucleus and the core electrons, namely, $V(r)$ which behaves as $-Ze^2/r$

near $r=0$ and as $-e^2/r$ for large r. That the whole series of $nf\,^2F$ levels is hydrogenic implies that the wave functions of these states are hydrogenic, with the same effective charge Z. Now these functions are apparently the eigenfunctions of the Hamiltonian

$$H=T-\frac{Z^*e^2}{r}.$$

That Z^* must be nearly equal to unity follows from the requirement that the eigenvalues be hydrogenic with quantum defects of the order 0.01, namely,

$$\int \Psi^*_{n3}H\Psi_{n3}dx=-\frac{Z^*}{n^2}=-\frac{1}{(n-0.01)^2}$$

To understand perhaps more clearly why the actual field $V(r)$ leads to practically the same f levels as the field Z^*e^2/r, we may either represent $V(r)$ by a Hartree-Fock field or the Thomas-Fermi field. The Schrödinger equation for the radial wave functions of the f states is, in atomic units,

$$\frac{d^2R}{dr^2}+\left[E-V(r)-\frac{12}{r^2}\right]R=0.$$

If we regard the function $V(r)+\frac{12}{r^2}$ as the effective potential, then it is seen that on account of the centrifugal term $12/r^2$, the region of classical motion, and hence the region where the $|R|^2$ is large, lies at large distance from the nucleus.

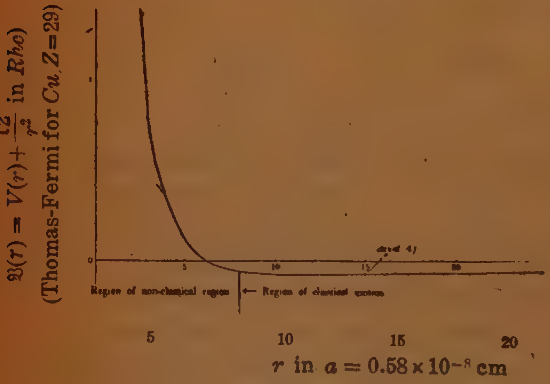

Fig. 1.

The deviation of $V(r)$ from $-\frac{e^2}{r}$ in the non-classical origin only introduces a small perturbation appearing finally as a small quantum defect(3).

The situation is shown in the following figure. It is seen that if the effective charge parameter $Z-s$ in the wave function of the $4f$ electron

$$R_{45}\simeq r^4\exp\left(-\frac{Z-s}{4}r\right)$$

is about 7 as contended by Araki, the wave function R_{43} would then have its maximum at $r=16/7$ atomic units, which lies in the non-classicl region of motion. This is clearly not possible. Furthermore, the wave function with $Z-s=7$ is not even asymptotically correct at large r, since at large r, $V(r)$ behaves as $-\frac{e^2}{r}$ and one must have $R_{43}\sim r^4e^{-\frac{1}{4}r}$.†

In his note(2), Araki also makes some new calculations of the $\zeta_{nl,43}$ with hydrogenic wave functions whose effective charge parameters are taken to be those determined for the "inner" region in Slater's method of representing the self-consistent field solution by a sum of a few expotentials. Thus the effective charge is taken to be 21.62×3 for 3s and 12.32×3 for $3p$, in the case of Cu. Now it is clear that hydrogenic wave functions with these values as the effective charge parameters have no meaning at all. One must either employ the whole Slater function (which consists of a sum of expotentials) or a hydrogenic function whose single expotential term mest be so adjusted as to give the best over-all fit with the self-consistent solution. In view of the use of these entirely meaningless wave function, no significance can be attached to the values for the $\zeta_{nl,43}$ computed by Araki.

In must be concluded that the criticism of Araki's theory as given in the previous hote(1) still stands.

Reference.

(1) T. Y. Wu, J. Phys. Soc. Jap., **4** (1949), 343.
(2) G. Araki, *ibid*, **4** (1949), 345.
(3) For details of such considerations and f states in the heavy atoms, see T. Y. Wu, Phys. Rev., **44** (1933), 727.

---

† In his note, Araki argues that in

$$Z^{*2}=(Z-s_1)^2-(s_1-s)^2,$$

Z^* is not equal to $Z-s$ since s_1 and s are in general different. This line of argument is not the correct one. One must see that s_1, which represents the screening due to the core electrons, is, for f electrons, very close to $Z-1$. Now the spectral terms give $Z^*=1$. Putting these values into the above expression, one then finds $s=Z-1$ so that $Z-s=1$.

Note added by G. Araki. After I submitted my remarks on Ta-You Wu's criticism to the editor of this journal, Tutihasi evaluated all the parameters by employing the self-consistent core functions, and recently he has finished the calculation for $Cu\,4f^2F$. Contray to my expectation he has not been able to fined the *over-screening* for larger values (probably larger than 3) of the effective charge for the $4f$ orbital. The over-screening has been expected for smaller values of the effective charge from the result of his calculation, but the absolute value of the term has been expected to be too small in agreement with Ta-You Wu's argument. Tutihasi will publish his result in Prog. Theor. Phys. when he will finish the calculation for Na3d^{2}D in which he is now engaged.

G. Araki

On the Depolarization of Electrons by Multiple Scattering and Reflection-Transmission Effect.

By Norio Ryu.

Department of Physics, Faculty of Science, Kyushu University, Fukuoka.

(Read May 21, 1948: Received May 13, 1950)

Abstract

In some experiments on the polarization of electrons, there is a discrepancy between their results and the theory. The effect of multiple scattering, as a depolarization factor, cannot explain the discrepancy as is shown by Rose and Bethe. As another cause of the discrepancy, the plural scattering, which is the combination of two rather large angle deflections in the same foil, is considered in some detail. Such a plural scattering gives rise to values of the so-called "reflection-transmission" effect agreeing with experimental results. It is shown that the negative experimental results obtained by Dymond, Thomson, and Richter can be accounted for, if this effect is taken into account.

§ 1 Intooduction.

Using Dirac's equation, Mott(1) has investigated, theoretically, the effect of the spin on the scattering of electrons, and showed if electrons were made to undergo double large angle scatterings by atoms of large atomic number, its intensity would have azimuthal asymmetry at the second scattering which is large enough to be observed. The experiments on the polarization of electrons carried out by Dymond(2), Thomson(3), and Richter(4) are guided by Mott's idea. The conditions to be fulfilled are; (1) only single scattering in each foil should take place, (2) the atomic number of scattering atoms should be large, (3) scattering angles should be large, and (4) the energy of the incident electrons should not be too small. Unfortunately, their results did not agree with the theory. To reconcile this discrepancy, the effect of the crystal structure of the scatterer has been considered by Weiskopf(5) and others, and the depolarization by multiple scattering and exchange scattering have been investigated by Rose and Bethe(6). In spite of these efforts, the discrepancy had been remaining.

It was, then, pointed out by Goertzel and Cox(9) that in the usual experimental arrangement, in which the scattering foil is set at an angle of 45° to the incident beam the effect of the beam scattered twice at large angles in the single foil cannot be neglected, even when Wentzel's criterion is fulfilled. In the beam scattered back to the reflection side, a large number of such doubly scattered electrons exist besides the singly scattered electrons. Recently, Shull, Chase, and Myers(8), using electrons of the energy of 400 kev, and Shinohara and Ryu(9), with electrons of the energy below 100 kev, both using the beam scattered to the transmission side of the foil to avoid such plural scattering, succeeded in obtaining the effect of polarization not much different from that predicted by the theory. The failure of the previous authors to observe the expected effect can be attributed partly to the so-called "reflection-transmission" effect. Since, however, Goertzel and Cox's calculated value is too small to explain the previous experimental results, a more precise calculation has been carried out. The effect of the multiple scattering is also investigated.

§ 2. The Polarization of Electrons.

Before discussing the multiple scattering it will be most convenient for later purposes to recapitulate some of the theory on the polarization. We consider an electron incident along the z-axis and scattered elastically in the direction θ, ϕ by some field of force. If we put the components of the amplitudes of the Dirac plane waves A and B, we have

$$-\frac{B}{A}=\cot\frac{\chi}{2}e^{i\omega}, \tag{1}$$

$$|A|^2+|B|^2=1, \tag{2}$$

where χ, ω indicate the direction of the spin axis and Eq. (2) gives the normalizing condition. The amplitudes after the scattering are given by Mott(1), as follows

$$\left.\begin{aligned} u_3 &= Af-Bge^{-i\phi} \\ u_4 &= Bf-Age^{i\phi} \end{aligned}\right\}, \tag{3}$$

where f and g depend only on θ. The differential cross section Φ is then

$$\begin{aligned}\Phi &= |f|^2+|g|^2-(fg^*-f^*g)(AB^*e^{i\phi}-A^*Be^{-i\phi}) \\ &= \Phi_0(1-\delta p),\end{aligned} \tag{4}$$

where

$$\begin{aligned}\Phi_0 &= |f|^2+|g|^2,\ \delta = (fg^*-f^*g)/\Phi_0, \\ p &= AB^*e^{i\phi}-A^*Be^{-i\phi} = i\sin\chi\sin(\omega-\phi).\end{aligned} \tag{5}$$

Now we see the largest azimuthal asymmetry of scattered intensity is given by electrons whose magnetic moment is in the direction $\chi \doteq \frac{\pi}{2}$, $w \doteq \frac{\pi}{2}+\phi$ when θ is fixed, that is, electrons whose spin axis is normal to the scattering plane give the maximum asymmetry that ip is caused by polarization. It can be easily shown proportional to the difference between the numbers of electrons in two directions normal to the scattering plane and it is proportional to azimuthal asymmetry.

To find out the experimental asymmetry, as shown by Mott(1), it is necessary to polarize the beam initially. Consider the non polarized beam — beam containing electrons which have the spin parallel to the z-axis and electrons antiparallel — which fell on the polarizer P as shown in Fig. 1, and scattered in the direction of PA. Using the above equations and Darwin's(10) spinor transformation, p about the axis PA becomes

$$p = \frac{(f_1g_1^*-f_1^*g_1)}{|f|^2+|g_1|^2}\cos\phi = \delta_1\cos\phi.$$

When these electrons are scattered by analyser A, the intensity after the second scatterings is

$$\Psi = \Phi_{01}\Phi_{02}(1-\delta_1\delta_2\cos\phi), \tag{6}$$

where the indices show the scattering at the polarizer and the analyser, respectively. δ_1 and δ_2 are pure imaginary quantities, so that AD_1 in Fig. 1. is the direction of the maximum intensity and the AD_2 the minimum.

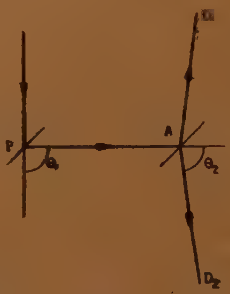

Fig. 1.

§ 3. Multiple Scattering

In the experiment on the polarization by double scattering, it is necessary to use thin foils so as to conform to the Mott's conditions(1). But even if we use the thinnest possible foils, we cannot avoid the large number of small angle scatterings, i. e. multiple scattering. As we will see later, multiple scattering does not polarize the beam, therefore, we need not take into account the multiple scattering which occurs before the first large angle deflection in the polarizer and also the one after the large angle deflection in the analyser. Rose and Bethe(6) have evaluated the change of $q=|A|^2-|B|^2$ by multiple scattering, but the change of q does not affect the experiment on the polarization of electrons. Therefore, our problem is to determine the change of p defined by Eq. (5) between two large angle deflections.

Consider an electron whose amplitudes are A and B at any point along the path PA in Fig. 1. After a small angle deflection given by θ and ϕ, p changes to

$$p'=-\frac{1}{\Phi}(p|f|^2+R).$$

The change of p per collision is, therefore,

$$\varDelta p=-\frac{1}{\Phi}(p|g|^2+R'), \tag{7}$$

where R and R' are functions depending on ϕ and cansel out in the later calculation. To get $\varDelta p$ at the next small angle scattering it is necessary to use Darwin's(10) transformation. Darwin's transformation is separable in two transformrtions about θ and ϕ, respectively, i. e. the rotation about y-axis and z-axis. The rotation about z-axis gives as the ratio of the amplitudes

$$-\frac{B'}{A'}=\cot\frac{\chi}{2}e^{i(\omega-\phi)},$$

that is, in this transformation, ω changes to $\omega-\phi$. In other words, the direction of spin does not change about the initial coordinate. In order to carry out the rotation about y-axis, let us use the matrix

$$\begin{pmatrix}\cos\frac{\theta}{2} & \sin\frac{\theta}{2}\\ -\sin\frac{\theta}{2} & \cos\frac{\theta}{2}\end{pmatrix}.$$

Considering that most of the scatterings treated here are of very small angles, we can take approximately the matrix as unity. We can, therefore, get the final change of p by adding $\varDelta p$ at each successive collisions, using a fixed coordinate.

The probability of scatteaing at an angle given by θ and ϕ, during the passage of electrons in the material of thickness dx is $N\Phi\sin\theta d\theta d\phi dx$ Where N is the number of scatterers per unit volume. The change of p after traversing the thickness dx in the foil will be, therefore,

$$dp=-2\pi Npdx\int_0^\pi|g|^2\sin\theta d\theta.$$

We can, thus write

$$p=\exp[-\gamma x] \tag{8}$$

where

$$\gamma=2\pi N\int_0^\pi|g|^2\sin\theta d\theta.$$

x is the distances traversed by the electron beam in crossing the foil.

Table. I.

kev	10.5	46.5	79.0	204.4
$\gamma\times10^{-3}$	2.58	0.59	0.49	0.31
$d\times10^{3}$	0.4	1.7	2.1	3.2

Fortunately, we are able to use, in evaluating the above expression, the results obtained by Massey and Mohr(11) using a screened field about gold atoms. Results are shown in Table I. p decreases to $1/e$ when the beam traverses a distance d. It is clear that if we use a foil thinner than 10^{-4}cm, the multiple scattering exerts no appreciable effects on the experiment.

§ 4. Reflection-Transmission Effect

Chase and Cox(12) have observed, in studying experimentally, the scattering of electrons incident at 45° on the thin aluminium foil, the scatering at 90° was greater toward the side from which the electrons were incident than toward the other side. Later, Goerzel and Cox(7) have shown theoretically that this asymmetry is caused by the combination of two rather large angle deflections in the same foil. A similar but more precise calculation is carried out. The electrons which most likely to undergo plural scattering will be those scattered into the foil, i. e. in the direction of OS in Fig. 2 which lies in the plane of the foil. The incident electrons are assumed to strike the foil along AO. The probability that electrons are scattered into the solid angle $d\theta d\phi$ is

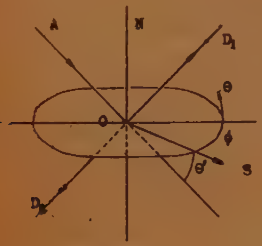

Fig. 2.

$$I=\surd 2\ Nh\Phi(\theta')\cos\phi d\theta d\phi,$$

where N is the number of scattering atoms per unit volume, h the thickness of the foil, θ' the deflected angle, and $\Phi(\theta')$ is the cross section of elastic scattering. These electrons will lose some energy in passing through the foil and the amount of loss being given approximately by the equation

$$v^4=v_0^4(1-nax),$$

where v_0 is a initial velocity and na the quantity to be decided by experiments of the energy loss of electrons. There is no empirical nor theoretical expression giving the intensity of the electron beam proceeding in a thin foil and parallel to its plane. The calculation of Goudsmit and Saunderson$^{(13)}$ treating the diffusion of electrons by multiple scattering cannot be applied. But, we will assume that the electron intensity should decrease rapidly when the electrons travel the distance determined by the condition that the distance multiplied by $<\sin\alpha>_{AV}$, the mean project angle, is equal to the thickness of the foil. Therefore, we will assume approximately the following intensity relation

$$I_x=I(1-ax)$$

where a is given by $h=\dfrac{1}{a}<\sin\alpha>_{AV}$. Since the result of the calculation does not depend critically on a, this assumption is expected to give sufficiently good results.

Let us, then, assume thst the electron undergoes a second deflection at some point on OS which brings it into the direction CD_1. The probability of the electrons scattering into the detector at D_1 is $NIx\Phi(\theta')dx\Omega$. Using the Mott's$^{(1)}$ formula for scattering and integrating it over all directions in the foil and dx, we get as the total intensity scattered into D_1;

$$P_{D1}=4\surd 2\,N^2hR^2\left(\frac{1-\beta^2}{\beta^4}\right)^2\int_0^\pi d\phi\int_0^{\pi/2}d\theta$$
$$\times\int_0^x dx\sum_{m=0}^{\infty}A_m a^m x^m\cos\theta$$
$$\times\operatorname{cosec}^5\frac{\theta'}{2}\left(1-\beta^2\sin^2\frac{\theta'}{2}\right.$$
$$\left.+\pi\beta Z\alpha\sin\frac{\theta'}{2}\cos^2\frac{\theta'}{2}\right)\Omega,$$

where A_m is given by

$$\frac{(1-ax)\,(1-\beta^2\surd\overline{1-nax})}{\beta^4(1-nax)}=\frac{1-\beta^2}{\beta^4}\sum_{m=0}^{\infty}A_m a^m x^m,$$

and $R=\left(\dfrac{Ze^2c^2}{2m}\right)^2$. In carrying out the integration by θ, it should be taken into accunt that for θ smaller than $\theta_0=\dfrac{ah}{2}$, the limit of integration should be from zero to $1/a$ and for θ larger than θ_0, the limit should be from zero to $h/2\sin\theta$. θ' and ϕ are connected by $\cos\theta'=\surd\overline{2}\cos\phi$. Then we get

$$P_{D1}=2\surd\overline{2}N^2h^2R^2\left(\frac{1-\beta^2}{\beta^4}\right)^2\left\{-ln\frac{ah}{2}\right.$$
$$\left.+1+\sum_{m=0}^{\infty}\frac{A_m}{m}\left(1-\frac{a^m h^m}{2^m(m+1)}\right)\right\}I_R\Omega \qquad (9)$$

$$I_R=996-354\beta^2+680\pi\beta Z\alpha$$
$$+112(\pi\beta Z\alpha)^2-112\pi\beta^3Z\alpha+36\beta^4.$$

P_{D2}, the intensity on the transmitted side, is obtained similarly if we replace I_R with I_T given by

$$I_T=106-106\beta^2+58\pi\beta Z\alpha+7(\pi\beta Z\alpha)^2-34\pi\beta^3Z\alpha+18\beta^4.$$

Dividing P_{D1} and P_{D2} by the single scattering intensity, respectively, we get the ratios r and t, for the reflection side and the tronsmission side, respectively. The reflection-transmission asymmetry can, then, be obtained by

$$\alpha=\frac{1+r}{1+t}, \qquad (10)$$

On neglecting the energy loss in the foil we get only the first term in the bracket in Eq. (9). This coresponds to the case with high speed electrons and a sufficiently thin foils.

Table II shows the comparison of the calculated reflection-transmission effect with the experimental results using the first term in the

Table II.

Substance	h (cm)	energy (kev)	α (exp.)	α (theo.)	Goertzel and Cox (α)	Reference
Au	4.1×10^{-5}	400	1.55	1.31	1.09	Shull et. al.
Au	3.8×10^{-5}	400	1.49	1.30	1.08	Trounson and Simpson
Al	0.5×10^{-5}	50	1.1	1.06	1.01	Chase and Cox
Al	1.0×10^{-5}	50	1.2	1.14	1.03	Chase and Cox
Al	1.1×10^{-3}	400	2.12	1.15	1.07	Shull et. al.

bracket in Eq. (9). The agreement can be considered as satisfactory in view of the roughness of approximation. Besides the double scattering in the foil, another processes such as the combination of more than two scatterings in the same foil or the combination of inelastic scatterings affect the reflection-transmission effect. But the probability of triple scattering is much smaller than the double scattering and also the cross-section of inelastic scattering above 45° is much smaller than that of the elastic scattering.

The plural scattering considered here plays an important role on the experiment by double scattering when electrons used are those scattered to the side of the foils from which they are incident, i. e. the reflection side, as in the experiments of Dymond(2), Thomson(3), and Richter(4). Since most of the electrons suffering such plural scattering are likely to undergo nearly 45° deflection twice, we may get a rough estimate of the asymmetry in scattering of these electrons in the foil by assuming that all those electrons had suffered two 45° scatterings in the foil. Using equations given in § 2 and an approximate value of $\delta(\theta')$ as given by Mott's theory(1), the asymmetry after the second scattering of the electrons which suffered such plural scatterings in either the polarizer or the anrlyser foil or in both can be calculated. The experimental asymmetry to be measured is caused by the beam composed of electrons which had suffered such plural scattering and also those suffering single scatterings in both foils. This is given by

$$Asymm. \doteqdot 1+\frac{2}{1+r}\,\delta^2\left(\frac{\pi}{2}\right). \tag{11}$$

Eq. (11) is obtained on the assumption that there is no depolarization by multiple scattering when the electrons are proceeding in the foils. But, as the path of the electrons in the foils, in case of plural scattering, is rather long, one may assume that the small angle multiple scatterings along the path may depolarize the beam. In this case we get

$$Asymm \doteqdot 1+\frac{2}{(1+r)^2}\,\delta^2\left(\frac{\pi}{2}\right). \tag{12}$$

When $r=1$, the amount of depolarization is 50~75%, and $r=2$ the amount is 60~90%, From Table III, it appears that it is imsossible to detect the asymmetay by double scattering if we use the foil 5×10^{-5} cm thick and the reflection side of the polarizer and the analyser foils. Even though we use foils thinner than 5×10^{-6} cm, it is necessary to use accelerating voltage higher than 100 kev. On the other hand if the transmission side and foils of 5×10^{-6} cm thickness is used, no disturbing effect from plural scatterings is expected.

Table III.

β	Energy (k ev)	$h=5\times10^{-5}$cm		$h=5\times10^{-6}$cm		$200\delta^2$ (Mott)
		r	t	r	t	
0.3	24.7	---	1.5	3.3	0.3	0.2
0.4	46.5	6.9	0.6	1.2	0.1	3.0
0.5	79.0	3.6	0.3	0.6	0.1	11.5
0.6	127.7	2.0	0.2	0.3	---	15.5
0.7	204.4	1.1	0.1	0.2	---	14.0
0.8	340.4	0.5	0.1	0.1	---	10.0

§ 5. Discussion.

In the experiment of polarization by double scatterings there is no appreciable effect by mul-

---

* *Note added in proof:* Recently we read the article published by Mohr, Proc. Roy. Soc., A 182 (1943) 189. Since his precise calculation shows the polarization effect by scattering at 45° is so small compared with the Mott's analytical formula, the depolarization by plural scattering above mentioned may be given approximately by Eq. (12).

ple scatterling when the thiceness of the gold foil is of the order of or less than 10^{-4} cm. Much more disturbing is the plural scatterings which gives rise to the reflection-transmission effect. Kikuchi⁽¹⁴⁾ have obtained experimental results which agrees with the theory of Mott, using the foil of about 10^{-3} cm as the polarizer. But from what has been discussed above, his use of the thick target makes his results open to question.

As we have seen above, the theoretical values of the reflection-transmission effect coincide with experimental results. The plural scattering composed of two large angle scatterings in the same foil cannot, therefore, be neglected in the double scattering experiment. In his experiment, Dymond obtained a very small asymmetry compared with the theory, using foils of 9×10^{-6} cm. It is, now, possible to understand the cause of the small asymmetry as he used the reflection side in his arrangement and r was nearly 2. In Dymond's later experiment, using a foil thinner than 5×10^{-6} cm, one would expected a larger asymmetry. The results, however, showed no asymmetry. In this case, the failure to observe the expected asymmetry must be attributed to other causes. A very small change in high voltage during the measurement may constitute such a cause. The error in the measured intensity of doubly scattered electrons is some eight times the error in measuring high voltage and moreover the asymmetry predicted by the theory is small. Therefore, if we derived the results using values observed at different times, the very small fluctuation in high voltage makes it impossible to detect the asymmetry. The fact that his measurement shows an appreciable fluctuation seems to show the correctness of this interpretation. The negative results in Thomson's and also in Richter's experiment can be understood in a similar manner.

Using the transmission side, Shull, Chase, and Myers⁽³⁾, Trounson and Simpson⁽¹⁵⁾, and also Shinohara and Ryu⁽⁹⁾ have obtained the experimental asymmetry nearly coinciding with the theory. Recently, Broer⁽¹⁶⁾ pointed out that there is a small discrepancy between the results from Shull et. al. and the theories concerning the reflection-transmission effect, but it seems impossible to get precise numerical coincideces sinee the theories are constructed on a rough approximation and moreover their experimental results are derived by a complicated procedure.

I wish to express my sincere thanks to Professor M. Nogami for his kind interest in this problem and also to Professor K. Shinohara for his kind discussions.

References.

(1) N. F. Mott: Proc. Roy. Soc., A **124** (1929) 425: *ibid* A **135** (1932) 429.

(2) E. G. Dymond: Proc. Roy. Soc., A **136** (1932) 638: *ibid* A **145** (1934) 657.

(3) G. P. Thomoson: Phil. Mag., **7** (1934) 1058.

(4) H. Richter: Ann. d. Physik, **28** (1937) 533.

(5) V. Weiskopf: Zeit. fur Physik, **92** (1935) 561: *ibid* **105** (1937) 747.

(6) M. F. Rose and H. A. Bethe: Phys. Rev., **55** (1939) 277.

(7) G. Goertzel and R. T. Cox: Phys. Rev., **63** (1943) 37.

(8) C. G. Shull, C. T. Chase, and F. E. Myers: Phys. Rev., **63** (1943) 29.

(9) K. Shinohara and N. Ryu: Phys. Rev., **75** (1949) 1762: J. Phys. Soc. Japan, **5** (1950) 119.

(10) C. G. Darwin: Proc. Roy. Soc., A **118** (1928) 654.

(11) H. S. W. Massey and C. B. O. Mohr: Proc. Roy. Soc., A **177** (1941) 341.

(12) C. T. Chase and R. T. Cox: Phys. Rev., **57** (1940) 243.

(13) S. Goudsmit and J. L. Saunderson: Phys. Rev., **57** (1940) 24: *ibid* **56** (1940) 36.

(14) K. Kikuchi: Proc. Phys-Math. Soc. Japan, **22** (1940) 805.

(15) E. Trounson and J. A. Sinpson: Phys. Rev., **63** (1943) 55.

(16) L. T. Broer: Phys. Rev., **74** (1948) 1887.

Revision of the Hyperfine Structure of the Mercury Spectrum.

By Kiyoshi Murakawa and Shigeki Suwa.

Institute of Science and Technology, Komaba, Meguro-ku, Tokyo.

(Received May 13, 1950)

Abstract.

The hyperfine structure of λ 5790, λ 5789.7, λ 5769 and λ 4047 of the spectrum of Hg I was studied, and the structure of some terms was determined. The ratio of the hyperfine structure constant of Hg^{199} to that of Hg^{201} was calculated for the terms $6p\ {}^1P_1$, $6p\ {}^3P_2$ and $7s\ {}^3S_1$, and it was found that the ratio is anomalous for the term $6p\ {}^1P_1$. The quadrupole moment of Hg^{201} was calculated to be $0.3_5 \cdot 10^{-24}$ cm².

Regularity in the displacement of even isotopes in lines of the mercury spectrum was found to exist in such a way that the ratio of the spacings $Hg^{204}-Hg^{202}$: $Hg^{202}-Hg^{200}$: $Hg^{200}-Hg^{198}$ is constant for all lines examined and is equal to 1 : 0.933 : 0.880. The same qualitative regularity was found in the isotopic displacement in lines of heavy elements consisting of at least three even isotopes.

§ 1. Introduction.

The object of the present paper is to describe the results of experiment which was undertaken in order to study whether the ratio of the hyperfine structure constant of Hg^{199} to that of Hg^{201} is constant for all terms of Hg I. For this purpose the terms $7\ {}^3S_1$, $6\ {}^1P_1$ and $6\ {}^3P_2$ were selected, and the hyperfine structure of the yellow lines of Hg I was studied, first of all, with a special care, and the structure of the term $6\ {}^1P_1$ was determined. The structure of the term $7\ {}^3S_1$ was determined from λ 4047 and λ 5461.

The hyperfine structure of the yellow lines has already been published in numerous papers, of which the most complete seems to be that of Görlich and Lau,⁽¹⁾ but the accuracy of their measurement is a little insufficient for the above mentioned purpose, in spite of the excellent resolving power of their spectroscopic apparatus. The work of one of the present authors was in progress at that time, but continuation of the work was hindered by subsequent events, and the investigation was resumed in 1945. Some of the results were reported, in an abstracted form, at another place.⁽²⁾

§ 2. Experimental Arrangement.

A Geissler tube which contained mercury and noble gas and was excited by a high voltage direct current, a specially constructed mercury arc lamp, and a hollow cathode discharge tube were used as the light source. For the purpose of resolving the fine structure, two quartz Lummer plates (thickness = 4 mm and 7 mm) and a Fabry-Pérot etalon were used. The Lummer plate was crossed with another one or with a Fabry-Pérot etalon.

§ 3. Experimental Results.

It was found that in order to obtain the structure of the term $6p\ {}^1P_1$ as accurately as possible, the structure of the line λ 5790 must be analyzed thoroughly.

The measurement of the structure of λ 5790 was sometimes disturbed by the presence of the line λ 5789.7 which lies very near to λ 5790. The hyperfine structure of the line λ 5789.7 had therefore to be fixed and was measured with the etalon with 1 mm, 2.4 mm and 6.5 mm spacers, and the result was taken into consideration in measuring the structure of λ 5790. The measured fine structure of λ 5789.7 is shown in Fig. 1, in which the transition scheme is also given. Numbers in parenthesis were calculated. The component due to Hg^{199} $(I=1/2)$ is represented by an arrow, while the component due to the even isotope $(I=0)$ is represented by a thick line. All the other components belong to the isotope Hg^{201} $(I=3/2)$. The accuracy of measurement of the

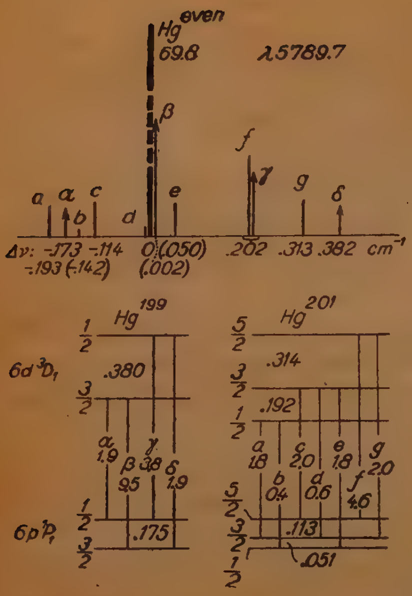

Fig. 1. Hyperfine structure of Hg I λ5789.7 ($6\,^1P_1-6\,^3D_1$).

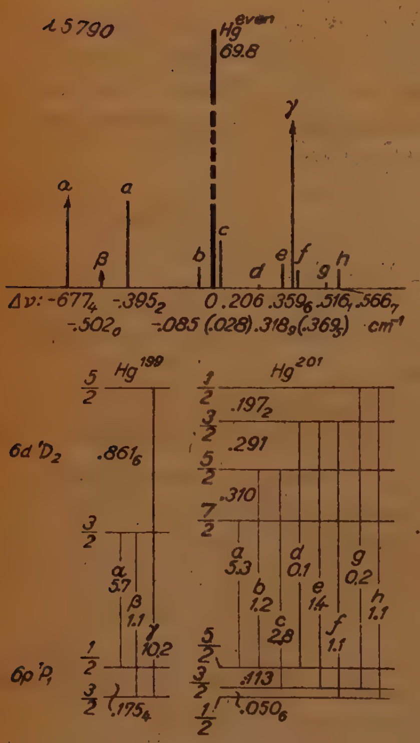

Fig. 2. Hyperfine structure of Hg I λ5790 ($6\,^1P_1-6\,^1D_2$).

structure of λ5789.7 is not great, but is sufficient for the above mentioned purpose. The calculated structure of λ5789.7 was given in a previous work,⁽³⁾ and is in general agreement with the observed one.

The structure of λ5790 is shown in Fig. 2. The interference pattern of this line taken with a 3.2 mm etalon is reproduced in Fig. 7, by which spacer every fine structure component of λ5790 was resolved without overlapping of orders. The splittings of $6\,^1P_1$ (Hg^{201}) namely $F_{\frac{5}{2}}-F_{\frac{3}{2}}$ and $F_{\frac{3}{2}}-F_{\frac{1}{2}}$ were determined from the distance $d-e$ and $g-h$ respectively. The component d is so weak that the accuracy of measurement of $F_{\frac{5}{2}}-F_{\frac{3}{2}}$ is ±0.002 cm^{-1}, although it is repeatedly measured on numerous plates.

The splitting of $6p\,^1P_1$ of Hg^{199} was determined by measuring directly the distance between the components α and β. But about 2/5 of the plates gave $\alpha-\beta=0.182_3\pm0.001$ cm^{-1}, while the remaining 3/5 gave $\alpha-\beta=0.175_4\pm0.0006$ cm^{-1}, and no intermediate values were obtained. At first it was decided to select one of these values by measuring the fine structure of λ4916 ($6\,^1P_1-8\,^1S_0$). The following structure was obtained for λ4916:

α(5.7%)	a(6.6%)	Hg$^{\text{even}}$ (69.8%)	b(4.4%)	β(11.4%)	c(2.2%)
−0.125	−0.065	0	?	0.055	0.098 cm^{-1}

The distance between the components α and β in

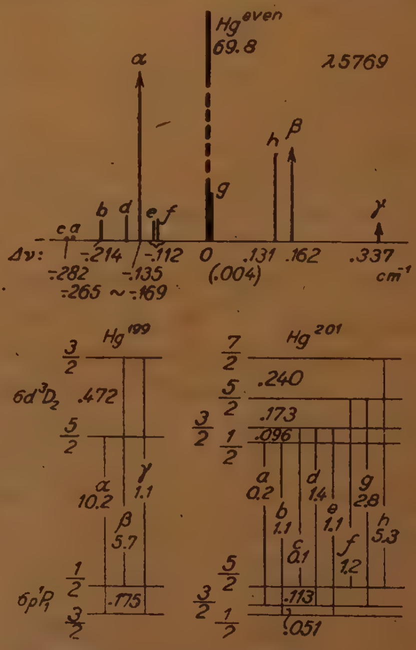

Fig. 3. Hyperfine structure of Hg I λ5769 ($6\,^1P_1-6\,^3D_2$).

λ 4916 should give approximately the required splitting of $6p\ ^1P_1$ (Hg^{199}), and this 0.180 cm^{-1} is in favour of the above mentioned 0.182 cm^{-1}.

Fig. 3 gives the fine structure of λ 5769. The accuracy of measurement of this line is not so good as λ 5790, but it serves to prove that the splittings of $6\ ^1P_1$ (Hg^{201}) that were deduced from λ 5790 are qualitatively correct. The components *c* and *a* were not satisfactorily resolved, but they appear as a patch diffuse to the red side.

The splitting of $6\ ^1P_1$ (Hg^{199}) can be obtained by measuring directly the distance $\beta-\gamma$. This gave the value 0.175 cm^{-1}, which is, contrary to λ 4916, in favour of 0.174 cm^{-1}. The cause of this discrepancy is not clear to us, but in view of the circumstance that the component β of λ 4919 is possibly disturbed by the unresolved component *b*, more weight was given to λ 5769, and the value 0.175 cm^{-1} was finally adopted. It is conceivable that on the plates which gave $\alpha-\beta = 0.182$ cm^{-1} for λ 5790 a weak line not corresponding to the transition $6\ ^1P_1-6\ ^1D_2$ appeared very close to the violet side of the component β and made the mutual distance $\alpha-\beta$ apparently larger.

Another proof, although less confirmatory, was obtained from λ 5789.7. From the measurement of λ 5789.7, the splitting of $6\ ^3D_1$ (Hg^{199}) was deduced to be 0.380 cm^{-1} or 0.373 cm^{-1} by adopting the value 0.175 cm^{-1} or 0.182 cm^{-1} respectively as the splitting of $6\ ^1P_1$ (Hg^{199}), whereas the splitting of $6\ ^3D_1$ was deduced to be 0.381 cm^{-1} from λ 3663 ($6\ ^3P_2-6\ ^3D_1$), which is again in favour of 0.175_4 cm^{-1}.

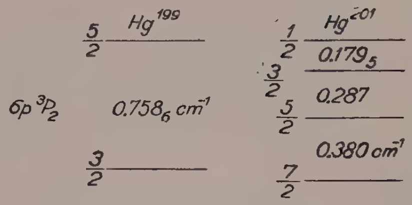

Fig. 5. Hyperfine structure of the term Hg I $6\ ^3P_2$.

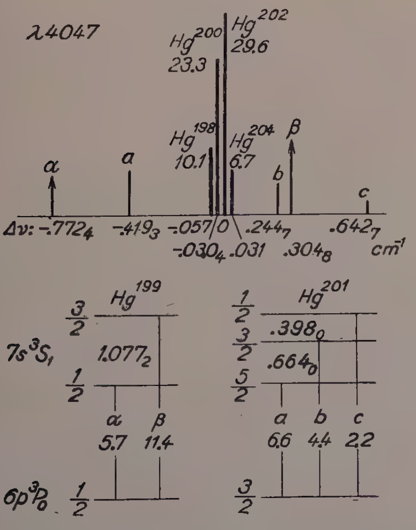

Fig. 4. Hyperfine structure of Hg I λ 4047 ($6\ ^3P_0-7\ ^3S_1$).

Accordingly the value of A^{199} for the term $6p\ ^1P_1$ which was given as −121.5 in reference 2 should be changed to −116.9.

The fine structure of λ 4047 is shown in Fig. 4. The structure of the term $7\ ^3S_1$ given here which was also confirmed by λ 5461 ($6\ ^3P_2-7\ ^3S_1$) is in agreement with the one given by previous workers⁽⁴⁾ ⁽⁵⁾ within experimental error.

The structure of the term $6p\ ^3P_2$ was determined (see Fig. 5) from λ 5461 ($6p\ ^3P_2-7s\ ^3S_1$) and λ 3654 ($6p\ ^3P_2-6d\ ^3D_2$). The splitting $F_{\frac{5}{2}}-F_{\frac{3}{2}}$ of

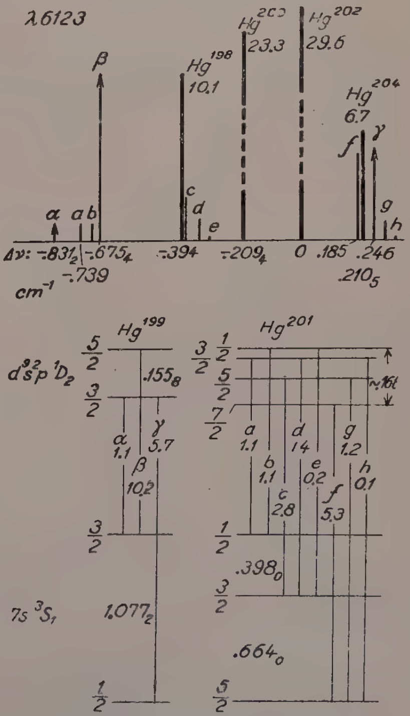

Fig. 6. Hyperfine structure of Hg I λ 6123 ($7\ ^3S_1-d^9\ s^2\ p\ ^1D_2$).

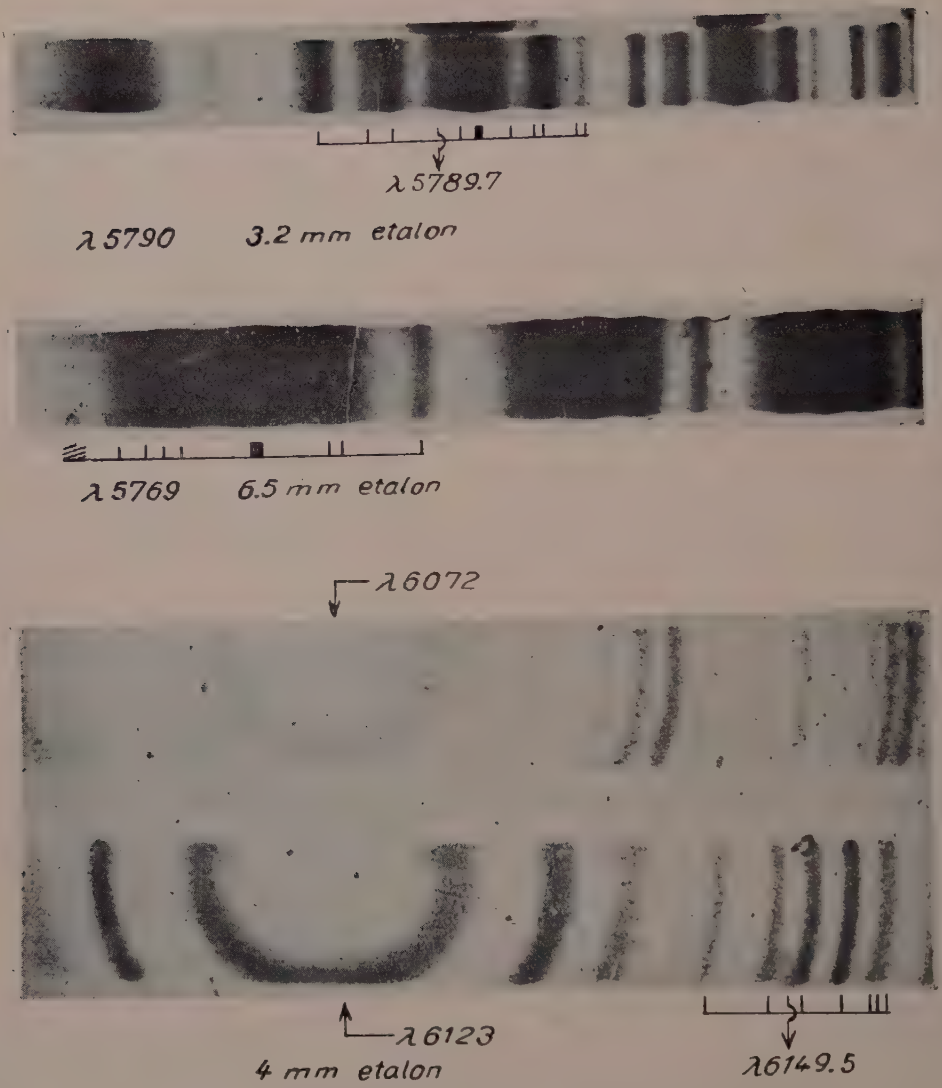

Fig. 7. Interference pattern of some lines of Hg I.

Hg^{199} and $F_{\frac{7}{2}}-F_{\frac{5}{2}}$ of Hg^{201} were determined from λ3654 only.

Finally. the fine structure of the line λ6123 is given in Fig. 6, which is, it is hoped, more accurate than the one given in a previous report.(4) In Fig. 7, the interference pattern of λ6123 taken with a 4 mm etalon is reproduced, by which the resolution of the component *f* was just attained without overlapping of orders. By the use of a thicker spacer this was resolved more clearly, but overlapping of orders occurred. Most of the components due to Hg^{201} are situated at positions so unfavourable to measurement that exact splittings of the upper term in Hg^{201} were not obtained. The displacement effect of the even isotopes will be discussed in § 6.

§ 4. Ratio of the Hyperfine Structure Constants of the Two Odd Isotopes.

Table 1 summarises the hyperfine structure constants of the three terms that could be determined with reasonable accuracy in the present work.

All the constants were calculated according to the expression

$$E = E_0 + \frac{A}{2} C + BC(C+1)\,,$$
$$C = F(F+1) - I(I+1) - J(J+1)\,.$$

Table 1. Hyperfine structure of the terms of Hg I. (in unit of $10^{-3}\cdot\text{cm}^{-1}$)

Term	A^{199}	A^{201}	B^{201}	A^{199}/A^{201}
$7\,^3S_1$	$718._1$	$-265._5$	0.0_2	-2.7047 ± 0.0006
$6\,^3P_2$	$303._4$	$-111._9$	0.26	$-2.713\ \pm0.004$
$6\,^1P_1$	$-116._9$	$42._4$	0.7_0	$-2.756\ \pm0.01$

In the last column the ratio A^{199}/A^{201} is given for the three terms. The ratio for the terms $7s\,^3S_1$ and $6p\,^3P_2$ do not differ much, but the ratio for the term $6p\,^1P_1$ is anomalous. It may be noted that this term is enough far away from other terms of the same parity to make it very unreasonable to ascribe the anomaly to a perturbation.

With respect to the ratio of the hyperfine structure constants of two odd isotopes belonging to an element, discrepancy between spectroscopic and nuclear induction experiment values has been noted in other elements.(6) (7) The discrepancy has been discussed by Bohr and Weisskopf(8) in a recent theoretical paper, but they predict the amount of the discrepancy only in the case of s and $p_{1/2}$ terms.

The terms that have been studied here belong to the configurations $6s\,7s\,^3S_1$, $6s\,6p_{3/2}\,^3P_2$, and $6s\,6p_{3/2}\,^1P_1$. According to our opinion, the value of B also must be taken into consideration in order to explain the above mentioned discrepancy.

§ 5. Quadrupole Moment of Hg^{201}.

In 1932 one of the authors determined the splittings of the term $6p\,^3P_2$ of Hg^{201} which deviated from the Landé interval rule to a large extent. Schüler and Schmidt interpreted this as due to the quadrupole moment of Hg^{201} which they calculated to be $0.5\cdot10^{-24}\,\text{cm}^2$. They also deduced the same value from the term $6p\,^3P_1$.

From the value of the constant B of $6p\,^1P_1$ (Hg^{201}) given in Table 1, the value of Q can be calculated according to the formula which is due to Casimir(9)

$$Q=\frac{BZ^*HI(2I-1)\cdot14.79}{\delta(R'\cdot c_1{}^2-2.83\cdot S\cdot c_1c_2)}10^{-24}\,\text{cm}^2,$$

in which B is measured in unit of $10^{-3}\,\text{cm}^{-1}$, and H, R' and S are relativity, correction factors and c_1 and c_2 are coupling constants of the term $6p\,^1P_1$, and δ is the doublet separation of the p-electron. Putting $B=0.7_0$, $Z^*=76$, $H=1.29$, $S=1.55$, $\delta=5624$, $c_1=0.907$, $c_2=-0.421$ in the above formula, we obtain

$$Q^{201}=0.2\cdot10^{-24}\,\text{cm}^2\quad(\text{from } 6s\,6p_{3/2}\,^1P_1),$$

which is not in good agreement with the value obtained from the term $6p\,^3P_1$ or $6p\,^3P_2$ (reference 5). The denominator in the formula for deducing the value of Q from the term $6p\,^3P_1$ has a small value, and this seems to cause uncertainty in calculating Q. The final value of Q^{201} seems, therefore, to be

$$Q^{201}=0.3_5\cdot10^{-24}\,\text{cm}^2,$$

taking the mean value of Q deduced from the terms $6p_{3/2}\,^1P_1$ and $6p_{3/2}\,^3P_2$.

§ 6. Displacement Effect of the Even Isotopes.

It is well known that the components due to the even isotopes show displacement effect in the hyperfine structure of numerous lines of mercury. The measured consecutive distances(10) between components due to even isotopes in each line and their ratio are summarized in Table 2.

Table 2. Displacement effect of even isotopes in lines of the mercury spectrum

Line	$\text{Hg}^{204}-\text{Hg}^{202}$	: $\text{Hg}^{202}-\text{Hg}^{200}$	: $\text{Hg}^{200}-\text{Hg}^{198}$
λ 6123	0.210_5	: 0.209_4	: $0.185\,\text{cm}^{-1}$
	= 1	: 0.995	; 0.885
λ 6072	0.122	: 0.121	: $0.108\,\text{cm}^{-1}$
	= 1	: 0.992	: 0.885
λ 4359	0.031	: 0.030_6	: $0.027\,\text{cm}^{-1}$
	= 1	: 0.99	: 0.87
λ 4078	0.031	: 0.031	: $0.027\,\text{cm}^{-1}$
	= 1	: 1.	: 0.87
λ 4047	0.031	: 0.030_4	: $0.027\,\text{cm}^{-1}$
	= 1	: 0.98	: 0.87
λ 3984	0.513_0	: 0.510_5	: $0.447\,\text{cm}^{-1}$
	= 1	: 0.995	: 0.87
Weighted mean	1	: 0.993	: 0.880

The ratio can be regarded as constant for all lines of mercury within experimental error.

Such a regularity was also found in the spectra of Pb I, Pb II and Pb III, about which the details will be published in a separate paper.

Further example of this kind can be found in the spectrum of W I, which was measured by Kiuchi, Hasunuma and Kawada.(11) Also the hyperfine structure of the spectrum of Os I measured by Kawada(12) and of the spectrum of Pt I measured by Tolansky and Lee(13) obey this regularity.

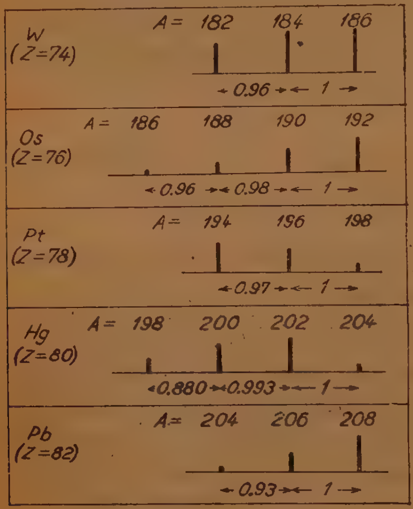

Fig. 8. Ratio of spacings of the components due to consecutive even isotopes

The ratio of spacings of the components due to consecutive even isotopes is given in Fig. 8 for each heavy element consisting of at least three even isotopes. It is seen that the ratio decreases towards lighter isotope in each element, and this regularity will be important in the theoretical explanation of isotope effect in the spectra of heavy elements.

References.

(1) P. Görlich u. E. Lau: Zeits. f. Physik **77** (1932), 746.

(2) K. Murakawa: Phys. Rev. **78** (1950), in press.

(3) K. Murakawa: Sci. Pap. Inst. Phys. Chem. Res. Tokyo **17** (1932), 299.

(4) K. Murakawa: Proc. Phys. Math. Soc. Japan **17** (1935), 14.

(5) H. Schüler u. T. Schmidt: Zeits. f. Physik **98** (1935), 239.

(6) F. Bitter: Phys. Rev. **75** (1949), 1326; **76** (1949), 150.

(7) S. Millman and P. Kusch: Phys. Rev. **58** (1940), 438; A. Berman, P. Kusch and A. K. Mann: Phys. Rev. **77** (1950), 140.

(8) A. Bohr and V. Weisskopf: Phys. Rev. **77** (1950), 94. See also G. J. Béné, P. M. Denis and R. C. Extermann: Phys. Rev. **78** (1950), 66.

(9) H. Casimir: Verh. Teylers Tweede Genootschap., Haarlem **11** (1936).

(10) Cf. also S. Mrozowski: Phys. Rev. **57** (1940), 207.

(11) M. Kiuchi, H. Hasunuma and T. Kawada: Proc. Phys. Math. Soc. Japan **19** (1937), 1019.

(12) T. Kawada: Proc. Phys. Math. Soc. Japan **20** (1938), 653.

(13) S. Tolansky and E. Lee: Proc. Roy. Soc. London (A) **158** (1937), 110.

On the Adiabatic Theorem of Quantum Mechanics.

By Tosio KATO.

Department of Physics, University of Tokyo.

(Read April 27, 1948, Received March 17, 1950)

§ 1. Introduction.

If the Hamiltonian H_t of a system is dependent on the time t, the Schrödinger equation of motion

$$\frac{d\psi_t}{dt} = -iH_t\psi_t \tag{1}$$

has in general no stationary solution (we put the Planck constant h equal to 2π). But in the limit when the change of H_t is made infinitely slow, the system, when started from a stationary state of H_0, passes through the corresponding stationary states of H_t for all t. This is the assertion of the adiabatic theorem of quantum mechanics.

The most complete proof hitherto given to the adiabatic theorem is due to Born and Fock(1) (hereafter quoted as BF). Their proof is very general so far as concerns the occurrence of crossing of eigenvalues, but in other respects it is still restricted by two essential assumptions:

i) the spectrum of H_t consists of purely discrete eigenvalues;

ii) these eigenvalues are non-degenerate except for accidental degeneracy caused by crossing.

Their argument cannot be extended to more general case without radical modification, for they consider simultaneously infinite number of solutions of (1) corresponding to the *complete system* of discrete eigenfunctions, which does not exist in general case.

From the physical point of view, these assumptions i), ii) are rather artificial, for it is not plausible that the solution of (1) corresponding to some particular eigenvalue λ_t of H_t should be influenced essentially by the nature, discrete or continuous etc., of those parts of the spectrum which are *distant* from λ_t.

In the present note we shall give a new proof of the theorem without these restrictive assumptions. In contrast with the method of BF, we have only to consider the solution of (1) starting from a *particular* eigenfunction of H_0(2) which may be degenerate, and we need not set up any hypothesis concerning the spectrum of H_t except in the immediate neighborhood of the eigenvalue under consideration.

In our opinion the contents of the adiabatic theorem is divided into two parts. In the first place it states the existence of virtual change of the eystem which may be called *adiabatic transformaticn* (abr. AT). Secondly, it asserts that the *dynamical transformation* (abr. DT) defined by the equation of motion (1) goes over to AT in the limit when the change of H_t is infinitely slow. These tranformations are represented by unitary operators, for they are real or virtual mechanical change.

Accordingly, our subject consists of two parts. First we have to find the unitary operator representing AT, and then we study the asymptotic behavior of DT defined by (1) and show its equivalence with AT. It should be noted that *the first part was quite trivial in the case of BF* where i), ii) are assumed, for AT should transform every eigenfunction of H_0 into the corresponding one of H_t and thus AT is already determined up to a phase factor for each eigenfunction. For this reason, only a half of the problem is solved in BF. The matter is not so simple in our general case, and *the construction of AT constitutes the main part of the present note.*

Our proof given below is rather formal and not faultless from the mathematical point of view. Of course it is possible to retain mathematical rigour by detailed argument based on clearly defined assumptions, but it would take us too far into unnecessary complication and obscure the essentials of the problem.

§ 2. Dynamical Transformation.

We consider the equation of motion (1) in the interval $0 \leq t \leq \tau$ and inquire into the behavior of the solution when $\tau \to \infty$, while the total change of H_t remains finite. For this purpose, it is convenient to introduce the new variable s by $t = \tau s$, $0 \leq s \leq 1$, according to BF, and to rewrite (1) as

$$\frac{d\phi_\tau(s)}{ds} = -i\tau H(s)\phi_\tau(s). \tag{2}$$

By hypothesis $H(s)$ is such that $dH(s)/ds$ remains finite when $\tau \to \infty$. In what follows we shall for simplicity assume that $H(s)$ is independent of τ, but it will be remarked that our argument applies without change also in the case of $H(s)$ depending on τ.

Let $\lambda(s)$ be a discrete eigenvalue of $H(s)$ with multiplicity $m \geq 1$, and let $E(s)$ be the projection⁽³⁾ on the associated m-dimensional eigenspace. We assume that $\lambda(s)$, $E(s)$ are continuous functions of s and that dE/ds, d^2E/ds^2 are piecewise continuous.

We have adopted the projection $E(s)$ because it is uniquely determined, while the corresponding eigenfunctions are not, especially when $m > 1$. It will be noted that $E(s)$ can easily be calculated if these eigenfunctions are given. Also $\lambda(s)$ and $E(s)$ are obtained from $H(s)$ by the well known perturbation method,⁽⁴⁾ and their continuity follows from that of $H(s)$.

Now we have by definition

$$\{H(s)-\lambda(s)\}E(s) = 0, \tag{3}$$

and there is an operator $S(s)$ such that⁽⁴⁾

$$E(s)\,S(s) = S(s)\,E(s) = 0, \tag{4}$$

$$\{H(s)-\lambda(s)\}S(s) = 1-E(s). \tag{5}$$

If the spectral decomposition⁽⁵⁾ of $H(s)$ is given by $H(s) = \int \lambda dE_s(\lambda)$, $S(s)$ is represented as⁽⁴⁾

$$S(s) = \int' [\lambda-\lambda(s)]^{-1}\, dE_s(\lambda), \tag{6}$$

where $\int'$ denotes integration except the point $\lambda = \lambda(s)$.

The solution of (2) is

$$\phi_\tau(s) = V_\tau(s)\,\phi_\tau(0). \tag{7}$$

$V_\tau(s)$ is a unitary operator* representing DT, and satisfies $(' = d/ds)$

$$V_\tau'(s) = -i\tau\, H(s)\, V_\tau(s), \quad V_\tau(0) = 1; \tag{8}$$

$$V_\tau^{+\prime}(s) = i\tau\, V_\tau^{+}(s)\, H(s), \quad V_\tau^{+}(0) = 1, \tag{9}$$

where $+$ denotes the adjoint operator. If we set

$$\overline{V}_\tau(s) = \exp\{i\tau\int_0^s \lambda(s)\, ds\}\, V_\tau(s), \tag{10}$$

we have by (9)

$$\overline{V}_\tau^{+\prime}(s) = i\tau\, \overline{V}_\tau^{+}(s)\, \{H(s)-\lambda(s)\}. \tag{11}$$

§ 3. Adiabatic Transformation.

We consider the differential equation

$$X'(s) = iA(s)\,X(s), \tag{12}$$

$$iA(s) = [E'(s),\, E(s)] \equiv E'E - EE'. \tag{13}$$

(12) is easily solved by successive approximation, and the solution is uniquely determined by the initial value $X(0)$. If we denote by $U(s)$ the solution of (12) with the initial value $U(0) = 1$, the general solution of (12) is clearly given by $X(s) = U(s)\,X(0)$. Also we have

$$U' = iAU, \quad U^{+\prime} = -iU^{+}A, \tag{14}$$

since $A(s)$ is Hermitian by (13). If follows that $(U^+U)' = (-iU^+A)\,U + U^+(iAU) = 0$ and hence $U^+U = U^+(0)\,U(0) = 1$. Also

$$(UU^+)' = (iAU)\,U^+ + U(-iU^+A) = i[A,\, UU^+]. \tag{15}$$

This is a linear differential equation for UU^+ and its solution is uniquely determined by its initial value $U(0)\,U^+(0) = 1$. Hence we must have $UU^+ = 1$, for it is certainly a solution of (15). Thus we have obtained

$$U^+U = UU^+ = 1, \tag{16}$$

showing that $U(s)$ is unitary.

On the other hand we have $E^2(s) = E(s)$ since $E(s)$ is a projection.⁽⁶⁾ Differentiation of both sides gives $E'E + EE' = E'$. Multiplying by E from left and right and noting $E^2 = E$, we have

$$EE'E = 0. \tag{17}$$

From (13) and (17) follows

---

* The proof is the same as in (16) below

$$iEA = -EE', \quad iAE = E'E. \tag{18}$$

Hence by $E'E + EE' = E'$ given above

$$E' = iAE - iEA = i[A, E]. \tag{19}$$

Next we consider EU. We have

$$(EU)' = (E' + iEA)U = iAEU \tag{20}$$

by (14) and (19). (20) means that $W \equiv EU$ is a solution of (12) so that we must have, by what is stated above, $W(s) = U(s)W(0)$ or

$$W(s) \equiv E(s)U(s) = U(s)E(0), \tag{21}$$

and hence

$$E(s) = U(s)E(0)U^{-1}(s). \tag{22}$$

We note further that

$$W(s) = E(s)W(s) = W(s)E(0), \tag{23}$$

$$W^+(s)W(s) = E(0), \quad W(s)W^+(s) = E(s) \tag{24}$$

by (21). Also we have

$$W'(s) = iAW = iAEW = E'EW = E'(s)W(s) \tag{25}$$

by (21), (20), (23) and (18), so that $W(s)$ satisfies a little simpler differential equation than $U(s)$. Finally we note that

$$E(s)W'(s) = EE'EW = 0 \tag{26}$$

by (25) and (17).

(22) means that the unitary operator $U(s)$ transforms the eigenspace $E(0)$ of $H(0)$ *isometrically* onto the eigenspace $E(s)$ of $H(s)$. By (21) and (23) we have $W(s)E(0) = U(s)E(0)$ so that $W(s)$ gives the same mapping as $U(s)$ when operated on functions of the eigenspace $E(0)$. We shall call $U(s)$ or $W(s)$ the AT operator corresponding to the eigenvalue $\lambda(s)$. In the fallowing section we shall show that $U(s)$ really represents the adiabatic change of the system initially in the eigenspace $E(0)$, and it will be seen that the relations (23) and (26) are essential for this purpose.

Remark. If $E(s)$ is a regular (analytic) function of s, it is easily seen that $U(s)$ is also regular. This is the case with the regular perturbation discussed in the paper cited above.(4)

§4. Proof of the Adiabatic Theorem.

We have by (11)

$$(\overline{V}_\tau^+ W)' = i\tau\overline{V}_\tau^+(H-\lambda)W + \overline{V}_\tau^+ W'.$$

The first term on the right vanishes by (23) and (3). Hence we have, on integrating both sides between 0 and s and noting

$$\overline{V}_\tau^+(0) = 1, \quad W(0) = E(0),$$
$$\overline{V}_\tau^+(s)W(s) - E(0) = \int_0^s \overline{V}_\tau^+ W' ds. \tag{27}$$

But we have by (26) and (5)

$$W' = (1-E)W' = (H-\lambda)SW',$$

so that by (11)

$$\overline{V}_\tau^+ W' = \overline{V}_\tau^+(H-\lambda)SW' = (i\tau)^{-1}\overline{V}_\tau^{+\prime} SW'.$$

Substituting this into (27) and integrating by part, we obtain

$$\overline{V}_\tau^+ W - E(0)$$
$$= (i\tau)^{-1}\Big[\overline{V}_\tau^+ SW'\Big]_0^s - (i\tau)^{-1}\int_0^s \overline{V}_\tau^+ (SW')' ds. \tag{28}$$

First let us assume that the eigenvalue $\lambda(s)$ does not cross other eigenvalues or continuous spectrum for $0 \leqq s \leqq 1$. Then $S(s)$ is finite as is seen from (6), and the right side of (28) is of the order τ^{-1} since $\overline{V}_\tau^+$ is unitary and hence of the order 1. Multiplying from left by the unitary operator $-V_\tau$ and noting $\overline{V}_\tau\overline{V}_\tau^+ = 1$, we obtain

$$\overline{V}_\tau(s)E(0) - W(s) = O(\tau^{-1})$$

or, by (10) and (23)

$$[V_\tau(s) - \exp\{-i\tau\int_0^s \lambda(s)ds\}W(s)]E(0) = O(\tau^{-1}). \tag{29}$$

It means that the DT $V_\tau(s)$ operated on any function of the eigenspace $E(0)$ tends to the AT $W(s)$ when $\tau \to \infty$ except for a phase factor, and thus (29) contains all the assertions of the adiabatic theorem.

For instance, let $\varphi_1(0), \cdots, \varphi_m(0)$ be an orthonormal system composed of eigenfunctions of $H(0)$ belonging to the eigenvalue $\lambda(0)$. Then we have $E(0)\varphi_j(0) = \varphi_j(0)$, and $\varphi_j(s) \equiv U(s)\varphi_j(0) = W(s)\varphi_j(0)$ are eigenfunctions of $H(s)$ belonging to the eigenvalue $\lambda(s)$ because $E(s)\varphi_j(s) = \varphi_j(s)$ by (23). Also $\varphi_j(s)$ form an orthonormal system since $U(s)$ is unitary. If we operate (29) on $\varphi_j(0)$, we have

$$V_\tau(s)\varphi_j(0) - \exp\{-i\tau\int_0^s \lambda(s)ds\}\varphi_j(s) = O(\tau^{-1}). \tag{30}$$

But $V_\tau(s)\varphi_j(0)$ is the solution of the equation of motion with the initial state $\varphi_j(0)$. Hence (30) means that this solution coincides with the eigenfunction $\varphi_j(s)$ of $H(s)$ up to the quantity of the order $O(\tau^{-1})$ and a phase factor.

Again let $\psi(0)$ be any wave function. Taking the scalar product of (30) with the function $V_\tau(s)\psi(0)$ and noting that $V_\tau(s)$ is unitary, we obtain

$$(\varphi_j(0),\ \psi(0)) - \exp\{-i\tau\int_0^s \lambda(s)\,ds\}(\varphi_j(s),\ V_\tau(s)\psi(0)) = O(\tau^{-1}). \tag{31}$$

If the system is initially represented by the wave function $\psi(0)$, the probability that the system is in the stationary state $\varphi_j(0)$ at $s=0$ is $|(\varphi_j(0), \psi(0)|^2$. The probability that the system is in the corresponding stationary state $\varphi_j(s)$ after the time s is $|(\varphi_j(s), V_\tau(s)\psi(0))|^2$. Therefore (31) shows that these probabilities are equal up to a quantity $O(\tau^{-1})$*.

Thus (29) is seen to contain all the assertions of the adiabatic theorem.

Next we consider the case where crossing takes place finite times between the eigenvalue $\lambda(s)$ and other eigenvalues. Let $s_1, \cdots, s_{N-1}$ be the points at which the crossing occurs. Then the operator $S(s)$ in general becomes infinite at these points (see (6)), and (28) is not valid. But if we take a small number $\delta>0$, we can apply (28) to each of the intervals $s_{k-1}+\delta \leqq s \leqq s_k-\delta$ $(k=1, \cdots, N;\ s_0=0,\ s_N=1)$ in place of the interval $(0, s)$, and we obtain

$$\lim_{\tau\to\infty}\left[\overline{V}_\tau{}^+W\right]_{s_{k-1}+\delta}^{s_k-\delta}=0$$

for *fixed* δ. On the other hand, if we apply (27) to the small interval $s_k-\delta\leqq s\leqq s_k+\delta$, we obtain

$$\lim_{\delta\to 0}\left[\overline{V}_\tau{}^+W\right]_{s_k-\delta}^{s_k+\delta}=0$$

uniformly with respect to τ because $\overline{V}_\tau{}^+$ is unitary. Consequently, if we take first δ small and then τ sufficiently large, we can easily conclude that

$$\overline{V}_\tau{}^+W-E(0)=o(1)$$

where $o(1)$ means a quantity which tends to zero when $\tau\to\infty$. It follows as before

$$[V_\tau(s)-\exp\{-i\tau\int_0^s\lambda(s)ds\}W(s)]E(0)=o(1), \tag{32}$$

which gives the complete proof of the adiabatic theorem in the general case.

Of course (32) holds for every eigenvalue of $H(s)$ provided the eigenvalue and the corresponding projection on the associated eigenspace has appropriate continuity with respect to s stated before. On the other hand, the adiabatic theorem can often fall to be valid if this continuity condition is not satisfied.⁽⁶⁾.

§ 5. Extension of the Adiabatic Transformation.

Hitherto we have considered only one eigenvalue $\lambda(s)$ of $H(s)$ and constructed the corresponding AT operator $U(s)$. Accordingly $U(s)$ does not necessarily represent AT if it is operated on functions outside the eigenspace $E(0)$, and we had to take different $U(s)$ for different eigenvalues of $H(s)$.

To remove this defect, we shall in this section show that we can construct a unitary operator $U(s)$ which describes AT *for all discrete eigenvalues* $\lambda_n(s)$, $(n=1, 2, \cdots)$, of $H(s)$ simultaneously.

Let $E_n(s)$ be the eigenspace associated with $\lambda_n(s)$. As is well known, they are mutually *orthogonal*:

$$E_n(s)\,E_m(s)=\delta_{nm}E_n(s), \quad (n,\ m=1, 2, \cdots).$$

But they are not necessarily *complete*, for we have not excluded the existence of the continuous spectrum. If we set

$$1-\sum_{n=1}^{\infty}E_n(s)=E_0(s), \tag{33}$$

$E_0(s)$ is therefore in general not zero, and is orthogonal to all $E_n(s)$, $(n\geqq 1)$.

If these $E_n(s)$ are appropriately continuous, we can construct the corresponding AT operator $W_n(s)$ defined in §3 (see (21)), and we have by (23), (24)

$$W_n(s)=E_n(s)\,W_n(s)=W_n(s)\,E_n(0), \tag{34}$$

$$W_n{}^+(s)\,W_n(s)=E_n(0),\quad W_n(s)\,W_n{}^+(s)=E_n(s). \tag{35}$$

In follows from (34) that for $m\neq n$

$$\begin{aligned} W_n{}^+(s)\,W_m(s)&=W_n{}^+(s)\,E_n(s)\,E_m(s)\,W_m(s)=0,\\ W_n(s)W_m{}^+(s)&=W_n(s)\,E_n(0)\,E_m(0)\,W_m{}^+(s)=0. \end{aligned} \tag{36}$$

---

* Or $O(\tau^{-2})$ if $(\varphi_j(0), \psi(0)=0$.

Now we set

$$U(s) = \sum_{n=0}^{\infty} W_n(s) . \qquad (37)$$

Then we have

$$U^+(s)\, U(s) = \sum_{m,n}^{0,\infty} W_n^+(s)\, W_m(s) = \sum_{n=0}^{\infty} E_n(0) = 1$$

by (35), (36) and (33). Similarly we can show $UU^+ = 1$ so that $U(s)$ is a unitary operator. Next we have by (34)

$$U(s)\, E_n(0) = \sum_m W_m(s)\, E_m(0)\, E_n(0) = W_n(s) .$$

Hence $U(s)$ coincides with $W_n(s)$ when operated on $E_n(0)$, so that $U(s)$ represents AT in each subspace $E_n(0)$. Thus we have obtained the desired operator.

In conclusion we note without proof that $U(s)$ satisfies the following differential equation

$$U'(s) = iB(s)\, U(s) ,$$

$$iB(s) \doteq \tfrac{1}{2} \sum_{n=0}^{\infty} [E'_n(s) ,\ E_n(s)] .$$

References.

(1) M. Born and V. Fock: Zs. f. Phys. **51** (1928), 165. See also M. Born and P. Jordan: Elementare Quantenmechanik. Berlin, 1930.

(2) In this respect, our method is analogous to that of Güttinger, Zs. f. Phys. **73** (1931), 169.

(3) J. v. Neumann: Mathematische Grundlagen der Quantenmechanik, Berlin, 1932, p. 40.

(4) Cf. T. Kato, Prog. Theor. Phys. **4** (1949), 514.

(5) See (3), p. 60.

(6) Cf. the classical example in M. Born, Vorlesungen über Atommechanik, Berlin, 1925, p. 112.

On the Standing Varicose and Sinuous Ripple of a Cylindrical Flow.

By Yoshimasa WADA.

Yamanashi University.

(Read in the Ordinary Meeting of April 1950, Received May 17, 1950)

§ 1. Experiment of Varicose Vibration.

The wave form in the up- and down-stream sides of an obstacle held stationary in the plane surface of running fluid was investigated by Lord Rayleigh.(2) In the case of a cylindrical jet the circumstance behind the disturbance is not observed in general and has been put out of consideration. But when the fluid is flowing out from a circular tube, such disturbance is always given to the flow at the orifice, neverthless we observe no ripples. In order to recognize the circumstances more clearly, the author made the following experiment.

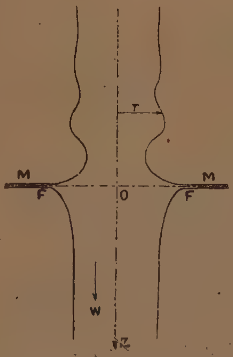

Fig. 1. Schematio sketch of varicose ripples.

M: metal plate,
F: film of fluid.

We make in a thin metal plate a circular hole of the radius which is a little greater than that of the jet, and insert the plate into the jet. In that hole we made a membrane of a film of the fluid previously. If the size of the hole is appropriate, the jet flows down through the membrane without breaking it. Then the disturbance of radial negative pressure is given by the surface tension of the film. And, as shown in Fig. 1, above the metal plate standing ripples are observed as a matter of course, below it there are none, but the radius of the jet decrease gradually as the distance from the plate increases. Thus we can see that for the disturbance of the same magnitude the ripples form in the up-stream side of it but none in the down-stream side.

§2. General Formula.

In order to require the mathematical foundation, when we intend to apply Lord Rayleigh's method[2] for the case of plane surface, there enters a combination of Bessel functions in place of algebraic terms in his case, so that the calculation becomes very difficult. But when we confine the problem only to the criterion of the wave-lengths before and behind the disturbance, assuming the wave forms to be represented by trigonometric functions, the following method may be applied.

Let us consider the case that the viscosity of the fluid is so small that it does not disturb the existence of the velocity potential. When the fluid has a common velocity W downwards, using the cylindrical coordinates z, r, θ, where the positive direction of z axis coincides with that of the common velocity, the equation of the velocity potential ϕ is

$$\frac{\partial^2\phi}{\partial r^2}+\frac{1}{r}\frac{\partial\phi}{\partial r}+\frac{1}{r^2}\frac{\partial^2\phi}{\partial\theta^2}+\frac{\partial^2\phi}{\partial z^2}=0. \qquad (1)$$

The slightly disturbed surface is given by

$$r=a+\xi,$$

where a is the mean radius of fluid column, and ξ may be given by the sum of the terms of the type $\alpha_n \exp(in\theta)\exp(ikz)$, each of which may be considered independent.

For the surface we have

$$-\left(\frac{\partial\phi}{\partial r}\right)_{r=a}=W\frac{\partial\xi}{\partial z}. \qquad (3)$$

From (1) we obtain

$$\phi=-\frac{W\alpha_n}{J_n'(ika)}J_n(ikr)\,e^{in\theta}\,e^{ikz}-Wz. \qquad (4)$$

Then ξ is written as

$$\xi=\alpha_n\,e^{in\theta}\,e^{ikz}. \qquad (6)$$

In the following discussion we assume that the disturbance is given at $z=0$.

Substituting (4) and (5) in the pressure equation

$$p/\rho=\nu(\phi+Wz)-q^2/2. \qquad (6)$$

and taking account of the effect of the variation due to the surface tension T in p, we have

$$kW^2-\frac{T}{\rho a^2}(k^2a^2+n^2-1)\frac{iJ_n'(ika)}{J_n(ika)}=i\nu W. \qquad (7)$$

Using $I_n(ka)$ for $J_n(ika)$, (7) can be transformed as follows.

$$kW^2-\frac{T}{\rho a^2}(k^2a^2+n^2-1)\left\{\frac{n}{ka}+\frac{I_{n+1}(ka)}{I_n(ka)}\right\}=i\nu W. \qquad (8)$$

This is the fundamental relation between W and k for a given disturbance of the mode of n. For the sake of simplicity we write the left side as follows

$$F(k)=kW^2-\frac{T}{\rho a^2}(k^2a^2+n^2-1)\left\{\frac{n}{ka}+\frac{I_{n+1}(ka)}{I_n(ka)}\right\}. \qquad (9)$$

Then

$$F(k)=0 \qquad (10)$$

gives the first approximation to k. To get the second approximation, we put

$$F'(k)\Delta k=i\nu W, \qquad (11)$$

or

$$\Delta k=i\nu W/F'(k) \qquad (12)$$

Thus $k+\Delta k$ is given as the second approximation. Introducing these expressions in (5), we see that ξ varies proportionally to

$$\exp[ik-\nu W/F'(k)]z \qquad (13)$$

So that we must select solutions of (10) such that (13) does not diverge, namely, for $z>0$, we must use k such as to make $F'(k)$ negative, and for $z>0$, such as to make $F'(k)$ positive.

§3. Application to Varicose Vibration.

For varicose vibration we put n to be zero. Then

$$F(k)=kW^2-\frac{T}{\rho a^2}(k^2a^2-1)\frac{I_1(ka)}{I_0(ka)}. \qquad (14)$$

To find the solutions of $F(k)=0$, we describe the curves representing kW^2 (curve a) and

$$(T/\rho a)(k^2a^2-1)\,I_1(ka)/I_0(ka)$$

(curve b) against k, as in Fig. 2. We have three points of intersection between them, and their ordinates give the solution of $F(k) = 0$. Thus the first approximation are κ_1, which is always zero, and $\pm\kappa_2$. (The numerical values of κ_2 were already calculated by the author in a previous paper⁽³⁾, but are not needed for the present purpose.) Since $F'(k)$ is given by the difference of the gradients of the two curves a, and b, as

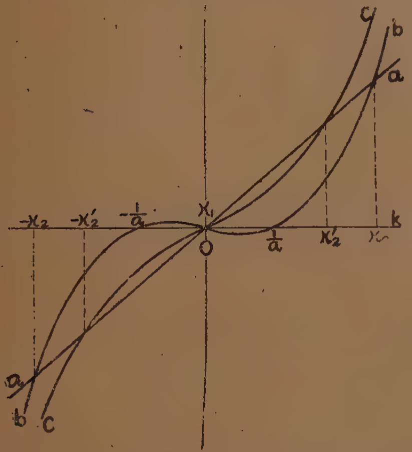

Fig. 2. Diagram for solving $F(k) = 0$ and deciding the signes of $F'(k)$.

we can understand easily in Fig. 2, $F'(\kappa_1)$ is always positive, and $F'(\kappa_2)$ and $F'(-\kappa_2)$ are always negative and equal. So that $\kappa_1 (= 0)$ corresponds to the state in $z > 0$, and κ_2 and $-\kappa_2$ to that in $z < 0$.

Thus the standing varicose ripples (corresponding to $\pm\kappa_2$) can be observed only above the disturbance, and below it no waves are to be seen.

§ 4. Application to Sinuous Vibration.

Next we investigate the sinuous vibration. As $n = 1$,

$$F(k) \doteq kW^2 - \frac{T}{\rho a^2} \cdot k^2 a^2 \left\{ \frac{1}{ka} + \frac{I_2(ka)}{I_1(ka)} \right\}. \quad (15)$$

The second term in the right-hand side of (15) is shown by the curve c in Fig. 2, and the points of intersection of it with the curve a give κ_1, which is equal to zero, and $\pm\kappa_2'$ as the solutions of $F(k) = 0$,

As the gradients of the curve c at the origin is $T/\rho a$, when W^2 is greater than $T/\rho a$, κ_1 and $\pm\kappa_2'$ are real. and similarly to the case of varicose vibration, the ripples corresponding to $\pm\kappa_2'$ are observed above the disturbance, because κ_2' as well as $-\kappa_2'$ makes $F'(k)$ negative and κ_1 makes $F'(k)$ positive. But below the disturbance there acts no restituting force as shown by Lord Rayleigh⁽¹⁾, we cannot obtain the distortion in this region from the above investigation.

As W^2 approaches toward $I/\rho a$, κ_2' decreases rapidly to zero, and when W^2 becomes less than $T/\rho a$, $\pm\kappa_2'$ become imaginary, but on the contrary $\kappa_1 (= 0)$ makes $F'(k)$ negative, and above the disturbance we observe aperiodic distortion.

§ 5. Experiment of Sinuous Vibration.

For the experiment of this case the disturbance was caused by the electrical method suggested Lord Rayleigh⁽²⁾. In this case the jet and a thin metal plate with its one edge placed very near the jet, formed the electrodes, and potential difference of about two thousand volts was applied between them.

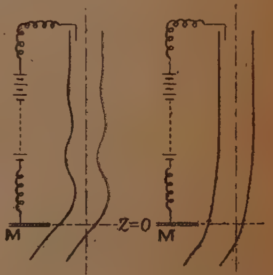

(a) $W^2 > T/\rho a$ (b) $W^2 < T/\rho a$

Fig. 3. Schematic sketch of sinuous ripples.
M: metal plate.

By the electrical attraction the distortion of jet appeared, but in nearly all cases sinuous ripples as shown in Fig. 3, a were observed. If we wish to observe the aperiodic distortion, we are to use the region where W^2 is less than $T/\rho a$. But in the perpendicular jet as used by the author, this region is limited to a very narrow space near the orifice for all quantity of flow by the influence of gravitation. As the velocity of flow decreased, the ripple-length increased very rapidly, far more rapidly than did in the case of varicose ripples. At last the wave form disappeared and the jet became as shown in Fig. 3, b. The critical state of transition is given by $W^2 = T/\rho a$. If we bring the metal electrode upward keeping the quantity of flow invariable, we can find the critical position on the jet. In this position the radius of the jet was measured by a sliding telescope, and then with the quantity of flow the critical velocity was calculated and the square of this velocity was compared with $T/\rho a$ as shown in Table 1. The fluid used was water and the surface tension was taken as 74 c.g.s., as the temperature wass 11°C.

Table 1.

Quantity of flow c.c./sec.	Radius of jet, a cm	Velocity of flow, W cm./sec.	W^2	$T/\rho a$
1.26	0.130	23.8	562	570
1.64	0.157	21.2	450	471

Thus the experimental investigation also supports the above-mentioned consideration.

§ 6. Acknowledgement.

The author is greateful to Professor H. Honda in Tokyo University for encouragement and to Professor I. Imai for suggestion and discussion.

References.

(1) Lord Rayleigh: Proc. Roy. Soc. **29** (1879) 71.
(2) Lord Rayleigh: Proc. London Math Soc. **15** (1883) 69.
(3) Wada, Y.: Journ. Phys. Soc. Japan **5** (1950) 259.

On the Electrical Conductivity of Alumina.

By Tetsuya ARIZUMI and Shoichiro TANI.

Kobe Kogyo Corp. Kobe.

(Received May 22, 1950)

§ 1. Introduction.

Almina is an excellent insulator at low temperatures, but it becomes slightly conductive beyond 1,000°C. W. Hartmann(1) whose experiments were carried out at 300~800°C has reported that alumina is an excess semi-conductor and its activation energy for the conductivity is 0.25~0.385 e.v. For the practical use in vacuum tube industry, however, the conductivity at higher temperatures should be the matter of concern and it is the present item to be studied.

§ 2. Experimental Procedure.

The conductivity was measured by the imbedded probe method. Fig. 1 shows three types of electrode arrangement used in the experiments. h is a W-Mo alloy wire of the diameter 0.09 mm., on which alumina was coated as thick as 0.3 mm. diameter by the dip method(2) or by the electro-deposition.(3) The coated wire was fired in hydrogen at 1,650~1700°C, to make alumina sintered to a rigid sheath (t). Then W-Mo alloy wire of 0.026 mm. was wound around the sheath t, on which a small amount of alumina was sprayed (u). The assembly was fired in hydrogen again. The sample thus prepared is shown in Fig. 1(a).

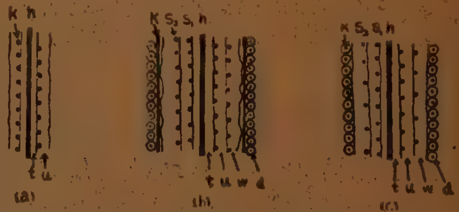

Fig. 1. Experimental electrode arrangements.

In the type (b) a second alloy wire was wound around the sample (a), on which the third alumina layer was sprayed and then the assembly was sintered. The sintered sample was inserted into a nickel sleeve *k*, around which an alumina coated wire d was wound closely. In the type (c) a spiral alloy wire, replaced the nickel sleeve in (b), served as both the heater and an electrode.

Each type has several defects; In the type (a), its temperature distribution is not always uniform and the potential drop along the heater cannot be neglected. The type (b) is the most ideal procedure, but it cannot be heated above 1,400°C. The type (c) lacks of these defects in (b), but cannot be free from similar weak points in (a). In each experiment, the best fitted type was chosen of these three ones. In every cases the coating length of alumina was about 30 mms. A prepared sample was mounted on a stem and the assembly was sealed and exhausted.

Appling a D.C. potential between *h* and *k*, the potential of two probes s_1 and s_2, were measured by a potentiometer. The temperature was determined by a micro-optical pyrometer, as well as by the resistance of the alloy wire. Both results agree within ±15°C.

Three kinds of fused alumina with different impurity contents were used. Their analytical results are presented in the table 1 and their average grain size is about 1 micron.

Table 1. Impurity contents (%)

Sample	SiO_2	Fe_2O_3	CuO	MgO	CaO	Na_2O
A	0.37	0.68	0.03	1.19	1.35	0.32
B	0.22	0.39	0.24	0.90	trace	
C	0.25	0.26	trace	0.18	0.03	0.25

§ 3. Ionic Current.

The electrode arrangement of the type (a) and (c) was mainly used for these experiments. In all tubes of insufficient ageing, the current through alumina decreases rapidly, when a D.C. potential is supplied between *k* and *h*. Fig. 2 is typical examples. Connecting *k* to −50V D.C. at first, the current decrease like a_1, and then changing the polarity of *k* to +50V suddenly, almost similar time change is observed (b_1). Changing the polarity to −50V, again, the curve a_2 is obtained. Other curves correspond to such alternation of polarity. The peak value i_0 is found to decrease slightly as the time of repeating.

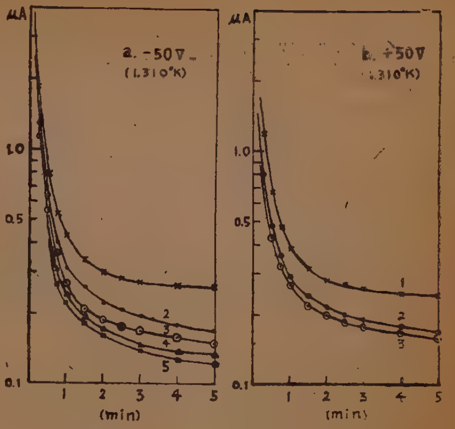

Fig. 2, Ionic Currents.

These curves seem to be an addition of a current with intense time change and a steady current. Thus, plotting $\log(i-i_\infty)$ versus time in min., the following expression is found to hold in every cases.

$$\log(i-i_\infty) = A-K \log t \tag{1}$$

K range from 0.6 to 1.6. The expression (1) is similar as that for the polarization current, suggesting that one part of the current is due to the polarization of ions or similar phenomena.

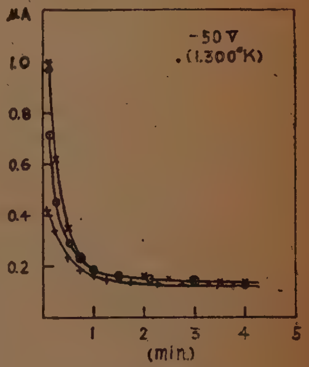

Fig. 3. Effect of Hysteresis.

This part of current is influenced sensitively by the hysteresis of the sample. When the potential of *k* is changed suddenly from positive to negative, after having been kept at +50V for 15 secs. 80 secs. and 5 mins., the time changes of current become like three curves 1, 2 and 3 in Fig. 3. respectively.

Although the steady currents are almost equal, the peak value i_0 is distinctly different. It holds the case for the interchange from negative to positive. Moreover the polarization current depends upon the pausing time, which means the time of lighting the sample without any potential. If a potential of the same sign is applied intermittently, the longer-pausing time gives the smaller current, while the larger one in the case of the opposite potential. In Fig. 4 (a) k is positive and in (b) negative and the curves (2) and (3) in both figures are those measured at 10 and 20 mins. pausing time respectively. K differs in both sides, probably because of the geometrical arrangement and other effects.

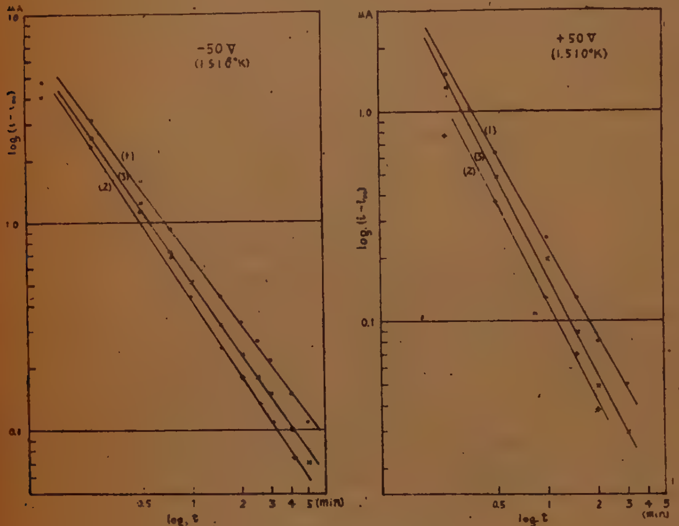

Fig. 4. Effect of Pausing.

Such large hysteresis effect probably masks almost all other effects. Generally speaking, however, following tendencies should be pointed out. (1) The polarization current becomes larger at higher potentials, but K is almost constant within the experimental error, and (2) i_0 does not increase so much but i_∞ increases at high temperatures.

These several results suggest that the polarization current is caused by the ionic motion in alumina. Appling a potential, both positive and negative ions move to two opposite electrodes, resulting in a non-uniform distribution of ion density in the alumina layer. Removing the potential, the density recovers by means of the thermal diffusion to an uniform distribution. But it takes rather long time for the recovering probably because of the difficulty in diffusion.

§ 4. Effects of Heat Treatment and Impurities.

Lighting the sample at a high temperature, say 1800°C, i_0 decreases gradually and i_∞/i_0 become larger. Fig. 5 (a) and (b) are time changes of the ionic current of alumina A fired at 1800°C for 1 hr. and about 80 hrs. respectively. As seen in the figure, it takes much shorter time to reach a steady current in (b) than in (a). In such a state as (b) an interesting phenomena happened to be observed. Connecting k to −20V at first, the current decreases slightly only for one min. as in (b). Changing to −40V after 10 mins' pause, the current increases to a steady value as in (c). Appling k to −60V after the second 10 mins. pause, the current increases similarly. This curious phenomena may well be also due to the ionic motion. Passing through such process the ionic current becomes to disappear thoroughly at last.

The ionic current is also sensitively affected by the purity of alumina. In alumina A i_∞/i_0 is 0.05—0.1, while it is 0.2—0.5 for alumina C at the initial stage and it takes several times longer at 1,800°C in alumina A than in alumina C that the ionic current disappears.

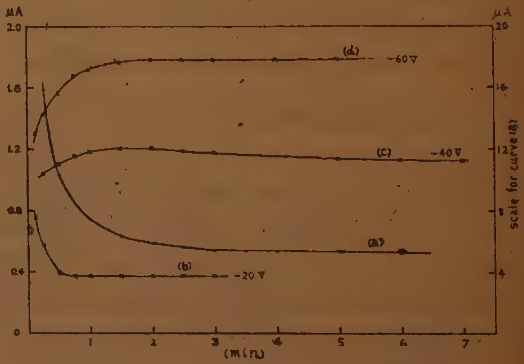

Fig. 5. The transient phenomena.

These results are evidences to that the ionic current is mainly caused by impurities in alumina. During the long heat run at high temperatures, some kind of volatile impurities, such as Na_2O and K_2O, evaporates to decrease the ionic current. The fact that black evaporated substances were found frequently to be condensed on the glass wall in the case of alumina A is a direct proof to the above conclusion.

§ 5. Breakdown.

During the measurement of ionic current, the phenomena which are thought to be preliminary for the breakdown were experienced frequently. Most of these phenomena occurs only when the ionic current is still predominant. Appling the potential, the current decreases rapidly as described in the foregoing section, but it begins to deviate gradually from the normal time change represented by (1) and at last develops to a sudden changes as seen iu Fig. 6.

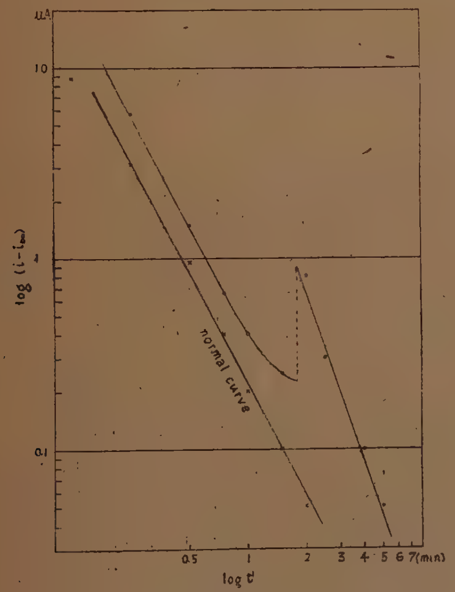

Fig. 6. A preceding phenomena of breakdown.

However, it does not proceed to a complete breakdown, but enters into a new decreasing curve (2), as if there has been no abnormality. This increased ionic current decreases again during the heat run. These phenomena like the breakdown is more frequently encountered at high temperature. Probably the accumulation of these phenomena proceds to the breakdown.

§ 6. Potential Distribution.

The electrode arrangement (b) was mainly available for this purpose. The applied voltage and the potentials of s_1 and s_2, measured by a potentiometer, are presented in Table 2. No proportionality is found in the table between v_0 and i, and almost all part of applied potential drops at the space $h-s_2$ and only remaining small voltage in the alumina layer. As the total drop v_3 in the layer can be evaluated, the relation of i upon v_0-v_3 is found to be expressed by

$$\log i = \kappa (v_0-v_3)^{\frac{1}{2}} \tag{2}$$

This formula is quite similar to the thermionic Schottky equation,

$$i = i_0 \exp\left(\frac{e\sqrt{v}}{kT}\right) \tag{3}$$

showing that the current from alumina to nickel or from nickel to alumina is a thermionic emission. As the practical cathode has a similar construction as the type (b) in Fig. 1, expect two probes, the leakage current, usually called i_{hk}, means the thermionic emission current.(4)

It is seen also in the Table 2 that v_2/v_1 is a function of temperature, but independent on the applied voltage. Its dependency on temperature is more remarkable in the sample with insufficient ageing, while v_2/v_1 becomes almost independent on temperature when the ionic current disappears.

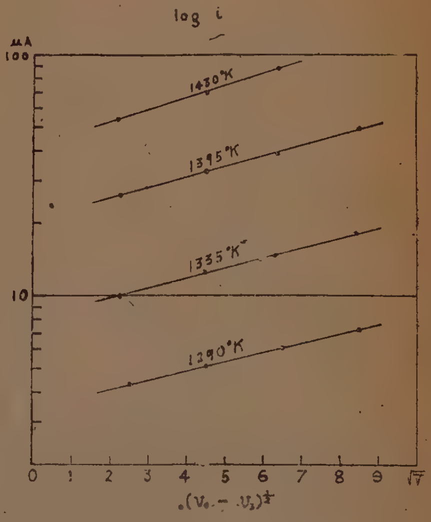

Fig. 7. Schottky plots.

Table 2. The potential distribution

v_0	1,480°K				1,418°K			
	i	v_1	v_2	v_2/v_1	i	v_1	v_2	v_2/v_1
5.0	17.2	0.44	0.72	1.64	2.5	0.16	0.30	1.88
10.0	19.6	0.48	0,79	1.65	4.4	0.29	0.53	1.83
20.0	22.8	0.58	0,95	1,64	5.1	0.35	0.63	1.80
50.0	28.5	0.70	1.15	1.64	5,8	0.40	0.72	1.80
90.0	32.0	0.76	1.26	1.66	9.0	0.44	0.82	1.86
Average				1.65				1.83

This means that, exactly speaking, the potential distribution is not linear, so long as the ionic current is still remarkable. As the impurities evaporate from alumina, the potential distribution becomes linear and at the same time the electronic conduction becomes predominant.

§ 7. Electronic Conduction.

Even in the steady state the ionic current should not be perfectly neglected, judging from the existence of the unsteady part and non-linear potential distribution. However, the potential drop between s_1 and s_2 is quite linear with respect to the current through alumina as in Fig. 8, showing that the Ohmic law holds in the steady state. In other words, the conduction becomes electronic.

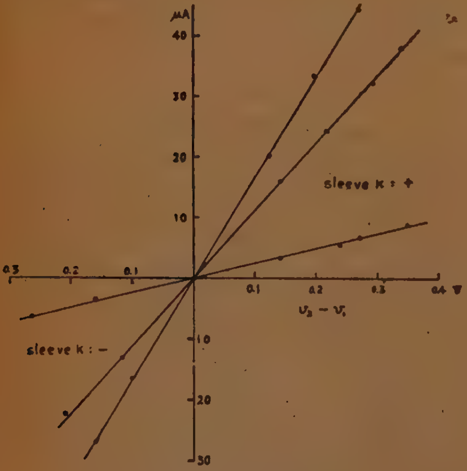

Fig. 8. Electronic currents.

The conductivity evaluated from the inclinations in Fig. 8 are plotted in Fig. 9 and it is represented in the form,

$$\sigma = \sigma_0 \exp\left(-\frac{\varepsilon-\mu}{kT}\right). \tag{4}$$

The curve (1) is that for the sample with insufficient heat run and the estimated activation energy is about 1.0 e.v. During the lighting at high temperature, the activation energy becomes larger gradually as the curves (2) and (3), and finally it reaches to 2.8—2.9 e.v. In these state no ionic current is observed and no further increase in the activation energy is experienced.

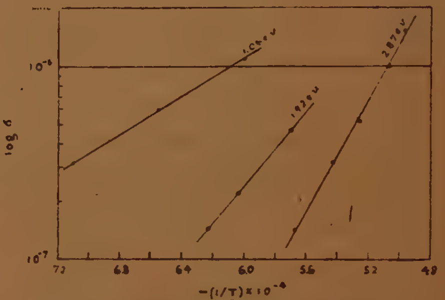

Fig. 9. The activation energy for electronic conduction.

The activation energy of alumina B and C are always larger than that of alumina A, except the final state at which all kinds of alumina have the same activation energy of 2.8—2.9 e.v. This leads to the conclusion that the low activation energy observed in the alumina with insufficient heat run is mainly due to the existence of some kinds of impurities. However, it seems still questionable to conclude that the activation energy 2.8—2.9 e.v. is the proper value of pure alumina. More detailed studies on the effects of impurities is now being carried out, the results of which will be published in a following paper.

§ 8. Conclusion.

The electric conduction of alumina at high temperature is composed of ionic and electronic conductions. Some kind of impurities has a remarkable effects on both types of conduction. Heating the sample at high temperatures for long time, volatile impurities evaporate to decrease the ionic current and to make the activation energy for electronic conduction larger. In the final state at which almost all volatile impurities have already evaporated, the activation energy becomes 2.8—2.9 e.v. Almost all part of applied voltage between the heater and the cathode drops in the space of alumina to cathode and the current is a thermionic emission obeying the Schottky law.

In conclusion we wish to acknowledge Miss. Mimura for her analytical works and other members in our laboratory for their discussions.

References.

(1) W. Hartmann: Zeits. f. Phys. **102** (1936) 709.
(2) T. Oshida: Kawanishi-Kikai, **1** (1948) No. 1.
(3) T. Oshida: ebenda, **2** (1949) No. 5.
(4) H. Miyazawa: He has reached to the same conclusion, (read at the metting of electron emission).

Ferromagnetic Resonance Absorption by Mo-Permalloy at 3000 Mc/sec.

By Junkichi ITOH and Tetsuo AKIOKA.*

(*Physical Institute and Research Institute of Acoustical Science, Osaka University.*)

(Received May 30, 1950)

Abstract.

Ferromagnetic resonance absorption and resonance dispersion were investigated by Mo-permalloy at 3000 mc/sec. The results obtained are in good agreement with Kittel's theory, provided that relaxation constant is assumed to be proportional to magnetic field strength. The *g*-factor is determined from the extrapolated value of resonance field to zero width of the sample which is 2.11.

§ 1. Introduction.

Ferromagnetic resonance absorption was investigated by various authors(1)(2)(3)(4) using various ferromagnetic specimens. Except in the very early experiment which was not accurate, all of the experiments were performed at 10000 mc/sec or higher frequencies. We performed the experiment at about 3000 mc/sec by Mo-permalloy plate. The preliminary report was published briefly in Physical Review.(5) Here, we want to report further experimental results and to discuss them comparing with the theory of Kittel.

According to the theory of Kittel,(6) the resonance field H_r is given by the following equation, provided that magnetization of the specimen already saturates at the field below H_r:

$$\omega = \gamma \sqrt{B_r H_r} \qquad (1)$$

where ω is the angular frequency of microwave used, γ is the gyromagnetic ratio of the specimen and B_r is the magnetic induction at H_r. Let M_s be the saturated magnetization of specimen, then $B_r = H_r + 4\pi M_s$. If the relaxation time of ferromagnetic specimen can be considered infinite, the value of imaginary part of complex permeability at resonance will be infinitely large and the absorption maximum will be also infinitely sharp. However, in actual specimens the relaxation time is considerably small and we must take into account the effect of relaxation to discuss the shape of absorption or dispersion curve. Let $\chi_x = \chi_x' - j\chi_x''$ be complex susceptibility at microwave frequency $\omega/2\pi$ which is equal to M_x/H_x where M_x is the intensity of magnetization in the direction of microwave field, H_x, which is perpendicular to the static field, H. Then, according to Kittel, χ_x is given by the following equation:

$$\chi_x = \chi_x' - j\chi_x'' = \chi_0 \frac{\omega_0^2 + \lambda^2 \mu + j\omega\lambda}{\omega_0^2 + \lambda^2 \mu - \omega^2 + j\omega\lambda(\mu+1)} \qquad (2)$$

where $\omega_0 = \gamma\sqrt{BH}$, λ is the relaxation constant,

---

* Now at Nihon Musen Co.

μ is the static permeability $(=B/H)$, χ_0 is the static susceptibility, and B is the static magnetic induction at static field H. The resonance condition is given by $\omega=\omega_0$. As to the relaxation constant, λ, no theoretical deduction can be obtainable in the present state, and Kittel first assumed it to be independent of H. But, lately Yager⁽⁵⁾ found experimentally that λ must be proportional to H and thus is expressed by AH where A is a constant independent of H.

Now, in all experiments using metallic samples which forms a part of walls of a cavity resonator, changes of the Q value of the cavity resonator were determined directly by experiments which will be given by the following equation:⁽⁷⁾

$$\Delta\left(\frac{1}{Q}\right)-2j\frac{\Delta\nu}{\nu}=\frac{1}{2}(1+j)\sqrt{\mu_x}\,\delta\int_S H_x^2\,dS \qquad (3)$$

where $\Delta\left(\frac{1}{Q}\right)$ is the change of $1/Q$ of the resonator by ferromagnetic specimen, $\Delta\nu$ is the change of resonant frequency ν of the resonator, μ_x is microwave permeability, δ is the skin depth of the sample at the frequency used assuming $\mu=1$, S is the surface area of specimen, and H_x is the microwave magnetic field normalized by the equation $\int_V H_x^2 dV=1$, where V is the total volume of the cavity resonator. As microwave permeability $\mu_x=1+4\pi\chi_x$ is a complex quantity $\mu'-j\mu''$, as given by (2), equation (3) will be transformed to the following equation

$$\Delta\left(\frac{1}{Q}\right)-2j\frac{\Delta\nu}{\nu}=\frac{1}{2}\left(\sqrt{\mu_R}+j\sqrt{\mu_L}\right)\delta\int_s H_x^2\,dS \qquad (4)$$

where

$$\sqrt{\mu_R}=\left[\sqrt{\mu'^2+\mu''^2}+\mu''\right]^{1/2} \qquad (5)$$

$$\sqrt{\mu_L}=\pm\left[\sqrt{\mu'^2+\mu''^2}-\mu''\right]^{1/2}$$
$$(+\text{ for }\mu'>0\text{ and }-\text{ for }\mu'<0) \qquad (6)$$

and

$$\mu'=1+4\pi\chi_x' \quad\text{and}\quad \mu''=4\pi\chi_x''.$$

All of μ_R, μ_L, μ' and μ'' are real quantities.

In all of previous experiments, only the absorption, or $\Delta\left(\frac{1}{Q}\right)$ was measured which is related to μ_R. We measured the absorption and also the dispersion curve, the latter which is the measurement of $\Delta\nu$ is related to μ_L.

Since the resonance field given by (1) is very low at 3,000 mc/sec in ordinary ferromagnetic material, we must choose the material which saturates magnetically at much lower field than the resonance field and also whose saturation magnetization is as small as possible. By these request, we used Mo-permalloy as absorbing material, as it saturates at very low field (about 10 oersted) and its saturation magnetization is 8500/4π gauss which is much smaller than that of pure iron or permalloy.

§ 2. Experimental Methods and Procedure.

To obtain the value of μ_R, we measured the change of Q of a rectangular resonant cavity excited by H_{101} mode in which a plate of Mo-permalloy was sometimes soldered and sometimes screwed on one side of the walls, by changing strength of static magnetic field which was perpendicular to high frequency magnetic field in the cavity resonator. As we used, in most part of the experiments, a magnetron as microwave oscillator, it was difficult to change the frequency of microwave over considerable range. Therefore, to tune the resonator, a plunger of 1.4 cm diameter was attached to it and by changing length of the plunger, exact resonance of the resonator was realized.

In the preliminary experiment, a magic T was used. But in the later work, standing wave method was adopted. The schematic diagram of the apparatus is shown in Fig. 1. The output of standing wave monitor made by a crystal detector was measured by a galvanometer. Let D is standing wave maximum when the resonator was completely detuned by changing greatly the length of the plunger, T is the standing wave maximum when the resonator was at exact resonance, and,

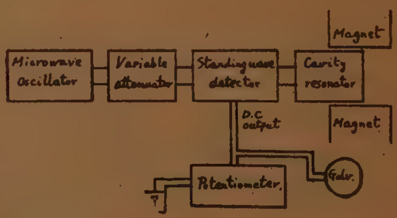

Fig. 1. Schematic diagram of apparatus.

T' is standing wave minimum at exact resonance. If direct current output of crystal detector is proportional to n-th power of microwave electric field strength induced in it, following equations will be hold:

$$T'/T=(Q_0/Q_1)^n \tag{7}$$

$$D/T=(1+Q_0/Q_1)^n \tag{8}$$

where Q_1 is the Q value of entrance slit of the resonator and Q_0 is the unloaded Q of the cavity resonator which was smaller than Q_1 in our experiment. Measuring T'/T and D/T, we calculated the value of n to be about 1.80 which does not vary with intensity of microwave field strength in the measured range. Thus in the later work we used this value of n, and obtained the value of Q_0/Q_1 only by the measurement of T'/T.

The relation between plunger length and resonant frequency of the resonator was obtained as follows: the frequency of microwave oscillator was changed by a small amount by changing the plate voltage of magnetron oscillator, the frequency change was measured by a cavity wavelength meter, and, at the same time, the change of plunger length to tune the resonator at exact resonance was measured. By plotting the change of plunger length with the frequency, we obtained the required relation. It was linear within the measured range, about 78 kc/sec per 1/100 mm change of plunger length. The resonance curve of the resonator was obtained by measuring the output of standing wave monitor set at minimum value by varying the plunger length. The Q value of the resonator which is $f/\varDelta f$ where f is the frequency of microwave, about 3000 mc/sec, and $\varDelta f$ is the width of resonance curve at $1/2^{n/2}$ of its maximum value was about 1000. Now, by the equation (7),

$$Q_1/Q=Q_1(1/Q_1+1/Q_0)=1+(T/T')^{1/n} \tag{9}$$

Thus, by measuring Q value of the resonator and standing wave ratio at resonance we can calculate the value of Q_1. Then we can calculate $1/Q_0$ by the equation (7), only by the measurement of the standing wave ratio at resonance.

We measured the value of $1/Q_0$ with Mo-permalloy plate set in the resonator and also with a copper plate of the same dimension set in the same position for various values of static magnetic field. The value of $1/Q_0$ with copper plate varies by a small amount with magnetic field strength beyond 1500 oersted. This effect was further investigated and was found to be the absorption effect by paramagnetic oxygen gas in the resonator.* So we measured the difference of $1/Q_0$ for the case of Mo-permalloy and for the case of copper at each value of magnetic field strength. The difference $\varDelta(1/Q_0)$ is given by the following relation using (4):

$$\varDelta\left(\frac{1}{Q_0}\right)=\frac{1}{2}\delta\int_S H_x^2\,dS\cdot[\sqrt{\mu_R}-\delta_0/\delta] \tag{10}$$

where δ_0 means skin depth of copper plate and δ means that of Mo-permalloy both for $\mu=1$. By known conductivities of copper and Mo-permalloy, δ_0/δ is calculated to be about 0.17 which has only small contribution to $\sqrt{\mu_R}$.

The calculate μ_R from experimental $\varDelta(1/Q_0)$ using (10), $\int_S H_x^2\,dS$ must be calculated. However, as we used rather large plunger, microwave magnetic field at Mo-permalloy plate cannot be calculated exactly. Therefore, we determined the value of $\int_S H_x^2\,dS$ so that experimental value of μ_R coincides with static permeability at very high field. This procedure was adopted in discussing all of the following experimental results.

Next, measurement of μ_L will be described. Plunger length at exact resonance of the resonator and hence relative frequency change were determined with various field strength. To obtain true μ_L for Mo-permalloy, we must know the difference of resonant frequency of the resonator when Mo-permalloy plate was put on the wall of the resonator and copper plate of the same dimension was put on the same place, as the oxygen gas in the resonator also shows the dispersion effect. As the frequency change for various field strength was very small, only a slight difference in the dimension of copper and Mo-permalloy plates or a slight difference in method of attaching the plate may affect very much the results.

---

* Further work on paramagnetic absorption by oxygen gas will be done in the future.

Therefore, only the difference in $\Delta\nu$ for different field was concerned, and we did not make much effort to determine the absolute value of μ_L.

The Mo-permalloy plate which was 0.05 cm thick was used always after electrolytically polishing.

The magnetic field was calibrated by nuclear resonance method at about few hundred oersted and was extrapolated to lower field by the use of a fluxmeter, as it was difficult to measure the field strength by nuclear resonance method at lower field.

§ 3. Experimental Results and Discussions.

A. Absorption measurement.

In our previous experiment,⑸ we reported that the resonance absorption curve did not agree well with that predicted by the theory of Kittel. Since then, we performed several experiments with samples of various geometrical figures, and found that the shape of sample affects the shape of absorption curve rather strongly. In Fig. 2, several absorption curves are shown for different shapes of the samples. In this figure, to show the difference of absorption curves clearly, the value $\mu_R/\mu_{R,max}$ where $\mu_{R,max}$ is the maximum value of μ_R, was adopted for the ordinate, and the value $H-H_{max}$, where H is the applied field strength and H_{max} is that corresponds to $\mu_{R,max}$, for the abscissa. Though the absorption curve for the sample of 2.9 cm hight and 2 mm width (the height means the length parallel to applied static field and the width means the length parallel to high frequency field), is not accurate enough because of very low intensity of absorption, it is sharpest and coincides with that for circular plate of 2.79 cm diameter. This means that the broader resonance in the case of wider samples, for example, 2.9 cm high and 3.4 cm wide used in our preliminary experiment, is due to inhomogeneities of inner field and magnetic induction. As the magnetization in wider sample is difficult to calculate accurately and moreover perhaps no significant result may be obtained from such consideration, we will not proceed further consideration about this point. In the case of circular plate or samples of very narrow width, the magnetization can be considered to be fairly homogeneous even at lower field. So, it is accepted that the absorption curve for these samples is the true one which can be compared with the theory. In previous reports in which cases the frequency used was much higher than that in our experiment, the resonant field was always several thousand oersted and the effect of inhomogeneity will probably have no effect for the shape of the absorption curve.

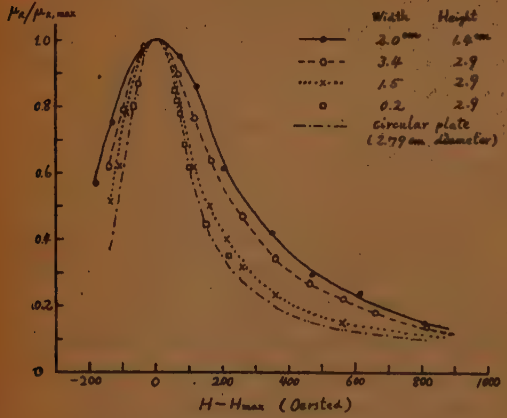

Fig. 2. Absorption curves.

In Fig. 3, we compare the experimental values of μ_R with that calculated from the theory of Kittel. As by the experiments which will be described in the following section, the resonant inner field is 113 oersted and the demagnetizing field can be considered as constant at the inner field larger than 10 oersted, we took the demagnetizing field to be the difference of applied field at resonance and 113 oersted, which was 127 oersted.

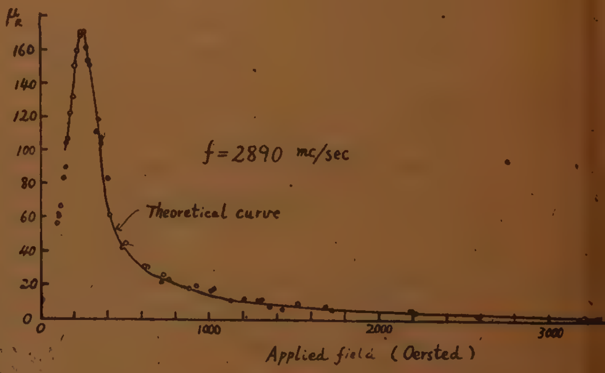

Fig. 3. μ_R.

The theoretical curve drawn in the figure was calculated by (2) and (5), assuming that λ is proportional to H or $\lambda = AH$ where A is a constant and determining the value of A by the experimental maximum value of μ_R by the relation $\mu_R = 2\mu'' = 2\omega(\mu-1)/\lambda(\mu+1)$ which can be deduced from (2) and (5) by substituting $\omega = \omega_0$. The value of A thus obtained was $1{\cdot}85 \times 10^6\ \mathrm{sec}^{-1}\ \mathrm{gauss}^{-1}$. The magnetic field for the theoretical curve was $H+127$ oersted which corresponds to the applied field for the inner field of H oersted. As to be seen from the figure the experimental points just coincide with the predicted theoretical curve and Kittel's theory is proved to hold exactly even at such lower field.

The value of A obtained above is larger than that obtained by Yager(3) and Yager and Herwitt(4) for Supermalloy and for Heusler alloy, the reason of which may be due to slight inner stress or slight anisotropy in our sample or A may not be constant for widely different value of magnetic field strength.

B. *g*-value for Mo-permalloy.

As, owing to the lowness of the frequency used in our experiment, the resonant field was comparable with demagnetizing field, the inner field at resonance cannot be determined accurately by approximate calculation of demagnetizing field. Therefore we determined it experimentally by the method just the same as described in our previous report. Field strengths at resonance for samples of different width which have all the same hight and thickness were measured successively and were plotted against the width of the sample as shown in Fig. 4. The field strength extrapolated to zero width must correspond to the resonant field with zero demagnetizing field. This was 113 oersted and the value of g calculated from it was 2.11 ± 0.03.

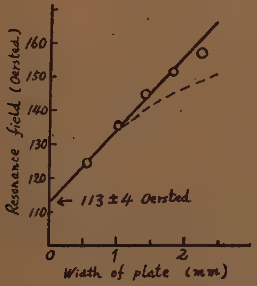

Fig. 4. Resonance field.

The demagnetizing field for very narrow sample can be calculated approximately by the formula of demagnetizing factor for ellipsoid. The dotted curve in Fig. 4 corresponds to the sum of resonant inner field which is 113 oersted and the demagnetizing field thus calculated. In the case of samples whose width was less than 1 mm, the calculated values just coincide with the experimental ones. In the case of 2.79 cm circular plate, the demagnetizing field can be calculated with good approximation which was 124 oersted, and thus the calculated resonant inner field is to be 116 oersted, which coincides with the experimental value obtained above within the experimental errors.

C. Dispersion measurement.

Next, we measured the change of resonant frequency of the cavity resonator for circular Mo-permalloy plate of 2.79 cm diameter set on one wall for various magnetic field strength. The same experiment was performed with copper plate. In Fig. 5, the difference of relative frequency change for copper and for Mo-permalloy was shown against the applied field. In this figure, the frequency at 400 oersted was assumed as standard, and the frequency change relative to this frequency was plotted. In this figure, the theoretical curve was calculated by (2), (4) and (6) assuming the same value of A obtained in the section A and the same value of $\int_S H_x^2\, dS$ used in the section A. As only relative values

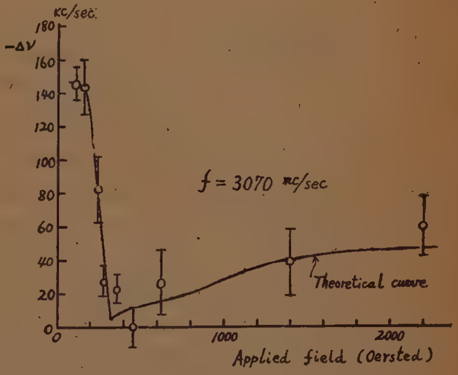

Fig. 5. $\Delta\nu$.

are concerned, we draw the theoretical curve to fit best with the experimental plots. Though the experimental results are not accurate enough, it may be concluded that the coincidence of the experiment and the theory is satisfactory. As mentioned in §2, no discussion concerning the absolute value of μ_L can be made from the present experiment.

References.

(1) Griffith: *Nature.* **158** 670 (1946).
(2) Yager and Bozorth: *Phys. Rev.* **72** 80 (1947).
(3) Yager: *Phys. Rev.* **75** 316 (1949).
(4) Yager and Herwitt: *Phys. Rev.* **75** 318 (1949).
(5) Itoh and Akioka: *Phys. Rev.* **77** 293 (1950).
(6) Kittel: *Phys. Rev.* **71** 270 and **73** 155 (1948).
(7) Slater: Microwave electronics. *Rev. Mod. Phys.* **18** 441 (1946).

Short Notes

Noise of Cuprous-Oxide Rectifier

By Shoji KOJIMA, Susumu OKAZAKI
and Akira SHIMAUCHI

Tokyo Bunrika University

(Received August 22, 1950)

Since the structure of copper-cuprous-oxide rectifier is well understood, the study for its noise is physically interesting. However, this does not generate large noises at high frequencies because of shunting by the capacity of barrier. Then small samples are favourable. The used samples have their area of 7.6∼0.66 $10^{-2}\,\mathrm{cm}^2$. The measuring instruments were a four-stage selected amplifier of 600 kc/s with band width of 10 kc/s and a output meter connected a square-law detector. The input circuit of the amplifier and its equivalent circuit are shown by Fig. 1. Where

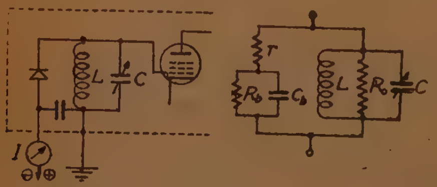

Fig. 1.

R_o is the resonance impedance of the LC circuit and R_b, C_b and r are barrier resistance, barrier capacity and bulk resistance of the rectifier respectively. The resistance r estimated from the forward current was negligibly small compared to R_b in the range of our measurement.

When a current I flows in the rectifier by a d.c. bias voltage, the mean square noise current in a frequency range Δf is represented as follows:

$$\overline{i^2}\Delta f = \{(4kT/R_e)+\overline{i_e^2}\}\Delta f,$$

where the first term corresponds to thermal noise being R_e the equivalent resistance of the input circuit(1) and the second term $\overline{i_e^2}$ is what we call excess noise. From the indication of output metter that is proportional to $R_e^3\,\overline{i^2}$ we can compute $\overline{i_e^2}$ or the noise temperature defined by

$$t_e = \overline{i_e^2}R/4kT,$$

where R is the tangential resistance of the rectifier(2).

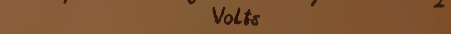

Fig. 2.

A typical result for the noise temperature as a function of the bias voltage is given in Fig. 2. The relations of log $\overline{i_c^2}$ versus log I are plotted in Fig. 3. It indicates that the excess noise is approximately proportional to the square of the current.

At the measurement the capacity C had to be adjusted to tune when the bias was varied. This

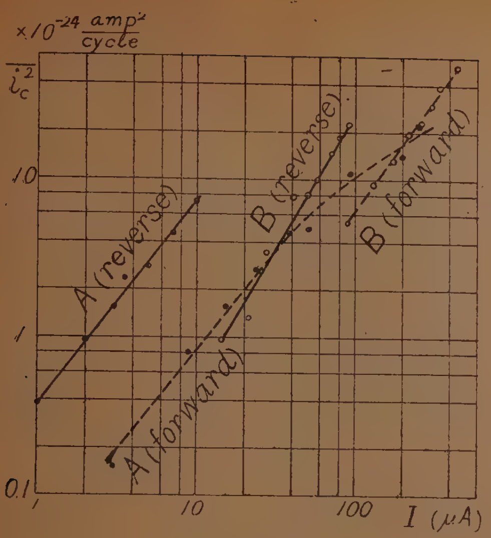

Fig. 3.

suggests that the capacity of barrier layer can be measured by the change of the condenser. The obtained capacity is give in Fig. 4. For the forward direction the correction factor $(1+r/R_b)^2$ was applied. This result has the same character as that of Schottky-Deutchmann⁽³⁾.

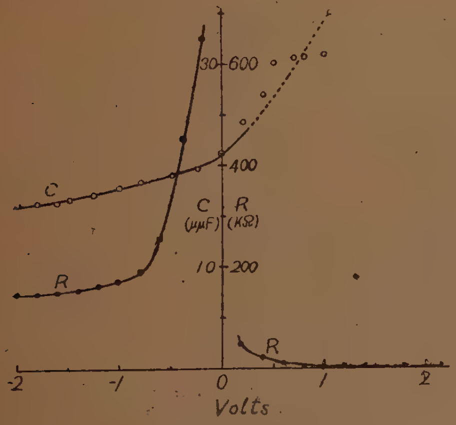

Fig. 4.

On the noise proportional to I^2 many theories are posturated. We adopt the formula $\int \overline{i_c^2} df = I/N$, where N is the total number of carriers or impurities⁽⁴⁾. If the noise spectrum has the inverse frequency behaviour as the crystal rectifier and if the integral of $1/f$ is the order of one, then the excess noise will be expressed by⁽⁵⁾

$$\overline{i_c^2} \approx \frac{I}{N}\frac{\Delta f}{f} \quad \text{or} \quad t_c \approx \frac{1}{Nf}\frac{RI^2}{4kT}.$$

Using this formula we can estimate the total number of carrier in the barrier layer. For example, when $t_c = 8.2$ and $RI^2 = 45\mu W$, we obtain $N = 5\times10^9$. The concentration of the carrier is given as 3.2×10^{15} with the area of 6.6×10^{-3} cm² and the barrier depth of 2.4×10^{-4} cm which is estimated from the obtained capacity. The same analysis applied for a germanium rectifier gives a concentration of 10^{18} provided that the contact volume is 10^{-11} cm³.

We are indepted to the Ministry of Education for the research grant.

References.

(1) Nyquist: Phys. Rev. **32** (1928) 110.
(2) Torrey and Whitmer: "Crystal Rectifiers".
(3) Schottky and Deutschmann: Phys. Zeits. **30** (1929) 839.
(4) Bernamont: Compt. Rend. Paris **198** (1934) 1755.
(5) Kojima: "Zatsuon" in press.

Crystal Structures of Lead Titanate and of Lead-Barium Titanate

By Gen SHIRANE, Sadao HOSHINO and Kazuo SUZUKI

Tokyo Institute of Technology,
Oh-okayama Tokyo.

(Received September 7, 1950)

It is known⁽¹⁾ that the solid solutions of $BaTiO_3$ and $PbTiO_3$ show the ferroelectric properties of barium titanate type having the Curie temperatures which rise with lead contents, attaining to about 500°C for pure $PbTiO_3$. An X-ray study of the phase change of (Pb20—Ba80) TiO_3 has been performed by Miyake and one of the authors⁽²⁾. According to Cole and Espenshied⁽³⁾ the crystal structure of $PbTiO_3$ belongs to the orthorhombic system, but more recent investigations⁽⁴⁾ have shown that it may possess tetragonal lattice with a large tetragonality.

To obtain more detailed informations about this series, we have performed an X-ray study over the whole range of (Pb – Ba)TiO_3. We used the ceramic specimens prepared by sintering at about 1200°C the mixtures of appropriate ratios of PbO, $BaCO_3$ and TiO_2. We have measured the permittivity as a function of the temperature and determined the Curie points for varied compositions of this series (Fig. 1). Specimens containing $PbTiO_3$ more than 50%, is porous and their Curie points are high, so that the dielectric measurements are difficult.

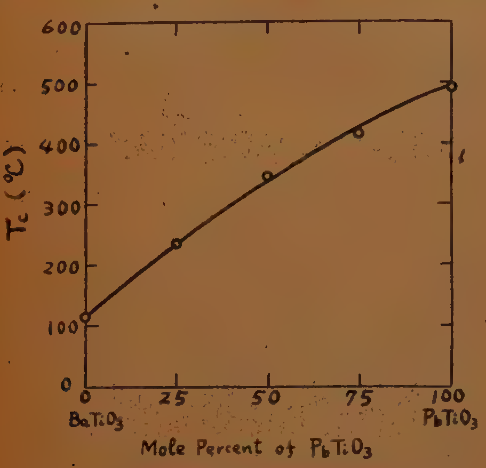

Fig. 1. Curie point *vs.* composition curve.

The Debye photographs of this series were taken on powdered specimens mixed with starch, using Cu Kα radiation. The camera radius is about 5 cm. These photographs were well explained if we assume the tetragonal structure having the same atomic arrangement as that of barium titanate, i.e. perovskite type. The precise lattice constants and the axial ratios c/a were calculated mainly from (*143*) and (*134*) lines on photographs taken by back reflection method. The results are shown in Figs. 2 and 3.

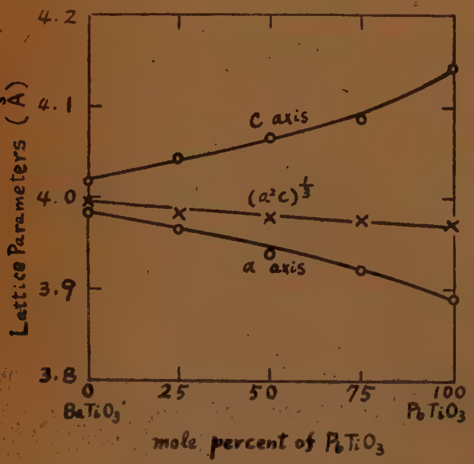

Fig. 2. Lattice constants and cube root of the unit cell volume as a function of composition.

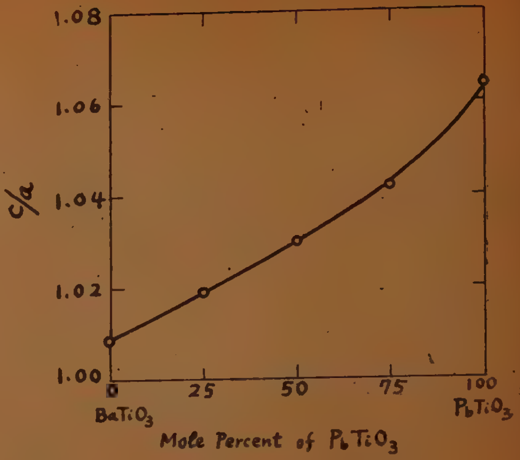

Fig. 3. c/a *vs* composition curve.

In these figures we see that the volume of unit cell decreases and the tetragonality c/a increases gradually towards the $PbTiO_3$ side. Lead titanate was found to possess a tetragonal lattice with $a = 3.891$ Å, $c = 4.141$ Å and $c/a = 1.064$, the result being in good agreement with the recent investigations⁽⁴⁾. It is remarkable that c/a of this crystal is rather great; therefore it may be expected that the values of spontaneous polarization and of coercive force are greatly different from those of $BaTiO_3$. Unfortunately, however, at least at the present stage, ceramic lead titanate obtained by us is too porous to perform these measurements.

We are now investigating the thermal properties of the ferroelectric transitions of this series (Fig. 1), and the detailed results will be reported later.

The authors express their sincere thanks to Mr. J. Hori for his suggestion to this problem and also to Professor S. Miyake and Professor Y. Takagi for their encouragements in the course of this research.

References.

(1) G. H. Jonker and J. H. Van Santen: Chem. Weekblad, **43** (1947) 672.

S. Waku and J. Hori: Unpublished yet, reported at the Committee for the Piezo-electric Material, held at Tokyo, on 1st May 1950.
S. Nomura and S. Sawada: J. Phys. Soc. Japan, **5** (1950) 279.
(2) K. Suzuki and S. Miyake: Unpublished yet, reported at the meeting of the Phys. Soc. Japan, held at Tokyo, on 3rd April 1950.
(3) S. S. Cole and H, Espenshied: J. Phys. Chem. **41** (1937) 445.
(4) I. Naray-Szabo: Naturw. **31** (1943) 202, 446.
H. D. Megaw: Proc. Phys. Soc., **58** (1946) 133.
W. G. Wyckoff: Crystal structures, Interscience Publisher, N. Y. 1948. Chap. 7. table page 12.

Electrical Properties of Cu_2O.

By Wataru Sakaki.

Material Division, Electrotechnical Laboratory.

(Received September 7, 1950).

Electrical resistivity and Hall effect of Cu_2O are measured between 30°C and 180°C. Samples are prepared by oxidation of copper plate in an electric furnace at 1040°C. After the plate is completely oxidized, the cuprite is cooled slowly to an annealing temperature, T_a, under the pressure of 10^{-2} mm Hg. After 2 hours' annealing, the sample is quenched to room temperature.

One of the results of the resistivity and Hall measurements is shown in Fig. 1. The concentration of charge carriers, n, is calculated by the following equation.

$$n = 3\pi/8cR,$$

where R is Hall coefficient. As is already known, resistivity, ρ, and n show an anomalous change over the temperature range from 100°C to 150°C, and heating and cooling curves do not agree under 150°C(1). There occurs an irreversible process which causes irreversible increase of resistivity and decrease of charge carriers.

In order to clarify the temperature of this transition from *quenched* state to *equilibrium* state, the temperature of the sample is raised stepwise against time, that is, the sample is kept at a constant temperature for 7 minutes, during which time the measurements are carried out, then is heated to the next temperature in 3 minutes. The reststivity is measured twice at an interval of 5 minutes during the temperature is kept constant. Between 100°C and 150°C the resistivity increases even when the temperature is kept constant. The ratio of the latter value of resistivity to the former value, ρ'/ρ, is shown in Fig. 2. This ratio corresponds to the reaction velocity of the transition process. Fig. 2 indicates that the transition velocity gets its highest value at 125°C and approaches zero at 150°C.

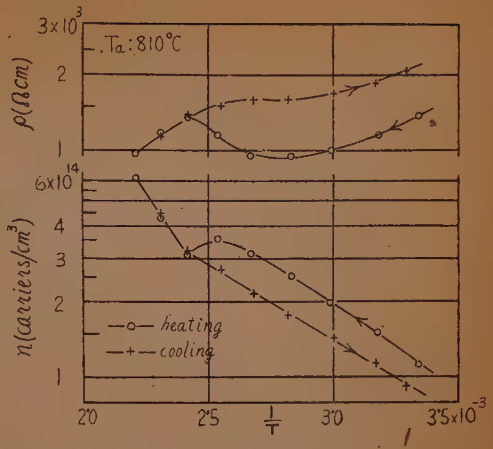

Fig. 1. Temperature dependency or ρ and n.

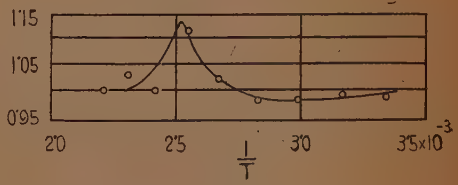

Fig. 2. Temperature dependency of ρ'/ρ.

The mobility of charge carriers, μ, is given by

$$\mu = 1/\rho ne,$$

and is shown in Fig. 3, which indicates a fact that the irreversible increase of ρ is due not only to the decrease of n but to the decrease of μ. The scattering centers for the movement of charge carriers are composed of thermal vibrations of ionic crystal lattice, ionized impurities, and neutral impurities. If the scattering by these centers

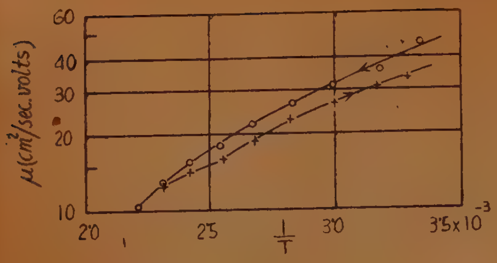

Fig. 3. Temperature dependency of μ.

are assumed to be additive, μ is represented by

$$\frac{1}{\mu}=\frac{1}{\mu_L}+\frac{1}{\mu_I}+\frac{1}{\mu_N},$$

where μ_L, μ_I, and μ_N represent contributions from lattice vibrations, ionized impurities, and neutral impurities respectively. By the experimental results, the irreversible decreae of μ is accompanined by the decrease of n, or the increase of μ_I, so that $(1/\mu_L+1/\mu_N)$ must be increased. Nothing has been reported in regard to the exsistence of transition phenomena of *quenched* Cu_2O crystal lattice in the temperature range from 100°C to 150°C. It is doubtful, however, that the increase of $(1/\mu_L+1/\mu_N)$ is completely explained by the change of μ_N only. The absolute values and the temperature dependency of μ are affected considerably by the annealing temperature.

Reference.

(1) Feldmann: Phys. Rev. 64, 113.

On Anomalous Phase Change of Ammonium Nitrate NH_4NO_3.

By Ryuzo Ueda and Takeo Ichinokawa.

Department of Applied Physics,
Waseda University, Tokyo.

(Received September 11, 1950).

It has been known that the ammonium nitrate NH_4NO_3 has many phase changes in temperature ranges from low temperature to the melting point 160°C. The accompanying table summarizes them(1),(2). These phase changes are reversible on heating or cooling, although there exists more or less thermal hysteresis in each transition. When the salt is cooled down from the highest phase I, however, an irrevrsible change which is rather peculiar in appearance occurs at about 50°C. The foregoing X-ray and microscopic studies have concluded that this transition corresponds to such a change from phase II to metastable phase IV′ which is stable at ordinary temperature(3).

The present authors have performed the dilatometer and specific heat measurements of this compound from low temperature up to nigher temperatures. One of the results of the dilatometer measurements is reproduced in the figure. The ordinate shows the readings of the oil meniscus in the capirally of the glass-in-oil dilatometer. The ammonium nitrate showed the first contraction at 125°C, when cooled from phase I, and transformed into phase II, which was kept without any further change even at 84°C until it expand suddenly in volume at about 50°C, whereat phase II appeared and continued between this temperature and 32°C. (A→E→F→C→G→). Then, a cycle (A→B→C→D→E→F→G→)

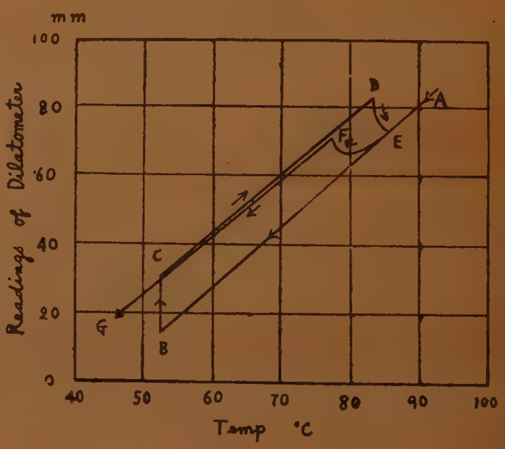

Fig. 1.

Phase	I	II	III	IV	V	VI	VII
Tr. Temp°C	125	84	32	−16	−60	−150	
Crys. Sys.	Cub.	Tetr.	Orthor.	Orthor.	Hex. ?	Hex. ?	?

indicate the fact that the appearance of the phase change at 50°C is closely related to the disappearance of that at 84°C. The anomalous specific heat about 50°C is measured by means of a heat conduction calorimeter. The energy change is the same order of that at 84°C, giving 160 cal./mol.deg.

From the above results, it has become clear that the irreversible transition at about 50°C is due neither to a change as formerly described nor to a kind of a large thermal hysteresis, but the one from phase II to phase III, presumably as the result of the excitation of state which takes place in the higher temperature phase I. The ionic radicals, both nitrate and ammonium, is considered to be rotating and the crystal may become plastic above 125°C.

X-ray studies on the phase change of this crystal from low temperature up to higher temperatures is now in progress. The detailed report of the investigation will be published in near future.

References.

(1) S. B. Hendriks, E. Posnjak and F. C. Kracek: J. Am. Chem. Soc., **54** (1932) 2766.
(2) M. J. Jaffray: Compt. rend., **224** (1947) 1346; J. Rech. Cen. Nat. Re. Scie., No. **3** (1947) 153.
(2) R. Tiemeyer; Z. Krist., **97** (1937) 386.

CONTENTS

(Vol. 5)

No. 1.

Page
Michika MIYANISHI: On the mechanism of the emission of the auroral green light in the night sky 1
Nobuhiko SAITÔ: Concentration dependence of the viscosity of high polymer solutions, I. 4
Shôhei MIYAHARA: A theory of initial permiability 8
Hiroshi KUBOTA: On the interference color of thin layers on glass surfaces 10
Ryukiti HASIGUTI: On the theory of recrystalization of cold-worked metals. 14
Heiji KAWAI & Noboru TOKITA: The new dynamical method for measuring Young's modulus and internal friction of fibres and film. 17
Shoji KOJIMA & Shizuko HASHIMOTO: Interaction of beta rays with matter 20
Ryosei UNO & Toshihiko OKADA: On the thermal expansion of cuprous oxide. 23
Kenji KONDO: On the properties of ferromagnetic alloy of manganese and bismuth at low temperature, I, Magnetic, dilatometoric and calorimetric studies. 26
Toyozo KAMBARA: Dissociation and Ionization of n-propylalcohol by electron impact . 31
Toyozo KAMBARA: Dissociation and Ionization of iso-propylalcohol be electron impact. 36
Yasuo MAKITA & Shin-ya MIYATANI: The time in which equilibrium state of auditory sensation is established, Part I. The damping constant of the inner ear . . . 39
Yasuo MAKITA & Shin-ya MIYATANI: The time in which equilibrium state of auditory sensation is established, Part II. The time constant of building up or decay of auditory sensation at the threshold. 43
Kenjiro KAMBE: On the paramagnetic susceptibilities of some polynuclear complex salts 48

No. 2.

Masateru SONODA: The efficiency of the G–M counter 53
Takasi HUZIMURA: On the displacement of a magnetic domain boundary by a large Barkhausen jump in a ferromagnetic substance 56
Tomoyoshi KAWADA: On the discontinuous elongation of aluminium crystal. I. 60
Tomoyoshi KAWADA: On the discontinuous elongation of aluminium crystal. II. . . . 64
Tomoyoshi KAWADA: On the discontinuous elongation of aluminium crystal. III. . . . 68
Tetsuya ARIZUMI and Seiichi KOTANI: On the oxidation of the evaporated barium film. 70
Takehiko OGUCHI: Statistics of the three-dimensional ferromagnet 75
Mitsuo MIWA, Shôichi MAMIYA, Tatsuo IGARASHI, and Yoshio ONAI: A note on the structure of amorphous carbon 81
Toyozo KAMBARA: Dissociation and ionization of acetone and acetic acid molecules by electron impacts. 84
Hazimu KAWAMURA and Akira SHINOHARA: On the resistance of interfrce of oxide-coated cathode. 90
Tutomu TANAKA and Zyun KOANA: Solar limb effect of the spectral lines in a prominence observed at the total eclipse in 1941. 95
Tutomu TANAKA and Hirobumi OURA: On the solar coronal lines at the total eclipse in 1943. 101
Tutomu TANAKA, Hirobumi OURA, Tosio MURAKAMI, and Tokio MITUNOBU: On the continuous spectrum of the solar corona at the total eclpse in 1943 106
Tutomu TANAKA: Supplementary report on the continuous spectrum of the solar corona. 110
Akira SAKURAI: On the thickness of plane shock wave in a gas in turbulent motion . 114

No. 3.

Kenichi SHINOHARA and Norio RYU: Polarization of electrons. 119
Takehiko ISHIDZU: On the energy levels of the configurations d^4p, d^5p and d^6p. . . . 124

Takehiko ISHIDZU and Shinya OBI: Structure of the f^n electron configurations. (I) Coefficients of fractional parentage of f^3 142
Takehiko ISHIDZU, and Shin-ya OAI: Structure of the f^n electron configurations. (II) Spin-orbit interaction of the configurations f^3. 145
Masaru WATANABE and Jun-ichi MIIDA: Ionization of the negative oxygen ion by electron impact. III. 149
Takahiko YAMANOUCHI: Probabilities of excitation and de-excitation of metastable states of oxygen atom by collision of slow electron. 154
Yutaka SHIGEMITSU: On experimental methods of the investigation of turbulent flow, I. 157
Tetsuya ARIZUMI and Leona ESAKI: On the thoria coated cathode 163
Tetsuya ARIZUMI and Kuninosuke IMAEDA: Absorption of nitrogen by evaporated film of barium 169
Tetsuya ARIZUMI and Leona ESAKI: Conductivity and electronic energy state of thoria coated cathode. 174
Mitsuo SAKAI: Researches and developments on the spiral orbit spectrometer (I) . . . 178
Mitsuo SAKAI: Researches and developments on the spiral orbit spectrometer (II). . . 184
Kozo ISHIGURO: Application of the double slit interferometer to the measurement of phase shift of light transmitted through thin films 187
Seiichi OYAMA: On the vapour flow in the diffusion pump. 192

No. 4.

Tokio SAKUKAI: Electromagnetic phenomena on ribbon elements gratings. 203
Yutaka SHIGEMITSU: On experimental methods of the investigation of turbulent flow, II. 207
Akira ISIHARA: Transport phenomena in degenerate systems. I. General theory in a mixed system 213
Akira ISIHARA: Transport phenomena in degenerage system. II. Degenerate Bose-Einstein Gas 217
Masao TOMURA: On the electric formation of the selenium rectifier. 222
Shoichiro NOMURA and Shozo SAWADA: D.C. resistance of barium titanate and its solid solution ceramic. 227
Shozo SAWADA and Shoichiro NOMURA: Specific heat and thermal expansion of barium strontium titanate ceramics. 231
Syû ONO: Statistical thermodynamics of multimolecular adsorption 232
Kazuhisa MATSUDA and Naoki ONO: Measurement of thermal diffusion ratio by "Bending Balance" 233
Yasuo MAKITA and Shinya MIYATANI: The time in which equilibrium state of audition is establishod. Part 2. A new method of measuring the damping constant of the mechanical system of the ear. 241
Seiichi SUEOKA: On the Stark effect of helium in strong electric field (I) 244
Juichi IGARASHI: The determination of sound absorption coefficient 249
Tunezo SATOH: On the mathematical analysis of the problem of the conduction of heat when emissivity is variable. 253
Koichi SHIMODA: A symmetrical six-arms wave-guide circuit for micro-wave bridge . 255
Yoshimasa WADA: On the steady surface ripples of cylindrical flow 259
Seikichi SAITO: On the phenomena of burning of insulators caused by gliding spark discharge 263
Takao SATO: Effects of the transformation process on the thermoelectric power of the superlattice alloy Cu_3Au. 268
Kazutake KOHRA: On the anomalies of the small angle reflection of cathode rays from the surface of a single crystal. Part 3. The effect of absorption 272

No. 5.

Takao SATO: On some properties of the Cu-Mn alloy system 287

Takasi HUZIMURA: On the Barkhausen jumps in the course of magnetic after effect . 293
Yutaka SHIGEMITSU: On the velocity fluctuations in the laminar boundary layer, I. . 298
Yutaka SHIGEMITSU: On the velocity fluctuations in the laminar boundary layer. II . 304
Kenzi KONDO: On the properties of ferromagnetic alloy of manganese and bismuth at low temperature, II. Electric conduction and galvanomagnetic effect 307
Zenya FUNATOGAWA: The change in the thermal e.m.f. produced by magnetization of a single crystal of iron 311
Tamotsu AWANO: On the negative energy photon hypothesis 316
Eiichi FUKADA: The vibration properties of wood, I. 321
Sôshin CAIKAZUMI: Ferromagnetic properties and superlattice formation of iron-nickel alloys (I). 327
Sôshin CHIKAZUMI: Ferromagnetic properties and superlattice formation of iron-nickel alloys (II) 333
Masaki HIRASHIMA: On the motion of electron in a B-K tube. 339
Yasaku WADA, Sotoshi SHIMBO and Minoru ODA: Dispersion of ultrasonic velocity in the liquid fatty acids 345
Masao TOMURA: On the characteristics of the selenium rectifier at low temperatures and the electric formation. 349
Ryosuke YOKOTA: On the structure of Na_2O—SiO_2 glasses 354
Shoji KOJIMA and Kazuo TAKAYAMA: Probe measurements for high frequency discharge II 357
Seijiro MAEDA: On the magnetic after effect due to the irreversible displacement of domain boundary (I). 358
Heiji KAWAI and Noboru TOKITA: On the Young moduli and the internal friction of papers. 365
Yoshinobu KAKIUCHI, Tosio SAKURAI and Tadasu SUZUKI: Anomalous specific heat and molecular rotation in normal solid alcohol 369
Seiichi KONDO and Tokuo SUITA: Dielectric dispersion of alkali halide crystals 375

No. 6.

Tokio SAKURAI: The theory of metal plates dielectric 389
Tokio SAKURAI: Artificial matter for electromagnetic wave 394
Itaru NONAKA and Shoji TANABE: Radioactivity of thoriated tungsten wire 398
Masateru SONODA: The efficiency of Geiger-Müller counter for the high energy γ-rays II. 403
Masateru SONODA: The efficiency of Geiger-Müller counter for the high energy γ-rays III. 408
Ken-ichi KUZUKAWA: On the spectrum of turbulence. 412
Mitsuo MIWA, and Seizaburo KAGEYAMA: Natural β-ray spectrum of BaC. 416
Ta-You-Wu: Further remarks on Araki's theory of inverted alkali doublets 421
Norio RYU: On the depolarization of electrons by multiple scattering and reflection-transmission effect 423
Kiyoshi MURAKAWA and Shigeki SUWA: Revision of the hyperfine structure of the mercury spectrum. 429
Tosio KATO: On the adiabatic theorem of quantum mechanics. 435
Yoshimasa WADA: On the standing varicose and sinuous ripples of a cylindrical flow. 439
Tetsuya ARIZUMI: On the electrical conductivity of alumina. 442
Junkichi ITO and Tetsuo AKIOKA: Ferromagnetic resonance absorption by Mo-permalloy. 447

SHORTE NOTES

No. 3.

Yoshihito TAKESADA: On the magnetostriction vibrator as a source of supersonics . . 197
Yoshiro KAINUMA and Ryozi UYEDA: Gn the structure adsorbed organic long-chain molecules on the cleavage surface of molybdenite 199
Seiichi KONDO and Tokuo SUITA: Absorption spectra of colored potassium chloride containing several kinds of impruities 200
Akira ISHIARA: Probable distribution of a polymer around the center of gravity . . . 201
Osamu SATO and Ayao AMEMIYA: On the solution of differential equations of the two-dimensional steady flow of compressible fluid. 201

No. 4.

Hirobumi OURA: On the rate of nucleatiou of ice. 277
Shoichiro NOMURA and Shozo SAWADA: On the anomalous dielectric properties of mixtures of lead titanate and strontium titanate 279
Giichi YOSHII: On fast neutron in cosmic rays. 280
Hiroshi WATANABE and Noboru TSUYA: On the electrical conductivity of magnetite. . 281
Itaru NONAKA and Zitsuo SHIMAZU: Long beaded counteres for x-ray measurements . 282
Isao IMAI: On Sneddon and Fulton's solution for the irrotational flow of a perfect fluid past two spheres. 284
Mitsu SAKAI: On the perfect velocity forcusing mass spectrograph 285

No. 5.

Shoji KOJIMA and Kiyoe KATO: On the noise of rochelle salt II. Barkhausen effect . 379
Kôzô ISHIGURO: An experiment on 16 times amplification of the phase shift of thin films. 380
Masakazu HAYASHI: Absorption spectrum of cuprous oxide 380
Kiyoshi MURAKAWA and Shigeki SUWA: On some regularities in the isotope effect in the spectrum of lead 382
Takao WAKABAYASHI: Photoelastic method for determination of stress in powered mass. 383
J. YAMAGUCHI and S. KATAYAMA: On cadmium selenide of selenium rectifiers 385
J. YAMAGUCHI and S. KATAYAMA: X-ray analysis on selenium layers of selenium rectifiers. 386

No. 6.

Shoji KOZJMA, Susumu OKAZAKI and Akira SHIMAUCHI: Noise of cuprous oxide rectifier 452
Gen SHIRANE, Sadao HOSHINO and Kazuo SUZUKI: Crystal structure of lead titanate and of lead-barium titanate. 453
Wataru SASAKI: Electrical properties of Cu_2O. 455
Ryuzo UEDA and Takeo ICHINOKAWA: On anomalous phase change of ammonium nitrate NH_4NO_3 456

AUTHOR INDEX

Page

AKIOKA T.
J. ITO and ———: Ferromagnetic resonance absorption of Mo-permalloy at 3,000 MC/sec 447

AMEMIYA A.
O. SATO and ———: On the solution of differential equations of the two-dimensional steady flow of compressible fluid 201

ARIZUMI T.
——— and S. KOTANI: On the oxidation of the evaporated barium film 70
——— and L. ESAKI: On the thoria coated cathode 163
——— and K. IMAEDA: Absorption of nitrogen by evaporated film of barium 169
——— and L. ESAKI: Conductivity and electronic energy state of thoria coated cathode 174
——— On the electrical conductivity of alumina 442

AWANO T.: On the negative energy photon hypothesis 316

CHIKAZUMI S.
——— Ferromagnetic properties and superlattice formation of iron-nickel alloys (I). 327
——— Ferromagnetic properties and superlattice formation of iron-nickel alloys (II). 333

ESAKI L.
T. ARIZUMI and ———: On the thoria coated cathode 163
T. ARIZUMI and ———: Conductivity and electronic energy state of thoria coated cathode 174

FUKADA E.: The vibration properties of wood, I 321

FUNATOGAWA Z.: The change in the thermal e.m.f. produced by magnetization of a single crystal of iron 311

HASHIMOTO S.
S. KOJIMA and ———: Interaction of beta rays with matter 20

HASIGUTI R.: On the theory of recrystallization of cold-worked metals 14

HAYASHI M.: Absorption spectrum of cuprous oxide 380

HIRASHIMA M.: On the motion of electrons in a B-K tube 339

HOSHINO S.:
G. SHIRANE, ——— and K. SUZUKI: Crystal structure of lead titanate and of lead-barium titanate 453

HUZIMURA T.: On the displacement of a magnetic domain boundary by a large Barkhausen jumps in the ferromagnetic substance 56
On the Barkhausen jumps in the course of magnetic after effect 293

ICHINOKAWA T.
R. UEDA and ———: On anomalous phase change of ammonium nitrate NH_4NO_3. 456

IGARASHI J.: The determination of sound absorption coefficient 249

IGARASHI T.
M. MIWA, S. MAMIYA, ——— and Y. ONAI: A note on the structure of amorphou carbon 81

IMAEDA K.
T. ARIZUMI and ———: Absorption of nitrogen by evaporated film of barium 169
IMAI I.: On Sneddon and Fulton's solution for the irrotational flow of a perfect fluid past two sphers 284
ISHIDZU T.: On the energy levels of the configurtions d^4p, d^5p and d^6p 124
and S. OBI: Structure of the f^n electron configurations. (I) Coefficients of fractional parentage of f^3 142
——— and S. OBI: Structure of the f^n electron configurations. (II) Spin-orbit interaction of the configurations f^3 145
ISIGURO K.: Application of the double slit interferometer to the measurement of phase shift of light transmitted through thin films 187
———: An experiment on 16 times amplifications of the phase shift of thin films .. 380
ISIHARA A.: Probable distribution of a polymer around the center of gravity 201
———: Transport phenomena in degenerate systems. I. General theory in a mixed system 213
———: Transport phenomena in degenerate system. II. Degenerate Bose-Einstein Gas 217
ITO J.
T. AKIOKA and : Ferromagnetic resonance absorption by Mo-permalloy at 3,000 MC-sec 447
KAGEYAMA S.
M. MIWA and ———: Natural β-ray spectrum of RaC 416
KAINUMA Y.
——— and R. UYEDA: On the structure of adsorbed organic long-chain molecules on the cleavage surface of molyddenite 199
KAKIUCHI Y.
———, T. SAKURAI and T. SUZUKI: Anomalous specific heat and molecular rotation in normal solid alcohol 369
KAMBARA T.: Dissociation and Ionization of n-propylalcohol by electron impact 31
———: Dissociation and ionization of iso-propylalcohol by electron impact 36
: Dissociation and ionization of acetone and acetic acid molecules by electron Impects 84
KAMBE K.: On the paramagnetic susceptibilities of some polynuclear complex salts 48
KATAYAMA S.
J. YAMAGUCHI and ———: On cadmium selenide of selenium rectifiers 385
J. YAMAGUCHI and ———: X-ray analysis on selenium layers of selenium rectifiers . 386
KATO T.: On the adiabatic theorem of quantum mechanics 435
KAWADA T.: On the discontinuous elongation of aluminium crystal. I 60
———: On the discontinuous elongation of aluminium crystal. II 64
———: On the discontinuous elongation of aluminium crystal III 68
KAWAI H.
and N. TOKITA: The new dynamical method for measuring Young's modulus

and internal friction of fibres and films.......... 17
——— and N. TOKITA: On the Young's moduli and the internal friction of papers 365

KAWAMURA H.
——— and A. SHINOHARA: On the resistance of interface of oxide-coated cathode 90

KOANA Z.
T. TANAKA and ———: Solar limb effect of the spectral lines in a prominence observed at the total eclipse in 1941.......... 95

KOHRA K.: On the anomalies of the small angle reflection of cathode rays from the surface of a single crystal. Part 3. The effect of absorption.......... 272

KOJIMA S.
——— and S. HASHIMOTO: Interaction of beta rays with matter.......... 20
——— and K. TAKAYAMA: Probe measurements for high frequency discharge II.. 357
——— and K. KATO: On the noise of rochelle salt II. Barkhausen effect.......... 375
——— and S. OKAZAKI and A. SHIMAUCHI: Noise of Cuprous Oxide Rectifier...... 452

KONDO K.: On the properties of ferromagnetic alloy of manganese and bismuth at low temperature, I. Magnetic, dilatometoric and calorimetric studies.......... 26
———: On the properties of ferromagnetic alloy of manganese and bismuth at low temperature, II. Electric conduction and galvanomagnetic effects.......... 307

KONDO S.
——— and T. SUITA: Absorption spectra of colored potassium chloride containing several kinds of impurities.......... 200
——— and T. SUITA: Dielectric dispersion of alkali halide crystals.......... 375

KOTANI S.
T. ARIZUMI and ———: On the oxidation of the evaporated barium films.......... 70

KUBOTA H.: On the interference color of thin layers on glass surfaces.......... 10

KUZUKAWA K.: On the spectrum of turbulence.......... 412

MAEDA S.: On the magnetic after effect due to the irreversible displacement of domain boundary (I).......... 358

MAKITA Y.
——— and S. MIYATANI: The time in which equilibrium state of auditory sensation is established, Part I. The damping constant of the inner ear.......... 39
——— and S. MIYATANI: The time in which equilibrium state of auditory sensation is established, Part II. The time constant of building up or decay of auditory sensation at the threshold.......... 43
——— and S. MIYATANI: The time in which equilibrium state of audition is estabilished. Part 3. A new method of measuring the damping constant of the mechanical system of the ear.......... 241

MAMIYA S.
M. MIWA, ———, T. IGARASHI and Y. ONAI: A note on the structure of amorphous carbon.......... 81

MATSUDA K.
——— and N. ONO: Measurement of thermal difusion ratio by "Bending Balance" 238

MIIDA J.
  M. WATANABE and : Ionization of the negative oxygen ion by electron impact. III. 149

MITUNOBU T.
  T. TANAKA, H. OURA, T. MURAKAMI and ———: On the continuous spectrum of the solar corona at the total eclipse in 1943 106

MIWA M.
  , S. MAMIYA, T. IGARASHI and Y. ONAI: A note on the structure of amorphous carbon 81
  ——— and S. KAGEYAMA: Natural β-ray spectrum 416

MIYAHARA S.: A theory of initial permiability 8

MIYANISHI M.: On the mechanism of the emission of the auroral green light in the night sky 1

MIYATANI S.
  Y. MAKITA and : The time in which equllibrium state of auditory sensation is established, Part III. The damping constant of the inner ear 39
  Y. MAKITA and ———: The time in which equibrium state of auditory sensation is establshed, Part II. The time constant of building up or decay of auditory sensation at the threshold 43
  Y. MAKITA and ———: The time in which equilibrium state of audition is established. Part 3. A new method of measuring the damping constant of the mechanical system of the ear 241
  ———, and S. KAGEAYAMA: Natural -ray spectrum of RaC ....

MURAKAMI T.
  T. TANAKA, H. OURA, ——— and T, MISTUNOBU: On the continuous spectrum of the solar corona at the total eclipse in 1943 106

MURAKAWA K.
  and S. SUWA: On some regularities in the isotope effect in the spectrum of lead 382
  ——— and S. SUWA: Revision of the hyperfine structure of the mercury spectrm ... 429

NOMURA S.
  and S. SAWADA: D. C. resistance of barium titanate and its solid solution ceramics 227
  ——— and S. SAWADA: Specific heat and thermal expansion of barium strontium titanate ceramics 231
  ——— and S. SAWADA: On the anomalous dielectric properties of mixtures of lead titanate and strontium titanate 279

NONAKA I.
  and Z. SHIMAZU: Long beaded counters for x-ray measurements 282
  and S. TANABE: Radioactivity of thoriated tungsten wire 398

OBI S.
  T. ISHIDZU and ———: Structure of the f^n electron configurations. (I) Coefcients of fractional parentage of f^3 142
  T. ISHIDZU and : Structure of the f^n electron configuration. (II) Spin-orbit interaction of the configurations f^3 145

Oda M.
  Y. Wada, S. Shimbo and ——— : Dispersion of Ultrasonic velocity in the liquid fatty acids.......... 345
Oguchi T. : Statistics of the three-dimensional ferromagnet.......... 75
Okada T.
  R. Uno and ——— : On the thermal expansion of cuprous oxide.......... 23
Okazaki S.
  S. Kojima ——— and A. Shimauchi : Noise of Cuprous Oxide Rectifier.......... 452
Onai Y.
  M. Miwa, S. Maniya, T. Igarashi and ——— : A note on the structure of amorphous carbon.......... 81
Ono N.
  K. Matsuda and ——— : Measurement of thermal diffusion ratio by bending balance.......... 238
Ono S. : Statistical thermodynamics of mnltimolecular adsorption.......... 232
Oura H. : On the rate of nucleation of ice.......... 277
  ——— and T. Tanaka : On the solar coronla lines at the total eclipse in 1943.......... 101
  ——— and T. Tanak, T. Murakami, T. Mitunobu : On the continuous spectrum of the solar corona at the total eclipse in 1943.......... 106
Oyama S. : On the vapour flow in the diffusion pump.......... 192
Ryu N.
  K. Shinohara and ——— : Polarization of elctrons.......... 119
  ——— : On the depolarization of elctrons by multiple scattering and reflection-transmission effect.......... 423
Saito N. : Concentration dependence of the viscosity of high polymer solution, I.......... 4
Saito S. : On the phenomena of burning of insulators caused by gliding spark discharge.......... 263
Sakai M. : Researches and developments on the spiral orbit spectrometer (I).......... 178
  ——— : Researches and developments on the spiral orbit spectrometer (II).......... 184
  ——— : On the perfect velocity forcusing mass spectrograph.......... 285
Sakurai A. : On the thickness of plane shock wave in a gas in turbulent motion.......... 114
Sakurai Tokio : Electromagnetic phenomena on ribbon elements gratings.......... 203
  ——— : Artificial matter for electromagnetic wave.......... 394
  ——— : The theory of metal plates dielectric.......... 389
Sakurai Tosio.
  Y. Kakiuchi, ——— and T. Suzuki : Auomalous sdecific heat and molecular rotation in normal solid alcohol.......... 369
Sasaki W. : Electrical properties of Cu_2 O.......... 455
Sato O.
  ——— and A. Amemiya : On the solution of differential equation of the two-dimensional steady flow of compressible fluid.......... 201
Sato T. : Effects of the transformation process on the thermoelctric power of the superlatice alloy Cu_3 Au.......... 268

Sato T.: On some properties of the Cu-Mn alloy system ... 287
Satoh T.: On the mathematical analysis of the problem of the conduction of heat when emissivity is variable ... 253
Sawada S.
  S. Nomura and ——: D.C. resistance of barium titanate and its solid solution ceramics ... 227
  —— and S. Nomura: Specific heat and thermal expansion of barium. strontium titanate ceramics ... 231
  S. Nomura and ——: On the anomalous dielectric properties of mixtures of lead titanate and strontium titanate ... 279
Shimauchi A.
  Kojima S. Okazaki T. and ——: Noise of cuprous oxide rectifier ... 452
Shigemitsu Y.: On experimental methods of the investigation of turbulent how, I ... 157
  ——: On experimental methods of the investigation of turbulent flow, II ... 297
  ——: On the velocity fluctuations in the laminar boundary layer, I ... 298
  ——: On the velocity fluctuations in the laminar boundary layer, II ... 304
Shimazu Z.
  I. Nonaka and ——: Long beaded counters for x-ray measurements ... 282
Shimbo S.
  K. Wada, —— and M. Oda: Dispersion of Ultrasonic velocity in the liquid fatty acids ... 345
Shimoda K.: A symmetrical six-arms wave-guide circuit for microwave bridge ... 255
Shinohara A.
  Kawamura H. and ——: On the resistance of interface of interface of oxide-coated cathode ... 90
Shinohara K.
  —— and N. Ryu: Polarization of electrons ... 119
Shirane G.
  —— S. Hoshino and K. Suzuki: Crystal structure of lead titanate and of lead-barium titanate ... 453
Sonoda M.
  ——: The efficiency of the G-M counter ... 58
  ——: The efficiency of Geiger-Müller counter for the high energy γ-rays II ... 403
  ——: The efficiency of Geiger-Müller counter for the high energy γ-rays III ... 408
Sueoka S.: On the Stark effect of helium in strong electrice field (I) ... 244
Suita T.
  S. Kondo and ——: Absorption spectra of colored potassium chloride containing several kinds of impurities ... 200
  S. Kondo and ——: Dielectric dispersion of alkali halide crysuals ... 375
Suwa S.
  K. Murakawa and ——: On some regularities in the isotope effect in the spectrum of lead ... 382

K. MURAKAWA and ——— : Revision of the hyperfine structure of the mercury spectrum 429

SUZUKI K.

G. SHIRANE, S. HOSHINO and ——— : Crystal Structure of lead titanate and of lead-barium titanate........ 453

SUZUKI T.

Y. KAKIUCHI, T. SAKURAI and ———: Anomalous specific heat and molecular rotation in normal solid alcohol........ 369

TAKAYAMA K.

S. KOJIMA and ——— : Probe measurements for high frquency discharge II 357

TAKESADA Y.: On the magnetostriction vibrator as a source of supersonics........ 197

TANABE S.

I. NONAKA and ———: Radioactivity of thoriated tungsten wire........ 398

TANAKA T.

——— and Z. KOANA: Solar limb effect of the spectral lines in a prominence observed at the total eclipse in 1941........ 95

——— and H. OURA: On the solar coronal lines at the total eclipse in 1933 101

——— H. OURA, T. MURAKAMI, and T. MITUNOBU: On the corona at the total eclipse in 1943........ 106

———: Supplementary report on the continuous spectrum of the solar corona.... 110

TA-YOU-WU: Further remarks on Araki'i theory of inverted alkali doublets........ 421

TOKITA N.

H. KAWAI and ———: The new dynamical method for measuring Young's modulus and internal friction of fibers and films 17

H. KAWAI and ———: On the Young's moduli and the internal friction of papers... 365

TOMURA M.: On the electric formation of the selenium rectifier 222

———: On the characteristics cf the selenium rectifies at low temperatures and the electric formation 349

TSUYA N.

H. WATANABE and ———: On the electrical conductivity of magnetite 281

UNO R.

——— and T. OKADA: On the thermal expansion of cuprous oxide........ 23

UYEDA R.

——— and T. ICHINOKAWA: On anomalous phase change of ammonium nitrate NH_4NO_3 456

——— and Y. KAINUMA: On the structure of absorbed organic long-chain molecules on the cleavage surface of molybdenite 199

WADA YASAKU:

——— S. SHIMBO and M. ODA: Dispersion of ultrasonic velocity in the liquid fatty acid........ 345

WADA YOSHIMATA: On the steady surface ripples of cylindrical flow........ 259

———: On the standing varicose and sinuos ripples of a cylindrical flow........ 431

WAKABAYASHI T.: Photoelastic method for determination of stress in powderde mass.. 383
WATANABE H.
——— and N. TUYA: On the elctrical conductivity of magnetite 281
WATANABE M.
——— and J. MIIDA: Ionization of the negative oxygenion by electron impact. III. 149

YAMAGUCHI J.
——— and S. KATAYAMA: On cadmium selenide of selenium rectifiers 385
——— and S. KATAYAMA: X-ray analysis on selenium layers of selenium rectifiers.. 386
YAMANOUCHI T.: Probabilities of excitation and de-excitations of metastable states of oxygen atom by collision of slow electron 154
YOKOTA R.: On the structure of Na_2O-SiO_2 Glasses 354
YOSHII G.: On fast neutron in cosmic rays 280

JOURNAL OF THE PHYSICAL SOCIETY OF JAPAN

Vol. 5, No. 6. 1950

Single Copy $1.00.

Yearly Rate $5.00.

(Postage Covered).

日本物理學會歐字報告

第5卷 第6號 (昭和25年11～12月號)

編集兼發行者	武藤俊之助 東京都世田谷區太子堂町四〇〇, WD18
印刷者	笠井重治 東京都中央區新富町3ノ17
印刷所	國際出版印刷社 東京都中央區新富町3ノ17
發行所	社團法人 日本物理學會 東京都文京區本富士町1 東京大學理學部內

昭和25年12月25日印刷・昭和25年12月30日發行

定價 1部 150圓

JOURNAL OF THE PHYSICAL SOCIETY OF JAPAN
Volume 5, Number 6, November～December 1950.

CONTENTS

Page
Tokio SAKURAI: The Theory of Metal Plates Dielectric 389
Tokio SAKURAI: Artifical Matter for Electromagnetic Wave 394
Itaru NONAKA and Shoji TANABE: Radioactivity of Theoriated Tungsten Wire ... 398
Masateru SONODA: The Efficiency of Geiger-Müller Counter for the High Energy γ-Rays II 403
Masateru SONODA: The Efficiency of Geiger-Müller Counter for the High Energy γ-Rays III 408
Ken-ichi KUZUKAWA: On the Spectrum of Turbulence 412
Mitsuo MIWA and Seizaburo KAGEYAMA: Natural β-Ray Spectrum of RaC 416
Ta-You-Wu: Further Remarks on Araki's Theory of Inverted Alkali Doublets ... 421
Norio RYU: On the Depolarization of Electrons by Multiple Scattering and Reflection-Transmission Effect 423
Kiyoshi MURAKAWA and Shigeki SUWA: Revision of the Hyperfine Structure of the Mercury Spectrum 429
Tosio KATO: On the Adiabatic Theorem of Quantum Mechanics 435
Yoshimasa WADA: On the Standing Varicose and Sinuous Ripples of a Cylindrical Flow 439
Tetsuya ARIZUMI: On the Electrical Conductivity of Alumina 442
Junkichi ITO and Tetsuo AKIOKA: Ferromagnetic Resonance Absorption by Mo-Permally 447

SHORT NOTES

Shoji KOZJMA, Susumu OKAZAKI and Akira SHIMAUCHI: Noise of Cuprous Oxide Rectifier 452
Gen SHIRAN , Sadao HOSHINO and Kazuo SUZUKI: Crystal Structure of Lead Titanate and of Lead-Barium Titanate 453
Wataru SAKAKI: Electrical Properties of Cu_2O 455
Ryuzo UEDA and Takeo ICHINOKAWA: On Anomalous Phase Change of Ammonium Nitrate NH_4NO_3 456
VOLUME CONTENTS .... i～xii